Lecture Notes in Electrical Engineering 498

Jiadong Sun · Changfeng Yang
Shuren Guo
Editors

China Satellite Navigation Conference (CSNC) 2018 Proceedings

Volume II

Springer

Lecture Notes in Electrical Engineering

Volume 498

**** Indexing: The books of this series are submitted to ISI Proceedings, EI-Compendex, SCOPUS, MetaPress, Springerlink ****

Lecture Notes in Electrical Engineering (LNEE) is a book series which reports the latest research and developments in Electrical Engineering, namely:

- Communication, Networks, and Information Theory
- Computer Engineering
- Signal, Image, Speech and Information Processing
- Circuits and Systems
- Bioengineering
- Engineering

The audience for the books in LNEE consists of advanced level students, researchers, and industry professionals working at the forefront of their fields. Much like Springer's other Lecture Notes series, LNEE will be distributed through Springer's print and electronic publishing channels.

For general information about this series, comments or suggestions, please use the contact address under "service for this series".

To submit a proposal or request further information, please contact the appropriate Springer Publishing Editors:

Asia:

China, *Jessie Guo, Assistant Editor* (jessie.guo@springer.com) (Engineering)

India, *Swati Meherishi, Senior Editor* (swati.meherishi@springer.com) (Engineering)

Japan, *Takeyuki Yonezawa, Editorial Director* (takeyuki.yonezawa@springer.com)
(Physical Sciences & Engineering)

South Korea, *Smith (Ahram) Chae, Associate Editor* (smith.chae@springer.com)
(Physical Sciences & Engineering)

Southeast Asia, *Ramesh Premnath, Editor* (ramesh.premnath@springer.com)
(Electrical Engineering)

South Asia, *Aninda Bose, Editor* (aninda.bose@springer.com) (Electrical Engineering)

Europe:

Leontina Di Cecco, Editor (Leontina.dicecco@springer.com)
(Applied Sciences and Engineering; Bio-Inspired Robotics, Medical Robotics, Bioengineering; Computational Methods & Models in Science, Medicine and Technology; Soft Computing; Philosophy of Modern Science and Technologies; Mechanical Engineering; Ocean and Naval Engineering; Water Management & Technology)

(christoph.baumann@springer.com)

(Heat and Mass Transfer, Signal Processing and Telecommunications, and Solid and Fluid Mechanics, and Engineering Materials)

North America:

Michael Luby, Editor (michael.luby@springer.com) (Mechanics; Materials)

More information about this series at http://www.springer.com/series/7818

Jiadong Sun · Changfeng Yang
Shuren Guo
Editors

China Satellite Navigation Conference (CSNC) 2018 Proceedings

Volume II

Springer

Editors
Jiadong Sun
China Aerospace Science
and Technology Corporation
Beijing
China

Shuren Guo
China Satellite Navigation
Engineering Center
Beijing
China

Changfeng Yang
China Satellite Navigation
Engineering Center
Beijing
China

ISSN 1876-1100 ISSN 1876-1119 (electronic)
Lecture Notes in Electrical Engineering
ISBN 978-981-13-0013-4 ISBN 978-981-13-0014-1 (eBook)
https://doi.org/10.1007/978-981-13-0014-1

Library of Congress Control Number: 2018938375

Printed on acid-free paper

This Springer imprint is published by the registered company Springer Nature Singapore Pte Ltd.
part of Springer Nature
The registered company address is: 152 Beach Road, #21-01/04 Gateway East, Singapore 189721, Singapore

Editorial Board

Vice-Chairman

Yanhong Kou, Beihang University, Beijing, China
Zheng Yao, Tsinghua University, Beijing, China

Topic: S4: Satellite Orbit and Satellite Clock Error

Chairman

Xiaogong Hu, Shanghai Astronomical Observatory, Chinese Academy of Sciences, Shanghai, China

Vice-Chairman

Rongzhi Zhang, Xi'an Satellite Control Center, Shaanxi, China
Geshi Tang, Beijing Aerospace Control Center, Beijing, China
Maorong Ge, Geo Forschungs Zentrum (GFZ), Potsdam, Germany

Topic: S5: Precise Positioning Technology

Chairman

Qile Zhao, Wuhan University, Hubei, China

Vice-Chairman

Jianwen Li, The PLA Information Engineering University, Henan, China
Shuli Song, Shanghai Astronomical Observatory, Chinese Academy of Sciences, Shanghai, China
Yanming Feng, Queensland University of Technology, Brisbane, Australia

Topic: S6: Time–Space Datum and Temporal Frequency Technologies

Chairman

Lianshan Gao, The 203th Research Institute of China Aerospace Science & Industry Corporation, Beijing, China

Vice-Chairman

Chunhao Han, Beijing Satellite Navigation Center, Beijing, China
Xiaohui Li, National Time Service Center, Chinese Academy of Sciences, Shaanxi, China
Nikolay Demidov, Vremya CH Corporation, Novgorod, Russia

Topic: S7: Satellite Navigation Augmentation Technology

Chairman

Junlin Zhang, OLinkStar Co., Ltd., Beijing, China

Vice-Chairman

Jinping Chen, Beijing Satellite Navigation Center, Beijing, China
Rui Li, Beihang University, Beijing, China
Shaojun Feng, Imperial College London Qianxun Positioning Network, Co., Ltd., Shanghai, China
Dun Wang, Space Star Aerospace Technology Applications Co., Ltd., Heilongjiang, China

Topic: S8: Test and Assessment Technology

Chairman

Xiaolin Jia, Xi'an Institute of Surveying and Mapping, Shaanxi, China

Vice-Chairman

Jun Yang, National University of Defense Technology, Hunan, China
Jianguang Qu, Heilongjiang Institute of Technology, Heilongjiang, China
Yang Gao, University of Calgary, Alberta, Canada

Topic: S9: User Terminal Technology

Chairman

Haibo He, Beijing Satellite Navigation Center, Beijing, China

Vice-Chairman

Baowang Lian, Northwestern Polytechnic University, Shaanxi, China
Hong Li, Tsinghua University, Beijing, China

Topic: S10: Multi-Source Fusion Navigation Technology

Chairman

Zhongliang Deng, Beijing University of Posts and Telecommunications, Beijing, China

Vice-Chairman

Hong Yuan, Academy of Opto-Electronics, Chinese Academy of Sciences, Beijing, China
Yongbin Zhou, National University of Defense Technology
Jinling Wang, University of New South Wales, Australia

Topic: S11: PNT New Concept, New Methods and New Technology

Chairman

Mingquan Lu, Tsinghua University, Beijing, China

Vice-Chairman

Wei Wang, The 20th Research Institute of China Electronics Technology Group Corporation, Shaanxi, China
Ying Xu, Academy of Opto-Electronics, Chinese Academy of Sciences, Beijing, China
Sang Jeong Lee, Chungnam National University, Daejeon, South Korea

Topic: S12: Policies and Regulations, Standards and Intellectual Properties

Chairman

Junlin Yang, Beihang University, Beijing, China

Vice-Chairman

Daiping Zhang, China Defense Science and Technology Information Center, Beijing, China
Yonggang Wei, China Academy of Aerospace Standardization and Product Assurance, Beijing, China
Huiying Li, Electronic Intellectual Property Center, Ministry of Industry and Information Technology, PRC Beijing, China

Preface

BeiDou Navigation Satellite System (BDS) is China's global navigation satellite system which has been developed independently. BDS is similar in principle to global positioning system (GPS) and compatible with other global satellite navigation systems (GNSSs) worldwide. BDS will provide highly reliable and precise positioning, navigation and timing (PNT) services and short-message communication for all users under all-weather, all-time and worldwide conditions.

China Satellite Navigation Conference (CSNC) is an open platform for academic exchanges in the field of satellite navigation. It aims to encourage technological innovation, accelerate GNSS engineering, and boost the development of the satellite navigation industry in China and in the world.

The 9th China Satellite Navigation Conference (CSNC 2018) is held during May 23–25, 2018, Harbin, China. The theme of CSNC2018 is Location, Time of Augmentation, including technical seminars, academic exchanges, forums, exhibitions, and lectures. The main topics are as followed:

Conference Topics

S1 Satellite Navigation Technology
S2 Navigation and Location Service
S3 Satellite Navigation Signal and Anti-Jamming Technologies
S4 Satellite Orbit and Satellite Clock Error
S5 Precise Positioning Technology
S6 Time–Space Datum and Temporal Frequency Technologies
S7 Satellite Navigation Augmentation Technology
S8 Test and Assessment Technology
S9 User Terminal Technology
S10 Multi-Source Fusion Navigation Technology
S11 PNT New Concept, New Methods and New Technology
S12 Policies and Regulations, Standards and Intellectual Properties

The proceedings have 208 papers in twelve topics of the conference, which were selected through a strict peer-review process from 588 papers presented at CSNC2018. In addition, another 274 papers were selected as the electronic proceedings of CSNC2018, which are also indexed by "China Proceedings of Conferences Full-text Database (CPCD)" of CNKI and Wan Fang Data.

We thank the contribution of each author and extend our gratitude to 279 referees and 55 session chairmen who are listed as members of editorial board. The assistance of CNSC2018's organizing committees and the Springer editorial office is highly appreciated.

Beijing, China

Jiadong Sun
Changfeng Yang
Shuren Guo

Scientific Committee

Chairman

Jiadong Sun, China Aerospace Science and Technology Corporation, Beijing, China

Vice-Chairman

Rongjun Shen, China Satellite Navigation System Committee, Beijing, China
Jisheng Li, China Satellite Navigation System Committee, Beijing, China
Qisheng Sui, China Satellite Navigation System Committee, Beijing, China
Changfeng Yang, China Satellite Navigation System Committee, Beijing, China
Zuhong Li, China Academy of Space Technology, Beijing, China
Shusen Tan, Beijing Satellite Navigation Center, Beijing, China

Executive Chairman

Jingnan Liu, Wuhan University, Hubei, China
Yuanxi Yang, China National Administration of GNSS and Applications, Beijing, China
Shiwei Fan, China Satellite Navigation Engineering Center, Beijing, China
Jun Xie, China Academy of Space Technology, Beijing, China

Committee Members: (By Surnames Stroke Order)

Xiancheng Ding, China Electronics Technology Group Corporation, Beijing, China
Qingjun Bu, China National Administration of GNSS and Applications, Beijing, China
Weixing Wan, Institute of Geology and Geophysics, Chinese Academy of Sciences, Beijing, China
Liheng Wang, China Aerospace Science and Technology Corporation, Beijing, China
Yuzhu Wang, Shanghai Institute of Optics and Fine Mechanics, Chinese Academy of Sciences, Shanghai, China

Guoxiang Ai, National Astronomical Observatories, Chinese Academy of Sciences, Beijing, China
Shuhua Ye, Shanghai Astronomical Observatories, Chinese Academy of Sciences, Shanghai, China
Daren Lv, The Institute of Atmospheric Physics, Chinese Academy of Sciences, Beijing, China
Yongcai Liu, China Aerospace Science & Industry Corporation, Beijing, China
Zhaowen Zhuang, National University of Defense Technology, Hunan, China
Qifeng Xu, PLA Information Engineering University, Henan, China
Houze Xu, Institute of Geodesy and Geophysics, Chinese Academy of Sciences, Hubei, China
Tianchu Li, National Institute of Metrology, Beijing, China
Jiancheng Li, Wuhan University, Hubei, China
Guirong Min, China Academy of Space Technology, Beijing, China
Xixiang Zhang, The 29th Research Institute of China Electronics Technology Group Corporation, Sichuan, China
Lvqian Zhang, China Aerospace Science and Technology Corporation, Beijing, China
Junyong Chen, National Administration of Surveying, Mapping and Geo-information, Beijing, China
Benyao Fan, China Academy of Space Technology, Beijing, China
Dongjin Luo, China People's Liberation Army, Beijing, China
Guohong Xia, China Aerospace Science & Industry Corporation, Beijing, China
Shuren Guo, China Satellite Navigation Engineering Center, Beijing, China
Peikang Huang, China Aerospace Science & Industry Corporation, Beijing, China
Chong Cao, China Research Institute of Radio Wave Propagation (CETC 22), Beijing, China
Faren Qi, China Academy of Space Technology, Beijing, China
Rongsheng Su, China People's Liberation Army, Beijing, China
Ziqing Wei, Xi'an Institute of Surveying and Mapping, Shaanxi, China

Executive Members: (By Surnames Stroke Order)

Qin Zhang, Chang'an University, Shaanxi, China
Yamin Dang, Chinese Academy of Surveying & Mapping, Beijing, China
Xiaochun Lu, National Time Service Center, Chinese Academy of Sciences, Shaanxi, China
Xiaogong Hu, Shanghai Astronomical Observatory, Chinese Academy of Sciences, Shanghai, China
Qile Zhao, Wuhan University, Hubei, China
Lianshan Gao, The 203th Research Institute of China Aerospace Science & Industry Corporation, Beijing, China
Junlin Zhang, OLinkStar Co., Ltd., Beijing, China

Xiaolin Jia, Xi'an Institute of Surveying and Mapping, Shaanxi, China
Haibo He, Beijing Satellite Navigation Center, Beijing, China
Zhongliang Deng, Beijing University of Posts and Telecommunications, Beijing, China
Mingquan Lu, Tsinghua University, Beijing, China
Junlin Yang, Beihang University, Beijing, China

Organizing Committee

Secretary-General

Haitao Wu, Satellite Navigation Headquarters, Chinese Academy of Sciences, Beijing, China

Executive Deputy Secretary-General

Weina Hao, Navigation Headquarters, Chinese Academy of Sciences, Beijing, China

Deputy Secretary-General

Wenhai Jiao, China Satellite Navigation Engineering Center, Beijing, China
Wenjun Zhao, Beijing Satellite Navigation Center, Beijing, China
Tonghuang Wang, Space Star Aerospace Technology Applications Co., Ltd., Heilongjiang, China
Bo Wang, Academic Exchange Center, China Satellite Navigation Office, Beijing, China

Committee Members: (By Surnames Stroke Order)

Qun Ding, The 20th Research Institute of China Electronics Technology Group Corporation, Shaanxi, China
Guang Yu, Harbin Institute of Technology, Heilongjiang, China
Li Wang, International Cooperation Research Center, China Satellite Navigation Office, Beijing, China
Chunsheng Wang, Haidian Investment Promotion Bureau, Beijing, China
Ying Liu, China Satellite Navigation Engineering Center, Beijing, China
Wanming Yang, Administrative Committee of Nanjing New & High Technology Industry Development Zone, Jiangsu, China
Jun Shen, Beijing UniStrong Science & Technology Co., Ltd., Beijing, China
Liquan Song, Heilongjiang Institute of Technology, Heilongjiang, China
Mingquan Lu, Tsinghua University, Beijing, China

Lu Chen, Beijing Institute of Space Science and Technology Information, Beijing, China
Xiuwan Chen, Peking University, Beijing, China
Gang Hu, Beijing Unicore Communications, Inc., Beijing, China
Qile Zhao, Wuhan University, Hubei, China
Min Shui, The National Remote Sensing Center of China, Beijing, China

Contents

Part I
Satellite Navigation Signal and Anti-jamming Technologies

A New Technique for Improving the Anti-jamming Performance of Vector Tracking Loop

Ruihua Zhang, Renbiao Wu and Qiongqiong Jia

Abstract The GNSS is vulnerable so that it often faces the risk of jamming, and blanket jamming is one of the interference. Power inversion algorithm is a commonly method used to solve this problem, however, the receiver will lose lock when GNSS satellites are close to RFI sources. To improve the receiver's anti-jamming performance in this harsh scene, a method of vector tracking loop (VTL) based on despread-respread (DR) algorithm is present. Firstly, this paper suppress oppressive interference. Secondly, local reference signal is reconstructed according to predicted tracking loop parameters. Thirdly, beamforming algorithm is present. Theoretical analysis and simulation experiments verify that the VTL based on DR algorithm can reduce phase discriminator output errors, improve receiver's positioning performance, and has superior anti-jamming performance in harsh scene. The method proposed in this paper can be applied to arbitrary array without prior information of satellites' directions and is not sensitive to the error of array. Copared to VTL based on EIG, VTL based on DR algorithm has lower complexity.

Keywords Vector tracking loop · Anti-jamming · Despread-respread algorithm Beamforming algorithm

1 Introduction

Satellite navigation is widely used in civil and military fields. The Global Navigation Satellite Systems (GNSS) signals are vulnerable to interference, because their powers are weak on the earth's surface. For example, the signal powers of L1 frequency signals are −160 dBw. Therefore, satellite navigation receivers are vulnerable to various interference, and blanket jamming is a kind of the common

R. Zhang (✉) · R. Wu · Q. Jia
Tianjin Key Lab for Advanced Signal Processing, Civil Aviation University of China, Tianjin, China
e-mail: htuzrh1993@163.com

J. Sun et al. (eds.), *China Satellite Navigation Conference (CSNC) 2018 Proceedings*, Lecture Notes in Electrical Engineering 498,
https://doi.org/10.1007/978-981-13-0014-1_1

jamming. It's an important guarantee for the successful application of satellite navigation to take research on anti-jamming technology effectively [1].

Vector tracking loop (VTL) algorithm, as a new tracking technology of GNSS in recent years, combines the navigation filter with tracking loop in the Kalman filter and has advantage of tracking attenuated signal in the scene of signal interruption. Therefore, VTL has a certain of anti-jamming ability compared with the traditional scalar receiver. Up to now, the anti-jamming technology of vector receiver is concerned and studied by many scholars of the world [2]. However, VTL will lose efficacy when the vector receiver is in the attenuation environment for a long time. Therefore, the combination of array signal processing technique and VTL can improve the anti-jamming performance of vector tracking loop. At present, the research of anti-jamming based on VTL is divided into interference detection technique and interference suppression technique [3]. Harbin Engineering University used predicted signal from vector tracking loop as reference signal in cross-SCORE algorithm to suppress interference. Xu Mingshan et al. combined blind beamforming algorithm with VTL to improve robustness of VTL [4, 5]. DLR firstly proposed VTL Based on EIG, but this method needs more correlators and has more complexity [6–10].

In order to improve the anti-jamming performance of VTL in harsh scene. On the basis of the existing VTL based on EIG, this paper combines despread-respread (DR) algorithm [11] with VTL to propose a kind of VTL based on DR. Firstly, the power inversion algorithm is used to suppress oppressive jamming. Secondly, the local reference signal is reconstructed. Finally, beamforming algorithm based on DR is present. This method has lower complexity and is not sensitive to the array error. It can suppress oppressive jamming and provide gain to satellite signals without knowing the direction of jamming and satellite signals. The contents of this paper are as follows: the second section introduces the data model, the third section introduces the VTL based on DR scheme, the fourth section gives the simulation results and analysis, and the fifth section is a summary of this paper.

2 Data Model

Jamming signals are usually considered as zero-mean additive white Gaussian noises (AWGN) with high power. G satellite signals and Q jamming signals are incident on an uniform linear array. The satellite signals' arrival angles are respectively $\theta_g (g = 1, 2 \ldots, G)$, and jamming signals' arrival angles are respectively $\theta_q (q = 1, 2 \ldots, Q)$. The received signals can be written as:

$$\begin{aligned} \mathbf{x}(t) &= \mathbf{x}_s(t) + \mathbf{x}_j(t) + \mathbf{e}(t) \\ &= \sum_{g=1}^{G} \mathbf{a}(\theta_g) s_g(t) + \sum_{q=1}^{Q} \mathbf{a}(\theta_q) j_q(t) + \mathbf{e}(t) \end{aligned} \tag{1}$$

Where $\mathbf{x}(t) = [x_1(t), x_2(t), \ldots, x_M(t)]^{\mathrm{T}}$ represents $M \times 1$ dimensional array data vector, $\mathbf{e}(t)$ is noise vector assumed to obey zero-mean gauss distribution, $s_g(t)$ is complex envelope of gth satellite signals, $j_q(t)$ is jamming signals, $\mathbf{a}(\theta_q)$ is steering vector of qth jamming signal, $\mathbf{a}(\theta_g)$ is steering vector of gth satellite signal. And the $\mathbf{a}(\theta_g)$ can be expressed as:

$$\mathbf{a}(\theta_g) = \left[1, e^{\frac{-j2\pi d \sin\theta_g}{\lambda}}, \ldots, e^{\frac{-j2\pi(M-1)d \sin\theta_g}{\lambda}}\right]^{\mathrm{T}} \tag{2}$$

where d means spacing of array element, λ means wavelength of incident signals. GPS signal can be expressed as:

$$s_g(t) = \sqrt{2A_g} D_g(t - \tau_g) C_g(t - \tau_g) \exp\left[j(2\pi f_0 t + \varphi_g)\right] \tag{3}$$

where A_g means the power of gth satellite navigation signal. $D_g(t)$ means the navigation message. $C_g(t)$ means the C/A code. τ_g means the code phase. f_0 means carrier frequency. φ_g means initial carrier phase. Therefore, the received signals can be expressed as as:

$$\begin{aligned}\mathbf{x}(t) = &\sum_{g=1}^{G} \sqrt{2A_g} D_g(t - \tau_g) C_g(t - \tau_g) \exp\left[j(2\pi f_0 t + \varphi_g)\right] \mathbf{a}(\theta_g) \\ &+ \sum_{q=1}^{Q} j_q(t) \mathbf{a}(\theta_q) + \mathbf{e}(t)\end{aligned} \tag{4}$$

Existing studies show that Power Invert (PI) algorithm can effectively suppress oppressive jamming signals when satellite signals direction θ_g is far from interference's direction θ_q. However, the satellite signals' direction and jamming signals' direction are gradually changing in the actual scene. In the case of satellite signals are near to RFI sources, PI algorithm will lose efficacy and this will make receiver lose lock. Because VTL can track attenuated signals, this paper combines DR algorithm with VTL to design beamforming algorithm, which can further give gain for satellite signals. This method can achieve the purpose of enhancing satellite signals while suppressing jamming signals, and it improves the anti-jamming performance of vector receiver in the harsh scene.

3 Proposed Method

We embed DR algorithm into VTL in this section and take the gth satellite signal as an example to introduce principle of the proposed method. The principle block diagram is shown in Fig. 1: Firstly, PI algorithm is used to suppress jamming signal. Secondly, the reference signal is reconstructed. Tirdly, beamforming algorithm is taken through coherent integration results between reference signal and

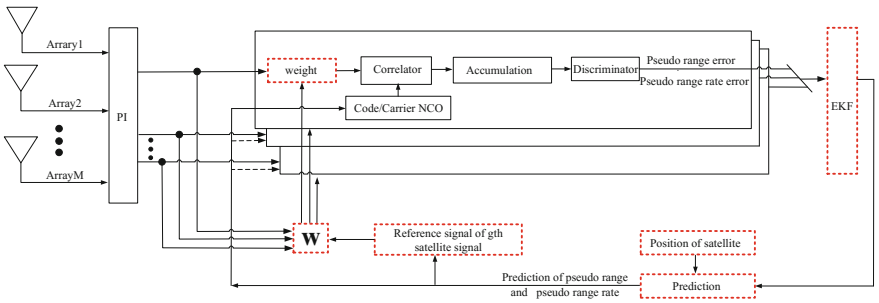

Fig. 1 Scheme diagram of VTL based on DR

data without blanket jamming. Lastly, the received data is weighted to complete the whole tracking process. Interference suppression algorithm and weight vector calculation are introduced in this section.

3.1 Suppression of Jamming

PI algorithm is usually used to suppress oppressive jamming and noise in satellite navigation system because of its simple principle. Inputs of the method is $\mathbf{x}(t)$, and the covariance matrix can be expressed as:

$$\mathbf{R}_x = E\{\mathbf{x}(t)\mathbf{x}^{\mathrm{H}}(t)\} = \mathbf{R}_{\mathrm{s}} + \mathbf{R}_j + \mathbf{R}_n \tag{5}$$

Where $E\{.\}$ means solving of mathematical expectation; $\{.\}^{\mathrm{H}}$ means conjugate transpose operation. As GPS signal is very weak, which is generally submerged in noise, the signal-to-noise ratio is about −20 dB. And the formula (5) can be approximately expressed as:

$$\mathbf{R}_x \approx \mathbf{R}_j + \mathbf{R}_n = \sigma_j^2 \mathbf{a}(\theta_j)\mathbf{a}^{\mathrm{H}}(\theta_j) + \sigma_n^2 \mathbf{I} \tag{6}$$

According to the inverse matrix theorem:

$$\mathbf{R}_x^{-1} = \frac{1}{\sigma_n^2}\left(\mathbf{I} - \mathbf{a}(\theta_j)\left(\frac{\sigma_n^2}{\sigma_j^2} + \mathbf{a}^{\mathrm{H}}(\theta_j)\mathbf{a}(\theta_j)\right)^{-1}\mathbf{a}^{\mathrm{H}}(\theta_j)\right) \tag{7}$$

Because the interference powers are far higher than the noise powers, $\mathbf{R}_x^{-1}$ can be expressed as:

$$\mathbf{R}_x^{-1} = \frac{1}{\sigma_n^2}\left(\mathbf{I} - \mathbf{a}(\theta_j)\left(\mathbf{a}^{\mathrm{H}}(\theta_j)\mathbf{a}(\theta_j)\right)^{-1}\mathbf{a}^{\mathrm{H}}(\theta_j)\right) \tag{8}$$

where $\mathbf{I}-\mathbf{a}(\theta_j)\left(\mathbf{a}^{\mathrm{H}}(\theta_j)\mathbf{a}(\theta_j)\right)^{-1}\mathbf{a}^{\mathrm{H}}(\theta_j)$ means orthogonal projection matrix of oppressive jamming.

In the practice, we usually use the sample covariance matrix instead of the theoretical covariance matrix

$$\hat{\mathbf{R}}_x=\frac{1}{K}\sum_{k=1}^{K}\mathbf{x}(k)\,\mathbf{x}^{\mathrm{H}}(k) \tag{9}$$

where K means the number of the sampling points. Therefore, the outputs of the power inversion algorithm can be obtained through the orthogonal projection to the received signal.

$$\mathbf{y}(t)=\hat{\mathbf{R}}_x^{-1}\mathbf{x}(t) \tag{10}$$

Therefore, we get the data after suppressing strong interference.

3.2 Calculation of Weight Vector

Traditional PI algorithm can only suppress interference, but can not give gain to the satellite signals. In addition, when the satellite signals are close to interference, the algorithm will fail. This section uses the prediction function of VTL and array processing technology to solve this problem. We combine the VTL and $\mathbf{y}(t)$ after suppressing interference to take beamforming algorithm, which can provide high gain to satellite signals and make up for the shortcomings of traditional PI algorithm. The calculation of weight vector mainly includes the following three steps: prediction of parameters, construction of reference signal and development of beamforming algorithm.

The prediction of receiver parameters mainly includes prediction of state vector and tracking loop parameters. The state vector can be defined as $\boldsymbol{x}=[x,y,z,ct_b,v_x,v_{y,},v_{z,},ct_d]^{\mathrm{T}}$ according to receiver's three dimensional coordinate $\boldsymbol{p}=[x\,y\,z]^{\mathrm{T}}$, three dimensional velocity $\boldsymbol{v}=\left[v_x\,v_y\,v_z\right]^{\mathrm{T}}$, clock error ct_b and clock drift ct_d. It is assumed that the receiver moves uniformly when time interval $t_{k,k+1}$ is short enough. Therefore, we can predict $\hat{\boldsymbol{x}}_{k+1}$ according to $\boldsymbol{x}_k$. The prediction process is as follows:

$$\begin{aligned}\hat{\boldsymbol{p}}_{k+1}&=\boldsymbol{p}_k+t_{k,k+1}\boldsymbol{v}_k\\ \hat{\boldsymbol{v}}_{k+1}&=\boldsymbol{v}_k\end{aligned} \tag{11}$$

The prediction of clock error and clock bias in $k+1$ is given by:

$$\begin{aligned}\hat{t}_{b,k+1}&=t_{b,k}+t_{k,k+1}t_{d,k}\\ \hat{t}_{d,k+1}&=t_{d,k}\end{aligned} \tag{12}$$

Through formula (11)–(12), the prediction of receiver's state vector in $k+1$ can be expressed as:

$$\hat{\boldsymbol{x}}_{k+1} = [\hat{x}_{k+1}, \hat{y}_{k+1}, \hat{z}_{k+1}, c\hat{t}_{b,k+1}, \hat{v}_{x,k+1}, \hat{v}_{y,k+1}, \hat{v}_{z,k+1}, c\hat{t}_{d,k+1}]^{\mathrm{T}} \tag{13}$$

Pseudo range $\hat{\rho}_{g,k+1}$ and pseudo range rate $\hat{\dot{\rho}}_{g,k+1}$ of gth satellite signal can be expressed as:

$$\begin{cases} \hat{\rho}_{g,k+1} = \hat{r}_{g,k+1} + c\hat{t}_{b,k+1} \\ \hat{\dot{\rho}}_{g,k+1} = \hat{\dot{r}}_{g,k+1} + c\hat{t}_{d,k+1} \end{cases} \tag{14}$$

Where $\hat{r}_{g,k+1} = \sqrt{\left(x_{g,k+1} - \hat{x}_{k+1}\right)^2 + \left(y_{g,k+1} - \hat{y}_{k+1}\right)^2 + \left(z_{g,k+1} - \hat{z}_{k+1}\right)^2}$ means geometric distance between the gth satellite and receiver in $k+1$. According to the formula (14), the doppler shift of satellite can be obtained as:

$$\hat{f}_{d,k+1} = -\frac{\hat{\dot{\rho}}_{g,k+1}}{\lambda} = -\hat{\dot{\rho}}_{g,k+1}\frac{f}{c} \tag{15}$$

The code frequency and carrier frequency in $k+1$ can be expressed as:

$$\hat{f}_{code,k+1} = f_{code} + \hat{f}_{d,k+1} = f_{code} - \hat{\dot{\rho}}_{g,k+1}\frac{f_{code}}{c} \tag{16}$$

$$\hat{f}_{0,k+1} = f_0 + \hat{f}_{d,k+1} = f_0 - \hat{\dot{\rho}}_{g,k+1}\frac{f_0}{c} \tag{17}$$

where f_{code} means C/A code frequency, and code phase in $k+1$ can be expressed as follows:

$$\hat{\tau}_{k+1} = \tau_k + \left(\hat{\rho}_{g,k+1} - \rho_{g,k}\right)\frac{f_{code}}{c} \tag{18}$$

According to code frequency $\hat{f}_{code,k+1}$, carrier frequency $\hat{f}_{0,k+1}$, code phase $\hat{\tau}_{k+1}$, and carrier phase $\hat{\varphi}_{k+1}$, the reference signal can be obtained as [1]:

$$\hat{s}_g(t) = D_g(t - \hat{\tau}_{k+1})C_g(t - \hat{\tau}_{k+1})\exp\left[j\left(2\pi\hat{f}_{0,k+1}t + \hat{\varphi}_{k+1}\right)\right] \tag{19}$$

Then prompt coherent integration results of $\mathbf{y}(t)$ and $\hat{s}_g(t)$ are obtained as:

$$\mathbf{P}_g(n) = \sqrt{2A_g}D_g R(\Delta\tau_{k+1})\sin c(\Delta f_{0,k+1}T_{coh})\exp\left(j\Delta\varphi_{k+1}\right)\mathbf{a}\left(\theta_g\right) \tag{20}$$

Where $R(\Delta\tau_{k+1})$ represents the autocorrelation function of the C/A code, $\Delta\tau_{k+1}$ is the time difference between the prompt local code and the received signal, $\Delta f_{0,k+1}$ is frequency tracking errors, T_{coh} is coherent time, $\Delta\varphi_{k+1}$ is carrier phase

tracking errors, **e** is AWGN. The coherent integration results for single antenna is defined as $P_g(n)$ and formula (20) can be expressed as:

$$\mathbf{P}_g(n) = P_g(n)\mathbf{a}\left(\theta_g\right) \tag{21}$$

The estimation of covariance matrix by $\mathbf{P}_g(n)$ in N ms can be expressed as follows:

$$\hat{\mathbf{R}}_p = \sum_{n=1}^{N} \mathbf{P}_g(n)\mathbf{P}_g(n)^{\mathrm{H}} \tag{22}$$

We get normalized weight vector $\mathbf{w}_l$ through eigenvector corresponding to the largest eigenvalue, which can enhance satellite signal.

$$\mathbf{w}_l = \hat{\mathbf{a}}\left(\theta_g\right) \tag{23}$$

The method proposed in this paper is a two-stage anti-jamming processor. In the first stage, the PI algorithm is used to suppress the interference. In the second stage processor, $\hat{\mathbf{a}}\left(\theta_g\right)$ is obtained through beamforming algorithm. Therefore, the weighted vector of the proposed method can be expressed as [1]:

$$\mathbf{w}_{lopt} = \mathbf{R}_x^{-1}\hat{\mathbf{a}}(\theta_g) \tag{24}$$

3.3 Comparison of Algorithm

On the basis of the existing VTL based on EIG, this paper combines despread-respread algorithm with VTL to propose a kind of VTL based on DR. This method proposed in this paper get weight through coherent integration results between local reference signal and data without blanket jamming. The VTL based on EIG get weight through coherent integration results of array received data without blanket jamming, and it needs more correlators.

Next, we analyze and compare complexity of the proposed method and the existing VTL based on EIG. The number of correlators required in each tracking channel is used as index to measure complexity when the number of array elements is M and the number of satellites is G. Table 1 is result of analysis.

As shown in Table 1, each tracking channel of VTL based on EIG needs $3 \times M \times G$ correlators according to the document [10], because this tracking system

Table 1 Comparison of complexity

Name of method	Number of correlators
VTL based on EIG	$3 \times M \times G$
VTL based on DR	$3 \times G$

requires early, prompt and late correlator outputs which are obtained through array received signal $\mathbf{y}(t)$ to get eigenbeamforming algorithm, and this tracking system has larger complexity. The method proposed in this paper get beamforming algorithm through coherent integration results of $\hat{s}_g(t)$ and $\mathbf{y}(t)$. this tracking system needs $3 \times G$ correlators and has lower complexity.

4 Simulation Analysis

This section verifies the effectiveness of the proposed method through simulation experiments in the scene of oppressive jamming. The anti-jamming performance of traditional VTL, VTL based on EIG and VTL based on DR is compared and analysed. In these simulation experiments, the number of linear array is 7, and 5 satellite signals with arrival direction of $50°, 35°, 10°, -10°, -35°$ are generated through GPS signal simulator. SNR is 20 dB, and JNR of interference is 30 dB.

4.1 Performance Analysis of Interference from Far Range

The oppressive jamming with arrival angle of $-75°$ appears persistly from 25 s. Figure 2 is result of the PRN3 satellite signal's C/No ratio processed by three tracking loops at different time. Figure 3 is phase detector output comparison result of three tracking loops. Table 2 is the statistical result of position errors through 10,000 Monte-Carlo RMS experiments.

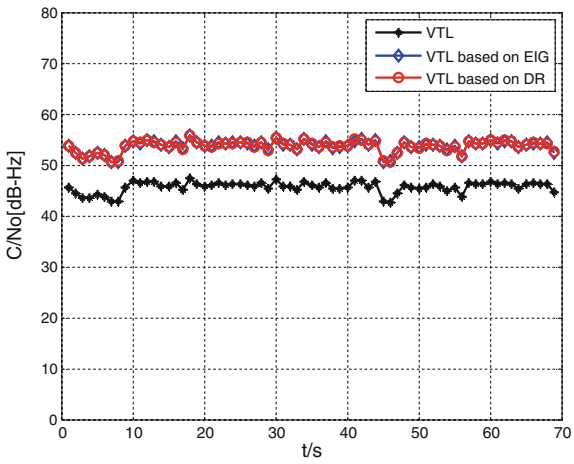

Fig. 2 C/No comparison for three kinds of VTL

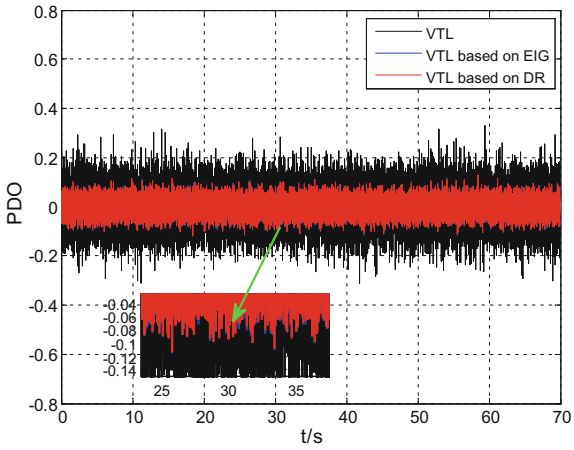

Fig. 3 Phase discriminator outputs for three kinds of VTL

Table 2 Position errors

Name of method	Position errors (m)
VTL	3.00
VTL based on EIG	2.64
VTL based on DR	2.64

As shown in Fig. 2, compared with the traditional VTL, the VTL based on DR and VTL based on EIG can improve carrier-to-noise ratio of satellite signals from 46 to 52 dB in this simulation condition. Since the two methods can provide gain to satellite signals by beamforming algorithm, the C/No ratio of the tracking loop is improved greatly.

As shown in Fig. 3, compared with the traditional VTL, the VTL based on DR and VTL based on EIG both can reduce the phase discriminator output (PDO) errors.

It can be seen from Table 2 that the VTL based on DR and VTL based on EIG can improve the positioning performance compared with the traditional VTL.

4.2 Performance Analysis of Interference from Near Range

The blanket jamming with arrival angle of $9°, 33°$ appears persistly from 25 s. Figure 4 is result of the PRN14 satellite signal's C/No ratio processed by three tracking loops at different time. Figure 5 is position error of three tracking loops.

As shown in Fig. 4, the VTL based on DR and VTL based on EIG can improve the C/No ratio of PRN 14 from 20 to 38 dB. This method proposed in this paper

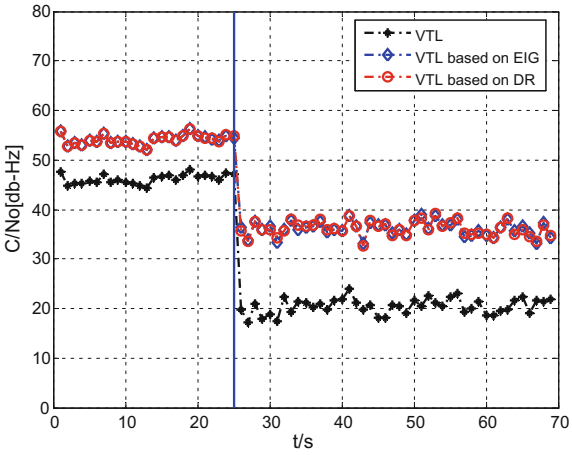

Fig. 4 C/No comparison for three kinds of VTL

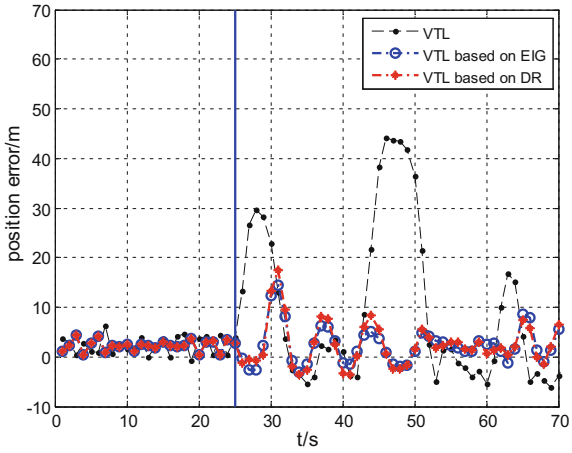

Fig. 5 Position errors for three kinds of VTL

can provide gain for the weakened satellite signal, which is guaranteed for satellite signal to be continuously tracked.

As shown in Fig. 5, the traditional VTL loses lock and the position error increases suddenly, because PRN3 and PRN14 is watered down at 25 s. The VTL based on DR and VTL based on EIG can provide gain to weakened satellite signals, which ensure that VTL can work within normal level after 25 s. Hence, the VTL based on DR has better anti-jamming ability in complex electromagnetic environment.

5 Conclusions

This paper combines DR algorithm with VTL to improve VTL's anti-jamming performance in complex electromagnetic environment. Theoretical analysis and simulations verify that the VTL based on DR algorithm has better robustness while reducing complexity. It can reduce discriminator output errors, improve the positioning performance, and has superior anti-jamming performance in complex electromagnetic environment.

Acknowledgements The work of this paper is supported by the The National Key Research and Development Program of China (Grant No. 2016YFB0502402).

References

1. WU R, WANG W, LU D et al (2015) Adaptive interference mitigation in GNSS. Science Press, Beijing, pp 1–30
2. Li F, Wu R, Wang W (2016) The anti-jamming performance analysis for vector tracking loop. In: China Satellite Navigation Conference (CSNC) 2016 Proceedings: vol 1, pp 665–675. https://doi.org/10.1007/978-981-10-0934-1_57
3. Jafarnia-Jahromi A, Lin T, Broumandan A et al (2012) Detection and mitigation of spoofing attacks on a vector-based tracking GPS receiver. Proceed ION ITM 2012:790–800
4. Li Q, Xu D, Wang W et al (2014) Anti-jamming scheme for GPS receiver with vector tracking loop and blind beamformer. Electron Lett 50(19):1386–1388. https://doi.org/10.1049/el.2014.2274
5. Xu M, Lv Y, Wang X et al (2016) Simulation research on optimal control of satellite navigation mitigation. Computer Simulation 33(3):52–55
6. Cuntz M, Konovaltsev A, Sgammini M et al (2011) Field test: jamming the DLR adaptive antenna receiver. In: Proceedings of the 24th International Technical Meeting of The Satellite Division of the Institute of Navigation (ION GNSS 2011), Portland, OR, pp 384–392
7. Cuntz M, Konovaltsev A, Hättich C et al (2012) Vector tracking with a multi antenna GNSS receiver. In: Proceedings of the 25th International Technical Meeting of The Satellite Division of the Institute of Navigation (ION GNSS 2012), Nashville, TN, pp 2050–2056
8. Sgammini M, Antreich F, Kurz L et al (2012) Blind adaptive beamformer based on orthogonal projections for GNSS. Proceedings of International Technical Meeting of the Satellite Division of the Institute of Navigation 137(1):926–935
9. Bek MK, Shaheen EM, Elgamel SA (2015) Classification and mathematical expression of different interference signals on a GPS receiver. Navigation 62(1):23–37
10. Cuntz M, Konovaltsev A, Meurer M (2016) Concepts, development, and validation of multiantenna GNSS receivers for resilient navigation. Proc IEEE 104(6):1288–1301. https://doi.org/10.1109/JPROC.2016.2525764
11. Dan L (2013). Robust anti-jamming techniques for global avigation satellite system. [Phd Thesis], Xi'an Electronic and Science University, 2013

A Novel Generation Method of TM-AltBOC Modulator and Demodulator

Jun Mo, Yi Zhang and Hui Liu

Abstract A novel generation method of TM-AltBOC modulator and demodulator based on binary-offset modulate is provided. This method is applied by modulating four signals on two sub-carriers with sub-carrier division and time division multiplexing. The signal can effectively process time division multiplexing satellite navigation signal without energy loss, and has the advantage of simple structure and easy to realize. It can adjust signal power of each component by software configuration.

Keywords Satellite navigation system · Navigation signal structure TM-AltBOC

1 Foreword

In order to get higher accuracy and better performance, BOC modulation technology was adopted by several new generation satellite systems [1, 2]. For example, AltBOC was used at E5 signal of Galileo in order to fully utilize the bandwidth [3]. A proper sub-carrier waveform needs to be selected to generate a constant envelop signal when doing the modulation. Galileo uses AltBOC modulation to have four different navigation signals E5a-data, E5a-pilot, E5b-data and E5b-pilot to be modulated into a complex signal and up convert to a wideband signal centered at 1191.795 MHz. With this modulation, E5a-data and E5a-pilot can be treated as a QPSK signal modulated at E5a frequency (1176.45 MHz), E5b-data and E5b-pilot can be treated as a QPSK aignal modulated at E5b frequency (1207.14 MHz).

Another modulation technology combining four binary signals into a wideband signal is introduced by Tsinghua University as ACE-BOC [4]. Comparing with

J. Mo (✉) · Y. Zhang · H. Liu
Wuhan Navigation & LBS, Inc, Wuhan, Hubei Province, China
e-mail: mojun@wnlbs.com

Y. Zhang
e-mail: zhangyi_hrb@126.com

J. Sun et al. (eds.), *China Satellite Navigation Conference (CSNC) 2018 Proceedings*, Lecture Notes in Electrical Engineering 498,
https://doi.org/10.1007/978-981-13-0014-1_2

AltBOC only having equivalent power on all four signals, ACE-BOC can adjust power ration between the modulated four signals on demand, which is more flexible. Two modulation methods are given to achieve this technology, one is lookup table method and the other is analytical method.

TD-AltBOC is also a similar technology introduced by Huazhong University of Science and Technology [5]. This technology needs a simpler lookup table comparing to AltBOC and ACE-BOC, but there are limitations in this technology: the four modulated signals have the same power and the pilot signals on high and low sub-band must use the same pseudo-random code.

Considering all technologies mentioned above have their limitations, either have complicate calculation or have fixed signal power ratio, a new modulation technology is invented and introduced as TM-AltBOC. Using this technology, power ration between signals can be flexibly adjusted while a much simpler modulation method is needed.

2 Modulation of TM-AltBOC

The block diagram of TM-AltBOC modulation is shown as following (Fig. 1).

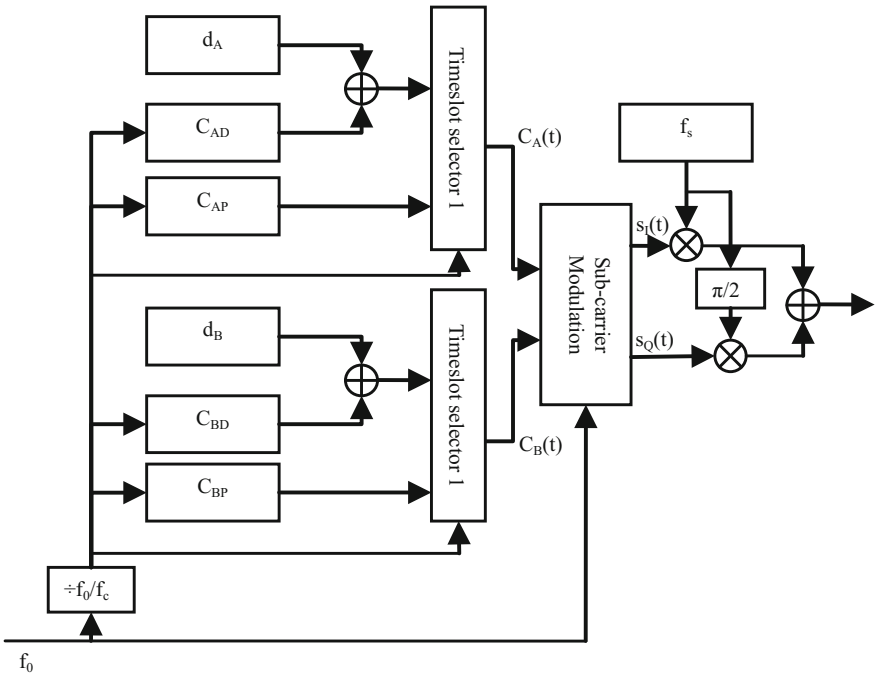

Fig. 1 Block diagram of TM-AltBOC modulation

In above diagram, f_0 is the clock used to generate baseband complex signal, it is divided by N to get code generation clock fc, which is used to generate four different pseudo-random codes: lower sub-band data code C_{AD}, lower sub-band pilot code C_{AP}, upper sub-band data code C_{BD} and upper sub-band pilot code C_{BP}. The data code C_{AD} and C_{BD} first need to XOR with the modulation data d_A and d_B respectively. Then data code and pilot code for lower sub-band are input into timeslot selector 1 to get binary signal of lower sub-band $C_A(t)$, data code and pilot code for upper sub-band are input into timeslot selector 2 to get binary signal of upper sub-band $C_B(t)$. These two timeslot selector can use the same configuration or use different configuration on timeslot selection. The sub-carrier modulator then use these two binary signal as input and will output complex baseband signal driven by clock f0. Finally, the complex baseband signal is up convert to a wideband signal centered at frequency fs.

As an example, a signal centered at 1191.795 MHz and has the same spectrum as E5 signal is generated with following steps:

(1) Use f0 = 60 × 1.023 MHz = 61.38 MH as reference clock and divided by 6 to get code generation clock at 10.23 MHz.
(2) Four different PRN code generation block to generate code C_{AD}, C_{AP}, C_{BD} and C_{BP} respectively, each code is 10230 in length and lasts 1 ms.
(3) Modulation data d_A and d_B exclusive-or with C_{AD} and C_{BD} respectively. The length of modulation data is multiple of 1 ms.
(4) Optionally, pilot code C_{AP} and C_{BP} can also be modulated by secondary codes C_{SA} and C_{SB}. C_{SA} and C_{SB} can be the same or different and each with length of multiple of 1 ms.
(5) Use the time selector to do selection from the data or pilot code to fill in the time slots to generate binary signal on lower or upper sub-band. The ratio of timeslot to fill in is adjustable by different configuration so power ratio will be different, e.g. if the data code occupies m timeslots within each n timeslots, the data channel takes m/n of the power and the pilot channel takes 1 − m/n of the power. The outputs of the time selector are $C_A(t)$ and $C_B(t)$ respectively.
(6) The sub-carrier modulator is used to put the binary code of lower and upper sub-band into a complex baseband signal. The formula used is:

$$s(t) = s1(t)e*(t) + s2(t)e(t)$$

in which s1(t) and s2(t) are modulated binary signal CA(t) and CB(t) respectively. s1(t) = 1/2 when CA(t) = 0 and s1(t) = −1/2 when CA(t) = 1, the same relationship applies to s2(t) and CB(t).
e(t) and e*(t) are complex sub-carriers of upper sub-band and lower sub-band:

$$e(t) = SCcos(t) + jSCsin(t)$$
$$e*(t) = SCcos(t) - jSCsin(t)$$

in which

$$SCcos(t) = sign(cos(2\pi fSCt))$$
$$SCcos(t) = sign(sin(2\pi fSCt))$$

are cosine and sine binary sub-carrier, the frequency of the sub-carrier f_{SC} = 15.345 MHz.

(7) Get the real part and the imaginary part of the baseband signal:

$$\begin{aligned} s(t) &= sI(t) + jsQ(t) \\ &= [s1(t) + s2(t)]SCcos(t) + j[s2(t) - s1(t)]SCsin(t) \end{aligned}$$

(8) An easy lookup table method can be used to get the real part and the imaginary part (Fig. 2).

The waveforms of cosine and sine binary sub-carrier are shown below:

In which, $T = 1/f_{SC}$ is the cycle of sub-carrier. When m takes 0, 1, 2, and 3 in t = (4n + m)/4T, SCcos(t) has the values of 1, −1, −1 and 1, SCsin(t) has the values of 1, 1, −1 and −1 respectively.

When the frequency of sub-carrier is 15.345 MHz, take f0 as four times of sub-carrier frequency. The real part and imaginary part of the baseband signal can be get from the following lookup table in each one fourth period of sub-carrier cycle (Table 1):

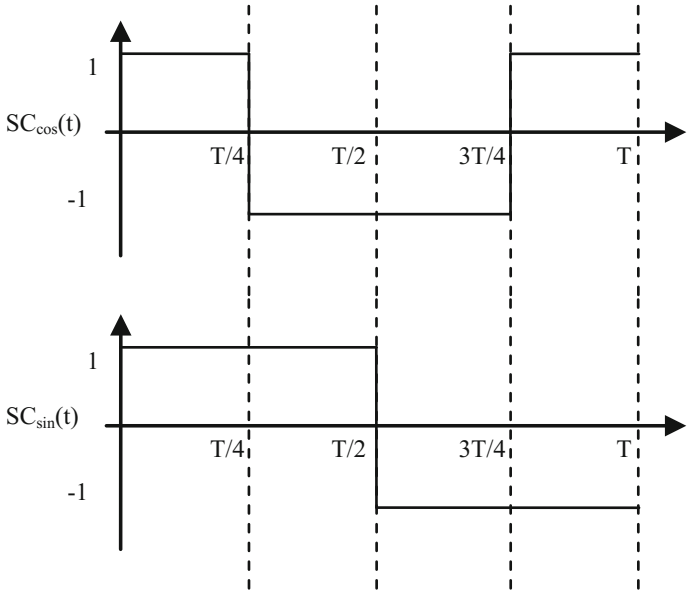

Fig. 2 Waveforms of cosine and sine sub-carrier

Table 1 Sub-carrier modulation lookup table

$C_A(t)$	$C_B(t)$	$s_I(t)$				$s_Q(t)$			
0	0	1	−1	−1	1	0	0	0	0
0	1	0	0	0	0	−1	−1	1	1
1	0	0	0	0	0	1	1	−1	−1
1	1	−1	1	1	−1	0	0	0	0

(9) The final step is to modulate the baseband signal up to frequency fs = 1191.795 MHz using formula $sI(t)\cos(2\pi fst) - sQ(t)\sin(2\pi fst)$.

The advantages of above method are lower frequency requirement of generation clock, simple lookup table, flexible power allocation between data and pilot channel and having the feature of constant envelop.

3 Signal Demodulation and Tracking

Several methods can be used to track and demodulate the signal generated in previous section. One method is used to track single side-band signal, another method is used to track and demodulate it as a whole wideband signal. These two methods are introduced below:

When tracking the lower or upper side-band signal solely, it is equivalent to track a BPSK signal modulated at 1176.45 MHz or 1207.14 MHz. The following block diagram can be used to do signal tracking (Fig. 3).

After the IF frequency is removed by multiplex local carrier, the digital baseband signal $I_B + jQ_B$ is get. Then local pilot signals with different delay as $C_{BP\text{-}E}$, $C_{BP\text{-}P}$ and $C_{BP\text{-}L}$ are used to correlate with input baseband signal. The timeslot selection signals S_E, S_P, S_L are synchronized to local pilot signals $C_{BP\text{-}E}$, $C_{BP\text{-}P}$ and $C_{BP\text{-}L}$ respectively. The integration will use timeslot selection information to determine correlated signal in which time slot will be summed up. The accumulation results represent early, prompt and late correlation $I_E + jQ_E$, $I_P + jQ_P$ and $I_L + jQ_L$ is then be used in carrier loop and code loop to track the signal.

On data demodulation, the data code C_D and time slot enable signal S_D is used instead of $C_{BP\text{-}P}$ and S_P in the correlation and integration step, and the sign of the

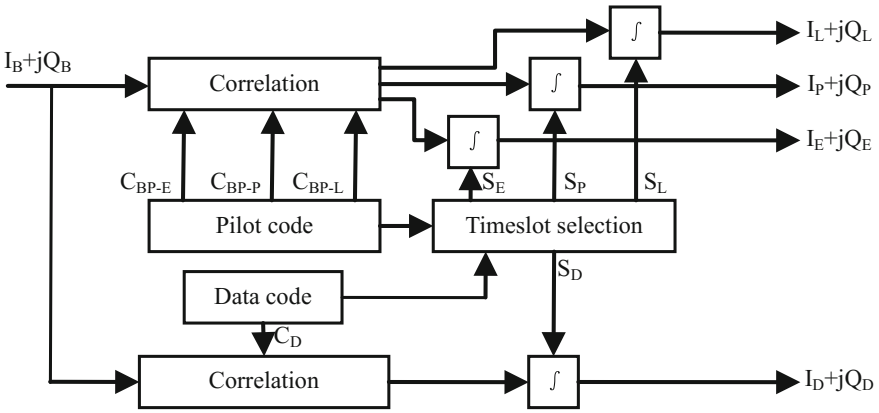

Fig. 3 Block of diagram of signal tracking

integration result can be used to determine the data value. The data integration result can also be used in signal tracking.

When tracking the whole signal, it is treated as a wideband signal centered at 1191.795 MHz, so local carrier of such frequency is first multiplied to get baseband signal $I_B + jQ_B$. The a similar method is used to do signal tracking with different correlation and integration block shown (Fig. 4).

Correlation is also a multiplication between baseband signal and conjugation of local complex signal. According to the method of signal generation, the local signal can be expressed as:

$$s(t) = [s1(t) + s2(t)]SCcos(t) + j[s2(t) - s1(t)]SCsin(t)$$

In which, SCcos(t) and SCsin(t) are cosine and sine binary sub-carrier. There are four different combination of the sub-carrier values as shown (Fig. 5).

The combinations are (1,1), (−1,1), (−1,−1) and (1,−1).

And

$$s1(t) = C_{AP}(t)S_{AP}(t) + C_{AD}(t)S_{AD}(t)$$
$$s2(t) = C_{BP}(t)S_{BP}(t) + C_{BD}(t)S_{BD}(t)$$

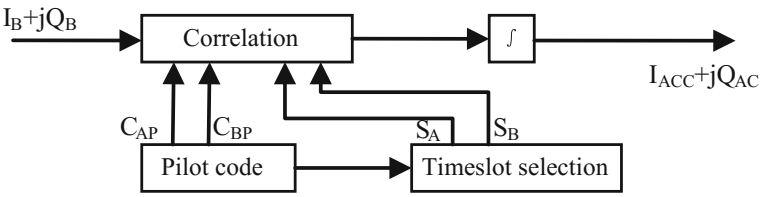

Fig. 4 Block diagram of coherent integration

Fig. 5 Value combination of sub-carrier within one cycle

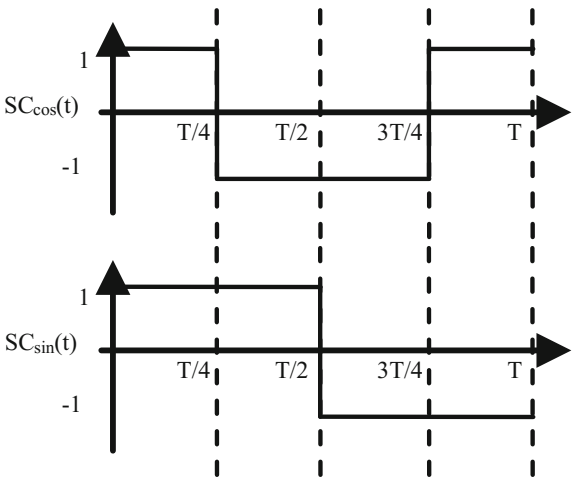

Table 2 lookup table of local complex signal

$s_1(t)/s_2(t)$	$SC_{cos}(t)/SC_{sin}(t)$			
	1/1	−1/1	−1/−1	1/−1
1/1	2	−2	−2	2
1/−1	−2j	−2j	2j	2j
−1/1	2j	2j	−2j	−2j
−1/−1	−2	2	2	−2
1/0	1 − j	−1 − j	−1 + j	1 + j
−1/0	−1 + j	1 + j	1 − j	−1 − j
0/1	1 + j	−1 + j	−1 − j	1 − j
0/−1	−1 − j	1 − j	1 + j	−1 + j
0/0	0	0	0	0

In which, $C_{AP}(t)$ and $C_{AD}(t)$ are pilot and data code in lower sub-band, $C_{BP}(t)$ and $C_{BD}(t)$ are pilot and data code in upper sub-band, the values of these code are 1 and −1. $S_{AP}(t)$ and $S_{AD}(t)$ are selection of pilot and data code with values be 1 or 0. Because pilot signal and data signal cannot be selected both, so $S_{AP}(t)$ and $S_{AD}(t)$ will not be all 1 at the same time. So as $S_{BP}(t)$ and $S_{BD}(t)$.

When tracking the pilot signal, the local complex signal will only contain the pilot signal part, so $s1(t) = C_{AP}(t)S_{AP}(t)$ and $s2(t) = C_{BP}(t)S_{BP}(t)$. And s1(t) and s2(t) have the value of 1, −1 or 0.

The following table gives the value of local complex signal with different value of s1(t) and s2(t) (Table 2):

The correlation can also use lookup table to give the multiply result of baseband signal and conjugation of local signal. The output of correlation is given in following table when baseband signal input to correlator is $I_B + jQ_B$ (Table 3):

Table 3 lookup table of correlation result

$s_1(t)/s_2(t)$	$SC_{cos}(t)/SC_{sin}(t)$			
	1/1	−1/1	−1/−1	1/−1
1/1	$2I_B + j2Q_B$	$-2I_B - j2Q_B$	$-2I_B - j2Q_B$	$2I_B + j2Q_B$
1/−1	$-2Q_B + j2I_B$	$-2Q_B + j2I_B$	$2Q_B - j2I_B$	$2Q_B - j2I_B$
−1/1	$2Q_B - j2I_B$	$2Q_B - j2I_B$	$-2Q_B + j2I_B$	$-2Q_B + j2I_B$
−1/−1	$-2I_B - j2Q_B$	$2I_B + j2Q_B$	$2I_B + j2Q_B$	$-2I_B - j2Q_B$
1/0	$I_B - Q_B + j$ $(I_B + Q_B)$	$-I_B - Q_B + j$ $(I_B - Q_B)$	$Q_B - I_B + j$ $(-I_B - Q_B)$	$I_B + Q_B + j$ $(Q_B - I_B)$
−1/0	$Q_B - I_B + j$ $(-I_B - Q_B)$	$I_B + Q_B + j$ $(Q_B - I_B)$	$I_B - Q_B + j$ $(I_B + Q_B)$	$-I_B - Q_B + j$ $(I_B - Q_B)$
0/1	$I_B + Q_B + j$ $(Q_B - I_B)$	$Q_B - I_B + j$ $(-I_B - Q_B)$	$-I_B - Q_B + j$ $(I_B - Q_B)$	$I_B - Q_B + j$ $(I_B + Q_B)$
0/−1	$-I_B - Q_B + j$ $(I_B - Q_B)$	$I_B - Q_B + j$ $(I_B + Q_B)$	$I_B + Q_B + j$ $(Q_B - I_B)$	$Q_B - I_B + j$ $(-I_B - Q_B)$
0/0	0	0	0	0

Table 4 correlation result with same timeslot

$s_1(t)/s_2(t)$	$SC_{cos}(t)/SC_{sin}(t)$			
	1/1	−1/1	−1/−1	1/−1
1/1	$I_B + jQ_B$	$-I_B - jQ_B$	$-I_B - jQ_B$	$I_B + jQ_B$
1/−1	$-Q_B + jI_B$	$-Q_B + jI_B$	$Q_B - jI_B$	$Q_B - jI_B$
−1/1	$Q_B - jI_B$	$Q_B - jI_B$	$-Q_B + jI_B$	$-Q_B + jI_B$
−1/−1	$-I_B - jQ_B$	$I_B + jQ_B$	$I_B + jQ_B$	$-I_B - jQ_B$
0/0	0	0	0	0

From above table, it is easy to be observed that the correlation results are addition or subtraction of real part and imaginary part of input signal.

Furthermore, if the pilot code of upper and lower sub-band occupy the same timeslot, the combination of (1,0), (−1,0), (0,1) and (0,−1) will not appear in above table, so the output of correlator can be further simplified to following table (Table 4):

In table above, the output of the correlation are divided by 2 and will not affect the result.

From above table, it is easy to see that both the real part and the imaginary part of the correlation result can simply select the real part or imaginary part of the input signal.

With above method, the integration result $I_{ACC} + jQ_{ACC}$ can be put into phase/frequency discriminator or delay discriminator and do signal tracking with traditional method.

On signal demodulation, the local signal is also [s1(t) + s2(t)]SCcos(t) + j[s2(t) − s1(t)]SCsin(t) and the same correlation and integration method is used. When the lower sub-band data is demodulated, using $s1(t) = C_{AD}(t)S_{AD}(t)$ and $s2(t) = 0$ and when the upper sub-band data is demodulated, using $s1(t) = 0$ and $s2(t) = C_{BD}(t)S_{BD}(t)$. The sign of the integration result gives the demodulated value when the signal is in tracking.

If the timeslot of the lower and upper sub-band data channel are the same, which is $S_{AD}(t) = S_{BD}(t)$, a simpler method can be used to do data demodulation:

Using $s1(t) = C_{AD}(t)S_{AD}(t)$ and $s2(t) = -C_{BD}(t)S_{BD}(t)$ to generate the local signal, the integration result gives the sum of the upper and lower sub-band data $D_{ADD} = D_A + D_B$. Using $s1(t) = C_{AD}(t)S_{AD}(t)$, $s2(t) = -C_{BD}(t)S_{BD}(t)$ to generate the local signal, the integration result gives the subtraction of the upper and lower sub-band data $D_{SUB} = D_A - D_B$. By adding or subtracting the above two values, the lower sub-band data and the upper sub-band data can be recovered: $D_A = (D_{ADD} + D_{SUB})/2$, $D_B = (D_{ADD} - D_{SUB})/2$.

4 Conclusion

A new binary offset carrier modulation technology TM-AltBOC is introduced, and technology to demodulate and tracking TM-AltBOC signal is also illustrated. This technology modulates four different signals with sub-carrier division and time

multiplex method. The signal generation logic is easy to implement, only four different phases are used in the four-entry phase lookup table. The frequency of clock used by signal generation block is only four times of sub-carrier frequency. The power ratio between data and pilot channel can also be adjusted without additional logic or calculation efforts.

References

1. Betz J (1999) The offset carrier modulation for GPS modernization. In: Proceedings of ION Technical meeting. Cambridge, Massachusetts, pp 639–648
2. Betz J (2013) Something old, something new: signal structures for satellite-based navigation: past, present, and future, Inside GNSS
3. Galileo Open Service Signal In Space Interface Control Document, Issue 1.1, Sept. 2010
4. Yao Z, Lu M (2013) Design, implementation, and performance analysis of ACE-BOC modulation. In: 26th international technical meeting of the satellite division of the institute of navigaiotn, ION GNSS, Nashville
5. Tang Z, Zhou H, Wei J et al (2010) TD-AltBOC: a new CPMPASS B2 modulation. In: China satellite navigation conference 2010, Shanghai

Generation Mechanisms and Experimental Verifications of Pseudo-range Biases for BDS Navigation Signals

Chengyan He, Ji Guo, Xiaochun Lu, Li Kang and Meng Wang

Abstract Due to the non-ideal characteristics of navigation satellite signals, pseudo-range observations of two satellites for the same signal are different in the same receiver, in addition to that, for zero-baseline receivers, pseudo-range observations between different receivers are different even for the same satellite and the same signal. Bias inconsistencies will lead to adverse effects for pseudo-range-based positioning applications and can also hinder carrier-phase ambiguity resolution. However, fewer article deals with the generation mechanisms of pseudo-range biases for BeiDou Navigation Satellite System. In order to mitigate the impact of biases on BDS to the greatest extent, the generation mechanisms and characteristics of pseudo-range biases are studied in detail in the beginning. Then based on this, experimental verification methods are designed using Haoping Radio Observatory (HRO) of Chinese Academy of Sciences to observe BDS signals. Pseudo-range biases of all visible BDS satellites are measured and evaluated with high accuracy thanks to the 40 m dish antenna and modern equipment of HRO. Finally, some important parameters for BDS receivers, such as the correlator spacing and front-end bandwidth, are provided or suggested to mitigate the ranging errors and positioning errors result from pseudo-range biases. The achievements of this paper could be a worthy reference for GNSS signal designers, GNSS monitoring and assessment and GNSS receiver designers.

Keywords BeiDou navigation satellite system · Pseudo-range bias
Generation mechanism · Experimental verification

C. He (✉) · J. Guo · X. Lu · L. Kang · M. Wang
National Time Service Center, Chinese Academy of Sciences,
No. 3 Shuyuan East Road, Lintong, Xi'an 710600, Shaanxi, China
e-mail: hechengyan@ntsc.ac.cn

J. Guo
School of Astronomy and Space Science, University of Chinese
Academy of Sciences, Beijing 100190, China

L. Kang · M. Wang
Graduate University of Chinese Academy of Sciences, Beijing 100190, China

J. Sun et al. (eds.), *China Satellite Navigation Conference (CSNC) 2018 Proceedings*, Lecture Notes in Electrical Engineering 498,
https://doi.org/10.1007/978-981-13-0014-1_3

1 Introduction

According to the on-board clock frequency, GNSS satellites transmit modulated navigation signals in specific format, which arrives at the terrestrial user receiver antenna after a lapse of time Δt from the satellite. Signals propagation time Δt multiplied by electromagnetic wave propagation velocity in space c, we can get the geometric distance ρ between satellite and the user's. By calculating the distances from at least three satellites to the user, it is possible to calculate the intersection position of three balls with each satellite as the center and the distance to the user as the radius. Here the intersection position is the exact position of the user.

In fact, however, the calculated Δt is not the exact propagation time from satellite to the user, due to the fact that there are also the effects of satellite clock errors, receiver clock errors, satellite ephemeris errors, receiver measurements noise, multipath, ionospheric delay and tropospheric delay on the propagation time Δt. Therefore, the calculated distance in practical applications is not the real geometric distance from station to satellite, which is conventionally called the pseudo-range.

For high-precision users, differential systems can eliminate some errors, but there still exists some errors such as multipath, receiver measurement noise, errors caused by satellite signal distortion, which cannot be eliminated by differential system. As a result, when two receivers of zero-baseline or short-baseline observe simultaneously the same satellite, the pseudo-range difference between the two receivers is a constant with non-zero mean. In addition, when two receivers of zero-baseline or short-baseline observe simultaneously two identical satellites, the pseudo-range difference between the two receivers also shows a constant with a non-zero mean. Moreover, the pseudo-range biases between different receivers and different satellites are different. The phenomenon above is called pseudo-range biases. This phenomenon was first discovered in 2011 by Gabriel Wong and R. Eric Phelts of Stanford University when studying the ranging and positioning results of the GPS and WAAS systems. Results show that, the signal characteristics of different satellites cannot be in full accord, when dual-frequency users eliminate ionospheric effects by dual-frequency linear combination, the impact of pseudo-range bias will be further amplified.

Those pseudo-range biases have already been studied by foreigners years ago, and this unnormal phenomenon was first been found in GPS satellites. Many foreigners attempt to solve this problem.

References [1–3] found pseudo-range biases when using dual-frequency techniques to eliminate ionospheric delays. At the same time, some suggestions to reduce the effect of pseudo-range biases are given. On the one hand, the influence of this phenomenon on users can be reduced by broadcasting parameters of time group delay (TGD) and Inter-Signal Corrections (ISCs) in navigation message. On the other hand, the effects of pseudo-range biases can be reduced by defining parameters such as receiver front-end bandwidth and correlator spacing in ICD (Interface Control Document). References [4–7] studied the possible causes of GPS

pseudo-range biases. Those articles pointed out that: the inconsistency among various satellites' signals is the essential cause of the pseudo-ranges biases.

However, the above references mainly focused on the phenomenon and stability of pseudo-range biases in GPS satellites. There are few articles mentioning whether there are any pseudo-range biases in China's BDS system. In later 2016, during the monitoring and evaluation process of BDS II and experimental satellites, it is found that pseudo-range biases also occurred in BDS satellites, but the characteristics are different from that of GPS. With the demand of continuous improvement of the positioning accuracy of BDS, researches on pseudo-range biases have been paid more and more attention in China. At present, however, researches on pseudo-range biases in China mainly focus on the phenomenon and their influence on positioning, while its causes and solutions of pseudo-range biases are not studied fundamentally.

Aiming at pseudo-range biases of BDS satellites, the phenomenon of pseudo-range biases will firstly be described in detail by the way of theoretical formula. Then based on this, a complete transmitting and receiving model of navigation signal transmitting, broadcasting, and receiving is established to analyze step by step the reasons of the biases from the whole route of satellite signal transmission. Then from the perspective of user terminals, the possible forms and characteristics of the pseudo-range biases are further analyzed respectively mainly from three aspects: the correlator spacing of receiver, the RF bandwidth and the elevation angle of satellites. The conclusion of this paper and suggestions for BDS users are given in the end.

2 Phenomenon of Pseudo-range Biases

The phenomenon of pseudo-range biases cannot be directly obtained by a single receiver, it is required that two receivers of zero-baseline or short-baseline observe simultaneously two satellites. The pseudo-range biases can be obtained by calculating the single difference or double difference of pseudo-ranges of the two receivers, which is possible to eliminate some of the common errors. Here we assume that the two receivers are denoted as r1 and r2 respectively and the two satellites are denoted as i and j respectively. Then we can calculate the O-C double difference from pseudo-ranges of B1I and B3I.

The pseudo-range equations of single frequency for r1 and r2 receivers and for i and j satellites are as follows:

$$P_{r1}^{i} = \rho_{r1}^{i} + c\delta t_{r1} - c\delta t^{i} + c \cdot IFB_{r1} - c \cdot Tgd^{i} - iono_{r1}^{i} - trop_{r1}^{i} - rel_{r1}^{i} - \alpha_{r1}^{i} + \varepsilon_{r1}^{i} + MP_{r1}^{i} + SDM_{r1}^{i} \quad (1)$$

$$P_{r1}^{j} = \rho_{r1}^{j} + c\delta t_{r1} - c\delta t^{j} + c \cdot IFB_{r1} - c \cdot Tgd^{j} - iono_{r1}^{j} - trop_{r1}^{j} - rel_{r1}^{j} - \alpha_{r1}^{j} + \varepsilon_{r1}^{j} + MP_{r1}^{j} + SDM_{r1}^{j} \quad (2)$$

$$P_{r2}^{i} = \rho_{r2}^{i} + c\delta t_{r2} - c\delta t^{i} + c \cdot IFB_{r2} - c \cdot Tgd^{i} - iono_{r2}^{i} - trop_{r2}^{i} - rel_{r2}^{i} - \alpha_{r2}^{i} + \varepsilon_{r2}^{i} + MP_{r1}^{i} + SDM_{r1}^{i} \quad (3)$$

$$P_{r2}^{j} = \rho_{r2}^{j} + c\delta t_{r2} - c\delta t^{j} + c \cdot IFB_{r2} - c \cdot Tgd^{j} - iono_{r2}^{j} - trop_{r2}^{j} - rel_{r2}^{j} - \alpha_{r2}^{j} + \varepsilon_{r2}^{j} + MP_{r1}^{j} + SDM_{r1}^{j} \quad (4)$$

Taking the receiver r1 and satellite i as an example: here P_{r1}^{i} is pseudo-range between receiver and satellite, ρ_{r1}^{i} is theoretical distance between receiver and satellite, δt_{r1} and δt^{i} are receiver clock error and satellite clock error respectively, IFB_{r1} and Tgd^{i} are inner-frequency biases between receivers and inner-frequency biases between satellites respectively, c is light speed, $iono_{r1}^{i}$ and $trop_{r1}^{i}$ are the ionosphere delay and the tropospheric delay respectively, rel_{r1}^{i} is relativistic effect delay, α_{r1}^{i} is receiver channel delay, ε_{r1}^{i} is thermal noise, MP_{r1}^{i} is multipath and SDM_{r1}^{j} is the error result from signal distortion.

Because of the zero-baseline connection of the two receivers, the ionosphere delay, the tropospheric delay and the relativistic effect delay from the same satellite to the two receivers are the same, the inner-frequency biases between satellites for the two receivers are the same, and the inner-frequency biases between receivers for the different satellites are the same. Therefore, the O-C double difference between the pseudo-ranges of the two receivers can be used to eliminate many main errors such as receiver clock error, satellite clock error, inner-frequency biases between receivers, inner-frequency biases between satellites, ionospheric delay, tropospheric delay, relativistic effects, and multipath. Therefore, the mean of O-C double difference is considered to be the pseudo-range biases between the two satellites.

During the measurement process of pseudo-range biases of BDS B1I signals, four different manufacturers of receivers are connected in zero-baseline. The four receivers are as follows: one Trimble receiver, one receiver of No. 20 institute of China Electronic Technology Group which is denoted as No. 20 receiver for brevity, one of No. 704 Institute denoted as No. 704 receiver for brevity, and one of National Defense University denoted as NDU receiver for brevity. Here we take the Trimble receiver as the reference receiver, the pseudo-range observations of all other three receivers are subtracted with that of the Trimble receiver respectively. The pseudo-range biases of B1I signal can be obtained by the O-C double difference of two receivers. Here we take the BDS GEO-1 (C01) satellite as the reference.

The blue column of R-1 in Fig. 1 represents means of double differences between No. 20 receiver and Trimble receiver, the red column of R-2 in Fig. 1 represents means of double differences between No. 704 receiver and Trimble receiver, and the green column of R-3 represents means of double differences between NDU receiver and Trimble receiver.

Figure 1 shows that the pseudo-range biases between different receivers and different satellites is not zero and is different from each other. Therefore, in the next section we will study the generate mechanism of pseudo-range biases in detail.

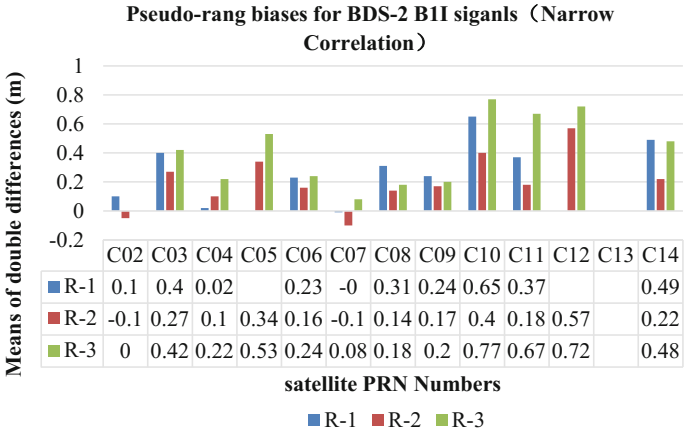

Fig. 1 Pseudo-range biases of BDS BI1I signals: R-1 represents means of double differences between No. 20 receiver and trimble receiver, R-2 represents that between No. 704 and trimble receivers, and R-3 represents that between NDU and trimble receivers

3 Generate Mechanism Analyses

If the transmission channel of satellite navigation signal is not ideal, that is, the amplitude-frequency and the phase-frequency characteristics of the channel transfer function H (f) are not ideal, when the satellite navigation signal arrives at the user receiver correlates with the corresponding local code, it will be obvious that the correlation curve is asymmetric and there are nonlinear distortions in the correlation curve. These distortions will lead to an offset of the lock point of the DLL discriminating curve, which is ranging error [8] and is shown in Fig. 2.

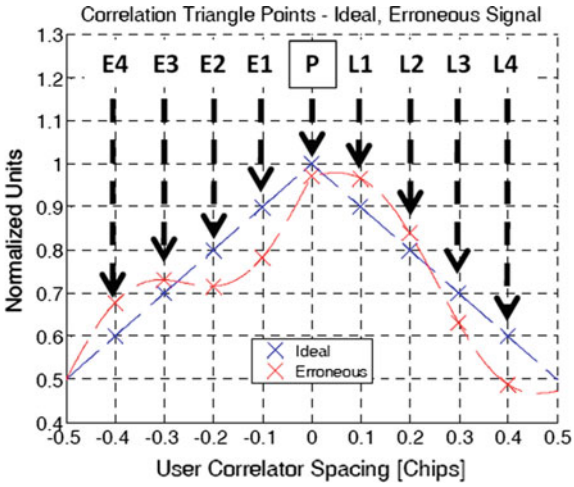

Fig. 2 Cross-correlation of the local code and broadcasted code

Taking the typical incoherent Early-Minus-Late Power discriminator as an example, here we assume the correlator spacing is δ, then the S curve can be calculate from the following equations [8]:

$$SCurve(\varepsilon, \delta) = \left| CCF\left(\varepsilon - \frac{\delta}{2}\right)\right|^2 - \left| CCF\left(\varepsilon + \frac{\delta}{2}\right)\right|^2 \tag{5}$$

The lock point error $\varepsilon_{bias}(\delta)$ meets the following equation:

$$SCurve(\varepsilon_{bias}(\delta), \delta) = 0 \tag{6}$$

S curve biases is defined as:

$$SCB = \max_{\substack{over \\ all\ \delta}}(\varepsilon_{bias}(\delta)) - \min_{\substack{over \\ all\ \delta}}(\varepsilon_{bias}(\delta)) \tag{7}$$

The blue dotted line in Fig. 2 represents the ideal signal correlation curve and the red dotted line represents that of the received signal. It can be seen that the correlation curve of received signal is seriously asymmetric, so the lock points of DLL discriminating curve for different correlator spacing are different. In this case, there still exists a non-zero constant that cannot be cancelled out in the double-difference of pseudo-ranges for two receivers with different correlator spacing.

Results show that if the distortion characteristics of each satellite signal are identical or the parameters of all receivers are in full accord, then the pseudo-range biases phenomenon can be completely eliminated during double-difference processing. Therefore, even if there is some distortions in received signal, different receivers of zero baseline or a short baseline will obtain a zero-mean Gaussian noise when performing pseudo-range double-difference processing [9]:

(A) Single pseudo-range difference of two receivers with different correlator spacing:

$$\rho_{mn} = c\left[\delta t_{u,m} - \delta t_{u,n}\right] + \varepsilon_{\rho,m} - \varepsilon_{\rho,n} + MP_{\rho,m} - MP_{\rho,n} + SDM_{\rho,m} - SDM_{\rho,n} \tag{8}$$

(B) Double pseudo-range difference of two receivers with different correlator spacing:

$$\rho^{ij}_{mn} = \varepsilon^{ij}_{\rho,mn} + MP^{ij}_{\rho,mn} + SDM^{ij}_{\rho,mn} \tag{9}$$

Here m and n are used to denote receivers, and i and j are used to denote satellites.

SDM^{j}_{r1} is signal distortion and is usually a constant. If $\varepsilon^{ij}_{\rho,mn}$ and $MP^{ij}_{\rho,mn}$ is small relative to signal distortion biases, we can see SDM^{j}_{r1} over a long time of

averaging, say an hour, to reduce $\varepsilon^{ij}_{\rho,mn}$ and $MP^{ij}_{\rho,mn}$. Here we assume $\varepsilon^{ij}_{\rho,mn}$ and $MP^{ij}_{\rho,mn}$ are zero mean random variables.

(C) Single pseudo-range difference of two receivers with the same correlator spacing:

$$\rho_{mn} = c\left[\delta t_{u,m} - \delta t_{u,n}\right] + \varepsilon_{\rho,m} - \varepsilon_{\rho,n} \tag{10}$$

Note that the multipath and signal distortion error terms are cancelled.

(D) Double pseudo-range difference of two receivers with the same correlator spacing:

$$\rho^{ij}_{mn} = \varepsilon^{ij}_{mn} \tag{11}$$

In this case, we should see that double difference should be zero-mean over a long time, say an hour.

For double-frequency users, the following formula is used to remove ionospheric delay:

$$P^{i}_{B1\,B3\,r1} = \frac{f_1^2}{f_1^2 - f_3^2} \cdot P^{i}_{B1\,r1} - \frac{f_3^2}{f_1^2 - f_3^2} \cdot P^{i}_{B3\,r1} \tag{12}$$

Then the double pseudo-range difference for two zero-baseline receivers is:

$$\mathrm{omc}^{i,j}_{B1B3\ r1,r2} = \frac{f_1^2}{f_1^2 - f_3^2} \cdot \mathrm{omc}^{i,j}_{B1\,r1,r2} - \frac{f_3^2}{f_1^2 - f_3^2} \cdot \mathrm{omc}^{i,j}_{B3\,r1,r2} \tag{13}$$

It is obvious that, for double-frequency users, the pseudo-range biases are amplified by 2.9 and 1.9 times respectively for B1I and B3I signal. In this case, if the signs of measured pseudo-range biases for B1I and B3I signal are opposite, then the measured pseudo-range biases of B1I–B3I double-frequency users is amplified seriously.

Research results show that if the distortion characteristics of each satellite signal are identical or the parameters of all receivers are in full accord, then the pseudo-range biases phenomenon can be completely eliminated during double-difference processing. Therefore, even if there is some distortions in received signal, different receivers of zero baseline or a short baseline will obtain a zero-mean Gaussian noise when performing pseudo-range double-difference processing.

Because it is almost impossible to adjust the navigation signals of on-orbit satellites and to guarantee the uniformity of all signals of different satellites, we studied the effects of pseudo-range biases mainly from the user perspective. Here the influence of font-end bandwidth, correlator spacing and satellite's elevation angle on the pseudo-range biases of BDS II is analyzed in detail. And finally suggestions of the setting range of receiver parameters are given to minimize the effects of pseudo-range biases on users.

4 Pseudo-range Biases with Correlator Spacing

The parameter of correlator spacing is of vital importance for a receiver to achieve high accuracy of DLL tracking. If it is not set appropriately, there will be large ranging error. To analyze the effect of correlator spacing on pseudo-range biases, we carried out lots of test-and-verifications using the 40 m antenna system of Haoping Radio Observatory (HRO) in November 2017. Each BDS B1I signal was collected for many times by NI data collecting equipment. According to the methods for S curve calculating introduced above, we calculated the lock points of all B1I S curves for each satellite using the "GNSS signal quality assessment software" developed by ourselves. Here we traversed all the correlator spacing from 0.01 to 1.0 chips and results are shown in Fig. 3.

As we can see from Fig. 3:

- For a particular bandwidth, there is much difference between lock points of S curves for different satellites.
- For a particular satellite, there is much difference between lock points of S curve for different correlator spacing.
- For the same type of satellites, there is less difference between lock points of S curve with the same correlator spacing.
- For different kinds of satellites, there is much difference between lock points of S curve with the same correlator spacing.

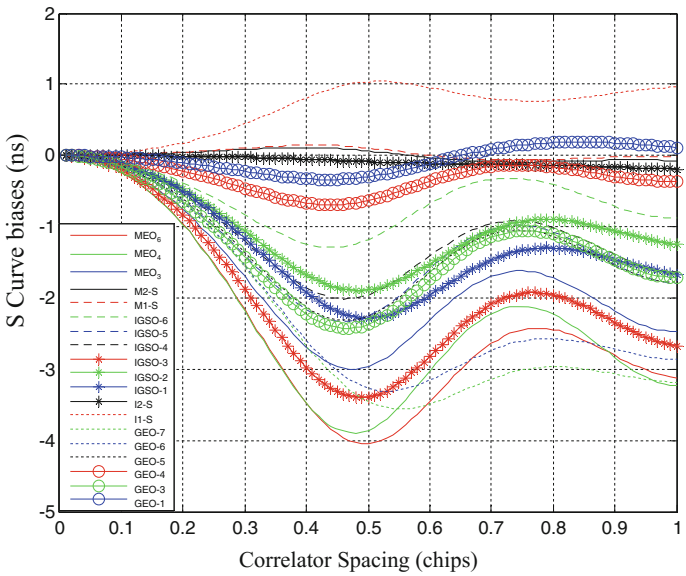

Fig. 3 Variation with correlator spacing of S curve biases for BDS B1I, with single side band of 8 MHz

If we assume the correlator spacing of the reference receiver is 0.5 chips, then the lock points of S curves of B1I signals of different satellites are shown in Fig. 4.

It is obvious that:

- If the correlator spacings of all user receivers are set to be 0.2 chips, then the double pseudo-range difference between user receiver and the reference receiver is 3 ns at most.
- If the correlator spacing of all user receivers are set to be 0.6 chips, then the double pseudo-range difference between user receiver and the reference receiver is 0.8 ns at most.
- Therefore, if there is less difference between correlator spacing of user receiver and the reference receiver, then there will much less pseudo-range biases.
- For example, if the correlator spacings of all user receivers are set to be in the range of [0.4–0.6 chips], then the double pseudo-range difference between user receiver and the reference receiver is 0.8 ns at most.

5 Pseudo-range Biases with RF Bandwidth

The radio front-end filter is used to guarantee the full pass of all useful signals while prevent out-band interference signals or other useless signals. It will bring in some useless signals if the filter bandwidth is too large, which will affect ranging accuracy.

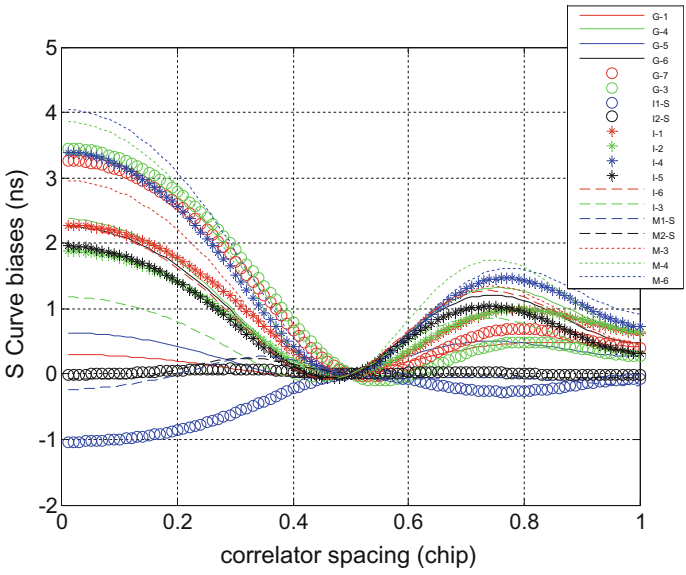

Fig. 4 S curve biases corresponding to a reference-receiver with its correlator spacing of 0.5 chips, in the condition of the single side bandwidths of 8 MHz

In this section, we will discuss about the effect of RF filter bandwidth on the measured pseudo-range biases. Here we assume the correlator spacing is identical for all receivers to better analyze the effect of bandwidth.

As we can see from Fig. 5:

- For a particular correlator spacing, there is much difference between lock points of S curves for different satellites.
- For a particular satellite, there is much difference between lock points of S curve for different bandwidths.
- For the same type of satellites, there is less difference between lock points of S curve with the same bandwidth.
- For different kinds of satellites, there is much difference between lock points of S curve with the same bandwidth.

If we assume the front-end bandwidth of the reference receiver is 4 MHz, then the lock points of S curves of B1I signals of different satellites are shown in Fig. 6.

It is obvious that:

- If the front-end bandwidths of all user receivers are set to be 2 MHz, then the double pseudo-range difference between user receiver and the reference receiver is 1 ns at most.
- If the front-end bandwidths of all user receivers are set to be 8 MHz, then the double pseudo-range difference between user receiver and the reference receiver is 2.8 ns at most.

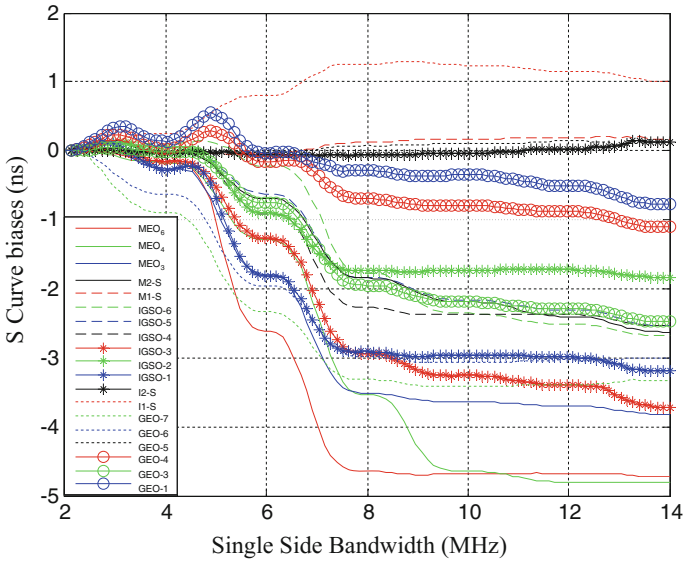

Fig. 5 Variation with single side band of S curve biases for BDS B1I, with correlator spacing of 0.5 chips

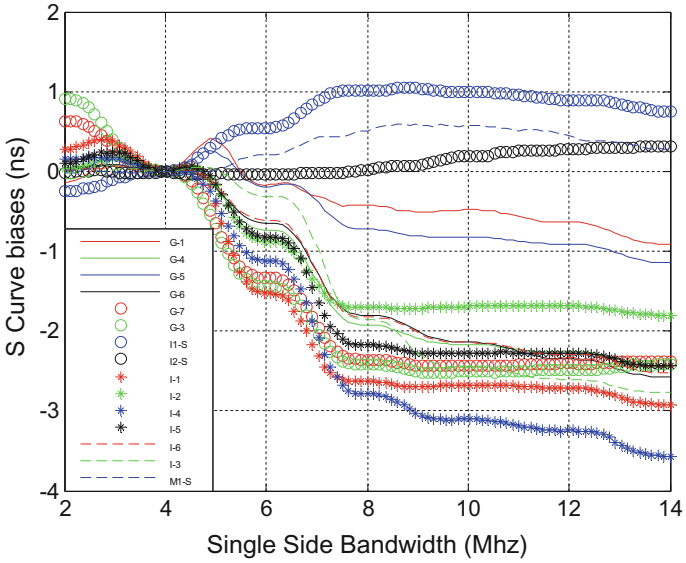

Fig. 6 S curve biases corresponding to a reference-receiver with single side bandwidth of 4 MHz, in the condition of correlators spacing of 0.5 chips

- Therefore, if there is less difference between front-end bandwidths of user receiver and the reference receiver, then there will much less pseudo-range biases.
- For example, if the front-end bandwidths of all user receivers are set to be in the range of [2–5 MHz], then the double pseudo-range difference between user receiver and the reference receiver is 1 ns at most.

6 Pseudo-range Biases with Satellite Elevation Angle

To analyze the effect of satellite elevation angle on pseudo-range biases, we collected each BDS satellite B1I signal every 10°. The ranging errors of B1I signals of BDS M1-S and M2-S experimental satellites with respect to satellite elevation angle are shown in Fig. 7.

We can get from Fig. 7 that the effect of satellite elevation angle on pseudo-range biases is in centimeter level and is less than 0.15 ns for BDS M1-S satellite and M2-S satellite. In fact, based on so many tests and verifications we have done, the effect of satellite elevation angle on pseudo-range biases is very less compared with RF front end bandwidth and correlator spacing. So it is safe to believe that for BDS system the effect of elevation angle is negligible. As a result, we would like to give some useful suggestions mainly on the bandwidth and correlator spacing for users in the end of this paper.

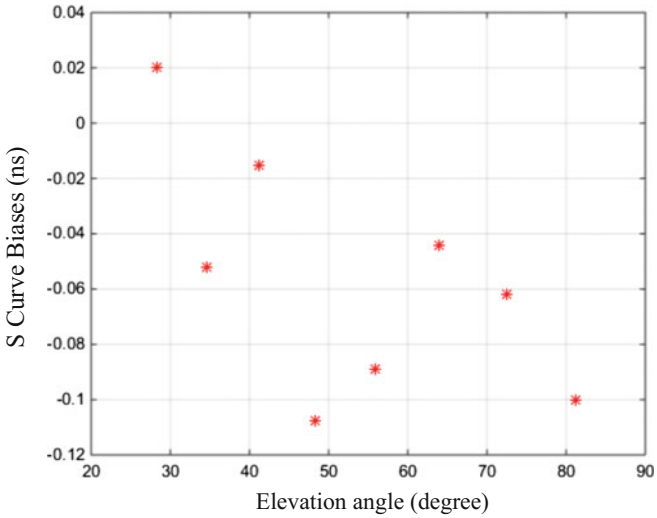

(a) S curve biases of M1-S B1I signal varies with elevation angels

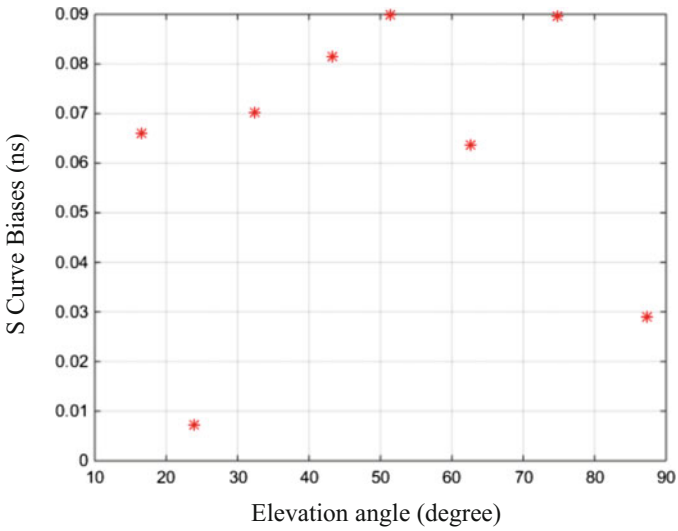

(b) S curve biases of M2-S B1I signal varies with elevation angels

Fig. 7 S curve biases with the variation of satellite elevation angle for BDS B1I signal: the upper picture Fig. 7a is that of M1-S satellite and the bottom picture Fig. 7b is that of M2-S satellite

7 Solutions and Conclusions

To sum up, the root cause of pseudo-range biases is the distortion of broadcasted signals, which is different for different satellites. This is why we obtained different ranging errors for different satellites, and it also explains well the pseudo-range biases phenomenon mentioned in the introduction of this paper.

In view of the pseudo-range biases occurred in BDS system, we carried out lots of test-and-verifications using the 40 m antenna system of HRO. Navigation signals of each BDS II satellite was collected by NI data collecting equipment and measurements were collected by different types of receivers. First, according to the phenomena and the characteristics of pseudo-range biases, the fundamental causes of pseudo-range biases were studied from theoretical analysis, formula derivation and experimental verification. Then the effects of pseudo-range biases on users were demonstrated in the condition of different correlator spacing, different front-end bandwidth and different satellite elevation angle. It is possible to draw the following conclusions:

- Satellite elevation angle has little effect on pseudo-range biase (centimeter level) and can be ignored;
- The difference of front-end bandwidth between different receivers will affect seriously the measurement result of pseudo-range biases: the smaller the difference of front-end bandwidth between receivers, the smaller the measured pseudo-range biases;
- The difference of correlator spacing between different receivers will also affect seriously the measurement result of pseudo-range biase: the smaller the difference of correlator spacing between receivers, the smaller the measured pseudo-range biases.

Therefore, it is suggested that all BDS receivers should better use the following settings:

- When the filter bandwidth and correlator spacing of reference receiver is known, then it is suggested that these parameters of user receiver is close to that of reference receiver, and the closer the better.
- If the filter bandwidth and correlator spacing of reference receiver is unknown, then it is suggested that these parameters of user receivers are close to each other and the closer the better. Only in this way, can we minimize the effect of pseudo-range biases on users. Here the choice of parameters setting is the trade-off between the performance and the cost of receivers.

Acknowledgements Test data for this work were provided by Haoping Radio Observatory (HRO), China. The authors would like to thank the staff in HRO of National Time Service Center, Chinese Academy of Sciences (CAS), for their support and data. The authors would like to acknowledge that this effort was sponsored by National Nature Science Foundation of China (No. 61501430) and Youth Innovation Promotion Association of the Chinese Academy of Sciences (CN). In particular, great thanks to the reviewers for their constructive comments.

References

1. Wong G, Phelts RE, Walter T et al (2011) Bounding errors caused by nominal GNSS signal deformations. In: Proceedings of the 24th international technical meeting of the satellite division of the institute of navigation, ION GNSS, Portland, OR
2. Coco DS, Coker C, Dahlke SR et al (1999) Variability of GPS satellite differential group delay biases. IEEE Trans Aerosp Electron Syst 27(6):931–938
3. Sardón E, Zarraoa N (1997) Estimation of total electron content using GPS data: how stable are the differential satellite and receiver instrumental biases? Radio Sci 32(5):1899–1910
4. Hauschild A, Montenbruck O (2016) A study on the dependency of GNSS pseudorange biases on correlator spacing. GPS Solutions 20(2):159–171
5. Hauschild AÉ, Montenbruck O (2016) The effect of correlator and front-end design on GNSS pseudorange biases for geodetic receivers. Navigation 63(4):443–453
6. Jefferson DC, Heflin MB, Muellerschoen RJ (2001) Examining the C1-P1 pseudorange bias. GPS Solutions 4(4):25–30
7. Wong G, Chen YH, Phelts RE et al (2012) Measuring code-phase differences due to inter-satellite hardware differences. In: Proceedings of the 25th international technical meeting of the satellite division of the institute of navigation, ION GNSS, Nashville
8. He C (2013) Research on evaluation methods of GNSS signal quality and the influence of GNSS signal on ranging performance. University of Chinese Academy of Sciences (National Time Service Center), China, p 2013
9. Wong G, Phelts R E, Walter T et al (2011) Alternative characterization of analog signal deformation for GNSS-GPS satellites. In: Proceedings of the 2011 international technical meeting of the institute of navigation, ION ITM, San Diego

Code Phase Bias Reduction in Spatial Adaptive Beam-Forming GNSS Receivers

Hailong Xu, Xiaowei Cui, Songtao Huangfu and Mingquan Lu

Abstract The adaptive beam-forming technique based on array antennas is an effective countermeasure towards suppressive interferences. However, it will induce distortions to the desired satellite signal, leading the code phase measurement in the receiver to be biased. This makes spatial adaptive beam-forming incompatible with high precision applications, so the high precision receivers have to be threatened by both intentional and unintentional interferences. To solve this issue, a method to reduce the code phase bias induced by spatial adaptive beam-forming is proposed in this paper. By constructing the beam steering vector properly and taking advantage of some common characteristics of the antenna element frequency response, the code phase biases can be estimated in all incident directions. Then these estimates can be used for bias compensation at the output of the code delay loop. The effectiveness of this method is validated by joint HFSS and Matlab simulations.

Keywords GNSS receiver · Antenna array · Anti-jamming · Adaptive beam-forming · High precision · Code phase measurement

1 Introduction

Due to that the power of the global navigation satellite system (GNSS) signal reaching the earth is very weak, the receiver is very easy to be blocked by jammers or unintentional interferences. To solve this issue, an effective countermeasure in the receiver is to use the adaptive beam-forming technique based array antennas. This technique can form nulls towards interferences in the composite array pattern, while maintain gains towards the desired satellite signals, thus the interferences are

H. Xu · X. Cui (✉) · M. Lu
Department of Electronic Engineering, Tsinghua University, Beijing 100084, China
e-mail: cxw2005@mail.tsinghua.edu.cn

S. Huangfu
Beijing Institute of Spacecraft System Engineering, Beijing 100094, China

J. Sun et al. (eds.), *China Satellite Navigation Conference (CSNC) 2018 Proceedings*, Lecture Notes in Electrical Engineering 498,
https://doi.org/10.1007/978-981-13-0014-1_4

suppressed and the signal to noise ratio (SNR) is enhanced [1]. Because of its outstanding anti-jamming performance to varied jamming patterns, this technique is widely used, especially in military fields.

Although the need for anti-jamming also exists in GNSS high-precision applications, high-precision receivers rarely adopt adaptive beam-forming arrays. This is because the latter will induce biases to the receiver code phase measurement, decreasing the final positioning accuracy [2, 3]. Under this condition, the high-precision receivers have to be threatened by jamming in some very critical applications, including land-based or sea-based aircraft auto-landing, and reference receiving or monitoring in differential positioning systems. Thus, some methods to reduce these biases should be adopted to let the adaptive beam-forming technique meet the high-precision requirements.

In this paper, an easy-to-implement method to reduce the code phase biases induced by the adaptive beam-forming arrays is proposed. By constructing the steering vector properly and taking advantage of some common characteristics of the antenna element frequency responses, estimation of these biases can be obtained. These estimates depends on the incident direction of the satellite signal, but are independent on the adaptive weights of the algorithm, thus can be prior calculated and stored in a look-up table (LUT). The receiver can use these estimates to compensate the biases at the output of the tracking loop. The effectiveness of the method is validated on an HFSS-designed seven-antenna array by simulation.

2 Adaptive Beam-Forming Technique

An adaptive beam-forming array can be regarded as a spatial filter, which adjusts the weights of different antenna elements according to the environment to achieve signal enhancement and interference mitigation. Typical algorithms include Minimum Variance Distortion-less Response (MVDR) and Minimum Power Distortion-less Response (MPDR). Considering the satellite signal power is well below the noise floor, these two algorithms have the same forms [4]. So MVDR is introduced below.

2.1 MVDR Algorithm

After orthogonally down conversion, the data received by the array can be expressed as

$$\mathbf{x}(n) = [x_1(n), x_2(n), x_3(n), \ldots, x_M(n)]^T \tag{1}$$

where n denotes the sampling period index. Then, the output weighted sum can be expressed as

$$y(n) = \mathbf{w}^H \mathbf{x}(n) \tag{2}$$

where $\mathbf{w}$ denotes the weighting vector. In this paper, lowercase bold letters denote vectors, and uppercase bold letters denote matrices.

Further, define the correlation matrix as

$$\mathbf{R} = \mathrm{E}\{\mathbf{x}(n)\mathbf{x}^H(n)\} \tag{3}$$

where $\mathrm{E}\{\cdot\}$ denotes the expectation operation. Then, the MVDR algorithm can be given as solving the optimal problem below [4]:

$$\mathbf{w_o} = \arg\min_{\mathbf{w}} \mathbf{w}^H \mathbf{R} \mathbf{w} \quad \text{s.t. } \mathbf{w}^H \mathbf{v_s} = 1 \tag{4}$$

which means minimizing the output power while keeping the signal incident along the direction described by the steering vector $\mathbf{v_s}$ undistorted. Considering that the interference power is above the thermal noise, while the satellite signal power is below, interferences can be mitigated under this optimal criterion. Using the Lagrange multiplier method, the optimal weighting vector can be solved as

$$\mathbf{w_o}^H = \frac{\mathbf{v_s}^H \mathbf{R}^{-1}}{\mathbf{v_s}^H \mathbf{R}^{-1} \mathbf{v_s}} \tag{5}$$

In practice, $\mathbf{R}$ is usually estimated through time averaging:

$$\hat{\mathbf{R}} = \frac{1}{K} \sum_{k=0}^{K-1} \mathbf{x}(k)\mathbf{x}^H(k) \tag{6}$$

where K denotes the number of used snapshots. The finity of K results that $\hat{\mathbf{R}}$ is perturbed from $\mathbf{R}$. But this perturbation will not change the distortionless feature of the desired signal along $\mathbf{v_s}$, which can be seen from Eq. (4), although it will possibly reduce the anti-jamming performance. It is worth noting that, the steering vector only represents the signal incident response on the array at a single frequency. However, the desired satellite signal is usually wideband. Derivations in the next section will show that, with the frequency response variations of the antenna, the distortionless feature at one frequency will not guarantee the code phase measurement is not biased.

2.2 Steering Vector Construction

In MVDR, the steering vector depends upon the array geometry and the incident direction of the desired signal. The antenna coordinate system is presented in Fig. 1, where the array lines in the X–Y plane, and the θ and φ denote the elevation and azimuth angles, respectively.

If all the antenna elements are assumed to be isotropic and have a frequency response of unity, the steering vector at the central frequency of the satellite signal can be calculated as

$$\mathbf{v_s} = \left[e^{-j\frac{2\pi f_c}{c}\mathbf{p}_1^T\mathbf{a}}, e^{-j\frac{2\pi f_c}{c}\mathbf{p}_2^T\mathbf{a}}, \cdots, e^{-j\frac{2\pi f_c}{c}\mathbf{p}_M^T\mathbf{a}} \right]^T \tag{7}$$

where f_c is the carrier frequency, c is the speed of light, $\mathbf{p}_i$ is the position of the i-th antenna element, and $\mathbf{a}$ is the incident vector of the satellite signal, which is given by

$$\mathbf{a} = -[\sin\theta_s \cos\varphi_s, \sin\theta_s \sin\varphi_s, \cos\theta_s]^T \tag{8}$$

where (θ_s, φ_s) denote the incident angles. Under the array narrowband assumption [4], this steering vector nearly completely describes the incident response, resulting no code phase biases.

In practice, the frequency response of the antenna element always varies along frequency, and is different in different directions, which can be described by $A(f, \theta, \varphi)$ [2, 3]. However, the steering vector still has to be calculated at a single frequency. Here, we still select the central frequency, then the steering vector turns to

$$\mathbf{v_{s,m}} = \mathbf{A}(f_c, \theta_s, \varphi_s)\mathbf{v_s} \tag{9}$$

where

$$\mathbf{A}(f_c, \theta_s, \varphi_s) = \mathrm{diag}\{A_1(f_c, \theta_s, \varphi_s), A_2(f_c, \theta_s, \varphi_s), \ldots, A_M(f_c, \theta_s, \varphi_s)\} \tag{10}$$

Steering vector $\mathbf{v_{s,m}}$ is used in the rest of this paper.

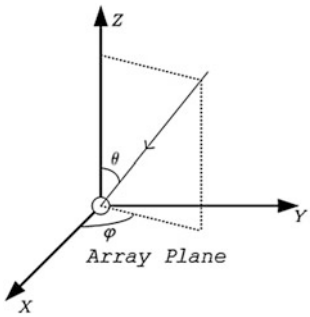

Fig. 1 The antenna coordinate system

3 Code Phase Bias Reduction

In this section, firstly, the theoretical calculation method of the code phase bias is given. Then, a more easy-to-implement bias reduction method is proposed.

3.1 Theoretical Calculation of the Code Phase Bias

The frequency response of the adaptive beam-forming array can be given by following transfer function:

$$H(f, \theta_s, \varphi_s) = \mathbf{w}_{\mathrm{o}}^H \mathbf{A}(f, \theta_s, \varphi_s)\mathbf{v_s} \tag{11}$$

From Eqs. (4) and (9) it can only be concluded that $H(f_c, \theta_s, \varphi_s) = 1$, rather than the linear phase response in the whole frequency band, which is the cause of the code phase bias.

In the receiver, a local ranging code replica is used to correlate with the received data after weighted summing. The correlation function is

$$R(\tau, \theta_s, \varphi_s) = \int d(t) d_r(t - \tau) \mathrm{d}t \tag{12}$$

where $d(t)$ is the received data and $d_r(t - \tau)$ is the time-delay code replica. By Wiener-Khintchine Theorem [4], the correlation function can be further written as

$$R(\tau, \theta_s, \varphi_s) = \int \Phi_{ss}(f) H(f, \theta_s, \varphi_s) \mathrm{e}^{\mathrm{j}2\pi f \tau} \mathrm{d}f \tag{13}$$

where $\Phi_{ss}(f)$ is the normalized spectrum density of $d(t)$. The code phase measurement is obtained in the at the peak of $R(\tau, \theta_s, \varphi_s)$, thus the code phase bias ρ_{bias} corresponds to the time shift of the peak τ_{bias}, i.e.,

$$\tau_{bias}(\theta_s, \varphi_s) = \arg\max_{\tau} |R(\tau, \theta_s, \varphi_s)| \tag{14}$$

$$\rho_{bias} = c \cdot \tau_{bias}(\theta_s, \varphi_s) \tag{15}$$

where ρ_{bias} is in meters [5].

3.2 Proposed Code Phase Bias Estimation and Reduction

The value ρ_{bias} calculated above can be used to compensate the biases at the output of the receiver tracking loop. However, in practice this method is difficult to

implement. The reasons are as follows: First, the adaptive weights are needed, meaning ρ_{bias} must be updated along with the weights, whose update rate is very rapid. Moreover, this update rate may be not synchronous with the integral interval of the tracking loop. Second, the integral operation (13) means lots of calculation amount. Third, calculation of $H(f, \theta_s, \varphi_s)$ needs the frequency response of all the antenna elements in the whole band and all directions, which means tremendous labor in the anechoic chamber.

Actually, the antenna frequency response is not arbitrary, and some common characteristics can be taken advantage of to derive a simpler bias estimation method. The derivations are given as below.

To investigate $H(f, \theta_s, \phi_s)$ more delicately, divide $A_i(f, \theta_s, \varphi_s)$ to two parts by amplitude and phase. Assume within the signal bandwidth, the amplitude response is flat enough, while the phase response can be fitted into a linear function, then we have

$$\begin{aligned} A_i(f, \theta_s, \varphi_s) &\approx |A_i(f_c, \theta_s, \varphi_s)| \mathrm{e}^{\mathrm{j}[\angle \mathrm{A}_i(f_c, \theta_s, \varphi_s) + \alpha_{i,1}(\theta_s, \varphi_s)(f - f_c)]} \\ &= A_i(f_c, \theta_s, \varphi_s) \mathrm{e}^{\mathrm{j}\alpha_{i,1}(\theta_s, \varphi_s)(f - f_c)} \end{aligned} \tag{16}$$

As a step further, assume $\alpha_{i,1}(\theta_s, \varphi_s)$ is similar between different i, i.e.,

$$\alpha_{i,1}(\theta_s, \varphi_s) \approx \alpha_1(\theta_s, \varphi_s), \quad i = 1, 2, \ldots, M \tag{17}$$

Then

$$\mathbf{A}(f, \theta_s, \varphi_s) = \mathbf{A}(f_c, \theta_s, \varphi_s) \mathrm{e}^{\mathrm{j}\alpha_1(\theta_s, \varphi_s)(f - f_c)} \tag{18}$$

Substitute this equation into (11), considering $\mathbf{w}_{\mathrm{o}}^H \mathbf{A}(f_c, \theta_s, \varphi_s)\mathbf{v_s} = 1$ in MVDR, the transfer function can be simplified as

$$H(f, \theta_s, \varphi_s) \approx \mathrm{e}^{\mathrm{j}\alpha_1(\theta_s, \varphi_s)(f - f_c)} \tag{19}$$

Substitute this equation into (13), then the estimate of ρ_{bias} is obtained by

$$\hat{\rho}_{bias} = -c \cdot \alpha_1(\theta_s, \varphi_s) \tag{20}$$

where $\alpha_1(\theta_s, \varphi_s)$ can be obtained through averaging, i.e.,

$$\hat{\rho}_{bias} = -\frac{c}{M} \sum_{i=1}^{M} \alpha_{1,i}(\theta_s, \varphi_s) \tag{21}$$

Compared with the theoretical method above, this method only needs the first order coefficients of Taylor expansion of the antenna phase response, so the measurement labor in the anechoic chamber is greatly decreased. Besides, the bias estimated values can be prior calculated and stored in a LUT indexed by the

incident direction angles, thus no on-the-fly calculation is required. While the receiver is running, the estimated value corresponding to the incident direction in the LUT is used for bias compensation in the tracking loop output. Note that this method is based on a few assumptions about the antenna frequency response, which are discussed below.

3.3 Discussion

The first assumption the method is based on is that, the amplitude response for each antenna element within the signal bandwidth is plain enough. This is a common requirement in the antenna design and is often strictly required. The second assumption is that the phase response for each antenna element can be approximated by Taylor first order expansion, and the first order coefficients which correspond to the group delay are nearly the same. This means that the signal transfer paths behind each antenna should have the same length, which can be required in the design [6]. Besides, the inconsistency between different radio frequency (RF) channels can also influence the code phase measurement. Compared with the antenna whose frequency response is stable after manufacturing, the frequency response of RF channels can vary rapidly with the environment and aging of the equipment, thus is difficult to calibrate priory. However, these inconsistencies can be reduced by on-the-fly equalisation effectively [7].

4 Simulation

Simulations are performed in this section to validate the proposed method. Instead of measuring the frequency response of a real array antenna in the anechoic chamber, a simulated antenna designed by ANSYS HFSS® is used. This software is the industry standard for simulating high-frequency electromagnetic fields and of high fidelity. Using it we can acquire the full characteristics of the designed antenna.

4.1 Antenna Array Characteristics

The geometry of the array antenna is hexagonal and consists of seven elements, which is presented in Fig. 2. Each element is a microstrip antenna resonating at 1575.42 MHz, with the bandwidth of 20 MHz. Separation distance between adjacent elements is half wavelength of the carrier frequency. Figure 3 presents the gain patterns of all the elements at the central frequency, in which the radial corresponds

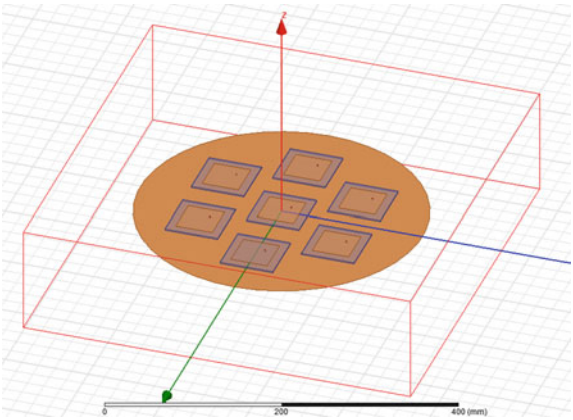

Fig. 2 The seven-element array designed by HFSS

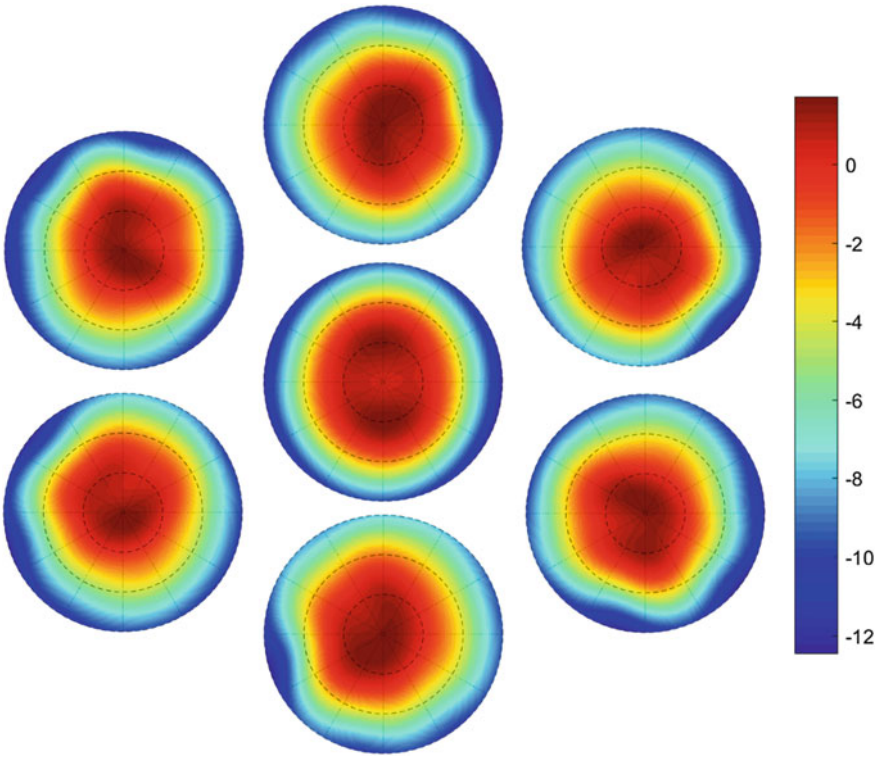

Fig. 3 Antenna element gain patterns at the carrier frequency

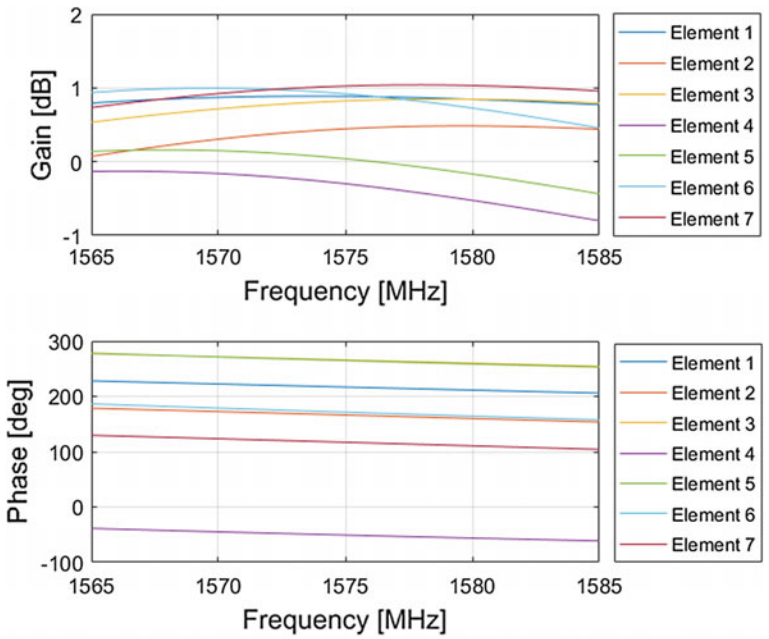

Fig. 4 Antenna element frequency response

to the elevation and the direction along the circle corresponds to the azimuth. Due to mutual coupling and the finite ground effect, the gain pattern is anisotropic.

Moreover, Fig. 4 presents the amplitude and phase responses of all the elements in a certain direction. It can be seen that the gain is quite flat in the bandwidth, and the phase response meet the second assumption declared in Sect. 3.3. It is worth noting that the phase response of this antenna is not specially designed, so the assumed phase response is a common character, further showing the rationality of the assumption.

4.2 Code Phase Bias Reduction Performance

On this array antenna above, the propose method is validated. The desired satellite signal is assumed to be Binary Phase Shift Keying (BPSK) modulated, with the chip rate of 10.23 MHz. Three white Gaussian noise (WGN) jammers are placed in the environment, with the interference-to-noise ratio (INR) being 60 dB. First, the code phase bias is calculated by the theoretical method given in Eq. (15), and the results are presented in Fig. 5. It shows that the biases are different for different directions. Except for the directions near the jammers where large biases occur, other directions also see bias variation of about 1 meters. This uncommon bias for between different satellite signals can lead the final solved position to be biased.

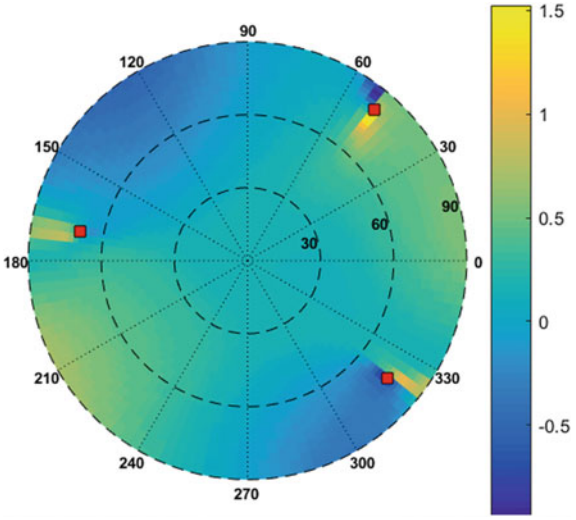

Fig. 5 Code phase bias in meters calculated by the theoretical method. Jammers are presented by the red blocks

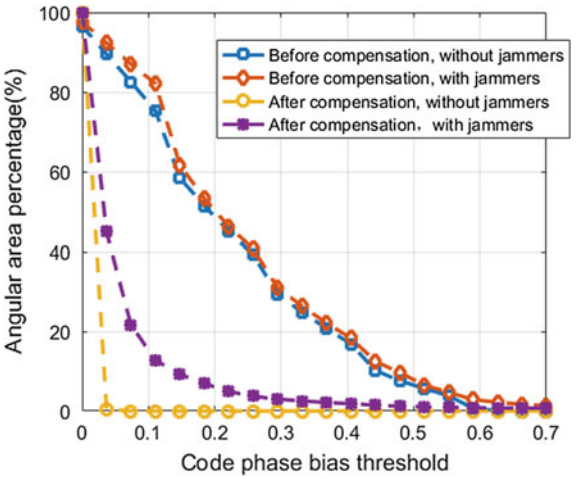

Fig. 6 Code phase bias reduction performance. The horizontal axis represents the code phase bias threshold. The vertical axis represents the angular area percentage in the whole upper hemisphere where the code phase bias (before compensation) or the residual bias (after compensation) is above the threshold. Both conditions with and without jammers are presented

Then, using the proposed method in Eq. (21), bias values are estimated in all directions, before which the bias in Fig. 5 are compensated. The bias reduction performance is described in Fig. 6. Before compensation, whether the jammers exit or not, in more than 70% directions the bias is larger than 0.1 m. After compensation, when the jammers are off, in nearly all directions, the residual bias is close to zero. When the jammers are on, only in about 15% directions, the residual bias is above 0.1 m. Further investigation shows that these directions are all near the jammers. These directions are not valid for the receiver, for the desired signal is severely degraded. Therefore, above results show that the proposed method can reduce the code phase bias very well.

5 Conclusion

Towards the issue of code phase bias induced by the adaptive beam-forming, a new method is proposed to reduce the bias. By taking advantage of the assumed common characters of the antenna, the implementation difficulty can be greatly decreased compared with the former theoretical method. These assumed characters can be met by laying reasonable requirements to the antenna design. The values of these requirements can be determined by further simulations and real experiments.

References

1. Fante L, Vaccaro J (2000) Wideband cancellation of interference in a GPS receive array. IEEE Trans Aerosp Electron Syst 36(2):549–564
2. Prades C, Arribas J, Closas P (2016) Robust GNSS receivers by array signal processing: theory and implementation. Proc IEEE 104(6):1207–1220
3. O'Brien J, Gupta J (2010) An optimal adaptive filtering algorithm with zero antenna-induced bias for GNSS antenna arrays. Navigation 57(2):87–100
4. Van T, Harry L (2002) Optimum array processing: Part IV of detection, estimation and modulation theory. Wiley, New York
5. Church M, Gupta J (2009) Estimation of adaptive antenna induced code and carrier phase bias in GNSS receivers. Navigation 56(3):151–160
6. Stutzman W, Thiele G (2013) Antenna theory and design. Wiley, New York
7. Farina A (2003) Digital equalisation in adaptive spatial filtering for radar systems: a survey. Sig Process 83(1):11–29

Multipath Mitigation Method for BOC Signals Dual Estimation Technology Based on Synthesized Correlation Function

Nengjie Yu, Jiantao Ruan, Qijia Dong and Dun Wang

Abstract Dual Estimation Technique (DET) is mainly used to achieve unambiguous tracking of high-order BOC signals. DET has a good tracking performance, but its anti-multipath performance need to be further improved. In this paper, the method of designing a synthesized correlation function(SCF) based on step-shape code symbol (SCS) is applied to the DET. Anti-multipath performance of DET is improved by introducing the special SCS signal to participate in the coherent integration process with the received signal. The improved DET is flexible in designing, no need of additional correlator, and only design a SCS vector to achieve anti-multipath performance improvement. The theoretical derivation and concrete implement of the improved DET are analyzed, and simulations are conducted in both anti-multipath and tracking performance. The results show that when the 4 order SCS vector is used, compared with the traditional DET, the multipath error envelope area of BOC (2,1) and BOC (14,2) signal tracked by the improved DET can be reduced 62.6 and 70.4% respectively. But at the same time, it will bring about 6 dB coherent integration gain loss. All of the above shows that this method is only suitable for the unambiguous and anti-multipath tracking of the strong BOC signals.

Keywords Dual estimation technique · BOC signal · Synthesized correlation function · Anti-multipath performance

N. Yu (✉)
Tsinghua University, Beijing 100084, China
e-mail: ynjfish@163.com

J. Ruan · Q. Dong · D. Wang
Beijing Institute of Satellite Information Engineering, Zhichunli
No. 82, Haidian District, Beijing, China

J. Sun et al. (eds.), *China Satellite Navigation Conference (CSNC) 2018 Proceedings*, Lecture Notes in Electrical Engineering 498,
https://doi.org/10.1007/978-981-13-0014-1_5

1 Introduction

Binary Offset Carrier (BOC) signal is widely used in the new generation of satellite navigation system. Compared with the traditional Binary Phase Shift Keying (BPSK) signal, the BOC signal has a larger Gabor bandwidth, higher code tracking accuracy, and better anti-interference and anti-multipath performance [1]. However, there are multiple peak points in the auto-correlation function (ACF) of BOC signals, and the number of peak points increases with the BOC signal order. Therefore, using the traditional tracking structure to track the BOC signal will be mistakenly locked in the side peak easily, which is tracking ambiguous.

A great deal of research has been done on the problem of ambiguous tracking of BOC signals and many solutions have been proposed [2–4]. The newly proposed DET uses the Delay-Locked Loop (DLL) and the Subcarrier Lock Loop (SLL) to track the pseudo-code and sub-carrier components of the BOC signal respectively and achieves a full accuracy of BOC signal without tracking ambiguity. The tracking structure of DET is simple and easy to implement, so it currently widely used in the new generation navigation signal receiver.

Though DET has better tracking performance, its anti-multipath performance is only equivalent to traditional DLL. The performance of DET depends on the sub-carrier tracking loop [5], and the anti-multipath performance of DET can be improved by using the correlator. However, in the band-limited channel, the capability of using correlator to improve the anti-multipath performance is limited [6].

In newly research, an effective anti-multipath algorithm for DET tracking structure is to modify the cross-correlation function (CCF) between the DLL signal supplied to the SLL and the pseudo-code component in the received BOC navigation signal [7, 8], which is hereinafter referred to as DET double-loop interactive CCF, to achieve effective multipath signals mitigation. GAO Yang et al. add an early phase shift to the prompt code signal provided by the DLL to the SLL, the coverage area of the DET double loop interactive CCF is advanced offset and the non-zero interval of CCF in the multi-path sensitive area is reduced, therefore, the anti-multipath performance of the algorithm is effectively improved [7]. Xu et al. use code correlation reference waveforms in phase with prompt code instead of prompt code to provide for SLL and reduce the non-zero interval of double loop interactive CCF to improve anti-multipath performance [8]. All of the above shows that DET anti-multipath performance can be effectively improved by designing DET double-loop interactive CCF.

Yao and Lu put forward a design framework for generating a SCF without side peaks based on SCS signal to achieve a unambiguity tracking of the BOC signal [9]. In this paper, we apply it to DET and propose a method to improve the anti-multipath performance of DET by designing double-loop interactive CCF. Compared to traditional DET, this method has reduced multipath error envelope area of 62.6% for BOC (2,1) signals and 70.4% for BOC (14,2) signals.

2 Improved Multipath Mitigation Method

2.1 Anti-multipath Improved DET Structure

The loop structure of DET consists of DLL and SLL. The DLL tracks the PRN code and an unambiguous time-delay of PRN code is estimated. Then the estimated PRN code time-delay $\hat{\tau}_c$ is provided to SLL to aid the tracking of subcarrier phase. And the SLL tracks the subcarrier time-delay $\hat{\tau}_{sc}$ and provided it to DLL. The DLL and SLL cooperate to achieve a stable tracking of the input signal phase.

The structure of anti-multipath improvement DET (hereinafter referred to as improved DET) is showed in Fig. 1. Different from the traditional DET structure, the improved DET adds an additional SCS signal generator to the DLL, and the generated SCS signal is provided directly to the SLL for the correlation integral with the receiving BOC signal. The SCS signal generator is controlled by the DLL NCO to generate a signal in phase with the prompt replica code in DLL.

Suppose that the input signal in Fig. 1 is the baseband signal and only has one multipath signal. The baseband input signal can be expressed as

$$\begin{cases} s_{BOC}(t-\tau) = c(t-\tau) * sc(t-\tau) \\ r(t) = a_0 s_{BOC}(t-\tau_0)\cos\varphi_0 + a_1 s_{BOC}(t-\tau_1)\cos\varphi_1 \end{cases} \tag{2.1}$$

In Eq. (2.1), τ is the time delay of the received signal. $c(t-\tau), s(t-\tau)$ denote the pseudo-code and subcarrier of the BOC modulated signal, respectively.τ_0, τ_1 are the direct and multipath signal delay. And φ_0, φ_1 are the carrier demodulation phase error of direct signal and multipath signal respectively. a_0, a_1 are the amplitudes of direct and multipath signals. The multipath-to-Direct Ratio (MDR) of the received signal can be expressed as $\alpha_1 = a_1/a_0$.

In traditional DET, we define the ACF of the pseudo-code as $R_{PRN}(\tau)$, the ACF of the subcarrier as $R_{SUB}(\tau)$, and the double-loop interactive CCF as $R_{DLL/SLL}(\tau)$,

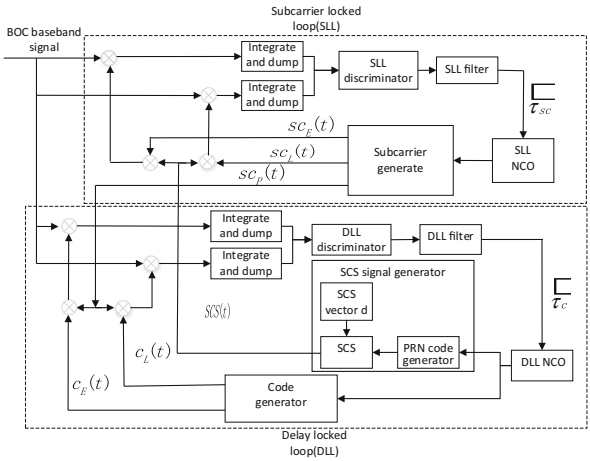

Fig. 1 Schematic representation of the modified DET

there is $R_{DLL/SLL}(\tau) = R_{PRN}(\tau)$. The correlation integral output of the local early replica signal and received signal in SLL can be expressed as [10]

$$\begin{aligned} R_{E\_SLL}(\tau) &= \frac{1}{T_c}\int_0^{T_c} S_{E\_SLL}(t-\hat{\tau}_c, t-\hat{\tau}_{sc}) \cdot S_{BOC}(t-\tau) \\ &= R_{PRN}(\hat{\tau}_c - \tau) \cdot R_{SUB}\left(\hat{\tau}_{sc} - \frac{d_s}{2} - \tau\right) \\ &= R_{DLL/SLL}(\hat{\tau}_c - \tau) \cdot R_{SUB}\left(\hat{\tau}_{sc} - \frac{d_s}{2} - \tau\right) \end{aligned} \tag{2.2}$$

The SLL use Early-Minus-Late (EML) discriminator. And denote the EML discriminator output of the subcarrier as $D_{SUB}(\tau)$, the EML discriminator output of the SLL under the influence of the multipath signal can be expressed as

$$\begin{aligned} D_{SLL}(\hat{\tau}_{sc}) = {} & a_0 \cdot R_{DLL/SLL}(\hat{\tau}_c - \tau_0) \cdot D_{SUB}(\hat{\tau}_{sc} - \tau_0) \\ & + a_1 \cdot R_{DLL/SLL}(\hat{\tau}_c - \tau_1) \cdot D_{SUB}(\hat{\tau}_{sc} - \tau_1) \end{aligned} \tag{2.3}$$

From Eq. (2.3), the MDR of the subcarrier signal components tracked in the SLL of the improved DET is no longer α_1, but changed into α_{1_SLL} as follows

$$\alpha_{1\_SLL} = \alpha_1 \cdot \frac{R_{DLL/SLL}(\hat{\tau}_c - \tau_1)}{R_{DLL/SLL}(\hat{\tau}_c - \tau_0)} \tag{2.4}$$

In order to simplify the analysis of the SLL, assuming that the phase of the BOC pseudo-code component is precisely synchronized, i.e. $\hat{\tau}_c = \tau_0$, then

$$\alpha_{1\_SLL} = \alpha_1 \cdot \frac{R_{DLL/SLL}(\hat{\tau}_c - \tau_1)}{R_{DLL/SLL}(0)} = \frac{\alpha_1}{A} R_{DLL/SLL}(\tau_1 - \tau_0) \tag{2.5}$$

where A is the peak of $R_{DLL/SLL}(\tau)$ and $R_{DLL/SLL}(\tau)/A$ is the normalized CCF. From Eq. (2.5), $R_{DLL/SLL}(\tau)$ determines the equivalent MDR of subcarrier signals tracked by the SLL. Therefore, we can effectively improve the anti-multipath performance of the algorithm by design a $R_{DLL/SLL}(\tau)$.

The anti-multipath $R_{DLL/SLL}(\tau)$ design criteria in multipath-sensitive regions ($0 < \tau < 1.5$ chips) can be summarized as follows:

(1) Cross-correlation peak should be as sharp as possible;
(2) CCF non-zero area should be as small as possible;
(3) CCF side peak should be as small as possible.

In the improved DET, the SCS signal $S_{SCS}(t)$ is substituted for the locally generated prompt code signal $c(t)$. The $R_{DLL/SLL}(\tau)$ in improved DET becomes

$$R_{DLL/SLL}(\tau) = \frac{1}{T_c}\int_0^{T_c} S_{SCS}(t) \cdot c(t+\tau)dt \tag{2.6}$$

The pseudo-code component $c(t+\tau)$ of the received BOC signal can't be changed, but the $S_{SCS}(t)$ can be generated locally in the receiver. So we can design a $S_{SCS}(t)$ signal to synthesize $R_{DLL/SLL}(\tau)$ that meets the CCF design criteria.

2.2 Design of Anti-multipath SCF

The navigation baseband signals can be represented by step-shape code symbols (SCS) [9]. The time-domain mathematical model of GNSS baseband signal can be expressed as

$$S(t) = \sum_{i=-\infty}^{\infty} c_i \sum_{k=0}^{M-1} d_k \varphi_k(t - iT_c) \tag{2.7}$$

$$\varphi_k(t) = \begin{cases} 1, & (k-1)T_s \le t \le kT_s \\ 0, & \text{otherwise} \end{cases} \tag{2.8}$$

The rectangular pulse signal set $\varphi_k(t - iMT_s)(0 \le i \le M-1)$ is an orthogonal basis. d_k is the mapping coefficient of the signal waveform on the set of orthogonal basis, and d_k needs to satisfy the energy normalization constraint

$$\frac{1}{M}\sum_{k=0}^{M-1} d_k^2 = 1 \tag{2.9}$$

Therefore, for a given rectangular pulse signal set $\varphi_k(t - iMT_s)$, the required waveform can be obtained by designing the SCS vector $d = [d_0 \ldots d_{M-1}]$, M is the order. The local waveform $S_{SCS}(t)$ is designed such that the DET double loop interactive CCF satisfies the design criteria. $S_{SCS}(t)$ and $S_{PRN}(t)$ can be expressed as

$$\begin{cases} S_{PRN}(t) = \sum\limits_{i=-\infty}^{\infty} \sum\limits_{k=0}^{M-1} c_i d_k \varphi_k(t - iMT_s) \\ S_{SCS}(t) = \sum\limits_{j=-\infty}^{\infty} \sum\limits_{l=0}^{M-1} c_i d'_l \varphi_l(t - jMT_s) \end{cases} \tag{2.10}$$

For pseudo-code signal, there is $d_k = 1(0 \le k < M)$. The SCF of under the SCS vector d_S expressed as

$$R(\tau; d_S) = \begin{cases} \left(\frac{\tau M - kT_c}{T_c}\right)(r_{k+1} - r_k) + r_k, & \frac{kT_c}{M} \le \tau < \frac{(k+1)T_c}{M} \\ \left(\frac{\tau M - kT_c + MT_c}{T_c}\right)(r_{k-M+1} - r_{k-M}) + r_{k-M}, & \frac{kT_c}{M} \le \tau < \frac{(k+1)T_c}{M} \\ 0, & \text{others} \end{cases} \tag{2.11}$$

And

$$r_k(d, d') = \begin{cases} \frac{1}{M} \sum_{i=0}^{M-1-k} d'_{k+i}, & 0 \le k \le M-1 \\ \frac{1}{M} \sum_{i=0}^{M-1-k} d'_i, & 1-M \le k < 0 \\ 0, & |k| \ge M \end{cases} \tag{2.12}$$

The $R_{DLL/SLL}(\tau)$ satisfies the anti-multipath CCF criterion can be expressed as follows

$$R_{DLL/SLL}(\tau; d_S) = \begin{cases} 1 - \frac{\tau M}{nT_c}, & 0 \le \tau < \frac{(n+1)T_c}{M} \\ 0, & \frac{(n+1)T_c}{M} \le \tau < T_c \end{cases} \tag{2.13}$$

To generate a synthesis CCF of Eq. (2.13), we can obtain the SCS vector in conjunction with Eqs. (2.11–2.13) as follows

$$d(i, n) = \begin{cases} d_i = d_{i+1} = \sqrt{\frac{M}{n}}, & 0 \le i \le n-1 \\ 0, & n < i \le M-1 \end{cases} \tag{2.14}$$

Taking $M = 4$ as an example, the SCS vector that satisfies the anti-multipath CCF criterion when the multi-path delay $\tau > 0$ can be expressed as follows

(1) $d_1 = [2/\sqrt{3}, 2/\sqrt{3}, 2/\sqrt{3}, 0]$;
(2) $d_2 = [\sqrt{2}, \sqrt{2}, 0, 0]$;
(3) $d_3 = [2, 0, 0, 0]$.

Besides, increasing M will design more SCS vectors that satisfy the anti-multipath CCF criteria.

2.3 Multipath Mitigation Performance Analysis

The waveform of the $S_{SCS}(t)$ signal designed by d_1, d_2 and d_3 is showed in Fig. 2a. From Fig. 2a the non-zero interval width of the SCS signal designed by vector d_1 is 0.75 chip, the d_2 vector is 0.5 chip, and the d_3 vector is only 0.25 chip.

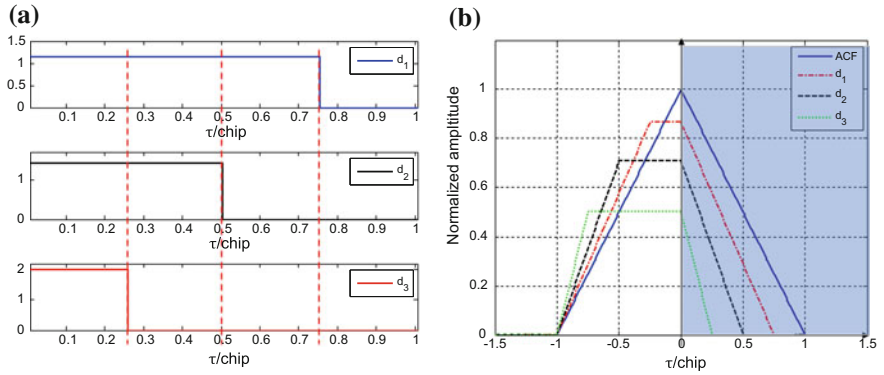

Fig. 2 **a** The waveform designed by vector d_1, d_2 and d_3 in a single chip; **b** synthesized correlation function

Figure 2b shows the SCF of $S_{SCS}(t)$ and $S_{PRN}(t)$ generated by using SCS vector d_1, d_2 and d_3. The shadow part is a multipath sensitive region (the relative multipath delay is greater than 0). The SCFs of d_1, d_2 and d_3 are not symmetrical triangles, and only have the correlation triangular spikes in the multipath-sensitive regions. From Eq. (2.5), the equivalent MDR of the signal tracked by SLL is only related to the $\tau > 0$ part of $R_{DLL/SLL}(\tau)$. Therefore, we mainly analyze the SCF of $R_{DLL/SLL}(\tau)$ at $\tau > 0$. The SCF $R_{DLL/SLL}(\tau)$ only affects the MDR of the subcarrier component of the received BOC signal tracked by the SLL, and does not affect its correlation function characteristics. So the asymmetry of the correlation function does not cause tracking ambiguity for the improved DET. From Fig. 2a, b, the width of the zero interval of the CCF is determined by the width of the zero-value interval of the signal waveform, which is constructed by the SCS vector. From Eq. (2.5), we can know that the MDR of the tracking signal is zero in the zero interval of the SCF, that is, the influence of multipath signals in this interval can be completely eliminated.

Taking d_1, d_2 and d_3 vectors for example, the SCF designed by d_1, d_2 and d_3 vector can be completely eliminate the effect of multipath signals whose delay larger than 0.75, 0.5 and 0.25 chip, theoretically.

Though the anti-multipath performance of improved DET is enhanced but the carrier-to-noise ratio (CNR) of the correlated integral output is reduced. From Fig. 2a, the *M* order SCS vector divides a single code chip into *M* small symbols. Suppose the number of sampling points per symbol is *N*, then the sampling points of one chip is $M \cdot N$, and $\sqrt{P_s}$ is the power of the received signal, the integrated output within one chip can be expressed as

$$\text{sum} = \sum_{i=1}^{M} d_i \left(N\sqrt{P_s} + \sum_{j=1}^{N} n((i-1)N + j) \right) \tag{2.15}$$

In Eq. (2.15), $n(\mathrm{i})$ is a Gauss white noise signal with a variance of σ, and the CNR of the correlation integral output can be expressed as

$$\mathrm{CN}_0 = \frac{\left(\sum_{\mathrm{i}=1}^{\mathrm{M}} \mathrm{d_i N}\sqrt{\mathrm{P_s}}\right)^2}{\left(\sum_{\mathrm{i}=1}^{\mathrm{M}} \mathrm{d_i} \sum_{\mathrm{j}=1}^{\mathrm{N}} \mathrm{n}((\mathrm{i}-1)\mathrm{N}+\mathrm{j})\right)^2} \tag{2.16}$$

If the nonzero coefficients in vector d are equal and the number is m, $1 \le m \le M$, then Eq. (2.16) can be simplified to

$$\mathrm{CN}_0 = \frac{\mathrm{m^2 N^2 P_s}}{\mathrm{mN}\sigma^2} = \mathrm{mN}\frac{\mathrm{P_s}}{\sigma^2} \tag{2.17}$$

In traditional DET, there is $m = M$. Therefore, if the non-zero coefficients of vector d are equal, the CNR loss of improved DET is

$$\mathrm{L_{CNR}} = 10\mathrm{lg}(\mathrm{m}/\mathrm{M}) \tag{2.18}$$

The root mean square error (RMS) of random phase caused by the thermal noise in the tracking loop can be expressed as

$$\sigma_{\mathrm{n}} = \sqrt{\frac{\mathrm{B_n}}{\mathrm{CN_0}}\left[1 + \frac{1}{2\mathrm{CN_0 T_I}}\right]} \tag{2.19}$$

In Eq. (2.19), $\mathrm{B_n}$ is the tracking loop bandwidth, $\mathrm{CN_0}$ is the CNR, and $\mathrm{T_I}$ is the integration time. The CNR loss in the improved DET will reduce the loop tracking accuracy.

From Eqs. (2.5) and (2.17), the magnitude of the SCS vector does not affect the anti-multipath performance and the correlation integral gain under ideal conditions. Taking signals constructed by $\mathrm{d}_1, \mathrm{d}_2$ and d_3 vectors as an example, the theoretical values of the CNR losses of using $\mathrm{d}_1, \mathrm{d}_2$ and d_3 are 1.25, 3 and 6 dB.

3 Simulation and Analysis of Improved DET Performance

3.1 Multipath Mitigation Performance Analysis

In this part,the anti-multipath performance of the traditional DET and improved DET is simulated and analyzed. BOC (2,1) and BOC (14,2) are selected as the representative of the low and high order BOC signal, and the bandwidth of them are 20, 32 MHz, respectively. The signals provided to the SLL by the DLL are generated using the previously designed $\mathrm{d}_1, \mathrm{d}_2$ and d_3. DET and improved DET both use EMLP discriminator in DLL, while SLL use DP discriminator. Simulation

signal contains only 1 path multipath signal, and the MDR of the multipath signal is −3 dB.

As showed in Figs. 3 and 4, compared to the traditional DET, the improved DET's anti-multipath performance has been significantly improved. The improved DET using d_1, d_2 and d_3 vectors can effectively mitigation the effects of multipath signals which phase delays greater than 0.75 chips, 0.5 chips, and 0.25 chips respectively. The anti-multipath performance of the improved DET using d_3 vector is the best,compared with the traditional DET, the envelope area of multipath error for input BOC (2,1) signal is reduced by 62.6%.

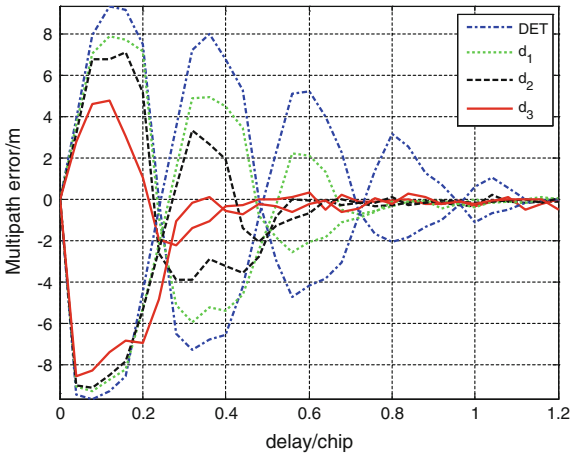

Fig. 3 Multipath error envelope of BOC (2,1)

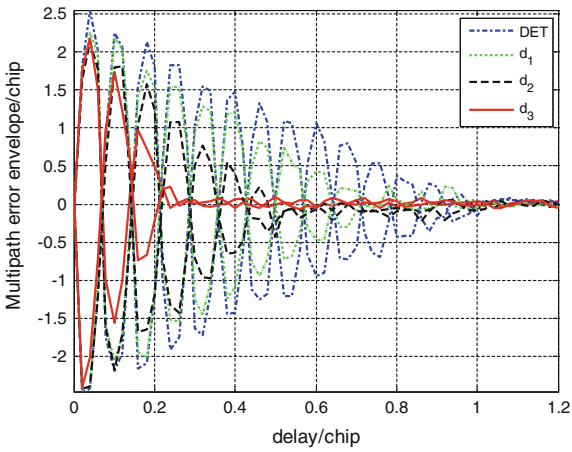

Fig. 4 Multipath error envelope of BOC (14,2)

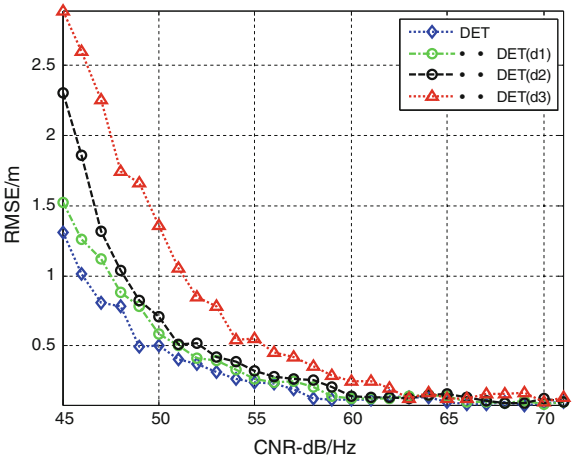

Fig. 5 Code tracking RMSE versus CNR

3.2 Tracking Performance

Figure 5 shows the simulation results of the tracking accuracy for BOC (2, 1) signal with the traditional DET and improved DET under different CNR. The front bandwidth of input BOC (2, 1) baseband signal is 20 MHz, and sampling rate is 61.38 MHz. The DLL of DET and improved DET both use EMLP discriminator, while SLL use DP discriminator. Loop bandwidth of DLL and SLL are both 2 Hz.

From Fig. 5, the improved DET adopting d_1, d_2 and d_3 vectors has a significantly lower tracking accuracy than the traditional DET. With the reduction of non-zero coefficients in the SCS vector, the zero-value region of the SCS signal is increased, which causes a coherent integration gain loss. Compared to traditional DET, the tracking accuracy of improved DET using d_1 vector is reduced about 1 dB (CNR), d_2 vector is reduced about 3 dB, and d_3 vector is reduced about 6 dB, which is nearly in line with the theoretical results.

4 Conclusions

In this paper, a method to improve the anti-multipath performance of DET by designing a special SCF is proposed, which can be used to conduct an unambiguous and anti-multipath tracking for BOC signals. The proposed method only needs to design the SCS signal locally generated in DLL to achieve different multipath mitigation effects, which is designing flexible. The anti-multipath and tracking performance are evaluated for the improved DET. From the simulation results, when the improved DET use 4 order SCS vector, the best result can reducing the multipath error envelope area by 62.6% compared to the traditional DET for BOC (2,1) signal. But the tracking accuracy of the improve DET has some loss, under the

situation of best anti-multipath performance, the CNR loss is about 6 dB. Therefore, when applying the algorithm, we must consider the trade-offs between the multipath mitigation and tracking performance. Compared with other algorithms, the proposed algorithm is more suitable for unambiguous and anti-multipath tracking for BOC signals under strong signal conditions.

References

1. Betz JW (2000) Design and performance of code tracking for the GPS M code signal. In: Proceedings of international technical meeting of the satellite division of the institute of navigation, pp 2140–2150
2. Fante R (2003) Unambiguous tracker for GPS binary-offset-carrier signals. In: Proceedings of the 2003 ION National Technical Meeting, Albuquerque, New Mexico
3. Ward PW (2003) A design technique to remove the correlation ambiguity in binary offset carrier (BOC) spread spectrum signals. In: Proceedings of annual meeting of the institute of navigation and CIGTF guidance test symposium
4. Hodgart MS, Blunt PD, Unwin M (2008) Double estimator—a new receiver principle for tracking BOC signals. Inside GNSS 3:26–36
5. Zhou B, Gao Y, Cui X-W et al (2005) Analysis on multipath performance of dual estimate technology for band-limited BOC signals. Radio Commun Technol 41(5)
6. Tang Z (2009) Analysis of multipath rejection performance in GNSS signal design. J Huazhong Univ Sci Technol 37(5):1–5
7. Gao Y, Yao Z, Zhu Y et al (2014) A two-dimension tracking based multipath mitigation method for BOC signals. In: Proceedings of the international technical meeting of the institute of navigation, pp 876–883
8. Xu C, Zhe L, Tang X et al (2017) Strobe double phase estimator: a multipath mitigating technique for BOC signal in GNSS based on double phase estimator. Int J Satell Commun Network 35(3):249–261
9. Yao Z, Lu M (2011) Side-peaks cancellation analytic design framework with applications in BOC signals unambiguous processing. In: Proceedings of ION international technical meeting, pp 775–785
10. Hodgart MS, Blunt PD (2007) Dual estimate receiver of binary offset carrier modulated signals for global navigation satellite systems. Electron Lett 43(16):877–878

Fast Parameter Estimation Method of Multi-components LFM Interference to GNSS Uplink Injection

Hang Ruan, Shuxian Zhang and Shuren Guo

Abstract As the amounts of satellite communication and radar devices increasing, the electromagnetic environment for global navigation satellite systems (GNSS) becomes more and more complex. High power radar signal in L-band has obvious interference to uplink injection of navigation satellites. If satellites has ability to detect and identify interference signals, it will be beneficial to take measures to avoid interference. For the typical linear frequency modulated (LFM) radar signal, a method based on Radon-Wigner Transform (RWT) is proposed to efficiently estimate parameters of multi-components LFM signals, and simulation is performed to verify the validation of the method. The results of this paper can be used to detect and identify the LFM radar interference for navigation satellites.

Keywords GNSS · Uplink injection · Linear frequency modulated (LFM) Multi-component · Parameters estimation · Radon-Wigner transform (RWT)

1 Introduction

The ground-based GNSS uplink injection station mainly aims to send navigation massages and control instructions to navigation satellites on orbit. When interference exists, it may increase the error rate and reduce the quality of the uplink data, which will essentially affect the operation of navigation satellites.

The working frequency band of GNSS uplink injection is partly overlaped by the working frequency band of radars allocated by International Telecommunication Union (ITU) [1], therefore the GNSS uplink injection confronts with potential interference. Especially, ground-based L band high-power radars have characteristics of high peak power and average power, and adjacent working frequency band with the GNSS uplink injection, which may cause interference to satellite uplink injection receiver. In order to avoid or decrease the affect of interference, GNSS

H. Ruan (✉) · S. Zhang · S. Guo
Beijing Institute of Track and Telecommunication Technology, Beijing, China
e-mail: ruanhang_bds@163.com

J. Sun et al. (eds.), *China Satellite Navigation Conference (CSNC) 2018 Proceedings*, Lecture Notes in Electrical Engineering 498,
https://doi.org/10.1007/978-981-13-0014-1_6

uplink injection receiver usually has the ability to detect and recognize interference signals. For the typical linear frequency modulated (LFM) radar signal, a method based on fractional Fourier transfer (FrFT) is proposed to estimate the signal parameters in Ref. [1]. However, the FrFT-based method demands a quite large amount of computation. In order to increase parameter estimation efficiency, this paper proposed a method based on Radon-Wigner transform (RWT). The method is capable of efficiently estimating the parameters of multi-component LFM interference from the ground-based radars with a high precision. Simulation experiments demonstrate the validation of the proposed method.

2 Parameter Estimation Method of LFM Radar Signals

When there is only a single LFM radar interference signal in space received by the spaceborne uplink injection receiver, a number of methods can be used to estimate the parameter of single-component LFM signal, such as short-time Fourier transform (STFT) [2] and Wigner-Ville distribution (WVD) [3]. However, when there are multiple LFM signals in the space, the above methods need to find balance between time-frequency resolution, cross-term suppression and computational efficiency. For this purpose, a method based on FrFT to estimate parameters of multi-component LFM signals is proposed in Ref. [1]. However, the computational efficiency of the FrFT-based method is still relatively high. Therefore, a method based on Radon-Wigner transform (RWT) is proposed in this paper to estimate the parameters of multi-component LFM signals, which not only has high computation efficiency but also good estimation accuracy.

Since the multi-component LFM signals appear as straight lines with different slopes in the Wigner distribution plane, they appear as multiple peak points in the Radon transform domain, and the cross terms will be scattered in the transform domain. Therefore, performing Radon transform to multi-component LFM signals not only suppresses the cross terms, but also estimates the parameters of multi-component LFM signals which are related to the positions of peaks. In addition, the RWT transform can be quickly implemented by using only one dechirping and Fourier transform [4], which therefore has high computational efficiency.

2.1 Estimation Method for a Single-Component LFM Signal

Supposing LFM radar signal can be expressed as [1]:

$$s(t) = A \exp[j2\pi(f_0 t + \frac{1}{2}\gamma t^2)] \tag{1}$$

In which, A is amplitude, f_0 is center frequency, γ is frequency modulation slope.

The RWT of can be implemented by using dechirping and Fourier transform. The result of dechirping can be expressed as:

$$\begin{aligned}\hat{s}(t) &= s(t)\exp\left(-j\pi kt^2\right) \\ &= A\ \exp\left(\mathrm{j}2\pi\left(f_0 t + \frac{1}{2}\gamma t^2\right)\right)\exp\left(-j\pi kt^2\right) \\ &= A\ \exp(\mathrm{j}2\pi f_0 t)\exp\left(-\mathrm{j}\pi(k-\gamma)t^2\right)\end{aligned} \tag{2}$$

When $k \neq \gamma$, the above signal is still a LFM signal, which becomes a energy dispersed wide spectrum after being Fourier transformed; When $k = \gamma$, the above signal is a single-frequency signal, which becomes a energy accumulated spike after being Fourier transformed, and the position of the spike in frequency domain is the very initial frequency. Therefore, the method based on RWT to estimate the single LFM signal are as follows:

STEP 1 Set a search scope $[k_{start}, k_{end}]$ for frequency modulation slope and a search step Δk with N points in the scope.
STEP 2 Calculate the dechirping result $\hat{s}_n(t)$ of $s(t)$ when $k_n = k_{start} + n \cdot \Delta k$, and then obtain the peak value $\hat{S}_{n,\max}$ of the Fourier transformed $\hat{s}_n(t)$.
STEP 3 Search all peak values after RWT in all N searching points of the frequency modulation slope, and obtain the largest peak value $\hat{S}_{\max}$ and its position.
STEP 4 The frequency modulation slope k_i and the frequency f_i related to the largest peak value $\hat{S}_{\max}$ are the estimated results.

To obtain high-precision parameter estimation results, a smaller search step of frequency modulation slope is necessary, which however, will increase the computational complexity. To solve this problem, a hierarchical search method can be used to estimate the optimal frequency modulation slope. The steps are not described here. For details, we can refer to the method in Ref. [1].

2.2 Estimation Method for Multi-component LFM Signals

Multi-component LFM signals with different amplitudes can be expressed as:

$$s(t) = \sum_{i=1}^{I} A_i \exp[j2\pi(f_{0,i}t + \frac{1}{2}\gamma_i t^2)] \tag{3}$$

The dechirping result of the above signal is:

$$\begin{aligned}\hat{s}_k(t) &= \sum_{i=1}^{I} A_i \exp[j2\pi(f_{0,i}t + \frac{1}{2}\gamma_i t^2)] \exp\left(-j\pi k t^2\right) \\ &= A_1 \exp[j2\pi(f_{0,1}t + \frac{1}{2}\gamma_1 t^2)] \exp\left(-j\pi k t^2\right) \\ &\quad + \sum_{i=2}^{I} A_i \exp[j2\pi(f_{0,i}t + \frac{1}{2}\gamma_i t^2)] \exp\left(-j\pi k t^2\right)\end{aligned} \tag{4}$$

Similarly, when $k = \gamma$, the first part of the above expression is a single frequency signal, while the others are still LFM signals due to frequency modulation slope mismatch. Compared to the original multi-component signals, the frequency modulation slope of each component changed the same value. What is more, after performing dechirping and Fourier transform, the first component becomes a energy accumulated spike in the frequency domain, while the others become energy dispersed wide spectrum due to frequency modulation slope mismatch in dechirping processing. When LFM signals with different intensities coexist, the strong signal components may cover up the weak signal components, even if the stronger ones are not focused in the frequency domain. Thus, there is a large error in the detection and estimation of weak signal components. To deal this problem, we can realize separation and parameters estimation between strong and weak signal components in the RWT transform domain by combining the CLEAN technique [5]. The steps in detail are as follows:

STEP 1 When estimating the i-th component, implement dechirping and Fourier transform to echo sequences with a step of Δk at different frequency modulation slopes, obtaining a two-dimensional distribution $\hat{S}_i(k,f)$ in the plane (k,f).
STEP 2 Search the peak value in the two-dimensional distribution plane (k,f), obtain the corresponding frequency modulation slope k_i and initial frequency f_i of the peak value, which are the estimated results of the i-th component.
STEP 3 Construct a narrow-band filter $W_i(f)$ with a center frequency f_i, perform band-stop filtering processing in (k_i,f) distribution plane of the i th component, and do inverse Fourier transform and then multiply $\exp(j\pi k_i t^2)$, which will be taken as the source signal for the next component's separation and parameter estimation, that is:

$$s_{i+1}(t) = F^{-1}\left[(1 - W_i(f))\hat{S}_i(k_i,f)\right] \exp\left(j\pi k_i t^2\right) \tag{5}$$

STEP 4 Replace i with $i + 1$, repeat the above steps, until no LFM component with significant peak can be detected.

3 Simulation Experiment

For a spaceborne uplink injection receiver, we consider two scenes with interference, one is that a single-frequency LFM radar interference signal exists and the other is multi-component LFM radar interference signals with different intensities exist. Simulation experiments are performed to validate the effectiveness of the proposed method.

3.1 Scene of a Single LFM Signal

The simulation parameters are: LFM signal initial frequency 10 MHz, frequency modulation slope 1.5×10^6 MHz/s, pulse width 10 μs, sampling frequency 51.1 MHz and 512 samples. In Ref. [1], the interference-to-signal ratio has been discussed and an example based on COBRA DANE radar is calculated, which shows that the interference-to-signal ratio is larger than 30 dB. Without loss of generality, here we set the interference-to-signal ratio to be 15 dB. The time-frequency distribution of a LFM signal can be fastly obtained by performing STFT, and hence the search scope for frequency modulation slope can be determined. After that, hierarchical search method is used to estimate the frequency modulation slope of the radar interference signal.

Figure 1 shows the time frequency distribution after STFT. The frequency distribution domain is from 0 to 20 MHz, and the pulse width is 10 μs, which means the corresponding search scope for frequency modulation slope is $[-2 \times 10^6, 2 \times 10^6$ MHz/s]. Therefore, we set the search scope as $[-2 \times 10^6, 2 \times 10^6$ MHz/s], initial search step 5×10^5 MHz/s, and end search step 1×10^5 MHz/s.

Figure 2a, b are the distribution of the signal in the (k,f) plane after performing RWT. In Fig. 2, from the peak point's position, we can obtain the value of frequency modulation slope is 1.5×10^6 MHz/s and the value of initial frequency is 10.08 MHz, which are very close to the actual values. Considering that each evaluation method has different search scope and steps, the time consumption comparison for a single estimation procedure is rational. The RWT method costs

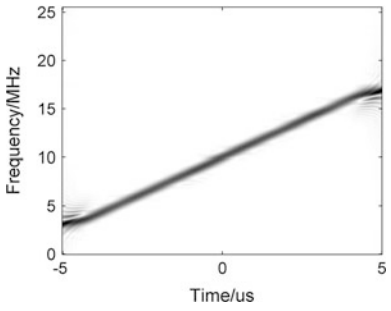

Fig. 1 Time-frequency distribution of a single LFM signal

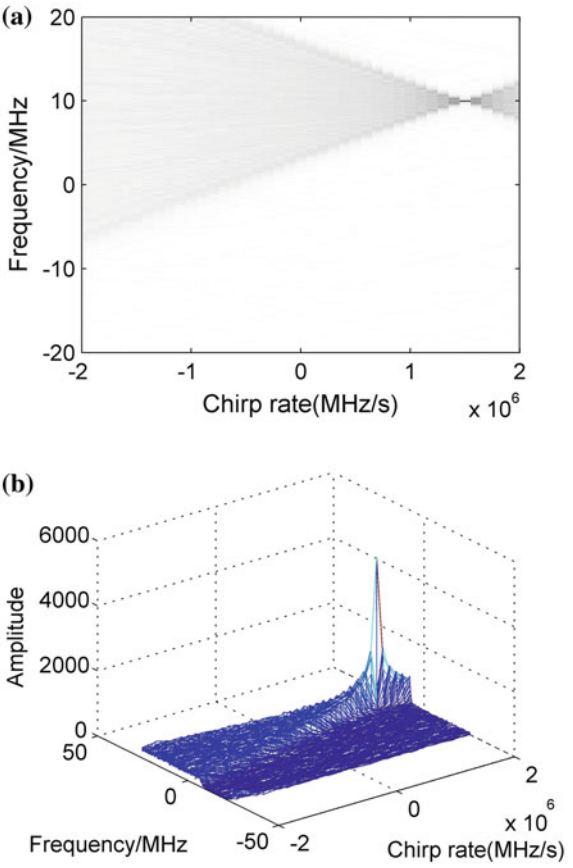

Fig. 2 RWT distribution of a single LFM signal

0.0006568s for one searching procedure averagely, while the FrFT method proposed in Ref. [1] costs 0.0044s. Therefore, the parameter estimation method proposed in this paper for single LFM signal is more effective than the FrFT based method.

3.2 Scene of Multiple LFM Signals

The simulation parameters are: initial frequencies of three LFM signals are 10, 20 and 15 MHz; frequency modulation slopes are 1.5×10^6, 2×10^6, and -2×10^6 MHz/s; amplitudes are 10, 5, and 5, respectively; pulse width is 10 μs and we have 512 sampling points; the interference-to-signal ratio is 15 dB; From the time-frequency distribution of multiple LFM signals (using short time Fourier transform) in Fig. 3, the initial search scope for frequency modulation slope can be set as $[-5 \times 10^6, 5 \times 10^6$ MHz/s]. The initial search step is 5×10^5 MHz/s, and the end search step is 1×10^5 MHz/s.

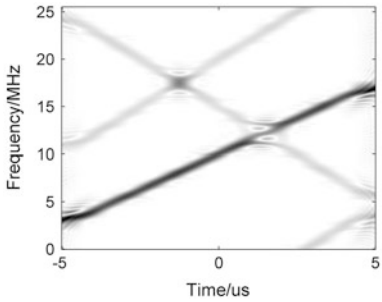

Fig. 3 Time-frequency distribution of multiple LFM signals

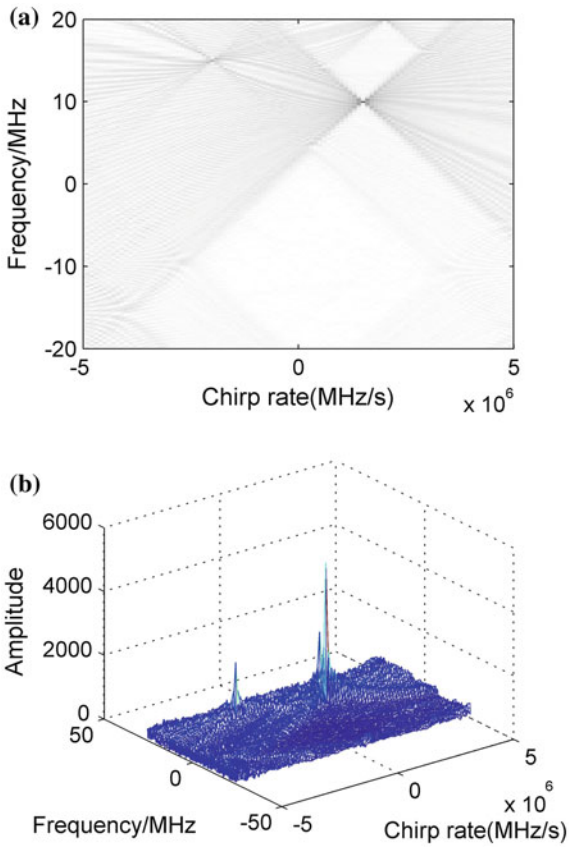

Fig. 4 RWT distribution of multiple LFM signals

Figure 4a, b are the distribution of the signals in the (k,f) plane after performing RWT. In Fig. 4, from three peak points' positions, we can obtain that the frequency modulation slopes are 1.5×10^6, -20×10^6 and 20×10^6 MHz/s, and the initial frequencies are 10.08, 15.07 and 20.06 MHz, respectively. As we can see, for the scene that multiple LFM interference signals exist, the estimated values are very

close to the actual values. Thus, the proposed parameter estimation method for multiple LFM signals is effective as well.

4 Summary

Considering that GNSS uplink injection is facing the threat of high-power LFM radar interference, this paper presents a method to detect and estimate parameter of a single LFM interference signal, which is also suitable for the multiple LFM signals with different intensities. The research results of this paper may contribute to improve the anti-jamming ability of the uplink injection receiver of GNSS in practice, and have reference significance for improving the GNSS safety performance.

References

1. Guo S, Ruan H, Wu H (2017) Parameter estimation method for LFM interference to GNSS uplink injection. In: The 8th China Satellite Navigation Conference, Shanghai, China, pp 985–995 (in Chinese)
2. Chi H, Wang H, Guo Q et al (2012) Application of STFT in time-frequency filtering of LFM signals. Telecommun Eng 52(2):155–159 (in Chinese)
3. He Y, Su F, Qu C (2004) A novel multiple LFM signals detection method. In: Proceedings of 4th international conference on microwave and millimeter wave technology, Beijing, China, pp 818–821
4. Zhang X, Bao Z (2001) Non-stationary signal analysis and process. National Defence Industry Press, pp 158–165 (in Chinese)
5. Ruan H, Wu Y, Ye W (2013) Inverse synthetic aperture Ladar imaging algorithm for maneuvering target based on FRFT-CLEAN. J Electron Inf Technol 35(7):1540–1546 (in Chinese)

Beidou Modulator Distortion Modeling and Compensation Algorithm

Fei Ling, Zuo Zhang, Zhe Su, Yisong Li, Lei Wang and Xiaoxia Tao

Abstract In order to improve the quality of the navigation signal in the Beidou global navigation system, a calibration and compensation algorithm for the distortion characteristic of the modulator is proposed. First of all, we analyze the distortion characteristics of the modulator; on this basis, we study the effects of the distortion characteristics of navigation signal quality through mathematical derivation and simulation experiments; and then we proposes a modulator distortion characteristic calibration and compensation algorithm, through actual modulator test, verify the validity of the methods.

Keywords Navigation system · Payload · Modulator · Distortion

1 Introduction

Satellite navigation system provides users with services through radio navigation signals, and the quality of navigation signals is directly related to the user's use and the realization of various services, which is the key element of the satellite navigation system [1]. The navigation signal is generated and broadcast from the satellite and propagate in the free space. After arriving the receiver, the navigation signal is captured, tracked and positioned, and its signal quality is affected by many factors. The satellite is the source of the signal, and determines the quality of the signal to a great extent. Therefore, optimizing the load of the navigation satellite and improving the signal quality are of great significance for improving the positioning accuracy [2].

The navigation satellite payload generates navigation signals, including base band/inter-frequency generation, modulation/frequency conversion and amplification [3]. Among them, modulation is an important part. For narrow band navigation signal, it can be realized by digital inter-frequency modulation, but for broadband

F. Ling · Z. Zhang · Z. Su (✉) · Y. Li · L. Wang · X. Tao
China Academy of Space Technology, Xi'an, China
e-mail: suzhe504@163.com

J. Sun et al. (eds.), *China Satellite Navigation Conference (CSNC) 2018 Proceedings*, Lecture Notes in Electrical Engineering 498,
https://doi.org/10.1007/978-981-13-0014-1_7

navigation signal, modulation function can only be realized by RF analog modulator. The non ideal characteristics introduced by the modulator will result in the distortion of the navigation signal. Therefore, in order to improve the signal quality, in this paper, distortion characteristics of modulator are mathematical modeling, and proposes a compensation algorithm for distortion characteristics, to maximize the signal quality through the modulator.

2 Modulator Mon-Ideal Model

2.1 Math Model of Modulator

The input signal of modulator is $I(t)$ and $Q(t)$, the output signal of modulator is $M(t)$, and the math model of modulator is

$$\begin{aligned} M(t) &= \mathrm{Rel}\left\{S(t)\cdot e^{j\omega t}\right\} = \mathrm{Rel}\left\{\begin{array}{l}[I(t)+jQ(t)]\cdot \\ [\cos(\omega t)+j\,\sin(\omega t)]\end{array}\right\} \\ &= I(t)\cos(\omega t) - Q(t)\sin(\omega t) \end{aligned} \tag{1}$$

where, $\mathrm{Rel}\{\cdot\}$ represents real operation, $\omega = 2\pi f$ and f is the center frequency of modulator.

2.2 Modeling of Modulators' Distortion Characteristics

Taking the Beidou ACE-BOC signal as an example, the influence of the amplitude and phase imbalance of the modulator on the quality of the navigation signal is analyzed.

The expression of the ACE-BOC baseband signal is as follows

$$\begin{aligned} S(t) = {} & Ad(t)\cdot e^{-j\omega_{SC}t} + 2Ap(t)\cdot e^{j\left(-\omega_{SC}t+\frac{\pi}{2}\right)} \\ & + Bd(t)\cdot e^{j\omega_{SC}t} + 2Bp(t)\cdot e^{j\left(\omega_{SC}t+\frac{\pi}{2}\right)} + IM(t) \end{aligned} \tag{2}$$

Among them, $Ad(t), Ap(t), Bd(t)$ and $Bp(t)$ represent four signal components of ACE-BOC signal, respectively. ω_{SC} represents the angular frequency 15.345 MHz of the ACE-BOC subcarrier, $IM(t)$ is inter-modulation product.

The I path of the ACE-BOC baseband signal is:

$$\begin{aligned} I(t) = \mathrm{Rel}\{S(t)\} = {} & Ad(t)\cos(\omega_{sc}t) + 2Ap(t)\sin(\omega_{sc}t) \\ & + Bd(t)\cos(\omega_{sc}t) + 2Bp(t)\sin(-\omega_{sc}t) \end{aligned} \tag{3}$$

The Q path of the ACE-BOC baseband signal is:

$$\begin{aligned} Q(t) = \mathrm{Img}\{S(t)\} = Ad(t)\sin(-\omega_{sc}t) + 2Ap(t)\cos(\omega_{sc}t) \\ + Bd(t)\sin(\omega_{sc}t) + 2Bp(t)\cos(\omega_{sc}t) \end{aligned} \tag{4}$$

The I and Q baseband signals are input to the ideal modulator. The output signal is:

$$\begin{aligned} M(t) &= I(t)\cos(\omega t) - Q(t)\sin(\omega t) \\ &= \{Ad(t)\cos(\omega_{sc}t)\cos(\omega t) - Ad(t)\sin(-\omega_{sc}t)\sin(\omega t)\} \\ &\quad + \{2Ap(t)\sin(\omega_{sc}t)\cos(\omega t) - 2Ap(t)\cos(-\omega_{sc}t)\sin(\omega t)\} \\ &\quad + \{Bd(t)\cos(\omega_{sc}t)\cos(\omega t) - Bd(t)\sin(-\omega_{sc}t)\sin(\omega t)\} \\ &\quad + \{2Bp(t)\sin(-\omega_{sc}t)\cos(\omega t) - 2Bp(t)\cos(-\omega_{sc}t)\sin(\omega t)\} \end{aligned} \tag{5}$$

The type of product and the difference after the merger of similar items, get:

$$\begin{aligned} M(t) = Ad(t)\cdot\cos[(\omega - \omega_{sc})t] - 2Ap(t)\cdot\sin[(\omega - \omega_{sc})t] \\ + Bd(t)\cdot\cos[(\omega + \omega_{sc})t] - 2Bp(t)\cdot\sin[(\omega + \omega_{sc})t] \end{aligned} \tag{6}$$

The upper expression of the signal component $Ad(t)$ and $Ap(t)$ and the lower band in the ACE-BOC modulation, and $Ad(t)$ and $Ap(t)$ each other orthogonal, $Ad(t)$ is in the same direction branch, $Ap(t)$ is in the orthogonal branch. $Bd(t)$ and $Bp(t)$ are on the upper band in the ACE-BOC modulation, and $Bd(t)$ and $Bp(t)$ each other orthogonal, $Bd(t)$ is in the same direction branch, $Bp(t)$ is in the orthogonal branch.

3 The Influence of the Non-ideal Characteristics of the Modulator on the Quality of the Signal

3.1 Mathematical Deduction and Analysis

The actual modulator products have a certain degree of non ideal characteristics, and this non ideal characteristic is mainly characterized by amplitude imbalance in the L band.

The amplitude imbalance is the difference between the modulators' I channel modulation channel and the Q channel modulation channel for the signal insertion loss. The expression of a mathematical expression is expressed as:

$$M(t) = A_I I(t)\cos(\omega t) - A_Q Q(t)\sin(\omega t) \tag{7}$$

Among them, A_I and A_Q represent the insertion loss of the I channel modulation channel and the Q channel modulation channel, $A_I \approx A_Q$.

If the amplitude characteristic of the modulator is not ideal, that is, the modulator is not balanced, the expression of $I(t)$ and $Q(t)$ is replaced by (7).

$$\begin{aligned} M(t) = & \left\{Ad(t)\cdot\cos(\omega_{sc}t)\cdot A_I\cdot\cos(\omega t) - Ad(t)\cdot\sin(-\omega_{sc}t)\cdot A_Q\cdot\sin(\omega t)\right\} \\ & + \left\{2Ap(t)\cdot\sin(\omega_{sc}t)\cdot A_I\cdot\cos(\omega t) - 2Ap(t)\cdot\cos(-\omega_{sc}t)\cdot A_Q\cdot\sin(\omega t)\right\} \\ & + \left\{Bd(t)\cdot\cos(\omega_{sc}t)\cdot A_I\cdot\cos(\omega t) - Bd(t)\cdot\sin(-\omega_{sc}t)\cdot A_Q\cdot\sin(\omega t)\right\} \\ & + \left\{2Bp(t)\cdot\sin(-\omega_{sc}t)\cdot A_I\cdot\cos(\omega t) - 2Bp(t)\cdot\cos(-\omega_{sc}t)\cdot A_Q\cdot\sin(\omega t)\right\} \end{aligned} \tag{8}$$

The type of product and the difference after the merger of similar items, get:

$$M(t) = M_{Ad}(t) + M_{Ap}(t) + M_{Bd}(t) + M_{Bp}(t) \tag{9}$$

Among them, $M_{Ad}(t), M_{Ap}(t), M_{Bd}(t)$ and $M_{Bp}(t)$ respectively represent the four signal components of the ACE-BOC signal, and the mathematical expressions of $M_{Ad}(t)$ is as follow:

$$M_{Ad}(t) = Ad(t)\cdot\left\{\left(\frac{A_I + A_Q}{2}\right)\cdot\cos[(\omega-\omega_{sc})t] + \left(\frac{A_I - A_Q}{2}\right)\cdot\cos[(\omega+\omega_{sc})t]\right\} \tag{10}$$

The upper formula is actually a general expression of the modulator. When $A_I = A_Q$, the upper formula can be simplified as the first item of (6) $Ad(t)\cdot\cos[(\omega-\omega_{sc})t]$. When $A_I \neq A_Q$ and $A_I \approx A_Q$, that is, $A_I - A_Q \approx 0$, most of the energy $\left(\frac{A_I+A_Q}{2}\right)$ is kept in the lower band; a small portion of the energy $\left(\frac{A_I-A_Q}{2}\right)\neq 0$ exists in the upper band. This is due to $A_I \neq A_Q$, which causes the signal of the upper part of the upper band to not completely offset, and the main effect is as follows:

(1) The correlation loss is deteriorated, and the value of the correlation loss is $10\log_{10}\left\{\frac{A_I+A_Q}{2A_I}\right\}$[dB].
(2) The signal component of $Ad(t)$ exists in the same direction component of the upper side, $Ad(t)$ interferes with $Bd(t)$, the influence of cross-correlation is intensified, the correlation peak produces more distortion, and the slope distortion of SCB and phase discrimination curve deteriorate.

3.2 *Simulation of Influence of Amplitude Imbalance of Modulator on Correlation Loss*

Correlation loss is an important index of the quality of satellite navigation signal. It measures the difference between the total power and the theoretical proportion of the effective power in the navigation signal.

The calculation method of the related loss [4] is as follows:

$$CL[\mathrm{dB}] = P_{\underset{Ideal}{CCF}}[\mathrm{dB}] - P_{\underset{Real}{CCF}}[\mathrm{dB}] \tag{11}$$

Among them,

$$P_{CCF}[\mathrm{dB}] = \max_{\substack{over \\ all\ \varepsilon}} \{20 \cdot \log_{10}[|CCF(\varepsilon)|]\} \tag{12}$$

$\max_{\substack{over \\ all\ \varepsilon}} \{\cdot\}$ Represents the maximum function value of all ε ranges, $CCF(\varepsilon)$ represents the normalized correlation function, which is defined as follows

$$CCF(\varepsilon) = \frac{\int_0^{T_p} S_{Real}(t) \cdot S^*_{Ref}(t-\varepsilon)dt}{\sqrt{\left\{\int_0^{T_p} |S_{Real}(t)|^2 dt\right\} \cdot \left\{\int_0^{T_p} \left|S_{Ref}(t-\varepsilon)\right|^2 dt\right\}}} \tag{13}$$

The radio frequency navigation signals of different amplitude and phase inconsistencies are simulated, and the correlation losses are calculated respectively, as shown in the following diagram. The calculation method for the correlation loss of the theory is $10\log_{10}\left\{\frac{A_I + A_Q}{2A_I}\right\}[\mathrm{dB}]$.

In Fig. 1, α is defined as the degree of amplitude imbalance, and the formula is as follows:

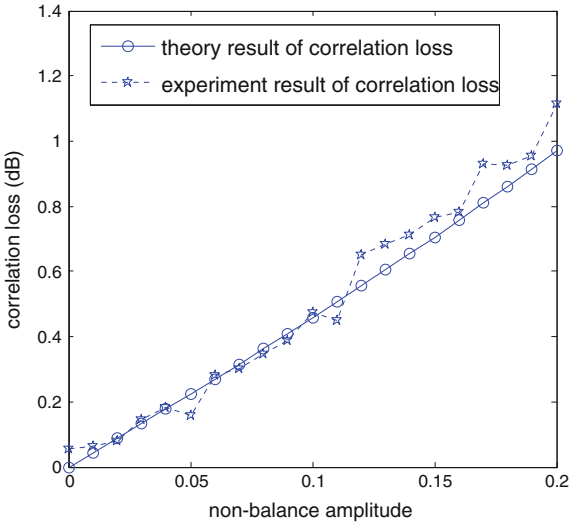

Fig. 1 Effect of non-balance amplitude on correlation loss

$$\alpha = \frac{A_I - A_Q}{A_I + A_Q} \tag{14}$$

From the simulation results above, we can see that the theoretical analysis is consistent with the simulation results. With the increase of the amplitude imbalance, the correlation loss increases rapidly.

3.3 Simulation of Influence of Amplitude Imbalance of Modulator on SCB

SCB (S-Curve Bias) [5, 6] is used to measure the symmetry of the correlation peaks, which are defined as follows:

$$\begin{aligned} SCB = &\max_{\substack{over \\ all\ \delta}} \{SCurve(\varepsilon, \delta)\} \\ &- \min_{\substack{over \\ all\ \delta}} \{SCurve(\varepsilon, \delta)\} \end{aligned} \tag{15}$$

$SCurve(\varepsilon, \delta)$ represents phase discrimination curve, ε represents the location of the zero crossing point of the phase discrimination curve, δ represents the relative spacing.

A radio frequency navigation signal with different amplitude and phase inconsistencies is simulated, and the SCB is measured respectively, as shown in the following diagram (Fig. 2).

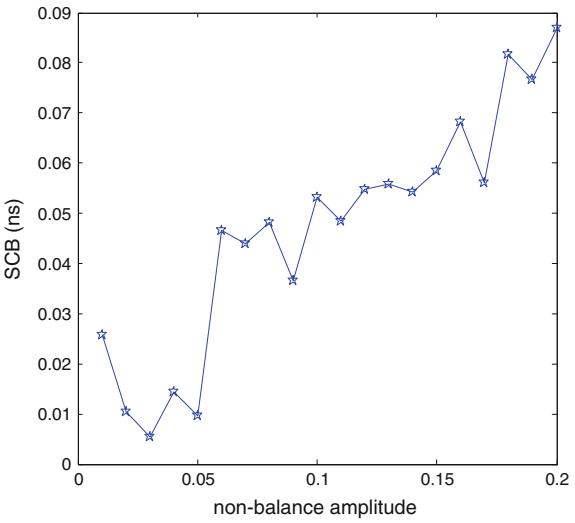

Fig. 2 Effect of non-balance amplitude on SCB

Through the simulation results, it can be seen that with the deterioration of the amplitude, the SCB increases rapidly.

4 The Measurement and Compensation Method of the Distortion Characteristic of the Modulator

In order to measure the distortion characteristic of the modulator, a method for detecting and compensating the amplitude imbalance of the filter is proposed in this paper.

(1) The I path input cosine carrier of the modulator $\cos(\omega_{sc}t)$, carrier frequency $\omega_{sc} = 2\pi f_{sc}, f_{sc} = 15.345$ MHz.
(2) The Q path input sine carrier of the modulator $\sin(-\omega_{sc}t)$.
(3) The signal of the output of the modulator is measured, the power value of the $\omega - \omega_{sc}$ is P_1 and the power value of $\omega + \omega_{sc}$ is P_2.
(4) $\frac{A_I + A_Q}{2} = P_1, \frac{A_I - A_Q}{2} = P_2$, figure out A_I and A_Q

$$\begin{cases} A_I = P_1 + P_2 \\ A_Q = P_1 - P_2 \end{cases} \tag{1.16}$$

If P_2 is zero, then $A_I = A_Q = P_1$, the insertion loss of the I channel modulation channel of the modulator and the Q channel modulation channel are equal; if P_2 is not zero, then $A_I \neq A_Q$, can be compensated according to the A_I and A_Q.
(5) The I channel and Q channel of the modulator are $\frac{1}{A_I}$ and $\frac{1}{A_Q}$ times respectively, which can compensate the amplitude imbalance of the modulator.

A modulator is tested. In the modulator's I Road, the cosine carrier is input, the modulator's Q path is input into the sinusoidal carrier, and the spectrum is measured at the output end. According to the annotation in the spectrum diagram, the value of P_1, P_2, A_I and A_Q can be solved and compensated according to the result of the measurement. The quality of the signal before and after compensation is compared and analyzed, as shown in the following Table 1.

Table 1 Contrast of signal quality before and after compensation

	Before compensation	After compensation
Correlation loss	0.06 dB	0.03 dB
SCB	0.02 ns	0.003 ns
Slope distortion of phase discrimination curve	3%	0.6%

It can be seen that compensating for the amplitude inconsistency of the modulator can obviously improve the signal quality indicators such as correlation loss, SCB, phase discrimination curve and slope distortion.

5 Conclusion

This paper gives the mathematical expression of non ideal characteristics—modulator amplitude unbalance, deduced the amplitude imbalance effect on signal quality, and through the numerical simulation, studied the amplitude imbalance effects on the power spectrum envelope, losses and SCB, this paper presents a calibration method and compensation method for unbalanced amplitude modulator through the experiment, verify the validity of the method.

Acknowledgements This work is supported by the National Natural Science Foundation of China (No. 91438107).

References

1. Phelts RE, Akos DM, Enge P (2000) Robust signal quality monitoring and detection of evil wveforms. In: Proceedings of the institute of navigation ION GPS. Salt Lake City, UT, pp 1180–1190
2. Rebeyrol E, Macabiau C, Julien O, Ries L, Bousquet M, Boucheret ML (2006) Signal distortions at GNSS payload level. In: ION GNSS 19th international technical meeting of the satellite division, vol 9, pp 26–29
3. Winkel J, Luck T, Bodenbach M, Gohler E, Falk N, Wolf H, Kubr H, Minelli L (2007) Galileo payload test system-the receiver subsystem. In: ION GNSS 20th international technical meeting of the satellite division, vol 9, pp 25–28
4. Sollner M, Kurzhals C, Kogler W, Erker S, Thölert S (2009) Innovation: one year in orbit, GIOVE-B E1 CBOC signal quality assessment. GPS World 9(1):28–37
5. Yang YK et al (2012) A simulation for impact of filter nonlinear phase on navigation payload. In: 2012 5th international congress on image and signal processing, CISP 2012, pp 1417–1420
6. Soellner M (2008) GNSS offline signal quality assessment. In: 21st international technical meeting of the satellite division of the institute of navigation, ION GNSS 2008

A Variable Step Frequency-Domain LMS Narrowband Interference Suppression Algorithm Based on Adaptive Noise Statistics

Yaohui Chen, Dun Wang, Hehe Guo, Zhenxing Xu, Peng Liu and Dongjun Li

Abstract In the inter-satellite communication system, the power of spread spectrum signal received by the receiving end has a large dynamic range due to the large distance between the senders and receivers. In order to ensure the stability of AD sampling data, it usually adds AGC in the RF channel to make the output of the IF signal power stable, and does not change along with the change of the input signal power. It also leads to a problem that the proportion of the effective signal (the number of bits) after AD sampling reduced with the increase of the interference signal power, thus affecting the anti-jamming performance of the fixed-step frequency domain LMS algorithm. Aiming at the above problems, this paper proposes a variable step frequency domain LMS narrowband interference suppression algorithm which based on adaptive noise statistics. In this paper, the simulation results show that the proposed approach can effectively solve the above problems.

Keywords Frequency domain · LMS · Adaptive · Variable step AGC · Anti-jamming

1 Introduction

In the satellite communication system, multiple satellites can be interconnected by establishing links for communication between satellites, so that information can be transmitted and exchanged between satellites, and information can be promptly transmitted back to the ground in real time, and avoiding set up ground stations around the world. In addition, establishing communication links between satellites can also improve the autonomous ability of constellations. The communication between satellites is accomplished through transceivers, which will face the threat of various jammers during their operations, especially in combat environments. Although its spread spectrum communication technology has certain anti-jamming

Y. Chen (✉) · D. Wang · H. Guo · Z. Xu · P. Liu · D. Li
Space Star Technology Co.,Ltd, Beijing 100095, China
e-mail: Chen_yaohui10@163.com

J. Sun et al. (eds.), *China Satellite Navigation Conference (CSNC) 2018 Proceedings*, Lecture Notes in Electrical Engineering 498,
https://doi.org/10.1007/978-981-13-0014-1_8

ability, when there exists strong jammers, it is unrealistic to rely solely on spread spectrum gain due to the limitation of the spread spectrum bandwidth. Therefore, it is necessary to research anti-jamming technology for inter-satellite communication to further enhance the anti-jamming ability of the system. This paper mainly studies the technique of narrowband interference suppression. According to industry standards, it will be considered to be narrowband interference if the ratio of interference signal bandwidth to useful signal bandwidth is less than 1/10.

The commonly used narrowband interference suppression techniques are mainly divided into three categories: prediction technology, transform domain technology and code assistance technology [1]. Due to its unique advantages, transform domain technology has been widely used in spread spectrum communication systems. Initially, Milstein et al. [2] proposed a transform domain filtering technique using FFT and SAW (Surface Acoustic Wave) devices to suppress narrowband interference in spread spectrum receivers. Later, this idea was further developed as transform domain interference suppression techniques based on Fourier Transform. The easiest frequency domain suppression technology is to set zero to the bins which beyond the threshold as in Literature [3]. However, it is not an optimal method based on some parameters. The LMS (Least Mean Square) algorithm proposed by Widrow and Hoff [4] in 1960 has been widely used due to its simple structure and robustness to changes of signal statistical characteristics. However, the step size is fixed in traditional LMS algorithm. Within the convergence range of the LMS algorithm, the larger the step factor, the faster the algorithm convergences, but the greater the imbalance of LMS algorithm. The contradiction between convergence speed and steady state error restricts the application of the algorithm in practice. Therefore, many scholars have studied and proposed a series of improved algorithms, including normalized LMS algorithm, variable step size LMS algorithm and adaptive frequency domain block LMS algorithm [5–7].

In the inter-satellite communication system, the power of the spread spectrum signal received by the receiver has a large dynamic range due to the large distance between the senders and receivers. In order to ensure the stability of AD sampling data, it usually adds AGC in the RF channel to make the output of the IF (intermediate frequency) signal power stable. It also leads to a problem that the proportion of the effective signal after AD sampling reduced with the increase of the interference signal power, thus affecting the anti-jamming performance of the fixed-step frequency domain LMS algorithm. The existing variable step algorithms are basically to solve the contradiction between convergence speed and steady state error, but don't aim at the situation that the step factor is not suitable for the noise variation so that the interference can't be effectively suppressed. Aiming at the above problems, this paper proposes a variable step frequency domain LMS narrowband interference suppression algorithm.

This paper is organized as follows, Sect. 1 is the introduction. Section 2 introduces the principle of frequency domain LMS algorithm and the convergence of the algorithm. Section 3 introduces a variable step frequency domain LMS narrowband interference suppression algorithm based on noise statistics. Section 4 shows the overall architecture of the system. Section 5 shows the simulation carried out with

the theoretical data. Finally, Sect. 6 summarizes the full text. Compared with the fixed-step LMS, the variable step frequency domain LMS narrowband interference suppression algorithm based on noise statistics which proposed in this paper can well solve the above problems and improve the anti-jamming performance of the system.

2 Frequency Domain LMS Algorithm

Here reference literature [8] to introduce the principle of frequency domain LMS algorithm and its convergence.

2.1 Frequency Domain LMS Algorithm Model

Frequency domain LMS algorithm is using LMS algorithm at each frequency bin. Figure 1 shows the principle of frequency domain LMS algorithm.

In Fig. 1, $\{x_n(l)\}$ are the buffer data, where $n = 0, 1, \cdots, N-1$. $\{\tilde{x}_k(l)\}$ are the outputs of buffer data after Fourier transform, where $k = 0, 1, \cdots, N-1$. $\{w_k(l)\}$ are the unknown weights, where $k = 0, 1, \cdots, N-1$. $\{e_k(l)\}$ are the errors, where $k = 0, 1, \cdots, N-1$. $\{y_n(l)\}$ are the time domain outputs after the inverse Fourier transform, note that index l denotes the block number.

The output of the kth bin for the lth block after Fourier transform is given by

$$\tilde{x}_k(l) = \sum_{n=0}^{N-1} x_n(l) e^{-j\frac{2\pi}{M}kn}, k = 0, 1, \cdots, N-1 \tag{1}$$

Using $\tilde{x}_k(l)$ as reference, so the error signals is given by

$$e_k(l) = \tilde{x}_k(l) - w_k(l)\tilde{x}_k(l), k = 0, 1, \cdots, N-1 \tag{2}$$

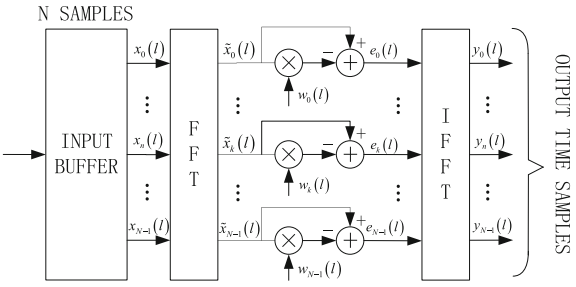

Fig. 1 Principle of frequency domain LMS algorithm

Introduces $\alpha(0<\alpha<1)$ as a weight leakage factor. Using the steepest descent method can get the kth bin weight

$$w_k(l+1) = \alpha w_k(l) + 2\mu_k e_k(l)\tilde{x}_k^*(l) \tag{3}$$

where μ_k is step factor.

Taking Eq. (2) into Eq. (3) can get

$$w_k(l+1) = \alpha w_k(l) + 2\mu_k[1 - w_k(l)]\tilde{x}_k(l)\tilde{x}_k^*(l) \tag{4}$$

From Eq. (3) one can see that weight update is related to the current weights and the input signal power, and the step factor and weight are both real.

The kth bin output for the lth block after the anti-jamming filter is given by

$$e_k(l) = [1 - w_k(l)]\tilde{x}_k(l) \tag{5}$$

Finally the outputs of the N bins after the anti-jamming filter are inverse Fourier transformed to obtain the time domain outputs. The nth time domain output for the lth block is given by

$$y_n(l) = \sum_{k=0}^{N-1} e_k(l)e^{j\frac{2\pi}{N}kn}, n = 0, 1, \cdots, N-1 \tag{6}$$

2.2 Algorithm Convergence

Take both sides of the Eq. (4) with the statistical average

$$E\{w_k(l+1)\} = \alpha E\{w_k(l)\} + 2\mu_k E\left\{|x_k(l)|^2\right\} - 2\mu_k E\left\{w_k(l)|x_k(l)|^2\right\} \tag{7}$$

Suppose $w_k(l)$ has nothing to do with $\tilde{x}_k(l)$, and the power of each frequency bin σ_k^2 remains unchanged, namely

$$E\left\{|x_k(l)|^2\right\} = \sigma_k^2 \tag{8}$$

Then Eq. (7) can be rewritten as

$$\begin{aligned} E\{w_k(l+1)\} &= \left(\alpha - 2\mu_k\sigma_k^2\right)E\{w_k(l)\} + 2\mu_k\sigma_k^2 \\ &= \left(\alpha - 2\mu_k\sigma_k^2\right)^{l+1}E\{w_k(0)\} + 2\mu_k\sigma_k^2\sum_{m=0}^{l}\left(\alpha - 2\mu_k\sigma_k^2\right)^m \end{aligned} \tag{9}$$

To ensure that the algorithm converges, it requires that $E\{w_k(l)\}$ tends to be a constant when l tends to infinity. So it should be independent of the initial value. Therefore, the step factor given by Eq. (9) should satisfy the following formula.

$$\left|\alpha - 2\mu_k\sigma_k^2\right| < 1 \tag{10}$$

As to be satisfied $\mu_k > 0$ at the same time, so the convergence condition is

$$\mu_k \in \left(0, (\alpha+1)/2\sigma_k^2\right) \tag{11}$$

When the step factor satisfies the convergence condition, the kth bin optimal weight after convergence is given by

$$w_{optk} = \frac{2\mu_k\sigma_k^2}{1-\alpha+2\mu_k\sigma_k^2} \tag{12}$$

Let $N_{th}(N_{th} = (1-\alpha)/2\mu_k)$ as threshold factor, then the kth bin optimal weight can be rewritten as

$$w_{optk} = \frac{\sigma_k^2}{N_{th}+\sigma_k^2} \tag{13}$$

From Eq. (13) one can see that the optimal weight tends to zero so that the signal is nearly straight through when σ_k^2 is much smaller than N_{th}, and the optimal weight tends to one so that the signal is greatly suppressed when σ_k^2 is much larger than N_{th}. Therefore, the threshold factor determines the input signal power threshold which is retained or suppressed.

In practical engineering applications, the step factor of each bin usually selects a fixed value, namely the threshold factor is fixed. The anti-jamming processing is generally based on noise. For noise-stable system, the narrowband interference can always be suppressed effectively when it uses fixed step. However, due to the special application conditions of the inter-satellite communication system, the proportion of the effective signal after AD sampling decreases with the increase of the power of the interference signal, which also makes the fixed-step frequency domain LMS algorithm unsuitable. It needs to adjust the step size according to the change of AD sampling signal in real time. Therefore, this paper proposes a variable step frequency-domain LMS narrowband interference suppression algorithm based on adaptive noise statistics.

3 Variable Step Frequency Domain LMS Algorithm

The principle of the variable step frequency domain LMS narrowband interference suppression algorithm based on adaptive noise statistics proposed in this paper is basically the same as that of fixed-step frequency domain LMS, except the step size

is adaptively adjusted according to real time noise statistics. Since noise can only be calculated by the frequency bins without interference in the band, it needs to detect the interference to identify the spectrum range.

3.1 Interference Detection

Due to the influence of the AGC in RF channel, it is not easy to judge the interference by the power of the signal in time domain. This situation is more suitable for interference detection in the frequency domain. Using the forward continuous mean elimination algorithm (FCME) [9] can obtain the bandwidth and the spectrum range of the interference.

3.2 Noise Statistics

The noise statistics is also carried out in frequency domain. According to the characteristics of the interference (mainly the spectrum range of the interference) given by the interference detection module, there takes the average power of M non-interfering frequency bins in the band from the l_1th bin as noise.

$$\sigma^2(l) = \gamma \frac{1}{M} \sum_{k=l_1}^{l_1+M-1} |\tilde{x}_k(l)|^2 \tag{14}$$

where γ is real, which can be adjusted according to the actual situation.

Select the threshold factor as

$$N_{th} = \sigma^2 \tag{15}$$

Then the step factor can be written as

$$\mu = \frac{1-\alpha}{2\sigma^2} \tag{16}$$

From the analysis in Sect. 2.2, one can see that the selection of the threshold factor is very important, and it can neither be too large nor too small. It will lead to the interference can't be suppressed effectively if the threshold factor is too large. However, if the threshold factor selection is too small, the interference can be suppressed effectively, but it will also have a greater impact on the useful signal. Therefore it needs to choose a reasonable threshold factor.

3.3 Algorithm Convergence

Quoting the conclusion showed in Eq. (11), which requires

$$\frac{1-\alpha}{2\sigma^2} \in \left(0, \frac{\alpha+1}{2\sigma_k^2}\right) \tag{17}$$

It can satisfy the above convergence condition which only need to reasonably choose α and γ according to the actual situation.

4 Overall Architecture

The overall system architecture is shown in Fig. 2. The analog IF signal is converted into digital IF signal by AD sampling and then divided into two channels. One of the channels is delayed, and then the two signals are added with windows, FFT, interference detection, noise statistics, adaptive filtering, IFFT, inverse window, overlap and DAGC processing.

The FFT operation of truncation of long sequences can cause spectral leakage due to the discontinuity of the data block edges, and the slow changing window can effectively suppress spectral leakage. However, the addition of window processing, while reducing the spectrum leakage, also introduces the distortion of the edges of the block data, which will cause some loss to the SNR (Signal-to-Noise Ratio). Most of the frequency domain anti-jamming techniques use overlap and inverse window processing to compensate the SNR loss caused by windowing.

In addition, due to the influence of the AGC in RF channel, the proportion of the effective signal after AD sampling reduced with the increase of the interference signal power, so that the signal power remaining after anti-jamming processing gradually decreases, which affects the signal acquisition and tracking. The DAGC can make the signal outputs to the acquisition and tracking module after anti-jamming processing basically stable and does not decrease with the increase of the interference, so as to ensure that the acquisition and tracking performance is not be affected. Next, this paper will also simulate the influence of DAGC.

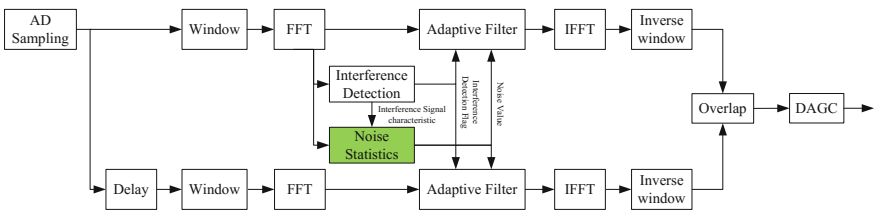

Fig. 2 System architecture diagram

5 Simulation and Verification

In order to verify the variable step frequency domain LMS narrowband interference suppression algorithm based on adaptive noise statistics proposed in this paper has advantages compared with the fixed-step LMS algorithm, then the simulation is carried out with the theoretical data. The values of the parameters are α=0.99, γ=16. Assuming the bandwidth of satellite signal is 20.46 MHz. The signals received by antenna are converted to digital IF signal through RF channel, AD sampling (65 MHz), then are carried out anti-jamming processing. In this paper, we consider the most harsh interference environment, and apply a narrowband interference signal with a bandwidth of 2 MHz near the center frequency. The anti-jamming performance of the two algorithms under different ISR (Interference-to-Signal Ratio) is compared through simulation.

5.1 Scene 1

This scenario contains one narrowband jammer, which is located near the center frequency of the satellite signal and has a bandwidth of 2 MHz. The ISR is assumed to be 25 dB, and the SNR is assumed to be −14 dB. Figure 3 shows the time-domain waveform and power spectrums (Gain) of the IF signal. From Fig. 3b one can see clearly that there is a narrowband interference signal.

Figure 4a and b show the power spectrums of the output signals after anti-jamming processing by the fixed step frequency domain LMS algorithm and the proposed variable step frequency domain LMS algorithm.

From Fig. 4a and b one can see clearly that both algorithms can effectively suppress the interference.

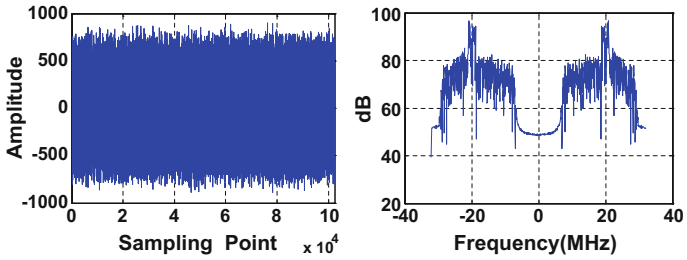

(a) Time-domain waveform (b) Power spectrums (Gain)

Fig. 3 Signal waveform and power spectrums (Gain) after BPF

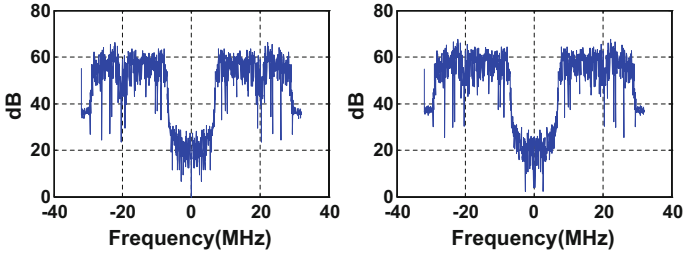

(a) Fixed-step (b) Variable step

Fig. 4 Signal power spectrums (Gain) after anti-jamming

5.2 *Scene 2*

This scenario shows that the interference can't be effectively suppressed by the fixed step frequency domain LMS algorithm due to the decrease of the proportion of the effective signal after AD sampling when the interference is strong, while the new method proposed in this paper is effective. This scenario contains one narrowband jammer, which is located near the center of the satellite signal and has a bandwidth of 2 MHz. The ISR is assumed to be 45 dB, and the SNR is assumed to be −14 dB. Figure 5 shows the time-domain waveform and power spectrums (Gain) of the IF signal.

Comparing Fig. 5a with Fig. 3a, one can see that the amplitude of the AD sample signal doesn't increase with the increase of the interference signal power, which is the function of the RF AGC. However, comparing Fig. 5b with Fig. 3b, one can see that the noise when the ISR is 45 dB is obviously lower than the noise when the ISR is 25 dB due to the influence of RF AGC.

Figure 6a and b show the power spectrums of the output signals after anti-jamming processing by the fixed step frequency domain LMS algorithm and the proposed variable step frequency domain LMS algorithm.

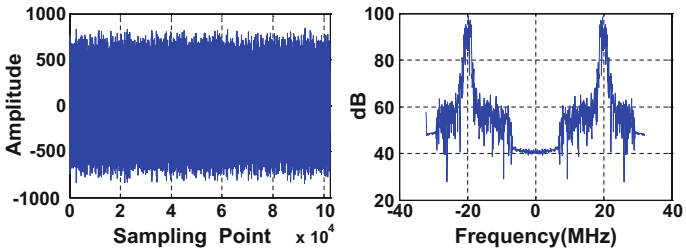

(a) Time-domain waveform (b) Power spectrums (Gain)

Fig. 5 Signal waveform and power spectrums (Gain) after BPF

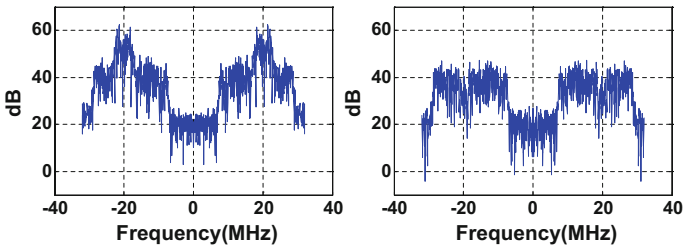

(a) Fixed-step (b) Variable step

Fig. 6 Signal power spectrums (Gain) after anti-jamming

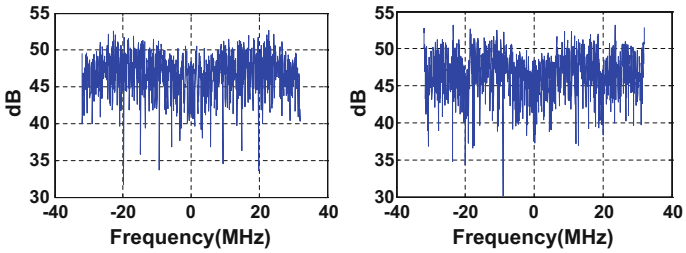

(a) Fixed-step (b) Variable step

Fig. 7 Signal power spectrums (Gain) after DAGC

From Fig. 6 one can see there still has obvious residual narrowband interference in the signal spectrums after anti-jamming processing by the fixed step frequency domain LMS algorithm. One can also see that the narrowband interference can be suppressed by the variable step frequency domain LMS algorithm proposed in this paper, which proves the effectiveness of the proposed algorithm.

Comparing Fig. 4b with Fig. 6b, one can see that the power of the signals after anti-jamming processing with the ISR of 25 dB is obviously greater than that with the ISR of 45 dB. It can seriously affect the accumulated value during the acquisition and tracking processing, which in turn affects the actual acquisition and tracking performance. In order to make the signal outputs to the acquisition and tracking module stay stable, the DAGC is added after the anti-jamming processing. Figure 7a and b show the signal power spectrums of the outputs of ISR with 25 and 45 dB after DAGC.

From Fig. 7a and b one can see that the DAGC can make the signal outputs to the acquisition and tracking module after anti-jamming processing basically stable and does not change with the increase of interference signal intensity, thus ensuring the acquisition and tracking performance.

6 Summary

In order to ensure the stability of AD sampling data in the inter-satellite communication system, it usually adds AGC in the RF channel. It also leads to a problem that the proportion of the effective signal after AD sampling reduced with the increase of the interference signal power, thus affecting the anti-jamming performance of the fixed-step frequency domain LMS algorithm. Aiming at the above problems, this paper proposes a variable step frequency domain LMS narrowband interference suppression algorithm based on adaptive noise statistics. In this paper, the simulation results show that the anti-jamming performance of the proposed algorithm based on adaptive noise statistics is obviously better than the fixed-step LMS algorithm, and it can effectively solve the above problems and further improve the anti-jamming performance.

The future research is to analyze signal acquisition and tracking features on the receivers.

References

1. Chen Y, An J, Luo W (2003) Technology of narrow-band interference rejection in a DS-SS System. Syst Eng Electron 25(2)
2. Milstein LB, Das PK (1980) An analysis of a real-time transform domain filtering digital communications system—Part I: narrow-band interference rejection. IEEE Trans. On Commun 28:816–824
3. Chen M, Zhang J (2005) A modified frequency domain method for suppressing narrowband interference in DSSS system. Sig Process 21(4A):399–402
4. Widrow B, Hoff ME Jr (1960) Adaptive switching circuits. IRE WESCON Conv REC. Part4 96–104
5. Nitzberg R (1985) Application of normalized LMS algorithm to MSLC. IEEE Trans AES 21 (1):79–91
6. Chen Y, Ding W, Liu C (2017) Variable step size frequency domain block LMS algorithm. Comput Eng Appl 53(4):140–144
7. Saulnier GJ (1992) Suppression of narrowband jammers in a spread-spectrum receiver using transform-domain adaptive filtering. IEEE JSAC 10(4):742–749
8. Gong Y (2003) Adaptive filtering (2nd ed)—Time domain adaptive filtering and smart antenna. Publishing House of Electronics Industry, Beijing
9. Yu H (2014) A study and implementation of jamming detection technology based on DSSS system. Xidian University, China

A Cooperative Anti-spoofing Technology Based on Subspace Projection

Mingyu Liu, Shuai Han, Yu Zhang and Weixiao Meng

Abstract With the development of GNSS, spoofing and anti-spoofing issues are gradually rising in modern applications. Effective spoofing sources can mislead common receivers and induce them to log the specific trajectory, and therefore many anti-spoofing technologies are proposed to distinguish the spoofing jamming. However, the existing anti-spoofing technologies are limited to a specific scenario, which reduces the reliability of receivers greatly. In this paper, we propose a cooperative anti-spoofing technology based on subspace projection that can extract two characters of the spoofing signals to construct orthogonal subspaces to eliminate the spoofing signals. We also present the receiver structure that includes spatial processing and data processing. Spatial processing can mitigate the spoofing sources with larger power and compensate the authentic signals. And data processing can suppress the spoofing signals not aligned with the authentic signals in the code domain. The two parts aim at different types of spoofing signals and spatial processing can also do help to data processing by eliminating the signals with larger power. At last, the proposed technology is verified by simulations.

Keywords Anti-spoofing · GNSS · Subspace projection

1 Introduction

Nowadays GNSS-dependent system is more and more popular in many fields. Its security and reliability have become a great matter of concern because of its low signal power and public known data structure. So the researches on how to protect GNSS receivers have been increasing in recent years [1].

GNSS receivers mainly suffer two types of interference that are blanket jamming and spoofing jamming. Blanket jamming can interfere with all receivers in a particular

M. Liu (✉) · S. Han · Y. Zhang · W. Meng
Communication Research Center, Harbin Institute of Technology,
Harbin, China
e-mail: liumingyu_1993@126.com

J. Sun et al. (eds.), *China Satellite Navigation Conference (CSNC) 2018 Proceedings*, Lecture Notes in Electrical Engineering 498,
https://doi.org/10.1007/978-981-13-0014-1_9

area. The spoofing jamming is hidden in the authentic signals that is not easily distinguished by a GNSS receiver. Meanwhile, rapid developments with SDR (software defined radio) technology have made spoofing jamming more flexible and low-cost, hence spoofing jamming is more threatening [2].

Typical anti-spoofing jamming technology can be classified into two categories, namely spoofing detection and spoofing mitigation. Some methods based on the signal power monitoring are proposed to detect the spoofing attack. Jafarnia-Jahromi et al. [3] gives a method using C/N_0 monitoring whose any unusual variation can be regarded as a sign of spoofing attack. Spoofing mitigation technologies mainly include RAIM (receiver autonomous integrity monitoring) and multiple antennas, which can help the spoofed receiver to retrieve its positioning and navigation abilities. Han et al. [4] proposes an improved RAIM to perform spoofing detection and spoofing identification with a particle filter which is more effective. Daneshmand et al. [5] provides a low computational complexity approach to mitigate the spoofing signals, but it is established on that all spoofing signals are transmitted from the same source in space. Hence we proposes a cooperative anti-spoofing technology based on subspace projection. The proposed technology can realize both spoofing detection and mitigation that has stronger robustness and validity.

The remainder of this paper is outlined as follows: Sect. 2 indicates the system model of our proposed technology in detail. Section 3 shows principles of the subspace projection, and it also gives the receiver structure. Section 4 analyzes the performance according to the simulation results. Section 5 gives the conclusion.

2 System Model

In this section, we give the anti-spoofing model. Assume that there is an M-element linear antenna array where r_1 is selected as the reference antenna to facilitate the subsequent analysis. The structure is shown in Fig. 1.

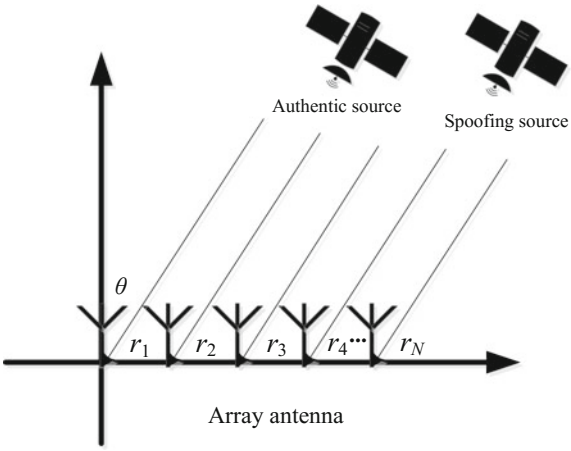

Fig. 1 The antenna array

The received IF signal that contains both authentic and spoofing signals can be expressed as

$$\mathbf{r}(nT_s) = \mathbf{r}_a(nT_s) + \mathbf{r}_s(nT_s) + \boldsymbol{\eta}(nT_s) \tag{1}$$

where $\mathbf{r}_a(nT_s)$ represents the vector of the authentic signals, $\mathbf{r}_s(nT_s)$ represents the vector of the spoofing signals and $\boldsymbol{\eta}(nT_s)$ is regarded as the additive white Gaussian noise.

In Eq. (1), the detail expressions of authentic and spoofing signals are shown as follows:

$$\mathbf{r}_a(nT_s) = \mathbf{A}_a\mathbf{Q}_a(nT_s) \tag{2}$$

$$\mathbf{r}_s(nT_s) = \mathbf{A}_s\mathbf{Q}_s(nT_s) \tag{3}$$

where $\mathbf{A}_a$ represents the space characteristic matrix of authentic signals, $\mathbf{A}_s$ represents the space characteristic matrix of spoofing signals, $\mathbf{Q}_a(nT_s)$ is the basic matrix of authentic signals and $\mathbf{Q}_s(nT_s)$ is the basic matrix of spoofing signals. The variables are respectively defined as

$$\mathbf{A}_a = [\,\mathbf{a}_1 \quad \mathbf{a}_2 \quad \cdots \quad \mathbf{a}_{N_a}\,] \tag{4}$$

$$\mathbf{A}_s = [\,\mathbf{b}_1 \quad \mathbf{b}_2 \quad \cdots \quad \mathbf{b}_{N_s}\,] \tag{5}$$

$$\mathbf{Q}_a(nT_s) = \left[\, q_a^1(nT_s) \quad q_a^2(nT_s) \quad \cdots \quad q_a^{N_a}(nT_s) \,\right]^{\mathrm{T}} \tag{6}$$

$$\mathbf{Q}_s(nT_s) = \left[\, q_s^1(nT_s) \quad q_s^2(nT_s) \quad \cdots \quad q_s^{N_s}(nT_s) \,\right]^{\mathrm{T}} \tag{7}$$

$$q_a^m(nT_s) = \sqrt{p_a^m}w_a^m(nT_s - \tau_a^m)c_a^m(nT_s - \tau_a^m)e^{j\phi_a^m + j2\pi f_a^m nT_s} \tag{8}$$

$$q_s^z(nT_s) = \sum_{k=1}^{N_k} \sqrt{p_s^{zk}}w_s^{zk}(nT_s - \tau_s^{zk})c_s^{zk}(nT_s - \tau_s^{zk})e^{j\phi_s^{zk} + j2\pi f_s^{zk} nT_s} \tag{9}$$

where N_s represents the number of spoofing sources, N_a represents the number of authentic signals, N_k represents the number of the spoofing signals contained by the spoofing source, T_s is the sampling interval, φ, f, p, τ mean the phase, carrier frequency, signal power and code delay of the received signals respectively. $w(nT_s)$ and $c(nT_s)$ are navigation data bits and PRN (pseudo random noise) code. And

$$a_m = \left[1\; e^{-j\frac{2\pi}{\lambda}d\sin\theta_m} \cdots e^{-j(M-1)\frac{2\pi}{\lambda}d\sin\theta_m}\right]^{\mathrm{T}} \tag{10}$$

$$b_z = \left[1\; e^{-j\frac{2\pi}{\lambda}d\sin\theta_z} \cdots e^{-j(M-1)\frac{2\pi}{\lambda}d\sin\theta_z}\right]^{\mathrm{T}} \tag{11}$$

where a_m means the steer vector of m-th authentic signals, b_z means the steer vector of z-th spoofing sources, λ means the incident wavelength, d means the distance between the antenna. Then the model is established.

3 The Anti-spoofing Technology Based on Subspace Projection

The anti-spoofing technology proposed in this paper mainly concerns on the character of the signal and ignores the detail navigation data information of the signal that means we do not need to acquire the PNT solutions to help mitigate the spoofing signal. So we utilize subspace projection [6] as our primary method. The key of the subspace projection algorithm lies in how to construct the subspace.

3.1 Spatial Processing

RELAX algorithm is very fit for estimating the DOA of the GNSS signal [7]. RELAX algorithm can calculate the waveform and DOA of a weak signal simultaneously, the waveform can be utilized by the following part. Further, the algorithm needs a prior input that is the number of the detected signal. And RELAX algorithm can detect the signals from big to small according to the signal power.

Before estimating the DOA of signals, RELAX algorithm first structures a cost function that is written as

$$\mathbf{F}_1[\,\theta\,\mathbf{s}(k)\,] = \sum_{k=1}^{K} [\mathbf{x}(k) - \mathbf{A}\mathbf{s}(k)]^H [\mathbf{x}(k) - \mathbf{A}\mathbf{s}(k)] \tag{12}$$

where θ is the DOA of the signal; $s(k)$ is the amplitudes of all signals at k-th time slot; $x(k)$ represents the $M \times 1$ matrix of the received signals at k-th time slot; A represents the space characteristic matrix of all incident signals; K is the number of time slots. Assuming that the noise is white Gaussian, the DOA and waveform evaluation of received signals $\left\{\,\hat{\theta} \quad \hat{\mathbf{s}}(\hat{\theta})\,\right\}$, can be gotten by minimizing Eq. (12).

Assuming that there exist $\bar{N}$ GNSS signals that are the unique parameter to acquire first, for the convenience of description, the n-th signal is selected to be illustrated as

$$\mathbf{x}_n(k) = \mathbf{x}(k) - \sum_{i=1, i\neq n}^{\bar{N}} \mathbf{a}(\hat{\theta}_i)\hat{s}_i(k) \tag{13}$$

Since $\left\{\,\hat{\theta}_i \quad \hat{s}_i(k)\,\right\}_{i=1,i\neq n}^{\bar{N}}$ can be acquired by the previous iterative operations, the cost function of the n-th signal can be updated into

$$\mathbf{F}_2[\,\theta_n \mathbf{s}_n(k)\,] = \sum_{k=1}^{K} [\mathbf{x}_n(k) - \mathbf{a}(\theta_n)\mathbf{s}_n(k)]^H [\mathbf{x}_n(k) - \mathbf{a}(\theta_n)\mathbf{s}_n(k)] \tag{14}$$

By minimizing Eq. (12), $\hat{\theta}$ and $\hat{s}(k)$ of the n-th signal can be calculated as

$$\hat{s}_n(k) = \frac{\mathbf{a}^H(\theta_n)\mathbf{x}_n(k)}{M}\Big|_{\theta_n=\hat{\theta}_n} \quad k = 1, 2, \ldots K \tag{15}$$

$$\hat{\theta}_n = \arg\min_{\theta_n} \sum_{k=1}^{K} \left\| \left[\mathbf{I} - \frac{\mathbf{a}(\theta_n)\mathbf{a}^H(\theta_n)}{M}\right] \mathbf{x}_n(k) \right\|^2 \tag{16}$$

As long as the number of the detected signals is acquired, we can get the DOA and waveform evaluation accurately. We can acquire all the DOAs of the spoofing signals that can be written as $\hat{\theta}_1, \hat{\theta}_2 \cdots \hat{\theta}_m$. Based on that we can get the subspace A_s of the spoofing signals that can be defined as

$$A_s = \left[b\left(\hat{\theta}_1\right) b\left(\hat{\theta}_2\right) \cdots b\left(\hat{\theta}_m\right) \right] \tag{17}$$

Then we can construct the orthogonal projection matrix of the spoofing signals that is written as

$$\mathbf{P}_{\perp 1} = \mathbf{I} - \mathbf{A}_s(\mathbf{A}_s^H \mathbf{A}_s)^{-1} \mathbf{A}_s^H \tag{18}$$

So the spoofing signals can be suppressed as

$$\begin{aligned} X(nT_s) &= P_{\perp 1} r(nT_s) \\ &= P_{\perp 1} A_a Q_a(nT_s) + P_{\perp 1} A_s Q_s(nT_s) + P_{\perp 1} \eta(nT_s) \\ &= P_{\perp 1} A_a Q_a(nT_s) + P_{\perp 1} \eta(nT_s) \end{aligned} \tag{19}$$

From Eq. (19), we can find that $P_{\perp 1} A_a$ can affect the authentic signals. So we should adopt some methods to maximize the output signals. Here we introduce a $M \times N_a$ arbitrary vector h to compensate the authentic signals. Then we should maximize the matrix $h^H P_{\perp 1} A_a$ to guarantee the signals' reliability. Let

$$\mathbf{h} = \frac{\mathbf{P}_{\perp 1}\mathbf{A}_a}{\|\mathbf{P}_{\perp 1}\mathbf{A}_a\|} \tag{20}$$

The output power will be maximized by h.

3.2 Data Processing

When the receiver acquires and tracks a spoofing signal, we can get the navigation data, the PRN code, the Doppler frequency, the carrier phase, the code delay and

signal power. Here the received signals V that are from spatial processing can be expressed as

$$\mathbf{V} = \sum_j \mathbf{q}_a^j + \sum_i \mathbf{q}_s^i + \boldsymbol{\eta}_K \tag{21}$$

When we acquire the navigation data w_s^m, the PRN code c_s^m, the Doppler frequency f_s^m, the carrier phase ϕ_s^m, the code delay τ_s^m and the signal power p_s^m, the orthogonal projection subspace of m-th spoofing signal can be written as

$$\mathbf{P}_{\perp 2}^m = \mathbf{I} - \mathbf{q}_s^m (\mathbf{q}_s^{mH} \mathbf{q}_s^m)^{-1} \mathbf{q}_s^{mH} \tag{22}$$

We can remove the spoofing signal q_s from V as

$$\begin{aligned} \mathbf{V}_f &= \mathbf{P}_{\perp 2}^m \mathbf{V} \\ &= \mathbf{P}_{\perp 2}^m \left(\sum_j \mathbf{q}_a^j + \sum_i \mathbf{q}_s^i + \boldsymbol{\eta}_K \right) \\ &= \mathbf{P}_{\perp 2}^m \sum_j \mathbf{q}_a^j + \mathbf{P}_{\perp 2}^m \sum_i \mathbf{q}_s^i + \mathbf{P}_{\perp 2}^m \boldsymbol{\eta}_K \\ &= \mathbf{P}_{\perp 2}^m \sum_j \mathbf{q}_a^j + \mathbf{P}_{\perp 2}^m \sum_{i \neq m} \mathbf{q}_s^i + \mathbf{P}_{\perp 2}^m \boldsymbol{\eta}_K \end{aligned} \tag{23}$$

Because the PRN code has better characters, the subspaces of different PRNs and the subspaces of the same PRN with different code delays are approximately orthogonal. So the result of Eq. (23) can be simplified as

$$\begin{aligned} \mathbf{V}_f &= \mathbf{P}_{\perp 2}^m \sum_j \mathbf{q}_a^j + \mathbf{P}_{\perp 2}^m \sum_{i \neq m} \mathbf{q}_s^i + \mathbf{P}_{\perp 2}^m \boldsymbol{\eta}_K \\ &\approx \sum_j \mathbf{q}_a^j + \sum_{i \neq m} \mathbf{q}_s^i + \boldsymbol{\eta}_K \end{aligned} \tag{24}$$

Then the spoofing signal can be eliminated by the subspace that need to be constructed by six parameters, the navigation data, the PRN code, the Doppler frequency, the carrier phase, the code delay and the signal power.

In [8], the signal power is proved to be independent with the orthogonal subspace. The navigation data is also proved to be needless to construct the orthogonal subspace when the data is long enough. The condition is easily achieved for the GNSS receiver. And the carrier phase is also proved to be independent with the orthogonal subspace when the signal is complex signal. Because the GNSS receiver usually use I/Q mixer, the carrier phase can be also neglected. When all the constraint conditions are met, we can utilize the PRN code, the Doppler frequency and the code delay to eliminate the spoofing signal, which will simplify the calculation.

3.3 The Receiver Structure

In this part the receiver structure is proposed in detail that is shown in Fig. 2. In data processing, the projection subspace is constructed for every spoofing signal instead of developing only one subspace for all signals because it has lower complexity [9], which can suppress the spoofing signals that are not aligned with the authentic one in the code domain. But when the spoofing signal is much stronger than the authentic signal that will brings strong cross-correlation interference. It may be hard to acquire the signals for data processing. For the new receiver, it can mitigate the strong spoofing signals in spatial processing. It not only guarantee the normal operation of data processing but also mitigate the spoofing signals that cannot be suppressed by data processing, which greatly enhances the reliability of the receiver. Then the processing procedure is introduced as follows:

- Estimate the DOA and waveform of the signals, pick up the spoofing signals, construct the space orthogonal subspace $P_{\perp 1}$;
- maximize the power of the output signals;
- Acquire, track all signals, obtain the parameters c, f, τ;
- Construct the i-th orthogonal subspace $P^{i}_{\perp 2}$ for the i-th signal with the parameters of i-th signals, project the received signals onto the subspaces respectively;
- Select the authentic signals, decode them and pass all signals to the baseband processing.

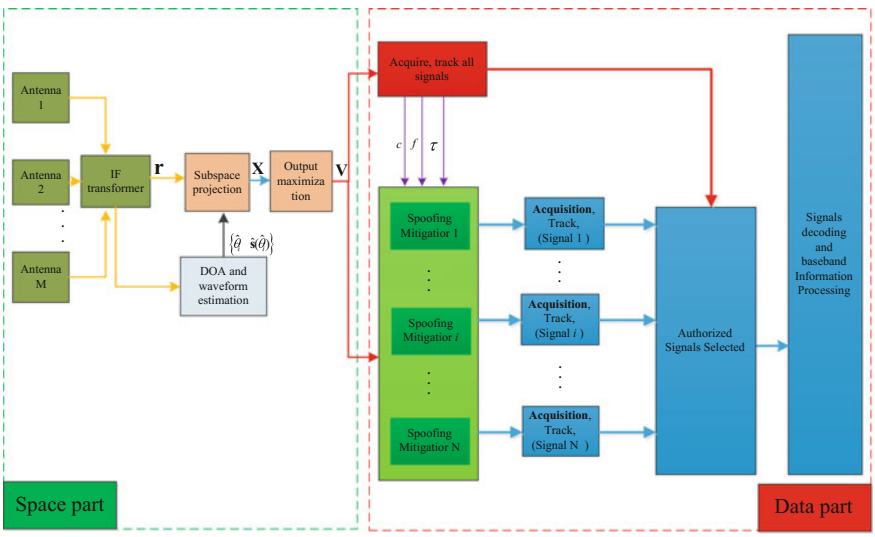

Fig. 2 The receiver structure

4 Simulation

In this section, the spatial processing is mainly to suppress the strong spoofing sources with higher power, while data processing can mitigate the spoofing signals not consistent with the authentic signals in the code domain. And the performances are evaluated respectively.

The acquisition of GPS signal is utilized to verify the performance of the new receiver. The parameters are shown in Table 1. In spatial processing, the receiver distinguishes the spoofing signals from the authentic ones with the DOA and waveform.

We conduct the simulation to get the detection and false alarm probability that are our primary indicators to evaluate our new receiver. And the threshold is set according to Neyman-Pearson criterion, false alarm probability is defined as 0.05. The results are shown in Figs. 3 and 4. Figure 3 shows the relation between probability and *ISR* (interference to signal ratio) where the dashed line means the detection probability and the solid line means the false alarm probability. And when the *ISR* is more than 7 dB, the detection probability is greater than 0.9 and the false alarm probability is very small. In Fig. 4, the relation between the average ratio

Table 1 Simulation parameters

Parameter	Value
DOA of authentic signals	20 30 40 50 60
DOA of spoofing sources	10 35 340
PRN	4 5 6
IF	1.405 MH
Sample frequency	5.714 MHz
C/N_0	45 dB-Hz
Frequency Search Bandwidth	5 kHz

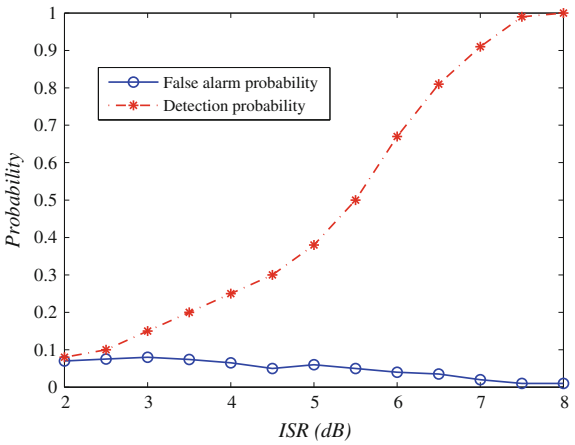

Fig. 3 The probability with three spoofing sources

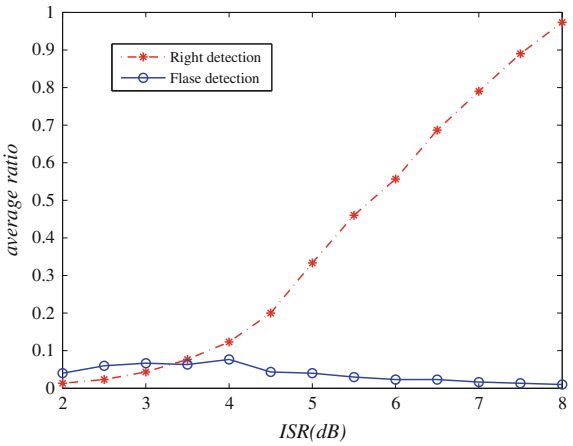

Fig. 4 The average ratio with three spoofing sources

(number of spoofing detected to number of all spoofing ratio) and *ISR* is shown, where the dashed line means the right detection ratio and the solid line means the false detection ratio. When *ISR* is more than 7 dB, the right detection ratio is more than 0.8 and the false detection ratio is also very small. In the whole simulation, the false alarm probability is very low that is below 0.1 all the time and the false detection ratio is less than 0.1. So spatial processing of the new receiver has good inhibitory performance to strong spoofing sources. If the detection is wrong, the receiver will eliminate the authentic signals. In this paper we adopt higher threshold to keep lower false alarm probability, because the weak spoofing signals can be distinguished better in data processing.

After strong spoofing signals are mitigated, the cross-correlation interference between the signals will be small. Then data processing will suppress the spoofing signals that not aligned with the authentic signals, the result is introduced in Fig. 5. In the figure, the probability means the acquisition probability. If the receiver can

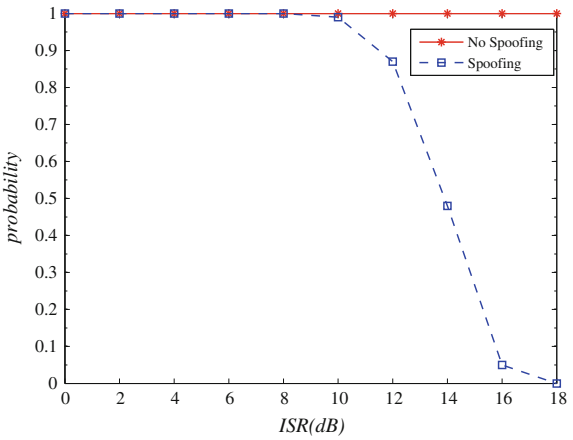

Fig. 5 Probability in data processing

acquire the signal again after mitigating the spoofing signals include the same PRN code, it means the receiver can get the authentic signals. So the probability also represents the detection and mitigation probability. From the result, we can find that if the *ISR* is below 10 dB, the probability is almost 100%. Hence data processing can suppress the spoofing signals with lower power validly.

5 Conclusions

In this paper, a cooperative anti-spoofing technology based on subspace projection is proposed, which includes spatial processing and data processing. They use different parameters A_s and Q_s to construct two subspaces. As the two parts are suitable for different scenarios, the new technology can deal with more kinds of spoofing signals. Meanwhile spatial processing can help data processing conduct spoofing signals more validly and robustly. In the simulations, the two parts show their validity in respective scenarios. The algorithm in spatial processing can detect one or more strong spoofing sources with high detection probability approaches to 100% and mitigate them. In data processing, the receiver can mitigate the weak spoofing signal that is not aligned with the authentic one. Certainly, the new technology can bring better performances.

Acknowledgements This work is supported by the National Natural Science Foundation of China (No.91438205) and Natural Science Foundation of Jiangsu Province (No. BK20171023).

References

1. Ganther C (2013) A survey of spoofing and counter-measures. In: Proceeding of navigation, Journal of the Institute of Navigation, pp 159–177
2. Kim T et al (2012) Analysis of effect of spoofing signal in GPS receiver. In: ICC 2012, IEEE, JeJu Island, ROK, pp 2083–2087
3. Jafarnia-Jahromi A et al (2012) GPS spoofer counter measure effectiveness based on signal strength, noise power and C/N0 observables. Int J Satell Commun Netw, 181–191
4. Han S, Luo D, Meng W, Li C (2014) A novel anti-spoofing method based on particle filter for GNSS. In: ICC 2014, IEEE, Sydney, AUS, pp 5413–5418
5. Daneshmand S et al (2012) A low-complexity GPS anti-spoofing method using a multi-antenna array. In: ION GNSS' 2012, pp 1233–1243
6. Landon J et al (2012) Model-based subspace projection beamforming for deep interference nulling. IEEE Trans Signal Process, 1215–1228
7. Han S, Zhang Y, Meng W, Li C (2015) GPS anti-spoofing technology based on RELAX algorithm in smart grid. In: Chinacom 2015, IEEE, Shanghai, PRC
8. Chen L, Meng W, Han S, Li C (2015) Subspace projection based anti-spoofing algorithm for GNSS receiver. In: CSNC 2015, Xi'an, PRC
9. Han S, Chen L, Meng W, Li C (2017) Improve the security of GNSS receivers through spoofing mitigation. In: IEEE Access, pp 21057–21069

Beidou B1I Signal Acquisition Scheme Based on Variable Length Data Accumulation

Menghuan Yang, Guoping Wang, Yingxin Zhao and Hong Wu

Abstract The Neumann-Hoffman code is modulated in Beidou D1 navigation message, which increases the possibility of bit sign transition. It puts a constraint on the coherent integration duration for possible bit sign transition. An acquisition scheme of Beidou B1I signal has been proposed in this paper. Firstly, the carrier and sign bit code are deprived by delay and multiplication. Then, the Doppler shift of the ranging code is searched. According to the Doppler shift of ranging code, the variable length of data block is accumulated to 1 ms data. Finally, the ranging code phase is detected by FFT-based synchronized algorithm. The carrier frequency offset, whose boundary is determined by the Doppler shift of ranging code, is accurately estimated by means of chirp-z transform. The experiment shows that the method can achieve long-term coherent integration and improve the acquisition probability.

Keywords BDS · Acquisition · Bit sign transition · Doppler shift
Chirp-z transform

1 Introduction

In the procedure of Beidou satellite signal reception, the first step is the signal acquisition. We need to acquire the approximate carrier frequency offset and ranging code phase, providing initial parameters for subsequent signal tracking. It is necessary to obtain sufficient gain by long-term coherent integration. However, the sign bit transition may be introduced in long-term coherent integration, causing

M. Yang · G. Wang · Y. Zhao · H. Wu (✉)
College of Electronic Information and Optical Engineering,
Nankai University, Tianjin, China
e-mail: wuhong@nankai.edu.cn

M. Yang · G. Wang · Y. Zhao · H. Wu
Tianjin Key Laboratory of Optoelectronic Sensor and Sensing
Network Technology, Tianjin, China

J. Sun et al. (eds.), *China Satellite Navigation Conference (CSNC) 2018 Proceedings*, Lecture Notes in Electrical Engineering 498,
https://doi.org/10.1007/978-981-13-0014-1_10

the correlation peak to be neutralized. The higher data rate of the signal, the more frequently the bit sign transition may occur. The data rate of GPS L1 signal is 50 bps. However, when it comes to Beidou B1I signal, the data rate of the D1 navigation message is 50 bps. After the second modulation Neumann-Hoffman (NH) code, the data rate becomes 1 kbps. The data rate of the D2 navigation message is 500 bps. Beidou B1I signal data rate is much greater than the GPS L1 signal, which means it is vulnerable to bit sign transitions, leading to acquisition failure.

In order to overcome the bit sign transition, commonly used methods include non-coherent integration and differential coherent integration. Non-coherent integration adds the result of coherent integration after square processing, which can eliminate the influence of bit sign transition [1], but it cannot eliminate the bit sign transition in pre-coherent integration process. Meanwhile, it introduces square loss, which reduces acquisition performance. Differential coherent integration cross multiply the adjacent moments I and Q channel and then accumulation, which avoid the loss of squared, but the adjacent data blocks require to have same bit sign. In view of NH code modulation, Beidou B1I signal cannot meet this point, resulting in acquisition failure. In order to improve the acquisition efficiency, Li Dengbo et al. proposed a secondary acquisition method. The search is not only for the ranging code phase but also for the NH code phase [2]. The method is computationally complex and works well for the D1 navigation message, but not suitable for the D2 navigation message. Macchi et al. proposed a zero-padding algorithm that adds zero to the local ranging code [3]. This method overcomes the bit sign transition in the process of coherent integration by adding a certain amount of computation, but it has a limited improvement for the integral time length and poor performance for weak signal acquisition. Tsui uses delay and multiplication to deprive carriers and data codes, which eliminates the bit sign transition, but only work for strong signal acquisition [4].

In this paper, we propose a Beidou B1I signal acquisition method based on variable length data accumulation. The carrier and sign bit code are deprived by delay and multiplication, which solve the problem of peak offset caused by bit sign transition. In the process of long-term coherent integration, the Doppler shift of the ranging code is searched by the variable length of the accumulated data block. The FFT-based acquisition algorithm is used on the accumulated signal to achieve the detection of the phase-ranging code. According to the frequency offset of the ranging code obtained from the search, the carrier frequency offset range is determined, and then the carrier frequency offset estimation is implemented by the chirp Z transform. The main innovations of this paper are as follows: The noise performance of signal processed by delay and multiplication is studied in detail; a method of acquisition based on the search of the frequency offset of ranging code is proposed, and the length of coherent integral is greatly extended.

The remainder of this paper is organized as follows: Sect. 2 analyses the principle of delay and multiplication process, and the change of SNR after the process. Section 3 presents an acquisition scheme based on variable length data accumulation. Section 4 conducts an experiment and analyses the results. Section 5 concludes the paper.

2 The Principle of Delay and Multiplication

2.1 The Structure of Signal Processed by Delay and Multiply

In view of Beidou B1I signal, the intermediate frequency (IF) signal $S(t)$ from the RF front-end can be expressed as:

$$S(t) = D(t)C(t)\sin(2\pi ft) + W(t) \tag{1}$$

where $D(t)$ is the navigation message data bit, $D(t) = \pm 1$, and $D(t)$ also contains the NH code for the D1 navigation message; $C(t)$ is the ranging code; f is the carrier frequency, $f = f_{IF} \pm 5\,\text{KHz}$, f_{IF} is the theoretical intermediate frequency; $W(t)$ is Gaussian white noise, $W(t) \sim \text{N}(0, \sigma^2)$. The carrier amplitude is normalized in (1), and the noise power becomes accordingly

$$\sigma^2 = \frac{N_0 B_w}{2A^2} \tag{2}$$

where A is the actual received carrier signal amplitude; B_w is the RF front-end bandwidth; $N_0/2$ is the bilateral band noise power spectral density. The signal-to-noise ratio of the RF signal is

$$SNR = \frac{1}{2\sigma^2} \tag{3}$$

The intermediate frequency signal $S(t)$ delay and multiplied by itself, after which the new signal $S_\tau(t)$ can be expressed as

$$S_\tau(t) = S(t)S(t-\tau) = D_0(t)C_0(t)F_0(t) + W_0(t) \tag{4}$$

$$D_0(t) = D(t)D(t-\tau) \tag{5}$$

$$C_0(t) = C(t)C(t-\tau) \tag{6}$$

$$F_0(t) = \frac{1}{2}\cos(2\pi f\tau) - \frac{1}{2}\cos[2\pi f(2t-\tau)] \tag{7}$$

$$W_0(t) = W(t)W(t-\tau) \tag{8}$$

In Eq. (5), as shown in Fig. 1, $D_0(t)$ can be regarded as a fixed value of 1. In Eq. (6), the product of a Gold code and its delayed version belongs to the same family as the Gold code, which indicates that its autocorrelation and the cross correlation can be used to find its beginning point. In Eq. (7), it consists of the DC term and the high frequency term. The DC term is constant value, while the high frequency term can be filtered out. In order to make this equation usable, the

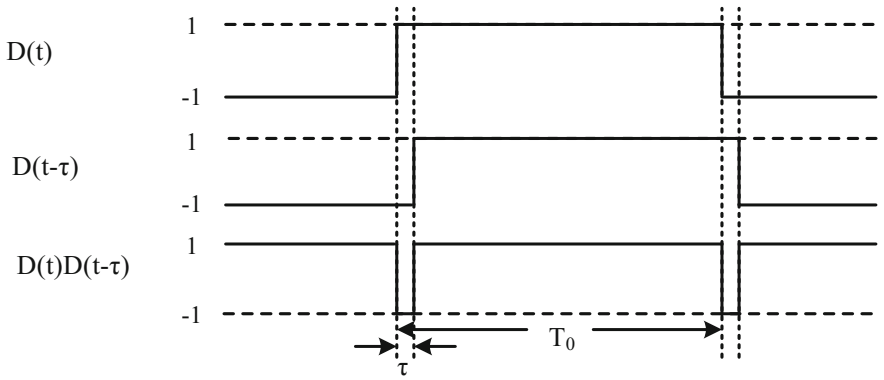

Fig. 1 bit sign transition in Delay-and-Multi approach

$\cos(2\pi f\tau)$ must be close to unity which can be achieved by certain value of τ. In Eq. (8), the cross-terms of signal and noise are ignored, because the noise power is much higher than the satellite signal. To simplify Eqs. (5)–(8), Eq. (4) can be written as

$$S_\tau(t) = \frac{1}{2}C_0(t) + W_0(t) \tag{9}$$

From Eq. (9), we can see that the carriers and the data codes are deprived after the delay and multiplication, leaving only the new ranging codes. The new ranging codes still have good correlation features, which is necessary for signal acquisition.

2.2 Noise Analysis

Although the delay and multiplication procedure can successfully deprive the carrier and data codes, it also introduces a lot of noise. The noise in Eq. (9) is analyzed below. When $W(t)$ is uncorrelated with $W(t-\tau)$, the noise power of $W_0(t)$ is the lowest. For the white Gaussian noise with band of $[f_1, f_2]$, the relevance between $W(t)$ and $W(t-\tau)$ can be given by their autocorrelation function:

$$R(\tau) = N_0 B \frac{\sin(\pi B\tau)}{\pi B\tau}\cos(2\pi f_0\tau) \tag{10}$$

where $B = f_2 - f_1$, $f_0 = (f_2 + f_1)/2$. As shown in Fig. 2, when τ takes a certain value, $R(\tau) = 0$ and $W(t)$ is uncorrelated with $W(t-\tau)$. For two normal random variables, irrelevance is equivalent to being independent with each other. The distribution of a product of two independent zero mean normal random variables is given by [5]

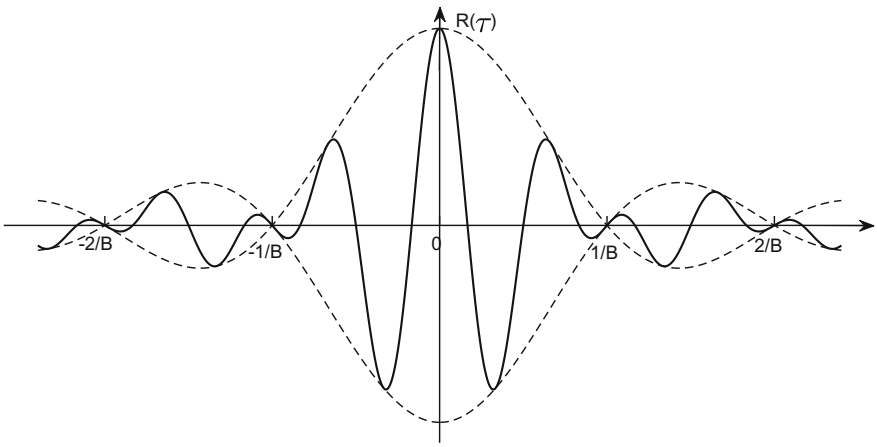

Fig. 2 Autocorrelation function of bandlimited white Gaussian noise

$$P(u) = \frac{K_0(|u|/\sigma^2)}{\pi\sigma^2} \tag{11}$$

where u = $W(t)W(t-\tau)$, $K_0(\cdot)$ is modified Bessel function of the second kind of order zero. The mean of u is 0 and the variance is σ^4. The power of noise u can be calculated as

$$\mathrm{E}\left(u^2\right) = [\mathrm{E}(u)]^2 + \mathrm{D}(u) = \sigma^4 \tag{12}$$

And the signal-to-noise ratio of $S_\tau(t)$ can be seen as

$$SNR_1 = \frac{1}{4\sigma^4} = SNR^2 \tag{13}$$

If the signal-to-noise ratio is expressed in dB, it becomes

$$SNR_1 = 2SNR \tag{14}$$

In order to further analyze the SNR after the delay and multiplication procedure, we need to estimate the SNR of the intermediate frequency signal. According to the Beidou Navigation Satellite System Signal in Space Interface Control Document, the minimum user-received signal power level is specified to be −163dBW for B1I signal [6]. The antenna equivalent noise temperature T_e is supposed to be 290 K. Then the minimum signal-to-noise ratio of Beidou B1I signal can be estimated as

$$SNR = S - 10\log_{10}(kT_eB_w) \approx -25\,\text{dB} \tag{15}$$

where k is Boltzmann constant, and B_w is the RF front-end bandwidth, which is set to be 4.092 MHz. Take Eq. (15) into Eq. (14), we can calculate $SNR_1 = -50$dB. Previous study have shown that the baseband SNR must be above 14 dB for reliable signal acquisition [7], which can be summarized as

$$SNR_1 + G \geq 14\,\text{dB} \tag{16}$$

The coherent gain G can be calculated by Eq. (17).

$$G = 10\log_{10}(B_wT_c) \tag{17}$$

Take Eq. (17) into Eq. (16), we can get the coherent integration time T_c 628 ms. In other word, the length of coherent integration is at least 628 ms to ensure signal acquisition.

3 Acquisition Scheme Based on Variable Length Data Accumulation

The coherent integration time of traditional FFT parallel code phase search algorithm is only a few milliseconds. However, the required coherent integration time is up to hundreds of milliseconds after the delay and multiplication procedure. Besides, the computation rises up greatly. From Eq. (8), it can be seen that the signal part of $\boldsymbol{S_\tau(t)}$ consists of only the new ranging code $\boldsymbol{C_0(t)}$, ***which*** is a periodic signal whose frequency is equal to the ranging code $\boldsymbol{C(t)}$. Obviously, it is feasible to reduce computation by periodically accumulate $\boldsymbol{C_0(t)}$.

At the transmitter, the period of ranging code $\boldsymbol{C(t)}$ is $\boldsymbol{T_0}$ = 1 ms. At the receiver, due to the relative speed between the satellite and the receiver, the period of ranging code changes in consideration of the Doppler shift, which cannot be ignored in the process of long-term coherent integration. The Doppler shift of carrier and ranging code has the following relation:

$$\frac{\Delta f_c}{\Delta f_B} = \frac{f_c}{f_B} \tag{18}$$

where $\boldsymbol{f_c}$ is carrier frequency, $\boldsymbol{f_c}$ = 1561.098 MHz; $\boldsymbol{f_B}$ is the ranging code rate, $\boldsymbol{f_B = 2.046\,MHz}$. Besides, $\Delta\boldsymbol{f_c}$ and $\Delta\boldsymbol{f_B}$ is the Doppler frequency shift of carrier and ranging code, respectively. The maximum value of $\Delta\boldsymbol{f_c}$ and $\Delta\boldsymbol{f_B}$ is 5 kHz and

6.5 Hz, respectively. Due to the existence of the Doppler shift of the ranging code, the period of the ranging code changes. When the frequency of ranging code is shifted by Δf_B, the number of sample points of the ranging code increases or decreases by 1 sample point per N periods. N and Δf_B have the following relationship:

$$N = \frac{f_B}{\Delta f_B} \cdot \frac{1}{L} \tag{19}$$

where L is the number of sample points of one period ranging code, $L = T_0 f_s$, and f_s is sample rate. After every N periods ranging codes are accumulated, the length of ranging codes is compensated by means of zero-padding or truncation. After the compensation of the ranging code, superimposed to get a period of the ranging code signal, and then conduct correlation operation with the local ranging code to achieve signal acquisition. As shown in Fig. 3, the algorithm can be expressed in the following flow.

(1) Delay and multiplication. The acquired intermediate frequency signal S(t) is delayed by τ and multiplied by itself to obtain a new signal $S_\tau(t)$.
(2) Accumulate $S_\tau(t)$ in blocks. The Doppler frequency shift of the ranging code is searched. According to the frequency shift Δf_B, a data block with a length of N period ranging codes is selected, and adjacent M data blocks are accumulated to obtain $S_N(t)$. When $\Delta f_B > 0$, the sample points of $S_N(t)$ is NL − 1; when $\Delta f_B < 0$, the sample points of $S_N(t)$ is NL + 1.
(3) The signal $S_N(t)$ is further accumulated. The sample points of $S_N(t)$ is NL ± 1, and is compensated to NL by truncation or zero-padding operation. The new sequence is accumulated every L sampling points to obtain a sequence $S_0(t)$ of length L.
(4) FFT-based Acquisition. The locally generated ranging code delay and multiplied by itself, then conduct the FFT transform and take the conjugate, afterwards multiplied by the frequency domain of $S_0(t)$. IFFT transform is conducted on the product, then take the absolute value and locate the peak value.
(5) If the peak value is greater than the threshold, then the acquisition is successful. The peak corresponding to the code phase and Δf_B is the acquisition result. Otherwise, change the value of Δf_B, then return to step 2).
(6) Estimate the carrier frequency. The carrier frequency range is determined by Eq. (18). According to the ranging code phase, the ranging code is deprived from satellite IF signal $S(t)$, then using chirp-Z transform to achieve accurate estimation of the carrier frequency.

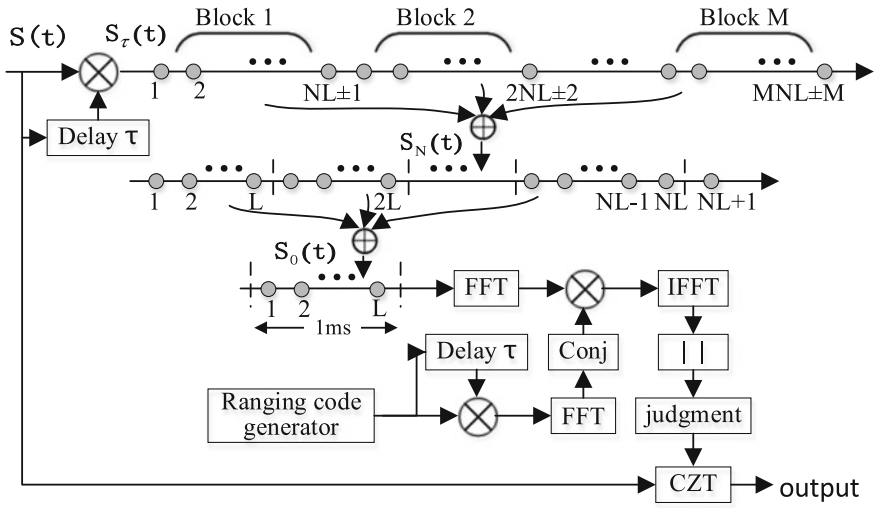

Fig. 3 BDS B1I signal acquisition scheme based on variable length data accumulation

By means of variable length data accumulation method, the data of T = MN milliseconds can be accumulated into 1 ms data, thereby greatly reducing the amount of calculation, and then realizing long-term coherent integration of satellite signals.

4 Experiments and Results

In order to verify the validity of the Beidou B1I signal acquisition method, this paper uses the practical data for signal acquisition. USRP 2920 is used as the hardware platform to acquire Beidou B1I signal. The sampling quantized level is 8 bit. The antenna was located in 38° 59′N, 117° 20′E and the signal reception took place at 15:54 on April 20, 2017.

Experiment 1: For the practical received signal, an acquisition method based on variable length data accumulation is realized by a software receiver on MATLAB. Software receiver parameters are shown in Table 1.

Figure 4 is the acquisition results for satellite No. 1. Positioning the peak point, we can get the Doppler frequency ranging code and code phase offset. In order to accurately estimate the carrier frequency, the ranging code is derived from the intermediate frequency signal, then accurate estimation of the carrier frequency is realized by using the CZT transform. Figure 5 shows the result of carrier frequency estimation for No. 1 satellite with a frequency resolution of 10 Hz, which provides an accurate carrier frequency value for subsequent signal tracking.

Table 1 The parameters of BDS software receiver

Sampling frequency f_s	10 MHz
Theoretical intermediate frequency f_{IF}	2.5 MHz
Delay τ	2.2 μs
The range of ranging code Doppler shift	[−6.5 Hz, 6.5 Hz]
The step of ranging code Doppler shift	0.5 Hz
Coherent integration time length	700 ms
CZT transform frequency resolution	10 Hz

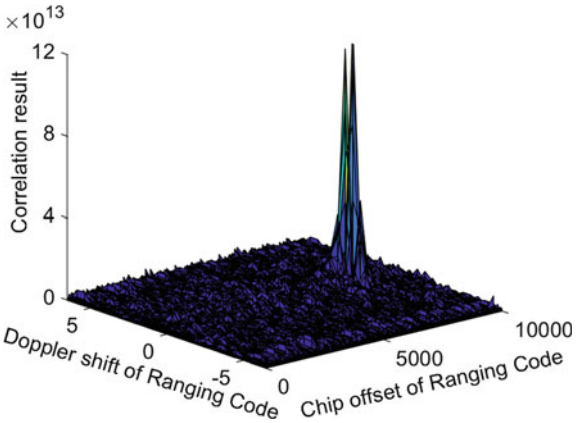

Fig. 4 The acquisition result of Beidou satellite No.1

In experiment 1, the acquisition of B1I signal of Beidou is realized by the method of variable length data accumulation, and the accurate estimation of the phase and carrier frequency of ranging code is also completed. The validity of this method has been verified.

Experiment 2: the ROC (Receiver Operating Characteristic) curve is analyzed by comparing the acquisition method based on the variable length data with the traditional coherent integration method, the non-coherent integration method and the difference coherent integration method. In this experiment, the acquisition parameters based on variable length data are consistent with experiment 1. The integral time length of coherent integration, non-coherent integration and differential coherent integration is 4 ms.

The formulas for the satellite No. **i** detection probability $\boldsymbol{P_{d,\mathbf{i}}}$ and the false alarm probability $\boldsymbol{P_{f,i}}$ are as follows:

$$\mathrm{P_{d,i}} = \mathrm{P}\{\mu_\mathrm{i} > \alpha | \mathrm{H_{1,i}}\} \tag{20}$$

$$\mathrm{P_{f,i}} = \mathrm{P}\{\mu_\mathrm{i} > \alpha | \mathrm{H_{0,i}}\} \tag{21}$$

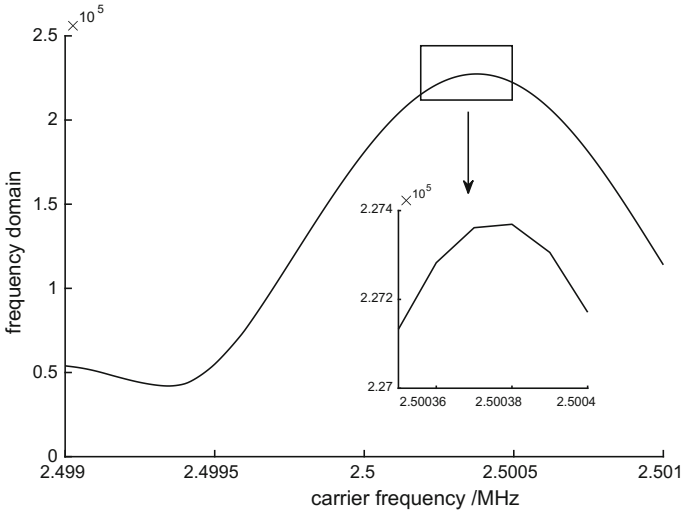

Fig. 5 The estimate of carrier frequency by CZT

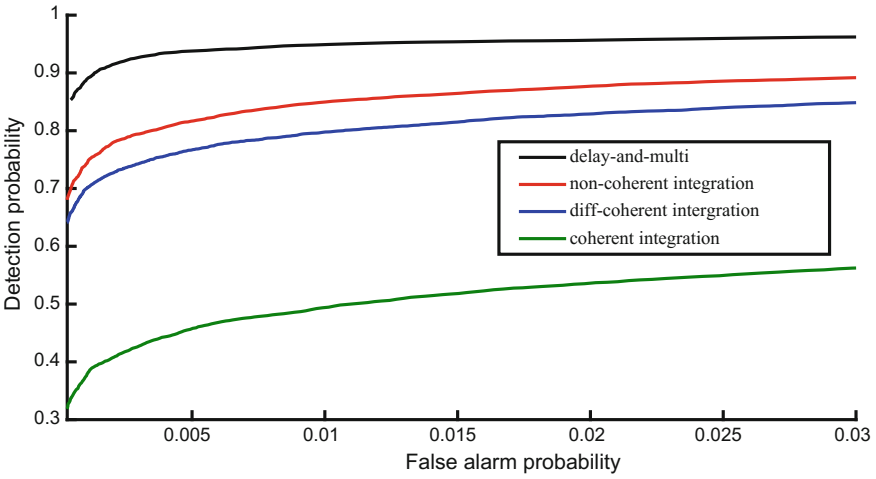

Fig. 6 ROC curve of acquisition results for satellite No. 32

where the events $\boldsymbol{H}_{1,i}$ and $\boldsymbol{H}_{0,i}$ represent that the practical received signal includes, excludes the signal of satellite No.**i**, respectively; $\boldsymbol{\mu_i}$ denotes the peak value correlative to the locally generated ranging code; and α is the acquisition threshold. Figure 6 shows the ROC curve for satellite No. 32 after $\mathbf{10^4}$ acquisitions. It can be seen from the figure that, under the same false alarm probability, the probability of successful acquisition based on variable length data accumulative acquisition method is obviously greater than the traditional coherent integration method,

non-coherent integration method and differential coherent integration method. In the case of false alarm probability $\boldsymbol{P_f = 0.01}$, the detection probability of coherent integral, non-coherent integral and differential coherent integral are 49.4, 84.9 and 79.8%, respectively. As a contrast, the acquisition probability based on variable length data accumulation is 94.9%, which is increased by 10% or more.

In Experiment 2, the signal acquisition method based on variable length data is compared with traditional coherent integration, non-coherent integration and difference coherent integration. In the case of the same false alarm probability, the probability of acquisition is higher than the traditional three methods.

5 Conclusion

In this paper, we propose a Beidou B1I signal acquisition scheme based on variable length data accumulation. This method solves the problem of bit sign transition by delay and multiplication. The Doppler shift of the ranging code is searched by changing the length of the accumulated data block. The experiment shows that the method can effectively capture the Beidou B1I signal, and the probability of capture is 94.9% when the false alarm probability is 0.01. This method, which can be widely used in the Beidou receiver, has high practical value.

Acknowledgements This work was supported in part by the National Natural Science Foundation of China under grant nos. 61571244 and 61501262, in part by Tianjin Research Program of Application Foundation and Advanced Technology under grant no. 16YFZCSF00540.

References

1. Li X, Guo W (2013) Efficient differential coherent accumulation algorithm for weak GPS signal bit synchronization. IEEE Commun Lett 17(5):936–939. https://doi.org/10.1109/LCOMM.2013.031913.130267
2. Li D-A, Niu W-H, Zhao J-M, Li S, Liu J-Q (2016) Twice acquisition algorithm of BDS signal based on the secondary code. 36(3):289–294. https://doi.org/10.15918/j.tbit1001-0645.2016.03.013
3. Macchi F, Petovello MG (2007) Development of a one channel Galileo L1 software receiver and testing using real data. In: Proceedings of the 20th international technical meeting of the satellite division of the Institute of Navigation (ION GNSS'07), vol 2, pp 2256–2269
4. Tsui JBY (2005) Fundamentals of global positioning system receivers: a software approach, vol 173. Wiley, Hoboken
5. Sharma RK, Wallace JW (2009) Improved spectrum sensing by utilizing signal autocorrelation. In: IEEE 69th vehicular technology conference. VTC Spring 2009, pp 1–5. https://doi.org/10.1109/vetecs.2009.5073595
6. BeiDou ICD (2013) BeiDou navigation satellite system signal in space interface control document open service signal B1I (Version 2.1)
7. Lu Y (2016) Beidou/GPS dual mode software receiver principle and implementation of technology. Publishing House of Electronic Industry

Design and Simulation of Synchronization Algorithm for Short Time Burst- Mode GMSK Signal

Guoshuai Ren, Wenquan Feng and Xi Liu

Abstract The AIS (Automatic Identification System) is a marine monitoring system with means of detection capabilities, providing multi-user applications for offshore services. The satellite-based AIS system send the received AIS signals for analysis by one or more low orbit satellites. The satellite-based AIS is a new navigation aid system which can be used as a complement to navigation system. The AIS system is a Non-real-time communication system, using GMSK modulation. The reception of short time burst AIS signal is facing frame synchronization, Doppler shift compensation, phase compensation, delay spread and other issues. This paper describes an innovative synchronization algorithm for the short burst-mode GMSK signal. There are several advantages of this synchronization algorithm. The signal is processed in real time. It voids the loss of data caused by commonly used loop structure. The devised algorithm provides an excellent performance against noise, delay spread, frequency offset and phase offset. The demodulator using this synchronization algorithm shows that the bit error's performance degradation is only about 0.3 dB.

Keywords Short burst-mode GMSK · Signal detection · Frequency offset estimation · Phase offset estimation · Timing synchronization

1 Introduction

Nowadays the Automatic Identification System (AIS) is the main means to help navigation. It is widely used in many fields, such as maritime traffic regulation, maritime rescue and fight against terrorism. Furthermore, AIS is considered as a navigation system to assist Beidou and GPS. When AIS works, it will use the positioning and timing servers from navigation satellites.

G. Ren (✉) · W. Feng · X. Liu
Beihang University, Beijing 100191, China
e-mail: twrgs@buaa.edu.cn

J. Sun et al. (eds.), *China Satellite Navigation Conference (CSNC) 2018 Proceedings*, Lecture Notes in Electrical Engineering 498,
https://doi.org/10.1007/978-981-13-0014-1_11

The Space-based AIS system consists of one or more LEO satellites, it forwards signals sent by sea users to ground stations for further analysis. Compared with traditional onboard AIS system, Space-based AIS system is a new type of marine surveillance system to represent a promising solution to provide AIS detection service coverage on any given area on the Earth. The marine security environment of China is complex and its rights are faced with many challenges. Therefore, accelerating the development of Space-based AIS system plays an important role in protecting marine environment and national security [1]. The signal format consists of a Gaussian minimum shift keying (GMSK) modulation. It transports in frame, each frame contains 576,000 bits data and lasts for 1 min. Each frame is composed by 2250 slots where the transmitters can transmit their bursts. Each slot has 256 bits and lasts for 26.67 ms [2].

The reception of short time burst AIS signal is facing time synchronization, frequency compensation, phase compensation, delay spread and other issues. The frequency shift is mainly caused by the high relative speed of satellites to mobile users. Each frame of the AIS signal are time-stamped by GPS/Beidou navigation system to maintain precise synchronization [3, 4]. This paper describes an innovative synchronization algorithm for the short burst-mode GMSK signal. The overall design of the algorithm is proposed. The key algorithms are studied. Finally, a software simulation platform is set up and the simulation results are given.

2 Design of Short Time Burst GMSK Signal Synchronization

In satellite mobile communications, frequency offset, phase offset and delay spread are major factors that cause the bit error rate to deteriorate and the communication quality to drop. The traditional loop does not suitable for short time burst mode signal. There are several advantages of this synchronization algorithm. The signal is processed in real time. The devised algorithm provides an excellent performance against noise, delay spread. It voids the loss of data caused by traditional loop structure. The synchronization algorithm is shown in Fig. 1. The key algorithms are as follows.

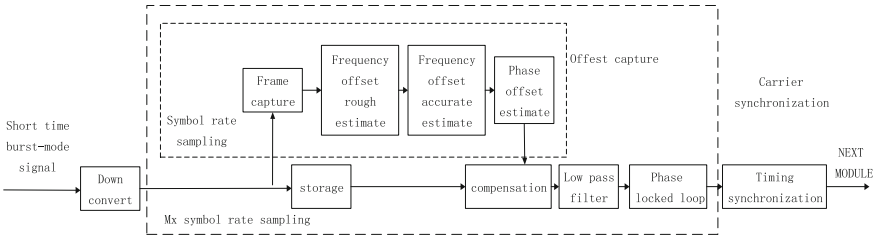

Fig. 1 Structure of synchronization algorithm of short burst signal

(1) Carrier synchronization: Convert the signal down, sampling the signal at M times speed and put the discrete-time sequences signal into storage. Then decimate the sampling signal by M into the frequency and phase capture module and estimate the offset. Compensate the offset to the signal from the storage and then finish the carrier synchronization.
(2) Timing synchronization: The algorithm in this paper is improved by the Gardner algorithm. Select the best sampling point from M points in each symbol. In this paper $M = 40$.

3 Carrier Synchronization

3.1 Header Capture and Rough Estimate Frequency Offset

The AIS signal is consisted by start time buffer (8 bits), training sequence (24 bits), start flag (8 bits), transmit data (168 bits), FCS (16 bits), end flag (8 bits) and end time buffer (24 bits).

The AIS signal's header is located at the 9th data bit. This paper use the data-assisted method for frame's header capture. Using training sequence and start flag, total 32 bit as header information. The specific method is shown in Fig. 2.

Stored the sampling signal which has M discrete points in each symbol. The discrete-time sequences can be expressed as the form of Eq. (3.1). Where $\mu(t)$ is additive white Gaussian noise, $\triangle f$ is the frequency offset, θ is the phase offset, τ is the timing error, and $\varphi_s(t)$ is the carrier frequency modulation phase.

$$s(t) = \exp\{j[\varphi_s(t-\tau)]\}\exp\{j(2\pi\triangle ft)+\theta\}+\mu(t) \tag{3.1}$$

Reference [5] pointed out that noise and time delay will interfere with the signal header detection. Put the signal $s(t)$ into storage, and then decimate by M to get sampling signal $r(t)$ into offset capture module. This paper proposes 1 bit difference method. First, the header information is used as a local training sequence (32 bits). The local detection sequence $\triangle a_n$ can be written as Eq. (3.2). Then the received sequence $\triangle r_n$ can be written as Eq. (3.3).

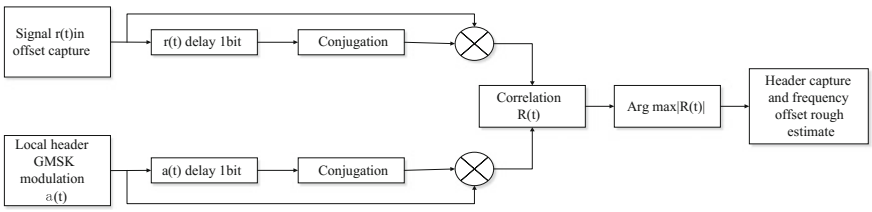

Fig. 2 Header capture and frequency offset rough estimate

$$\triangle a_n = a(nT) \cdot a^*((n+1)T) \tag{3.2}$$

$$\triangle r_n = r(nT) \cdot r^*((n+1)T) \tag{3.3}$$

Where *a(t)* is a modulated GMSK signal generated by local training sequence (32 bits) without frequency and phase offset, $(\cdot)^*$ denotes the complex conjugate of $(\cdot)$, T is the symbol period, n = 1…31. Using $\triangle a_n$ to search the starting position of header from the sequence $\triangle r_n$. It will search the header every 31 bits and find the Maximum $R_n = \sum \triangle a_n \cdot \triangle r_n$. The maximum position is the starting position of header of the AIS signal. When E_b/N_0 = 10 dB, the result is shown in Fig. 3.

It can rough estimate the frequency offset while detecting the position of the header.

$$\triangle f_1 = f_d \cdot \arctan(Q_{\max}/I_{\max})/2\pi \tag{3.4}$$

In Eq. (3.4), $Q_{\max} = imag(R_{\max})$, $I_{\max} = real(R_{\max})$. Enter the precise frequency offset estimation module after compensating the frequency offset to *r(t)*, as Eq. (3.5).

$$r_1(t) = r(t) \cdot \exp[-j(2\pi \triangle f_1 t)] \tag{3.5}$$

3.2 *Frequency Offset Accurate Estimation and Phase Offset Estimation*

After the rough frequency offset compensation, the signal still have residual frequency offset. After the phase-locked loop, short time burst signal may lose data. In order to lock the signal as soon as possible, the frequency offset needs to be estimated and compensated more accurately. The specific method is as follows.

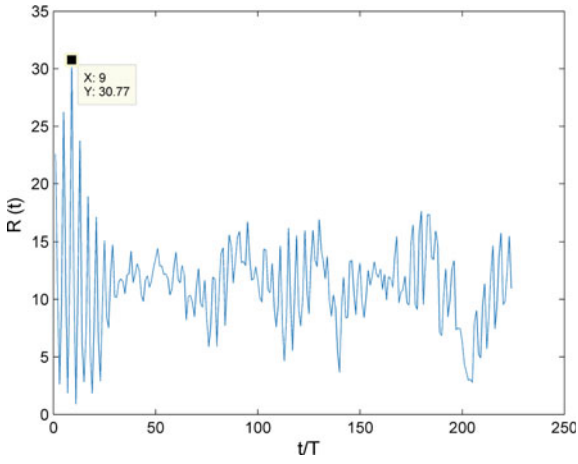

Fig. 3 Frame's header capture

$$\psi(n) = r_1(nT) \cdot a^*(nT) \tag{3.6}$$

In Eq. (3.6), n = 1…32. Then do N-point Fast Fourier Transform (FFT) to get $\psi(k)$. In this paper $N = 2048$, $R_b = 9600$. The resolution of the algorithm is $R_b/N = 4.7$ Hz. The peak position of $\psi(k)$ is due to the residual offset $\triangle f_2$ in this module. When $\triangle f_2 = 0$, the peak appears at $k = 1$ or $k = N$. When $\triangle f_2 > 0$, $k_{\max} \in \{0, N/2\}$; when $\triangle f_2 < 0$, $k_{\max} \in \{N/2+1, N\}$. The relationship can be seen in Eq. (3.7).

$$\Delta f_2 = \begin{cases} R_b \cdot (k_{\max} - 1)/N, k_{\max} \in \{0, N/2\} \\ R_b \cdot (N - k_{\max})/N, k_{\max} \in \{N/2+1, N\} \end{cases} \tag{3.7}$$

The estimated frequency offset in frequency offset capture module is shown as $\triangle f_0 = \triangle f_1 + \triangle f_2$, so the compensation signal in capture module is shown in Eq. (3.8).

$$\mathrm{r}_0(t) = r(t) \cdot \exp[-j(2\pi \triangle f_0 t)] \tag{3.8}$$

The signal's initial phase can not be the same as the local carrier phase. In phase offset estimation module, take the received header information sequence conjugate multiply by local header information sequence. Accumulate, calculate tangent and then estimate the phase offset θ_0. The specific method is as

$$\begin{aligned} Q_\theta &= imag\left[\sum\nolimits_{n=1}^{32} r_0(nT) \cdot a^*(nT)\right] \\ I_\theta &= real\left[\sum\nolimits_{n=1}^{32} r_0(nT) \cdot a^*(nT)\right] \\ \theta_0 &= \arctan(Q_\theta / I_\theta) \end{aligned} \tag{3.9}$$

3.3 Phase Locked Loop

Compensate $\triangle f_0$ and θ_0 into sampling signal *s(t)* which has *M* discrete points in each symbol from the storage and pass through low-pass filter to reduce noise interference. The preceding steps do not completely eliminate the effects of offset, so phase locked loop mean to eliminate the residual frequency offset and phase offset, otherwise the error rate will be severely deteriorated. This paper designs a second-order PPL. It is shown in Fig. 4.

In Fig. 4, $I_\mathrm{p} = I \cdot \cos u - Q \cdot \sin u$, $Q_\mathrm{p} = Q \cdot \cos u - I \cdot \sin u$. Default setting cosu = 2048, sinu = 0. $e = \mathrm{sgn}(\mathrm{Q}_p) \cdot I_p - \mathrm{sgn}(I_p) \cdot \mathrm{Q}_p$, $K_p = 9.32 \times 10^7$, $K_i = 3.29 \times 10^6$, $K_a = 1$. The loop output signal $s_0 = I_p + j \cdot Q_p$. By now it has completed carrier synchronization. Loop output waveform is shown in Fig. 5.

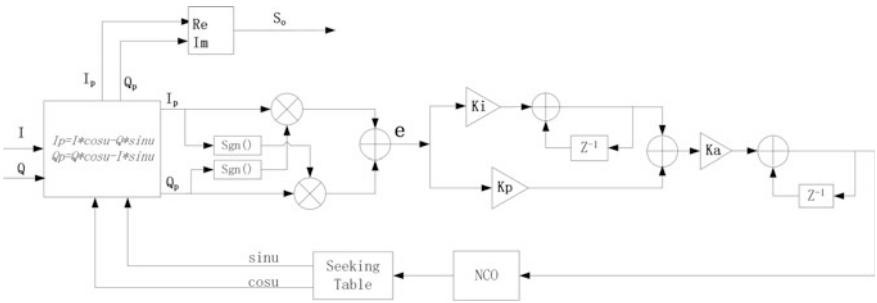

Fig. 4 Phase locked loop

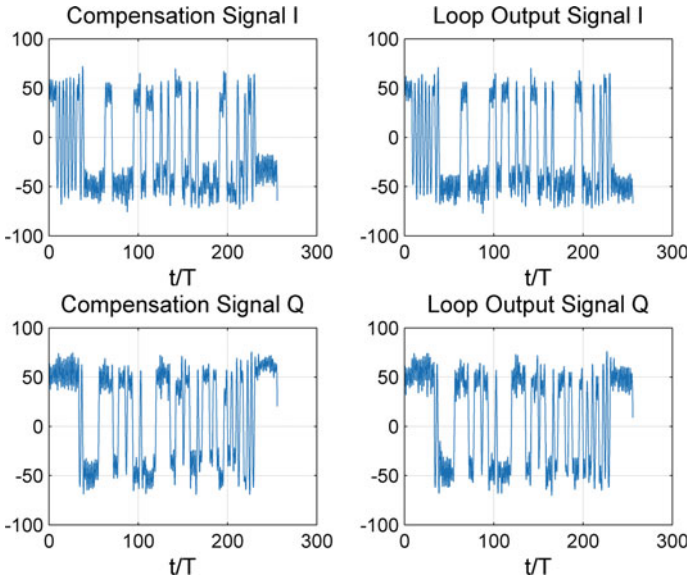

Fig. 5 Phase-locked loop output signal

4 Timing Synchronization

People usually use the timing synchronization method based on maximum likelihood algorithm in the literature [6] in GMSK modulation. However, this method is more suitable for MSK signal. Combined with the characteristics of short time burst-mode AIS signal, this paper proposes an improved Gardner timing synchronization method. It compares the discrete sampling points in the time domain and selects the point closest to the ideal sampling point in each symbol. This algorithm does not need to estimate and compensate the accurate timing errors. The

algorithm is feasible when the error is in the range of $-T/2 \sim T/2$. The algorithm with good reliability and accuracy is simple to implement.

Gardner classic algorithm [7] requires two samples per symbol, ideally one at the best sampling position and the other at the middle of the two symbols, as Eq. (4.1) shows.

$$\tau(n) = x(n-1/2) \cdot [x(n) - x(n-1)] \tag{4.1}$$

When the received signal is complex, two such computations, one each from the I and from the Q channel, are added when processing a demodulated carrier signal. The equation can be rewritten as

$$\begin{aligned} \tau(n) &= x_I(n-1/2) \cdot [x_I(n) - x_I(n-1)] \\ &\quad + x_Q(n-1/2) \cdot [x_Q(n) - x_Q(n-1)] \\ &= \mathrm{Re}\{x(n-1/2) \cdot [x^*(n) - x^*(n-1)]\} \end{aligned} \tag{4.2}$$

Because the amplitude of GMSK signal envelope is different and the value of the middle sampling point of two ideal sampling points is not 0. The improved Gardner timing synchronization method is based on the amplitude of intermediate sampling point and symbol hopping situation to determine the timing error. When the sampling clock delay, the principle shown in Fig. 6.

As shown in Fig. 6, t_1 is the ideal sampling time, t_2 is the actual sampling time, $\triangle t = t_2 - t_1$ is the residual timing error. When $x(n) < x(n-1)$, $\triangle t$ is increasing, the value of $x(n-1/2)$ is smaller. When $x(n) > x(n-1)$, $\triangle t$ is increasing, the value of $x(n-1/2)$ is larger, so that

$$\tau(k,n) = \begin{cases} x(n-1/2), x(n) > x(n-1) \\ -x(n-1/2), x(n) < x(n-1) \end{cases} \tag{4.3}$$

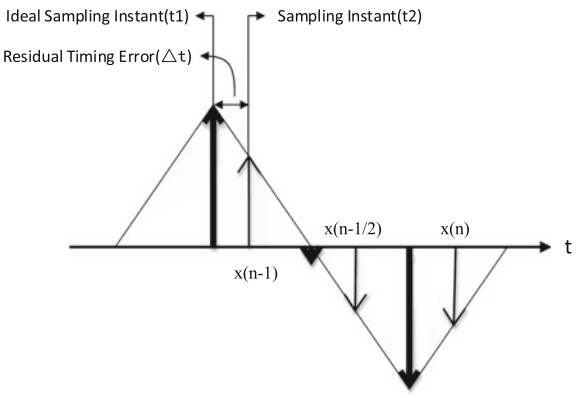

Fig. 6 The principle of timing synchronization

Where $\tau(k)$ represents the total error of the kth sample sequence, $\tau(k) = \sum_{n=1}^{256} \tau(k,n)$. In this algorithm, it does not contribute to the useful time error when adjacent symbols do not jump, so we only consider when adjacent symbol hopping. In GMSK signal when adjacent symbol hopping, the polarity of ideal sampling point in each symbol may not hop. So we set a threshold σ to determine if the adjacent symbol hopping. In this paper $\sigma = 0.3$. It shows as Eqs. (4.4) and (4.5).

$$\tau(k,n) = \begin{cases} x(n-1/2), x(n) - x(n-1) > \sigma \\ -x(n-1/2), x(n-1) - x(n) > \sigma \\ 0, \ others \end{cases} \tag{4.4}$$

$$\tau(k,n) = \tau_I(k,n) + \tau_Q(k,n) \tag{4.5}$$

The algorithm will select a 256-point sequence form M sequences. The result is shown in Fig. 7.

Where $\tau(k) = \sum_{n=1}^{256} \tau(k,n)$, $k = 1 \ldots M$. When $\tau(k)$ at the minimum, the kth sampling sequence is the output sample sequence. As shown in Fig. 7, when $k = 12$, the sampling point of each symbol is the closest to the ideal sampling point, and the 12th sampling point of each symbol will output to enter the final module. The capture range of demodulator is usually required ± 100 ppm [8]. Within 256 symbol periods, its relative deviation is 2.56%. In this paper $M = 40$, the accuracy of the algorithm is 1/40 = 2.5%. It meets the requirements of the demodulator, while improving system performance and reducing the algorithm complexity.

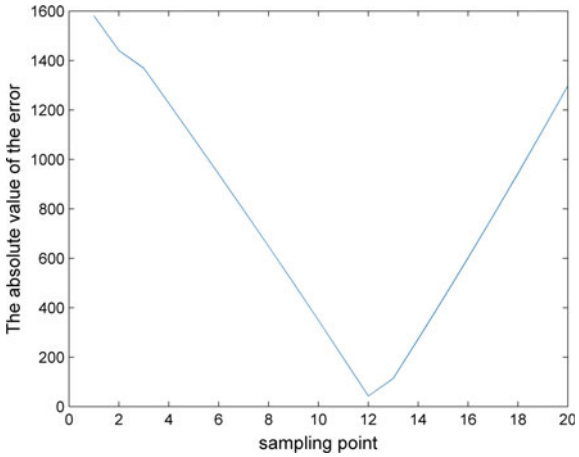

Fig. 7 The waveform of τ(k)

5 Simulation Results and Analysis

The initial frequency and phase offset has nothing to do with the performance of frequency and phase offset estimation in this algorithm. The range of frequency offset capture is $-R_b \sim R_b$ and the range of phase offset capture is $-\pi/2 \sim \pi/2$. This paper verifies the performance of the synchronization algorithm through simulation. Figure 8 shows the performance of the algorithm in the range of offset capture when E_b/N_0 = 10 dB. It also shows the performance of the algorithm in the range of E_b/N_0 = 0 dB to E_b/N_0 = 10 dB.

In Fig. 8, it shows that the initial frequency and phase offset has nothing to do with the performance of frequency and phase offset estimation in this algorithm. Noise has little effect on the performance of the algorithm. When the noise increases, the stability of the algorithm decreases slightly. After frequency offset estimation module and phase offset estimation module. The residual frequency offset is around 2 Hz and the residual phase offset is around 0.05 rad. So phase-locked loop can quickly eliminate the residual offset. It voids the loss of data caused by commonly used loop structure.

In space-based AIS communication systems, the Gaussian channel is the best approximation. Simulation parameter setting: BT = 0.4, data bit rate R_b is 9.6 kbps. Using Matlab software to demodulate GMSK signal, each symbol in the demodulator has M sampling points (M = 40), the sampling frequency is f_s = 384 kHz. Storage the sampling sequences. Decimate by M = 40 times the sequences (reducing the sampling frequency to $f_s = R_b = 9.6$ kHz), go into the offset estimation module. Then compensating the estimated offset to the sequences from the storage. After low-pass filtering, PLL, timing synchronization and other steps it finally finish the demodulation. The signal used for demodulation in simulation is generated by Matlab software. The generated GMSK signal with Gaussian white noise is added

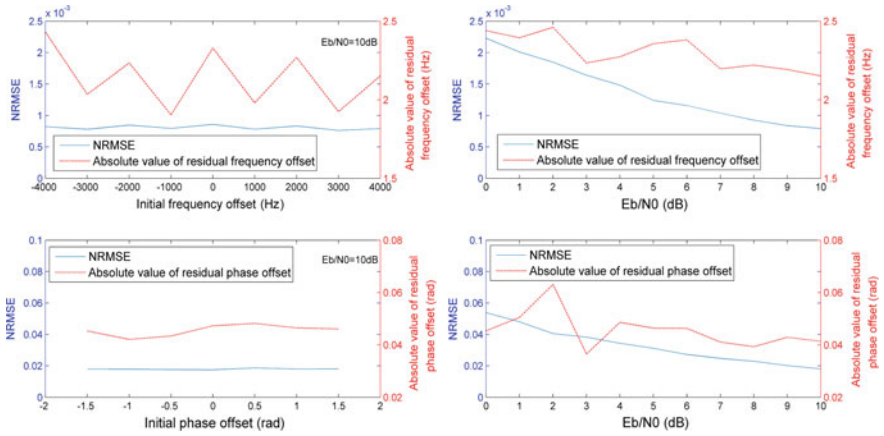

Fig. 8 The performance of offset estimation

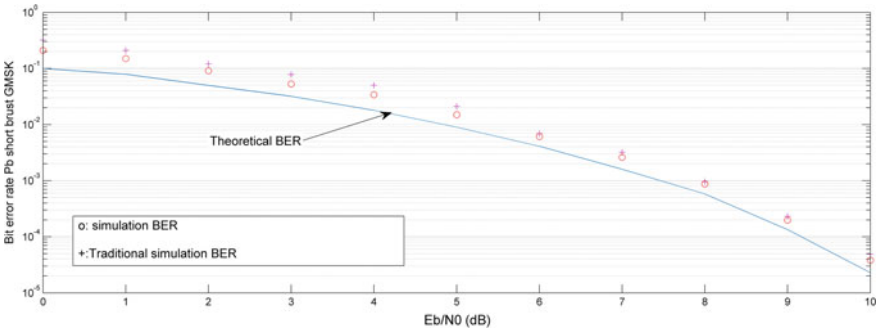

Fig. 9 The performance of bit error rate when Eb/N0 = 0 ~ 10 dB

frequency offset and phase offset which are random values in the range of $\pm R_b/2$ and $\pm\pi/2$, respectively. The simulation results are shown in Fig. 9. The bit error rate performance degradation of only 0.3 dB and its performance is better than the traditional algorithm in the literature [6].

6 Conclusion

LEO satellites equipped with AIS systems complement the navigation satellite network. The space-based AIS system needs navigation satellite positioning and timing service support in its work. This paper proposes a synchronization algorithm adapted to short time burst-mode GMSK signals. The algorithm can accurately detect the signal. The signal is processed in real time and the offset estimation has higher accuracy. It locks fast in PLL and voids the loss of data caused by commonly used loop structure. At the same time, an improved Gardner timing synchronization method is proposed. And its performance is better than commonly used existing algorithms. When $E_b/N_0 = 10$ dB, the bit error rate $P_b \leq 10^{-4}$. It is proved that this algorithm can be used for the actual AIS signal demodulation [9].

References

1. Zhu K (2008) Application of BeiDou satellite system to offshore vessels. Radio Eng 38(9): P35–P38
2. He C (2013) Acquisition of ship AIS data via Beidou satellite navigation system. J Shanghai Marit Univ P6
3. Ji K (2013) Review and assessment of maritime surveillance based on small satellite-based AIS. Radar Sci Technol P3–P4
4. Wang Y, Wang X (2011) Application of combination of AIS and Beidou terminal in dynamic ship monitoring. J Shanghai Marit Univ P17–P21

5. Yao N (2006) Modulation and demodulation technique of GMSK in AIS system. University of Electronic and Technology of China, China
6. Morelli M, Vitetta GM (1999) Joint phase and timing synchronization algorithms for MSK-type signals. In: Proceedings of the communication theory mini-conference F6–F10
7. Gardner FMA (1986) BPSK/QPSK timing-error detector for sampled receiver. IEEE Trans Commun COM-34(5):P423–P429
8. Vaughan RG, Scott NL, White DR (1991) The theory of band-pass sampling. IEEE Transitions on Sig Process 39(9):P1973–P1984
9. Zhang X (2015) Research and implementation of automatic identification system. Beijing University of posts and telecommunication, Beijing

A Novel Analog Threat Analysis of BDS Signal and Effect on Ranging Performance

Meng Wang, Chengyan He, Xiaochun Lu, Ji Guo and Li Kang

Abstract Satellite navigation analog threat generate unit abnormal will lead to signal distortion, navigation signal analog threat will directly affect the ranging, positioning performance and other user experience. In this paper, the analog threat signal of BDS are researched and analyzed. Firstly, the large-diameter antenna receiving system is used to obtain the off-line satellite navigation signal data. Using the cumulative average method to process the baseband waveforms. Then, the standard chip correlation technique is used to obtain the optimal symbol waveform. Secondly, the optimal symbol is modeled based on the 2OS model to determine the initial value of the σ (damping factor) and f_d (damped frequency) of oscillation. The two-dimensional search is used to search σ and f_d respectively. The mean of the difference between ideal signal and the real signal waveform are based for the σ and f_d of oscillation values. Finally, the simulation and experimental data are used to verify, the estimation method of the analog distortion parameters of the navigation signal and its influence on the ranging performance are given in detail.

Keywords BDS signal · Analog threat · Ranging performance

M. Wang (✉) · C. He · X. Lu · J. Guo · L. Kang
National Time Service Center, Chinese Academy of Sciences, Xi'an 710600, China
e-mail: wangmengntsc@163.com

M. Wang · C. He · X. Lu · L. Kang
Key Laboratory of Precision Navigation and Timing Technology, Xi'an 710600, China

M. Wang · X. Lu · J. Guo
School of Astronomy and Space Sciences, Chinese Academy of Sciences University, Beijing 1014082, China

L. Kang
School of Electronic, Chinese Academy of Sciences University, Beijing 1014082, China

J. Sun et al. (eds.), *China Satellite Navigation Conference (CSNC) 2018 Proceedings*, Lecture Notes in Electrical Engineering 498,
https://doi.org/10.1007/978-981-13-0014-1_12

1 Introduction

The SQM (signal quality monitoring) is an important indicator to detect the normal orbiting satellites, and the normal orbiting satellites also occur subtle distortion [1]. As a result, the cross-correlation function curve of the local signal and the ground receiving signal will be deteriorated, and the zero crossings of the S curve will occur move, thus causing ranging error [2]. The failure of the satellite payload in the satellite navigation system will lead to distortion of the navigation signal, thus affecting the user's ranging performance [2]. Since 1997 GPS-SV19 satellite failure, the satellite signal failure model analysis has drawn people's attention [3–5]. The foreign scholars Alexanhder Michael Miteman, Robert Eric Phelts, P Enge and soon on, have studied the evil signal model in dept [5]. The most typical research about the chip distortion model is the 2nd-order step (2OS) model proposed by Robert Eric Phelts. The model summarizes three possible fault signal models: TMA (digital distortion), TMB (analog distortion), and TMC (mixed distortion) [3, 5]. ICAO Annex 10 sets the parameters of the 2OS distortion model for GPS and GLONASS navigation signal [5]. For GPS and GLONASS systems, chip distortion model has been quite successful, qualitative and quantitative analysis have achieved remarkable results. In this paper, the digital threat and analog threat models in the 2nd-order step (2OS) model are introduced, and the analog threat model is introduced in detail. The second section introduces the chip extraction method, from the collection of raw data to the finally selected optimized chip. The third section is based on the 2nd-order step (2OS) model, the analog threat model of the measured BDS signal is established, and the two-dimensional accurate search method is proposed to obtain the precise parameter values of the simulation distortion. In the fourth section, the measured signals and the simulated signals with determined parameters in the third section are respectively used for verification. The locking points bias are given. It is further confirmed that the method to determine the simulated distortion parameters in Step 3 is feasible and effective. In conclusion, the determination of the simulated distortion parameters plays a supporting role in the signal quality assessment and has important reference significance for the BDS signal analysis.

2 2OS (2nd-Order Step)

2.1 Digitial Threat (TMA)

Digital threat occurs inside the NDU (navigation data unit), independent analog threat, this failure as either an advance or delay in the falling edge of C/A code chip [3], the positive and negative chip waveform width inconsistencies, correlation peak expansion [2, 6]. This kind of distortion mode generates the dead-zones in the correlation peak. Figure 1 depicts a delay of 0.3 chips of a chip period, and its effect on the correlation peak like Fig. 2. We can be get from the Figs. 1–2, the chip is

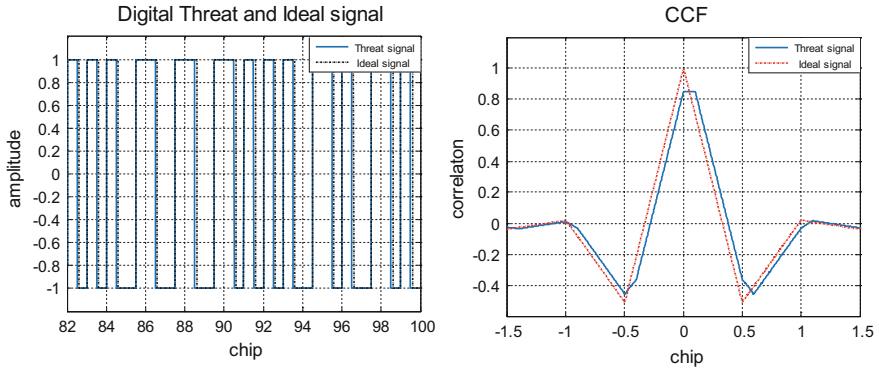

Fig. 1 Digital threat model

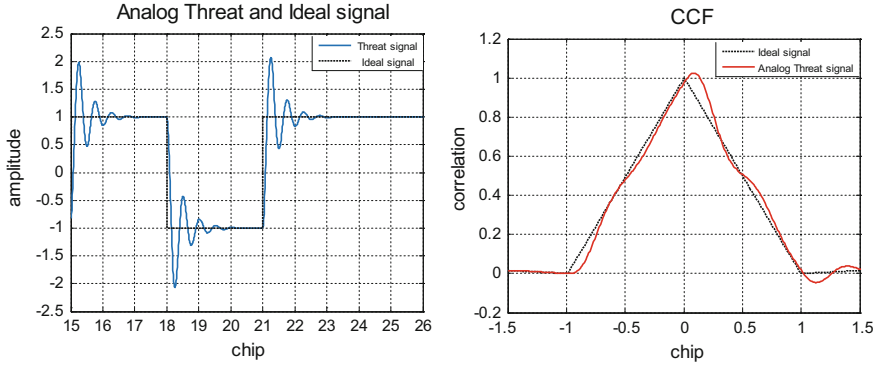

Fig. 2 Analog threat model

delayed (or advanced), the correlation curves also translates entirely backwards or forwards, and the correlation peak shows a dead-zones. The proposed range of single TMA parameter Δ, is ±0.12 of a code chip, since larger values produce waveforms that are easily detectable by multi-correlation signal quality monitors [6]. At present, a great deal of research has been done on the current BDS digital threat, so this article only briefly introduces and the follow-up no longer discussed in detail.

2.2 Analog Threat (TMB)

Analog threat (TMB) occurs in the satellite analog payload module, which is mainly caused by the on-board transmitter baseband filtering or radio frequency filtering anomaly [2]. As shown in Fig. 3, analog threat waveform like the

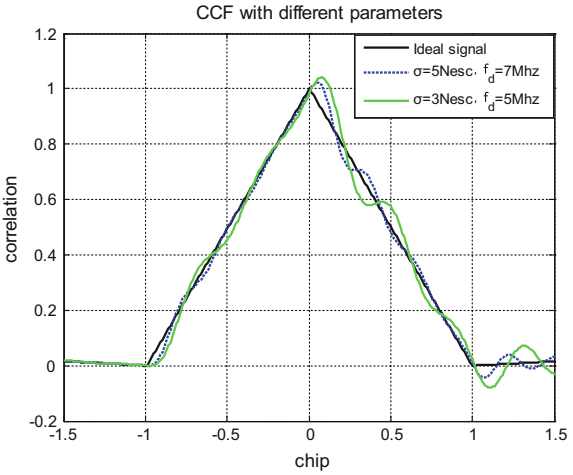

Fig. 3 Analog threat correlation curve with different parameters

amplitude modulation and ringing joint effect, independent of digital threat module [3]. The expression is the jitter of the time-domain chip waveform, the distortion of the correlation peak, left-right asymmetry, etc. [3, 5]. The analog threat signal can be regarded as the response of the ideal signal after passing through the second-order filter [3]. The mathematical expression is as follows:

$$e(t) = \begin{cases} 0 & t < 0 \\ 1 - \exp(-\sigma t)\left[\cos\omega_d t + \frac{\sigma}{\omega d}\sin\omega_d t\right] & t \geq 0 \end{cases} \quad (1)$$

From the above equation, the corresponding impulse response function is:

$$h_{(\sigma,f_d)}(t) = \frac{\sigma^2 + \omega_d^2}{\omega_d} e^{-\sigma t}\sin(\omega_d)u(t) \quad (2)$$

TMB signal that is:

$$x_{TMB}(t) = x_{nom}(t) * h_{(\sigma,f_d)}(t) \quad (3)$$

among them:

$$\omega_d = 2\pi f_d, x_{nom}(t) \text{is ideal signal;}$$

From Fig. 2 and Eq. (1), When σ is constant, the larger the f_d is, the higher the dithering frequency of the waveform is. When f_d is constant, the larger the σ is, the faster the waveform attenuation tends to the amplitude of the chip; thus, f_d affects the oscillation frequency of the waveform, While δ affects the oscillation amplitude of the waveform [3]. The second-order step (2OS) model proposed by Robert Eric Phelts gives the specific parameter values under different navigation system and threat models in detail. We can get from Table 1, For TMB, f_d range from 4 to

Table 1 .

	GPS	GLONASS
TMA	-0.12 chip $\ll \Delta \ll 0.12$ chip	-0.11 chip $\ll \Delta \ll 0.11$ chip
TMB	$\Delta = 0$ 4 MHz $\ll$ fd $\ll$ 17 MHz 0.8 Nesc $\ll \sigma \ll$ 8.8 Nesc	$\Delta = 0$ 4 MHz $\ll$ fd $\ll$ 17 MHz 0.8 Nesc $\ll \sigma \ll$ 8.8 Nesc
TMC	-0.12 chip $\ll \Delta \ll 0.12$ chip 7.3 MHz $\ll$ fd $\ll$ 13 MHz 0.8 Nesc $\ll \sigma \ll$ 8.8 Nesc	-0.11 chip $\ll \Delta \ll 0.11$ chip 4 MHz $\ll$ fd $\ll$ 17 MHz 0.8 Nesc $\ll \sigma \ll$ 8.8 Nesc

17 MHz, and σ ranges from 0.8 to 8.8 M/s. f_d only extends as low as 4 MHz since lower frequencies would impact the military signal (P(Y)code), which is more closely monitored than the C/A code. Frequencies above 17 MHz would be difficult for the satellite signal hardware to generate. A lower σ would unrealistically result in unstable oscillations on the code chips, larger values of σ would not introduce additional constraints on the avionics since this would future attenuate the oscillations [6].

2.3 Analog Threat Model Correlation Function

The correlation function of analog threat is written as $R(\tau)$, TMB threat model:

$$\begin{aligned} \frac{\partial R(\tau)}{\partial \tau} &= u(\tau + T_c) - 2u(\tau) + u(\tau - T_c) \\ h_{2nd}(t) * \frac{\partial R(\tau)}{\partial \tau} &= e(\tau + T_c) - 2e(\tau) + e(\tau - T_c) \end{aligned} \tag{4}$$

Analog threat correlation peak function as follows:

$$R(\tau, \sigma, f_d) = h_{2nd}(\tau, \sigma, f_d) \ * \ R(\tau) = E\begin{vmatrix} \tau + T_c \\ 0 \end{vmatrix} - 2E\begin{vmatrix} \tau \\ 0 \end{vmatrix} + E\begin{vmatrix} \tau - T_c \\ 0 \end{vmatrix} \tag{5}$$

And E(t) is one-order response;

$$E(t) = \int_0^t e(\alpha)d\alpha = \begin{cases} 0 & t \le 0 \\ t - \frac{2\sigma}{\sigma^2 + \omega_d^2} + \frac{\exp(-\sigma t)}{\sigma^2 + \omega_d^2}\left[2\sigma\omega_d t + \left(\frac{\sigma^2}{\omega_d} - \omega_d\right)\sin\omega_{dt}\right] & t \ge 0 \end{cases} \tag{6}$$

Analog threat correlation curve is affected by the sine and cosine function at the same time, which directly leads to the jitter and asymmetry of the correlation curve [3]. As shown in the Fig. 3, the correlation curves under different σ and f_d

parameters are simulate respectively. The smaller the f_d is, the smaller the frequency of the relevant curve jitter is. When f_d is constant, the smaller σ is, the smaller the jitter amplitude of the correlation curve is.

3 Optimal Chip Extraction

Using the 40-m large aperture antenna to obtain the original BDS signal data with high signal-to-noise ratio and low multipath interference. Firstly, use the software receiver to process the raw data to obtain the baseband signal Fig. 4a. Then, the baseband signal is processed with the averaging processing method, we can see that the baseband waveform amplitude envelope significantly neat. Figure 4c shown take the standard chip-correlation technology (signal waveform and code impulse sequence related) [7] to process the signal shown in Fig. 4b for chip recovery. Figure 4d shown the enlarged view of Fig. 4c. Figure 5 shows the optimized symbols extracted.

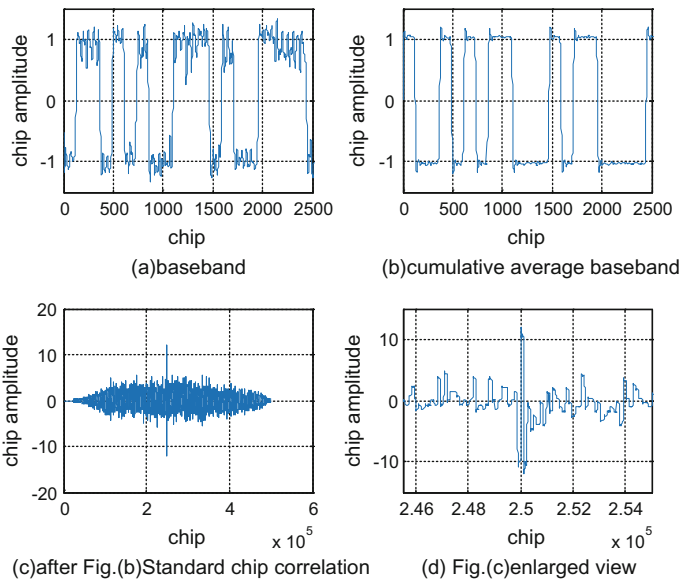

Fig. 4 Chip extraction process

4 Analog Distortion Model Parameters to Determine the Method

As shown in Fig. 5, the decay trend of the envelope curve is σ, and the difference between adjacent wave peaks is f_d. In order to obtain the initial values of σ and f_d, we first extract the special points such as the peak and trough of the optimal chip waveform. Then, the extracted data are fixed function interpolation fitting. According to the result of the fitting curve envelope, we obtain initial value about σ and f_d. In order to get more accurately estimate σ and f_d, the chart of the program structure is proposed as follows Fig. 6. After the pre-processing obtains the initial values of σ and f_d, the σ and f_d with 1000 Hz step search respectively. Based the mean of difference between the actual signal chip and ideal signal, the minimum mean difference is the needed ideal waveform, and the corresponding σ and f_d is finally determined precise parameter values. Figure 7 shown the minimum mean difference between the ideal signal and the actual signal chip waveform, we can see a good fit.

5 Ranging Performance

As shown in Fig. 3, Analog threat will produce the correlation curve fluctuation, jitter and lead to the left-right asymmetry situation, directly produce the ranging error. Ideally, the zero crossings of the receiver's loop phase curve (S-curve), code ring lock points, should be at a code loop tracking error of 0 [5]. Due to the influence of analog threat, the lock phase of the code phase detection phase will shift. Set the lead- lag correlator interval is d, the corresponding S-curve expression is:

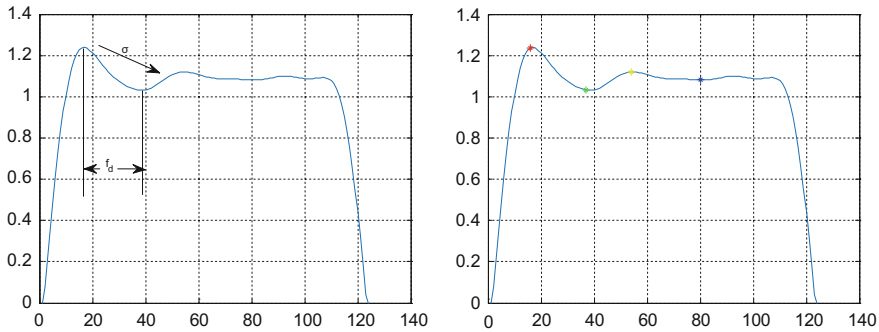

Fig. 5 Optimized symbol waveforms

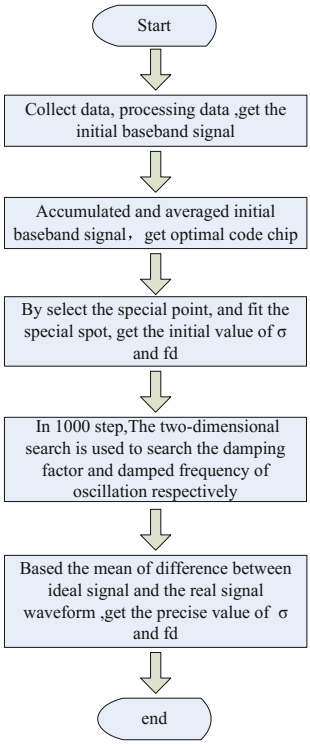

Fig. 6 Two-dimensional search flow chart

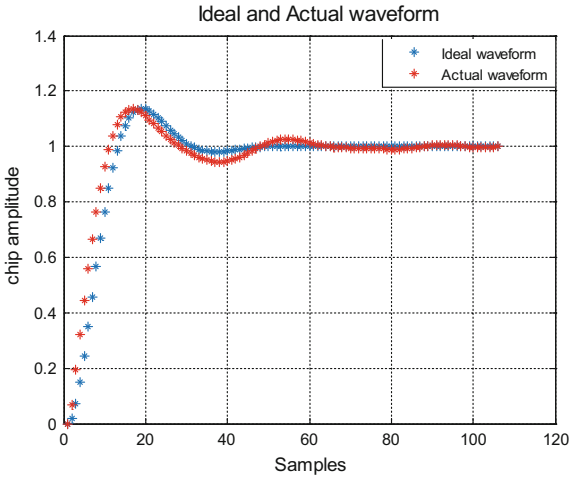

Fig. 7 Ideal and measured signal fitting plots

$$S_{Curve}(\varepsilon, d) = \left|CCF\left(\varepsilon - \frac{d}{2}\right)\right|^2 - \left|CCF\left(\varepsilon + \frac{d}{2}\right)\right|^2 \quad (7)$$

The locking point deviation ε_bias (d) is satisfied:

$$S_{Curve}(\varepsilon_{bias}(d), d) = 0 \quad (8)$$

As shown in the Fig. 8, it is the ranging error generated by the measured signal. As shown in the Fig. 9 which is the ranging error of the simulate signal calculated by the analog threat parameter adopted in this paper.

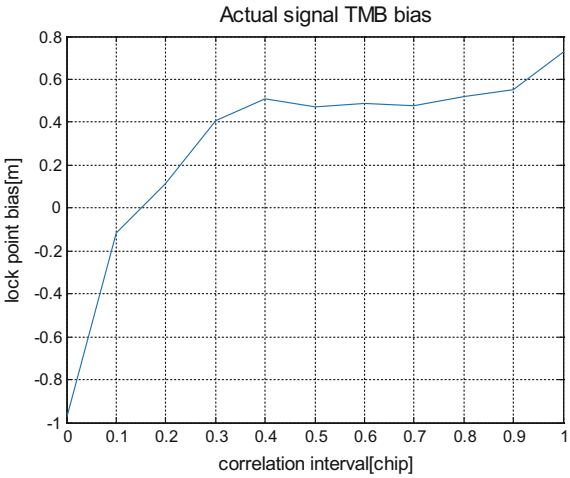

Fig. 8 Measured signal ranging error

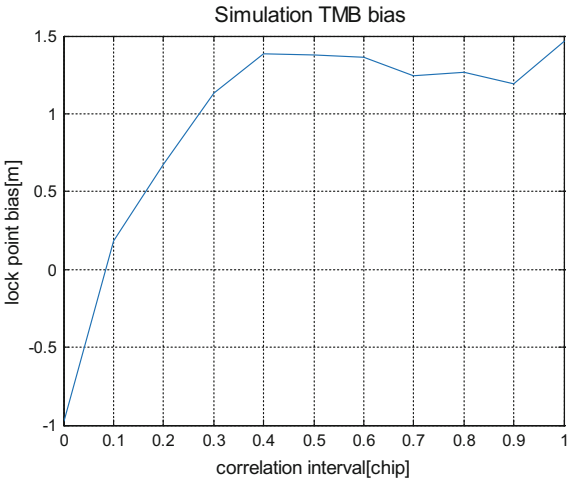

Fig. 9 Simulationsignal ranging error

6 Conclusion

In this paper, the model of BDS signal simulation distortion is discussed in detail, and the parameters of analog threat model are quantitatively deduced. The ideal signal obtained from the calculated σ and f_d parameters fits well with the measured signal. To a certain extent, this article provides support for the quantitative analysis of the simulated distortion parameters of BDS signals. Based on this, the effect of analog distorted signal on the ranging performance is verified. The results show that: (1) the analog threat calculated by the parameters are better fitted to the measured waveforms; (2) the higher the simulated distortion, the greater the impact on the ranging performance. These are of great importance to the subsequent BDS signal quality assessment.

Acknowledgements This study is funded by Youth Innovation Promotion Association of the Chinese Academy of Science (CN). This work is also supported by National Science Foundation of China (No. 61501430).

References

1. Wong G, Phelts RE, Walter T et al (2010) Characterization of signal deformations for GPS and WAAS satellites. In: Proceedings of the 23rd international technical meeting of the satellite division of institute of navigation, ION GNSS, pp 3143–3151, 21–24 Sept 2010
2. Chengyan HE (2013) Research on evaluation methods of GNSS signal quality and the influence of GNSS signal on ranging performance. National Time Service Center, Chinese Academy of Sciences, Xi'an, Shanxi, P.R. China
3. Phelts RE, Akos DM (2006) Effects of signal deformations on modernized GNSS signals. J Glob Pos Syst 5(1–2):2–10
4. Liu J, Fan J (2015) Estimation method of ranging bias caused by navigation satellite signal distortion. Aerosp Control, Beijing 36:1296–1302
5. Zhao Q (2016) Monitoring and evaluation on time and frequency domain of Beidou signal in space. Civil Aviation University of China, Tianjin
6. Liu R (2016) Research on digital distortion of signal in space for Beidou satellite navigation system. Aerosp Control, Beijing x(34):38–43
7. Wu D (2016) Evaluation of GNSS signal at low SNR. Huazhong University of Science & Technology, Wuhan 430074, P.R. China

Analysis of Positioning Performance of the GNSS Receiver Under Complete and Incomplete Spoofing

Ya Qi, Rui Xu, Jianye Liu and Weihao Dai

Abstract The GNSS receiver is susceptible to malicious spoofing attack and further estimates a wrong position which is considered as an arbitrary preset site from the spoofer. However, when the target receiver is far away from the spoofer, authentic signals are weak rather than submerged by spoofing signals and some authentic satellite signals are survival due to satellite geometry. In this case, the spoofing attack is incomplete and its effects on the positioning estimation of target receivers become complex. In this study, an improved transmitter-based spoofer is realized employing the software-defined receiver and used to analyze the positioning performance of the target receiver under the complete and incomplete spoofing attack. Simulation results show that the target receiver is possibly controlled by the spoofer under complete spoofing attack and its estimated position is equal to the spoofer preset position. Under incomplete spoofing, the estimated position is between the preset position and the genuine position, but is neither.

Keywords GNSS · Software-defined receiver · Spoofing attack
Transmitter-based spoofer · Positioning performance

1 Introduction

Global Navigation Satellite Systems (GNSS) like GPS and Beidou are widely applied in many fields of civilian and military [1]. Unfortunately, the power level of GNSS signal received by ground receivers is extremely low due to the large

Y. Qi · R. Xu (✉) · J. Liu · W. Dai
Navigation Research Centre, Nanjing University of Aeronautics and Astronautics, Nanjing, China
e-mail: ruixu@nuaa.edu.cn

Y. Qi
e-mail: nuaaqiya@nuaa.edu.cn

Y. Qi · R. Xu · J. Liu · W. Dai
Satellite Communication and Navigation Collaborative Innovation Center, Nanjing, China

J. Sun et al. (eds.), *China Satellite Navigation Conference (CSNC) 2018 Proceedings*, Lecture Notes in Electrical Engineering 498,
https://doi.org/10.1007/978-981-13-0014-1_13

distances between the satellites and the receiver, and finally causes the signals highly vulnerable to interference under complex electromagnetic environment [2, 3].

Spoofing attack is one of the interference and can be divided into generated spoofing and transmitter/repeater spoofing. Due to low-cost and simple implementation, repeater spoofing is carried out in many important researches on spoofing countermeasures over the last decade [4, 5]. Through controlling the time offsets, Doppler frequency offsets and signal power of spoofing signals, the spoofer can perform an aggressive spoofing attack with the help of the techniques, software [6, 7] and hardware tools [8, 9]. Generally, the majority of repeater spoofers emit their received authentic signals with a certain time delay (referring to pseudorange) [10]. As the result, the spoofer simply deceives the target receiver estimating its position near to the transmitter rather than an arbitrary preset position [11, 12]. When the time delays of different signals are controlled and different, the spoofer is able to deceive the target receiver estimating its position to an arbitrary preset site [13, 14].

However, when the target receiver is far away from the spoofer, the spoofing signal power is not strong enough to suppress all the authentic signals and part of authentic satellite signals can also be received by the receiver. In such situation, the spoofing signals are unable to cover all the received authentic signals, the spoofing is incomplete. To analyze the incomplete spoofing effects on positioning performance of the GNSS receiver, a repeater spoofer based on GNSS Software-Defined Receiver (SDR) is constructed in this paper by varying the time delay and signal strength of each satellite spoofing signal. The remainder of this paper consists of four sections. Section 2 presents the influence of complete and incomplete spoofing. Section 3 presents the implementation of repeater spoofing. Section 4 presents the experiments for testing the positioning performance of the GNSS receiver under incomplete spoofing. Finally, conclusions are given in Sect. 5.

2 Repeater Spoofing System

2.1 *Signal Model Under Complete and Incomplete Spoofing Attack*

Under spoofing attack, the signal s received by the target receiver can be considered as mixed signals of the authentic signals s_{au} from N satellites and the spoofing signals s_{sp} referring to M satellites, as well as noise ε, which is written as:

$$s = s_{au} + s_{sp} + \varepsilon = \sum_{i=1}^{N} s_{au}^{i} + \sum_{j=1}^{M} s_{sp}^{j} + \varepsilon \tag{1}$$

Generally, the spoofing signals are GNSS-like signals, with the same signal structure to the authentic GNSS signals. For example, the GPS L1 signals are

composed by 1.023 MHz C/A code, 1575.42 MHz carrier wave and 50 Hz navigation data. The model of the received signal from one satellite is written as:

$$s_{au}^{i} = \sqrt{2P_{au}^{i}}\left[C_{au}^{i}\left(t-\tau^{i}\right)D_{au}^{i}\left(t-\tau^{i}\right)\right]\sin\left(2\pi f_{au}^{i}t+\theta_{au}^{i}\right) \tag{2}$$

where, the superscript i represents the i-th satellite, the subscript au represents the authentic signal while the spoofing signal is denoted by the subscript sp in (3), P_{au}^{i} is the average power, $C_{au}^{i}(\cdot)$ is the C/A code and τ^{i} is the time delay which equals the propagation time of the signal from the satellite to the receiver, $D_{au}^{i}(\cdot)$ is the navigation data, the item of $\sin\left(2\pi f_{au}^{i}t+\theta_{au}^{i}\right)$ is the carrier wave, and f_{au}^{i} is the carrier frequency including the Doppler frequency.

Similarly, the spoofing signals can be expressed as:

$$s_{sp}^{j} = \sqrt{2P_{sp}^{j}}\left[C_{sp}^{j}\left(t-\tau^{j}+\tau_{sp}^{j}\right)D_{sp}^{j}\left(t-\tau^{j}+\tau_{sp}^{j}\right)\right]\sin\left(2\pi f_{sp}^{j}t+\theta_{sp}^{j}\right) \tag{3}$$

where, P_{sp}^{j} and $C_{sp}^{j}(\cdot)$ are the average power and the C/A code of spoofing signals. Nominally, the spoofed signals have the same C/A code sequence $C_{sp}^{j}(\cdot) = C_{au}^{j}(\cdot)$ as the corresponding authentic signals, but with an additional time delay τ_{sp}^{j} which is set according to the spoofing requirement such as the artificial spoofing position. The navigation data $D_{sp}^{j}(\cdot)$ of the spoofing signals is same to that of the corresponding authentic signals for the transmitter-based spoofing and different for the generator-based spoofing. For the spoofing carrier $\sin\left(2\pi f_{sp}^{j}t+\theta_{sp}^{j}\right)$, the frequency is usually same to the authentic frequency or match to the variation of code time delay. For focusing on the position estimation performance of the target receiver, the carrier wave of spoofing signals, in this study, are simplified as the same as authentic signals, that is $f_{sp}^{j} = f_{au}^{j}$ and $\theta_{sp}^{j} = \theta_{au}^{j}$.

An powerful spoofer is considered to control the target receiver completely. In such case, $P_{sp} \gg P_{au}$ and $M \geq N$, the authentic signals vanish in the received signals and the signal model can be shorten as

$$s = \sum_{j=1}^{M} s_{sp}^{j} + \varepsilon \tag{4}$$

In practice, the spoofer is commonly fixed in the ground and its signals are attenuated gradually during the propagation to a long-distance target receiver. In this case, the authentic signal is weak but not totally suppressed, $P_{sp} \approx P_{au}$. On the other hand, long distance possible leads to different satellite geometry, and hence different satellites observed by the target receiver, $M < N$. The two incomplete spoofing situations cause that the target receiver collects authentic and spoofing signals simultaneously and the effects of the authentic signals cannot be ignored. The signal model under incomplete spoofing attack is same to (1).

- Situation 1: $P_{sp} \approx P_{au}$

When spoofing signal power is not strong enough, $P_{sp} \approx P_{au}$, it is obvious that the spoofing signal still has influence on the target receiver operating in tracking, and an illustration of complete and incomplete spoofing attack is given in Fig. 1.

When the spoofing signal power is much larger than the authentic signal power, as shown in Fig. 1 (upper), the spoofer will drag the correlation peak away from the genuine peak to the counterfeit peak when the spoofing occurs. The estimating error τ'_{sp} equals to preset time delay τ_{sp}, which is the signal delay of the spoofing signal. The correlation peak calculated from the value of non-coherent integration is influenced by the signal power. For lower spoofing signal power, as shown in Fig. 1 (bottom), the spoofing signals are no longer dominant in the tracking loop, and the correlation curve of received signals, which is the combination peak in Fig. 1 (bottom), will be bilaterally asymmetric. In this case, the phase detector of code tracking loop will adjust code phase to correct the output of correlation, and the introduced estimating error τ'_{sp} is smaller than the preset time delay τ_{sp}.

- Situation 2: $M < N$

When the satellite geometry received by the target receiver changes, the positioning performance will vary accordingly. Assuming that several satellite signals from a certain region are attacked by spoofing signals, the estimated position of the target receiver will deviate from the authentic site. According to the principle of three-sphere intersection measurement as shown in Fig. 2, the influence in the line between the target receiver and the area where satellite signals are deceived is the most obvious. When the preset signal delays lag behind the authentic signals, $\tau_{sp} > 0$, the estimated position will shift to the opposite direction of the area where the satellite signals are spoofed. The relation between the preset signal delay τ_{sp} and the offset distance is nonlinear, which needs further research in the future.

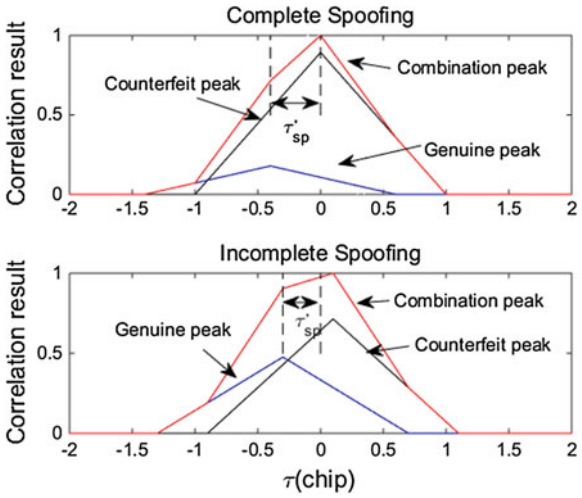

Fig. 1 Correlation results under complete spoofing (upper) and incomplete spoofing (bottom) attacks

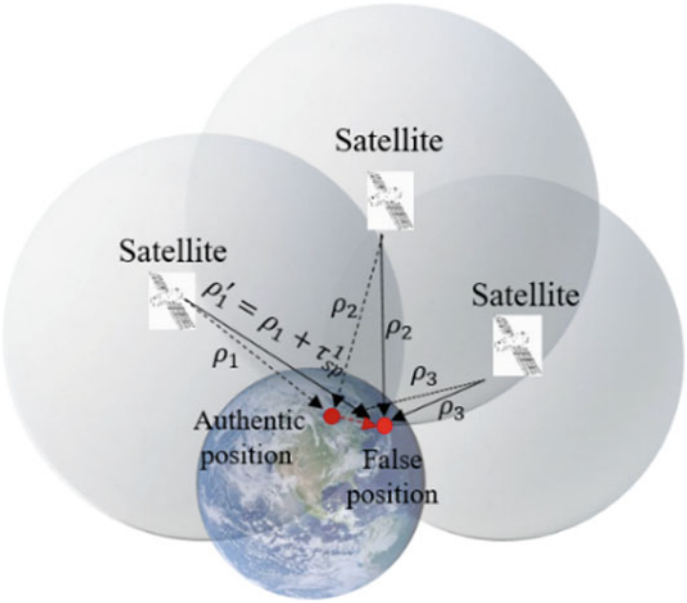

Fig. 2 The illustration of three-sphere intersection measurement of the incomplete spoofing

2.2 *Positioning Model Under Spoofing Environment*

The GNSS receiver obtains the pseudoranges between the receiver and satellites and then estimates the position with at least four pseudoranges. The pseudorange of the i-th authentic GNSS signal ρ_i^{au} can be expressed as:

$$\rho_i^{au} = r_i + \delta t_u + \varepsilon_p \tag{5}$$

$$r_i = \sqrt{(x_i - x)^2 + (y_i - y)^2 + (z_i - z)^2} \tag{6}$$

where, r_i is the distance between the receiver and the i-th satellite, δt_u is the clock error of the receiver, which is related to the GNSS receiver clock, ε_p is the sum of other errors. x_j, y_j, z_j $(j = 1, 2, 3, 4\ldots)$ and x, y, z represent the coordinates of the i-th satellite and the receiver under Earth Center Fixed coordinate system. The j-th spoofing GNSS signal ρ_j^{sp} has the same pseudorange model as the authentic signal:

$$\rho_j^{sp} = \rho_j^{au} + \tau_{sp}^j + \varepsilon_j = r_j + \delta t_u + \tau_{sp}^j + \varepsilon_j' \tag{7}$$

where, τ_{sp}^j is the product of the preset time offset τ_{sp} and the speed of light c $\left(\tau_{sp}^j = \tau_{sp} \times c\right)$, ε_j is the noise produced by the spoofer.

For complete spoofing, all the authentic signals are submerged by spoofing signals. The positioning equations can be expressed as:

$$\begin{cases} \rho_1 = \rho_1^{sp} = r_1 + \delta t_u + \tau_{sp}^1 + \varepsilon_1' \\ \vdots \\ \rho_M = \rho_M^{sp} = r_M + \delta t_u + \tau_{sp}^M + \varepsilon_M' \end{cases} \tag{8}$$

Under complete spoofing, when all the spoofing signals have the same preset time delay $\tau_{sp}^j = \tau_{sp}$, the common time delay τ_{sp} can be viewed as the clock error increment of the target receiver, $\delta t_u' = \left(\delta t_u + \tau_{sp}\right)$, and the preset site of the spoofer can only be the position of the transmitter. When time delays vary from spoofing signals, theoretically, the spoofer can drag the target receiver to any excepted location through the control of preset time delay τ_{sp}^i.

For incomplete spoofing, the authentic signals are weak but not totally suppressed. The positioning equations can be expressed as:

$$\begin{cases} \rho_1 = \rho_1^{sp} = r_1 + \delta t_u + \tau_{sp}^1 + \varepsilon_1' \\ \vdots \\ \rho_M = \rho_M^{sp} = r_M + \delta t_u + \tau_{sp}^M + \varepsilon_M' \\ \rho_{M+1} = \rho_{M+1}^{au} = r_{M+1} + \delta t_u + \varepsilon_{M+1} \\ \vdots \\ \rho_N = \rho_N^{au} = r_N + \delta t_u + \varepsilon_N \end{cases} \tag{9}$$

In this case, the position of the target receiver is influenced by both spoofing signals and authentic signals. The effect of incomplete spoofing is analyzed in the Sect. 2.1. The change on estimated pseudoranges can be viewed as the change on distance between the receiver and the *i*-th satellite, as shown in (10), and revealed in the deviation of estimated position, as shown in (11).

$$\begin{cases} r_1' = r_1 + \tau_{sp}^1 \\ \vdots \\ r_M' = r_M + \tau_{sp}^M \\ r_{M+1}' = r_{M+1} \\ \vdots \\ r_N' = r_N \end{cases} \tag{10}$$

$$r_j' = \sqrt{\left(x_j - x'\right)^2 + \left(y_j - y'\right)^2 + \left(z_j - z'\right)^2} \tag{11}$$

where, x', y', z' represent the coordinates of the target receiver under Earth Center Fixed coordinate system.

3 Implementation of Repeater Spoofing

The spoofer receives the GPS L1 signals, where the necessary parameters of the spoofing signals are obtained through sampling, acquisition and tracking. According to (2), the authentic satellite signals are composed by spreading code, carrier wave and navigation data, which are obtained from tracking results. Though separating and reconstructing each satellite signal, we can get a replica of the authentic signals. To affect the target receiver operating in tracking mode, the C/A code sequence, navigation data and carrier wave of spoofing signal are same to the authentic, as shown in (3), with the preset time offsets τ_{sp} reflecting in spreading code phase and signal power P_{sp} different.

Considering the possibility of incomplete spoofing, the number of spoofing signals and the spoofing signal power are under control in accordance with the requirements of tests. Through adjusting the parameters of spoofing signals, spoofing attacks are simulated to analyze the positioning performance of the target receiver under the incomplete spoofing.

4 Experiment and Analysis

4.1 Experiment Method and Environment

Data was received by the GNSS Software-Defined Receiver on the roof of No. 1 building, college of automation engineering, Nanjing University of Aeronautics and Astronautics, on September 18, 2017. The position measured by a dual-frequency commercial receiver is 118.7926358°E, 31.9388758°N, 51.82-m Height. The parameters of the target GNSS receiver are shown in the Table 1.

In the simulation, the GPS satellites are divided into four regions according to satellite distribution with the azimuth angle 0–360° at intervals of 90°, as shown in Fig. 3. The satellites respectively contained by the four regions are PRN 24 and 15 (Northeast Region—Region I), PRN 10 and 32 (Southeast Region—Region II), PRN 21 (Southwest Region—Region III), PRN 12 and 25 (Northwest Region—Region IV).

To analyze the positioning performance of GNSS receiver under the incomplete spoofing, two tests are carried out:

Table 1 The parameters of the target GNSS receiver

Sampling frequency	16.3676 MHz
Intermediate frequency	4.12397 MHz
PLL bandwidth@Integration time	10 Hz@1 ms
DLL bandwidth@Integration time	1 Hz@1 ms
Early-late chip spacing	0.5 chip

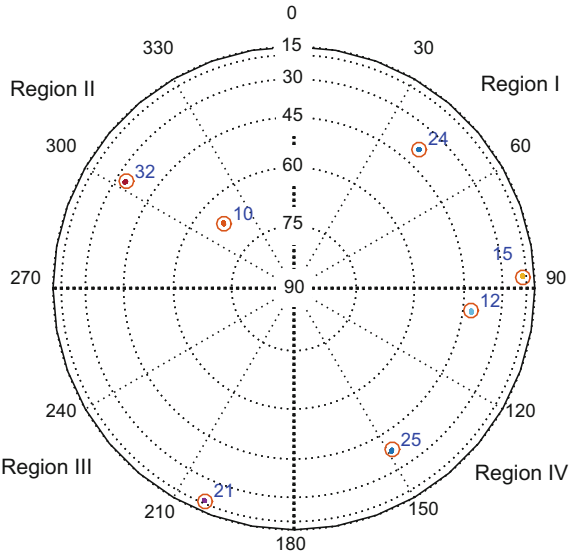

Fig. 3 Satellite spatial distribution

Test 1: The spoofing attack is complete. According the preset position (50 m away from the receiver-spoofer in the direction toward the east), the preset time delays τ_{sp}^{i} vary from different satellite signals $\left(\tau_{sp}^{i} \neq \tau_{sp}^{j}, i \neq j, i \in [1, N], j \in [1, N]\right)$. In this test, the preset time delays of PRN 24, 15, 12, 25, 21, 32, 10 are −28, −13, −18, −12, 38, 60, 50 m respectively.

Test 2: The spoofing attack is incomplete. We assume that one region of the satellite distribution is attacked by spoofing signals, and the preset time delay of spoofing signals is 50 m $\left(\tau_{sp}^{i} = 50\,\mathrm{m}, i \in [1, M], M < N\right)$. Considering the influence of spoofing signal power, the test is divided into two cases: (a) the spoofing signal power is large enough to submerge the authentic signals $\left(P_{au} \ll P_{sp}\right)$ and (b) the spoofing signal power decays during the propagation and is similar to the authentic signal power $\left(P_{au} \approx P_{sp}\right)$.

4.2 *Simulation Results and Analysis*

Figure 4 shows the positioning results of target receiver under complete spoofing of Test 1. In the results, we set the authentic position of target receiver as the reference position. To a certain extent, the estimated position of target receiver is nearly same as the preset position, which is in agreement with the analysis in Sect. 2.2. In this case, the spoofing signals play a dominant role in the position and fool the target receiver to any position with suitable settings of time delay $\tau_{sp}^{i}(i \in [1, N])$.

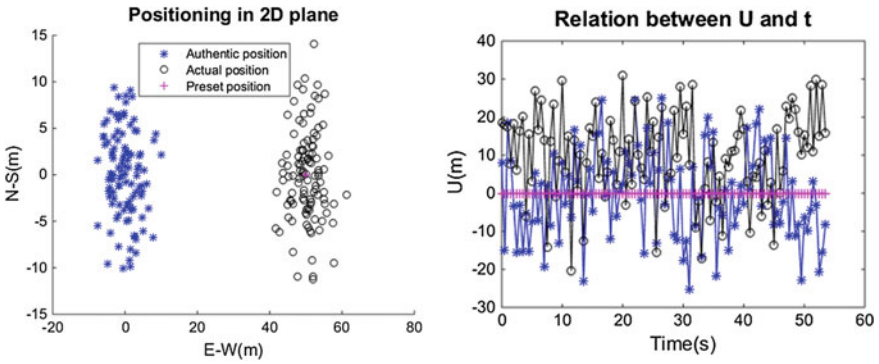

(a) Horizontal position (b) Height direction position

Fig. 4 Positioning results of target receiver under complete spoofing

Figure 5 shows the positioning results of target receiver under incomplete spoofing of Test 2. As shown in Fig. 5a, c, the estimating error τ'_{sp} reflecting in the deviation is related to spoofing signal power. The deviations of case (b) are mostly smaller than that of case (a). Compared with complete spoofing, the incomplete spoofing with smaller spoofing power is influenced by authentic signals and the positioning deviation is smaller accordingly. Under incomplete spoofing, the estimated position deviation of target receiver is related to satellite geometry obtained by the receiver. In the horizontal direction, the estimated location of target receiver is related to the azimuth angle of spoofed satellites. For example, when the signals from satellites in the Region I (Azimuth: 0–90°) under spoofing attack, the target receiver position shifts to the Region III (Azimuth: 180–270°), and the deviations are 9.47 m and 6.63 m in the north, 30.98 m and 8.88 m in the east respectively. The offset distance depends on the time delay which is affected by the spoofing signal power and authentic signal power. However, the position of the target receiver in height direction does not show a clear regularity, as shown in Fig. 5b, d. Though experiments carried out in this paper, the analyses of the incomplete spoofing influence on the GNSS receiver in the Sect. 2 are verified.

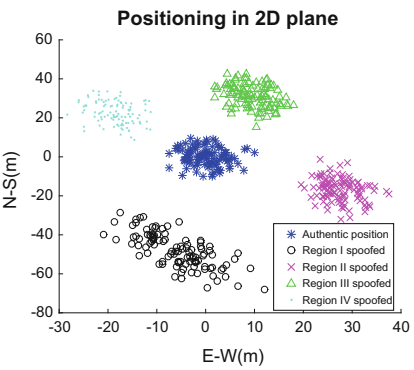

(a) Horizontal position ($P_{au} \ll P_{sp}$)

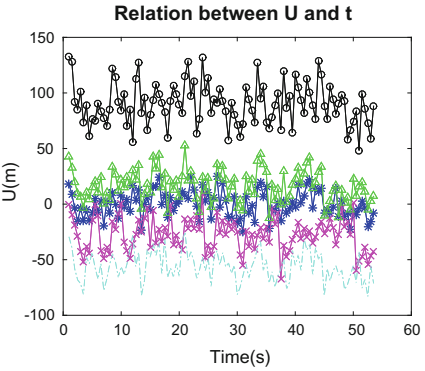

(b) Height direction position ($P_{au} \ll P_{sp}$)

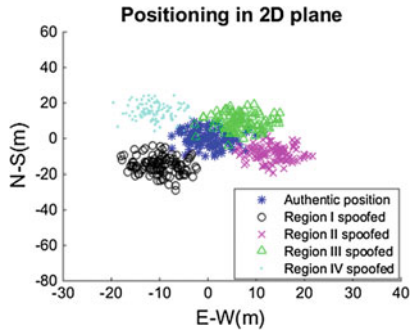

(c) Horizontal position ($P_{au} \approx P_{sp}$)

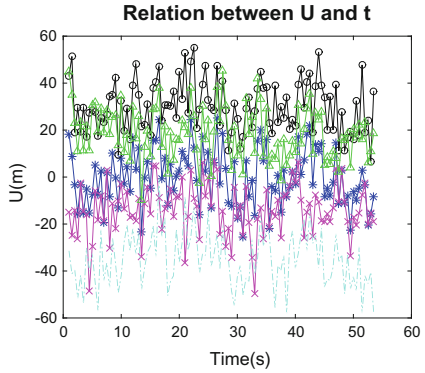

(d) Height direction position ($P_{au} \approx P_{sp}$)

Fig. 5 Positioning results of target receiver under incomplete spoofing

5 Conclusion

The GNSS repeater-based spoofer poses a greater threat to civilian receiver at present. When the site of the spoofer is far away from the target receiver, the influence of spoofing signals will be complex. In this paper, the positioning performance of a GNSS receiver under complete and incomplete spoofing are described in detail. The theoretical analyses and simulation results show the following conclusions:

(a) Complete spoofing attack, theoretically, can deceive the positioning result of the target receiver to any expected position with suitable settings of signal delays.
(b) Under incomplete spoofing attack, which revealing in the spoofing power or the coverage of signals incomplete, the existence of authentic signals has influence on the positioning results. When the spoofing power is incomplete, the actual

deviation τ'_{sp} is smaller than the preset deviation τ_{sp}; when the coverage of signals is incomplete, the actual position will shift in the line between the authentic position and the area where the spoofed satellites lie, and the deviation is related to the distance between the receiver and the satellite, the preset time delay and spoofing signal power.

Further study will consider the influence of incomplete spoofing on the spoofing process, such as the influence on code loop and tracking state.

Acknowledgements The authors are grateful for financial support from the National Natural Science Foundation of China (NSFC, www.nsfc.gov.cn) which supports this work under grant No. 61603181.

References

1. Ioannides RT, Pany T, Gibbons G (2016) Known vulnerabilities of global navigation satellite systems, status, and potential mitigation techniques. Proc IEEE 104(6):1174–1194
2. Motella B, Pini M, Fantino M, Mulassano P, Nicola M, Fortuny-Guasch, J et al (2011) Performance assessment of low cost GPS receivers under civilian spoofing attacks. Satellite Navigation Technologies and European Workshop on GNSS Signals and Signal Processing, IEEE, pp 1–8
3. Haider Z, Khalid S (2017) Survey on effective GPS spoofing countermeasures. In: Sixth international conference on innovative computing technology, IEEE, pp 573–577
4. Gao Y, Li H, Lu M, Feng Z (2013) Intermediate spoofing strategies and countermeasures. Tsinghua Science and Technology 18(6):599–605
5. Bhatti J, Humphreys TE (2017) Hostile control of ships via false GPS signals: demonstration and detection. Navigation 64(1):51–66
6. Psiaki ML, Humphreys TE (2016) GNSS spoofing and detection. Proc IEEE 104(6):1258–1270
7. Huang L, Lv ZC, Wang FX (2012) Spoofing pattern research on GNSS receivers. J Astronaut 33(7):884–890
8. Shepard DP, Bhatti JA, Humphreys TE, Fansler AA (2012) Evaluation of smart grid and civilian UAV vulnerability to GPS spoofing attacks. In: ION GNSS conference, pp 3591–3605
9. Humphreys TE, Ledvina BM, Psiaki ML, O'Hanlon BW, Kintner PM (2008) Assessing the spoofing threat: development of a portable GPS civilian spoofer. In: International technical meeting of the satellite division of the institute of navigation, pp 2314–2325
10. Broumandan A, Jafarnia-Jahromi A, Lachapelle G (2015) Spoofing detection, classification and cancelation (SDCC) receiver architecture for a moving GNSS receiver. GPS Solutions 19 (3):475–487
11. Bian S, Hu Y, Ji B (2017) Research status and prospect of GNSS anti-spoofing technology. SCIENTIA SINICA Informationis 47(3):275–287
12. Chen L, Han S, Meng W, Gong Z (2015) A spoofing mitigation algorithm based on subspace projection for GNSS receiver. In: China satellite navigation conference (CSNC) 2015 proceedings: vol I, pp 727–737. Springer, Berlin, Heidelberg
13. Huang J, Presti LL, Motella B, Pini M (2016) GNSS spoofing detection: theoretical analysis and performance of the ratio test metric in open sky. ICT Express 2(1):37–40
14. Kerns AJ, Shepard DP, Bhatti JA, Humphreys TE (2014) Unmanned aircraft capture and control via GPS spoofing. J Field Robot 31(4):617–636

Subcarrier-Abstracted Multi-frequency Constant-Envelope Multiplexing and Its Implementation Optimization

Junjie Ma, Zheng Yao and Mingquan Lu

Abstract More and more signals are broadcast by navigation satellite systems nowadays to satisfy users' diversified needs in positioning, navigation and timing (PNT). We usually adopt multiplexing techniques to combine several signals into an integrated signal to save transmission link resources. Since the high-power amplifier on satellite operates at the nonlinear saturation region, the multiplexed signal is required to have constant-envelope characteristic. At present, single frequency constant-envelope multiplexing (CEM) techniques have been studied thoroughly. However, the research in multi-frequency constant-envelope multiplexing still needs to be strengthened. In this paper, we propose a subcarrier-abstracted multi-frequency constant-envelope multiplexing (SAMCEM) technique. We substitute the continuous sinusoidal subcarrier by step-shape subcarrier, and construct the signal space using the view of orthogonality. Based on these mathematical preliminaries, we set up an optimization problem, which maximizes multiplexing efficiency under the constraint of constant envelope. The output of our method is a phase look-up table (LUT). Our method breaks the limitations in subcarriers, the number of signals, and power and phase relationship among signals, overcoming drawbacks of the existing multi-frequency multiplexing techniques with better flexibility and universality and can achieve optimal multiplexing efficiency. This technique serves as a candidate technique to support the improvement in signal scheme of BDS III. In this paper, we also improve the engineering implementation of multi-frequency CEM. A low-redundancy LUT storage scheme is proposed, which can save half of the storage resource in dual-frequency multiplexing. Besides, pipeline structure is adopted to generate multi-frequency CEM signals, which can help avoid transmitted phase error in multi-frequency CEM.

Keywords Multi-frequency constant-envelope multiplexing · Subcarrier Orthogonal basis · Multiplexing efficiency · Pipeline

J. Ma · Z. Yao (✉) · M. Lu
Department of Electronic Engineering, Tsinghua University,
Beijing 100084, China
e-mail: yaozheng@tsinghua.edu.cn

J. Sun et al. (eds.), *China Satellite Navigation Conference (CSNC) 2018 Proceedings*, Lecture Notes in Electrical Engineering 498,
https://doi.org/10.1007/978-981-13-0014-1_14

1 Introduction

The design of navigation signals is a crucial part in the construction of global navigation satellite systems (GNSSs). Superior signal scheme can boost the performance of the whole navigation system. Multiplexing technology is an important part in navigation signal design. Because the high-power amplifier on satellite operates in the nonlinear saturation region, the multiplexed signal is required to have constant-envelope characteristic. In single-frequency CEM, all signals involved in multiplexing have the same central frequency, while in multi-frequency CEM signals may have several different central frequencies. In existing GNSSs, multi-frequency CEM usually means dual-frequency CEM. Therefore, we mainly focus on dual-frequency CEM case in this paper.

After years of research, the single-frequency constant-envelope multiplexing technology has gradually become mature. A series of single-frequency CEM methods are proposed, such as majority voting (MV) [1], Interplex [2] and POCET [3]. POCET sets no restrictions in the number of signals, power and phase relationship among signals, and multiplexing efficiency can always be optimal. As for multi-frequency CEM technology, alternate binary offset carrier (AltBOC) modulation [4], asymmetric constant envelope binary offset carrier modulation (ACEBOC) [5], and equilong segment asymmetric constant-envelope binary offset carrier (ES-ACEBOC) modulation [5] are most representative. However, these methods are limited in the number of signals, power and phase relationship among signals, the number of subcarrier segments and so on. In [6] a universal multi-frequency CEM method named rotating POCET (R-POCET) is proposed, which overcomes the above limitations but the multiplexing efficiency is not optimal. To solve these problems in multi-frequency CEM, this paper proposes subcarrier-abstracted multi-frequency constant-envelope multiplexing (SAMCEM) technique. Our method can achieve optimal multiplexing efficiency without the limitations in traditional multi-frequency CEM methods.

Improvements in engineering implementation of multi-frequency CEM are also discussed in this paper. We propose a low-redundancy phase look-up table (LUT) storage scheme based on the inherent symmetry of multi-frequency CEM subcarrier waveforms, which consumes only half of the storage resources compared with traditional implementation structure. Apart from this, pipeline structure is utilized in the generation of multi-frequency CEM signals to help avoid transmitted phase error caused by high clock frequency in multi-frequency CEM.

2 Model and Methodology

2.1 Discrete Equivalent Subcarriers

Considering the combination of n independent signals with certain power and phase relationship among them, the integrated signal by direct superposition can be expressed as

$$s(t) = \sum_{i=1}^{n} \sqrt{P_i} \exp(j\phi_i) s_{i,RF}(t), \tag{1}$$

where P_i and ϕ_i are the transmitted power and phase of component i respectively. $s_{i,RF}(t)$ is the ith radio frequency signal.

$$\begin{aligned} s_{i,RF}(t) &= \sum_{k=-\infty}^{+\infty} (-1)^{c_i[k]} d_i(t) p_i(t - kT_c^{(i)}) \exp(j2\pi f_i t) \\ &= s_i(t) \exp(j2\pi f_i t) \end{aligned} \tag{2}$$

where $c_i[k]$, $d_i(t)$, $\exp(j2\pi f_i t)$ are the spreading code with chip rate $1/T_c^{(i)}$, navigation data, and complex carrier with frequency f_i of signal i respectively. $p_i(t)$ is chip waveform of the spreading code, which is zero outside interval $t \in [0, T_c)$, the definition is given in (3)

$$p_i(t) = \sum_{q=0}^{M_i - 1} m_i[q] \psi_{T_p^{(i)}}(t - qT_p^{(i)}), \tag{3}$$

in which $\psi_{T_p^{(i)}}(t)$ and $T_p^{(i)}$ are

$$\psi_{T_p^{(i)}}(t) = \begin{cases} 1, & 0 \le t < T_p^{(i)} \\ 0, & \text{else} \end{cases} \tag{4}$$

$$T_p^{(i)} = \frac{T_c^{(i)}}{M_i}. \tag{5}$$

M_i is the number of waveform segments, and $m_i[q]$ denotes the value of chip waveform in the qth segment. Most of the existing spreading chip waveforms in GNSSs are bipolar, which means $m_i[q] = \pm 1$ in (3).

Since high-power amplifiers on satellites operate at the nonlinear saturation region, the fluctuation of signal envelope will cause amplitude and phase distortion, and degrade the performance of navigation signals. However, multiplexing by direct superposition defined in (1) usually does not meet the constant-envelope requirements. Therefore we have to introduce additional signals to the integrated

signal so that the envelope of the integrated signal is constant, as shown in (6). We should also diminish the interference of these additional signals to initial signal components.

$$\begin{aligned} s_{CE}(t) &= \left[\sum_{i=1}^{n} \sqrt{P_i}\exp(j\phi_i)s_i(t)\exp(j2\pi(f_i - f_0)t) + \tilde{s}(t)\right]\exp(j2\pi f_0 t) \\ &= s_{CE0}(t)\exp(j2\pi f_0 t) \end{aligned} \tag{6}$$

In (6), $\tilde{s}(t)$ is the introduced additional signal, and f_0 is the central frequency of CEM signal. $s_{CE0}(t)$ denotes the base-band CEM signal, which can always be expressed as the form of phase modulation, as shown in (7),

$$s_{CE0}(t) = \sum_{l=-\infty}^{+\infty} A\ \exp(j\theta[l])\psi_{T_l}(t - lT_l) \tag{7}$$

where $\theta[l]$ is the transmitted phase when $t \in [lT_l, (l+1)T_l)$. T_l should guarantee the value of $s_i(t)$ is constant when $t \in [lT_l, (l+1)T_l)$ for $i = 1, \ldots, n$. A is the envelope of CEM signal. $f_i - f_0$ is the subcarrier frequency of signal i, which is denoted as f_{si} for simplicity. In dual-frequency CEM, $|f_{si}|$ is constant. The key point in (7) is that the transmitted phase of the integrated signal in interval $t \in [lT_l, (l+1)T_l)$ does not vary. Accordingly, we can substitute complex sinusoidal subcarrier by step-shape subcarrier with the same receiving effect. Figure 1 depicts the equivalent step-shape subcarrier and the original sinusoidal subcarrier.

We further transform the step-shape subcarrier into discrete signal vectors. Let $F = f_l / |f_{si}|$, then the step-shape subcarrier could be abstracted as a vector $\mathbf{e_i}$, where sgn(■) means the sign function.

$$\begin{aligned} \mathbf{e_i} = \frac{F}{\pi}\sin(\frac{\pi}{F})[&\exp(j\frac{\pi}{F}\mathrm{sgn}(f_{si}))\exp(j\frac{3\pi}{F}\mathrm{sgn}(f_{si}))\ldots \\ &\exp(j\frac{2\pi}{F}(l+\frac{1}{2})\mathrm{sgn}(f_{si}))\ldots\exp(j\frac{(2F-1)\pi}{F}\mathrm{sgn}(f_{si}))]^{\mathrm{T}} \end{aligned} \tag{8}$$

We use normalized subcarrier vector $\tilde{\mathbf{e}}_\mathbf{i} = \mathbf{e_i}/\|\mathbf{e_i}\|$ in other parts of this paper for simplicity.

2.2 *Multiplexing Efficiency Optimization Based on Orthogonal Basis*

Multiplexing efficiency is an important criterion to evaluate a CEM scheme, which is defined as the power proportion of useful signals in the integrated signal. Most CEM techniques aim at optimizing multiplexing efficiency [3, 5–7]. In [7], a method for optimizing the multiplexing efficiency based on orthogonal basis is

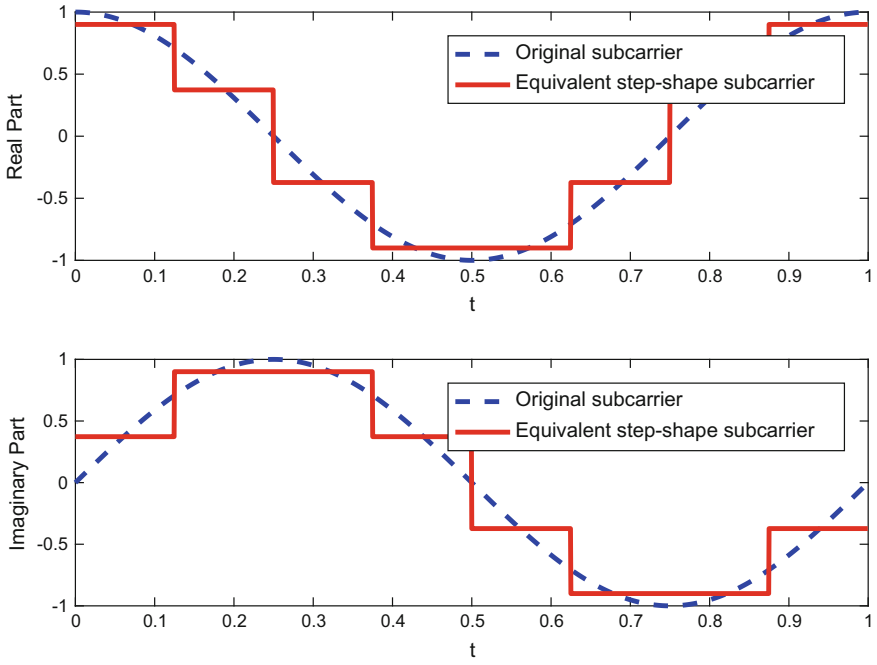

Fig. 1 Equivalent step-shape subcarrier of original sinusoidal subcarrier

proposed with outstanding performance and clear physical meaning. This subsection will use the orthogonal basis opinion to optimize multiplexing efficiency.

Since superposition of signals generally do not have constant-envelope characteristics, additional signals need to be introduced to make the composite signal has a constant envelope, as shown in Eq. (6). The additional signals will degrade multiplexing efficiency, and cause interference to the original signals. In order to reduce this interference, it is pointed out in [7] that the additional signals should fall in the orthogonal complementary space of the original signal. Therefore, we need to clarify the vector space of the original signals first.

For n BPSK signals, all possible combinations of signal values can be taken as the first n columns of the 2^n order Hadamard matrix [8, 9]. The corresponding Hadamard matrix of three-signal case is given in Fig. 2 as an example, and the first three columns of the matrix correspond to the three signals participating in the multiplexing. We denote the ith signal as $\mathbf{s_i}$.

In Sect. 2.1, we give the normalized equivalent subcarrier vector. Therefore in multi-frequency CEM the ith signal could be expressed as

$$\tilde{\mathbf{s}}_\mathbf{i} = \mathbf{s_i} \otimes \tilde{\mathbf{e}}_\mathbf{i}, \tag{9}$$

where $\otimes$ denotes Kronecker product. All the n signals span multi-frequency signal space, which is the column space of $\mathbf{S}$.

Fig. 2 Hadamard matrix of three-signal case

$$\begin{bmatrix} -1 & -1 & -1 & -1 & -1 & -1 & -1 & -1 \\ -1 & -1 & 1 & -1 & 1 & 1 & 1 & -1 \\ -1 & 1 & -1 & 1 & -1 & 1 & 1 & -1 \\ -1 & 1 & 1 & 1 & 1 & -1 & -1 & -1 \\ 1 & -1 & -1 & 1 & 1 & -1 & 1 & -1 \\ 1 & -1 & 1 & 1 & -1 & 1 & -1 & -1 \\ 1 & 1 & -1 & -1 & 1 & 1 & -1 & -1 \\ 1 & 1 & 1 & -1 & -1 & -1 & 1 & -1 \end{bmatrix}$$

$$\mathbf{S} = [\tilde{\mathbf{s}}_1 \quad \tilde{\mathbf{s}}_2 \quad \ldots \quad \tilde{\mathbf{s}}_n] \tag{10}$$

As mentioned above, the introduced additional signals must fall in the orthogonal complementary space of the original signal space, whose basis could be constructed by Gram-Schmidt orthogonalization. These basis vectors are the columns of matrix $\mathbf{S}^{\perp}$. Let $\mathbf{C} = [\mathbf{S} \quad \mathbf{S}^{\perp}]$, we require that $\mathbf{C}$ satisfy $\mathbf{C}\mathbf{C}^{H} = 2^{n}\mathbf{I}$.

A CEM scheme is a mapping between the combination of signal values and the transmitted phases, as shown in (11), where $\boldsymbol{\theta}$ consists of the transmitted phases of the integrated signal for different signal combinations.

$$\mathbf{S} = [\tilde{\mathbf{s}}_1 \quad \tilde{\mathbf{s}}_2 \quad \ldots \quad \tilde{\mathbf{s}}_n] \rightarrow \exp(\mathrm{j}\boldsymbol{\theta}) \tag{11}$$

Based on orthogonal basis, multi-frequency CEM signal can be constructed by

$$\mathbf{S}\mathbf{w}_{\mathbf{s}} + \mathbf{S}^{\perp}\mathbf{w}_{\mathbf{m}} = A\ \exp(j\boldsymbol{\theta}) \tag{12}$$

in which $\mathbf{w}_{\mathbf{s}}$ is the linear combination coefficients of original signal vectors reflecting power and phase relationship among signals, the ith component of $\mathbf{w}_{\mathbf{s}}$ is

$$\mathbf{w}_{\mathbf{s}}(i) = \|\mathbf{e}_{\mathbf{i}}\|^{-1}\sqrt{P_i}\exp(j\phi_i). \tag{13}$$

P_i and ϕ_i have the same definition as in Eq. (1). $\mathbf{w}_{\mathbf{m}}$ is the linear combination coefficients of the additional signal vectors. A is the amplitude of the integrated CEM signal. $\boldsymbol{\theta}$ is the transmitted phase vector of the multiplexed signal, whose ith component corresponds to the ith combination case of signal values, that is the ith row of $\mathbf{S}$.

In addition to minimizing the interference of the additional signals on the original signal, we also need to minimize the power of the additional signals to achieve better multiplexing efficiency. The calculation formula of multiplexing efficiency in multi-frequency constant-envelope multiplexing is shown in (14), which reflects the power proportion of useful signals in the integrated signal.

$$\eta = \frac{F^{-1}\sum_{i=1}^{n} P_i}{\|\mathbf{w_s}\|^2 + \|\mathbf{w_m}\|^2} \tag{14}$$

$\sum_{i=1}^{n} P_i$ and $\|\mathbf{w_s}\|^2$ are decided by signal designers, therefore we only need to minimize $\|\mathbf{w_m}\|^2$.

Let $\mathbf{w} = [\mathbf{w_s}^{\mathrm{T}}\ \mathbf{w_m}^{\mathrm{T}}]^{\mathrm{T}}$, $\mathbf{s_{CE}} = \mathbf{Cw}$, $\mathbf{s_{CE}}(i)$ denotes the ith component of $\mathbf{s_{CE}}$. We build the optimization problem as below

$$\begin{cases} \arg\min\limits_{\mathbf{w_m}} \quad \|\mathbf{w_m}\|^2 \\ \text{s.t.} \quad \max\limits_{i}(\|\mathbf{s_{CE}}(i)\|) - \min\limits_{j}(\|\mathbf{s_{CE}}(j)\|) = 0 \end{cases}. \tag{15}$$

We can use gradient descent method in [7] or other numerical methods to solve this optimization problem. When $\mathbf{w_m}$ is determined, we substitute it into the expression of $\mathbf{s_{CE}}$ and solve the optimal transmitted phase vector $\boldsymbol{\theta}$. We name the multi-frequency CEM technique in this paper as Subcarrier-Abstracted Multi-frequency Constant-Envelope Multiplexing (SAMCEM).

3 Implementation Issues

3.1 Phase Look-up Table

In Sect. 2, we have introduced the mathematical model of multi-frequency CEM, and abstracted the equivalent subcarrier vector of the original sinusoidal subcarrier, then an optimization problem is set up to solve the optimal transmitted phase vector $\boldsymbol{\theta}$. However, the phase vector $\boldsymbol{\theta}$ is difficult to be implemented directly in engineering and it is necessary to convert it to a more easily-realized form.

It is stated that constant-envelope multiplexing scheme is actually a mapping between the combination of signal values and the transmitted phase, as shown in (11). In multi-frequency CEM, the combination of the multi-frequency signals' values is related to both the current value of original signals (without subcarriers) and the current value of the equivalent subcarriers. In practical engineering implementation, there is no need to reproduce the equivalent subcarriers, because values of equivalent subcarriers can be determined by the time information. Suppose current time is t, let $T_{sc} = 1/|f_{si}|$, if $\mathrm{mod}(t, T_{sc})/T_{sc}$ belongs to interval $[(i-1)/F,\ i/F)$, current time corresponds to the ith component of the subcarrier vector. (T_{sc} and F have been defined in Sect. 2.) Therefore we can construct a phase look-up table (LUT) with dimension $F \times 2^n$. The transmitted phase is determined according to current time and the current value combination of the original signals.

Table 1 Phase LUT of CEM in three-signal case with F = 8

$\mathbf{s}_1$	−1	−1	−1	−1	1	1	1	1
$\mathbf{s}_2$	−1	−1	1	1	−1	−1	1	1
$\mathbf{s}_3$	−1	1	−1	1	−1	1	−1	1
$[0, \frac{1}{8})T_{sc}$	$\boldsymbol{\theta}_1$	$\boldsymbol{\theta}_9$	$\boldsymbol{\theta}_{17}$	$\boldsymbol{\theta}_{25}$	$\boldsymbol{\theta}_{33}$	$\boldsymbol{\theta}_{41}$	$\boldsymbol{\theta}_{49}$	$\boldsymbol{\theta}_{57}$
$[\frac{1}{8}, \frac{1}{4})T_{sc}$	$\boldsymbol{\theta}_2$	$\boldsymbol{\theta}_{10}$	$\boldsymbol{\theta}_{18}$	$\boldsymbol{\theta}_{26}$	$\boldsymbol{\theta}_{34}$	$\boldsymbol{\theta}_{42}$	$\boldsymbol{\theta}_{50}$	$\boldsymbol{\theta}_{58}$
$[\frac{1}{4}, \frac{3}{8})T_{sc}$	$\boldsymbol{\theta}_3$	$\boldsymbol{\theta}_{11}$	$\boldsymbol{\theta}_{19}$	$\boldsymbol{\theta}_{27}$	$\boldsymbol{\theta}_{35}$	$\boldsymbol{\theta}_{43}$	$\boldsymbol{\theta}_{51}$	$\boldsymbol{\theta}_{59}$
$[\frac{3}{8}, \frac{1}{2})T_{sc}$	$\boldsymbol{\theta}_4$	$\boldsymbol{\theta}_{12}$	$\boldsymbol{\theta}_{20}$	$\boldsymbol{\theta}_{28}$	$\boldsymbol{\theta}_{36}$	$\boldsymbol{\theta}_{44}$	$\boldsymbol{\theta}_{52}$	$\boldsymbol{\theta}_{60}$
$[\frac{1}{2}, \frac{5}{8})T_{sc}$	$\boldsymbol{\theta}_5$	$\boldsymbol{\theta}_{13}$	$\boldsymbol{\theta}_{21}$	$\boldsymbol{\theta}_{29}$	$\boldsymbol{\theta}_{37}$	$\boldsymbol{\theta}_{45}$	$\boldsymbol{\theta}_{53}$	$\boldsymbol{\theta}_{61}$
$[\frac{5}{8}, \frac{3}{4})T_{sc}$	$\boldsymbol{\theta}_6$	$\boldsymbol{\theta}_{14}$	$\boldsymbol{\theta}_{22}$	$\boldsymbol{\theta}_{30}$	$\boldsymbol{\theta}_{38}$	$\boldsymbol{\theta}_{46}$	$\boldsymbol{\theta}_{54}$	$\boldsymbol{\theta}_{62}$
$[\frac{3}{4}, \frac{7}{8})T_{sc}$	$\boldsymbol{\theta}_7$	$\boldsymbol{\theta}_{15}$	$\boldsymbol{\theta}_{23}$	$\boldsymbol{\theta}_{31}$	$\boldsymbol{\theta}_{39}$	$\boldsymbol{\theta}_{47}$	$\boldsymbol{\theta}_{55}$	$\boldsymbol{\theta}_{63}$
$[\frac{7}{8}, 1)T_{sc}$	$\boldsymbol{\theta}_8$	$\boldsymbol{\theta}_{16}$	$\boldsymbol{\theta}_{24}$	$\boldsymbol{\theta}_{32}$	$\boldsymbol{\theta}_{40}$	$\boldsymbol{\theta}_{48}$	$\boldsymbol{\theta}_{56}$	$\boldsymbol{\theta}_{64}$

For example, for the multi-frequency CEM of three-signal case, we assume $F = 8$, the LUT of CEM scheme is shown in Table 1, where $\boldsymbol{\theta}_\mathbf{i}$ denotes the ith component of $\boldsymbol{\theta}$.

3.2 Low-Redundancy LUT Storage Scheme

Since the transmitted phase is not only related to current value combination of the original signals but also to the current time, the storage consumption of the multi-frequency CEM LUT is much larger than that of single-frequency CEM. We hope to minimize redundant storage by analyzing the intrinsic structure of phase LUT.

We can reduce the storage consumption to half of the original LUT for dual-frequency CEM. The reduction in storage is due to the fact that there are identical rows in matrix $\mathbf{S}$, that is, the combination of signal values (including subcarriers) are the same. We denote the kth component of $\mathbf{s}_\mathbf{i}$ by $\mathbf{s}_\mathbf{i}(k)$, then we have

$$\mathbf{s}_\mathbf{i}(k) = -\mathbf{s}_\mathbf{i}(2^n + 1 - k) \tag{16}$$

When F is even, we have

$$\tilde{\mathbf{e}}_\mathbf{i}(m) = -\tilde{\mathbf{e}}_\mathbf{i}(\mathrm{mod}(F/2 + m - 1, F) + 1), \tag{17}$$

where $\tilde{\mathbf{e}}_\mathbf{i}(m)$ is the mth component of $\tilde{\mathbf{e}}_\mathbf{i}$. Furthermore, we can deduce that

$$\tilde{\mathbf{s}}_\mathbf{i}(F(k-1) + m) = \tilde{\mathbf{s}}_\mathbf{i}(F(2^n - k) + \mathrm{mod}\,(F/2 + m - 1, F) + 1) \tag{18}$$

$$\boldsymbol{\theta}(F(k-1) + m) = \boldsymbol{\theta}(F(2^n - k) + \mathrm{mod}\,(F/2 + m - 1, F) + 1). \tag{19}$$

In Fig. 3, we show this intrinsic symmetry when $n = 3$ and $F = 8$.

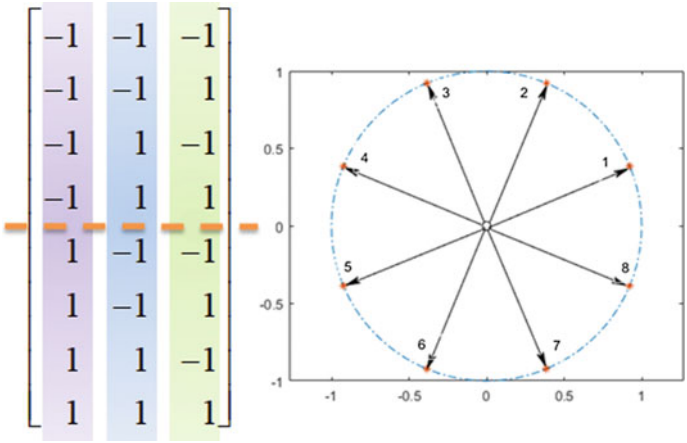

Fig. 3 Symmetry of $\mathbf{s_i}$ and $\sqrt{F}\tilde{\mathbf{e}}_\mathbf{i}$

From (18) and (19), we can assert that the transmitted phase in row m, column k is the same as the phase in row $(\mathrm{mod}(F/2+m-1,F)+1)$ and column (2^n+1-k). For example, if Table 1 corresponds to dual-frequency CEM, we only need to store the left half of the original LUT, the phases on the right half of LUT can be found on the left because of the intrinsic symmetry of LUT.

The phase LUT for dual-frequency CEM schemes such as AltBOC [4], ES-ACEBOC [5] and ACEBOC [5] all have the intrinsic symmetry analyzed in this section and can apply the low-redundancy storage scheme.

3.3 *Pipeline Structure in the Generation of Multi-frequency CEM Signals*

Pipeline structure has successful applications in the design of circuits and processors. It divides the whole process into several stages. Each stage occupies a single clock cycle, and different stages can be executed in parallel. Therefore, pipeline structure helps to improve the throughput rate of the program and relax the requirements in hardware performance.

The clock frequency is much higher in multi-frequency CEM than in single-frequency CEM. As a result, the transmitted phase look-up should be finished in much shorter interval. The multi-frequency CEM signal generation could be divided in three stages.

1. Time chip counting for subsequent phase look-up and signal generation.
2. Access to memory to get PRN code, navigation data and so on.
3. Phase look-up according to the value combination of signals and current time.

Traditional single cycle structure requires that the above three steps are accomplished in the same clock cycle, as shown in Fig. 4.

When hardware performance is not good enough or the driving clock frequency is too high, the traditional single cycle structure may cause transmitted phase error. However, for pipeline structure the three stages can be executed in parallel in a single clock cycle. This feature helps relax the requirements in hardware performance and could avoid phase error. Pipeline structure for multi-frequency CEM is shown in Fig. 5.

In order to ensure the correctness of results in each stage, pipeline registers need to be added between stages to save the execution results of current stage so that next stage could use them. The data path diagram of pipeline structure is shown in Fig. 6.

Pipeline structure can be partitioned into several units, including COUNTER, ROM, ALU and PHASE MUX, responsible for time chip counting, storage, operation, and phase look-up respectively. When we generate multi-frequency

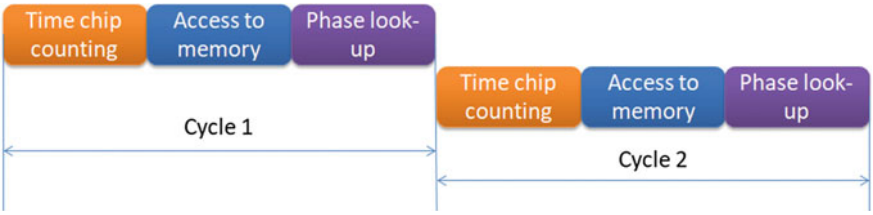

Fig. 4 Single cycle structure of multi-frequency CEM

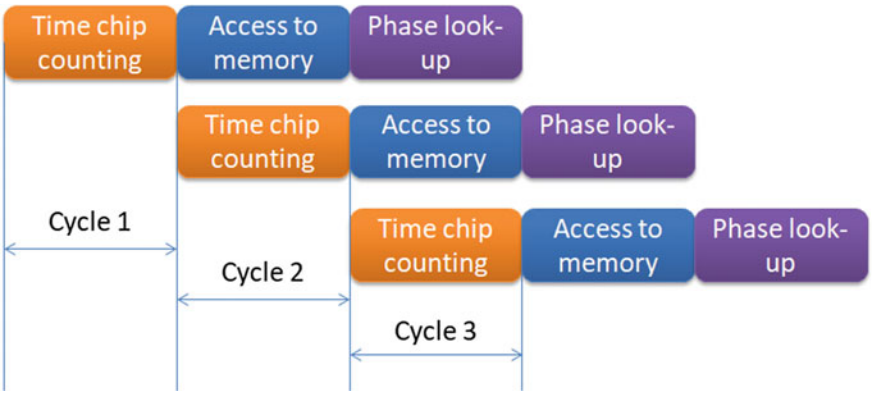

Fig. 5 Pipeline structure of multi-frequency CEM

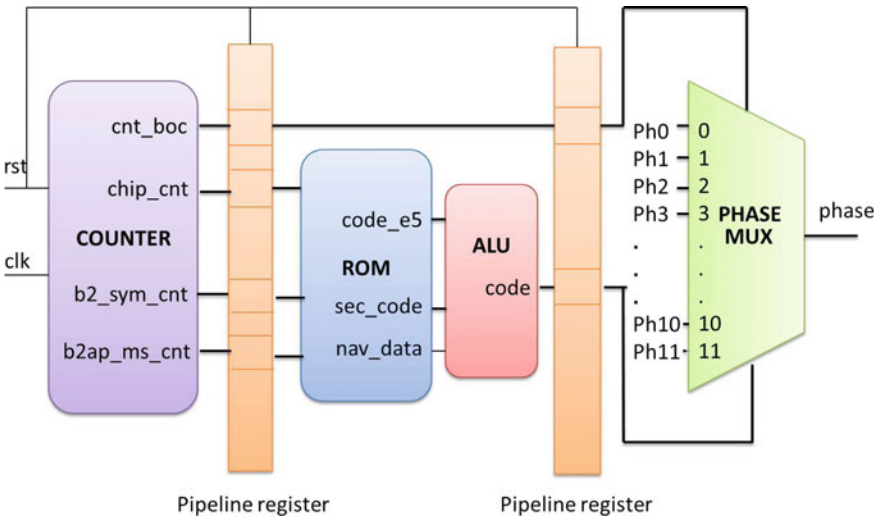

Fig. 6 Data path diagram of pipeline structure

CEM signal in experiment, we found that the output of PHASE MUX is incorrect sometimes if we adopts traditional single cycle structure, while the result is always right if pipeline structure is applied.

4 Simulation Results

In this section we compare the performance of SAMCEM with ES-ACEBOC, an advanced multi-frequency CEM technique to highlight the advantages of SAMCEM in flexibility, universality, and multiplexing efficiency. Let UI, UQ denote signals on the upper frequency band with phases in quadrature, and LI, LQ denote signals on the lower band also with phases in quadrature. The power allocation among the four signals is $P_{UI} : P_{UQ} : P_{LI} : P_{LQ} = 1 : 3 : 1 : 3$. In the SAMCEM method, we need to determine the number of subcarrier segments F, the linear combination coefficients of the signal vectors $\mathbf{w_s}$ and the equivalent subcarrier vectors $\tilde{\mathbf{e}}_\mathbf{i}$. We set the number of subcarrier segments to 8 to compare with ES-ACEBOC. We could choose $\mathbf{w_s} = [\,1 \quad \sqrt{3}j \quad \exp(j\theta) \quad \sqrt{3}j\exp(j\theta)\,]^{\mathrm{T}}$, where θ denotes the angle between UI and LI. The equivalent subcarriers of the four signals are

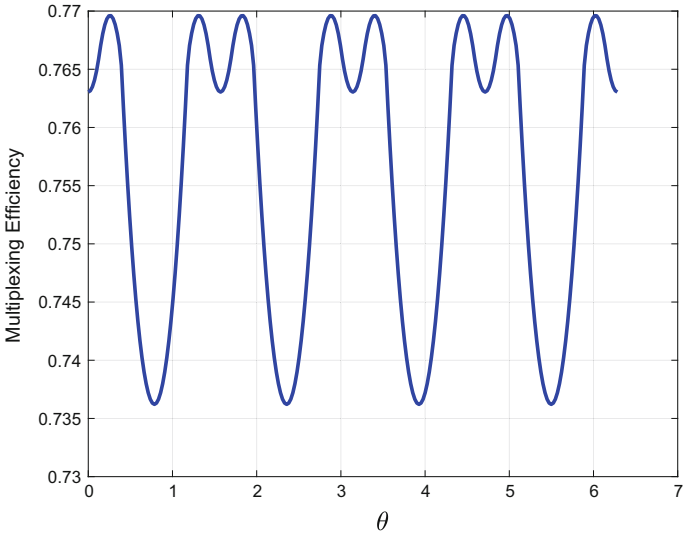

Fig. 7 Multiplexing efficiency of SAMCEM with respect to θ

$$\tilde{\mathbf{e}}_1 = \frac{1}{2\sqrt{2}}[\exp(j\frac{\pi}{8})\ \exp(j\frac{3\pi}{8})\ \exp(j\frac{5\pi}{8})\ldots\exp(j\frac{15\pi}{8})]^{\mathrm{T}}$$
$$\tilde{\mathbf{e}}_2 = \tilde{\mathbf{e}}_1 \quad \tilde{\mathbf{e}}_3 = \tilde{\mathbf{e}}_4 = conj(\tilde{\mathbf{e}}_1)$$

$conj(\cdot)$ means conjugation. Now we are able to solve problem (15), and calculate the optimal transmitted phases and multiplexing efficiency. The multiplexing efficiency of SAMCEM with different θ is depicted in Fig. 7.

Multiplexing efficiency changes with θ, as shown in Fig. 7. As a consequence, we could select appropriate θ to maximize multiplexing efficiency by using SAMCEM. Under the above circumstance, the optimal multiplexing efficiency reaches 76.9%, while multiplexing efficiency of ES-ACEBOC is only 75.6%. This is because ES-ACEBOC can only deal with the case where the angle between UI and LI is zero, and there are some unnecessary constraints in the optimization problem.

Furthermore, we study the multiplexing efficiency of SAMCEM with different θ and F, as Fig. 8 shows. The value of F is set to $4, 6, \ldots, 24$. Simulation results show that optimal multiplexing efficiency is 81.06% when F is 12 or 24. For the simplicity of engineering implementation, we set F to 12 and θ to 0. As ES-ACEBOC can only handle the cases with $F = 8$, its multiplexing efficiency is inferior.

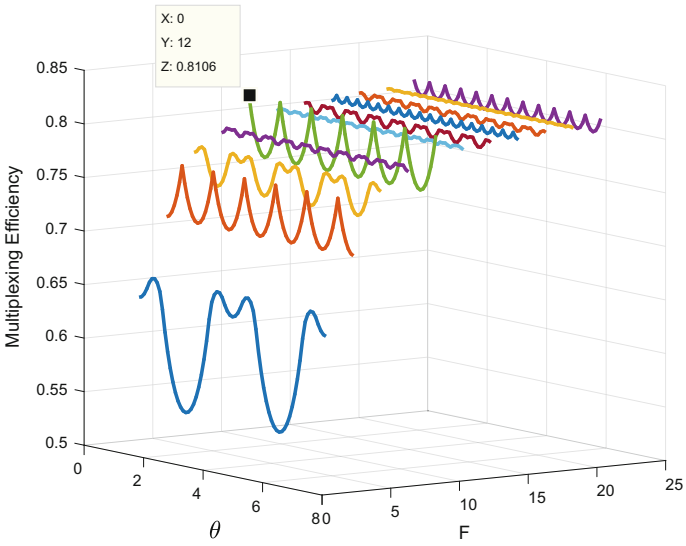

Fig. 8 Multiplexing efficiency of SAMCEM with respect to θ and F

5 Conclusions

In this paper we propose a subcarrier-abstracted multi-frequency constant-envelope multiplexing (SAMCEM) technique. SAMCEM substitutes the sinusoidal subcarriers by equivalent discrete subcarriers, and construct the signal space in the view of orthogonality. Based on these mathematical preliminaries, we set up an optimization problem, which maximizes multiplexing efficiency under the constraint of constant envelope. We will get the optimal transmitted phases after solving the numerical optimization problem. SAMCEM breaks through the limitations of existing multi-frequency constant-envelope multiplexing methods in terms of the number of signals, the number of subcarrier segments, and power and phase constraints in signals, which greatly increases the design flexibility and generality. SAMCEM could provide technical support for BDS III in further improvement of navigation signals.

In addition, this paper improves the engineering implementation of multi-frequency constant-envelope multiplexing by adopting pipeline structure to generate multi-frequency multiplexing signal, which solves the problem of phase output error at high clock rate. Besides, we reduce the redundancy in phase look-up table by exploiting the inherent symmetry of equivalent subcarriers. For dual-frequency constant-envelope multiplexing, the low-redundancy storage scheme reduces the amount of storage to 50% of the original.

References

1. Spilker JJ, Orr RS (1998) Code multiplexing via majority logic for GPS modernization. In: ION GNSS 11th international technical meeting of the satellite division. Nashville, TN, pp 265–273
2. Rebeyrol E, Macabiau C, Ries L et al (2006) Interplex modulation for navigation systems at the L1 band. In: ION NTM 2006. Monterey, CA, pp 100–111
3. Dafesh PA, Cahn CR (2009) Phase-Optimized Constant-Envelope Transmission (POCET) modulation method for GNSS signals. In: ION GNSS 2009. Savannah, GA, pp 2860–2866
4. Lestarquit L, Artaud G, Issler J-L (2008) AltBOC for dummies or everything you always wanted to know about AltBOC. In: ION GNSS 2008. Savannah, GA, pp 961–970
5. Yao Z, Zhang J, Lu M (2016) ACE-BOC: dual-frequency constant-envelope multiplexing for satellite navigation. IEEE Trans Aerosp Electron Syst 52(1):466–485
6. Dafesh PA, Cahn CR (2011) Application of POCET method to combine GNSS signals at different carrier frequencies. In: ION ITM 2011. San Diego, CA, pp 1201–1206
7. Yao Z, Guo F, Ma J, Lu M (2017) Orthogonality-based generalized multicarrier constant envelope multiplexing for DSSS signals. IEEE Trans Aerosp Electron Syst 53(4):1685–1698
8. Zhang X, Zhang X, Yao Z, Lu M (2012) Implementations of constant envelope multiplexing based on extended Interplex and Inter-Modulation construction method. In: ION GNSS 2012. Nashville, TN, pp 893–900
9. Ma J, Yao Z, Lu M (2017) Analytic efficiency optimal constant-envelope multiplexing technique for GNSS signals. In: ION GNSS 2017. Portland, Oregon, pp 1579–1588

Design and Field Test of a GPS Spoofer for UAV Trajectory Manipulation

Minghan Li, Yanhong Kou, Yong Xu and Yachuan Liu

Abstract With the frequent occurrence of unmanned aerial vehicle (UAV) accidents, GPS spoofing has become a hot technology in the field of low-altitude UAV management and control. Nowadays several cases of successful live UAV deception by generating GPS spoofing signals have been reported. The description of the spoofing strategy for manipulating UAV trajectories, however, is not detailed. In addition, most spoofing devices on the market rely on bulky commercial GNSS signal simulators. In order to spoof the UAV in actual flight environments, this paper designs and implements a miniature GPS spoofer, and proposes a spoofing strategy for the calculation of the misleading position of the UAV. The model of the spoofing signal transmitted by the spoofer is established, and the difference of signal state parameter calculation between a spoofer and a common simulator is comparatively analyzed. Finally, a field test is conducted, where error position and velocity outputs of a commercial receiver and a target receiver onboard an UAV are under control. In addition, we successfully make the UAV land on the spoofing position by using the intelligent return function of the UAV. The results verify the correctness of the spoofing strategy and the signal model, as well as the effectiveness and feasibility of the designed spoofer.

Keywords GPS spoofing · Spoofing strategy · Spoofer · UAV

1 Introduction

At present, UAV applications and flight ranges are expanding, which brings great potential security problems to other aircraft in the complex airspace environment as well as ground personnel and property [1]. Therefore, it is necessary to control and disperse the UAV. It will make the control more threatening and covert to control the UAV with the help of the GPS spoofing technology. Generative GPS spoofing

M. Li · Y. Kou (✉) · Y. Xu · Y. Liu
No. 37 Xueyuan Road, Haidian District, Beijing, People's Republic of China
e-mail: buaakyh@126.com

J. Sun et al. (eds.), *China Satellite Navigation Conference (CSNC) 2018 Proceedings*, Lecture Notes in Electrical Engineering 498,
https://doi.org/10.1007/978-981-13-0014-1_15

technology can simulate and transmit GPS spoofing signals at any given time and position autonomously, and guide the target receiver to lock the signal and output controlled error positions and velocities [2].

In the field of spoofing technology, several successful cases of live UAV deception by generating GPS spoofing signals have been reported. The most active study came from Professor Todd and his team at Texas University, who proposed the feasibility of GPS spoofing [3] and succeeded in spoofing an UAV in 2008 [4]. The team implemented GPS spoofing of a yacht, making it deviate from its scheduled route on the map [5]. Similar tests have been conducted by the German Aerospace Center (DLR) [6]. In 2011, Tippenhauer et al. analyzed in detail the conditions for successful spoofing [7]. Daniel [8] and Farin [9] analyze the effects of spoofing on target receivers taking account of different stages of receiver working. In June 2015, a researcher at the University of Bath verified that a common GPS signal simulator can work effectively as a spoofer against a standard civil GPS receiver by using a fully functional software-defined GPS signal simulator posted to github [10]. Psiaki [10] made a relative assessment of the difficulties of various types of attacks and defenses. Early researches on spoofing technology in China mainly focused on reradiating spoofing and can be found in [11–14]. Researches on the more concealed and harmful generative spoofing have been increasing in recent years [15–18]. GPS spoofing technology has already been applied to anti-UAV area. A set of spoofing civilian anti-UAV system—ADS2000 was released in May 2016 [19]. A test of inducing the descent of an UAV by spoofing signals was conducted in [20]. Li [21] simulated the effects of spoofing based on the control characteristics of UAV GPS/INS integrated navigation system [21]. However, there is still a lack of field testing and a description of the spoofing strategy aiming at UAV trajectory manipulation. In addition, most spoofers on the market rely on bulky commercial GNSS signal simulators.

The purpose of this paper is to explore the spoofing strategy capable of not only misleading the UAV position and velocity outputs, but also manipulating its trajectory, assuming that the UAV's autonomic navigation is completely controlled by the GPS sensor; The detailed model of the spoofing signal is given, and the difference of signal state parameter calculation between a spoofer and a common simulator is analyzed. A miniaturized generative GPS spoofer based on DSP + FPGA + RF architecture is designed and implemented. Finally, the field experiment is conducted to successfully make the target receiver on the UAV output controlled error position and velocity, and then to make it land on the spoofing position by using its return function. The results demonstrate the feasibility of the spoofing strategy and the signal calculation model as well as the effectiveness of the system design.

2 Spoofing Signal Simulation Method

2.1 Spoofing Signal Model

The RF signal transmitted by the spoofer at GPS system time t can be expressed as [22]:

$$x_{RF}(t) = \sum_{j=1}^{N(t)} \sqrt{2P_s^j(t)} C^j\left[t - \tau^j(t)\right] D^j\left[t - \tau^j(t)\right] \cos\left[\phi^j(t)\right] + n(t)$$

where t is the transmit time (in GPS system time) of the simulated spoofing signal, $N(t)$ the number of all visible satellites at time t, j the sequence number of the visible satellite, $P_s^j(t)$ the signal power at time t, $C^j(\cdot)$ the C/A code of the jth satellite, $D^j(\cdot)$ the navigation message of the jth satellite, $\tau^j(t)$ the code time delay at time t, $\phi^j(t)$ the L1 carrier phase at time t, and $n(t)$ the noise term. Note that the time t in the model of a common signal simulator is the signal receive time, as the simulator simulates the signals received by the receiver antenna at GPS system time t. In contrast, the time t in the model of the spoofer is the signal transmit time. The calculation model of the main signal state parameters of the spoofing signal will be discussed in the following.

2.2 Signal State Parameter Calculation Model

2.2.1 Signal Power

The power of the jth satellite signal in the transmitted spoofing signal at time t is calculated as:

$$P_s^j(t) = P_r^j[t + \tau_{su}(t)] - G_T(t) + 20\log\frac{4\pi d_{su}(t)}{\lambda}$$

where λ is the GPS L1 carrier wavelength, $G_T(t)$ the gain of the transmit antenna in the direction of the target receiver at time t, $d_{su}(t)$ the signal propagation distance from the phase center of the spoofer's transmission antenna to that of the target receiver's antenna at time t, and $P_r^j[t + \tau_{su}(t)]$ the signal power of the jth true satellite at time $t_r(t) = t + \tau_{su}(t)$.

In the determination of the signal power of a common simulator, if the transmit power of the true satellite is known, the method of simulating various space fading effects can be used; otherwise, the power can be determined by using the $C/N0$ and corresponding elevation data recorded by a receiver to find out how the signal power changes with the elevation through curve fitting, taking account of the

receiver antenna gain. However, in the spoofing environment, since the distance between the spoofer and the target receiver varies in real time during the UAV's flight, the propagation delay must be taken into account.

The propagation delay $\tau_{su}(t)=\frac{d_{su}(t)}{c}$ can be calculated by the transmit antenna phase center position $\mathbf{p}_s(t)$ at time t and the predicted target receiver antenna phase center position $\mathbf{p}_u[t+\tau_{su}(t)]$ at $t_r(t)=t+\tau_{su}(t):\tau_{su}(t)=\frac{1}{c}|\mathbf{p}_s(t)-\mathbf{p}_u[t+\tau_{su}(t)]|$; and $\mathbf{p}_u[t+\tau_{su}(t)]$ depends on the calculation of $\tau_{su}(t)$. So the dichotomy can be used to solve $\tau_{su}(t)$, until the difference between the two iterations is below the pseudo range error limit.

2.2.2 Code Phase

The code delay of the jth satellite signal in the transmitted spoofing signal at time t is calculated by the following formula:

$$\tau^j(t)=\frac{1}{c}\left|\mathbf{p}^j_{sv}\left[t^j_T(t)\right]-\mathbf{p}_m[t+\tau_{su}(t)]\right|+\tau^j_{iono}(t)+\tau^j_{trop}(t)+\tau^j_{rel}(t)$$
$$\tau^j(t)=t+\tau_{su}(t)-t^j_T(t)$$

where $t^j_T(t)$ is the transmit time of the jth satellite signal corresponding to time t, $\mathbf{p}_m[t+\tau_{su}(t)]$ the misleading position at $t+\tau_{su}(t)$, $\tau^j_{iono}(t)$ and $\tau^j_{trop}(t)$ the ionospheric and tropospheric delay at the misleading position $\mathbf{p}_m[t+\tau_{su}(t)]$ at $t+\tau_{su}(t)$, and $\tau^j_{rel}(t)$ the delay caused by the relativistic effect.

Different from the common simulator, the delay $\tau_{su}(t)$ also needs to be considered in the signal state parameter calculation of the generative GPS spoofer. As mentioned above, $\tau_{su}(t)$ can be calculated from the iteration of $\mathbf{p}_s(t)$ and $\mathbf{p}_u[t+\tau_{su}(t)]$ using dichotomy to achieve higher accuracy. It is worth noting that for the code phase simulation of an asynchronous generative GPS spoofer, even though it is impossible to obtain the location of the receiver antenna phase center in a real application, a fixed $\tau_{su}(t)$ (e.g. $\tau_{su}(t)=\frac{1500\ \mathrm{m}}{c}\approx 5\ \mu\mathrm{s}$) can still be employed. Because $\tau_{su}(t)$ is same for each simulated satellite and will be attributed to the receiver clock error in navigation solution, it will not affect the final positioning results of the target receiver.

3 Spoofing Strategy

For the convenience of analysis, it is generally assumed that the UAV's navigation flight control system will guide the UAV to fly from the current location to the next planned waypoint at a fixed direction and speed. As shown in Fig. 1, it is assumed that the current true position A of the target receiver onboard the UAV is known

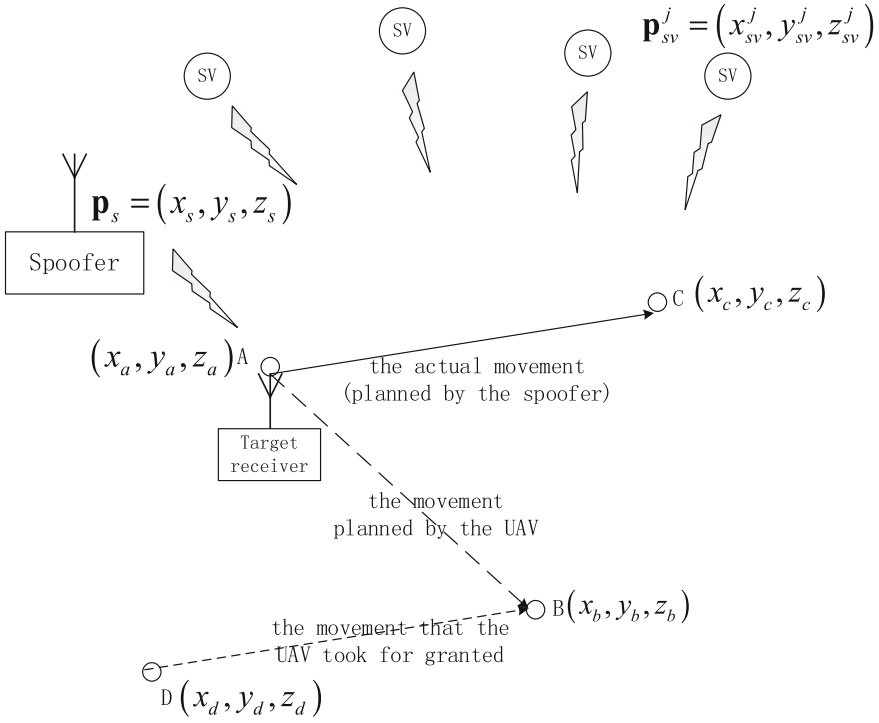

Fig. 1 Illustration of spoofing strategy

and the current true target position is point B, then the dotted line between A and B is the planned movement; if the current spoofing target point C is known, the misleading position D as the basis of spoofer signal calculation and outputted by the target receiver as expected can be found out. Under successful spoofing the UAV's navigation flight control system will adjust its fly in the direction from D to B, but in fact the UAV will fly from A to C. In other words, the solid line from A to C is the actual movement, whereas the dotted line from D to B is the movement the UAV took for granted.

From the spoofing principle we know that in Fig. 1, AC and BD must be parallel and equal: $\overrightarrow{AC} = \overrightarrow{DB}$; the coordinates of point A, B, C, D are (x_a, y_a, z_a), (x_b, y_b, z_b), (x_c, y_c, z_c), (x_d, y_d, z_d), respectively; so the misleading point D is at $(x_d, y_d, z_d) = (x_b - x_c + x_a, y_b - y_c + y_a, z_b - z_c + z_a)$.

If an UAV encounters obstacles, strong winds or other non-ideal conditions in an actual flight, it will produce a large offset inconsistent with the original path planned by the spoofer. As shown in Fig. 2, assuming that the straight line AC is the initial planned trajectory, a threshold can be set to distinguish the offset of the true UAV position to this plan. If the UAV arrives at A′ at a time t away from AC and the distance between A′ and AC exceeds this threshold, the misleading position needs

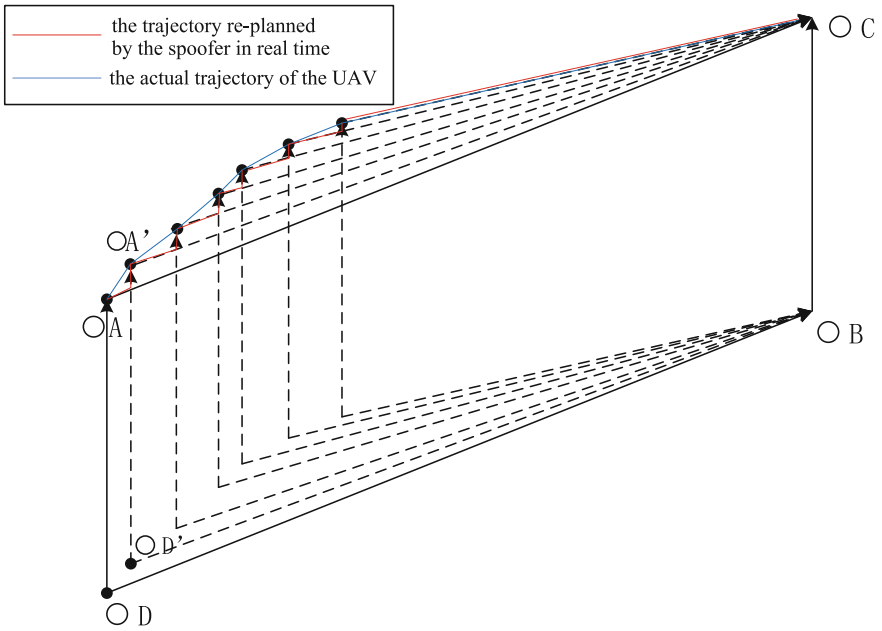

Fig. 2 Illustration of real-time manipulation of UAV trajectory

to be recalculated and the path needs to re-planned. In this case, the misleading position D′ at the time t can be calculated according to the current true position A′ of the UAV and the above model, then the planned trajectory of the UAV can be changed from AC to A′C after time t. If an offset occurs in subsequent flight, and thus the re-planned trajectory can be utilized in the similar manner to drive the UAV reaching the spoofing target position C eventually. By setting the threshold small enough the actual trajectory and the planned trajectory will be very close to each other.

The simulation of the above analysis is shown in Fig. 3, assuming that the original true position of the UAV is (200 m, 300 m) in the horizontal plane of the ENU coordinate system, and the UAV encounters a south wind during the flight. Under the northward offsets of the actual UAV movement caused by the south wind, the UAV finally arrives at the spoofing target position (600 m, 100 m) by adjusting the planned trajectory of the target receiver and thus the corresponding misleading position in real time in the spoofer.

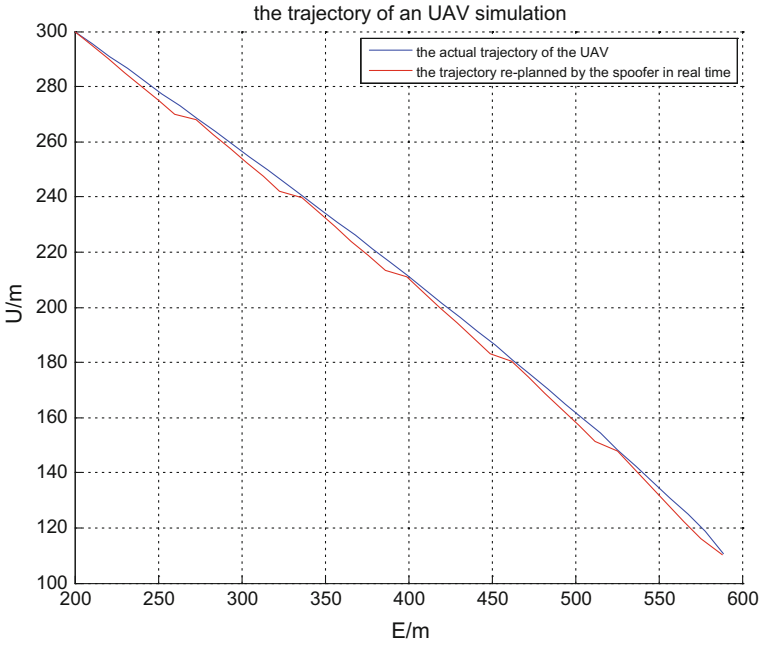

Fig. 3 Simulation results of UAV trajectory manipulation in real time

4 Design and Experiment

4.1 Overall Design

A miniaturized GPS spoofer is designed and implemented with a combination of hardware, firmare and software. The hardware part mainly consists of a spoofing signal processing module, an up-conversion and RF conditioning module, a timing receiver, a power adapter, a receive antenna, and a transmit antenna. The first two modules are developed by ourselves, and the latter three utilizes purchased shelf products. As shown in Fig. 4, the software and firmware part mainly includes the main control software, the main control DSP firmware, the operation DSP firmware, and the FPGA firmware.

The spoofing signal processing module is the core module responsible for receiving commands and simulation parameters from the master device software and generating the intermediate-frequency spoofing signal, which can be accurately controlled in real time. A "DSP + FPGA" architecture is employed. where FPGA is more suitable for parallel multi-channel signal processing, and DSP features convenient programming and powerful floating-point operations, which can be used for complex computations and process control. The up-conversion and RF conditioning module mainly up-convert and power-control the IF signal to form the GPS L1 RF signal with the specified power.

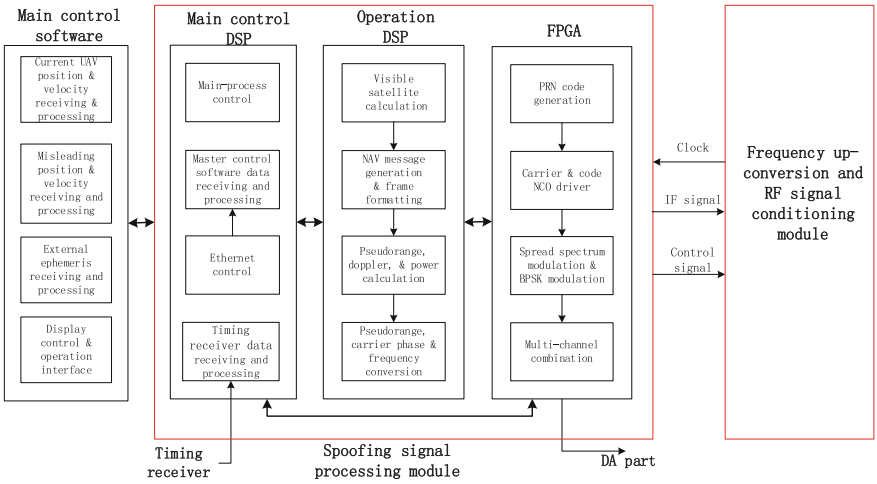

Fig. 4 Block diagram of software and firmware of the miniaturized GPS spoofer

4.2 Experiment of Spoofing a Static Commercial Receiver

The experiment was carried out in our laboratory in Beihang University with a commercial receiver mainly applied in timing and survey [23]. Both the receiver antenna and the spoofer transmit antenna are placed outside the window and on the top of the six-story building. The receiver positioning results show the local coordinates (40.192824°N, 116.272792°E, 70 m) by using only the true satellite signals at first. Then the spoofer is turned on and the misleading coordinates of a static scenario are set to be (40°N, 116°E, 10 m). This misleading position and the receiver positioning results are shown in WGS-84 geodetic coordinates in Fig. 5, and their changes with time are shown in ECEF Cartesian coordinates in Fig. 6. It can be seen that the receiver acquires and tracks the spoofing signal as expected, and the positioning results coincide with the misleading position set by the spoofer.

Next, with the experimental environment unchanged, the spoofer switches to a dynamic scenario with an initial position at (40°N, 116°E, 0 m), a horizontal velocity of $6\sqrt{2}$ m/s, and a vertical velocity of 6 m/s in ENU coordinates. The trajectory set by the spoofer and the receiver positioning results are shown in WGS-84 geodetic coordinates in Fig. 7, and velocity results are shown in ENU coordinates in Fig. 8, where the two trajectories and velocity results fit well into each other.

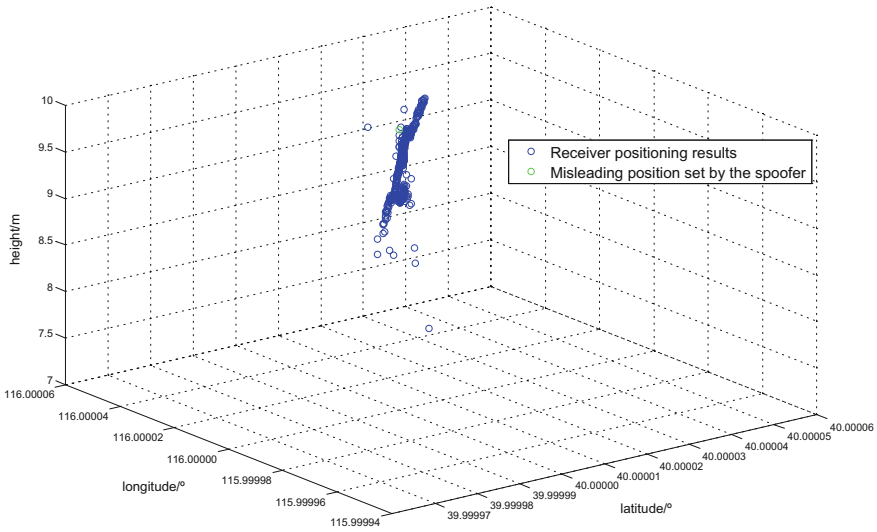

Fig. 5 Comparison of the misleading position set by spoofer and the receiver positioning results in a static scenario

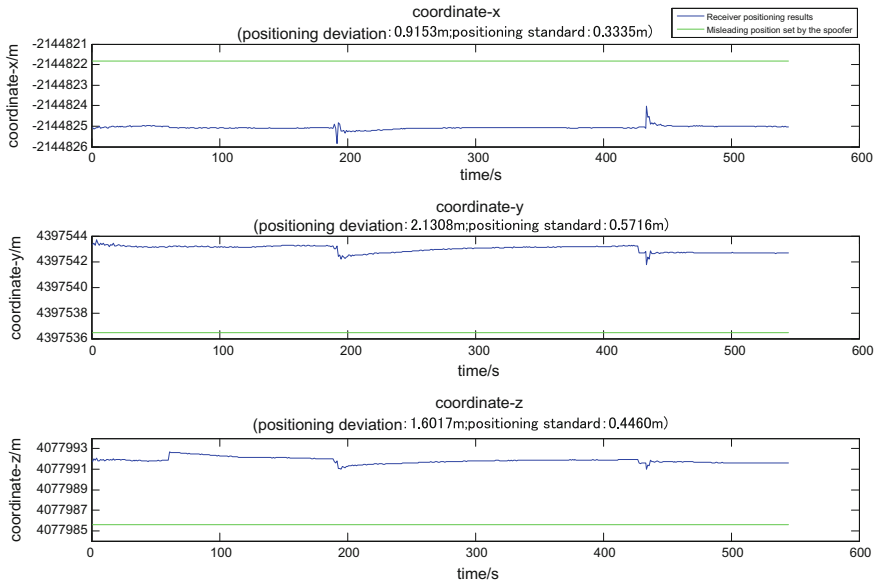

Fig. 6 Receiver positioning results in static scenario

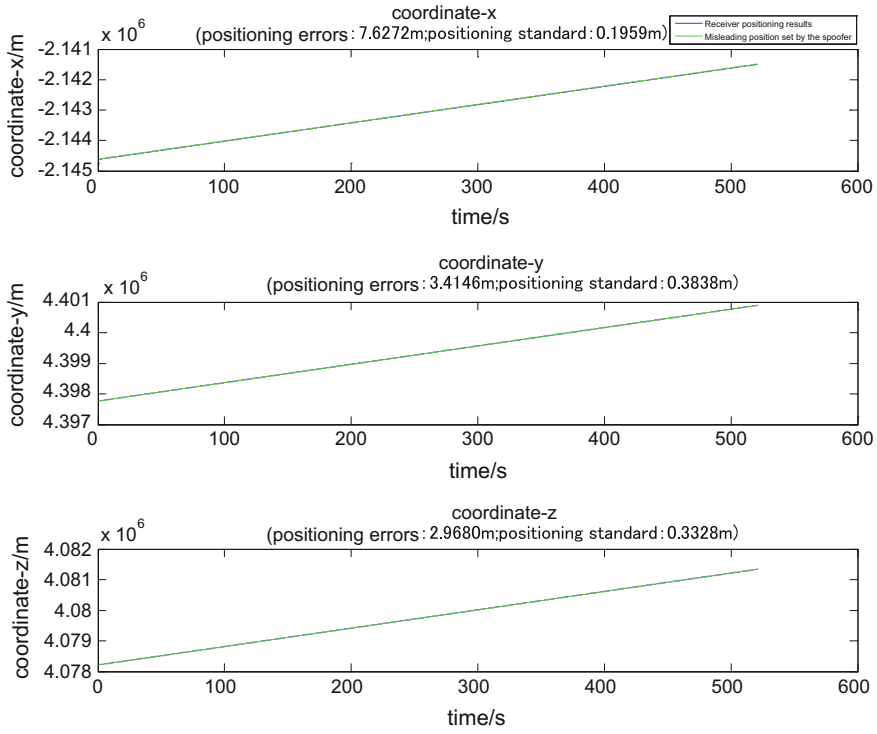

Fig. 7 Trajectory set by spoofer and receiver positioning results in a dynamic scenario

4.3 Field Test of Spoofing an UAV

A field test of spoofing a consumer-level UAV [24] was carried out in November 2017 at the non-no-fly zone in Changping District of Beijing. Figure 8 shows the picture of the test site and equipment. The UAV output the local coordinates of (40.192824°N, 116.272792°E) when receiving only the true GPS satellite signal.

Then the spoofer was turned on and the misleading position of the static scenario was set to be at (34°N, 119°E) located in Suqian city, Jiangsu Province. The UAV real-time positioning results shown Fig. 9 coincides with the misleading position set by the spoofer (Fig. 10).

Since the height information of this UAV is obtained by data fusion from its sensors including not only GPS receiver but also barometer, ultrasound, and vision navigation system, the spoofing in the height direction has not been successful. In spite of this, we can still use the UAV's return function to land the UAV to the spoofing target position. This field test was conducted at a coastal test site in Lianyungang city, Jiangsu Province. The misleading position of the spoofer was set to be the spoofing target position of (34.764988°N, 119.329960°E, 20 m), and the UAV was placed about 100 m away. When the UAV was powered on and hovered

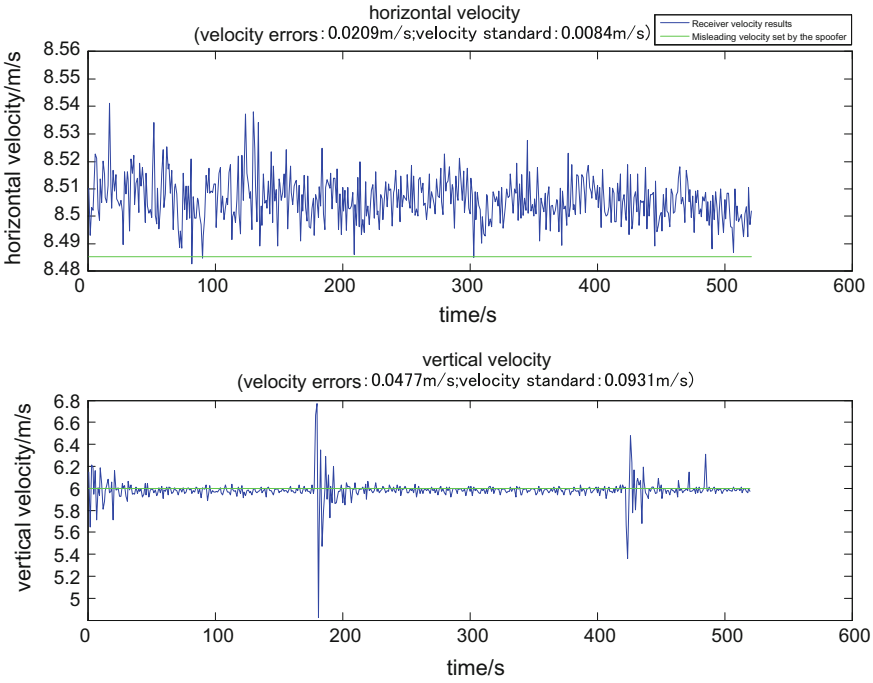

Fig. 8 Velocity set by spoofer and receiver velocity results in a dynamic scenario

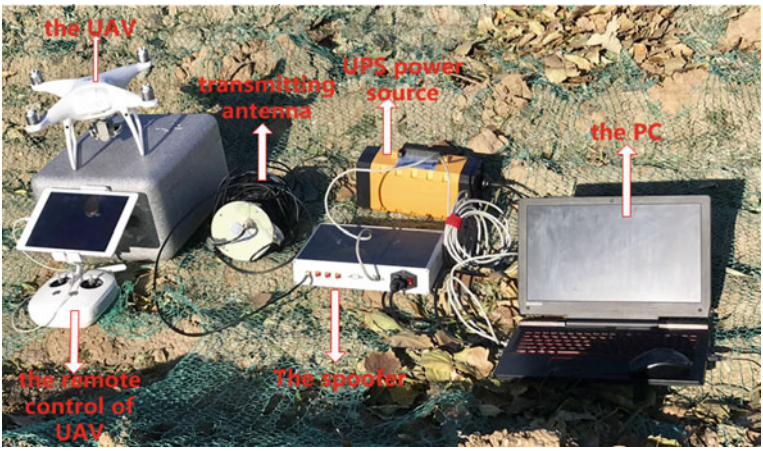

Fig. 9 Picture of field test site and equipment of spoofing an UAV

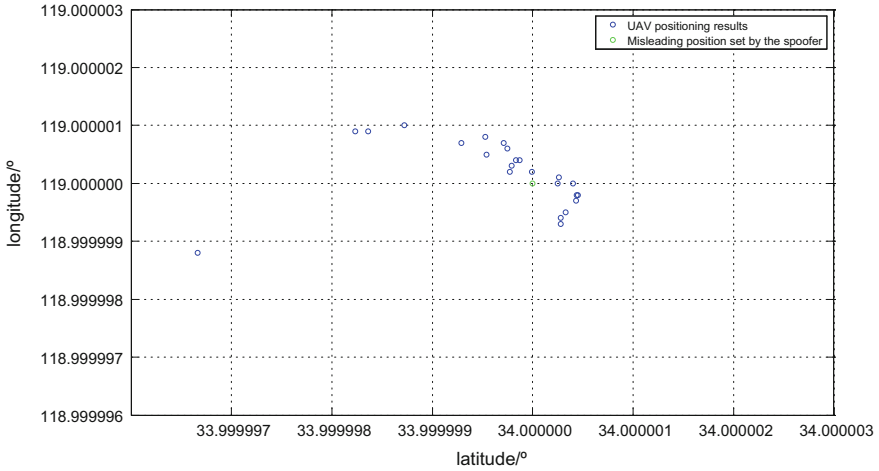

Fig. 10 Comparison of the misleading position set by spoofer and UAV positioning results in a static scenario

over the air through the remote control, the UAV output position was the misleading position set by the spoofer. We set this position as the UAV return point, turned off the spoofer, and then choose the UAV function of returning to home. The UAV was seen to fly towards the spoofing position and finally land at that position accurately.

5 Conclusions

This paper has designed and implemented a miniaturized GPS spoofer. The model of the RF signal transmitted by the spoofer has been established, and the difference of signal state parameters between a spoofer and a common simulator has been comparatively analyzed. A spoofing strategy for real time manipulation of UAV trajectory is proposed. Then the feasibility tests were conducted, where controlled error positions and velocities were outputted by the commercial receiver and the target receiver on the UAV. In addition, a spoofing test using the UAV's return function landed the UAV at the spoofing position successfully. In the future, the effectiveness of the spoofing strategy on UAVs needs to be further studied in combination with the real-time UAV position and velocity measurements provided by the UAV target monitoring system.

References

1. Loh R, Bian Y, Roe T (2009) UAVs in civil airspace: safe requirements. IEEE Aerospace and Electronic Systems. Piscataway: Institute of Electrical and Electronics Engineers Inc
2. Pang J, Ni SJ, Nie JW, Ou G (2016) An overview to GNSS spoofing technologies. Fire Control Command Control 41(7):1–4
3. Humphreys TE, Ledvina BM, Psiaki ML et al (2008) Assessing the spoofing threat: development of a portable GPS civilian spoofer. Proceedings of the ION GNSS international technical meeting of the satellite division 55:56
4. Kerns AJ, Shepard DP, Bhatti JA, Humphreys TE (2014) Unmanned aircraft capture and control via GPS spoofing. J Field Robot 31(4):617–636
5. Bhatti J, Humphreys T (2015) Hostile control of ships via false GPS signals: demonstration and detection, submitted to Navigation, in review
6. Konovaltsev A, Cuntz M, Haettich C, Meurer M (2013) Autonomous spoofing detection and mitigation in a GNSS receiver with an adaptive antenna array. In: Proc. ION GNSS + , Nashville, TN, pp 2937–2948
7. Tippenhauer NO, Popper C, Rasmussen KB, Capkun S (2011) On the requirements for Successful GPS spoofing attacks. In: Computer and Communications Security, New York
8. Daniel PS, Todd EH (2011) Characterization of receiver response to spoofing attacks. ION GNSS, Portland, pp 2608–2618
9. Farin é, Aleksandat J, Botteron C et al (2014) Multi-test detection and protection algorithm against spoofing attacks on GNSS receivers. ION PLANS, monterey, pp 1258–1271
10. Psiaki ML, Humphreys TE (2016) GNSS spoofing and detection. Proc IEEE 104(6):1258–1270
11. Yang J, Zeng F, Hu S (2005) A jamming system through section mapping for GPS navigation. Acta Electronica Sinica 33(06):1036–1038
12. Zhang S, Yang J, Pan G, Wang L (2011) Station embattling optimization and moving model of the GPS area-mapping deceiving unites battlefield navigation integrative system. J Univ Sci Technol China 41(08):746–752
13. Zhanjie Y, Wu D, Liu H (2013) Analysis of time-delay in GPS repeater deception jamming. J Air Force Eng Univ (Nat Sci Ed) 14(04):67–70
14. Huang L, Gong H, Zhu X, Wang F (2013) Research of re-radiating spoofing technique to GNSS timing receiver. J Nat Univ Defense Technol 34(04):93–96
15. Huang L, Lv Z, Wang F (2012) Spoofing pattern research on GNSS receivers. J Astronaut 33 (07):884–890
16. Bi C, Guo C (2016) Study on GPS spoofing pattern process. Bull Sci Technol 32(10):164–169
17. Liang HE, Li W, Guo C (2016) Study on GPS generated spoofing attacks. Appl Res Comput 33(08):2405–2408
18. Ma K, Sun X, Nie Y (2014) Research on key technologies of GPS generated spoofing. Aerosp Electron Warfare, 30(06):24–26 + 34
19. http://www.gnssopenlab.org/show_content.php?id=1769. Accessed 19 May 2016
20. Lin S, Wei L (2017) UAV management and control technology based on satellite navigation spoofing jamming. Command Inf Syst Technol 8(01):22–263
21. Li C, Wang X (2017) Jamming of unmanned aerial vehicle with GPS/INS integrated navigation system based on trajectory cheating. J Nanjing Univ Aeronaut Astronaut 3 (49):420–427
22. Zhao Y, Kou Y, Huang Z, Zhang Q (2009) Architecture of software-based GNSS signal simulator and implementation of its IF signals generation. J Beijing Univ Aeronaut Astronaut 35(07):789–793
23. http://www.wintekgps.com/pro_details.aspx?nid=5&pid=12&id=25. Accessed 6 Jan 2018
24. https://www.dji.com/cn/phantom-4-pro?site=brandsite&from=nav. Accessed 6 Jan 2018

The Difference Analysis on the Effect of Third-Order Intermodulation Between Single Antenna and Antenna Arrays Anti-jamming

Zukun Lu, Zhengrong Li, Shaojie Ni, Baiyu Li and Gang Ou

Abstract The time domain and frequency domain anti-jamming technology based on single antenna, and the space domain anti-jamming technology based on antenna arrays, which can realize the interference suppression under the different interference bandwidth. The interference intermodulation would be generated in single antenna and antenna arrays, and the most obvious is the third-order intermodulation. The essence of interference suppression is to zero the interference spectrum in single antenna anti-jamming. When the third-order intermodulation is submerged under the noise, the intermodulation has little effect on frequency domain anti-jamming. However, in the application of antenna arrays anti-jamming, the nature of anti-jamming is to achieve interference cancellation by amplitude and phase weighting, and the consistency between different elements are emphasized. If the non-linear characteristics are the same in different elements, the third-order intermodulation can still be achieve cancellation through the amplitude and phase weighting. Therefore, in antenna array, the anti-jamming performance is not affected by third-order intermodulation on single channel but the non-linear consistency. In this paper, the difference effects on single antenna and antenna arrays of the third order intermodulation are analyzed. Aim to the relationship between interference and intermodulation, a part of the third-order intermodulation could be suppressed, and the suppression method is proposed. The simulation results show that the effectiveness of the analysis and the proposed method.

Keywords Time and frequency domain · Antenna array · Anti-jamming
Third-order intermodulation · Satellite navigation system

Z. Lu · Z. Li · S. Ni · B. Li · G. Ou (✉)
College of Electronic Science, National University of Defense Technology,
417000 Changsha, China
e-mail: ougangcs@139.com

J. Sun et al. (eds.), *China Satellite Navigation Conference (CSNC) 2018 Proceedings*, Lecture Notes in Electrical Engineering 498,
https://doi.org/10.1007/978-981-13-0014-1_16

1 Introduction

The global navigation satellite system (GNSS) represented by GPS has been rapidly developed since the 1970s and has brought great convenience to people's travel. It is also widely used in the military field [1–3]. Satellites are distanced from the ground about 27,000 km, and the signal is very weak when the satellite signal arrives at the ground. The navigation receiver received the signal with signal to noise ratio (SNR) about −20 dB, which makes the navigation receiver vulnerable to a variety of intentional or unintentional interference. The anti-jamming performance of the navigation receivers must be considered in the application of military or civilian core areas [4–6].

The two signals with the same power and similar frequency pass through a device such as an antenna, a low-noise amplifier, a filter, and other analog devices. Due to uncontrollable reasons such as virtual welding, surface oxidation and unreliable connections in analog devices, intermodulation parts are generated which called the intermodulation distortion [7]. In general, the third-order intermodulation distortion (IMD3) measures crosstalk. The larger the third-order intermodulation value, the better the linearity of the system or module.

This paper analyzes the third-order intermodulation model. The analysis results show that the third-order intermodulation is generated by the nonlinear characteristics of the channel. When frequency domain anti-jamming is adopted, the third-order intermodulation can lead to excessive suppression of spectral lines in the frequency domain, resulting in excessive SNR loss. However, when the anti-jamming of the antenna array is adopted, the coherence between the intermodulation and the interference is considered to achieve the interference suppression. Adopting the space-time adaptive processing can achieve to suppress the partial of the third-order intermodulation. The influence of the third-order intermodulation on the anti-jamming of single antenna and antenna array is different.

2 Third-Order Intermodulation Model

The ideal channel is linear. In this paper, the nonlinear model is used in [8] to simulate the nonlinearity by adding a sine function to the linear model. The nonlinearity of the channel is controlled by adjusting the amplitude, phase and frequency of the sine function.

Third-order intermodulation value measurement method is that using the signal source to transmit a dual-tone signal to the input of the channel, and observe the spectrum of the channel output through the spectrum analyzer. In the case of using the above model, the signal source spectrum analyzer spectrum is shown in Fig. 1.

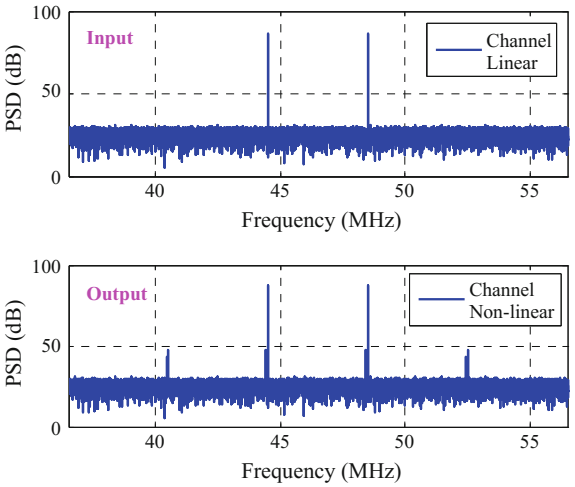

Fig. 1 Test result for third-order intermodulation

The ratio of the power between the original signal and the intermodulation is the third-order intermodulation rejection ratio for the channel. According to the Fig. 1, the third-order intermodulation rejection ratio of the above model is 40 dB.

Intermodulation can be considered as "interference from the input interference", the output of the RF module contains not only interference itself, but also includes the intermodulation section. For broadband interference, the intermodulation can be divided into two parts: part of the intermodulation spectrum falls within the interference band, raising the interference power, while the other part of the intermodulation spectrum falls outside the interference band, which is equivalent to raising the noise floor. The relationship between the input and output is shown in Fig. 2.

In Fig. 2, the nonlinear factor can be equivalent to a system, so the input and output have certain relevance.

According to Fig. 2, assuming the input is x_n, the output is y_n, then the relationship between the two are as follows:

$$\begin{aligned} y_n &= x_n + x_{nIMD3} \\ &= x_n + f_n(x_n) \end{aligned} \tag{1}$$

where, $f_n()$ represents the channel transfer function.

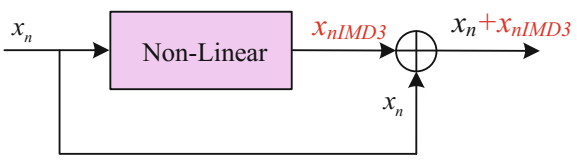

Fig. 2 Equivalent for intermodulation decomposition

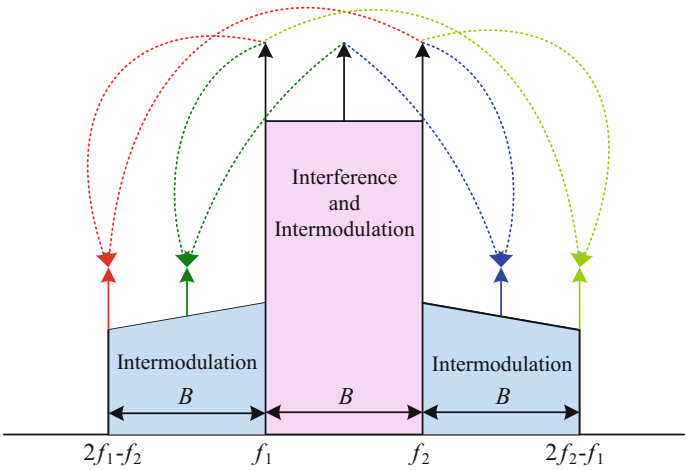

Fig. 3 Influence of interference bandwidth on third-order intermodulation bandwidth

For wideband interference, the third order intermodulation is produced between every two frequencies in the bandwidth. The impact of interference bandwidth on the third-order intermodulation bandwidth is shown in Fig. 3.

Using the same channel model of Fig. 1, the spectrum of 2, 20, 30 MHz interference bandwidth in the channel ideal and channel non-linearity is shown in Fig. 4. It can be clearly seen that the noise floor in nonlinear case is higher than in linear case, no matter the interference bandwidth, that is, the channel non-linearity raises the noise floor.

According to Fig. 4, channel non-linearity caused by interference, intermodulation, noise floor power (digital power) changes shown in Table 1.

3 Influence of Third Order Intermodulation on Frequency Domain Anti-jamming

The basic idea of anti-jamming in the frequency domain is to set the interference spectrum to zero in the frequency domain. The ideal frequency-domain stop-band filter can be expressed as [9, 10]:

$$H(f) = \begin{cases} 0 & |f - f_i| \le B/2 \\ 1 & else \end{cases} \tag{2}$$

Among them, the center frequency of interference is f_i, the interference bandwidth is B.

In the frequency domain anti-jamming, usually set a fixed threshold or adaptive real-time estimation of noise power to determine the interference spectrum.

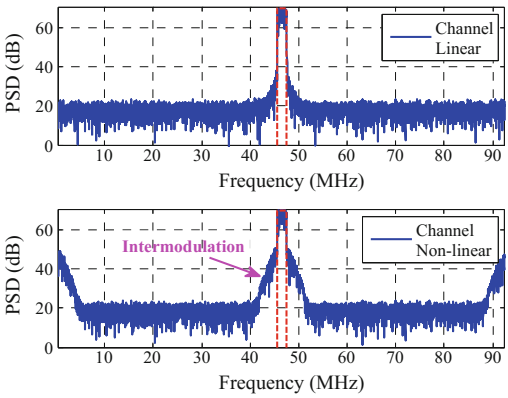

(a) Interference Bandwidth 2MHz

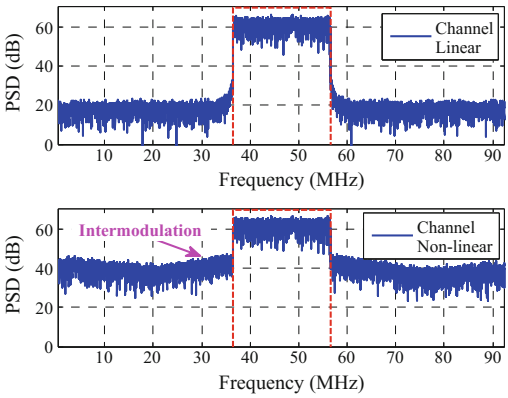

(b) Interference Bandwidth 20MHz

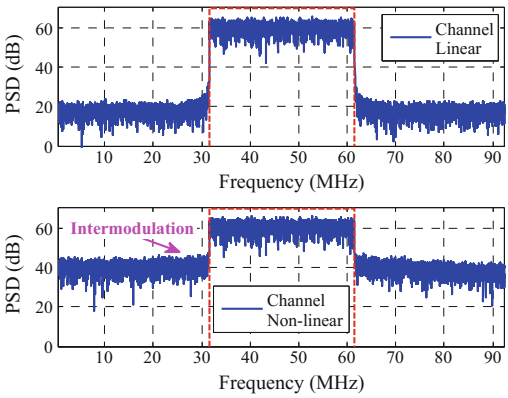

(c) Interference Bandwidth 30MHz

Fig. 4 Influence of channel non-linear on interference spectrum. **a** Interference bandwidth 2 MHz, **b** Interference bandwidth 20 MHz, **c** Interference bandwidth 30 MHz

Table 1 The power cased by channel nonlinear (Unit: dB)

	Interference bandwidth 2 MHz		Interference bandwidth 20 MHz		Interference bandwidth 30 MHz	
	Linear	Non-linear	Linear	Non-linear	Linear	Non-linear
Interference Power	72.8	72.8	71.7	71.7	72.7	72.7
Intermodulation Power	−88.8	68.3	−90.4	67.3	−90.6	68.2
Noise Power	1.0	1.0	1.0	1.0	1.0	1.0
INR	71.8	71.8	70.7	70.7	71.7	71.7
IINR	72.8	**4.5**	71.7	**4.4**	72.6	**4.4**

where, IINR stands for the interference to intermodulation and noise ratio
Bold indicates that there are differences with other data

As can be seen from the Fig. 4b, the presence of third-order intermodulation results in the broadening the interference bandwidth. Therefore, during the anti-jamming in the frequency domain, the zero width of the spectrum will increase, which will directly lead to set the signal line to zero, resulting in decreased the SNR loss.

Figure 4a, b shows the data for anti-jamming in the frequency domain. The adaptive threshold method is used, and the spectrum after anti-jamming is shown in Fig. 5a, b. It can be seen from Fig. 5 that in the case of channel non-linearity, the width of the zero line is obviously larger than the linear width of the channel.

The navigation signal is added to the data shown in Fig. 4a, b, and the navigation signal set to the Beidou B3 PRN1. The carrier to noise ratio (CNR) is 54 dBHz. The theoretical loss of the carrier to noise ratio caused by anti-interference in the frequency domain is [11, 12]:

$$CNR_{LOSS} = \frac{\left(\int_{-\beta_r/2}^{\beta_r/2} H(f)G_s(f)\,df\right)^2}{\int_{-\beta_r/2}^{\beta_r/2} |H(f)|^2 G_s(f)\,df} \tag{3}$$

The theoretical values and the simulation values of CNR, under the conditions of channel input nonlinearity and channel nonlinearity, which are shown in Fig. 6 under different interference to noise ratio (INR).

As can be seen from Fig. 6, when the INR is small, there is no significant difference between the channel linearity and the channel non-linearity, because the third-order intermodulation is under the noise. When the INR is large, especially at 70 dB, there is a significant difference in the CNR under the linear and nonlinear channel conditions. When the INR is 80 dB, the difference is about 8 dB, which is consistent with the theoretical analysis.

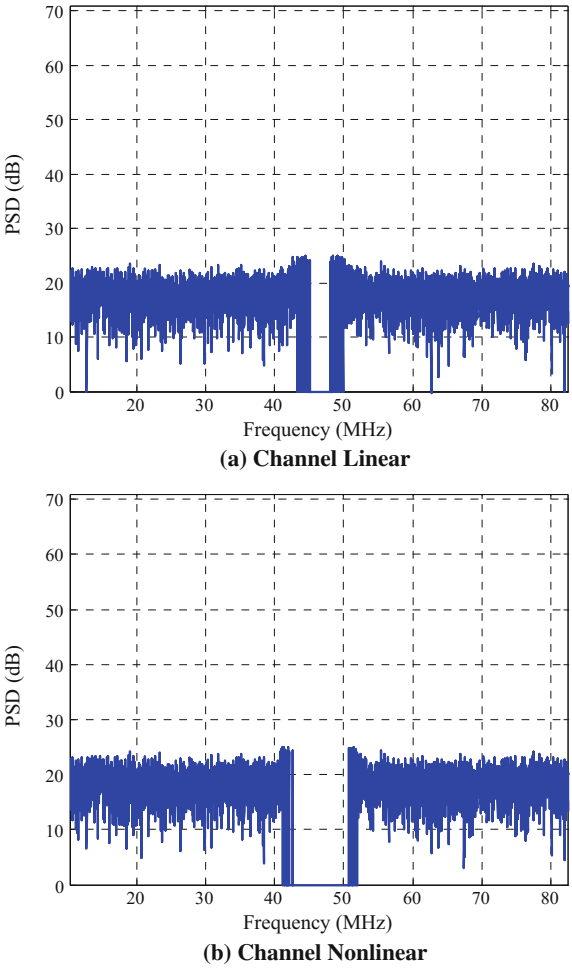

Fig. 5 Spectrum after frequency domain anti-jamming

4 Influence of Third Order Intermodulation on Anti-jamming of Antenna Arrays

The basic principle of the anti-jamming of the antenna array is to cancel the interference according to the correlation between the data of different channels. In Table 1 under the experimental conditions, the interference, intermodulation, noise, the correlation between the two are shown in Table 2.

The conclusions of Table 2 are consistent with the equivalent decomposition of Fig. 2, that is, interference is strongly correlated with intermodulation. As a result, crossover causes a rise in the noise floor, and the crosstalk cannot be equated to noise because the crosstalk is related to interference, and noise and interference are not relevant.

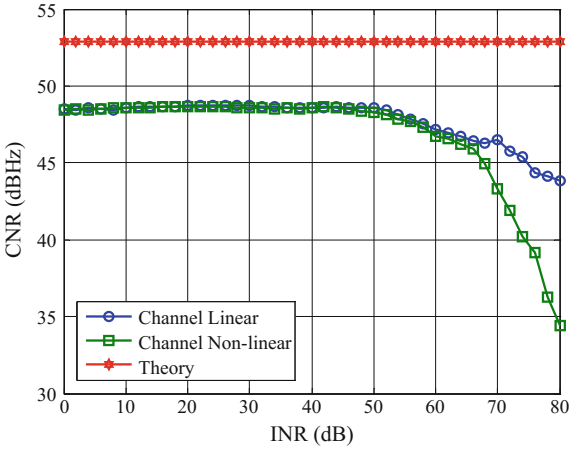

Fig. 6 CNR after frequency domain anti-jamming

Table 2 Related value between the various conditions

	Interference bandwidth 2 MHz		Interference bandwidth 20 MHz		Interference bandwidth 30 MHz	
	Linear	Non-linear	Linear	Non-linear	Linear	Non-linear
Interference-intermodulation	0.00	**0.99**	0.00	**0.99**	0.00	**0.99**
Interference-noise	0.00	0.00	0.00	0.00	0.00	0.00
Intermodulation-noise	0.00	0.00	0.00	0.00	0.01	0.01

Bold indicates that there are differences with other data

It is not the non-linear characteristic of the channel that affects the anti-interference of the antenna array, but the inconsistency of the non-linear characteristic of the channel. Assuming that the nonlinear characteristics of each array element channel are exactly the same, the intermodulation and interference of each channel have the same spatial domain characteristics, and the interference can be effectively suppressed. However, in reality, the nonlinear characteristics of each array element channel cannot be exactly the same. Therefore, an FIR filter is required after each element to equalize the non-linear characteristics of each element channel, that is, the space-time adaptive processor is used to equalize the channel non-linearity inconsistencies and enhance the consistency of the nonlinear features. The effect of the space-time adaptive processor in the antenna array is shown in Fig. 7 [13, 14].

According to (1), the input, output and intermodulation in the case of multi-channel, which relationship can be expressed as:

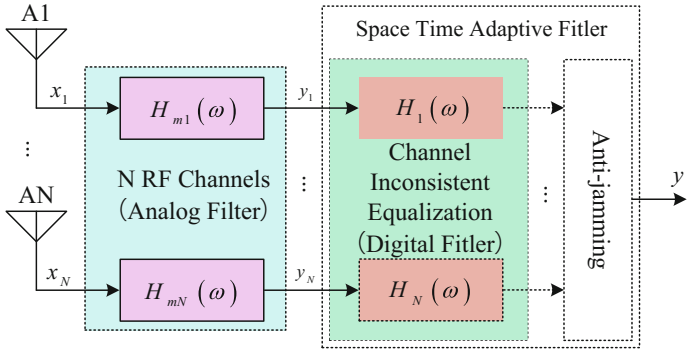

Fig. 7 Channel inconsistency equilibrium by STAP

$$\begin{aligned} y_1 &= x_1 + f_1(x_1) \\ &\vdots \\ y_N &= x_N + f_N(x_N) \end{aligned} \tag{4}$$

where, $f_1()\ldots f_N()$ are the transfer function from channel 1 to N. In the case of ideal channels, there is no crosstalk, and the reason that the interference can be effectively suppressed is that there is a strong correlation between $x_1 \ldots x_N$. The weighting of the array can achieve the purpose of anti-interference. The input of $f_n(x_n)$ is x_n, $(1 \leq n \leq N)$, therefore, $f_n(x_n)$ and x_n are related, so there is a possibility of being suppressed the $f_n(x_n)$.

The antenna array with four elements is used. The sampling rate is 62 MHz, the IF frequency is 46.52 MHz, the interference direction is (60°, 30°), the interference type is Gaussian white noise, the interference bandwidth is 3, 20, 30 MHz, Than 0–80 dB, step 5 dB, with a pure space-based anti-jamming way to weight, using power inversion [15]. A group of channel nonlinear models are randomly generated, but the third order intermodulation rejection ratio of the constraint is 40 dB. The four channels of the four elements adopt the same model. The effect of the input interference-noise ratio on the interference rejection ratio is shown in Fig. 8a. Four groups of channel non-linear model is generated randomly, and constrained third-order intermodulation suppression ratio of 50 dB, the input noise ratio on the interference rejection ratio as shown in Fig. 8a. As can be seen from Fig. 8, when the antenna array channels are non-linearly consistent, the interference rejection ratio linearly changes with the input interference-noise ratio, and the interference is effectively suppressed. However, when the antenna arrays have non-linear channels, the interference suppression ratio has an extreme value, and the limit value is about the third-order intermodulation rejection ratio, which verifies the traditional analysis method of the third-order intermodulation interference rejection effect.

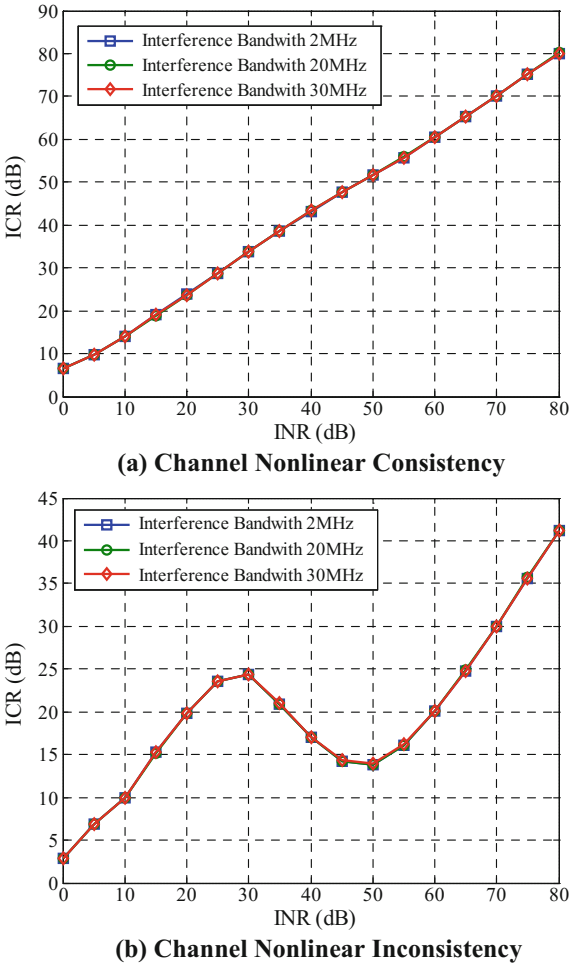

Fig. 8 Influence of channel consistency on anti-jamming

In the scenario shown in Fig. 8, when the input dry-noise ratio is 70 dB, the channels of the antenna array are non-linearly consistent, and the spectrum of the array output data in the case of inconsistency is shown in Fig. 9.

Combining with Fig. 4, we can see that under non-linearity of channel, the noise power after anti-jamming is equal to the noise under channel linearity, indicating that the intermodulation component is effectively suppressed with the interference component in the case of non-linear channel. Under non-linear channel inconsistencies, the noise power after anti-jamming is significantly higher than that of channel non-linearity, indicating that the cross-talk components are not effectively suppressed and the signal quality is affected.

In order to further analyze the impact of the third-order intermodulation caused by noise floor lifting on the signal to noise ratio, set the interference bandwidth of 20 MHz, the signal using Beidou B3 frequency code PRN1, carrier to noise ratio of

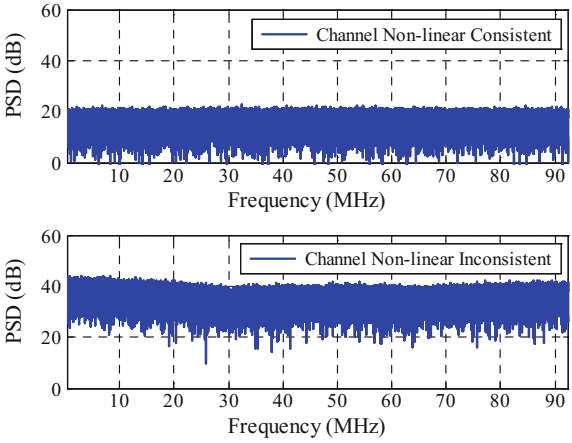

Fig. 9 Spectrum after space domain anti-jamming

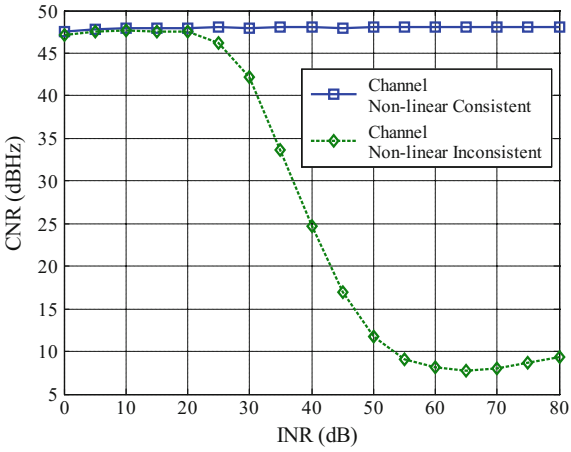

Fig. 10 Influence of INR on CNR

45 dBHz, using the channel characteristics shown in Fig. 9, Noise ratio on the output carrier to noise ratio as shown in Fig. 10. Figure 10 further verifies the effect of third-order intermodulation on signal quality. The third-order intermodulation causes a decrease in anti-jamming performance, resulting in increased residual interference and noise floor uplift, eventually resulting in a decrease in carrier-to-noise ratio.

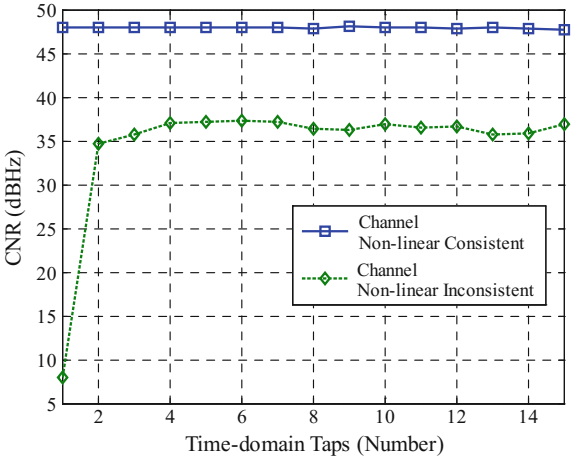

Fig. 11 Influence of time domain taps on CNR

According to the analysis of Fig. 7, the space-time adaptive processing can balance the intermodulation mismatch of each array element channel. Assuming an interference-free ratio of 70 dB, the other conditions are the same as those in Fig. 10, The effect is shown in Fig. 11.

As can be seen from Fig. 11, the carrier-to-noise ratio remains stable irrespective of the number of taps in the time domain with non-linear channels. In the case of channel non-linearity, the carrier-to-noise ratio tends to increase with the number of taps in the time domain, especially when the number of taps in the time domain is from 1 to 2, and the signal to noise ratio increases obviously. The amount of lifting is more than 25 dB and the number of taps in the time domain is 12 When the carrier to noise ratio increased by about 30 dB. Space-time adaptive processing can effectively reduce the third-order intermodulation interference performance.

5 Conclusion

Aiming at the problem of anti-jamming caused by the third-order intermodulation, the third-order intermodulation is analyzed in frequency domain based on single antenna and the difference of anti-jamming effect based on space array. The influence of the third-order intermodulation on the anti-interference in the frequency and spatial domains is different from the anti-interference on the air-time. The traditional view that third-order intermodulation cannot be suppressed, so the third-order intermodulation appears above the noise will result in a sharp decline in anti-interference performance of the frequency domain, airspace. However, the source of intermodulation is still interference, so intermodulation and interference have a certain relevance, the use of space-time processing, after each array of FIR filter interference, intermodulation amplitude and phase consistency adjustment, Eventually, space-time processing can weaken the third-order intermodulation interference performance.

Based on the single-antenna anti-interference in the frequency domain, the third-order intermodulation causes the noise floor to rise, which eventually leads to the decrease of anti-jamming performance. The noise floor rise caused by the third-order intermodulation does not affect the anti-jamming performance based on the space domain/space—The third-order intermodulation coherence of each array element channel is the fundamental reason that decides the third-order intermodulation influences anti-interference. Therefore, the influence of third-order intermodulation on the anti-interference of single antenna and antenna array is different.

Acknowledgements This work was supported by the National Natural Science Foundation of China under grant No. 61403413, 41604016 and 61601485.

References

1. Kaplan E, Hegarty C (2005) Understanding GPS: principles and applications. Artech House
2. Engel U (2008) A theoretical performance analysis of the modernized GPS signals. In: 2008 IEEE/ION position, location and navigation symposium, pp. 1067–1078
3. Tan S The engineering of satellite navigation and positioning. National Defense Industry Press
4. Fante R, Vaccaro JJ (2000) Wideband cancellation of interference in a GPS receive array. IEEE Trans Aero Elec Sys 36(2):549–564
5. Chen F, Nie J, Li B, Wang F (2015) Distortionless space-time adaptive processor for GNSS receiver. Electron Lett 51(25):2138–2139
6. Junwei N (2011) Study on GNSS antenna arrays anti-jamming algorithm and performance evaluation key techniques. Ph.D. dissertation, Chinese National University of Defense Technology, Oct 2011
7. Tan Q, Zhang J (2014) Research on the third-order intermodulation in wireless communication system. Electron R & D 12:20–21
8. Lu Z, Li P, Li J, Nie J, Wang F (2016) Channel consistency indexes of satellite navigation antenna arrays receivers. In: Proceedings of the 5th international conference on computer science and network technology (ICCSNT 2016), Changchun, China, 2016.12, pp 553–557
9. Zhang T, Zhang X, Lu M (2013) Effect of frequency domain anti-jamming filter on satellite navigation signal tracking performance. In: China satellite navigation conference (CSNC), pp 507–516
10. Betz J (2000) Effect of narrowband interference on GPS code tracking accuracy. In: ION NTM 2000, Anaheim, CA, pp 16–27, 26–28 Jan 2000
11. Rinder P, Bertelsen N (2004) Design of a signal frequency GPS software receiver. Master Thesis, Aalborg University, Denmark
12. Li J, Nie J, Li, Chen H, Wang F (2017) Frequency domain anti-jamming based on symmetric cancellation consecutive mean excision for power-enhanced signal GNSS receiver. In: 2017 ION/PNT, pp 809–813
13. Lu Z, Nie J, Chen F, Ou G (2016) Impact on anti-jamming performance of channel mismatch in GNSS antenna arrays receivers. Int J Antennas Propag, pp 1–9
14. Lu Z, Nie J, Chen F, Chen H, Ou G (2017) Adaptive time-taps of STAP under channel mismatch for GNSS antenna arrays. IEEE Trans Instrum Meas 66(11):2813–2824
15. Compton RT (1979) The power-inversion adaptive array: concept and performance. IEEE Trans Aerosp Electron Syst 15:803–814

Subspace Based Joint Delay and Direction of Arrival Estimation for GNSS Multipath Signals

Ning Chang, Xi Hong, Wenjie Wang and Zhaonian Wang

Abstract Multipath signals formed by signal reflecting from objects around the receiver in Global Navigation Satellite System result in tracking performance reduction and positioning error increase. Based on parameter estimation, multipath signals can be recognized, separated, restrained, and then position accuracy get improved. This paper proposed a new method focusing on joint estimation of multipath delays and direction of arrivals utilizing characteristics of spatial and code domain in GNSS signals. Considering the acquisition results, we first despread the received signal to obtain the gain. Also, the despreaded signal is truncated to reduce the dimension. Then, to overcome the coherent sources, the matrix is constructed by introducing some spatial degrees of freedom to frequency domain. Furthermore, subspace based method is adopted to estimate delay and direction of arrival of each path. Finally, simulation results and complexity analysis demonstrate that the proposed method has excellent performance and low complexity, which make the proposed method attractive in practical project.

Keywords Subspace method · Multipath · Delay and DOA · Multi-antenna GNSS receiver · Joint estimation

1 Introduction

In reality, multipath signals formed by signal reflecting from objects around the receiver in Global Navigation Satellite System (GNSS) [1] result in tracking performance reduction and positioning error increase. Based on parameter estimation of multipath signals, different paths can be separated, restrained, and then position accuracy get improved. Traditional receiver will encounter tracking loop jitter

N. Chang (✉) · X. Hong · W. Wang · Z. Wang
Ministry of Education Key Lab for Intelligent Networks and Network Security, Xi'an Jiaotong University, Xi'an 710049, China
e-mail: changning@stu.xjtu.edu.cn

J. Sun et al. (eds.), *China Satellite Navigation Conference (CSNC) 2018 Proceedings*, Lecture Notes in Electrical Engineering 498,
https://doi.org/10.1007/978-981-13-0014-1_17

which increases position error and extends tracking time in multipath scenario. Moreover, the pseudorange error caused by traditional receiver can be reached to meters or even hundreds meters which is large enough to influence the reliability and positional accuracy of the whole system [2].

Multi-antenna receiver has the ability of spatial parameter analysis and it can promote spatial resolution as the number of sensors and array length arise. There is evidence in the literature that fine parameter estimation has been applied to GNSS signals. Such as SAGE [3] and corresponding algorithms [4] based on the principle of maximum likelihood separate multipath signals in multi-antenna situation using iteration, and then estimate parameters of each multipath in turn. The performance can be approximate to the theoretical value but with high complexity. In view of performance and complexity tradeoffs, subspace based methods such as ESPRIT [5] and DOAMatrix [6] are proposed. Based on rotational invariance structure, these methods can provide a near SAGE performance but with reduced complexity, thus leading to easy implementations in engineering project. Nevertheless, these methods are all restricted in telecommunication systems. Due to its long distance transmission, GNSS signals have weak power that are almost buried in the background noise when they reaches the receiver. There are few contributions about ESPRIT-like method applied to GNSS yet and this motivates out work.

In the light of the aforementioned discussion, this paper proposed a new method focusing on joint estimation of multipath delays and direction of arrivals utilizing characteristic of spatial and code domain in GNSS signals. To address the relative delays within one chip after acquisition that may cause low resolution, considering the acquisition result [7], we first despread the received signal to bring back the gain. Also, the despreaded signal is truncated to reduce the dimension at the same time. Then, to overcome the coherent sources problem, we reconstruct the matrix by introducing spatial degrees of freedom. Furthermore, ESPRIT-like is adopted to estimate each path's delay and direction of arrival. Finally, simulation results demonstrate that the proposed method with reduced complexity can also provide the near performance compared to SAGE, these features make the proposed method attractive in practical project.

2 Model

In this paper, we assume GPS signal as our target study object. When GPS signals, multipath interferences and noise exist simultaneously, the received baseband signal at element of an M-element antenna uniform linear array is given by

$$x_m(t) = \sum_{p=1}^{P} \left(\sum_{q=1}^{Q} a_m(\theta_{p,q}) b_{p,q} s_p(t - \tau_{p,q}) \right) + n_m(t) \tag{1}$$

where P and Q are the number of satellites and multipath respectively, $a_m(\theta_{p,q})$ is the response of the *mth* antenna to the *qth* path arriving in *pth* satellite signal from angle $\theta_{p,q}$, $b_{p,q}$ is the complex envelope of the path fading, $\tau_{p,q}$ is the path delay, and $s_p(\cdot)$ is the transmitted GPS signal, given by $s_p(t) = D_p(t)\tilde{c}_p(t)$ and $\tilde{c}_p(t) = \sum_i c_p(i)g(t - iT_c)$, where $\{D_p(t)\}$ is the GPS navigation message and $\{c_p(t)\}$ is the sequence of spreading code bits, $g(t)$ is the pulse-shaping function, and T_c is the chip period. $n_m(t)$ is the additive Gaussian noise with variance σ^2 and mean value zero. Here, we consider that signals and noises are uncorrelated.

For illustration purposes, the satellites signals can be seen as noises except the target satellite signals, thus we have

$$x_m(t) = \sum_{q=1}^{Q} a_m(\theta_q) b_q s(t - \tau_q) + \tilde{n}_m(t) \tag{2}$$

Sample the signal $x_m(t)$ at rate S_a. L denotes the length of C/A code. Thus we obtain Eq. 3 with matrix format as

$$\mathbf{X}^{(n)} = \mathbf{A}(\boldsymbol{\theta})\mathbf{B}\mathbf{S}^{\mathrm{T}}(\boldsymbol{\tau}) + \widetilde{\mathbf{N}}^{(n)} \tag{3}$$

where $\mathbf{A}(\boldsymbol{\theta})$ is the collection of steering vectors, $\mathbf{A}(\boldsymbol{\theta}) = [\mathbf{a}(\theta_1), \ldots, \mathbf{a}(\theta_Q)]$, each steering vector can be written as $\mathbf{a}(\theta_q) = \left[1, e^{j2\pi d \sin(\theta_q)/\lambda}, \ldots, e^{j2\pi d(M-1)\sin(\theta_q)/\lambda}\right]^{\mathrm{T}}$. $\mathbf{B} = diag\{b_1, b_2, \ldots, b_Q\}$ denotes the complex amplitudes diagonal matrix, and $\mathbf{S}^{\mathrm{T}}(\boldsymbol{\tau}) = D\widetilde{\mathbf{C}}^{\mathrm{T}}(\boldsymbol{\tau})$, $\widetilde{\mathbf{C}}^{T}(\boldsymbol{\tau}) = \begin{bmatrix} \tilde{c}(t_0 - \tau_1) & \cdots & \tilde{c}(t_{LS_a-1} - \tau_1) \\ \vdots & \ddots & \vdots \\ \tilde{c}(t_0 - \tau_Q) & \cdots & \tilde{c}(t_{LS_a-1} - \tau_Q) \end{bmatrix}$.

3 Joint Delay and Direction of Arrival Estimation for Multipath Signals

3.1 *Joint Delay and Direction of Arrival Estimation for GNSS Multipath Signals Based on Subspace*

Based on the acquisition of the GPS signals, the C/A code and delay τ_z of the target satellite signals can be acquired subsequently. With these information, we can construct a signal

$$\mathbf{d} = [s(t_0 - \tau_z), s(t_1 - \tau_z), \ldots, s(t_{LS_a-1} - \tau_z)]. \tag{4}$$

where pulse-shaping function is applied to both received signals and constructed signals. To eliminate the effects that caused by the pulse-shaping function, the amplitudes of the pulse-shaping function should be divided

$$\mathbf{d}_f = \left[S(0)/|G(0)|^4, \ldots, S(LS_a - 1)e^{-j\frac{2\pi(LS_a-1)\tau_z}{LS_a}}/|G(LS_a - 1)|^4\right] \tag{5}$$

$S(k), G(k), 0 \le k \le LS_a - 1$ are DFT values of $s(t)$ and $g(t)$, respectively. Since the high frequency components of $\mathbf{d}_f$ are almost zero, the frequency response of the received signals become abnormal if we compensate the amplitudes of pulse-shaping function at all the frequency components. Only low frequency components of $\mathbf{d}_f$ are compensated here. Multiply $\mathbf{d}_f$ by the conjugate received signals, and we obtain

$$\mathbf{X}'^{(n)} = \mathbf{A}(\theta)\mathbf{B}\mathbf{R}_c^{\mathrm{T}}(\tau) + \widetilde{\mathbf{N}}'^{(n)} \tag{6}$$

where $R_c(t)$ is the autocorrelation function of C/A code. It forms a whole matrix $\mathbf{R}_c^{\mathrm{T}}(\tau) = \begin{bmatrix} R_c(t_0 + \tau_z - \tau_1) & \cdots & R_c(t_{LS_a-1} + \tau_z - \tau_1) \\ \vdots & \ddots & \vdots \\ R_c(t_0 + \tau_z - \tau_Q) & \cdots & R_c(t_{LS_a-1} + \tau_z - \tau_Q) \end{bmatrix}$. Because of the low value of the cross correlation between different satellites C/A codes, $\widetilde{\mathbf{N}}'^{(n)}$ can be seen as DFT of Gaussian white noise approximately.

In order to diminish the effect of noise, $\mathbf{X}'^{(n)}$ is truncated according to F_t, where $F_t = \begin{cases} 1, & -K/2 + 1 < t < K/2 \\ 0, & else \end{cases}$. Here, the value of K should be judged according to the empirical value. If K is too large, too much spreading noise and operand will be brought in. On the other hand, if K is too small, estimation will be wrong due to the under-sampling points. Plenty of simulation results show that the empirical value of K should be $4 \cdot S_a$.

As far as we know, each point of $P_{cc}(k), 0 \le k \le K - 1$ can be approximated as P_{cc}. Perform a DFT to the sampled signals mentioned above then we have

$$\begin{aligned} \mathbf{X}_f'^{(n)} &= \mathbf{A}(\theta)\widetilde{\mathbf{B}}\mathbf{P}^T(\tau) + \widetilde{\mathbf{N}}_f'^{(n)} \\ &= [\mathbf{a}(\theta_1), \ldots, \mathbf{a}(\theta_Q)] \begin{bmatrix} \tilde{b}_1 & & \\ & \ddots & \\ & & \tilde{b}_Q \end{bmatrix} \begin{bmatrix} \mathbf{p}(\tau_1) \\ \vdots \\ \mathbf{p}(\tau_Q) \end{bmatrix} + \widetilde{\mathbf{N}}_f'^{(n)} \end{aligned} \tag{7}$$

where $\widetilde{\mathbf{B}} = \mathbf{B}P_{cc}$, $\mathbf{p}(\tau_q) = \left[1, \ldots, e^{-j\frac{2\pi(K-1)(\tau_z-\tau_q)}{K}}\right]$.

In this paper, it is note worthy that multipath signals with relative delays within one chip belong to coherent signals. To increase the resolution of multipath signals,

smoothing method is adopted to construct the expanding matrix which introduces some spatial degrees of freedom to frequency domain.

Let $\mathbf{x}_f^{\prime(n)} = vect\left(X_f^{\prime(n)}\right)$ be a vector of length MK obtained by taking the transpose of each row of the matrix $X_f^{\prime(n)}$ and stacking it below the transpose of the previous row. Equation (7) can be written as

$$\mathbf{x}_f^{\prime(n)} = \mathbf{U}(\theta,\tau)\boldsymbol{\beta} + \tilde{\mathbf{n}}_f^{\prime(n)} \tag{8}$$

where $\tilde{\mathbf{n}}_f^{\prime(n)}$ is the vectored noise of $\widetilde{\mathbf{N}}_f^{\prime(n)}$. The qth column of $\mathbf{U}(\theta,\tau)$ is $\mathbf{a}(\theta_q) \otimes \mathbf{p}(\tau_q)$, where $\otimes$ denotes the kronecker product. The $MK \times Q$ matrix $\mathbf{U}(\theta,\tau)$ is called the space-time matrix, and being parametrized by the DOA and the path delays.

Form the sub matrix $\mathbf{U}_J(\theta,\tau)$ by taking the first JK rows of $\mathbf{U}(\theta,\tau)$, where each column of it is $\left(\Psi_J\mathbf{a}(\theta_q)\right) \otimes \mathbf{p}(\tau_q)$ with $\Psi_J = \left[\mathbf{I}_J, \mathbf{0}_{J,(M-J)}\right]$. There are $M-J+1$ groups totally through sliding K rows each time and each group can be described as $\mathbf{x}_{fJ\gamma}^{\prime(n)} = \mathbf{U}_J(\theta,\tau)(\Phi)^{\gamma-1}\boldsymbol{\beta} + \tilde{\mathbf{n}}_{fJ\gamma}^{\prime(n)}$, $\gamma = 1,\ldots,M-J+1$, where $\Phi = diag\left\{e^{j2\pi d\,\sin(\theta_1)/\lambda},\ldots,e^{j2\pi d\,\sin(\theta_Q)/\lambda}\right\}$.

Design a new matrix

$$\begin{aligned}\mathbf{X}_{new}^{(n)} &= \left[\mathbf{x}_{fJ1}^{\prime(n)}, \mathbf{x}_{fJ2}^{\prime(n)}, \ldots, \mathbf{x}_{fJ(M-J+1)}^{\prime(n)}\right] \\ &= \mathbf{U}_J(\theta,\tau)\left[\mathbf{I}\boldsymbol{\beta}, \Phi\boldsymbol{\beta}, \ldots, (\Phi)^{M-J+1}\boldsymbol{\beta}\right] + \left[\tilde{\mathbf{n}}_{fJ1}^{\prime(n)}, \tilde{\mathbf{n}}_{fJ2}^{\prime(n)}, \ldots, \tilde{\mathbf{n}}_{fJ(M-J+1)}^{\prime(n)}\right]\end{aligned} \tag{9}$$

As we can see, the dimension of $\mathbf{X}_{new}^{(n)}$ is $JK \times (M-J+1)$. Then, $\mathbf{X}_{sub}$ is obtained by taking the first $M-J$ columns of $\mathbf{X}_{new}^{(n)}$. Similarly, $\mathbf{Y}_{sub}$ is obtained by taking the last $M-J$ columns of $\mathbf{X}_{new}^{(n)}$. The two matrix both possess the characteristic of invariance principle, and any ESPRIT-like method can be adopted to estimate DOA and delay of each multipath.

DOAMatrix [6] constructs the DOA matrix based on the rotational invariance structure, in which the DOA elements and steering vectors are acquired after eigen decomposition within two parallel linear array.

In order to get the multipath parameters, this paper apply the DOAMatrix method into the matrix constructed before to obtain the DOA elements and the spatial-frequency submatrix.

Firstly, compute the autocorrelation matrix with $\mathbf{X}_{sub}^{(n)}$ by

$$\begin{aligned}\mathbf{R}_{xx} &= \varepsilon\left(\mathbf{X}_{sub}^{(n)}\mathbf{X}_{sub}^{(n)H}\right) \\ &= \mathbf{U}_J(\theta,\tau)\varepsilon\left(\left[\mathbf{I}\boldsymbol{\beta}, \Phi\boldsymbol{\beta}, \ldots, (\Phi)^{M-J}\boldsymbol{\beta}\right] \cdot \left[\mathbf{I}\boldsymbol{\beta}, \Phi\boldsymbol{\beta}, \ldots, (\Phi)^{M-J}\boldsymbol{\beta}\right]^H\right)\mathbf{U}_J^H(\theta,\tau) + \sigma^2\mathbf{I}\end{aligned} \tag{10}$$

The auto-covariance matrix of $\mathbf{R}_{xx}$ is recorded as

$$\mathbf{R}_{xx0} = \mathbf{R}_{xx} - \sigma^2\mathbf{I} \tag{11}$$

Meanwhile, compute the cross correlation matrix

$$\begin{aligned}\mathbf{R}_{yx} &= \varepsilon\left(\mathbf{Y}_{sub}^{(n)}\mathbf{X}_{sub}^{(n)H}\right) \\ &= \mathbf{U}_J(\theta,\tau)\Phi\varepsilon\left(\left[\mathbf{I\beta},\Phi\mathbf{\beta},\ldots,(\Phi)^{M-J}\mathbf{\beta}\right]\cdot\left[\mathbf{I\beta},\Phi\mathbf{\beta},\ldots,(\Phi)^{M-J}\mathbf{\beta}\right]^H\right)\mathbf{U}_J^H(\theta,\tau)\end{aligned} \tag{12}$$

Here, make a reasonable assumption that each multipath signal's direction of arrival is different from others. $\left[\mathbf{I\beta},\Phi\mathbf{\beta},\ldots,(\Phi)^{M-J}\mathbf{\beta}\right]\cdot\left[\mathbf{I\beta},\Phi\mathbf{\beta},\ldots,(\Phi)^{M-J}\mathbf{\beta}\right]^H$ in (10) and (12) is full rank.

According to (11) and (12), we have

$$\mathbf{R} = \mathbf{R}_{yx}\mathbf{R}_{xx0}^* \tag{13}$$

where $\mathbf{R}_{xx0}^* = \sum_{i=1}^{Q}\mu_i^{-1}V_iV_i^H$. μ_i, V_i are the *ith* eigenvalue and the corresponding eigenvector of $\mathbf{R}_{xx0}$ respectively. Assume that the number of multipath Q is known. In order to determine Q, several methods can be applied, e.g. methods using Akaike information criterion (AIC) or methods using the minimum description length (MDL) criterion.

Then we have

$$\mathbf{R}\mathbf{U}_J(\theta,\tau) = \mathbf{U}_J(\theta,\tau)\Phi \tag{14}$$

The sub special-time matrix and DOA information are obtained from eigen decomposition of $\mathbf{R}$. From that, DOAs and delays can be computed by

$$\hat{\theta}_q = \sin^{-1}\left\{\frac{\lambda}{2\pi d}Arg\left(\lambda_q\right)\right\} \tag{15}$$

$$\begin{aligned}\hat{u}_q &= diag^{-1}\left\{I,\Phi\left(\hat{\theta}_q\right),\ldots,\left(\Phi\left(\hat{\theta}_q\right)\right)^{J-1}\right\}u_q \\ \hat{\tau}_q &= \frac{1}{J}\sum_{i=1}^{J}\frac{K}{2\pi}\sum_{k=2}^{K}\frac{1}{(k-1)}Arg\left\{\frac{\hat{u}_q(i,k)}{\hat{u}_q(1)}\right\}\end{aligned} \tag{16}$$

where λ_q and u_q are the *qth* eigenvalue and the corresponding eigenvector of $\mathbf{R}$, respectively. $\hat{u}_q(i,k)$ is the *kth* element of *ith* group in processed $\hat{u}_q$.

3.2 Complexity Analysis

In this section, complexity analysis results are carried out and compared with that of SAGE. The complexity of proposed algorithm mainly reflect on dispreading. Take complex multiplication as example, the complexity of two times FFT is $o(LS_aN \cdot \log_2(LS_a))$. However, the complexity of proposed algorithm after truncation is only $o\left((JK)^3\right)$, which is far less than that of FFT.

In contrast, SAGE algorithm is based on the principle of maximum likelihood separate multipath signals, and then estimate parameters of each multipath in turn using iteration. The complexity of SAGE is $o(LS_aN \cdot S_{num} \cdot Iter)$, where S_{num} is the number of searching points and *Iter* denotes the number of iteration. The number of searching points changes according to searching precision. In general, *Iter* should be more than 5 and S_{num} may be reached to 200. From that, the operand of SAGE algorithm is almost ten times larger than that of the proposed algorithm.

4 Simulation Analysis

In this section, the performance of the proposed approach and SAGE are assessed by computer simulations. For each parameter setting, 200 Monte Carlo runs are performed and we adopt the root mean square error (RMSE).

We assume a uniform linear array (ULA) with $M = 10$ sensor elements. The number of GPS satellites is 4. 3 of them have only one path for each satellite, with DOA $[60, 0, 10]^\circ$ and the corresponding relative delays $[5.5, 2.5, 3.5]T_c$. We adopt C/A code with sampling rate 2 and code period $T = 1$ ms, 1023 chips per code period each with a time duration $T_c = 977.52$ ns. The iteration of SAGE here is 5.

4.1 Scenario A: Single Path

In the extreme case, the studied satellite has only one direct path with relative delay zero and DOA 30°.

At this situation, SAGE algorithm evolves into maximum likelihood searching. As shown in Fig. 1, the single path delay estimation performances of SAGE are only almost 3 dB better than that of the proposed algorithm over a wide range of chip SNRs, because of the intrinsic difference between ML and subspace based method. At the same time, truncation of the autocorrelation function is applied to reduce the spreading noise which performs well.

As shown in Fig. 2, the performance of the proposed algorithm is 5 dB lower than that of SAGE. This is because the intrinsic difference between subspace decomposition and maximum likelihood principle on one hand, and on the other

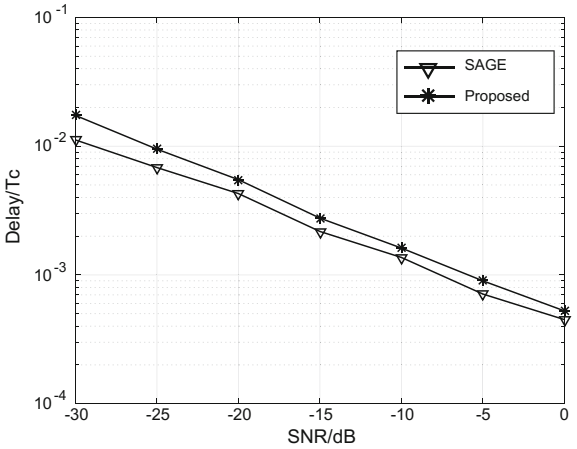

Fig. 1 RMSEs of single path delay estimation versus SNR

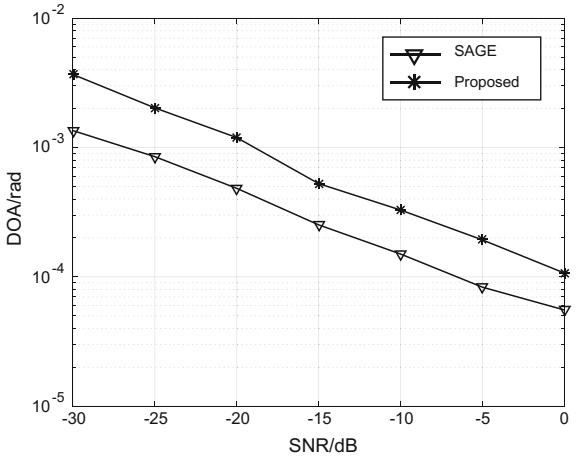

Fig. 2 RMSEs of single path DOA estimation versus SNR

hand, some spatial degrees of freedom are introduced into frequency domain, the spatial performance deteriorates. For illustration purposes, when $SNR = -15$ dB, the performance of the proposed scheme has a 0.015° less comparing with the performance of SAGE. However, the corresponding complexity cost can be considerably reduced at the same time. Therefore, the proposed scheme is a promising alternative to achieve the tradeoffs between performance and complexity in practice.

4.2 Scenario B: Multipath

In multipath situation, two paths of the studied satellite are considered, path1 and path2, where the amplitude of path2 equals 0.7 times of path1. Path1 and path2 have relative delays $[0.3, -0.3]T_c$ respectively, with the corresponding DOAs $[30, -40]^\circ$. There are 5 groups totally included by setting of $J = 6$.

Figure 3 compares the RMSE of the multipath delay estimates of SAGE and the proposed algorithm with respect to the SNRs from −30 dB to 0 dB. As shown in Fig. 3, the proposed algorithm outperforms the SAGE at low SNR. This is because path2's energy is lower than path1 for almost 3 dB, and multipath with relative delays less than one chip are seen as correlated signals, which can not be separated by SAGE at low SNR. In the contrast, our proposed algorithm introduces some spatial information into frequency domain by smoothing, which increases distinction of each path in order to obtain a better performance. However, the RMSE curves of the proposed algorithm become flat at high SNRs, where multiple access interference caused by several satellites spreading codes dominate the RMSE of the proposed algorithm performance. With respect to SNRs from −25 dB to −5 dB, the proposed algorithm is 3 dB lower than that of SAGE. And the reason it does is because of the mitigation of other paths in SAGE when estimating the wanted one. Figure 3 continue to show that the proposed algorithm approaches the performance of SAGE and has the lower complexity which is a big boost in real-time processing.

Figure 4 demonstrates the RMSE of the multipath DOA estimates of SAGE and the proposed algorithm. At low SNRs, the proposed algorithm outperforms SAGE, but SAGE is better than ours as SNR increases. There are two main reasons, one is the difference between subspace decomposition method and maximum likelihood principle, and the other one is that the decrease of spatial degrees of freedom.

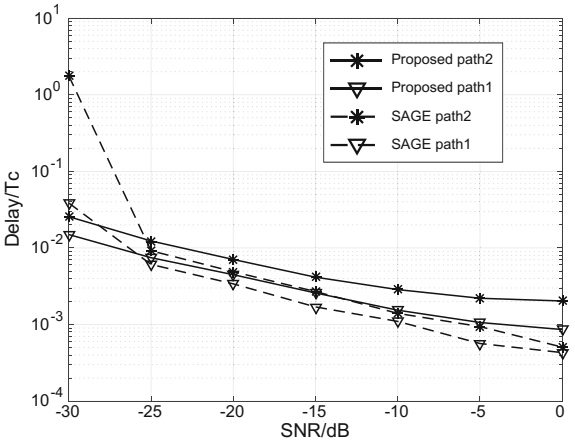

Fig. 3 RMSEs of multipath delays estimation versus SNR

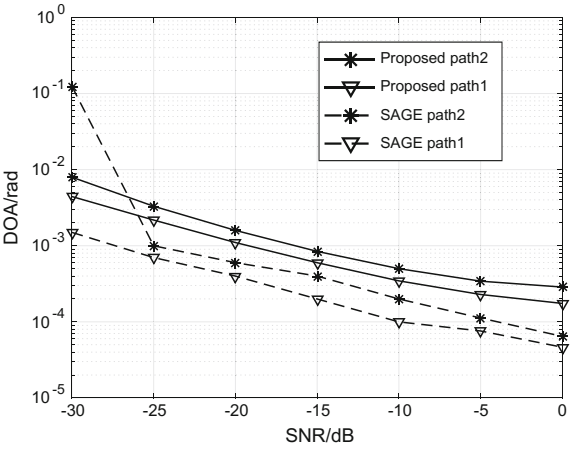

Fig. 4 RMSEs of multipath DOA estimation versus SNR

5 Conclusions

This paper proposes a novel algorithm with outstanding performance and low complexity focusing on joint estimation of multipath delays and direction of arrivals utilizing characteristic of spatial and code domain in GNSS signals. To address the relative delays within one chip after acquisition that may cause low resolution, considering the acquisition results, we first despread the received signal to obtain the spreading gain. Also, the despreaded signal is truncated to reduce the dimension at the same time. Then, to overcome the coherent sources problem, we reconstruct the matrix by introducing spatial degrees of freedom. Furthermore, ESPRIT-like is adopted to estimate each path's delay and direction of arrival.

Simulation results for delay and DOA estimation in GPS application were presented for both single and multipaths case. It demonstrates that the proposed approach almost attains the performance of delay estimation under SAGE algorithm. Complexity analysis also demonstrates that the complexity of proposed approach is several times lower than SAGE which possess excellent feasibility in engineering.

Acknowledgements The work of this paper is supported by the Project of the National Natural Science Foundation of China (NFNC) (Grant No. 61671366).

References

1. Cuntz M, Konovaltsev A, Meurer M (2016) Concepts, development, and validation of multiantenna GNSS receivers for resilient navigation. Proc IEEE 104(6):1288–1301
2. Kos T, Markezic I, Pokrajcic J (2010) Effects of multipath reception on GPS positioning performance. In: Proceedings of the ELMAR, pp 399–402

3. Fleury BH, Tschudin M, Heddergott R, Dahlhaus D, Ingeman Pedersen K (1999) Channel parameter estimation in mobile radio environments using the SAGE algorithm. IEEE J Sel Areas Commun 17(3):434–450
4. Antreich F, Nossek JA, Seco-Granados G, Swindlehurst AL (2011) The extended invariance principle for signal parameter estimation in an unknown spatial field. IEEE Trans Signal Process 59(7):3213–3225
5. Roy R, Kailath T (1989) ESPRIT-estimation of signal parameters via rotational invariance techniques. IEEE Trans Acoust Speech Signal Process 37(7):984–995
6. Yin QY, Zou LH, Newcomb RW (1991) A high resolution approach to 2-D signal parameter estimation: DOA matrix method. J China Instit Commun 12(4):1–7
7. Misra P, Enge P (2004) Global positioning system signals, measurements, and performance. Ganga-Jamuna Press, Lincoln, MA
8. Akaike H (1974) A new look at the statistical model identification. IEEE Trans Autom Control 19(6):716–723
9. Wax M, Kailath T (1985) Detection of signals by information theoretic criteria. IEEE Trans Acoust Speech Signal Process 33(2):387–392

An Improved CCRW Algorithm for BOC Signals with Odd Modulation Coefficient

Hongbo Zhao, Songlin Du and Chao Sun

Abstract Along with the advancement of the process of GNSS modernization, BOC modulation has been widely used. Tough it has a certain anti-multipath capability, reflected BOC signals with the large amplitude and short delay cannot be suppressed. Additionally, some of the traditional multipath suppression algorithms are no longer applicable for the BOC signals, so the multipath mitigation algorithms for BOC signals need to be studied further. CCRW is a kind of anti-multipath algorithm for BOC modulation, but it unsuitable for BOC signals with odd coefficient. In order to overcome its shortcoming, this paper proposes an improved CCRW algorithm for BOC signals with odd modulation coefficient, and simulation results prove the effectiveness of the proposed algorithm.

Keywords BOC modulation · Anti-multipath algorithm · CCRW
Multipath error envelope

1 Introduction

Satellite navigation has been widely used in civil applications such as positioning, navigation, timing and geological surveying in view of its high accuracy, global coverage, all-weather conditions, convenience, flexibility and low cost [1]. However, the accuracy of satellite navigation cannot meet the requirements of weapon guidance or aircraft precision approach [2]. The multipath effect is one of the main factors affecting the positioning accuracy [3].

At present, the methods to reduce the multipath errors are mainly categorized into non-parametric and parameterized class [4]. The parameterization method establishes the model of multipath signals, and then estimates the parameters in the model. This technology can estimate the delay of the direct signal and weakens the

H. Zhao · S. Du (✉) · C. Sun
School of Electronics and Information Engineering, Beihang University, Beijing, China
e-mail: 13141455941@163.com

J. Sun et al. (eds.), *China Satellite Navigation Conference (CSNC) 2018 Proceedings*, Lecture Notes in Electrical Engineering 498,
https://doi.org/10.1007/978-981-13-0014-1_18

multipath effect. It includes MEDLL [5] algorithm, Kalman filter [6] and so on. Although these methods can significantly reduce the multipath effect, they require a number of correlators which caused large computation burden. In contrast, non-parametric methods do not need to estimate the parameters, so their calculation amount is small and they are widely used [4]. Non-parametric methods include narrow correlation technique [7], Double-Delta technique [8], Gated-PRN technique [9] etc.

The CCRW method is one of the non-parametric methods. It uses a PRN code signal (excluding subcarriers) to generate a local reference waveform in the receiver. The reference waveform is related to the received signal in the tracking loop. Compared with the autocorrelation function (ACF), its cross-correlation function (CCF) has less parasitic responses which are pushed further in delay [10]. The original CCRW method is only applicable to SinBOC (n, n) signals, and an improved algorithm is proposed in [4], which can be applied to SinBOC (m, n) signals with even modulation coefficient.

In this paper, the CCRW method is further improved so that it can be applied to the SinBOC (m, n) signal whose modulation coefficient is odd. In order to understand the improved algorithm in this paper, we introduce the basic principle of CCRW in the second chapter. In the third chapter, we will introduce the improved CCRW algorithm which is suitable for the BOC signals with odd modulation coefficients. Finally, we will analyse the performance of the improved algorithm and show the simulation results.

2 The CCRW

The CCRW method makes use of the PRN code waveform to generate a reference code waveform for the correlation operation. Compared with the autocorrelation function, its CCF has less parasitic responses which are pushed further in delay. Therefore, the CCRW method has a better performance in multipath mitigation. The reference code waveforms of CCRW can be classified into two sub-categories: "transition-based" versus "per-chip" reference waveforms. The former includes the Narrow Correlator (NC, W1) waveform, and the other contains W2, W3 and W4 waveforms [10]. In this paper, we proposed a CCRW method for odd-order binary offset carrier signals which is a kind of "transition-based" waveform. In order to understand the proposed method, the basic principle of NC waveform is introduced.

Let the PRN code sequence waveform be given by:

$$C(t) = \sum_{k} c_k w(t - kT_c) \tag{2.1}$$

where $w(t), 0 \leq t \leq T_c$ is a rectangular pulse, Tc is the code duration, and $c_k = \pm 1$ is the chip at the time slot k.

The non-zero values of the NC sequence appear only at the original PRN code transitions symmetrically, and the sign is same as the latter chip of the code transitions. The width of non-zero values is $2T_c/M$. Based on these principles, the NC sequence can be given by:

$$S_{NC}(t) = \frac{1}{2}[C(t + \frac{T_c}{M}) - C(t - \frac{T_c}{M})] \tag{2.2}$$

Figure 1 displays the NC sequence waveform for BOC (1, 1), and the cross-correlation function between the BOC (1, 1) signal and the NC sequence waveform is shown in Fig. 2 in solid lines. The auto-correlation function for BOC (1,1) is shown in dot dash lines for comparison. It can be seen from the figure that the parasitic responses of CCF are further away from the main peak. It indicates that the NC method has a stronger anti-multipath capability.

According to the above analysis, NC method can improve the anti-multipath ability for even-order SinBOC signals. However, it is not suitable for SinBOC signals with odd modulation coefficient. Take SinBOC (3, 2) for example, we obtain the NC sequence waveform according to the formula (2.2), and the result is shown in Fig. 4. The correlation result between the NC waveform and the SinBOC (3, 2) signal is zero. As a result, we cannot track the signals with this method.

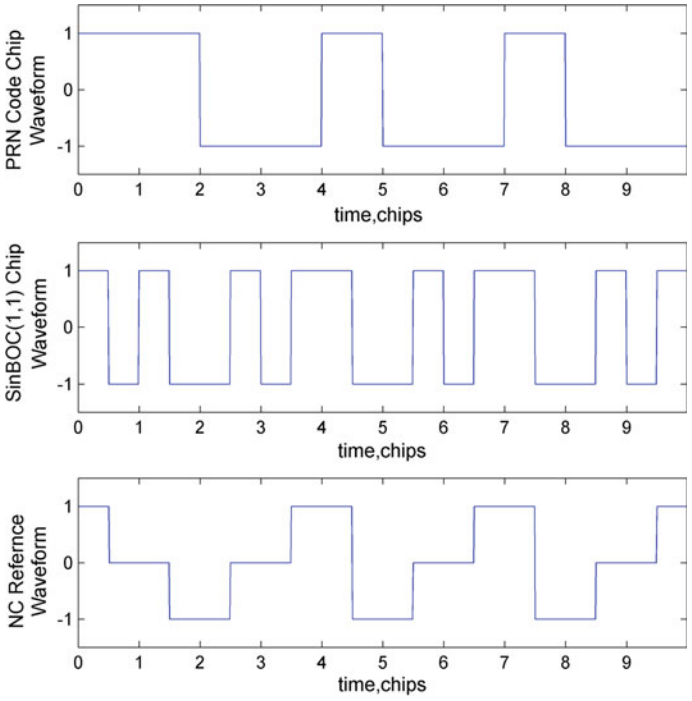

Fig. 1 The narrow correlator sequence waveform

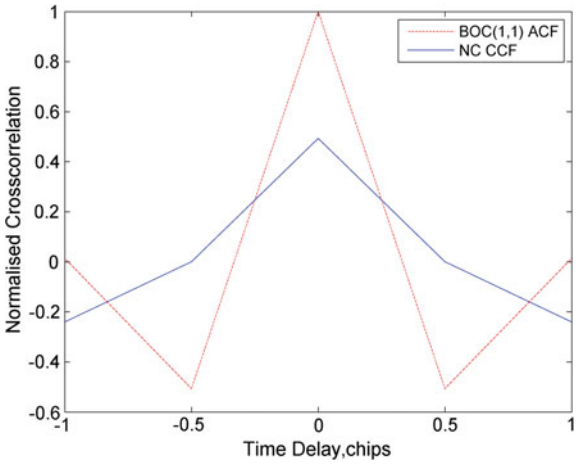

Fig. 2 The CCF between the NC sequence waveform and the BOC (1, 1) signal

3 The Improved CCRW

In order to solve the problem that the BOC signals with odd modulating coefficient cannot produce a correlation peak with the NC reference waveform, the NC sequence waveform is multiplied by a subcarrier whose frequency is $nf_0/2$, half of the PRN code rate. Then the subcarrier can be expressed as:

$$S_{CCRW-subcarrier}(t) = sign(\cos(2\pi * (nf_0/2)t)) \tag{3.1}$$

where $sign()$ is the sign function, it is given by:

$$sign(t) = \begin{cases} 1 & t > 0 \\ -1 & t < 0 \end{cases} \tag{3.2}$$

and the improved CCRW sequence waveform can be expressed as:

$$S_{CCRW\_improved}(t) = S_{CCRW}(t) \cdot S_{CCRW\_subcarrier}(t) \tag{3.3}$$

The structure of the improved CCRW generator is shown in Figs. 3 and 4 shows the improved CCRW waveform, and the CCF between SinBOC (3, 2) signal and the improved CCRW waveform is shown in Fig. 7 in solid line. The CCF only has two side peaks, whose centers are located at ± 1 chips away from the main peak, while the ACF has 4 side peaks at $\pm 1/3, \pm 2/3$ chips late. Therefore, the proposed improved CCRW method has a better performance in multipath suppression.

In order to further improve the anti-multipath capability for proposed method, we subtract the improved CCRW left shift and right shift two chips with aptitude from the improved CCRW waveform. It is expressed as:

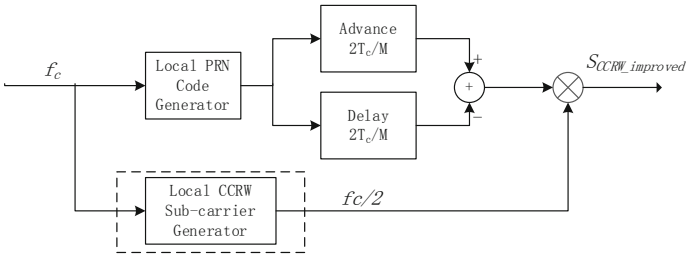

Fig. 3 The structure of the improved CCRW generator

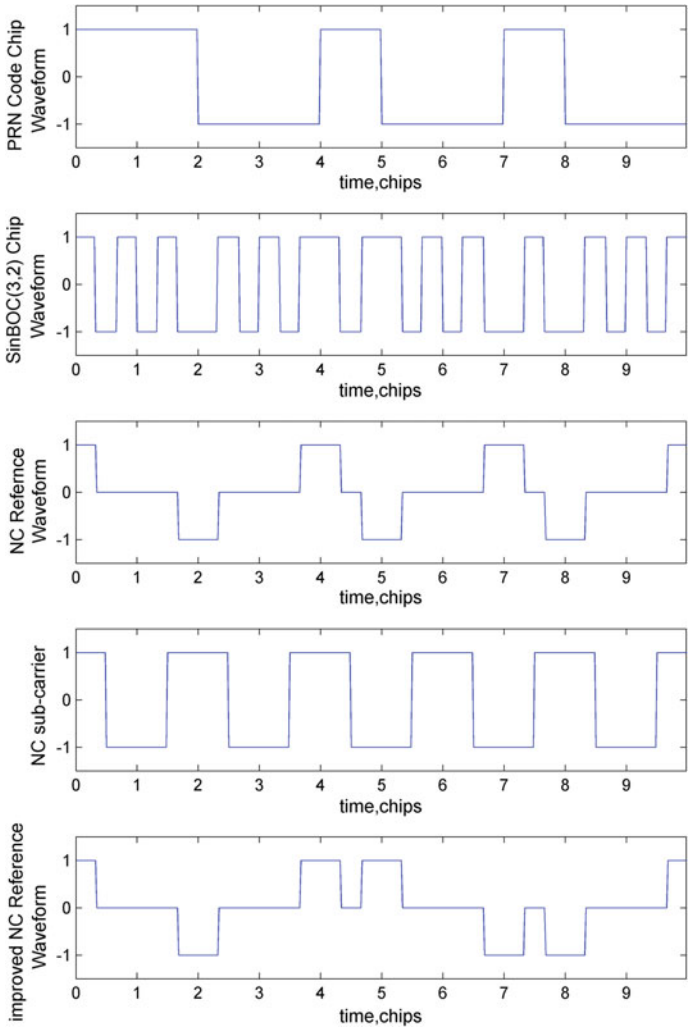

Fig. 4 The CCRW sequence waveforms for BOC (3, 2)

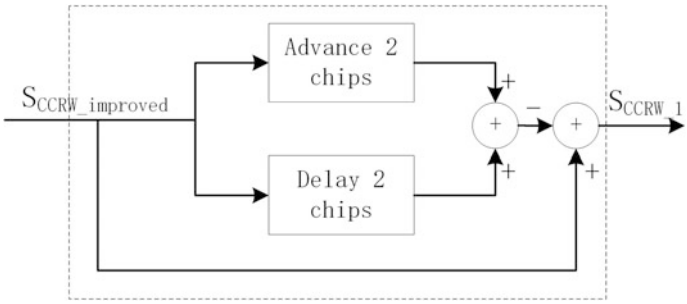

Fig. 5 The structure of the further improved CCRW generator

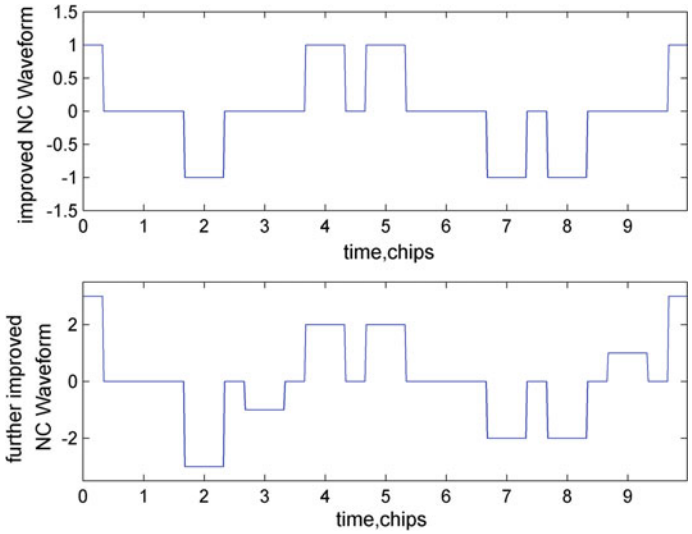

Fig. 6 The CCRW sequence waveforms for BOC (3, 2)

$$S_{CCRW\_1}(t) = S_{CCRW\_improved}(t) - [S_{CCRW\_improved}(t - 2T_c) - S_{CCRW\_improved}(t + 2T_c)] \tag{3.4}$$

The structure of further improved CCRW generator is shown in Fig. 5, and the further improved CCRW is shown in Fig. 6. As a result, the side peaks at ±1 chips away from the main peak are eliminated. The CCF between the further improved CCRW waveform and SinBOC (3, 2) signal is shown in Fig. 7 in dot dash line. Though the further improved CCRW method increase the amount of side peaks to 4, the centers of the side peaks are located at 2 chips away from the main peak at least. Hence the multipath error induced from the side peaks is negligible.

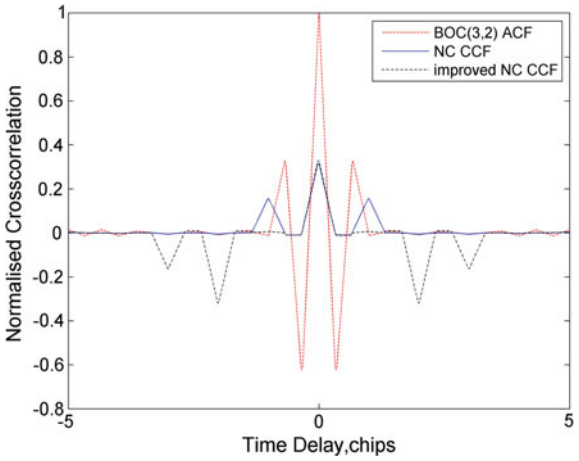

Fig. 7 The CCF between the CCRW waveform and the BOC (3, 2) signal

4 Performance Analysis

In this chapter, we take SinBOC (3, 2) as an example to analyze the anti-multipath and tracking performance of the improved CCRW algorithm.

4.1 Anti-multipath Performance

When the received signal contains multipath component, the symmetry of the correlation peak is destroyed, and the stable tracking point of the discriminator is located at a non-zero point thus resulting in a tracking error [4].

Assuming that the received GNSS signal contains a direct signal and one reflected signal, and the amplitude of the reflected signal is half that of the direct signal. Under the condition that the spacing of early-late correlators is 0.1 chips, the multipath error envelopes for two algorithms are shown in Fig. 8. When the reflected signal is in-phase or out-phase with the direct signal, the pseudo-range measurement error reaches the maximum [11]. From the figure, we can observe that the further improved CCRW algorithm has stronger ability to suppress the reflected signal whose delay is more than 0.6 chips and less than 1.6 chips. Considering the effect of the channel attenuation, the amplitude of the reflected signals with more than 1.6 chips is small, so they have less impact on tracking loop compared with reflected signals with less than 1 chips. Therefore, the further improved CCRW algorithm has better anti-multipath performance.

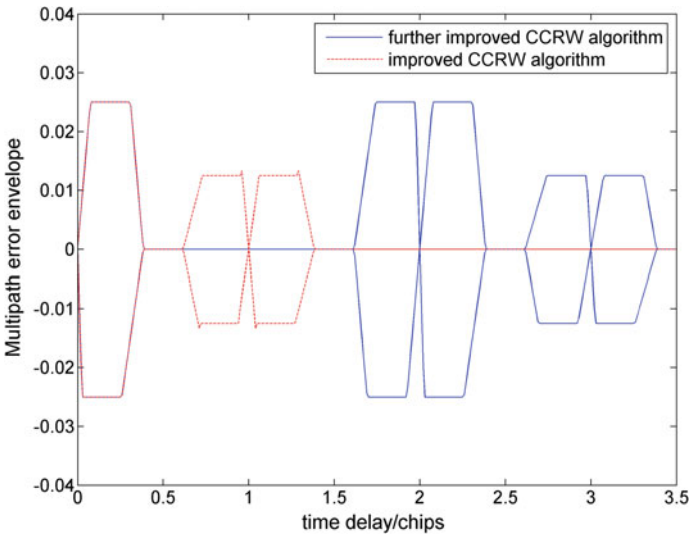

Fig. 8 The multipath error envelope for improved CCRW algorithms

4.2 Tracking Performance

Without considering multipath and interference, the dominant code tracking error source is noise, so we will analyse the tracking performance of the proposed method for coherent EML code tracking loop by calculating the code tracking error standard deviation in various SNR.

For $0 < B_L T_I < 0.5$, where B_L is the single-side equivalent rectangular loop bandwidth, T_I is the integration time. Under the assumption that there is only white Gaussian noise, the estimated code delay tracking error variance is given by [12]:

$$\sigma^2 = \frac{B_L(1 - 0.5B_L T_I)\int_{-\beta_r}^{\beta_r} G_s(f)\sin^2(\pi f\Delta)df}{(2\pi)^2 \frac{C}{N_0}\int_{-\beta_r}^{\beta_r} f G_s(f)\sin(\pi f\Delta)df} \tag{4.1}$$

where $G_s(f)$ is defined as a power spectral density normalized to unit power over infinite bandwidth, β_r is pre-correlation bandwidth, Δ is the spacing between the early and late correlators.

The setting of the simulation parameters is concluded in Table 1, and the code tracking standard deviation of the proposed method is shown in Fig. 9 under the condition that SNR ranges from 25 dB Hz to 50 dB Hz. From the figure we conclude that the tracking performance of the further improved CCRW method is worse than that of the improved CCRW method. It is mainly because that the further improved CCRW method has more side peaks and the amplitude of the side peaks is larger than improved CCRW method.

Table 1 Setting of simulation parameters

Parameters	Values
B_L	2 Hz
T_I	20 ms
β_r	Infinite
Δ	0.2 chips

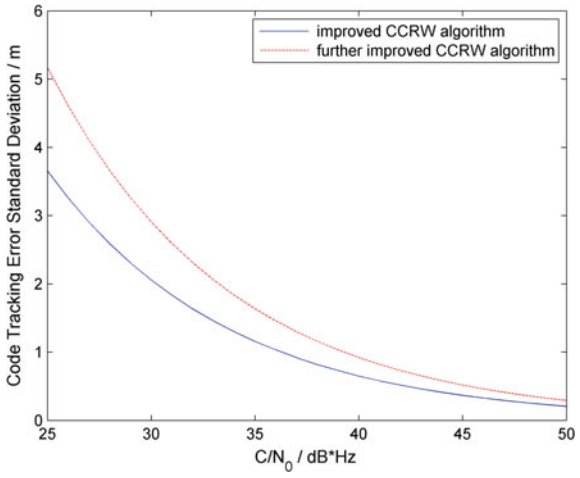

Fig. 9 The code tracking error standard deviation for the proposed method

5 Conclusion

In this paper, an anti-multipath algorithm for BOC (m, n) signals with odd modulation coefficients is proposed. By adding subcarriers to the NC reference waveform, the reference waveform has a cross-correlation peak with the BOC (m.n) signal, and by further improvement, the center of the side peaks are pushed farther away from the main peak. Although further improvements increase the number of side peaks and reduce the tracking performance of the receiver, it has better anti-multipath performance and more obvious suppression for the multipath signal with delay between 0.6 chips and 1.6 chips.

References

1. Xie G (2009) Principles of GPS and receiver design. Publishing House of Electronics Industry, Beijing, China
2. Gan XL (2008) Research on quality monitoring technology of GPS local area augmentation system. Unpublished doctorial dissertation, Harbin Engineering University, Harbin, China
3. Ji FY, Shi HL, Sun YX, Ji Y-F, Shi H-L, Sun X-Y (2007) Study on multipath mitigation performance of strobe correlator. J Astronaut 05:1094–1099

4. Zhou Y, Tang Z (2014) Multipath mitigation technique for sine-phased binary offset carrier signal. In: International conference on information and communications technologies, pp 1.011–1.011, IET
5. Van NDJR (1997) Method of estimating a line of sight signal propagation time using a reduced-multipath correlation function. US, US5615232
6. Peng J, Su Y, Li J, Wang F (2014) Research on multipath mitigation based on the variable length reduced sigma point kalman filter. Lecture Notes in electrical engineering, vol 303, pp 739–749
7. Dierendonck AJV, Fenton P, Ford T (1992) Theory and performance of narrow correlator spacing in a gps receiver. Navigation 39(3):265–283
8. Qu B, Li L, Bian L, Wang X, Meng Y (2016) An unambiguous multipath mitigation method based on double-delta correlator for BOC modulation signal. In: China satellite navigation conference (CSNC) 2016 proceedings, vol I, Springer Singapore
9. Wu J, Dempster AG (2011) "boc-gated-prn" a multipath mitigation technique for boc(n, n) waveforms. IEEE Trans Aerosp Electron Syst 47(2):1136–1153
10. Garin LJ (2005) The "shaping correlator", novel multipath mitigation technique applicable to GALILEO BOC (1,1) modulation waveforms in high volume markets. In: Proc. ENC-GNSS
11. Rouabah K, Saifeddine C, Atia S, Flissi M, Chikouche D (2013) Mathematical model of non-coherent-dll discriminator output and multipath envelope error for boc (α, β) modulated signals. Positioning 4(1):65–79
12. Betz JW, Kolodziejski KR (2009) Generalized theory of code tracking with an early-late discriminator part i: lower bound and coherent processing. IEEE Trans Aerosp Electron Syst 45(4):1538–1556

MC-BOC: A New Interoperable Modulation and Performance Analysis for BeiDou B1 Signal

Xinming Huang, Xin Zhao, Xiangwei Zhu and Gang Ou

Abstract B1/L1/E1 frequency (1575.42 MHz) is one of the main interoperability frequency bands in the Global Navigation Satellite Systems (GNSS). The MBOC (Multiplexed BOC) modulation is adopted on this frequency by GPS and Galileo systems, which is also a candidate for BeiDou B1C signal. This paper starts with the definition of MBOC modulation, and proposes a generalized MBOC modulation, i.e. MC-BOC (Multi Carrier BOC) modulation. The MC-BOC modulation is a multi-carrier modulation, which contains four sub-carriers. Compared with the existing MBOC modulation, the proposal has independent intellectual property right. And it has superiorities in anti-multi-path and tracking, as well as in the flexibility. The study results can be regarded as a choice for the design and optimization of the BeiDou signals.

Keywords MC-BOC · MBOC · Constant envelope modulation
BeiDou B1

1 Introduction

In order to improve the receiving performance of navigation signals, MBOC is proposed as the modulation type for E1 and L1 frequency by Galileo and GPS [1]. MBOC modulation is defined on frequency domain, whose power spectral density is a mixture of BOC (1, 1) spectrum and BOC (6, 1) spectrum. The Composite BOC (CBOC) is chosen as the candidate for Galileo L1 OS signal, and the Time-Multiplexed BOC (TMBOC) is used by the GPS L1C signal [2, 3]. Different MBOC implementations would require different receiving complex. Thus, the MBOC implementation type should be carefully designed in order to acquire a better receiving performance.

BeiDOu B1C signal is considered to choose MBOC modulation, in order to achieve the interoperability and compatibility with GPS and Galileo. TMBOC and

X. Huang (✉) · X. Zhao · X. Zhu · G. Ou
National University of Defense Technology, Changsha 410073, China
e-mail: hxm_kd@163.com

J. Sun et al. (eds.), *China Satellite Navigation Conference (CSNC) 2018 Proceedings*, Lecture Notes in Electrical Engineering 498,
https://doi.org/10.1007/978-981-13-0014-1_19

CBOC are two candidates, while all the two modulations face patent risks. Quadrature Multiplexed BOC (QMBOC) is a new modulation remaining the MBOC spectral constraints [4]. By Placing the narrowband BOC component and the wideband BOC component in phase quadrature, the new modulation can provide a more flexible application as the narrowband BOC component and the wideband BOC component can modulate different data. A more generalized application is to transfer more data on MBOC modulation, thus, we need the BOC component transfer data on both the upper and lower sideband, which is similar as the 2 code AltBOC modulation. On the basis of this idea, we propose a new modulation, i.e. MC-BOC (Multi Carrier BOC) modulation. The MC-BOC modulation is a multi-carrier modulation, which contains four sub-carriers. Compared with the existing MBOC modulation, the proposal has independent intellectual property right. And it has superiorities in anti-multi-path and tracking, as well as in the flexibility.

2 MC-BOC Modulation

2.1 Generalized MBOC Modulation

The Multiplexed Binary Offset Carrier (MBOC) modulation has been recommended by the GPS-GALILEO Working Group on Interoperability and Compatibility. The power spectral density of MBOC modulation is a mixture of BOC (1, 1) spectrum and BOC (6, 1) spectrum, whose definition can be expressed as

$$\Phi_{\mathrm{MBOC}(m,n,\gamma)} = (1-\gamma)\Phi_{\mathrm{BOC}(n,n)} + \gamma\Phi_{\mathrm{BOC}(m,n)} \tag{1}$$

$\gamma : (1-\gamma)$ is the power ratio between the wideband BOC signal and the narrow band BOC signal.

The definition can be extended as

$$\Phi_{\mathrm{MBOC}(m,n,\gamma)} = (1-\gamma)(\Phi^{up}_{\mathrm{BOC}(n,n)} + \Phi^{down}_{\mathrm{BOC}(n,n)}) + \gamma(\Phi^{up}_{\mathrm{BOC}(m,n)} + \Phi^{down}_{\mathrm{BOC}(m,n)}) \tag{2}$$

$\Phi^{up}_{\mathrm{BOC}(n,n)}, \Phi^{down}_{\mathrm{BOC}(n,n)}$ are defined as the up sideband and low sideband of BOC (n, n) signal, and $\Phi^{up}_{\mathrm{BOC}(m,n)}, \Phi^{down}_{\mathrm{BOC}(m,n)}$ are defined as the up sideband and low sideband of BOC (m, n) signal.

We can regard the upper and lower sideband as two independent sub-carriers, thus, a new expression can be achieved as following:

$$\begin{aligned}\Phi_{GMBOC(m,n,\gamma)} &= (1-\gamma)(\Phi_1(f-nf_0)+\Phi_2(f+nf_0)) \\ &\quad +\gamma(\Phi_3(f-mf_0)+\Phi_4(f+mf_0))\end{aligned} \tag{3}$$

We define the new modulation as the generalized MBOC modulation. The new modulation equals to MBOC modulation when and $\Phi_1(f) = \Phi_2(f)$ and $\Phi_3(f) = \Phi_4(f)$.

2.2 MC-BOC Modulation

We first discuss the case as $\gamma = 0.5$.

Assume that $s_1(t)$, $s_2(t)$, $s_3(t)$ and $s_4(t)$ represent four components of the sub-carrier signals, $s_0(t)$ represents the multicarrier multiplexed signal, which combines the above four signals $s_1(t)$, $s_2(t)$, $s_3(t)$ and $s_4(t)$ on four subcarriers, with the centre frequencies of each two signals $2f_{sc}$ apart, into an integrated signal. The multi-carrier multiplexed signal can be expressed as

$$s(t) = \left(s_1(t)e^{-j2\pi nf_s t} + s_2(t)e^{j2\pi nf_s t}\right) + e^{j\theta}\left(s_3(t)e^{-j2\pi mf_s t} + s_4(t)e^{j2\pi mf_s t}\right) \tag{4}$$

where $e^{-j2\pi nf_s t}$, $e^{j2\pi nf_s t}$, $e^{-j2\pi mf_s t}$ and $e^{j2\pi mf_s t}$ are the complex exponential functions used to realize multi-carrier modulation.

The three level cosine-phased and sine-phased BOC subcarriers, shown as Fig. 1, are used to express the complex exponential function, thus the multi-carrier multiplexed signal can be expressed as

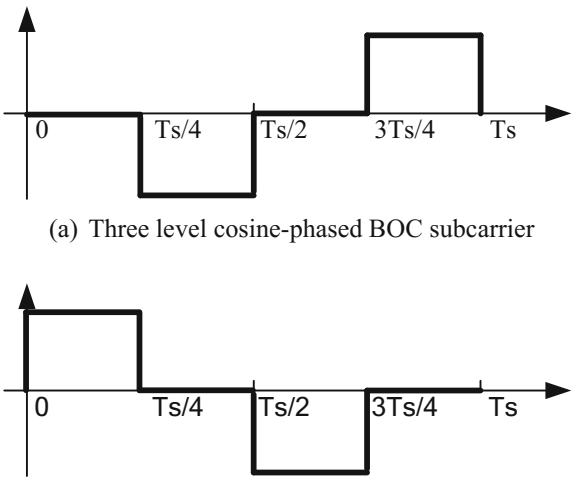

Fig. 1 Three level BOC subcarrier

(a) Three level cosine-phased BOC subcarrier

(b) Three level sine-phased BOC subcarrier

$$\begin{aligned} s(t) = {} & s_1(t)\left(\left[SC_{3c}^n(t) + jSC_{3s}^n(t)\right]\right) + s_2(t)\left(\left[SC_{3c}^n(t) - jSC_{3s}^n(t)\right]\right) \\ & + e^{j\frac{\pi}{4}}\left\{s_3(t)\left(\left[SC_{3c}^m(t) + jSC_{3s}^m(t)\right]\right) + s_4(t)\left(\left[SC_{3c}^m(t) - jSC_{3s}^m(t)\right]\right)\right\} \end{aligned} \tag{5}$$

$SC_{3c}^n(t), SC_{3s}^n(t), SC_{3c}^m(t), SC_{3s}^m(t)$ are the three level cosine-phased and sine-phased BOC (n, n) and BOC (m, n) subcarriers respectively.

In order to make the multi-carrier multiplexed signal constant envelope, the complex exponential functions are firstly divided into a discrete multi-level complex exponential functions. The multicarrier multiplexed signal with discrete multi-level complex exponential functions can be expressed as [5]

$$s(t) = s_1(t)e^{j\frac{\pi}{4}k_1(t)} + s_2(t)e^{j\frac{\pi}{4}k_2(t)} + s_3(t)e^{j\frac{\pi}{4}k_3(t)} + s_4(t)e^{j\frac{\pi}{4}k_4(t)} \tag{6}$$

where the phase rotating indices $k_1(t)$, $k_2(t)$, $k_3(t)$, $k_4(t)$ stand for varying phase of complex sub-carriers, which are defined as Tables 1 and 2.

T_{sc}^n and T_{sc}^m are the periods of sub-carriers of $k_1(t)$, $k_2(t)$ and $k_3(t)$, $k_4(t)$ respectively.

By employing the multi-level waveforms like the AltBOC subcarrier as the subcarriers for inter-modulation products, we can get the four-component multi-carrier constant envelope baseband signal, which makes the multicarrier multiplexed signal with discrete multi-level complex exponential functions into a constant envelope signal, as following [6]

$$\begin{aligned} s(t) = {} & s_1(t)e^{j\frac{\pi}{4}k_1(t)} + s_2(t)e^{j\frac{\pi}{4}k_2(t)} + s_3(t)e^{j\frac{\pi}{4}k_3(t)} + s_4(t)e^{j\frac{\pi}{4}k_4(t)} \\ & + 0.4142\left[s_{aI}(t)e^{j\frac{\pi}{4}k_5(t)} + s_{aQ}(t)e^{j\frac{\pi}{4}k_6(t)} + s_{bI}(t)e^{j\frac{\pi}{4}k_7(t)} + s_{bQ}(t)e^{j\frac{\pi}{4}k_8(t)}\right] \end{aligned} \tag{7}$$

Table 1 Phase rotating indices for multi-carrier BOC modulation

t modulo $T_{sc}^n/4$	$k_1(t)$	$k_2(t)$
[0, $T_{sc}^n/4$)	2	6
[$T_{sc}^n/4$, 2 $T_{sc}^n/4$)	4	4
[2 $T_{sc}^n/4$,3 $T_{sc}^n/4$)	6	2
[3 $T_{sc}^n/4$, T_{sc}^n)	0	0

Table 2 Phase rotating indices for multi-carrier BOC modulation

t modulo $T_{sc}^m/4$	$k_3(t)$	$k_4(t)$
[0, $T_{sc}^n/4$)	3	7
[$T_{sc}^n/4$, 2 $T_{sc}^n/4$)	5	5
[2 $T_{sc}^n/4$,3 $T_{sc}^n/4$)	7	3
[3 $T_{sc}^n/4$, T_{sc}^n)	1	1

where $s_{aI}(t)$, $s_{aQ}(t)$, $s_{bI}(t)$, $s_{bQ}(t)$ are the inter-modulation products, which can be defined as

$$\begin{aligned} s_{aI}(t) &= s_2(t)s_3(t)s_4(t), s_{aQ}(t) = s_1(t)s_3(t)s_4(t) \\ s_{bI}(t) &= s_1(t)s_2(t)s_4(t), s_{bQ}(t) = s_1(t)s_2(t)s_3(t) \end{aligned} \tag{8}$$

The phase rotating indices $k_5(t)$, $k_6(t)$, $k_7(t)$, $k_8(t)$ stand for varying phase of complex subcarriers for inter-modulation products. $k_5(t)$, $k_6(t)$ equals to $k_1(t)$, $k_2(t)$, and $k_7(t)$, $k_8(t)$ equals to $k_3(t)$, $k_4(t)$.

2.2.1 Generalized MC-BOC Modulation

A more generalized problem is to multiplex signals with unequal power allocation on two different subcarrier signals into a multiplexed signal with constant envelope. Assume the power ratio between $s_1(t)$, $s_3(t)$ and $s_2(t)$, $s_4(t)$ is $1{:}p^2$ ($p > 0$), thus the multi-frequency constant envelope baseband signal can be achieved with the same way as multi-carrier BOC modulation, which can be expressed as

$$\begin{aligned} s(t) = {} & s_1(t)e^{j\frac{\pi}{4}k_1(t)} + ps_2(t)e^{j\frac{\pi}{4}k_2(t)} + s_3(t)e^{j\frac{\pi}{4}k_3(t)} + ps_4(t)e^{j\frac{\pi}{4}k_4(t)} \\ & + as_{aI}(t)e^{j\frac{\pi}{4}k_5(t)} + as_{aQ}(t)e^{j\frac{\pi}{4}k_6(t)} + bs_{bI}(t)e^{j\frac{\pi}{4}k_7(t)} + bs_{bQ}(t)e^{j\frac{\pi}{4}k_8(t)} \end{aligned} \tag{9}$$

where $s_{aI}(t)$, $s_{aQ}(t)$, $s_{bI}(t)$, $s_{bQ}(t)$ are the inter-modulation products, $k_1(t)$, $k_2(t)$, $k_3(t)$, $k_4(t)$ and $k_5(t)$, $k_6(t)$, $k_7(t)$, $k_8(t)$ stand for varying phase of complex subcarriers for useful singles and inter-modulation products respectively. All the values of these parameters are the same as multi-carrier BOC modulation. a and b are the coefficients of the inter-modulation products that can be achieved by following [8]

$$\begin{aligned} & p = \sqrt{\frac{\gamma}{1-\gamma}} \\ & a(1+b) = p(b-1) \\ & b = \begin{cases} -\frac{3}{4} + \frac{1}{4}\sqrt{d} + \frac{1}{2}\sqrt{\frac{1}{2} + 7\left(\frac{4}{3c}\right)^{1/3}p^2 - \left(\frac{2c}{9}\right)^{1/3} + \frac{1-16p^2}{2\sqrt{d}}}, & p < \frac{1}{4} \\ -\frac{3}{4} - \frac{1}{4}\sqrt{d} + \frac{1}{2}\sqrt{\frac{1}{2} + 7\left(\frac{4}{3c}\right)^{1/3}p^2 - \left(\frac{2c}{9}\right)^{1/3} - \frac{1-16p^2}{2\sqrt{d}}}, & p > \frac{1}{4} \\ -\frac{3}{4} + \frac{1}{4}\sqrt{3+2\sqrt{17}}, & p = \frac{1}{4} \end{cases} \end{aligned} \tag{10}$$

where c and d can be calculated by

$$\begin{aligned} c &= -9p^2 + 9p^4 + \sqrt{3}\sqrt{27p^4 + 632p^6 + 27p^8} \\ d &= 1 - 28\left(\frac{4}{3c}\right)^{1/3}p^2 + 4\left(\frac{2c}{9}\right)^{1/3} \end{aligned} \tag{11}$$

As can be seen, the multi-carrier BOC modulation is the special case as equal power allocation.

3 The MC-BOC Modulation for BeiDou B1 Signal

We consider BeiDou B1 signal adopts MC-BOC (6, 1, 1/11) modulation, and the modulation and frequency characteristics are analyzed.

The constellation diagram below is used to analyze the characteristics of constant envelope modulation. Figure 2 depicts the sketch of the in-phase and quadrature-phase components of the MC-BOC (6, 1, 1/11) modulated signal. It can be seen that the MC-BOC modulated signal has 16 phase points spaced on the constant envelope circle.

Assume the pseudo-code has ideal auto-correction and cross-correction characteristics, frequency characteristics of the constant envelope MC-BOC (6, 1, $\frac{p^2}{1+p^2}$) signal and useful signals are analyzed.

$$S(f) = \frac{1+b^2}{1+p^2+a^2+b^2} \cdot \frac{8f_c sin^2\left(\frac{\pi f}{2f_c}\right) sin^2\left(\frac{\pi f}{4f_c}\right)}{\pi^2 f^2} + \frac{p^2+a^2}{1+p^2+a^2+b^2} \cdot \frac{8f_c sin^2\left(\frac{\pi f}{12f_c}\right) sin^2\left(\frac{\pi f}{24f_c}\right)}{\pi^2 f^2} \cdot \frac{sin^2\left(\frac{\pi f}{f_c}\right)}{sin^2\left(\frac{\pi f}{6f_c}\right)} \tag{12}$$

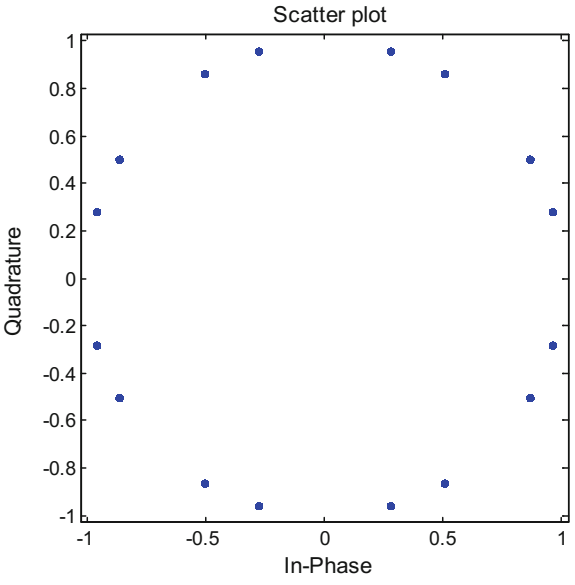

Fig. 2 Constellation of MC-BOC (6, 1, 1/11) modulated signal

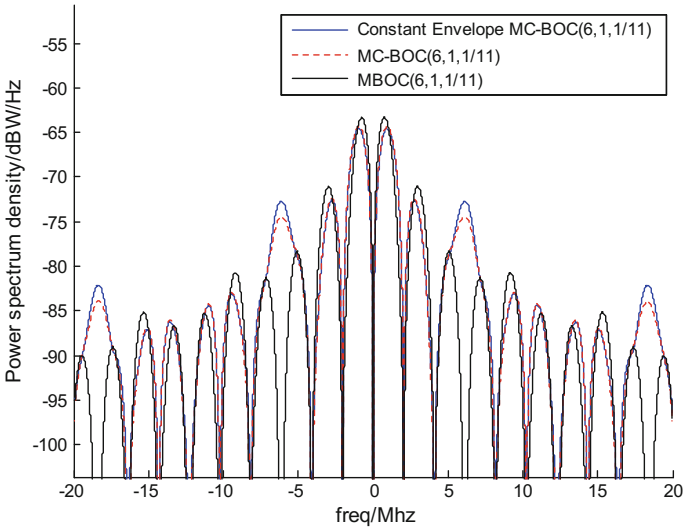

Fig. 3 PSD of MC-BOC (6, 1, 1/11)

The PSD of the MBOC (6, 1, 1/11) signal and the normal and constant envelope MC-BOC (6, 1, 1/11) signals are shown as the following Fig. 3. As can be seen, MC-BOC (6, 1, 1/11) has the similar frequency characteristics of MBOC (6, 1, 1/11).

4 Receiving Performance Analysis

4.1 Ranging Performance

Ranging performance is in direct proportion with the Gabor bandwidth, thus we use Gabor bandwidth to evaluate signal ranging performance [7]. Gabor bandwidth is defined in the form in Hz, namely

$$\Delta f_{Gabor} = \sqrt{\int_{-\beta_r/2}^{\beta_r/2} f^2 G_s(f) df(Hz)} \tag{13}$$

where f is the frequency in Hz; $G_s(f)$ is the equivalent normalized power spectral density of the baseband signal in 1/Hz; β_r is receive bandwidth in Hz.

Figure 4 shows the Gabor bandwidth of the MC-BOC (6, 1, 1/11) modulation and MBOC (6, 1, 1/11) modulation for a given receiver bandwidth assumed to have rectangular bandwidths. As can be seen, when the receiving bandwidth is broader than 5 MHz, ranging performances of either the constant envelope

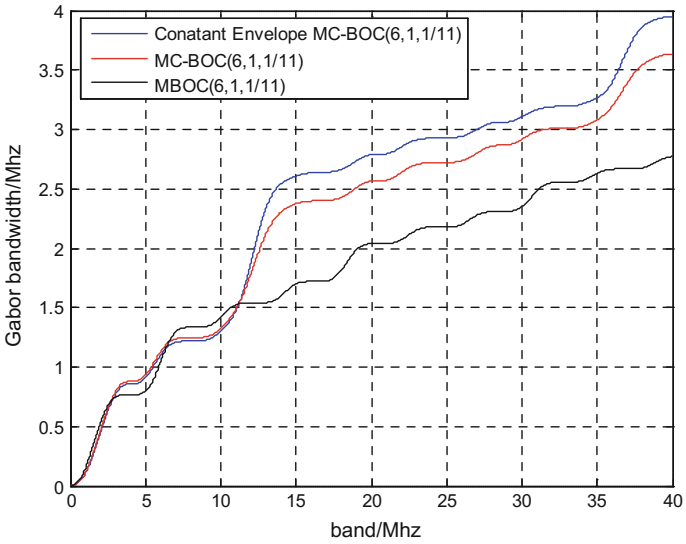

Fig. 4 Gabor bandwidth of MBOC modulation and MC-BOC modulation

MC-BOC modulation or the normal MC-BOC modulation have been greatly improved compared with the traditional MBOC modulation when the bandwidth is larger than 12 MHz.

4.2 Multipath Performance

Evaluation of navigation signal's multipath resistance capability is usually based on a static model with one direct and one reflected path, with a multipath to direct path signal power ratio (MDR) that is independent of delay. Navigation signal's multipath resistance capability can be measured by the code tracking multipath error envelope and the average multipath error which based on the non-coherent early-late delay locked loop. Multipath error envelope is the maximum deviation caused by multipath effects under the conditions of different multipath delay. It could reflect the worst instance in multipath error under condition of a particular multipath, and is chosen as index to evaluate the multipath resistance capability.

The code tracking multipath error envelope lower bound based on the early-late delay-locked loop is defined as [8]

$$\lim_{d\to 0}\varepsilon_r(\tau_1) \approx \frac{\pm a_1 \int_{-\beta_r/2}^{\beta_r/2} f\cdot S(f)\sin(2\pi f\tau_1)df}{2\pi \int_{-\beta_r/2}^{\beta_r/2} f^2\cdot S(f)[1\pm a_1\cos(2\pi f\tau_1)]df} \tag{14}$$

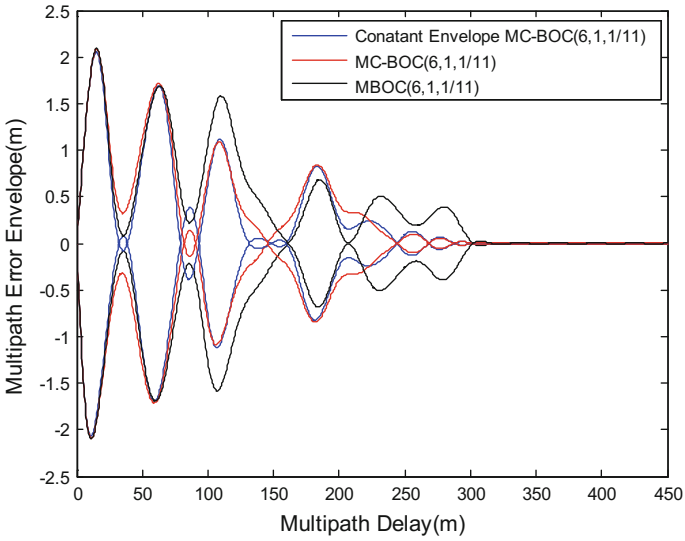

Fig. 5 Multipath error envelope of the MBOC and MC-BOC modulations

where, $S(f)$ is power spectrum normalized in the transmission bandwidth, the unit is Hz, β_r is receive bandwidth in Hz. τ is the delay of multipath signal relative to the direct signal, the unit is Second, a_1 is MDR.

Figures 5 and 6 shows MC-BOC modulated and MBOC modulated signal multipath error envelopes with that the front-end bandwidth is 30 MHz and MDR $a_1 = -6\text{dB}$.

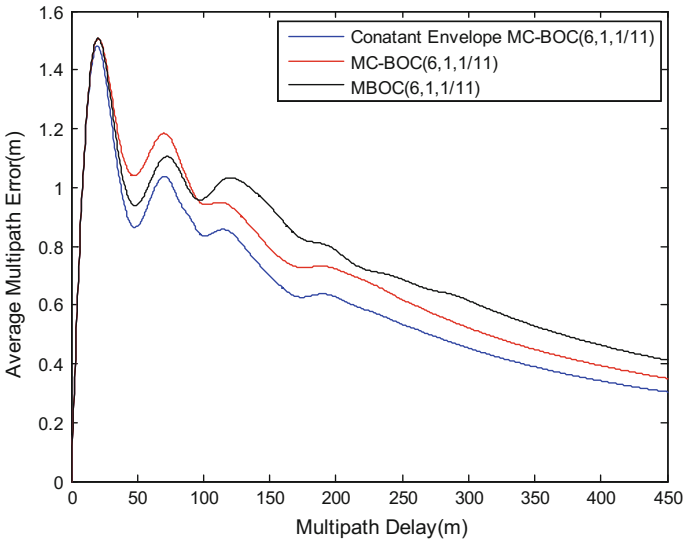

Fig. 6 Average multipath errors of the MBOC and MC-BOC modulations

It can be seen that both the constant envelope and the nonconstant envelope MC-BOC modulations have better performances in terms of mitigation of short-delay, medium-delay and long-delay multipath than the normal MBOC modulation.

5 Conclusions

A generalized MBOC modulation, named MC-BOC modulation, is proposed. Compared with the existing MBOC modulation, the new modulation satisfies the MBOC constraint condition, and has better receiving performances on tracking and multipath resistance. The study results can be regarded as a choice for the design and optimization of the BeiDou signals.

References

1. Hein G, Avila-Rodriguez J et al (2006) MBOC: the new optimized spreading modulation recommended for Galileo L1 OS and GPS L1C. In: Proceedings of IEEE/ION PLANS, San Diego, CA, pp 883–892
2. Hein G, Avila-Rodriguez J et al (2005) A candidate for the Galileo L1 OS optimized signal. In: Proceedings of ION GNSS, Long Beach, CA
3. Avila-Rodriguez JA (2008) On generalized signal waveforms for satellite navigation. University FAF Munich, Munich
4. Yao Z, Lu M, Feng Z (2010) Quadrature multiplexed BOC modulation for interoperable GNSS signals. Electron Lett 46(17):1234–1236
5. Lestarquit L, Artaud G, Issler J AltBOC for dummies or everything you always wanted to know about AltBOC. In: Proceedings of the 21st international technical meeting of the satellite division of the institute of navigation, Savannah, GA, pp 16–19 Sept 2008:961–970
6. Zhang K (2013) Generalized constant-envelope DualQPSK and AltBOC modulation for modern GNSS signals. Electron Lett 49(21):1335–1337
7. Tang Z, Zhou H, Hu X, Ran Y, Liu Y, Zhou Y (2010) Research on performance evaluation of COMPASS signal. In: Proceedings of the 1st China satellite navigation conference, Beijing, 19–21 May 2010
8. Tang Zuping Z, Hu X (2009) Analysis of multipath resistance performance in GNSS signal design. J Huazhong Sci Technol Univ 37(5):1–4

A New Signal Quality Monitoring Method for Anti-spoofing

Chao Sun, Joon Wayn Cheong, Andrew G. Dempster, Hongbo Zhao, Laure Demicheli and Wenquan Feng

Abstract Intermediate spoofing, identified as an efficient spoofing attack method, can launch a spoofing attack without interrupting the regular functioning of Global Navigation Satellite System (GNSS) receivers. GNSS is vulnerable and easily interfered by spoofing because of its opening signal structure and low signal power, and this threatens the security and integrity of GNSS, especially for the safety critical applications such as maritime and aviation. Signal Quality Monitoring (SQM) techniques, originally designed for multipath detection, are recently found to be useful to identify the deformation on the correlation function of a GNSS signal due to an intermediate spoofing attack. Conventional SQM-based methods directly employ the values of the SQM metric to detect spoofing attacks. In this paper, we develop an enhanced SQM technique for spoofing detection. It is known that the value of SQM metric fluctuates significantly during the interaction between the counterfeit signal and authentic signal. As the variance of metric can better reflect this fluctuation of metric, we choose the moving variance (MV) of the SQM metric as a new "metric" to detect the occurrence of spoofing. The basic principle of the proposed method is well introduced and tested on four different SQM metrics. Its ability to detect spoofing has been validated using the dataset collected using our SPIRENT simulators. The results show that the proposed moving variance-based SQM method is advantageous in the detection of spoofing attacks.

Keywords Spoofing detection · Signal quality monitoring (SQM) Moving variance · Receiver operator characteristic (ROC)

C. Sun (✉) · H. Zhao · W. Feng
School of Electronics and Information Engineering,
Beihang University, Beijing, China
e-mail: sunchao@buaa.edu.cn

C. Sun · J. W. Cheong · A. G. Dempster · L. Demicheli
Australian Centre for Space Engineering Research,
University of New South Wales, Sydney, Australia

J. Sun et al. (eds.), *China Satellite Navigation Conference (CSNC) 2018 Proceedings*, Lecture Notes in Electrical Engineering 498,
https://doi.org/10.1007/978-981-13-0014-1_20

1 Introduction

Spoofing is a deliberate interference that intends to mislead the target Global Navigation Satellite System (GNSS) receivers into generating false position or navigation solutions by broadcasting a fake signal [1]. As the low power level and opening signal structure, GNSS open service signals are very vulnerable to the spoofing attacks. Thus, spoofing attack has become one of the most harmful threats for the user receivers, especially for the safety critical applications such as maritime and aviation.

Recent successful implementations of spoofing trials have further reinforced the awareness of the hazard of spoofing attacks. In 2013, a research group from The University of Texas at Austin successfully carried out a spoofing attack to control the trajectory of a yacht [2]. They later performed effective capture and control of an unmanned aerial vehicle (UAV) via GNSS signal spoofing in 2014 [3]. Thus, many research works have been focused on the development of detection and mitigation techniques against the spoofing threats, such as the methods based on the signal power monitoring and carrier noise ratio monitoring [4, 5], the methods based on receiver antenna defence techniques [6–8], the methods based on Time of Arrival (TOA) discrimination [9], consistency checks among different measurements [1], and the methods based on cryptographic modulation of the civil GNSS signal [10].

Recently, Signal Quality Monitoring (SQM) techniques are found to be effective to detect the distortion of the correlation function caused by a spoofing attack. SQM techniques were originally developed particularly for signal deformation monitoring and multipath detection [11]. As structures of the spoofed and multipath signals are very similar which had led several research groups to the assumption that such metrics can also detect spoofing, so that performances of SQM metrics were also explored for spoofing detection in [12]. Detailed performance assessment has been done over a set of spoofing scenarios [13, 14]. To further improve the reliability of spoofing detection, a two-dimensional SQM method was developed by introducing a monitoring metric in Doppler frequency domain [15]. The SQM-based countermeasures mentioned above all directly employ the raw values of the SQM metric to detect spoofing attacks.

In this paper, a new SQM technique is presented for spoofing detection. It is known that the value of SQM metric fluctuates significantly during the interaction between the counterfeit signal and authentic signal. As the variance can better reflect this fluctuation of metrics, we choose the moving variance (MV) of the SQM metric as a new "metric" to judge the occurrence of spoofing. The basic principle of the proposed method is well introduced. Its ability to detect spoofing has been validated using the dataset collected using SPIRENT simulators. The results show that the proposed moving variance-based SQM method outperforms the basic SQM method for spoofing detection.

2 Recall of SQM Metrics

During an intermediate spoofing attack, the spoofer generates a counterfeit signal for each satellite signal used in the navigation solution. The three typical steps of launching an intermediate spoofing attack can be concluded as three stages. In the first stage, the spoofed signals are generated with the same code delay and Doppler shift as authentic signal to ensure that their correlation functions are perfectly aligned with each other. Then in the second stage, the spoofer gradually increases the power of the spoofed signal and finally exceeds the authentic signal's power level. In the last stage, the spoofer slowly leads the spoofed signal away from the authentic signal to manipulates the victim receiver.

When the counterfeit signal interacts with the authentic signal, the phase and power of the signal admixture fluctuate strongly at this moment and during the period when the counterfeit signal is moving away from the authentic signal. Such fluctuation affects the complex correlation shape and thus causes the abnormality of correlator output values. Thus, we can employ this abnormality to detect the spoofing attack. It is worth noting that as the multipath has quite similar effect with spoofing attacks, all the SQM-based anti-spoofing techniques face the challenge that how to distinguish spoofing from multipath. Generally, some extra detection techniques, such as power detection [16] or doppler domain detection [15], are required to perform joint detection and make the detection more robust.

SQM techniques typically employ the correlator outputs to detect the distortion of correlation peak in the tracking loop of the user receivers. Figure 1 gives the complex correlation function in the presence of spoofing. $I_{E,d}(t)$, $I_{P,d}(t)$ and $I_{L,d}(t)$ refer to the Early, Prompt and Late In-Phase correlator output at time t, respectively; $Q_{E,d}(t)$, $Q_{P,d}(t)$ and $Q_{L,d}(t)$ denote the Early, Prompt and Late Quadrature correlator output at time t, respectively. We can see that both In-Phase and Quadrature

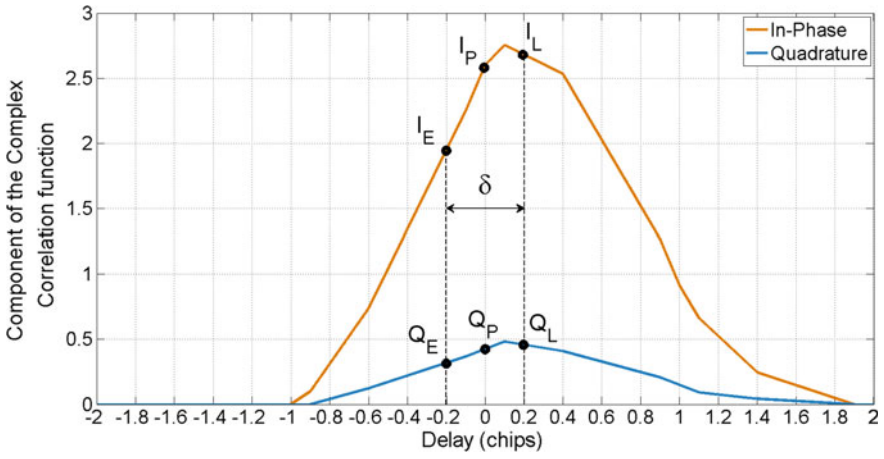

Fig. 1 In-phase and quadrature complex correlation component at time t. d = 0.2 chip

correlation functions are distorted due to the spoofing attack which allows us to develop countermeasures by analyzing these correlator outputs.

Employing the multiple samples of the complex correlation function given above, different strategies have been proposed to compute metrics. In this paper, we mainly consider the following four metrics:

- Delta Metric [13]:

$$\Delta_d(t) = \frac{I_{E,d}(t) - I_{L,d}(t)}{2I_P} \tag{1}$$

- Ratio Metric [13]:

$$RT_d = \frac{I_{E,d}(t) + I_{L,d}(t)}{2I_P} \tag{2}$$

- Early Late Phase Metric [17]:

$$ELP_d(t) = \tan^{-1}\left(\frac{Q_{L,d}(t)}{I_{L,d}(t)}\right) - \tan^{-1}\left(\frac{Q_{E,d}(t)}{I_{E,d}(t)}\right) \tag{3}$$

- Magnitude Difference Metric:

$$MD_d(t) = \frac{|x_{E,d}(t)| - |x_{L,d}(t)|}{2|x_P|} \tag{4}$$

where $|x(t)|$ denotes the magnitude of the complex correlation function computed as:

$$|x(t)| = \sqrt{I(t)^2 + Q(t)^2} \tag{5}$$

The SQM-based anti-spoofing methods mentioned above directly employ the raw values of the SQM metric to detect spoofing attacks. They are usually very sensitive to the system noise which results in the reduction of detection rate for a given false alarm rate.

3 Moving Variance

The moving variance technique has already been used for spoofing detection by monitoring the C/N0 variation caused by a spoofing attack [18]. As we have presented above, the raw values of different SQM metrics fluctuate significantly during the interaction stage of the counterfeit signal and authentic signal.

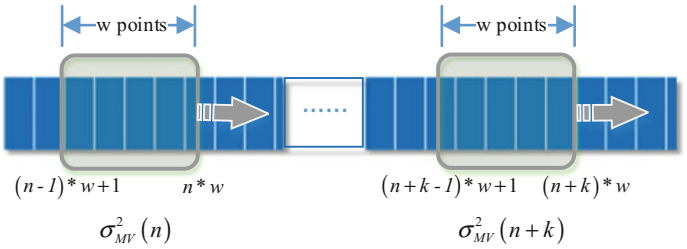

Fig. 2 Illustration of the computation of moving variance

Considering the variance is typically used to show the dispersion degree of a set of data, it can be employed to further magnify the changings of correlator outputs to make it more significant. Therefore, the moving variance of each SQM metric has the potential to be a better "metric" to detect the occurrence of spoofing.

Figure 2 illustrates the principle of moving variance calculation. Through a predefined window sizing a subset of metrics values, the moving variance formula evaluates the difference between the mean of the squares of the subset and the square of the mean over this subset. Then, the window shifts forward. Hence, it creates a series of variances of different subset of the full data set. The general expression of moving variance is given by:

$$\sigma^2_{MV}(n) = \frac{1}{w}\sum_{i=(n-1)*w+1}^{n+w} x(i)^2 - \left(\frac{1}{w}\sum_{i=(n-1)*w+1}^{n+w} x(i)\right)^2 \tag{6}$$

where $x(i)$ is the value of the i-th sample in the data, w denotes the length of each subset and n is the total number of the subsets of the entire data.

The typical profile of metrics responses to a spoofing attack is illustrated in Fig. 3. As mentioned in Sect. 2, the spoofing attack can be divided into three stages. For the second stage (from the 150th to the 300th second), both authentic and counterfeit signals reach the receiver and interact with each other. They lead to distortion of the correlation function of the mixed-signal and bring in noticeable risings and declines of the metric values over time. Whereas for the first stage (before the 150th second) and the third stage (after the 280th second), because either the authentic signal or the counterfeit signal is stably tracked, the final metric values keep a steady behavior. Thus, we can detect the attack during the second stage of the spoofing attack, thanks to these remarkable metrics variations.

Figure 4 plots the moving variance for different metrics. compared with raw metric values, the operation of moving variance makes the spoofing behavior more outstanding. The main peaks locate around the 220th second. It is much easier to search for these abnormal peaks or impulses among the moving variance of each SQM metric and thus identify any potential hazards from spoofing attacks.

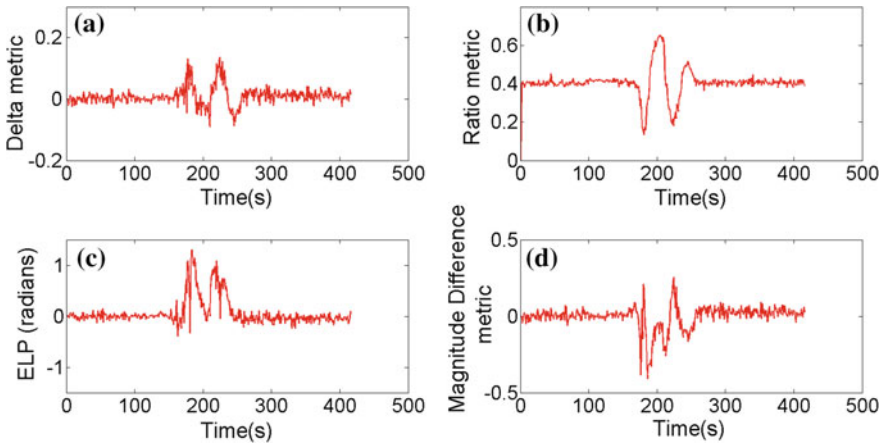

Fig. 3 Four metrics responses to a matched-power spoofing scenario computed with a 0.5 chip correlator spacing

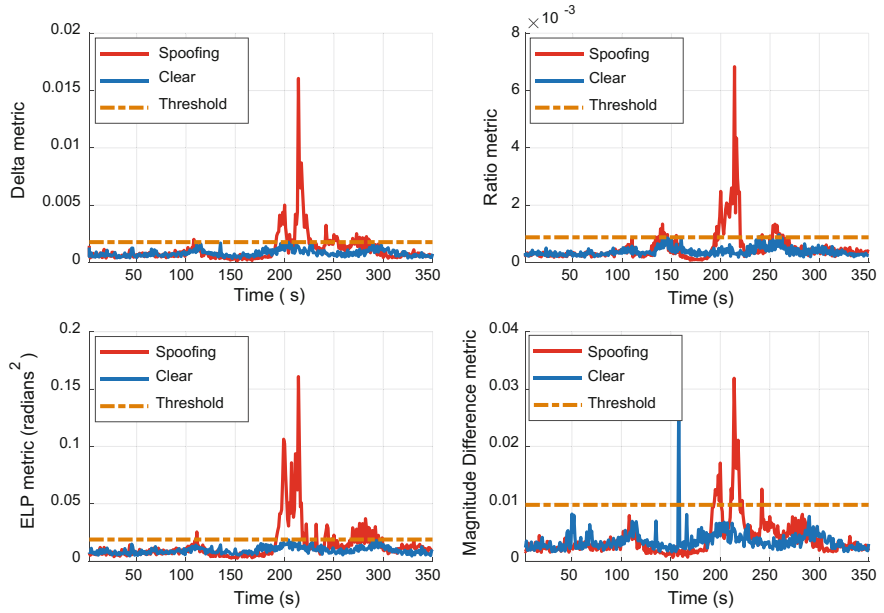

Fig. 4 Moving variance responses to a spoofing attack. The correlator spacing is 0.5 chip

4 Performance Evaluation

In order to evaluate the spoofing detection performance of the moving variance-based SQM method, we plot the receiver operator characteristic (ROC) curves of the proposed method and compare them with the conventional SQM-based methods that directly employ the raw values of SQM. Its ability to detect spoofing is validated using the dataset collected using our SPIRENT simulators.

4.1 Determination of the Threshold

The spoofing detection method is implemented by comparing the values of moving variance with a threshold. Thus, a spoofing-present decision is made if the threshold value is exceeded, and a spoofing-absent decision is made otherwise. Given the time-varying nature of the metrics, the operations of computing the thresholds and probability analysis are performed within a detection window of several seconds. In the following test, this detection window is from the beginning of the spoofing attack to the end of the dataset.

Generally, the threshold value is a function of the designated false alarm probability (P_{fa}) and the level of thermal noise. For a designated C/N_0, the final P_{fa} and P_d can also be seen as functions of the threshold value. For a certain threshold Th, P_{fa} and P_d are computed as follows:

$$\begin{aligned} P_{fa} &= \int_{Th}^{\infty} f_c(x)\mathrm{d}x \\ P_d &= \int_{Th}^{\infty} f_s(x)\mathrm{d}x \end{aligned} \tag{7}$$

where $f_c(x)$ represents the probability density function of the clear signal moving variance, and $f_s(x)$ denotes the probability density function of moving variance values in the presence of a spoofing attack.

We can see that, in order to calculate P_{fa} and P_d, the moving variance distributions for both spoofing-absent and spoofing-present circumstances have to be obtained. However, the distributions of moving variance are quite complicated. Besides, they also depend on the window size used in the method, the number of samples of correlator's outputs, the receiver's sampling frequency and the specific spoofing attack pattern. It is impractical to derive the analytical expression of the probability density functions. So this paper evaluates the performance of the moving variance-based algorithm using the statistical method. The distributions of moving variance are analyzed and computed using computer softwares. Then by

varying the value of threshold, we are able to obtain the P_{fa} and P_d curves versus threshold values. Furthermore, we can plot the ROC curves with horizontal axis of P_{fa} and vertical axis of P_d. One of benefits of such process is we can get the actual ROC curves without the knowledge of the exact mathematical expression of the probability distribution.

4.2 Scenario Created with the SPIRENT Simulator

A self-made spoofing scenario is built in order to show the effectiveness of the anti-spoofing algorithm and test its performance. As is shown in Fig. 5, it was created through the GPS signal simulator GSS6560, a product of the SPIRENT Communications Company. The SimGen software was used to run the GSS6560 GPS signal simulator. A NordNav receiver software was used to post-process the generated GPS signals. The NordNav front-end is directly connected to the GPS simulator, and the data obtained include correlator output values, navigation data, and the channel properties.

Figure 6 illustrates the spoofing pattern we used in the test. The scenario consists of a spoofer with a low power advantage over the LOS (+0.4 dB) that performs a spoofing attack from seconds 150 to 580 of the total simulation time. In this scenario, the spoofer first aligns its code delay with the authentic signal, and when the relative delay is zero, it starts increasing its power and thus takes control of the receiver.

Figure 7 shows the ROC curves for Ratio, Delta, MagDiff, and ELP metrics. The window size used to calculate moving variance is set to 1 s and the correlator spacing is 0.4 chip. We can see that the four metrics have quite similar performance, so all of them can be used for anti-spoofing. But for the P_{fa} of a small value, such as 0.1, the P_d for each metric is around 0.8, which is not high enough and can lead to missed detection problem. However, the computation of moving variance is helpful to improve the performance of each metric. It can be seen that the moving-variance-based methods all outperform the according raw SQM metrics. For a given false alarm rate of 0.1, the detetction probabilities of the four metrics go up to around 0.9. Thus, the introduction of the concept of moving variance is proved to be an effective improvement.

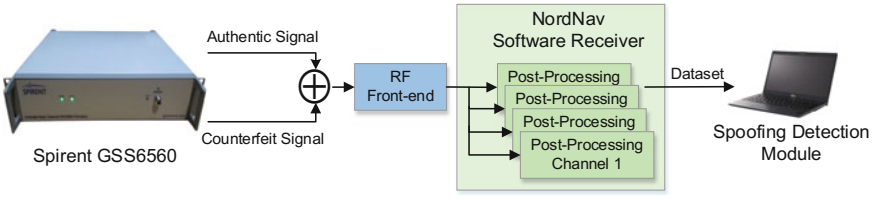

Fig. 5 Spoofing generation and detection setup

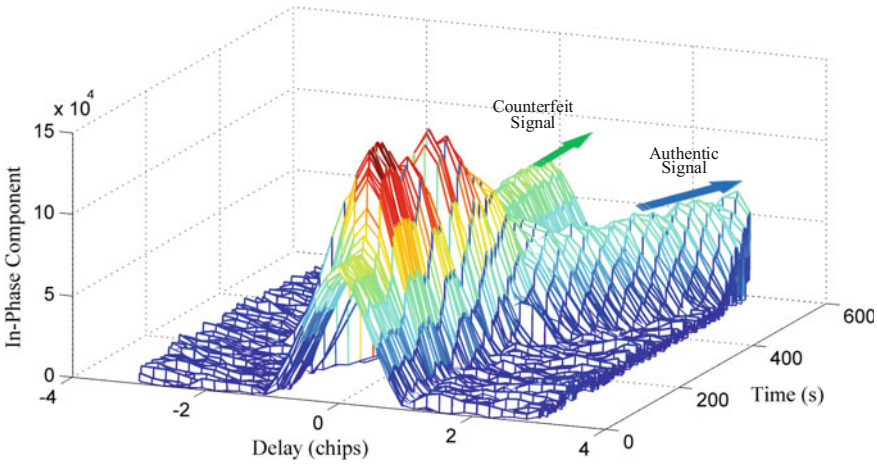

Fig. 6 The in-phase correlation component of spoofing scenario

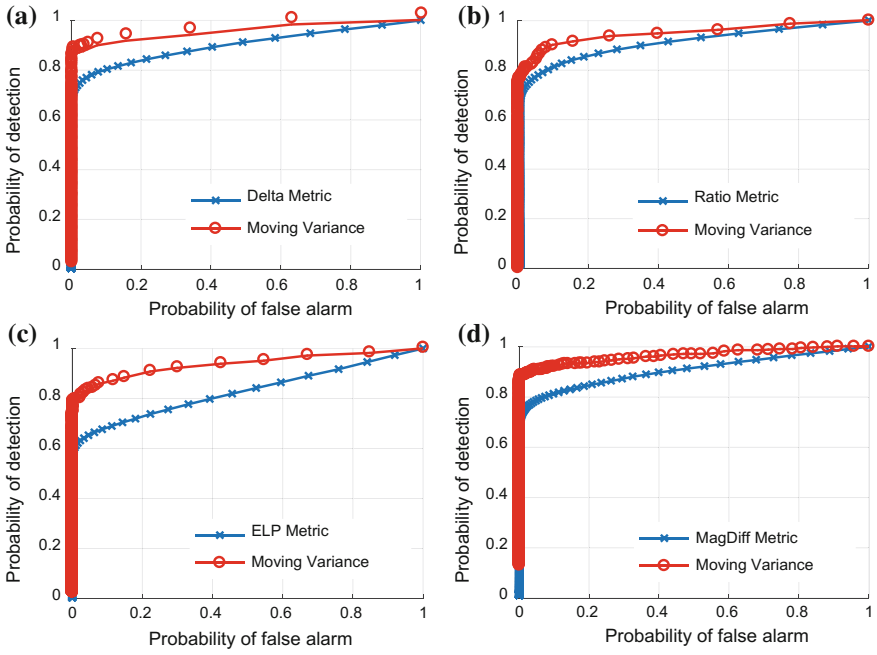

Fig. 7 Comparison of ROC curves for **a** Delta test metric, **b** Ratio test metric, **c** ELP test metric and **d** MagDiff test metric over the dataset created with the SPIRENT simulator

5 Conclusions

This paper has developed a new SQM-based anti-spoofing technique. It calculates the moving variance instead of raw metric values to perform spoofing detection. Four different SQM metrics have been considered and the performance of the proposed method has been evaluated using the dataset collected by SPIRENT simulators. Results show that, compared with the basic SQM method, this enhanced method has higher ROC performance for all the four metrics. Particularly when Pfa is 0.1, the Moving variance-based method with the window time of 1 s increases the probability of detection from an average value of 0.8–0.9, which demonstrates the effectivity of the proposed method.

As multipath has quite similar effect with a spoofing attack in the correlation domain, the next step of the research will be focused on how to distinguish spoofing from multipath in terms of moving variance-based SQM method and a more detailed performance analysis should be given.

Acknowledgements The work of C. Sun was also supported by the China Scholarship Council with No. 201606020020.

References

1. Jafarniajahromi A, Broumandan A, Nielsen J, Lachapelle G (2012) GPS vulnerability to spoofing threats and a review of antispoofing techniques. Int J Navig Obs 2012(9)
2. UT Austin Researchers Successfully Spoof an $80 million Yacht at Sea (2013) Retrieved 29 July 2013, from http://www.utexas.edu/news/2013/07/29/ut-austin-researchers-successfully-spoof-an-80-million-yacht-at-sea/
3. Kerns AJ, Shepard DP, Bhatti JA, Humphreys TE (2014) Unmanned aircraft capture and control via GPS spoofing. J Field Rob 31(4):617–636
4. Jahromi AJ, Broumandan A, Nielsen J, Lachapelle G (2012) GPS spoofer countermeasure effectiveness based on signal strength, noise power, and c/n0 measurements. Int J Satell Commun Netw 30(4):181–191
5. Dehghanian V, Nielsen J, Lachapelle G (2012) GNSS spoofing detection based on receiver c/n0 estimates. In: Proceedings of international technical meeting of the satellite division of the institute of navigation, pp 2878–2884
6. Psiaki ML, O'Hanlon BW, Bhatti JA, Shepard DP, Humphreys TE (2011) Civilian GPS spoofing detection based on dual-receiver correlation of military signals. In: Proceedings of the Institute of navigation GNSS, pp 2619–2645
7. Montgomery PY, Humphreys TE, Ledvina BM (2009) A multi-antenna defense: receiver-autonomous GPS spoofing detection. Inside GNSS 4(2):40–46
8. Konovaltsev A, Cuntz M, Haettich C, Meurer M (2013) Autonomous spoofing detection and mitigation in a GNSS receiver with an adaptive antenna array. In: Proceedings of ION GNSS+ 2013, pp 17–20
9. Humphreys TE, Ledvina BM, Psiaki ML, O'Hanlon BW, Kintner PM (2008) Assessing the Spoofing Threat: Development of a Portable GPS Civilian Spoofer. In: International technical meeting of the satellite division of the institute of navigation, pp 2314–2325
10. Wesson K, Rothlisberger M, Humphreys T (2012) Practical cryptographic civil GPS signal authentication. Navigation 59(3):177–193

11. Phelts RE (2001) Multicorrelator techniques for robust mitigation of threats to GPS signal quality. Doctoral dissertation, Stanford University
12. Manfredini EG, Dovis F, Motella B (2014) Validation of a signal quality monitoring technique over a set of spoofed scenarios. In: Satellite navigation technologies and european workshop on GNSS signals and signal processing, pp 1–7
13. Yang Y, Li H, Lu M (2015) Performance assessment of signal quality monitoring based GNSS spoofing detection techniques. CSNC 2015:783–793
14. Jahromi AJ, Broumandan A, Daneshmand S, Lachapelle G, Ioannides RT (2016) Galileo signal authenticity verification using signal quality monitoring methods. In: International conference on localization and GNSS, IEEE, pp 1–8
15. Pirsiavash A, Broumandan A, Lachapelle G (2016) Two-dimensional signal quality monitoring for spoofing detection. In: ESA/ESTEC NAVITEC 2016 conference
16. Wesson KD, Evans BL, Humphreys TE (2013) A combined symmetric difference and power monitoring GNSS anti-spoofing technique. In: Global conference on signal and information processing, IEEE, pp 217–220
17. Mubarak OM, Dempster AG (2010) Analysis of early late phase in single-and dual-frequency GPS receivers for multipath detection. GPS Solutions 14(4):381–388
18. Jovanovic A, Botteron C, Farine PA (2014) Multi-test detection and protection algorithm against spoofing attacks on GNSS receivers. In: Position, location and navigation symposium —PLANS 2014, 2014 IEEE/ION, pp 1258–1271

An Unfuzzy Acquisition Algorithm Based on Matched Filtering for BOC (n, n)

Xiyan Su, Fang Hao, Yuanfa Ji, Weimin Zhen, Baoguo Yu and Xingli Gan

Abstract Due to ambiguous acquisition caused by multiple peaks of auto-correlation function (ACF) of Binary Offset Carrier (BOC) modulation technology, an Odd-even Correlation Side-peak Cancellation Technology (OCSCT) is proposed in this paper. The side-peak elimination is obtained by multiplying and transforming the odd-even branch and received signals. In order to make full use of the received signals and further improve the acquisition performance, a corresponding optimization algorithm is put forward. The methods of BPSK-LIKE, ASPeCT and this paper are analyzed and compared. The results show that the proposed side-peak elimination method can effectively solve the acquisition ambiguity problem, and reduce the span of the main peak to half a chip, which further improves the acquisition probability. Compared with the ASPeCT method, the acquisition sensitivity, and the peak to average ratio is increased by 2 dB, 10%, respectively. While the calculation amount is reduced by about 50.11%.

Keywords Satellite navigation · Binary offset carrier · Unambiguous acquisition Side-peak elimination · Half chip

1 Introduction

Recently, with the rapid development of global satellite navigation technology, global positioning technology has not only applied to the military but also permeated in daily life. At present, many countries are developing their own global

X. Su · F. Hao · Y. Ji (✉)
Guangxi Key Laboratory of Precision Navigation Technology and Application, Guilin University of Electronic Technology, Guilin 541004, China
e-mail: jiyuanfa@163.com

W. Zhen
State Key Laboratory of Satellite Navigation System and Equipment Technology, Shijiazhuang 050000, China

B. Yu · X. Gan
Key Laboratory of Radio Wave Environment and Modeling Technology, Qingdao, China

J. Sun et al. (eds.), *China Satellite Navigation Conference (CSNC) 2018 Proceedings*, Lecture Notes in Electrical Engineering 498,
https://doi.org/10.1007/978-981-13-0014-1_21

satellite navigation systems such as the United States' GPS, European Galileo satellite navigation system and China's Beidou satellite navigation system, which may cause different satellite navigation systems and the same navigation system to send Multi-channel signals on the same frequency band. Therefore, in order to reduce the mutual interference between signals, a new signal modulation technique is proposed, that is, BOC modulation technique. Compared with traditional binary phase shift keying (BPSK) modulation, BOC modulation divides the spectrum of the signal into two parts symmetrically, reducing the interference between navigation signals and making full use of the bandwidth resources. Second, the correlation peak of the auto-correlation function becomes steeper, improving the acquisition performance. However, the disadvantage of BOC modulation is the occurrence of multiple secondary peaks on both sides of the main peak of the correlation peak, which may easily trap the secondary peak during acquisition and lead to acquisition ambiguity.

There are mainly two approaches to eliminate ambiguity. One is the frequency domain processing scheme, another one is the time-domain processing scheme. The typical frequency domain processing techniques, such as BPSK-LIKE method, considers received signal as two BPSK signal superposition, and each sideband can be regarded as a separate BPSK signal, respectively obtaining a single correlation peak, and then completely eliminate ambiguity. However, this method may stretch the signal peak span and lose the advantage of BOC signal. In addition, filtering the sideband not only increases the complexity, but also causes energy loss of the signal 0–3 dB. As for time-domain processing scheme, the auto-correlation edge peak cancellation technology (ASPeCT) is a typical processing options. Auto-correlation side-peak cancellation technology (ASPeCT) reduces edge peaks by algorithmic operations between the auto-correlation function (ACF) of the BOC signal and the cross-correlation function (CCF) between the BOC signal and the PRN sequence. This method effectively suppresses edge peaks, however, the elimination of multiple secondary peaks is not completely and only applicable to BOC (n, n) signals.

In this paper, the Odd-even Correlation Side-peak Cancellation Technology (OCSCT) and matched filtering methods are used to eliminate the ambiguity in the BOC signal in the frequency domain. The local code is stored in the acquisition module and sliding matched with the input signal for code phase. At a specific point of search frequency, every time take a correlate processing with local code when receiving a code phase of the input signal. Searching the code phase of the frequency point until received a complete code cycle [1]. Among them, the local BOC signal is divided into two branch signals, an odd signal and an even signal. The two are respectively associated with the received BOC (n, n) signals to obtain two symmetric correlation functions. The odd-even correlation function is then reconstructed based on the new reconstruction rule, by which the main peak span is reduced to half a chip and the side-peaks are completely eliminated while maintaining the narrowband correlation peak. This innovative odd-even correlation method can achieve better acquisition performance.

2 Algorithm Analysis

2.1 ACF Function of BOC Modulation Signals

The auto-correlation function (ACF) can be obtained by the correlation between the BOC signal and the sub-carrier modulated PRN sequence. The ACF for the BOC (1, 1) signal can be modeled as:

$$R_{BOC(1,1)}(\tau) = tri_0(\frac{\tau}{l}) + \frac{1}{2}tri_{\frac{1}{2}}(\frac{\tau}{l}) - \frac{1}{2}tri_{-\frac{1}{2}}(\frac{\tau}{l}) \tag{2.1}$$

where $R_{BOC(1,1)}(\tau)$ is ACF. τ is chip delay.$\frac{1}{2}tri_{\frac{1}{2}}(\frac{\tau}{l})$ represents the peak nearby $\frac{T_c}{2}$ (T_c is a pseudo code period) related peaks, 1/2 is the amplitude value. The auto-correlation curve of BOC (1, 1) signal and the local BOC sequence simulated with Matlab is illustrated in Fig. 1.

As can be seen from the figure, the auto-correlation function of the BOC signal has an obvious main peak and two secondary peaks. The GPS C/ A code has only one main peak, but the main peak span is twice that of the main peak of the BOC (1, 1) auto-correlation function.

2.2 Odd-Even Correlation Side-Peak Cancellation Technology(OCSCT) Acquisition Algorithm

2.2.1 Separation of $R_o(\tau)$ and $R_E(\tau)$ Functions

To solve the $R_o(\tau)$ and $R_E(\tau)$ functions, the odd branch signal and the even branch signal should be solved firstly. The odd signal and the even signal are separated by the local BOC signal.

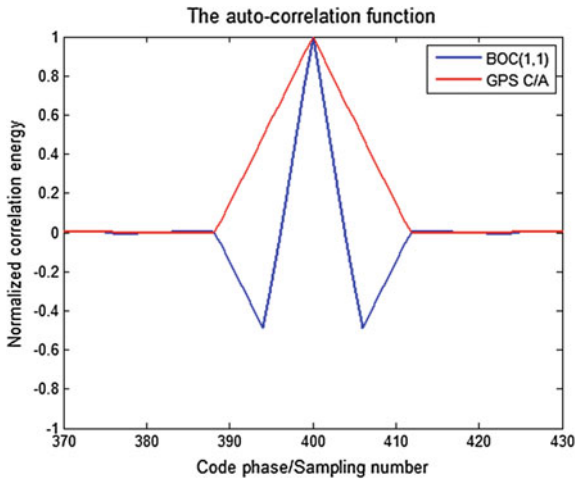

Fig. 1 BOC (1, 1) auto-correlation function

First, the mathematical model of local pseudo-random-noise code sequence is:

$$PRN(t) = \sum_{i=-\infty}^{\infty} C_i P_{T_C}(t - iT_C) \tag{2.2}$$

P_{T_C} is a rectangular pulse of period T_C and an amplitude of 1, T_C is the width of one chip, and C_i is the symbol of the chip, $C_i \in (-1, 1)$. The local sub-carrier mathematical model is:

$$s_{sc}(\mathrm{t}) = \sum_{j=0}^{M-1} d_j P_{T_{sc}}(\mathrm{t} - \mathrm{j}T_{sc}) \tag{2.3}$$

$P_{T_{sc}}$ is a rectangular pulse with a period of T_{sc}, that is, the width of one sub-carrier pulse, with an amplitude of 1. d_j is the pulse symbol of sub-carrier with the duration being T_{sc}, M is the total number of pulses in one PRN chip. For BOC (1, 1) signals, $d_j \in (-1, 1)$, $T_{sc} = \frac{T_c}{2}$, M = 2.

The local BOC baseband sequence is obtained by multiplying the local PRN code sequence with the local sub-carrier, that is,

$$s_{BOC}(\mathrm{t}) = \sum_{i=-\infty}^{\infty} C_i P_{T_C}(\mathrm{t} - \mathrm{i}T_C) \times \sum_{j=0}^{M-1} d_j P_{T_{sc}}(\mathrm{t} - \mathrm{j}T_{sc}) \tag{2.4}$$

Due to the strict synchronization of the sub-carriers with the local PRN sequences, Eq. (2.4) can be changed to

$$s_{BOC}(\mathrm{t}) = \sum_{i=-\infty}^{\infty} \sum_{j=0}^{M-1} C_i d_j P_{T_{sc}}(\mathrm{t} - iT_c - \mathrm{j}T_{sc}). \tag{2.5}$$

Then, based on the length of each PRN chip, the sub-carriers are divided into two equal parts according to the pulse duration of the sub-carriers. The first half of the chip and the second half of the chip patch zero to make up the odd branch BOC signal and the first half of the chip patch zero and the second half of the chip to make up the even branch BOC signal. Figure 2 is a partial figure of the generation of a BOC (1, 1) sequence.

BOC signal separation according to sub-carrier pulse duration can be expressed as:

$$s_n = s_n^o(\mathrm{t}) + s_n^e(\mathrm{t}) \tag{2.6}$$

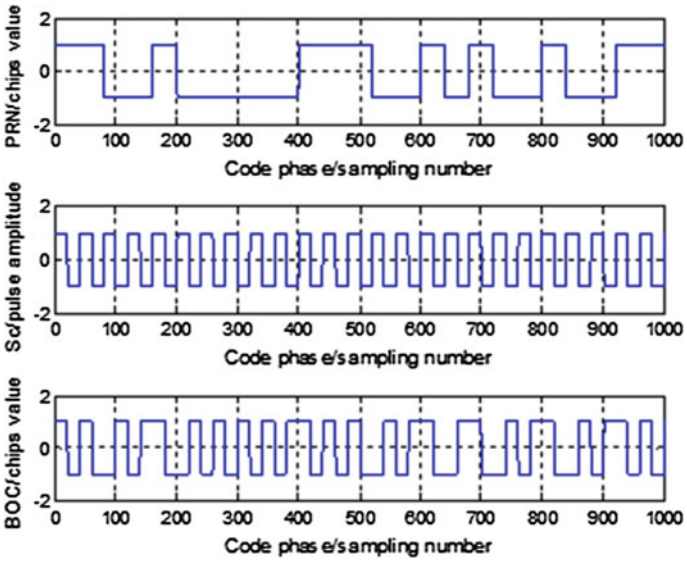

Fig. 2 The generation of a BOC (1, 1) sequence

$s_n^o(\mathrm{t})$ represents an odd part and $s_n^e(\mathrm{t})$ is the even part:

$$s_n^o(\mathrm{t}) = \sum_{\mathrm{i}=0}^{N_c-1} C_i P_{T_{SC}}(\mathrm{t} - iT_C) \tag{2.7}$$

$$s_n^e(\mathrm{t}) = \sum_{i=0}^{N_c-1} C_i P_{T_{SC}}(\mathrm{t} - \mathrm{i}T_C - T_{sc}) \tag{2.8}$$

N_c in the above formula is the number of chips in one cycle.

Suppose the signal of the input IF signal stripped by the carrier wave is $s_{\mathrm{iq}}(\mathrm{t})$. The output results of the integrator output of the local BOC odd branch signal and the even branch signal are as follows:

$$R_O(\tau) = \int_0^{T_S} s_{iq}(t)\, s_n^o(t+\tau)dt \tag{2.9}$$

$$R_E(\tau) = \int_0^{T_S} s_{iq}(t)\, s_n^{\mathrm{e}}(t+\tau)dt \tag{2.10}$$

Figure 3 is a partial view of a parity branch.

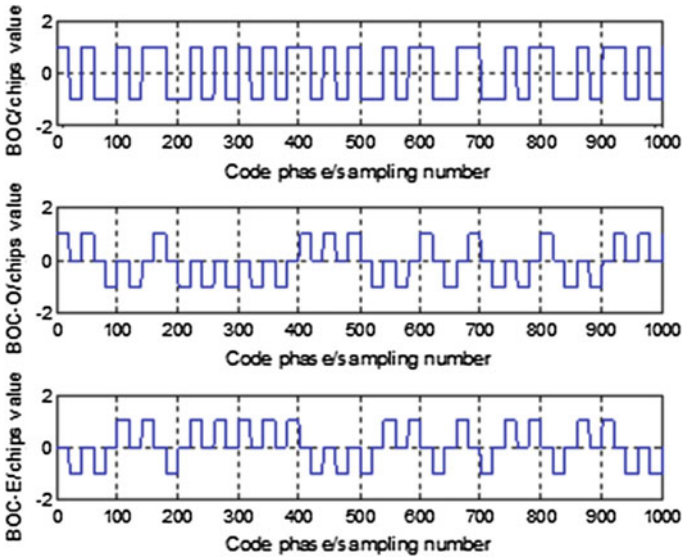

Fig. 3 The generation of the parity branch sequence

2.2.2 The Implementation of Acquisition Algorithm for OCSCT

Based on the SMF-FFT acquisition system, the Odd-even Correlation Side-peak Cancellation Technology acquisition algorithm is introduced, which is to replace the locally generated BOC code in the SMF-FFT acquisition system with the odd unit signal and the even unit signal, that is, to split the local BOC code into two parts: an even one and an odd one, which based on sub-carrier length. Two branch signals may be respectively correlate with the input signal and generate an odd branch correlation function and an even branch correlation function. Under the new reconstruction rules proposed in this paper, the side peaks can be well eliminated, and the final detection results in a clear detection variable. The concrete implementation schematic diagram is shown in Fig. 4.

The satellite signals acquisition is essentially a three-dimensional search process on PRN code, frequency and time [2]. For a satellite, a certain carrier and code phase signal is generated on artificially-set acquisition strategy, and then perform carrier stripping and correlate action with real signal [2]. If the relevant acquisition peak value exceeds the acquisition threshold after the correlate action, then the acquisition is successful. At this time, the carrier and code phase can be considered as the carrier and code phase of the actual signal, that is, the best estimation process of the carrier and code phase of the actual signal [2].

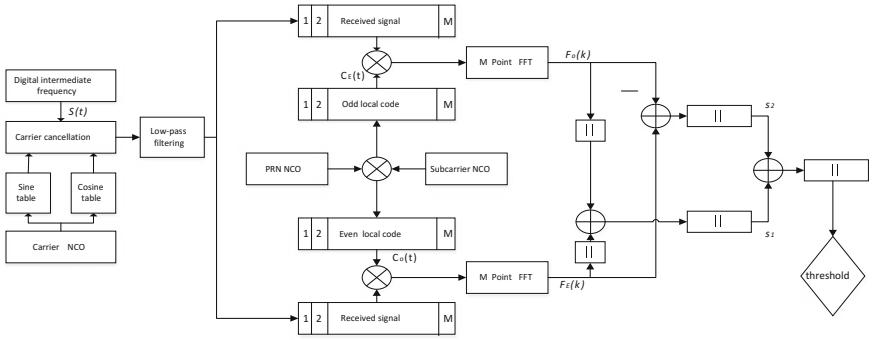

Fig. 4 SMF-FFT combined with OCSCT

Down-converted digital IF signal can be expressed as

$$y_t = Ad(\mathrm{t})c(\mathrm{t})sc(\mathrm{t})cos(\omega_0 t + \varphi) + n(\mathrm{t}) \tag{2.11}$$

where A is the signal amplitude, c(t) is the spreading code modulated on the carrier, $d(\mathrm{t})$ is the navigation message modulated on the carrier, ω_0 and φ are angular frequency and the initial phase of the signal respectively. n(t) is the Gaussian white noise with mean zero and the variance is σ_n^2, $X \sim N(0, \sigma_n^2)$. Because the noise and signals have weak cross-correlations, so the noise is not to be considered for the time being for the convenience of derivation.

Using quadrature demodulation method and separating carriers to demodulate signal, then I and Q branch signals are obtained after low-pass filter:

$$\mathrm{s(t)} = \mathrm{i(t)} + \mathrm{jq(t)} \approx Ad(\mathrm{t})\, c_i(\mathrm{t})sc(\mathrm{t})\, e^{j(\omega_d \mathrm{t} + \varphi_d)} + jAd(\mathrm{t})\, c_q(\mathrm{t})sc(\mathrm{t})\, e^{j(\omega_d \mathrm{t} + \varphi_d)} \tag{2.12}$$

ω_d is Carrier frequency difference and φ_d is initial phase difference in Eq. 2.12.

Match filter with total sample point L, Doppler frequency shift f_d, sample period T_s which perform match filtering action can obtain the odd and even branch match-filtering correlate value.

Then carry out subsection of two branch signals, $L = MX$, M taps, the length of each segment is X, and the correlation value of m segment matching filter is

$$\begin{aligned} S^o_{PMF}(\mathrm{k}) &= Ad(\mathrm{t})\, R^o_m(\tau)\, \frac{\sin(\pi f_d \,\mathrm{L}\, T_s)}{\sin(\pi f_d\, T_s)} \\ &\quad \times e^{-j(2\pi f_d(\mathrm{L} - mX - 1)\, T_s\, +\, \varphi_d)} \quad (\mathrm{m} = 1, 2, 3 \ldots, \mathrm{M}\ - 1) \end{aligned} \tag{2.13}$$

$$S_{PMF}^{E}(\mathrm{k}) = Ad(\mathrm{t})\, R_{m}^{E}(\tau) \frac{\sin(\pi f_d \,\mathrm{L}\, T_s)}{\sin(\pi f_d\, T_s)} \times e^{-j(2\pi f_d(\mathrm{L}-mX-1)\, T_s\, +\, \varphi_d)} \quad (\mathrm{m} = 1, 2, 3\ldots, \mathrm{M}\ -1) \tag{2.14}$$

$R_o(\tau)$ is the correlation function of an odd branch signal and the received signal, and $R_E(\tau)$ is the correlation function of an even branch signal and the received signal.

M point fast Fourier transform, and the output value is:

$$F_O(k) = \sum_{m=0}^{\mathrm{M}-1} S_{PMF}^{O}(m)\, e^{-j\frac{2\pi mk}{M}} \tag{2.15}$$

$$F_E(k) = \sum_{m=0}^{\mathrm{M}-1} S_{PMF}^{E}(m)\, e^{-j\frac{2\pi mk}{M}} \tag{2.16}$$

Finally, the output of SPMF-FFT acquisition is:

$$F_O(k) = Ad(\mathrm{t})\, R_{m}^{o}(\tau) \frac{\sin(\pi f_d\, X\, T_s)}{\sin(\pi f_d\, T_s)} \times \frac{\sin(\frac{\pi k}{M} - \pi f_d\, X)M}{\sin(\frac{\pi k}{M} - \pi f_d\, X)} \times e^{-j[2\pi f_d(\mathrm{L}-1)\, T_s\, +\frac{2\pi k}{M}(M-1)-2\pi f_d(M-1)X\, +\, \varphi_d]} \tag{2.17}$$

$$F_E(k) = Ad(\mathrm{t})\, R_{m}^{E}(\tau) \frac{\sin(\pi f_d\, X\, T_s)}{\sin(\pi f_d\, T_s)} \times \frac{\sin(\frac{\pi k}{M} - \pi f_d\, X)M}{\sin(\frac{\pi k}{M} - \pi f_d\, X)} \times e^{-j[2\pi f_d(\mathrm{L}-1)\, T_s\, +\frac{2\pi k}{M}(M-1)-2\pi f_d(M-1)X\, +\, \varphi_d]} \tag{2.18}$$

Then acquisition algorithm for OCSCT is implemented:

$$F_1 = |F_O(K)| + |F_E(K)| \tag{2.19}$$

$$F_2 = |F_O(K) - F_E(K)| \tag{2.20}$$

$$F = |F_1 - F_2| \tag{2.21}$$

2.3 Simulation Results of Matlab

Based on the Matlab platform, the IF of the input signal is 4.092 MHz, the sampling rate is 16.368 MHz, the setting code phase offset is 5 chips and the Doppler is 1100 Hz. The BOC (1, 1) signal acquisition results are obtained by using the OCSCT and matched filtering method. The results are shown in Fig. 5.

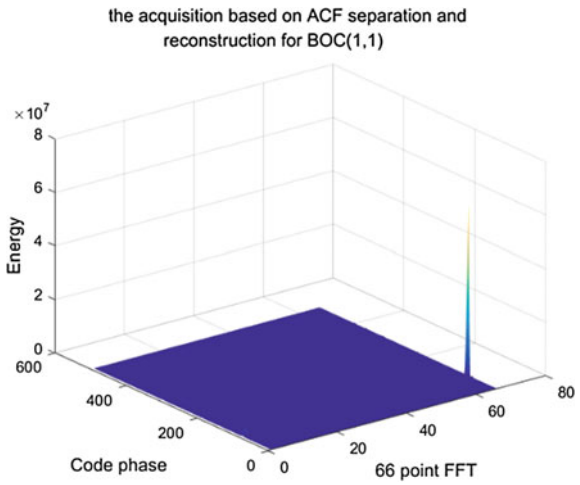

Fig. 5 SPMF+FFT acquisition results diagram

Figure 6 is an odd-even correlation function normalized two-dimensional simulation results.

$|F_O| + |F_E|$ has multiple peaks, one of the main peaks is at the code phase $\tau = 81$ and two side peaks. The code phases of the two peaks of $|F_O - F_E|$ correspond to the code phases of the two side peaks of $|F_O| + |F_E|$, and the zero point between the two peaks of $|F_O - F_E|$ and the main peak of $|F_O| + |F_E|$ lie in the same phase . The span of the main peak of F is 8 points, that is, half chip width. The acquisition probability is greatly improved.

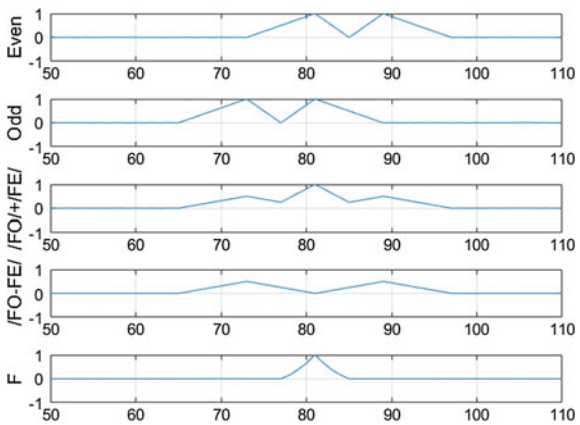

Fig. 6 Reconstruction of odd and even branch correlation function

3 Detection Performance Analysis

The input BOC signal can be expressed as:

$$s(t) = Ad(\mathrm{t}-\tau)c(\mathrm{t}-\tau)sc(\mathrm{t}-\tau)cos(2\pi(f_{IF}+f_d)\mathrm{t}+\varphi)+n(\mathrm{t}) \tag{3.1}$$

A is the amplitude of the input signal, c(t) is the PRN code, d(t) is the navigation data, τ is the code delay of the input signal, f_d is the Doppler frequency of the input signal, is the intermediate frequency and sc(t) is the sub-carrier.

Separate carriers and multiply the odd and even branch signals:

$$S_E(t) = S(t)C_E(t)[\cos[2\pi(f_{IF}+f_D)t]+\cos[2\pi(f_{IF}+f_D)T_s]]+n_E \tag{3.2}$$

$$S_O(t) = S(t)C_O(t)[\cos[2\pi(f_{IF}+f_D)t]+\cos[2\pi(f_{IF}+f_D)T_s]]+n_O \tag{3.3}$$

The navigation data d(t) is a constant and can be omitted here. $C_E(t)$ indicates the local even branch signal and $C_O(t)$ represents the local odd branch signal. Then carry out the coherent integration, the output is

$$\bar{S}_E = AR_E(\Delta\tau)T_s \sin c(\pi\Delta f_d T_s)\times[\cos(\pi\Delta f_d T_s)+\sin(\pi\Delta f_d T_s)]+N_E \tag{3.4}$$

$$\bar{S}_O = AR_O(\Delta\tau)T_s \sin c(\pi\Delta f_D T_s)\times[\cos(\pi\Delta f_D T_s)+\sin(\pi\Delta f_D T_s)]+N_O \tag{3.5}$$

N_O, N_E are uncorrelated Gaussian white noise with the mean of zero and a variance of σ_n^2, $X\sim N(0,\sigma_n^2)$. The density function probability $P(n)$ is

$$P(n) = \frac{K_0(|n|/\sigma^2)}{\pi\sigma^2} \tag{3.6}$$

$$\int_0^\infty t^\mu K_n(t)dt = 2^{\mu-1}\Gamma\left(\frac{\mu+n+1}{2}\right)\Gamma\left(\frac{\mu-n+1}{2}\right) \tag{3.7}$$

$K_n(t)$ is Modified Bessel function of the second kind, and $\Gamma(\cdot)$ is the Gamma function. The variance σ_n^2 is

$$\sigma_n^2 = \int_{-\infty}^{\infty} n^2 P_n(n)dn = 16\sigma^4 \tag{3.8}$$

The odd and even signals can obtain F_O and F_E via FFT, F can be obtained by OCSCT algorithm.

$$\begin{aligned} F &= \sum_{j=1}^{M} \left(|F_{E+O}|_j^2 - |F_{E-O}|_j^2 \right) \\ &= \sum_{j=1}^{M} \left(|F_E(k)|_j \times |F_O(k)|_j \right) + \sum_{j=1}^{M} \left(|F_E(k)|_j \times N_O \right) \\ &\quad + \sum_{j=1}^{M} \left(|F_O(k)|_j \times N_E \right) + \sum_{j=1}^{M} (N_E \times N_O)_j \end{aligned} \tag{3.9}$$

The noise term $\sum_{j=1}^{M} (N_E \times N_O)_j$ meets Gaussian distribution according to the Central Limit Theorem, and its variance is

$$\sigma_n^2 = 16M\sigma^4 \tag{3.10}$$

So F obeys Gaussian distribution.

Assume X_0 is the case that only noise presents in the received signal, and X_1 is the other case that both signal and noise are exist. These two cases are analyzed here.

The signal processing can be deemed as linear operation of Gaussian noise under condition X_0. The detection variable v is subject to Rayleigh distribution, and its mean value and variance are

$$\mathrm{E}(v) = 0 \tag{3.11}$$

$$\mathrm{D}(v) = 16M\sigma^4 \tag{3.12}$$

And the Probability Density Function (PDF) is

$$f_n(v) = \frac{v}{{\sigma_n}^2} e^{-\frac{v^2}{2{\sigma_n}^2}} \tag{3.13}$$

The false alarm probability P_{fa} corresponds to threshold value V_t is

$$P_{fa} = \int_{V_t}^{\infty} f_n(v)dv = \int_{V_t}^{\infty} \frac{v}{{\sigma_n}^2} e^{-\frac{v^2}{2{\sigma_n}^2}} dv = e^{-\frac{{v_t}^2}{2{\sigma_n}^2}} \tag{3.14}$$

that is,

$$v_t = \sigma_n \sqrt{-2 \ln P_{fa}} \tag{3.15}$$

linear operation can be regarded as the adding Gaussian noise under condition X_1, The detection variable obeys Rician distribution, its PDF $f_s(v)$ is

$$f_s(v) = \frac{v}{{\sigma_n}^2} \exp\left\{ -\frac{v^2 + a^2}{2\sigma_n^2} \right\} I_0\left(\frac{av}{\sigma_n^2}\right) \tag{3.16}$$

where $v \geq 0$, $I_0(\cdot)$ is Modified Bessel function of the first kind. the signal power of v is a^2, and noise power is $2\sigma_n^2$, hence, the signal-to-noise ratio (SNR) is

$$SNR = \frac{a^2}{2\sigma_n^2} \tag{3.17}$$

The mean value and average power of v can be obtained according to Eq. 3.16

$$E(v) = \sqrt{\frac{\pi}{2}} \sigma_n L_{1/2}(-\frac{a^2}{2\sigma_n^2}) \tag{3.18}$$

$$E(v^2) = a^2 + 2\sigma_n^2 \tag{3.19}$$

Lagrange polynomials $L_{1/2}(\cdot)$ is

$$L_{1/2}(x) = e^{\frac{x}{2}}((1-x) I_0(-\frac{x}{2}) - x I_1(-\frac{x}{2})) \tag{3.20}$$

$I_1(\cdot)$ is first order Modified Bessel function of the first kind.
The detection probability (real alarm probability) P_d is

$$P_d = \int_{V_t}^{\infty} f_s(v) dv \tag{3.21}$$

Suppose the coherent integration time is 1 ms, the false alarm probability is $P_{fa} = 10^{-3}$. There is no code phase and carrier frequency error. The detection probability of the proposed method, BPSK method and ASPeCT method varies with the CNR of input signal, as shown in Fig. 7. The ASPeCT method can detect the signal of CNR about 42 dBHz. The OCSCT method can detect the signal of CNR about 40 dBHz, and the acquisition sensitivity increases about 2 dBHz. This is due to the fact that there is no secondary peak at all for the parity-dependent method to affect acquisition.

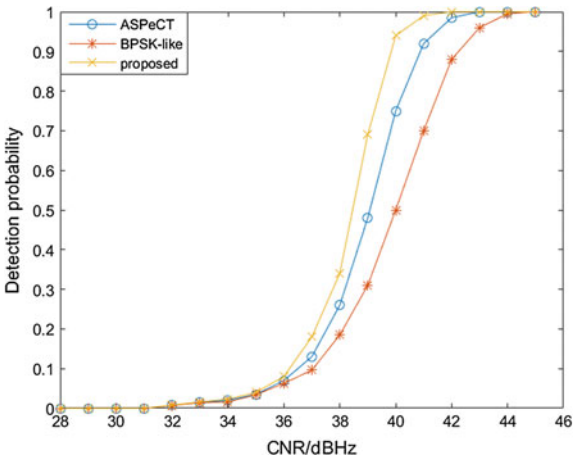

Fig. 7 The detection probability of three methods

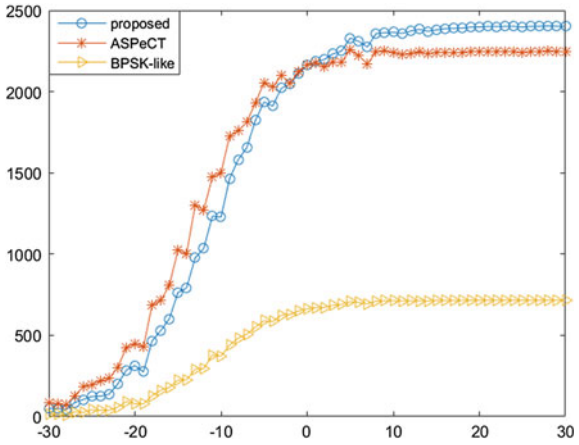

Fig. 8 Three methods of peak to average comparison diagram

In detection performance, the peak to average ratio is also a feasible way to measure the performance of the acquisition, that is, the ratio of the maximum peak to the average. As shown in Fig. 8, the new method is significantly higher than the other two methods, 10% and 200%, which greatly improves the acquisition performance.

It can be seen from the above performance analysis that the OCSCT is significantly superior to the ASPeCT and BPSK-LIKE methods, regardless of the detection probability or the peak-to-average ratio.

4 Computational Complexity Analysis

Taking the parameters set in 3.3 as an example, the matched filter acquisitions the frequency interval of 500 Hz, the frequency range is ±10 kHz and the code phase is set as 1 sample point. The FFT parallel code phase acquisition frequency interval is 500 Hz and the frequency range is ±10 kHz. SPMF-FFT acquisition is divided into 66 segments, each segment length of 248 points, and the code phase is also set to 1 sample point.

Matched filter acquisition requires the search unit number is $(\frac{2\times 10{,}000}{500}+1)\times 1023 = 41,943$, which is 41,943 correlated operations. The sampling points are used to calculate in the paper, so the matched filter acquisition needs $1023 \times 16 = 16,368$ multiplication operation and 16367 addition operations to complete a correlation operation. So matched filter acquisition requires $41,943 \times 16,368 = 686,523,024$ multiplications and $41,943 \times 16,367 = 686,481,081$ additions.

FFT parallel code phase acquisition method adopts parallel code phase search method. It needs two times FFT operation, one IFFT operation, which means a total of three times FFT operations. Completion of a 16,368 point FFT requires computation of complex additions:

$$N \lg_2^N = 16,368 \lg_2^{16,368} = 229,152$$

Complex multiplication:

$$\frac{N}{2} \lg_2^N = \frac{16,368}{2} \lg_2^{16,368} = 114,576$$

In general, a complex multiplication can be divided into four real multiplications and three real additions, and one complex addition can be turned into two real additions.

SPMF-FFT acquisition computation can be divided into two parts, namely, the serial partial matching filter and the FFT operation, so the required total addition amount is

$$(66 \lg_2^{66} \times 5 + 66 \times 248) \times 16,368 = 300,559,857$$

The total number of multiplications required is

$$(33 \lg_2^{66} \times 4 + 66 \times 248) \times 16,368 = 280,970,796$$

It can be seen that the required addition of SPMF-FFT acquisition method is only 43.7% of the matched filter algorithm and the multiplication is 40.9%, which greatly reduces the difficulty of hardware design and the resources consumed.

The sampling rate is 16.368 MHz on the premise of using the SPMF-FFT acquisition method. The OCSCT method proposed in this paper undergoes $2 \times 16,368 = 32,736$ multiplication and $2 \times 16,366 = 32,732$ addition, and then undergoes two FFTs and 198 complex additions to obtain the detection quantity. The ASPeCT method needs to go through $4 \times 16,368 = 65,472$ multiplications and $4 \times 16,367 = 65,468$ additions, and then twice FFT operations, $2 \times 66 = 132$ complex multiplication and 66 complex additions to obtain quantity. The BPSK-LIKE method needs to go through $4 \times 16,368 = 65,472$ multiplications and $4 \times 16,367 = 65,468$ additions, and then twice FFT operations, $2 \times 66 = 132$ complex multiplication and 66 complex additions to obtain quantity. Assuming that one multiplication and one addition last for the same time, it can be seen that in the case of no two FFT, 33,128 additions and 32,736 multiplications are performed by the OCSCT method. The BPSK-LIKE and ASPeCT methods performs 65,996 additions and 66,000 multiplications. Therefore, the computation of the proposed method is 49.89% of the ASPeCT and BPSK-LIKE methods. However, the BPSK-LIKE method uses a large number of filters compared to the ASPeCT method, achieving more complicated implementation.

5 Conclusion

Based on the fast acquisition, a new method of eliminating the BOC (n, n) signal ACF ambiguity based on the odd-even correlation is proposed by using the fast acquisition method of the serial partial matching filter combined with FFT to improve the system speed, reducing the use of system resources and completely eliminating side peaks during fast acquisition while preserving the narrow correlation of the main peak. In this paper, the performance of detection, the amount of computation and the simulation show that compared with other two traditional acquisition methods, the proposed method is less computationally intensive and has better performance of acquisition, which can cope with the existing signal acquisition.

References

1. Xu F, Qiu L, Wang Y (2013) APSK signal mixed blind equalization method. J Chongqing Univ Posts Telecommun (Natural Science Edition) 25(5):605–610
2. Ceng Q, Tang L, Wang Q et al (2013) GPS L1/L2C signal fast acquisition algorithm based on segmented FFT. J China Inertial Technol 21(5):640–645
3. Zhang H, Ba X, Chen J et al (2017) The fuzzy acquisition technology for BOC (m, n) signals. Acta Aeronaut Acta 38(4):217–226
4. Ji Y, Liu Y, Zhen W, Sun X, Yu B (2017) An unambiguous acquisition algorithm based on unit correlation for BOC (n, n) signal. IEICE Trans Commun (08)

5. Signal Acquisition in GALILEO Receiver (2006) Beijing Aeronaut Astronaut 32(6):687–690 (in Chinese). Received Revised Online Accepted Abstract
6. Chen Z, Dong DD (2015) Improved algorithm of pseudo-code acquisition based on PMF. J Harbin Univ Commer (Natural Sciences Edition) 31(4):447–485
7. Lohan ES (2006) Statistical analysis of BPSK-like techniques for the acquisition of Galileo signals. J Aerosp Comput Inf Commun 3(5):234–243
8. Julien O, Macabiau C, Cannon ME, Lachapelle G (2007) ASPeCT: unambiguous sine-BOC (n, n) acquisition/tracking technique for navigation applications. Aerosp Electron Syst IEEE Trans 43(1):150–162
9. Sousa FMG, Nunes FD (2013) New expressions for the autocorrelation function of BOC GNSS signals. Navig-J Inst Navig 60(1):1–9
10. Chen HH, Ren JW, Yao ML (2012) Side-peak cancellation general framework designed for BOC signals unambiguous processing. J Astronaut 33(11):1646–1653
11. Pan Y, Zhang TQ, Li JW (2013) Unambiguous algorithm analysis for BOC signal based on PCF. Sci Technol Eng 13(28) (Oct 2013)
12. Xie G (2009) Principles of GPS and receiver design. Publishing House of Electronics Industry, Beijing, pp 349–389
13. Guo SC, Chen AL, Han FJ (2010) Pseudo-noise code acquisition method based on partial matched filter. Electron Inf Warfare Technol 25(2):20–23
14. Yang P, Guo LL, Yan HQ (2012) A method of synchronization capture using match filter based on FPGA in spread spectrum communication system. Tech Autom Appl 31(12):28–31

Part II
Satellite Orbit and Satellite Clock Error

A New Satellite Clock Offsets Prediction Method Based on the IGS RTS Products

Hongzhou Yang, Yang Gao, Liang Zhang and Zhixi Nie

Abstract Satellite clock offsets prediction is crucial for GNSS applications and has attracted much attention from the GNSS community. However, previous satellite clock offset prediction was mostly carried out based on the IGS rapid products or IGS final products. Limited by the long latency of the above products, the predicted satellite clock offset cannot meet the requirements of high precision real-time applications such as real-time PPP. In this paper, a new satellite clock offsets prediction method based on the IGS real-time service (RTS) products is proposed, in which the satellite clock drifts from the broadcast ephemeris are used as the pseudo-observations. For the polynomial part, only clock drift and clock drift rate are estimated while the latest clock offsets are directly applied. The GPS satellite clock offsets are predicted all together by considering the datum change involved in the IGS combination process, which is observed in the IGS01 clock products. The results show that the standard deviations of the predicted IGS01 products are 1.408 ns and 0.079 ns for the traditional method and proposed method, respectively. For the IGS03 products, the corresponding standard deviations are 0.243 ns and 0.080 ns. The proposed satellite clock offset prediction method provides better clock prediction performance based on the IGS RTS products.

Keywords IGS RTS · Satellite clock offset prediction · Clock drift constraint

1 Introduction

To meet the increasing demands from real-time users, the IGS Real-Time Service (RTS) has been available to public users since April 2013 [1]. These corrections are disseminated via a networked transport of RTCM via Internet protocol (NTRIP) [7]. Abundant researches have been carried out about the real-time PPP with different

H. Yang (✉) · Y. Gao · L. Zhang · Z. Nie
Department of Geomatics, University of Calgary, 2500 University Drive NW, Calgary, AB T2N 1N4, Canada
e-mail: honyang@ucalgary.ca

J. Sun et al. (eds.), *China Satellite Navigation Conference (CSNC) 2018 Proceedings*, Lecture Notes in Electrical Engineering 498,
https://doi.org/10.1007/978-981-13-0014-1_22

real-time products [2, 3, 6, 8, 9]. Satellite clock prediction is of great importance to real-time GNSS applications [4, 5]. However, most research to date is based on the IGS final products or other products with long latency. This makes the predicted clocks generated from those products cannot meet the requirement of high precision real-time applications.

In this paper, a new satellite clock offsets prediction method will be proposed based on the IGS RTS clock products. In the new method, the satellite clock drifts from the broadcast ephemeris will be applied as pseudo-range observations in the estimation, and only clock drifts and clock drift rates are estimated in the polynomial fitting while the latest clock offsets are directly applied. Last but not least, the clock offsets of all GPS satellites will be predicted together.

The paper will be organized as follows: Sect. 2 briefly introduces the current atomic clocks onboard the GPS satellites and the IGS RTS products; Sect. 3 evaluates the stability of the IGS RTS clock products by differencing between consecutive epochs, meanwhile, the Allan Variance is applied for the analysis. In Sect. 4, the proposed prediction method is introduced in details. The comparison results between existing satellite clock offset prediction model and the newly proposed prediction model are presented in Sect. 5. Finally, the conclusions are summarized in Sect. 6.

2 Current Active Clocks Onboard GPS Satellites and IGS RTS Clock Products

The current active atomic clocks onboard GPS satellites can be divided into four types regarding the orbit block type and clock type as shown in Table 1.

As we can see from Table 1, there are 12 active Rubidium (Rb) clocks onboard the GPS IIR satellites, which accounts for the largest clock group and followed by 10 active Rb clocks onboard the GPS IIF satellites. While 7 active Rb clocks are onboard the GPS IIR-M satellites, only two active Caesium (Cs) clocks are onboard the GPS IIF satellites. The ages of the total 31 active clocks up to August of 2017 are given in Fig. 1. The oldest clock group is the active Rb clocks onboard the GPS IIR satellites and the second oldest clock group is the 7 active Rb clocks onboard the GPS IIR-M satellites. The active clocks onboard the GPS IIF satellites are the youngest.

Table 1 Block-type, PRN and clock type of GPS (up to 21st Aug 2017)

	Satellite PRN
IIR/Rb	16,28,20,19,2,21,11,22,18,14,23,13
IIR-M/Rb	31,7,12,29,17,5,15
IIF/Rb	30,25,26,27,1,6,3,10,9,32
IIF/Cs	24,8

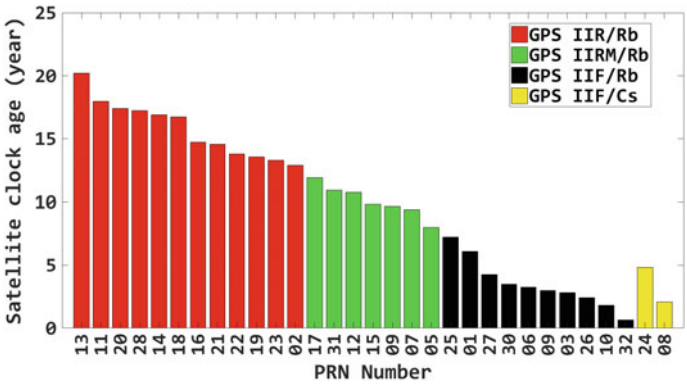

Fig. 1 Ages of the GPS satellite clocks up to 21st Aug 2017

The IGS RTS corrected orbits are expressed in the International terrestrial reference frame 2014 and the commonly used IGS RTS products are listed in Table 2.

The IGS01 and IGC01 products are the single-epoch combination solutions produced using software developed by ESA/ESOC and the orbit reference points for the two products are different. The update rates are as high as 5 s for both orbit and clock corrections. The IGS02 and IGS03 products are combination solutions using Kalman filter approach with orbit and clock update rates at 60 and 10 s correspondingly. The contents of the satellite clock corrections include Delta Clock C0, Delta Clock C1 and Delta Clock C2, and they are applied using the following equations,

$$\begin{aligned} \delta C &= C_0 + C_1(t - t_0) + C_2(t - t_0)^2 \\ t_{satellite} &= t_{broadcast} + \frac{\delta C}{speed\ of\ light} \end{aligned} \tag{1}$$

Table 2 Technical contents of IGS RTS

	Combination	Orbit ref point	RTCM messages
IGS01	Single-epoch	APC	GPS code bias (5), Combined orbit and clock corrections (5)
IGC01	Single-epoch	CoM	GPS orbit and clock corrections (5), GPS code bias (5)
IGS02	Kalman filter	APC	GPS orbit corrections (60), clock corrections (10), GPS code bias (10)
IGS03	Kalman filter	APC	GPS orbit corrections (60), GPS clock corrections (10), GPS code bias (10), GLONASS orbit corrections (60), GLONASS clock corrections (10), GLONASS code bias (10)

Note CoM: Center of Mass; APC: Antenna Phase Center

where δC is the correction for the clock offset based on the broadcast navigation message, t is the calculation epoch, t_0 the reference epoch, C_i is the polynomial term, $t_{satellite}$ is the precise clock offsets, $t_{broadcast}$ is the clock offsets calculated from the broadcast ephemeris.

3 Stability Analysis of the IGS RTS Clock Products

To investigate the stability of the IGS RTS clock products, the raw real-time satellite clock offsets on July 7th of 2017 from IGS01 and IGS03 are collected and stored. Furthermore, four satellites with different types of clocks are selected to present all the 31 active clocks onboard the GPS satellites, namely PRN 16, PRN 31, PRN 30 and PRN 8. The raw satellite clock offsets are shown in Fig. 2. As we can see that, the IGS03 clock products are more stable than the IGS01 clock products and the linear trend is obvious. While for IGS01 clock products, there are lots of jumps for all types of clocks.

The mean offset rates for the above four satellites clocks are calculated as well by differencing satellite clock offsets between consecutive epochs, which are shown in Fig. 3. The IGS final clock products with a sample rate of 30 s for the same day are downloaded and used here as the reference. The magnitude of the mean offset rates for IGS01 can be more than one ns per second due to the jump, which are

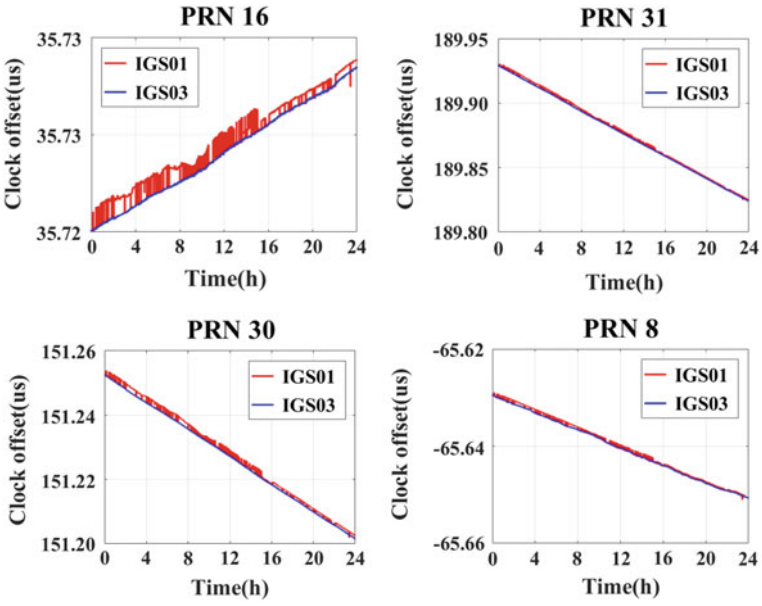

Fig. 2 IGS01 (in red) and IGS03 (in blue) satellite clock offsets for PRN 16, PRN 31, PRN 30 and PRN 8 with one-day length

much larger than that of IGS03. The mean offset rates for the IGS03 and the IGS final clock products have the same magnitude at a level of several tens ps per second. Meanwhile, another phenomenon needs to be mentioned is that the big jumps for different satellites seem to happen at the same time, which may due to different strategies adopted for IGS clock combination.

Additionally, the Allan Variance is applied to analyze the stability of different clock products. The Allan Variances of the PRN 16, PRN 31, PRN 30 and PRN 8 from IGS01, IGS03 and IGS final products are shown in Fig. 4. It is obvious the IGS01 has the poorest stability while the performance of the IGS03 and the IGS final products are quite similar when comes to the Allan Variance. The Cs clock onboard GPS IIF satellites shows the poorest stability among the four selected satellite clocks.

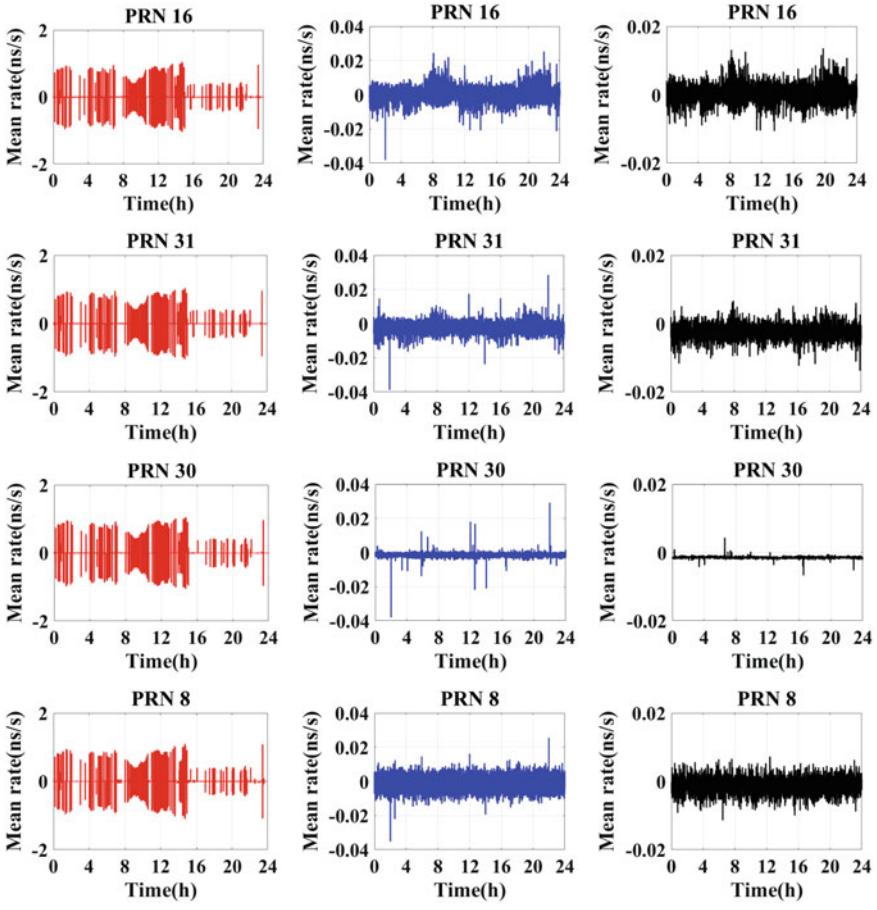

Fig. 3 Mean clock offset rate of IGS01, IGS03 and IGS final products

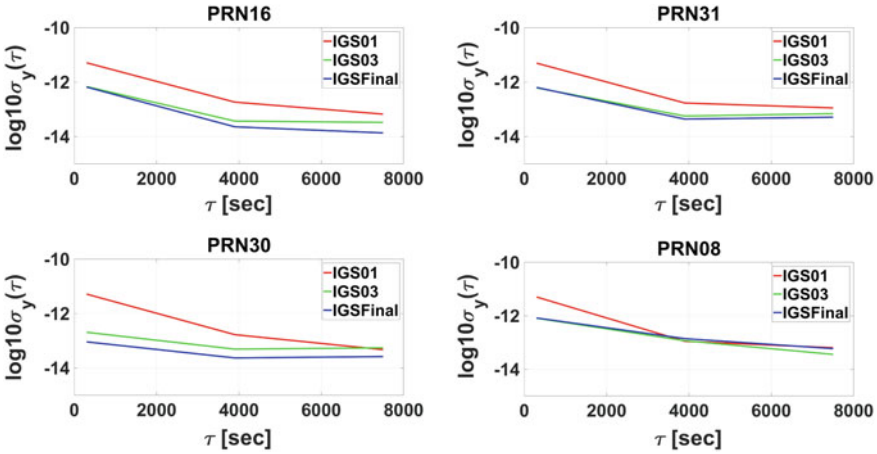

Fig. 4 Allan Variance of PRN 16, PRN 31, PRN 30 and PRN 8 from IGS01, IGS03 and IGS final products

4 A New Satellite Clock Offset Prediction Method

The traditional satellite clock offset prediction equations can be expressed as follows:

$$x(t) = x_0 + y_0 t + \frac{z_0 t^2}{2} + \sum_{l=0}^{k} A_l \sin(\omega t + \varphi_l) + \Psi(t) \tag{2}$$

where x_0, y_0 and z_0 are the polynomial parameters associated with the time offset, the drift and the drift rate, k denotes the number of periodic terms, A_l denotes the amplitude, ω is the frequency, φ_l is the phase shift of the sinusoidal variation and $\Psi(t)$ is the generic random noise process. In the traditional model, the satellite clock offsets are assumed as a combination of the polynomial and periodic terms, which fits well with IGS final products and IGS03 products. For products with lots of jumps such as the IGS01, the traditional prediction model may not fit anymore. The satellite clock offset can be expressed in another form,

$$Offset_{AC}^{Sat}(t) = O_{AC} + I_{AC}^{Sat} + V_{AC}^{Sat}(t) \tag{3}$$

where O_{AC} denotes the AC specific time offset, I_{AC}^{Sat} is the initial satellite specific clock offset and $V_{AC}^{Sat}(t)$ is the clock offset at the time t. The above equation is primarily used for the combination of different RTS products or the accuracy evaluation process.

For each satellite clock offsets, the proposed model can be expressed as follows,

$$\begin{aligned} x(t)^j - x_{tref}^j &= y_0^j t + \frac{\beta z_0^j t^2}{2} + \sum_{l=0}^{k} A_l^j \sin(\omega t + \varphi_l^j) + \Psi(t)^j, \\ y_{Brdc}^j &= y_0^j, \qquad \delta^{j2} \end{aligned} \tag{4}$$

where y_{Brdc} is the satellite clock drift from the latest broadcast ephemeris; x_{tref} is the satellite clock offset from RTS; δ is the standard deviation term for y_{Brdc}; j denotes the GPS PRN number. The other parameters have the same denotes as Eq. 2. Note that the first polynomial term is not included in the estimation and the satellite clock offsets at the epoch closest to current are directly used. The clock drifts from the broadcast ephemeris are used in the estimation process as pseudo-observations. Furthermore, all the satellite clocks are predicted together and the whole prediction model for all satellites can be expressed as,

$$\begin{aligned} x(t)^1 - x_{tref}^1 &= O_{AC} + y_0^1 t + \frac{\beta z_0^1 t^2}{2} + \sum_{l=0}^{k} A_l^1 \sin(\omega t + \varphi_l^1) + \Psi(t)^1, \\ y_{Brdc}^1 &= y_0^1, \qquad \delta^{1^2} \\ x(t)^2 - x_{tref}^2 &= O_{AC} + y_0^2 t + \frac{\beta z_0^2 t^2}{2} + \sum_{l=0}^{k} A_l^2 \sin(\omega t + \varphi_l^2) + \Psi(t)^2, \\ y_{Brdc}^2 &= y_0^2, \qquad \delta^{2^2} \\ x(t)^j - x_{tref}^j &= O_{AC} + y_0^j t + \frac{\beta z_0^j t^2}{2} + \sum_{l=0}^{k} A_l^j \sin(\omega t + \varphi_l^j) + \Psi(t)^j, \\ y_{Brdc}^j &= y_0^j, \qquad \delta^{j^2} \end{aligned} \tag{5}$$

where O_{AC} is added in the estimation process and assumed to be the same for all satellite clocks at the same epoch and varies over different epochs. In the filter, satellite clock offsets are modelled by two polynomial parameters and 2 * k periodic parameters (k is usually set as 2 or 4). O_{AC} is estimated as random walk parameters. When the total epoch number is m and satellite number at an epoch in the RTS products is n, then the filter can be solved as long as the following requirement can be met.

$$m \times n > m + n \times (2 + 2 \times k) \tag{6}$$

For example, if k equals to 4 and n equals to 31, the epoch number will be larger than 11. For IGS01 and IGS03, the minimum lengths for fitting are 11 * 5 and 11 * 10 s, respectively.

5 Experiments and Results

In this Section, several experiments are carried out to analyze and evaluate the proposed satellite clock offsets prediction model. Firstly, the variance for clock drifts from the broadcast ephemeris as the pseudo-observation is investigated. Afterwards, the predicted results with the proposed model are compared with IGS final products.

5.1 Evaluation of Satellite Clock Drifts from Broadcast Ephemeris

The proper weighting for broadcasted satellite clock drifts as pseudo-observations is important in the new method. To investigate the accuracy of the satellite clock drift from broadcast ephemeris, the broadcast ephemeris and IGS final clock products of whole 2016 year are downloaded. The satellite clock drifts calculated from the IGS final clock products are used as a reference. The satellite clock drifts from both broadcast ephemeris and IGS final clock products for PRN 16, PRN 31, PRN 30 and PRN 8 are shown in Fig. 5. As we can see that, the satellite clock drifts have linear trend for PRN 16, PRN 31 and PRN 30. PRN 30 has the largest drift rate and the clock drift over one year is more than four ps per second. For GPS PRN 8, the satellite clock drift doesn't have linear trend and the value ranges in −2 ps per second to −1 ps per second. Meanwhile, the satellite clock drifts from broadcast ephemeris can keep the same value for several days.

Afterwards, the difference between satellite clock drifts from the broadcast ephemeris and IGS final clock products are calculated over the year 2016 and the Root Mean Square errors (RMS) are computed accordingly for each satellite, which is shown as Fig. 6. As we can see that, the RMS for most satellite clocks are smaller than 0.05 ps per second and the average RMS of all satellites is 0.05 ps per second. The RMS for GPS PRN 8, PRN 24, PRN 28 and PRN 32 are larger than 0.1 ps per second. The RMS for each satellite will be used for the weighting of the satellite clock drift from broadcast ephemeris as a pseudo-observation.

5.2 Satellite Clock Offset Prediction with the New Method

In this part, the satellite clock offset prediction will be carried out with the proposed method. The satellite clock products of IGS01, IGS03 and IGS final on July 7th of 2017 are used for prediction. More specifically, satellite clock products of a very short period, from 12:30 to 12:36 pm are used for fitting, which are shown as following Fig. 7.

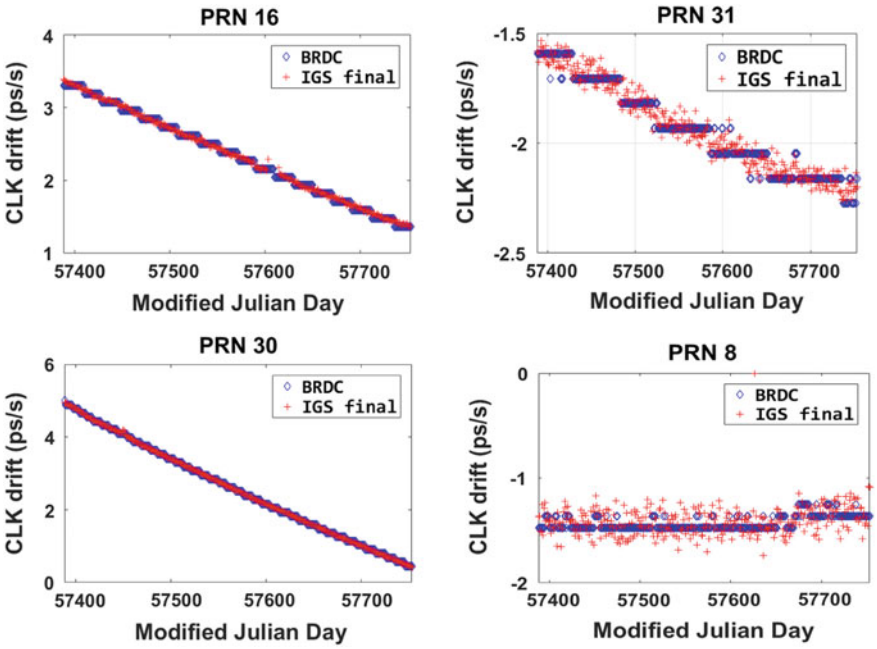

Fig. 5 Satellite clock drifts of PRN 16, PRN 31, PRN 30 and PRN 8 from broadcast ephemeris and IGS final clock products over 2016

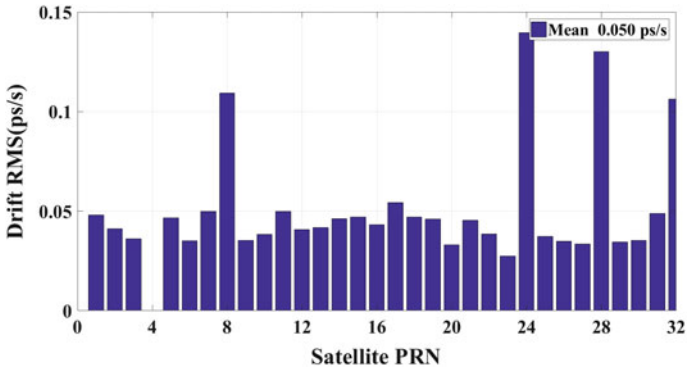

Fig. 6 Satellite clock drift RMS of broadcast ephemeris for all GPS satellites

As we can see from Fig. 7, the IGS03 and IGS final products have quite similar trend over time and the bias between them is at ns level for four selected satellites clocks. The satellite clock offsets from IGS01 showed different characters and jumped a lot during the very short period of 6 min. The epoch number of the IGS01, IGS03 and IGS final products are 72, 36 and 12 correspondingly due to different sample rates at 5, 10 and 30 s. Afterwards, the satellite clock offsets

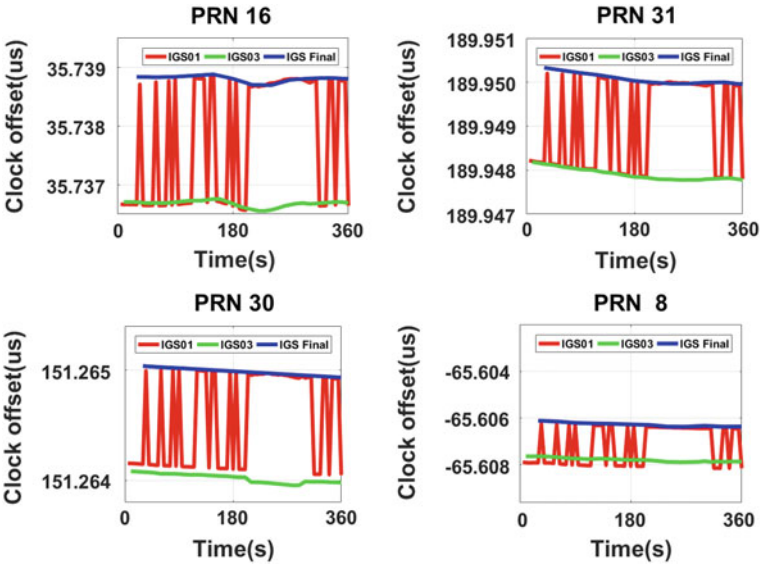

Fig. 7 Satellite clock offsets of IGS01, IGS03 and IGS final products for fitting

prediction with the traditional method and proposed method are carried out for IGS01, IGS03 and IGS final. The satellite clock drifts of IGS01, IGS03 and IGS final derived from the traditional method are shown in Fig. 8.

As we can from Fig. 8, the derived satellite clock drifts for IGS03 and IGS final with the traditional satellite clock offset prediction method are similar, which are quite different to the IGS01 resutls. The main reason for the differences is the jumps in the satellite clock offsets from IGS01. For some satellites such as PRN 1 and PRN 5, the clock drift differences between IGS01 and IGS final can be more than

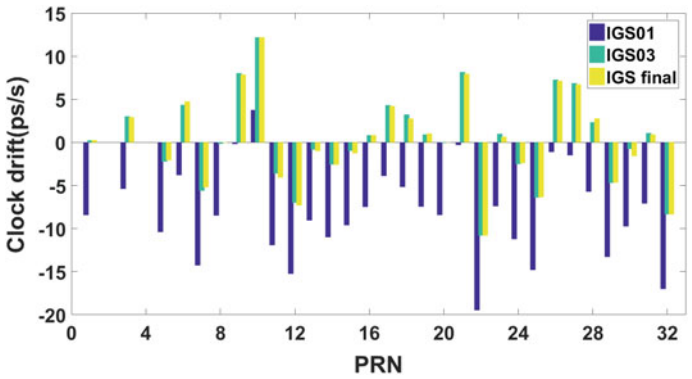

Fig. 8 Satellite clock drifts obtained with traditional prediction method for IGS01, IGS03 and IGS final products

five ps per second, which equals to 4.5 ns difference with prediction over half hour. Furthermore, the fitting residuals of IGS01, IGS03 and IGS final products are shown as Fig. 9. As we can see that, the residuals of IGS01 products are very large, which accounts for poor internal reliability of the traditional prediction model. While the residuals of IGS03 and IGS final products are much smaller and the values are less than one ns.

The proposed new prediction method is then applied and the satellite clock drifts are shown as following Fig. 10.

We can see that, the derived satellite clock drifts from IGS01, IGS03 and IGS final products with the proposed new method are quite similar with each other. The fitting residuals are shown in Fig. 11. The residuals for IGS01 are at the same level with IGS03 and IGS final products, and all the residuals are less than 0.3 ns. When compared to the traditional method, the residuals for IGS01 are much smaller with the new prediction method, which indicates the internal reliability of the proposed new method is much better.

Apart from above comparisons regarding the internal reliability, the extern reliability is also briefly investigated here. Both the traditional prediction method and the proposed prediction method are applied for the same data of IGS01 and IGS03 products. The reference is the IGS final clock products and the standard deviation of the predicted satellite clocks over ten minutes are shown in Fig. 12.

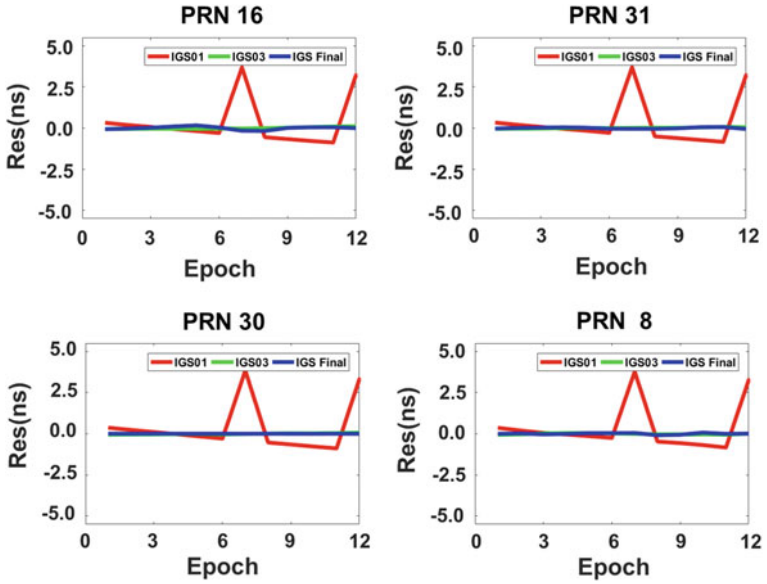

Fig. 9 Residuals of satellite clocks of PRN 16, PRN 31, PRN 30 and PRN 8 after fitting with the traditional method for IGS01, IGS03 and IGS final products

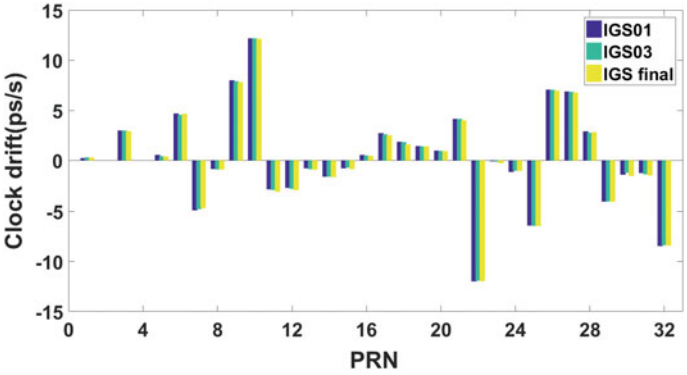

Fig. 10 Satellite clock drifts obtained with proposed prediction method for IGS01, IGS03 and IGS final products

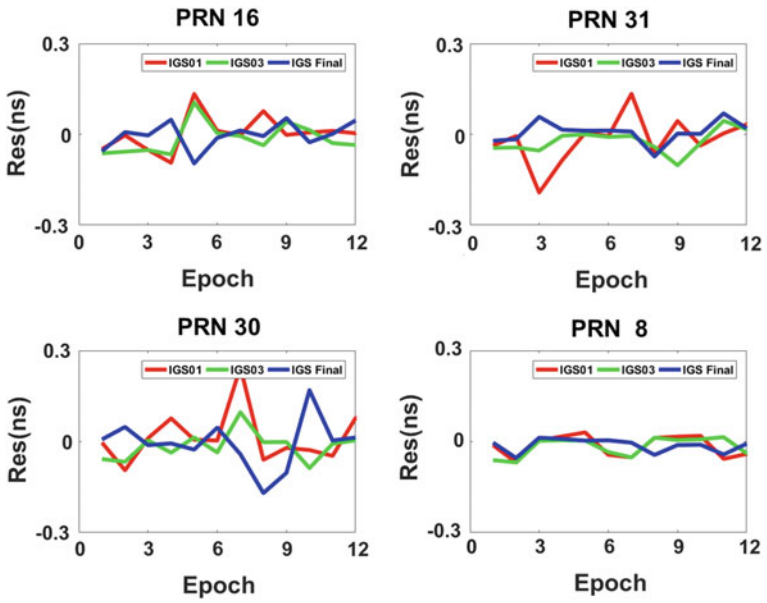

Fig. 11 Residuals of satellite clocks of PRN 16, PRN 31, PRN 30 and PRN 8 after fitting with the new prediction method for IGS01, IGS03 and IGS final

As we can see, the improvement for IGS01 is obvious for all the satellites. The improvements can be more than 2 ns for some satellites such as PRN 5 and PRN 12. The average standard deviation of the traditional method for IGS01 is 1.408 ns while that with the proposed new method is 0.079 ns. When comes to IGS03, the average standard deviation of the traditional method is 0.243 ns and that with the proposed new method is 0.080 ns. Thus, the external reliability of the proposed method is also proved.

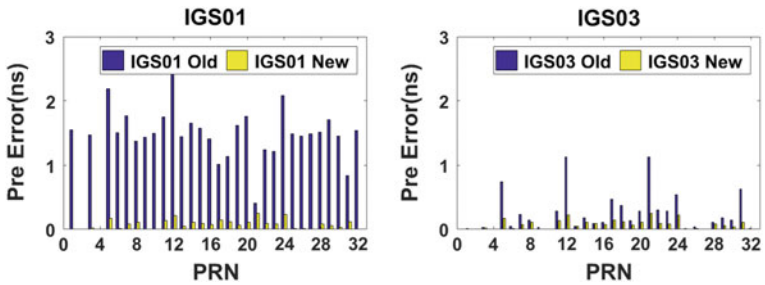

Fig. 12 Comparison of the proposed (new) and traditional (old) method for satellite clock offset prediction with IGS01 and IGS03 products

6 Conclusions

A new satellite clock offset prediction method based on the IGS RTS is proposed in this paper. The IGS RTS combined clock products are firstly investigated regarding stability. The results show the stability of IGS03 is similar to IGS final clock products and the mean clock offset rate between consecutive epochs is at several tens ps per second level. The IGS01 show obvious jump over time and the mean clock offset rate between consecutive epochs can be around one ns. Meanwhile, those jumps for different satellite clocks occurred at similar epoch which may due to the datum change in the combination process. Afterwards, the new satellite clock offset prediction method is introduced, in which all the active GPS satellite clocks are predicted together and one common parameter for all satellite clocks is added for every epoch. The satellite clock drifts from broadcast ephemeris are used as pseudo-observations in the estimation process and the weighting is based on the comparison with IGS final clock products. The average RMS of satellite clock drifts for satellites from broadcast ephemeris is 0.05 ps per second when the IGS final clock products are used as the reference. Finally, the comparison is carried out between the proposed satellite clock offset prediction method and the traditional method. Both the internal and external reliability are investigated and compared. The residuals with traditional method for IGS01 can reach several ns while those with proposed method are less than 0.3 ns. The standard deviation for predicted IGS01 products are 1.408 ns and 0.079 ns with proposed method and tradition method. For IGS03, the values are 0.243 ns and 0.080 ns correspondingly. In a word, the proposed satellite clock offsets prediction method shows better performance with IGS RTS products.

Acknowledgements The first author would thank for the support from the China Scholarship Council and the IGS is appreciated for providing the RTS products and final products.

References

1. Caissy M et al (2012) The international GNSS real-time service. GPS World 23(6):52–58
2. Gao Y, Chen K (2004) Performance analysis of precise point positioning using rea-time orbit and clock products. J Glob Position Syst 3(1&2):95–100
3. Gao Y, Zhang W, Li Y (2017) A new method for real-time PPP correction updates. Int Assoc Geodesy Symp :0939–9585
4. Huang G, Zhang Q (2012) Real-time estimation of satellite clock offset using adaptively robust Kalman filter with classified adaptive factors. GPS Solutions 16(4):531–539
5. Huang GW, Zhang Q, Xu GC (2014) Real-time clock offset prediction with an improved model. GPS Solutions 18(1):95–104
6. Li X et al (2015) Accuracy and reliability of multi-GNSS real-time precise positioning: GPS, GLONASS, BeiDou, and Galileo. J of Geodesy 89(6):607–635. Available at: http://dx.doi.org/10.1007/s00190-015-0802-8
7. Weber G, Dettmering D, Gebhard H (2005) Networked transport of RTCM via internet protocol (NTRIP). In: A Window on the future of geodesy. Springer, Berlin, pp 60–64
8. Yang H, Gao Y (2017) GPS satellite orbit prediction at user end for real-time PPP system. Sensors 17(9):1981
9. Yang H, Xu C, Gao Y (2017) Analysis of GPS satellite clock prediction performance with different update intervals and application to real-time PPP. Surv Rev :1–10

Study on Solar Radiation Pressure Model Considering the Yaw Attitude of the BDS

Kewei Xi, Xiaoya Wang and Qunhe Zhao

Abstract The solar radiation perturbation is an important factor affecting the accuracy of satellite orbit, it related to the satellite attitude and satellite radiation characteristics. The special constellation of Beidou navigation system lead to a difference attitude control with GPS/GLONASS, therefore, the traditional solar radiation pressure model can not meet the pressure of IGSO/MEO high precision orbit determination during the satellite attitude switching. It is necessary to establish a suitable high precision pressure model in Beidou navigation system. The thesis establish a new model which based on the BOX-WING model and also considering about radiation model parameters change during satellite attitude switch, the applicability and accuracy of the model was verified by measured data of Beidou tracking network(form MGEX). The results show that compared to the BERN model, IGSO and MEO orbit residuals improve the accuracy of 10–30% during the attitude switching period. Compared with the GBM final orbit, the residual values decreased. Meanwhile, in orbit prediction, the residual error of long arc prediction is significantly decreased.

Keywords Solar radiation pressure model · Beidou navigation system
Yaw attitude · Orbit determination

1 Introduction

The solar radiation perturbation is one of the most important factors affecting the accuracy of satellite orbit determination, the maximum level of acceleration can reach to 1e-8 according to the orbit height and the intrinsic characteristics of

K. Xi (✉) · X. Wang · Q. Zhao
Shanghai Astronomical Observatory, Chinese Academy of Sciences,
Shanghai, China
e-mail: xkw@shao.ac.cn

K. Xi · X. Wang · Q. Zhao
University of Chinese Academy of Sciences, Beijing, China

J. Sun et al. (eds.), *China Satellite Navigation Conference (CSNC) 2018 Proceedings*, Lecture Notes in Electrical Engineering 498,
https://doi.org/10.1007/978-981-13-0014-1_23

different radiation pressure. The effect of pressure perturbation influence on navigation satellite orbit including photon, satellite attitude control error, parameter changes in optical properties of the surface of the planet, solar radiation constant and the change of quality of satellite [1, 2]. Because there is a strong correlation between the influence factors and the parameters, it's difficult to use a simple model to accurately describe the characteristics of pressure, so the study of solar radiation model has become an important work in the way of high precision orbit determination.

The traditional solar radiation model is mainly of experience model which based on a long time observed data in large range observation network. The establishment of the BERN series model has tremendous improve the accuracy of GPS satellite precision orbit determination. In order to meet the demand of satellite navigation tasks, it must be ensure that the solar panel is perpendicular to the sun, at the same time as the downlink antenna is as close as possible perpendicular to the ground. The way to solve the problem is according to the satellite sensor and satellite orbit attitude to adjustment the yaw angle, which is called yaw-steering mode; when the sun angle is less than a certain angle, the satellite will shift control strategy, it gives priority to ensuring the alignment of downlink antenna, thus the yaw angle is fixed to zero, which is called orbit-normal mode. For the BDS constellation, Geosynchronous Earth Orbit (GEO) satellite always keep in the orbit-normal mode, Inclined Geosynchronous Satellite Orbit (IGSO) and Medium Earth Orbit (MEO) using combination of yaw-steering and orbit-normal, the Satellite attitude mode can switching within a year at least two times. If the influence of attitude switching is not considered properly, it will lead to a decline in the accuracy of satellite orbit [3–5]. According to the research of Guo Jing et al., The approximate condition of BDS satellite attitude switching is that when the sun angle is less than 4°, the satellite attitude is converted to orbit-normal. Until the sun angle is greater than 4°, the orbit-normal will change to the yaw-steering [6, 7].

The related research shows that it can basically meet the requirement of precision orbit determination when using BERN model for BDS in yaw-steering. However, due to the satellite's characteristics and constellation differences, the accuracy of orbit determination will decrease significantly. The solar radiation perturbation error is mainly due to solar radiation model does not estimate the corresponding changes between the orbit-normal and yaw-steering as soon as possible. Considering the construction of BDS constellation is not complete and the limited factors such as network data tracking, a physical solar radiation pressure model with the BDS attitude control strategy differences was established based on the Box-wing model. Compared with the BERN model, the new model takes into account the structural characteristics and the yaw information. It can reflect changes of satellite area by using the subdivision body modeling area element. It can be better at reaction radiation characteristics and reflect the pressure force of the continuous variable.

2 BDS Solar Radiation Model

According to the principles of the Box-wing model, the navigation satellite can be decomposed into 7 parts with different shapes, including the axis of X/Y/Z forward or backward and the solar panels [8–10]. The solar radiation perturbation for the area differential element can be represented as following:

$$d\overrightarrow{F} = -\lambda \frac{\Phi_0}{c}\left(\frac{AU}{r_{ss}}\right)\cos\theta \quad dA\left\{\begin{array}{l} 2v\left[\mu\cos\theta + \frac{1-\mu}{3}\right]\hat{n} \\ +(1-\mu v)\hat{p} \end{array}\right\} \tag{1}$$

where λ is the eclipse factor for satellite, Φ_0 is the solar radiation at distance of 1AU, c is speed of the light, r_{ss} is the distance from satellite to the sun, dA is the satellite area differential area element, $\hat{n}$, $\hat{p}$ respectively, is the area element normal vector and satellite direction vector to the sun, θ is the angle between the area element normal and the satellite to the sun, μ is specular reflection coefficient, v is reflectivity. m is the mass of the satellite, then the total acceleration is given by:

$$\overrightarrow{a}_{SRP} = \int_A \mathrm{d}\overrightarrow{F}/\mathrm{m} \tag{2}$$

When the satellite maintains its nominal attitude, the satellite antenna points to the center of the earth, and the solar panels is always point to the sun, it can be writen as:

$$\cos\varepsilon = -\cos\beta_0\cos\Delta\mathrm{u} \tag{3}$$

where ε is the angle between the satellite antenna to the earth center and the solar panel to the sun direction, β_0 is the angle of sun elevation, Δu is the angle between the satellites to earth. In order to remove the parameter correlation, the estimation parameters are combined in the process of partial derivative. Let $\alpha = (1-v)$, $\rho = \mu v$, $\delta = (1-\mu)v$. For the solar panels, there is $\cos\theta = 1$, then:

$$\frac{\partial \overrightarrow{a}_{SP}}{\partial\left(1+\rho+\frac{2}{3}\delta\right)} = -\lambda\frac{\Phi_0}{\mathrm{cm}}Asp\left(\frac{AU}{r_{ss}}\right)^2\hat{\rho} \tag{4}$$

For the satellite body in the +X bus surface direction, there is $\cos\theta = \sin\varepsilon$:

$$\frac{\partial \overrightarrow{a}_{+X_i}}{\partial(\alpha+\delta)} = -\lambda\frac{\Phi_0}{\mathrm{cm}}A_{+X_i}\left(\frac{AU}{r_{ss}}\right)^2\sin\varepsilon\left(\hat{\rho}+\frac{2}{3}\overrightarrow{e}_{+X}\right) \tag{5}$$

$$\frac{\partial \overrightarrow{a}_{+X_i}}{\partial(\rho)} = -\lambda\frac{\Phi_0}{\mathrm{cm}}A_{+X_i}\left(\frac{AU}{r_{ss}}\right)^2 2\sin^2\varepsilon\,\overrightarrow{e}_{+X} \tag{6}$$

In the direction of +Z bus surface, $\cos\theta = \cos\varepsilon$, then:

$$\frac{\partial \overrightarrow{a}_{+Z_i}}{\partial(\alpha+\delta)} = -\lambda\frac{\Phi_0}{\mathrm{cm}}A_{+X_i}\left(\frac{AU}{r_{ss}}\right)^2\cos\varepsilon\left(\overset{\wedge}{\rho} + \frac{2}{3}\overrightarrow{e}_{+Z}\right) \tag{7}$$

$$\frac{\partial \overrightarrow{a}_{+Z_i}}{\partial(\rho)} = -\lambda\frac{\Phi_0}{\mathrm{cm}}A_{+X_i}\left(\frac{AU}{r_{ss}}\right)^2 2\cos^2\varepsilon\overrightarrow{e}_{+Z} \tag{8}$$

For the BDS satellite, use the Box-wing model to calculate the prior value, adding five parameters of the ECOM model, and consider the yaw attitude of IGSO/MEO satellite to adjust the parameters of the radiation model, which is called SRPM model (Shao solar radiation pressure model, SRPM). It can be written as:

$$\overrightarrow{a} = a_{apri} + D(u)\overrightarrow{e}_D + Y(u)\overrightarrow{e}_Y + B(u)\overrightarrow{e}_B \tag{9}$$

where a_{apri} is calculated using the Box-wing model of the prior solar radiation pressure acceleration, u is the angle between satellite in the orbit plane and the midnight, $\overrightarrow{e}_D$ is the pressure in the direction from the sun to the satellite, $\overrightarrow{e}_Y$ the solar wing axis, $\overrightarrow{e}_B$ is the cross direction of the two directions, $D(u)$, $Y(u)$, $B(u)$ respectively, is the corresponding direction of acceleration which being estimated parameters and used to adjust the model. We need to pay attention to that when the satellite is in the orbit-normal mode, the DYB coordinate system need to rotation, then:

$$\begin{aligned}\overrightarrow{e}_{D'} &= \overrightarrow{\mathrm{e}}_{B'} \times \overrightarrow{\mathrm{e}}_{Y'}\\ \overrightarrow{\mathrm{e}}_{Y'} &= \overrightarrow{\mathrm{e}}_R\\ \overrightarrow{\mathrm{e}}_{B'} &= \overrightarrow{\mathrm{e}}_D \times \overrightarrow{\mathrm{e}}_{Y'}\end{aligned} \tag{10}$$

where $\overrightarrow{\mathrm{r}}$ is the satellite position in the ECI and $\overrightarrow{\mathrm{e}}_R = \frac{\overrightarrow{\mathrm{r}}}{\mathrm{r}}$.

3 Processing Strategy

In order to analyze the applicability and accuracy of the SRPM model in different yaw attitude, chose the observation data from 55 sites of MGEX tracking network to carry out the precise orbit determination experiment. In the three day arc length of orbit determination, pending track interval in the middle orbit arc, such as the orbit of the day of year 170 is determined using the observed data of 169/170/171. Considering errors include the phase correction of the earth tide, antenna pco and so on, the parameters of the satellite orbit and clock are estimated. The estimation strategy of the specific parameters is given in Table 1.

Table 1 Correction model and Parameter estimation strategy

	Parameter	Strategy	
Observation and correction model	Observation	LC + PC(UD)	
	Interval	300 s	
	Cut elevation	5°	
	Troposphere model	Dry and Wet	NIELL
		Map function	NIELL
	Phase center offset	IGS_08.ATX (update to 2017)	
	Phase winding correction	Model	
	Relativistic effect	IERS convention	
	Solid tide	IERS convention	
	Ocean tide	FES2004	
	Pole tide	IERS convention	
	Site coordinates(priori)	ITRF2008	
Parameter estimation	Orbit Sat clk Rec clk Ambiguity Site coordinates Srp model Eop Tropospheric parameter	Estimation Estimation Estimation Estimation Constraint (1 sigma) BERN or SRPM Estimate xp, yp, dxp, dyp, DUT1, UT1(1 sigma) 1 h per site	

Try to analysis each direction pressure perturbation variation of acceleration, and analyses the changes of pressure perturbation when the IGSO/MEO satellite attitude switching. The orbit determination accuracy of the SRPM model under the orbit-normal and yaw-steering conditions is studied and the results of the BERN model is also given as a comparison. The observation data of 170–185 in 2015 are selected for orbit determination. In the selected time period, C08, C11 and C12 are in the orbit-normal during the day of year 172–182. The rest of the satellites are in yaw-steering(without considering GEO satellites), the precise orbit determination results during the period of attitude switching was analyzed.

4 Orbit Determination Result

4.1 Pressure Variation

When analysis of the orbit accuracy, the satellite orbit coordinate system is convenient for described and analyzed. So the pressure perturbation acceleration in the RTN direction of the perturbation acceleration calculate by the SRPM was plotted

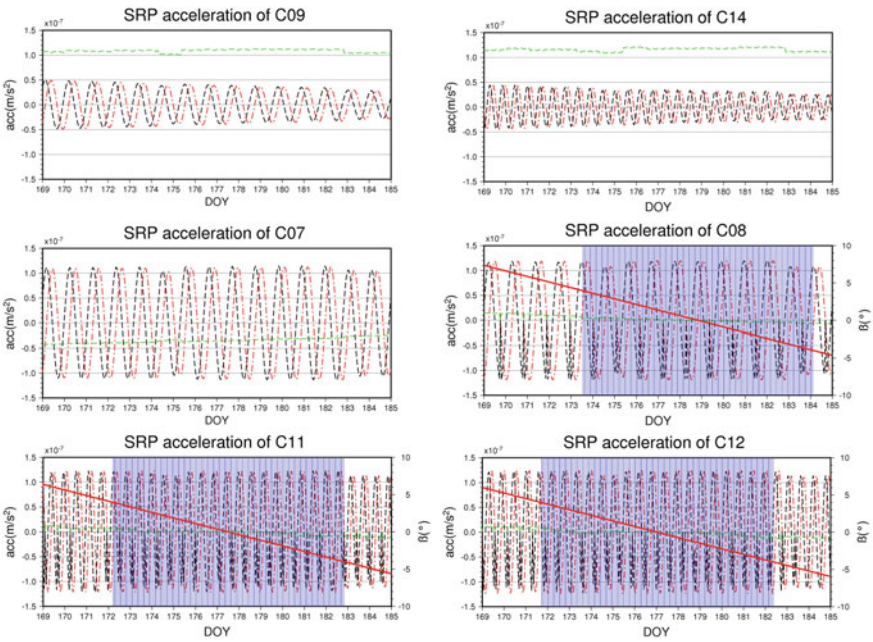

Fig. 1 Acceleration change during attitude conversion (The R/T/N was plotted in black/red/green dot line. It was covered by blue shadow and the sun elevation is drawn with red lines when the satellite in orbit-normal.)

in Fig. 1. The C06/C07/C09/C10/C14 is in the mode of yaw-steering and the C08/C11/C12 in the orbit-normal which was represented as light blue shadow.

It can be seen from the figure that satellite radiation pressure in each axial acceleration changes with a certain regularity. The pressure perturbation acceleration is in the level of 1e-7 of the satellites. It has a strong cyclical changes in R and T direction, and the amplitude changes with the height of the sun elevation; The direction of R and T amplitude of the amplitude decreases, and the acceleration in the direction of N is negative in the forward direction, and the value varies greatly. It is shown that there is a great difference the force between yaw-steering and orbit-normal.

4.2 Analysis

In order to analyze the orbit determination accuracy of BERN and SRPM models under yaw-steering/orbit-normal situation, the orbit calculated is compared with the precise orbit products of GFZ, and the three-dimensional RMS is plotted in Fig. 2.

It can be seen from Figure that when doy 170, all the satellites are in yaw-steering, the orbit determination accuracy of the SRPM model is better than the BERN model, and the orbit determination result is better than 0.2 m. The C11 and C12 are in the

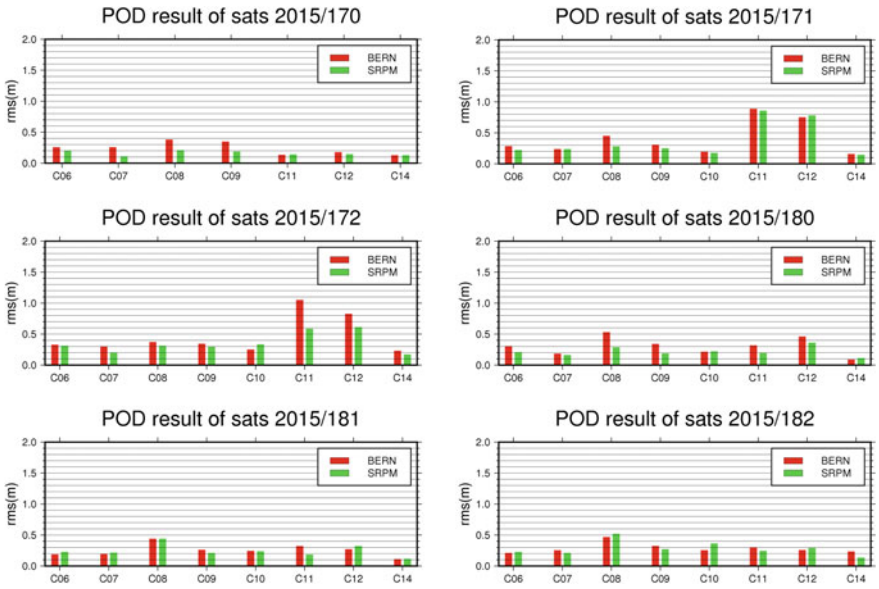

Fig. 2 Orbit determination precision during attitude conversion

direction of yaw attitude transformation during doy 171, the orbit determination accuracy of all two satellites has decreased, but the orbit determination results of other satellites remain stable. This shows that when the data of the tracking network is sufficient, the accuracy of the overall orbit determination can be stabilized during the attitude switching, and the satellite accuracy in the attitude switching will be reduced. The attitude conversion of satellite C11 and C12 at doy 172 shows that the residual value of the SRPM model is smaller, which lower than the BERN model 0.4 m and 0.2 m respectively. At the doy of 180/181, the satellite C08/C11/C12 is in orbit-normal, but the rest of the satellites are in yaw-steering. From the orbit determination residuals, the orbit residuals of SRPM at yaw-steering are smaller than that of BERN models, and the overall performance is better than that of 0.5 m. It is obvious that the orbit determination results for satellites are smaller when the yaw-steering. However, the orbit determination residuals of many satellites are smaller by using BERN models, the reasons for that should be further studied.

The accuracy of orbit determination can be reflected by the overlapped arcs, where gives out the three dimensional RMS information of two models overlapped for 2 days in the BERN and SRPM of two models, as shown in Fig. 3.

From Fig. 3, we can see that IGSO satellite residual error of overlapped arc is smaller than that of BERN model during the yaw-steering, which can reduce 0.2 m. While the MEO satellite performs better under the BERN model. The C11 and C12 satellites have higher accuracy and can maximum 1 m reduction in the SRPM model during the attitude switching. It can make sure the overlapped better than 0.5 m and avoid the significantly descend of orbit accuracy during the autitude switch.

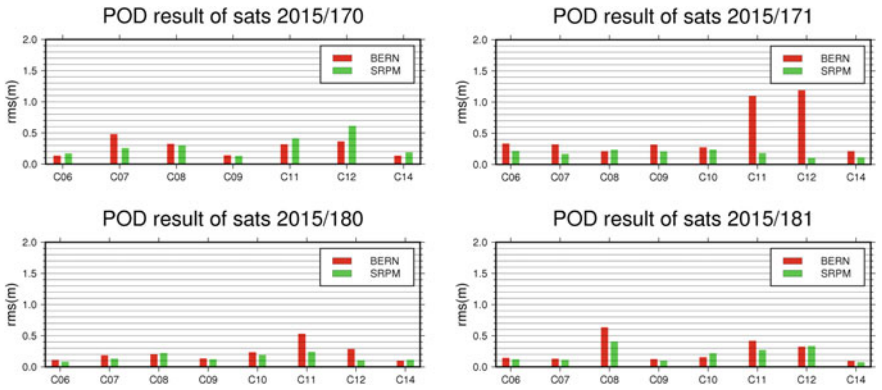

Fig. 3 Overlapping arcs during attitude conversion

One of the most important way to checking orbit accuracy is to predict the orbit using the same model as the orbit determination, then use statistical results to reflect the accuracy of the dynamic model. Respectively doing the orbit determination by using two models and the prediction method is shown in Fig. 4. The three dimensional RMS statistical of results was listed in Table 2.

Statistical results show that when predicting 12 h, the accuracy of the two models is approximately the same. For the satellite with attitude switching, the prediction accuracy of SRPM can be increased by about 0.3 m. The prediction of 24 h, BERN model of satellite attitude switching accuracy decreases rapidly, mainly there is a big error in attitude switching in which the error in predicting the maximum C08 reached 17.86 m, at the same time the error of the SRPM only 3.8 m. statistical results show that the prediction accuracy of partial SRPM can be increased by about 0.4 m of satellites in the yaw-steering. The statistical accuracy of the orbit prediction of the BERN model is seriously reduced when the 48 h is predicted, and the reason for this phenomenon is consistent with the prediction of 24 h. However, the SRPM model has maintained a better prediction effect. From the yaw-steering satellite statistics, the prediction results show that the maximum RMS can reduce the maximum of 0.7 m compared with the BERN model.

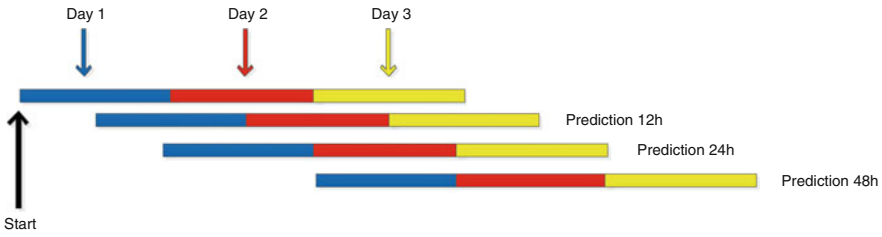

Fig. 4 Forecasting method

Table 2 BERN and SRPM predict 12/24/48 h orbit RMS

	Pre 12 h		Pre 24 h		Pre 48 h	
Satellite\model	BERN	SRPM	BERN	SRPM	BERN	SRPM
C06	0.295	0.264	0.604	0.335	1.394	0.513
C07	0.288	0.258	0.761	0.298	1.571	0.458
C08	0.960	0.649	2.705	1.158	7.566	2.545
C09	0.286	0.248	0.560	0.299	1.434	0.526
C10	0.403	0.356	0.949	0.430	1.766	0.608
C11	0.834	0.527	2.020	0.804	5.381	1.488
C12	0.694	0.424	1.633	0.670	3.965	1.364
C14	0.344	0.244	0.674	0.325	1.228	0.578

5 Conclusion

Through analysing BDS orbit products under the yaw-steering and orbit-normal, we can conclude the results: the satellite's force are greater differences during attitude switching and cyclical changes the R and T direction keeps the relative stability, but there is a big change in N direction. If the change is not considering the stress situation and influence of the yaw attitude will lead to a decline in the accuracy of orbit. The new SRPM model is more elaborate than the BERN model, and the physical meaning is clearer. The calculation results also show that the SRPM model has higher accuracy in orbit-normal; it can also make the IGSO and MEO satellite orbit error is reduced by 10–30% when the satellite is in the yaw-steering, close to the normal yaw period reference value. The orbit residuals decrease when compared with GBM precise orbit. The orbit overlap of the SRPM model can maintain a high stability and avoid a sharp drop in the accuracy of the attitude conversion. At the same time, in orbit prediction, the predicted residual decreases significantly, which greatly improves the accuracy and availability of orbit.

Acknowledgements This study is funded by the Ministry of Science and Technology of China (No. 2015FY310200), the National Basic Research Program of China (No. 2016YFB0501405), the National Natural Science Foundation of China (No. 11173048, 10873029), the Shanghai Key Laboratory of Space Navigation and Position Techniques (No. 06DZ22101). thanks !

References

1. Zhao Q, Wang X, He B et al (2014) The solar radiation pressure modeling on high-altitude earth orbit satellite. China Satellite Navigation Conference CSNC
2. Zhao Q (2017) Research on high precision solar radiation pressure model determination for BeiDou satellites. University of Chinese Academy of Sciences
3. Zhou P, Du L, Fang S et al (2016) Analysis of characteristics of QZSS satellite orbit and clock products during yaw attitude model switching. Acta Geodaetica Cartogr Sin 45(03):274–281

4. Mao Y, Song X, Wang W et al (2015) Beidou IGSO and MEO navigation satellites' yaw-seering and orbit-normal attitude control modes and solar radiation pressure fifference analysis. Acta Geodaet et Cartographica Sinica 40(08):129–134
5. Tan H, Guo R, shiXie J (2017) Design yaw control modes of the navigation satellite and analyze the solar radiation pressure. China Satellite Navigation Conference CSNC
6. Guo J (2014) The impacts of attitude, solar radiation and function model on precise orbit determination for GNSS Satellites. Wuhan University, China
7. Dai X (2016) Real-time precise GNSS satellite orbit determination using the srif method: theory and implementation. Wuhan University, China
8. Kouba J (2009) A simplified yaw-attitude model for eclipsing GPS satellites. GPS Solutions 13(1):1–12
9. Rodriguez-Solano CJ, Hugentobler U, Steigenberger P (2011) Precise GNSS orbit determination using an adjustable box-wing model for solar radiation pressure/Iugg
10. Rodriguez-Solano CJ, Hugentobler U, Steigenberger P (2012) Adjustable box-wing model for solar radiation pressure impacting GPS satellites. Adv Space Res 49(7):1113–1128

Quality Analysis of Observation Data of BeiDou-3 Experimental Satellites

Yilei He, Qianxin Wang, Zhiwen Wang and Ya Mao

Abstract Five new-generation BeiDou global experimental satellites (BDS-3) have been launched into inclined geosynchronous orbit (IGSO) and medium orbit (MEO) since March 2015. The quality of observation data has a direct impact on the performance of navigation, positioning and timing service. Therefore, it is very important to analyze the observation data quality of new-generation BDS satellites, for evaluating the service performance of BDS-3. In this paper, the practical observation data of 16 iGMAS stations and 6 MGEX stations from 21 August to 20 September 2017 are selected, because they can receive the observation data of BDS-3, BDS-2 (BeiDou regional navigation system) and GPS (Global Positioning System). The observation data quality of BDS-3, BDS-2 and GPS are analyzed and compared, including the data integrity rate, multipath, signal-to-noise ratio (SNR), ionospheric delay and cycle slip ratio. The results show that the data integrity rate on the B1 and B3 frequency of BDS-3 and BDS-2 are at the same level. The SNR of BDS-3 are outperformed that of BDS-2. The multipath error and the ionospheric delay error of BDS-3 are slightly better than those of BDS-2. And the cycle slip ratio of BDS-3 is similar to that of BDS-2. Therefore, the new-generation BDS-3 satellites can meet the normal working requirements and the data quality of BDS-3 is better than that of BDS-2 in general.

Keywords BDS · Global experimental satellites · Evaluation index Quality analysis

Y. He · Q. Wang (✉) · Z. Wang · Y. Mao
School of Environment Science and Spatial Informatics, China University of Mining and Technology, Xuzhou 221116, Jiangsu, China
e-mail: wqx@cumt.edu.cn

J. Sun et al. (eds.), *China Satellite Navigation Conference (CSNC) 2018 Proceedings*, Lecture Notes in Electrical Engineering 498,
https://doi.org/10.1007/978-981-13-0014-1_24

1 Introduction

Beidou Satellite Navigation System (BDS), which is independently developed by China, is an important part of global navigation satellite system [1]. Its implementation process is steadily carried out follows the "three steps" strategy. In the first phase, three satellites in geostationary orbit (GEO) were successfully launched from 2000 to 2003, and the Beidou navigation demonstration system (BDS-1) was initially built; In the second phase, until 27 December, 2012, the constellation with five satellites in GEO, five satellites in inclined geosynchronous orbit (IGSO) and five satellites in medium earth orbit (MEO) was successfully built, and the extension of regional navigation system (BDS-2) had been formed, which provides continuous passive positioning, navigation and timing services for the whole Asia-Pacific region; In the third phase, the full constellation of BDS global system that is expected to launch 35 global satellites by 2020, including 5 satellites in GEO, 3 satellites in IGSO and 27 satellites in MEO, which can provide positioning and navigation services to global users [2]. On March 30, 2015, the successfully launch of the first new-generation Beidou global experimental satellites (BDS-3) signaled the beginning of the BDS from regional extension system to global coverage. As of September 2017, two satellites in IGSO and three satellites in MEO were launched into the orbit. Currently, four satellites (C31–C34) are already in operation and broadcasting signals, while C35 is still being tested. The ground tracks of BDS-3 as shown in Fig. 1, and the status of BDS-3 is summarized in Table 1 [3]. In order to improve the compatibility and interoperability with other navigation system, besides broadcasting B1I at 1561.098 MHz and B3I at 1269.520 MHz, BDS-3 also broadcasts several new signals which overlap with the GPS L1/L5 and Galileo

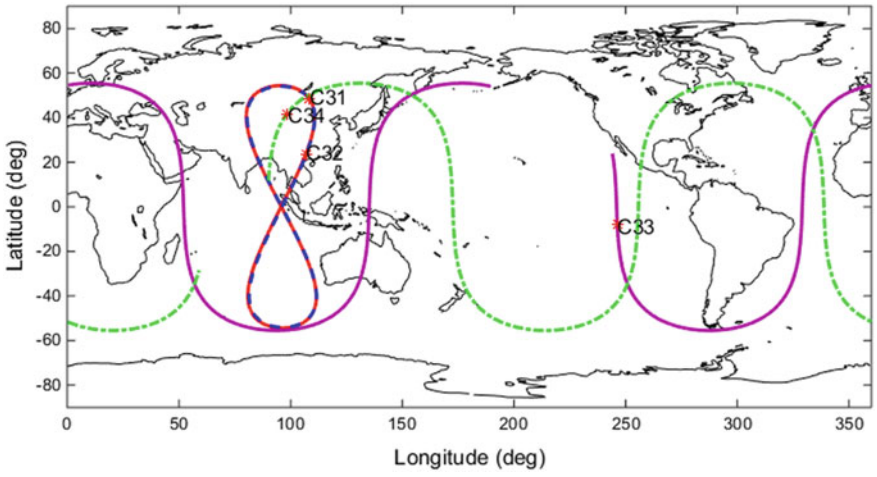

Fig. 1 The ground tracks of the new-generation BDS-3 on 21 August, 2017

Table 1 Status of BDS-3 satellites

Satellite	PRN	Type	Launch date	Status
I1-S	C31	IGSO	2015/03/30	Operational
M1-S	C33	MEO	2015/07/25	Operational
M2-S	C34	MEO	2015/07/25	Operational
I2-S	C32	IGSO	2015/09/29	Operational
M3-S	C35	MEO	2015/09/29	Test

E1/E5a/E5b signals in space, namely B1C at 1575.42 MHz, B2a at 1176.45 MHz and B2b at 1207.14 MHz, respectively [4].

The launch of BDS-3 is to verify the new technology, including new satellite signals, intersatellite link, different satellite platforms, and so on. The quality of observation data has a direct impact on the globalization process of Beidou navigation system in China. There are many researchers have evaluated the quality of BDS-2 satellite observation data, Hong et al. [5] used the data to analyze the quality by multipath effect, signal-to-noise ratio and positioning accuracy, the results showed that the accuracy of the BeiDou is slightly lower than that of GPS. Xu and Ji [6] assessed the quality of BeiDou pseudorange and carrier phase observations in terms of availability, integrity and positioning accuracy with practical data in Hong Kong. The experiment results showed that the noise and multipath of GEOs pseudorange measurement fluctuates within 1.5 m, while the variations of IGSOs and MEOs are more obvious. Bramanto et al. [7] assessed the data quality and positioning performance of BeiDou in respect with GPS in Bandung, Indonesia, the results showed that the SNR for B1, B2, and B3 vary from 40 to 50 dB-Hz, the multipath variation of GEOs varies within 1 m, while the multipath variation of IGSOs and MEOs vary larger than GEOs'. However, the research on the BDS-3 experimental satellite is relatively few, especially in comprehensive assessment of the quality of its observation data. Tan et al. [3] and Zhao et al. [4] evaluated the precision orbit and clock of the BDS-3 experimental satellites, respectively. The initial results indicated that the BDS-3 satellites show slightly better performance than BDS-2 satellites; Zhang et al. [2] evaluated the five kinds of signals of C32–C34 from the aspects of carrier-noise-ratio density ratio (C/N_0) and pseudorange multipath, the results show that the quality of BDS-3 observation data are comparable to those of GPS L1/L2/L5 and Galileo E1/E5a/E5b. This paper systematically analyze the quality of the new-generation BDS-3 experimental satellite data in terms of data integrity, signal-to-noise ratio (SNR), multipath effect, ionospheric delay and cycle slip, etc. so as to facilitate the evaluation of the performance of the new-generation experimental satellite.

2 Data Collection

At present, the International GNSS Monitoring and Assessment System (iGMAS) tracking network and a little of the Multi-GNSS Experiment (MGEX) tracking network can receive the BDS-3 experimental satellite observation data, but most of the

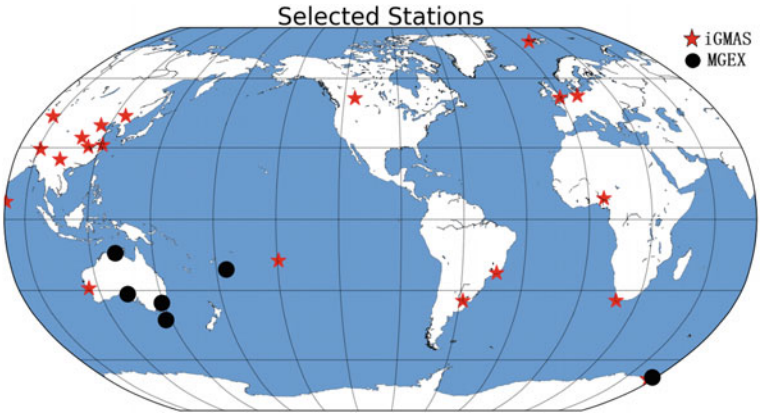

Fig. 2 Distribution of selected tracking stations from MGEX and iGMAS

receiver can only receive the B1I and B3I dual-frequency observation data of BDS-3. Therefore, this paper selected the real multi-GNSS observations of 16 iGMAS stations and 6 MGEX stations from 21 August (doy 233) to 20 September 2017 (doy 263), the stations distribution as shown in Fig. 2, and the details of the stations are summarized in Table 2. The quality of the Beidou new-generation experimental satellite B1I and B3I dual-frequency observation data are analyzed in terms of the evaluation indexes of data integrity rate, SNR, multipath effect, ionospheric delay and cycle slip. In order to intuitive comparison analysis, the above-mentioned satellites are divided into 8 categories: GPS (G01–G32), GEO (C01–C05), IGSO (C06–C10), MEO (C11–C14), C31, C32, C33 and C34. Through comparing with the data quality of BDS-2 and GPS of the homologous stations, the performance indexes and winding level of new-generation experimental satellite are obtained.

3 Data Quality Evaluation Indexes

3.1 GNSS Observation Equation

The quality analysis software for multi-GNSS observation data was selected in this paper, which is independent research by Beidou Data Processing and Analysis Center of China University of Mining and Technology [8]. Similar to the data quality checking software TEQC (Translation, Editing and Quality Checking) which is most widely used [9], the principle of the software is based on GNSS dual-frequency observation data. The basic observation equations of the pseudorange and carrier-phase can be expressed as [10]:

Table 2 Information of the selected tracking stations from MGEX and iGMAS

Station	Location	Country	Receiver	Antenna	Notes
CEDU	Ceduna	Australia	SEPT POLARX5	AOAD/M_T NONE	MGEX
DAV1	Davis	Antarctica	SEPT POLARX5	LEIAR25.R3 LEIT	MGEX
HOB2	Hobart	Australia	SEPT POLARX5	AOAD/M_T NONE	MGEX
KAT1	Katherine	Australia	SEPT POLARX5	LEIAR25.R3 LEIT	MGEX
STR1	Stromlo	Australia	SEPT POLARX5	ASH701945C_M NONE	MGEX
TONG	Nuku'alofa	Tonga	SEPT POLARX5	TRM59800.00 NONE	MGEX
ABJA	Abuja	Nigeria	GNSS_GGR	RINT-8CH CETD	iGMAS
BJF1	Beijing	China	CETC-54-GMR-4016	LEIAR25.R4 LEIT	iGMAS
BRCH	Brunswick	Germany	CETC-54-GMR-4016	NOV750.R4 NOVS	iGMAS
CANB	Canberra	Australia	CETC-54-GMR-4011	GNSS-750	iGMAS
CHU1	Changchun	China	GNSS_GGR	RINT-8CH CETD	iGMAS
CLGY	Calgary	Canada	CETC-54-GMR-4016	LEIAR25.R4 LEIT	iGMAS
DWIN	Darwin	Australia	CETC-54-GMR-4011	GNSS-750	iGMAS
GUA1	Wulumuqi	China	GNSS_GGR	RINT-8CH CETD	iGMAS
HMNS	Hermanus	South Africa	GNSS_GGR	RINT-8CH CETD	iGMAS
ICUK	London	Britain	CETC-54-GMR-4016	NovAtel-750	iGMAS
KNDY	Kandy	Sri Lanka	CETC-54-GMR-4016	GNSS-750	iGMAS
LHA1	Lasa	China	CETC-54-GMR-4016	NOV750.R4 NOVS	iGMAS
PETH	Perth	Australia	CETC-54-GMR-4011	GNSS-750	iGMAS
WUH1	Wuhan	China	CETC-54-GMR-4016	LEIAR25.R4 LEIT	iGMAS
XIA1	Xi'an	China	GNSS_GGR	RINT-8CH CETD	iGMAS
ZHON	Zhongshan Station	Antarctica	CETC-54-GMR-4011	GNSS-750	iGMAS

$$\begin{aligned} P_i(t) &= \rho(t) + c(t_r - t_s) + Ion_i + Trop_i + MP_i + \varepsilon_P \\ L_i(t) &= \rho(t) + c(t_r - t_s) - Ion_i + Trop_i + mp_i + n_i\lambda_i + \varepsilon_L \end{aligned} \tag{1}$$

where, the subscript i indicates the band (B1 and B3) of observations, $P_i(t)$ and $L_i(t)$ are pseudorange and carrier-phase observations, ρ is the geometric distance between satellite and receiver in meters, c is the speed of light (299792458 m). t_r and t_s are the receiver clock error and the satellite clock error, respectively. Ion_i and $Trop_i$ are ionospheric delay and tropospheric delay in meters, respectively. MP_i and mp_i are the multipath error of pseudorange and carrier-phase in meters, respectively. n_i and λ_i are the ambiguity and wavelength, respectively. ε_P and ε_L are the observation noise of pseudorange and carrier-phase, respectively.

3.2 Data Integrity Rate

During the process of generation and transmission of satellite signals, the lack of necessary data may be caused by many different reasons, resulting in the decline of the quality of the observation data. Data integrity is an important index of the observational data, which refers to the availability and integrity of data of the observation period. It not only reflects the influence of observation environment, but also reflects the performance of receiver [11]. The data integrity *Int* is defined as:

$$Int = Have(i)/Expert(i) \tag{2}$$

where, *Have(i)* is the number of the real complete observations of the *i* satellite, and *Expert(i)* is the number of theoretical observations of the *i* satellite. Complete observation value means a satellite must has the observation value of P1 or C/A code, P2 or C2 code, B1 and B3 carrier-phase data at the same epoch, and the SNR of B1 and B3 are greater than or equal to the minimum specified value, the elevation angle of the satellites is greater than or equal to the satellite elevation cut-off angle [12]. The theoretical observation value is the use of the broadcast ephemeris to calculate satellite elevation angle in the observation period. If the elevation angle is greater than the elevation cut-off angle, the satellite can be observed by the receiver theoretically.

The data integrity rate of GPS and BDS of 22 stations from doy 233 to doy 263 in 2017 were calculated. In order to verify the reception of B1I and B3I signals, the cut-off angle was set to zero in this paper. According to the above-mentioned satellites classification, the average values of 31 days of each station as shown in Table 3, and mapped in Fig. 3.

Table 3 and Fig. 3 shows the maximum of data integrity of BDS experimental satellites is 100% and the minimum is 89.79%, among them, the data integrity of 91.94% IGSO experimental satellites (C31-C32) are more than 95%, and 98.39% MEO experimental satellites (C33-C34) are more than 95%. The phenomena of inferior data integrity are concentrated in TONG, ABJA and ICUK stations, but the receivers and antenna types of three stations are not the same, probably due to the environmental impact around the station. Compared with the BDS-2 and GPS of the homologous stations, the data integrity of the BDS-3 experimental satellites is comparable to the same type of BDS-2, and in most cases it is slightly better than BDS-2 and GPS.

3.3 Signal-to-Noise Ratio

The Signal-to-Noise Ratio (SNR) is the ratio of the carrier signal intensity to the noise intensity of the receiver, and the unit is dB-Hz. It is mainly affected by the gain of the satellite launch equipment, the status of the correlator of the receiver,

Table 3 Data integrity rate of different satellites at different stations

Station	GPS	GEO	IGSO	MEO	C31	C32	C33	C34	Station	GPS	GEO	IGSO	MEO	C31	C32	C33	C34
CEDU	97.41	99.63	99.76	98.91	99.75	99.63	98.17	98.58	CLGY	96.56	–	97.24	98.36	97.92	98.18	98.81	98.60
DAV1	99.68	93.28	99.52	99.47	99.23	99.54	99.45	99.53	DWIN	96.39	99.98	99.18	95.99	99.94	100	97.81	96.02
HOB2	96.47	99.00	99.59	97.99	99.79	99.74	98.28	98.15	GUA1	94.75	99.51	98.66	97.95	97.44	99.27	96.15	96.69
KAT1	96.68	97.97	99.28	95.65	99.99	100	95.39	97.21	HMNS	97.80	99.90	97.29	98.30	96.53	98.62	98.48	99.35
STR1	96.65	98.63	98.32	95.86	99.29	99.43	97.97	97.17	ICUK	99.57	46.37	85.51	92.39	91.08	92.10	97.87	97.52
TONG	92.63	98.06	94.78	92.18	93.08	94.63	90.65	95.62	KNDY	99.60	99.97	99.98	99.38	100	100	99.67	99.45
ABJA	87.77	95.27	91.91	97.16	89.79	96.90	97.32	98.67	LHA1	98.52	98.66	98.70	97.99	99.24	99.74	98.02	98.62
BJF1	94.33	95.74	97.51	95.36	98.44	98.77	95.76	95.96	PETH	96.20	99.98	95.82	97.17	97.81	97.26	97.60	97.53
BRCH	93.78	99.98	93.99	94.75	95.56	96.28	97.97	98.09	WUH1	98.13	99.98	98.13	97.85	99.45	98.04	97.73	97.16
CANB	96.46	99.72	98.59	97.64	98.71	99.12	97.74	97.81	XIA1	96.43	99.95	99.09	98.19	99.51	99.81	98.07	99.08
CHU1	95.75	99.72	99.51	99.12	99.54	99.71	98.72	98.65	ZHON	99.39	92.48	96.57	97.09	97.93	99.07	98.69	98.11

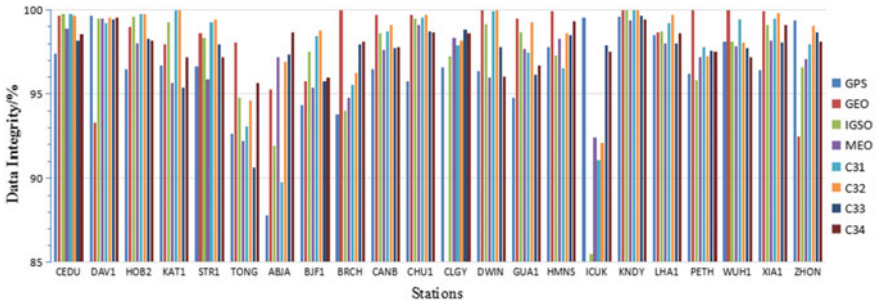

Fig. 3 Data integrity rate of different satellites at different stations

the geometric distance between the satellite and the receiver, and the multipath effect. It not only reflects the performance of the receiver, but also reflects the quality of the satellite signal [13]. The greater the SNR, the better the quality of the signal and the greater the accuracy of the observations. The SNR of each satellite can be obtained from the observation file directly.

The SNR of GPS and BDS of 22 stations from doy 233 to doy 263 in 2017 were calculated. According to the above-mentioned satellites classification, the average values of 31 days of each station as shown in Table 4, and the average SNR of each station are drawn to Fig. 4. Because of the limited space, only the HMNS station is selected to show the fluctuates of the SNR of various satellites during the experimental period, as shown in Figs. 5 and 6. The SNR1 and SNR3 represent the SNR of BDS B1 and B3 frequency points, or the SNR of GPS satellite L1 and L2 frequency points, respectively (Fig. 7).

Table 4 and Fig. 4 shows the average SNR of the experimental satellites are more than 43 dB-Hz, the SNR of C31 and C32 have a slight increase over than those of BDS-2 working IGSO satellites, only the SNR1 of B1 frequency of C31 is slightly lower than the BDS-2 IGSO satellites. The SNR of C33 and C34 are greater than those of the BDS-2 working MEO satellites, which indicates that the two MEO experimental satellites carrier-phase observations have less noise and better quality. The SNR1 of GPS is obviously larger than SNR3, while the SNR1 of BDS is slightly lower than SNR3. Figures 5 and 6 shows the fluctuates of SNR1 and SNR3 of all kinds of satellites observed by HMNS stations are consistent. It is more intuitive that the SNR1 and SNR3 of BDS-3 are better than BDS-2 working satellites.

3.4 Multipath Effect

The influence of observation environment on the transmission process of satellite signal will cause multipath effect. Generally, the multipath error of carrier-phase observation does not exceed 1/4 wavelength, while the pseudorange multipath error

Table 4 SNR of different satellites at different stations

Station	SNR1								SNR3							
	GPS	GEO	IGSO	MEO	C31	C32	C33	C34	GPS	GEO	IGSO	MEO	C31	C32	C33	C34
CEDU	43.72	42.67	44.87	44.64	43.14	46.51	44.88	45.51	33.89	42.91	45.40	46.22	45.25	46.47	47.19	47.28
DAV1	46.04	40.57	45.42	46.45	44.90	48.03	47.05	47.38	33.34	39.10	45.45	47.02	46.49	47.86	48.30	48.04
HOB2	44.37	42.72	44.19	44.56	42.33	45.60	45.49	45.89	34.96	44.33	46.77	48.05	46.15	47.59	49.57	49.43
KAT1	44.54	44.42	44.26	44.08	42.87	46.48	45.28	45.08	32.85	45.19	44.87	45.70	44.38	46.09	47.42	46.66
STR1	43.41	42.17	42.93	43.07	41.11	43.99	44.29	44.42	32.02	38.32	38.89	40.36	38.29	39.19	42.07	41.93
TONG	43.27	45.90	37.70	41.88	35.14	38.59	43.80	44.44	30.90	46.81	39.66	44.50	38.80	40.17	47.18	47.36
ABJA	45.29	41.14	38.96	45.34	38.16	41.03	47.10	48.14	41.92	43.20	40.85	47.72	41.97	42.64	50.13	50.60
BJF1	46.19	42.28	44.93	44.73	43.76	47.08	45.16	45.04	36.18	41.13	44.61	45.03	45.27	46.60	45.76	45.41
BRCH	45.75	38.11	41.92	45.08	42.25	45.17	46.13	46.59	33.43	36.17	39.72	43.81	41.20	42.25	45.39	45.46
CANB	46.69	43.82	43.85	44.84	42.66	45.82	46.05	46.32	36.91	43.70	44.04	45.78	43.98	45.19	47.55	47.24
CHU1	43.94	45.98	50.07	49.55	48.47	51.63	49.38	50.01	40.81	42.59	47.04	47.39	47.11	48.34	47.95	48.07
CLGY	47.75	–	40.64	44.99	40.77	42.62	46.80	47.14	37.62	–	38.28	44.42	39.46	39.65	46.94	46.41
DWIN	46.12	43.73	43.67	44.32	42.37	45.85	45.33	45.59	34.60	43.83	43.02	44.41	42.91	44.30	45.98	45.58
GUA1	44.11	44.00	49.32	48.88	49.40	52.48	48.27	49.06	46.65	43.74	51.03	51.32	52.23	53.60	51.50	51.70
HMNS	43.51	40.48	39.88	45.78	40.55	42.55	47.12	47.84	40.66	41.25	40.88	47.08	42.15	42.64	49.16	49.27
ICUK	47.38	38.86	41.15	44.97	41.87	44.88	46.28	46.67	35.32	37.66	37.80	42.64	39.17	40.30	44.49	44.34
KNDY	45.30	45.49	44.23	45.39	44.50	48.18	46.07	45.96	32.96	45.41	43.98	45.90	45.97	47.50	46.99	46.35
LHA1	46.90	43.56	45.05	46.09	44.59	48.31	46.60	47.03	36.87	42.69	44.88	46.23	45.84	47.37	46.95	47.16
PETH	46.14	44.05	44.44	44.80	43.55	46.95	45.73	45.57	34.30	42.45	43.25	44.26	44.04	45.29	45.59	44.82
WUH1	46.66	44.20	45.14	45.79	44.44	47.79	46.30	46.97	36.22	44.08	45.54	46.53	46.25	47.72	47.27	47.76
XIA1	44.58	45.60	50.09	49.49	49.28	52.68	49.71	49.90	46.97	47.09	50.49	51.03	51.35	52.88	51.96	51.84
ZHON	46.69	39.85	44.66	45.71	44.61	47.81	46.32	46.68	35.71	37.78	44.58	45.66	45.47	46.90	46.74	46.63
AVE	45.38	42.84	43.97	45.47	43.21	46.36	46.32	46.69	36.59	42.35	43.68	45.96	44.26	45.48	47.37	47.24

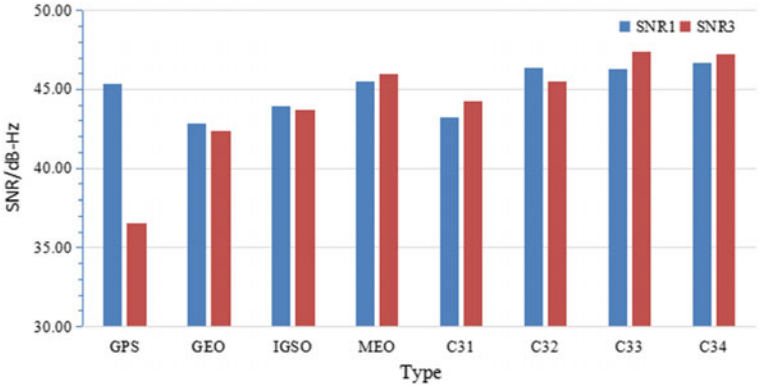

Fig. 4 SNR of classified satellites

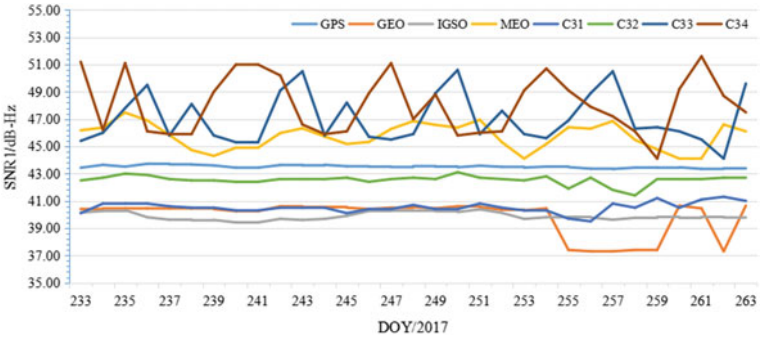

Fig. 5 SNR1 from doy 233 to doy 263 of HMNS station

can reach 0.5 code width. The multipath effect has the characteristics of periodic and random noise, which can not be completely separated from the noise [14]. Therefore, this paper mainly considers the effect of the pseudorange multipath and noise. Due to the difference of the frequencies, the influence of signals during the transmission process are different, while the multi-frequency data can form different data combinations, dual-frequency pseudorange multipath effect can be obtained by the linear combination of pseudorange and carrier-phase observations [11]. The multipath error of the satellite can be expressed as [9, 13]:

$$\begin{aligned} MP_1 &= P_1 - (1 + \frac{2}{\alpha - 1})\lambda_1\varphi_1 + \frac{2}{\alpha - 1}\lambda_3\varphi_3 - B_{P1} \\ MP_3 &= P_3 - \frac{2\alpha}{\alpha - 1}\lambda_1\varphi_1 + (\frac{2\alpha}{\alpha - 1} - 1)\lambda_3\varphi_3 - B_{P3} \end{aligned} \tag{3}$$

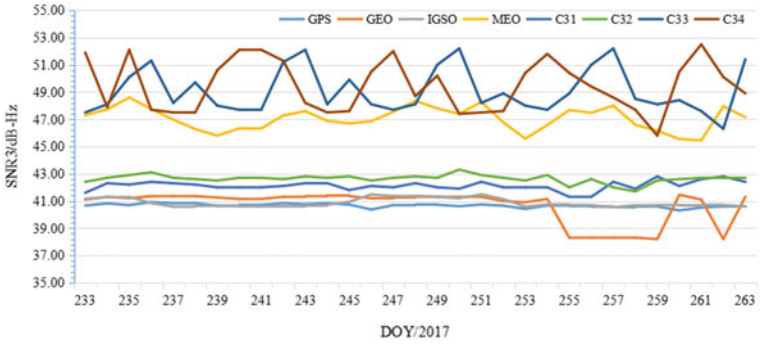

Fig. 6 SNR3 from doy 233 to doy 263 of HMNS station

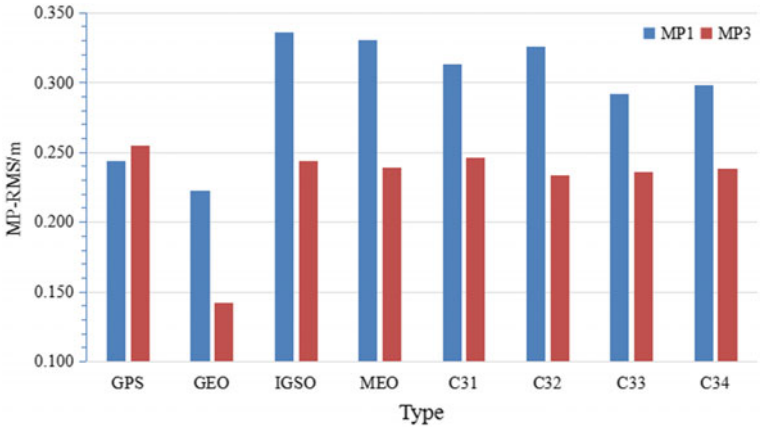

Fig. 7 Multipath error of classified satellites

where, MP_1 and MP_3 represent the combined multipath of B1/B3 band pseudorange and carrier-phase observations, respectively, P_i is the pseudorange observations, λ_i is the wavelength corresponding to the frequency, φ_i is the carrier-phase observations, $\alpha = (f_1^2/f_3^2)$, f_i is the frequency of carrier-phase observations, B_{Pi} includes the ambiguity and frequency bias.

In case of no cycle slip, B_{P1} and B_{P3} are constants. If the real multipath needs to be calculated, ambiguity must be solved accurately, but the resolution of ambiguity is complicated. In this paper, the moving average method is used to calculate the pseudorange multipath [12]. Moving average method, which is calculate the average value of combined multipath of the mobile window, then using the combined multipath of current epoch minus the moving average, the multipath of the epoch can be obtained, so as to eliminate the system error and the hardware delay which are not included in Eq. (3). The multipath effect has a period of about 5–

10 min, in order to eliminate the influence of the periodicity, the length of the mobile window should be the multiple of the period.

The root mean square (RMS) of multipath errors of GPS and BDS of 22 stations from doy 233 to doy 263 in 2017 are calculated. According to the above-mentioned satellites classification, the average values of 31 days of each station can be seen as Table 5, and the average multipath errors RMS of each station are drawn to Fig. 7. The HMNS station is selected to show the variation of the multipath errors RMS of various satellites during the experimental period, as shown in Figs. 8 and 9. The MP1-RMS and MP3-RMS represent the multipath error RMS of BDS B1 and B3 frequency points, or the multipath error RMS of the GPS satellite L1 and the L2 frequency points, respectively.

Table 5 and Fig. 7 shows the RMS mean values of all satellites are below 0.35 m, the maximum multipath error RMS of BDS-3 up to 0.757 m, the phenomena of larger than 0.5 m are concentrated in TONG, CLGY and ICUK stations, which is similar to the data integrity, the environment around these stations is poor. The multipath errors of C31 and C32 are comparable to those of the BDS-2 working IGSO satellites, while the C33 and C34 multipath errors are significantly reduce compared with the BDS-2 working MEO satellites, indicating that the pseudorange observations of C33 and C34 are superior. It can be seen that the MP1-RMS of GPS is slightly smaller than MP3-RMS, while MP1-RMS of BDS is obviously greater than MP3-RMS, which indicates that the pseudorange observations of the L1 frequency point of GPS and the B3 frequency point of BDS have better quality, and the ability to suppress multipath error is stronger. Because of the geostationary characteristic of the GEO satellites, its multipath error is far less than those of other satellites. Figures 8 and 9 shows the fluctuates of MP1-RMS and MP3-RMS of all kinds of satellites observed by HMNS station are consistent, except a few outliers. It reflects the periodicity of multipath error, and shows that the pseudorange observations quality of C31–C34 are better than those of BDS-2 working satellites.

3.5 Ionospheric Delay and Change Rate

The electromagnetic wave will be delayed when it passes through the ionosphere, assumes that the propagation path of two frequency carriers are same in the atmosphere, the ionospheric delay of two frequencies can be expressed as [9]:

$$\begin{aligned} I_1 &= \frac{1}{\alpha - 1}[(B_1 - B_3) - (n_1\lambda_1 - n_3\lambda_3 + mp_1 - mp_3)] \\ I_3 &= \frac{\alpha}{\alpha - 1}[(B_1 - B_3) - (n_1\lambda_1 - n_3\lambda_3 + mp_1 - mp_3)] \end{aligned} \tag{4}$$

where, I_i is the ionospheric delay error, B_i is the carrier-phase observation, and the other parameters are the same as above-mentioned.

Table 5 RMS of multipath error of different satellites at different stations

Station	MP1-RMS								MP3-RMS							
	GPS	GEO	IGSO	MEO	C31	C32	C33	C34	GPS	GEO	IGSO	MEO	C31	C32	C33	C34
CEDU	0.226	0.107	0.166	0.232	0.171	0.169	0.215	0.207	0.176	0.041	0.110	0.138	0.094	0.097	0.149	0.144
DAV1	0.285	0.285	0.294	0.350	0.226	0.237	0.282	0.287	0.164	0.147	0.129	0.140	0.115	0.108	0.142	0.144
HOB2	0.205	0.185	0.262	0.319	0.242	0.241	0.233	0.232	0.138	0.071	0.089	0.138	0.107	0.104	0.138	0.141
KAT1	0.340	0.288	0.410	0.530	0.340	0.338	0.377	0.406	0.168	0.085	0.110	0.175	0.137	0.128	0.171	0.193
STR1	0.216	0.086	0.275	0.324	0.254	0.265	0.251	0.257	0.193	0.043	0.155	0.187	0.180	0.180	0.185	0.182
TONG	0.480	0.093	0.850	0.734	0.706	0.757	0.604	0.582	0.499	0.050	0.522	0.508	0.513	0.511	0.451	0.445
ABJA	0.383	0.311	0.344	0.268	0.359	0.377	0.239	0.226	0.367	0.366	0.313	0.244	0.298	0.315	0.231	0.210
BJF1	0.380	0.359	0.148	0.197	0.142	0.162	0.204	0.222	0.216	0.492	0.645	0.308	0.683	0.353	0.264	0.225
BRCH	0.350	0.118	0.538	0.441	0.513	0.494	0.417	0.422	0.408	0.143	0.451	0.385	0.381	0.387	0.395	0.419
CANB	0.161	0.261	0.349	0.358	0.330	0.371	0.318	0.324	0.238	0.098	0.197	0.245	0.211	0.226	0.239	0.246
CHU1	0.282	0.082	0.172	0.189	0.177	0.194	0.197	0.197	0.257	0.043	0.114	0.137	0.123	0.142	0.154	0.149
CLGY	0.188	0.000	0.645	0.420	0.593	0.620	0.347	0.359	0.222	0.000	0.405	0.320	0.442	0.483	0.278	0.292
DWIN	0.137	0.342	0.298	0.265	0.313	0.319	0.260	0.254	0.248	0.133	0.176	0.239	0.210	0.217	0.263	0.262
GUA1	0.118	0.058	0.054	0.096	0.049	0.052	0.082	0.082	0.190	0.036	0.041	0.074	0.036	0.040	0.083	0.072
HMNS	0.210	0.055	0.215	0.153	0.203	0.208	0.127	0.128	0.264	0.027	0.155	0.116	0.135	0.140	0.110	0.114
ICUK	0.260	0.094	0.563	0.450	0.551	0.563	0.424	0.391	0.286	0.053	0.477	0.361	0.447	0.438	0.363	0.353
KNDY	0.181	0.234	0.323	0.283	0.270	0.277	0.269	0.279	0.299	0.069	0.203	0.262	0.166	0.162	0.286	0.306
LHA1	0.124	0.205	0.232	0.228	0.224	0.236	0.218	0.203	0.213	0.086	0.124	0.158	0.123	0.124	0.169	0.164
PETH	0.133	0.219	0.338	0.436	0.318	0.369	0.430	0.529	0.223	0.110	0.161	0.202	0.177	0.169	0.207	0.244
WUH1	0.264	0.200	0.380	0.404	0.374	0.402	0.413	0.382	0.306	0.117	0.235	0.296	0.231	0.237	0.326	0.293
XIA1	0.222	0.225	0.239	0.272	0.261	0.246	0.202	0.278	0.240	0.206	0.229	0.251	0.243	0.235	0.194	0.255
ZHON	0.209	1.088	0.293	0.318	0.272	0.277	0.319	0.305	0.294	0.713	0.313	0.382	0.357	0.337	0.398	0.388
AVE	0.243	0.222	0.336	0.330	0.313	0.326	0.292	0.298	0.255	0.142	0.243	0.239	0.246	0.233	0.236	0.238

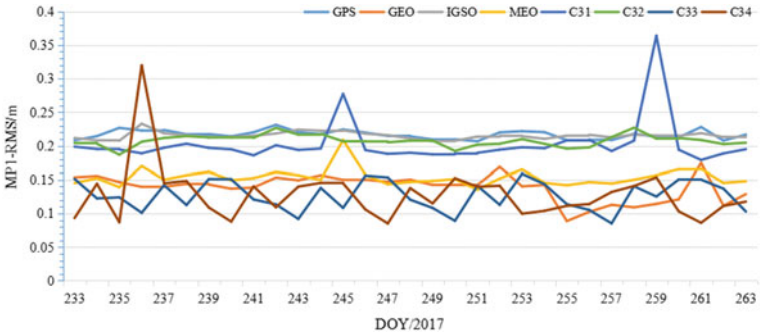

Fig. 8 MP1-RMS from doy 233 to doy 263 of HMNS station

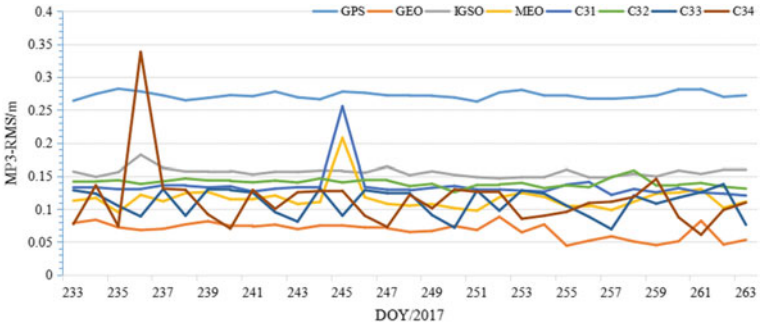

Fig. 9 MP3-RMS from doy 233 to doy 263 of HMNS station

The ionospheric delay change rate can reflect the activity of the ionosphere, and it is also one of the indexes to detect the cycle slip. Taking the B3 frequency as an example, the ionospheric delay change rate is defined as [15, 16]:

$$IOD_{(3)} = \frac{\alpha}{\alpha - 1}[(B_3 - B_1)_j - (B_3 - B_1)_{j-1}]/(t_j - t_{j-1}) \quad (5)$$

where, t_j is the observation time for the j epoch. When the $IOD_{(3)}$ is larger than or equal to 4 m/min, it is considered that the ionospheric slip had occurred.

The RMS of ionospheric delay change rates of GPS and BDS of 22 stations from doy 233 to doy 263 in 2017 are calculated. According to the above-mentioned satellites classification, the average values of 31 days of each station as shown in Table 6, and mapped in Fig. 10. The GUA1 station is selected to show the fluctuates of the ionospheric delay change rate RMS (IOD-RMS) of various satellites in the experimental period, as shown in Fig. 11.

Table 6 and Fig. 10 shows the maximum RMS of the ionospheric delay rate of C31–C34 experimental satellites can reach 1.04 m/min, while 97.58% of IOD-RMS are less than 0.30 m/min, which is at the same magnitude as BDS-2

Table 6 IOD-RMS of different satellites at different stations

Station	GPS	GEO	IGSO	MEO	C31	C32	C33	C34	Station	GPS	GEO	IGSO	MEO	C31	C32	C33	C34
CEDU	0.25	1.27	0.09	0.10	0.03	0.02	0.03	0.05	CLGY	0.05	–	0.06	0.07	0.05	0.03	0.05	0.07
DAV1	0.41	1.24	0.23	0.32	0.22	1.04	0.38	0.29	DWIN	0.41	0.34	0.27	0.58	0.20	0.13	0.31	0.48
HOB2	0.24	0.11	0.04	0.08	0.04	0.03	0.07	0.05	GUA1	0.63	0.13	0.06	0.05	0.05	0.06	0.05	0.07
KAT1	0.41	0.13	0.03	0.12	0.02	0.02	0.07	0.07	HMNS	0.63	0.09	0.06	0.06	0.08	0.14	0.12	0.07
STR1	0.31	0.06	0.12	0.37	0.03	0.06	0.03	0.06	ICUK	0.07	0.17	0.03	0.04	0.06	0.03	0.07	0.04
TONG	1.40	0.03	0.10	0.27	0.02	0.02	0.17	0.24	KNDY	0.36	0.17	0.23	0.27	0.19	0.24	0.26	0.23
ABJA	1.50	0.23	0.16	0.16	0.16	0.16	0.20	0.16	LHA1	0.20	0.15	0.07	0.05	0.09	0.13	0.10	0.06
BJF1	0.21	0.16	0.09	0.10	0.09	0.13	0.10	0.11	PETH	0.26	0.15	0.32	0.30	0.26	0.28	0.26	0.18
BRCH	0.44	0.10	0.04	0.06	0.04	0.04	0.06	0.07	WUH1	0.12	0.05	0.06	0.06	0.12	0.09	0.05	0.07
CANB	0.15	0.13	0.12	0.14	0.15	0.12	0.08	0.13	XIA1	0.74	0.26	0.24	0.17	0.16	0.14	0.09	0.15
CHU1	0.52	0.03	0.03	0.03	0.03	0.03	0.04	0.03	ZHON	0.22	0.76	0.30	0.20	0.22	0.24	0.17	0.20

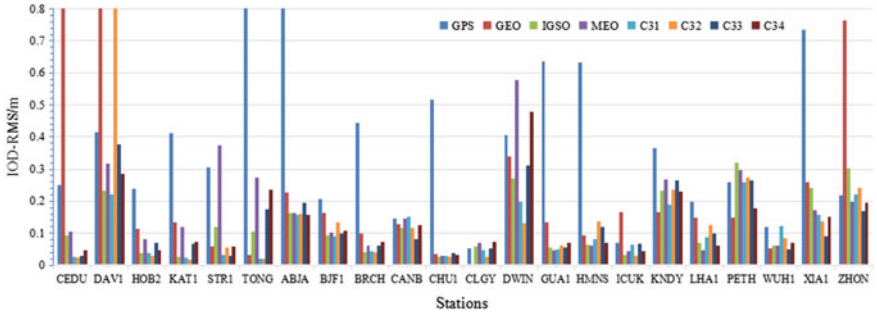

Fig. 10 IOD-RMS of different satellites at different stations

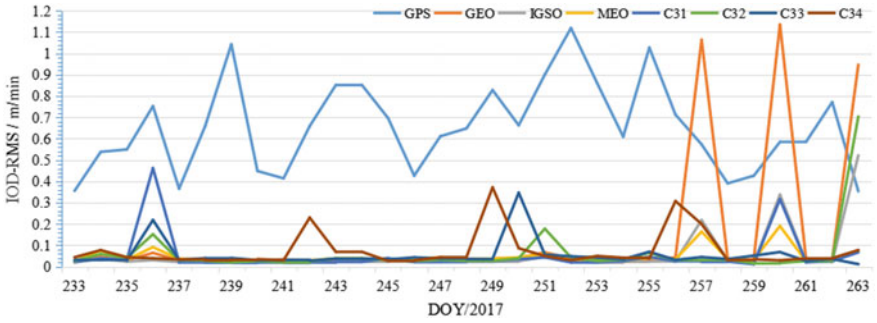

Fig. 11 IOD-RMS from doy 233 to doy 263 of GUA1 station

working satellites, and slightly better than those of BDS-2. Figure 11 shows the IOD-RMS of GPS satellites are significantly higher than those of BDS in various kinds of satellites, and there are obvious fluctuations on the doy 236, 242, 250, 257, 260 and 263, which may be caused by the ionosphere anomalies.

3.6 Cycle Slip Ratio

Cycle slip refers to the phenomenon of cycle counting slip or interruption in carrier-phase observation due to the loss of locking of satellite signals. This paper combined the Geometry-free combination (LG combination) and Melbourne-Wübbena combination (MW combination) to detect the cycle slip.

(1) LG combination [17]

$$\varphi_{LG} = \lambda_1\varphi_1 - \lambda_3\varphi_3 = (I/f_3^2 - I/f_1^2) + (\lambda_1 n_1 - \lambda_3 n_3) \tag{6}$$

where I is the ionospheric delay

(2) MW combination [17]

$$N_{MW} = n_1 - n_3 = (\varphi_1 - \varphi_3) - \frac{f_1 - f_3}{f_1 + f_3}\left(\frac{P_1}{\lambda_1} + \frac{P_3}{\lambda_3}\right) \tag{7}$$

The two combinations are independent of the geometric distance between the receiver and the satellite, orbit error, receiver clock error, satellite clock error and tropospheric error. The LG combination only includes the influence of ionosphere, and the real ambiguity combination of B1 and B3 [18]. If there is no cycle slip in carrier-phase observation, φ_{LG} should be a gentle curve, and N_{MW} is a constant theoretically. Due to the influence of observation noise, the N_{MW} sequence fluctuates near a certain value. Cycle slip ratio (CSR) is usually used to measure the cycle slip of the observation data, and the greater of the CSR, the more serious of the cycle slip [9].

$$CSR = \frac{1000}{O/Slps} \tag{8}$$

where the O/Slps indicates the ratio of the number of the observation value to the number of cycle slip.

The CRS of GPS and BDS of 22 stations from doy 233 to doy 263 in 2017 are calculated. According to the above-mentioned satellites classification, the average values of 31 days of each station as shown in Table 7, and mapped in Fig. 12. Table 7 and Fig. 12 shows that CRS of C31–C34 experimental satellites can reach a maximum of 53.62, and the larger CRS are concentrated in DAV1 and ZHON station, which may be due to the fact that both stations were built in Antarctica, high latitude causes serious cycle slip. Apart from these two stations, the CSR of 76.72% satellites is less than 10, which is generally stable. Compared with the homologous station BDS-2, the accuracy of BDS-3 is comparable, so there is no obvious improvement. But it is superior to the majority of the GPS satellites of the homologous station.

4 Conclusions

This paper selected the real multi-GNSS observations of 22 iGMAS and MGEX stations. The B1I and B3I dual-frequency observation data quality of BDS-3 are analyzed, including the data integrity rate, multipath, SNR, ionospheric delay and

Table 7 CRS of different satellites at different stations

Station	GPS	GEO	IGSO	MEO	C31	C32	C33	C34	Station	GPS	GEO	IGSO	MEO	C31	C32	C33	C34
CEDU	3.82	0.11	0.55	1.29	0.77	0.19	3.18	2.01	CLGY	5.79	–	12.31	13.96	8.34	1.64	4.98	8.48
DAV1	61.85	54.27	43.31	47.53	41.86	48.65	48.36	45.93	DWIN	23.53	1.48	3.15	23.27	1.46	1.52	15.33	15.76
HOB2	2.23	0.12	0.56	1.44	1.04	0.61	1.92	1.80	GUA1	2.36	0.76	0.48	1.09	0.38	0.96	0.56	1.32
KAT1	30.79	0.19	2.09	21.03	0.23	0.40	17.93	19.61	HMNS	2.70	9.43	1.89	1.62	0.83	1.00	0.47	0.75
STR1	2.63	0.07	0.22	0.71	0.47	0.18	2.15	1.32	ICUK	2.90	1.20	1.07	1.01	0.80	0.62	1.81	1.83
TONG	36.95	0.13	1.49	20.52	1.67	2.50	24.63	23.97	KNDY	7.54	2.41	2.92	6.04	2.91	3.00	4.62	6.03
ABJA	33.29	16.56	14.21	9.51	14.82	7.01	6.70	8.08	LHA1	31.56	1.28	10.80	11.27	17.16	28.14	15.90	18.96
BJF1	3.65	1.54	2.02	1.75	8.53	11.47	1.98	2.87	PETH	4.23	1.21	1.72	5.51	1.25	1.80	4.25	5.70
BRCH	7.41	1.82	2.84	3.43	3.09	2.71	3.71	3.16	WUH1	17.74	1.18	9.52	10.26	16.33	24.85	13.47	21.30
CANB	5.51	1.40	2.01	2.96	2.65	2.49	3.41	2.78	XIA1	11.47	14.91	18.33	19.63	25.25	20.68	13.71	19.26
CHU1	2.00	0.66	0.45	0.58	0.66	0.75	1.07	0.79	ZHON	61.48	59.35	48.96	56.61	44.30	53.62	52.34	52.88

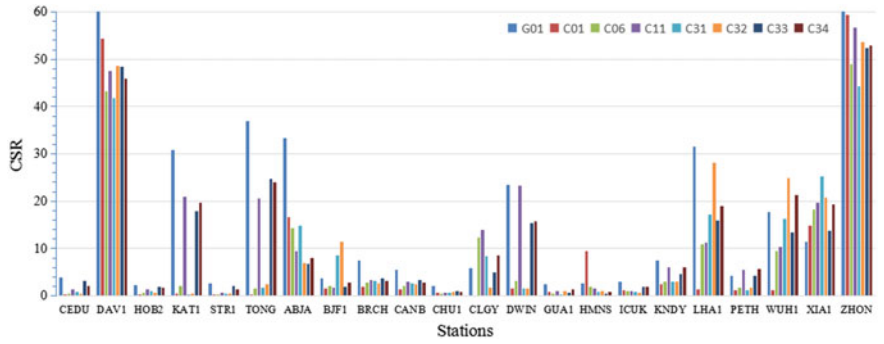

Fig. 12 CRS of different satellites at different stations

cycle slip ratio, and the results were compared with BDS-2 and GPS of the homologous stations.

(1) The data integrity of 91.94% IGSO experimental satellites (C31–C32) are more than 95%, and 98.39% MEO experimental satellites (C33–C34) are more than 95%.
(2) The SNR of C31 and C32 have a slight increase over than those of BDS-2 working IGSO satellites, only the SNR1 of B1 frequency of C31 is slightly lower than that of the BDS-2 IGSO satellites, and the SNR of C33 and C34 are greater than those of the BDS-2 working MEO satellites.
(3) The multipath errors of C31 and C32 are comparable to those of the BDS-2 working IGSO satellites, while the C33 and C34 multipath errors are significantly reduce compared with the BDS-2 working MEO satellites, indicating that the pseudorange observations of C33 and C34 are superior.
(4) In terms of ionospheric delay, 97.58% of IOD-RMS is less than 0.30 m/min, which is at the same level as BDS-2 working satellites, and slightly better than those of BDS-2 and GPS satellites.
(5) The CSR of most satellites is less than 10, which is generally stable. Compared with the homologous station BDS-2, the accuracy of BDS-3 is comparable, so there is no obvious improvement. But it is superior to the majority of the GPS satellites of the homologous station.

Overall, the performance of the Beidou new-generation experimental satellites have been further improved, which can meet the normal working requirements of the Beidou satellite navigation system, and lay the foundation for the Beidou satellite navigation system from the regional system to the global system.

Acknowledgements This paper was supported by the National Science Foundation of China (Grant No. 41404033), the National Science and Technology Basic Work (Grant No. 2015FY310200). And thanks the International GNSS Monitoring and Assessment Service (iGMAS) and the International GNSS Service (IGS) for the data and products.

References

1. Yang Y (2010) The progress, contribution and challenge of the Beidou satellite navigation system. J Survey Mapp 39(01):1–6
2. Zhang X, Wu M, Liu W et al (2017) Initial assessment of the COMPA-SS/BeiDou-3: new-generation navigation signals. J Geodesy 1:1–16
3. Tan B, Yuan Y, Wen M et al (2016) Initial results of the precise orbit determination for the New-Generation BeiDou satellites (BeiDou-3) Based on the iGMAS Network 5(11):196
4. Zhao Q, Wang C, Guo J et al (2018). Precise orbit and clock determination for BeiDou–3 experimental satellites with yaw attitude analysis.GPS Solut, 22(4)
5. Hong M, Zhao W, Chen G et al (2017) Quality check and analysis of BeiDou and GPS observation data in the experiment of Air-Gun in reservoir. IEEE Int Conf Cyber Secur Cloud Comput :104–107
6. Xu Y, Ji S (2015) Data quality assessment and the positioning performance analysis of BeiDou in Hong Kong. Empire Survey Review 47(345):446–457
7. Bramanto B, Gumilar I, Abidin HZ et al (2017) Assessment of the BeiDou data quality and the positioning performance: a perspective from Bandung, Indonesia. J Aeronaut Astronaut Aviat 49(2)
8. He Y, Wang Q (2017) Quality analysis and preprocess software for multi-GNSS observation data V1.0. Software copyright: 2017SR426408,2017
9. Estey LH, Meertens CM (1999) TEQC: the multi-purpose toolkit for GPS/GLONASS Data. GPS Solut 3(1):42–49
10. Li Z, Huang J (2005) GPS measurement and data processing. Wuhan University Press, Wuhan
11. Zhu J (2015) A multi system GNSS Real-time data quality analysis and software implementation of. Southeast University
12. Tan Y, Yuan B, Bao Z (2013) GPS/BD/GLONASS multi constellation quality inspection and implementation. Fourth Annual China Satellite Navigation Academic Annual Meeting
13. Wu D, Wang L, Zhang Q et al (2015) The implementation and verification analysis of GNSS data quality assessment software. J Survey Mapp Sci Technol 32(04):344–348
14. Vaclavovic P, Dousa J (2016) G-Nut/Anubis: open-source tool formultiGNSS data monitoring with a multipath detection for new signals, frequencies and constellations. In: AG 150 years: proceedings of the IAG scientific assembly in Postdam, 2013. Springer, Germany, pp 775–782
15. Li J, Wang J (2006) Quality checking and analysis on GPS data in Northeast Asia. Geomat Inform Sci Wuhan Univ 31(3):P209–P212
16. Zhang Q, Yuan Y, Peng X et al (2016) Design of GNSS observation data quality analysis software. Coal Technol 35(04):100–102
17. Fang R, Shi C, Wei N et al (2009) Research on real-time cycle slip detection in GPS data quality control. J Wuhan Univ (Inf Sci Ed) 34(09):1094–1097
18. Wei Z, Ge M (1998) GPS relative positioning mathematical model. Surveying and Mapping Publishing House, Beijing

Research on Adaptability of BDS Satellite in-Orbit Attitude Control Mode of Precise Orbit Determination

Jin Chang, Qiuli Chen and Haihong Wang

Abstract Orbit dynamics model is one of the most important factors determining the precision of orbit determination. It also determines navigation and positioning accuracy of navigation satellite system. The orbital perturbation force can be divided into two parts, conservative force and non-conservative force. For medium and high earth orbit navigation satellites, solar radiation pressure is the non-conservative force, that is closely related to the in-orbit attitude control mode and engineering parameters of the satellite. Taking BDS navigation satellite as example, the satellite in-orbit attitude control mode and the change of key parameters has been analyzed. On the basis of that, the difference of solar radiation pressure for three attitude control modes have been calculated and proposed, that are normal yaw-steering, yaw-fixed, and high-angle maneuvering. Seven-parameter optical pressure analysis model has been established. Based on precise ephemeris determined by laser range data, adaptability of solar radiation pressure models of different attitude control modes and precise orbit determination has been analyzed and studied. The results show that, the attitude control mode is the decisive factor of solar radiation pressure model which can not be ignored. Any other amendments are not considered. The solar radiation pressure models suitable for attitude control modes have been adopted. T precision of orbit determination is sub-meter level, which be not affected by the attitude control mode.

Keywords BDS satellite · Precise orbit determination · Attitude control mode Adaptability

1 Introduction

Satellites in the movement around the Earth will be subjected to a variety of forces. These forces can be divided into two categories: one is conservative, the other is non-defensive [1]. Conservative forces include the gravitational forces of the Earth,

J. Chang (✉) · Q. Chen · H. Wang
Beijing Institute of Spacecraft System Engineering, Beijing, China
e-mail: chj_cast@163.com

J. Sun et al. (eds.), *China Satellite Navigation Conference (CSNC) 2018 Proceedings*, Lecture Notes in Electrical Engineering 498,
https://doi.org/10.1007/978-981-13-0014-1_25

the Sun and the Moon gravitational forces. Non-conservative forces include atmospheric resistance that can be negligible for the high orbit satellite, solar radiation pressure perturbation, and relativistic effects. To the navigation satellites, whether the orbit dynamics model can accurately and truly represent the real on-orbit stress state, which affects the precision of orbit and positioning and navigation accuracy.

Different from other kinds of perturbation force, solar radiation pressure SRP and satellite attitude control mode, complex surface three-dimensional structure, the surface area of components, optical properties of materials and other engineering parameters are closely related. This also determines that SRP is the most difficult to accurately model [2]. It is the most important source of error for the navigation satellite orbit dynamics model.

There are three kinds of yaw attitude control modes of in-orbit BDS satellite, such as normal yaw-steering, yaw-fixed, and high angle maneuver. Taking BDS satellite as an example, a detailed analysis of three kinds of attitude control modes was proposed. On this basis, the acceleration of SRP under different attitude control modes were simulated and analyzed. The orbit determined by laser range data was chose as benchmark. By using SRP model established in different control modes, precise orbit was determined. The orbit determination result was compared with precise ephemeris afterwards named external compliance verification method. It is verified that the SRP model built for different attitude control modes were adapted to precise orbit determination.

2 Analysis on BDS Satellite Orbital Attitude Control Mode

At present, the BDS system has geostationary earth orbit, inclined geosynchronous satellite orbit, and medium earth orbit three types satellites. Three types of satellite attitude control methods are used full three-axis stability. In order to meet the energy security requirement, the IGSO/MEO satellite needs to control the attitude of yaw attitude and windsurfing corner. The result is that the included angle between the normal of windsurfing and sun rays is not greater than $\pm 5°$. So that the yaw attitude changes with the orbital position. The GEO satellite maintains its own energy needs by controlling the yaw attitude to 0° while keeping the sailboard cruising.

In order to meet the requirements of yaw control at different solar elevation angles, there are three kinds of yaw control modes for the in-orbit BDS IGSO/MEO satellites, which are respectively (1) yaw attitude dynamic bias mode (referred to as normal yaw-steering mode); (2) yaw attitude zero bias mode (referred to as yaw-fixed mode); (3) yaw attitude large-angle motor control (referred to as the high-angle motor mode).

In order to facilitate the explanation, we agree that the origin of the satellite is located at the satellite centroid. The +Z axis is perpendicular to the floor and points to the center of the earth. The +Y axis along one of the windsurfing shafts, and the X, Y and Z axes conform to the right hand spiral. As shown in Fig. 1.

2.1 Satellite Attitude Control Mode Analysis

The orbital inclination of inclined geosynchronous satellite orbit and medium earth orbit is 55°. The angle between the sun and the orbital plane is between 31.5 and 78.5°. Under normal conditions, the satellite yaw angle is shown in formula (1).

$$\psi = ATAN2(-\tan\beta, \sin\gamma) \tag{1}$$

where, ψ is yaw angle. β is the angle between solar vector and orbital plane. γ is the angle between satellite vector and orbit midnight, which is the farthest point on the orbit from the Sun.

According to the yaw angle in Eq. (1), the required yaw rate of satellite is formula (2).

$$\dot{\psi} = \dot{\gamma}\tan\beta\cos\gamma/(\sin^2\gamma + \tan^2\beta) \tag{2}$$

When $\gamma = 0°$, $\dot{\psi} = \dot{\gamma}/\tan\beta$. When $\gamma = 180°$, $\dot{\psi} = -\dot{\gamma}/\tan\beta$.

It can be concluded that the yaw rate will be very large when the included angle between the sun vector and the orbital plane is small. When $\beta = 0°$, theoretically $\dot{\psi}$ is infinite. The momentum wheel used to control the attitude can not track the nominal yaw rate. Therefore, depending on β, different attitude control modes need to be designed to meet the yaw attitude control needs.

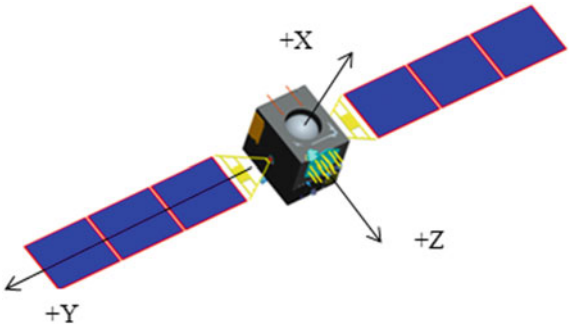

Fig. 1 Satellite body-fixed coordinate system

(1) Normal yaw-steering mode
When $\beta > 4°$, the control moment and angular momentum provided by the momentum wheel satisfied the requirement of yaw attitude control, and the continuous dynamic control of yaw angle was realized according to the yaw attitude offset determined by Formula (1).

Figure 2 is a IGSO satellite yaw attitude changes and solar panels rotation rules under normal conditions. The angle between solar vector and orbital plane angle is relatively large, yaw control mode of which called the normal yaw-steering in this article.

(2) Yaw-fixed mode
When $\beta < 4°$, one way was to make $\psi = 0°$. The solar panel is perpendicular to projection of the sun's vector in the orbit. Due to the small solar elevation angle, yaw-fixed can meet the energy needs of satellite. It also is a protection for on-board attitude control hardware. For yaw-fixed mode, the satellite body fixed coordinate system coincides with the orbital orbit coordinate system. The sun vector moves on the cone with the included angle with the XOZ plane of the present system (coincident with the orbital plane at this time).

(3) High-angle maneuvering mode
When β is small, yaw attitude control can also be implemented by means of yawing large-angle maneuvers. According to the reordered maneuvering trajectory of yaw attitude, the method of early maneuver and delayed maneuver is adopted to reduce the yaw maneuvering angular velocity and reduce the variation of yaw momentum so that the momentum wheel still has enough control torque margin and yaw angle Momentum margin.

Figure 3 shows the variation of yaw attitude, yaw rate and sailboard corner at high angle maneuvering at small solar altitude. In the maneuvering mode, the yaw attitude is controlled according to the planned trajectory. The sun vector is not

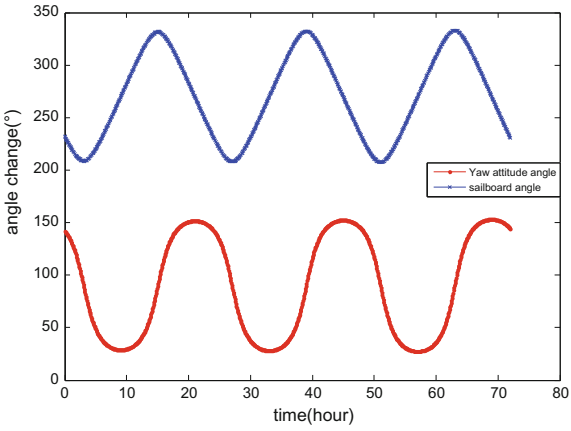

Fig. 2 Satellite yaw attitude and solar panel change for normally yaw-steering

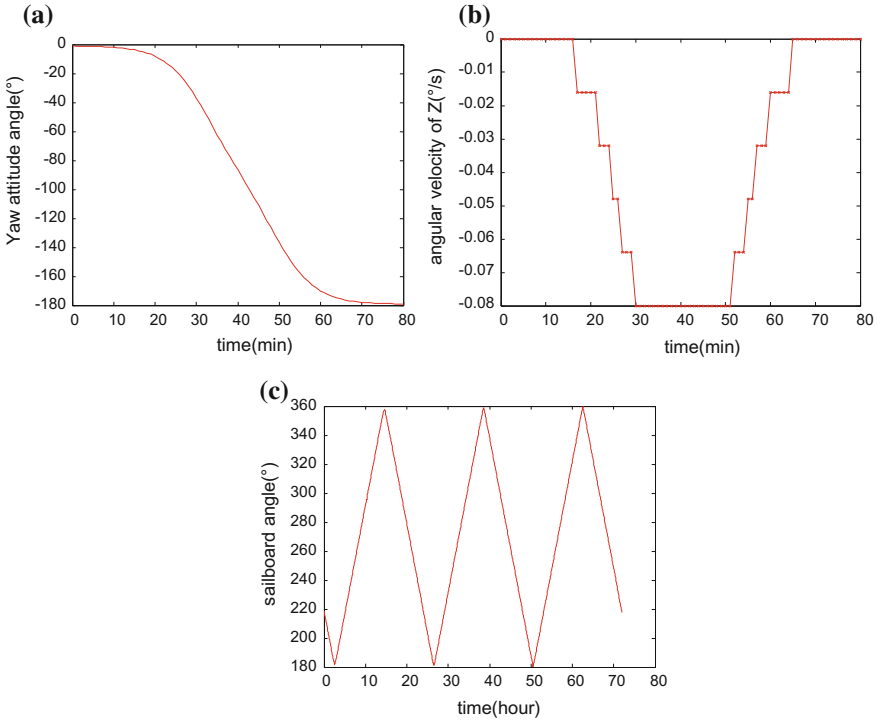

Fig. 3 **a** Yaw attitude during satellite maneuvering. **b** Yaw rate during satellite maneuvering. **c** Sailboard corner during satellite maneuvering of three days

completely within the XOZ plane of the present system, but has a small angle with the XOZ plane. With noon and midnight around the maneuver, the satellite has been +X facing the sun exposure.

2.2 Influence of Attitude Control Mode on SRP and TRP

The generalized pressure radiation is dominated by the direct solar radiation pressure, and also includes the satellite's own thermal radiation, the earth's albedo, and the high-power antenna electromagnetic radiation.

SRP analysis modeling is the calculation process from mechanism to result. By calculating the pressure perturbation force of each surface element and each surface element, the whole-star light pressure perturbation force and acceleration are obtained. This requires accurate description of the geometry of the surface elements exposed to sunlight, which is the real-time motion of the Sun vector in the star body coordinate system. This movement of the sun's vector is determined by the attitude control mode of the satellite.

Similarly, satellite thermal radiation means that when the temperature gradient exists between the surface of the satellite and the space environment. The satellite surface component radiates heat energy to the space background to maintain its own thermal balance [3]. Besides the heat generated by the work of the internal parts of the satellite body, the temperature of the outer surface component also absorbed from the sun and the earth's light energy. Different attitude control mode causes different radiated relations, the surface temperature of difference components is different, which will produce thermal radiation perturbation acceleration.

3 SRP and TRP Modeling and Difference Analysis for Different Control Modes

About the modeling method of the perturbation of pressure perturbation, it is the same with [2] in the literature, no longer elaborate here. The mass of the satellites is calculated on the basis of the orbital mass and the propellant consumed by each orbit of the orbit. In addition, the perturbation accelerations produced by Earth's albedo and antenna electromagnetic radiation are much lower than SRP and TRP, and are not included in the simulation in this paper.

3.1 Direct SRP Modeling and Analysis

To the normal yaw-steering, yaw-fixed and large-angle yaw maneuvering different attitude control models, taking the actual engineering parameters and on-orbit telemetry of a certain satellite as examples, direct SRP acceleration changes were shown in Figs. 4, 5 and 6. Y component is $2 \times 10^{-9} \sim 3 \times 10^{-9}$ m/s^2 during yaw-fixed. During high-angle yaw maneuvering, the difference between X and Z perturbation accelerations and normal yaw-steering is less than 10^{-11} m/s^2. It can consider that is same with normal yaw-steering. In addition, theoretically there is $3 \times 10^{-11} \sim 4 \times 10^{-11}$ m/s^2 Y-component during high-angle yaw maneuvers.

During the normal yaw-steering and the high-angle yaw maneuvering, the Sun moves within the XOZ plane of the satellite body-fixed coordinate system. Computation of acceleration of SRP and TRP perturbation taked the angle between the solar vector and +Z axis the satellite body-fixed coordinate system as an independent variable, denoted as θeps. During the yaw-fixed, there is an angle β between the sun and the XOZ plane of the star body which is also the orbital plane. In this case, the acceleration of SRP and TRP perturbation is the angle between the projection of the Sun vector in the orbital plane and +Z as an argument, which is also denoted as θeps.

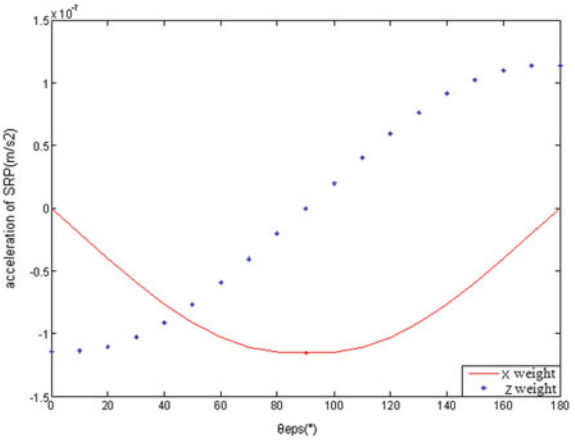

Fig. 4 Direct SRP acceleration for normal yaw-steering

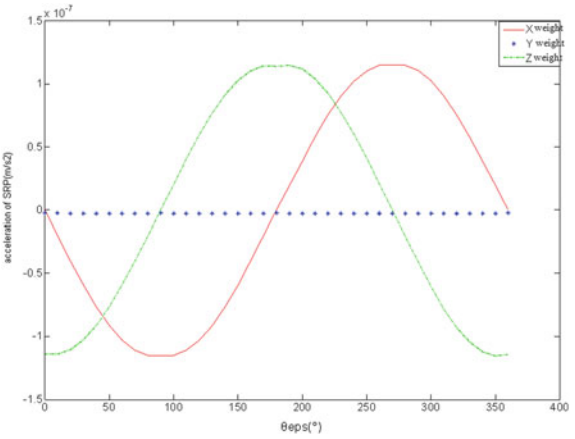

Fig. 5 Direct SRP acceleration for yaw-fixed

3.2 TRP Modeling and Analysis

Combined with the changes of in-orbit satellite temperature telemetry and the thermal simulation of the node grid method, Fig. 7 shows the X and Z perturbation accelerations caused by thermal radiation of in-orbit satellites for a period of time. North and South cooling plate is a uniform thermal design. In theory, there is no +Y or −Y direction of thermal radiation acceleration.

According to the simulation results of the optical perturbation, the seven-parameter form shown in the formula (3) is finally selected as the mathematical model of the optical perturbation analysis model after screening and comparison. And through the Fourier polynomial fitting, get each on-orbit satellite specific optical parameters.

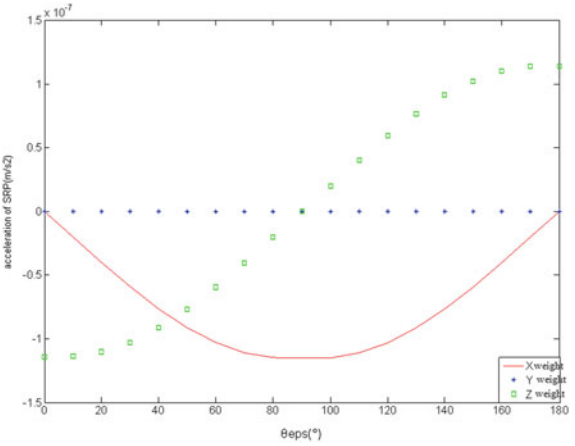

Fig. 6 Direct SRP acceleration for high-angle yaw maneuvering

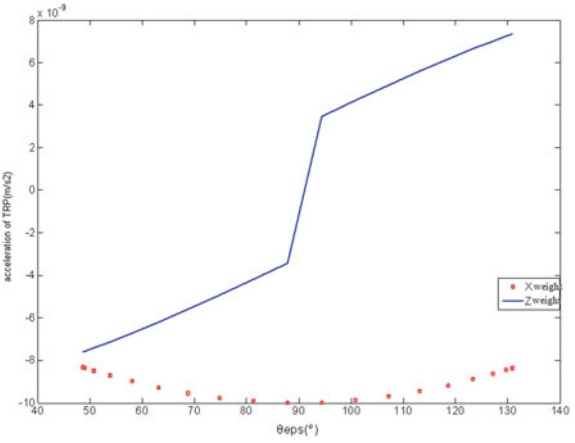

Fig. 7 TRP acceleration of in-orbit satellite

$$\begin{cases} \mathrm{X} = X_s \cdot \sin(\theta_{eps}) + X_c \cdot \cos(\theta_{eps}) + X_a \\ \mathrm{Y} = Y_a \\ \mathrm{Z} = Z_s \cdot \sin(\theta_{eps}) + Z_c \cdot \cos(\theta_{eps}) + Z_a \end{cases} \tag{3}$$

4 Precision Orbit Adaptation Verification

This section takes BDS C10 and C13 satellites as an example to conduct precise orbit determination. Precise orbit calculation determined by the laser ranging data around the world about 70 stations. Earth's gravitational field model uses 70*70 Joint Gravity Model 3 [4]. Sun and Month position was calculate through the ephemeris. Then, Sun and Moon gravity was solved. The SRP and TRP model uses

the simulation results described in Sect. 3, respectively. Every 15 min as a sampling point, the 2016 annual precise orbit has been determined. C10 satellite with the normal yaw-steering and yaw-fixed control mode, as the international laser tracking satellite, use laser ranging value of which as a benchmark. The root-mean-square (RMS) of the difference between the precision orbit determination result obtained by the precision measurement of the laser ranging and the orbit result determined in this paper in the 2016 full year has been compared. C13 satellites, using the normal yaw-steering and large-angle motor control mode, chose the same laser ranging as a benchmark. Precision orbit determination results through laser ranging and assess from the result in this paper has also been calculated.

Figure 8 shows the results of precision orbit determination and laser ranging and orbit determination under the normal continuous bias and zero offset modes of C10 satellite. The resulting evaluation results show that the precision of orbit determination is 0.785 m. Figure 9 shows the results of the calibration of precision orbit

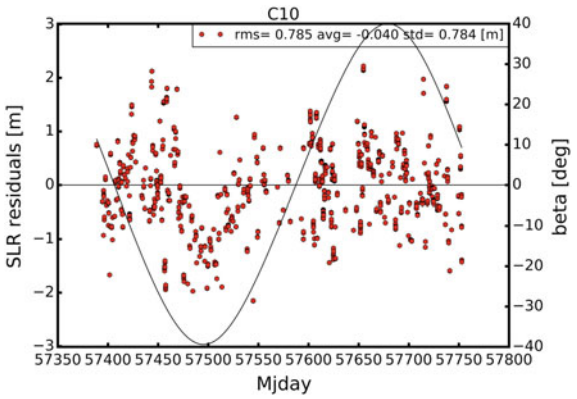

Fig. 8 In-orbit adaptability verification results of SRP +TRP model for C10 satellite

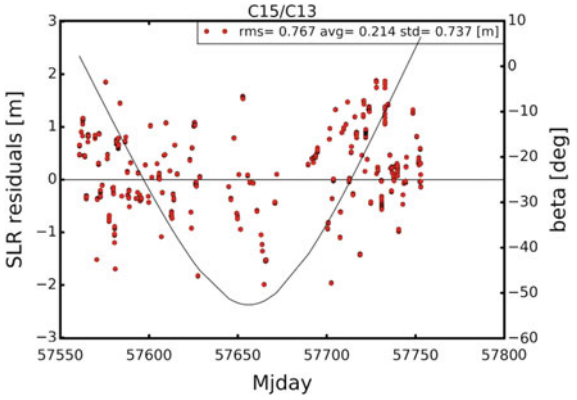

Fig. 9 In-orbit adaptability verification results of SRP +TRP model for C13 satellite

determination and laser ranging orbit determination during normal continuous maneuvering and high-angle maneuvering of C13 satellite. The orbit determination accuracy is 0.767 m.

In the same vein, we also tried to use the SRP model for yaw-steering mode during yaw-fixed mode or use the SRP model parameter under the yaw-fixed model during the yaw-steering mode. Both of them will cause the orbit determination to show signs of divergence in a short period of time. It shows that the model of SRP and the actual state of on-track are adaptive to each other, which is very necessary for the precision orbit determination.

5 Conclusion

Radiated parts and exposure is different due to BDS satellite different in-orbit attitude control modes, which causes different SRP model parameters. In this paper, the BDS inclined geosynchronous satellite orbit and medium earth orbit satellite were taken as examples to describe the different attitude control modes in orbit. The differential acceleration perturbations under different attitude control modes are simulated and analyzed. For the actual in-orbit attitude control mode, satellite telemetry parameters, engineering parameters established by the optical perturbation simulation model for the BDS satellite orbit determination. Based on the orbit determined by the laser ranging data, the results of the precision orbit determination of the simulation model are validated by comparing the outer coincidences with each other.

The results of laser inspection show that, the C10 satellite adopting the normal yaw-steering and yaw-fixed modes, C13 satellite adopting the normal yaw-steering and large-angle maneuver modes, adopts the light-pressure simulation model for the orbit calculation without adding any other corrections, precision orbit determination accuracy were both about 0.7 m. It provides a reference for further research on orbit dynamics model, especially for the in-depth study and application of light pressure perturbation.

References

1. Li J (1995) Satellite precision orbit determination. The People's Liberation Army press, Beijing (Ch)
2. Chen Q, Chen Z, Wang H (2014) Study on high precision solar radiation pressure for navigation satellite. CSNC (Ch)
3. Polar Lunar Regions: Exploiting Natural and Augmented Thermal Environments, NASA Tech Briefs, 2010.7
4. Tapley BD et al (1996) The joint gravity model 3. J Geophys Res 101(B12):28029–28050
5. Tapley BD et al (1996) The joint gravity model 3. J Geophys Res 101(B12):28029–28050

High-Precision GLONASS Orbit Prediction for Real-Time Precise Point Positioning

Peiyuan Zhou, Yang Gao and Hongzhou Yang

Abstract With the revitalization of GLONASS constellation, it becomes feasible to integrate the GLONASS into the conventional GPS-only real-time precise point positioning (PPP) processing to enhance system availability and reliability. As generation of real-time orbit corrections is a crucial part of the real-time PPP system, a high-precision GLONASS orbit prediction method is proposed and evaluated in this paper. First, the concept of a new real-time PPP system will be briefly introduced. Then, GLONASS orbit prediction method is presented with an emphasis on assessing the differences of the full 9 parameters empirical CODE orbit model (ECOM) solar radiation pressure (SRP) model and the reduced 5 parameters ECOM SRP model. Finally, the generated orbits are compared with the observed part of the GFZ ultra-rapid products. Furthermore, the orbit quality is assessed in both static and kinematic PPP experiments. It is shown that an average accuracy for 12 h orbit prediction using the full ECOM model are 0.019, 0.085, and 0.029 m in the radial, along-track and cross-track direction, respectively. The average accuracy of static PPP positioning for 5 global IGS stations are 0.019, 0.019, 0.031 m in the east, north and up direction, respectively; while the average accuracy of kinematic PPP is 0.136, 0.090, 0.256 m in the east, north and up direction, respectively. Meanwhile, utilization of the reduced 5 parameters ECOM solar radiation pressure model will not degrade the orbit prediction accuracy significantly and therefore comparable positioning performance can be achieved.

Keywords GLONASS · Orbit prediction · Real-time precise point positioning Solar radiation pressure

P. Zhou (✉) · Y. Gao · H. Yang
University of Calgary, Calgary T2N 1N4, Canada
e-mail: peiyuan.zhou@ucalgary.ca

J. Sun et al. (eds.), *China Satellite Navigation Conference (CSNC) 2018 Proceedings*, Lecture Notes in Electrical Engineering 498,
https://doi.org/10.1007/978-981-13-0014-1_26

1 Introduction

Precise point positioning (PPP) is a widely-used technique for derivation of accurate positioning solutions using a single receiver [1]. The conventional PPP data processing relies heavily on post-processed IGS final satellite orbits and clocks to obtain the highest accuracy, thus suffering from latencies up to about two weeks [2, 3].

In order to generate precise orbits and clocks for real-time PPP, the IGS launched the IGS real-time service (IGS RTS, http://www.igs.org/rts) [4]. Currently, the IGS RTS is transmitting real-time precise satellite orbit and clock corrections through the Networked Transport of RTCM via Internet Protocol (NTRIP) [5], with which the PPP user can obtain decimeter to centimeter level positioning accuracy [6–8]. However, the current user of real-time PPP system requires reliable and continuous access to the real-time orbit and clock correction streams, which is very challenging in real applications. Therefore, a new method for real-time correction update is proposed to solve this problem in previous work [9]. In the new real-time correction package, the orbit and clock are represented by initial conditions and generated in the server-end and then are sent to PPP users for derivation of precise orbit and clock corrections. The update rate of these orbit and clock initial conditions can be very low so that the PPP user's dependency on network access is significantly decreased.

In previous works, the generation of real-time orbit and clock initial conditions for GPS has been studied extensively [10, 11]. With a total number of 25 satellites in the GLONASS constellation, it is possible to add GLONASS to the conventional GPS-only processing to enhance system availability and reliability in challenging environments [12], such as city canyons, etc. However, the applicability of the GPS orbit prediction models to the GLONASS constellations remains to be investigated. For instance, the appropriate a priori SRP acceleration value should be determined for GLONASS satellites.

This paper will investigate the generation of GLONASS orbit initial conditions for real-time PPP system. The method used for generating GLONASS orbit initial conditions will be presented first and then an analysis of different solar radiation pressure models will be carried out. After that, the performance of the GLONASS orbit prediction will be fully examined. Finally, GLONASS based PPP experiments are conducted to demonstrate the quality of the predicted orbits.

2 GLONASS Orbit Prediction Method

It is well-known that satellite motions in space are under the influences of many forces, such as Earth gravity, Sun gravity, Moon gravity, solar radiation pressure, etc., which can be described by the differential equation [13]:

$$\ddot{r} = \frac{F(t, r, v)}{m} \tag{1}$$

where m is the mass of the satellite, r and v are satellite position and velocity in the inertial frame, respectively.

Considering the magnitude of different forces, a set of forces are selected and properly modeled. The EGM2008 model up to both degree and order of 12 is applied for modeling of Earth gravity [14]; the Sun and Moon gravity are calculated by point mass gravity [13]; and the solar radiation pressure forces are modeled by the empirical CODE orbit model (ECOM) developed by the Center for Orbit Determination in Europe (CODE) [15, 16]. A further detailed description of used models and methods can refer to [11, 17]. Accurate modeling of the solar radiation pressure forces is the key to achieve high-precision orbit prediction. The ECOM model can be described by [15]:

$$\ddot{r}_{SRP} = \frac{a_u^2}{|r_s - r|^2} \cdot [D(u) \cdot e_D + Y(u) \cdot e_Y + B(u) \cdot e_B] \tag{2}$$

where a_u represents the length of astronomical unit; r_s and r are positions of Sun and satellite in the initial frame. e_D is the unit vector from the sun to the satellite; e_Y is the Y axis of the satellite; and $e_B = e_D \times e_Y$.$D(u), Y(u)$ and $B(u)$ are expressed as [15]:

$$\begin{bmatrix} D(u) \\ Y(u) \\ B(u) \end{bmatrix} = D_0 \begin{bmatrix} \lambda \cdot DRAD & DCOS & DSIN \\ YRAD & YCOS & YSIN \\ BRAD & BCOS & BSIN \end{bmatrix} \begin{bmatrix} 1 \\ \cos(u) \\ \sin(u) \end{bmatrix} \tag{3}$$

where $DRAD, YRAD, BRAD \ldots BSIN$ are 9 ECOM parameters. u is the argument of latitude of the satellite, D_0 is the theoretical acceleration value caused by the solar radiation pressure given by ROCK model [16].

Instead of the full 9 parameters ECOM SRP model, a reduced 5 parameters empirical CODE orbit model is used in orbit determination activities of some IGS analysis centers [18]. The reduced ECOM SRP model differs in only taking harmonic terms in the B-direction into account as follows:

$$\begin{bmatrix} D(u) \\ Y(u) \\ B(u) \end{bmatrix} = D_0 \begin{bmatrix} \lambda DRAD & 0 & 0 \\ YRAD & 0 & 0 \\ BRAD & BCOS & BSIN \end{bmatrix} \begin{bmatrix} 1 \\ \cos(u) \\ \sin(u) \end{bmatrix} \tag{4}$$

With the above models, the orbit initial conditions, namely, the satellite position, velocity and ECOM parameters at the reference epoch, can be solved properly and then broadcasted to real-time PPP users for recovering high-frequency precise orbits through communication link [11]. Currently, the 9 parameters ECOM SRP model is routinely used in generation of GPS orbit initial conditions in the new real-time PPP system. However, since the theoretical acceleration value D_0 is

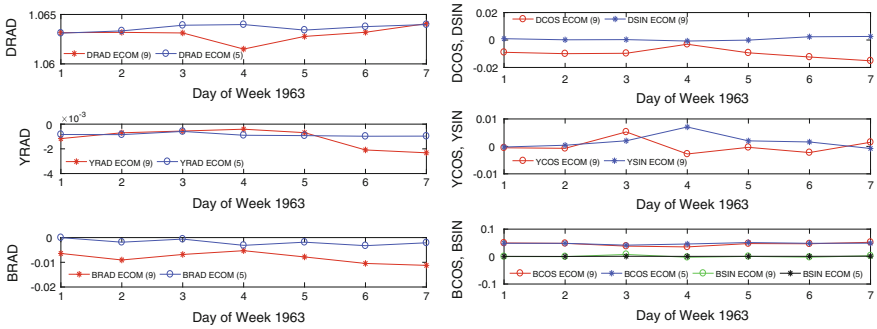

Fig. 1 Variations of ECOM SRP coefficients for GLONASS R01 in GPS week 1963

unknown for GLONASS satellites, it is necessary to set a reasonable value based on satellite properties. Therefore, the theoretical acceleration value for GPS satellites has been modified to serve the modeling of GLONASS satellite solar radiation pressure forces. The variations of ECOM coefficients for GLONASS R01 in GPST Week 1963 are shown in Fig. 1 for checking the validity of the model.

As can be seen, the DRAD parameter for both the full ECOM and the reduced ECOM are near 1, which shows the correctness of the theoretical acceleration value for GLONASS. The harmonic terms in the D and Y direction are basically an order of magnitude smaller than the B direction. Overall, the D and BCOS are two of the largest terms contributed to the SRP force modeling. Considering that the SRP forces are rather small compared to other forces acting on the satellite, it is expected that the elimination of harmonic terms in the D and Y direction will only slightly degrade recovered orbit quality while reduce computation efforts for recovering orbits from the initial conditions in the PPP user-end.

3 Orbit Prediction Accuracy

The GFZ multi-GNSS products are used for validation of the orbit prediction strategies. Firstly, the GFZ ultra-rapid orbits for GPS week 1963 with sampling interval of 5 min are downloaded from the GFZ online archive (https://www.gfz-potsdam.de/pub/home/GNSS/products/mgex/). 21 GLONASS satellites are available in this week. The GFZ ultra-rapid GLONASS orbits has an accuracy of several centimeters. It is remarked that we are using only the first update (i.e. 00:00) of each day in this paper. Then, the observed part of the GLONASS orbits in each day are used for generation of the orbit initial conditions. After that, the predicted orbits recovered from the initial conditions using a numerical integrator are compared with GFZ observed orbits of the next day.

The average fitting root mean square error (RMS) of each day for all GLONASS satellites is given in Table 1. It can be seen that the average fitting RMS using

Table 1 Average 24-h fitting RMS of all GLONASS satellites for GPS week 1963 (unit: m)

Day of week	SRP	Radial	Along	Cross
1	ECOM (9)	0.003	0.002	0.003
	ECOM (5)	0.017	0.006	0.008
2	ECOM (9)	0.003	0.003	0.003
	ECOM (5)	0.015	0.007	0.006
3	ECOM (9)	0.004	0.003	0.003
	ECOM (5)	0.015	0.008	0.005
4	ECOM (9)	0.004	0.003	0.003
	ECOM (5)	0.013	0.007	0.009
5	ECOM (9)	0.003	0.002	0.003
	ECOM (5)	0.015	0.007	0.005
6	ECOM (9)	0.004	0.005	0.003
	ECOM (5)	0.020	0.008	0.017
7	ECOM (9)	0.003	0.004	0.003
	ECOM (5)	0.018	0.007	0.012
Mean	ECOM (9)	0.003	0.003	0.003
	ECOM (5)	0.016	0.007	0.009

ECOM 9 parameters SRP model is 0.3 cm in each direction, while the average fitting RMS using ECOM 5 parameters SRP model are 1.6, 0.7 and 0.9 cm in radial, along-track and cross-track direction, respectively. The fitting RMS in the radial direction is an order of magnitude larger than using full ECOM SRP. The differences in fitting accuracy of the two SRP models are attributed to the different number of SRP parameters used for modeling of SRP force. Since the ECOM 5 parameters SRP model neglect harmonic terms in the D- and Y-direction, it might induce insufficient modeling of periodic force component in these directions. On the other hand, as the GFZ orbits are computed using the reduced 5 parameters SRP model [18], there also might be an overfitting problem when using the 9 parameters ECOM SRP model.

Next, the predicted orbits recovered from the generated orbit initial conditions are compared to the observed orbits. Figures 2 and 3 shows the 12-hour prediction accuracy of GLONASS R01 and R17 in the first day of GPS week 1963. It is clearly shown that the prediction errors in the radial and cross-track direction over 12 h are generally smaller than 0.05 m. Meanwhile, we can see accumulating errors in the along-track direction due to orbit dynamics. This might also be partly attributed to the fact that orbit prediction accuracy are closely correlated to the orbit quality used for generation of orbit initial conditions. The along-track direction of GFZ GLONASS orbits are poorer than the radial direction, which can lead to poor orbit initial condition estimates. As a result, the predicted orbit accuracy in the along-track direction are also poor. Furthermore, the ECOM model are designed for GPS satellites, it may not be fully capable of modeling SRP forces acting on GLONASS satellites. Therefore, the SRP model for GLONASS orbit prediction may need to be optimized in future work. Figure 4 shows the average orbit

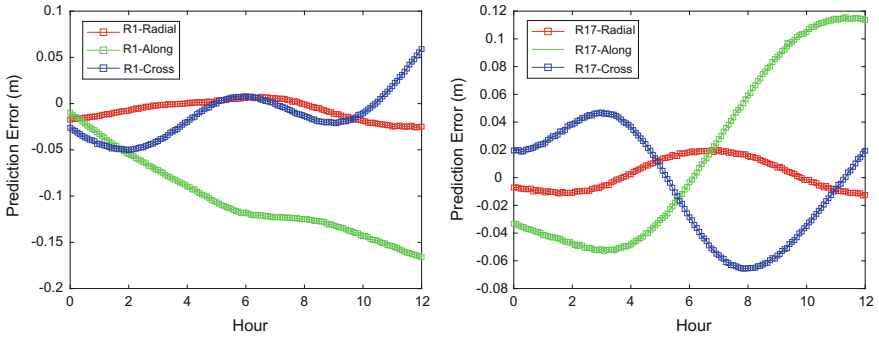

Fig. 2 GLONASS orbit prediction errors using full ECOM SRP model

prediction errors over 12 h for GPS week 1963. Overall, the average prediction error in the radial, along-track and cross-track direction over 12 h are 0.019, 0.085, 0.029 m for the full ECOM SRP model, and 0.026, 0.087, 0.033 m for the reduced ECOM SRPM model, respectively.

For evaluating orbit errors in the total positioning error budget, the orbit-only contribution to the signal-in-space range error (SISRE) for GLONASS is calculated by [19]:

$$SISRE(orb) = \sqrt{(0.98 \cdot R)^2 + (A^2 + C^2)/45} \tag{5}$$

where R, A and C are RMS of radial, along-track and cross-track directions.

The SISRE (orb) for the predicted orbits are plotted in Fig. 5. It indicates that the orbit-only SISRE of full ECOM SRP model is several millimeters better than the reduced ECOM SRP. Both the full ECOM and reduced ECOM model can satisfy PPP orbit accuracy requirement with an average SISRE (orb) of 3 cm. Therefore,

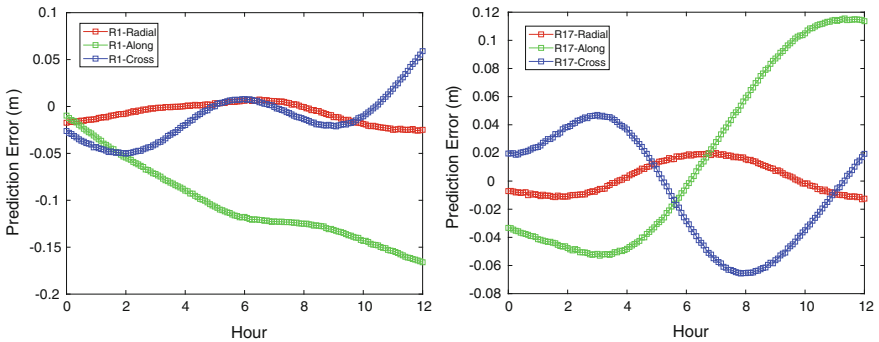

Fig. 3 GLONASS orbit prediction errors using reduced ECOM SRP model

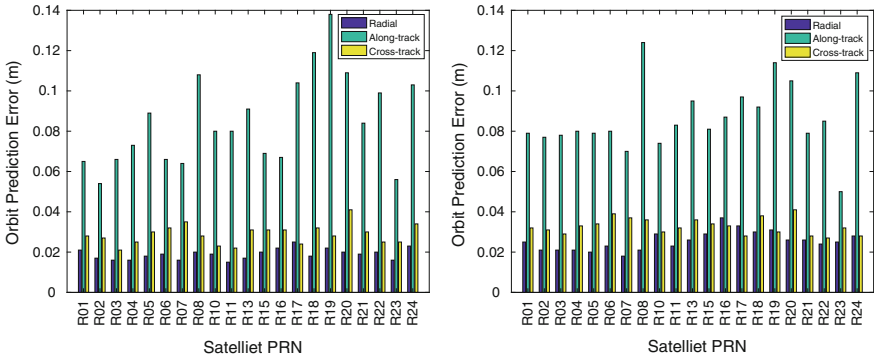

Fig. 4 Average orbit prediction errors over 12 h using full ECOM (left) and reduced ECOM (right) SRP model for GPS week 1963

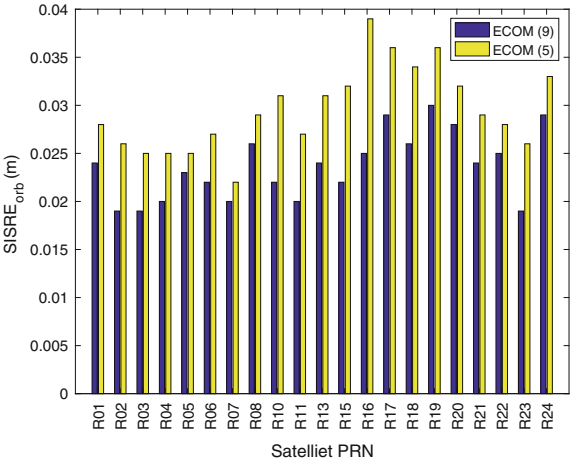

Fig. 5 SISRE (orb) of predicted orbits using different ECOM SRP models

the orbit-only SISRE of the two ECOM SRP models will not induce significant impacts on positioning accuracy.

4 PPP Experiments and Analysis

Since the positioning performance using the predicted orbits is our major concern, the accuracy of the predicted GLONASS orbits are further verified in both static and kinematic GLONASS-only PPP experiments. The experiments are carried out in the first day of GPS week 1963, 00:00 $\sim$ 06:00. The observation data with 30 s sampling interval are taken from the IGS global stations as shown in Fig. 6. The precise clocks are taken from the GFZ observed part of the ultra-rapid products,

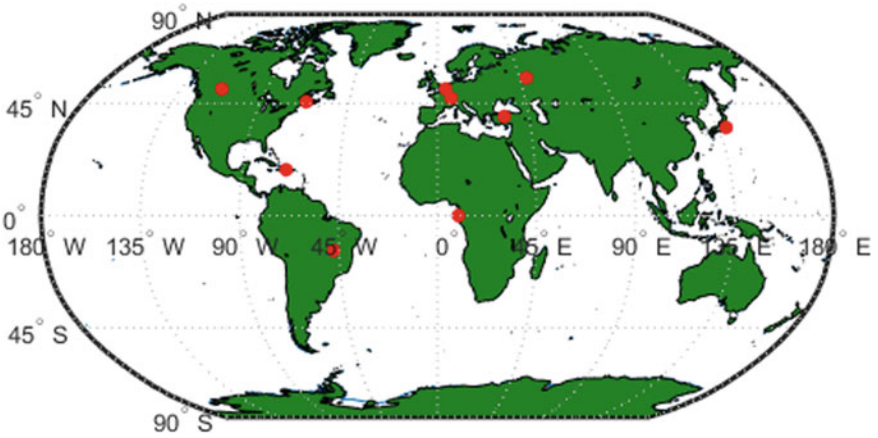

Fig. 6 Distribution of selected IGS stations

Table 2 Positioning accuracy of GLONASS-only static PPP (m)

Station	Orbits	East	North	Up
BRAZ	Observed	0.012	0.007	0.028
	Predicted with ECOM (9)	0.016	0.007	0.030
	Predicted with ECOM (5)	0.019	0.014	0.062
BRUX	Observed	0.024	0.017	0.015
	Predicted with ECOM (9)	0.043	0.019	0.017
	Predicted with ECOM (5)	0.044	0.013	0.030
RDSD	Observed	0.008	0.008	0.015
	Predicted with ECOM (9)	0.007	0.004	0.056
	Predicted with ECOM (5)	0.014	0.007	0.012
UCAL	Observed	0.004	0.013	0.009
	Predicted with ECOM (9)	0.017	0.037	0.020
	Predicted with ECOM (5)	0.012	0.030	0.026
UNB3	Observed	0.015	0.012	0.021
	Predicted with ECOM (9)	0.011	0.030	0.029
	Predicted with ECOM (5)	0.012	0.018	0.033
Mean	Observed	0.013	0.011	0.018
	Predicted with ECOM (9)	0.019	0.019	0.031
	Predicted with ECOM (5)	0.020	0.016	0.033

while the predicted orbits and the GFZ observed orbits are used for comparison. Both orbits and clocks have a sampling interval of 5 min. The positioning accuracy is calculated using the positioning solutions after the solution reach a fully convergence with respect to the IGS daily SINEX solution as a reference. The positioning accuracy of static PPP and kinematic PPP are listed in Tables 2 and 3, respectively.

Table 3 Positioning accuracy of GLONASS-only kinematic PPP (m)

Station	Orbits	East	North	Up
ANKR	Observed	0.024	0.026	0.053
	Predicted with ECOM (9)	0.032	0.021	0.080
	Predicted with ECOM (5)	0.026	0.022	0.079
BRAZ	Observed	0.040	0.023	0.063
	Predicted with ECOM (9)	0.038	0.042	0.097
	Predicted with ECOM (5)	0.044	0.039	0.089
BRUX	Observed	0.018	0.025	0.064
	Predicted with ECOM (9)	0.035	0.026	0.104
	Predicted with ECOM (5)	0.037	0.029	0.084
CHOF	Observed	0.362	0.221	0.747
	Predicted with ECOM (9)	0.445	0.278	0.942
	Predicted with ECOM (5)	0.441	0.271	0.917
KZN2	Observed	0.036	0.022	0.095
	Predicted with ECOM (9)	0.119	0.074	0.211
	Predicted with ECOM (5)	0.120	0.087	0.187
NKLG	Observed	0.057	0.064	0.083
	Predicted with ECOM (9)	0.067	0.074	0.104
	Predicted with ECOM (5)	0.090	0.071	0.086
RDSD	Observed	0.154	0.061	0.369
	Predicted with ECOM (9)	0.145	0.077	0.187
	Predicted with ECOM (5)	0.110	0.057	0.215
UCAL	Observed	0.058	0.074	0.089
	Predicted with ECOM (9)	0.095	0.127	0.158
	Predicted with ECOM (5)	0.085	0.122	0.171
UNB3	Observed	0.386	0.096	0.530
	Predicted with ECOM (9)	0.314	0.115	0.503
	Predicted with ECOM (5)	0.360	0.111	0.540
ZIM2	Observed	0.033	0.044	0.112
	Predicted with ECOM (9)	0.075	0.062	0.170
	Predicted with ECOM (5)	0.065	0.065	0.169
Mean	Observed	0.117	0.066	0.220
	Predicted with ECOM (9)	0.136	0.090	0.256
	Predicted with ECOM (5)	0.138	0.087	0.254

From the results, we can see that the average static PPP accuracy using the predicted orbits with ECOM 9 parameters SRP model are 0.019, 0.019, 0.031 m in the east, north and up direction; while the average accuracy of kinematic PPP is 0.136, 0.090, 0.256 m in the east, north and up direction, respectively. The positioning performance of predicted orbits using ECOM 5 parameters SRP model are comparable to the 9 parameters ECOM SRP model. On the other hand, the

performance of GFZ observed orbits are several centimeters better than using the predicted orbits. These results are in good agreements with analysis of SISRE (orb) statistics.

5 Conclusions

The high-precision GLONASS orbit prediction method for the new real-time PPP system are discussed and validated in this paper. The prediction method is presented first with an analysis of two variants of the ECOM SRP model. Then the generated orbits are compared to the GFZ observed orbit for direct accuracy analysis. It is shown that the proposed method can achieve high-precision GLONASS satellite orbit prediction with an average SISRE (orb) of smaller than 0.03 m. Furthermore, the predicted orbits are verified in PPP experiments with data acquired at the IGS global stations. The average accuracy of static PPP for 5 global IGS stations are 0.019, 0.019, 0.031 m in the east, north and up direction, respectively; while the average accuracy of kinematic PPP for 10 IGS stations are 0.136, 0.090, 0.256 m in the east, north and up direction, respectively. Based on our comparisons, it is concluded that the two ECOM SRP models has insignificant impacts on GLONASS orbit prediction accuracy and both models can satisfy real-time PPP requirements on orbit accuracy.

Acknowledgements GFZ is appreciated for providing the data. The first author is supported by the China Scholarship Council which is greatly acknowledged.

References

1. Zumberge JF, Heflin MB, Jefferson DC et al (1997) Precise point positioning for the efficient and robust analysis of GPS data from large networks. J Geophys Res 102:5005–5017. https://doi.org/10.1029/96JB03860
2. Kouba J (2009) A guide to using international GNSS Service (IGS) products
3. Bisnath S, Gao Y (2009) Current state of precise point positioning and future prospects and limitations. Observing our changing earth. Springer, Berlin, Heidelberg, pp 615–623
4. Agrotis L, Schoenemann E, Enderle W et al The IGS real time service
5. Weber G, Dettmering D, Gebhard H (2005) Networked transport of RTCM via internet protocol (NTRIP). A window on the future of geodesy. Springer, Berlin, Heidelberg, pp 60–64
6. Kazmierski K, Sośnica K, Hadas T (2018) Quality assessment of multi-GNSS orbits and clocks for real-time precise point positioning. GPS Solut 22:11. https://doi.org/10.1007/s10291-017-0678-6
7. Hadas T, Bosy J (2015) IGS RTS precise orbits and clocks verification and quality degradation over time. GPS Solut 19:93–105. https://doi.org/10.1007/s10291-014-0369-5
8. Elsobeiey M, Al-Harbi S (2016) Performance of real-time precise point positioning using IGS real-time service. GPS Solut 20:565–571. https://doi.org/10.1007/s10291-015-0467-z

9. Gao Y, Zhang W, Li Y (2016) A new method for real-time PPP correction updates. Springer, Berlin Heidelberg, Berlin, Heidelberg
10. Yang H, Xu C, Gao Y (2017) Analysis of GPS satellite clock prediction performance with different update intervals and application to real-time PPP. Surv Revi 0:1–10. https://doi.org/10.1080/00396265.2017.1359473
11. Yang H, Gao Y (2017) GPS satellite orbit prediction at user end for real-time PPP system. Sensors 17:1981. https://doi.org/10.3390/s17091981
12. Li X, Ge M, Dai X et al (2015) Accuracy and reliability of multi-GNSS real-time precise positioning: GPS, GLONASS, BeiDou, and Galileo. J Geod 89:607–635. https://doi.org/10.1007/s00190-015-0802-8
13. Montenbruck O, Gill E (2012) Satellite orbits: models, methods and applications. Springer Science & Business Media
14. Pavlis NK, Holmes SA, Kenyon SC, Factor JK (2008) An earth gravitational model to degree 2160: EGM2008. EGU General Assembly 2008:4–2
15. Beutler G, Brockmann E, Gurtner W et al (1994) Extended orbit modeling techniques at the CODE processing center of the international GPS service for geodynamics (IGS): theory and initial results. Manuscr Geod 19:367–386
16. Springer TA, Beutler G, Rothacher M (1999) A new solar radiation pressure model for gps satellites. GPS Solutions 2:50–62. https://doi.org/10.1007/PL00012757
17. Herring TA, King RW, McClusky SC (2010) Introduction to Gamit/Globk. Massachusetts Institute of Technology, Cambridge, Massachusetts
18. Deng Z, Fritsche M, Uhlemann M et al (2016) Reprocessing of GFZ multi-GNSS product GBM. In: Proceedings of IGS Workshop, Sydney, Australia. pp 8–12
19. Montenbruck O, Steigenberger P, Hauschild A (2015) Broadcast versus precise ephemerides: a multi-GNSS perspective. GPS Solut 19:321–333. https://doi.org/10.1007/s10291-014-0390-8

The Filtered GNSS Real-time Precise Orbit Solution

Xiaolei Dai, Zhiqiang Dai, Yidong Lou, Min Li and Yun Qing

Abstract The reliable real-time precise satellite orbit is the prerequisite and foundation of real-time precise positioning service for Global Navigation Satellite System. Recently, real-time precise orbit products are usually predicted from the post precise products that are determinate by the batch-processing method based on the history data. This method bears some obvious drawbacks that degrade the performance of real-time orbit products, especially for the Chinese BeiDou Satellite System (BDS). Firstly, the predicted orbit depends heavily on the accuracy of dynamic force model and responses slowly to the model accuracy degradation and variation. Secondly, the predicted precise orbit exhibits uncontinuity between two consecutive orbit arcs, which will affect the position accuracy. In this paper, the Square Root Information Filter (SRIF) method is adopted to update the satellite orbit in real-time and response quickly to orbit maneuver. The strategy is validated for the POD of GNSS satellites using one-month data. The results show that the 3D RMS of SRIF orbit for GPS and GLONASS satellites is 6.7 and 9.3 cm, respectively. The mean value of SLR validation residual for BDS IGSO and MEO satellites is less than 10 cm and for GEO satellite is about 20.7 cm. At last, the real time products were used to for kinematic PPP. The positioning results show that, compared to the predicted real time product, the real time product generated by the proposed real time filtering method improves the BDS-only kinematic positioning accuracy significantly and the accuracy of 3 cm in the horizon and 5 cm in height can be reached for the multi-GNSS positioning.

Keywords GNSS · BDS · Real-time orbit determination · SRIF

X. Dai (✉) · Y. Lou · M. Li · Y. Qing
GNSS Research Center, Wuhan University, 129 Luoyu Road, Wuhan 430079, Hubei, China
e-mail: xldai@whu.edu.cn

Z. Dai
Hi-Target Surveying Instrument Co., Ltd, 13th Building, Tian'an Technology Zone,
No. 555 the North of Panyu District, Guangzhou 511400, China
e-mail: dzq@whu.edu.cn

J. Sun et al. (eds.), *China Satellite Navigation Conference (CSNC) 2018 Proceedings*, Lecture Notes in Electrical Engineering 498,
https://doi.org/10.1007/978-981-13-0014-1_27

1 Introduction

GNSS technology has been committed to providing users with real-time, high-precision and high-reliability navigation services, especially in recent years, many countries and regions have been or are being established the real-time precise point positioning service system. High-precision satellite orbit is the prerequisite and guarantee for the global real-time positioning service system. There are two methods for real-time orbit determination. One is the orbital forecasting mode based on post-batch processing, the other is the filtering solution based on real-time data stream. The orbit prediction is realized based on the satellite dynamic model. First, the precise orbit states are determinated using post-batch processing, and then the satellite orbit is predicted based on the solved parameters by using numerical integration. The accuracy and reliability of such an orbit is heavily dependent on the stability of satellite motion and the force modelling, and as well as the predicting time. This strategy has been employed to generate the BDS orbit for the real-time positioning. Generally, the batch processing can achieve real-time orbit precision of decimeter level for IGSO and MEO, and about 1 m for GEO [1, 2]. However, when the satellite is during eclipsing season or maneuver period, it is hard to maintain the accuracy and reliability of the real-time orbit because the satellite dynamic is difficult to be modeled. This problem is more severe for BDS GEO satellites that have to keep pace with the Earth rotation by frequent maneuvers.

In principle, the filter-based real-time orbit determination strategy is superior to the traditional method at least in two ways. Firstly, this method can update the satellite orbit state as soon as the observation is obtained, so that the estimates can immediately reflect any unusual behaviour in satellite dynamics. Secondly, based on the real-time data stream, the estimated orbit using a filter is continuous and smooth over the whole filtering period, whereas orbit jumps between the consecutive arcs are inevitable in batch processing, especially for the BDS GEOs. Poor geometric condition and inaccurate solar radial pressure model may lead to 1 m jumps in the along-track direction [3].

In this paper, the square root information filter (SRIF) is used to determinate the satellite precise orbit in real-time. By using this method, the satellite orbit states are estimated in real-time which can avoid the accuracy degradation of the dynamic model predicted over time. The real-time GNSS orbits estimated by SRIF method are compared with the final products of IGS and MGEX ACs and analysed by the Satellite Laser Ranging (SLR) residuals. Finally, the SRIF real-time orbit products are validated by the real-time kinematic PPP.

2 Methodology

2.1 Square Root Information Filter

The SRIF is an improved Kalman filter method with high numerical accuracy and stability which is originally proposed by Bierman [4]. In its sequential recursive, an elementary Householder orthogonal transformation and a square root of the information matrix is employed. Generally, the SRIF process comprises of measurement and time update steps.

Assumed the normalized a priori information of the unknowns and linear measurement equations are:

$$\begin{cases} \tilde{z}_0 = \tilde{R}_0 x + \tilde{v}_0 \\ z = Ax + v \end{cases} \tag{1}$$

By applying Householder transformation to Eq. (1), then

$$T\begin{bmatrix} \tilde{R}_0 \\ A \end{bmatrix} x = T\begin{bmatrix} \tilde{z}_0 \\ z \end{bmatrix} + T\begin{bmatrix} \tilde{v}_0 \\ v \end{bmatrix} \Rightarrow \begin{bmatrix} \hat{R}_0 \\ 0 \end{bmatrix} x = \begin{bmatrix} \hat{z}_0 \\ e \end{bmatrix} + \begin{bmatrix} \hat{v}_0 \\ v_e \end{bmatrix} \tag{2}$$

where T is an orthogonal transformation, $\|e\|^2$ is the sum of squares residual error. The SRIF measurement update can be expressed as

$$\tilde{R}_0 x = \tilde{z}_0 \xrightarrow[T]{Ax=z} \begin{cases} e \\ \hat{R}_0 x = \hat{z}_0 \end{cases} \tag{3}$$

The estimate state vector x is divided into determined parameters y and process parameters p, then $x = [p \quad y]^T$. The dynamic equations for process noise parameters can be written as:

$$R_{w_j} p_{j+1} = M_j p_j + w_j \tag{4}$$

where the covariance matrix of the process noise ϖ_j is $Q_j = R_{w_j}^{-1} R_{w_j}^{-T}$, m_j is the transition matrix and set $M_j = R_{w_j} m_j, w_j = R_{w_j} \varpi_j$. The SRIF time update can be expressed as:

$$\hat{R}_j x_j = \hat{z}_j \xrightarrow[T]{R_{w_j} p_{j+1} = M_j p_j + w_j} \begin{cases} \tilde{R}_{p_j} p_j + \tilde{R}_{p_j p_{j+1}} p_{j+1} = \tilde{w}_{j+1} \\ \tilde{R}_{j+1} x_{j+1} = \tilde{z}_{j+1} \end{cases} \tag{5}$$

2.2 Measurement and Orbit Models

The real-time precise orbit determination software developed in this paper uses the SRIF method to simultaneously determine the orbit states of multi-GNSS satellites under the same space and time reference frame. The space and time reference frame, the dynamic model and the observed model are shown in Tables 1, 2 and 3.

Table 1 Space and time reference frame

Item	Applied models
Time system	GPS time
Inertial reference system	J2000.0 ICRF frame
Geocentric reference system	ITRF2008 reference frame
Earth rotation parameters (ERP)	Initial values are from file gpsrapid.daily (http://maia.usno.navy.mil/ser7/gpsrapid.daily)

Table 2 Orbit dynamic model

Item	Applied models
Geopotential	EGM96 model (12 × 12)
M-body gravity	Sun, Moon and planets
Tidal forces	Solid Earth, pole, ocean tide IERS conventions 2010
Solar radiation pressure	Reduced CODE 5-parameter with no initial value
Earth albedo	GPS/GLONASS: SR ERPFBOXW by Rodriguez-Solano with antenna thrust applied by Rodriguez-Solano et al. [5]; BDS: no

Table 3 Observation models

Item	Applied models
Basic observables	un-differenced ionosphere-free combination of code and phase based on GPS L1/L2, BDS B1/B2
Processing sampling	300 s
Cutoff elevation	7°
Weighting	Elevation dependent weight
Satellite antenna phase center	GPS/GLONASS: PCOs and PCVs from IGS; BDS: PCO from IGS MGEX no PCVs
Receiver phase center	igs08.atx for GPS/GLONASS, none for BDS
Phase wind-up	Wu [6]
Tropospheric delay	Initial model + random-walk process
Satellite clock	Estimated as white noise
Receiver clock	Estimated as white noise
Earth rotation parameters (ERP)	Estimated with tight constraint
Inter-system biases	Estimated as constant parameters with zero mean condition
Ambiguity	Fixed for GPS/BDS(IGSO, MEO) separately

3 Experiment and Result Analysis

In this paper, the post data were processed simulated in real-time to validate the algorithm and software. The data stream time delay which was exist in the real situation was regardless in this case. The experiments were performed on the precise orbit determination of GPS, GLONASS and Beidou satellites from DOY 039 to DOY 069 in 2015. The observations were from IGS, MGEX and BETS (Beidou Experimental Network) networks for a total of about 110 stations. The station distribution is shown in Fig. 1.

3.1 The Accuracy of Real-Time Orbit Solution

To evaluate the orbit accuracy, the GPS and GLONASS real-time orbit solutions are compared with the IGS final products, while the BDS real-time orbit is validated by the SLR data.

The real-time orbit solutions from 040, 2015 to 069, 2015 are used to assess the orbit accuracy, with the orbit during the convergence day excluded. Figure 2 presents the orbit accuracy of GPS and GLONASS in radial-, cross- and along-direction. As it is shown, the RMS of all GPS satellites is less than 7 cm, with the mean RMS of 2.9, 3.7 and 4.8 cm in the radial-, cross- and along-direction respectively. The orbit accuracy of GLONASS is comparable to that of GPS in radial-direction, and slight worse in another two directions, especially in cross-direction, with the largest RMS of about 12 cm. The mean RMS of all GLONASS satellites is 3.3, 4.2 and 7.6 cm in the radial-, cross- and along-direction, respectively. The statistical results show that orbit accuracy of GPS and GLONASS real-time orbit is comparable with that of the predicted part of IGS ultra-fast orbit products.

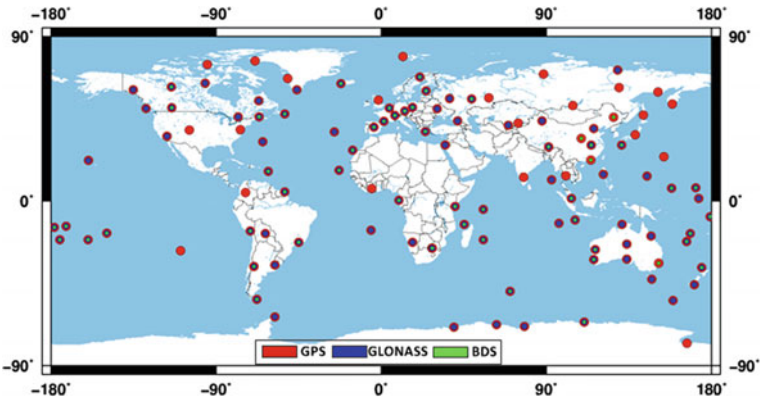

Fig. 1 The station distribution

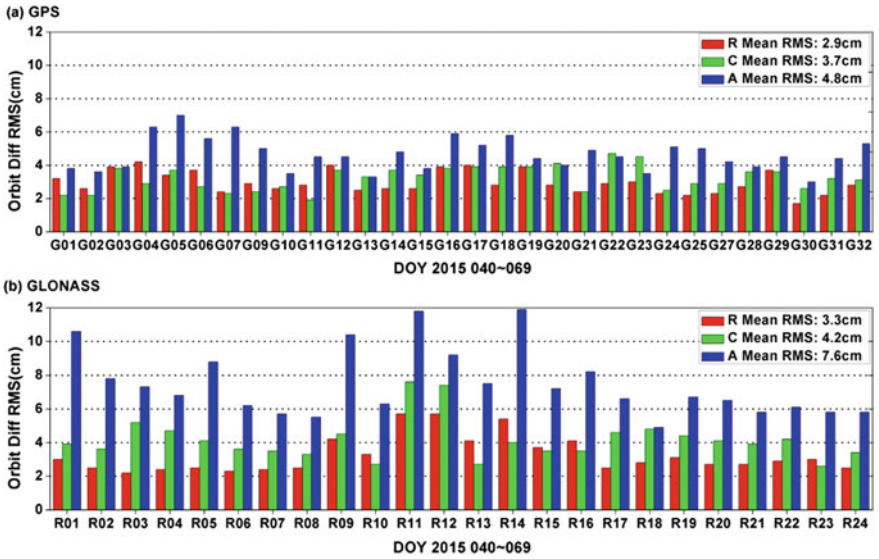

Fig. 2 Accuracy of the GPS (up) and GLONASS (bottom) filtered orbit solutions

The real-time BDS orbit solutions and the least-squares post solutions from 040, 2015 to 069, 2015 are compared respectively with the SLR data to assess the orbit accuracy which is listed in Table 4. As shown in table, the standard deviation (STD) of the IGSO and MEO SLR residuals of the real-time orbit solutions is large than that of the post orbit solutions. Of all the satellites, C08 has the large SLR residuals, of which the bias and STD are −5.8 and 9.7 cm respectively. The mean bias of C10 and C11 SLR residuals is −2.2 and −0.4 cm. There is significant bias, about −20.7 cm, found in the SLR residual of the filtered GEO orbit solution, which is 21 cm smaller than the post solutions, same as the STD. In real-time POD, the process noise is introduced to reduce the effect of force model error and increase the weight of observations may contribute to the improvement compared to the post solution. To further reduce the GEO SLR residuals, more accurate solar radiation pressure is needed.

Table 4 Mean and STD of SLR residuals of SRIF solutions and post 3-day solutions (Units: cm)

		Filtered Solution	Post 3-day solution
C01	Bias	−20.7	−41.7
	STD	18.8	29.2
C08	Bias	−5.8	−3.8
	STD	9.7	8.6
C10	Bias	−2.2	−1.7
	STD	7.9	4.7
C11	Bias	−0.4	−0.6
	STD	5.1	2.3

3.2 Analysis of the Real-Time Orbit Series

To assess the accuracy of real-time orbit solutions, the orbit difference series of real-time orbit solution and reference orbit is analyzed too.

Figure 3 presents the orbit difference series of GPS and GLONASS in the along-, cross- and radial-direction from 039, 2015 to 044, 2015. As it is shown in the figure, after convergence, the orbit difference of GPS is between ±10 cm in the cross- and radial-direction, and between ±20 cm in the along-direction. GLONASS has larger orbit differences than GPS in all directions, of which the orbit differences of most satellites are between ±10 cm in the radial- and cross-direction, and the orbit difference in the along-direction is up to 40 cm. Further analysis shows that, the R11, R12, R14 and R16 satellites, having rather larger orbit differences in the POD period, are eclipse satellites. The orbit differences exhibit significant jumps in the along- and cross-direction around the day boundary, especially for the eclipse satellite. Since the filtered orbits are continuous, the jumps in orbit differences result from the IGS reference orbits. Thus, orbit error of the reference solutions and filtered solutions becomes larger for the eclipse satellites which contributes to the apparent larger orbit differences than the other satellites.

Recently, the GNSS Research Center of Wuhan University has been providing the precise final products (code is WUM) for GPS, GLONASS, BDS and GALILEO. The filtered orbits are compared with the WUM products to compute the orbit differences in along-, cross- and radial-direction which are shown in Fig. 4. As it is shown, the orbit differences with WUM are the largest in along-direction, and the smallest in radial-direction. As the filter progresses, the orbit differences between filtered solution and WUM final products become smaller. As the WUM final products are the 1-day solutions, the orbit differences exhibit apparent jumps as much as 80 cm around the day boundary. The filtered solutions of BDS IGSO and MEO exhibit good continuity, of which the orbit differences converge to stable status as the filter progresses. After convergence, the orbit accuracy of the filtered solutions is about 10–20 cm.

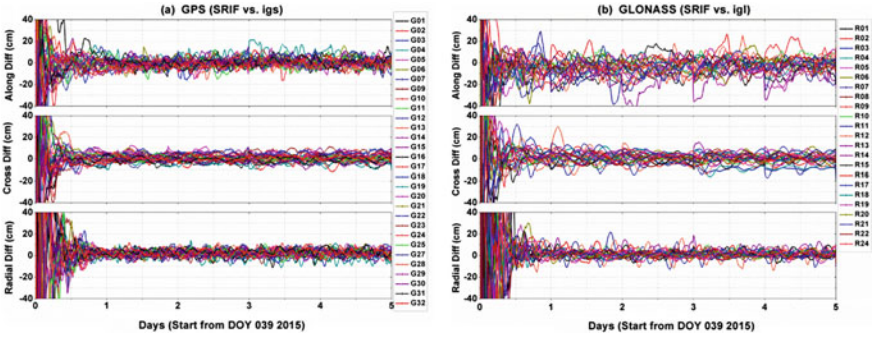

Fig. 3 Orbit difference series of GPS (left) and GLONASS (right)

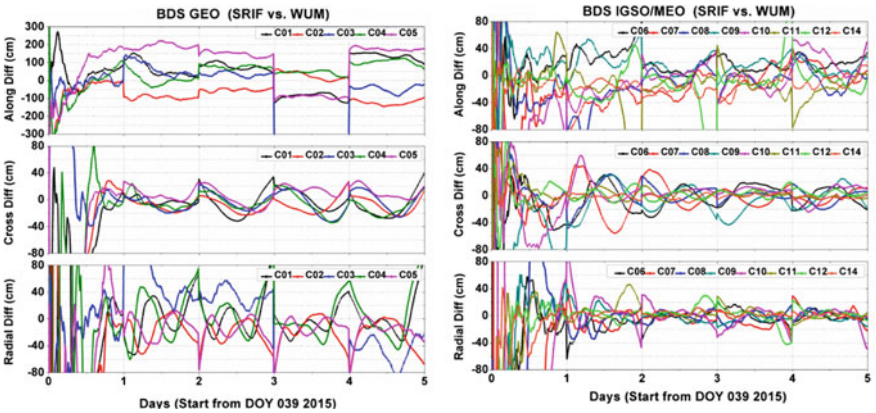

Fig. 4 Orbit differences between the filtered solutions and the WUM final products for BDS GEO (left), IGSO and MEO (right)

4 PPP Validation of the Filtered Orbit Products

In order to validate the positioning performance of the filtered real-time precise orbit products, the filtered orbits and predicted orbits are used to estimate precise satellite clock corrections with the same stations in POD. Two sets of products are respectively used to carry out kinematic PPP, and the positioning results are compared with the static PPP solution of the IGS post products. The E/N/U series are shown in Fig. 5. It can be seen from the figure that the multi-GNSS kinematic PPP solutions of the two schemes are superior to the GPS-only solutions in terms of accuracy and convergence speed, mainly because multi-GNSS can increase the available satellite number and improve the geometric conditions dramatically. For MROI station, the GPS and BDS combined solution shows apparent improvements in three directions, especially in the U direction, with an

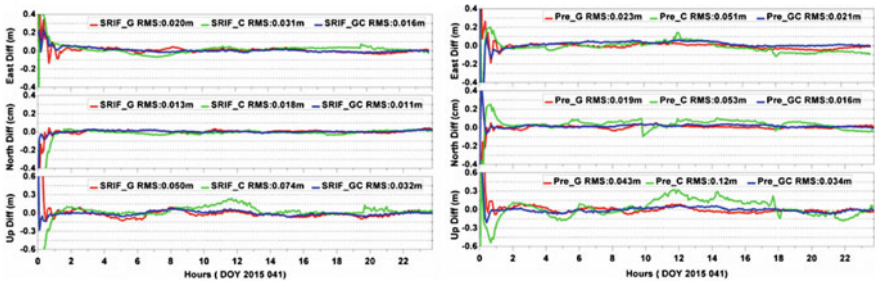

Fig. 5 Different kinematic PPP series in E/N/U directions (left: filtered products, right: predicted products)

improvement of 36% for scheme 1 and 21% for scheme 2. The GPS-only PPP solutions have comparable accuracy for the two schemes, while the BDS-only solution of scheme 1 is better than that of scheme 2, with the improvements of 39, 66 and 38% in E, N and U directions, because the predicted BDS orbit is rather worse. The GPS and BDS combined solutions of scheme 1 are better than that of scheme 2, with the accuracy of 1.6, 1.1 and 3.4 cm in E/N/U directions, which demonstrate that the filtered real-time products are capable to support real-time PPP application.

5 Conclusions

In this paper, the real-time orbit of satellite is determined by the SRIF method based on real-time observation data to generate high-precision real-time orbit, which effectively solves the problem that the precision of satellite dynamics model degrades with time. The experimental results show that the three-dimensional accuracy of real-time orbits of GPS and GLONASS are 6.7 and 9.3 cm, respectively. The mean bias of SLR residuals of the BDS IGSO and MEO real-time orbit is within 10 cm, while that of the GEO satellites is 20.7 cm, with an improved of 20 cm, compared with the post orbit solutions. After convergence, the filtered orbit exhibits better continuity in time, which can avoid inconsistencies between two arcs in the predicted orbit. At the same time, the filtered orbit can detect and response to the satellite orbit maneuver events in real-time. Based on the filtered real-time orbit product, the real-time PPP solution is improved by 2 cm, 3.5 cm, and 4.6 cm in E/N/U directions respectively, which demonstrate the filtered real-time orbit products can provide reliable and precise real-time positioning service.

Acknowledgements This work is supported by National Key Research and Development Program of China (No.2016YFB0501802).

References

1. Li X, Ge M, Dai X, Ren X, Fritsche M, Wickert J, Schuh H (2015) Accuracy and reliability of multi-GNSS real-time precise positioning: GPS, GLONASS, BeiDou, and Galileo. J Geod 89 (6):607–635
2. Tegedor J, de Jong K, Liu X, Vigen E, Øvstedal O (2015) Real-time precise point positioning using BeiDou. In: Rizos C, Willis P (eds) IAG 150 Years, International Association of Geodesy Symposia, vol 143. Springer, Cham
3. Ma H, Zhao Q, Xu X (2017) A new method and strategy for precise ultra-rapid orbit determination. In: China satellite navigation conference (CSNC) 2017 Proceedings, vol III. pp 191–205
4. Bierman GJ (1977) Factorization methods for discrete sequential estimation. Academic press, New York

5. Rodriguez-Solano C, Hugentobler U, Steigenberger P, Lutz S (2011) Impact of earth radiation pressure on GPS position estimates. J Geod 86:309–317. doi: http://www.doi.org/10.1007/s00190-011-0517-4
6. Wu J, Wu S, Hajj G, Bertiger W, Lichten S (1993) Effects of antenna orientation on GPS carrier phase. Manuscripta Geodaetica 18:91–98

Systematic Error Estimation and Accuracy Evaluation for Two-Way Satellite Time and Frequency Transfer Observing Data

Rui Guo, Li Liu, Shan Wu, GuiFen Tang and XiaoJie Li

Abstract The time delay could hardly be calibrated accurately for the two-way satellite time and frequency transfer equipment. Therefore the time delay error and its secular drift would not only restrict the time synchronization accuracy, but also restrict the broadcast parameters accuracy for the satellite navigation system. In order to solve this problem in the self-sending-self-receiving observation, we bring forward two systematic error estimation methods, named SLR co-location comparison method and combined precise orbit determination (POD) method. We also introduce a across sending and receiving systematic error estimation method based on the restriction from the station clock offsets estimated by multiple precise orbit determination (MPOD). And the three-station circle error and clock offset consistency are introduced to evaluate the systematic error estimation accuracy. Tests are carried out with the Beidou satellite navigation system (BDS) real data. Results show that the accuracy of the SLR co-location comparison method is better than 0.3 ns, while the combined POD method better than 0.5 ns for the self-sending-self-receiving observation. And for the across sending and receiving systematic error, the estimation accuracy is better than 0.4 ns, with circle errors among three stations better than 0.1 ns. The station clock offset consistency from two different C-band antennas is better than 0.3 ns. The high accuracy time synchronization can be achieved among different stations in the satellite navigation system, and two different C-band equipment could backup with each other.

Keywords Two-Way satellite time and frequency transfer · Systematic error Time delay · Circle error · Clock offset · Satellite laser ranging

R. Guo (✉) · L. Liu · S. Wu · G. Tang · X. Li
Beijing Satellite Navigation Center, Beijing 100094, China
e-mail: shimbarsalon@163.com

J. Sun et al. (eds.), *China Satellite Navigation Conference (CSNC) 2018 Proceedings*, Lecture Notes in Electrical Engineering 498,
https://doi.org/10.1007/978-981-13-0014-1_28

1 Introduction

High-accuracy interstation time synchronization is not only an important basis of satellite navigation system's high-precision punctuality and time service, but also an important premise for processing various satellite navigation message parameters [1, 2]. Especially for Beidou system, solving the problem of orbit determination and fast post-maneuver orbit recovery of GEO satellites depends on high-precision time synchronization among ground stations [3–5].

Commonly used interstation time synchronization method mainly includes satellite common-view method, satellite bidirectional common-view method and c-band satellite two-way frequency transfer method. Satellite common-view method is unable to completely eliminate satellite orbit error, and when station distance increases, alignment error also increases and meanwhile influence of pseudo-range measurement error is obvious. Satellite bidirectional common-view method relies on the two-receiving channels of uplink, which are high in precision but with limited application. C-band satellite two-way frequency transfer method is high in precision without high requirement on satellite load, and time synchronization between two stations can be realized by both communication satellite and navigation satellite, and therefore this method is preferred for time synchronization in Beidou system [6, 7].

However, affected by time delay error of satellite and ground equipment, accuracy of this method is decreasing significantly and unable to achieve high-precision time synchronization among stations with equipment's factory calibrated time delay value. There is significant systematic deviation in three-station clock offset and circle error, which makes it difficult to support navigation system's high-precision message parameters processing [8, 9].

This paper selects a suitable reference benchmark for interstation two-way frequency transfer data's time delay systematic error, and designs systematic error integrated computation and accuracy evaluation methods for interstation self-sending-self-receiving observation and across-sending-and-receiving observation, which effectively solves interstation time synchronization clock offset error, and significantly improves synchronization accuracy among stations and achieves high-precision GEO satellite orbit determination.

2 Interstation Two-Way Frequency Transfer

Interstation two-way frequency transfer is mainly used for time synchronization among multiple stations. Its basic principle is to assume that there are n stations under control of local clock and gather single-sending-multiple-receiving pseudo-range measurement at the same time, including self-sending-self-receiving observation and across-sending-and-receiving observation, details are shown below (Fig. 1).

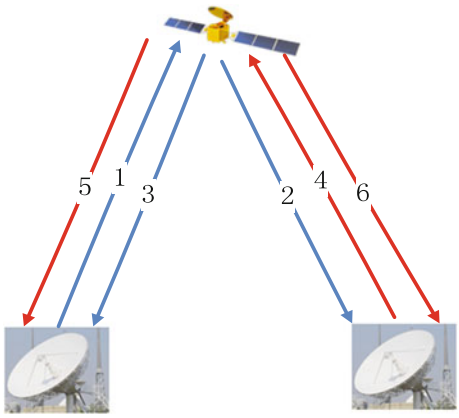

Fig. 1 Station–station two-way frequency transfer sketch map

Station 1 sends satellite uplink signal (link 1 in Fig. 1), which after resent by satellite turns to downlink signal (link 2 in Fig. 1) received by station 2. This is a complete Station-1-sending—Station-2-receiving observation ρ'_{12}, station 1 also receives the resent downlink signal (link 3 in Fig. 3), completing Station-1-sending—Station-1-receiving observation ρ'_{11}. If station 2 sends uplink signal (link 4 in Fig. 1), then station 1 completes across-sending-and-receiving observation ρ'_{21} and station 2 completes self-sending-self-receiving observation ρ'_{22}. The measurement model is shown in Eq. (1).

ρ'_{12} and ρ'_{21} are across-sending-and-receiving observations; ρ_{1_Sat} and ρ_{2_Sat} are planet geostrophic theory distance of two stations; ΔT_1 and ΔT_2 are clock offsets of the two stations; τ_{1_Tran} and τ_{2_Tran} are uplink time delay; τ_{Sat} is satellite resent time delay; τ_{1_Rcv} and τ_{2_Rcv} are downlink receiving time delay; τ_{Err12} and τ_{Err21} are propagation errors in two across-sending-and-receiving observations. Station 1's self-sending-self-receiving observation measurement model is shown in Eq. (2).

$$\begin{cases} \rho'_{12} = \rho_{1\_Sat} + \rho_{Sat\_2} + c \cdot (\Delta T_2 - \Delta T_1) + \tau_{1\_Tran} + \tau_{Sat} + \tau_{2\_Rcv} + \tau_{Err12} \\ \rho'_{21} = \rho_{2\_Sat} + \rho_{Sat\_1} + c \cdot (\Delta T_1 - \Delta T_2) + \tau_{2\_Tran} + \tau_{Sat} + \tau_{1\_Rcv} + \tau_{Err21} \end{cases} \quad (1)$$

$$\rho'_{11} = \rho_{1\_Sat} + \rho_{Sat\_1} + \tau_{1\_Tran} + \tau_{Sat} + \tau_{1\_Rcv} + \tau_{Err11} \quad (2)$$

Two-way time comparison of two across-sending-and-receiving observations from station 1 and station 2 can be used to determine relative clock offset between the two stations. As for self-sending-self-receiving data, the observation result does not include satellite clock offset and station clock offset, and therefore can be used for satellite orbit determination.

3 Systematic Error Sources and Calculation Benchmark Selection

Interstation time synchronization observation shows three types of time delay: launch delay, receiving delay and satellite transponder delay.

Generally speaking, launch delay and receiving delay are measured by ground equipment, which is defined as the delay value from c-band antenna phase center to 1PPS.

Since self-sending-self-receiving data does not contain satellite clock offset and station clock offset, the data could be converted into distance observation, and applied directly to satellite precise orbit determination, after deducting satellite transponder delay and self-sending-self-receiving combined time delay. In measured-data-based orbit determination calculation process, if adopting equipment's calibrated time delay value, then orbit determination residuals of different stations show obvious systematic error, largely concentrated in large overlapping arc segment, which led to over 10 m position error.

When processing interstation time synchronization data, if adopting directly equipment's measured time delay value, three-station clock offset and circle error are bigger, and clock offset calculated based on different satellite and different antenna displayed obvious difference, and there are also obvious error in GEO satellite orbit determination precision, which is based on interstation time synchronization system.

In order to accurately calculate c-band two-way frequency transfer data systematic error, appropriate reference benchmark needs to be selected. SLR (Satellite Laser Ranging) has very high accuracy at centimeter or millimeter level, which makes it an effective orbit determination and evaluation method. Therefore, SLR data of main stations can be selected as reference benchmark to complete comprehensive calculation of all self-sending-self-receiving data systematic error.

Since station clock offset cannot separate directly from equipment time delay, it is necessary to select appropriate benchmark to determine station clock offset. Multi-satellite orbit determination can comprehensively utilize pseudo-range phase data of multiple stations for combined orbit determination by using main station as reference benchmark and calculating clock offset of other stations and all satellites corresponding to the benchmark [10]. Therefore, calculation benchmark of interstation across-sending-and-receiving data systematic error can select multi-satellite orbit determination calculation's station clock offset.

4 Self-sending-self-receiving Data Systematic Error Calculation Method and Test Analysis

4.1 SLR Colocation and Comparison Method

When SLR station and c-band station carry out colocation observation of GEO satellite, tracking data of tracking station can be deducted to SLR station, using SLR data to calculate precisely time delay of c-band equipment in tracking station.

Using known GEO satellite orbit, the theoretical distance between c-band distance tracking station and laser station and their distance difference can be calculated precisely, and the difference value is insensitive to GEO orbit accuracy.

For C band range, satellite transponder delay can be measured before satellite launch, the value can be considered accurate and the inaccurate part is reduced to time delay of station equipment, therefore equipment delay within system achieves self-consistent. Eliminate errors related to propagation path from measured c-band ranging data and SLR data, and accurately calibrate equipment delay of tracking station. For detailed theory, please refer to Ref. [10].

4.2 Combined Orbit Determination Method

Due to limited number of SLR colocation stations, it is impossible to use colocation comparison method to calculate time delay for all c-band distance tracking stations. Therefore, it is necessary to find an effective method for equipment delay calculation. SLR observation data is highly accurate, and can be combined with c-band self-sending-self-receiving data collection for GEO combined orbit determination, and using SLR data as reference standard to estimate equipment delay error of other stations [10].

In addition to central attraction of the earth, mechanical model also includes non-spherical earth gravity, lunisolar attraction and planetary perturbation, earth tide, sea tide and solar radiation pressure, in which earth gravitational field using 10×10 order JGM-3 model and planetary ephemeris using JPL DE405 parameters, nutation model using IAU80 model, and solar radiation pressure model using Box–Wing model.

Orbit determination strategy observes one arc per day and multiple c-band ranging stations, and calculates other stations' equipment delay and meanwhile estimate satellite preliminary orbit and solar radiation pressure, using SLR station as benchmark.

4.3 Accuracy Evaluation Method

Calculation accuracy evaluation of self-sending-self-receiving data systematic error includes two aspects: internal and external consistency. Internal precision consistency evaluation is based on stability of root mean square and multi-day systematic error.

External precision consistency is mainly based on self-sending-self-receiving orbit determination precision method using SLR data, which processes orbit determination precisely using c-band self-sending-self-receiving data, and uses clock offset SLR data to evaluate calculation accuracy of self-sending-self-receiving data systematic error. It is important to note that SLR data used for evaluation cannot be used for equipment systematic error calculation.

4.4 Test Analysis

4.4.1 SLR Colocation Comparison Method

Measured SLR and c-band colocation observation data of Beidou GEO satellite is used in comparison test, and SLR station (No. 7821) and c-band tracking station (No. 1013) are located in Beijing.

The table has listed calibration result of 3 days from June 9 to 11, 2009. It can be seen from the results that time delay calibration results are very stable for 3 consecutive days, the average value is −2.0 m, standard deviation is 0.08 m, and daily delay change is very small, about 0.25 ns. Since satellite transponder delay jitter is also around 0.2 ns, and meanwhile considering the influence of propagation delay model error, SLR colocation comparison method's systematic error calculation internal precision consistency is better than 0.3 ns (Fig. 2 and Table 1).

4.4.2 Combined Orbit Determination Approach

Since SLR colocation station data are limited, it is impossible to use SLR colocation observation approach for time delay calibration of all resending tracking stations. Combined orbit determination approach is adopted in interstation time synchronization for self-sending-self-receiving data systematic error calculation. The calculation uses precise SLR data and c-band resent ranging data (time delay has been accurately calibrated) as reference and estimates systematic error of other tracking stations.

Orbit determination strategy uses 1 day observation segment and 3 c-band self-sending-self-receiving range tracking stations. Beijing laser station is used as benchmark to calculate combine time delay of other stations' c-band self-sending-self-receiving equipment, and meanwhile estimate satellite preliminary orbit and solar radiation pressure parameters. Three consecutive days' equipment time delay calculation results for three stations are presented in Table 2.

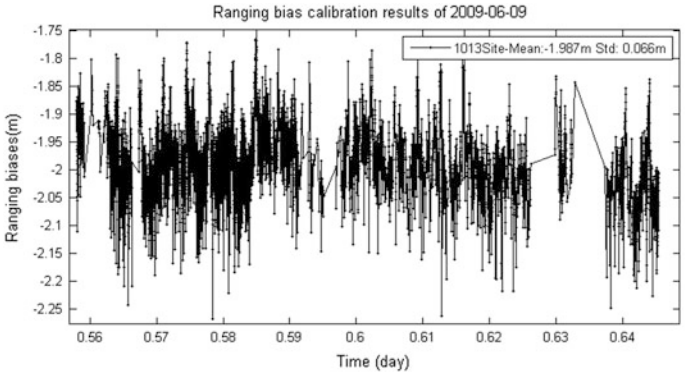

Fig. 2 Detailed ranging bias calibration results of SLR co-location comparison approach on June 9, 2009 (SLR co-location comparison approach)

Table 1 Ranging bias results of Beijing station (unit: m)

Date	2009/6/9	2009/6/10	2009/6/11	Average	Standard deviation
Time delay	−1.99	−2.08	−1.94	−2.00	0.08

It can be seen that equipment calibration results of the other three stations are very stable, except for Sichuan station, time delay variation of the other stations are better than 0.3 ns. Sichuan station has greater variation, about 0.6 ns, mainly because measurement noise of Sichuan station is large, about 40 cm.

In view of stability and accuracy of equipment time delay calculation results, mean value of the three day calibration results in table can be used as the final calibration result. Considering consistency of different stations' systematic error, SLR data residuals and orbit determination total residuals, it can be considered that based on combined orbit determination approach, the accuracy of self-sending-self-receiving data systematic error is better than 0.5 ns.

4.4.3 Self-sending-self-receiving Data Systematic Error Calculation Precise Evaluation Based on GEO Orbit Determination

This paper uses self-sending-self-receiving data of May and June in 2009 and carries out 5 orbit determination testing to further evaluate interstation self-sending-self-receiving data systematic error accuracy. Different from combined orbit determination, c-band range tracking station's equipment time delay used calibration results of June 9 to 11, 2009, and fixed time delay value without solving orbit determination algorithm. Orbit determination calculation strategy adopts one-day arc observation and estimates parameters only include satellite preliminary orbit and solar radiation pressure, and mechanical model is exactly the same as the previous one. It is important to note that SLR data in 4-day orbit determination test was not considered in calibration of orbit determination and equipment time delay, so SLR residuals can reflect orbit determination visual direction accuracy (Table 3).

It can be seen from the results in the table that 4-day GEO orbit determination results' residual internal consistent average precision is 0.21 m, SLR evaluated average external consistent visual direction precision is 0.13 m. Precision of orbit determination is very stable, changes are within 0.05 m. According to the ratio

Table 2 Ranging bias results for consequent 3 days by combined POD method (unit: m)

Time	Hainan	Xinjiang	Sichuan	SLR residual	POD residual
2009/6/9	−3.28	−2.01	−0.80	0.05	0.22
2009/6/10	−3.22	−2.12	−0.52	0.06	0.18
2009/6/11	−3.24	−2.05	−0.86	0.12	0.21
Average	−3.25	−2.06	−0.72	0.07	0.21
Standard deviation	0.03	0.06	0.18	0.04	0.02

between GEO satellite's visual direction accuracy and three-dimensional position accuracy (about 1:20) and external-consistent error precision, it can be inferred that accuracy of GEO satellite's three-dimensional position is better than 2.7 m.

At the same time, it is estimated that time delay of c-band tracking station equipment is about one month, looking from systematic error calculation time and orbit determination testing time. Therefore, with supported SLR data, it is completely possible to carry out regular calibration of equipment time delay using SLR colocation comparison approach and combined orbit determination approach, correct equipment time delay and improve GEO satellite orbit determination accuracy.

Based on accuracy of self-sending-self-receiving data's orbit determination precision based on SLR evaluation, visual direction accuracy of GEO satellite is 0.13 m, which can be considered as external-consistent precision of self-sending-self-receiving data's systematic error is better than 0.4 ns.

5 Across-Sending-and-Receiving Data's Systematic Error Calculation Method and Test Analysis

5.1 Constraint Method Based on Multi-satellite Orbit Determination Station Clock Offset

Since station clock offset is unable to separate directly from equipment time delay, it is necessary to select appropriate benchmark, which requires determining station clock offset first. We choose multi-satellite orbit determination calculation's station clock offset as a reference benchmark, separate station clock offset and equipment time delay, and then deduct geometry distance, transfer error and station clock offset from across-sending-and-receiving data, so combined time delay will be calculated for self-sending-self-receiving data. As GEO satellite orbit error influences across-sending-and-receiving data's systematic error accuracy, and in order to reduce the influence of this error, self-sending-self-receiving data could be used as benchmark (systematic error calculation completed) to achieve high-precision theoretical value, detailed computation formula is as follows:

$$\Delta\tau_{12} = \rho_{12} - R_{12} - (\tau_2 - \tau_1) - \frac{1}{2}(\rho_{11} - R_{11} - \Delta\tau_{11}) - \frac{1}{2}(\rho_{22} - R_{22} - \Delta\tau_{22}) \tag{3}$$

Table 3 GEO orbit determination accuracy statistic (unit: m)

Time	2009/5/17	2009/5/18	2009/6/22	2009/6/23	Average	Standard deviation
Orbit determination residuals	0.22	0.15	0.22	0.21	0.21	0.03
SLR residuals	0.17	0.16	0.15	0.13	0.13	0.05

In the equation, $\Delta\tau_{12}$ is the combined time delay of sending from Station 1 and receiving from Station 2; ρ_{12} is c-band ranging value sent by Station 1 and received by Station 2; R_{12} is the approximate earth-satellite distance when sending from Station 1 and receiving from Station 2; τ_1 and τ_2 are station clock offset of Station 1 and 2 respectively; ρ_{11} and ρ_{22} are self-sending-self-receiving range value of Station 1 and 2 respectively; R_{11} and R_{22} are approximate earth-satellite distance from Station 1 and 2 respectively; $\Delta\tau_{11}$ and $\Delta\tau_{22}$ are self-sending-self-receiving systematic error of Station 1 and 2 (please refer to part 4).

It is important to note that R_{12}, R_{11} and R_{22} are earth-satellite distance calculated based on the same orbit calculation and after correction of various transfer error. Above equation is able to eliminate GEO satellite orbit's error influence, and complete comprehensive calculation of all interstation across-sending-and-receiving data systematic error.

5.2 Accuracy Evaluation Method

This paper evaluates interstation time synchronization systematic error's internal-consistent accuracy, with root mean square of systematic error calculation and stability of multi-day systematic error. Evaluation method is completely the same with previous one.

External-consistent accuracy of interstation time synchronization's across-sending-and-receiving systematic error mainly evaluates by three-station circle error and clock offset consistency checking approach.

The calculation principle of three-station circle error is as follows:

$$\Delta = \tau_{12} - \tau_{13} + \tau_{23} \tag{4}$$

In the equation, τ_{12} is clock offset of station 1 comparing with station 2, τ_{13} is clock offset of station 1 comparing with station 3, τ_{23} is clock offset of station 2 comparing with station 3.

Clock offset consistency check can compare clock offset of different c-band antennas in the same station calculated by different GEO satellites, and then calculate standard deviation.

5.3 Test Analysis

5.3.1 Across-Sending-and-Receiving Data Systematic Error Calculation Based on Station Clock Offset of Multi-satellite Orbit Determination

In order to complete interstation time synchronization across-sending-and-receiving data systematic error calculation, this paper uses c-band data on Aug 4 in 2011 for

test calculation. Tables 4 and 5 have shown detailed calculation result of interstation across-sending-and-receiving data systematic error based on satellite C01 and C03.

Standard deviation of table shows result is 0.46 ns, so it can be considered that internal-consistent accuracy of this calculation is better than 0.5 ns.

Table 4 Inter-send/receive systematic error by C01 (unit: ns)

Received by	Sent by	Combined time delay				
		2011-8-4	2011-8-5	2011-8-6	Average	Standard deviation
Beijing	Hainan	2509.98	2510.62	2510.80	2510.47	0.43
	Xinjiang	5696.61	5696.27	5695.97	5696.28	0.32
	Sichuan	1084.03	1084.73	1084.95	1084.57	0.48
Hainan	Beijing	2593.28	2592.64	2592.45	2592.79	0.44
	Xinjiang	5324.47	5323.43	5322.95	5323.62	0.78
	Sichuan	694.00	693.96	694.00	693.99	0.02
Xinjiang	Beijing	3177.95	3178.33	3178.64	3178.31	0.34
	Hainan	2706.09	2707.13	2707.56	2706.93	0.75
	Sichuan	1280.81	1281.78	1282.32	1281.64	0.77
Sichuan	Beijing	3219.34	3218.73	3218.53	3218.87	0.43
	Hainan	2752.05	2752.09	2752.02	2752.05	0.03
	Sichuan	5944.19	5943.24	5942.71	5943.38	0.75
Average						0.46

Table 5 Inter-send/receive systematic error by C03 (unit: ns)

Received by	Sent by	Combined time delay				
		2011-8-4	2011-8-5	2011-8-6	Average	Standard deviation
Beijing	Hainan	2551.78	2552.37	2552.54	2552.23	0.40
	Xinjiang	5544.86	5544.61	5544.35	5544.61	0.25
	Sichuan	925.58	926.28	926.62	926.16	0.53
Hainan	Beijing	2625.98	2625.35	2625.24	2625.52	0.40
	Xinjiang	5462.08	5461.24	5460.79	5461.37	0.66
	Sichuan	842.89	842.99	843.14	843.01	0.13
Xinjiang	Beijing	3002.33	3002.59	3002.82	3002.58	0.25
	Hainan	2844.02	2844.89	2845.34	2844.75	0.67
	Sichuan	1225.48	1226.45	1227.00	1226.31	0.77
Sichuan	Beijing	2978.56	2977.91	2977.59	2978.02	0.50
	Hainan	2821.11	2821.03	2820.89	2821.01	0.11
	Sichuan	5815.22	5814.30	5813.75	5814.42	0.74
Average						0.45

5.3.2 Three-Station Circle Error

Three-station clock offset and circle error is an important indicator for c-band data systematic error calculation. In order to further analyze accuracy of above systematic error calculation, this paper uses c-band data on Aug 4 in 2011 for three-station circle error check, and compares with circle error before calculation. Detailed comparison results are presented in Table 6.

Above results have shown that interstation time synchronization's three-station circle error has improved from 3.84 ns to better than 0.1 ns after across-sending-and-receiving data systematic error calculation.

5.3.3 Clock Offset Check Based on Clock Offset Consistency

When a station has two sets of c-band interstation time synchronization equipment, two GEO satellite observations and two different interstation clock offsets could be achieved and consistency of clock offsets calculated by two set of equipment is also an important indicator for interstation time synchronization data systematic error calculation precision.

This paper uses c-band data on Aug 4 in 2011 for test analysis, compares two sets of antenna's station clock consistency based on satellite C01 and C03, detailed results are presented in Table 7.

Above results have shown that clock offset consistency based on different antennas and satellites has improved from over 10 to 0.3 ns after across-sending-and-receiving data systematic error calculation, and therefore two different C-band equipment could backup with each other.

Table 6 Three station circle error of station–station time synchronization (unit: ns)

Satellite	Testing station combination	Circle error before calculation		Circle error after calculation	
		Average	Standard deviation	Average	Standard deviation
C01	Beijing-Hainan-Xinjiang	3.20	0.32	0.04	0.32
	Beijing-Hainan-Sichuan	5.09	0.26	0.05	0.26
	Beijing-Xinjiang-Sichuan	2.06	0.37	0.01	0.37
	Hainan-Xinjiang-Sichuan	3.05	0.26	0.01	0.26
C03	Beijing-Hainan-Xinjiang	5.15	0.15	0.01	0.15
	Beijing-Hainan-Sichuan	6.19	0.19	0.02	0.19
	Beijing-Xinjiang-Sichuan	1.30	0.23	0.02	0.23
	Hainan-Xinjiang-Sichuan	4.64	0.22	0.01	0.22
Average		3.84	0.25	0.02	0.25

Table 7 Station clock offset consistency (unit: ns)

Test station combination	Relative clock offset before calculation		Relative clock offset after calculation	
	Average	Standard deviation	Average	Standard deviation
Beijing-Hainan	51.43	0.34	0.09	0.34
Beijing-Xinjiang	1.56	0.57	0.34	0.57
Beijing-Sichuan	136.31	0.43	0.01	0.43
Hainan-Xinjiang	53.10	0.60	0.43	0.60
Hainan-Sichuan	84.54	0.50	0.12	0.50
Xinjiang-Sichuan	138.24	0.58	0.33	0.58
Average	77.53	–	0.22	–

6 Conclusions

To sum up, this paper systematically analyzed source of systematic error for c-band interstation two-way frequency transfer's data systematic error, adopted high-precision SLR data and multi-satellite orbit determination calculation's station clock as reference benchmark, deduced and established two self-sending-self-receiving data systematic error calculation methods of SLR colocation comparison and combined orbit determination, and across-sending-and-receiving data systematic error calculation method based on multi-satellite orbit determination station clock offset, and then designed accuracy evaluation method that combined internal and external consistency, and carried out verification tests with Beidou measured data. Main conclusions are as follow:

(1) For self-sending-self-receiving data systematic error calculation, precision of SLR colocation comparison method is better than 0.3 ns, internal-consistent accuracy of combined orbit determination method is better than 0.5 ns, external-consistent accuracy is better than 0.4 ns, orbit determination accuracy based on self-sending-self-receiving data has improved from over 10 to 2.7 m, which consequently solves interstation self-sending-self-receiving data systematic error problem.
(2) For across-sending-and-receiving data systematic calculation, its internal-consistent accuracy is better than 0.4 ns, three-station circle error has improved from 3.84 to 0.1 ns, clock offset consistency based on different antennas and satellites has improved from over 10 to 0.3 ns, thus realizing high-precision interstation time synchronization and two different C-band equipment could backup with each other.
(3) For timeliness of systematic error calculation, effectiveness of c-band tracking station equipment delay is about 1 month, and navigation system can periodically carry out time delay check and maintain corresponding ground equipment.

Acknowledgements This work was funded by the National Natural Science Foundation of China (Grant No. 41204022, 41374038, 61603397).

References

1. Tang C, Hu X, Zhou S et al (2016, June) Improvement of orbit determination accuracy for Beidou navigation satellite system with two-way satellite time frequency transfer. Adv Space Res 2889–2898. https://doi.org/10.1016/j.asr.2016.06.007
2. Guo R, Chen J et al (2017) Beidou satellite ultra short arc kenematic orbit determination improvement and test analysis. J Surveying Mapp 46(4):411–420
3. Li X, Zhou J, Hu X et al (2015) Orbit determination and prediction for Beidou GEO satellites at the time of the spring/autumn qeuinox. Sci China Phys Mech Astron 58(8):089501. https://doi.org/10.1007/s11433-015-5675-6
4. Guo R, Zhou J, Hu X et al (2015) Precise orbit determination and rapid orbit recovery supported by time synchronization. Adv Space Res 2889–2898. https://doi.org/10.1016/j.asr.2015.03.001
5. Guo R, Hu X, Liu L et al (2010) Orbit determination for geostationary satellites with the combination of transfer ranging and pseudorange data. Sci China Phys Mech Astron 53 (9):1746–1754
6. Liu L, Tang G, Han C et al (2015) The method and experiment analysis of two-way common-view satellite time transfer for compass system. Sci China Phys Mech Astron 58 (8):089502. https://doi.org/10.1007/s11433-015-5679-2
7. Liu L (2004) Relativistic theory of time transfer and techniques of clock synchronization. Dissertation for Doctoral Degree, PLA Information Engineering University, Zhengzhou
8. Zhou J, Xu B (2015) Heterogeneous constellation POD and AOD theory and practices. Sci Publishing 104–106
9. Li Z, Yang X, Shi H et al (2008) A new method for determination of satellite orbits by transfer. Sci China Ser G Phys Mech Astron 38(12):1711–1722
10. Zhou S, Cao Y, Zhou J et al (2012) Positioning accuracy assessment for the 4GEO/5IGSO/2MEO constellation of COMPASS. Sci China Phys Mech Astron 55(12):2290–2299
11. Guo R, Hu X, Tang B et al (2010) Precise orbit determination for geostationary satellites with multiple tracking techniques. Chinese Sci Bull 55(8):687–692

Accuracy Analysis of BDS-3 Experiment Satellite Broadcast Ephemeris

Ya Mao, Qianxin Wang, Chao Hu and Yilei He

Abstract Currently, five BDS-3 experiment satellites are transmitting both BDS-2 signals and new signals for users. They are equipped with high-precision rubidium or/and passive hydrogen maser clocks. In view of the inconsistency of BDS-3 experiment satellites signals received by iGMAS and MGEX network, the experiment to determine BDS-3 orbits is carried out by the step by step method through one year. In order to improve the efficiency and avoid the inverse anomalies caused by too large matrix dimension in the inversion process, the normal equation matrix is decomposed by Cholesky. In this paper, the internal accuracy of BDS-3(C31/C32/C33/C34) satellites orbit and clock offset is evaluated by overlapping arcs, and the average values in one year are 36.5 cm/38.4 cm/44.1 cm/48.8 cm and 2.27 ns/2.40 ns/1.88 ns/1.87 ns respectively. In addition, satellite laser ranging (SLR), as an important external inspection tool, has been widely used in satellite orbit accuracy assessment. Using SLR to evaluate the orbit outside accuracy, and the average values of one year is 51.4 cm/40.2 cm/62.9 cm/82 cm. Finally, the precision of BDS-3 satellites broadcast-clock offset and broadcast-orbit is evaluated by BDS-3 precise ephemeris, and the SLR observation data is taken as the external inspection tool to evaluate the orbits. The results show that the BDS-3 experiment satellite broadcast-clock accuracy is better than 40 ns, and the broadcast-orbit accuracy is about 1 m.

Keywords SLR check · BDS-3 broadcast ephemeris · Step-by-step method Accuracy analysis

This paper was funded by The Natural Science Foundation of China (41404033), Supported State Key Laboratory Lake Science and Environment (SKLGIE2014-Z-1-1) and the Fundamental Research Funds for the Central Universities (2015QNA31).

Y. Mao · Q. Wang (✉) · C. Hu · Y. He
School of Environment Science & Spatial Informatics,
China University of Mining and Technology, Xuzhou 221116, China
e-mail: wqx@cumt.edu.cn

J. Sun et al. (eds.), *China Satellite Navigation Conference (CSNC) 2018 Proceedings*, Lecture Notes in Electrical Engineering 498,
https://doi.org/10.1007/978-981-13-0014-1_29

1 Introduction

In recent years, BeiDou satellite navigation system has been developed rapidly. As of 2012, there are 14 BDS navigation satellites in orbit, including 5 GEO (C01-C05), 5 IGSO (C06-C10) and 4 MEO (C11-C14), which can provide services to the Asia Pacific region. In March 30, 2015, the first BDS-3 experiment satellite was launched successfully, marking the beginning of the Beidou satellite navigation system covering from the region navigation system to the global navigational. Up to 2017, BDS-3 has been launched 5 experiment satellites (C31-C35) as follows: I1-S, M1-S, M2-S, I2-S, M3-S, and transmit some new signals namely B1C at 1575.42 MHz, B2a at 1176.45 MHz, B2b at 1207.14 MHz to users [1]. The Beidou navigation system plans to achieve 35 (5 GEO, 27 MEO and 3 IGSO) satellites in orbit, and provide PNT service to global users by the end of 2020. In the 5 experiment satellites, there are 4 (C31/C32/C33/C34) are in normal working state, the C35 is in testing mode, and there is no information about the 5 satellites in the ICD file because of the 5 experiment satellite is still in the experimental condition. Table 1 show the status of BDS-3 experiment satellites.

In satellite navigation and positioning, the main factor affect the navigation and positioning accuracy include the broadcast ephemeris accuracy and geometric precision factor [2]. It make great senses to analyze the broadcast ephemeris accuracy. At present, there are many scholars have been analysed the broadcast ephemeris accuracy, but the work is mostly focus on the four conventional system that is BDS, GPS, GLONASS, GALILEO, there is no literature to evaluate the BDS-3 satellites ephemeris accuracy. Literature [3] has been evaluate the GNSS broadcast ephemeris, and draws some meaningful conclusions; and the GPS broadcast ephemeris accuracy is analysed by Guo et al. [4], the result show that the GPS broadcast ephemeris accuracy is better than 2 m, and the clock offset accuracy is about 10 ns; and then Guo et al. [5] analysed the GLONASS broadcast ephemeris accuracy through the space signal ranging error, and the result show that the whole accuracy is better than 4.5 m; Lucas Rodriguez carried out the evaluation of Galileo broadcast ephemeris preliminary accuracy, first in 2013 [6]; Guo et al. [7] analysed the Beidou broadcast ephemeris orbit and clock offset accuracy, the results show that the radial accuracy of GEO satellite is better than 2 m, and the MEO and IGSO broadcast ephemeris accuracy is equivalent to GPS, that radial accuracy is better than 0.5 m. In addition, the studies have validated that SLR data is an important external inspection tool to evaluate the satellites orbits accuracy [1, 8–10]. It is

Table 1 BDS-3 satellites status [1, 17]

Satellite	PRN	SVN	Type	Lunch data
I1-S	C31	C101	IGSO	2015/3/30
I2-S	C32	C104	IGSO	2015/9/29
M1-S	C33	C102	MEO	2015/7/25
M2-S	C34	C103	MEO	2015/7/25
M3-S	N/A	N/A	MEO	2015/9/29

reliable to analyse the broadcast ephemeris accuracy by SLR data, Sun et al. [1] have been used SLR data to analyse the BDS-2 satellite broadcast-orbit accuracy, and the results show that the accuracy of C01, C08, C10, C11 satellites is 0.97, 0.43, 0.41, 0.44 m, and there was a constant laser residual deviation by SLR data to evaluate BDS-2 broadcast-orbit, but in this research, does not evaluate broadcast ephemeris accuracy by the precise ephemeris. There are two obvious defects to check the orbits accuracy by SLR [11, 12]: (1) There are less SLR stations, and the obtained broadcast ephemeris accuracy only in sight line of the SLR station; (2) It is impossible to carry out Omni-directional and full-time evaluation with less observation data. When using precise ephemeris to evaluate broadcast ephemeris, although, it is more robustly and practically, but it is easy to be affected by the accuracy of the precision ephemeris.

In this paper, the multi GNSS monitoring station data provided by MGEX stations network and iGMAS stations network are selected to calculate the BDS-3 experiment satellite orbit and clock offset in three days arcs by PANDA software, and then the BSD-3 experiment satellite broadcast ephemeris accuracy is evaluated by the precise ephemeris which are calculated above. In view of the advantage and disadvantage of evaluate the BDS-3 experiment satellites broadcast-orbit accuracy by SLR observation data and precise ephemeris data, the SLR observation data is used as an important external inspection tool to evaluate the broadcast-orbit accuracy.

2 Determine the BDS-3 Satellite Orbit and Clock Offset

In China, in order to provide high-precision satellite orbit, clock offset and other products and improve the signal availability, reliability, accuracy, since 2007, China have been build GNSS international monitoring system (iGMAS) to monitor Chinese Beidou satellite and other global navigation satellite system. In addition, to meet the needs of scientific research and engineering construction, iGMAS have been built the continuous operation tracking stations, which can receive BDS, GPS, GLONASS, GALILEO the four system signals. In 2016, there are 9 iGMAS stations can receive BDS-3 dual frequency observation data of B1/B3. By the end of the experiment, there are 17 stations have the capable to receive BDS-3 dual frequency observation data of B1/B3, as shown in Fig. 1. The MGEX monitoring station build by IGS can receive multi system observation data, but only four stations (roap, stj3, tlsg and yel2) have the capable to receive BDS-3 single frequency observation data of B1. According to the literature [13] research, the existing stations which can receive BDS-3 signals are not enough to carry out high-précis BDS-3 orbits; In addition, the literature [14] pointed out that making full use of the global distribution monitoring station data can effectively improve the parameters accuracy. In order to overcome the problem of that the less station that can receive BDS-3 singles, this section adopts the step by step method to determine BDS-3 satellites orbits and clock offset in three-day arcs, and this is a

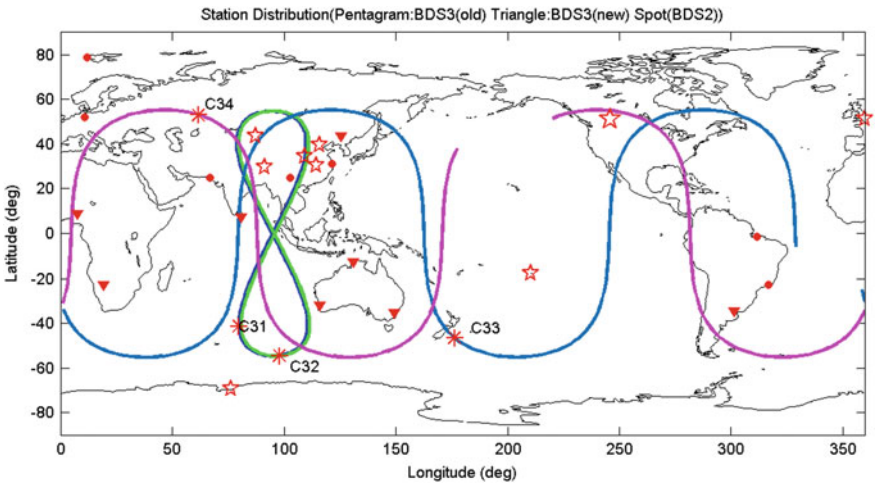

Fig. 1 The iGMAS station distribution

method that can makes full use of redundant observation data in orbit determination. The parameters and models setting to determine orbit and clock offset is shown in Table 2.

Considering the inconsistency between the received BDS-3 signals by iGMAS tracking network and MGEX tracking network, and it is useful to determine the BDS-3 orbit and clock offset by using MGEX observation data to calculate the related parameters (station coordinates, troposphere and clock errors). In order to making full use of the two networks observation data to determine BDS-3 experiment satellites orbit and clock offset, this paper adopt step by step method to determine orbit.

The equation of the two observation networks as follows [15]:

(1) The normal equation when determining the BDS-3 experiment satellite orbit and clock offset by iGMAS station:

$$\begin{bmatrix} NN_{11} & NN_{12} \\ NN_{21} & NN_{22} \end{bmatrix} \begin{bmatrix} X \\ Y \end{bmatrix} = \begin{bmatrix} U_1 \\ U_2 \end{bmatrix} \tag{1}$$

Among them, X is the parameters of troposphere, station coordinates, clock offset and others related to iGMAS station; Y is the orbit, clock offset and other parameters related to BDS-3 experiment satellites. NN is the normal matrix, U is the constant term.

Table 2 Configuration of calculation parameters

Parameter name	Configuration	Parameter name	Configuration
Observation data type	LC+PC	Solid earth tide	SUN MOON
Observation mode	Undifferent	Ocean tide	YES
Observation weight	Elevation	Point	SUN MOON MERC VENU MARS JUPI SATU URAN NEPT
Observation interval	30 s	Solar radiation	Kd_BERN Ky_BERN Kb_BERN Kbc1_BERN Kbs1_BERN
Estimator	LSQ	Atmosphere drag	NONE
Receiver ISB/IFB	Auto+CON	Relativity	YES
Receiver and satellite PCV	A_E_E	Variation	YES
Remove bias	YES	Tide displacement	SOLID_FREQ_POLE_OCEAN! SOLID_FREQ_OCEAN
Orbit reference frame	CRS	Estimate ERP	XPOLE_YPOLE_DXPOLE_DYPOLE_UT1_DUT1
Ambiguity fixing mode	ROUND	ERP constraint	0.300 0.030 0.0001 0.002
Baseline length limit	3500	Parameter to be estimated	PXSAT PYSAT PZSAT VXSAT VYSAT VZSAT +
Minimum common time	900 s		Kd_BERN Ky_BERN Kb_BERN Kbc1_BERN Kbs1_BERN
Estimate satellite orbit	YES	Orbit parameter constraint	10 m(X/Y/Z) 0.1 m(V_X/V_Y/V_Z) 0.1 m(F1-F9)
ZTD model	PWC:120	Sat. clock error constraint	5000 m

(2) The following is the normal equation to determine the common parameters by iGMAS and MGEX station:

$$\begin{bmatrix} NN'_{11} & NN'_{12} \\ NN'_{21} & NN'_{22} \end{bmatrix} \begin{bmatrix} X \\ Y' \end{bmatrix} = \begin{bmatrix} U'_1 \\ U'_2 \end{bmatrix} \tag{2}$$

Among them, X is the same parameter as the formula (1), that is, iGMAS station coordinate, clock offset and troposphere; Y' is the parameter related to MGEX station and the orbit and clock offset of GPS and BDS-2 satellite.

The same parameter X is calculated by formula (2):

$$X = \left[NN'_{11} - NN'_{12}\left(NN'_{22}\right)^{-1}NN'_{21}\right]^{-1}\left(U'_1 - N'_{12}\left(NN'_{22}\right)^{-1}U'_2\right) \tag{3}$$

In order to improve the efficiency and avoid the inversion anomaly caused by too large matrix dimension in the inversion process, Cholesky decomposition is used to the real symmetric matrix $NN'_{11} - NN'_{12}\left(NN'_{22}\right)^{-1}NN'_{21}$, that is $NN'_{11} - NN'_{12}\left(NN'_{22}\right)^{-1}NN'_{21} = S^T S$, S is a lower triangular matrix.

$$X = S^{-1}S^{-T}\left(U'_1 - N'_{12}\left(NN'_{22}\right)^{-1}U'_2\right) \tag{4}$$

The orbits and clock offset of the BDS-3 test satellite can be calculated by the formula (4) back to the formula (1):

$$Y = NN_{12}^{-1}(U_1 - NN_{11}X) \tag{5}$$

The parameters related to BDS-3 satellites can be solved by the upper form, and the satellite orbit and clock offset at any time can be obtained through the corresponding state transition matrix.

In order to describe the strategy to determine BDS-3 experiment satellites orbit by the step by step method, the flow chart of that method is given in Fig. 2.

3 Experimental Analysis

In order to analyze the BDS-3 experiment satellites orbit and clock offset accuracy calculated by the step by step method, the experiment to determine orbit was carried out by iGMAS and MGEX tracking stations observation data in per day from 154 days of 2016 to 154 days of 2017. In this experiment, there are 16 iGMAS stations (9 contain BDS-3 observation data), and 54 MGEX stations. And with the updating and construction of the iGMAS tracking network equipment, the number of iGMAS stations that can receive BDS-3 experiment satellites singles increased to 17 at the later stage of the experiment, and the distribution of that is showing in Fig. 1.

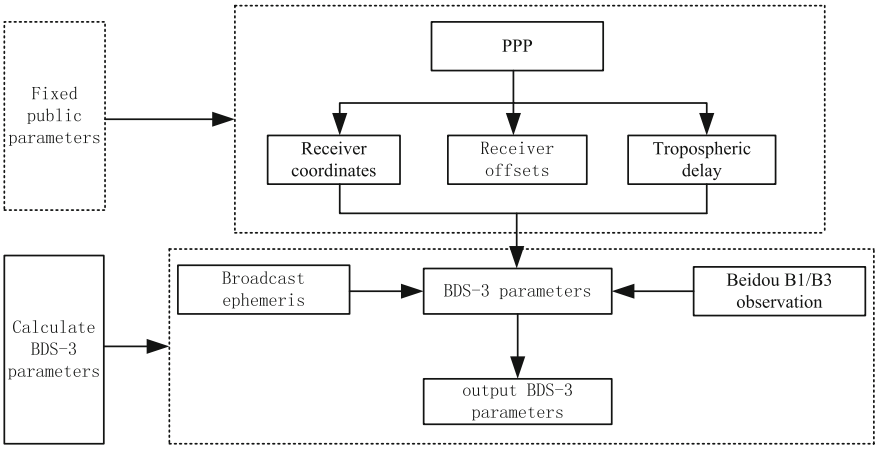

Fig. 2 The flow chart of step by step method to determine BDS-3 experiment satellites orbit and clock offset parameters

Because of the BDS-3 experiment satellites is a new generation experimental satellites, temporarily, satellites parameters cannot be obtained accurately, so that, the determine orbit model is same with GPS. In this experiment, 3 day arcs observation data is adopted to determine orbit, and the orbit accuracy is checked through the inside accuracy and outside accuracy, due to the BDS-3 experiment satellites clock offset accuracy cannot provide a stable external inspection tool, the clock offset accuracy is only checked by inside accuracy. The method to evaluate the orbit and clock offset as follows: (1) The non-attachment value between the overlap arc in one day, compare the orbit and clock offset difference in the same arc section between the two process, as shown in Fig. 3; (2) Taking into account that all the BDS-3 experiment satellites are equipped with laser reflection device, the external inspection of BDS-3 orbit is carried out by SLR observation data.

The BDS-3 (C31/C32/C33/C34) satellite orbit and clock offset accuracy is shown in Figs. 4 and 5, and the trend of the internal coincidence precision was fitted. The discontinuity in follow figure about C31 that is because there is no C31 broadcast data in that section. In Fig. 6 show the outside accuracy of orbit; Table 3

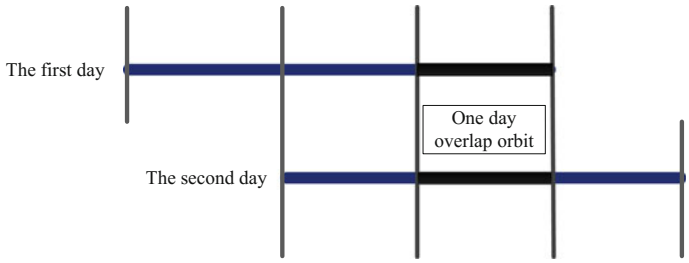

Fig. 3 Sketch map of precision of overlap segment of orbits and clock offset

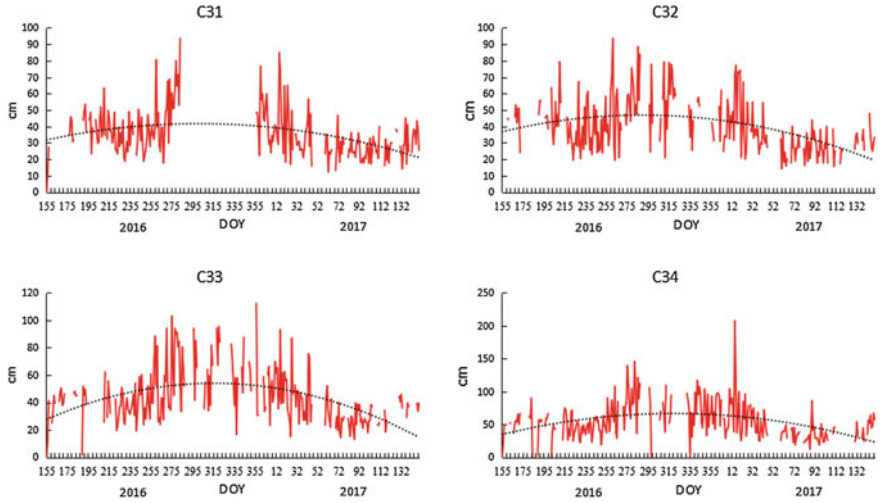

Fig. 4 The orbits inside precision of overlapping arcs of BDS-3 satellites with step by step method

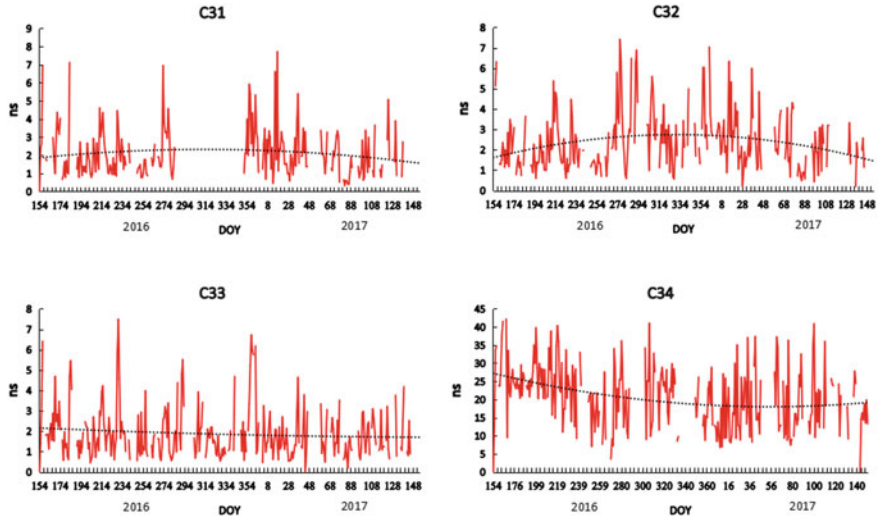

Fig. 5 The clock offset inside precision of overlapping arcs of BDS-3 satellites with step by step method

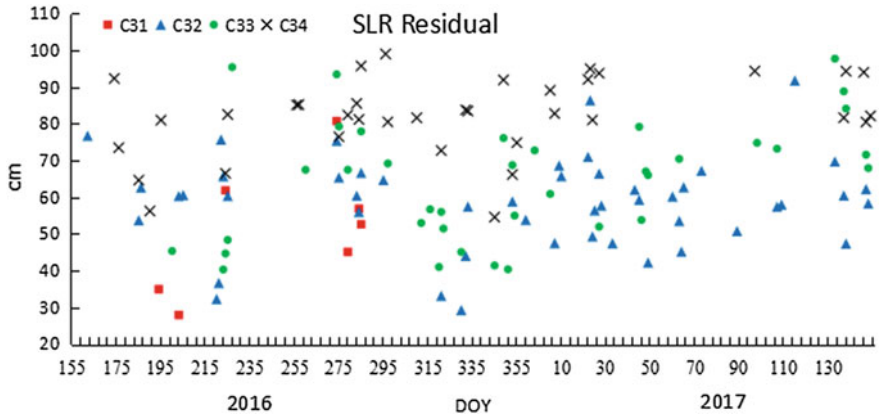

Fig. 6 The outside precision of BDS-3 test satellites orbits

Table 3 The orbits and clock offset average accuracy of the inside and outside precision internal in one year

	The inside precision/(cm/ns)		The outside precision/(cm/ns)	
Satellite	Orbit	Clock offset	Satellite	Orbit
C31	36.5	2.27	51.4	–
C32	38.4	2.40	40.2	–
C33	44.1	1.88	62.9	–
C34	48.8	1.87	82	–

show the average value of orbit and clock offset inside accuracy of one year, and the average value of outside orbit precision of one year.

The experimental results show that the inside accuracy and outside accuracy of the BDS-3(C31/C32/C33/C34) satellite orbit determined by step by step is 36.5 cm/38.4 cm/44.1 cm/48.8 cm and 51.4 cm/40.2 cm/62.9 cm/82 cm, respectively. And the inside precision of clock offset is 2.27 ns/2.40 ns/1.88 ns/1.87 ns.

4 Analyze the BDS-3 Broadcast Ephemeris Accuracy

In order to analyze the broadcast ephemeris accuracy, the broadcast ephemeris at the same time with upper section is selected to evaluate its orbit accuracy and clock offset accuracy. Considering the advantage and disadvantage of evaluate broadcast-orbit by the precise ephemeris and SLR observation data, this paper uses precise ephemeris of the upper section calculated as reference to check the BDS-3 broadcast ephemeris accuracy, and use SLR observations data as the external check method to check the orbits.

4.1 Analyze the BDS-3 Broadcast-Orbit Accuracy

At present, BDS transmit a set of broadcast ephemeris parameters in per 1H, and its ephemeris parameter gives the position of the satellite centroid [1]. In order to check the broadcast-orbit accuracy, it is necessary to calculate the satellite three-dimensional coordinates in the geocentric earth coordinate system by the broadcast ephemeris parameters, and the 6 Kepler orbital parameters and ECOM5 radiation model parameters were used to fit orbits, the orbit fitting model is shown in Table 4. Because the difference between the CGCS2000 coordinate system and the ITRF frame is less than 2 cm, so it can be neglected; but the BDS-3 precise ephemeris calculated on the upper section is using GPST as the reference epoch time scale, so when using the precise ephemeris as reference to evaluate the BDS-3 broadcast ephemeris accuracy will need transform it from GPST into BDT. Figure 7 show the accuracy of BDS-3 (C31, C32, C33 and C34) experiment satellites broadcast-orbit evaluated by precise ephemeris. Figure 8 show the results of BDS-3 broadcast-orbit evaluated by SLR observation data, Table 5 is the mean value of the inside accuracy and outside accuracy of the BDS-3 broadcast ephemeris.

Table 4 Dynamic model of BDS-3 satellite

Perturbation force	Module
Gravity field	EGM2008 12 steps
Tide	SOLID TIDE, OCEAN TIDE
Precession, nutation	IERS2000, IAU2000
N-body perturbation	DE405

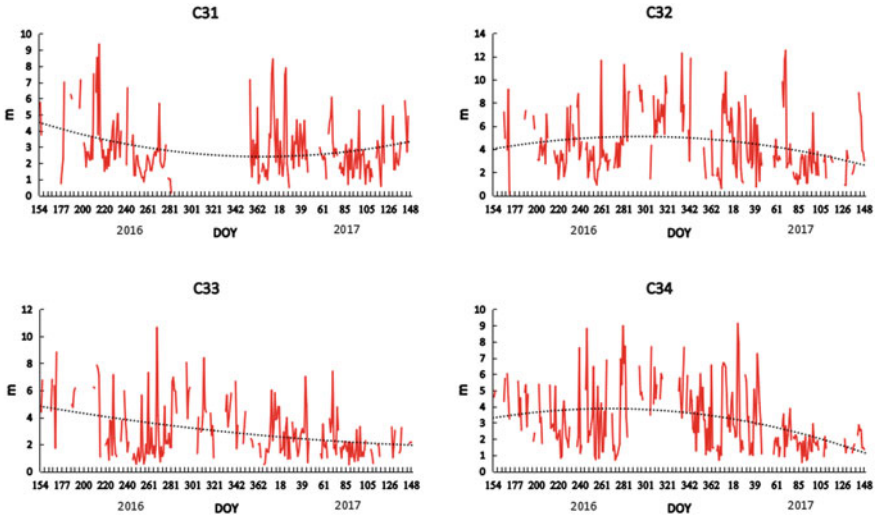

Fig. 7 The evaluate results of BDS-3 broadcast ephemeris orbits by satellites precise ephemeris

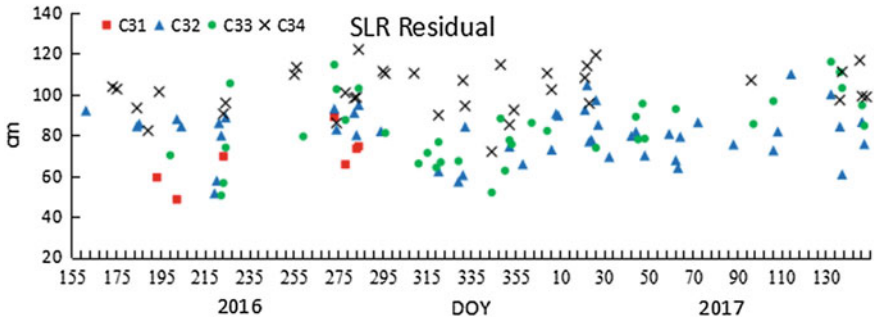

Fig. 8 The evaluate results of BDS-3 broadcast ephemeris clock offset by SLR

Table 5 BDS-3 the mean value of the inside and outside precision of the BDS-3 broadcast ephemeris

	Precision ephemeris/ (m, ns)		SLR/m
Satellites	Orbit	Offset	Orbit
C31	3.07	43.87	0.88
C32	4.69	39.87	0.79
C33	3.28	21.59	1.03
C34	3.17	20.81	0.93

The result of BDS-3 (C31/C32/C33/C34) broadcast-orbit accuracy is 3.07 m/ 4.69 m/3.28 m/3.17 m and 0.88 m/0.79 m/1.03 m/0.93 by precise ephemeris and SLR observation data, respectively. The evaluate result is differ greatly between the result that evaluated by the precise ephemeris and the SLR observation data because of the poor accuracy of the precise ephemeris.

4.2 Analyze the BDS-3 Broadcast-Clock Offset Accuracy

In this paper, the two order difference method is used to the clock offset accuracy statistics [16]. Because BeiDou broadcast-clock space time reference point is the antenna center of B3 frequency, and space-time reference points of BDS-3 precision clock offset is B1/B3 ionosphere-free combination, so it is necessary to TGD correction for clock offset (Eq. 6). Figure 9 is the check result of the BDS-3 broadcast-clock offset.

$$\Delta t_{B1/B3} = \Delta t_{B3} - \frac{TGD1 \cdot f_1^2}{f_1^2 - f_2^2} \tag{6}$$

Among them, $\Delta t_{B1/B3}$ is the clock offset corrected by TGD, f_2, f_2 stands for the frequency of *B1*, *B2*. Δt_{B3} is the broadcast ephemeris clock offset.

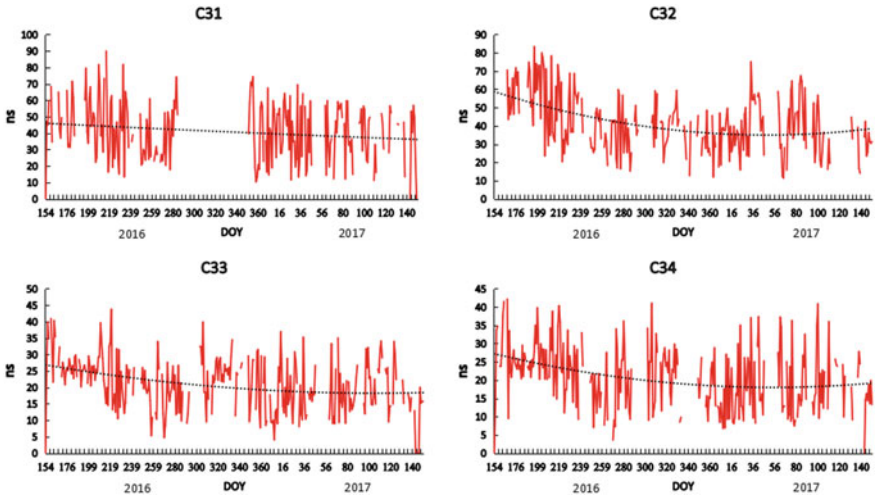

Fig. 9 The check result of the BDS-3 broadcast ephemeris offset

The above is the accuracy of the BDS-3 broadcast-clock offset evaluated by the BDS-3 precise clock offset calculated by this paper as the reference. Through the experimental analysis, the accuracy of the 4 BDS-3 experiment satellite broadcast ephemeris of C31/C32/C33/C34 is 43.87 ns/39.87 ns/21.59 ns/20.81 ns. The evaluate results of BDS-3 broadcast-clock offset accuracy are poor, mainly because of the poor accuracy of the precise clock offset, in addition, may be due to the system errors exist in the RMS statistical results, and the further analysis is needed.

5 Conclusion

In this paper, the BDS-3 experiment satellite broadcast-orbit and broadcast-clock offset accuracy through 12 months in 2016–2017 is evaluated by precise ephemeris. And the SLR observation data is used as a powerful external inspection tool to evaluate the orbit accuracy by the improved Bernese software.

At present, iGMAS and IGS do not provide BDS-3 experiment satellites precise ephemeris, in order to get BDS-3 experiment satellites precise orbit and clock offset, this paper based on the iGMAS and MGEX network observation data through one year to calculate the precise orbit of BDS-3 (C31/C32/C33/C34) in 3 day arcs by step by step method, and then statistical the overlap arc accuracy, the result show that: the inside accuracy of broadcast-orbit and broadcast-clock offset is: 36.5 cm/38.4 cm/44.1 cm/48.8 cm and 2.27 ns/2.40 ns/1.88 ns/1.87 ns, respectively; in order to evaluate the precise orbit more accurately, the outside accuracy of the orbit is evaluated by SLR observation data, and the average values are 51.4 cm/40.2 cm/62.9 cm/82 cm of one year. In addition, by fitting the inside

precision series, it can be found that the orbit and clock offset accuracy at the later stage is obviously improved, that is due to the more stations that can receive BDS-3 signals and the quality of data becomes more better. Because the number of SLR observation data of BDS-3 is less, cannot meet the fitting conditions, and its change trend cannot be obtained.

The BDS-3 precise ephemeris is combined with the SLR observation data to evaluate the BDS-3 broadcast ephemeris. Because BeiDou broadcast ephemeris satellite clock space time reference point is the antenna center of B3 frequency, and space-time reference points of BDS-3 precision clock offset is B1/B3 ionosphere-free combination, in this paper, the TGD correction for the clock offset is carried out before evaluate the accuracy of broadcast. The statistical results show that the RMS accuracy of C31 and C32 clock is about 40 ns, and the RMS accuracy of C33 and C34 clock is about 20 ns, the orbit accuracy is about 1 m, and the accuracy of BDS-3 broadcast ephemeris is improved obviously in the later period.

Acknowledgements We would like to thank the International GNSS Monitoring Assessment System (IGMAS) for their support for this paper.

References

1. Zhang X, Wu M, Liu W et al (2017) Initial assessment of the compass/BeiDou-3: new-generation navigation signals. J Geodesy 1:1–16
2. Kong Y, Sun B, Yang X et al (2017) Precision analysis of BeiDou broadcast ephemeris by using SLR data. Wuhan Daxue Xuebao 42(6):831–837
3. Montenbruck O, Steigenberger P, Hauschild A (2015) Broadcast versus precise ephemerides: a multi-GNSS perspective. GPS Solutions 19(2):321–333
4. Guo F, Zhang X, Li X et al (2009) Precision analysis on orbit and clock of GPS satellites broadcast ephemeris. Geomatics Info Sci Wuhan Univ 34(5):589–592
5. Guo J, Meng X (2011) Accuracy analysis of glonass satellites broadcast ephemeris. J Geodesy Geodyn 31(1):68–71
6. Rodriguez RL (2013) Galileo IOV status and results. In: Proceedings of international technical meeting of the satellite division of the institute of navigation
7. Guo Z, Gao J, Cao Y (2015) The precision analysis of coal technology, Beidou broadcast ephemeris and clock track 34(7):113–116
8. Degnan JJ, Pavlis EC (1994) Laser ranging to GPS satellites with centimeter accuracy 62–70
9. Watkins MM, Bar-Sever YE, Yuan DN (1996) Evaluation of IGS orbits with satellite laser ranging. Supercond. Ind.; (United States), 66(3):284–295
10. Behncke H, Remling C (1997) Apropos laser tracking to GPS satellites. J Geodesy 71 (7):423–431
11. Langley RB, Jannasch H, Peeters B et al (2000) The GPS broadcast orbits: an accuracy analysis. Cospar Sci Assembly
12. Roulston A, Talbot N, Zhang K (2000) An evaluation of various GPS satellite ephemerides. In: Proceedings of international technical meeting of the satellite division of the institute of navigation
13. Hu C, Wang Q, Wang Z et al (2017) An optimal stations selected model based on the GDOP value of observation equation. Wuhan Daxue Xuebao 42(6):838–844

14. Li M (2011) Multimode GNSS fusion precise orbit determination theory and its application. Wuhan University
15. Wang Q, Tianhe XU (2011) Adaptively changing reference station algorithm and its application in GPS long range airborne kinematic relative positioning. Acta Geodaetica Cartogr Sin 40(4):429–434
16. Huang G (2012) GNSS satellite atomic clock quality evaluation and precision clock algorithm. Chang'an University
17. Tan B, Yuan Y, Wen M, et al (2016) Initial results of the precise orbit determination for the new-generation BeiDou satellites (BeiDou-3) based on the iGMAS network 5(11):196

Multi-frequency Combined POD and Clock Estimation for BDS

Guang Zeng, Yanan Fang, Jie Li and Jun Zhu

Abstract MGEX (The Multi-GNSS Experiment) and iGMAS (international GNSS Monitoring & Assessment System) are two important global tracking networks of the BDS satellite navigation system. At present, all MGEX stations that can receive the BDS signal can track the BDS B1 and B2 signals. More than 20 stations can only track B1, B3 signals, and most iGMAS stations can only track B1, B3 signals. At the same time, BDS regional satellite navigation system broadcast B1, B2, B3 three frequency signal, and a new-generation BDS experimental satellite broadcast transitional signal of B1, B3. Based on this situation, a multi-frequency data fusion processing method is studied. The multi-frequency data fusion orbit determination and clock error estimation of BeiDou are realized by introducing the observation data of different frequency points from different observation networks. The proposed method has been applied and verified in the fusion of the BDS II and BDS experimental satellites. This method can introduce more MGEX stations and improve the BDS II MEO orbit accuracy by about 29%, 1DRMS to 5.5 cm; through the PPP verification of the BDS orbit and clock accuracy, PPP positioning accuracy increased by about 60%. The method can be applied to the BDS Global satellites construction for the early POD mission.

Keywords BDS · Multi frequency · Precise orbit determination
Satellite clock offset determination

G. Zeng (✉) · J. Li · J. Zhu
State Key Lab of Astronautic Dynamics, Xi'an, China
e-mail: zengguang_04@163.com

G. Zeng · J. Li · J. Zhu
Xi'an Satellite Control Centre, Xi'an, China

Y. Fang
Xi'an Jiaotong University, Xi'an, China

J. Sun et al. (eds.), *China Satellite Navigation Conference (CSNC) 2018 Proceedings*, Lecture Notes in Electrical Engineering 498,
https://doi.org/10.1007/978-981-13-0014-1_30

1 Introduction

The accuracy of navigation satellite Orbit and clock errors is a decisive factor in the precision location service performance of navigation systems. Domestic and foreign scholars have done a great deal of research on BDS precision orbit [1–5]. Compared with GPS system, BDS satellite navigation system lacks IGS densely distributed observation network. There are only a limited number of BDS observatories provided by the Multi-GNSS Experiment (MGEX) and the International GNSS Monitoring & Assessment System (iGMAS), with uneven global distributed only about 60 MGEX stations and 20 iGMAS stations. In order to improve the orbit determination and time synchronization accuracy, it is the best solution to use as many stations as possible. However, under the current conditions, the scheme is subject to the following constraints: At present, all MGEX stations that can receive the BDS signal can track the BDS B1 and B2 signals, but only more than 20 stations can track the B3 signal. All iGMAS stations can track B1, B3 signals, of which only four stations can track the B2 signal. At the same time, BDS regional satellite navigation system broadcasts B1, B2 and B3 tri-band signals. In order to achieve a smooth transition with the BDS II downlink navigation signal, the new generation of BDS experimental satellite and the BDS III satellite will still broadcast transition signals B1 and B3. In this case, Most of the BDS satellite orbit determination uses dual-frequency signal B1, B2 combination [6–8] or B1 and B3 combination, as a result, the observation stations used are bound to have some trade-offs. In order to realize the data fusion processing of different tracking network and BDS satellite at different stages of construction, a multi-frequency data fusion processing method is studied in this paper. Stations belonging to different observation networks introduce observation data of different frequency points to realize multi-frequency Data fusion orbit determination and clock error estimation. Finally, the method is applied to the BDS II and BDS experimental satellites fusion orbit determination experiment. The validity and correctness of this method is verified through the overlapping arc orbit and static PPP.

2 Mathematical Model

The receiver i receives the signal of the satellite j, and the observation equation of the code and the phase data is [1, 2]:

$$\begin{cases} P_{i,f}^{j} = \rho_i^j + c\left(\Delta t_i - \Delta t^j + b_{i,f} - b^{j,f}\right) + \varepsilon_{P,i}^{j} \\ L_{i,f}^{j} = \rho_i^j + c\left(\Delta t_i - \Delta t^j + b_{i,f} - b^{j,f}\right) + \lambda^{j,k} N_i^{j,k} + \varepsilon_{L,i}^{j} \end{cases} \tag{1}$$

where ρ_i^j is the distance between the satellite and the station (including the spatial delay correction of the troposphere and ionosphere), Δt_i and Δt^j are the clock errors

of the station and the satellite respectively, $b_{i,f}$ and $b^{j,f}$ are the channel delays of the station and the satellite, and $N_i^{j,k}$ is the ambiguity. Ignoring the observation noise, only the code data is taken into account and the following variables are introduced:

$$\begin{cases} K_1^{B12} = \frac{f_{B1}^2}{f_{B1}^2 - f_{B2}^2}, & K_2^{B12} = \frac{-f_{B2}^2}{f_{B1}^2 - f_{B2}^2} \\ K_1^{B13} = \frac{f_{B1}^2}{f_{B1}^2 - f_{B3}^2}, & K_2^{B13} = \frac{-f_{B3}^2}{f_{B1}^2 - f_{B3}^2} \end{cases} \tag{2}$$

where $f_{B1} = 1561.098$ MHz, $f_{B2} = 1207.14$ MHz, $f_{B3} = 1268.52$ MHz are BDS B1, B2, B3 signal frequency value respectively.

For B1 & B2 and B1 & B3 data, the ionosphere-free observation equation can be expressed as

$$\begin{cases} P_3^{B12} = \rho_{i1,ion\_free}^j + c\left(\Delta t_{i1} + K_1^{B12} b_{i1,B1} + K_2^{B12} b_{i1,B2}\right) \\ \qquad - c\left(\Delta t^j + K_1^{B12} b^{j,B1} + K_2^{B12} b^{j,B2}\right) \\ P_3^{B13} = \rho_{i2,ion\_free}^j + c\left(\Delta t_{i2} + K_1^{B13} b_{i2,B1} + K_2^{B13} b_{i2,B3}\right) \\ \qquad - c\left(\Delta t^j + K_1^{B13} b^{j,B1} + K_2^{B13} b^{j,B3}\right) \end{cases} \tag{3}$$

Equation (3) can be simplified as:

$$\begin{cases} P_3^{B12} = \rho_{i1,ion\_free}^j + c\left(\Delta t'_{i1} - \Delta t'_j + t_{bias}\right) \\ P_3^{B13} = \rho_{i2,ion\_free}^j + c\left(\Delta t'_{i2} - \Delta t'_j\right) \end{cases} \tag{4}$$

where

$$\begin{cases} \Delta t'_{i1} = \Delta t_{i1} + K_1^{B12} b_{i1,B1} + K_2^{B12} b_{i1,B2} \\ \Delta t'_{i2} = \Delta t_{i2} + K_1^{B13} b_{i2,B1} + K_2^{B13} b_{i2,B3} \\ \Delta t'_j = \Delta t^j + K_1^{B13} b^{j,B1} + K_2^{B13} b^{j,B3} \\ t_{bias} = \left(K_1^{B13} - K_1^{B12}\right) b^{j,B1} + K_2^{B13} b^{j,B3} - K_2^{B12} b^{j,B2} \end{cases} \tag{5}$$

When dealing with zero-difference pseudo-range data, the parameter solved is not the actual receiver clock error Δt_i, but the $\Delta t'_i$ that has been doped with channel delay. Since each receiver either processes the B1B2 data or processes the B1B3 data, it is only necessary to solve $\Delta t'_i$ for station clock error and station channel delay parameters during the fusion processing of different observation networks. The satellite clock error processing strategy is that for all receivers set parameter $\Delta t'_j$ for each satellite in each epoch, and for the B1B2 data receiver it is necessary to additionally add t_{bias} for each satellite (constants, not related to epochs). An extra restraint condition need to be introduced in order to prevent the normal equation system from becoming singular.

$$\sum_{j=1}^{ns} t_{bias}^{j} = 0 \tag{6}$$

When dealing with zero-difference phase data, since t_{bias} is linearly related to the ambiguity, it is not necessary to solve the parameter t_{bias} but solve the ambiguity-float solution.

For double-difference observations, the double-difference observation data can be expressed as:

$$\begin{cases} DDP(i_1, i_2, j_1, j_2) = \left(P_{i_1}^{j_1} - P_{i_1}^{j_2}\right) - \left(P_{i_2}^{j_1} - P_{i_2}^{j_2}\right) \\ DDL(i_1, i_2, j_1, j_2) = \left(L_{i_1}^{j_1} - L_{i_1}^{j_2}\right) - \left(L_{i_2}^{j_1} - L_{i_2}^{j_2}\right) \end{cases} \tag{7}$$

If both receivers i_1 and i_2 select either B1B2 data or B1B3 data, the channel delay parameters can be completely eliminated and the ambiguities remain integer. If one of the receivers a and b receives B1B1 data and the other receives B1B3 data, the channel delay difference between the different frequencies needs to be taken into consideration and solving process becomes complicated. In order to simplify the processing, when using double-difference data to solve the orbital parameters, the observation network needs to be grouped. Receivers that receive B1B2 data are classified as the first group and that receive B1B3 data are classified as the second group. Only the stations of the same group can form the baseline.

3 Processing Strategies and Procedure

BDS satellite multi-frequency data fusion processing has three key elements:

(1) The program needs to recognize the frequency of observed data when forming ionosphere-free combination;
(2) When dealing with double-difference data, only the stations of the same group can form baselines;
(3) When dealing with zero-difference data, identify the receiver that receives the B1B3 data and add parameter t_{bias} for each satellite.

The software used in the BDS multi-frequency combined processing test in this paper is developed by the iGMAS analysis centre on the basis of Bernese GNSS Software Version 5.2. The software now has the following combined processing capabilities:

(1) GPS & GLONASS & BDS & Galileo four systems combined processing;
(2) BDSII satellite and BDS experimental satellite combined processing;
(3) Joint processing of BDS B1 & B3 and B1 & B2 frequency combination.

The scheme adopted in BDS multi-frequency data combined processing is as follows:

In the joint processing of GPS&BDS & Galileo, the dynamic model and observation model used in the solution are the same as those in Ref. [1]. A two-step method that the orbit and the clock error are solved respectively in two steps is adopted: The first step is to use double-difference data to solve satellite orbits. The observation data are first divided into two groups, the iGMAS group (with B1 & B3 data included) and the MGEX group (with B1 & B2 data included), forming a baseline within the respective group with no baseline between the two groups. When estimating the parameters, all the baseline data are introduced to solve the orbital parameters of the three navigation systems, the tropospheric parameters, the earth rotation parameters and the station coordinate parameters. The second step is to solve the satellite and station clock errors using zero-difference data. The B1 & B3 data of IGS group and the B1 & B2 data of MGEX group are used together and the orbit, the tropospheric parameters, the Earth's rotation parameters and the station coordinates obtained in the first step are fixed and introduced. First, the DCB parameters (including t_{bias} parameters) are solved using the code data. Then the satellite and station clock errors are solved with combined code and phase data and fixed DCB parameters. Specific strategies shown in Table 1, the data processing flow shown in Fig. 1.

Table 1 Multi-frequency combined processing strategy

	POD with double-difference data	Clock error estimation with zero-difference data
Data source	iGMAS + MGEX: PHASE	iGMAS + MGEX: CODE + PHASE
Cluster scheme for difference	iGMAS in one cluster and MGEX in another	Zero-difference, mixed with iGMAS and MGEX
Coordinate parameters	Introducing rapid products of analysis center, tight constraints	Introducing the result of double-difference solution
Orbit parameters	6 orbit elements, 5 RPR parameters and pseudo-random pulse in tangential with tight constraints	Introducing the result of double-difference solution
Earth rotation parameter	Xp, Yp and LOD	Introducing the result of double-difference solution
Tropospheric delay	ZPD parameters, 2 h a group, relatively loose constraint. Horizontal gradients, 24 h a group, relatively loose constraint	Introducing the result of double-difference solution
Ambiguity parameters	Float solution	Float solution
DCB parameters	None	Bias between system inter-system biases, GPS P1-C1, t_{bias} of BDS
Arcs	3-days solution	1-day solution

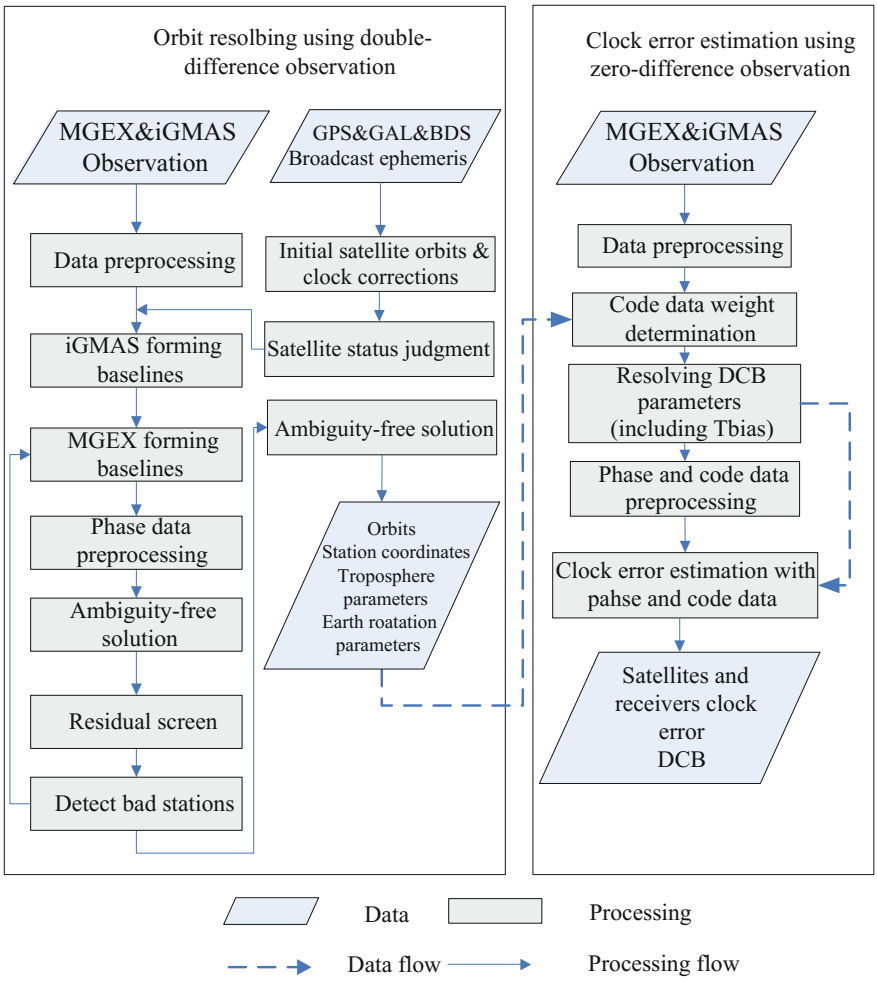

Fig. 1 Multi-frequency combined processing flow chart

4 Multi-frequency Orbit and Clock Error Estimation Test

4.1 Test Data

The stations used in the experiment included 17 stations in iGMAS and 65 stations in MGEX (only 25 stations could receive B3I signals). The station distribution is shown in Fig. 2. The test data are collected from these stations at 271 days in 2017–277 days in 2017. In multi-frequency processing trials (denoted as Scheme 1), iGMAS stations introduce B1 & B3 dual-band data, while MGEX introduce B1 & B2 data (65 stations).

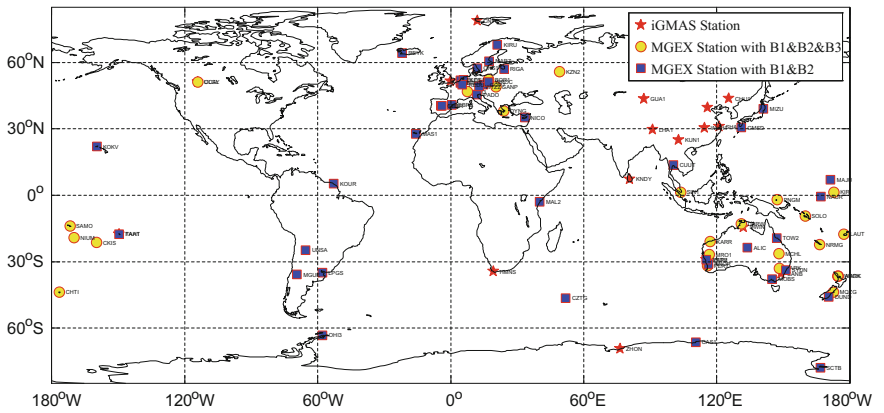

Fig. 2 Station distribution of POD and clock estimation experiment

Table 2 The data used in first and second scheme

	Multi-frequency	Dual-frequency
iGMAS	Code: B1I & B3I Phase: B1I & B3I	Code: B1I & B3I Phase: B1I & B3I
MGEX	Code: B1I & B2I Phase: B1I & B2I	Code: B1I & B3I Phase: B1I & B3I

To compare the test results, dual-frequency processing is introduced as the comparison scheme and denoted as Scheme2. The difference from Scheme 1 is the introduction of only iGMAS and MGEX stations (25 stations in total) that can receive B1I & B3I signals, as shown in the Table 2.

4.2 Test Results

The orbit obtained by the two schemes is respectively compared with overlapping arcs (3-day arcs, overlapping 2 days). The comparison results are shown in Fig. 3.

Compared with scheme 2, the multi-frequency processing scheme improved the MEO orbit of BDS II by 29%, while the increase of MGEX stations improves the observation conditions of MEO. However, for IGSO and GEO satellites, the satellite orbital loci are located in the Asia-Pacific region. The addition of B1I & B2I stations has seen little improvement in the observation conditions for satellites in this region. So in the overlapping arc of IGSO and GEO orbit, the proposed scheme has no obvious advantage.

In the multi-frequency processing scheme, additional satellite parameter t_{bias} is required for solving clock errors. To verify the rationality of this parameter setting, the repeatability of the single-day solution within 7 days is calculated. The results are shown in Fig. 4 (subtracting t_{bias} of C14). It can be seen that the daily t_{bias}

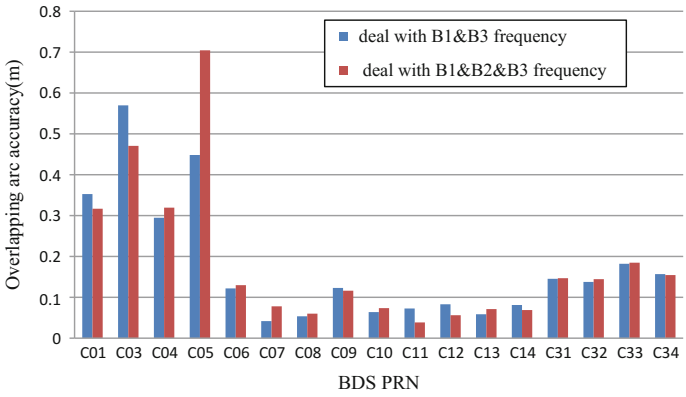

Fig. 3 Overlap arc accuracy of orbit product

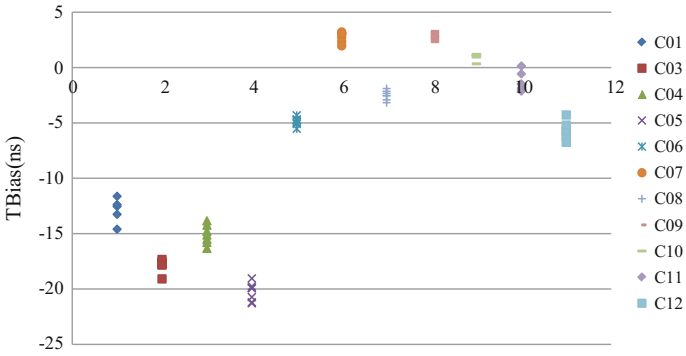

Fig. 4 Daily solution stability of BDS t_{bias} parameters

solved for each satellite is relatively stable, RMS = 0.465 ns, which proves the rationality of the solution.

In order to verify the BDS orbit and clock accuracy of the multi-frequency processing scheme, the static PPP method is used. The specific steps are as follows: 22 MGEX stations are selected and the BDS orbit and clock error, which are solved in Scheme I and Scheme II respectively, are used to complete the static PPP solution of station coordinates. The results of the solution are compared with iGMAS final coordinate products and statistical comparison result is shown in Fig. 5. The accuracy of static PPP reaches 45.14 mm in horizontal and 79.40 mm in vertical with the orbit and clock error obtained in scheme 1; and for Scheme 2, the accuracy in horizontal and vertical are 139.01 and 164.91 mm respectively. Compared to scheme 2, the BDS orbit and clock error products that are solved by the multi-frequency processing scheme improve the static PPP positioning accuracy of the station by about 60%.

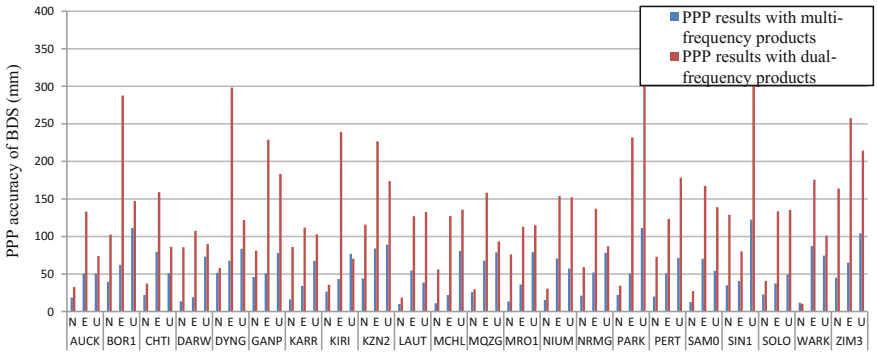

Fig. 5 Static PPP accuracy verification results

5 Conclusions

In this paper, a multi-frequency data combined processing method is studied. Stations belonging to different observation networks introduce observation data of different frequency points to realize multi-frequency Data fusion orbit determination and clock error estimation. The method has been applied and verified in the BDS II and BDS experimental satellite combined orbit determination:

(1) Compared with the traditional dual-frequency method, this method introduced more MGEX stations and improved the MEO observation conditions of BDS II. The MEO orbit of BDS II increased by 29% and 1DRMS reaches 5.5 cm.
(2) The accuracy of BDS orbit and clock errors are verified through the static PPP. The results show that static PPP accuracy increased by about 60%, the horizontal direction of 45.13 mm, the vertical direction of 79.40 mm.
(3) This method realizes the data fusion processing of different tracking network and BDS constellation at different stages of construction, and can be applied to the precise orbit determination and clock error estimation in the initial stage of BDS global satellite construction.

Thanks The authors are grateful to the observation data provided by the International GNSS Monitoring and Evaluation System (www.igmas.org).

References

1. Dai X, Shi C, Lou Y (2016) Multi-GNSS precise orbit determination and its precision analysis. Rev Surveying Mapp 2:P12–P16
2. Liu W, Hao J, Wei W et al (2016) Comparison of two methods of precise orbit determination of BDS satellites. J Geodesy Geodyn 36(3):211–215

3. Lou Y, Shi C et al (2015) Precise orbit determination of BDS constellation: method comparison. GPS Solutions P1–P10
4. Li M (2011) Multi-GNSS combined precise orbit determination: theory and application. Wuhan University, Wuhan
5. Li R, Zhao C, Zheng Z, He Z (2015) BDS navigation constellation orbit determination based on MGEX data. J Geodesy Geodyn 35(4):662–665
6. Zeng G, Gong B, Wang JS, Li J, Zhu J (2014) BDS/GPS indirect fusion precision orbit determination. In: Sun J, Jiao W, Wu H, Lu M (eds) China satellite navigation conference (CSNC) 2014 proceedings: volume III. Lecture notes in electrical engineering, vol 305. Springer, Berlin, Heidelberg
7. Zhu J, Wang J, Zeng G, Li J, Chen J (2013) Precise orbit determination of BDS regional navigation satellite system via double-difference observations. In: Sun J, Jiao W, Wu H, Shi C (eds) China satellite navigation conference (CSNC) 2013 proceedings. Lecture notes in electrical engineering, vol 245. Springer, Berlin, Heidelberg
8. Dach R, Lutz S, Walser P et al (2015) User manual of the bernese GNSS software, version 5.2. Astronomical Institute, University of Bern

Assessment of iGMAS Final Combination with Nearly Three-Year Solutions

Hongliang Cai, Xing Li, Guo Chen and Wenhai Jiao

Abstract To monitor and assess the performance of Chinese Beidou System as well as other navigation satellite systems (i.e. GPS, GLONASS, Galielo), the international GNSS continuous Monitoring and Assessment System (iGMAS) is developed by China. As the products reprocess center, the Product Integration and Service Center (ISC) provides global users with different time-delay products. With nearly three-year products from iGMAS, the present paper focuses on the timeliness and precision of products. The results show that there are four analysis centers with products timeliness more than 95% and keep stable, currently, the timeliness of combined solutions are better than 99%. Compared to the IGS products, the precision of final orbit and clock products differs between different satellite system, the GPS shows best among the four systems, the precision of orbit and clock are 1 cm and 0.05 ns, respectively, followed by GLONASS, 2 cm and 0.1 ns for satellite orbit and clock, respectively, while the BDS IGSO/MEO and Galileo satellites show identical results, the orbit precision of both systems is about 4–8 cm, and about 0.2 ns for the satellite clock products. The precision of combined final tropospheric delay products is 2 mm, with respect to the products from JPL, while the difference between the combinations of iGMAS and IGS is about 2TECU.

Keywords iGMAS · Orbit · Clock bias · Combination · Precision

H. Cai (✉) · X. Li · W. Jiao
Beijing Institute of Tracking and Telecommunication Technology, Beijing 100094, China
e-mail: caibanyu@126.com

H. Cai
Shanghai Astronomical Observatory of Chinese Academy of Sciences,
Shanghai 200030, China

G. Chen (✉)
School of Geodesy and Geomatics, Wuhan University, Wuhan 430079, Hubei, China
e-mail: wuhandaxuexinxibu@163.com

J. Sun et al. (eds.), *China Satellite Navigation Conference (CSNC) 2018 Proceedings*, Lecture Notes in Electrical Engineering 498,
https://doi.org/10.1007/978-981-13-0014-1_31

1 Introduction

With the establishment of the global navigation satellite systems (GNSS) from different nations, GNSS technology is extensive and profound applied in various scientific research and engineering fields. In 20 IUGG meeting, 1991, the concept of IGS (i.e. International GPS Service) was proposed, and with the continuous development during the last over twenty years, the international GNSS service organization (IGS) has been able to provide open access and high-quality GNSS products. The precision of final GPS satellites orbits and clock can reach to about 2.0 cm and 0.075 ns. Meanwhile, with the set-up and development of the Multi-GNSS Experiment (MGEX), IGS has been dedicated to generate and provide multi-GNSS products to global users [1–3].

The iGMAS is built by China at the beginning of 2011 to provide monitoring and assessment services for global navigation satellite systems. It consists of thirty global-distributed tracking stations, three data centers, more than eight analysis centers, one monitor and assessment center, one function management center and one Product Integration and Service Center (ISC). The main task of iGMAS is to provide the global GNSS users with tracking data from global stations and high quality products, such as satellite orbit/clock, Earth Rotation Parameters (ERP), station coordinates, global ionosphere maps, station zenith troposphere delay products and GNSS integrity products, as well as the monitoring and assessment results for the GNSS. The ISC is responsible for the combination of products from different analysis centers, including three types combined products, that is ultra-rapid, rapid and final products with different timeliness, the ultra-rapid products are updated every six hours with a delay by three hours, the rapid products are updated every day with a delay about fourteen hours and the final products are produced one time for each week with a delay about twelve days.

The differences of softwares and data processing strategies used by analysis centers, lead to the different products accuracy, timeliness and reliability during different analysis centers. The importance of products combination from ISC is make fully use of products from each analysis center to generate high-precision, stable and reliable combined solutions.

With nearly three-year products of iGMAS analysis centers and ISC, the present paper focuses on assessment of product timeliness and precision of final orbit, clock, troposphere and ionosphere maps.

2 Timeliness of IGMAS Products

Currently, thirteen analysis centers participate in the products combination and assessment. In order to provide users with different timely products to meet the different requirements in the various fields, analysis centers and ISC need to provide or reprocess products within the required time. In this section, the timeliness of products of analysis centers and ISC is analyzed. It is worth noting that the failure of

products generation due to power outages and network problems is excluded in the statistics of products timeliness. The time period is from Jan 1, 2015 to Oct 22, 2017.

For analysis center's product timeliness, that is the ability of submitting all kinds of products before the deadline to ISC. There are 84 ultra-rapid products per week, including satellite orbits, clock, Earth Rotation Parameters (ERP) and zenith tropospheric path delay estimates. There are 28 rapid products per week, including satellite orbits, clock, ERP and global ionosphere maps. For the final product, including station coordinates, satellite orbits, clock, ERP, zenith tropospheric path delay estimates and global ionosphere maps, there is a total of 45 products per week. The products timeliness is computed by the ratio between the number of products submitted by analysis centers on time and the required number. Figure 1 shows the products timeliness of each analysis center for each year.

For the products timeliness, most of the analysis centers have an improvement over time except AC09, compared to the products timeliness in 2015, the statistics results of products timeliness in 2017 period show an improvement about 6.7, 1.3 and 3.5% for ultra-rapid, rapid and final products, respectively. However, some analysis centers show decreasing performance of products timeliness. For example, there is a decrease about 7.2% for the rapid products of AC01, a decrease about 17.5% of final products for AC06 and 11.6% for AC13 final product. The analysis centers with the best product timeliness performance are AC02, AC03, AC08 and AC11, the average products timeliness during the three years are better than 95% for ultra-rapid, rapid and final products.

Table 1 lists the products timeliness of combined solutions for the ultra-rapid, rapid and final products, the performance shows a tendency of improvement year by year, especially for the ultra-rapid and rapid products. Compared to the products timeliness in 2015, there is an improvement by about 3.3, 5.1 and 1.7% in 2017 for the ultra-rapid, rapid and final products, respectively, and the products timeliness of ISC is better than 99%.

3 Precision of Final Combined Solutions

The precision of combined solutions is focused in this section and the external reference products from IGS are collected from Jan 01, 2015 to Sep 23, 2017. The combined final solutions include satellite orbits, clock, ERP, zenith tropospheric path delay estimates and global ionosphere maps.

3.1 Satellite Orbits

For the method of orbits combination, please reference to literature [4–8], in this present paper, we adopt the algorithm in the literature [8] to generate the combined solutions. To obtain the precision of orbits products, we take the combined solutions from IGS as references for GPS and GLONASS satellite orbits. Figure 2

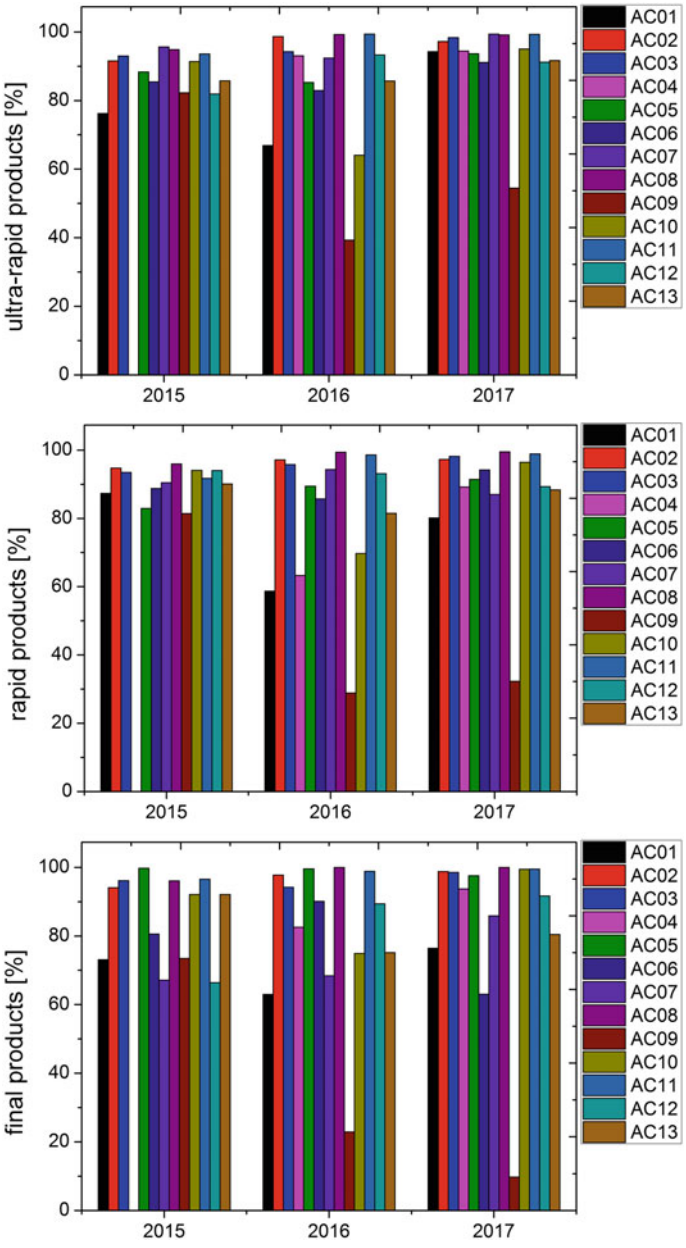

Fig. 1 Timeliness of analysis centers products. Top: ultra-rapid, middle: rapid, bottom: final products

Table 1 Timeliness of combined solutions (unit: %)

Year	Ultra-rapid	Rapid	Final
2015	96.43	94.94	98.25
2016	99.67	99.95	100.00
2017	99.77	100.00	100.00

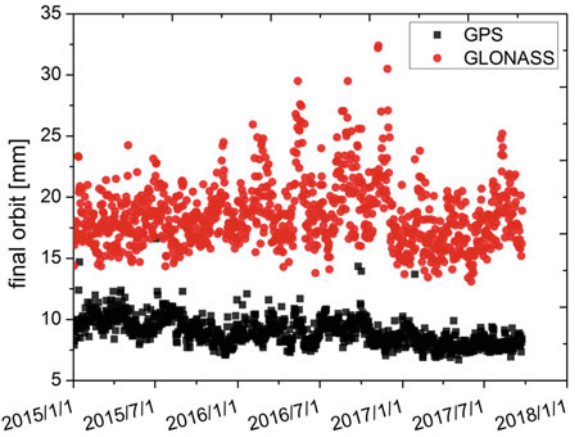

Fig. 2 Precision of GPS and GLONASS combined orbits

shows the precision of mean root mean square errors (RMS) over the three XYZ geocentric components.

For GPS and GLONASS satellite orbit, the precision of iGMAS combined solutions fluctuate around 1 and 1.8 cm respectively, and the precision of GPS satellite orbit has a tendency of improve over the time, at the end of 2016, the precision of combined GLONASS satellite orbits has an obvious improvement.

For BDS and Galileo satellite orbit products, the products from TUM and GFZ are used as reference. The average root-mean-square of orbit difference is used as the precision indicator, and the BDS GEO and IGSO/MEO satellites are separated in the statistics, the precision variation over time is shown in Fig. 3, the precision of GEO satellite is not shown in the figure, due to the lareger difference among the analysis centers.

In contrast to the reference orbits, the IGSO/MEO in the BDS has a tendency of improvement over time. At the end of 2017, the precision has reached 4 cm, which could be attributed to the enhancement of the model and more observations used by most of the iGMAS analysis centers. However, the variation of precision for the Galileo satellite orbit is relatively small, it fluctuates around 7 cm in the last three years. On the one hand, there is only a few analysis centers of iGMAS, which improve the solar pressure model, as a result, the beta-dependent systematic error in the Galileo satellite orbits is not removed. On the other hand, the orbit products of TUM also have the same systematic error before 2017 (http://mgex.igs.org/analysis/slrres_GAL.php).

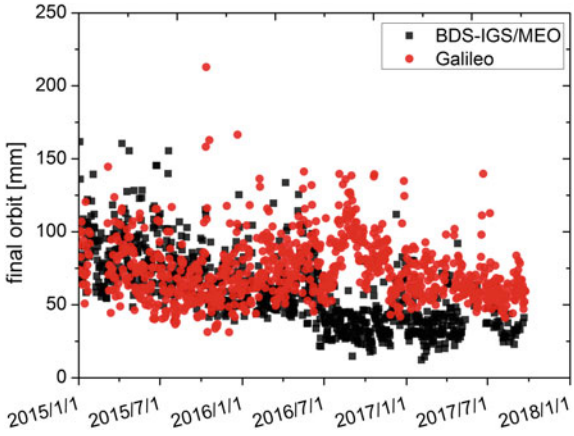

Fig. 3 Precision of BDS and Galileo combined orbits

Table 2 Precision of combined orbit (unit: mm)

Year	GPS	GLONASS	BDS-GEO	BDS-IGSO/MEO	Galileo
2015	9.6	18.1	2133.2	78.3	71.2
2016	9.1	19.8	1628.5	50.9	81.6
2017	8.1	17.4	1408.5	38.7	65.0

The statistic results for the precision of each navigation satellite system is presented in Table 2. The orbit of GPS and GLONASS products have a precision within 2 cm, while for BDS IGSO/MEO and Galileo satellite, the precession are better than 10 cm. Due to the limited changes of observation geometry, the precision of BDS GEO is between 1.4 and 2.2 m. With the increasement of global stations, there is still room to further improve the performance of precise orbit determination for BDS IGSO/MEO and Galileo satellites.

3.2 Satellite Clock Products

To keep the consistency between satellite orbit and clock products, the consistency corrections should also be accounted in the clock product combination. The detail method of satellite clock products combination is introduced in Refs. [9–11]. The difference between iGMAS and IGS for GPS satellite clock products, as well as the difference between iGMAS and ESA for GLONASS satellite clock products are shown in Fig. 4. The root mean square error is used as the clock products quality.

For BDS and Galileo satellite clock products, the MGEX products of GBM are used as reference and the iGMAS combined solutions are compared. The precision

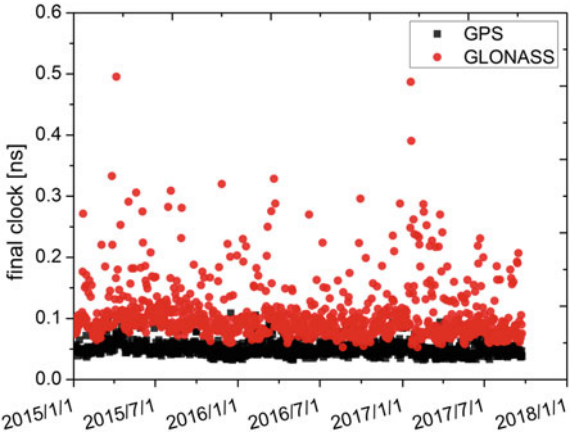

Fig. 4 Precision of combined satellite clock bias products for GPS and GLONASS

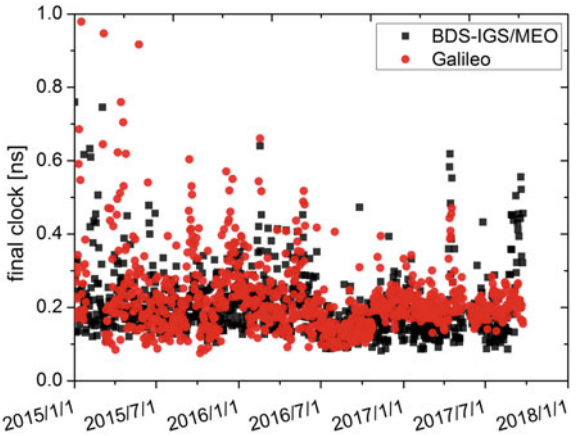

Fig. 5 Precision of combined satellite clock bias products for BDS and Galileo

of BDS GEO and IGSO/MEO satellites separately computed in statistics, the specific statistical accuracy change as shown in Fig. 5, the precision of BDS GEO satellites clock products is not shown in the figure as the larger difference compared to other satellites.

Table 3 lists the precision of the satellites clock products, it is clear from the figures and the table, the precision of GPS and GLONASS satellite clock is more stable, the precision of GPS satellite clock is at the level of 0.05 ns, and the GLONASS satellite clock products is about 0.11 ns. Compared with the reference products, the precision of BDS and Galileo satellites clock have an improvement over time. At the end of 2017, BDS GEO satellites clock have a precision about 0.5 ns, while BDS IGSO/MEO satellites and Galileo satellites clock are 0.2 ns.

Table 3 Precision of combined satellite clock products (unit: ns)

Year	GPS	GLONASS	BDS-GEO	BDS-IGSO/MEO	Galileo
2015	0.053	0.112	0.494	0.216	0.280
2016	0.052	0.100	0.464	0.195	0.204
2017	0.049	0.106	0.452	0.195	0.212

3.3 Tropospheric Delay Products

The zenith tropospheric path delay estimates are important for studying atmospheric water vapor, and the accuracy of tropospheric products directly influence the accuracy of water vapor content. Compared to the JPL troposphere products, the precision of iGMAS combined final products is computed, and Fig. 6 shows the precision variation over time. The precision is about 2.5 mm for 2015. A small improvement is found for 2016 and 2017, the precision is about 2.2 and 2.3 mm, respectively. The meteorological observation will be used to further verify the accuracy of iGMAS tropospheric products in the future.

3.4 Global Ionosphere Maps

For iGMAS combined global ionosphere maps, they are obtained as a simple weighted mean of the available analysis centers products. The iGMAS ionospheric products are compared to the IGS products for different latitudes (i.e. the northern high-latitude areas (NHL): 60–87.5°N, the northern hemisphere mid-latitude (NML): 30–60°N, the northern low-hemisphere (NLL): 0–30°N, the southern high-latitude areas (SHL): 60–87.5°S, the southern hemisphere mid-latitude (SML): 30–60°S, the southern low-hemisphere (SLL): 0–30°S). Figure 7 shows the precision of different latitude areas for iGMAS combined solution.

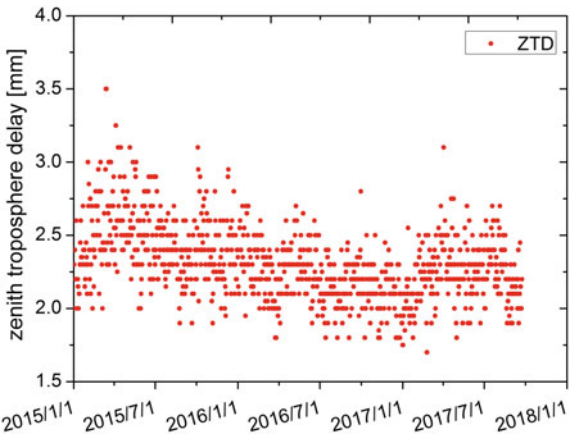

Fig. 6 Precision of iGMAS combined tropospheric delay products

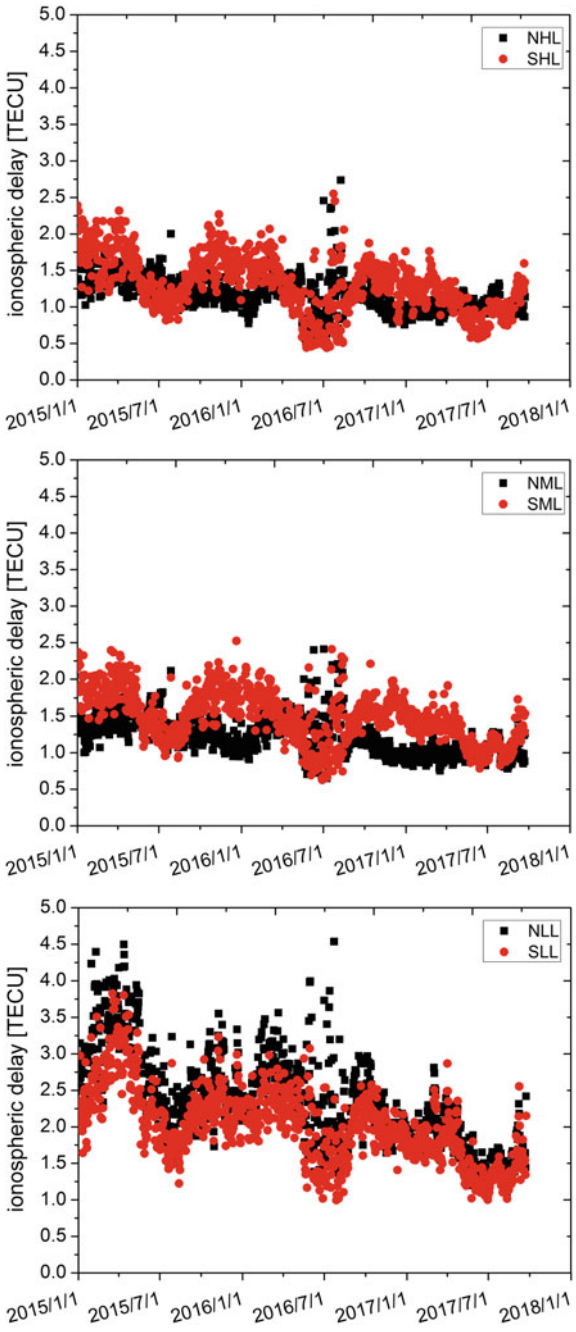

Fig. 7 Precision of iGMAS combined ionospheric delay products. Top: high latitude (HL) area, middle: middle latitude (ML) area, bottom: low latitude (LL) area

Table 4 Precision of iGMAS combined ionospheric delay products (unit: TECU)

Year	NHL	NML	NLL	SHL	SML	SLL
2015	1.31	1.34	2.78	1.53	1.68	2.33
2016	1.12	1.24	2.32	1.24	1.44	1.96
2017	1.01	0.99	1.73	1.07	1.23	1.59

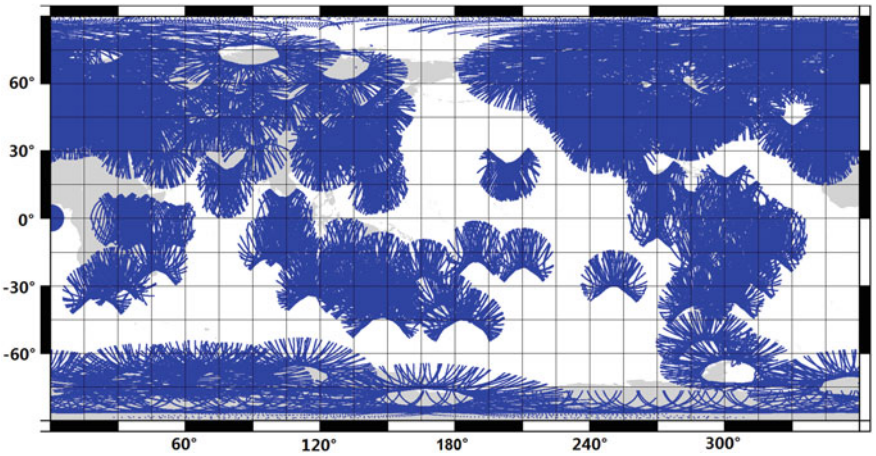

Fig. 8 Distribution of ionospheric pierce points

Table 4 summarizes the root mean square error of iGMAS global ionosphere maps. On the one hand, the maps in the northern hemisphere high and middle latitude areas have a better precision than the maps in southern hemisphere, while it is opposite for the low latitude area. On the other hand, the precision of ionosphere products in low latitude areas is less than the high and middle latitude areas, which is associated with the stronger activity of low latitude ionosphere. Moreover, stations in low latitude areas are not evenly distributed, here we choose 173 global stations with well distribution to calculate the ionosphere products, and the corresponding ionospheric pierce points are shown in Fig. 8. It is clear that there are less pierce points in low latitude areas, regardless of whether north or south hemispheres, what is worse, the stations are located in the mainland, the sea areas is more serious as the lack of data.

According to the characteristics of the solar-geomagnetic reference frame, the longitude of these areas with less observations in land under the framework are constantly changing, which means some pierce points under the framework could be observed at some periods. Therefore, it is possible to impose constraints on the parameters of the ionosphere model in the adjacent periods, as a result, the estimation of model parameters can be less affected by the less observations areas. In order to further improve the accuracy of ionospheric products, we can integrate multiple data sources, such as GNSS data, oceanic altimetry satellite and DORIS data.

4 Conclusion

With nearly three-year iGMAS products, this present paper firstly analyzes the timeliness of the products for analysis centers and combined solutions. The products timeliness of four analysis centers is relatively stable and better than 95%. For most analysis centers, compared the products timeliness in 2015, the timeliness in 2017 show a improvement. However, a few analysis center s need to be further improved for their products timeliness.

The combined products make full use of the products from different analysis centers, not only its timeliness, but also the precision are benefited. the timeliness of combined products in 2017 can reach 99%. Moreover, the precision of combined solutions is stable. Among the four satellite systems, the precision of GPS orbit and clock products show the best performance in four system, the GLONASS related products are better than BDS IGSO/MEO and Galileo satellites products (i.e. satellite orbit and clock), with more and more stations used for BDS and Galileo precise orbit determination and improvement of solar pressure model, there is still room to improve the precision of BDS and Galileo related products. At the end of 2017, the precision of combined tropospheric final product is about 2 mm, while it is about 2TECU for the final combined ionospheric products.

Further improvement of products performance for the iGMAS combined solutions can be considered from the analysis centers and the products consistency of combined solutions. For analysis centers, more efforts of data processing strategy, such as the orbit dynamic model (i.e. solar pressure model), ambiguity resolution should be studied to improve the performance of satellite orbit clock products. More data sources can be used to generate ionospheric products to improve the current performance of global ionosphere maps. For combined products consistency, the orbit/clock and ERP need to be validated in the future work.

References

1. Beutler G, Moore A, Mueller I (2009) The international global navigation satellite systems service (IGS): development and achievements. J Geodesy 83(3–4):297–307
2. IGS (2014) IGS quality of service. https://www.igs.org
3. Steigenberger P, Rothacher M, Rülke A, Dietrich R (2009) Quality of reprocessed GPS satellite orbits. J Geodesy 83(3–4):241–248
4. Yao Y (2007) Theory and realization of GPS orbit integration. Geomatics Info Sci Wuhan Univ 6:510–514
5. Feng L, Jia X (2010) A method of combining orbit by M estimation and dynamic smoothing. Scientia Sinica Pysica, Mechanica & Astronomica 5:603–607
6. Mireault Y, Kouba J, Lahaye F (1996) IGS combination of precise GPS satellite ephemerides and clocks. In Beutler G et al (ed) GPS trends in precise terrestrial, airborne, and spaceborne applications. Springer Berlin Heidelberg, Heidelberg, pp 14–23
7. Beutler G, Kouba J, Springer T (1995) Combining the orbits of the IGS analysis centers. Bulletin géodésique. 69(4):200–222

8. Tan C, Chen G, Wei N, Cai H (2016) Combined satellite orbits of the iGMAS analysis centers: method and precision. Geomatics Info Sci Wuhan Univ 41(11):1469–1475
9. Yang Y (1993) Theory and application of robust estimation. Ba Yi Press, Beijing
10. Jikun O (1996) Design of a new scheme of robust estimation by three steps. Acta Geodaetica Cartogr Sin 8:173–179
11. Chen K, Xu T, Yang Y, Cai H (2016) Combination and assessment of GNSS clock products from iGMAS analysis centers. Acta Geodaetica Cartogr Sin 45(z2):46–53

Analysis on the Representation of Polar Motion in GNSS Applications

Pu Li and Urs Hugentobler

Abstract In modern technology, the daily polar motion parameters are estimated with the orbit parameters in the precise orbit determination process. So, the precision of polar motion parameters affects that of orbit parameters as well as the reference frame. During current estimations, both the x-pole and y-pole are represented by a linear model. However, controversial of using the offset and rate model or the piecewise linear model remains unsolved. In this article, the behavior of polar motion is studied and simulated, then estimated using both models mention above. The attempt of implementing the least square cubic spline (LSCS) model is realized, and the comparison of these models are conducted. Consequently, the LSCS model revealed a significant improvement in the sense of residuals with the simulated polar motion data with less parameters per estimation period compared to the traditional offset and rate model. Furthermore, hypothesis testing show that higher order parameters are significant. It is then worth studying how much will the LSCS model affect orbit parameters.

Keywords Polar motion · Least square cubic spline · Time-frequency analysis POD

1 Introduction

In GNSS applications, the polar motion (PM) parameters are estimated by individual analysis centres (ACs) with the orbit parameters in the precise orbit determination process. During this procedure, the PM a priori model provided by the IERS conventions are subtracted, and the remains are estimated using linear model with two parameters (including an intercept and a slope) per day. However,

P. Li (✉) · U. Hugentobler
Technische Universität München, Arcisstraße 21, 80333 Munich, Germany
e-mail: pu.li@tum.de

U. Hugentobler
e-mail: urs.hugentobler@bv.tum.de

J. Sun et al. (eds.), *China Satellite Navigation Conference (CSNC) 2018 Proceedings*, Lecture Notes in Electrical Engineering 498,
https://doi.org/10.1007/978-981-13-0014-1_32

controversial of whether there should be daily continuity constraints remains unsolved and thus two models are distinguished—the "piecewise linear model" (with constraints) and the "offset and rate model" (without constraints). Many attempts to decide the performance of the two models, Kouba [7] and Ray [11–13] interpreted from the frequency domain of pole parameters themselves, while Gross et al. [3, 4] and Gross [5, 6] interpreted from that of the PM excitation. Their conclusions diverge.

In this article, the behaviour of polar motion is studied and the simulation of PM data is described in Sect. 2. The currently used two simple linear models, one simple linear model with (almost) doubled number of parameters, and the new LSCS model is introduced in Sect. 3. Afterwards, these models mentioned above are realised in Sect. 4, their residuals compared, followed by a hypothesis testing for the significance of higher order parameters. Finally, in Sect. 5 conclusions and further work are depicted.

2 Data Simulation

The simulation of data is mainly based on the estimations of PM in different ACs over the years. According to Ray [11], the power spectrum of the estimated x-pole and y-pole follows nearly a single power-law behavior in high frequencies (higher than 0.1 cpd) with a negative spectral index around −4. Further studies of the power spectrum showed that the index of x-pole has a slight larger absolute value than y-pole. For lower frequencies, periodic signal (the Chandler wobble) is dominant. So, the simulation is generated as the sum of a power law signal and a periodic signal.

The power law signal part of the simulated data is generated base on a discrete generation method [8]. The power of the noise in the x-pole is set to be −4.5 and in the y-pole −4.1 [11]; the Allan Variance at 1 s where the data are tabulated at 1 s of both poles are set to be 1e-8 (in order not to disturb the PM behavior in the time domain too much). The Chandler wobble part is generated as sinusoidal signals with yearly and 14-monthly periods; the magnitude of both periods are set to be 0.1 mas. During the simulation, the time resolution is set to be hourly.

3 Models

Linear model in this article means linear regression model with the form

$$y = X\beta + \varepsilon \tag{1}$$

where each symbol stands for a matrix, with β ($p{\cdot}1$ with p the number of parameters) the to be solved parameters, X ($m{\cdot}p$ with m the number of observations)

including the independent variables, y $(m{\cdot}1)$ the dependent variables, and ε $(m{\cdot}1)$ a random error component [9]. Basic assumptions include that the errors have zero mean, constant unknown variance, and are uncorrelated.

Simple linear models applied in the experiments are the offset and rate model, and the piecewise linear model. Polynomial regression models include the interpolating cubic spline model, and the least square cubic spline model. In this section, theories of the currently used models as well as the altered parameterization are presented, followed by the cubic splines.

3.1 Current Models

In current pole representation, a simple linear regression model is used, thus the independent variables have a maximum order of 1, and only two parameters—one intercept and one slope.

3.1.1 Offset and Rate Model

The offset and rate model is a simple linear regression model, which for each day has the form

$$y_i = \beta_{0i} + \beta_i x + \varepsilon_i \tag{2}$$

In the upper formula, β_{0i} is the intercept, β_i is the slope, and ε is a random error. There is no dependency between day to day results. If we define the day boundaries as $x_i (i = 1, 2, \ldots, n)$ for n days, then $x \in [x_i, x_{i+1}]$ in each day i.

As common to all, least-squares is applied to estimate unknown parameters and afterwards a parameter transformation [1] is applied to the intercept and slope of each day to get the offset and rate at 12UTC of each day.

3.1.2 Piecewise Linear Model

The piecewise linear model is also a simple linear regression model, which for each day has the form (2). However, different from the offset and rate model, there is dependency between day to day results. This dependency comes from the assumption that the estimates overall should be continuous (same value at day boundaries) and the form then becomes

$$y_i = A\beta_i + B\beta_{i+1} + \varepsilon_i \tag{3}$$

with

$$A = \frac{x_{i+1} - x}{x_{i+1} - x_i}, \quad B = \frac{x - x_i}{x_{i+1} - x_i} \tag{4}$$

where $x_i (i = 2, \ldots, n-1)$ has the same meaning as in the offset and rate model. Thus, the unknown parameters $\beta_i' (i = 1, 2, \ldots, n+1)$ in n days become the value at day boundaries and with our assumption (same value at day boundaries), the unknowns reduced from $2n$ to $n + 1$.

There is another way to achieve the assumption for day boundaries—instead of changing the original model itself, constraints are set up as "the difference of two boundary values shall be zero". These pseudo-observations are added in the least-squares normal equation level with high weights. The number of unknown parameters then remains the same, though the slopes (except the last one) are no longer free-variables, thus again only $n + 1$ parameters are freely estimated.

Since the second way is more convenient to realise, it is used in the orbit determination software for certain ACs. Same as the offset and rate model, the estimated intercepts and slopes are transformed to offsets and rates at 12UTC of each day.

Alternatives of the models can also be defined, for example, to leave the number of parameters like the offset and rate model, a piecewise linear model with half-day estimation period (thus with $2n + 1$ parameters) is also realised in the experiment part.

3.2 New Models

Currently used single regression model can only describe relationship of a single independent variable x and a dependent variable y that is a straight line. However, by observing the estimates of PM and its power spectrum, both x-pole and y-pole showed obvious curvature behavior. As polynomials are widely used in situations where the response is curvilinear [9], attempts of introducing the polynomial regression model shall be conducted.

Polynomial model with order k (with one independent variables) can be written in the following from

$$y = \beta_0 + \beta_1 x + \beta_2 x^2 + \cdots + \beta_k x^k + \varepsilon \tag{5}$$

Splines are piecewise polynomials with a certain order k. Usually we call the joint points of the pieces "knots". Commonly, the function values and the first $k - 1$ derivatives shall agree at the knots, which indicates the spline is a continuous function with $k - 1$ continuous derivatives. Since the cubic spline (with $k = 3$) is normally adequate for most practical cases [9], it is chosen.

According to Press et al. [10], a cubic polynomial can be described as

$$y_i = A\beta_i + B\beta_{i+1} + C\beta_i'' + D\beta_{i+1}'' \tag{6}$$

where

$$C = \frac{1}{6}(A^3 - A)(x_{i+1} - x_i)^2, \quad D = \frac{1}{6}(B^3 - B)(x_{i+1} - x_i)^2 \tag{7}$$

and A, B the same as (4). The unknown parameters $\beta_i (i = 1, 2, \ldots, n+1)$ and its second derivatives $\beta_i'' (i = 1, 2, \ldots, n+1)$ are now unknown parameters.

By directly calculating the 1st and 2nd derivative of Eq. (6), we get

$$\frac{dy}{dx} = \frac{y_{i+1} - y_i}{x_{i+1} - x_i} - \frac{3A^2 - 1}{6}(x_{i+1} - x_i)y_i'' + \frac{3B^2 - 1}{6}(x_{i+1} - x_i)y_{i+1}'' \tag{8}$$

and

$$\frac{d^2y}{dx^2} = Ay_i'' + By_{i+1}'' \tag{9}$$

Then with the continuity restrictions at knots for the 1st derivatives, we may write

$$\frac{x_i - x_{i-1}}{6}y_{i-1}'' + \frac{x_{i+1} - x_{i-1}}{3}y_i'' + \frac{x_{i+1} - x_i}{6}y_{i+1}'' = \frac{y_{i+1} - y_i}{x_{i+1} - x_i} - \frac{y_i - y_{i-1}}{x_i - x_{i-1}} \tag{10}$$

3.2.1 Interpolating Cubic Spline

For the interpolating cubic spline, observations at knots (y_i with $i = 1, 2, \ldots n$) are used, according to (10), the $n - 2$ linear equations have n unknowns (y_i'' with $i = 1, 2, \ldots n$). So, two boundary conditions need to be specified.

One way (the natural cubic spline) is to set the second derivatives of both of boundaries equal to zero. The other way is to calculate the second derivative of both of boundaries from (8) to make the first derivative of the interpolating function have a specific value [10].

3.2.2 Least-Squares Cubic Spline

To establish a least-squares fit of the cubic splines, we rewrite (10) as

$$\begin{aligned} 0 = {} & \frac{x_i - x_{i-1}}{6}y_{i-1}'' + \frac{x_{i+1} - x_{i-1}}{3}y_i'' + \frac{x_{i+1} - x_i}{6}y_{i+1}'' \\ & - \frac{1}{x_i - x_{i-1}}y_{i-1} + \left(\frac{1}{x_{i+1} - x_i} + \frac{1}{x_i - x_{i-1}}\right)y_i - \frac{1}{x_i - x_{i-1}}y_{i+1} \end{aligned} \tag{11}$$

The Eqs. (6) and (11) are both linear w.r.t the parameters and can be formally written as

$$\begin{aligned} y &= f(x, \beta_k) = X\beta \quad k = 1, 2, \ldots, n+1 \\ 0 &= g_i(\beta_k) = H\beta \quad i = 1, 2, \ldots, n-1 \end{aligned}$$

with one Lagrange multipliers λ_i for each of the $n - 1$ conditions, the function

$$F = (f - y)^T P(f - y) + 2\lambda^T g \tag{12}$$

is minimised. Partial derivatives of (12) w.r.t β and λ to maintain the minimal condition gives the normal equation (NEQ)

$$\begin{pmatrix} X^T PX & B^T \\ B & 0 \end{pmatrix} \begin{pmatrix} \beta \\ \lambda \end{pmatrix} = \begin{pmatrix} X^T Py \\ 0 \end{pmatrix}$$

Solving the NEQ gives the parameters and estimates of LSCS.

In the experiment part, both the interpolating cubic spline and LSCS are implemented. For comparison, the embedded Matlab function for LSCS with adjustable knot positions is also included.

4 Experiments

In this part, simulated data generated as described in Sect. 2 are treated as pseudo-observations, and least-squares fit of the offset and rate model, piecewise linear model, and LSCS model are carried out. After the adjustment, residuals of each model are analyzed and compared. To further determine the performance of these models, hypothesis testing based on the simulated data are implemented.

Figure 1 is a 3D-plot of the simulated data, where the x-axis is the amplitude of the x-pole in arcseconds, the y-axis is the amplitude of the y-pole in arcseconds, and the z-axis is the timespan in days.

The simulated data shows a smoother behavior than that according to Folgueira and Souchay [2] and the EOP 14 C04 (IAU 2000) combined solution, this could cause by a missing of short term periodic signals (with frequency between 1 and 365 cycles per year). Overall, the simulated data agree well with the two in the time domain and thus is considered usable.

The realized model types are the daily offset and rate model (Daily O&R), the daily piecewise linear model (Daily PL), the 12-hourly piecewise linear model (12 h PL), the interpolating cubic splines (Interp CS), the LSCS model, and the Matlab embedded LSCS model (Matlab LSCS). For each model, the corresponding number of parameters (NoP) in n days are shown in Table 1.

Residuals of each fit, and the mean and standard deviation (STD) of the residuals are displayed in the Fig. 2 and Table 2 respectively.

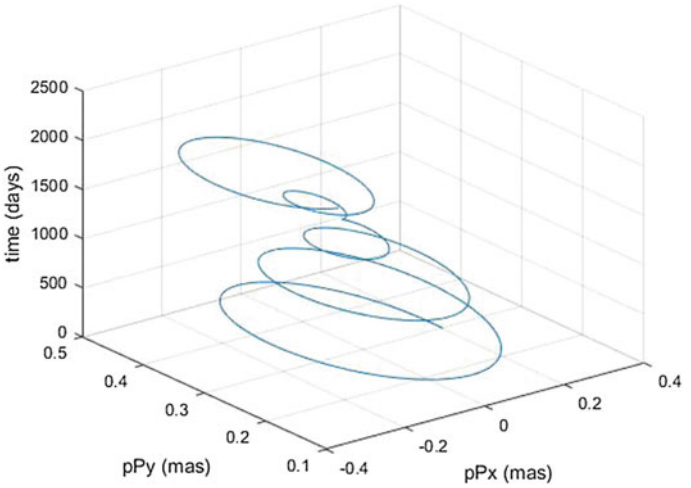

Fig. 1 3D-plot of the simulated data

Table 1 Model types and corresponding number of parameters in *n* days

Model type	Daily O&R	Daily PL	12 h PL	Interp CS	LSCS	Matlab LSCS
NoP	2n	n + 1	2n + 1	n + 1	n + 3	n + 3

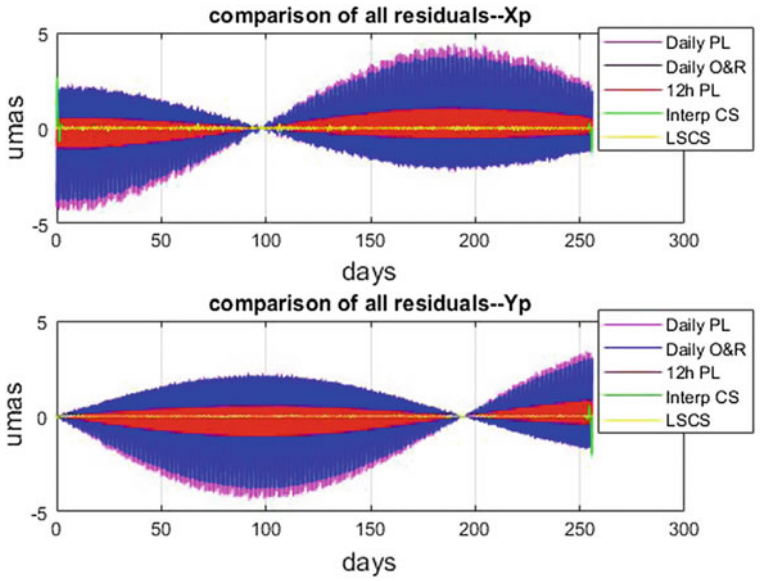

Fig. 2 Residuals of each fit

Table 2 Mean and STD of the residuals (micro arcsecond)

model type		Daily O&R	Daily PL	12 h PL	Interp CS	LSCS	Matlab LSCS
Mean	X	0	0	0	0.016	0	0
	Y	0	0	0	−0.037	0	0
STD	X	1.4034	1.4209	0.3643	0.1463	0.0488	0.0462
	Y	1.2581	1.2732	0.3269	0.0997	0.0236	0.0232

From the point of view of the residuals, the Daily O&R model has a similar performance with the Daily PL model. For the 12 h PL model where a similar number of parameters ($2n + 1$) is used as the Daily O&R model, variance of residuals reduced by more than a factor of three for both x-pole and y-pole. The residuals of all these three models show a periodic pattern. The residuals of the LSCS model show a more stable behavior and the variance of residuals reduced more than a factor of 20 for x-pole component and 50 for y-pole component. The embedded Matlab LSCS show similar behavior as the LSCS algorithm.

To further prove the significance of linear polynomial regression, model adequacy tests are conducted [9] with the simulated data. The first test is done by residual plots—a zoom-in of both Fig. 2 and the plot of residuals against fitted values are shown in Fig. 3.

Obvious nonlinear behavior can be seen in both residual plots from the three simple linear models. As expressed before, the nonlinearity could indicate that higher order independent variables e.g. quadratic or cubic terms are necessary. In this case, hypotheses testing (partial F test) based on the subsets of coefficients of the cubic polynomial regression is shown below.

The hypothesis testing can be described mathematically as

$$H_0 : \beta_2 = 0, \quad H_1 : \beta_2 \neq 0 \tag{13}$$

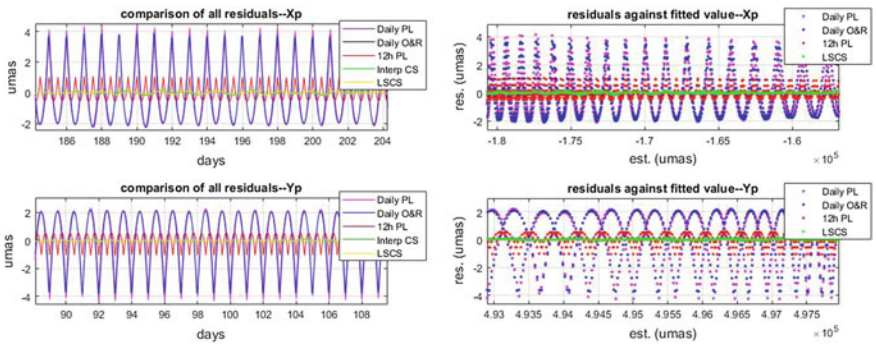

Fig. 3 Zoom-in of two residuals plots

As described before, the linear regression model can be written as (1) with β the parameters (p quantities). We want to determine the significance of the subset of higher order parameters β_2 (r quantities), so the model can be rewritten as

$$y = X_1\beta_1 + X_2\beta_2 + \varepsilon \tag{14}$$

with $\beta = (\beta_1, \beta_2)^T$, β_1 the linear terms ($p - r$), and β_2 the higher order terms (r). The model (14) is called the full model and its *SSE* (the sum of squares of estimations) is defined as

$$SSE(\beta) = (\hat{y} - \bar{y})'(\hat{y} - \bar{y}) \tag{15}$$

with $\hat{y}$ the fitted values and $\bar{y}$ the average of observations. The *SSR* (the sum of squares of residuals) of the full model is defined as

$$SSR(\beta) = (y - \hat{y})'(y - \hat{y}) \tag{16}$$

with the same notation for $\hat{y}$ and $\bar{y}$ as in (15).

We can further define the *MSR* (mean squares of residuals) as

$$MSR(\beta) = \frac{SSR(\beta)}{m - p} \tag{17}$$

with m the number of observations and p the number of parameters in the full model.

The contribution of the terms in β_2 to the estimates is find out by fitting the model assuming that the null hypothesis $H_0 : \beta_2 = 0$ is true. The reduced model is

$$y = X_1\beta_1 + \varepsilon \tag{18}$$

Corresponding sum of squares of the estimation of the reduced model $SSE(\beta_1)$ is defined like $SSE(\beta)$. So that the sum of squares of estimations due to β_2 given that β_1 is already in the model is

$$SSE(\beta_2|\beta_1) = SSE(\beta) - SSE(\beta_1) \tag{19}$$

And the F test can be written as

$$F_0 = \frac{SSE(\beta_2|\beta_1)/r}{MSR} \tag{20}$$

The null hypothesis is rejected if $F_0 > F_{p-1,m-p,\lambda}$, with p and m the same meaning as in (17) and λ the right-tail probabilities. And the reject of null hypothesis implies that the subset of parameters β_2 is significant. For more details, please refer to Montgomery et al. [9]. The result of F test with simulated data of 256 days for both x-pole and y-pole quadratic and cubic terms are shown in the Table 3.

Table 3 Relative terms of the hypothesis testing

	$SSE(\beta_2\|\beta_1)$	$MSR(\beta)$	F_0
X	4.4126e + 09	7.3279	3.0108e + 08
Y	5.3883e + 10	1.7075	1.5778e + 10

With such large F_0 values, $F_0 > F_{513,5631,\lambda}$ is established for any common value of λ, and the hypothesis H_0 is rejected for both x-pole and y-pole, so that we can conclude that the subset of higher order parameters is significant.

5 Conclusions and Further Work

In this article, polar motion data is simulated with hourly resolution, by a combination of low-frequency periodic terms and power-law terms. The simulated data coincide well with real data and is thus used as the pseudo-observations to study the performance of each linear model. Linear models as three simple linear models and two polynomial models with cubic order are realized in the experiments and their performance are compared. By simply looking at the residuals, the LSCS model has the best fit with less than 1/20 of the residuals of the most commonly used offset and rate model. Then the significance of the introduced quadratic and cubic terms are calculated using the hypothesis test (F test), which shows that it would be necessary to add the higher polynomial terms in the estimations.

In further studies, firstly, data source other than just the frequency domain of PM of the IGS ACs may be studied to complete the noise analysis of the simulated data, and thus the conclusions are more credible. Real data like the VLBI measured subdaily PM time series could also be useful. Secondly, effects of changing the PM parameterizations to the orbit parameters and to the reference frame shall be considered. If the influence is significant, the realization of LSCS model in GNSS software packages shall be conducted.

References

1. Brockmann E (1997) Combination of solutions for geodetic and geodynamic applications of the global positioning systems (GPS). Goed-Geophys Arb Schweiz 55
2. Folgueira M, Souchay J (2005) Free polar motion of a triaxial and elastic body in hamiltonian formalism: application to the earth and mars. A&A 432(3):1101–1113
3. Gross R, Hamdan K, Boggs D (1996) Evidence for excitation of polar motion by fortnightly ocean tides. Geophys Res Lett 23(14):1809–1812
4. Gross R, Chao B, Desai S (1997) Effect of long-period ocean tides on the earth's polar motion. Prog Oceanogr 40:385–397
5. Gross R (2009) Validating earth orientation series with models of atmospheric & oceanic angular momenta. American geophysical union meeting, 14–18 Dec. California, San Francisco

6. Gross R (2010) External comparison of EOP results. In IGS 2010 workshop, 28 June–1 July, Newcastle upon Tyne, England
7. Kouba J (2003) Testing of the IERS2000 sub-daily earth rotation parameter model. Stud Geophys Geod 47(4):725–739
8. Kasdin N, Walter T (1992) Discrete simulation of power law noise (for oscillator stability evaluation). Frequency Control Symposium, 27–29 May. Hershey, PA, USA
9. Montgomery D, Peck E, Vining G (2012) Introduction to linear regression analysis. Wiley, USA
10. Press W, Teukolsky S, Vetterling W, Flannery B (1986) Numerical recipes. Cambridge University, New York
11. Ray J (2008) Analysis effects in IGS polar motion estimates. Unpublished. Available via IGS ACC. http://acc.igs.org/erp-index.html. Accessed 04 Jan 2018
12. Ray J (2009a) Future improvements in determinations of earth orientation parameters. In IAG 2009 scientific assembly, 2 Sep, Buenos Aires
13. Ray J (2009b) IGS reprocessed GPS satellite orbits. Unpublished. Available via IGS ACC. http://acc.igs.org/erp-itrf2008.html. Accessed 04 Jan 2018

Real-Time Monitoring of Inter-device Distance Based on Same-Beam Interferometry

Yunpeng Gao, Tianpeng Ren, Lan Du, Zejun Liu and Sirui Chen

Abstract In this paper, we propose a real-time monitoring of the separation between devices by using very long baseline interferometry (VLBI) technology, which is already mature in the mission of the lunar flight. In particular, during the separation process, using the same beam interference measurement (SBI) based on two downstream signals between the detectors, and the relative delay resolution to improve the relative distance resolution. Based on the principle of monitoring the relative distance between devices by using the same beam interference measurement, the real-time monitoring algorithm is given and the effects of orbit error, observation delay error and satellite attitude error on the monitoring are analyzed. And select a reasonable number of samples and confidence intervals to determine the separation process. Simulation analysis shows that considering the influence of 10 km satellite orbit error, 10 ps observation delay error and 0.5° satellite attitude error, this method can realize the real-time monitoring of the separation between Chang'e 5's equipment.

Keywords Same beam interference measurement (SBI) · Chang'e 5
Relative distance

1 Introduction

China's lunar exploration project is divided into three stages: "winding, landing and returning". Chang'e 1 and Chang'e 2 detectors had accomplished a series of important scientific research achievements. They completed the missions of the lunar flight and the landing area imaging. Chang'e 3 is a lunar rover, with the lander and the "Yutu" rover inside, which successfully achieved a soft landing on

Y. Gao (✉) · L. Du · Z. Liu · S. Chen
Institute of Geospatial Information, Information Engineering University, Zhengzhou, China
e-mail: 465335929@qq.com

T. Ren
Beijing Aerospace Control Center, Beijing, China

J. Sun et al. (eds.), *China Satellite Navigation Conference (CSNC) 2018 Proceedings*, Lecture Notes in Electrical Engineering 498,
https://doi.org/10.1007/978-981-13-0014-1_33

December 14, 2013, and carried out the lunar reconnaissance mission. The "Chang'e 5" probe is expected to be launched in November 2017 (postponed) and plans to complete the lunar sampling and returning mission in the third phase of China's lunar exploration project.

The Chang'e 5's composition includes the orbiter, the returner, the lander and the riser. During the round-moon flight phase, the real-time monitoring of the separation between the orbiter-returner assembly and the lander-riser assembly is the key detection section of the Chang'e 5 flight control. In the separation phase, many facilities have yet to start up and the information not timely sent to the ground; there is no better method to measure relative distance between the orbital-reducer assembly and the lander-riser assembly in real time.

Very long baseline interferometry (VLBI) can realize the real-time continuous observations [1, 2]. When two signal source in the perspective of sense is very close, they can be observed within the same beam by the antenna on the ground. Using two deep space network source for observation at the same time, it can generate differential interferometry, called the same beam interference measurement (SBI). By using relative time delay to improve the relative distance decoding accuracy in the process of separation, we can realize real-time accurate monitoring of the separation distance between equipment.

2 Real-Time Monitoring Principle

2.1 SBI Principle

VLBI uses two ground stations, among which there are thousands of kilometers, to receive the arrival of the delay of the same deep signals. By using the distance difference between the two stations and signal source target, we can measure signal source of angular position information accurately.

If the angular distance is close to two sources, the signal can be observed by ground station within the same beam of the antenna; this can generate differential interferometry (referred to the same beam interference measurement).

The SBI measuring principle is shown in Fig. 1 [3–5]. Station 1 working as the time reference station, station 2 standing from a long distance away, the signal to station 1 time is t_0; S_R signal launch time is t_1; S_C signal emission time is t_2; station 2 receives S_R and S_C signal at the moment of t_3 and t_4. The SBI observation equation is derived as following,

$$\begin{aligned} c\triangle\tau_{t_0} &= c[\tau_R - \tau_C] \\ &= [|S_R(t_1) - T_K(t_0)| - |S_R(t_1) - T_J(t_3)|] \\ &\quad - [|S_C(t_2) - T_K(t_0)| - |S_C(t_2) - T_J(t_4)|] \end{aligned} \tag{1}$$

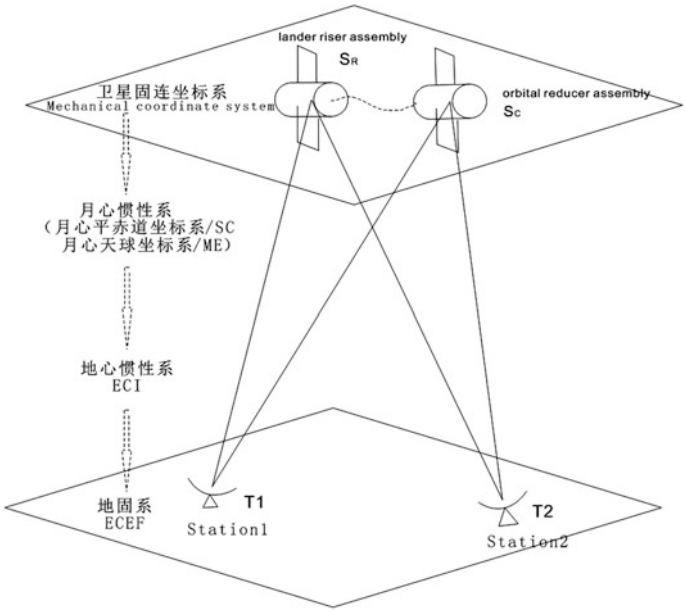

Fig. 1 SBI principle

where τ_C and τ_R are respectively the time delay corresponding to the antenna phase center of the orbital-reducer assembly and the lander-riser assembly. $T_K = [\mathrm{x}_k, \mathrm{y}_k, \mathrm{z}_k]^T$, $T_J = [\mathrm{x}_j, \mathrm{y}_j, \mathrm{z}_j]^T$ are the corresponding coordinates in the ECEF of antenna phase centers of Kashi Station, Jiamusi Station $S_C = [\mathrm{x}_c, \mathrm{y}_c, \mathrm{z}_c]^T$, $S_R = [\mathrm{x}_R, \mathrm{y}_R, \mathrm{z}_R]^T$ are the corresponding coordinates in the solid-state coordinate system of antenna phase centers of the orbital-reducer assembly and the lander-riser assembly.

The solid-state coordinate system (mechanical coordinate system) of the Chang'e 5 detector is defined as following (Fig. 2):

(1) Origin: The geometric center of the satellite and launch vehicle docking surface.
(2) X-axis: Along the longitudinal axis of the satellite, pointing in the direction of the ascender (in the direction of the satellite's movement);
(3) Z-axis: Perpendicular to the X-axis, perpendicular to the sun flaps, pointing to the moon direction;
(4) Y-axis: Point to Z, X-axis right-handed rectangular coordinate system.

The coordinate transformation of the lunar inertial system to the geocentric inertial system consists of two steps:

(1) The lunar equatorial coordinate reference system to the lunar celestial sphere coordinate reference system

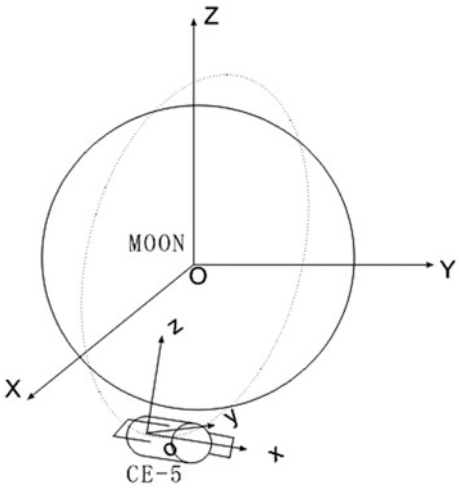

Fig. 2 CE-5 fixed coordinate system

The IAU defines the lunar horizontal axis coordinate system through its defined orientation model of the planet and its satellites, as shown in Fig. 3. We use the approximate transformation between the flat-axis coordinate system and the lunar celestial coordinate system provided by IAU2009:

$$\vec{r}_{ME} = R_z(W) \cdot R_x(90^\circ - \delta_0) \cdot R_z(90^\circ + \alpha_0) \cdot \vec{r}_{SC} \tag{2}$$

where $\vec{r}_{ME}$ and $\vec{r}_{SC}$ respectively represent the lunar position vector in the horizontal coordinate system and in the lunar celestial coordinate system.

(2) Selenocentric celestial coordinate system to the Geocentric inertial system

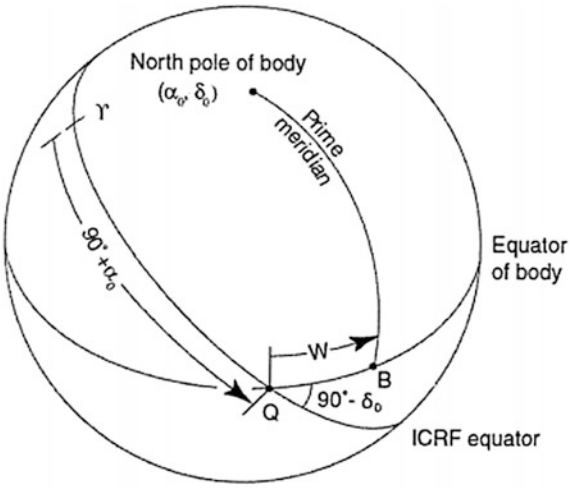

Fig. 3 IAU orientation model

As the selenocentric celestial coordinate system and the J2000 define the same coordinate direction, only the lunar celestial world coordinate system can be used to translate the GCRS to the selencenter.

Specific calculation methods and the derivation of other rotation matrices can be referred to [6, 7], which will not be repeated here.

At this point, we can get the rotating coordinate system of Chang'e 5 satellite rotating to the corresponding rotation matrix $\Phi_{\mathrm{MCI}}^{\mathrm{SF}}$.

2.2 SBI Based Separation Monitoring Method

(1) Measurement equation

In the reference system, finishing the measurement Eq. (3)

$$\begin{cases} c\triangle\tau_{t_0} = l_{t_0}(x_r, y_r, z_r) = |\boldsymbol{\rho}_1 - \boldsymbol{\rho}_2| - |\boldsymbol{\rho}_3 - \boldsymbol{\rho}_4| \\ \boldsymbol{\rho}_{1,2} = \Phi_{\mathrm{ECEF}}^{\mathrm{ECI}} \boldsymbol{r}_{\mathrm{moon_{ECI}}} + \Phi_{\mathrm{ECEF}}^{\mathrm{ECI}} \Phi_{\mathrm{ECI}}^{\mathrm{MCI}} \boldsymbol{r}_{\mathrm{c_{MCI}}} - \boldsymbol{T}_{1,2} \\ \boldsymbol{\rho}_{3,4} = \Phi_{\mathrm{ECEF}}^{\mathrm{ECI}} \boldsymbol{r}_{\mathrm{moon_{ECI}}} + \Phi_{\mathrm{ECEF}}^{\mathrm{ECI}} \Phi_{\mathrm{ECI}}^{\mathrm{MCI}} \boldsymbol{r}_{\mathrm{c_{MCI}}} + \Phi_{\mathrm{ECEF}}^{\mathrm{ECI}} \Phi_{\mathrm{ECI}}^{\mathrm{MCI}} \Phi_{\mathrm{MCI}}^{\mathrm{SF}} \boldsymbol{D} - \boldsymbol{T}_{1,2} \end{cases} \tag{3}$$

In this formula, $\boldsymbol{r}_{\mathrm{moon_{ECI}}}$ is the coordinate of the moon in geocentirc inertial system. $\boldsymbol{D}$ is the position vector of the orbital-reducer assembly relative to the lander-riser assembly in ECEF. $\Phi_{\mathrm{ECI}}^{\mathrm{MCI}}$ is the rotation matrix of selenocentric inertial system to geocentric inertial system. $\Phi_{\mathrm{ECEF}}^{\mathrm{ECI}}$ is the rotation matrix of the geocentric inertial system to ECEF. $\boldsymbol{T}_{1,2}$ are Jiamusi, Kashi stations' coordinates in ECEF.

(2) Separation process kinetic model

Within a few minutes of the initial separation of the lander-riser assembly from the orbital-reducer assembly, the linear velocity can be approximated as a constant linear motion in the fixed coordinate system due to the relatively slow separation speed.

Assuming that the direction of separation is the direction of flight velocity, the relative position of the separation body in satellite solidified coordinate system changes as:

$$\Delta\mathbf{D} = \mathrm{v}dt \tag{4}$$

According to the separation of kinematic equations and measurement equations, $\Delta\mathbf{D}$ can be calculated by the epoch. According to the separation distance, we can attain the separation process starting moment and the separation process to reach the safety distance of the moment.

2.3 Error Source Analysis

In this simulation, the main consideration of the error sources included as following [8, 9]:

(1) CE-5 orbit error: In front of the separate operation, generally to determine the satellite orbit, due to the track error of measurement, CE-5 satellite orbit will have certain deviation.
(2) SBI observation error: By the SBI observation system receiving equipment phase fluctuations, the detector frequency drift, and the Earth's rotation error.
(3) Attitude error of satellite: Due to the phase center deviation of satellite antenna and orbit error, the attitude of satellite has about 0.1° error.

Considering the influences of orbital accuracy, observational delay error and satellite attitude error, the result of the calculation has some deviations. The sample data confidence interval is used to process the solution data to obtain a relatively smooth result of the separation process.

3 Simulation Results and Error Analysis

3.1 Simulation Conditions

The Jiamusi-Kashi baseline and Shanghai-Kashi baseline were selected to measure the same-beam interferometry with Chang'e 5 satellite. The orbital elements of Chang'e 5 satellite during the separation phase is set to be 80° orbital inclination, 15 km perigee, 100 km apogee and the rests are 0 [10]. At 9:33, September 21, 2018, UTC, the separation start time was taken as 0.1, 0.2, 0.5 and 1 m/s, respectively. SBI sampling rate of 1 s, the error model includes 10 ps white noise observation [11]. The priori position error of Chang'e 5 is 10 km, and the attitude error is 0.5° (Fig. 4).

Fig. 4 CE-5 subastral point at 9.33, September 21, 2018

3.2 Simulation Results

Taking the Jiamusi-Kashi baseline as an example, the separation speed is 0.2 m/s, and the results are obtained shown in Figs. 5 and 6. We can see that the absolute error of the solution is about 1 m. As the separation distance increases, the absolute error of the solution results tends to increase.

The experimental process was repeated on Jiamusi-Kashi baseline and Shanghai-Kashi baseline. The different separation rates were selected as following: 0.1, 0.2, 0.5 and 1 m/s. The simulation results are shown in Fig. 7.

On these basis, the reasonable confidence intervals are selected as the basis for the separation distance to realize the automatic real-time separation monitoring. Taking 10 consecutive observations as samples, a confidence interval of 98% was constructed to determine whether the Chang'e-5 detector's orbital-reducer assembly was separated from the lander-riser assembly (separation distance increased from 0)

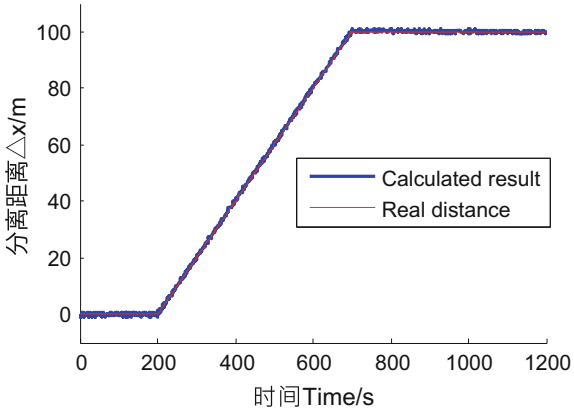

Fig. 5 The calculated results

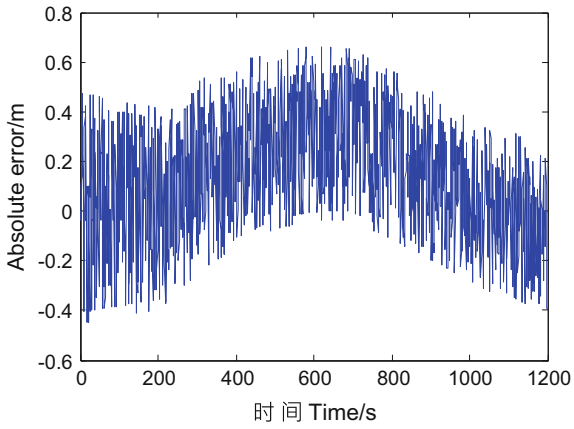

Fig. 6 Absolute error

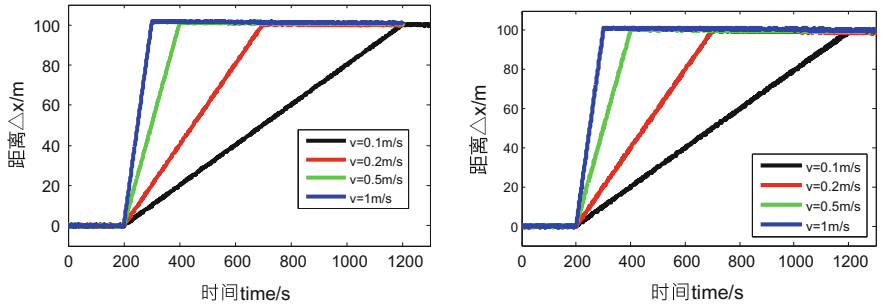

Fig. 7 Separation distance calculation result

Fig. 8 Judgment of separation distance

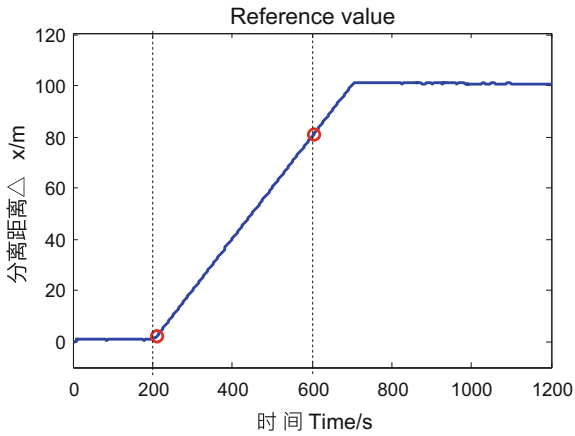

and both reached in the safety distance (taking 80 m as an example), the result obtained is shown in Fig. 1. Under these conditions, the corresponding moments are T = 210 s and T = 606 s respectively, and the true values should be T = 200 s and T = 600 s (Fig. 8).

Assessing the above separation process, we can get the moment of the start and the moment of the reaching of the safe distance. The results shown in Table 1, which can be learned:

(1) The separation monitoring and safety distance monitoring delay are less than 30 s. This method is superior to radar and visual sensor ranging methods in real-time, which realized the basic real-time separation between real-time monitoring.
(2) As the separation speed increases, the results of separation monitoring and safety distance monitoring are closer to the real time. This is because when the speed is faster, the data changes more obviously, so that the relative error is

Table 1 Time delay of separating and reaching safe distance

Base line	Separation speed V(m/s)	Separation time T_0/S	Monitor latency $\Delta T_0/S$	Safe distance moment T_1/S	Monitor latency $\Delta T_1/S$
Hamusi-Kashi	0.1	200	25	1000	14
	0.2	200	10	600	4
	0.5	200	9	360	6
	1	200	6	280	5
Shanghai-Kashi	0.1	200	26	1000	20
	0.2	200	14	600	10
	0.5	200	9	360	7
	1	200	6	280	6

reduced, the judgment time is shortened, and the judgment is more timely and accurate.

(3) The real-time performance of Jiamusi-Kashi baseline monitoring and separation process is better than that of Shanghai-Kashi baseline monitoring. This is due to the different geographical locations of the two baselines and the longer baseline length of the Jiamusi-Kashi, which has a higher angular resolution when performing SBI observations on Chang'e-5.

4 Conclusion

In this paper, for the "Chang'e 5" lunar probe lunar orbit phase, which based on the two downlink signals of the orbiter-returner assembly and the lander-riser assembly, we realized real-time separation monitoring using SBI data. The confidence interval of 10 consecutive observations and 98% confidence level was selected to judge independently.

The simulation results show that, under the influence of 10 km satellite orbit error, 10 ps observation delay error and 0.5° satellite attitude error, this method can achieve accurate and reliable monitoring for Chang'e-5 separation between the monitors, with delay less than 30 s with the separation distance of 80 m.

Acknowledgements This research work was supported by the National Natural Science Foundation of China (Grant No. 41774038), the opening Project of Shanghai Key Laboratory of Space Navigation and Positioning Techniques fund No. KFKT_201707 and State Key Laboratory of Geo-Information Engineering Laboratory fund No. SKLGIE2016-Z-2-4.

References

1. Du L, Zheng Y, Li J (2006) VLBI-augmented orbit determination for geostationary satellites. J Zhengzhou Inst Surveying Mapp
2. Zheng X, Liu Q, Wu Y, He Q (2014) The same beam VLBI technique for relative positioning of bimetallic detectors. J Astronaut 35(9):1030–1035
3. Chen M, Liu QH (2010) Calculation and analysis of same beam VLBI differential phase delay closure of lunar satellite. Prog Astron 28(4):415–423
4. Weiren WU, Liu Q, Huang Y et al (2015) Design and realization of same-beam interferometry measurement of CE-3. J Deep Space Explor
5. Liu QH, Chen M, Xiong WM et al (2010) Relative position determination of a lunar rover using high-accuracy multi-frequency same-beam VLBI. Sci China 53(3):571–578
6. Lei W, Zhang H, Li K (2016) Calculation and comparison of two coordinate transformation models of GCRS and ITRS. J Geomatics Sci Technol 33(3):236–240
7. Lan D, Zhang H, Zhou Q et al (2012) Correlation of coordinate transformation parameters. Geodesy Geodyn 3(1):34–38
8. Kikuchi F, Liu Q, Hanada H et al (2009) Picosecond accuracy VLBI of the two subsatellites of SELENE (KAGUYA) using multifrequency and same beam methods. Radio Sci 44(2):1–7
9. Liu W, Hao J, Li Z (2010) Analysis of satellite position, velocity and accuracy by broadcast ephemeris. J Geodesy Geodyn 30(2):144–147
10. Huang Y, Chang S, Li P et al (2014) Orbit determination of Chang'e-3 and positioning of the lander and the rover. Chin Sci Bull 59(29–30):3858–3867
11. Huang Y, Shan Q, Li P et al (2016) The application of the seam beam VLBI technique for the orbit determination of CE-5 in the rendezvous and docking phase. Sci China (Ser G) 46 (8):92–99

Analysis of BDS Satellite Clock Prediction Contribution to Rapid Orbit Recovery

Qian Chen, Junping Chen, Yize Zhang, Shan Wu and Xiuqiang Gong

Abstract The BDS-2 system is designed as a GEO/IGSO/MEO mixed constellation. Generally, there exists satellite maintaining operation for GEO or IGSO satellite every 7–10 days. During this period the maneuver satellite is out of service. It will be about 5–6 h starting from the beginning of satellite maneuver to the release of the first group of recovery orbit. Strategy of satellite clock assisted precise orbit determination (POD) is normally implement, where the most critical factor that contributes to the availability of maneuver satellites is the length of accumulation of data. However, the last hour of real-time observed pseudo-range data of tracking station could not be included in POD, due to the reason that the satellite clock could not be observed in real-time. In this paper, we propose to use the polynomial fitting method to forecast the satellite clocks and use it in POD. We analyze the accuracy of satellite clocks prediction and its contribution to the rapid orbit recovery. Results show that the satellite unavailability time could be shortened by at least 1 h, which effectively improves satellite availability. And it improves the accuracy of orbit determination and prediction by more than 15 and 70%.

Keywords BDS · Time synchronization · Satellite clock · Precise orbit determination · Rapid orbit recovery · Satellite availability

Q. Chen · J. Chen (✉) · Y. Zhang · X. Gong
Shanghai Astronomical Observatory Chinese Academy of Sciences, Shanghai 200030, China
e-mail: junping@shao.ac.cn

Q. Chen · J. Chen · X. Gong
School of Astronomy and Space Science, University of Chinese Academy of Sciences, Beijing 100049, China

S. Wu
Beijing Satellite Navigation Center, 22 Beiqing Road, Beijing 100094, China

J. Sun et al. (eds.), *China Satellite Navigation Conference (CSNC) 2018 Proceedings*, Lecture Notes in Electrical Engineering 498,
https://doi.org/10.1007/978-981-13-0014-1_34

1 Introduction

The Global Navigation Satellite System (GNSS) provides important spatiotemporal information and plays an increasingly prominent role in social life. Precise Orbit Determination (POD) and prediction are one of the important processes for GNSS PNT (Positioning, Navigation and Timing) service [1, 2]. Among different methods, multi-satellite orbit determination and prediction using data of 3–7 days are widely used [3]. Due to various perturbations on the satellites, orbit maneuver control is required to maintain satellite constellation configuration [4]. During the orbit maneuver periods, the satellite dynamics is normally different from previous arcs. Thus, strategies have to be developed for the fast orbit recovery to support the recovery of satellite availability, which is the key factor in the GNSS applications of life safety, such as aviation etc. [5].

BDS' constellation is composed of GEO/IGSO/MEO satellites. The unique system design makes the satellite maneuver more frequently. Every 7–10 days there will be a GEO or IGSO satellite under orbit control operation, during which the maneuver satellite is unavailable. During the period of maneuver, tracking data has to be re-accumulated for POD, as the orbit dynamics change. In this period, strategy of satellite clock assisted POD is developed [4, 6, 7], where the satellite clocks and station clocks from the technique of Two Way Time Transfer (TWTT) are normally used as known parameters in the POD process. It may take 5–6 h starting from the beginning of orbit control until the first group of rapid recovered orbit is released.

This paper studies the strategy to shorten the satellite maneuver period. As discussed previously, the clocks from TWTT is the key parameters in the fast POD process. However, the TWTT technique is normally in post-processing with latency of around 1–2 h. To make the first group of recovered orbit released earlier, we propose to use a polynomial fitting method to forecast the satellite clocks from TWTT technique. The accuracy of predicted satellite clocks and its contribution in satellite clock assisted POD is discussed.

2 Methods of Rapid Orbit Recovery and Clock Processing

Conventional POD use longer arcs using data of 3–7 days for multi-satellite orbit determination, but the orbit dynamics are changed during the satellite maneuver periods. In order to recover satellite orbit as soon as possible, short arcs are used to improve orbit accuracy and system availability [8].

2.1 Dynamic Model

Satellites suffer from a variety of forces during the rotation around the earth. The dynamic model used in orbit determination is as the following:

$$F = f_{\mathrm{TB}} + f_{\mathrm{NB}} + f_{\mathrm{NS}} + f_{\mathrm{TD}} + f_{\mathrm{RL}} + f_{\mathrm{SR}} + \mathrm{f}_{AL} \tag{1}$$

where $\mathrm{f_{TB}}$ is the gravity of the earth on the satellite, $\mathrm{f_{NB}}$ is the N-body perturbation, $\mathrm{f_{NS}}$ is the non-spherical gravitation perturbation of the earth, $\mathrm{f_{TD}}$ is the solid tide and ocean tide perturbation, $\mathrm{f_{RL}}$ is the relativistic perturbation, $\mathrm{f_{SR}}$ is the solar pressure, and $\mathrm{f_{AL}}$ is the Earth's albedo radiation Pressure perturbation (Table 1).

2.2 Observation Model

Rapid orbit recovery use pseudo-range observations of a tracking network. The pseudo-range observation equation is as the following [9, 10]:

$$\begin{aligned}\rho_{\mathrm{j}}^{i} = &\sqrt{(x^i - x_j)^2 + (y^i - y_j)^2 + (y^i - y_j)^2} + c \cdot dt_j \\ &- c \cdot dt^i + \delta_{trop} + \delta_{ion} + \delta_{\mathrm{rel}} + \varepsilon\end{aligned} \tag{2}$$

where $(\mathrm{x^i}, \mathrm{y^i}, \mathrm{z^i})$ is the satellite position, $(\mathrm{x_j}, \mathrm{y_j}, \mathrm{z_j})$ is the station location, $\mathrm{dt_j}$ is the station clock error, $\mathrm{dt_i}$ is the satellite clock error, δ_{trop} is the tropospheric correction, δ_{ion} is Ionospheric correction, δ_{rel} stands for relativistic correction, and ε is the multipath effects and other kinds of noise.

The location of the station are normally accurately determined previously and the tropospheric and ionospheric errors can be corrected by the model. Technique of carrier phase smoothing pseudo-range is applied here to obtain higher precision pseudo-range observation.

2.3 Satellite Clock Error Prediction Model

The clock accuracy in the satellite clock assisted POD should be better than 0.5 ns [11].

As satellite clock from TWTT is not broadcasted in real-time, only the clock parameters of previous hours could be used in rapid orbit recovery. To realize

Table 1 Model description

	Model
The gravity of the earth's gravity center	10 × 10 JGM-3 model
N body perturbation	Sun and moon gravity perturbation
Planetary calendar	JPL DE403
Nutation model	IAU80 model
Solid tide	IERS96 model
Solar pressure and earth's albedo radiation pressure	Box-wing model

real-time processes, the quadratic polynomial model could be used to fit and predict the satellite clocks, the model can be modeled as the following:

$$T_i = a_0 + a_1(t_i - t_0) + a_2(t_i - t_0)^2 \tag{3}$$

where t_0 is the reference time, t_i is the user epoch, (a_0, a_1, a_2) are the constant, linear and acceleration terms of satellite clocks, which can estimated from least square estimation [12–14].

Assuming that the clock error with respect to time t_i is x_i and the observation error is v_i, we can establish the error equation:

$$x_i + v_i = a_0 + a_1(t_i - t_0) + a_2(t_i - t_0)^2$$

Setting $\hat{a} = [\hat{a}_0, \hat{a}_1, \hat{a}_2]^T$ as (a_0, a_1, a_2) estimates, the coefficient matrix is as the following:

$$A = \begin{bmatrix} 1 & (t_1 - t_0) & (t_1 - t_0)^2 \\ 1 & (t_2 - t_0) & (t_2 - t_0)^2 \\ \cdots & \cdots & \cdots \\ 1 & (t_i - t_0) & (t_i - t_0)^2 \end{bmatrix}, \quad L = \begin{bmatrix} x_1 \\ x_2 \\ \cdots \\ x_i \end{bmatrix}$$

And it could be estimated by the equation: $\hat{a} = (A^T A)^{-1} A^T L$.

3 Analysis of Rapid Orbit Recovery

3.1 Orbit Determination Strategy

Satellite clock assisted POD strategy is applied for rapid orbit recovery. The station clocks can be retrieved from the multi-satellite POD, while the satellite clocks estimation include two parts: the satellite clocks can be corrected directly for the arc using the TWTT technique, and predicted when there is no TWTT satellite clocks in the last hour. The pseudo-range data can be smoothed using carrier phase data to reduce pseudo-range noise and multipath effect in data preprocessing.

Figure 1 shows the different data accumulation processes during rapid orbit recovery, where t_0 is the epoch when the orbit control is terminated and the start of data re-accumulation, t is the current epoch. From the figure we see that the accumulation of satellite clock data are late than the observation, due to the latency of TWTT process.

We define two types of processing methods of POD for comparison and analysis.

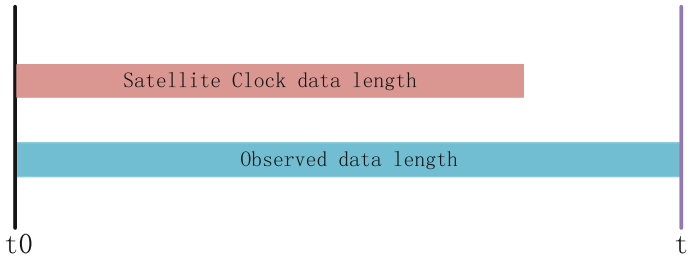

Fig. 1 Rapid orbit recovery of data accumulation diagram

Strategy 1: Only use the observed TWTT clocks and re-accumulated observations in POD.

Strategy 2: TWTT observed and predicted satellite clocks are both used, which can make full use of the observed data.

3.2 Introduction of Experiment Data

Data of 7 tracking stations evenly distributed in China are used, which is shown in Fig. 2. Three periods where GEO satellites experienced maneuver in October 2017 are selected for the experiment. The maneuvering information is shown in Table 2.

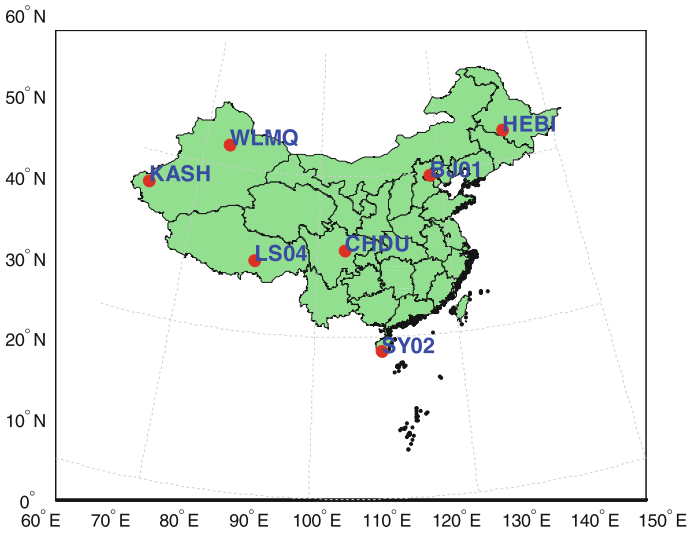

Fig. 2 Selected stations

Table 2 Satellite maneuvering information

SatID	Start time	End time	Available time
C01	2017-10-31 8:55	2017-10-31 10:15	4 h after maneuver
C02	2017-10-19 8:59	2017-10-19 11:15	4 h after maneuver
C03	2017-10-23 8:46	2017-10-23 11:15	4 h after maneuver

3.3 Analysis of Experiment Results

Firstly, the satellite clocks fitting and prediction accuracy is analyzed. The fitting accuracy of 1-h interval is within 0.3 ns and clock prediction errors is below 1.5 ns, which can be concluded from Table 3.

Using data spanning from 3 to 8 h, POD are carried out 6 using strategy 1 and strategy 2. With the observation data from The POD residuals, UERE and UERE after 1 h prediction are assessed, as shown in Table 4 and Figs. 3 and 4, respectively.

Table 3 Accuracy of fitting and predicted satellite clock for 1 h (unit: ns)

SatID	Accuracy	Predicted 1 h
C01	0.11	0.81
C02	0.09	0.80
C03	0.06	0.78
C04	0.11	1.14
C05	0.07	0.93
C06	0.24	1.23
C07	0.23	1.30
C08	0.17	1.33
C09	0.21	1.41
C10	0.26	1.44

Table 4 Residuals of orbit determination (unit: m)

SatID (h)	C01		C02		C03	
	Strategy 1	Strategy 2	Strategy 1	Strategy 2	Strategy 1	Strategy 2
3	1.120	1.070	0.631	0.688	0.524	0.516
4	1.070	0.961	0.682	0.679	0.513	0.521
5	0.962	0.608	0.677	0.678	0.522	0.509
6	0.610	0.641	0.676	0.642	0.509	0.495
7	0.611	0.582	0.641	0.650	0.496	0.490
8	0.585	0.621	0.652	0.679	0.492	0.512

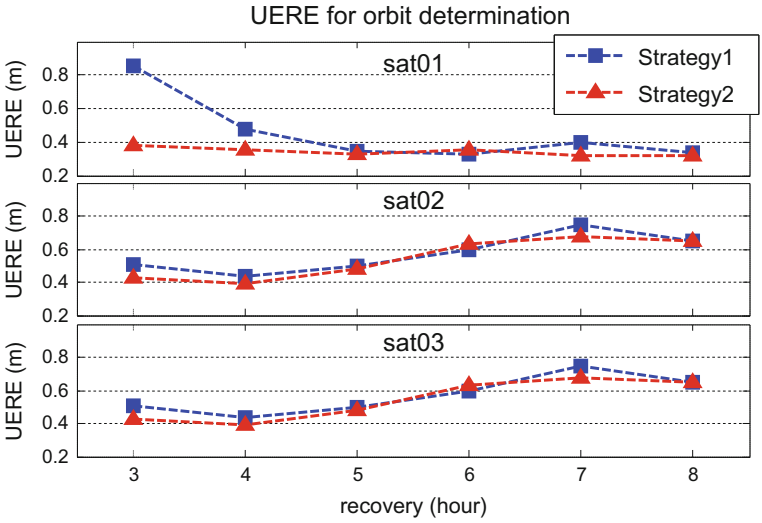

Fig. 3 UERE of each satellite during rapid orbit recovery

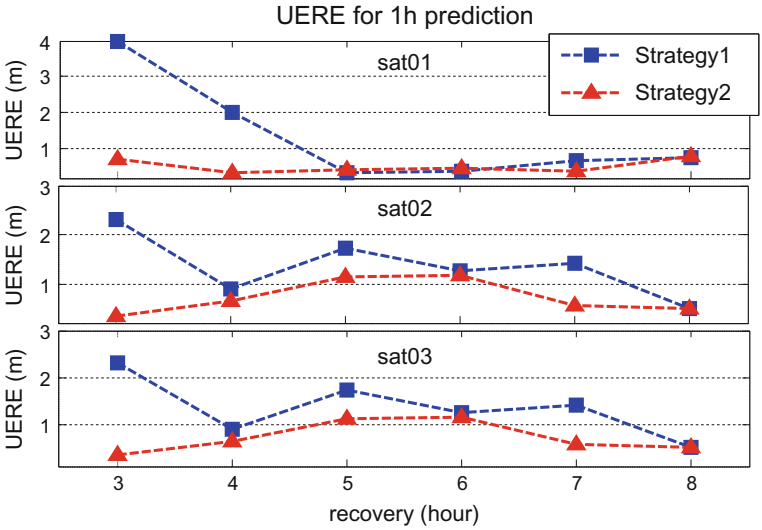

Fig. 4 UERE after 1 h prediction of each satellite during rapid orbit recovery

From the result we can see that the POD residuals of the two strategies are about 0.6 m, the differences is at millimeter level.

As for UERE results, the prediction accuracy of 3 h for strategy 1 is 1.9–3.9 m, while it is less than 1 m for strategy 2. This may due to the inclusion of more observation data, where satellite clocks are predicted. According to the Fig. 4, the

Table 5 Statistics of orbit determination (unit: m)

SatID	Time (h)	Orbit determination UERE			Forecast for 1 h UERE		
		Strategy 1	Strategy 2	Improvement (%)	Strategy 1	Strategy 2	Improvement (%)
C01	3	0.856	0.378	55.848	3.982	0.717	81.996
	4	0.476	0.354	25.672	1.997	0.341	82.919
	5	0.341	0.326	4.368	0.367	0.435	−18.484
	6	0.331	0.352	−6.377	0.400	0.486	−21.600
	7	0.402	0.323	19.497	0.697	0.376	46.114
	8	0.336	0.320	4.911	0.744	0.819	−10.052
C02	3	0.505	0.423	16.261	2.308	0.338	85.369
	4	0.436	0.394	9.529	0.889	0.632	28.941
	5	0.502	0.483	3.845	1.733	1.130	34.785
	6	0.600	0.628	−4.600	1.251	1.163	7.049
	7	0.750	0.679	9.433	1.415	0.564	60.158
	8	0.647	0.650	−0.526	0.502	0.501	0.179
C03	3	0.801	0.673	15.980	1.929	0.568	70.561
	4	0.670	0.680	−1.462	0.503	0.502	0.219
	5	0.683	0.643	5.801	0.842	0.546	35.139
	6	0.645	0.672	−4.169	0.506	0.476	5.873
	7	0.638	0.638	−0.063	0.494	0.513	−3.742
	8	0.611	0.614	−0.541	0.461	0.463	−0.456
Mean		**0.568**	**0.513**	**8.523**	**1.168**	**0.587**	**26.943**

POD precision and prediction accuracy of the strategy 2 is more stable, especially during the first few hours. The contribution to the orbit prediction for strategy 2 gradually decreases over time as more data are accumulated. The detailed comparison of strategy 1 and strategy 2 is listed in Table 5.

According to the statistics of the experiment results, it can be seen that the satellite clock prediction contributes the most to the first few hours where very few data are available. It improves orbit determination accuracy by more than 15% and over 70% on orbit prediction accuracy.

4 Conclusions

The accuracy of orbit determination during satellite orbit recovery is mainly limited by the amount of observation data. However, with the increase of the observation length, the orbit accuracy is mainly limited by the model accuracy and the quality of observed data. Aiming at reducing the recovery time after satellite's maneuver, we propose a method to use the predicted satellite clocks in POD. By using quadratic polynomials, the accuracy of short-term prediction is better than 0.3 ns. The

contribution of predicted satellite clocks to orbit determination and prediction is particularly significant during the first few hours of rapid orbit recovery. The contribution to orbit determination accuracy is above 15% and the contribution of orbit prediction accuracy is more than 70%. The optimization strategy can shorten the satellite unavailable period by at least one hour during satellite maneuvering, which would benefit the system service.

Acknowledgements This research is supported by the National Natural Science Foundation of China (Grant No. 11673050, 11273046).

References

1. Zhang J, Dong K, Qiu H et al (2008) Analysis of orbit determination of compass—MEO navigation satellite with pseudorange. J Spacecraft IT&C Technol 27(6):60–64
2. Lei H (2011) Research on precise orbit determination of navigation satellites based on transponder randing. National Time Service Center Chinese Academy of Sciences
3. Lou W (2011) Study on fast orbit determination and prediction for navigation satellite. PLA Information Engineering University
4. Guo R, Chen J et al (2017) Rapid orbit determination for BDS satellites constrained with clock offsets and dynamic parameters (in Chinese). Chin J Space Sci 37(4):468–475
5. Department O D U S A (2008) Global positioning system standard positioning service performance standard. GPS Augmentation Syst 35(2):197–216
6. Li X, Guo R, Hu G et al (2015) Research on technique of orbit rapid recovery for GEO satellite of partial subsatellite point. Scientia Sinica Physica, Mechanica & Astronomica (7):79507
7. Guo R, Zhou J, Hu X, Liu L, Tang B, Li X, Wu S (2015) Precise orbit determination and rapid orbit recovery supported by time synchronization. Adv Space Res 55(12):2889–2898
8. Du L (2006) A study on the precise orbit determination of geo stationary satellites. PLA Information Engineering University
9. Liu D (1996) The principle and data processing of the global positioning system (GPS). Tongji University Press
10. Li J (1995) Artificial satellite orbit determination. Chinese People's Liberation Army Publishing House
11. Li X (2012) Research on high precision orbit determination and prediction technology for regional navigation satellite. PLA Information Engineering University
12. Liu X, Wu X et al (2010) Study on atomic prediction of time based on interpolation model with tchebytchev polynomiais. J Geodesy Geodyn 30(1):77–82
13. Wang Y, Lu Z, Wang N et al (2016) Prediction of navigation satellite clock bias considering clock's stochastic variation behavior with robust least square collocation. Acta Geodaetica Cartogr Sin 45(6):646–655
14. Wang Y, Lu Z, Sun D et al (2016) A new navigation satellite clock bias prediction method based on modified clock-bias quadratic polynomial model. Acta Astronomica Sinica 57 (1):78–90

Centralized Autonomous Orbit Determination of Beidou Satellites Under the Constraint of Anchor Station

Xufeng Wen, Jinming Hao, Xiaogong Hu, Chengpan Tang, Dongxia Wang, Jie Xin, Bo Jiao and Jing Wang

Abstract Autonomous Navigation Based on Inter-Satellite Link (ISL) is a hot spot in the future development of satellite navigation system. The new generation Beidou navigation satellites are equipped with Ka-band ISL test verification platform. The processing flow of ISL observation data and the algorithm of centralized orbit determination are derived. Analysis of centralized orbit determination for 3 day arcs is carried out with measured data of five new generation BD satellites and an anchor station. Some 4 experiments were carried out on the effect of anchor station. Meanwhile, some 2 experiments were carried out on the effect of observation frequency. The result shows that: (a) The working time length of anchor station has little influence on the accuracy of orbit determination; (b) When the intersatellite observation is healthy, the anchor station and single satellite chain can maintain the orbit determination accuracy of 1 m, otherwise the improvement of anchor station's observation quantity will not improve its constraint function. (c) When the anchor station is well linked to all the satellites, the centralized algorithm can survive a lower number of observations, which means the orbit determination accuracy can remain being better than 1 m even though all links' observational frequencies dropped to 240 min.

X. Wen (✉) · J. Hao · B. Jiao
Information Engineering University, Zhengzhou, China
e-mail: wenxufeng201@126.com

X. Hu · C. Tang
Shanghai Astronomical Observatory, Chinese Academy of Science, Shanghai, China

D. Wang · J. Xin
Beijing Satellite Navigation Center, Beijing, China

D. Wang
State Key Laboratory of Geodesy and Earth's Dynamics, Wuhan, China

J. Wang
The 96633 Troops of PLA, Beijing, China

J. Sun et al. (eds.), *China Satellite Navigation Conference (CSNC) 2018 Proceedings*, Lecture Notes in Electrical Engineering 498,
https://doi.org/10.1007/978-981-13-0014-1_35

Keywords Beidou navigation satellite system · Inter-satellite link
Autonomous orbit determination · Anchor station · Observation frequency

1 Introduction

Based on the Inter-Satellite Link (ISL) ranging and communication, we can achieve the autonomous orbit determination and time synchronization of the satellite navigation system, and improve the survivability of the satellite navigation system under the condition of ground transportation control is blocked or weakened [1–7]. In addition, high precision ISL observation can be used to assist the ground transportation and control, and it can make up the defects of the station layout for the Beidou System in China 8.

For a long time, most of the domestic research on autonomous navigation of GNSS constellations is mostly in the stage of algorithm deduction and simulation verification [9–13]. In 2015–2016 years, Beidou(BDS) launched five new generation experimental navigation satellites (including 2 IGSO and 3 MEO satellites). These satellites have carried an inter satellite link test verification platform based on the Ka band time division observation system. The measured data have been obtained and the relevant technical research is being carried out. Therefore, the domestic research on autonomous navigation using ISL is transferred to the measured data test and evaluation. The preliminary analysis results of centralized autonomous orbit determination show that the dual one-way observation accuracy of Ka-band ISL is better than 10 cm [14], and the orbit determination precision of R direction under the support of a ground station is better than 0.5 m [15].

The autonomous orbit determination using ISL-only observations might lead to the problem of constellation rotation, which is caused by rank deficiency problem in the observation equation of ISL and the unobservability of the change of right ascension of ascending node (RAAN). With the prolongation of the time of independent orbit determination, this problem is mainly embodied in the accumulation of the error of the RAAN. To solve this problem, predicted orbits with good precision can be used as a priori information to constrain the estimated satellite orbit parameters. With the prior orbit of 15 m precision, the orbit determination accuracy is better than 6 m [16]. However, adding ground anchor stations is the general mean to solve the problem. And this scheme is used in BDS, who provides the means of satellite-ground observation in Ka-band.

In this paper, the problem of orbit determination with ISL under the constraint of anchor station is analysed. Data processing algorithm for ISL dual one-way observation is derived. Data from all 5 new generation satellites (compared with only 4 satellites in literature [16]) and an anchor station were collected. The influence of the observation of the anchor station on the orbit determination accuracy is analysed according to the different conditions, and the influence of the observation frequency on the orbit determination results is analysed, either.

2 ISL Observation Equation and Preprocessing

The ISL of the Beidou new generation satellite adopts the Ka bi-directional time division system, which means the routing table is pre-injected and each satellite (or anchor station) build chains with all visible satellites in order according to the table. Each pair of satellites (or anchor station) produce dual one-way measurement. Each of every pair of measurements, although produced in very close time, are actually not synchronous. Therefore, epoch deduction must be performed before the decoupling calculation. The ISL observational equation can be expressed as follows:

$$\begin{aligned}\rho_{\mathrm{AB}}(t_1) &= \left|\overrightarrow{r}_{\mathrm{B}}(t_1) - \overrightarrow{r}_{\mathrm{A}}(t_1 - \Delta t_1)\right| + c(\tau_{\mathrm{B}}(t_1) - \tau_{\mathrm{A}}(t_1)) + \delta_{\mathrm{AB}} \\ \rho_{\mathrm{BA}}(t_2) &= \left|\overrightarrow{r}_{\mathrm{A}}(t_2) - \overrightarrow{r}_{\mathrm{B}}(t_2 - \Delta t_2)\right| + c(\tau_{\mathrm{A}}(t_2) - \tau_{\mathrm{B}}(t_2)) + \delta_{\mathrm{BA}}\end{aligned} \tag{1}$$

where $\rho_{\mathrm{AB}}(t_1)$ and $\rho_{\mathrm{BA}}(t_2)$ are one-way measurement for satellite (anchor) A, B at corresponding time (forward and backward). $\overrightarrow{r}_{\mathrm{B}}$ and $\overrightarrow{r}_{\mathrm{A}}$ represent the positions of the two satellites when the signals are transmitted or received. Δt_1 and Δt_2 represent the light travel time of the dual one-way observation signals. c is the speed of light. τ_A and τ_{B} are the clock error of A and B compared with BDT. δ_{AB} and δ_{BA} are the amount of error to be corrected in two view measurements, respectively, which mainly includes the delay of the satellite and ground equipment and the geometric deviation like the antenna phase center deviation, the relativistic effect, the atmospheric influence (mainly the satellite ground link), and the Sagnac effect. Among them, the equipment delay can be calibrated accurately by the later period as a parameter to be estimated [17, 18]. The Ka ISL atmospheric delay is at subcentimeter level, negligible, and the rest can be modeled accurately. Imputed the dual measurements to the same epoch t_0:

$$\begin{aligned}\rho_{AB}(t_0) &= \rho_{\mathrm{AB}}(t_1) + d\rho_{\mathrm{AB}} = \left|\overrightarrow{r}_{\mathrm{B}}(t_0) - \overrightarrow{r}_{A}(t_0)\right| + c(\tau_{\mathrm{B}}(t_0) - \tau_{\mathrm{A}}(t_0)) + \delta_{\mathrm{AB}} \\ \rho_{\mathrm{BA}}(t_0) &= \rho_{\mathrm{AB}}(t_2) + d\rho_{\mathrm{BA}} = \left|\overrightarrow{r}_{A}(t_0) - \overrightarrow{r}_{\mathrm{B}}(t_0)\right| + c(\tau_{\mathrm{A}}(t_0) - \tau_{\mathrm{B}}(t_0)) + \delta_{\mathrm{BA}}\end{aligned} \tag{2}$$

where A and B are epoch imputation correction using forecasting euhemerist, including distance correction and satellite clock error correction. Adding two to each other, the information of the star clock can be eliminated and the orbital parameters are reserved only, and it can be used directly for the calculation of orbit determination:

$$Z_{AB}(t_0) = \frac{\rho_{AB}(t_0) + \rho_{BA}(t_0)}{2} = \left|\overrightarrow{r}_{\mathrm{B}}(t_0) - \overrightarrow{r}_{\mathrm{A}}(t_0)\right| + \frac{\delta_{\mathrm{AB}} + \delta_{\mathrm{BA}}}{2} \tag{3}$$

Thus, the orbit of the Ka bi-directional pseudo distance measurement is decoupled from the clock difference, and the residual term of the error can be pre-processed according to the previous method.

3 Centralized Orbit Determination Algorithm with Anchor Station

According to the dynamic equation of the satellite, we establish the connection between the input quantity, the normalized inter satellite link distance measurement, and the output, initial satellite information and all dynamic parameters. Then the adjustment can be carried out, and the output will be measured and corrected. The centralized orbit determination of this paper uses the least square batch processing algorithm, and the arc length of the fixed orbit is 3 days. The models considered in the satellite dynamics equation include two-body motion, the third body attracting forces model of sun and moon, the 30 order earth's non-spherical gravitational field model, the solar radiation pressure model, the earth tide and the sea tide perturbation model. The output parameters to be estimated include the initial orbit of the satellite ($\vec{r}$, $\dot{\vec{r}}$), the parameters of the solar radiation pressure $\vec{p}$ (Bernese ECOM 5) and the time delay $\vec{d}$ of the ISL equipment for the satellites or the anchor station.

The state of the satellite is $\vec{X} = \left(\vec{r}, \dot{\vec{r}}, \vec{p}\right)^T$. Let $f\left(\vec{X}\right) = \left(\dot{\vec{X}}, \ddot{\vec{X}}, 0\right)^T$. Then the dynamic equations and initial conditions of the satellite can be expressed as follows:

$$\begin{cases} \dot{\vec{X}}(t) = f\left(\vec{X}, t\right) \\ \vec{X}(t_0) = \vec{X}_0 \end{cases} \tag{4}$$

By the method of numerical integration, the relation between the initial state quantity and the time state of the target can be established, and the reference orbit and the state transfer matrix of the target time can be obtained. Thus, the numerical calculation of the motion equation of the satellite can be converted to the solution of the initial value of the ordinary differential equation. The Taylor expansion is carried out by the observation Eq. (3), and the residual equation after linearization can be expressed as:

$$\begin{aligned} z_{AB} &= Z_{AB} - Z_{AB}^* \\ &= H_A\left(\vec{X}_A - \vec{X}_A^*\right) + H_B\left(\vec{X}_B - \vec{X}_B^*\right) + D + v \\ &= H_A\vec{x}_A + H_B\vec{x}_B + D + v \\ &= H_A\Phi_{A,t}\vec{x}_{A,0} + H_B\Phi_{B,t}\vec{x}_{B,0} + D + v \end{aligned} \tag{5}$$

where Z_{AB}^* refers to the range estimation on target time calculated according to the satellite orbit prior information, $H = \frac{\partial z}{\partial \vec{X}}$ is the measurement matrix, $\Phi = \frac{\partial \vec{X}}{\partial\left(\vec{r}_0, \dot{\vec{r}}_0, \vec{p}\right)}$ is the state transition matrix, $\vec{x} = [\,\Delta\vec{r} \quad \Delta\dot{\vec{r}} \quad \Delta\vec{p}\,]^T$ is the State correction, and

$D = [\, dD_A \quad dD_B \,]^T$ refers to correction of distance deviation caused by device delay of two satellites (or anchor) respectively. D is contained in δ in formula (3). v is residual error.

After obtaining sufficient observation within 3 days, the state parameter correction calculation based on least squares estimation is carried out based on the above observation equation, and the modified orbit and ISL device delay is finally obtained. In the calculation, the anchor station is considered as a virtual satellite, but its exact coordinates are known, so the covariance is zero. Theoretically, the anchor station provides a spatial datum for the navigation constellation, which can solve the problem of the unobservability of overall rotation of the ISL measurements.

4 Example Analysis

4.1 Data Sets

In this paper, we collected the ISL data of all five new generation BDS satellites (I1S, I2S, M1S, M2S and M3S, respectively) and an anchor station. The data starts from 00:00 in July 15, 2016 (BDT) and end at 00:00 in July 18, 2016 (BDT). Available survey statistics are shown in Table 1. The coverage of the ISLs chain arc section is shown in Fig. 1. It can be seen that except the I1S-I2S link, which is not visible all the time, all the other links have observable data. But the data of the I1S-M2S and I2S-M3S links can be less. Figure 2 shows the chain construction.

4.2 The Influence of Anchor Station

The document [14] points out that, with the support of a ground anchor station, the laser residual of centralized orbit determination using ISL data is superior to 15 cm. Therefore, in this calculation example, the orbit determination results using all the observed data are used as the precision results. In order to analyse the influence of the anchor station on the accuracy of the autonomous orbit determination, the conditions of the observation of the anchor station are set according to the different strategies. And the accuracy is evaluated by comparing the calculated results with the preceding precision results. Radial direction (R direction), tangential direction (T direction), normal direction (N direction) and position error are selected as evaluation indexes. Each star completes the chain with all the visible stars (stations) within 30 s. The test scheme is shown in Table 2.

Figures 3, 4, 5 and 6 shows the test results of each test scheme. It can be seen that in scheme 1, with all the satellites retain the building chain with anchor station, the RMS of orbit determination is very small (within 1 m), even though the number of observation links of each anchor station is reduced. The contrast between

Table 1 Observable measurement information

Link	I1S-I2S	I1S-M1S	I1S-M2S	I1S-M3S	I1S-Anchor	I2S-M1S	I2S-M2S	I2S-M3S
Measurement number	0	1215	1277	170	5247	1226	4025	172
Link	I2S-Anchor	M1S-M2S	M1S-M3S	M1S-Anchor	M2S-M3S	M2S-Anchor	M3S-Anchor	
Measurement number	7425	6146	4583	1472	2634	995	1777	

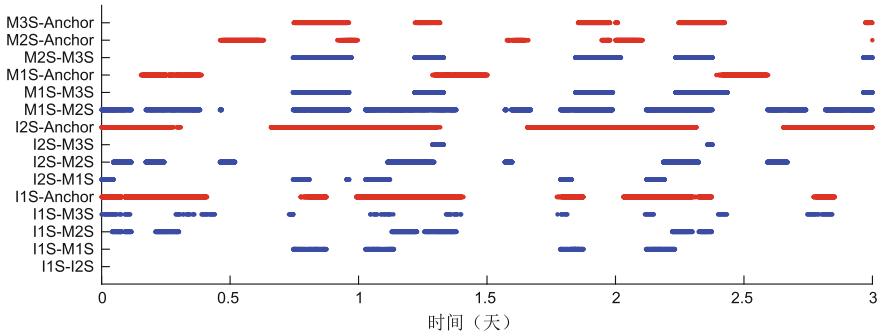

Fig. 1 Visibility of ISL observations. (The red part represents the anchor station links)

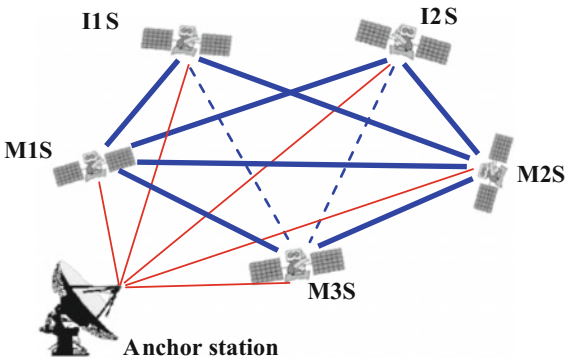

Fig. 2 Schematic diagram of link building in ISLs (The red lines represent the anchor station links, and the dotted lines represent inadequate data)

scheme 2 and scheme 3 is sharp: in a similar case with only one satellite building chain with anchor station, although the measurement number of anchor station in scheme 3 is more than 5 times that of scheme 2, the orbit determination error of the former, with 3 meters in T direction and N direction and even worse for I1S and I2S, is still much larger than the latter, which is not quite different from the result of scheme 1. Combined with the analysis of Fig. 2, this should be due to that the observations between M1S and all the other satellites are sufficient, which can transfer the anchor station's constraints well to other satellites. Conversely, not only can't I1S build chain with I2S, but it doesn't have a healthy link with M3S, which, to a large extent, restricts the transmission of anchor station's constraints. The result of scheme 4 shows the importance of the anchor station in the autonomous orbit determination, and the anchor station mainly plays a restraining effect on the T direction and the N direction.

Table 2 Observable measurement information

	Strategy	I1S-Anchor measurement number	I2S-Anchor measurement number	M1S-Anchor measurement number	M2S-Anchor measurement number	M3S-Anchor measurement number
Scheme 1	Anchor in 2nd day only	1825	2427	497	170	583
Scheme 2	Anchor station linked with M1S only	0	0	1472	0	0
Scheme 3	Anchor station linked with I2S only	0	7424	0	0	0
Scheme 4	No anchor station	0	0	0	0	0

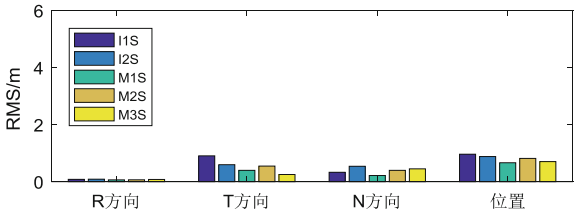

Fig. 3 The orbit determination accuracy of anchor station on only the second day

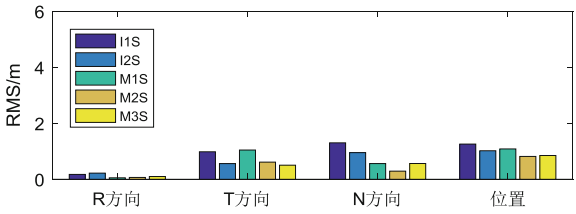

Fig. 4 The orbit determination accuracy of anchor station linked with M1S only

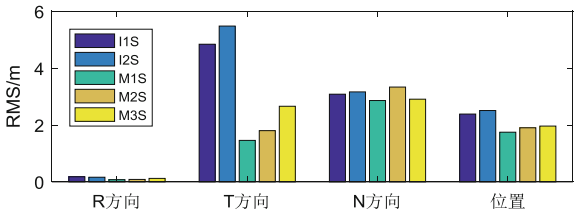

Fig. 5 The orbit determination accuracy of anchor station linked with I2S only

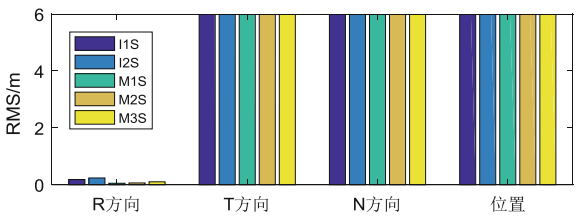

Fig. 6 The orbit determination accuracy with no anchor station (RMS on T and N are more than 100 m)

4.3 The Influence of the Observational Frequency of ISLs

In this paper, the influence of the observational frequency of ISLs on the orbit determination is also analysed. The test scheme is shown in Table 3. The so-called observational frequency of 1 min (240 min) means that the observation of each link within 1 min (240 min) is not more than once. The orbit determination results of the two schemes are shown in Figs. 7 and 8. It can be seen that even if the observation frequency is low to four hours in scheme 6, and the number of observations per star is only a few, its orbit determination accuracy is still within 1 m.

Table 3 Test scheme for the observational frequency strategy of inter-satellite links

	Strategy	Links	I1S measurement number	I2S measurement number	M1S measurement number	M2S measurement number	M3S measurement number
Scheme 5	Observation frequency of 1 min	All	2487	3160	3975	4122	2390
		-anchor station	1460	2016	561	386	613
Scheme 6	Observation frequency of 240 min	All	29	29	37	40	31
		-anchor station	12	13	6	6	7

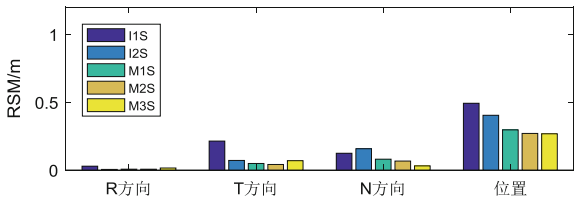

Fig. 7 Orbit determination accuracy with observation frequency of 1 min

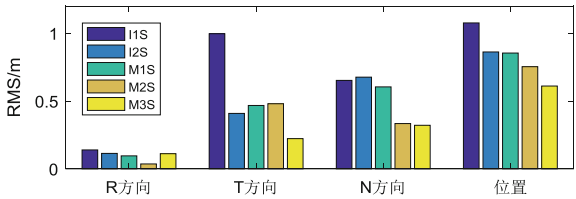

Fig. 8 Orbit determination accuracy with observation frequency of 240 min

The results show that the centralized orbit determination algorithm can tolerate ISL observation with low frequency under the presence of an anchor station. On the one hand, it shows the optimality of the centralized algorithm, and on the other hand, it shows the sensitivity of the anchorage station to the control of the autonomous orbit determination.

5 Summary and Discussion

The measurement on the Beidou ISL is based on the time division dual one-way strategy. The preprocessing algorithm for ISL observation data is derived, and the centralized orbit determination algorithm under the constraint of anchor station is deduced. Using measured data from five new-generation satellites of BDS and an anchor station, a centralized orbit determination of 3-day arc section is carried out. In order to analyze the influence of the anchorage station as well as the observation frequency of ISL on the accuracy of the orbit determination, some 6 experimental schemes are designed. The test results show that:

(A) The anchorage station is necessary in the autonomous orbit determination. Lacking of external constraints, the result of the autonomous orbit determination based on the ISL will be diverged.

(B) The constraint of anchorage station needs perfect ISLs to be transmitted to the whole constellation. The satellite linked to anchorage station needs to build enough links with other satellites, so as to guarantee the anchorage station's constraint function. When the condition is satisfied, an anchor station building chains with a single satellite can ensure that the centralized orbit determination accuracy is better than 1 m in 3-day arc section. Otherwise, the orbit determination accuracy will not be guaranteed, even if the number of observations increases.

(C) The centralized orbit determination is not sensitive to the observation frequency when the anchor station is built up chain with all satellites. The orbit determination accuracy on T and N direction of all satellites is better than 1 m, Despite that the observation frequency of each link is less than 240 min.

The analysis of this article is limited by the number of ISL-capable satellites and anchorage stations. With the completion of the Beidou-3 global system, more measured data can be used for the autonomous orbit determination of the whole constellation. In addition, the centralized algorithm is adopted in this paper, but the distributed autonomous orbit determination algorithm adapting to the satellites' environment using measured data needs further research.

References

1. Ananda MP, Bernstein H, Cunningham KE, Feess WA (1990) Global positioning system (GPS) autonomous navigation. Position location and navigation symposium, 1990. Record. The 1990's—a decade of excellence in the navigation sciences. In IEEE Plans '90. IEEE, vol. 27, pp 497–508. IEEE
2. Guo FX (2013) Research on navigation satellite autonomous orbit determination based on ground anchor stations. Doctoral dissertation, PLA Information Engineering University
3. Hofmann-Wellenhof B, Lichtenegger H, Wasle E (2008) GNSS—global navigation satellite systems. Springer
4. Menn MD, Bemstein H (1994) Ephemeris observability issues in the global positioning system (GPS) autonomous navigation (AUTONAV). In Position location and navigation symposium, vol 94, pp 677–680. IEEE
5. Rajan JA, Brodie P, Rawicz H (2003) Modernizing gps autonomous navigation with anchor capability. In Proceedings of international technical meeting of the satellite division of the institute of navigation, 1534–1542
6. Rajan JA (2002) Highlights of gps ii-r autonomous navigation. In Proceedings of annual meeting of the institute of navigation & Cigtf guidance test symposium, 354–363
7. Rajan J, Orr M, Wang P (2003) On-orbit validation of GPS IIR autonomous navigation. In Proceedings of the institute of navigation 59th annual meeting, vol 23–25, pp 411–419
8. Shuai P, Qu G, Chen Z (2006) Studies on autonomous navigation techniques for navigation constellations. Eng Sci 8(3):22–30
9. Han S, Gui Q, Li J (2013) Establishment criteria, routing algorithms and probability of use of inter-satellite links in mixed navigation constellations. Adv Space Res 51(11):2084–2092
10. Song XY (2009) Study on the orbit determination of compass navigation satellites. Doctoral dissertation, Chang'an University
11. Xu H, Wang J, Zhan X (2012) Autonomous broadcast ephemeris improvement for GNSS using inter-satellite ranging measurements. Adv Space Res 49(6):1034–1044
12. Xu Y, Chang Q, Yu ZJ (2012) On new measurement and communication techniques of GNSS inter-satellite links. Sci China Tech Sci 55(1):285–294
13. Zhenghang LI (2011) Influence of error and prior information to AOD of navigation satellites. Geomatics Info Sci Wuhan Univ 36(7), 797–796
14. Tang CP, Hu XG, Zhou SS (2017) Centralized autonomous orbit determination of Beidou navigation satellites with inter-satellite link measurements: preliminary results. Scientia Sinica Physica, Mechanica & Astronomica 47(2):95–105

15. Song X, Mao Y, Feng L, Jia X, Jianfeng JI (2017). The preliminary result and analysis for bd orbit determination with inter-satellite link data. Acta Geodaetica Et Cartographica Sinica 46 (5):574–553
16. Ren X, Yang Y, Zhu J, Xu T (2017) Orbit determination of the next-generation Beidou satellites with intersatellite link measurements and a priori orbit constraints. Adv Space Res 2155–2165
17. Pan JY, Hu X, Tang CP, Zhou SS, Ran LI, Zhu LF et al (2017) System error calibration for time division multiple access inter-satellite payload of new-generation beidou satellites. Chin Sci Bull 62(23):2671–2679
18. Ruan R, Feng L, Jia X (2014) Equipment delay estimation for GNSS satellite combined orbit determination with satellite-ground link and inter-satellite link observations. Acta Geodaetica Et Cartographica Sinica 43(2):137–142, 157

Part III
Precise Positioning Technology

Research on Atmosphere Refraction Modification of Radio Wave on TT&C System in Close-Shore Environment

Demin Qiu, Bo Liang, Tianyu Pan, Yuxuan Li, Haitao Fan, Qing Sun, Hongchao DiAO, SHAO Junfei, Maolin Xie and Shaohui Wei

Abstract As for the problem that the non-stationary fluctuating wind induces dramatic changes of atmosphere refraction at tens of meters height above the rough ocean surface, which reduces the accuracy of orbit measurement and control system while tracking spacecraft at low elevation. A new atmosphere refraction modification method is investigated based on the modified Monin-Obukhov approximation, with the consideration of the influence by random rough ocean surface which is established by Monte-Carlo method. Experimental results of several in-orbit spacecraft measurement data indicate that precision can be dramatically improved compared with traditional methods.

Keywords Atmosphere refraction modification · Random rough ocean surface Monte-Carlo method · PM spectrum

1 Introduction

With the increasing accuracy of the orbit determination and the accuracy of orbit determination, the accuracy of the atmospheric refraction correction model of electromagnetic wave propagation has become one of the important factors affecting the accuracy of the measurement [1]. The probability of evaporation of waveguides in the southeastern coastal areas of China is very high. Especially when the monitoring and control system in the coastal area tracks the low-elevation spacecraft, the surface roughness is affected by the gust of the tens of meters in the sea. Change more intense [2].

Some scholars have carried out research on the characteristics of evaporative waveguides based on the theory of ocean-atmosphere interaction in the 1970s [3]. However, such studies have been carried out under the assumption that the sea is

D. Qiu (✉) · B. Liang · T. Pan · Y. Li · H. Fan · Q. Sun · H. DiAO · S. Junfei
M. Xie · S. Wei
63756 Unit of PLA, Wannianquanstr. 33, Qingdao 266110, China
e-mail: Murray001@sina.com

J. Sun et al. (eds.), *China Satellite Navigation Conference (CSNC) 2018 Proceedings*, Lecture Notes in Electrical Engineering 498,
https://doi.org/10.1007/978-981-13-0014-1_36

calm. On this basis, the atmospheric correction method does not take full account of the influence of sea surface roughness [4], thus limiting the further improvement of the accuracy of spacecraft external measurement.

In this paper, a precision atmospheric refraction correction method is proposed for the high precision correction of radio propagation error in the coastal area. This method takes full account of the influence of sea surface roughness on the evaporative waveguide, based on Pierson-Moscowitz Gravitational Spectroscopy. The Monte-Carlo method is used to generate three-dimensional random rough sea surface, which accurately describes the change of atmospheric refractive index in the wave propagation environment. Using the meteorological data of Qingdao area to establish an empirical model of atmospheric meteorological parameters consistent with the climate and seasonal characteristics of the station area. Based on the theory of atmospheric refraction index and the statistical method, the empirical model of vertical distribution of atmospheric refractive index is proposed, and the atmospheric transmission error correction of the radio and television is measured to improve the accuracy of data correction. It is better for accurate tracking and measurement of spacecraft.

2 Evolving Waveguide Causes and Formation Conditions

The troposphere, especially the surface layer of the atmosphere, is adjacent to the surface and sea surface. Its electromagnetic properties have a strong influence on the propagation of radio waves. The electromagnetic properties of the atmosphere surface layer can be modelled as an function of temperature, pressure and humidity in the atmosphere. The random weather change the process. So that these parameters have complicated changes, affecting the ground measurement and control system measurement accuracy and performance. Since the discovery of atmospheric waveguide theory and low altitude atmospheric waveguide exploration since World War II, it has been shown that the atmospheric waveguides in the marine environment can be classified into three types: surface waveguide, floating waveguide and evaporative waveguide according to the spatial distribution of atmospheric refractive index. Evaporation of the waveguide is due to the evaporation of seawater caused by the increase in the surface humidity with the height of the rapid decline in the formation of the sea waveguide, generally occurred in the 40 m below the height of the sea atmosphere. According to Patterson and other global sea area atmospheric waveguide law, evaporation waveguide summer in China's southeastern coastal probability of up to 85% [5].

A large number of studies have shown that the atmospheric refraction effect causes the propagation delay and the path bending, which is one of the key factors to control the improvement of radio measurement accuracy. In order to further improve the accuracy of radiofrequency refraction correction, the tropospheric zenith delay of the traditional Hopfield model, Saastamoinen model and the minimum operational performance standard (MOPS) model and sounding rocket and

other methods, but these methods in the measurement days. There are some limitations in the top delay, and the accuracy needs to be improved.

2.1 Evaporative Waveguide Prediction Model

The atmospheric troposphere is the most recent atmospheric section from the ground. Its atmospheric composition, pressure, temperature and humidity all change with height. Therefore, it belongs to inhomogeneous medium, which usually reduces the atmospheric refraction index in the vertical direction with increasing height and horizontal Refractive index changes can be ignored [6]. The refractive index can be expressed by the refractive index.

$$N = (n-1) \times 10^6 = \ 77.6\frac{P}{T} + 3.73 \times 10^5 \times \frac{e}{T^2} \tag{1}$$

where: P for atmospheric pressure; T for thermodynamic temperature; e for vapor pressure. When the electromagnetic wave propagation distance is comparable to the Earth's radius, considering the influence of the Earth's curvature and assuming that the Earth's atmosphere is a uniform spherical stratification, the modified refractive index can be obtained by Snell's law

$$m(z) = n(z)(1 + \frac{z}{a_e}) \approx n(z) + \frac{z}{a_e} \tag{2}$$

where: z for the sea above the vertical height; $n(z)$ for the height z of the atmospheric refraction index; a_e = 6370 km for the Earth's average radius. Thus, the atmosphere can be corrected for the refractive index

$$M = N + \frac{z}{a_e} \times 10^6 = N + 0.157z \tag{3}$$

The main physical processes in the atmospheric boundary layer are the turbulent transport of physical quantities such as heat, momentum, water vapor and so on. The key to the momentum exchange of the oceanic surface is its accurate. The main physical process of atmospheric boundary layer is the turbulence of the atmospheric boundary layer affected by the near sea. To describe the dependence of atmospheric stability and sea surface aerodynamic roughness, the similarity theory of Monin-Obukhov can describe the dependence of stability, and the accuracy and universality of aerodynamic roughness calculation method are of great significance to the study of wind and waves development and sea-air interaction [7].

The similarity theory of Monin-Obukhov is closely related to the structure of the atmospheric surface, and it is believed that the atmosphere of the near sea is in a thermodynamically equilibrium state. The heat and water vapor are transmitted through the turbulence to the upper atmosphere, and the evaporation waveguide

modeling is used in the range of tens of meters above sea level [8]. Several common radio refraction is shown in Fig. 1.

According to Monin-Obukhov theory

$$\frac{\partial \bar{\sigma}}{\partial z} = \frac{\sigma^*}{\mathrm{K}z} \Phi\left(\frac{z}{L}\right) \tag{4}$$

where: $\bar{\sigma}$ for the turbulence average; σ' for the turbulence pulsation; σ^* for the turbulence feature scale; K for the Karman constant; L for the Monin-Obukhov length, Φ is the function of the stability parameter z/L. When using the formula (4) from the rough height z_0 of the sea to the height, there are

$$\bar{\sigma}(z_1) - \bar{\sigma}(z_0) = \frac{\sigma^*}{\mathrm{K}z} A \tag{5}$$

where $A = \int_{z_0}^{z} \frac{\Phi\left(\frac{z}{L}\right)}{z} \mathrm{d}z$. Substituting Eq. (5) into Eq. (4)

$$\frac{\partial \bar{\sigma}}{\partial z} = \frac{\bar{\sigma}(z_1) - \bar{\sigma}(z_0)}{z} \frac{\Phi\left(\frac{z}{L}\right)}{A} \tag{6}$$

Ignore the impact of other parameters near the sea surface, take the standard sea surface atmospheric conditions, so that P_0 = 1013.25 hPa, T_0 = 288 K, e_0 = 10.13 hPa. From formula (1) can be affixed to the sea atmospheric refractive index gradient

$$\frac{\mathrm{d}N(z)}{\mathrm{d}z} \approx 0.269 \frac{\mathrm{d}P(z)}{\mathrm{d}z} - 1.265 \frac{\mathrm{d}T(z)}{\mathrm{d}z} + 4.5 \frac{\mathrm{d}e(z)}{\mathrm{d}z} \tag{7}$$

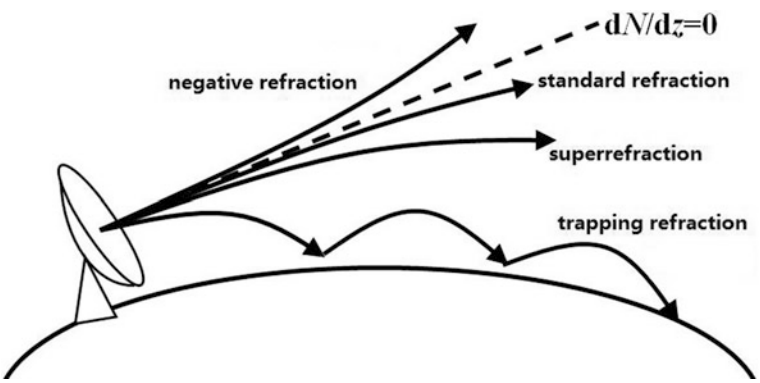

Fig. 1 Atmospheric refraction classification

$P(z)$ can be given by the exponential form

$$P(z) = P_0 e^{(-z/z_P)} \tag{8}$$

where: z_P is the homogeneous atmosphere height; $z_P = R^* T/g\mu$; R^* is the universal gas constant; g is the acceleration of gravity; u is the air molecular weight. For the sea atmosphere, take u = 28.84, z_P = 8467 m, then $\frac{dP(z)}{dz} \approx 0.1192$ hPa/m.

From formula (7) available in the vicinity of the sea atmospheric refractive index

$$\frac{dN(z)}{dz} \approx -0.032 - 1.265\frac{dT(z)}{dz} + 4.5\frac{de(z)}{dz} \tag{9}$$

At the height z_e of the evaporative waveguide

$$\left.\frac{dN(z)}{dz}\right|_{z=z_e} \approx -0.157 \text{ N/m} \tag{10}$$

This is available

$$4.5 \times \left.\frac{de(z)}{dz}\right|_{z=z_e} - 1.265 \times \left.\frac{dT(z)}{dz}\right|_{z=z_e} \approx -0.125 \tag{11}$$

Let $N_P(z) = 4.5 \times e(z) - 1.265 \times T(z)$, And defined $N_P(z)$ as the pseudo-refractive index, if the physical quantity $\sigma = N_P$, then formula (6) becomes

$$\frac{dN_P}{dz} = \frac{N_P(z_1) - N_P(z_0)}{z}\frac{\Phi\left(\frac{z}{L}\right)}{A} \tag{12}$$

where: $N_P(z_0)$, $N_P(z_1)$ are the pseudo-refractive index at the height of the sea surface roughness and the reference height, respectively. $b = -0.125$ When the pseudo-refractive index vertical gradient is equal to the critical gradient d, it is the evaporation waveguide height. Formula (12) is rewritten as

$$b = \frac{N_P(z_1) - N_P(z_0)}{d}\frac{\Phi\left(\frac{d}{L}\right)}{A} \tag{13}$$

By formulas (3), (12) and (13) available

$$\frac{dM}{dz} = 0.125 - 0.125 \times \frac{d\Phi\left(\frac{z}{L}\right)}{z\Phi\left(\frac{d}{L}\right)} \tag{14}$$

Formula (14) from the points z_0 to z get close to the sea surface of the evaporation waveguide refractive index of the logarithmic model

$$M(z) = M(z_0) + 0.125z - 0.125z_0 - 0.125d\ln(z/z_0) \quad (15)$$

where: $M(z_0)$ for the sea surface roughness height z_0 of the modified refractive index; d for the evaporation waveguide height. When d = 0 is the standard atmospheric refractive index profile. Evaporation waveguide characteristic parameter changes shown in Fig. 2.

Figure 2 shows the refractive index profile of the different waveguide type, where Fig. 2a is the refractive index profile of the standard atmosphere, and Fig. 2b is the refractive index profile of the evaporative waveguide, where M is the waveguide strength unit.

2.2 *Rapping Angle and Cutoff Wavelength of Evaporative Waveguides*

The necessary conditions for the propagation of radio waves in the atmospheric waveguide include the following conditions: (1) The elevation angle of the radio wave must be less than a critical angle, that is, the trapping angle; (2) The radio frequency must be higher than the maximum trapping frequency.

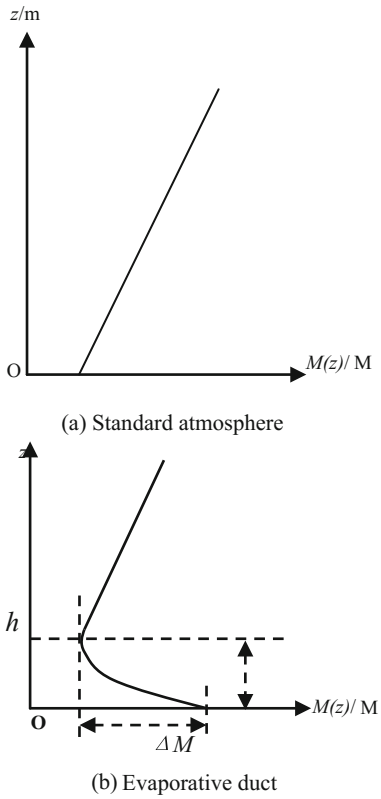

Fig. 2 Cutaway view on atmosphere refraction index

The trapping angle is that under certain atmospheric parameters, the wave can be captured by the atmospheric waveguide, thus forming the maximum elevation of atmospheric waveguide propagation. The expression is

$$\theta_c = \sqrt{2(\frac{\Delta N}{n_T dh} \times 10^{-6} - \frac{1}{r_e + h_T})dh} \tag{16}$$

The cutoff frequency expression is

$$\left.\begin{aligned} f_H &= c/\left[0.25 n_T (\frac{\Delta N}{n_T dh} - \frac{10^6}{r_e + h_T})^{1/2} dh^{3/2}\right] \\ f_V &= c/\left[0.75 n_T (\frac{\Delta N}{n_T dh} - \frac{10^6}{r_e + h_T})^{1/2} dh^{3/2}\right] \end{aligned}\right\} \tag{17}$$

In the formulas (16) and (17): c is the speed of light; n_T is the refractive index of the antenna where the antenna is located; r_e is the radius of the earth; h_T is the height of the antenna; dh is the thickness of the waveguide layer; ΔN is the index profile of the refractive index of the waveguide; f_H/f_V is the horizontal/vertical polarization wave cutoff frequency.

In the evaporative waveguide layer, when the angle between the wave path and the waveguide horizontal boundary is small, based on the spherical stratified atmosphere, Snell's law, we have

$$\Delta N = |M_d| + \frac{d}{r_e} \times 10^{-6} \tag{18}$$

where $|M_d|$ is the waveguide strength, since $h_T \ll r_e$, $n_T \approx 1$, the trapping angle and the horizontal polarization cutoff frequency can be approximated as (Fig. 3).

$$\left.\begin{aligned} \theta_c &\approx \sqrt{2 \times |M_d|} \times 10^{-3} \\ f_{Hmax} &= c/\left(0.25 d \sqrt{|M_d|}\right) \\ f_{Vmax} &= c/\left(0.75 d \sqrt{|M_d|}\right) \end{aligned}\right\} \tag{19}$$

Table 1 shows the cutoff frequency corresponding to the height and intensity of the different evaporative waveguides. It can be seen from the change rule of Table 1 that the trapping angle is proportional to the increase of the waveguide strength, and the cutoff frequency is inversely proportional to the increase of the waveguide strength, the higher the cutoff frequency of the evaporative waveguide layer is, the lower the cutoff frequency is.

The distribution of waveguide intensity in different regions is shown in Table 2. It can be seen that the average waveguide intensity in Qingdao is 13.1 M units. From formula (19), the trapping angle and horizontal cutoff frequency are 0.29° and

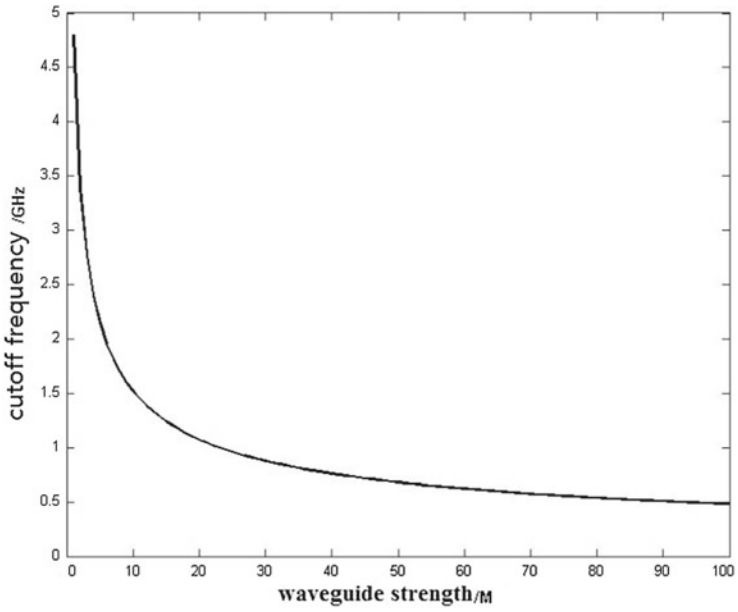

（a）Trapping angle

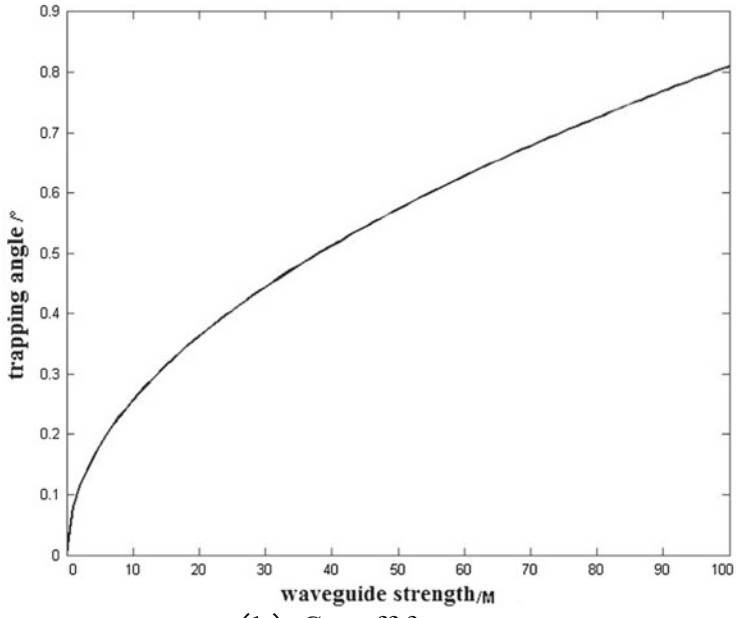

（b）Cut-off frequency

Fig. 3 Trapping angle and cut-off frequency of evaporation duct

Table 1 Cut-off frequency of different waveguides

Waveguide height/m	Waveguide strength/M	Cut-off frequency/MHz
10	10	3794.733
	20	2683.282
	30	2190.890
20	10	1897.367
	20	1341.641
	30	1217.161
30	10	1264.911
	20	894.427
	30	730.297

Table 2 Distribution of waveguide intensity in different areas

Place	Waveguide strength/M									
	0	0–2	2–5	5–10	10–15	15–20	20–30	30–40	>40	平均
QingDao	0.0	16.1	10.7	23.2	21.4	12.5	7.1	3.6	5.4	13.1
JiNan	0.0	32.0	20.0	16.0	4.0	8.0	4.0	0.0	16.0	11.4
DaLian	0.0	28.3	20.8	15.1	9.4	5.7	1.9	3.8	15.1	10.9
ShenYang	2.9	17.1	28.6	28.6	2.9	2.9	0.0	2.9	14.3	13.1
ZhengZhou	0.0	27.5	31.4	15.7	3.9	0.0	7.8	2.0	11.8	13.4
ShangHai	0.0	25.9	21.3	19.4	11.1	11.1	4.6	2.8	3.7	8.7
XiaMen	0.0	24.1	31.0	27.6	3.4	6.9	3.4	0.0	3.4	7.7
SanYa	0.0	18.4	20.4	28.6	14.3	6.1	4.1	4.1	4.1	11.0

1.66 GHz, respectively. It is shown that the radio and the received radio waves are not trapped by the evaporative waveguides to form the over-the-horizon propagation in the S-band (near 2200 MHz) in the coastal area of Qingdao. The atmospheric refractive index in the pitching direction will be significantly affected by the evaporation of the waveguide, which needs to be more precisely corrected.

3 Windy Environment Random Rough Surface Modeling

The scattering of radio waves in the rough sea surface makes the propagation path of the waveguide more complicated. The traditional atmospheric refraction correction method approximates the sea surface as a smooth plane, and does not fully consider the influence of the wave height on the atmospheric refractive index in the windy environment. According to the theory of Longuet-Higgins, the waves under steady sea conditions can be regarded as stationary stochastic processes, that is, the superposition of sine wave with infinite number of different periods, amplitudes and initial phases.

3.1 Rough Sea Surface Statistical Characteristics

The probability density function of the ups and downs of the waves reflects the distribution of the undulating distribution, denoted by $p(f)$, then $p(f)\mathrm{d}f$ is the probability of the average height $z \sim z + \mathrm{d}z$, and the mean of the undulating is

$$\bar{f} = \int_{-\infty}^{\infty} fp(f)\mathrm{d}f \tag{20}$$

The undulating mean square root is

$$\delta = \sqrt{\int_{-\infty}^{\infty} f^2 p(f)\mathrm{d}f - \int_{-\infty}^{\infty} fp(f)\mathrm{d}f} \tag{21}$$

The autocorrelation function is

$$\rho(R) = \frac{E[f(x)f(x+R)]}{\delta^2} \tag{22}$$

The power spectral density is

$$S(k) = \frac{1}{2\pi} \int_{-\infty}^{\infty} G(R)e^{ikR}\mathrm{d}R \tag{23}$$

where: $R = |x_1 - x_2|$.

3.2 Monte-Carlo Method to Generate Random Rough Sea Surface

The method of generating a stationary random process by Fast Fourier Transform (FFT) is used to generate a random rough surface sample [9]. The correlation function and spectral density function of rough surface fluctuation can be expressed by the corresponding Fourier transform relation, which is

$$\left.\begin{aligned} C(x,y) &= \iint W\left(K_x, K_y\right) e^{i\left(K_x x + K_y y\right)} \mathrm{d}K_x \mathrm{d}K_y \\ W\left(K_x, K_y\right) &= \frac{1}{4\pi^2} \iint C(x,y) e^{-i\left(K_x x + K_y y\right)} \mathrm{d}x\mathrm{d}y \end{aligned}\right\} \tag{24}$$

Monte-Carlo method is used to filter the power spectrum in the frequency domain, and the inverse fast Fourier transform (IFFT) can be used to obtain the ups and downs of the rough sea surface. The length of the two-dimensional random rough sea in the x and y directions is Lx, Ly, and the interval of the interval is M, N, the distance between adjacent two points is Δx, Δy, then the height of any point on the sea $x_m = m\Delta x$, $y_n = n\Delta y$, $m = -M/2+1, M/2$, $n = -N/2+1, \cdots, N/2)$ is

$$f(x_m, y_n) = \frac{1}{L_x L_y} \times \sum_{m_k=-M/2+1}^{M/2} \sum_{n_k=-N/2+1}^{N/2} F(k_{m_k}, k_{n_k}) e^{i\left(k_{m_k} x_m + k_{n_k} y_n\right)}$$

$$F(k_{m_k}, k_{n_k}) = 2\pi\sqrt{L_x L_y W(k_{m_k}, k_{n_k})} \times \left\{ \begin{array}{l} \sqrt{2}[N(0,1) + iN(0,1)], \begin{pmatrix} m_k \neq 0, M/2 \\ n_k \neq 0, N/2 \end{pmatrix} \\ N(0,1), \begin{pmatrix} m_k = 0, M/2 \\ n_k = 0, N/2 \end{pmatrix} \end{array} \right\} \tag{25}$$

where: $W(k_{m_k}, k_{n_k})$ is the power spectral density of a two-dimensional random rough surface; $k_{m_k} = 2\pi m_k / L_x$; $k_{n_k} = 2\pi n_k / L_y$.

3.3 Three-Dimensional Rough Sea Surface Simulation

The random rough sea surface is the Fourier transform of the wave height correlation function, which reflects the second order statistical properties of the random distribution process of the relative spatial frequency and position of each harmonic component. The commonly used wave spectrum is Pierson-Moskowitz spectrum (PM spectrum), Fung complete sea spectrum, JONSWAP spectrum [10]. The PM spectrum is the empirical spectrum of the wave observation with wind speed as the parameter. The polar coordinate expression of the three-dimensional PM spectrum is

$$W(D, \varphi) = \frac{\alpha}{2|D|^4} \times \exp\left(-\frac{\beta g_0^2}{D^2 U_{19.5}^4}\right) \Phi(\varphi) \tag{26}$$

where: $\alpha = 0.008$; $\beta = 0.74$; D is the spatial wave number; $U_{19.5}$ is the average wind speed at 19.5 m above the sea surface; g_0 is the gravitational acceleration; $\Phi(\varphi)$ is the diffusion function. Converts the polar coordinate expression of the PM spectrum to the Cartesian coordinate system

$$W(K_x, K_y) = \frac{\alpha}{2\left(K_x^2 + K_y^2\right)^2} \times \exp\left(-\frac{\beta g_0^2}{\left(K_x^2 + K_y^2\right) U_{19.5}^4}\right) \times \frac{\cos^2\left(\tan^{-1}\left(K_y / K_x\right) - \varphi_v\right)}{\pi} \tag{27}$$

where: φ_v is the average wind direction; $\varphi_v = 0$ corresponds to x positive.

According to Phillips, the relationship between surface roughness height z_0 and wind speed $U_{19.5}$ is obtained

$$z_0 = \sqrt{\frac{\alpha U_{19.5}^4}{4\beta g_0^2}} \tag{28}$$

The correlation length of the sea surface is 51.2 m and the sampling point is 512. The simulation results of the rough sea surface with different wind speed are shown in Fig. 4.

According to formulas (15) and (28) can be obtained in the environment near the rough sea near the atmospheric correction of the refractive index with the height of the curve shown in Fig. 5.

In order to evaluate the accuracy of the correction model and the traditional model, the tracking data of multiple satellites were verified by the coastal station. The results are shown in Figs. 6 and 7.

It can be seen from Figs. 6 and 7 that the correction of the elevation angle is 0.22° at the elevation angle of 3°, and the double exponential model as well as the Hopfield model are 0.28° and 0.32° respectively. At the elevation angle of 40°, the three models The correction amount is basically the same, that is, the low angle of elevation is close to the sea surface evaporation waveguide when the refraction angle correction amount is large, the high elevation angle over the top when the correction amount is the smallest. The results of the anomalous correction of the

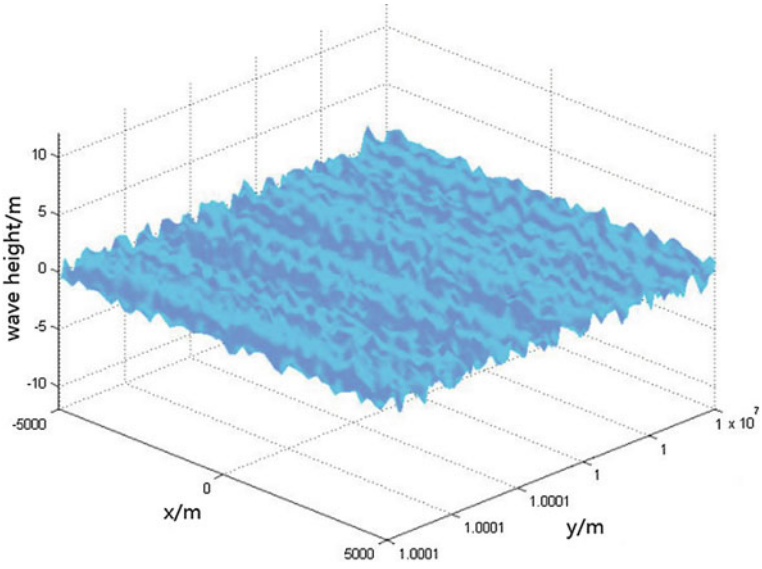

Fig. 4 Three-dimensional random rough sea

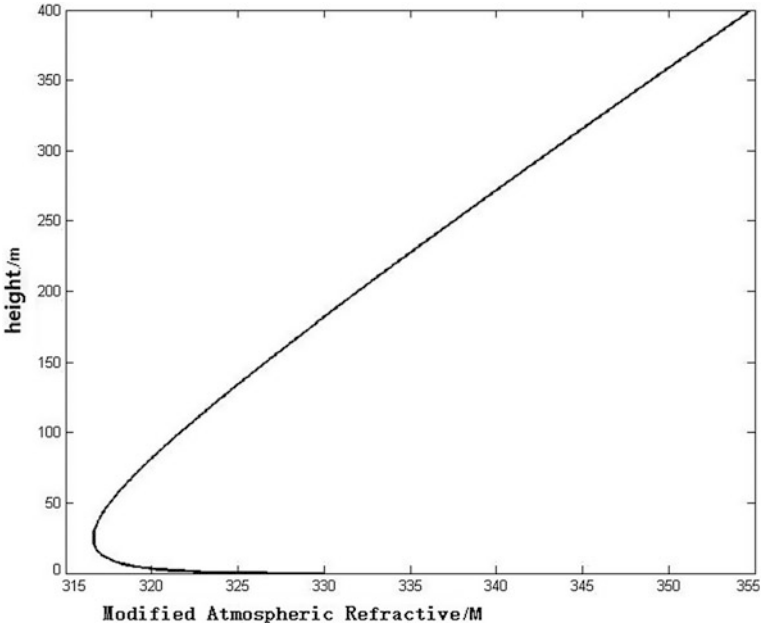

Fig. 5 Correction curve of atmosphere refraction index

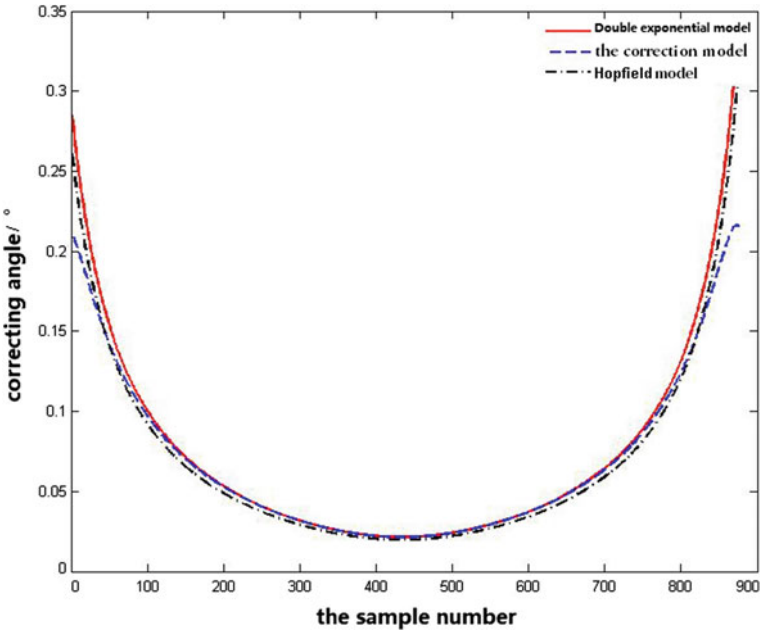

Fig. 6 Comparison of measured atmospheric refraction correction

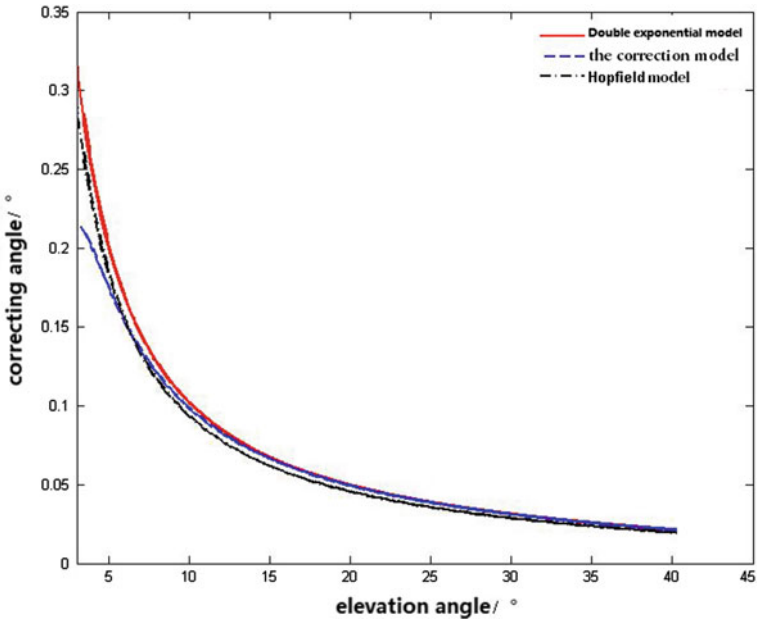

Fig. 7 Atmospheric refraction correction changing with the elevation angle

atmospheric correction model are compared with the traditional double exponential model and the Hopfield model, which is closer to the satellite orbit data.

From the above analysis, we can see that the model of the atmospheric correction model can reflect the change of the atmospheric refractive index over the coastal station and improve the accuracy of the orbital orbit measurement data.

4 Conclusion

Evaporative waveguides as the common form of atmospheric waveguide in the ocean has great influence on the propagation of radio waves in the near stratum, especially when the low altitude of the station in the coastal area is used to track the spacecraft, the atmospheric refraction error will greatly reduce the accuracy of angle measurement. In this paper, based on the Monte-Carlo method and Monin-Obukhov's similarity theory, the atmospheric refraction model is based on the assumption that the sea surface is a smooth surface condition. Considering the random rough sea surface effect of non-stationary pulsating winds, and the trapping angle and cutoff frequency of the S-band radio waves propagating in the evaporative waveguide are given. By using this model, the atmospheric refraction correction of the data of orbiting satellites is carried out. The accuracy of the correction is improved obviously compared with the traditional method, which provides a

technical means for the subsequent extension of the measurement of radians in the coastal area and improving the accuracy of the external test data.

In this paper, the demand for high-precision correction of atmospheric refraction error of low-elevation sea-level radio waves is measured in the observation and control of the spacecraft in the coastal area. The influence of sea surface roughness on the evaporation waveguide under the gust disturbance is considered. Based on the Pierson-Moscowitz gravity The Monte-Carlo method is used to generate three-dimensional random rough sea surface. The variation law of atmospheric refractive index in the environment of radio wave propagation is described accurately. A modified method of precision atmospheric refraction based on Monin-Obukhov similarity theory is proposed.

Domestic and foreign research status: Since World War II foreign scholars through the atmospheric waveguide theory, low-altitude atmospheric waveguide detection and other research, the marine environment in the atmospheric waveguide is divided into surface waveguide, floating waveguide and evaporation waveguide 3 categories. Patterson and other statistics summed up the global sea area atmospheric waveguide occurred in the law. The Hopfield model, the Saastamoinen model and the Minimum Operational Performance Standards (MOPS) model, as well as the ray tracing method and the sounding rocket.

The research on the propagation of radio waves in atmospheric waveguide is mainly from the 1990s, mainly based on the parabolic equation theory and the ray tracing theory. The Chinese Institute of Radio Propagation has carried out a large number of theoretical and experimental studies, such as ionospheric radio error correction based on microwave radiometer, Inversion of atmospheric refractive index based on GNSS, and so on.

References

1. Han X (2016) New method for the atmospheric refraction error correction in the range. Electron Measur Technol 39(5):P57–P60
2. Jiao P, Zhang Z (2007) Radar environment and wave propagation characteristics (pp 2–3). Electronic Industry Press, Beijing
3. Liu C, Pan Z, Guo L (1996) Statistical analysis of probability and characteristics of low-altitude atmospheric waveguide in China. J Radio Sci 11(2):60–66
4. Li L, Zhang H, Kan R (2014) Application of Monin-Obukhov similarity theory in evaporation duct PJ mode. Mod Defence Technol 42(2):P89–P94
5. Huang X, Zhang Y, Luo N (2007) Numerical simulation and experimental validation of electromagnetic waves trapped propagation in atmospheric ducts environments. J Microwaves 23:P177–184
6. Nghiem SV, Li FK, Neumann G (1997) The dependence of ocean backscatter at Ku-Band on oceanic and atmospheric parameters. IEEE Trans Geosci Remote Sens 35(3):P581–P600
7. Thorsos EI (1988) The validity of the kirchhoff approximation for rough surface scattering using a gaussian roughness spectrum. J Acoust Soc Am 83(1):78–92
8. Dai F (1998) The refractivity models in the marine atmospheric surface layer and their applications in the evaporation duct analysis. J Radio Sci 13(3):P280–P286

9. Kuttler JR, Dockery GD (1991) Theoretical description of the parabolic approximation fourier split-step method of representing electromagnetic propagation in the troposphere. Radio Sci 26(2):P381–P393
10. Mao C, Qiu Z, Liu Z (2013) Monte-carlo simulation of the random rough ocean surface. Ship Sci Technol 35(10):25–28

A Novel Triple-Frequency Cycle Slip Detection and Correction Method for BDS

Ye Tian, Lixin Zhang and Qibing Xu

Abstract A novel triple-frequency cycle slip detection and correction method for BDS is proposed to detect and correct cycle slips when the ionosphere is active. Firstly, two sets of phase combinations whose sum equals zero are selected, and the corresponding pseudorange coefficients are obtained by the optimization algorithm, which effectively reduces the ionospheric amplification factor. Then, a set of phase combinations whose sum not equal to zero is adopted to reduce the condition number of coefficient matrices, meanwhile, the ionospheric delay variation between the epochs of this combination data is estimated and corrected. Thus, three linear independence sets of geometry-free and ionosphere-free pseudorange-phase combinations are constructed. Finally, the covariance matrix of the combined observations is obtained by employing observation error and ionospheric correct error, accordingly, the search space and objective function of cycle correction are constructed, which improves the correction accuracy. Based on BDS triple-frequency observations, the experiment results show that the proposed method possesses a good cycle slip detection and correction performance under active ionospheric situation.

Keywords BDS · Three-frequency cycle slip detection and correction
Geometry-free and ionosphere-free · Covariance matrix of observations

1 Introduction

Carrier phase observations are always used in precise GNSS applications and accurate carrier phase observation is the key to precise GNSS applications [1]. Due to interruption of the GNSS transmitted signal, low signal-to-noise ratio and some other reasons, a cycle slip presents a sudden jump of phase ambiguity by an integer number [2]. Detection and correction of cycle slips are necessary before the carrier

Y. Tian (✉) · L. Zhang · Q. Xu
Academy of Space Electrical Information Technology, Xi'an 710100, China
e-mail: tianye_504@163.com

J. Sun et al. (eds.), *China Satellite Navigation Conference (CSNC) 2018 Proceedings*, Lecture Notes in Electrical Engineering 498,
https://doi.org/10.1007/978-981-13-0014-1_37

phases are used as high-precision measurements. At present, 3 or more than 3 carrier frequencies are used in GNSS, and it is a common and effective method to construct the multi-frequency linear combination observation for cycle slips detection and correction [2].

BDS has been able to provide triple-frequency signals. Cycle slip detection using multi-frequency BDS observations has been investigated for a long time. Based on the principle of ionospheric amplification factor and noise minimization, Ref. [3] selected the combination of geometric phase combination and pseudorange-phase combination to detect cycle slips. Reference [4] use wide-lane pseudorange-phase combinations with low ionosphere value as the first and second detectable amount, geometry-free phase combination with low ionosphere value as third detectable amount to detect cycle slip. Due to the current method is difficult to detect cycle slip when the ionosphere is active, a new triple-frequency TurboEdit method for weakening the ionosphere influence is proposed in Ref. [5]. Reference [6] selected two geometry-free phase combinations and one geometry-free pseudorange minus phase linear combination to detect and correct cycle slip in real time. In Ref. [7], a systematic study of BDS multi-frequency linear combination is carried out, and different optimal linear combinations are selected for long and short baselines. In Ref. [8], a robust polynomial adaptive algorithm is proposed for the small cycle of BDS GEOs at low elevation angles, which allows identification of such small cycle slips with high reliability. In above reference, Cycle slips detection and correction methods are studied in detail, but the method of Refs. [3–6] has a large condition number of coefficient matrix. The methods in the above reference don't fully consider the covariance of observations, which simplifies the search space and cause some correction errors.

In this paper, by choosing the two sets of coefficients in the group S_0 [7], the corresponding pseudorange coefficients are solved by using the optimization algorithm firstly. A set of coefficients is selected in the group S_1, meanwhile, the ionospheric delay variation is eliminated. Three sets of linearly independent, geometric-free ionospheric-free pseudorange-phase combinations are formed, which has better cycle slip detection capability. Through the covariance matrix of the combined observations, a corresponding search space is formed, and the correct cycle slip is searched under the influence of the weight coefficient to minimize the residual of the combined observation. Finally, the method is verified by the BDS triple-frequency data.

2 BDS Triple-Frequency Cycle Slip Detection Method

BDS now has the service capabilities in the Asia Pacific region. Currently the satellites in orbits are able to broadcast triple-frequency navigation signals, respectively, B1: 1561.098 MHz, B2: 1207.14 MHz, B3: 1268.52 MHz. Generally, the frequencies are arranged in descending order, which the three frequencies f_1, f_2, f_3 correspond to B1, B3 and B2 respectively.

2.1 Cycle Slip Detections Using Triple-Frequency Geometric-Free Ionospheric-Free Pseudorange-Phase Combinations

The carrier phase observation in any frequency at epoch t_0 is expressed as:

$$\lambda_i \varphi_i(t_0) = \rho(t_0) + t_r(t_0) - t^s(t_0) + T(t_0) + \lambda_i N_i(t_0) - \eta_i I_1(t_0) + \lambda_i \varepsilon_{\varphi_i}(t_0) \quad (1)$$

where, λ is carrier wavelength, φ is carrier phase, ρ is satellite-to-receiver geometric distance, t_r is receiver clock error, t^s is satellite clock error, T is tropospheric delay, I_1 is ionospheric delay of the B1 carrier phase, N is integer ambiguity, η_i is ionosphere amplification factor, ε_φ is phase noise, subscripts i represent signals of different frequencies. Pseudorange at epoch t_0 is expressed as:

$$P_l(t_0) = \rho(t_0) + t_r(t_0) - t^s(t_0) + T(t_0) + \eta_l I_1(t_0) + \varepsilon_{P_l}(t_0) \quad (2)$$

where, ρ, t_r, t^s, T have the same meaning with (1), η_l is ionospheric amplification factor, ε_P is pseudorange noise, the subscript l represents different frequencies. Let the combination coefficients of the triple-frequency carrier phase be i, j, k and the combination coefficients of the triple-frequency pseudorange be l, m, n ($l, m, n \in R$, $l + m + n = 1$). The combination of the phase and pseudo-range of the triple-frequency is expressed as:

$$\begin{aligned} \lambda_{ijk}\varphi_{ijk} &= \lambda_{ijk}(i\varphi_1 + j\varphi_2 + k\varphi_3) \\ &= \rho + T + \lambda_{ijk}N_{ijk} - \eta_{ijk}I_1 + T + (\delta_s - \delta_r) + \lambda_{ijk}\varepsilon_{ijk} \end{aligned} \quad (3)$$

$$\begin{aligned} P_{lmn} &= lP_1 + mP_2 + nP_3 \\ &= \rho + T + \eta_{lmn}I_1 + T + (\delta_s - \delta_r) + \varepsilon_{lmn} \end{aligned} \quad (4)$$

where, the ionospheric amplification factors are:

$$\eta_{ijk} = \frac{\lambda_{ijk}}{\lambda_1}\left(i + j\frac{\lambda_2}{\lambda_1} + k\frac{\lambda_3}{\lambda_1}\right) \quad (5)$$

$$\eta_{lmn} = l + m\left(\frac{\lambda_2}{\lambda_1}\right)^2 + n\left(\frac{\lambda_3}{\lambda_1}\right)^2 \quad (6)$$

Here, the first-order ionospheric delay terms are mainly discussed. The influences of second-order terms and subsequent terms have little effect on the final result and can be ignored [9]. Differencing (3) and (4), the combined ambiguity of pseudorange-phase can be expressed as:

$$N_{lijk,lmn} = \varphi_{ijk} - \frac{P_{lmn}}{\lambda_{ijk}} + \eta_{ijk,lmn} I_1 + \varepsilon \tag{7}$$

$$\eta_{ijk,lmn} = (\eta_{ijk} + \eta_{lmn}) / \lambda_{ijk} \tag{8}$$

where, $N_{ijk,lmn}$ is integer ambiguity, $\eta_{ijk,lmn}$ is ionospheric amplification factor and ε is noise. Difference (7) can be obtained difference of ambiguities between adjacent epochs, that is, the cycle slip detection value:

$$\Delta N_{ijk,lmn} = \Delta\phi_{ijk} - \frac{\Delta P_{lmn}}{\lambda_{ijk}} + \eta_{ijk,lmn} \Delta I_1 + \Delta\varepsilon' \tag{9}$$

Assuming that the standard deviation of the carrier phase noise of triple-frequency is same as σ_ϕ and the standard deviation of the pseudorange noise at the triple-frequency is same as σ_P, then the standard deviation of ambiguity is (9):

$$\sigma_{\Delta N_{lmn,ijk}} = \sqrt{2} \sqrt{(i^2 + j^2 + k^2)\sigma_\phi^2 + (l^2 + m^2 + n^2)\sigma_P^2} \Big/ \lambda_{ijk}^2 \tag{10}$$

Make three times the standard deviation of ambiguity estimation (confidence level of 99.7%) as the threshold of cycle slip judgment, and when the following formula holds, it is determined that cycle slip has occured.

$$i\Delta\phi_1 + j\Delta\phi_2 + k\Delta\phi_3 - \frac{l\Delta P_1 + m\Delta P_2 + n\Delta P_3}{\lambda_{ijk}} > 3\sigma_{\Delta N_{lmn,ijk}} \tag{11}$$

2.2 *Selection of Triple-Frequency Geometric-Free and Ionosphere-Free Pseudorange-Phase Coefficient*

From (7), (9), (11), when the change of ΔI_1 is large and the ionospheric amplification factor is large, the ionospheric amplification factor $\eta_{ijk,lmn}$ affect the result of the cycle slip detection. The standard deviation of the ambiguity estkimation $\sigma_{\Delta N_{lmn,ijk}}$ also has an impact on the accuracy of cycle slip detection. Therefore, it is necessary to select the appropriate parameters for pseudorange-phase combination to reduce the standard deviation of ambiguity estimation and the ionospheric amplification factor.

2.2.1 Method of Selecting Pseudorange-Phase Coefficient

From (5), (6), (8), the ionospheric amplification factor can be expressed as:

$$\eta_{ijk,lmn} = i\frac{1}{\lambda_1} + j\frac{\lambda_2}{\lambda_1^2} + k\frac{\lambda_3}{\lambda_1^2} + l\frac{1}{\lambda_{ijk}} + m\left(\frac{\lambda_2}{\lambda_1}\right)^2\frac{1}{\lambda_{ijk}} + n\left(\frac{\lambda_3}{\lambda_1}\right)^2\frac{1}{\lambda_{ijk}} \tag{12}$$

As can be seen from (10), when the phase coefficient is fixed, the smaller $l^2+m^2+n^2$ is, the smaller standard deviation of the ambiguity estimation. From the inequality $l^2+m^2+n^2 \geq 3lmn$ and $l+m+n=1$, we can see when $l=m=n=1/3$, $l^2+m^2+n^2$ has the minimum value, so let $l=m=n=1/3$, we can get the smallest $\sigma_{\Delta N_{lmn,ijk}}$.

Although when $l=m=n=1/3$, $\sigma_{\Delta N_{lmn,ijk}}$ has the minimum value, most of the references use this set of pseudorange coefficients. By analysing the Eq. (10) and the cycle slip correction processing, the influence of the ionosphere on the detection results is considerable. If the ionospheric delay can't be eliminated, the detection and correction of cycle slip will be affected. While the standard deviation of ambiguity estimation can be accurately corrected by search algorithm as long as the deviation is within a certain range. Therefore, the following optimization of pseudorange coefficients is given to further eliminate the ionospheric delay.

$$\begin{aligned} &\min_{l,m,n} \left\| \eta_{ijk,lmn} \right\|_2^2 \\ &s.t. \quad l+m+n=1 \quad \sigma_{\Delta N_{lmn,ijk}} < \sigma_{\Delta N_{\min}} + \omega \end{aligned} \tag{13}$$

where, the phase coefficient is fixed and $\sigma_{\Delta N\_\min}$ is the result when $l=m=n=1/3$. ω is used to limit the standard deviation of the ambiguity estimation, and being adjusted according to the pseudorange noise, the general empirical value is 0.001–0.01.

According to the sum of the coefficients, the phase combination coefficients are classified [7]. Let $S=i+j+k$, S_x represent the combination of $i+j+k=\pm x$. In the following table, the appropriate phase combination coefficients are chosen in the group S_0 and S_1, and the corresponding pseudorange coefficients are calculated by using the above-mentioned pseudorange coefficients optimization algorithm, compared with the pseudorange coefficients given in [5] and [10], and also compared with the case $l=m=n=1/3$. The standard deviations of the ambiguity estimation and ionospheric amplification factor are mainly compared. The subscript 1 represents the optimization method in this paper, the subscript 2 represents the method in the Refs. [5, 10], and the subscript 3 represents the case when $l=m=n=1/3$. The pseudorange noise is 0.3 m and the phase noise is 0.01 cycle.

It can be seen from Table 1 that the proposed method can further reduce the ionospheric amplification factor. In the above table, the coefficients (0, 1, −1) and (1, −2, 1) are selected as the two sets of cycle slip detection combinations. In order to constitute three linear independent equations and reduce the condition number of the coefficient matrix, another set of phase coefficients are selected in the S_1

Table 1 The optimal combination in S_0 region

i	j	k	l	m	n	λ	η_1	η_2	η_3	$3\sigma_{\Delta N1}$	$3\sigma_{\Delta N2}$	$3\sigma_{\Delta N3}$
0	1	−1	0.020517	0.425042	0.554441	4.88	5.27×10^{-9}	-1.46×10^{-8}	0.04	0.1918	0.1918	0.1620
1	−2	1	0.750578	0.208140	0.041282	1.30	1.48×10^{-10}	2.56×10^{-8}	0.20	0.7726	0.7726	0.5762
1	−4	3	1.576600	0.035441	0.541159	2.76	-5.32×10^{-8}	4.30×10^{-5}	0.28	0.7975	0.7975	0.3427
1	−1	0	0.597330	0.254020	0.148650	1.02	1.77×10^{-8}	2.51×10^{-7}	0.16	0.8293	0.8293	0.7197
1	0	−1	0.497229	0.283998	0.218773	0.85	2.05×10^{-7}	-4.10×10^{-6}	0.13	0.9231	0.9231	0.8697
1	−5	4	3.597093	0.596986	2.000107	6.37	1.21×10^{-9}	-2.02×10^{-7}	0.32	0.8751	0.8751	0.2982
1	−6	5	11.786113	4.017404	8.768709	20.93	-5.26×10^{-9}	1.01×10^{-6}	0.36	0.9844	0.9844	0.3359

group. Subscript 1 represents the optimization method proposed in this paper, and subscript 2 is the case when $l = m = n = 1/3$.

It can be seen from Table 2 that although the optimized pseudorange coefficients can greatly reduce the ionospheric amplification factor, the standard deviation of the ambiguity estimation becomes very large. Therefore, the set of $l = m = n = 1/3$ is used for the S_1 group. (−4, 3, 2) is selected from S_1 group. This set of coefficient has longer wavelength, the standard deviation of ambiguity estimation is smaller. However, the ionospheric amplification factor of (−4, 3, 2) is larger, which needs to eliminate the influence of ionospheric delay.

2.2.2 Method of Eliminating Ionospheric Delay of S_1

To eliminate the ionospheric delay, we need to estimate the ionospheric delay variation between adjacent epochs at the B1 frequency. We can calculate ΔI_1 and its standard deviation using Eq. (14). There is no cycle slip in the phase observation [10].

$$\Delta I_1 = \frac{\lambda_i \Delta\varphi_i - \lambda_j \Delta\varphi_j}{\eta_j - \eta_i}, \sigma(\Delta I_1) = \frac{2\sigma_\varphi}{|\eta_j - \eta_i|} \tag{14}$$

When there are cycle slips in the phase observation, there is a difference ΔN between epochs. ΔN_i and ΔN_j between the frequencies can't offset each other, which have a greater impact on the ΔI_1 estimation. When three frequency exist the same cycle slip ΔN, the first two sets of coefficients can't detect the cycle slip. The ionospheric quadratic difference defined by (15) can be used to detect it. Due to the second epoch difference of the ionospheric delay is very smooth, if there is a large deviation, we can consider triple-frequency exist the same cycle slip.

$$\nabla\Delta I_1(\alpha) = \Delta I_1(\alpha) - \Delta I_1(\alpha - 1) \tag{15}$$

When any one of $\Delta N_{(0,1,-1)}$, $\Delta N_{(1,-2,1)}$, and $\nabla\Delta I_1(\alpha)$ exceeds threshold, it is determined that cycle slips have occurred. Therefore, ΔI_1 of the current epoch can't be calculated using Eq. (14) and can be corrected by the following equation.

$$\Delta I_1(\alpha) = \Delta I_1(\alpha - 1) + \nabla\Delta\bar{I}_1(\alpha - 1) \tag{16}$$

where $\nabla\Delta\bar{I}_1$ is the smoothed value of $\nabla\Delta I_1$ without cycle slips. The calculation equation is expressed as:

$$\nabla\Delta\bar{I}_1(\alpha) = \theta \cdot \nabla\Delta I_1(\alpha) + (1 - \theta) \cdot \nabla\Delta I_1(\alpha - 1) \tag{17}$$

θ is the weight factor. The ionospheric delay of the S_1 group coefficients (−4, 3, 2) can be corrected by using the calculated ΔI_1.

Table 2 The optimal combination in S_1 region

i	j	k	l	m	n	λ	η_1	η_2	$3\sigma_{\Delta N1}$	$3\sigma_{\Delta N2}$
−3	−3	7	149.196238	45.575365	104.620873	−7.71	2.18×10^{-8}	12.11	31.0028	0.3601
−4	4	1	152.981506	−46.031951	105.949556	8.14	-1.67×10^{-7}	11.71	29.9740	0.2599
−4	3	2	228.222347	65.007206	164.215140	−12.21	1.16×10^{-7}	11.75	30.0816	0.2363
−3	2	6	256.260891	−71.185352	184.075539	13.32	-7.02×10^{-9}	12.07	30.9075	0.3021
−3	0	4	39.898772	−11.431826	−27.466946	2.06	-1.22×10^{-7}	11.99	30.6957	0.4145

3 A New Cycle Slip Correction Method

Three pseudorange-phase combinations are used to construct cycle slip detection with geometry-free and ionosphere-free, and the above method is used to correct the ionospheric delay of S_1 group observations. The combined observations can be obtained from:

$$\mathbf{L} = \mathbf{C}\mathbf{L}' \tag{18}$$

$$\mathbf{C} = \begin{bmatrix} i_1 & j_1 & k_1 & \frac{-l_1}{\lambda_{i_1 j_1 k_1}} & \frac{-m_1}{\lambda_{i_1 j_1 k_1}} & \frac{-n_1}{\lambda_{i_1 j_1 k_1}} \\ i_2 & j_2 & k_2 & \frac{-l_2}{\lambda_{i_2 j_2 k_2}} & \frac{-m_2}{\lambda_{i_2 j_2 k_2}} & \frac{-n_2}{\lambda_{i_2 j_2 k_2}} \\ i_3 & j_3 & k_3 & \frac{-l_3}{\lambda_{i_3 j_3 k_3}} & \frac{-m_3}{\lambda_{i_3 j_3 k_3}} & \frac{-n_3}{\lambda_{i_3 j_3 k_3}} \end{bmatrix} \tag{19}$$

$$\mathbf{L}' = \begin{bmatrix} l_{\varphi_1} & l_{\varphi_2} & l_{\varphi_3} & l_{P_1} & l_{P_2} & l_{P_3} \end{bmatrix}^T \tag{20}$$

where, the phase coefficients (i_1, j_1, k_1) and (i_2, j_2, k_2) correspond to (0, 1, −1) and (1, −2, 1) in S_0 group, and the corresponding pseudorange coefficients are in Table 1. In this equation, The phase coefficient (i_3, j_3, k_3) corresponds to (−4, 3, 2) in S_1 group and the pseudorange coefficient is $l = m = n = 1/3$. l_{φ_i} and l_{P_i} are phase and pseudorange observations in $\mathbf{L}'$ respectively. The relationship between the combination coefficient and the cycle slip valuation is expressed as:

$$\mathbf{A}\mathbf{X} = \mathbf{L} \tag{21}$$

$$\mathbf{A} = \begin{bmatrix} i_1 & j_1 & k_1 \\ i_2 & j_2 & k_2 \\ i_3 & j_3 & k_3 \end{bmatrix} \mathbf{X} = \begin{bmatrix} \Delta N_1 & \Delta N_2 & \Delta N_3 \end{bmatrix}^T \tag{22}$$

where, the coefficient matrix $\mathbf{A}$ is reversible, and the cycle slip can be determined by $\mathbf{X} = \mathbf{A}^{-1}\mathbf{L}$. But for the first and second observations, in order to reduce ionospheric amplification factor, the standard deviation of ambiguity estimation is increased. Ambiguity estimation of the third detection amount is affected by the error of ionospheric delay estimation. Therefore, it is not easy to correct cycle slip by calculating $\mathbf{X} = \mathbf{A}^{-1}\mathbf{L}$ and rounding.

Assuming that the covariance matrix of the combined observation $\mathbf{L}$ is $\mathbf{Q}$ and the third combined observation is also affected by the variance of the ionospheric delay estimation, we consider it into the covariance matrix, then $\mathbf{Q}$ is defined as follows:

$$\mathbf{Q} = [\mathbf{C}\,\mathbf{e}_3]\mathbf{Q}_0[\mathbf{C}\,\mathbf{e}_3]^T \tag{23}$$

where $\mathbf{Q}_0 = diag(\sigma^2_{\varphi_1}, \sigma^2_{\varphi_2}, \sigma^2_{\varphi_3}, \sigma^2_{P_1}, \sigma^2_{P_2}, \sigma^2_{P_3}, \sigma^2_{\Delta I_1})$ $\mathbf{e}_3 = \begin{bmatrix} 0 & 0 & 1 \end{bmatrix}^T$, σ_{φ_i}, σ_{P_i}, $\sigma_{\Delta I_1}$ denote the standard deviation of phase and pseudorange and ionospheric correct error respectively. In order to determine the integer cycle slip $\mathbf{X}_N$, the corresponding search space is set up as:

$$(\mathbf{X}_N - \hat{\mathbf{X}})^T \mathbf{Q}^{-1} (\mathbf{X}_N - \hat{\mathbf{X}}) < \chi \tag{24}$$

The threshold χ is generally based on the observation noise. The target equation is expressed as:

$$(\mathbf{A}\mathbf{X}_N - \mathbf{L})^T \mathbf{Q}^{-1} (\mathbf{A}\mathbf{X}_N - \mathbf{L}) = \min \tag{25}$$

Under the influence of weight coefficient, the correct cycle slip minimizes the residuals of $\mathbf{A}\mathbf{X}_N$ and combined observations $\mathbf{L}$.

4 Experimental Analysis

The experiment adopts the data in JFNG observation station ($30°31'N, 114°29'E$) at a large magnetic storm on December 21, 2015, the satellite elevation cutoff angle is set to 15°. The geomagnetic Dst index from 0 to 6 h on that day was abnormal, indicating that a large magnetic storm occurred. Using the above method, the C04 satellite data (without cycle slips) are processed. As can be seen from Fig. 1, the large magnetic storms do not affect the detection value due to the elimination of the ionospheric effects.

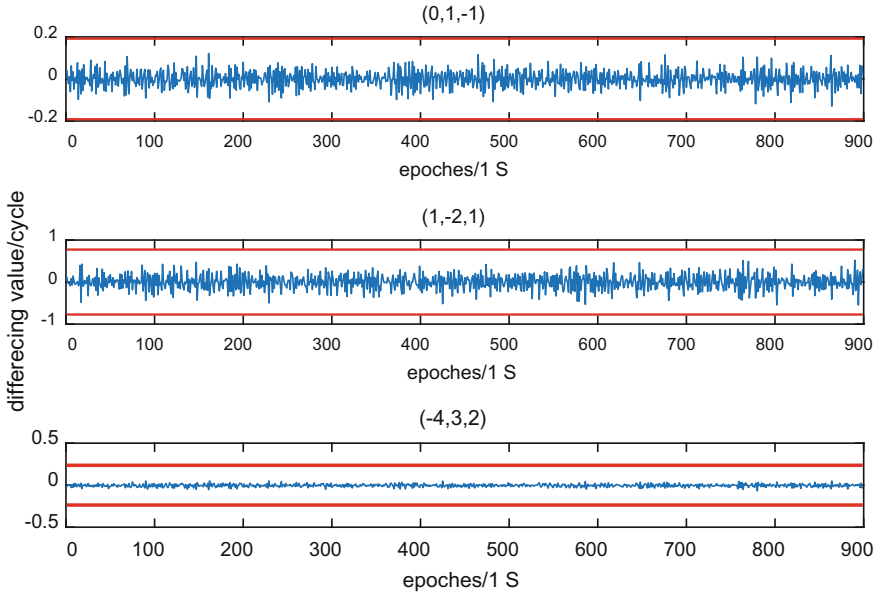

Fig. 1 Detection of three groups when no cycle slips occur

Figure 2 shows the results of four sets of special cycle slips. The special cycle slips include the cycle slips which are not sensitive to each set of coefficients and the small jumps which occur simultaneously in triple-frequency. As can be seen from Fig. 2, when a group of coefficients is not sensitive to the cycle slips, other coefficients can detect cycle slip. For $\Delta N_1 = \Delta N_2 = \Delta N_3 = 1$ this type of cycle slip, coefficients in S_1 group can be detected.

In order to further verify the performance of this cycle slip detection and correction method, different cycle slips combinations are added in different epochs of carrier phase observations of C08 and C12 satellites, including small cycle slips, large cycle slips and special cycle slips. As can be seen from Table 3, this method eliminates the effect of the ionospheric delay between epochs and can detect and correct the cycle slip. When some cycle slips occur, it is not correct to use the $\mathbf{X} = \mathbf{A}^{-1}\mathbf{L}$ directly to get the cycle slips. Using the method mentioned in this paper to search the optimal value in a certain region can avoid the problems caused by pseudorange, phase and ionospheric repair errors.

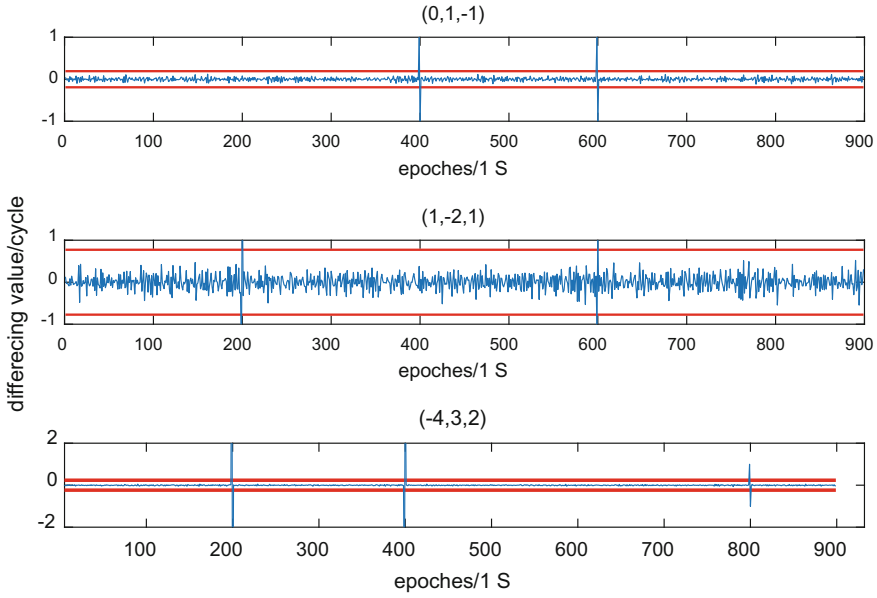

Fig. 2 Detection of three groups when special cycle slips occur

Table 3 Cycle slips detection and correct results

Satellite number	Epochs	Simulation cycle slips	$\Delta N_{(0,1,-1)}$	$\Delta N_{(1,-2,1)}$	$\Delta N_{(-4,3,2)}$	$\mathbf{A}^{-1}\mathbf{L}$	$\|\mathbf{AX}_N - \mathbf{L}\|^2_{\mathbf{Q}^{-1}}$	Search results	$\min\|\mathbf{AX}_N - \mathbf{L}\|^2_{\mathbf{Q}^{-1}}$
	60	(1, 0, 0)	−0.0262	0.7700	−3.9892	(0, −1, −1)	0.3517	(1, 0, 0)	0.0130
	150	(1, 1, 1)	0.0630	0.2749	0.9843	(2, 2, 2)	0.3675	(1, 1, 1)	0.0185
C08	310	(−3, 2, 1)	1.0037	−6.0796	19.9819	(−3, 2, 1)	0.0014	(−3, 2, 1)	0.0014
	420	(2, 2, 1)	1.0444	−1.0967	−0.0224	(2, 2, 1)	0.0022	(2, 2, 1)	0.0022
	550	(5, 8, 7)	1.0654	−4.0397	17.9885	(5, 8, 7)	0.0006	(5, 8, 7)	0.0006
	80	(0, 1, 1)	−0.0353	−1.2825	4.9998	(−2, 0, 0)	3.1367	(0, 1, 1)	0.0189
	170	(−1, −1, −1)	0.0515	0.0098	−1.0296	(−1, −1, −1)	0.0004	(−1, −1, −1)	0.0004
C12	350	(−1, 0, 1)	−0.9696	−0.0630	6.0065	(0, 0, 1)	5.5673	(−1, 0, 1)	0.0008
	460	(2, 1, 1)	−1.0415	2.1533	−1.0123	(2, 1, 2)	0.0064	(2, 1, 1)	0.0064
	600	(2, 5, 2)	3.0066	−6.0911	10.9947	(2, 5, 2)	0.0019	(2, 5, 2)	0.0019

5 Conclusions

A new triple-frequency cycle slip detection and correction method for BDS is proposed when the ionosphere is active. Firstly, two sets of phase combinations are selected from group S_0, and the corresponding pseudorange coefficients are obtained by the optimization algorithm, which effectively reduces the ionospheric amplification factor. Then, a set of phase combinations is selected from group S_1 to reduce the condition number of coefficient matrices, meanwhile, the ionospheric delay variation between the epochs of this combination data is estimated and corrected. Thus, three linear independence sets of geometry-free and ionosphere-free pseudorange-phase combinations are constructed. Finally, the covariance matrix of the combined observations is obtained by using observation and ionospheric correct error, which is employed to establish searching space. Under the influence of weight coefficient, the correct cycle slip is searched to minimize the residual of the combined observation. At last, the performance of proposed method is verified by BDS triple-frequency data. When the ionosphere is active, this method possesses a good cycle slip detection and correction performance.

References

1. Zhang X, Zeng Q, He J, Kang C (2017) Improving TurboEdit real-time cycle slip detection by the construction of threshold model. Geomatics and Information Science of Wuhan Univers 42(3):285–292
2. Cocarf M, Bourgon S, Kamali O et al (2008) A systematic investigation of optimal carrier-phase combinations for modernized triple-frequency GPS. J Geodesy 82(9):555–564
3. Huang L, Song L, WANG Y et al (2012) BeiDou triple-frequency geometry-free phase combination for cycle-slip detection and correction. Acta Geodaet Cartographica Sinica 41 (5):763–768
4. Yao Y, Gao J, Wang J et al (2014) Real-time detection and repair for compass triple-frequency carrier phase observations. J China Univer Min Technol 43(6):1140–1148
5. Huang L, Zhai G, Ouyang Y, et al (2015) Triple-frequency TurboEdit cycle-slip processing method of weakening ionospheric activity. Acta Geodaet Cartographica Sinica 44(8):840–847
6. Huang L, Lu Z, Zhai G et al (2015) A New Triple-frequency cycle slip detecting algorithm validated with BDS data. GPS Solutions 20(4):1–9
7. Zhang XH, He XY (2015) BDS triple-frequency carrier-phase linear combination models and their characteristics. Sci China Earth Sci 58(6):896–905
8. Ju B, Gu D, Chang X et al (2017) Enhanced cycle slip detection method for dual-frequency BeiDou GEO carrier phase observations. Gps Solutions 1–12
9. Banville S, Langley RB (2013) Mitigating the impact of ionospheric cycle slips in GNSS observations. J Geodesy 87(2):179–193
10. Wang X, Liu W, Li B et al (2016) Detection and repair of cycle slips for undifferenced bds triple-frequency observations. J Nat Univ Defense Technol 38(3):12–18

Stratified Weighting Method Based on Posterior Residual Error

Fangchao Li, Jingxiang Gao, Zengke Li, Yifei Yao, Ren Wang and Ruoxi Li

Abstract In order to enhance positioning accuracy and reliability, improve data utilization, improve the success rate of epoch result, a stratified weighting algorithm based on posterior residual error was designed for multi-GNSS. The algorithm can greatly improve reliability, accuracy and the success rate of epoch result without affecting positioning accuracy. Firstly, the GNSS date to be processed was solved based on weight allocated by priori information, then the system weight is allocated by posterior residual error of above results of each system, and this is the first layer weight allocation. Then the weight of satellite type is allocated by posterior residual error of each type satellite, and this is the second layer weight allocation. Then satellites' weight is allocated by residual residuals of each single satellite and this is the third layer weight allocation. Finally, stochastic model matrix is determined by multiplying above results, and the least square is used to process GNSS data based on the stochastic model. The algorithm is validated by 11 IGS stations date, and the result shows that it can increase hypothesis-test pass rate to more than 99% of dual-system BDS/GPS and BDS/GLO, triple-system BDS/GPS/GLONASS without affecting positioning accuracy, and it could get a similar effect for single-system BDS without the first layer weight allocation.

Keywords Stratified weighting · Hypothesis-test pass rate · Multi-GNSS Posterior residual error

F. Li · J. Gao (✉) · Z. Li · R. Wang · R. Li
School of Environment Science and Spatial Inofrmatics, China University of Mining and Technology, Xuzhou, Jiangsu 221116, China
e-mail: jxgao@cumt.edu.cn

Y. Yao
College of Water Resources and Architectural Engineering, Northwest A&F University, Yangling 712100, China

J. Sun et al. (eds.), *China Satellite Navigation Conference (CSNC) 2018 Proceedings*, Lecture Notes in Electrical Engineering 498,
https://doi.org/10.1007/978-981-13-0014-1_38

1 Introduction

After GPS and GLONASS, BDS II has achieved networking in Asia Pacific after launching 14 satellites, and BDS III has launched satellites in November 2017 and plans to achieve global networking by 2020. The BDS III is composed of 3 GEO (geostationary orbit satellite), 3 IGSO (inclined geosynchronous satellite orbit), 24 MEO (medium earth orbit) and other reserved satellites, and BDS is the only GNSS with three hybrid orbits in world [1]. Meanwhile, GALIEO, a new generation of civilian GNSS, has launched 18 satellites by European, and plans to realize global deployment by 2019. Multi-GNSS could provide large redundant information for error detection and processing, which could improve positioning accuracy and reliability, so multi-GNSS and multi observation is a trend of navigation and positioning [2] Meanwhile different observation types and frequencies bring different observation precision, and it is necessary to use suitable stochastic model for observation when using least square or Kalman filtering to process data.

At present, stochastic model used in multi-GNSS is relatively simple, and prior information is often used to construct stochastic model matrix, such as elevation model and the signal to noise ratio (SNR) model. It's most widely used model in GNSS is satellite elevation stochastic model, which is also used in four famous GNSS software. The Bernese GNSS software developed by University of Bern for precise positioning and orbit determination uses cosine function model [3]. The GAMIT GNSS software developed by Massachusetts Institute of Technology (MIT) and Scripps Institution of Oceanography(SIO) for calculation ultra-long baseline uses sine function model [4]. The Position and Navigation Date Analysis (PANDA) software developed by Wuhan University for precise positioning and orbit determination uses 30 degrees as dividing line for building stochastic model matrix [5]. If satellite altitude angle is greater than 30 degrees, weight matrix is unit array, otherwise, weight allocation is designed by sine function. There are also some other stochastic models based on satellite elevation angle, such as exponential function model designed by Barnes [6]. The model based on satellite elevation angle can improve positioning accuracy obviously compared with equal weight model, but it is difficult to reflect true quality of observation directly. In order to reflect true quality, domestic and foreign experts and scholars have proposed a variety of VCE (variance component estimation). MINQUE (Minimum norm quadratic unbiased), HELMERT (Helmert VCE) and BIQUE (best invariant quadratic unbiased estimation) are most widely used in the course of GNSS data processing [7–9]. Yu deduced rigorous formula of HELMERT VCE [10]. Wang studied L1/C1 iono-free combination (LC) stochastic model based on HELMERT VCE [11]. Amiri-simkooei studied zero-difference stochastic model based on LS (least square) [8]. There are also lots of studies about VCE by distinguishing GPS and BDS [12–14], and Li found there are significant differences in the magnitude of variance component and changing characteristics over time among three types of BDS orbit [15].

Although stochastic models based on prior information have been widely used, the information affects positioning precision is dynamic, which causes weight matrix could not reflect accuracy and reliability of observations. Residual error has been used in HELMERT VCE, but the relationship among observations in same system is neglected. We propose a stratified weighting algorithm based on posterior residual. In the algorithm, system weight allocation is determined by each system posterior error, then weight allocation among satellite types and satellites is determined by posterior error of each satellite. Finally, stochastic model matrix is determined by multiplying results above. This algorithm could dynamically update the weight of observation without any external information, and directly reflect observations accuracy, and greatly improve hypothesis-test pass rate.

2 Stratified Weighting Method Based on Posterior Residual Error of SPP

2.1 Pseudo-range SPP Theory

Time systems unification is foundation of GNSS high precision measurement. Although GPS, GLONASS and BDS all use international atomic time, the definition of time origin and the way of maintaining are different, which leads to a minor item except for integer multiple seconds between any two time systems. Because it requires integration to calculate the minor items, we often estimate the difference as a parameter when processing multi GNSS data. Time system can be unified after parameter estimation, and multi-GNSS SPP (single point positioning) date process can be written as follows:

$$\begin{aligned} P^{\mathrm{g}} &= \rho^{\mathrm{g}} + c\Delta t_{\mathrm{R}} - c\Delta t^{\mathrm{g}} + V_{\mathrm{ion}}^{\mathrm{g}} + V_{\mathrm{trop}}^{\mathrm{g}} + \delta\rho^{g} + \delta\rho_{\mathrm{mul}}^{\mathrm{g}} + \varepsilon^{\mathrm{g}} \\ P^{\mathrm{c}} &= \rho^{\mathrm{c}} + c\Delta t_{\mathrm{R}} + cT^{\mathrm{c}} - c\Delta t^{\mathrm{c}} + V_{\mathrm{ion}}^{\mathrm{c}} + V_{\mathrm{trop}}^{\mathrm{c}} + \delta\rho^{\mathrm{c}} + \delta\rho_{\mathrm{mul}}^{\mathrm{c}} + \varepsilon^{\mathrm{c}} \\ P^{\mathrm{r}} &= \rho^{\mathrm{r}} + c\Delta t_{\mathrm{R}} + cT^{\mathrm{r}} - c\Delta t^{\mathrm{r}} + V_{\mathrm{ion}}^{\mathrm{r}} + V_{\mathrm{trop}}^{\mathrm{r}} + \delta\rho^{\mathrm{r}} + \delta\rho_{\mathrm{mul}}^{\mathrm{r}} + \varepsilon^{\mathrm{r}} \end{aligned} \tag{1}$$

In the form, the superscript of g, r, c represents GPS, GLONASS, BDS, ρ represents geometric distance between satellite and receiver, P represents pseudo range observation, Δt_{R} represents receiver clock error, Δt^{g}, Δt^{r}, Δt^{c} represents satellite clock errors respectively, V_{ion} represents ionospheric delay, V_{trop} represents tropospheric delay, $\delta\rho$ represents distance error caused by satellite ephemeris errors, $\delta\rho_{\mathrm{mul}}$ represents multipath effect delay, ε represents other item correction.

Products of precise ephemeris and clock provided by GFZ (Helmholtz-Centre Potsdam-German Research Centre for Geosciences) is used for processing data. It can be considered that satellite orbit error and clock error have been eliminated, and multi-GNSS LC combination can be described as follows:

$$\begin{aligned} P_{\mathrm{IF}}^{\mathrm{g}} &= \rho^{\mathrm{g}} + c\Delta t_{\mathrm{R}} + V_{\mathrm{trop}}^{\mathrm{g}} + \varepsilon_{\mathrm{P_{IF}}}^{\mathrm{g}} \\ P_{\mathrm{IF}}^{\mathrm{c}} &= \rho^{\mathrm{c}} + c\Delta t_{\mathrm{R}} + cT^{\mathrm{c}} + V_{\mathrm{trop}}^{\mathrm{c}} + \varepsilon_{\mathrm{P_{IF}}}^{\mathrm{c}} \\ P_{\mathrm{IF}}^{\mathrm{r}} &= \rho^{\mathrm{r}} + c\Delta t_{\mathrm{R}} + cT^{\mathrm{r}} + V_{\mathrm{trop}}^{\mathrm{r}} + \varepsilon_{\mathrm{P_{IF}}}^{\mathrm{r}} \end{aligned} \tag{2}$$

In the form, P_{IF} represents LC of pseudo-range, $\varepsilon_{\mathrm{P_{IF}}}$ represents other errors.

2.2 *Stratified Weighting Method Based on Posterior Residual Error*

The construction time, maturity, orbit and clock accuracy of GNSS are different, and there are discrepancies in precision when one receiver receives signal rooted in different systems, which causes positioning accuracy of different system is different. There are great differences and similarity among each system, and accuracy of observation within same system is nearly. But the difference between system is greater than same satellite type, especially BDS, and BDS is only GNSS with three hybrid orbits in world. The differences among GEO, IGSO and MEO satellites is great in BDS system, which leads to different data processing strategies and observation precision, thus it is necessary to consider the differentia. Meanwhile, the launch time, orbit and environment of satellites are different, once observation environment becomes challengeable, it's difficult for positioning results to pass hypothesis-test. For this, we should consider similarities and differences among satellites.

Firstly, we design stochastic model matrices according to prior information and linearize location equation, which could be described as follows:

$$\begin{cases} \varepsilon_1 = \lambda_{11}X + \lambda_{12}Y + \lambda_{13}Z + \lambda_{14}\delta - \Delta_1 \\ \cdots \qquad\qquad \cdots \\ \varepsilon_n = \lambda_{n1}X + \lambda_{n2}Y + \lambda_{n3}Z + \lambda_{n4}\delta - \Delta_n \end{cases} \tag{3}$$

In the form, there are n kinds of observations, $\lambda_{ij}(i = 1 \cdots n, j = 1 \cdots 4)$ represents the coefficient of jth to be estimated parameters of ith type observation, Δ_i represents discrepancy of ith type, ε_i represents residuals of ith type, X, Y, Z, δ represents parameters to be estimated.

In the form, there are n kinds of observations totally, $\lambda_{ij}(i = 1 \cdots n, j = 1 \cdots 4)$ represents coefficient of jth parameters to be estimated of ith type observation, Δ_i represents discrepancy of ith type, ε_i represents residuals of ith type, X, Y, Z, δ represents parameters to be estimated.

It is assumed that all observations are independent with each other, and the weight of each kind of observations is $\vartheta_1, \cdots \vartheta_n$, and $\vartheta_{ij} = 0$ if $i \neq j$.

We assume as follows:

$$\varepsilon = \begin{bmatrix} \varepsilon_1 \\ \cdots \\ \varepsilon_n \end{bmatrix}, \lambda = \begin{bmatrix} \lambda_{11} & \cdots & \lambda_{14} \\ \cdots & \cdots & \cdots \\ \lambda_{n1} & \cdots & \lambda_{14} \end{bmatrix}, \vartheta = \begin{bmatrix} \vartheta_1 & 0 & 0 \\ 0 & \cdots & 0 \\ 0 & 0 & \vartheta_n \end{bmatrix}, \Delta = \begin{bmatrix} \Delta_1 \\ \cdots \\ \Delta_2 \end{bmatrix} \tag{4}$$

We can get following formula:

$$\xi = \lambda^T \vartheta \lambda = \lambda_1^T \vartheta_1 \lambda_1 + \cdots + \lambda_n^T \vartheta_n \lambda_n = \xi_1 + \cdots + \xi_n \tag{5}$$

In the formula, $\lambda_i = [\lambda_{i1}, \cdots, \lambda_{i4}]$

The solution of parameter to be estimated can be described as follow:

$$[X, Y, Z, \delta]^T = (\lambda^T \vartheta \lambda)^{-1} \lambda^T \vartheta \Delta = (\xi)^{-1} \zeta \tag{6}$$

Posterior residual weights are estimated as follow.

$$\varphi \hat{\vartheta} = W_\vartheta \tag{7}$$

In the formula, $\hat{\vartheta} = \begin{bmatrix} \hat{\vartheta}_{0_1}^2 & \hat{\vartheta}_{0_2}^2 & \cdots & \hat{\vartheta}_{0_n}^2 \end{bmatrix}$, $W_\vartheta = \begin{bmatrix} \varepsilon_1^T \vartheta_1 \varepsilon_1 & \varepsilon_2^T \vartheta_2 \varepsilon_2 & \cdots \varepsilon_n^T \vartheta_n \varepsilon_n \end{bmatrix}^T$,

$$\varphi = \begin{bmatrix} n_1 - 2tr(\xi^{-1}\xi_1) + tr(\xi^{-1}\xi_1) & tr(\xi^{-1}\xi_1\xi^{-1}\xi_2) & \cdots & tr(\xi^{-1}\xi_1\xi^{-1}\xi_n) \\ tr(\xi^{-1}\xi_1\xi^{-1}\xi_2) & n_2 - 2tr(\xi^{-1}\xi_2) + tr(\xi^{-1}\xi_2) & \cdots & \cdots \\ \cdots & \cdots & \cdots & \cdots \\ tr(\xi^{-1}\xi_1\xi^{-1}\xi_n) & \cdots & \cdots & n_n - 2tr(\xi^{-1}\xi_n) + tr(\xi^{-1}\xi_n) \end{bmatrix}$$

The solution of above equations can be written as follow:

$$\hat{\vartheta} = \varphi^{-1} W_\vartheta \tag{8}$$

It is inappropriate for weight allocation based on prior information at first, so it is necessary to iterate until the unit weight variance of each type observation is basically equal [16].

Firstly, initial weight matrix should be estimated by prior information, such as observations type and satellite elevation, which could be written as $\vartheta_1, \vartheta_2 \cdots \vartheta_n$. Then the first adjustment is carried out to get $\varepsilon_i^T \vartheta_i \varepsilon_i$, and residual error of each observation is calculated according to above process, and the unit weight variance of each type observation is obtained as $\hat{\vartheta}_{0_1}^2$. Then we can get stochastic model with formula $\hat{\vartheta}_i = p_i^{-1} / \hat{\vartheta}_{0_1}^2$, and the process is repeated until the unit weight variance ratio of all type observations is close to 1.

In accordance with data processing process as above, we can get weight ratio between GPS, GLONASS and BDS as $\vartheta_G : \vartheta_R : \vartheta_C$. Satellites in the system are classified according to satellites type. Nowadays there is three types of GPS satellites, IIA, IIR and IIF, and GPS satellites are divided into three categories, whose weight ratio are decided according to above algorithms, and the weight ratio

is $\vartheta_{G,A} : \vartheta_{G,R} : \vartheta_{G,F}$. There are M and K satellites in GLONASS. which is divided into two categories to decide weight ratio, and weight ratio can be described as $\vartheta_{R,M} : \vartheta_{R,K}$. We divide the most special system BDS into MEO, GEO and IGSO to allocate weight, and weight ratio could be written as $\vartheta_{C,M} : \vartheta_{C,G} : \vartheta_{C,I}$. Then all observation are taken as independent classes to determine stochastic model. The stratified result can be drawn as Fig. 1.

Finally, all observations are taken as an independent classes and stochastic model matrix is determined by multiplying results above. The weights can be calculated according to following formulas:

$$\begin{aligned} \vartheta_1 &= \vartheta_G \cdot \vartheta_{G,IIR} \cdot \vartheta 1 \\ \vartheta_2 &= \vartheta_G \cdot \vartheta_{G,IIR} \cdot \vartheta 2 \\ \cdots & \qquad \cdots \\ \vartheta_{m+n+q} &= \vartheta_C \cdot \vartheta_{C,G} \cdot \vartheta(m+n+q) \end{aligned} \tag{9}$$

3 Statistics and Analysis of SPP Result

Data utilization and accuracy are main indexes to evaluate GNSS algorithm. The data rejection rate should be less than 10% in the same period advised by China's GB/T 18314-2009. In order to weaken the error caused by troposphere when signal passes through the atmosphere, satellite cut-off elevation angle set as 15° advised by Li [17]. In order to evaluate positioning accuracy of stratified weighting model objectively, the SPP results of stochastic model are verified by 11 IGS multi-GNSS experiment (MGEX) stations located at the Asian-Pacific region. The dates are collected by Trimble R9 on October 1, 2016, and the sampling interval is 30 s continued for 86400. The selected station distribution is shown in Fig. 2.

Whether parameter estimation or error model is used to eliminate error, it is possible that the accuracy of location result is greatly reduced due to the incomplete elimination of system errors, thus it is indispensable to make hypothesis-testing for parameter estimation results. We assume that the systematic error is completely eliminated and the residual error of observation is random error at date process, thus

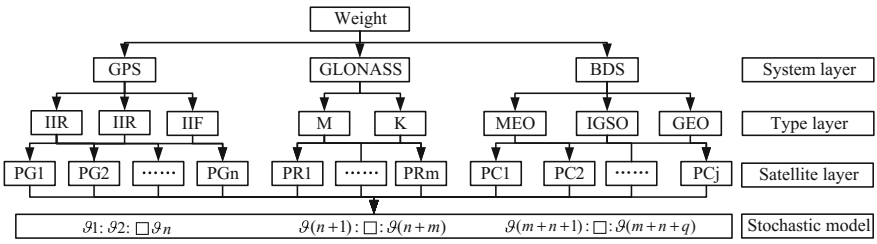

Fig. 1 Stratified weighting graph for multi-GNSS

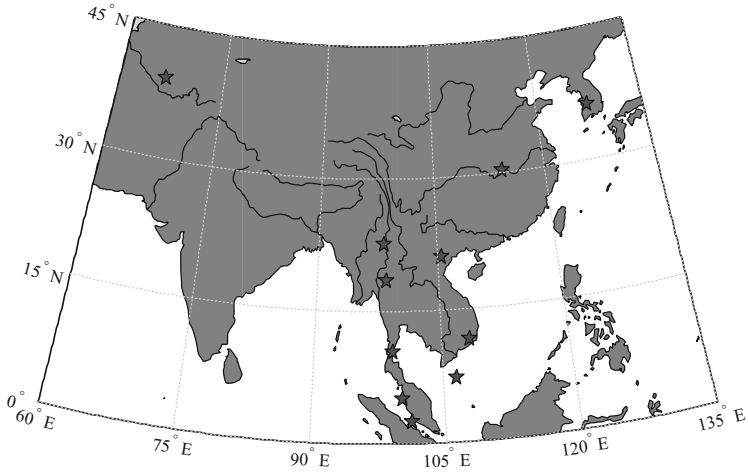

Fig. 2 The selected IGS MGEX station distribution map

the residual error v_i obeys normal distribution whose mean value is zero and standard deviation is δ_i, which could be expressed as follows:

$$v_i' = v_i/\delta_i \sim N(0,1) \tag{10}$$

In the formula, i stands for ith observation, δ_i stands for standard deviation of ith observation.

We take $v' = (v_1', v_2', v_3' \cdots v_m')$, and we can get follow:

$$\frac{v_i'^T v_i'}{m-n-1} \sim \chi^2(m-n-1) \tag{11}$$

In the formula, m represents there are m observations in all, n represents there are n observations to be estimated in all. We take a significant level $\alpha = 0.001(0.1\%)$ when taking hypothesis-testing.

The hypothesis-testing pass rate of 11 stations is processed by single-system BDS, dual-system BDS/GPS and BDS/GLO and three system BDS/GPS/GLO, and the statistical results are shown as Fig. 3.

It can get that there are some epochs are difficult to pass the hypothesis-test because of inadequate error elimination at GNSS date processing. After using stratified weighting algorithm, the pass rate of single-system BDS increased to more than 99.5%, dual-system BDS/GPS increased to more than 99.3% and BDS/GLO increased to more than 99.2%, triple-system BDS/GPS/GLO increased to more than 99.3%. From above analysis, we could obtain the succeed rate is greatly improved after using stratified weighting algorithm, and the stochastic model can greatly increase the utilization rate of navigation and positioning.

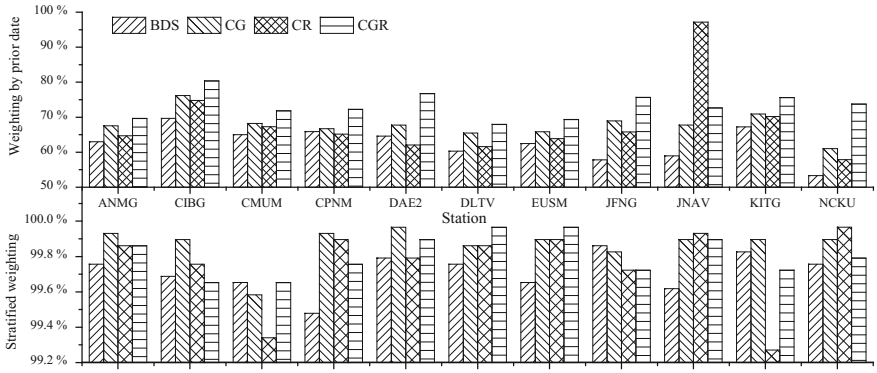

Fig. 3 The statistics figure of hypothesis-test succeed rate

The result accuracy is one of important indicators to evaluate GNSS algorithm, and in order to evaluate the stochastic model algorithm more objectively and effectively, the IGS MGEX stations coordinate provided by Jet Propulsion Laboratory (JPL) are used as reference truth values to gain residual error of each epoch. The residual error in east (E), north (N) and upon(U) directions of above 11 stations is calculated in four combination methods (C, C/G, C/R, C/G/R) of GNSS systems, and the weight allocation is determined by prior date and stratified algorithm respectively. The mean of squared residual error is also calculated, and the location results' accuracy of each combination method is shown in Figs. 4, 5, 6 and 7.

According above results, the changes of accuracy in three directions are counted, and there are 97.3% estimation results of the accuracy change is less than 1.5 m, 88.2% less than 1 m, and the mean value of accuracy change is less than 0.30 m; The accuracy changes slightly large in single-system BDS, because of the instability of BDS system and the system layer weight isn't allocated; The accuracy changes slightly in double-system BDS/GPS and BDS/GLO, and the improvement and reduction of precision are basically equal; The accuracy changes slightly little in triple-system BDS/GPS/GLO, and the advantages of stratified weighting is

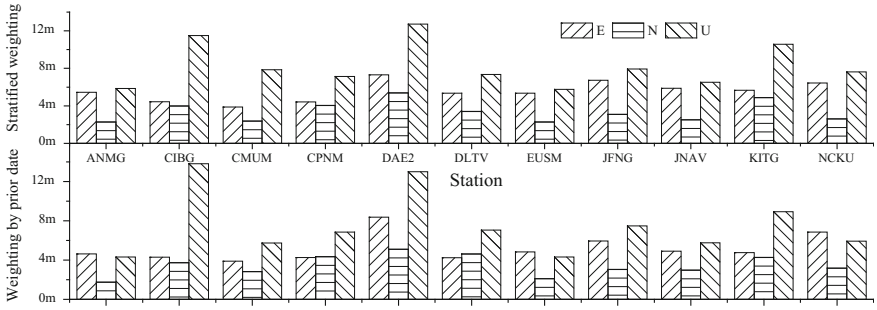

Fig. 4 The accuracy contrast figure of single-system BDS

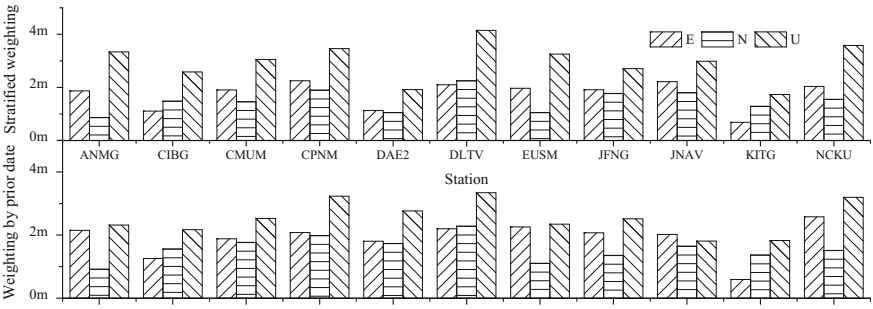

Fig. 5 The accuracy contrast figure of double-system BDS/GPS

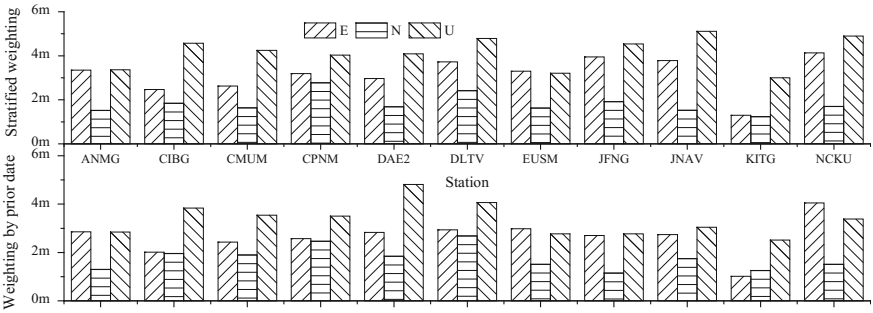

Fig. 6 The accuracy contrast figure of double-system BDS/GLO

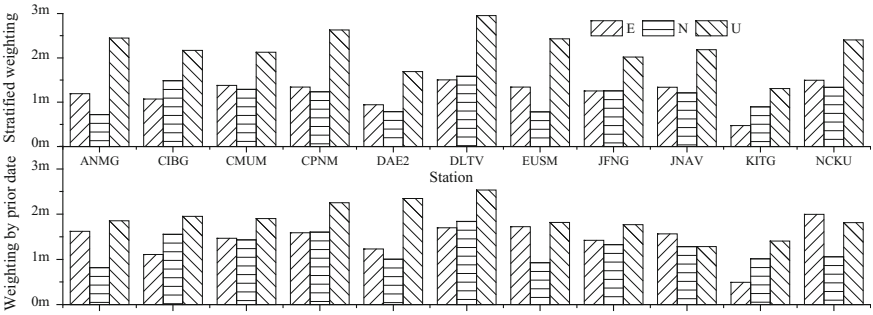

Fig. 7 The accuracy contrast figure of triple-system BDS/GPS/GLO

gradually reflected, and there are 69.7% estimation results of accuracy is improved. Meanwhile, the mean value of results' accuracy changes is only 0.01 m, which is far less than the location accuracy of SPP. We can get a conclusion from above analysis that the positioning accuracy doesn't change after using stratified weighting algorithm.

4 Conclusion

According to above experimental results, it is more reasonable to allocate weight of each system, satellites types and different satellites after using stratified weighting algorithm. It doesn't need additional information to update stochastic model matrix and the accuracy of observation is reflected dynamically by the algorithm, and 11 IGS MGEX stations data are used to verify the algorithm. The experimental results all show that the algorithm can greatly improve the pass rate of hypothesis-test and improve positioning reliability of results without affecting positioning accuracy.

Acknowledgements Contribution of data from IGS is greatly appreciated, and this research is supported by the National Natural Science of China (41604006, 41674008) and Postgraduate Research & Practice Innovation Program of Jiangsu Province (SJCX17_0522).

References

1. Yang Y, Tianhe XU, Xue S (2017) Progresses and prospects in developing marine geodetic datum and marine navigation of China. Acta Geodaet Cartographica Sinica
2. Yang Y (2016) Concepts of Comprehensive PNT and related key technologies. Acta Geodaetica Cartogr Sin 45(5):505–510
3. Dach R, Hugentobler U, Fridez P et al (2007) Bernese GPS software version 5.0. User manual. Astron Institute
4. King BRW, Bock Y (1999) Documentation for the GAMIT GPS analysis software. Mass. Inst. of Technol, Paper presented atIgs Technical Reports
5. Ge M, Gendt G, Rothacher M et al (2008) Resolution of GPS carrier-phase ambiguities in Precise Point Positioning (PPP) with daily observations. J Geodesy 82(7):389–399
6. Barnes (2000) Real time kinematic GPS and multipath: characterisation and improved least squares modelling. University of Newcastle Upon Tyne
7. Bischoff W, Heck B, Howind J et al (2006) A procedure for estimating the variance function of linear models and for checking the appropriateness of estimated variances: a case study of GPS carrier-phase observations. J Geodesy 79(12):694–704
8. Amiri-Simkooei AR, Zangeneh-Nejad F, Asgari J (2013) Least-Squares variance component estimation applied to GPS geometry-based observation model. J Survey Eng 139(4):176–187
9. Teunissen PJG, AmiriSimkooei AR (2008) Least-squares variance component estimation. J Geodesy 82(2):65–82
10. Yu Z (1991) The goneral formulas of helmert type for estimating variance and covarince caomponents. J Wuhan Technical Univer Survey Mapp
11. Wang JG, Gopaul N, Scherzinger B (2009) Simplified algorithms of variance component estimation for static and kinematic gps single point positioning. J Global Positioning Syst 8:43–52
12. Odolinski R, Odijk PJGT (2014) First combined COMPASS/BeiDou-2 and GPS positioning results in Australia. Part I: single-receiver and relative code-only positioning. J Spat Sci 59 (1):3–24
13. Odolinski R, Teunissen PJG, Odijk D (2013) Quality analysis of a combined COMPASS/ BeiDou-2 and GPS RTK positioning model. Paper presented atInternational Global Navigation Satellite Systems Society
14. Tang W, Deng C, Shi C et al (2014) Triple-frequency carrier ambiguity resolution for Beidou navigation satellite system. GPS Solutions 18(3):335–344

15. Li Y, Meng L, Xi M et al (2017) Real-time estimating different types of BDS observations stochastic model. Geomatics Inf Sci Wuhan Univ 42(2):263–269
16. Cui X (2009) Generalized measurement of adjustment. Wuhan University Press, Wuhan
17. Li F, Wang H, Gao J et al (2017) Influence of elevation masking angle and system integration on GNSS PPP Precision. Journal of Geodesy and Geodynamics

Characterization and Mitigation of BeiDou Triple-Frequency Code Multipath Bias

Xing Wang, Guoqiang Zhao, Feng Zhang and Yongan Yang

Abstract Regarding the problem of systematic multipath bias on BeiDou navigation system code observations, ten days BeiDou triple-frequency observations of multi-stations were collected, the relationships between the characteristic of multipath bias and the type of the satellite, the signal frequency and the satellite elevation angle were analyse d. In order to solve this problem, a modified sidereal filtering based on zero-phase filter was proposed to mitigate the multipath bias on GEO and IGSO satellites code observations, and elevation-angle correction method was introduced to decrease the multipath bias of IGSO and MEO satellite code observations. The experimental results show that the modified sidereal filtering can decrease the multipath bias of B1, B2 and B3 frequencies code observations for GEO and IGSO satellites over 17.0, 18.6 and 10.5%, respectively, and the elevation-angle correction method can reduce the multipath bias of IGSO and MEO satellite B1, B2 and B3 frequencies code measurements by 5.0, 6.8, and 4.1%, respectively. After mitigating the multipath bias of BeiDou code observations, the precision of single point position for east, north and up directions can be improved about 34, 45 and 51%, respectively.

Keywords BeiDou navigation system · Triple-frequency multipath bias on code observations · Modified sidereal filtering · Elevation-angle correction

1 Introduction

BeiDou navigation satellite system (BDS) is a self-developed and independently operated global satellite navigation system in China. The constellation is composed of Geostationary Earth Orbit (GEO) satellites, Inclined Geosynchronous Satellite Orbits (IGSO) satellites and Medium Earth Orbit (MEO) satellites. BDS satellites

X. Wang (✉) · G. Zhao · F. Zhang · Y. Yang
State Key Laboratory of Astronautic Dynamics, Xi'an, China
e-mail: wangxing-1010@163.com

J. Sun et al. (eds.), *China Satellite Navigation Conference (CSNC) 2018 Proceedings*, Lecture Notes in Electrical Engineering 498,
https://doi.org/10.1007/978-981-13-0014-1_39

broadcast triple-frequency signals, and create new opportunities for positioning, navigation and timing services.

Recent studies have shown that the code observations of BDS satellites have systematic bias errors, which may be caused by the multipath effect at the satellite, and closely related to the satellite elevation angle [1]. Wanninger and Beer analysed the relationship between the fluctuation amplitude of multipath series for BeiDou IGSO and MEO satellites and the elevation angle, azimuth angle and signal frequency, and gave the empirical correction model [2]. On this basis, Yang et al. proposed a two-order polynomial fitting model to simplify the correction parameters [3]. However, the above method has a poor capability of correcting the IGSO satellite multipath bias, only about 5% improvement can be reached, and it cannot be applied to eliminate the multipath bias of GEO satellite. Zhang et al. pointed out that although the elevation angle for GEO satellites is almost no change, there is still obvious systematic multipath bias existing in GEO code observations [4]. Based on the periodicity of satellite orbit, Wang et al. introduced sidereal filtering to mitigate the multipath effect of GEO satellite [5]. A modified sidereal filtering method was proposed by Wang et al. to improve the performance of multipath mitigation for GEO code observations [6]. However, these two methods only consider the GEO satellite, and not involve other satellite types. Therefore, there are still few researches on the analysis of the characteristics and mitigation methods for the multipath bias of all satellite types of BeiDou constellation.

To solve above problems, we chose 10 receiving stations with ideal environment and little multipath effect of ground, and collected 10 consecutive days triple-frequency observables to analyse the characteristics of multipath bias for BDS code observations, and used the modified sidereal filtering and the elevation-angle correction method to mitigate the multipath biases of different satellite types. Finally, Single Point Position (SPP) is involved to show the validity of the multi-path mitigation method in this paper.

2 Characterization of BeiDou Triple-Frequency Code Multipath Bias

2.1 Multipath Extraction for BeiDou Triple-Frequency Code Observation

A linear combination of code and carrier phase observations can be used to extract triple-frequency multipath series:

$$MP_i = P_i - (c_{1i} \cdot \Phi_1 + c_{2i} \cdot \Phi_2 + c_{3i} \cdot \Phi_3) - B_i \quad (1)$$

where MP is the multipath bias error; c represents the combined coefficient, sub-script i (i = 1, 2, 3) represents the frequency number; P and Φ are the code and carrier phase observations in meters; B is the offset term, which contains the satellite and receiver hardware delay, carrier ambiguity and other constant items.

Constraint the noise variance of the combination reach minimum, and geometry-ionospheric-free, the optimal combination will be obtained:

$$\mathrm{Min}\left\{c_{1i}^2+c_{2i}^2+c_{3i}^2\middle|c_{1i}+c_{2i}+c_{3i}=1;\frac{1}{f_i^2}+\frac{c_{1i}}{f_1^2}+\frac{c_{2i}}{f_2^2}+\frac{c_{3i}}{f_3^2}=0\right\} \tag{2}$$

We utilize BDS triple-frequency values to get the solution of the constraint equations, the combinations can be approximately expressed as:

$$\begin{aligned} MP_1 &= P_1-(4.1665\cdot\Phi_1-2.3483\cdot\Phi_2-0.8182\cdot\Phi_3)-B_1\\ MP_2 &= P_2-(5.2424\cdot\Phi_1-3.1010\cdot\Phi_2-1.1414\cdot\Phi_3)-B_2\\ MP_3 &= P_3-(4.9897\cdot\Phi_1-2.9242\cdot\Phi_2-1.0655\cdot\Phi_3)-B_3 \end{aligned} \tag{3}$$

Normally, the hardware delay is stable, and if we assume that there are no cycle slips during the observed period, the constant term B can be determined by average the MP series for a long observed time. Compared with multipath series extraction methods using dual-frequency combination [2, 3], this method reduces the combination coefficients, and decrease the noise variance of the combination.

2.2 Characteristics Analysis for BeiDou Code Multipath Bias

In order to analyze the characteristics of multipath bias for BDS code observations, we selected ten receiving stations in Asia-Pacific region, and collected BeiDou triple-frequency observed data from Day of Year (DoY) 137–146 in 2015. Figure 1 shows the distribution of receiving stations. Among them, five Multi-GNSS Experiment (MGEX) stations are all equipped with Trimble NetR9 receivers. The international GNSS Monitoring and Assessment System (iGMAS) stations CAN1, BJF1 and WUH1 are equipped with CETC-54 GMR-4011 receivers, while KUN1 and SHA1 stations are equipped with Unicore UB4B0I receivers. All observed data were sampled with 30 s interval.

2.2.1 The Characteristics of Multipath Bias for BeiDou GEO Satellite

Although the geometrical positions of GEO satellites and ground station are almost unchanged, the systematic multipath bias is still obviously. Figure 2 shows the elevation angle and multipath series of C01 and C04 satellite at CUT0 station.

The multipath bias for GEO satellite has followed characteristics: (1) are almost elevation-dependent, (2) daily periodical patterns can be easily found from all multipath series, (3) the amplitudes of MP1 and MP2 series are significantly larger than those of MP3 series.

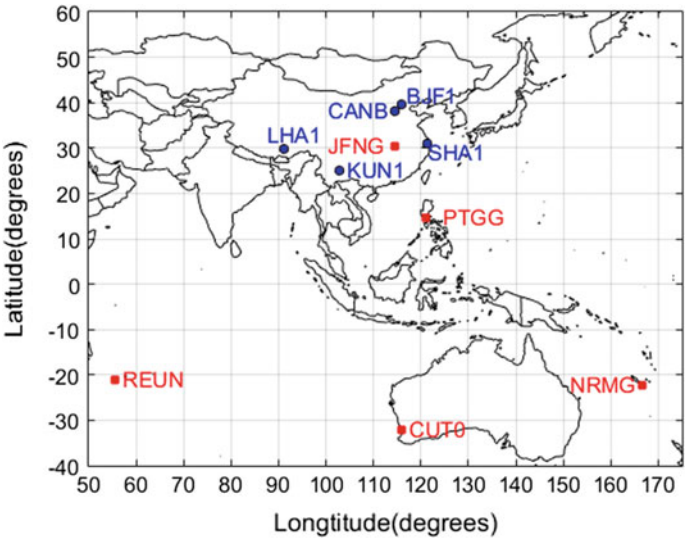

Fig. 1 Receiving stations of MGEX (red) and iGMAS (blue) used in this study

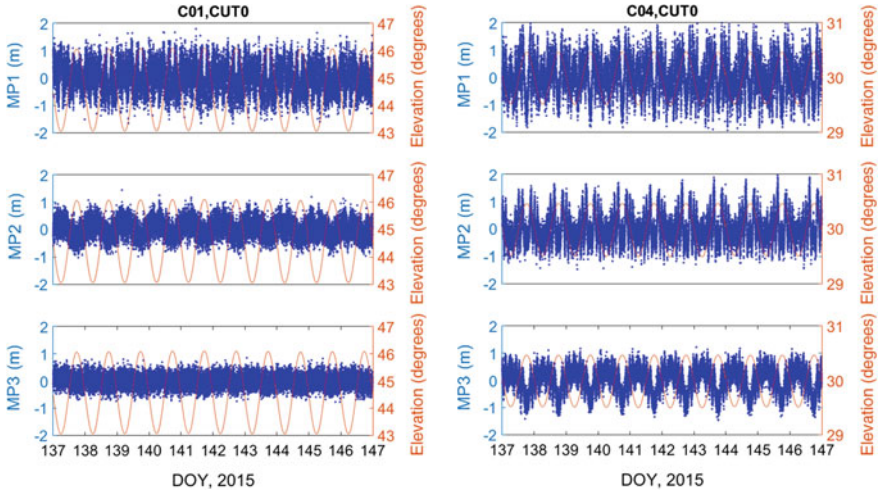

Fig. 2 The elevation angle and the multipath series for C01 and C04 during DoY 137–146, 2015 at CUT0 station

We introduced Power Spectral Densities (PSD) of multipath series to illustrate the spectral characteristics of multipath bias. As Fig. 3 shown that, although multipath series in time domain are satellite-dependent and frequency-dependent, they all have obviously low-frequency components, which verify that the multipath series for BeiDou GEO satellite have significant daily periodical patterns.

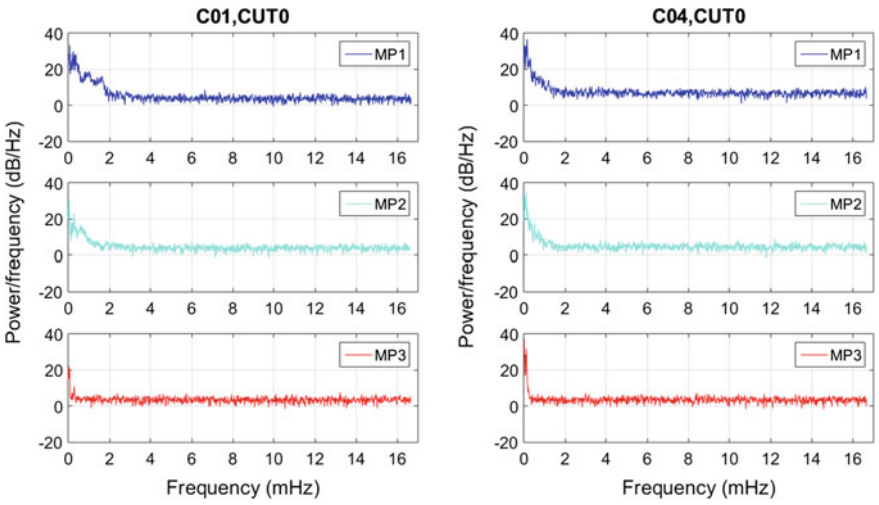

Fig. 3 The PSD results of multipath series for C01 and C04

2.2.2 The Characteristics of Multipath Bias for BeiDou IGSO Satellite

When it comes to BeiDou IGSO satellite, the orbit repetition period is about a sidereal day. For the receivers in the Asia Pacific region, a longer observed period and a larger range of changes in elevation angle will be obtained. Figure 4 shows the multipath series and elevation angle of C06 and C10 at CUT0 station. Figure 5 illustrates the PSD of these multipath series.

For stationary receivers, the multipath biases of IGSO satellite not only have the significantly periodic repeatability, but also have a close correlativity with the satellite elevation angle. So we make a statistic of all IGSO satellites observed data and show the multipath bias as a function of elevation angle (separated by 10° of elevation) in Fig. 6. We can conclude that the multipath bias for BeiDou IGSO satellite has followed characteristics: (1) have daily periodical patterns, (2) are elevation-dependent, but receiver-independent and station-independent, (3) have small difference in variation amplitude for B1, B2, and B3 frequencies, and the maximums of variation are almost 0.4 m.

2.2.3 The Characteristics of Multipath Bias for BeiDou MEO Satellite

The orbit repetition period of BeiDou MEO satellite is about 7 days, and the daily visible interval is not the same. Therefore, we only take the relationship between multipath bias and elevation angle into consideration, and show the multipath series with elevation angles of C11 and C12 at CUT0 station in Fig. 7.

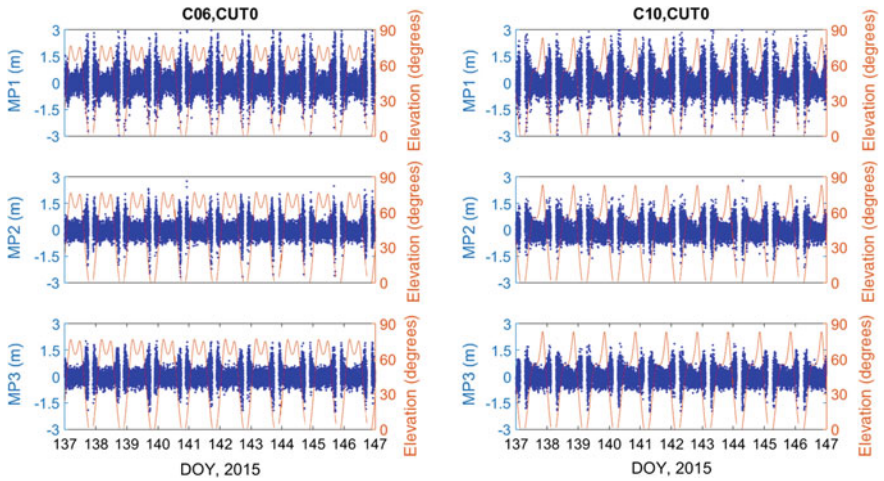

Fig. 4 The elevation angle and the multipath series for C06 and C10 during DoY 137–146, 2015 at CUT0 station

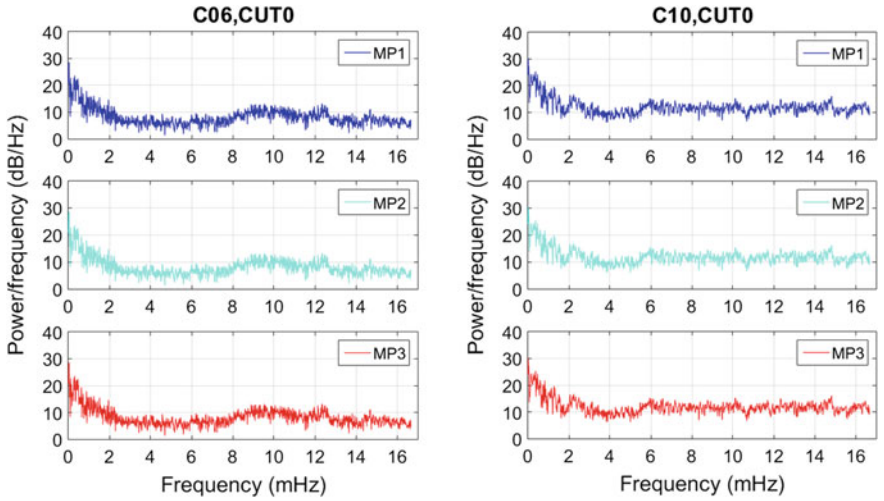

Fig. 5 The PSD results of multipath series for C06 and C10

Furthermore, we illustrate the multipath bias of MEO satellite as a function of elevation angle (separated by 10° of elevation) in Fig. 8. Obviously, we can conclude that the multipath bias for BeiDou MEO satellite has followed characteristics: (1) are elevation-dependent, but receiver-independent and station-independent, (2) variation amplitudes are 1.3, 0.8 and 0.4 m for B1, B2, and B3 frequencies, respectively.

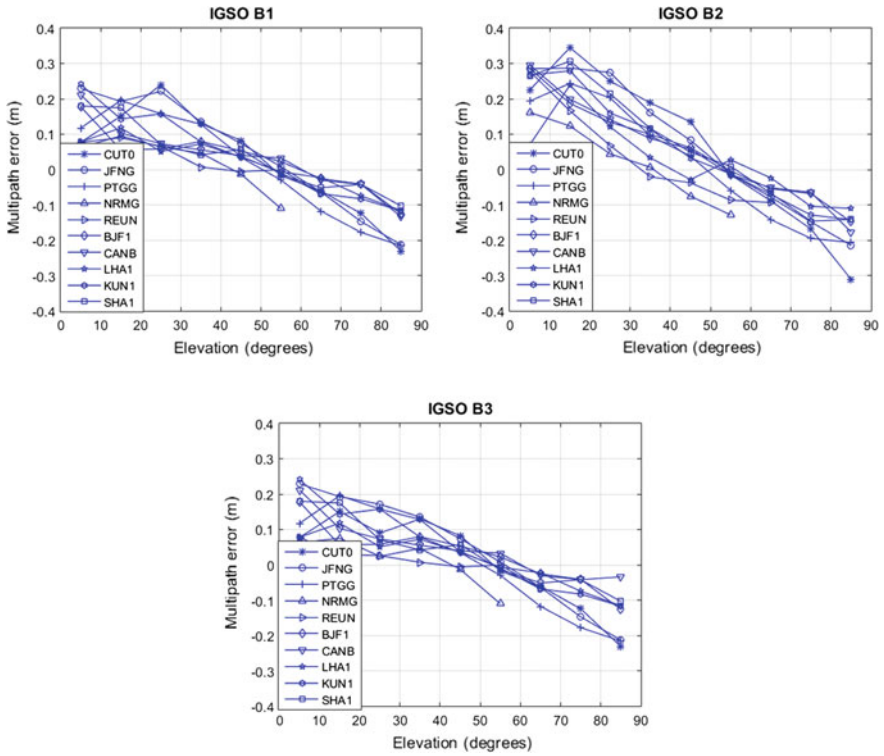

Fig. 6 The elevation-dependent code multipath bias models for BDS IGSO satellites

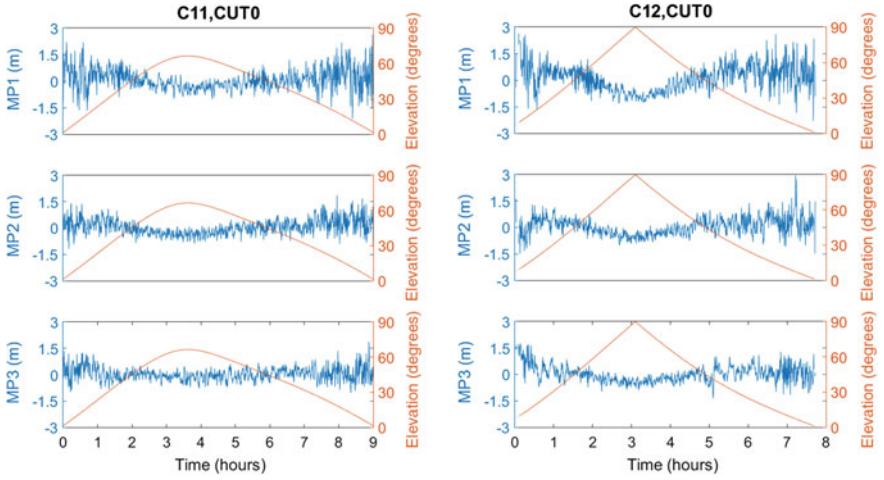

Fig. 7 The elevation angle and the multipath series for C11 and C12 during the visibility time of DoY 137–138, 2015 at CUT0 station

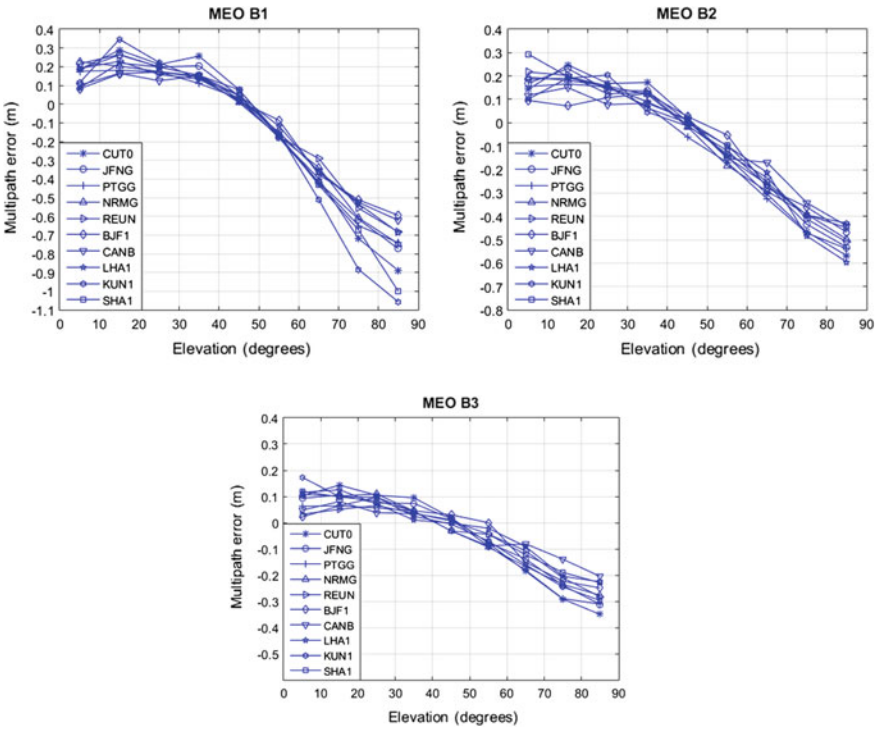

Fig. 8 The elevation-dependent code multipath bias models for BDS MEO satellites

3 The Multipath Mitigation Method for BeiDou Code Observation

3.1 The Modified Sidereal Filtering Based on Zero-Phase Filter

For stationary receivers, sidereal filtering can be used to mitigate daily periodical patterns. So it is necessary to extract the periodical components from multipath series, otherwise the observable noise will be amplified by using sidereal filtering. As foregoing statements, multipath bias and observable noise are tightly coupled in time domain, but can be easily distinguished from the frequency domain by utilizing a digital filter. So we introduce the modified sidereal filtering method, which utilize zero-phase filter to extract the low-frequency components of the multipath series as the correction values for nest sidereal day. Figure 9 illustrates the implementation of flow chart [6, 7]. The digital filter in modified sidereal filtering method can be easily designed and verified, and no phase distortion correction values with original series can be obtained, and a better performance for multipath mitigation will be got, and the computation will be great reduced.

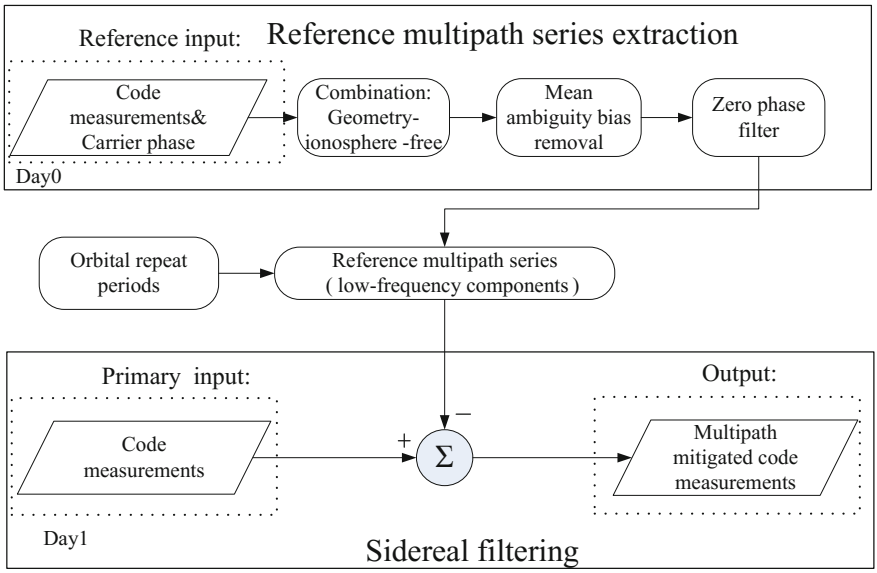

Fig. 9 The implementation flow chart of the modified sidereal filtering

We extend the modified sidereal filtering to the application of low sampling rate (30 s sampling interval) observed data by utilizing Lagrange interpolation to get the correction value at reference time. The interpolation is expressed as:

$$MP_i'(t) = \sum_{i=0}^{n} MP_i(t_i) \prod_{\substack{j=0 \\ j \neq i}}^{n} \frac{t_i - t}{t_i - t_j} \tag{4}$$

where n is the order for the interpolation, t is the specified reference time, t_i and t_j are the time series near the reference time, and MP_i' is the correction value after interpolation. We show the performance of the modified sidereal filtering as Figs. 10 and 11. After the mitigation, the periodic patterns have been significantly weakened, especially B1 and B2, periodical components have been almost completely eliminated.

Table 1 illustrates the Root Mean Square (RMS) of MP for BDS GEO and IGSO satellite before and after the modified sidereal filtering. It can be seen that the multipath bias of GEO satellite can correct about 24.65, 20.11 and 10.51% for B1, B2 and B3 frequencies, respectively, while the improvement in IGSO satellite can reach about 17.03, 18.64 and 14.24% for B1, B2 and B3 frequencies, respectively.

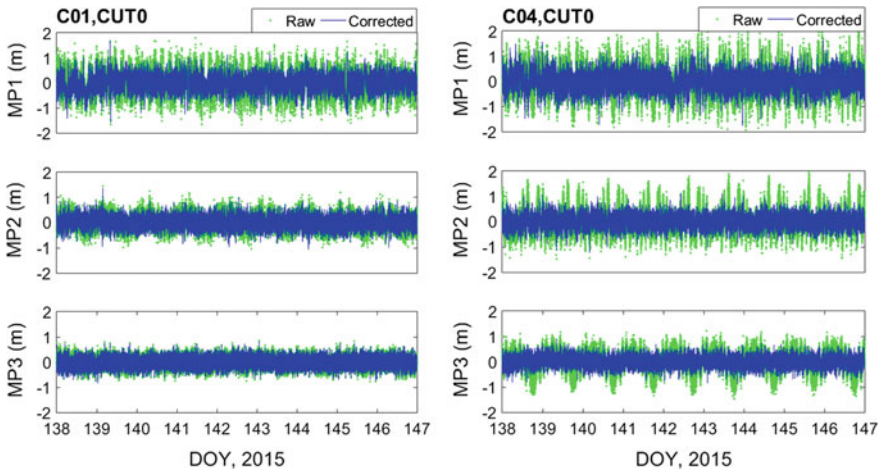

Fig. 10 The multipath correction by the modified sidereal filtering method for C01 and C04 satellites code observations

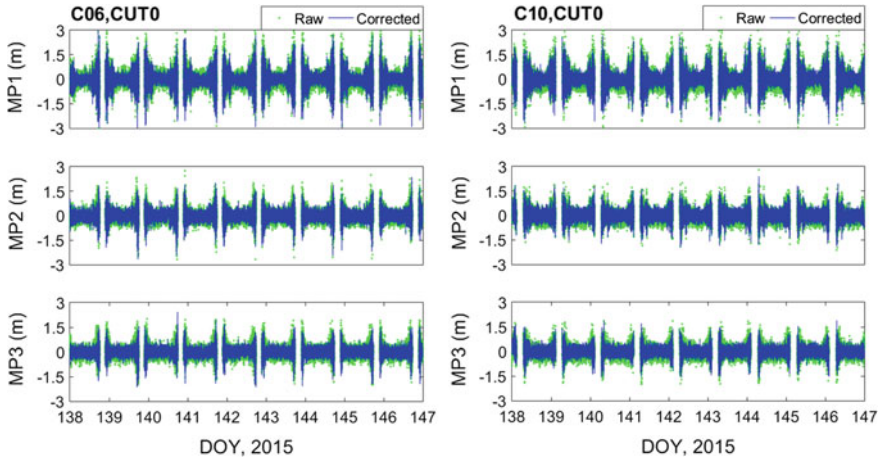

Fig. 11 The multipath correction by the modified sidereal filtering method for C06 and C10 satellites code observations

Table 1 MP RMS of BDS GEO and IGSO code observations corrected by the modified sidereal filtering

RMS (m)	GEO			IGSO		
	MP1	MP2	MP3	MP1	MP2	MP3
Raw data	0.434	0.353	0.295	0.499	0.338	0.316
Corrected	0.327	0.282	0.264	0.414	0.275	0.271
Improvement (%)	24.65	20.11	10.51	17.03	18.64	14.24

3.2 The Multipath Corrected by Elevation-Angle Correction Method

As foregoing statements, multipath biases of IGSO and MEO satellite are elevation-dependent. So we set up a two-order polynomial fitting function of the multipath bias of IGSO and GEO satellite for B1, B2 and B3 frequencies to the satellite elevation angle:

$$\widehat{MP}_i(EL) = a_2(EL)^2 + a_1(EL) + a_0 \tag{5}$$

where the $\widehat{MP}$ is the multipath correction value; EL represents the elevation angle; a_2, a_1 and a_0 are polynomial coefficients. The fitting coefficients are calculated by the Minimum Square Error (MSE) estimator for each frequency of IGSO and MEO satellite, and are illustrated with Table 2.

In application, we can subtract the multipath correction value of the original code observations to obtain corrected code observations. Figures 12 and 13 show the multipath series before and after the multipath corrected by elevation-angle correction method.

Table 3 shows the RMS of MP for BDS IGSO and MEO satellite before and after the elevation-angle correction method. It can be seen that the improvements in IGSO satellite code observation are only 5.01, 6.80 and 4.11% for B1, B2 and B3 frequencies, respectively, which is worse than that of the modified sidereal filtering The improvements in MEO satellites code observation are about 9.00, 8.35 and 4.85% for B1, B2 and B3 frequencies, respectively.

3.3 The Improvements in Precision of SPP

We involve SPP results to verify the validity of multipath mitigation method of this paper. The strategies applied for SPP validation are listed as follows: broadcast ephemeris is applied for orbital error and clock error correction, the cutoff elevation angle is set as 10°, Saastamoinen model is employed for tropospheric delay correction, ionosphere delay error is eliminated by constructing dual-frequency ionospheric-free code combination:

Table 2 The elevation-dependent two-order polynomial fitting coefficients for BDS IGSO and MEO code observations

		a_2	a_1	a_0
IGSO	B1	−0.0000267	−0.0015076	0.1597005
	B2	−0.0000004	−0.0055530	0.2877854
	B3	−0.0000219	−0.0017440	0.1543974
MEO	B1	−0.0002104	0.0059580	0.1665971
	B2	−0.0001040	0.0001606	0.1935616
	B3	−0.0000582	0.0003248	0.0979699

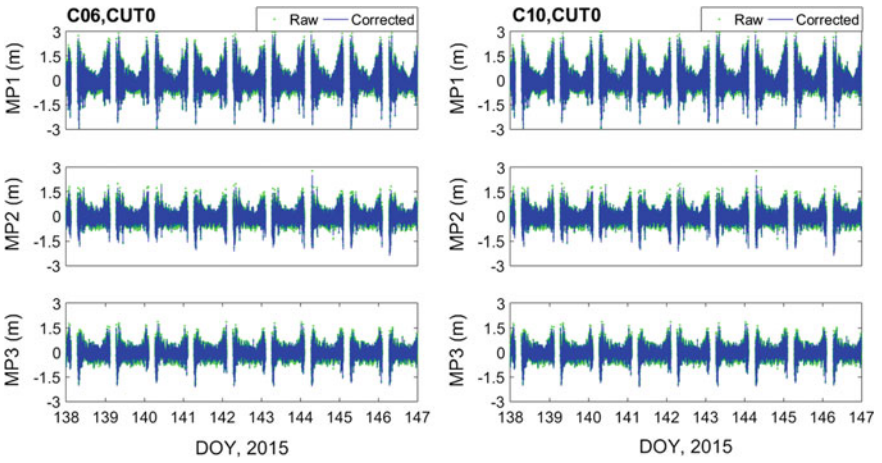

Fig. 12 The multipath correction by the elevation-angle correction method for C06 and C10 satellites code observations

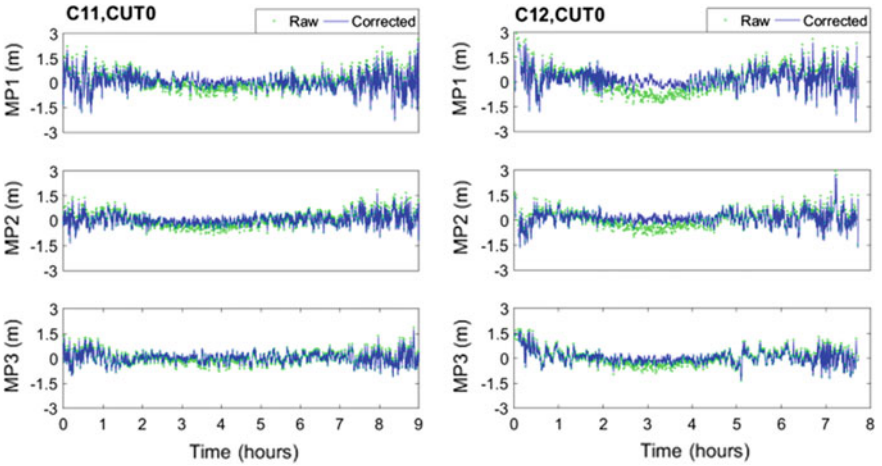

Fig. 13 The multipath correction by the elevation-angle correction method for C11 and C12 satellites code observations

Table 3 MP RMS of BDS IGSO and MEO code observations corrected by the elevation-angle correction method

RMS (m)	IGSO			MEO		
	B1	B2	B3	B1	B2	B3
Raw data	0.499	0.338	0.316	0.562	0.383	0.330
Corrected	0.474	0.315	0.303	0.512	0.351	0.314
Improvement (%)	5.01	6.80	4.11	9.00	8.35	4.85

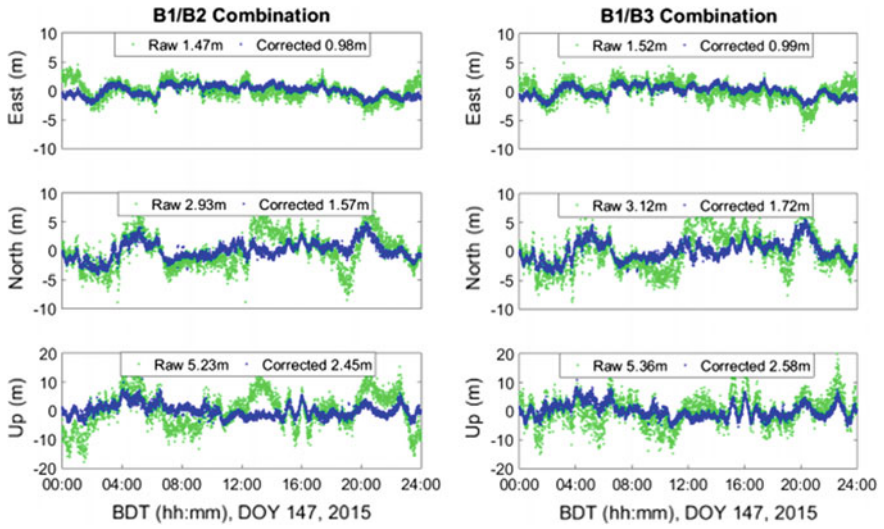

Fig. 14 SPP results before and after multipath bias mitigation at CUT0 station

$$\begin{cases} PIF_{12} = \frac{f_1^2}{f_1^2 - f_2^2} P_1 - \frac{f_2^2}{f_1^2 - f_2^2} P_2 \\ PIF_{13} = \frac{f_1^2}{f_1^2 - f_3^2} P_1 - \frac{f_3^2}{f_1^2 - f_3^2} P_3 \end{cases} \tag{6}$$

where PIF_{12} is B1 and B2 ionospheric-free code combination, PIF_{13} means B1 and B3 ionospheric-free code combination.

Figure 14 shows the improvement in precision of SPP after mitigating the multipath biases. Obviously, after eliminating the multipath bias of code observations, the precision of SPP at CUT0 station has been improved by 34, 45 and 51% for east, north and up directions, respectively.

4 Conclusion and Outlook

There are systematic multipath biases in code observation of BeiDou satellite. For stationary receivers, the multipath series of GEO and MEO satellite have daily periodical patterns, and can be mitigated by the modified sidereal filtering. The multipath bias of IGSO and MEO satellite are elevation-dependent, and can be corrected by elevation-angle correction method. After mitigating the multipath bias in code observations, the precision of SPP for stationary receivers has greatly improved. The precision of SPP for dynamic receivers can be investigated for the future research.

References

1. Montenbruck O, Rizos C, Weber R, Weber G, Neilan R, Hugentobler U (2013) Getting a grip on multi-GNSS: the international GNSS service MGEX campaign. GPS World 24(7):44–49
2. Wanninger L, Beer S (2015) BeiDou satellite-induced code observations variations: diagnosis and therapy. GPS Solutions 19(4):639–648
3. Yang W, Tong H, Pan L, Xu D, Guo W, Yang J (2016) Analysis and correction of BDS code multipath bias. In: China satellite navigation conference (CSNC) 2016 Proceedings, vol III, pp 503–513, Springer, Singapore
4. Zhang F, He H, Tang B, Shen F, Chen R (2013) Analysis of signal characteristic and positioning performance affected by code observations multipath for COMPASS. In: China satellite navigation conference (CSNC) 2013 proceedings, pp 493–503, Springer, Berlin, Heidelberg
5. Wang G, de Jong K, Zhao Q, Hu Z, Guo J (2015) Multipath analysis of code measurements for BeiDou geostationary satellites. GPS Solutions 19(1):129–139
6. Wang X, Liu W, Li B, Sun G (2017) A modified sidereal filtering for mitigating the code measurement multipath effects of BeiDou GEO satellites. Surv Rev 49(357):428–436
7. Wang X, Liu W, Li B, Sun G (2015) The application of zero phase filter on BDS geostationary satellite code multipath mitigation. In: 4th international conference on computer science and network technology (ICCSNT), 2015, vol 1, pp 1012–1015, IEEE

Comparison of Performances of Three Multi-constellation Precise Point Positioning Models Based on iGMAS Products

Yangyang Liu, Ke Su, Baoqi Sun, Yulong Ge, Guoqiang Jiao and Shengli Wang

Abstract The paper focuses on the performance of multi-GNSS (GPS, BDS, GLONASS, and Galileo) precise point positioning (PPP) of three commonly used models including Un-differenced (UD) model, UofC model and Un-combination (UC) model with the products from international GNSS Monitoring and Assessment System (iGMAS). The convergence time and positioning accuracy are investigated. As a comparison, the same processing strategy is employed by using the GBM products provided by Helmholtz-Centre Potsdam-German Research Centre for Geosciences (GFZ). Daily GNSS measurements from 10 stations observed during 30 days in 2015 are used. The result shows that: (1) the convergence time of three multi-constellation PPP models are 22.25, 18.92 and 20.21 min, respectively. The UofC model has the shortest convergence time and the convergence speed of the UD model is slightly slower than the UC model. The RMS values of the UD model in N, E and U components are 6.1, 7.8 and 21.1 mm, respectively. The ones in UofC model are 5.4, 6.4 and 19.5 mm while the ones in UC model are 5.6, 6.7 and 19.9 mm. The positioning accuracy of three

Y. Liu · B. Sun (✉) · Y. Ge
National Time Service Center, Chinese Academy of Sciences, Xi'an, China
e-mail: sunbaoqi@ntsc.ac.cn

Y. Liu · B. Sun · Y. Ge
Key Laboratory of Precise Positioning and Timing Technology, Chinese Academy of Sciences, Xi'an 710600, China

B. Sun
School of Astronomy and Space Science, University of Chinese Academy of Sciences, 100049 Beijing, China

Y. Liu · K. Su · Y. Ge · G. Jiao
University of Chinese Academy of Sciences, Beijing 100049, China

K. Su · G. Jiao
Shanghai Astronomical Observatory, Chinese Academy of Sciences, Shanghai, China

S. Wang
Institute of Ocean Engineering, Shandong University of Science and Technology, Qingdao 266590, China

J. Sun et al. (eds.), *China Satellite Navigation Conference (CSNC) 2018 Proceedings*, Lecture Notes in Electrical Engineering 498,
https://doi.org/10.1007/978-981-13-0014-1_40

multi-constellation PPP models is consistent in three components. (2) Using the same observation data, the final positioning accuracy of multi-constellation PPP based on both iGMAS products and GBM products in three models could reach millimeter in the horizontal and millimeter-centimeter in the up component. Although the convergence time of three models using iGMAS products are slightly slower, the results could prove the stability and reliability of iGMAS products.

Keywords iGMAS products · Multi-constellation PPP · PPP models
Positioning accuracy · Convergence time

1 Introduction

PPP is the technology which uses the precise satellites orbit and clock offset products provided by the organizations like IGS to process the pseudorange and carrier-phase observations to obtain the coordinate of a single receiver [1, 2]. With the construction and development the GNSS, there will be approximately more than 100 navigation satellites in orbit in the sky. Multi-constellation PPP gradually becomes the research hotspot at home and abroad [3–6]. Multi-constellation GNSS combination can improve the positioning accuracy and accelerate the convergence speed, which can help improve the performance of navigation and other applications. Helmholtz-Centre Potsdam-German Research Centre for Geosciences (GFZ) provides GBM precise products for the users to resolve after observing. China has also built international GNSS Monitoring and Assessment System (iGMAS), which can also provide the products of precise orbit, satellite clock offset, Earth Orientation Parameters (EOP) and so on [7]. Ge et al. employed the precise products provided by iGMAS to analyze the performance of multi-constellation PPP in the aspect of convergence time and demonstrated the stability of iGMAS products [8]. In processing, two methods to deal with ionosphere delay can be employed in PPP, which are the combinations of the observations and estimation of the parameters, to develop different PPP models. Commonly used PPP models are Un-differenced (UD) model, UofC model and Un-combination (UC) model based on the raw observations [2, 9, 10]. Li et al. analyzed the relationship of three models in the aspect of ambiguity and proved that UC model is equivalent to UofC model, which are both better than UD model [11]. At the same time, Shen et al. did some equivalent research to analyze different methods of combinations with observations [12, 13].

This contribution focuses on three multi-GNSS PPP models including UD model, UofC model and UC model with iGMAS products. Daily GNSS measurements from 10 stations observed during 30 days in 2015 are used. The convergence time and positioning accuracy are investigated to analyze the performance of multi-GNSS PPP with iGMAS products. GBM products are also used with the same processing strategy to verify the PPP results based on iGMAS products.

2 Three PPP Models with Multi-constellation

GNSS pseudorange and carrier-phase observation equations can be expressed as:

$$p_{r,j}^{s} = \rho_r^s + c(dt_r - dt^s) + T_r^s + I_{r,j}^s + c(d_r + d_{r,j}^s) + \varepsilon_p \tag{1}$$

$$\varphi_{r,j}^{s} = \rho_r^s + c(dt_r - dt^s) + T_r^s - I_{r,j}^s + \lambda_{r,j} N_{r,j}^s + \varepsilon_\varphi \tag{2}$$

where the superscript s represents the GNSS satellite, the subscript r and j represent the receiver and the frequency, $p_{r,j}^s$ is the pseudorange observed at the frequency f_j, $\varphi_{r,j}^s$ is the corresponding carrier-phase, ρ_r^s is the geometrical range from satellite position to receiver position,c is the vacuum speed of light, dt_r is the receiver clock offset from the GNSS time, dt^s is the satellite clock offset from the GNSS system time, T_r^s is the tropospheric delay in meter, $I_{r,j}^s$ is the ionospheric delay at different frequencies, d_r and $d_{r,j}^s$ are receiver and satellite terminal hardware delay deviation, $\lambda_{r,j}$ is the wavelength of carrier-phase at different frequencies, $N_{r,j}^s$ is the float ambiguity at different frequencies, ε_p and ε_φ are the relevant measurement noise components, including multipath of the pseudorange and carrier-phase observations.

UD model [1, 2] uses dual-frequency pseudorange and carrier-phase observations of ionosphere-free positioning model, which is expressed as follows [1]:

$$p_{r,IF}^{s} = \frac{f_1^2 \cdot P_1 - f_2^2 \cdot P_2}{f_1^2 - f_2^2} = \rho_r^s + c(dt_r - dt^s) + T_r^s + \varepsilon_{PIF} \tag{3}$$

$$\varphi_{r,IF}^{s} = \frac{f_1^2 \cdot \varphi_1 - f_2^2 \cdot \varphi_2}{f_1^2 - f_2^2} = \rho_r^s + c(dt_r - dt^s) + T_r^s + \lambda_{r,IF} N_{r,IF}^s + \varepsilon_{\varphi IF} \tag{4}$$

where $p_{r,IF}^s$ is ionosphere-free code observation, $\varphi_{r,IF}^s$ is the ionosphere-free carrier-phase observation.

UofC model [8] uses dual-frequency carrier-phase observations combination and half-sum linear combination of code and phase observations, which can be expressed as (4) and (5).

$$p_{r,j,IF}^{s} = \frac{p_{r,j}^s + \varphi_{r,j}^s}{2} = \rho + c(dt_r - dt^s) + T_r^s + \frac{\lambda_{r,j}}{2} N_{r,j}^s + \varepsilon_{j,IF} \tag{5}$$

where $p_{r,j,IF}^s$ is half-sum linear combination of code and phase observations at the frequency f_j.

UC model can be developed by the Eqs. (1) and (2). The effect of the ionospheric delay on different frequency observations has the relation: $I_{r,j_1}^s = (\lambda_{j_1}^2 / \lambda_{j_2}^2) I_{r,j_2}^s$, where j_1, j_2 are the different frequency. Hence, if observations at n frequencies are used, we can acquire $2n$ equations every epoch.

Multi-constellation GNSS combination can improve the positioning accuracy and accelerate the convergence speed, which can help improve the performance of navigation and other application. But there is a problem of compatibility between different systems, which exists in different navigation system and the difference of signal system. Hence, strategies and models of multi-constellation PPP models need to be modified. When the GPS system is chosen as the reference time scale, the multi-constellation PPP observation equations can be expressed as follows:

$$p_{r,j}^{g} = \rho_{r}^{g} + cdt_{r} + \varepsilon_{p}^{g} \tag{6}$$

$$\varphi_{r,j}^{g} = \rho_{r}^{g} + cdt_{r} + \lambda_{r,j} N_{r,j}^{g} + \varepsilon_{\varphi}^{g} \tag{7}$$

$$p_{r,j}^{o} = \rho_{r}^{o} + cdt_{r} + cdt_{sys} + \varepsilon_{p}^{o} \tag{8}$$

$$\varphi_{r,j}^{o} = \rho_{r}^{o} + cdt_{r} + cdt_{sys} + \lambda_{r,j} N_{r,j}^{o} + \varepsilon_{\varphi}^{o} \tag{9}$$

where the superscript g and o represent the GPS satellite and other system's satellite, dt_{sys} is the time difference between GPS and different systems. ε_{p}^{g}, $\varepsilon_{\varphi}^{g}$, ε_{p}^{o} and $\varepsilon_{\varphi}^{o}$ include noise and other measurement error.

3 Data Description and Strategy Analysis

The data used are collected at 10 stations on 30 days, from December 1, 2015 to December 30, 2015. The experiment tests 30 days of observation data. All selected stations can receive the observations from GPS, BDS, GLONASS, and Galileo constellations. The data has a sampling interval of 30 s. The orbit and clock offset of iGMAS integrated products have a sampling of 15 min and 5 min respectively and the time system of products is BDT. The sampling rate of GBM products are 5 min and 30 s and time system is GPST. The time system is unified to GPST in PPP processing. The 'igs08_1861. atx' file data is used to correct GNSS satellite phase center offset (PCO). The Kalman filtering algorithm is applied in the multi-constellation PPP processing. The PPP parameters to be estimated include the coordinates, the receiver offset, time difference between different satellite systems, the delay of the wet troposphere component, the ambiguities and the ionosphere parameters when only processing the UC model. The cutoff elevation of 5° is applied. Figure 1 shows the distribution of the selected station in MGEX. The solution strategy diagram is shown in Table 1.

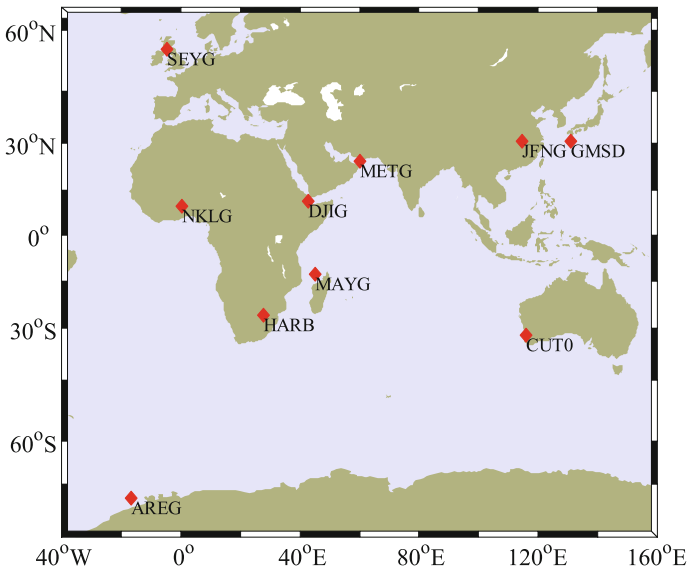

Fig. 1 Distribution of the selected MGEX stations

Table 1 Summary of data processing strategies

Parameters		Method
Observations	Pseudorange and carrier-phase	Ionosphere-free linear combination and half-sum linear combination
	Cutoff elevations	5°
Error model	Relativistic effects	IERS 2010 [14]
	Earth rotation	IERS 2010 [14]
	Tides	IERS 2010 [14]
	Receiver antenna	IERS 2010 [14]
	Satellite antenna	IERS 2010 [14]
	Wind-up of satellite	IERS 2010 [14]
	Satellite clock offset	GBM or iGMAS products
	Satellite obit	GBM or iGMAS products
	Troposphere	GPT2+VMF1 [15]
Estimated parameters	Receiver coordinate	Estimation
	Troposphere	Estimation
	Receiver clock offset	Estimation
	Ambiguity	Estimation and float
	System time difference	Estimation

4 Analysis of Positioning Results

The static quad-constellation PPP is carried out by using iGMAS products and mainly analyzes three PPP models, which are UD model, UofC model and UC model. In the study, the positioning filter is considered to have converged when the positioning errors reach ±1 dm and remains within ±1 dm. The convergence time is the period from the first the epoch the converged epoch. Figure 2 provides the root mean square (RMS) statistics in the north (N), east (E), and up (U) coordinate components to demonstrate a static positioning accuracy. For MAYG station, UD model and UC model have the same accuracy before convergence, and the convergence time of UD, UofC and UC model are 17, 22.5 and 18 min respectively. The three positioning models can achieve the accuracy of millimeter-centimeter positioning after convergence and remain the accuracy in three components.

Figure 3 provides the number of satellites and position dilution of precision (PDOP) values at MAYG station. It shows that there are more than 20 satellites observed at MAYG and the PDOP values is less than 0.4, which can ensure the integrity of the satellite space structure and improve the geometry of the satellite. Hence, multi-constellation GNSS positioning can accelerate the convergence speed, and improve the positioning accuracy and the performance of navigation positioning in the severe environment. Figure 4 shows the zenith tropospheric delay (ZTD) in three multi-constellation PPP models at SEYG station. The difference of the ZTD by different models is in the level of centimeter. Figure 5 shows the receiver clock offset and time difference of different time systems at SEYG station and the difference is below 1 ns.

Table 2 shows the parameter estimation method in three multi-constellation PPP models, where m, n, p and q represent the satellite's number of GPS, BDS, GLONASS, and Galileo, respectively. In the observation value of UD model, the ambiguous parameters have to be estimated as a real parameter, which cannot make full use of characteristic of integer ambiguity. At the same time, the original

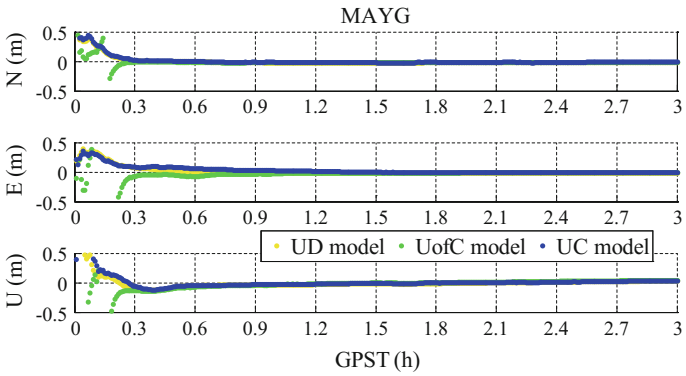

Fig. 2 Positioning errors of three multi-constellation PPP models at MAGY station

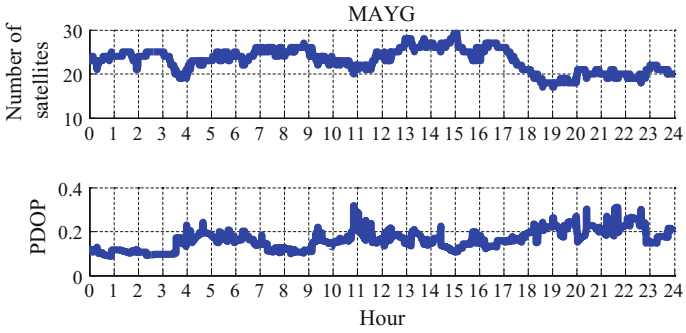

Fig. 3 The number of satellites and PDOP values at MAGY station

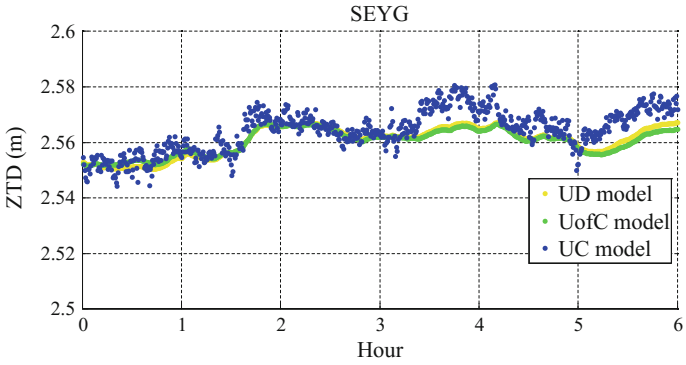

Fig. 4 The zenith tropospheric delay in three multi-constellation PPP models at SEYG station

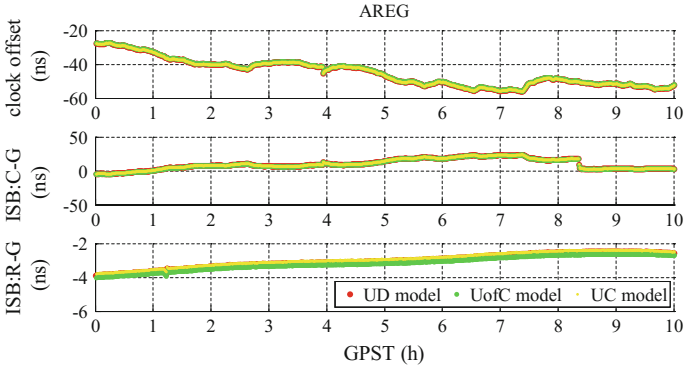

Fig. 5 The receiver clock offset and time difference of different time systems at SEYG station

Table 2 Comparison of three multi-constellation PPP models in parameter estimation method

	UD model	UofC model	UC model
Observed quantity	2m + 2n + 2p + 2q	3m + 3n + 3p + 3q	4m + 4n + 4p + 4q
Number of the parameter	m + n + p + q + 8	2m + 2n + 2p + 2q + 8	3m + 3n + 3p + 3q + 8
Redundancy	m + n + p + q − 8	m + n + p + q − 8	m + n + p + q − 8
Type of the parameters	Position, receiver clock offset, troposphere delay and ambiguity	Position, receiver clock offset, troposphere delay and ambiguity	Position, receiver clock offset, ionosphere delay, troposphere delay and ambiguity

observation noise is magnified three times. UofC model and UD model can both eliminate the influence of first-order ionosphere, while the former can also reduce the noise level of the combined observed value. UofC model can estimate the ambiguity of carrier phase in each frequency, but there is still systematic delay and errors in the model. In UC model, the ionosphere delay are regarded as the parameters, and by estimating the ionosphere delay, the troposphere delay, the receiver clock offset, the carrier phase ambiguity and the station coordinate parameters together, the model can ensure the convergence speed and reliability of the PPP.

5 Comparative Analysis of Positioning Results

iGMAS products are analyzed and compared with GBM products from the aspects of positioning accuracy, the convergence time, the tropospheric delay and so on. As a comparison, the same processing is employed by using GBM products provided by GFZ.

Table 3 provides the average RMS values of positioning errors by using iGMAS products and GBM in the component of N, E and U. The statistics of RMS value begins from the convergence time and sustains for 30 days. It shows that the final positioning accuracy of multi-constellation PPP based on both iGMAS products and GBM products in three models can reach millimeter in the horizontal and millimeter-centimeter in the up component. Figure 6 shows the average convergence time of three multi-constellation PPP models by using different products. The convergence time of UD model, UofC model and UC model are 22.25, 18.92 and 20.21 min, respectively by using iGMAS products. And the convergence time of UD model, UofC model and UC model are 21.78, 18.54 and 19.98 min, respectively by using GBM products. The convergence time of three models using iGMAS products is slightly slower than that of using GBM products.

Table 3 The average RMS values of positioning errors by three multi-constellation PPP models

	iGMAS products			GBM products		
	N (mm)	E (mm)	U (mm)	N (mm)	E (mm)	U (mm)
UD model	6.1	7.8	21.1	5.8	7.6	19.7
UofC model	5.4	6.4	19.5	4.5	6.7	18.2
UC model	5.6	6.7	19.9	5.1	6.0	19.3

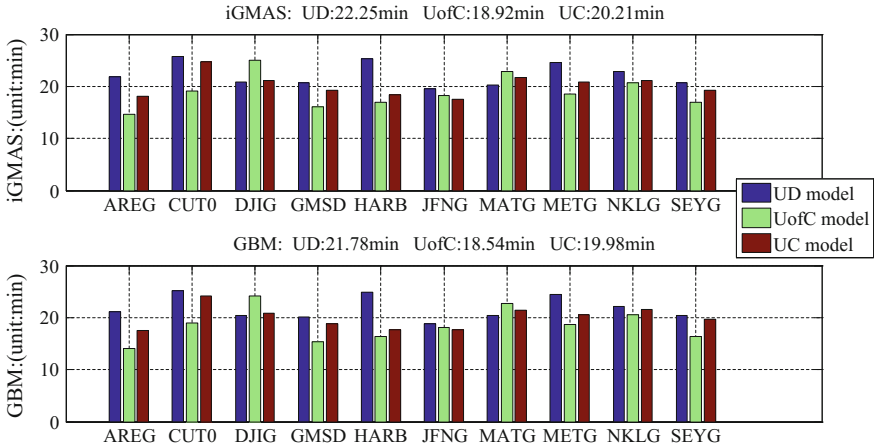

Fig. 6 Mean convergence time of three multi-constellation PPP models based on iGMAS and GBM products

By comparing the positioning accuracy and convergence time of three multi-constellation PPP with iGMAS products and GBM products, we can conclude that the results are in the same order of magnitude, which can partly prove the stability and reliability of iGMAS products.

6 Conclusions

UD model, UofC model and UC model are the most commonly used models in PPP, which differ in the combination of the observation and the processing of ambiguity. We use daily GNSS measurements from 10 stations observed during 30 days in 2015 and process the data using the above three multi-constellation PPP models with iGMAS products. The convergence time and positioning accuracy are investigated. As a comparison, the same processing strategy is employed by using GBM products provided by GFZ. The result shows that: (1) the convergence time of UD model, UofC model and UC model are 22.25, 18.92 and 20.21 min, respectively. The convergence speed of UofC model is the fastest and UD model is

the slowest. The positioning accuracy of three models is consistent in three components. The RMS values of the UD model for the north, east and vertical components are 6.1, 7.8 and 21.1 mm, respectively. The RMS values for the north, east and vertical components in UofC model are 5.4, 6.4 and 19.5 mm while the RMS values in UC model are 5.6, 6.7 and 19.9 mm. (2) Using the same observation data, the final positioning accuracy of multi-constellation PPP based on both iGMAS products and GBM products in three models can reach millimeter in the horizontal and millimeter-centimeter in the up component. Meanwhile, the convergence time of three models using iGMAS products is relatively slow. One possible is that the sampling rate of iGMAS products is larger, and the other is that iGMAS products adopt BDT, which will both be affected in the PPP processing. However, the positioning performance difference between the two products is not obviously, which can partly prove the stability and reliability of iGMAS products.

Acknowledgements This work is supported by National Natural Science Foundation of China (No.41104021; No.11173026; No.11703033). The authors gratefully acknowledge iGMAS for providing precise orbit and clock products. We would like to thank the National R&D Infrastructure and Facility Development Program of China, "Fundamental Science Data Sharing Platform" (DKA2017-12-02-24) who funded the project. Many thanks to the IGS MGEX for providing multi-GNSS ground tracking data and precise orbit and clock products.

References

1. Zumberge JF, Heflin MB, Jefferson DC, Watkins MM, Webb FH (1997) Precise point positioning for the efficient and robust analysis of GPS data from large networks. J Geophys Res: Solid Earth 102(B3):5005–5017
2. Kouba J, Héroux P (2001) Precise point positioning using IGS orbit and clock products. GPS Solutions 5(2):12–28
3. Li X, Ge M, Dai X, Ren X, Fritsche M, Wickert J, Schuh H (2015) Accuracy and reliability of multi-GNSS real-time precise positioning: GPS, GLONASS, BeiDou, and Galileo. J Geodesy 89(6):607–635
4. Li X, Zhang X, Ren X, Fritsche M, Wickert J, Schuh H (2015) Precise positioning with current multi-constellation global navigation satellite systems: GPS, GLONASS, Galileo and BeiDou. Scientific reports 5
5. Li P, Zhang X (2014) Integrating GPS and GLONASS to accelerate convergence and initialization times of precise point positioning. GPS Solutions 18(3):461–471
6. Cai C, Gao Y, Pan L, Zhu J (2015) Precise point positioning with quad-constellations: GPS, BeiDou, GLONASS and Galileo. Adv Space Res 56(1):133–143
7. Jiao W, Ding Q, Li J, Lu X, Feng L, Ma J, Chen G (2011) Monitoring and assessment of GNSS open services. J Navig 64(S1):S19–S29
8. Ge Y, Sun B, Wang S, Shen P, Liu J (2016) Convergence time analysis of multi-constellation precise point positioning based on iGMAS products. In: China satellite navigation conference (CSNC) 2016 Proceedings, vol III, Springer, Singapore, pp 297–306
9. Gao Y, Lahaye F, Heroux P, Liao X, Beck N, Olynik M (2001) Modeling and estimation of C1–P1 bias in GPS receivers. J Geodesy 74(9):621–626
10. Abdel-Salam MAT (2005) Precise point positioning using un-differenced code and carrier phase observations. 69(04)

11. Li B, Ge H, Shen Y (2015) Comparison of ionosphere-free, UofC and uncombined PPP observation models. Acta Geodaetica Cartogr Sin 44(7):734–740
12. Shen Y, Xu G (2008) Simplified equivalent representation of GPS observation equations. GPS Solutions 12(2):99–108
13. Shen Y, Li B, Xu G (2009) Simplified equivalent multiple baseline solutions with elevation-dependent weights. GPS Solutions 13(3):165–171
14. Petit G, Luzum B (2010) IERS conventions (2010) (No. IERS-TN-36). Bureau International des Poids et Mesures Sevres (France)
15. Urquhart L, Nievinski FG, Santos MC (2014) Assessment of troposphere mapping functions using three-dimensional ray-tracing. GPS Solutions 18(3):345–354

Influence of Three Ionospheric Models on Navigation Positioning Accuracy in China

Cunjie Zhao, Yibin Yao, Jian Kong and Leilei Li

Abstract Ionospheric delay error is one of the most important errors in navigation and positioning. Ignoring the effects of the second and the upper order terms of the ionosphere, dual-frequency/multi-frequency receivers eliminate the effects of ionospheric delay error through ionosphere-free combination model, while single frequency receivers can only weak the ionospheric delay error through the ionospheric model parameters broadcasted by satellite navigation and positioning systems. In the current major satellite navigation systems, GPS uses the Klobuchar ionosphere model, BDS uses the improved Klobuchar ionosphere model, and Galileo uses the NeQuick ionosphere model. Analysing the influence of GPS Klobuchar model, BDS Klobuchar model and NeQuick model on navigation and positioning accuracy in China has great significance to guide the single frequency receivers in China to select the suitable ionospheric parameters broadcasted by satellite navigation and positioning systems. In this paper, GPS L1 single-frequency observation data of 8 sites in Crustal Movement Observation Network of China are used, the GPS Klobuchar model, BDS Klobuchar model and NeQuick model are selected for single point positioning. The final positioning results are compared to evaluate the correction accuracy of the three models in China. The results show that choosing the NeQuick ionosphere parameters in China is more conducive to improving the navigation positioning accuracy in the region, followed by selecting the BDS Klobuchar ionosphere parameters and finally selecting the GPS Klobuchar ionosphere parameters.

Keywords Ionospheric delay · NeQuick model · GPS klobuchar model
BDS klobuchar model · Single point positioning

C. Zhao (✉) · Y. Yao
School of Geodesy and Geomatics, Wuhan University, Wuhan, China
e-mail: zhao.cunjie@163.com

J. Kong
Chinese Antarctic Center of Surveying and Mapping, Wuhan, China

L. Li
College of Aerospace Engineering, Chongqing University, Chongqing, China

J. Sun et al. (eds.), *China Satellite Navigation Conference (CSNC) 2018 Proceedings*, Lecture Notes in Electrical Engineering 498,
https://doi.org/10.1007/978-981-13-0014-1_41

1 Introduction

The ionosphere is an atmosphere which is about 60 to 1000 km above the ground. It is an important part of the space environment over the Earth and is responsible for the scattering, reflection, refraction and absorption of the radio waves passing through it [1]. The ionospheric delay error is one of the most important sources of error in GNSS navigation and positioning. It can reach more than 10 m in the zenith direction and more than 50 m when the satellite elevation angle is small [2]. Ignoring the effects of the second and the upper order terms of the ionosphere, dual-frequency/multi-frequency receivers eliminate the effects of ionospheric delay error through ionosphere-free combination model, while single frequency receivers can only weak the ionospheric delay error through the ionospheric model parameters broadcasted by satellite navigation and positioning systems [3]. In the current major satellite navigation systems, GPS uses the Klobuchar ionosphere model, BDS uses the improved Klobuchar ionosphere model, and Galileo uses the NeQuick ionosphere model. Analysing the influence of GPS Klobuchar model, BDS Klobuchar model and NeQuick model on navigation and positioning accuracy in China has great significance to guide the single frequency receivers in China to select the suitable ionospheric parameters broadcasted by satellite navigation and positioning systems.

2 Model Introduction

2.1 GPS Klobuchar Model

Globe Positioning System uses GPS Klobuchar model as its broadcast ionospheric correction model. In this paper, we call it GPS Klobuchar model. The GPS Klobuchar model is an ionospheric empirical model proposed by Klobuchar in 1987 [4] and is one of the ionospheric models most familiar to single-frequency navigation users. The advantage of the GPS Klobuchar model is that it has a simple formula and a high calculation time [5]. The model has eight parameters, which are broadcasted by GPS ephemeris to the users. The model is a piecewise function that describes the daytime ionospheric delay as the positive part of the cosine function and consists of the initial phase, cycle, and amplitude, setting the nighttime ionospheric zenith delay to 5 ns. These representations basically reflect the changing characteristics of the ionosphere and ensure the reliability of the ionospheric prediction from a large scale. The global correction accuracy of the model is about 50–60%. Corrections are better in mid-latitudes and lower in polar and equatorial regions where the ionospheric variation is greater [6, 7].

2.2 BDS Klobuchar Model

BDS satellite navigation system uses improved Klobuchar ionosphere model which is adapted for the Chinese region. In this paper, we call it the BDS Klobuchar model. The BDS Klobuchar model and the GPS Klobuchar model are roughly the same in calculation but slightly different. First of all, the GPS Klobuchar model uses the geomagnetic coordinate system, while the BDS Klobuchar model uses the solar solid geographic coordinate system. The advantage is that the unity of the geographical longitude and time is better, and the daily variation of the ionosphere is in good agreement with it. Second, there are differences between the two models in the choice of model-related parameters [8]. The broadcasting parameters of the BDS Klobuchar model are calculated based on the data of the monitoring stations in China. There is no data in the southern hemisphere. Therefore, the symmetrical mode with the northern hemisphere is adopted in the southern hemisphere. BDS Klobuchar model calculation can refer to < BeiDou Navigation Satellite System Signal In Space Interface Control Document > (version 2.0) [9].

2.3 NeQuick Model

The real-time single-frequency ionospheric correction model of the Galileo satellite navigation system is the NeQuick model. The NeQuick model is a three-dimensional ionospheric model developed by the International Center for Theoretical Physics (ICTP) in Italy and the University of Graz in Austria [10]. NeQuick model uses an improved DGR model [11, 12] to describe electron densities of 90–20,000 km above a given time and position. The NeQuick model divides the model into two parts based on the peak height of the F2 layer, hmF2: (a) the bottom part of the hmF2 is the bottom model, represented by the three Epstein layers; (b) the top part of the hmF2 is the top model, represented by the semi-Epstein layer. The input parameters include: position, time, effective ionospheric level factor AZ (determined by three coefficients broadcasted by Galileo ephemeris), and the output parameters is the electron density at a given position and time. The ionospheric STEC values along the propagation path from the satellite-to-site can be numerically integrated. NeQuick model calculation can refer to < Ionospheric Correction Algorithm for Galileo Single Frequency Users > [13].

3 Experiments and Analysis

In this paper, we divide the state of the ionosphere into two different situations: the ionospheric calm state and the ionospheric disturbance state, according to the geomagnetic activity index (Dst). A total of 8 sites in Crustal Movement

Observation Network of China are used, which are HRBN, SHA2, GDZH, HBXF, GSDX, YNJD, LHAS and XJWL. The exact coordinates of the sites are calculated by the Gamit software with GNSS observations in 2015 065–067 days. The satellite-to-site ionospheric delays are calculated at the observation epoch using the GPS Klobuchar model, the BDS Klobuchar model, and the NeQuick model, respectively. Since we only use the GPS L1 single-frequency observation data for the single-point positioning in this paper, the satellite-to-site ionospheric delay calculated by the BDS Klobuchar model and the NeQuick model needs to be reduced to the GPS L1 frequency. The single-point positioning results of each station are decomposed into two-dimensional horizontal direction and elevation direction. The root mean square error (RMS) is compared to evaluate the positioning accuracy of the three models in China.

3.1 Ionospheric Calm State

The day 065 in 2015 is selected as the ionospheric calm state, when the Dst index is 0nT. It can be seen from Figs. 1, 2 and 3 that when the ionosphere is calm, the accuracy of using the NeQuick model in the sites except HRBN and XJWL is significantly improved both in the horizontal direction and in the elevation direction compared with the GPS Klobuchar model and the BDS Klobuchar model. The accuracy of using the BDS Klobuchar model is significantly improved in the horizontal direction and is limited improved in the elevation direction compared with the GPS Klobuchar model. In HRBN and XJWL, the positioning accuracy of the three models is similar. It may be because the activity of the ionosphere decreased at higher latitudes and the effects of the three models on the improvement of the ionosphere are similar.

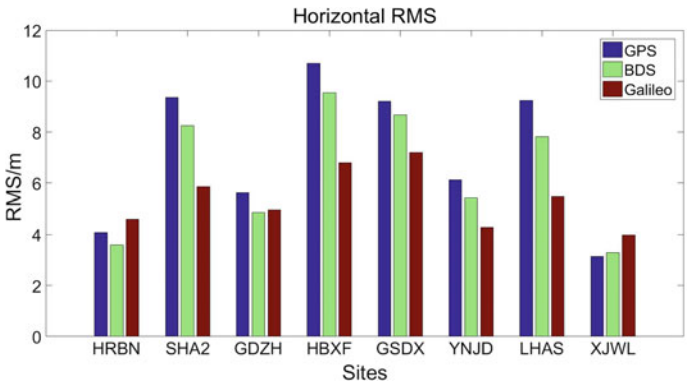

Fig. 1 Horizontal RMS for ionospheric calm state

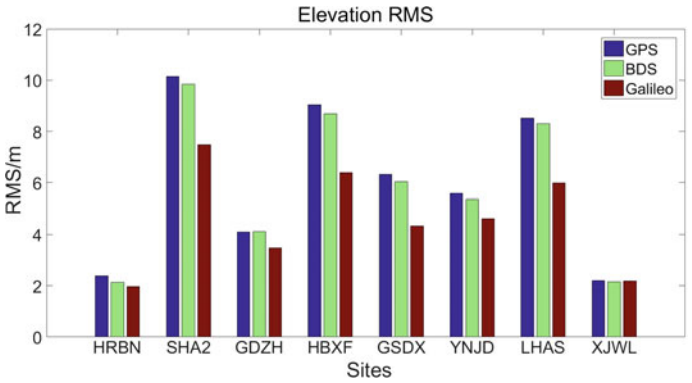

Fig. 2 Elevation RMS for ionospheric calm state

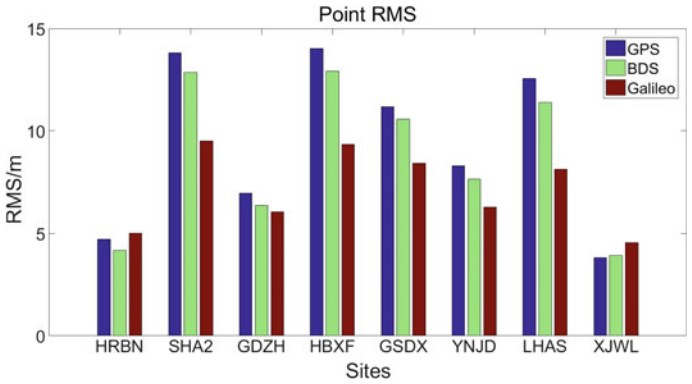

Fig. 3 Point RMS for ionospheric calm state

3.2 Ionospheric Disturbance State

The day 077 in 2015 is selected as the ionospheric disturbance state, when the Dst index is −105nT. As seen from Figs. 4, 5 and 6 that in the ionospheric disturbance state, the NeQuick model has the same or significantly improved in the horizontal direction accuracy compared with the BDS Klobuchar model and the GPS Klobuchar model. In addition to the YNJD and LHAS sites, significant improvements have been made in the elevation direction. For the YNJD and LHAS sites, it is probably because that most of the monitoring stations covered by Galileo in the world are located in Europe and the marine regions as of the end of 2014, while the altitude is high in Yunnan and Tibet. Maybe the calculated effective ionospheic level factor AZ is inconsistent with the actual situation. Compared with the GPS Klobuchar model, the BDS Klobuchar model improves the positioning accuracy in

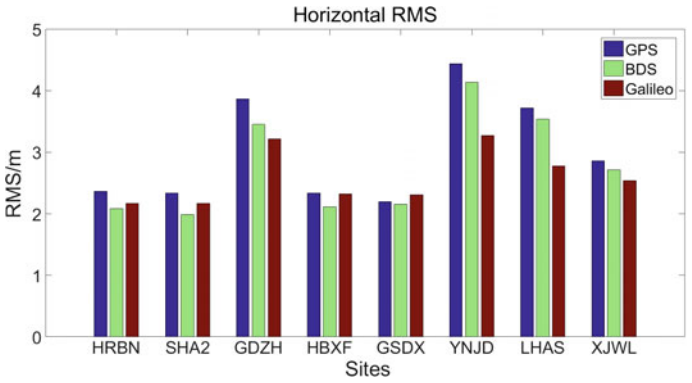

Fig. 4 Horizontal RMS for ionospheric disturbance state

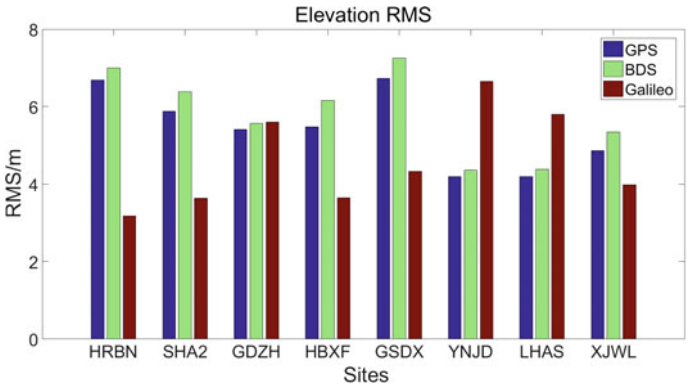

Fig. 5 Elevation RMS for ionospheric disturbance state

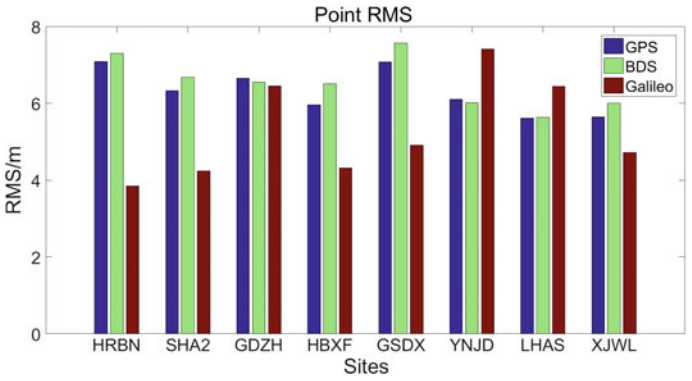

Fig. 6 Point RMS for ionospheric disturbance state

the horizontal direction slightly and decreases the positioning accuracy in the elevation direction slightly, but it is not obvious. In general, the two models perform similarly during periods of ionospheric disturbance state.

4 Conclusion

In this paper, the GPS L1 single frequency observation data of a total of 8 sites in Crustal Movement Observation Network of China are used for single point positioning. GPS Klobuchar model, BDS Klobuchar model and NeQuick model are used to calculate the satellite-to-site ionospheric delays, respectively. In order to reflect the influence of three models on positioning accuracy under different ionospheric conditions, we divide the state of ionosphere into two different situations: the ionospheric calm state and the ionospheric disturbance state, according to the geomagnetic activity index (Dst). The results show:

(1) In the case of ionospheric calm state: In middle and low latitude regions, the positioning accuracy of using the NeQuick model is significantly improved both in the horizontal direction and in the elevation direction compared with GPS Klobuchar model and BDS Klobuchar model. The positioning accuracy of using the BDS Klobuchar model is significantly improved in the horizontal direction and is slightly improved in the elevation direction compared with the GPS Klobuchar model. In the mid-high latitude regions, the positioning accuracy of the three models is comparable.
(2) In the case of ionospheric disturbances state: except for Yunnan and Tibet region, the positioning accuracy of using NeQuick model is close to or better than GPS Klobuchar model and BDS Klobuchar model both in horizontal direction and elevation direction. The GPS Klobuchar model and the BDS Klobuchar model perform equally well during periods of ionospheric disturbance state.

In general, choosing the NeQuick ionosphere parameters in China is more conducive to improving the navigation positioning accuracy, followed by selecting the BDS Klobuchar ionosphere parameters and finally selecting the GPS Klobuchar ionosphere parameters.

References

1. XU JiSheng, ZOU YuHua, Time-dependent 3-D computerized ionospheric tomography with ground-based GPS network and occultation observations. Wuhan University
2. Li Z, Huang J (2005) GPS Surveying and Data Processing. Wuhan University Press, Wuhan
3. Wang N, Yuan Y, Li Z et al (2016) An examination of the Galileo NeQuick model: comparison with GPS and JASON TEC. GPS Solutions 21(2):1–11

4. Klobuchar JA (2007) Ionospheric time-delay algorithm for single-frequency GPS Users. IEEE Trans Aerospace Electr Syst 23(3):325–331
5. Zhe Y (2012) SONG. Accuracy assessment of klobuchar model and NeQuick model in China. Geomatics Info Sci Wuhan Uni 37(6):704–708
6. Zhang Q, Zhao Q, Zhang H et al (2014) Evaluation on the precision of Klobuchar model for BeiDou navigation satellite system. Geomatics Info Sci Wuhan Uni
7. Zhang Q, Zhao Q, Zhang H et al (2013) Research on Beidou navigation satellite system Ionosheric model accuracy. In: China satellite navigation conference (CSNC) 2013 Proceedings, Wuhan
8. Wen-Wen LI, Min LI, Zhi-Gang HU et al (2013) Comparative analysis of BDS and GPS ionospheric model on positioning and navigation precision. J Navig Positioning
9. Ran C (2013) BeiDou navigation satellite system signal in space interface control document (Version 2.0). Management office of Beidou Navigation Satellite System, Beijing
10. Nava B, Coïsson P, Radicella SM (2008) A new version of the NeQuick ionosphere electron density model. J Atmos Solar Terr Phys 70(15):1856–1862
11. Giovanni GD, Radicella SM (1990) An analytical model of the electron density profile in the ionosphere. Adv Space Res 10(11):27–30
12. Radicella SM, Zhang ML (1995) The improved DGR analytical model of electron density height profile and total electron content in the ionosphere. Ann Geophys 38(1)
13. Centre E G S. IonospherIc CorrectIon AlgorIthm For Galileo Single Frequency Users. 2016

Analyzing the Precision and Regional Modeling Method of Tropospheric Delay Based on Multi-base Station GPS Observations

Wenchao Jin and Zhiyong Liu

Abstract Tropospheric delay is one of the main factors that affect obtaining a higher precision of long-distance RTK. In order to optimize the tropospheric delay modeling method and obtain a higher positioning precision, this paper uses the measured zenith tropospheric delay data of BJFS and URUM station to calculate the tropospheric zenith delay and RMS of four classical tropospheric delay correction models, the precision and applicability of classical model are analyzed, Hopfield model and Saastamoinen model have a higher precision. But for high precision baseline solution, the precision can not meet the requirements. Therefore, the GPS measurement method based on multi-base station GPS network is adopted. In order to analyze the factors that should be considered in the model, the tropospheric delay of several CORS stations calculated by a classical model is compared and analyzed. It is concluded that there is a positive correlation between the tropospheric delay and elevation, which provides evidence for modeling. And the applicability of several regional modeling methods is theoretically analyzed. The best method to choose base stations of multi-base station modeling is analyzed by several experiments and it is concluded that when the base station is laid in the mountainous area with gentle troposphere change, it should take into account the uniformity of the plane position distribution of the station under the condition of giving priority to the regional elevation range. By this way, the model can reflect regional characteristics better and obtain a higher degree of precision. And the precision and applicability of region modeling method of tropospheric delay is studied through three experimental networks. The tropospheric delay modeling methods based on multi-base station GPS observations obtained in this paper will obtain a higher degree of precision and a better applicability with regional range reducing. In different regions, the different method of tropospheric delay modeling should be chosen. In small-sized and medium-sized areas with gentle tropospheric change, the H1QM3 is the most suitable model for tropospheric delay calculation and the precision is better than 1 cm.

W. Jin (✉) · Z. Liu
Chengdu Institute of Surveying and Mapping, Chengdu, China
e-mail: 18380120378@163.com

J. Sun et al. (eds.), *China Satellite Navigation Conference (CSNC) 2018 Proceedings*, Lecture Notes in Electrical Engineering 498,
https://doi.org/10.1007/978-981-13-0014-1_42

Keywords Tropospheric delay · Regional modeling · H1QM3
Precision analysis of models

1 Introduction

Due to its high performance, high precision and high degree of automation, the Global Positioning System (GPS) suits the needs of surveying and mapping and is applied in various fields. Atmospheric refraction always limites the improvement of GPS positioning precision, of which tropospheric delay is the key factor [1]. Due to the complexity of the troposphere and accompanying changes, the conventional atmospheric models are difficult to show its characteristics. Therefore, Regional modeling of tropospheric delay based on the multi-base station GPS observation network becomes a solution to real-time monitoring of the troposphere and improve the real-time dynamic positioning precision [2]. In addition, the modeling of the troposphere will also break down the obstacles of the limited working distance of traditional RTK technology and broaden the application fields.

In this paper, first, the precision and applicability of the classic models of tropospheric delay correction are analyzed using the measured data; Second, the general law to select reference stations of tropospheric delay modeling based on multi-base station GPS observations is discussed in the experimental networks; Finally, The precision and applicability analysis were carried out, and the regional modeling methods meting the requirements of high precision baseline solution was selected.

2 Precision Analysis of Classical Tropospheric Delay Correction Model

Tropospheric delay values of Hopfield [3], Saastamoinen [4] and Black [5] are calculated by the five-day meteorological data from IGS product of BJFS and URUM station of Continuous Operational Reference System (CORS) sampling interval of 2 h. Using Pressure, temperature, vapor pressure, temperature gradient and water vapor gradient of mean sea level calculates the tropospheric delay value of the EGNOS [6]. The Normalized Root Mean Square (NRMS) in the solution results of GAMIT software is less than 0.3, which indicates that the precision of the baseline solution is high and the tropospheric delay value can be used as a standard value. Therefore, the RMS of the tropospheric delay error of the classical model can be obtained. The result is shown in Tables 1 and 2.

As Tables 1 and 2 shows, Hopfield and Saastamoinen obtain a higher precision in classical models, which can reach up 3–4 cm.

Table 1 RMS of classical models in several days of BJFS m

Model	Time					
	170616	170715	170815	170915	171010	Mean
Hopfield	0.016	0.058	0.033	0.039	0.039	0.037
Saastamoinen	0.015	0.046	0.020	0.034	0.039	0.031
Balck	0.105	0.289	0.263	0.182	0.115	0.191
EGNOS	0.075	0.061	0.080	0.033	0.036	0.057

Table 2 RMS of classical models in several days of URUM m

Model	Time					
	170616	170715	170815	170915	171010	Mean
Hopfield	0.105	0.122	0.095	0.070	0.048	0.088
Saastamoinen	0.060	0.072	0.049	0.030	0.010	0.044
Balck	0.133	0.190	0.129	0.081	0.039	0.114
EGNOS	0.216	0.200	0.217	0.211	0.215	0.212

3 Tropospheric Delay Regional Fitting Modeling Based on GPS Observations of Multiple Base Station

Although the precision of the Hopfield and Saastamoinen model is higher in classical models, the precision can not suit the need for high-precision baseline solution. Therefore, the tropospheric delay regional fitting model based on multi-base station GPS observations is used to improve the precision.

3.1 Tropospheric Delay Modeling

According to the complexity of the model and the choice of parameters, this paper selects the following seven models [7]:

1. Three-parameter Flat model with one elevation factor (H1QM3)

$$d_t = a_0 + a_1 x + a_2 y + a_3 h$$

2. Four-parameter Surface model with one elevation factor (H1QM3)

$$d_t = a_0 + a_1 x + a_2 y + a_3 xy + a_4 h$$

3. Quadratic surface model with one elevation factor (H1QM6)

$$d_t = a_0 + a_1 x + a_2 y + a_3 xy + a_4 x^2 + a_5 y^2 + a_6 h$$

4. Curve model with one elevation factor (H1QX1)

$$d_t = a_0 + a_1 h$$

5. Quadratic curve model with one elevation factor (H1QX2)

$$d_t = a_0 + a_1 h + a_2 h^2$$

6. Surface model with two elevation factor (H2QM3)

$$d_t = a_0 + a_1 x + a_2 y + a_3 xh + a_4 yh$$

7. Surface model with three elevation factor (H1QM6)

$$d_t = a_0 + a_1 x + a_2 y + a_3 xh + a_4 yh + a_5 h$$

Where: a is a polynomial coefficient, x, y and h were north coordinates, east coordinates and elevation, dt is tropospheric delay.

3.2 Analyzing Precision of Models

To establish a regional tropospheric delay model, the best method to choose reference stations is required. Therefore, this paper selects a part of SCIGN (South California Integrated GPS Net), which consists of 27 points and covers an area of about 60 km × 60 km. Its distribution is shown in Fig. 1.

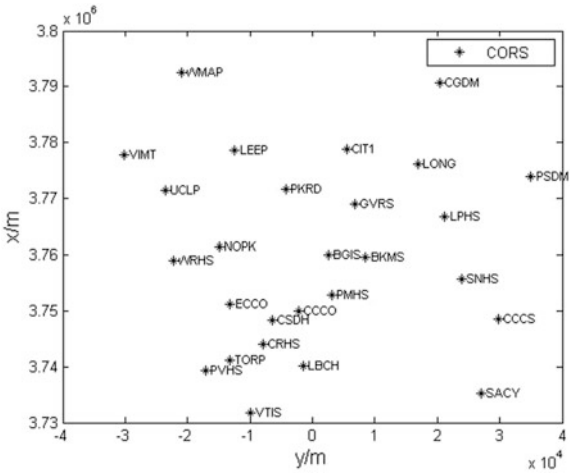

Fig. 1 Distributing graph of reference station in SCIGN

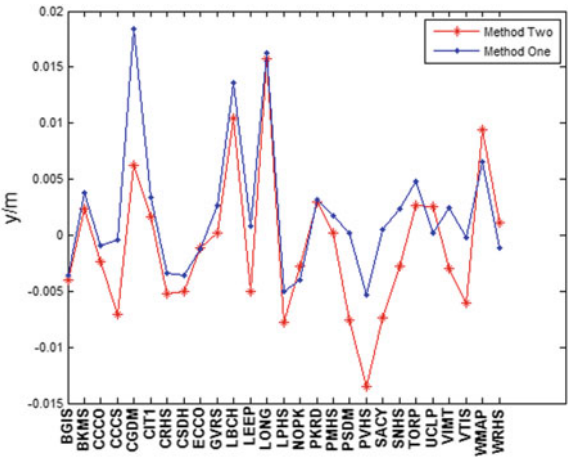

Fig. 2 Tropospheric delay error of CORS station by two methods

This paper selects H1QM3 model and the full-network to ananlyze the best method to choose reference stations. Two methods to choose reference stations are applied to calculate the error and the RMS of tropospheric delay using station meteorological data on the 350th day of 2002. The result is shown in Fig. 2.

As Fig. 2 shows, the tropospheric delay error of the two methods are generally same, and the precision of the two methods is calculated to be 6–7 mm. The almost absolute value of tropospheric delay error of stations is less than 1 cm. Analysis shows that CGDM and LBCH stations beyond the elevation range of the reference stations in Method 1, so the correlation will be reduced which result in a lower precision. However, values of stations such as VIMT, WMAP and LEEP that beyond the base station range in the X or Y direction are all less than 1 cm; the three-dimensional coordinates of LONG in Method 1 and PVHS and LONG in Method two are within the range of the reference stations, but the value are larger than 1 cm, which reflects the limitation of H1QM3.

In summary, when laying out base stations in mountainous areas where the troposphere changes gently, covering elevation range is prior to covering flat coordinates for reference stations and the uniformity of the location distribution should be taken into account. In this way, the information will better reflect the regional characteristics and improves the positioning precision in the network.

3.2.1 Test One: Application Analysis of Models in SCIGN

This experiment network locates at mountain. Basing on the general law of choosing base stations mentioned in the previous content, CCCS, CGDM, LBCH, PSDM, PVHS, UCLP, VTIS and WRHS are selected as the base stations for regional modeling. In order to verify the precision of the model, The results of GAMIT software show that the NRMS values are less than 0.3, so the tropospheric

Table 3 RMS of models in several time interval m

Time	Model						
	H1QM3	H1QM4	H1QM6	H1QX1	H1QX2	H2QM3	H3QM3
0	0.0053	0.0053	0.0145	0.0597	0.0628	0.0095	0.0056
2	0.0051	0.0053	0.0068	0.0600	0.0657	0.0063	0.0054
4	0.0039	0.0040	0.0088	0.0627	0.0674	0.0074	0.0035
6	0.0048	0.0043	0.0105	0.0614	0.0635	0.0064	0.0038
8	0.0053	0.0051	0.0121	0.0618	0.0644	0.0104	0.0059
10	0.0043	0.0044	0.0128	0.0615	0.0643	0.0069	0.0037
12	0.0048	0.0046	0.0073	0.0612	0.0660	0.0043	0.0034
14	0.0062	0.0062	0.0162	0.0605	0.0619	0.0101	0.0065
16	0.0041	0.0048	0.0069	0.0605	0.0641	0.0053	0.0047
18	0.0069	0.0074	0.0122	0.0573	0.0623	0.0094	0.0070
20	0.0080	0.0080	0.0129	0.0572	0.0612	0.0076	0.0080
22	0.0091	0.0076	0.0181	0.0626	0.0633	0.0060	0.0054
24	0.0105	0.0116	0.0201	0.0659	0.0675	0.0073	0.0092
Mean	0.0060	0.0060	0.0122	0.0609	0.0642	0.0074	0.0055

delay value at the sampling interval of 2 h on the 350th day of 2002 is obtained as the standard value to calculate the tropospheric delay error RMS. The results are shown in the following Table 3.

As Table 3 shows, the RMS of H1QM3, H1QM4, H2QM3 and H3QM3 models are all less than 1 cm, and the precision is significantly higher than that of the traditional methods. The precision of H1QM6 is also about 1 cm, which is higher than the traditional method. The RMS of H1QX1 and H1QX2 models are all more than 4 cm, which is bigger than RMS of Saastamoinen and Hopfield.

In SCIGN, the H1QM3 model is the best choice considering the precision and complexity of modeling.

3.2.2 Test Two: Application Analysis of Models in Chinese GPS Network

The experimental network consists of 10 CORS stations covering an area about 2900 km × 2000 km. Basing on the general law of choosing base stations mentioned in the provious content, the test selects six CORS stations as reference stations. Its distribution is shown in Fig. 3.

The results of GAMIT software show that the NRMS values are less than 0.3, so the eight-day tropospheric delay value at the sampling interval of 2 h is obtained as the standard value to calculate the tropospheric delay error RMS every two hour except for H1QM6 and daily RMS can be obtained by average. The result are shown in the following Table 4.

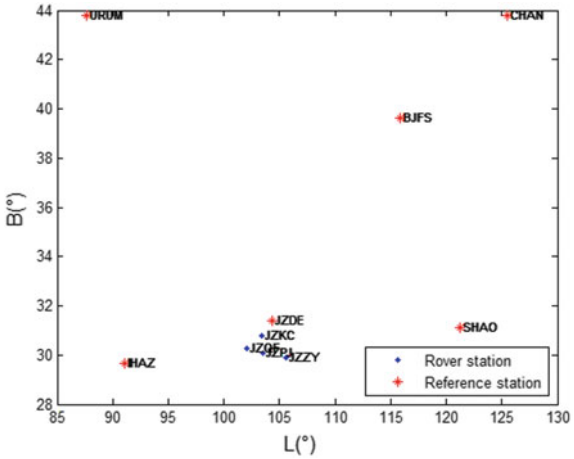

Fig. 3 Distributing graph of reference station in Chinese GPS Network

Table 4 RMS of models in several time interval m

Time	Model					
	H1QM3	H1QM4	H1QX1	H1QX2	H2QM3	H3QM3
170515	0.009	0.010	18.177	47583.608	0.013	0.009
170616	0.048	0.021	18.573	41592.467	0.041	0.020
170715	0.027	0.020	21.224	63031.177	0.021	0.014
170815	0.020	0.010	16.900	54816.317	0.018	0.012
170915	0.023	0.012	14.246	54511.272	0.019	0.015
171010	0.020	0.015	10.110	58594.716	0.016	0.012
171116	0.036	0.016	15.825	46417.840	0.014	0.005
171215	0.027	0.009	18.345	47852.556	0.010	0.008
Mean	0.026	0.014	16.675	51799.994	0.019	0.012

As Table 4 shows, The precision of models are better than that of classical model except for H1QX1 and H1QX2.

In the Chinese trial network, taking into account the precision and complexity of modeling, H1QM4 model is the best choice.

3.2.3 Test Three: Application Analysis of Models in Sichuan GPS Net

The experimental network consists of some Sichuan GPS stations, covering an area about 300 km × 300 km. Basing on the general law of choosing base stations mentioned in the previous content, the test uses CORS stations such as MYAN, PIXI, ZHJI, YAAN, RENS, ROXI, YBIN and LUZH as reference stations. Its distribution is shown in Fig. 4.

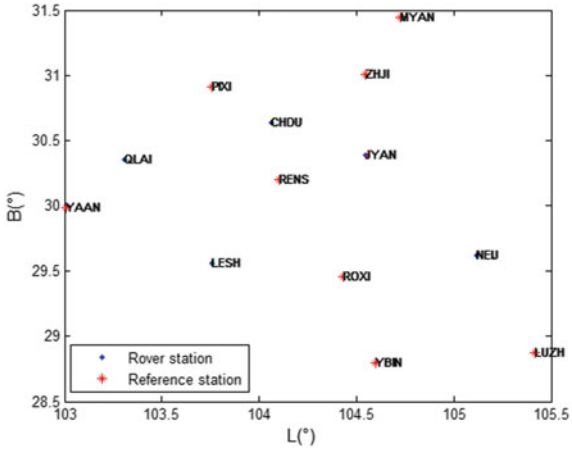

Fig. 4 Distributing graph of reference station in Sichuan GPS Network

The results of GAMIT software show that the NRMS values are less than 0.3, so the tropospheric delay value at the sampling interval of 2 h on May 12, 2014 is obtained as the standard value to calculate the tropospheric delay error RMS. The results are shown in the following Table 5.

As Table 5 shows, the precision of models are all 1–2 cm in experimental conditions and higher than the traditional method.

Therefore, in the Sichuan experimental network, the precision of H1QM6 is the highest. but H1QM3 is the best optimal choice for regional modeling.

Table 5 RMS of models in several time interval m

Time	Model				
	H1QM3	H1QM4	H1QM6	H2QM3	H3QM3
0	0.0090	0.0098	0.0096	0.0089	0.0143
2	0.0099	0.0101	0.0092	0.0091	0.0130
4	0.0084	0.0103	0.0078	0.0077	0.0139
6	0.0087	0.0088	0.0077	0.0088	0.0091
8	0.0065	0.0068	0.0046	0.0067	0.0084
10	0.0065	0.0067	0.0046	0.0067	0.0084
12	0.0064	0.0067	0.0045	0.0066	0.0083
14	0.0064	0.0067	0.0045	0.0066	0.0084
16	0.0064	0.0066	0.0045	0.0066	0.0083
18	0.0064	0.0066	0.0045	0.0066	0.0083
20	0.0063	0.0066	0.0045	0.0065	0.0083
22	0.0063	0.0066	0.0045	0.0065	0.0083
24	0.0703	0.0705	0.0698	0.0704	0.0710
Mean	0.0121	0.0125	0.0108	0.0121	0.0145

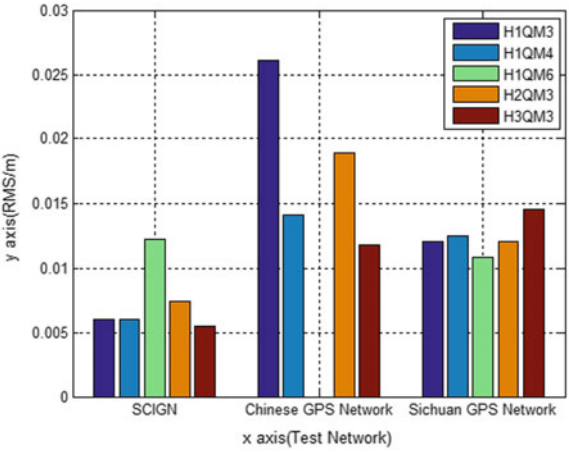

Fig. 5 Histogram of RMS in three test network

To analyze the precision and applicability of the tropospheric delay modeling method based on multi-base station GPS observations, a histogram of mean value of RMS of models over the three experimental networks is plotted in Fig. 5.

As Fig. 5 shows that, H1QM3, H1QM4, H1QM6, H2QM3 and H3QM3, have a higher precision than that of classical models.

4 Conclusion

After analysis of the three tests, a series of conclusions can be drawn:

- From Chinese Test Network to Sichuan Test Network and then to SCIGN, the precision of models is generally improved. In SCIGN, the precision of models can reach up several millimeters except for H1QM6. Thus, as the area of tropospheric delay modeling methods based on the multi-base station GPS observations is reduced, the higher the precision, the better the applicability.
- The model with the highest precision and the best choice in the test are not always same, and the applicability of the model is different. In SCIGN, the precison of H3QM3 is the best, and H1QM3 is the best choice. Therefore, we can draw a conclusion that H1QM3 has the best applicability in small areas where the tropospheric gradients are not significant changing along the elevation in the x and y directions. In Sichuan network, the precision of H1QM6 is the best, and H1QM3 is the best choice. Therefore, we can draw the conclusion that the H1QM3 has the best applicability in medium-sized regions where the non-linear change of the troposphere with the plane position change is not significant. In the Chinese network, the precision of H1QM6 is the best and the

H1QM4 model is the optimal choice. Therefore, the model based on the linear relationship with x, y and h can not show the tropospheric variation when the area is large enough, and the nonlinear variation should be considered; In summary, H1QM3 is most suitable for tropospheric delay solution in small and medium-sized regions where the tropospheric changes are gentle.

- The fitting error of model H1QX1 and H1QX2 in China and Sichuan experiment network is too large, which reach up several meters, and the precision of model H1QX1 and H1QX2 in SCIGN is the worst. Therefore, models considering only the troposphere change with elevation can not objectively reflect the regular pattern of tropospheric changes.
- The troposphere has regional characteristics. Establishing a regional GPS control network, it is advisable to consider whether the span of the area will cause the tropospheric characteristics change in addition to considering the size of the regional network, which will influence the parameters selection and precision of the tropospheric modeling. In order to further study the scope of the model, it is suggested to refine the range gradient of the experimental network. Building a balanced relationship between the data sample interval and the volume of data will ensure the high precision and high efficiency of regional modeling.

Acknowledgements This work is supported by the updating maintenance of Chengdu city control network fund project (No. 2016022).

References

1. Yin H (2006) Study on the regional tropospheric delay 4-dimension modeling and applications based on the multiple reference stations network. Southwest Jiaotong University, Doctor Degree Dissertation 1–7
2. Maorong G, Jingnan L (1996) Study on tropospheric refraction estimation in GPS positioning. J Mapping 25(4):84–91
3. Bock O, Doerflinger E (2001) Atmospheric modeling in gps data analysis for high accuracy positioning. Phys Chem Earth (A) 26:373–383
4. Tang W, Wang J Jin Y (2004) Design and establishment of virtual reference station system. Mod Mapping 02
5. Dick G, Gendt G, Reigber C (1999) Operational water vapor estimation in a dense german network. IGS 1999 Technical Report 375–384
6. Collins P, Langley RB (1999) Tropospheric delay: prediction for the WAAS user. GPS World 10(7):52–58
7. Yongliang X, Dingfa H, Xiaoli D, Haitao Y (2005) Tropospheric delay correction model based on multiple GPS reference stations. J Eng Invest 5:56–57

A Modified LLL-MIGS Decorrelation Algorithm and Time Efficiency Assessment Measure

Mingkun Su, Jiansheng Zheng, Yanxi Yang and Qiang Wu

Abstract LLL reduction algorithm has been used as a new technique of decorrelation to GNSS ambiguity resolution for recent years. The basic idea of this method is to make the variance-covariance matrix as orthogonal as possible by virtue of integer Gram-Schmidt orthogonalization, based on this we also refer to as LLL-IGS. Although LLL-IGS can indeed be used for decorrelation, the experiments indicated that it performs worse and deteriorates in some cases, especially for real GNSS data. In this contribution, (i) A modified LLL-MIGS decorrelation algorithm is proposed by improving the sorting method and removing the error of orthogonalization. (ii) The time efficiency is introduced as a new assessment criterion to measure the performance of the decorrelation algorithm directly. The time efficiency includes the decorrelation time efficiency and searching time efficiency. (iii) Real GNSS observations which including short baseline, network-based medium and long baselines have been used to compare the LLL-MIGS with LLL-IGS and also to analyze them in depth. The results of the experiments show that the LLL-MIGS method performs better than LLL-IGS method in decreasing condition number and reducing time consumption which includes the decorrelation time consumption and searching time consumption. Moreover, both of them indicate that the modified LLL-MIGS algorithm is more stable than the traditional LLL-IGS method.

Keywords Decorrelation algorithm · LLL-MIGS · Time efficiency GNSS

J. Zheng (✉) · Q. Wu
School of Electronic Information, Wuhan University, Wuhan 430079, China
e-mail: jszwhu@gmail.com

M. Su · Y. Yang
Research Center of GNSS, Wuhan University, Wuhan 430079, China

J. Sun et al. (eds.), *China Satellite Navigation Conference (CSNC) 2018 Proceedings*, Lecture Notes in Electrical Engineering 498,
https://doi.org/10.1007/978-981-13-0014-1_43

1 Introduction

In the realm of high precision GNSS positioning, decorrelation algorithm can reduce the correlation of the variance-covariance matrix effectively and improve the efficiency of ambiguity resolution. Among these ambiguity resolution approaches, the most successful method is the LAMBDA, which was proposed by Teunissen [1–3]. Based upon the LAMBDA algorithm, Chang [4] developed the modified LAMBDA (MLAMBDA) method. Numerous simulations demonstrated that the MLAMBDA method can reduce the computational complexity effectively and perform faster than LAMBDA method on decreasing the correlation of the variance-covariance. In addition, based on the direct high dimensional Gaussian transformation, a recursive decorrelation method has been proposed by Li and Gao [5]. After that, Liu et al. [6] proposed the united integer ambiguity decorrelation algorithm and introduced the condition number as a assessment measure to assess the performance of the decorrelation algorithms. Theoretically, these methods are all based on Gaussian transformation.

Xu [7] developed the inverse integer Cholesky decorrelation algorithm (ICHOL) and also presented a random simulation method. Zhou [8] proposed the inverse paired Cholesky integer transformation. Mathematically speaking, both of them are based on Cholesky decomposition. On the basis of LLL [9] reduction algorithm, Hassibi [10] presented a new decorrelation method, namely LLL decorrelation algorithm. Xu [7] and Lannes [11] studied and analyzed the performance of the LLL-IGS algorithm. The experiment results indicate that although LLL-IGS decorrelation algorithm can be used as a new technique for decorrelation, it performs worse and deteriorates in some cases, especially for real GNSS data.

In this research, in order to improve the performance of LLL-IGS method and make it better applied in the realm of decorrelation, the limitation and the source of the error of the LLL-IGS have been analyzed deeply. A modified LLL-MIGS decorrelation algorithm is proposed by improving the sorting method and removing the error of orthogonalization. The new method LLL-MIGS performs better than LLL-IGS significantly and is more stable in real GNSS data. In addition, we also introduce the time efficiency as a new measure criterion to assess the performance of the LLL-MIGS decorrelation algorithms directly.

2 A Modified LLL-MIGS Method

2.1 LLL-IGS Algorithm

Normally, the original variance-covariance matrix Q always can be decomposed by means of the Cholesky lower triangular decomposition into:

$$Q = LL^T \tag{1}$$

where L is a lower triangular matrix, and L^T is the transpose matrix. Theoretically, because Q is non-singular and full rank, the factorization is unique. To reach the goal of orthogonal, we can further decompose L by Gram-Schmidt orthogonalization, and express it as

$$L = GO \tag{2}$$

where G is unimodular, and O is almost orthogonalization. The process works as follows:

$$o_i = l_i - \sum_{j=1}^{i-1} g_{ij} o_j \tag{3}$$

$$g_{ij} = \left[(l_i, o_j)/(o_j, o_j) \right]_{in} \tag{4}$$

where l_i and O_i denote the row vectors of L and O, respectively. $(\cdot)$ denotes the ordinary inner product. $[\cdot]_{in}$ means rounded to the nearest integers. g_{ij} is the factors of the orthogonaliztion.

Then we have

$$Q = LL^T = GOO^T G^T \tag{5}$$

Then, we will achieve an almost diagonal matrix Q1, by left multipling Q by G^{-1} and right multipling it by $(GT)^{-1}$, respectively. It can be expressed as

$$Q_1 = G^{-1} Q \left(G^T \right)^{-1} \tag{6}$$

where the elements of G^{-1} are all integers, and it can be seen from Eq. 4. When transformation matrix G^{-1} is defined as Z, then the transformation matrix is achieved. At the same time, if the dimension is sufficiently large, one can improve the orthogonality by attempting to iterate the process from Eqs. 1–6. Then we have

$$\begin{aligned} Z &= Z_n Z_{n-1} \ldots Z_2 Z_1 \\ &= G_n^{-1} G_{n-1}^{-1} \ldots G_2^{-1} G_1^{-1} \end{aligned} \tag{7}$$

where n denotes the number of the iteration.

Xu [7] studied and analyzed the effect of different decomposition matrices L, different vectors for the orthogonalization and different orderings of the vectors during orthogonalization. Numerous results have shown that the way of decomposition does not affect the performance of decorrelation, and initial vector will largely determine the effect of decorrelation. He also showed that the LLL-IGS has greatest performance if the L in order of descending norm, but the performance of LLL-IGS is still worse and deteriorates in some cases, especially for real GNSS data.

2.2 A Modified LLL-MIGS Algorithm

In order to make the coefficient of the orthogonalization as small as possible, Xu [7] sort the vectors by the norm of the row vectors. The sorting method can improve the effect of decorrelation in a certain degree, but not significantly. Al Borno [12] proposed that, contrary to the common belief, decorrelation should pursue the permutation of the ordering of the diagonal entries. Hence, the other decorrelation algorithms reach the goal of decorrelation by using integer Gauss transformation and permutation. Specifically, they use the L^TDL decomposition and strive for the permutation of the diagonal entries of D.

Since the norm ranking method can only affect the factors of the orthogonalization, it cannot make the spectrum of conditional variances more flatten. Thus, we try to sort the diagonal entries of original matrix Q distributed in increasing order instead of sorting the norm of vectors. The sorting matrix is F

$$Q1 = FQF^T \tag{8}$$

where Q is original covariance matrix, F is the sorting matrix. The process of generating sorting matrix F as follows:

Algorithm 1: forming sorting matrix F

Given original matrix Q
Step 1: sort the diagonal entries of Q in increasing order and record the corresponding location before sorting. Then, we will obtain a sorting vector m(i:n)
Step 2: if the j of f_{ij} equal to m(i), $f_{ij} = 1$, or $f_{ij} = 0$
Step 3: loop step 2 from i = 1 to i = n
Step 4: form the sorting matrix F
Output the sorting matrix F

After algorithm 1, the new matrix Q1 can be achieved.

At the same time, it is obvious that Eq. 4 means the coefficient of orthogonalization g_{ij} will be rounded to the nearest integer before used to process the next orthogonalization vector. Hence, this fact can result in orthogonalization error especially in the following two situations: (i) with the increase of the dimension of covariance matrix, the error of orthogonalization will be gradually accumulated. (ii) the multi-time iteration also lead to magnify the error.

In order to remove the error of orthogonalization accumulation and improve the effect of transformation matrix diagonalization, we conduct the Gram-Schmidt orthogonalization procedure firstly, and then round the elements of G into integers. The procedure can be expressed as follows:

$$o_i = l_i - \sum_{j=1}^{i-1} g_{ij} o_j \tag{9}$$

$$g_{ij} = (l_i, o_j)/(o_j, o_j) \tag{10}$$

$$G = \begin{vmatrix} 1 & & & \\ [g_{21}]_{in} & 1 & & \\ . & . & 1 & \\ [g_{n1}]_{in} & [g_{n2}]_{in} & . & 1 \end{vmatrix} \tag{11}$$

The process of forming orthogonalization matrix G can be described as follows:

Algorithm 2: forming orthogonalization matrix G

Given lower triangular matrix L
Step 1: use Eqs. 9 and 10 orthogonal L(i:n) by the row vector of L. Recording the factors g_{ij}.
Step 2: rounding $[g_{ij}]_{in}$.
Step 3: generate the orthogonalization matrix G using the elements of step 2.
Output orthogonalization matrix G.

After achieving the orthogonalization matrix G, left and right multiplied by G^{-1} and $(G^{-1})^T$, we can obtain transformation variance-covariance matrix Qa, expressed as

$$Qa = G^{-1}FQF^T(G^{-1})^T \tag{12}$$

Then, the transformation matrix Z can be achieved

$$Z_1 = G^{-1}F \tag{13}$$

Similarly, we can further improve the orthogonality by attempting to iterate the process from Eqs. 8 to 12. In addition, in order to avoid deterioration of recursion, we set the maximum of the iteration number as 30. Hence, the iteration will be terminated when the G is identity matrix or the iteration number equal to 30. Thus, the transformation matrix is

$$\begin{aligned} Z &= Z_n Z_{n-1} \ldots Z_2 Z_1 \\ &= G_n^{-1} F_n G_{n-1}^{-1} F_{n-1} \ldots G_2^{-1} F_2 G_1^{-1} F_1 \end{aligned} \tag{14}$$

where n denotes the number of the iteration. The LLL-MIGS decorrelation algorithm has been implemented in following the flowchart in Fig. 1.

3 Comparative Study and Analysis

In this research, the experimental data are double difference static resolution for static receiving. Short baseline and Network-based baseline will be analyzed. The condition numbers and time efficiency will be used to compare the traditional

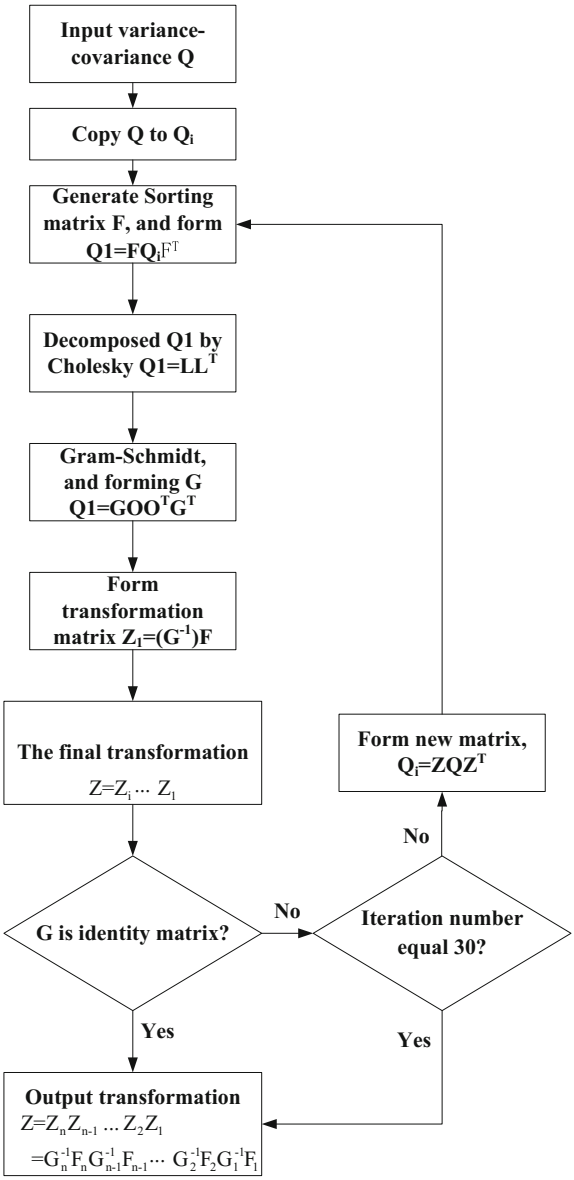

Fig. 1 Flowchart of proposed LLL-MIGS algorithm

LLL-IGS with new LLL-MIGS algorithm. The time efficiency contains the decorrelation time and searching time. To make a fair comparison, both of them are searched by the same search method. All presented results in this section are performed in Visual Studio 2010 on a PC, 3.09 GHz with 3.42 GB memory running Windows XP professional.

3.1 Short Baseline

The length of short baseline is 8 km. The base station and rover station are both equipped with Trimple NETR3 receiver. Experiment was conducted at 13:00 UT and ended at 15:00 UT on July 31, 2014. The time interval between the data is 15 s, and the cut-off angle is 10°.

Figure 2 shows the results of the condition numbers of the traditional LLL-IGS (red) and new LLL-MIGS (blue). It is obvious that the LLL-MIGS performs better than LLL-IGS in decreasing the condition numbers. The averages of condition numbers can be decreased from 8.69604 (LLL-IGS) to 1.3608 (LLL-MIGS). Meanwhile, LLL-IGS fluctuates more significantly than LLL-MIGS. The maximum of the condition number by LLL-IGS is 12.4989, and the minimum is 6.038144. However, the LLL-MIGS fluctuates from 2.7112 to 0.9089. Thus, the LLL-MIGS performs more stable than LLL-IGS.

Tables 1 and 2 show the statistics of the 200 numbers of time efficiency of traditional LLL-IGS algorithm and the LLL-MIGS method in unites of seconds. In these tables, the average means the average time of the 200 numbers of each method. The max and min mean the maximum one and minimum one of the 200

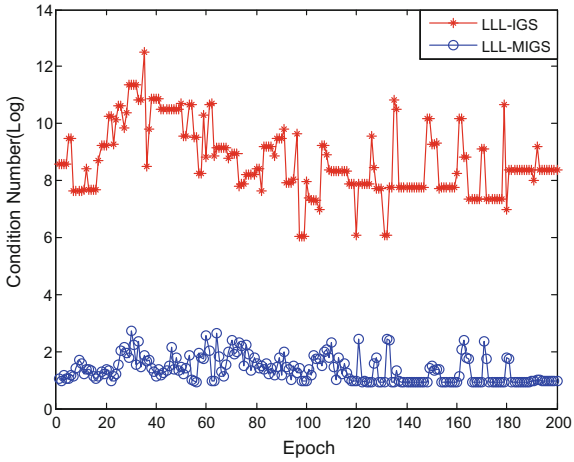

Fig. 2 Comparison of the condition numbers of the 200 examples after applying the LLL-IGS (red) and LLL-MIGS (blue) for short baseline, respectively

Table 1 The statistics of 200 numbers of epochs of decorrelation time (s), which was repeat 100 times by each decorrelation

	Max	Min	Average
LLL-IGS	0.0782	0.0156	0.0307
LLL-MIGS	0.0471	0.0151	0.0291

Table 2 The statistics of 200 numbers of search time (s), which was repeat 500 times by each search

	Max	Min	Average
LLL-IGS	0.2351	0.1152	0.1839
LLL-MIGS	0.0161	0.001	0.0045

numbers of the experiment indexes. Specifically, Table 1 shows the decorrelation time efficiency. From the Table 1, the minimum time of the LLL-IGS is almost same as the LLL-MIGS. And the maximum time is slightly less than LLL-IGS. Similarly, the average time of the LLL-MIGS is less than the LLL-IGS slightly. Therefore, in terms of the decorrelation time efficiency, Table 1 shows that the LLL-MIGS performs slightly better than the LLL-IGS algorithm in reducing decorrelation time consumption.

Table 2 presents the results of the searching time of the LLL-IGS and LLL-MIGS. It is obvious that the maximum and minimum time of the LLL-MIGS is far less than that LLL-IGS algorithm. Particularly for the minimum time, the LLL-IGS is 0.1151, but the modified LLL-MIGS method is only 0.001. Meanwhile, as a whole, the average of searching time can be decreased from 0.1839 to 0.0045. The LLL-MIGS is nearly 41 times faster than LLL-IGS. Hence, the modified LLL-MIGS method can effectively improve the search computational efficiency, and to further increase the speed of ambiguity resolution.

3.2 Network-Based Baseline

The modified LLL-MIGS is verified by the short baseline. Whether LLL-MIGS works well in complex application will be tested by network-based experiments. The location of the network is situated in western China as shown in Fig. 3. The base station ZYAN and two rover stations ZYXT, ZYSN. The length of the baseline ZYAN-ZYXT is 31.6 km and the ZYAN-ZYSN is 74.3 km. This experiment started at 17:00 UT and ended at 19:00 UT on November 25, 2013. The interval between data is 15 s. The cut-off angle is 10°.

Fig. 3 The locations of stations ZYAN, ZYXT, and ZYSN in western China

Figures 4 and 5 show the results of the condition numbers of two baselines for LLL-IGS and LLL-MIGS algorithm. The red star line represents the LLL-IGS and the blue dot line represents the LLL-MIGS. Figure 4 shows the results of baseline ZYAN-ZYXT, while Fig. 5 shows the results of baseline ZYAN-ZYSN. Both Figs. 4 and 5 show that the LLL-MIGS performs better than the LLL-IGS in decreasing the condition numbers significantly. The averages of the numbers of condition numbers can be decreased from 10.3083 (LLL-IGS) to 1.5118 (LLL-MIGS) for Fig. 4 and from 10.4177 (LLL-IGS) to 2.0736 (LLL-MIGS) for Fig. 5, respectively. Meanwhile, both Figs. 4 and 5 indicate that the red lines has obvious fluctuations, but the blue line is found to be very stable with hardly any fluctuations. Therefore, the LLL-MIGS performs more stable than the LLL-IGS in decreasing condition numbers in network-based.

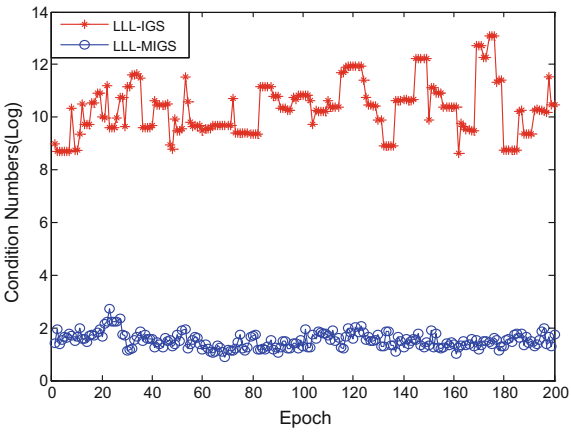

Fig. 4 Comparison of the condition numbers of the 200 examples after applying the LLL-IGS (red) and LLL-MIGS (blue) for ZYAN-ZYXT baseline, respectively

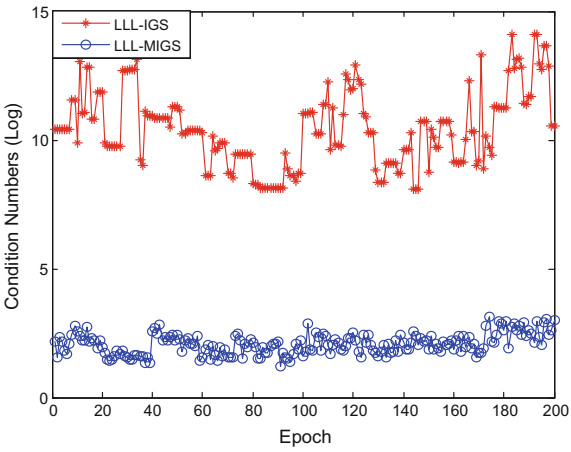

Fig. 5 Comparison of the condition numbers of the 200 examples after applying the LLL-IGS (red) and LLL-MIGS (blue) for ZYAN-ZYSN baseline, respectively

Table 3 The statistics of 200 numbers of epochs of decorrelation time (s), which was repeat 100 times by each decorrelation

	Max	Min	Average
ZYAN-ZYXT:			
LLL-IGS	0.2815	0.1541	0.2154
LLL-MIGS	0.064	0.001	0.0064
ZYAN-ZYSN:			
LLL-IGS	0.3127	0.1575	0.2186
LLL-MIGS	0.0714	0.001	0.0085

Table 3 presents the results of the decorrelation time efficiency of the LLL-IGS and LLL-MIGS for two network baselines. For ZYAN-ZYSN baseline, the maximum time is reduced from 0.1411 to 0.0947 and the minimum time is reduced from 0.0366 to 0.0301. Both of the averages of the decorrelation time for two baselines indicate that the LLL-MIGS consumes less time than LLL-IGS algorithm. Actually, the values of Table 3 show that although the improvement for decorrelation time efficiency is not obvious, the LLL-MIGS still performs better than LLL-IGS slightly in reducing decorrelation time consuming.

Table 4 shows the results of the search time efficiency of the LLL-IGS and LLL-MIGS for two network baselines. It is clear that the LLL-MIGS algorithm performs better than LLL-IGS in reducing the search time. The averages of the search time can be decreased from 0.2154 (LLL-IGS) to 0.0064 (LLL-MIGS) for ZYAN-ZYXT and 0.2186 (LLL-IGS) to 0.0085 (LLL-MIGS) for ZYAN-ZYSN, respectively. As a whole, the modified LLL-MIGS method is nearly 34 times faster than LLL-IGS for ZYAN-ZYXT and 26 times faster than LLL-IGS for ZYAN-ZYSN, respectively. Meanwhile, compared to LLL-IGS method, both the maximum and minimum time of the LLL-MIGS for these baselines are significantly improved.

Tables 3 and 4 show that not only the modified LLL-MIGS algorithm can be used for short baseline, but also it can by applied for network-based medium and long baselines. The proposed LLL-MIGS method can decrease the condition

Table 4 The statistics of 200 numbers of epochs of search time (s), which was repeat 500 times by each search

	Max	Min	Average
ZYAN-ZYXT:			
LLL-IGS	0.0945	0.0352	0.0487
LLL-MIGS	0.0781	0.0311	0.0452
ZYAN-ZYSN:			
LLL-IGS	0.1411	0.0366	0.0655
LLL-MIGS	0.0947	0.0301	0.0629

numbers more significantly than LLL-IGS method and reduce the time consumption in decorrelation and search procedures more effectively. Meanwhile, both the short baseline and network-based experiments indicate that the LLL-MIGS performs more stably and effectively than LLL-IGS method.

4 Conclusions

In recent years, LLL-IGS algorithm has been introduced into the realm of GNSS decorrelation as a new technique. Although LLL-IGS can indeed be used for decorrelation, numerous experiments demonstrated that it performs worse and deteriorates in some cases, especially for the real GNSS data.

In this contribution, we improve the LLL-IGS from two aspects: (i) Sorting the diagonal entries of original matrix Q distributed in increasing order instead of sorting the norm of vectors. (ii) Removing the error of orthogonalization by conducting the Gram-Schmidt orthogonalization procedure firstly, and then rounding the elements of G into integers. In addition, in order to assess the performance of the decorrelation algorithm directly, we introduce the time efficiency as a new criterion to evaluate the performance of the modified LLL-MIGS method. The time efficiency measure includes the decorrelation time efficiency and searching time efficiency.

For the short baseline, the LLL-MIGS can reduce the condition numbers more effectively than LLL-IGS method and the performance is more stable. Moreover, although the LLL-MIGS performs slightly better than LLL-IGS in decorrelation time consumption, it can reduce the search time significantly.

For the network-based, the LLL-MIGS method still performs better than LLL-IGS in decreasing the condition numbers, reducing the decorrelation and searching time efficiency. These results show that the proposed modified LLL-MIGS algorithm performs better than LLL-IGS not only for short baseline, but also for network-based medium and long baselines. Moreover, the LLL-MIGS algorithm is still more stable than LLL-IGS.

In these experiments, the results indicate that the modified LLL-MIGS algorithm performs much better than the LLL-IGS method in reducing condition numbers and consumption of searching time consuming, even though the LLL-MIGS improves decorrelation time efficiency slightly. Moreover, the performance of the modified LLL-MIGS algorithm is more stable than that of LLL-IGS method.

References

1. Teunissen PJG (1993) Least-squares estimation of the integer GPS ambiguities. In: LGR-Series No. 6. Delft Geodetic Computing Centre. Delft University of Technology, pp 59–74

2. Teunissen PJG (1995) The least-squares ambiguity decorrelation adjustment: a method for fast GPS integer ambiguity estimation. J Geod 70:65–82
3. Teunissen PJG (1994) A new method for fast carrier phase ambiguity estimation. In: Processings of the IEEE PLANS'94, Las Vegas, NV, 11–15 April 1994, pp 562–573
4. Chang X, Yang X, Zhou T (2005) MLAMBDA: a modified LAMBDA algorithm for integer least-squares estimation. J Geod 79(9):552–565
5. Li Z, Gao Y (1997) Direct construction of high dimension ambiguity transformation for the Lambda method. In: Proceedings of KIS97, Banff, 1997, 3–6 June
6. Liu LT, Hsu HT, Zhu YZ, Ou JK (1999) A new approach to GPS ambiguity decorrelation. J Geod 73:478–490
7. Xu PL (2001) Random simulation and GPS decorrelation. J Geod 75(7–8):408–423
8. Zhou Y (2012) A new practical approach to GNSS high-dimensional ambiguity decorrelation. GPS Solut 15(4):325–331. https://doi.org/10.1007/s10291-010-0192-6
9. Lenstra AK, Lenstra HW, Lovász L (1982) Factorizing polynomials with rational coefficients. Math Ann 261:515–534
10. Hassibi A, Boyd S (1998) Integer parameter estimation in linear models with applications to GPS. IEEE Trans Signal Process 46(11):2938–2952
11. Lannes A (2013) On the theoretical link between LLL-reduction and LAMBDA-decorrelation. J Geod 87:323–335
12. Al Borno M, Chang X, Xie X (2015) On "decorrelation" in solving integer least-squares problems for ambiguity determination. Survey Review 46:37–49

FCB Estimation Using IGS Real-Time Products and Its Application in Precise Point Positioning

Bo Jiao, Yishuai Shi, Jinming Hao, Cheng Fang, Xufeng Wen and Baofeng Song

Abstract Real-time capability, positioning accuracy and convergence time ar e the keys to the performance of Precise Point Positioning (PPP). In recent years, the development of IGS Real-Time Services (RTS) has improved the performance of real-time PPP to a large extent. Meanwhile, the PPP ambiguity resolution technique, which significantly improves the positioning accuracy and convergence time, has become mature gradually. If the advantages of both techniques can be combined to realize real-time PPP with ambiguity resolution, the application of PPP would be greatly expanded. In this paper, a real-time satellite-satellite single-difference fractional cycle bias (FCB) estimation method based on RTS products is proposed. To meet the demand of real-time PPP, narrow-lane FCBs are forecasted by short-term linear extrapolation. Taking accuracy levels and data amount into consideration, the forecasting interval for real-time wide-lane and narrow-lane FCBs are determined. Finally, the performance of real-time PPP with ambiguity resolution using real-time FCBs is evaluated in both static and kinematic modes. The results show that wide-lane FCBs to be forecasted daily and narrow-lane FCBs to be forecasted every 5 min can satisfy the need of real-time PPP with ambiguity resolution. In static mode, the average time to first fix (TTFF) is 15.97 min, and the average precision of the north, east and up components for hourly solution are 1.51, 1.64 and 2.18 cm respectively. As for kinematic mode, an average TTFF of 24.36 min is needed, and the 3D position error in fixed solution is decreased by 42.59% compared with float solution.

Keywords Precise point positioning · Fractional cycle bias · Ambiguity resolution Real-time solution · Least square fit

B. Jiao (✉) · Y. Shi · J. Hao · C. Fang · X. Wen · B. Song
Information Engineering University, Zhengzhou, China
e-mail: jiaobojob@qq.com

J. Sun et al. (eds.), *China Satellite Navigation Conference (CSNC) 2018 Proceedings*, Lecture Notes in Electrical Engineering 498,
https://doi.org/10.1007/978-981-13-0014-1_44

1 Introduction

PPP has the advantage of determining the position of a single receiver with high precision [1], thus it has been widely used in deformation monitoring, engineering survey, geodynamics and so on. The accuracy of PPP largely depends on the quality of satellite orbit and clock products. However, the high-precision products usually have a certain delay. Therefore, traditional PPP can only be used in post-processing mode. In order to meet the growing demands for real-time PPP, IGS launched the Real-time Pilot Project (RTPP) in 2007, which is dedicated to building a global IGS real-time tracking network, developing the formats for real-time data delivery and combining real-time products from different analysis centers [2]. IGS has been providing real-time service (RTS) since April 1, 2013 [3]. The accuracy of its orbits is better than 5 cm and the accuracy of clocks is better than 0.3 ns [4]. The real-time products are generated based on RTCM-SSR (state space representation) format and distributed via the Internet according to the Ntrip (networked transport of RTCM via Internet protocol) [5, 6].

Due to the effect of uncalibrated phase delay (UPD), the ambiguity in PPP usually appears as a real number, while the correct integer ambiguity is conducive to improving the convergence speed and accuracy [7]. Several methods have been proposed to fix ambiguities [8–10]. Among them, Ge's satellite-satellite single-difference FCB method has already been widely used. It eliminates the effects of receiver hardware delays and only estimates the fractional part of satellite UPDs, which eases the calculation burden and is easy to be implemented.

Real-time PPP (RT-PPP) and PPP ambiguity resolution (PPP-AR) are two principal development trends of PPP at present. However, there are few studies about real-time PPP-AR with the combination of these two techniques. Laurichesse had promoted the integer clock method into real-time applications with ambiguity resolution, enabling users to achieve real-time positioning accuracy of 1 cm horizontally and 3 cm vertically [11]. Using igu orbits from IGS, Li calculated real-time clocks and then generated real-time FCBs to realize real-time PPP-AR, which was proved to significantly improve the convergence time and accuracy compared with the float solution [12]. Considering that the delay of RTS products has been reduced to about 10 s and the accuracy of real-time clocks provided by RTS is significantly better than that of the igu products [13], it is possible to generate real-time FCBs using RTS products. Therefore, this paper presented a real-time satellite-satellite single-difference FCB estimation method using IGS real-time products. A linear extrapolation method is used to forecast narrow-lane FCBs in a short term to meet real-time needs. To Balance the accuracy and the data transmission burden, the forecast intervals for real-time wide-lane (WL) and narrow-lane (NL) FCBs are determined. Finally, the performance of real-time PPP with ambiguity resolution using real-time FCBs is evaluated in both static and kinematic modes.

2 Real-Time FCB Estimation Method

2.1 Calculation of Single-Difference FCBs

The single-difference FCB method estimate only the satellite FCBs. It uses ionosphere-free (IF) combination to solve PPP, and decomposes IF ambiguities into WL ambiguities and NL ambiguities with integer characteristics, FCBs of which is estimated separately.

When solving WL FCBs, the WL float ambiguities can be obtained from MW (Melbourne-Wubbena) combination:

$$N_{wl,r}^{s} = \frac{L_{wl,r}^{s} - P_{nl,r}^{s}}{\lambda_{wl}} = \tilde{N}_{wl,r}^{s} + b_{wl}^{s} + b_{wl,r} + \varepsilon_{MW,r}^{s} \tag{1}$$

where r and s denote station and satellite, $L_{wl,r}^{s}$ is the WL carrier observation, $P_{nl,r}^{s}$ is NL the pseudo-range observation, and λ_{wl} means the WL wave-length. $N_{wl,r}^{s}$ is composed of four parts: the integral part $\tilde{N}_{wl,r}^{s}$, the UPD influences of satellites b_{wl}^{s}, the UPD influences of receivers $b_{wl,r}$, and the MW observation noise $\varepsilon_{MW,r}^{s}$. Since the integral part of UPD has no influence on the AM fixation, so what we need to calculate is only the fractional part (FCB). After $b_{wl,r}$ has been eliminated by single-difference between s_1 and s_2, the WL ambiguity can be obtained by eliminating $\varepsilon_{MW,r}^{s}$ using elevation-angle weighting. Then the decimal part of WL ambiguity is the WL FCB of the current station:

$$\begin{cases} \hat{N}_{wl,r}^{s_1,s_2} = \hat{N}_{wl,r}^{s_1} - \hat{N}_{wl,r}^{s_2} = \tilde{N}_{wl,r}^{s_1,s_2} + b_{wl}^{s_1,s_2} \\ b_{wl,r}^{s_1,s_2} = \hat{N}_{wl,r}^{s_1,s_2} - \mathrm{int}\left[\hat{N}_{wl,r}^{s_1,s_2}\right] \end{cases} \tag{2}$$

After making average over $b_{wl,r}^{s_1,s_2}$ from different stations, the current estimate of WL FCB $\hat{b}_{wl}^{s_1,s_2}$ and its standard deviation (STD) $\sigma_{\hat{b}_{wl}^{s_1,s_2}}$ are:

$$\begin{cases} \hat{b}_{wl}^{s_1,s_2} = \left\langle b_{wl,r}^{s_1,s_2} \right\rangle \\ \sigma_{\hat{b}_{wl}^{s_1,s_2}} = \sqrt{\left\langle \left(b_{wl}^{s_1,s_2} - \hat{b}_{wl,r}^{s_1,s_2} \right)^2 \right\rangle / n_{\mathrm{sta}}} \end{cases} \tag{3}$$

Where <•> means the average between stations, n_{sta} is the amount of stations.

NL FCBs are calculated epoch-wisely. Supposing the single-difference IF ambiguity of k-epoch is $\left(N_{IF,r}^{s_1,s_2}\right)_k$ and the fixed WL ambiguity is $\left(\tilde{N}_{wl,r}^{s_1,s_2}\right)_k$, the float NL ambiguity can be obtained from the relationship between ambiguities as follow:

$$\left(N_{nl,r}^{s_1,s_2}\right)_k = \frac{f_1+f_2}{f_1}\left(N_{IF,r}^{s_1,s_2}\right)_k - \frac{f_2}{f_1-f_2}\left(\tilde{N}_{wl,r}^{s_1,s_2}\right)_k = \left(\tilde{N}_{nl,r}^{s_1,s_2}\right)_k + \left(b_{nl}^{s_1,s_2}\right)_k + \left(\varepsilon_{nl,r}^{s_1,s_2}\right)_k \tag{4}$$

By eliminating the integer part $\left(\tilde{N}_{nl,r}^{s_1,s_2}\right)_k$, the fractional part of $\left(b_{nl}^{s_1,s_2}\right)_k$ is obtained, which is the NL FCB of current station. After averaging different $b_{wl,r}^{s_1,s_2}$, the estimated WL FCB $\hat{b}_{wl}^{s_1,s_2}$ and its STD $\sigma_{\hat{b}_{wl}^{s_1,s_2}}$ are:

$$\begin{cases} \left(\hat{b}_{nl}^{s_1,s_2}\right)_k = \left\langle \left(N_{nl,r}^{s_1,s_2}\right)_k - \mathrm{int}\left[\left(N_{nl,r}^{s_1,s_2}\right)_k\right] \right\rangle \\ \left(\sigma_{\hat{b}_{nl}^{s_1,s_2}}\right)_k = \sqrt{\left\langle \left(\left(b_{nl,r}^{s_1,s_2}\right)_k - \left(\hat{b}_{nl}^{s_1,s_2}\right)_k\right)^2 \right\rangle / n_{\mathrm{sta}}} \end{cases} \tag{5}$$

But single-difference FCBs using one reference satellite cannot cover all satellites all the time, which requires differential transmission to convert the FCB estimated using other reference satellites to a unified one. Assuming that s_1–s_3 and s_2–s_3 are common-satellites pairs and that FCB $\hat{b}^{s_1,s_3}, \hat{b}^{s_2,s_3}$ and their STDs $\sigma_{\hat{b}^{s_1,s_3}}, \sigma_{\hat{b}^{s_2,s_3}}$ are known, the FCB of s_2 refer to s_1 can be obtained through transmission:

$$\begin{cases} \hat{b}^{s_2,s_1} = \hat{b}^{s_2,s_3} - \hat{b}^{s_1,s_3} = \left(\hat{b}^{s_2} - \hat{b}^{s_3}\right) - \left(\hat{b}^{s_1} - \hat{b}^{s_3}\right) \\ \sigma_{\hat{b}^{s_2,s_1}} = \sqrt{\left(\sigma_{\hat{b}^{s_1,s_3}}\right)^2 + \left(\sigma_{\hat{b}^{s_2,s_3}}\right)^2} \end{cases} \tag{6}$$

In order to limit the error accumulation, only one transmission between reference satellites is performed. And single-difference FCBs available for the whole period are obtained by robust estimation.

2.2 Real-Time FCBs Forecast

The estimation of FCBs needs precise products and GNSS observations, for which it is usually implemented in a post-processing mode. In order to satisfy the needs of real-time applications, the server should forecast and broadcast short-term extrapolations based on the FCBs from the pre-epochs. Then clients can use the forecasted FCBs to fix the ambiguity in real-time PPP.

The WL FCBs are derived by the MW combinations, which are independent of the accuracy of real-time orbits and clocks. Studies have proven that WL FCBs have a good long-term stability, typically less than 0.1 cycles within 30 days [7], which

can be regarded as a constant for several days in forecast. For real-time applications, WL FCB from previous day is treated as the forecasts. The NL FCBs' long-term stability is poor, but it still has a good short-term stability. The least squares linear fit of NL FCBs of the current period is used to extrapolate the forecasts of the next period according to the fitting function [14]. Assuming that the prediction period of NL FCBs is n epochs and the FCBs of the i epoch are b_i (i = 1, 2 … n) in pre-period, the observation equations of the least squares linear fit are:

$$\begin{cases} a_1 + a_0 = b_1 \\ 2a_1 + a_0 = b_2 \\ \quad\vdots \\ na_1 + a_0 = b_n \end{cases} \tag{7}$$

where a_0 and a_1 are fitting coefficients. After the weight matrix has been determined according to variances of b_i, a linear function of the fitting is resolved through the least squares solution. Subsequently, the extrapolation obtains the forecasts $\tilde{b}$ s at the mid-point of the next period for clients to use:

$$\tilde{b} = \frac{3n+1}{2} a_1 + a_0 \tag{8}$$

After the forecasting method has been determined, the accuracy and data burden of the forecast FCBs are directly related to the forecast interval. The forecast interval should be determined based on the stability of the NL FCBs and forecast errors.

3 Generation of Real-Time FCBs

3.1 Generation Strategies

IGS-RTS has provided real-time streams including IGS01, IGC01, IGS02 and IGS03 [15]. In this paper, real-time precision orbits and clocks saved from IGC01 is used. The products' suffix name is igc. Using 30 s sampling data from 150 IGS stations that are shown in Fig. 1, real-time single-difference FCBs are generated, and the reference satellite is G01. The period is from 260 to 266 days in 2017. The length of continuous arcs in WL FCBs solution should be longer than 20 min. When solving NL FCBs, the parameters and settings of IF combination PPP are shown in Table 1. The complete generation process of real-time is shown in Fig. 2.

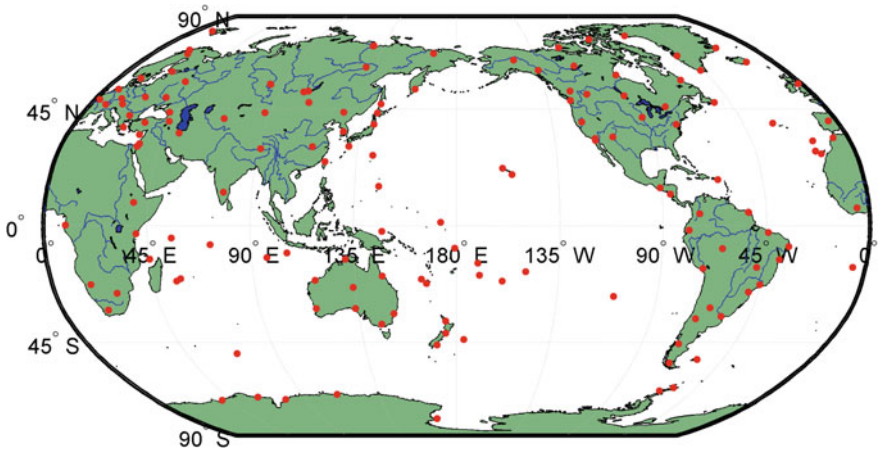

Fig. 1 The distribution of stations used in FCBs generation

Table 1 Strategies of parameter estimation and error handling

	Items	Strategy
Parameter estimation	Receiver position	Fixed to IGS weekly solution
	Receiver clocks	White noise process
	Ionosphere delay	IF combination
	Troposphere delay	Estimate ZTD
	Calculation method	Extended Kalman filter
	Elevation cut-off	10°
Error handling	Satellite orbit and clocks	Real-time igc products
	Cycle slip detection	GF-MW combination
	Clock jump	Difference between epochs
	Phase center correction	igs14.atx
	Earth tide and ocean tide	IERS2003 and FES2004
	DCB correction	P1C1.dcb from CODE
	Earth orientation parameter	ERP files from IGS
	Phase windup effect	Corrected by model
	Relativity effect	Corrected by model

3.2 Determination of Forecast Interval

3.2.1 Stability Analysis of Real-Time FCBs

Because WL FCBs don't require precise products, its real-time results are as stable as the post-processing results. As shown in Fig. 3, the maximum variation of WL FCBs for each satellite over a week is 0.27 cycles.

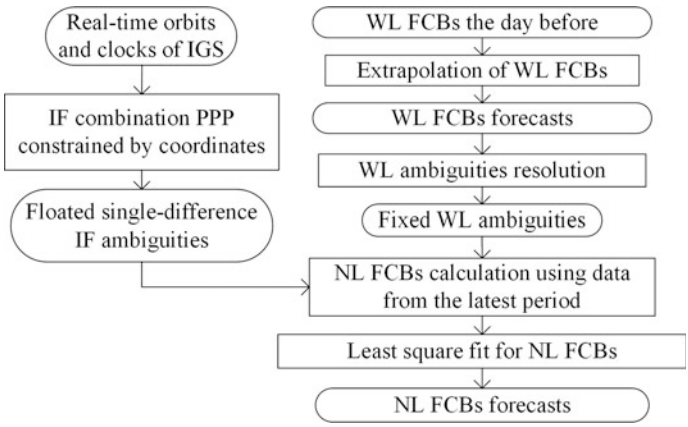

Fig. 2 The generation process of real-time FCBs

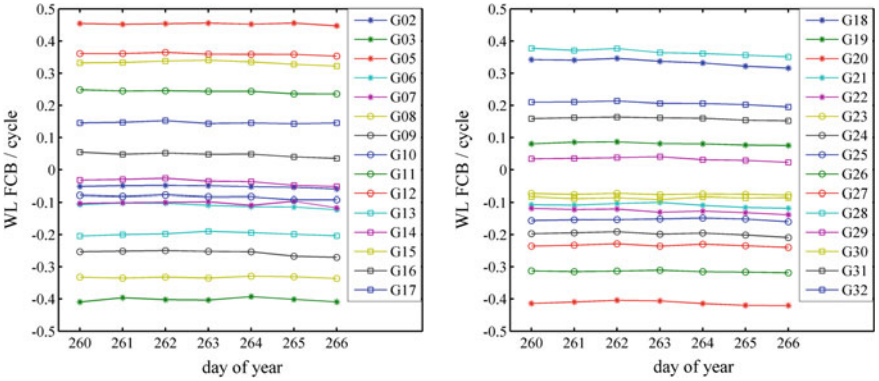

Fig. 3 Time series of real-time WL FCBs

Since the accuracy of real-time orbits and clocks is not as good as the post-processing products, the accuracy of real-time IF ambiguities is not as accurate as the post-processing results, which would degrade the stability of NL FCBs through Formula (4). To compare stability differences between real-time and post-processing NL FCBs, this paper uses final orbits and clocks from IGS to generate post-processing NL FCBs. The post-processing NL FCBs' daily changes are less than 0.2 cycles, while the real-time products might change more than 1 cycle. However, 98.45% changes of real-time NL FCBs between adjacent epochs are less than 0.05 cycles, which shows that it has good stability in short-time and can meet the requires of short-term forecast. As shown in Figs. 4 and 5, partial satellites are selected to show the difference between real-time and post-processing NL FCBs' sequences.

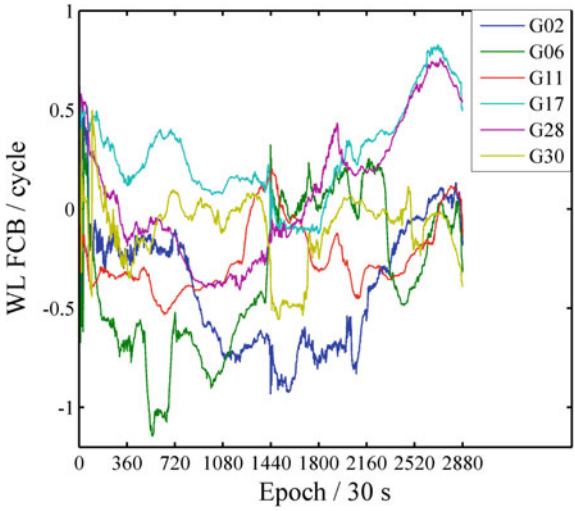

Fig. 4 Time series of real-time NL FCBs

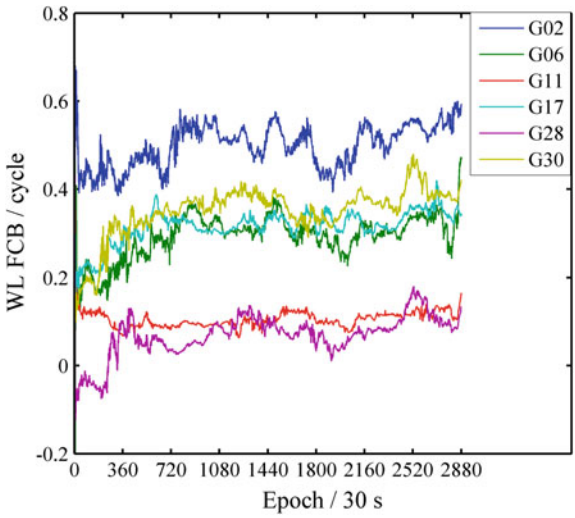

Fig. 5 Time series of post-processing NL FCBs

3.2.2 Accuracy of Forecasted FCBs

Referring to the overlapped arc test method used in forecast orbit accuracy evaluation, we can get the forecast errors of FCBs through comparing forecast FCBs and the measured values of the same period. WL FCBs have a better stability, so the results of the last day are directly used as forecasts. The average forecast error is 0.0044 cycles, and the STD is 0.0055 cycles, which can meet the needs to fix WL ambiguities. However, the real-time NL FCBs are less stable compared with the post-processing results. Therefore, it is impossible to select a 15-minute interval as

mentioned in [8] for real-time NL FCBs [8]. The forecast interval needs to be re-determined. In order to do this, using the prediction method proposed in Sect. 2.2, different forecast intervals were adopted to generate forecast NL FCBs for 7 days. Table 2 shows the calculated forecast errors of different intervals. The errors within 0.05 cycles does not affect the fixity of ambiguity. Therefore, 0.05 cycles is chosen as the threshold to judge whether NL FCBs can meet the needs of PPP. The experimental results show that only STDs at 2.5 and 5-minute intervals can meet the requirements. The prediction accuracy of 2.5-minute promotes slightly comparing with that of 5-minute, but the data burden would double. So 5-minute is determined as the NL FCBs' interval.

Real-time FCBs are generated according to the selected interval and the distribution of the residuals is shown in Fig. 6. The statistics show that 92.47% of WL FCBs residuals are less than 0.01 cycles and 90.53% of NL FCBs residuals are less than 0.05 weeks.

Table 2 Forecast errors of NL FCBs at different intervals

Forecast interval/minute	2.5	5	10	15	20
Average error/cycle	0.016	0.023	0.036	0.048	0.058
STD/cycle	0.031	0.040	0.057	0.074	0.087

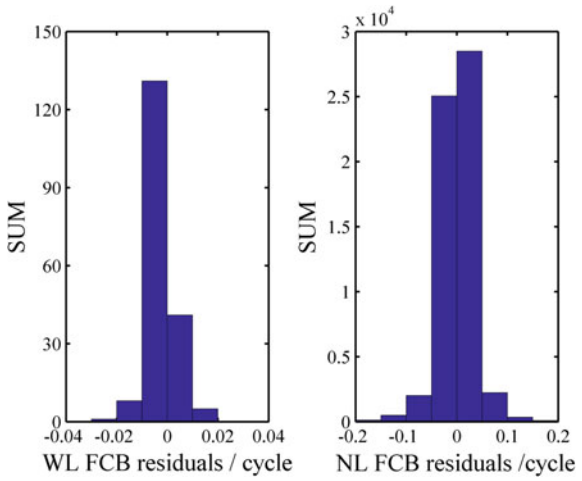

Fig. 6 Forecast residual distribution of WL and NL FCBs

4 Application of Real-Time FCBs in PPP

To verify the performance of real-time FCBs in PPP, 10 IGS stations shown in Fig. 7 are selected for fixed PPP experiments in both static and kinematic modes. Except for that station coordinates are calculated epoch-wisely, the rest of the settings are same as Table 1. For comparison purposes, post-processing fixed solutions are also given using post-processing FCBs. For WL ambiguities, the rounding method is used to fix ambiguities and the success rate of Bootstraping with a threshold of 0.999 is used for verification. NL ambiguities were searched using LAMBDA algorithm and checked using ratio-test with a threshold of 3.0 [8]. To ensure the fixed correctness, the fixed solution results are updated only after the successive 5 epochs pass the tests and the three-dimensional (3D) STD is less than 0.15 m. If 3D errors are greater than 0.15 m after fixing and exceed 1.5 times the errors of the corresponding float solution, then the ambiguities are considered to be incorrectly fixed.

4.1 Static PPP

The 7-day observation data are divided into 1-hour sessions, and their float and fixed solutions in static mode using real-time FCBs are calculated. As a comparison, static post solutions are also resolved. Figure 8 shows the convergence process of static PPP of station ALTT during 19:00 to 20:00 on the DOY 260 in 2017. The blue and red curves show the positioning errors in north, east and up (NEU) components of fixed and float solutions compared with the IGS weekly solutions respectively. The green vertical dashed line indicate the TTFF of fixed

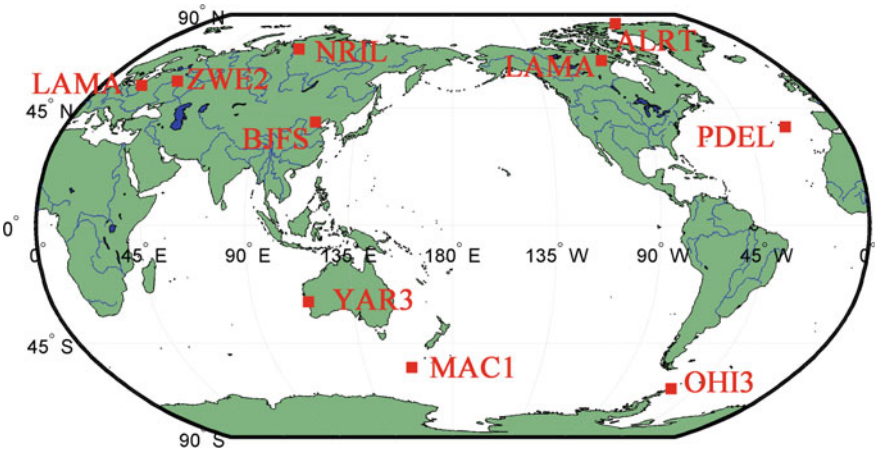

Fig. 7 The distribution of experimental stations

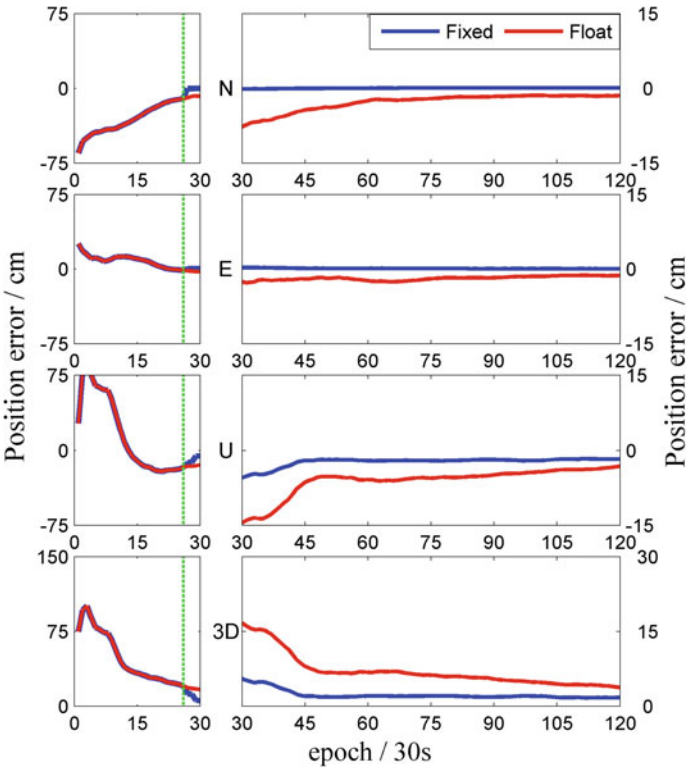

Fig. 8 Position errors of static PPP in ALRT

solution. To emphasize the difference between fixed and float solutions, the longitudinal axis is enlarged by 5 times after fixation.

When the errors of NEU components are all less than 10 cm and maintain more than 20 epochs, it is recognized that PPP achieves convergence [17]. The convergence rate of float solutions is the percentage of convergence periods in all periods, and that of fixed solutions is the proportion of successfully fixed periods. Though fixed solutions have better converge speed and accuracy, its convergence rate is lower. Table 3 shows convergence rates, average convergence time and average positioning errors of different components of float solutions and fixed solutions in static mode. According to results in static mode, real-time PPP-AR converge faster than that of float solutions, and position errors are significantly reduced and remain stable after the ambiguity being fixed. Compared with the float results, the 3D errors of real-time fixed PPP are reduced by 44.56%, and the convergence speed is accelerated by 26.94, 83.33% periods can be successfully converged, the average positioning error after convergence is 3.67 cm. The convergence rates and speeds of post-processing PPP are better than real-time PPP, which is consistent with existing researches.

Table 3 Convergence and accuracy of 1 h static PPP

Mode	Ambiguity strategy	Convergence		Position error/cm			
		Rate/%	Time/min	N	E	U	3D
Real-time	Float	95.83	21.86	2.78	3.67	3.81	6.62
	Fixed	83.33	15.97	1.51	1.64	2.18	3.67
Afterwards	Float	99.17	17.71	0.95	2.07	2.54	3.84
	Fixed	94.17	13.87	0.72	1.01	1.63	2.33

4.2 Kinematic PPP

Using the same observations, we set the processing noise of the coordinate estimation as white noise with a variance of 10^4 m^2 for PPP in kinematic mode. The solutions of real-time fixed and float PPP are divided in 1-hour sessions, and the post-processing solutions are used as a contrast. As the kinematic solution needs to re-estimate the coordinates epoch by epoch, which is more likely to be affected by measurement noise, its convergence efficiency and positioning accuracy are inferior to the static mode. Figure 9 shows the process of kinematic PPP convergence of

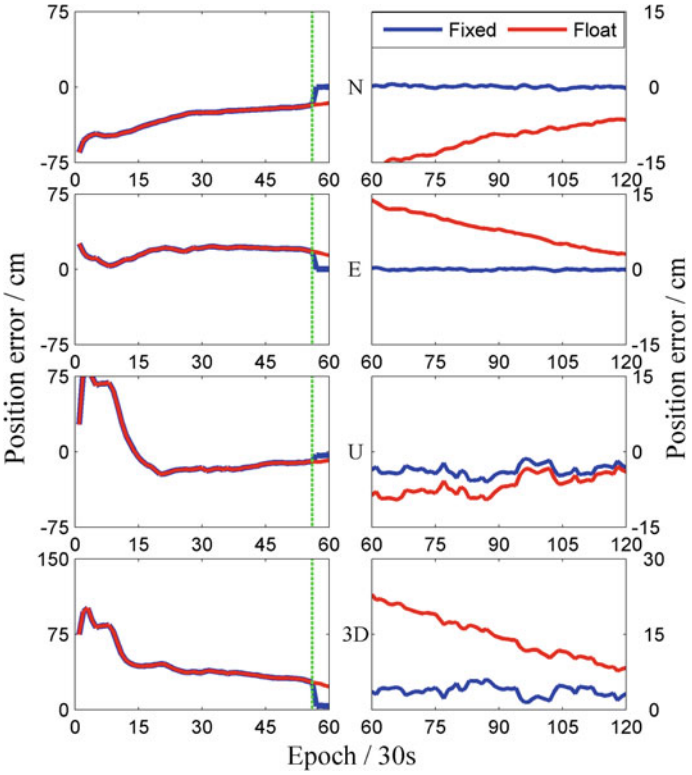

Fig. 9 Position errors of kinematic PPP in ALRT

Table 4 Convergence and accuracy of 1 h kinematic PPP

Mode	Ambiguity strategy	Convergence		Position error/cm			
		Rate/%	Time/min	N	E	U	3D
Real-time	Float	81.67	32.96	3.39	4.56	4.84	8.57
	Fixed	64.17	24.36	1.95	2.41	2.66	4.92
Afterwards	Float	93.75	27.75	2.45	2.89	3.51	5.92
	Fixed	74.58	19.82	1.35	0.91	2.16	3.02

station ALRT during the same period in Fig. 8. Table 4 shows the statistical results in kinematic mode. The positioning errors of fixed solutions decrease by 1.14 cm, 2.15 and 2.18 cm respectively in NEU components compared with float solutions. The average convergence time is shortened by 8.6 min, but only 64.17% sessions converge successfully.

5 Conclusion

In this paper, single-difference FCBs are generated using IGS real-time orbits and clocks, and the linear extrapolation method is used to forecast the NL FCBs in a short term for real-time application. The stability of the real time FCBs, as well as the performance of real-time PPP-AR both in static and kinematic modes, have been evaluated and analyzed. The results are concluded as follow:

(1) The stability of real-time NL FCBs is worse than that of post-processing products. According to the analysis of prediction errors, a 5-minute interval should be chosen for NL FCBs forecast, in which situation 90.53% of linear extrapolation residuals are within 0.05 cycles. However, the stability of real-time WL FCBs is much better, with 92.4% residuals within 0.01 cycles at a 1-day interval.
(2) The real-time PPP with ambiguity resolution using real-time FCBs can significantly improve the position accuracy and convergence time comparing with the float solution. In the static mode with ambiguity resolution: the convergence rate is 83.33%; the deviation of the NEU direction is 1.51, 1.64 and 2.18 cm, respectively; and the 3D deviation is reduced by 44.56% compared to the floating point solution. In the kinematic mode with ambiguity resolution: it takes an average time of 24.36 min to converge; after convergence, the deviations of NEU components are 1.95, 2.41 and 2.66 cm, respectively.

Acknowledgements This research work was supported by the Natural Science Foundation of China (41604032).

References

1. Zumberge JF, Heflin MB, Jefferson DC, Watkins MM, Webb FH (1997) Precise point positioning for the efficient and robust analysis of GPS data from large networks. J Geophys Res Solid Earth 102(B3):5005–5017
2. Dow JM, Neilan RE, Rizos C (2007) The International GNSS service (IGS): preparations for the coming decade. Bulletin of the American Astronomical Society
3. Caissy M, Agrotis L, Weber G, Fisher S (2013) The IGS real-time service. EGU General Assembly, 07–12 Apr. 2013, Vienna Austria
4. Hadas T, Bosy J (2015) IGS RTS precise orbits and clocks verification and quality degradation over time. GPS Solutions 19(1):93–105
5. Wubbena G, Schmitz M, Bagge A (2005) PPP-RTK: precise point positioning using state-space representation in RTK Networks. ION GNSS 2005, Long Beach, CA, September 2584–2594
6. Gebhard H, Weber G (2003) NTRIP: networked transport of RTCM via internet protocol—internet radio technology for real-time GNSS purposes. AGU Fall Meeting. AGU Fall Meeting Abstracts
7. Li P (2016) Research on methodology of rapid ambiguity resolution for GNSS precise point position. Wuhan University, Wuhan
8. Ge M, Gendt G, Rothacher M, Shi C, Liu J (2008) Resolution of gps carrier-phase ambiguities in precise point positioning (PPP) with daily observations. J Geodesy 82(7):389–399
9. Laurichesse D, Mercier F, Berthias JP, Broca P, Cerri L (2009) Integer ambiguity resolution on indifference GPS phase measurements and its application to PPP and satellite precise orbit determination. Navigation 56(2):135–149
10. Collins P, Bisnath S, Lahaye F et al (2010) Undifferenced GPS ambiguity resolution using the decoupled clock model and ambiguity Datum fixing. Navigation 7(2):123–135
11. Laurichesse D (2011) The CNES Real-time PPP with undifferenced integer ambiguity resolution demonstrator. Proc Int Tech Meeting Satellite Div Inst Navig 10(1):654–662
12. Li X, Ge M, Zhang H, Wickert J (2013) A method for improving uncalibrated phase delay estimation and ambiguity-fixing in real-time precise point positioning. J Geodesy 87(5):405–416
13. Shao K, Gu D, Tu X, Duan X, Liu H (2016) Applications of IGS real-time products in precise point positioning and LEO satellites precise orbit determination. China satellite navigation conference (CSNC), Changsha
14. Wang J, Zhou L, Jiang T, Sun G (2014) A simple linear fitting method based on weighted total least square. Bull Surveying Mapp 4:33–35
15. International GNSS Service (IGS). IGS Real-time Service. http://www.igs.org/rts/products/. Accessed 12 June 2016
16. National Aeronautics and Space Administration (NASA). igc orbits and clocks [DB/OL]. ftp://cddis.gsfc.nasa.gov/gps/products/rtpp/1967/. Accessed 17 Sept 2017
17. Zhang X, Li P, Guo F (2013) Ambiguity resolution in precise point positioning with hourly data for global single receiver. Adv Space Res 51(1):153–161

Improved TCAR Algorithm for BDS Over Medium-Long Baseline

Yijun Tian, Lifen Sui, Dongqing Zhao, Shaolei Peng and Yuan Tian

Abstract In the paper, a modified TCAR method was proposed to investigate triple-frequency ambiguity resolution (AR) performance with real BDS data. At first, the extra-wide-lane (EWL), wide-lane (WL) and narrow-lane (NL) ambiguities were determined with the classical TCAR method, and then analysis of the influence of the residual double-differencing (DD) ionospheric delay on the NL ambiguity resolution was given, and concluded that the residual ionospheric delay was the main error in the resolution of NL ambiguity over medium-long baseline. In the modified TCAR method, the estimated DD ionospheric delay was used to modify the NL ambiguity resolution. As the noise term of the DD ionospheric delay estimated from the ambiguity-fixed EWL is very large, the smooth method is employed to correct the estimated DD ionospheric delay. As a result, the NL ambiguity resolution modified by the smooth DD ionospheric delay shows a much better performance than the classical TCAR method over medium and long baseline.

Keywords BDS real data · TCAR method · Smooth DD ionospheric delay NL

1 Introduction

BDS satellite navigation system has already become the world's third largest navigation system, following the United States GPS, and Russia GLONASS [1]. After the BDS satellite navigation system formally provides regional services, the number of visible satellites of the combined BDS and GPS systems can reach 20 [2]. Domestic and foreign scholars have done a great deal of work in using BeiDou to achieve high-precision static and dynamic relative positioning and

Y. Tian (✉) · L. Sui · D. Zhao · Y. Tian
Information Engineering University, Zhengzhou 450000, China
e-mail: tianyijun56@163.com

S. Peng
91404 Armed Forces, Qinhuangdao 066000, China

J. Sun et al. (eds.), *China Satellite Navigation Conference (CSNC) 2018 Proceedings*, Lecture Notes in Electrical Engineering 498,
https://doi.org/10.1007/978-981-13-0014-1_45

demonstrating their feasibility and accuracy [3]. With the advent of GNSS multi-frequency signals, many scholars have started to study various multi-frequency linear combinations to improve the efficiency of ambiguity resolution, the detection and repair of cycle slip, and the navigation and positioning accuracy. Wu Yue analyzed the positioning accuracy of some GPS triple-frequency phase observation [4]. Cocard systematically studied the linear combination of GPS triple-frequency integer coefficients and found that the sum of the linear combination coefficients is closely related to the observed error characteristics of GPS triple-frequency carrier phase combinations [5]. Urquhart analyzed the possible benefits of combination of GPS and Galileo triple frequency phase observations to ambiguity resolution and positioning accuracy [6]. Hatch analyzed the impact of GPS third frequency on navigation and positioning users and pointed out that the third frequency mainly improves the ambiguity resolution under short baseline and its contribution is still limited under long baselines [7].

Under the "3 GEO + 3IGSO" regional constellation configuration of Beidou satellite navigation system, Shi conducted a preliminary quality analysis of Beidou GEO and IGSO satellites and evaluated the accuracy of dual-frequency carrier phase differential positioning [8]. In the case of short baselines, Montenbruck analyzed the success rate of the ambiguity resolution of the Beidou triple frequency geometry-free carrier combination [9]. Tang proposed a method to improve the TCAR model based on the geometric model and greatly improved the success rate of ambiguity fixed in the case of short baseline [10]. In general, ambiguity resolution in the geometry-free combination at short baseline is mainly affected by ionospheric delay error and multipath error [11, 12], and the ionospheric delay error can be roughly neglected after double differencing.

Under medium and long baseline, the ambiguity resolution in the geometric model is not affected by the orbit and tropospheric delay errors, but the third-step narrow-lane ambiguity resolution is easily affected by the double-difference ionospheric delay error. Therefore, many scholars started to study the solution of the narrow-lane ambiguity over medium-long baseline. Simsky presented a triple frequency geometry-free and ionosphere-free combination, and analyzed its application in ambiguity resolution and multipath error extraction. Hatch proposed a method of calculating the ambiguity of narrow lane with medium and long baselines by using triple-frequency optimal ionosphere combination smoothing (ultra) wide-lane combination [14]. Wang and Rothacher propose a simplified geometry-free and ionosphere-free model by minimizing noise effects [15]. Zhao and Zhang has improved the traditional TCAR method by using the combination of ultra-wide-lane and wide-lane combination with pseudo-range combination to eliminate the geometric and ionospheric terms [16, 17]. The non-geometric, ionosphere-free methods above are essentially equivalent, all based on the good properties of a tri-band, geometric-free, ionosphere combination that is unaffected by geometric terms and ionospheric delay errors. The geometry-free and ionosphere-free methods above are essentially equivalent, all based on the good properties of the triple frequency combination that is unaffected by geometric terms and ionospheric delay errors.

Although geometry-free and ionosphere-free ambiguity resolution scheme eliminates systematic errors such as ionospheric delays, due to the error associated with the epoch, the convergence speed of ambiguity is slow, and even it cannot converge to the true value due to long-period multipath error (especially for BDS GEO satellite). In this paper, aiming at the problem that it is difficult to accurately fix the ambiguity of the narrow lane in the TCAR method under medium and long baselines, an improved method is proposed to estimate the double-difference ionospheric delay by smoothing the two wide-lane combinations with ambiguity fixed. Then, the smoothed double-difference ionospheric delay can be used to correct the narrow-lane ambiguity, which can obviously improve the rounding success rate of floating ambiguity.

2 GNSS Observation Model

2.1 The Linear Combination of Observations

From the original observations and different linear combination coefficient, we can get the observed combination of different characteristics, which can be expressed as follows:

$$\begin{aligned}\nabla\Delta\Phi_{(i,j,k)} &= \frac{i\cdot f_1\cdot\nabla\Delta\Phi_1 + j\cdot f_2\cdot\nabla\Delta\Phi_2 + k\cdot f_3\cdot\nabla\Delta\Phi_3}{i\cdot f_1 + j\cdot f_2 + k\cdot f_3} \\ &= \nabla\Delta\rho - \beta_{(i,j,k)}\nabla\Delta I + \nabla\Delta T + \lambda_{(i,j,k)}\nabla\Delta N_{(i,j,k)} + \zeta_{\nabla\Delta\Phi}\end{aligned} \tag{1}$$

$$\begin{aligned}\nabla\Delta P_{(i,j,k)} &= \frac{i\cdot f_1\cdot\nabla\Delta P_1 + j\cdot f_2\cdot\nabla\Delta P_2 + k\cdot f_3\cdot\nabla\Delta P_3}{i\cdot f_1 + j\cdot f_2 + k\cdot f_3} \\ &= \nabla\Delta\rho + \beta_{(i,j,k)}\nabla\Delta I + \nabla\Delta T + e_{\nabla\Delta P}\end{aligned} \tag{2}$$

where $\nabla\Delta\Phi_{(i,j,k)}$ and $\nabla\Delta P_{(i,j,k)}$ denote the double-difference phase and pseudo range observations respectively, and correspondingly, $\zeta_{\nabla\Delta\Phi}$ and $e_{\nabla\Delta P}$ denote their respective observed noise; $\nabla\Delta I$ and $\nabla\Delta T$ denote the double-difference ionospheric delay and tropospheric delay error, respectively; $\lambda_{(i,j,k)}$ is the combined observation wavelength; $\mu_{(i,j,k)} = \sqrt{\frac{(i\cdot f_1)^2 + (j\cdot f_2)^2 + (k\cdot f_3)^2}{(i\cdot f_1 + j\cdot f_2 + k\cdot f_3)^2}}$ is the noise amplification factor; $\nabla\Delta N_{(i,j,k)}$ represents the double-difference ambiguity; $\beta_{(i,j,k)}$ is the double-difference combination coefficient of ionospheric delay.

2.2 Selection of Combined Observations

Feng and Cocard study the selection of the optimal combination of triad frequencies systematically, and put forward the standard of determining the optimal

combination of observations is to select the linear combination which has a longer wavelength, smaller ionospheric delay and smaller linear noise effects. According to the criterion and method of optimal combination coefficients proposed by Feng, three optimal linear combinations of EWL (0, −1, 1), EWL (1,4, –5) and NL (4, 0, −3) are adopted to conduct the experiments in this paper, and the characteristics of the three combinations are shown in Table 1.

3 The Classical TCAR Method

3.1 Model of the TCAR Method

(1) The first step is to use the pseudo-range to solve the ultra-wide lane ambiguity (EWL).

$$\hat{N}_{(i_e,j_e,k_e)} = \varphi_{(i_e,j_e,k_e)} - \frac{P_{(m,n,l)}}{\lambda_{(i_e,j_e,k_e)}} + \frac{\beta_{(i_e,j_e,k_e)} + \beta_{(m,n,l)}}{\lambda_{(i_e,j_e,k_e)}} I_1 - \varepsilon_{(i_e,j_e,k_e)} + \frac{e_{(m,n,l)}}{\lambda_{(i_e,j_e,k_e)}} \tag{3}$$

For GPS or BDS, the wavelength of the combined EWL observation is very long. In the case of short baseline, the neglected double-difference ionospheric delay error and observation noise have little influence on the ambiguity resolution [21], so the EWL ambiguity can easily be fixed.

(2) The second step is to solve wide-lane ambiguity (WL) by combined observation of EWL with fixed ambiguity.

$$\begin{aligned} \hat{N}_{(i_w,j_w,k_w)} = \varphi_{(i_w,j_w,k_w)} &- \frac{\lambda_{(i_e,j_e,k_e)}\left(\varphi_{(i_e,j_e,k_e)} - \breve{N}_{(i_e,j_e,k_e)}\right)}{\lambda_{(i_w,j_w,k_w)}} \\ &+ \frac{\beta_{(i_w,j_w,k_w)} - \beta_{(i_e,j_e,k_e)}}{\lambda_{(i_w,j_w,k_w)}} I_1 + \frac{\lambda_{(i_e,j_e,k_e)}\varepsilon_{(i_e,j_e,k_e)} - \varepsilon_{(i_w,j_w,k_w)}\lambda_{(i_w,j_w,k_w)}}{\lambda_{(i_w,j_w,k_w)}} \end{aligned} \tag{4}$$

Table 1 Characteristics of optimal observation combinations

$\nabla\Delta\Phi_{(i,j,k)}$	$\lambda_{(i,j,k)}$	$\beta_{(i,j,k)}$	$\mu_{(i,j,k)}$
(0, −1, 1)	4.884	−1.592	28.529
(1, 4, −5)	6.371	0.652	172.6
(4, 0, −3)	0.1229	0.1972	2.9984

(3) The third step is to solve narrow-lane ambiguity (NL) by combined observation of WL with fixed ambiguity.

$$\begin{aligned}\hat{N}_{(i_n,j_n,k_n)} = \varphi_{(i_n,j_n,k_n)} - \frac{\lambda_{(i_w,j_w,k_w)}\left(\varphi_{(i_w,j_w,k_w)} - \breve{N}_{(i_w,j_w,k_w)}\right)}{\lambda_{(i_n,j_n,k_n)}} \\ + \frac{\beta_{(i_n,j_n,k_n)} - \beta_{(i_w,j_w,k_w)}}{\lambda_{(i_n,j_n,k_n)}} I_1 - \varepsilon_{(i_n,j_n,k_n)} + \varepsilon_{(i_w,j_w,k_w)} \frac{\lambda_{(i_w,j_w,k_w)}}{\lambda_{(i_n,j_n,k_n)}}\end{aligned} \tag{5}$$

When the double-difference ionospheric error and double-difference measurement noise of WL and NL combinations are less than half of the wavelength of the combined observations, the floating ambiguities can be directly rounded to the integers. In this paper, the steps are slightly changed. Firstly, the first EWL (0, −1, 1) and second EWL (1, 4, −5) are determined according to the first step and then the WL (1, −1, 0) is obtained according to the equation $\breve{N}_{(1,-1,0)} = 5\breve{N}_{(0,-1,1)} + \nabla\Delta\breve{N}_{(1,4,-5)}$, and finally the NL (4, 0, −3) is obtained according to the Eq. (5). It can be seen that from Table 2 the influence coefficient of double-difference ionospheric delay in NL observations is 12.125, that is to say, the effect of the double-difference ionospheric delay on the NL ambiguity resolution can be neglected only when the double-difference ionospheric delay residual is within 4 cm.

3.2 Analysis of Experiments

Three baselines of 8, 17 and 72 km are selected in this paper (Table 3). The double-difference ambiguities correctly fixed by LAMBDA method are taken as reference values to calculate the double-difference ambiguities of EWL, WL and NL in TCAR experiments.

Table 4 shows the RMS of the double-difference ambiguity resolution of different combinations for all BDS satellites. For short baselines of 8 and 17 km, the

Table 2 Influence of ionospheric coefficient on EWL (0, −1, 1), (1, 4, −5) and NL (4, 0, −3)

Equations	Ionospheric coefficient	$\nabla\Delta I_1$		
		0.04 m	0.1 m	0.2 m
(3)	0.061	0.002	0.006	0.012
(4)	0.305	0.001	0.03	0.06
(5)	12.125	0.48	1.2	2.4

Table 3 Data of free-geometry ambiguity resolution

Length of baseline (km)	Date	Sampling interval (s)	Data length
8	2014.07.31	10	3 h 30 min
17	2014.07.01	10	3 h 12 min
72	2013.12.14	1	24 h

Table 4 RMS of EWL (0, −1, 1), WL (1, 4, −5), NL (4, 0, −3) DD ambiguity residual

RMS/cycles		8 km			17 km			72 km		
		(1)	(2)	(3)	(1)	(2)	(3)	(1)	(2)	(3)
GEO	C02	0.08	0.10	0.12	0.11	0.12	0.24	0.09	0.19	3.43
	C03	0.06	0.08	0.10	0.12	0.11	0.19	0.05	0.09	0.97
	C04	0.10	0.12	0.17	0.06	0.11	0.21	0.06	0.11	0.94
	C05	0.08	0.10	0.13	0.13	0.17	0.23	*	*	*
IGSO	C06	*	*	*	0.06	0.08	0.18	0.06	0.10	1.35
	C07	0.06	0.09	0.13	0.07	0.10	0.18	0.06	0.10	0.52
	C08	0.06	0.07	0.11	0.07	0.09	0.20	0.08	0.13	1.74
	C09	*	*	*	*	*	*	0.05	0.10	1.44
	C10	0.06	0.07	0.09	0.06	0.08	0.22	0.07	0.14	3.37
MEO	C11	0.07	0.09	0.11	*	*	*	*	*	*
	C12	*	*	*	*	*	*	0.06	0.10	1.20
	C13	*	*	*	*	*	*	0.07	0.12	2.19
	C14	*	*	*	*	*	*	0.06	0.12	2.47

RMSs of the double-difference ambiguities for both EWL and NL combinations are less than 0.3 cycles, and the accuracy of EWL (1, 4, −5) is almost the same as that of EWL (0, −1, 1). For a medium-long baseline of 72 km, the double-difference ambiguity residuals of the two EWL combinations can still reach high accuracy, but the accuracy of double-difference NL ambiguity is obviously deteriorated, indicating that the effect of baseline length on the direct rounding of the EWL ambiguity resolution is not significant but the direct rounding effect on the NL ambiguity resolution is obvious. The success rate of rounding ambiguities to the correct integers is listed in Table 5. As mentioned earlier, the direct rounding rates of the

Table 5 Success rate of ambiguity resolution

Success rate/%		8 km			17 km			72 km		
		(1)	(2)	(3)	(1)	(2)	(3)	(1)	(2)	(3)
GEO	C02	100	100	100	100	100	94.3	100	99.7	26.8
	C03	100	100	100	100	100	100	100	100	58.2
	C04	99.8	99.7	99.6	100	100	99.0	100	100	62.7
	C05	100	100	99.5	100	99.6	95.0	*	*	*
IGSO	C06	*	*	*	99.2	99.1	96.2	100	99.9	39.4
	C07	100	100	100	100	100	99.9	100	99.9	49.5
	C08	100	100	100	100	100	99.1	99.9	99.8	37.7
	C09	*	*	*	*	*	*	99.9	99.9	35.8
	C10	100	100	100	99.1	99.0	93.7	100	99.7	42.5
MEO	C11	0.07	0.09	0.11	*	*	*	*	*	*
	C12	*	*	*	*	*	*	0.06	0.10	1.20
	C13	*	*	*	*	*	*	0.07	0.12	2.19
	C14	*	*	*	*	*	*	0.06	0.12	2.47

two EWL combinations at three baselines are above 99%, even up to 100%, while for the 72 km baseline, the narrow-lane ambiguity rounding success rate become significantly worse. Therefore, in the following, the resolution of the NL ambiguity at medium-long baselines is mainly considered (Fig. 1).

4 The Modified TCAR Method

Aiming at the low success rate of NL ambiguity resolution over the medium-long baseline, an improved TCAR method is proposed, which is to use the smoothed double-difference ionosphere estimation to correct the NL ambiguity in the classical TCAR method in this paper.

4.1 The Smoothed Double-Difference Ionosphere Estimation

It can be seen from the foregoing statement that both the EWL (0, −1, 1), (1, 4, −5) double-difference ambiguities can be easily fixed in the first two steps of the TCAR method, regardless of the short or medium long baseline. Therefore, the double difference ionospheric delay can be estimated by using these two ambiguous fixed EWL observations. The equation can be expressed as follows:

$$\hat{I}_1 = \frac{\tilde{\Phi}_{(0,-1,1)} - \tilde{\Phi}_{(1,4,-5)}}{\beta_{(0,-1,1)} - \beta_{(1,4,-5)}} \tag{6}$$

where $\tilde{\Phi}_{(0,-1,1)} = \Phi_{(0,-1,1)} - \lambda_{(0,-1,1)} \cdot \breve{N}_{(0,-1,1)}$ and $\tilde{\Phi}_{(1,4,-5)} = \Phi_{(1,4,-5)} - \lambda_{(1,4,-5)} \cdot \breve{N}_{(1,4,-5)}$ are the two EWL combinations after correction.

It is assumed that the accuracy of the phase observations at each frequency point is equal, namely, $\sigma_{\nabla\Delta\Phi_1} = \sigma_{\nabla\Delta\Phi_2} = \sigma_{\nabla\Delta\Phi_3} = \sigma_{\nabla\Delta\Phi}$, and then the accuracy of double differential ionospheric delay estimation can be obtained.

$$\begin{aligned}\sigma_{\hat{I}_1} &= \frac{\sigma_\Phi}{\beta_{(0,-1,1)} - \beta_{(1,4,-5)}} \sqrt{\frac{f_1^2}{f_{(1,4,-5)}^2} + \left(\frac{f_2}{f_{(0,-1,1)}} + \frac{4f_2}{f_{(1,4,-5)}}\right)^2 + \left(\frac{f_3}{f_{(0,-1,1)}} + \frac{5f_3}{f_{(1,4,-5)}}\right)^2} \\ &= 89.38\sigma_\Phi\end{aligned} \tag{7}$$

As it can be seen from the Eq. (7), the noise of the double-difference ionospheric delay estimated by the two EWL combinations is very large, so it needs to adopt the smoothing algorithm. The term that is used to smooth the estimated double difference ionospheric delay can be expressed as follows:

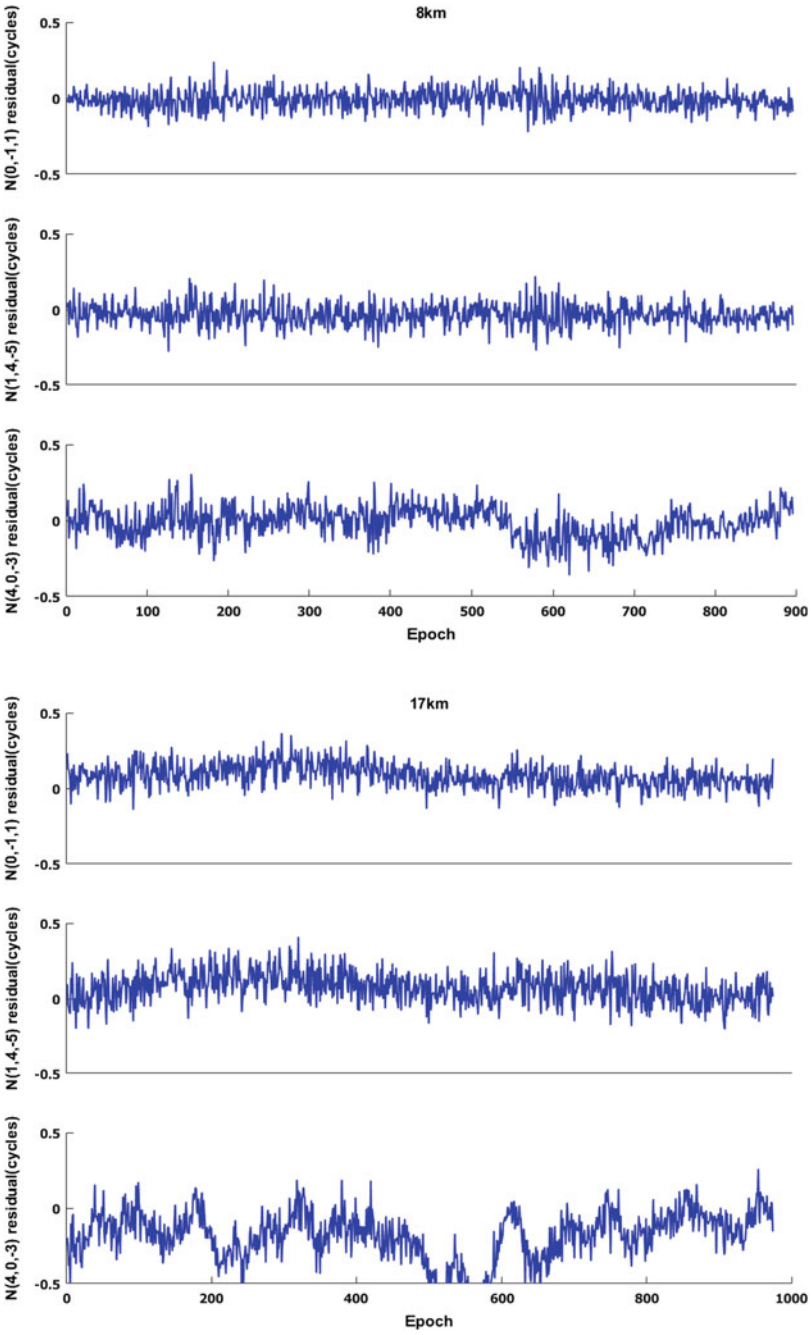

Fig. 1 The EWL (0, −1, 1), (1 ,4, −-5) and NL (4, 0, −3) ambiguity residual of different baselines

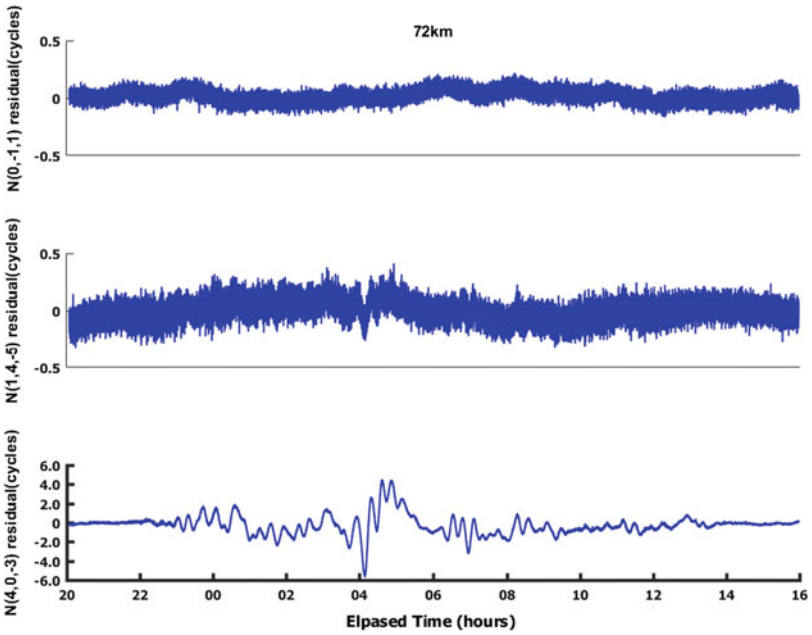

Fig. 1 (continued)

$$\bar{I}_1 = \frac{(\Phi_{(1,0,0)} - \lambda_1 N_1) - (\Phi_{(0,1,0)} - \lambda_2 N_2)}{\beta_{(1,0,0)} - \beta_{(0,1,0)}} \tag{8}$$

where ambiguity terms $\nabla\Delta N_1$ and $\nabla\Delta N_2$ are unknown, but they can be eliminated by differencing between epochs, so in the event of cycle slip it needs to repair the cycle slips or restart the procedure of smoothing. The double-difference ionospheric delay can be obtained by combining the Eqs. (6) and (8).

$$\breve{I}_1(n) = \frac{\sum_{t=1}^{n} \hat{I}_1(t)}{n} + \frac{(n-1)\bar{I}_1(n) - \sum_{t=1}^{n-1} \bar{I}_1(t)}{n} \tag{9}$$

In Fig. 2, the double differential ionospheric delay estimation obtained in Eq. (6) and the smoothing value obtained in (9) is compared. As mentioned above, no matter whether the short baseline or the medium long baseline, noise of the double-difference ionospheric delay estimation is very large, even up to 1 m. The smoothed double-difference ionospheric delay noise is significantly smaller, with an accuracy over short baseline smaller than 5 cm. The double-difference ionospheric delay of 72 km in the medium long baseline is significantly larger than that of the short baseline, and is still on the decimeter scale even after the double difference. In the meantime, the strategy of partial ambiguity fixing in LAMBDA method is used

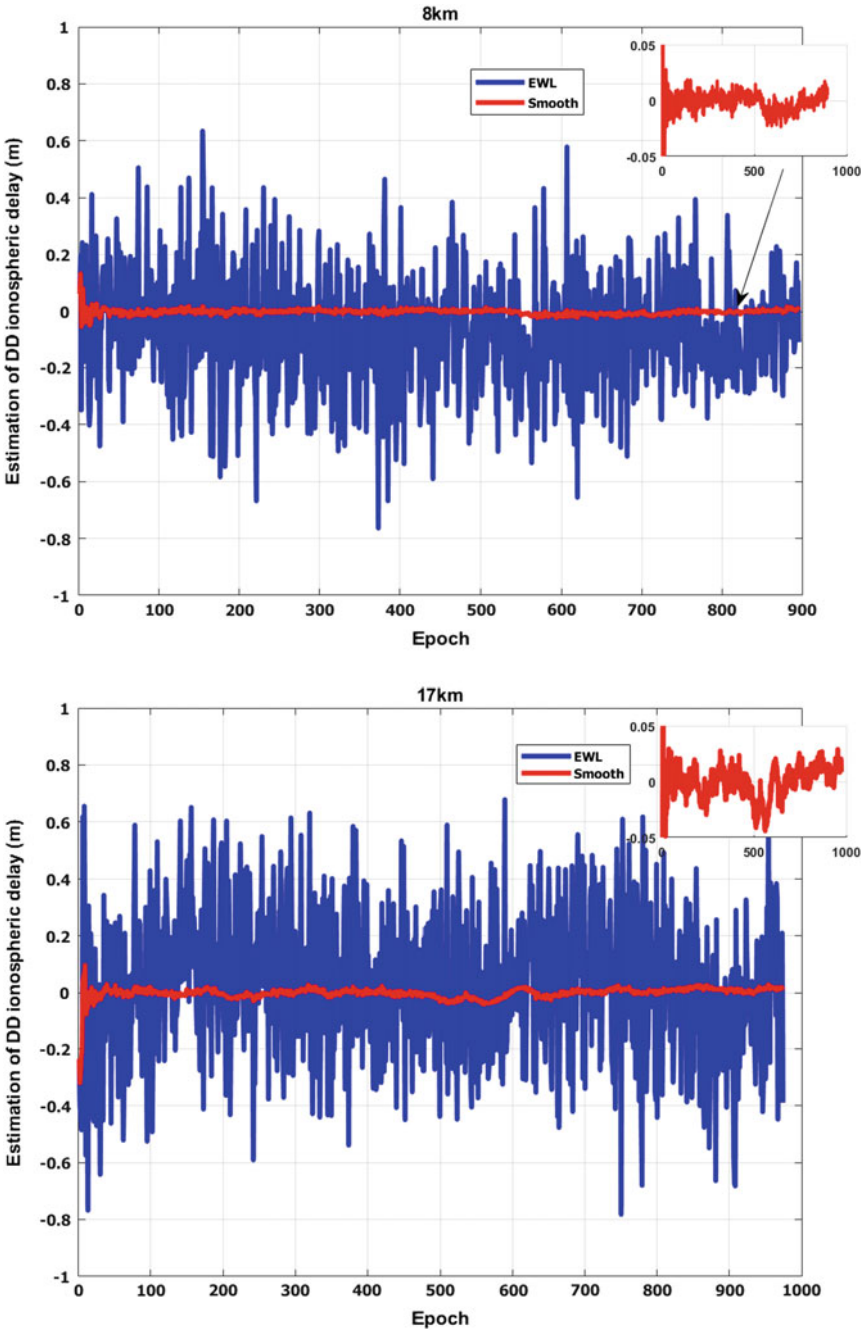

Fig. 2 Estimation of DD ionospheric delay

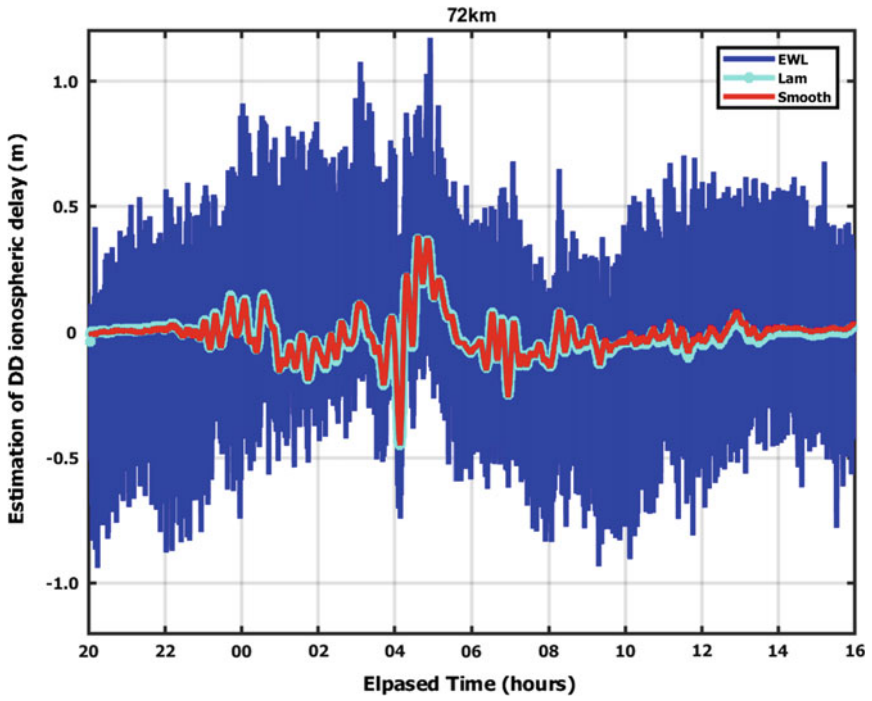

Fig. 2 (continued)

to estimate the double-difference ionospheric delay which can be regarded as the reference value for the TCAR method. It can be seen from the Fig. 2, the smoothed double-difference ionospheric delays derived from the TCAR method are in good agreement with the value obtained in the LAMBDA method.

4.2 Corrections of the NL Ambiguity

Using the double difference ionospheric smoothing value obtained in the previous section, the narrow lane ambiguity NL in TCAR method is corrected as follows:

$$\begin{aligned}\hat{N}_{(i_n,j_n,k_n)} = \varphi_{(i_n,j_n,k_n)} - \frac{\lambda_{(i_w,j_w,k_w)}\left(\varphi_{(i_w,j_w,k_w)} - \breve{N}_{(i_w,j_w,k_w)}\right)}{\lambda_{(i_n,j_n,k_n)}} \\ + \frac{\beta_{(i_n,j_n,k_n)} - \beta_{(i_w,j_w,k_w)}}{\lambda_{(i_n,j_n,k_n)}}\breve{I}_1 - \varepsilon_{(i_n,j_n,k_n)} + \varepsilon_{(i_w,j_w,k_w)}\frac{\lambda_{(i_w,j_w,k_w)}}{\lambda_{(i_n,j_n,k_n)}}\end{aligned} \tag{10}$$

The estimated double-difference ionospheric delay after smoothing are plotted in Fig. 3. At the same time, referring to the correct integer ambiguities, residuals of the

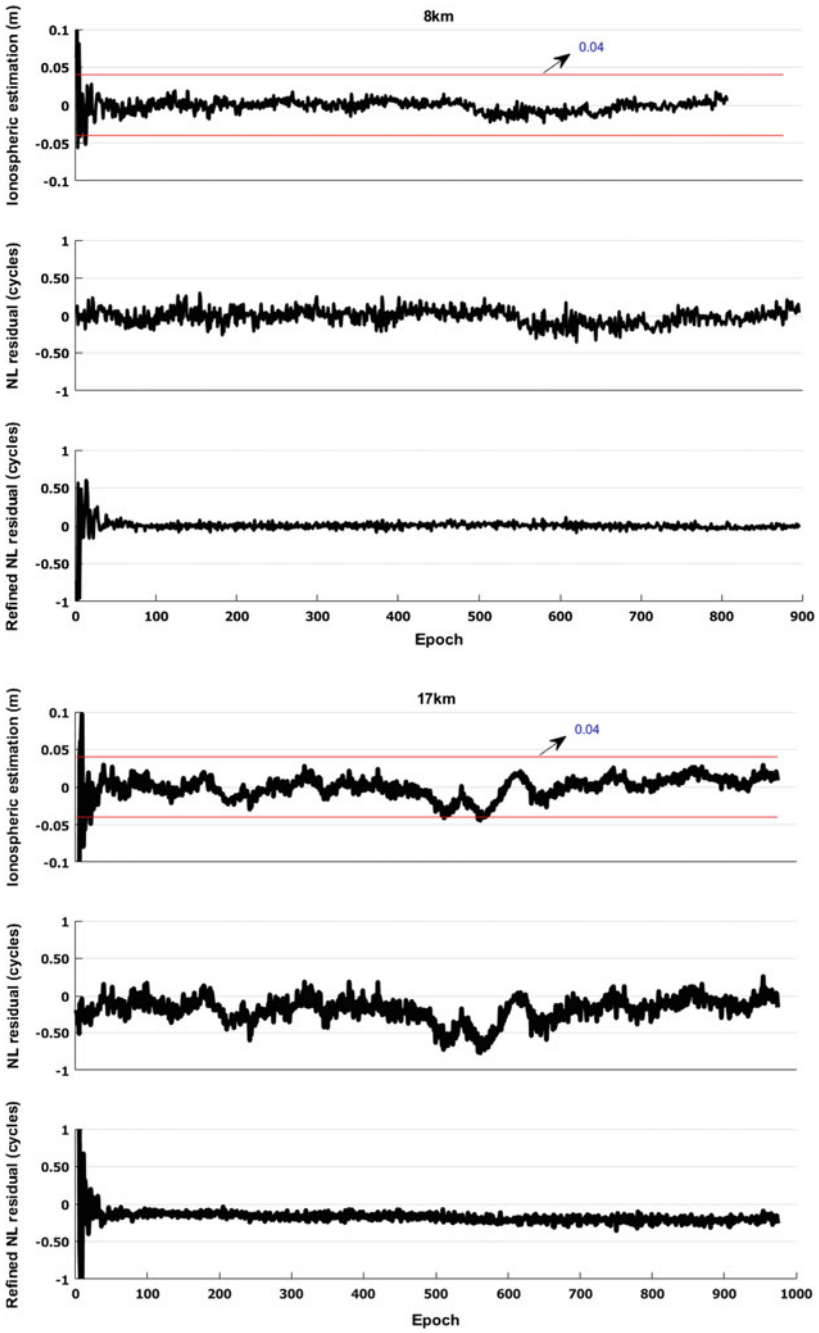

Fig. 3 The smooth DD ionospheric delay, classical and modified NL ambiguity residual

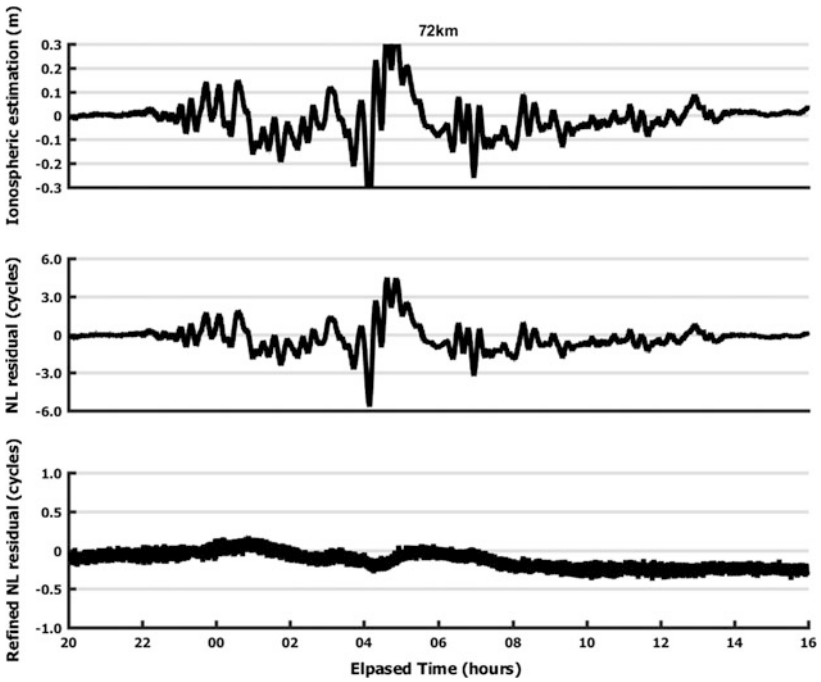

Fig. 3 (continued)

double-difference NL floating ambiguities under three baselines compared with values after correction are shown in Fig. 3, too. It can be seen that residuals of the double-difference NL ambiguity and double-difference ionospheric smoothing values always maintain the same trend. For the short baseline, the double difference ionospheric delay residuals are very small. Except for several epochs in the initial convergence stage, other epochs are all within 4 cm, which cannot affect the NL ambiguity resolution as depicted in Sect. 3.1. However, at medium-long baseline, the double-difference ionospheric delay residuals can still reach the decimeter level, resulting in poor precision of narrow-lane ambiguity resolution, the effects of which can reach up to 6 cycles. It is noticed that the accuracy of NL ambiguity corrected by the ionospheric smoothing values is obviously improved.

The RMS values of the double-difference NL ambiguities for BDS satellites in the classical and modified TCAR method are given in Table 6 over three baselines. It can be seen from the comparison that as the baseline length increases, accuracy of the NL ambiguity resolution will gradually deteriorate, and for the medium long baseline, the RMSs of the double-difference NL ambiguity are even close to 4 cycles. The accuracy of NL ambiguity resolution after corrections by the double-difference ionospheric smoothing values is significantly improved. Most of the errors can be corrected to within 0.5 cycles even at medium-long baseline. Success rates of rounding NL ambiguities to the correct integers under different baseline are listed,

and correspondingly, success rates of the corrected NL ambiguity are displayed, too. It is worth noting that the success rates of the corrected NL ambiguity are even larger than that of the NL ambiguity resolution without correction for short baseline, the mainly reason of which is that success rate of NL ambiguity resolution is already very high, and it needs time to converge during the procedure of ionospheric smoothing, which affect the NL ambiguity resolution in the initial stage. However, for the medium-long baseline success rate of NL ambiguity resolution has been greatly improved, and for some satellites it can even reach 100% (Table 7).

Table 6 RMS of NL and modified NL ambiguity residual

RMS		8 km		17 km		72 km	
		NL	NL-Smo	NL	NL-Smo	NL	NL-Smo
GEO	C02	0.12	0.10	0.24	0.18	3.43	1.06
	C03	0.10	0.08	0.19	0.20	0.97	0.16
	C04	0.17	0.07	0.21	0.14	0.94	0.11
	C05	0.13	0.07	0.23	0.12	*	*
IGSO	C06	*	*	0.18	0.20	1.35	0.27
	C07	0.13	0.08	0.18	0.14	0.52	0.27
	C08	0.11	0.06	0.20	0.13	1.74	0.45
	C09	*	*	*	*	1.44	0.56
	C10	0.09	0.05	0.22	0.19	3.37	0.73
MEO	C11	0.11	0.06	*	*	*	*
	C12	*	*	*	*	1.20	0.54
	C13	*	*	*	*	2.19	1.5
	C14	*	*	*	*	2.47	0.7

Table 7 Success rate of ambiguity resolution for NL and modified NL

Success rate/%		8 km		17 km		72 km	
		NL	NL-Smo	NL	NL-Smo	NL	NL-Smo
GEO	C02	100	99.1	94.3	98.9	26.8	30.2
	C03	100	99.3	100	99.0	58.2	100
	C04	99.6	99.0	99.0	98.3	62.7	100
	C05	99.5	98.7	95.0	96.1	*	*
IGSO	C06	*	*	96.2	96.0	39.4	95.7
	C07	100	99.3	99.9	98.8	49.5	79.6
	C08	100	99.0	99.1	99.4	37.7	91.2
	C09	*	*	*	*	35.8	77.6
	C10	100	99.5	93.7	98.9	42.5	60.4
MEO	C11	100	99.2	*	*	*	*
	C12	*	*	*	*	45.7	67.7
	C13	*	*	*	*	22.5	56.5
	C14	*	*	*	*	22.3	27.4

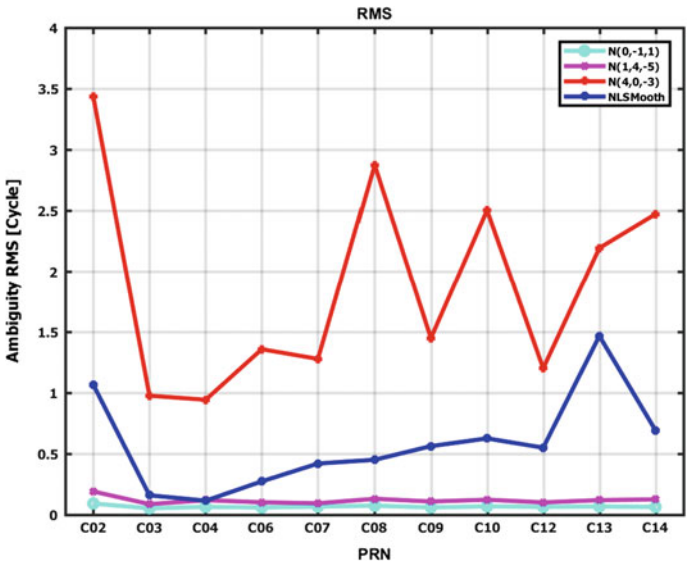

Fig. 4 Comparison of RMS in baseline of 72 km

The RMS comparison of EWL (0, −1, 1), (1, 4, −5) NL (4, 0, −3) and the corresponding NL corrections for BDS satellites at 72 km length is given in Fig. 4. For the medium-long baseline, accuracies of the double-differenced ambiguity resolution for the two EWL combinations are very high, and it is very poor for the NL ambiguity resolution, but it is greatly improved after ionospheric correction.

5 Conclusions

Performances of TCAR method over different baseline are investigated in the paper. First of all, according to the classical TCAR method, the evaluation accuracy and rounding success rate of the two double-difference EWL and NL ambiguity resolution are analyzed, it is found that the result of the two EWL ambiguity resolution is not affected by the increase of the baseline length. However, the performance of the NL ambiguity is very poor in the medium-long baseline. And then, the main factors influencing NL ambiguity resolution are analyzed experimentally. It is found that the ambiguity resolution in geometric model is mainly affected by the double difference ionospheric delay. In the case of short baseline, residual of the double difference ionospheric delay Which is within 4 cm, and its influence on NL ambiguity resolution can be neglected. However, the residual double-difference ionospheric delay is still large at medium-long base line, even reaching 3 decimeters, which largely affects the NL ambiguity resolution. Therefore, the two EWL combinations with ambiguities successfully fixed is used to estimate the

double-difference ionospheric delay residual, but the accuracy is poor, and then the smoothing procedure is adopted to obtain the double-difference ionospheric delay. At last, the smoothed double-difference ionosphere delay is used to correct the NL double-difference ambiguity. It can be seen that although the smoothing process requires several epoch convergence, the accuracy of the accuracy of the double-difference NL ambiguity resolution has been greatly improved both in the short baseline and in the mid-long baseline. The success rate of ambiguity rounding has increased significantly, the maximum increasing rate can be up to 151.1%.

References

1. China Satellite Navigation Office (CSNO) (2013) BeiDou navigation satellite system signal in space interface control document open service signal (Version 2.0)
2. Yang Y, Li J, Wang A et al (2014) Preliminary assessment of the navigation and positioning performance of BeiDou regional navigation satellite system. Sci China Earth Sci 57(1):144–152
3. Yang Y, Li J, Xu J et al (2011) Contribution of the Compass satellite navigation system to global PNT users. China Sci Bull 56(26):2813–2819
4. Yue W, JinLai G, Yang M, Wei S (2006) Analysis of GPS multi-frequency carrier phase combinations. Geomatics Info Sci Wuhan Uni 31(12):1082–1085
5. Cocard M et al (2008) A systematic investigation of optimal carrier-phase combinations for modernized triple-frequency GPS. Geod 82:555–564
6. Urquhart L (2009) An analysis of muti-frequency carrier phase linear combinations for GNSS. Senior technical report, Department of Geodesy and Geomatics Engineering Technical Report No. 263, University of New Brunswick, Fredericton, New Brunswick, Canada
7. Hatch R, Jung J, Enge P, Pervan B (2000) Civilian GPS: the benefits if three frequencies. GPS Solutions 3(4):1–9
8. Shi C et al (2013) Precise relative positioning using real tracking data from COMPASS GEO and IGSO satellites. GPS Solutions 17(1):103–119
9. Montenbruck O, Hauschild A, Steigenberger P, Hugentobler U, Teunissen P, Nakamura S (2012) Initial assessment of the COMPASS/BeiDou-2 regional navigation satellite system. GPS Solutions, Published online: 12 June 2012. https://doi.org/10.1007/s10291-012-0272-x
10. Tang W, Deng C, Shi C, Liu J (2013) Triple-frequency carrier ambiguity resolution for Beidou navigation satellite system. GPS Solutions 18:335–344
11. Vollath, U et al (1998) Analysis of three-carrier ambiguity resolution (TCAR) technique for precise relative positioning in GNSS-2. In: Proceedings of ION GPS-98 the 11th international technical meeting of the satellite division of the institute of navigation, Nashville, Tennessee, USA, pp 417–426
12. Odijk D et al (2008) ADOP in closed form for a hierarchy of multi-frequency single-baseline GNSS models. J Geodesy 82(473–492)
13. Simsky A (2006) Three's the charm: triple-frequency combinations in future GNSS. July/August, Inside GNSS, pp 38–41
14. Hatch R (2006) A new three-frequency, geometry-free technique for ambiguity resolution. In: Proceedings of ION GNSS 2006, 26–29 Sept, Fort Worth, TX, pp 309–316
15. Wang K, Rothacher M (2013) Ambiguity resolution for triple-frequency geometry-free and ionosphere-free combination tested with real data. J Geod 87:539–553
16. Zhao Q, Dai Z, Hu Z, Sun B, Shi C, Liu J (2014) Three-carrier ambiguity resolution using the modified TCAR method. GPS Solutions 1–11

17. Zhang, X. He, X (2015) Performance analysis of triple-frequency ambiguity resolution with BeiDou observations. *GPS* Solutions 1–13
18. Jinlong Li (2011) Research on the algorithms of GNSS triple frequency precise positioning. Information Engineering University, Zhengzhou
19. Fengyanming GNSS (2008) Three carrier ambiguity resolution using ionosphere-reduced virtual signals. J Geodesy 2008(82):847–862
20. Zhang W (2005) Triple Frequency Cascading Ambiguity Resolution for Modernized GPS and GALILEO. UCGE Reports, Number 20–28, July 2005

Analysis of the Effect of the 06-09-2017 Solar Flare on GNSS Signal and Positioning Performance

Wei Zhou, Shegnfeng Gu, Maorong Ge and Jungang Wang

Abstract This paper investigates the effect of 06-09-2017 X9.3 solar flare on Global Navigation Satellite System (GNSS) signal and positioning performance. To conduct the study we select 60 IGS stations and collect the observations and ephemeris from August 30 to September 13, 2017. The Solar activity Indexes of Ap, Kp, Dst are evaluated and the global ROTI maps are constructed to indicate and define the magnitude of the storm. As for the GNSS signal, signal-in-space-ranging-errors (SISRE) is used to assess the solar flare's effect on the accuracy of broadcast ephemeris, and the cycle slip occurrence is used to assess it's impact on observation quality, especially phase observation. Furthermore, the kinematic GNSS PPP solution is used to evaluate the GNSS positioning performance during the storm. After processing, root mean square errors (RMS) of north, east and up component were calculated for each station on each day. The results indicate that at eight of all the selected IGS stations three-dimensional (3D) accuracy of PPP has degraded significantly and the GNSS are unreliable during the storm.

Keywords GNSS · Solar flare · ROTI · SISRE · PPP · Performance

W. Zhou (✉) · S. Gu · M. Ge · J. Wang
LEETC, Wuyue Road.2, Luoyang 471003, China
e-mail: zhouwei_0611@163.com

W. Zhou
Geo Forschungs Zentrum (GFZ) Potsdam, Telegrafenberg,
D14473 Potsdam, Germany

S. Gu
GNSS Research Center, Wuhan University, Luoyu Road 129, Wuhan 430079,
Hubei, China

J. Sun et al. (eds.), *China Satellite Navigation Conference (CSNC) 2018 Proceedings*, Lecture Notes in Electrical Engineering 498,
https://doi.org/10.1007/978-981-13-0014-1_46

1 Introduction

Ionosphere is a dispersive medium of gases and molecules. It produces ionospheric irregularities when local electron density differs significantly, thus inducing rapid Scintillation in the amplitude and phase of the radio signals [1]. Scintillation, especially in the L-band, has the capacity to degrade the accuracy and reliability of GNSS by increasing the tracking error, occurrence of cycle slips and probability of loss of lock. The WAAS performance in Canada, Alaska, and CONUS were affected on March 17 and March 18, 2015 by ionospheric activity [2]. Scintillations on L band have been frequently observed from GNSS receivers [3, 4] at low latitudes and high latitudes [5]. During intense magnetic storm periods they have also been reported at middle latitudes [6].

Solar flares occurred on September 6, 2017, at 12:02 UTC [7]. This event was classified as an X9.3 and the largest flare so far in the current solar cycle. The X9.3 solar flares were accompanied by a coronal mass ejection (CME) and impacted the Ionosphere and Earth's magnetic field around early morning on September 8, 2017.

This paper focuses on the performance of GNSS during the 2017-09-06 X9.3 solar flare. In the sections to follow we first introduce the data set and the methodology for analyzing the effect of the 2017-09-06 X9.3 flare on GNSS performance. The comparisons results during the event as well as the relevant discussions are given in Sect. 3. Finally, we summarize the main findings in Sect. 4.

2 Dataset and Methodology

We select 60 MGEX stations to analyze the effect of the 2017-09-06 X9.3 flare on GNSS. Figure 1 shows the distribution of the stations with different geographic locations. All the 60 MGEX stations have GPS, GLONASS, BDS and Galileo observations. To analyze the overall performance, also for comparison, we collect the observations for two weeks from August 30 to September 13, 2017. The Multi-GNSS precise orbits and clocks provided by GFZ, i.e., the GBM final products, are used here for precise positioning. The Rate of TEC Index (ROTI), Dst, Kp, Ap, SISRE, the occurrence of GNSS phase cycle slips and the positioning errors are analyzed in this study to evaluate the GNSS signals and positioning performance.

2.1 Solar Activity Index

Solar index Kp and Ap are used to define the magnitude of a geomagnetic storm. Kp is a worldwide weighted average metric which indicates a geomagnetic storm when the value of Kp is more than 5. On the basis of Ap thresholds, we classified the geomagnetic storms into three grade as a minor storm when $29 < Ap < 50$,

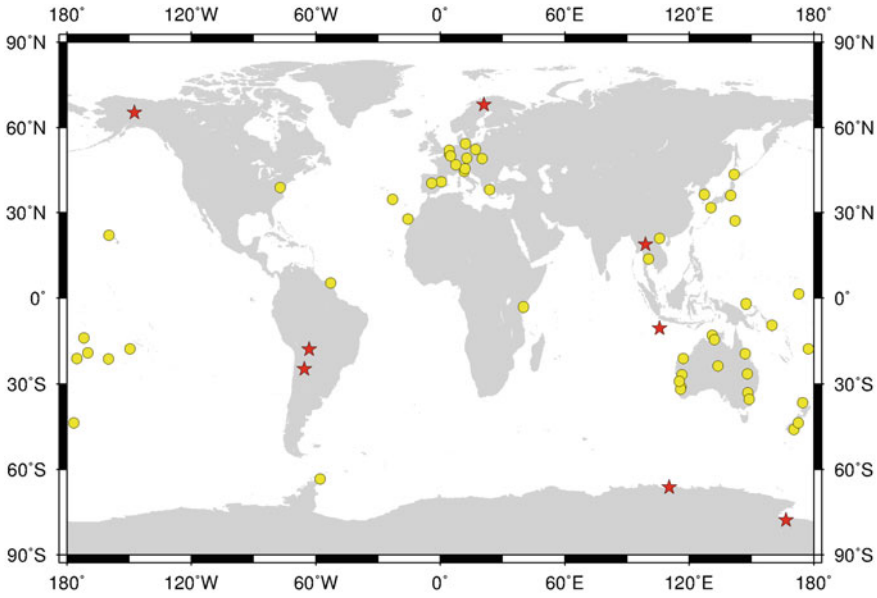

Fig. 1 IGS stations distribution

a major storm when 50 <= Ap < 100 and a severe storm when Ap >= 100 [8]. The geomagnetic storms can also be characterized by the Dst. The worldwide magnetic storm level is categories as weak storms (Dst $\geqslant -50$nT), moderate storms (-100nT < Dst $\leqslant -50$nT) and intense storms (Dst $\leqslant -100$nT) [9].

ROTI is defined as the standard deviation of the rate of TEC and widely used in the services of space weather monitoring [10] and investigations of the ionospheric irregularities occurrence [11]. ROTI is estimated by dual-frequency GNSS data with the time interval of 5 min as:

$$ROTI = \sqrt{\langle ROT^2 \rangle - \langle ROT \rangle^2} \tag{1}$$

where ROT is the rate of TEC [12], which is defined as the slant TEC variation rate of two successive epochs:

$$ROT = \frac{TEC^i_{t+\Delta t} - TEC^i_t}{\Delta t} \tag{2}$$

2.2 GNSS Positioning Indices

To analyze the impact of the X9.3 flare on GNSS signal and positioning performance we use three data parameters: SISRE, the number of cycle slips and the positioning accuracy.

The signal-in-space ranging error (SISRE) describes the combined impact of orbit and clock errors, which is defined as a weighted average [13]:

$$SISRE = \sqrt{[rms(w_R \cdot R - c \cdot \Delta t)]^2 + w_{A,C}^2 (A^2 + C^2)} \quad (3)$$

where $c \cdot \Delta t$ denotes the error of the clock offset, w_R and $w_{A,C}^2$ denote the weight of radial and along/cross orbit errors, respectively. For different GNSS systems and different types of satellites (GEO, IGSO, MEO), w_R and $w_{A,C}^2$ have different values, and we refer Montenbruck for the detailed values.

The most important negative impact on GNSS by ionosphere scintillation is the loss of lock and the frequent cycle slip occurrence of the phase observations. Therefore, when a solar flare occurs it is expected that the cycle slips will be much more frequent compared with other times when the ionosphere activities are quiet. In this paper we pay special attention to the cycle slips statistics of the phase observations during the flare. We adopt the widely used Turboedit algorithm [14] to detect the cycle slips automatically. This method uses the wide-lane combination and the ionospheric combination to detect cycle slip and could be implemented on a single receiver.

Precise GNSS positioning mainly counts on the accurate phase observations, which has an accuracy of mm-level. However, it is impossible to obtain the precise estimates due to the ambiguity, which needs some time to convergent to a precise value. The convergence time for PPP usually takes half an hour or more, depending on the pseudo-range accuracy, the satellite geometry, et al. With more cycle slips the estimated parameters will suffer some accuracy degradation. Moreover, if the cycle slips occur at the same epoch or within a short period, which is equivalent to a reconvergence, the solution will become extremely unreliable. Even though some method has been proposed to speed up the reconvergence by constraining the atmosphere [15], the occurrence of cycle slips will still degrade the positioning accuracy.

3 Results and Discussion

3.1 Solar Activity Index Analysis

To detect the variations of solar activity and geomagnetic conditions during the X9.3 solar flares, we first evaluate the Ap index, Kp index and Dst index. From the Fig. 2 we find that since late September 7, 2017, the Ap index reached value up to more than 200. Moving to the scale of another index, a value of 8 or more for the Kp index and a value of −150 for the Dst index also indicated an intense storm.

Furthermore, to construct the global ROTI maps, we selected 262 IGS stations with GPS observations for the period of September 7–9, 2017. The distribution of tracking stations is shown in Fig. 3. All the ROTI values derived from the GPS data along all visible satellite passes are averaged and binned into cells of $1° \times 1°$

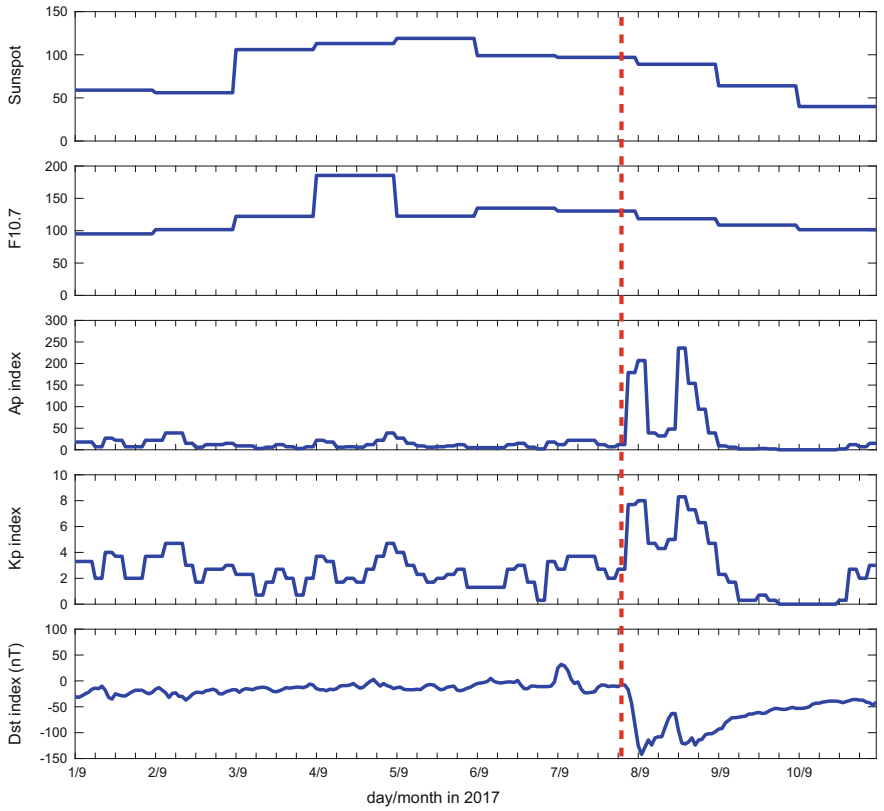

Fig. 2 Variations of solar activity and geomagnetic conditions during 1–10 September 2017. From up to bottom: Sunspot, F10.7, Ap index, Kp index, Dst Index

resolution in geographic latitude and longitude, and the ROTI values are calculated every hour. Four epochs' ROTI maps are presented in Figs. 4, 5, 6, and 7. As we can see from Figs. 4, 5, 6, and 7, this Geomagnetic Strom occurs since late September 7 and lasts until the early morning of September 9.

3.2 Sisre

SISRE is a key indicator to monitor the GNSS performance. We calculate the daily SISRE values by Eq. 3 for each satellite from August 30 to September 17, 2017 (DOY 241 to 256), using the GBM final precise orbits and clocks as reference. Figures 8, 9, 10 and 11 show SISRE values of GPS, Glonass, Beidou and Galileo, respectively. As we can see, the SISRE values do not show significant variations during the intense geomagnetic storm. The comparison results indicate that the X9.3 solar flare doesn't affect the accuracy of the broadcast ephemeris.

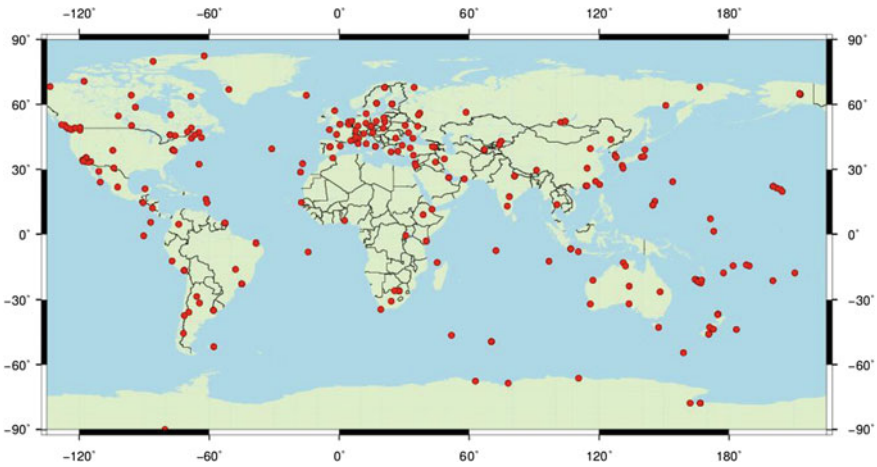

Fig. 3 Geographical distribution of tracking stations in global for ROTI calculation

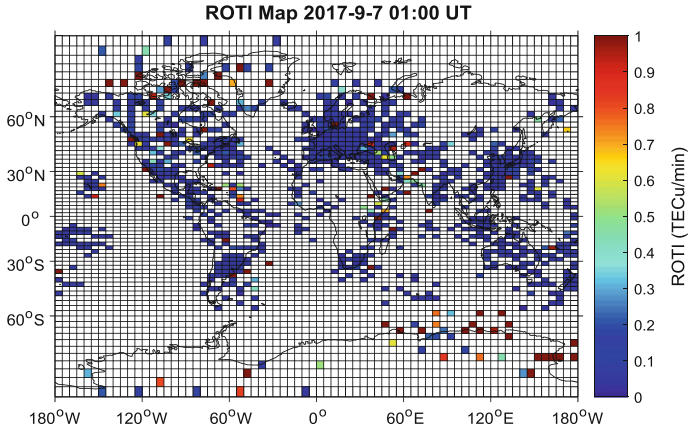

Fig. 4 ROTI map for 2017-9-7 01:00 UT

3.3 Detection of Cycle Slip

As described in Sect. 2, we select 60 globally distributed IGS stations and obtain all the GNSS observations from August 30 to September 13, 2017. We count the number of cycle slips occurred on different frequencies of all the satellites for GPS, GLONASS, Beidou and Galileo and then we take an average for each day at each station. This cycle slips number of each station on each day is shown in Fig. 12. For most of the stations, the numbers of cycle slip hold slow fluctuation during the two-week period, while 8 of them show significant variation on DOY 251, when the

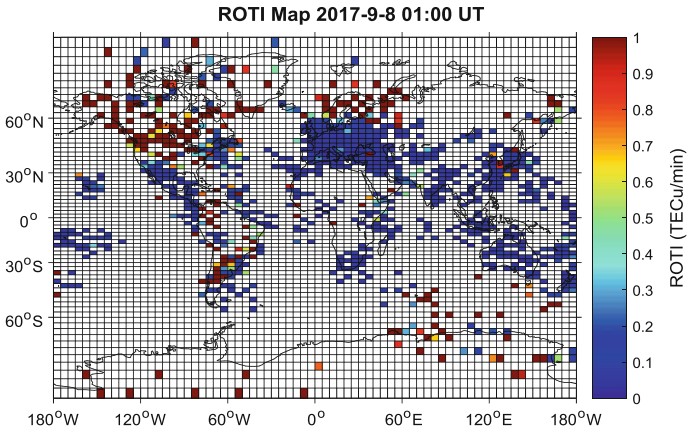

Fig. 5 ROTI map for 2017-9-8 01:00 UT

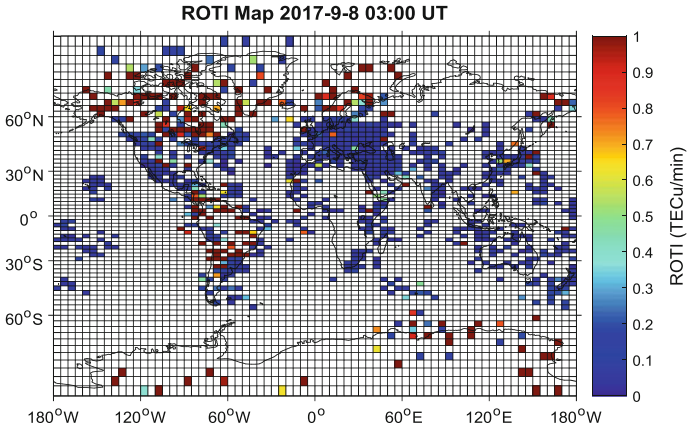

Fig. 6 ROTI map for 2017-9-8 03:00 UT

geomagnetic storm occurs. The 8 stations marked with star in Fig. 1, i.e., CAS1, CMUM, KIRU, PFRR, SCRZ, SCTB, UNSA, XMIS, are distributed in low and high latitudes.

We take Station PFRR and Station KIRU as examples and present the daily cycle slip number in Figs. 13 and 15. The daily averages cycle slip numbers for both stations fluctuate slightly from August 30 to September 7 (DOY 241-250), while the cycle slip numbers abruptly increase on September 8. For station PFRR, the daily average cycle slip number rises from 106 up to 193 on DOY 251, and that for station KIRU goes up from 61 to 157. The daily average cycle slips return to normal level on September 9. To evaluate the effect on the GNSS phase observation of the X9.3 solar flare, we also analyze the time series of the cycle slip number on

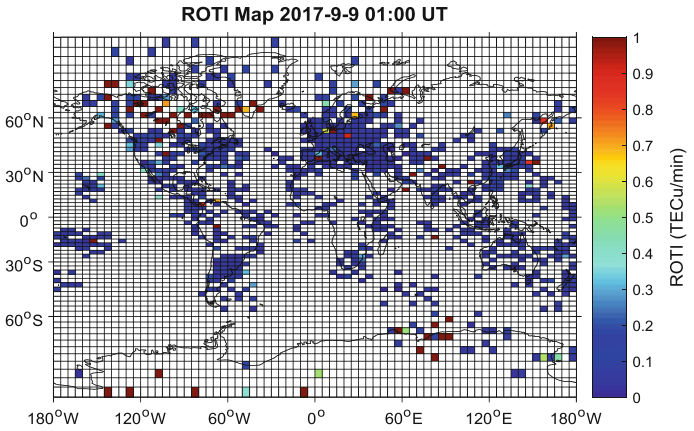

Fig. 7 ROTI map for 2017-9-9 01:00 UT

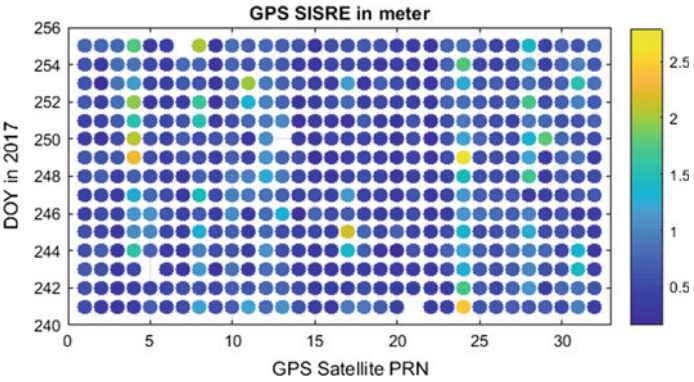

Fig. 8 GPS SISRE

September 8 at both PFRR and KIRU, which is shown in Figs. 14 and 16. As we can see, the series of the cycle slip number exhibit a significant increase during 47,000 –52,000 s of DOY 251, which may degrade the positioning precision.

3.4 Precise Positioning

To investigate whether the X9.3 solar flare degrades the GNSS precise positioning or not, we conduct Multi-GNSS kinematic Precise Point Positioning (PPP) on the 8 stations from DOY41-255, 2017. We take Station PFRR and Station KIRU as examples. The root mean square (RMS) values on all the north, east, up components and the 3-D accuracy for all these two stations on each day are presented in

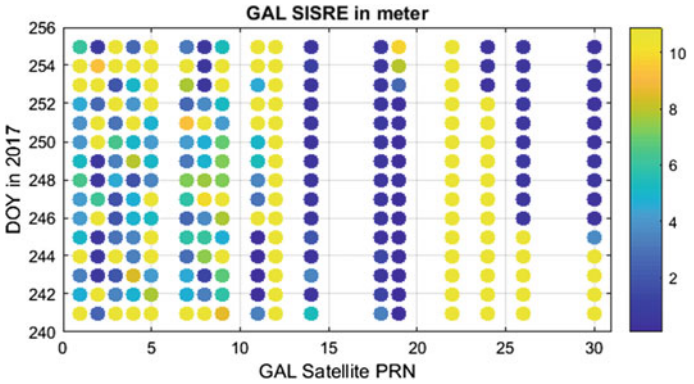

Fig. 9 Galileo SISRE

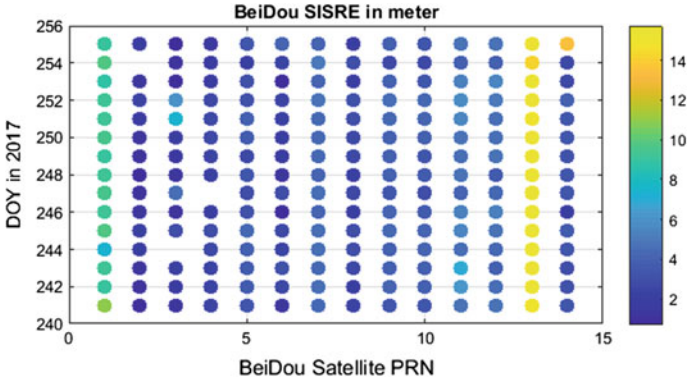

Fig. 10 Beidou SISRE

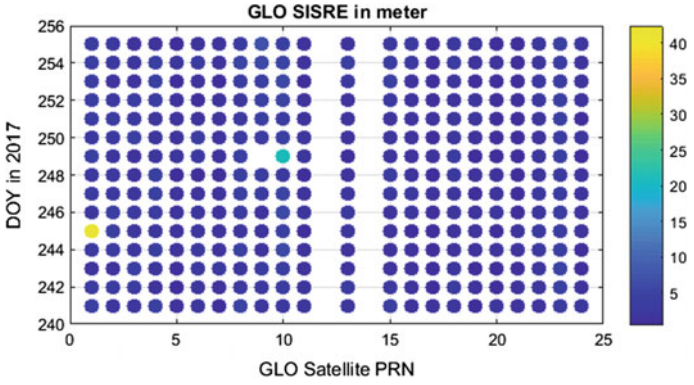

Fig. 11 GLONASS SISRE

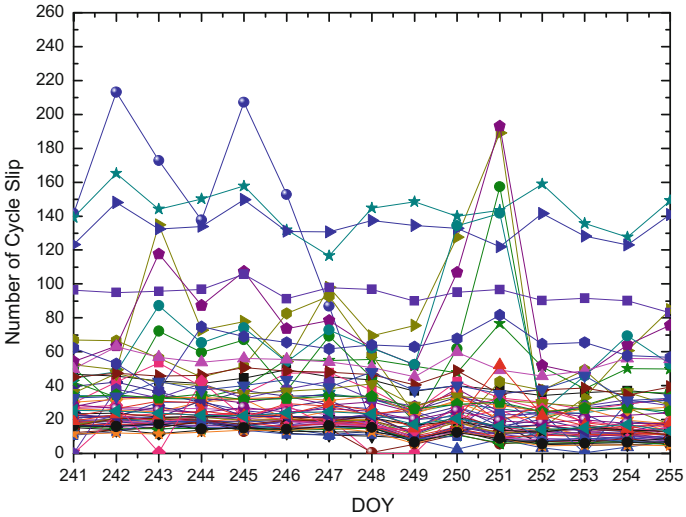

Fig. 12 Daily average of GNSS cycle slips

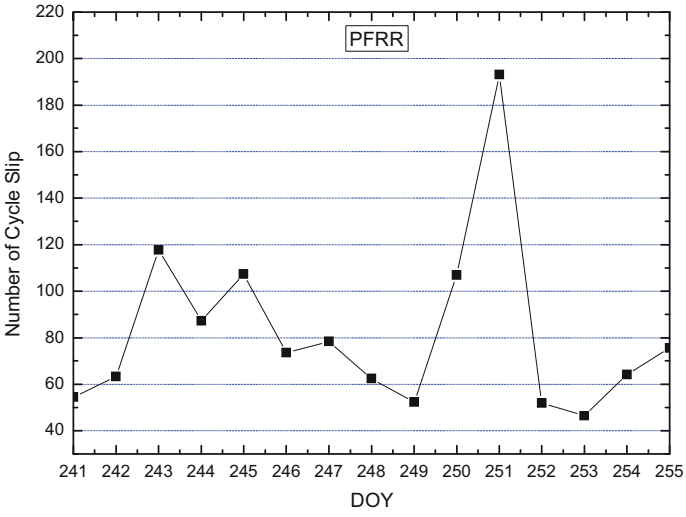

Fig. 13 PFRR Daily average cycle slips

Figs. 17 and 19, respectively. Similar to the cycle slip behaviors mentioned above, for station PFRR the positioning accuracy shows a significant decrease on September 8. The RMS values for DOY 251 are 0.19/0.13/0.45/0.50 m for north, east, up and 3-D components, which are about two times larger than that of other days. On the other hand, KIRU station also shows the same pattern like PFRR. The RMS values on DOY 251 are 0.19/0.29/0.38/0.51 m, for the north, east, up and

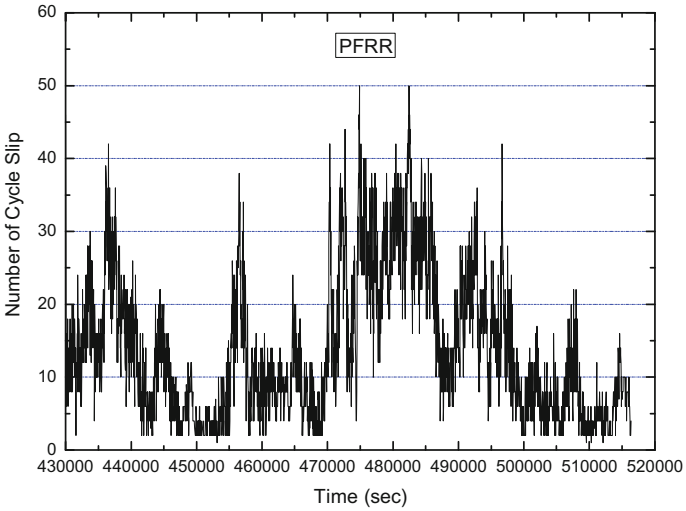

Fig. 14 PFRR cycle slip occurrence on DOY 251

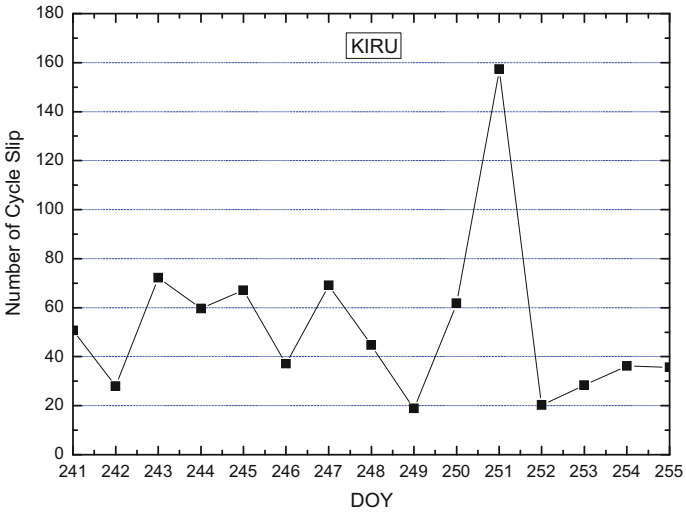

Fig. 15 KIRU daily average cycle slips

3D components respectively, which are more than 5 times larger than that of other days. The epoch-to-epoch coordinate estimates on DOY 251 for both PFRR and KIRU are presented in Figs. 18 and 20, respectively. Corresponding to the period when the X9.3 sun flare occurs, the coordinate estimates show obvious degradation during this period, which is attributed to the cycle slips cause by the sun flare.

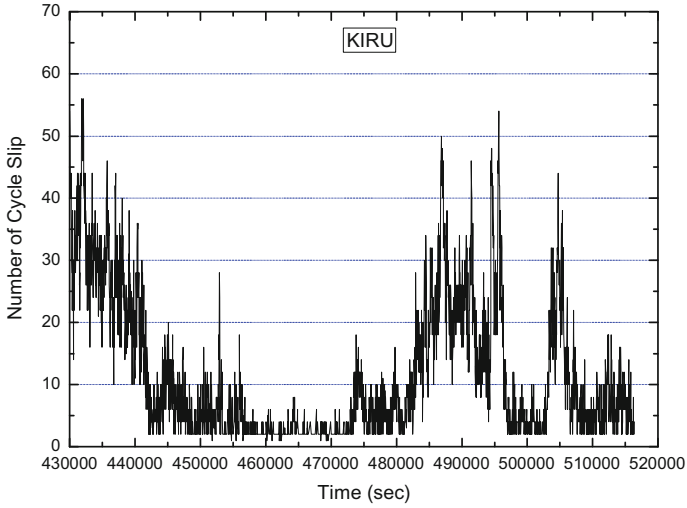

Fig. 16 KIRU cycle slip occurrence on DOY 251

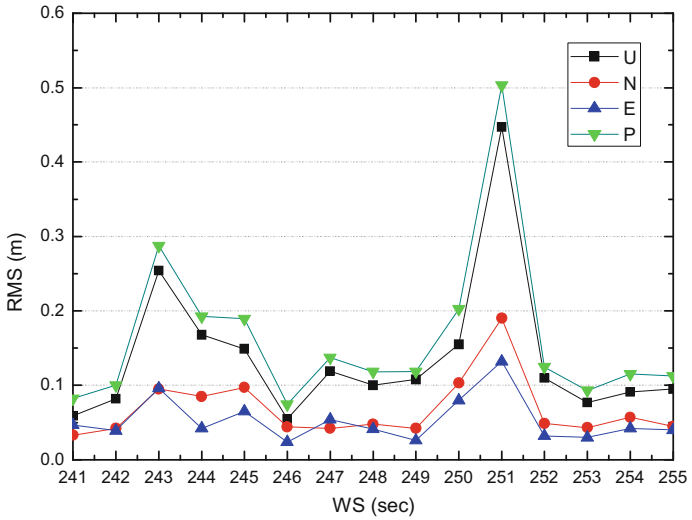

Fig. 17 PFRR daily PPP positioning accuracy

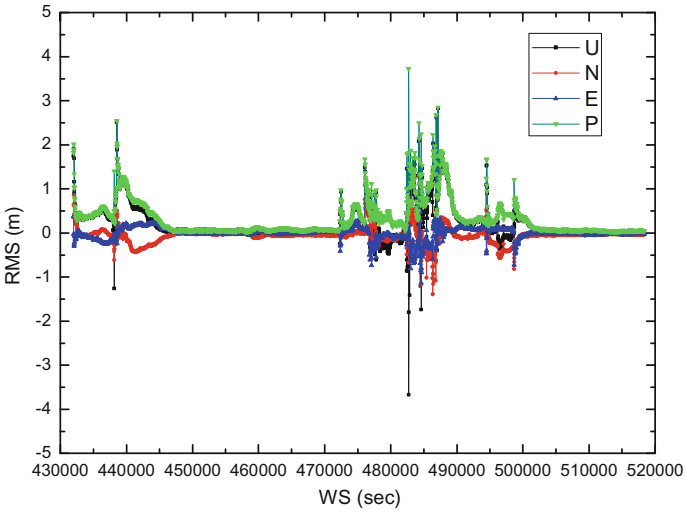

Fig. 18 PFRR PPP positioning accuracy on DOY 251

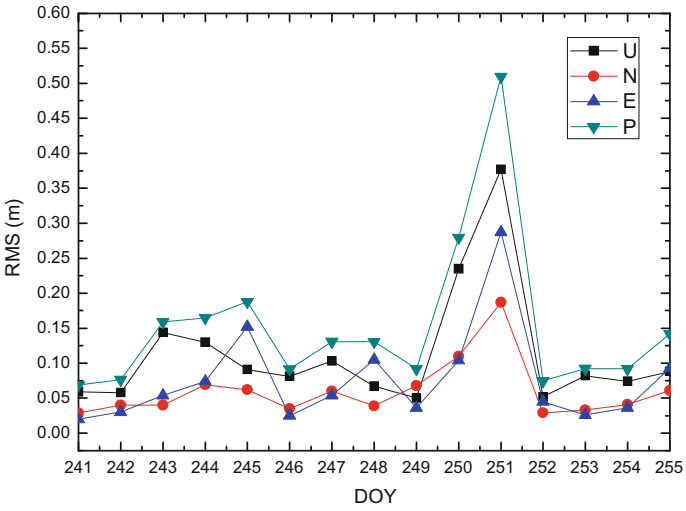

Fig. 19 KIRU daily PPP positioning accuracy

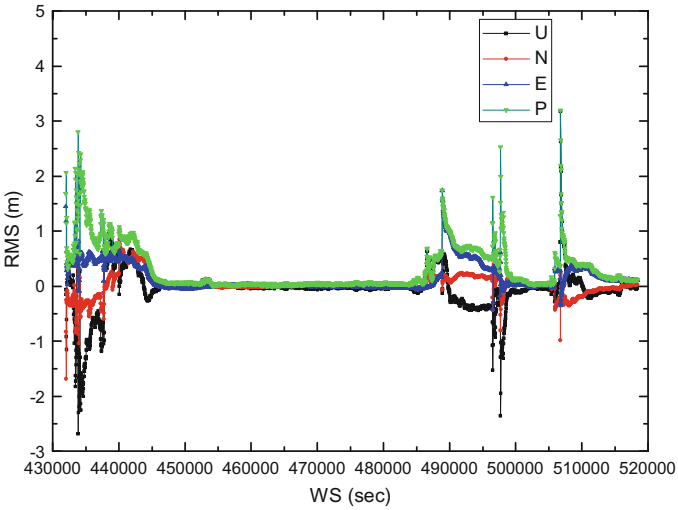

Fig. 20 KIRU PPP positioning accuracy on DOY 251

4 Conclusion

We summarize the main results of our investigation as follows:

- During the period of the intense geomagnetic storm since late September 6, 2017, the indexes, including Ap, Kp, Dst and ROTI all show an intense Geomagnetic storm.
- To investigate the effect of the X9.3 solar flare on the GNSS signal,we assess the GNSS broadcast ephemeris using the GBM final product as reference, and also use the cycle slips statistics to demonstrate the phase observations quality. The results show that the X9.3 solar flare has an insignificant impact on the broadcast ephemeris, since the SISRE statistics behave similarly with other days. On the other hand, cycle slip number has a significant increase during the intense Geomagnetic storm.
- The Multi-GNSS combined kinematic PPP solution of 60 IGS stations is used to evaluate the GNSS positioning performance during the solar flare. 8 of the stations located in low and high latitude show significant accuracy degradation, especially on vertical component. The period of accuracy decrease is highly correlated with the period of the solar flare, and is attributed to the cycle slips surge. The solar storm makes the kinematic PPP solution extremely unreliable.

References

1. Mansoori AA Purohit PK (2017) Effect of ionospheric irregularities on GPS signals during declining phase of solar cycle 23 at Bhopal. J Phys Conf Ser 836:012043
2. Wanner B (2015) Effect on WAAS from Iono Activity on March 17–18. WAAS Technical Report William J. Hughes Technical Center Atlantic City International Airport, NJ March 19, 2015
3. Kintner PM, Ledvina BM, de Paula ER, Kantor IJ (2004) Size, shape, orientation, speed, and duration of GPS equatorial anomaly scintillations. Radio Science 39:2004. https://doi.org/10.1029/2003RS002878
4. Dymond KF (2012) Global observations of L band scintillation at solar minimum made by COSMIC. Radio Science, 47, https://doi.org/10.1029/2011rs004931
5. A White Paper SBAS Ionospheric Working Group November (2010) Effect of Ionospheric Scintillations on GNSS
6. Jakowski J et al (2012) Monitoring, tracking and forecasting ionospheric perturbations using GNSS techniques. Space Weather Space Clim 2:2012. https://doi.org/10.1051/swsc/20120222012
7. Sun Erupts With Significant Flare, Sept. 11, 2017, https://www.nasa.gov
8. Rangarajan GK, Iyemori T (1997) Time variations of geomagnetic activity indices Kp and Ap: an update. Ann Geophys 15:1271–1290
9. Cherniak I, Zakharenkova I (2017) New advantages of the combined GPS and GLONASS observations for high-latitude ionospheric irregularities monitoring: case study of June 2015 geomagnetic storm. Earth Planets Space 69:66. https://doi.org/10.1186/s40623-017-0652-0
10. Miyake W, Jin H (2009) Derivation of near real-time TEC for monitoring ionospheric disturbances. J Natl Inst Inf Commun Technol 56(1–4):377–389
11. Cherniak I (2015) Dynamics of the high-latitude ionospheric irregularities during the 17 March 2015 St. Patrick's Day storm: Ground-based GPS measurements, Space Weather, 13 (9), September 2015 Pages 585–597
12. Cherniak L, Krankowski A, Zakharenkova I (2017) ROTI Maps: a new IGS's ionospheric product characterizing the ionospheric irregularities occurrence. IGS Workshop 2017
13. Montenbruck O, Hauschild A, Steigenberger P, Hugentobler U, Teunissen P, Nakamura S et al (2013) Initial assessment of the COMPASS/Beidou-2 regional navigation satellite system. GPS Solution 17(2):211–222
14. Blewitt G (1990) An automatic editing algorithm for GPS data. Geophys Res Lett 17(3):199–202
15. Li Xingxing, Zhang Xiaohong, Guo Fei (2013) Predicting atmospheric delays for rapid ambiguity resolution in precise point positioning. Adv Space Res 54(2014):840–850

BeiDou Reliable Integer Ambiguity Resolution in the Presence of Time-Correlated Obversion Errors

Zeyu Xin, Liang Li, Chun Jia, Hui Li and Lin Zhao

Abstract Time to first fix of ambiguity is always finished by using multiple sequential epochs in real-time kinematic (RTK). Among different epochs, the residual observation errors exist the time correlation each other, which increases with the increase of distance of baseline. However, the characteristics of time correlation is always neglected by traditional RTK stochastic model to limit the performance of ambiguity resolution. In this paper, the characteristics of time correction among different epochs with BeiDou observations are analyzed. The magnitudes of the time correction from GEO satellites of BeiDou show larger than the MEO and IGSO satellites of BeiDou and all MEO satellites of GPS. Therefore, in this paper, the characteristics of time correction are modeled by using first-order Gaussian Markov processing to further adjust the RTK stochastic model. The proposed method is tested by a Monte-Carlo simulation and actual BeiDou observations. The simulated test shows that the proposed method can get more real probability of correct fix, compared with the model neglecting the characteristics of time correction. The actual test show that the proposed method deceases the probability of false alarm and missed detection by 50 and 15%, respectively, compared with the model neglecting the characteristics of time correction. As a result, the proposed method achieves the optimal ambiguity resolution performance taking the probability of success, false alarm and missed detection into account, simultaneously.

Keywords BeiDou satellite navigation system · Time correlation
Stochastic model · Multiple epochs · Monte carlo

1 Introduction

Integrity ambiguity resolution is one of significantly point of carrier phase based difference technique for achieving centimeter level positioning. The stochastic model of BeiDou satellite navigation system is one of the main factor that restricts

Z. Xin · L. Li (✉) · C. Jia · H. Li · L. Zhao
College of Automation, Harbin Engineering University, Harbin 150001, China
e-mail: liliang@hrbeu.edu.cn

J. Sun et al. (eds.), *China Satellite Navigation Conference (CSNC) 2018 Proceedings*, Lecture Notes in Electrical Engineering 498,
https://doi.org/10.1007/978-981-13-0014-1_47

the ambiguity resolution efficiency. By accurately describing the stochastic model, the ambiguity can be calculated more correctly to achieve high-precision positioning results [1]. The observational error of BeiDou can be roughly divided into two variables, slow variables including atmospheric delay and multipath effects [2]. Normally, slow variables cause a strong charismatics of temporal correlation. Under the condition of long baseline, slow variables cannot be eliminated by double difference. As a result, there will be a temporal-related characteristic of double-difference observations among epochs, which will cause adverse effects [1, 3]. In order to describe precisely stochastic model, not only the stochastic characteristics of various types of errors need to be described accurately, but also the impact of various types of error-time related characteristics of the system should be considered.

Precisely stochastic model is the precondition for realizing the high precision positioning. In recent studies, Euler and Goad proposes weighted model based on satellite elevation angles and obtains significant effects in practical applications. However, they don't consider the correlation of among satellite observations. Anangaza [4] applies variance component estimation to Global Positioning System (GPS) network data processing to get a stable adjustment results. Howind [5] and EI-Rabbany [6] consider the influence of time correlation on the baseline accuracy and prove that the time correlation has less effect on the coordinate results.

In the process of applying dynamic Kalman filtering of GPS, Yang Yuanxi [7] estimates variance and covariance matrix based on historical information and new information on real-time, which makes the filtering not only make full use of the historical information but also express the current information as much as possible. Li Bofeng [8], under the condition of short baselines, analyzes the Beidou and GPS stochastic characteristics and concludes that there are varying degrees of correlation between accuracy and elevation angle on Beidou and GPS. Through the above analysis, the time correlation will affect the accuracy of the ambiguity assessment, then affecting the validation of the ambiguity resolution. Therefore, the time-dependent stochastic model is important for improving reliability of ambiguity resolution.

In this paper, we use Beidou data of short-baseline to analyze time correlation. on this basis, simulation and time-related stochastic model is studied and discussed.

2 Zero Baseline Single Difference Observation Model

The test uses zero baseline single-difference observations, ignoring the effects of atmospheric delays and multipath errors. The single-difference observation equation is:

$$\nabla P_L^s = \nabla \rho^s + \nabla \delta t_L + \nabla \delta t_{0,L} - \lambda \nabla N_L^s + \nabla \varepsilon_L^s \tag{1}$$

$$\nabla P_P^s = \nabla \rho^s + \nabla \delta t_P + \nabla \delta t_{0,P} + \nabla \varepsilon_P^s \tag{2}$$

where ∇ is a single difference operator, and ∇P_L^s and ∇P_P^s are single-difference carrier observations and single-difference pseudo range observations, and $\nabla \rho^s$ is the single difference guard distance. $\nabla \delta t_L, \nabla \delta t_P, \nabla \delta t_{0,L}, \nabla \delta t_{0,P}, \nabla \varepsilon_L^s, \nabla \varepsilon_P^s$ respectively are single-difference carrier receiver clock error, single-difference pseudo range receiver clock error, the receiver hardware delay and observation noise. ∇N_L^s are single-difference integer ambiguities, $\boldsymbol{\lambda}$ is the carrier phase wavelength, and $\boldsymbol{s}$ is the satellite number.

In order to introduce the whole-week characteristic of double-difference ambiguity, the reference satellite number is set as $\boldsymbol{r}$, and the above equation can be written as:

$$\begin{aligned} \nabla P_L^s &= \nabla \rho^s + \nabla \delta t_L + \nabla \delta t_{0,L} - \lambda\left(\nabla N_L^s - \nabla N_L^r + \nabla N_L^r\right) + \nabla \varepsilon_L^s \\ &= \nabla \rho^s + \nabla \delta_L - \lambda \Delta N_L^{sr} + \nabla \varepsilon_L^s \end{aligned} \tag{3}$$

In Eq. (3), the constant items are combined into one item that is the phase equivalent clock error $\nabla \delta_L = \nabla \delta t_L + \nabla \delta t_{0,L} - \lambda \nabla N_L^r . \lambda \Delta N_L^{sr}$ is double-difference integer ambiguity. Receiver clock error and the receiver hardware delay in the single difference pseudorange observation equation are combined into:

$$\nabla P_P^s = \nabla \rho^s + \nabla \delta_P + \nabla \varepsilon_P^s \tag{4}$$

With the known observations, baseline and double-difference ambiguity plugged into (1, 2), the single difference observation equation is:

$$\nabla \tilde{P}_L^s = \lambda \nabla \phi_L^s - \nabla \rho^s + \lambda \Delta N_L^{sr} = \nabla \delta_L + \nabla \varepsilon_L^s \tag{5}$$

$$\nabla \tilde{P}_P^s = \nabla P_P^s - \nabla \rho^s = \nabla \delta_P + \nabla \varepsilon_P^s \tag{6}$$

Assuming that the number of public satellites in the base station mobile station is m at this moment, the single-epoch pseudo range observation equation can be written as:

$$\nabla \tilde{\boldsymbol{P}}_P = \boldsymbol{e}_m \nabla \delta_P + \nabla \boldsymbol{\varepsilon}_P \tag{7}$$

In the formula, observation vector $\nabla \tilde{\boldsymbol{P}}_P = \left(\nabla \tilde{P}_P^{s1} \nabla \tilde{P}_P^{s2} \ldots \nabla \tilde{P}_P^{sm}\right)^T, m \times 1$ dimension matrix $\boldsymbol{e}_m = \begin{pmatrix} 1 & \cdots & 1 \end{pmatrix}^T$, noise vector $\nabla \boldsymbol{\varepsilon}_P = \left(\nabla \varepsilon_P^{s1} \nabla \varepsilon_P^{s2} \ldots \nabla \varepsilon_P^{sm}\right)^T$, superscript $\boldsymbol{s}$ corresponds to satellite number. The carrier phase observation equation can be similarly introduced.

Assuming that the observations of m satellites completely satisfy the stochastic distribution at this moment, the common constant term $\nabla \delta_P = \boldsymbol{e}_m \boldsymbol{e}_m^T \nabla \tilde{\boldsymbol{P}}_P / m$ can be calculated by solving the expectation, so that the residual vector v of single-epoch single-difference pseudo-range observations can be calculated as follows:

$$\boldsymbol{v} = \nabla\tilde{\boldsymbol{P}}_P - \boldsymbol{e}_m\boldsymbol{e}_m^T\nabla\tilde{\boldsymbol{P}}_P/m \tag{8}$$

Due to the fixed ambiguity parameter, the carrier phase observation equation is similar to the pseudo range observation equation, so the residual vector of single difference carrier phase can be calculated.

3 Time Correlation

3.1 Time Correlation Estimation

The time correlation coefficient ρ is defined as:

$$\rho_\tau = \rho_{ij} = \rho_{ji} \quad ,\tau = |i-j| \quad , \quad (i,j = 1,2,\ldots,n) \tag{9}$$

where i, j are the number of epoch, and τ is the epoch interval.

The formula for deriving the correlation coefficient of available time is:

$$\rho_\tau = \frac{1}{2(n-\tau)}\sum_{i=1}^{n-\tau}\frac{\boldsymbol{v}_i^T\boldsymbol{v}_{i+\tau}}{\sqrt{r_i r_{i+\tau}}\sigma_{P,i}\sigma_{P,i+\tau}} \quad , \quad 1 \le \tau \le n-1 \tag{10}$$

where $\boldsymbol{v} = \nabla\tilde{\boldsymbol{P}}_{P,i} - \boldsymbol{e}_m\boldsymbol{e}_m^T\nabla\tilde{\boldsymbol{P}}_{P,i}/m$ is the residual of the ith epoch single-difference pseudo range observation; $\sigma_{P,i}$ and $\sigma_{P,i+\tau}$ are respectively the mean-squared error of the pseudorange observations for the epoch i and $i+\tau$ ephemeris; the corresponding pseudorange observations of the epoch i and $i+\tau$ are r_i and $r_{i+\tau}$, r_i=$r_{i+\tau} = m-1$. Similarly, the carrier phase time correlation coefficient can be obtained.

3.2 Multiple Epoch-Time Related Stochastic Models

According to the known time-dependent characteristics, the multi-epoch, single-difference time-related covariance matrix is constructed as follows:

$$\mathrm{cov}\begin{bmatrix}\nabla\widetilde{\boldsymbol{P}}_{P,1}\\ \nabla\widetilde{\boldsymbol{P}}_{P,2}\\ \cdots\\ \nabla\widetilde{\boldsymbol{P}}_{P,n}\end{bmatrix} = \begin{bmatrix}\sigma^2_{\nabla P,1}\boldsymbol{I}_m & \rho_{12}\sigma_{\nabla P,1}\sigma_{\nabla P,2}\boldsymbol{I}_m & \cdots & \rho_{1n}\sigma_{\nabla P,1}\sigma_{\nabla P,n}\boldsymbol{I}_m\\ \rho_{21}\sigma_{\nabla P,2}\sigma_{\nabla P,1}\boldsymbol{I}_m & \sigma^2_{\nabla P,2}\boldsymbol{I}_m & \cdots & \rho_{2n}\sigma_{\nabla P,2}\sigma_{\nabla P,n}\boldsymbol{I}_m\\ \cdots & \cdots & \cdots & \cdots\\ \rho_{n1}\sigma_{\nabla P,n}\sigma_{\nabla P,1}\boldsymbol{I}_m & \rho_{n2}\sigma_{\nabla P,n}\sigma_{\nabla P,2}\boldsymbol{I}_m & \cdots & \sigma^2_{\nabla P,n}\boldsymbol{I}_m\end{bmatrix} \tag{11}$$

The time correlation coefficient is defined as:

$$\rho_\tau = \frac{1}{2(n-\tau)} \sum_{i=1}^{n-\tau} \frac{\boldsymbol{v}_i^T \boldsymbol{v}_{i+\tau}}{\sqrt{r_i r_{i+\tau}} \sigma_{P,i} \sigma_{P,i+\tau}} \quad , \quad 1 \le \tau \le n-1 \tag{12}$$

4 Experimental Results and Analysis

4.1 Time Correlation

In this paper, the data measured by the Observatory of Curtin University in Australia on January 28th, 2016 is used. The sampling rate is 30 s, and the cut-off height angle is 10°. The time correlations for the baseline of zero, baseline of 4.27 m and baseline of 8.42 m, are extracted respectively, and calculate the auto-correlation coefficient based on the time-related consideration method mentioned above.

Figure 1 shows that the time correlation of zero baseline is very weak. The reason is that the inter station error is strongly correlated. The observed noise after single difference is a white noise without time correlation.

As the baseline increases, the residual error of the observed noise increases, and the observed noise contains colored noise terms [9, 10], making it time-related. Figure 2 shows the time correlation coefficient of 4.27 m baseline extraction. It can be clearly seen that the autocorrelation coefficient decays gradually until zero as the time interval increases. It is verified that there is a temporal correlation in the observed data. The autocorrelation coefficient of the 8.42 m baseline in Fig. 3 also confirms the existence of time correlation.

In addition, data of 7.98 m baseline is used to analyze the time correlation of GPS and BDS. It can be seen from the comparison of Figs. 4 and 5 that the time correlation of BDS is stronger than that of GPS system. The specific reason can be analyzed from Figs. 6 and 7. From Fig. 7, it can be seen that the correlation between the time correlation of IGSO and MEO satellites in BDS is approximate to the GPS time. From Fig. 6, it can be concluded that the GEO satellites in BDS is

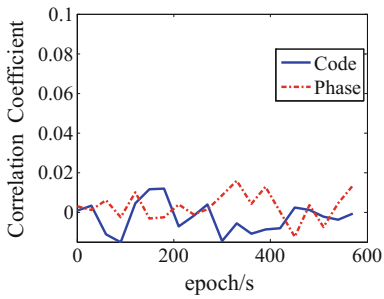

Fig. 1 Zero baseline time correlation coefficient

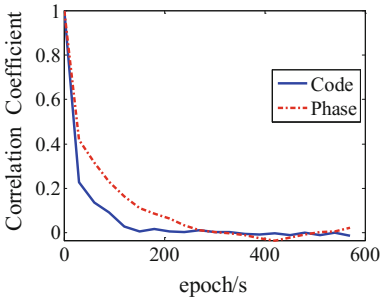

Fig. 2 4.27 m baseline time correlation coefficient

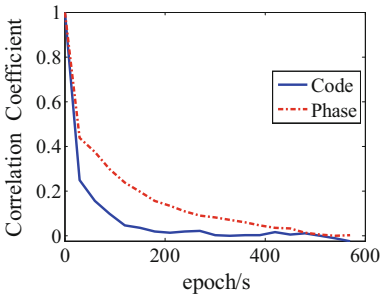

Fig. 3 8.42 m baseline time correlation coefficient

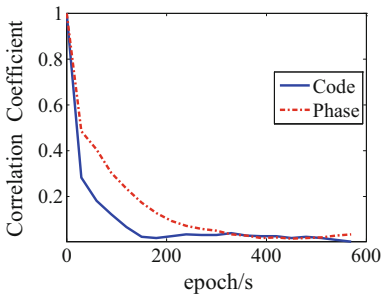

Fig. 4 GPS 7.98 m baseline time correlation coefficient

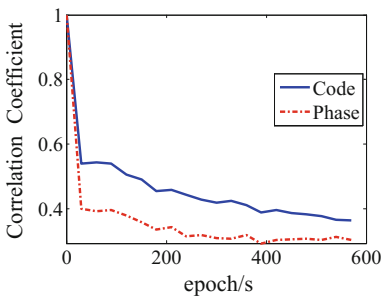

Fig. 5 BDS 7.98 m baseline time correlation coefficient

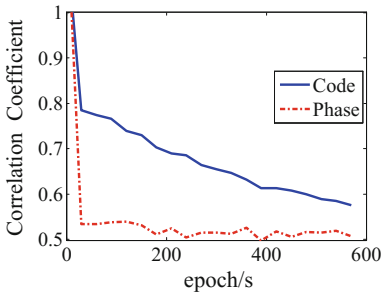

Fig. 6 BDS GEO time correlation coefficient

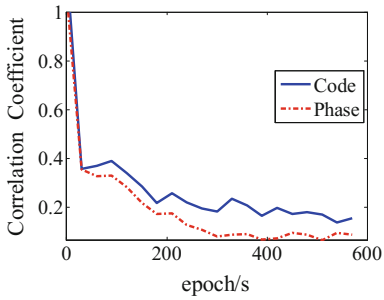

Fig. 7 BDS no-GEO time correlation coefficient

the reason why the time correlation of BDS is stronger than that of GPS. For GEO is a geostationary satellite, the change in relative ground position is smaller, so the time correlation of GEO is stronger than that of MEO and that of IGSO.

4.2 Simulation

4.2.1 Time-Related Simulation

A total of 7 different scenarios are evaluated. The scheme ignores the effects of the atmosphere and these scenarios may be useless for all base stations except for very short baselines, but they are able to independently research on multi-path standard deviation and time-dependent effects. Scenario A is the basic case and Scenarios B to E independently consider the changes of each of the four multipath parameters.

According to Kyle [11], we consider the time-dependent error as a first-order Gaussian Markov model [1, 12]:

$$\rho_\tau = e^{-\frac{\nabla t}{T}} \quad , \quad (\tau = 1, 2, \ldots, n-1) \tag{13}$$

where the interval ∇t between the epochs in the data is known, and in the covariance matrix only T and σ are unknown. At this moment, the time-related covariance matrix can be written as:

$$\boldsymbol{Q}_T = \begin{bmatrix} \sigma^2 \boldsymbol{I}_m & \rho_1 \sigma^2 \boldsymbol{I}_m & \cdots & \rho_{n-1} \sigma^2 \boldsymbol{I}_m \\ \rho_1 \sigma^2 \boldsymbol{I}_m & \sigma^2 \boldsymbol{I}_m & \cdots & \rho_{n-2} \sigma^2 \boldsymbol{I}_m \\ \cdots & \cdots & \cdots & \cdots \\ \rho_{n-1} \sigma^2 \boldsymbol{I}_m & \rho_{n-2} \sigma^2 \boldsymbol{I}_m & \cdots & \sigma^2 \boldsymbol{I}_m \end{bmatrix} \tag{14}$$

On the basis of the zero-time data with very weak time correlation, the time-related simulation is performed on the stochastic model. Also, the single-difference measurement noise term is suppose to be 0.3 m for pseudo ranges and 1 mm for phases. In each case, the state covariance matrix for each epoch is calculated using the previously mentioned multi-epoch accumulations. This is achieved by applying the LAMBDA algorithm to decorrelate the ambiguity state [13]. During the process, submatrices corresponding to the state of the ambiguity are extracted from the global state covariance matrix to determine the PCF for each epoch (Table 1).

Basic scenario: scenario A

The results from this scene will be used to compare with all other scenes to determine the effect of changing each different simulation parameter.

Deviations: Cases B and C

Schemes B deals with the effects of tripling the pseudo range and schemes C tripling the carrier phase multipath standard deviation. It can be seen from Fig. 8 that increasing the pseudo range multipath standard deviation has a smaller effect on the correct correction probability, whereas multiplying the carrier phase multipath by a factor of three greatly affects the PIF. The reason is that the estimated variance of the ambiguity state mainly depends on the phase observations, and code multipath only affects the position solution and is mostly average over time.

Programs D and E.

The scheme D and E increase the correlation time of the pseudo range or carrier phase by three times respectively. As can be obtained from Fig. 9, the increase of pseudo range multipath correlation time has little effect on PIF. However, the effect is seen with an increase in relative phase multipath. Again, the dependence on phase

Table 1 The standard deviation of each scene multipath and related time settings

	Code Multipath		Phase Multipath	
Scenario	σ(m)	T(s)	σ(m)	T(s)
A	0.3	40	0.01	40
B	0.9	40	0.01	40
C	0.3	40	0.03	40
D	0.3	120	0.01	40
E	0.3	40	0.01	120
F	0.3	120	0.01	120
G	0.9	40	0.03	40

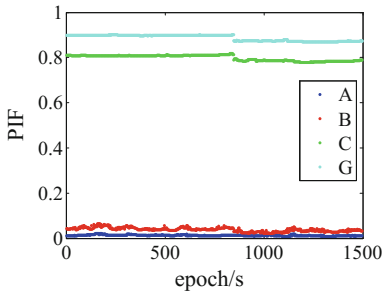

Fig. 8 Scenarios A, B, C, G PIF

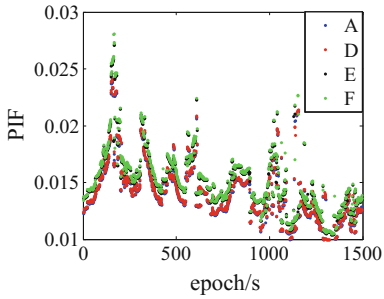

Fig. 9 Scenarios A, D, E, F PIF

multipath can be explained by the fact that phase observations more directly affect the ambiguity state than code observations. However, it can be seen in the case of increasing carrier phase multipath correlation time. That the carrier phase has more direct influence on the fuzzy state than the pseudo range.

Increase the relevant time: Scene F

As shown in Fig. 9, increasing both the pseudo range and carrier phase correlation time results in a result similar to that obtained by adding only the phase-dependent time in scheme E.

Increase multipath standard deviation: Case G

Much of the results obtained by increasing the standard deviation of pseudo range and carrier phase multipath follow the results obtained when the standard deviation of multipaths for carrier phase increases, and the small part is affected by the standard deviation of pseudo range multipath. The reason is simple, and the probability of correction depends on the variance of the estimated ambiguity, which in turn depends mainly on the quality of the phase observations.

4.2.2 Monte Carlo Simulation

In order to verify the effect of the time-related stochastic model, the following simulation will be used to compare and analyze. Firstly, with the Monte Carlo algorithm, the ambiguity of single epoch is fixed for 100 thousand times to

determine the success real value of the ambiguity, then the ambiguities of the traditional stochastic model and time-related stochastic model are fixed. Finally, the results of ambiguity resolution of the above three ways are comparatively analyzed.

As can be seen from Fig. 10, with the existence of time correlation, if the stochastic model does not consider the time-related part of the data, the lower limit of the success rate of ambiguity resolution will be overly optimistic.

However, if the stochastic model takes the time correlation into consideration, the lower limit of the success rate of ambiguity resolution obtained by the LAMBDA algorithm will match the success rate of ambiguity resolution produced by the Monte Carlo method. From Figs. 11 and 12, we can see that the phenomenon above will become more and more obvious with the increase of the time-related parameters [11].

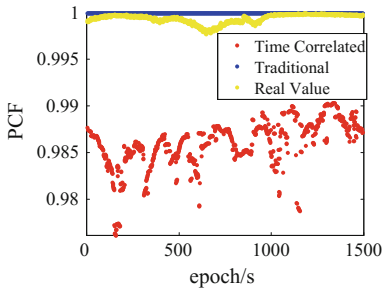

Fig. 10 Scenarios A PCF

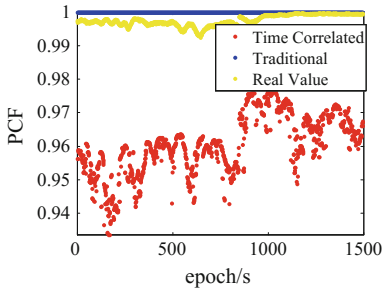

Fig. 11 Scenarios B PCF

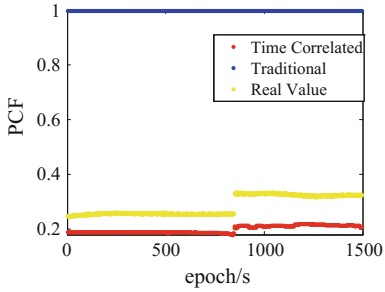

Fig. 12 Scenarios C PCF

4.3 The Actual Data Validation

According to the time-related characteristics mentioned before, the corresponding parameters are substituted into the model to obtain the location results of the traditional stochastic model and the time-related stochastic model.

The following indicators are introduced to analyze the effect of ambiguity resolution.

Ambiguity correct number of epochs divided the number of all epochs is the success rate of ambiguity resolution:

$$P_C = n_{corr}/n_{total} \times 100\% \tag{15}$$

The success rate of ambiguity resolution which passes Ratio test:

$$P_S = n_{pass}/n_{total} \times 100\% \tag{16}$$

The miss rate, the rate of fixing ambiguity unsuccessfully and passing Ratio test:

$$P_{\mathrm{I}} = n_{pass}^{\mathrm{I}}/n_{pass} \times 100\% \tag{17}$$

The false alarm rate, the rate of fixing ambiguity successfully and failing Ratio test:

$$P_{\Pi} = n_{pass}^{\Pi}/n_{corr} \times 100\% \tag{18}$$

where, $n_{pass}, n_{corr}, n_{pass}^{\mathrm{I}}, n_{pass}^{\Pi}, n_{total}$ respectively, are the number of epochs when the ambiguity passes the test, the number of epochs when the ambiguity is fixed successfully, the number of epochs when the ambiguity passes the test and is fixed unsuccessfully, the number of epochs when the ambiguity fails the test and is fixed successfully and the number of all epochs.

Table 2 shows the comparison between the traditional stochastic model and the time-related stochastic model for solving the ambiguity effect. The second column of the table shows the success rate of the correct ambiguity resolution from which it can be seen that the time-related stochastic model can improve the success rate of ambiguity solution. With the Ratio test and different thresholds of the test, the success rate of the ambiguity resolution of the time-related stochastic model is higher than that of the traditional model, which indicates that the using of the time-related stochastic model increases the success rate of ambiguity resolution and system continuity. In addition, the false alarm rate and miss detection rate of the time-related stochastic model are both less than those of the traditional model, which shows that the time-related stochastic model can reduce the miss detection and the false alarm and ensure the reliability of the system results. From the 8.42 m baseline data, it is showed that the miss detection rate is always lower than 50% of the traditional stochastic model, which is important in the ambiguity resolution. The increase of the miss detection rate will make the wrong ambiguity pass the Ratio

Table 2 Analysis of ambiguity resolution in stochastic model with time correlation

Random model	P_C	Category	Ratio test result				
			C < 1/3	C < 1/2.5	C < 1/2	C < 1/1.7	C < 1/1.5
Traditional model	99.44	P_S	92.38	94.57	96.59	97.60	98.33
	–	P_I	0	0	0.036	0.0713	0.141
	–	P_{Π}	7.098	4.895	2.902	1.923	1.259
Timerelated model	99.51	P_S	93.50	95.83	97.36	97.98	98.50
	–	P_I	0	0	0	0.0355	0.0706
	–	P_{Π}	6.045	3.704	2.166	1.572	1.083

indicator test. Using the wrong ambiguity will result in incorrect positioning results, and this is supposed to be avoided.

The table shows that with the Ratio test threshold loosening, the success rate of ambiguity resolution increases, but the miss detection rate also increases. However, the missed detection rate of the traditional stochastic model is so large that the fuzzy success rate of the stochastic model is higher than the true value, which verifies the result of the simulation. As to the time-related stochastic model, its success rate of ambiguity resolution is higher, and its false alarm rate and missed detection rate are lower. Compared to the traditional model, the time-related stochastic model reaches a better balance between the missed detection rate and the false alarm rate.

We usually use three Ratio test thresholds, and they are 1, 1/2, 1/3. When the threshold value is 1, all the ambiguity resolution can pass the test, and then if this error is smaller than 0.1 m, the ambiguity will be fixed successfully. Then, the success rate of true ambiguity resolution can be calculated. The table shows that the time-correlated random model can improve the success rate of ambiguity resolution, caused by the more exact description of the error. When the threshold is 1/2, the traditional stochastic model begins to miss detection, while the time-related stochastic model can still keep the undetected rate being 0. Besides, the success rate of ambiguity resolution and the false alarm rate are better than the traditional model. When the threshold is 1/3, the strict threshold test makes the missing detection rate of both models become zero, but with the time-related stochastic model, the success rate of ambiguity resolution is higher and the false alarm rate is lower.

5 Conclusion

In this paper, we mainly study the influence of time correlation on ambiguity resolution and construct a time-related stochastic model by analyzing the time-related characteristics of observations. We compare the effect traditional stochastic model and time-related stochastic model on ambiguity resolution by simulation. Finally, the following conclusions are obtained from several experiments:

(1) The time correlation among epochs using Beidou observations is more obvious than that of GPS, especially the geostationary characteristics of GEO satellites.
(2) The time-related enhancement will reduce the success rate of ambiguity resolution, and the success rate of ambiguity resolution without considering the temporal correlation will excess optimistic which causes missing detection of ambiguity resolution.
(3) The time-related stochastic model can improve the success rate of ambiguity resolution, while the miss detection rate and the false alarm rate are reduced by 50% and 15% respectively compared with the traditional model, and can achieve a better performance in terms of the ambiguity resolution success rate, miss detection rate and error rate.

Acknowledgements This research was jointly funded by National Natural Science Foundation of China (Nos. 61773132, 61633008, 61374007, 61304235), the Fundamental Research Funds for Central Universities (No. HEUCFP201768), and the Post-Doctoral Scientific Research Foundation, Heilongjiang Province (No. LBH-Q15033).

References

1. Yi-He L, Yun-Zhong S (2011) Effect of time correlation of gps observations on baseline solution. J Wuhan Uni (Info Sci Edn) 04:427–430
2. Wang Q (2007) Preliminary study on GPS time correlation. Modern Commerce and Industry, 024
3. Sheng Z, Liang W, Zhao-liang D (2010) Research on pseudorange smoothing technology of GNSS receiver. J Radio Eng 04:32–34
4. Ananga N, Coleman R, Rizos C (1994) Variance-covariance estimation of GPS networks. J Geodesy 68(2):77–87
5. Howind J, Kutterer H, Heck B (1999) Impact of temporal correlations on GPS-derived relative point positions. J Geodesy 73:246–258
6. El-Rabbany AE (1994) The effect of physical correlation on the ambiguity resolution and accuracy estimation in GPS differential positioning. Ph.D. thesis, Department of Geodesy and Geomatics Engineering, University of New Brunswick, Fredericton
7. Yuan-Xi Y, Tian-he X (2003) Adaptive filtering based on covariance and variance components estimation of mobile windowing. J Wuhan Uni Sci Edn 28(6):714–718
8. Bo-feng L, Yun-zhong S, Pei-liang X (2008) Stochastic model evaluation of different GPS receivers. Chin Sci Bull 53(16):1967–1972
9. Changsheng Z (2013) Kalman filtering under noise-related conditions. Proc Bull 1:14–15
10. Mei S, Yun Z (2003) Kalman filtering of correlated noise systems. Aerosp Meas Technol 23 (4):38–42
11. O'Keefe K, Petovello M, Lachapelle G et al (2006) Assessing probability of correct ambiguity resolution in the presence of time-correlated errors. Navigation 53(4):269–282
12. Haonan Z, Cuilin K, Wujiao D (2013) Application of Kalman filter considering colored noise in GPS high-frequency dynamic deformation monitoring. J Eng Investigation 04:50–54
13. Li L, Jia C, Zhao L et al (2016) Integrity monitoring-based ambiguity validation for triple-carrier ambiguity resolution. Gps Solutions 1–14

An Optimal Satellite Selection Model of Global Navigation Satellite System Based on Genetic Algorithm

Shuyue Zhu

Abstract With the increasing number of global navigation satellites and redundant information, the problem of the positioning accuracy and timeliness cannot be taken into account simultaneously has been raised. An optimal satellite selection model of global navigation satellite system based on genetic algorithm (GA) has been suggested. This algorithm is combined with the characteristic of geometric factor calculation model and GA. According to the users' requirement of positioning accuracy, the number of selected satellites is adjusted adaptively to ensure timeliness. The mutation crossover method is used to overcome the premature convergence of the satellite selection result caused by the intrinsic defect of GA. Experimental results show that the model can quickly select the satellite under the condition of the required positioning accuracy and improve the comfort of users.

Keywords Genetic algorithm · Geometric dilution precision · Mutation crossover Global navigation satellite system · Optimal satellite selection

1 Introduction

With the development of global navigation satellite system, the main global navigation and positioning system's number of satellites on orbit have been increased to over 100 by December 31st in 2016 according to the national union of concerned scientist website. Due to the large increase in the number of visible satellite, integrated satellite navigation system is obviously better than the single navigation system on accuracy, integrity, availability, et al. Integrated navigation is the trend of future navigation. The higher positioning accuracy and however, the larger redundancy will be simultaneously achieved by increasing the number of visible satellites. Positioning calculating volume of rapid growth improves the requirements of the receiver's load ability of data processor and processing speed. At the

S. Zhu (✉)
61920, troops, Chengdu 610000, China
e-mail: 744643443@qq.com

J. Sun et al. (eds.), *China Satellite Navigation Conference (CSNC) 2018 Proceedings*, Lecture Notes in Electrical Engineering 498,
https://doi.org/10.1007/978-981-13-0014-1_48

same time, the increase of positioning accuracy is getting smaller and smaller, which seriously affects the timeliness. Therefore, how to select suitable satellites to position is a hotspot in the navigation field.

In a single navigation system, the minimum GDOP method [1] or the maximum volume method [2] is usually used to select the optimal constellation to participate in the localization solution. Due to the ergodicity, the minimum GDOP method has large computation cost and poor timeliness. The computation of maximum volume method is increased with the number of visible satellites. It is difficult to achieve fast selection of satellites. The traditional integrated navigation selection algorithm also has a large amount of operations, which cannot meet the requirements of fast positioning. It is difficult to use traditional algorithm for combining navigation and selection of satellites. At present, for the problem of selecting satellites of integrated navigation system, some scholars have proposed a non-traditional algorithm-GA [3–6]. GA is a simulation of Darwin's genetic choice and a calculation model of natural selection of biological evolution process, which searching the optimal solution by simulating the natural evolution process. As a fast, simple and fault-tolerant algorithm, GA shows obvious advantages in the optimization of all kinds of structure objects. In recent 40 years, it has been widely applied in computer science, engineering, management science and social science and many other fields because it is simple, fast and robust. It has become one of the core technologies of intelligent computing in the 21st century.

In this paper, an improved adaptive GA is adopted to solve the contradiction between convergence speed and global convergence. The initial population can be better distributed in the solution space to accelerate the global convergence speed, improve the timeliness of data processing and reduce the navigation calculation.

2 The Point of Selecting Satellites

2.1 GDOP of Integrated Navigation

The size of DOP value is directly proportional to the error of the navigation positioning system. The positioning error and the lower the positioning accuracy increase with the DOP value.

Relationship between several precision factors is shown as follows:

$$HDOP^2 + VDOP^2 = PDOP^2$$
$$PDOP^2 + TDOP^2 = GDOP^2$$

where PDOP is the three-dimensional position dilution precision factor, TDOP is the clock error precision factor, HDOP is the horizontal component precision factor and VDOP is the vertical component precision factor.

GDOP directly reflects the geometric distribution relationship between the receiver and the visible satellite and it is an important index to measure the accuracy of satellite positioning. The smaller GDOP value is, the better geometric distribution and the higher positioning accuracy will be achieved. The threshold value of GDOP depends on the rigor of the positioning accuracy requirements under the environment. Generally, the threshold of GDOP is 2–6. The accuracy range of GDOP is defined as follows:

$$\begin{cases} 2 \le GDOP < 3 & \text{high accuracy} \\ 3 \le GDOP < 4 & \text{superior accuracy} \\ 4 \le GDOP < 6 & \text{general accuracy} \end{cases}$$

For a single navigation system, the GDOP value decreases monotonically with the increase of satellites numbers [7]. Assuming H is the navigation system observation matrix, GDOP is defined as:

$$GDOP = \sqrt{trace\left[(H^T H)^{-1}\right]}$$

The trace is the matrix trace. For a single navigation system, assuming that the number of visible satellites is n, so the H matrix is:

$$H = \begin{bmatrix} \alpha_1 & \beta_1 & \gamma_1 & 1 \\ \vdots & \vdots & \vdots & \vdots \\ \alpha_n & \beta_n & \gamma_n & 1 \end{bmatrix}$$

For the multi-star satellite navigation system, the time difference of the system should be considered. Taking COMPASS/GPS dual mode receiver as an example, the observation matrix needs to increase the inter-system clock, so at least 5 satellites need to be used to locate and service time. The measurement matrix can be expressed as:

$$H = \begin{bmatrix} \alpha_1 & \beta_1 & \gamma_1 & 1 & 0 \\ \vdots & \vdots & \vdots & \vdots & \vdots \\ \alpha_{n1} & \beta_{n1} & \gamma_{n1} & 1 & 0 \\ \alpha_{n1+1} & \beta_{n1+1} & \gamma_{n1+1} & 0 & 1 \\ \vdots & \vdots & \vdots & \vdots & \vdots \\ \alpha_n & \beta_n & \gamma_n & 0 & 1 \end{bmatrix}$$

where α_i,β_i and γ_i $(i = 1, 2, \ldots, n1, n1+1, \ldots, n)$ represent the direction cosine of the ith satellite, $n1$ represents the visible satellites' number of navigation system 1, $n - n1$ represents the visible satellites' number of navigation system 2. The GDOP of three satellite navigation systems or more satellite navigation systems can be on the analogy of this.

2.2 Number of Selected Satellites

Due to the sharp increase numbers of visible satellite in the integrated navigation system, the reasonable allocation is extremely important for the rapid selection of satellites. In order to effectively reduce the redundant information, the balance between positioning accuracy and navigation computation should be considered. Comprehensively determine the maximum satellites number should consider the total channel number of the receiver, the amount of locating computation and the need of fault detection. For dual constellation global positioning system, it is no more than 10 generally.

Using GA to select the satellites should configure the initial number of selected satellites to determine the initial population. For single navigation system, at least four stars are required to be located. For multi-navigation system, it should take the clock difference between the navigation systems into account. The initial selected satellite threshold is not less than the minimum satellites number. The computation costs and features of GA also should be considered.

3 Genetic Algorithm

GA is a random search algorithm which simulates biological natural selection and genetic mechanism. The basic idea is to simulate the evolution of the natural evolution phenomenon. The search space is the space of genetic mapping. Put the possible solution into a vector chromosome. Chromosome's each element is called genes. The optimal chromosome is selected and the optimal solution is obtained by continuously calculating the fitness of each chromosome.

3.1 Fitness Function

The adaptation degree of each individual to the environment is called fitness. The fitness function is the evaluation function that guides the search. The greater fitness function value is, the better quality of the solution will be achieved. In GA, the fitness is the main indicator of individual performance. The size of the fitness is used to preserve the good results and discard the bad ones. The selection of fitness function can directly affect the convergence speed of GA and whether or not to find the optimal solution.

According to the rule that the higher the fitness should be combined with the higher probability, the fitness function is chosen as the reciprocal of the GDOP in the selecting satellite problem.

The number of visible satellites is n and m satellites are to be selected to make the selection of its option optimal. The selected problem can be described as:

$$\begin{cases} f(X) = \frac{1}{GDOP(X)} \\ X = [x_1, x_2, \ldots, x_{n-1}, x_n] \\ s.t. \sum_{i=1}^{n} x_i = m \end{cases}$$

where X represents the selection of star plan. $x_i = 0 \, or \, 1$, $i = 1, 2, \ldots, n$.

3.2 Basic Operator

Every evolution in nature keeps excellent individual in population and eliminated unsatisfactory individuals. Continuously evolution makes the population become more outstanding. Genetic operators include selection, crossover and mutation.

The principle of selection operator is adaptable individual has the higher probability to contribute to the next generation with one or more offsprings. Namely the excellent individuals in a population genetic directly to the next generation or through matching cross to produce new individual genetic to future generations. The selection operation is based on the fitness assessment of the individual in the group. The commonly used selection operators have the fitness proportional method. The commonly used methods are fitness ratio method, stochastic universal sampling and local selection method. The roulette method is the simplest and most commonly used method and its selection probability and fitness value of each individual are proportional.

Crossover is the most important genetic manipulation in GA. The new generation of individuals can be obtained through crossover operation. Binary coded genetic exchange process is similar to the process of homologous chromosomal association process. Random put several genes in the same location of the exchange of coding to produce new individual. The commonly used methods include a single point of intersect, two-point crossover, uniform hybridization and shuffle hybridization, etc. In the literature [4], only 1 or 0 genes are used to achieve cross-operation to produce the original offspring. The legalization of future generations is realized by means of variation.

Gene mutation is one of chromosome changes in gene loci, which makes a gene into its alleles and usually has a certain phenotype change. It provides chances for the emergence of new individual. The genetic manipulation of binary coding is very similar to that of biology and the “0” or “1” on the gene string has a certain chance of becoming the opposite of “1” or “0”. Genetic mutations occur randomly and the general mutation frequency is low. In the literature [5], through the selection process of chromosome selection through crossover and mutation, the selection of the GA can easily get into the disadvantage of local optimality.

3.3 Algorithm Process

Basic steps of GA:

Step1: encoding

The common coding methods of GA include binary coding, floating-point coding and symbolic coding. According to the properties of the satellite question, setting each satellite as a gene by binary coding. All visible satellites in order to row. The first one means no. 1 satellite. 1 gene means satellite visible. 0 gene means satellite is not visible. When selecting the satellite, 1 and 0 are used to indicate the selection of the satellite. 1 gene indicates that the satellite was selected and the 0 gene indicates that the satellite was not selected.

Step2: generating the initial population

The initial population of the selected satellites scheme consisting of an initial selection of stars is constructed. The initial population size is N. Randomly generated initial population $S = \{s_1, s_2, \ldots, s_N\}$, from $U = C_n^{m_0}.T = 1$.

Step3: solving the adaptive value of the selected star schemes in the population

According to the rule that the higher the fitness should be combined with the higher probability, the fitness function is chosen as the reciprocal of the GDOP in the selecting satellite problem:

$$f(s_i) = \frac{1}{GDOP_i}$$

where s_i represents the satellite option. $i = 1, 2, \ldots, N$.

Step4: judgment

If the conditions of termination are met, choosing the maximum fitness of the individual as the result and the algorithm ends. If not satisfied, the algorism enters the next step.

The termination conditions of the algorithm are:

1. The predetermined evolutionary algebra $T_{\max}$ is completed.
2. The optimal individual continuous generation of the population did not have an evolutionary or average fitness continuous generation.
3. The optimal value is less than the specified threshold.

Step5: choosing

Using roulette betting selection method, an individual fitness is selected. And the probability of selection is:

$$P_i = \frac{f(s_i)}{\sum_{i=1}^{N} f(s_i)}$$

Select one of the selected individuals at random as P_i, copy the chromosomes and then make a new population S_1.

Step6: crossover

Using the reshuffle, crossover rate is randomly selected to participate as P_c in the cross on the number of chromosomes as a midpoint gene switch points. Exchange parts of a gene between paired chromosomes. Replace the original chromosome with the resulting new chromosome S_2.

Step7: variation

According to the mutation rate P_m, select chromosome randomly and reverse the original gene value of the mutation. Replace the original chromosome with the resulting new chromosome. Replace the group as a new generation S_3. $T = T + 1$. Then move to step 3.

Step8: output

The algorithm satisfies the termination conditions. Output the optimal chromosome in the population.

3.4 Algorithm Improvement

In order to solve the contradiction between convergence speed and global convergence, an improved adaptive GA is adopted. The threshold switch is introduced in the selection of the population to increase the diversity of the population, so that the initial population can better spread in the solution space and speed up the global convergence.

The crossover probability P_c and mutation probability P_m of GA are adaptive adjusted. The following adaptive genetic rules should be followed in the operation:

1. When the individual fitness of the population tends to be consistent, P_c and P_m increases.
2. When the group fitness is more diffuse, P_c and P_m decreases.
3. For individuals with high fitness, reduce P_c and P_m to protect their entry into the next generation.
4. Conversely, for individuals with low fitness, P_c and P_m should increase.

The improved algorithm flow chart is shown in Fig. 1.

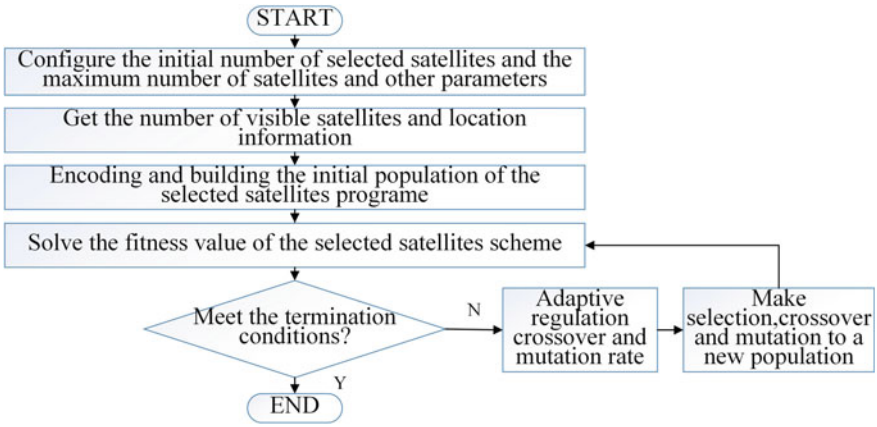

Fig. 1 Improved genetic algorithm selection of satellite flow chart

4 Experimental Verification and Analysis

4.1 The Experimental Environment

Considering that the GPS is the most perfect global navigation system and the binary navigation and positioning system has certain universality and applicability, GPS and COMPASS navigation system are used to experiment.

Currently, the COMPASS system operates a constellation of 15 satellites, which includes six GEO satellites, six IGSO satellites and three MEO satellites. The GPS constellation is designed to be 24 satellites. The actual constellation contains 32 satellites, all of which are MEO satellites.

4.2 Determination of Genetic Algorithm Parameters

The selection parameters of GA include the number of initial selected satellites m_0, the maximum number of satellites $m_{\max}$, population size N, crossover probability P_c, variation probability P_m, genetic algebra k, and maximum evolutionary algebra $T_{\max}$ and so on. At present, the parameter selection method is not yet clear in GA. Usually within a certain scope, the quality of the convergence of reconciliation is distinguished through numerous experiments and the suitable parameter values are chosen. The range of the normal population size, cross probability, variation probability and algebra is 20–100, 0.4–0.99, 0.001–0.01 and usually 100–500, respectively.

In the case of a COMPASS/GPS dual mode receiver, the receiver can receive up to 18 COMPASS satellites and 16 GPS satellites at the same time. The time period of data analysis is 08:00 on November 16th in 2017 to 08:00 on November 17th in

2017. The sampling interval is 60. The satellite shielding angle is 5 degrees. Statistical analysis shows that the mean number of stars is 20.

According to the conventional value range of each parameter of GA and the characteristics of the selected star, the control variable method is adopted to select the GA parameters applicable to this situation after repeated experiments. The number of initial selected stars, the most general election star, the population size N, the genetic algebra k and the maximum evolution algebra is 6, 10, 20, 5 and 20, respectively.

The crossover probability and mutation probability were increased when $4 \leq GDOP < 6$. The crossover probability and mutation probability were reduced when $2 \leq GDOP < 3$, as follows:

$$\begin{cases} \mathrm{P}_c = \mathrm{P}_c + 0.1 & \text{when} 4 \leq GDOP < 6 \\ \mathrm{P}_m = \mathrm{P}_m + 0.001 & \text{when} 4 \leq GDOP < 6 \\ \mathrm{P}_c = \mathrm{P}_c - 0.1 & \text{when} 2 \leq GDOP < 3 \\ \mathrm{P}_m = \mathrm{P}_m - 0.001 & \text{when} 2 \leq GDOP < 3 \\ s.t. \quad 0.4 \leq P_c \leq 0.8, 0.001 \leq P_m \leq 0.01 \end{cases}$$

4.3 Experimental Verification and Analysis

The average satellite number of the constellation was 20 and the number of satellite constellation was 7 during 24 h. The starry sky comparison chart of the star constellation was shown in Fig. 2:

The traditional selection algorithm, traditional GA and improved GA are compared. The experiment results are shown as follows:

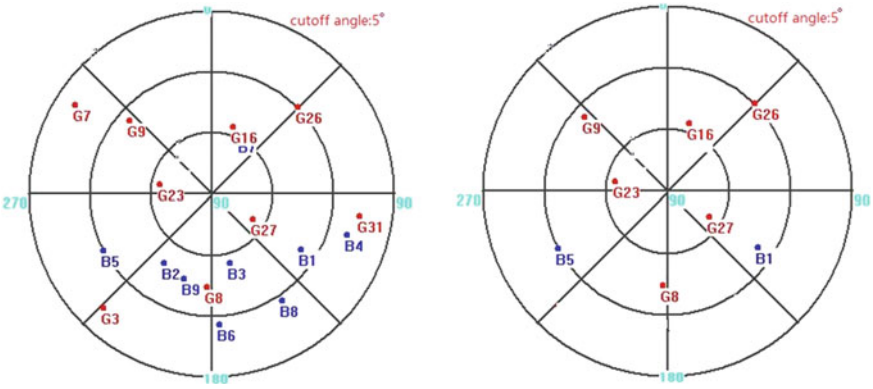

Fig. 2 Satellite comparison chart before and after selection

Table 1 Analysis of GDOP after selecting of different algorithms

GDOP after satellite selection				
	Min	Max	Mean	Variance
Traditional algorithm	2.5	6.0	4.6	0.766
Traditional GA	2.0	4.9	3.3	0.372
Improved GA	2.0	4.2	3.0	0.317

Table 2 Analysis of time after selecting of different algorithms

Time consuming				
	Min	Max	Mean	Variance
Traditional algorithm	0.031	0.044	0.037	2.2885e-5
Traditional GA	0.023	0.032	0.028	9.1342e-6
Improved GA	0.018	0.025	0.021	5.3067e-6

The statistical results of Tables 1 and 2 can be obtained as follows:

1. Compared with the traditional algorithm, the GA chooses fewer satellites, but the positioning accuracy is not reduced and the time efficiency is enhanced.
2. Compared with the traditional GA, the improved GA converges faster.
3. The improved GA can select the optimal scheme more quickly.

5 Conclusions

A new algorithm based on GA is proposed. In this paper, the key points of the selected star problem of the combined navigation system are analysed detailedly. The algorithm process is given and the GA is improved and the configuration of GA parameters is determined. The experiment results show that the improved GA overcomes the disadvantages of the traditional method. At the same time, the satellite number can be adaptively adjusted according to actual situation. It is more intelligent and has a faster convergence rate compared with the traditional genetic selection algorithm.

References

1. Bai Y, Chen Dong (2006) Calculation of the geometrical precision factor of satellite navigation and selecting satellite method. Navigation 42(3):88–94
2. Kaplan ED, Hegarty CJ (2007) GPS principles and applications, Kou yanhong translation Version 2. Beijing, Electronic Industry Press, China, pp 240–268
3. Huo Y, Zhang X (2015) A rapid selection of satellite navigation system. J Beijing Uni Aeronautics and Astron 02

4. Chen C, Zhu H, Zhan J, Wu J, Sun J (2015) A new crossover operator of genetic algorithm and its application in the selection of GNSS constellation. Comput Measur Contr, 23(10)
5. Song D, Xu C, Hu C, Zhang P (2015) A multi-satellite selection method based on genetic algorithm. J. Aerospace 03
6. Ying S, Li J, Liu W, Qiu L (2013) Selecting satellite algorithm and positioning analysis of BD-2/GPS integrated navigation system. J Shanghai Maritime Uni 06
7. Sairo H, Akopian D, Takala J (2003) Weighted dilution of precision as quality measure in satellite positioning. IEEE Rader Sonar Nav 150(6):430–436

BDS Cycle Slips Detection and Repair Based on Compressive Sensing

Dengao Li, Zhiying Ma, Wenjing Li, Jumin Zhao and Zheng Wei

Abstract In case of obstacle or low signal to noise ratio, the satellite signal will lose lock, which will occur cycle slips and affect the accuracy of navigation and positioning. To solve this problem, this paper proposes a method of cycle slips detection and repair for INS aided BDS based on compressive sensing from the perspective of Bayesian statistics. In our algorithm, the Kalman filter is used to establish a tightly combined positioning model of BDS and INS. Meanwhile, a sparse cycle slips detection model based on compressive sensing is constructed, and according to the statistical test method to determine whether the cycle slips are generated. After analysing, under the framework of Bayesian learning, we introduce the hierarchical priori in the relation vector machine of machine learning theory and transform the reconstruction of the cycle slips into the reconstruction of the hyperparameters, which is obtained by an iterative generalized maximum expectation algorithm to estimate the hyperparameters, as a result, the cycle slips repair are realized. In this paper, the cycle slips detection error rate is considered as the performance index of the algorithm. The experimental results show that the proposed algorithm can effectively reduce the error rate of BDS cycle slips detection and improve the positioning accuracy.

Keywords Bayesian compressive sensing · Statistical test · Kalman filter
Cycle slips · BDS/INS

1 Introduction

At present, carrier phase positioning is widely used in high precision positioning service, including navigation of aircraft and land vehicles. However, when carrier phase is used as a location measurement, carrier phase fault detection must be performed prior to positioning. Cycle slip detection is one of the important problems

D. Li (✉) · Z. Ma · W. Li · J. Zhao · Z. Wei
College of Information Engineering, Taiyuan University of Technology, Jinzhong, China
e-mail: lidengao@tyut.edu.cn

J. Sun et al. (eds.), *China Satellite Navigation Conference (CSNC) 2018 Proceedings*, Lecture Notes in Electrical Engineering 498,
https://doi.org/10.1007/978-981-13-0014-1_49

that need to be overcome in BDS carrier phase positioning system. Because of the weak carrier phase signal or other interference, the cycle slips occur frequently.

The algorithms of cycle slips detection and repair have been researched and developed for decades. The combination of code and carrier phase residuals, ionospheric Doppler integral and carrier phase time difference method has been used to detect cycle slips [10]; Bisnath et al. proposed carrier phase measurements based on L1 and L2 to detect cycle slip [5]; Banville et al. proposed the algorithm of cycle slip detection, which is not affected by the high ionospheric activity [1]. In Ref. [13], a set of adaptive threshold model is constructed to improve the performance of cycle slips detection for the TurboEdit method. However, these algorithms have a high cost and no cost effectiveness. In addition, due to the low data rate of BDS receiver, Doppler integration and carrier phase time difference method also have a limited cycle slip detection accuracy in dynamic environment [2]. Since BDS satellite signals are easily influenced by external factors such as geographical environment and noise, the error will not accumulate over time, while INS will not be affected by geographical environment. In order to overcome these limitations, INS can be combined with BDS to detect cycle slip. Altmayer et al. used the GPS/ INS integrated system to detect and repair the cycle slips. The distance between the satellite and the current position of the INS is equivalent to the measured carrier phase, and the cycle slip is detected by comparing the carrier phase obtained with the GPS receiver [7]. An effective adaptive GPS/ INS fusion method is presented in [4]. Younsil et al. [12] proposed a carrier phase cycle slips detection method based on satellite geometry for inertial-aided GPS, and the covariance is used to calculate the threshold for the occurrence of a cycle slip from the GPS/INS filter. What's more, the algorithm mentioned above does not consider the effect of noise on cycle slip detection. Up to now, the research on the detection and repair of cycle slips by combining BDS and INS systems is relatively few, which is worth further exploration.

Aiming at the influence of observation noise on BDS cycle slips detection and repair, a method of cycle slips detection and repair based on Bayesian compressive sensing is proposed in this paper for INS-aided BDS. On the basis of the complementary combination of BDS and INS, the undetermined equation about cycle slip is obtained after the epoch and station difference of carrier phase observations. The cycle slips are first detected by statistical test, then the method of Bayesian compression sensing is used to repair cycle slips. The flow chart of this algorithm is shown in Fig. 1.

2 Integrated Positioning Model of BDS and INS

Inertial kinetic model is derived from the INS error model based on angle ψ [6].

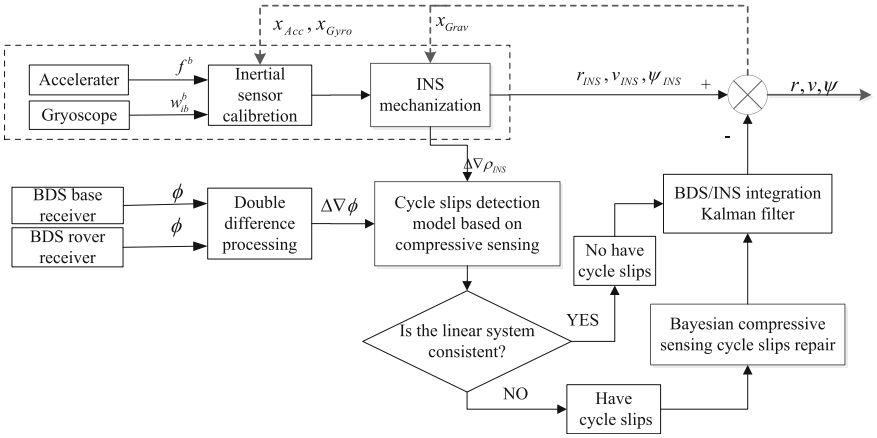

Fig. 1 Cycle slips detection and repair of BDS/INS tightly integrated based on Bayesian compressive sensing

$$\begin{cases} \delta\dot{r} = -w_{en} \times \delta r + \delta v \\ \delta\dot{v} = -(2w_{ie} + w_{en}) \times \delta v - \delta\psi \times f + \delta g + \nabla \\ \delta\dot{\psi} = -(w_{ie} + w_{en}) \times \delta\psi + \varepsilon \end{cases} \tag{1}$$

where $\delta r, \delta v$ and $\delta\psi$ represent the position, velocity, and attitude error vectors, respectively. w_{ie} denotes the rate of earth with respect to an inertial frame, w_{en} denotes the rate of navigation frame with respect to earth, f is the specific force vector δg is the gravity uncertainty error vector, ∇ and ε are the accelerometer error and gyro error vectors, respectively.

In this paper, Kalman filtering is used to integrate BDS and INS in a tightly integrated manner. In order to describe the errors and corrections of the integrated navigation more accurately, the established navigation system model adopts the state parameters of 27 dimensions, including 9 navigation parameter errors, 12 inertial sensor error states, namely three biases and three scale factors for accelerometer and gyroscope, respectively, three gravity uncertainty errors, and three lever arm errors [8]. The complete error states can be written as:

$$\begin{aligned} x_{Nav} &= [\delta r_N, \delta r_E, \delta r_D, \delta v_N, \delta v_E, \delta v_D, \delta\psi_N, \delta\psi_E, \delta\psi_D]^T \\ x_{Acc} &= \left[\nabla_{bx}, \nabla_{by}, \nabla_{bz}, \nabla_{fx}, \nabla_{fy}, \nabla_{fz}\right]^T \\ x_{Gyr} &= \left[\varepsilon_{bx}, \varepsilon_{by}, \varepsilon_{bz}, \varepsilon_{fx}, \varepsilon_{fy}, \varepsilon_{fz}\right]^T \\ x_{Gra} &= [\delta g_N, \delta g_E, \delta g_D]^T \\ x_{Ant} &= \left[\delta L_{bx}, \delta L_{by}, \delta L_{bz}\right]^T \end{aligned} \tag{2}$$

Inertial sensor errors are expressed as first-order Gaussian-Markov processes. The system error equation of state is (3)

$$\dot{X}_{k+1} = F_k X_k + G_k W_k \tag{3}$$

where X is the system error state vector, F is the system state transition matrix, G is the system dynamic noise matrix, and W is the Gauss white noise vector with mean zero. The observation equation of the system is expressed as:

$$Z = HX + e = \nabla\Delta\phi - \lambda^{-1} \cdot \nabla\Delta\rho \tag{4}$$

$$H = [A_{M\times 3} C_n^e \quad 0_{M\times 21} \quad A_{M\times 3} C_b^e] \tag{5}$$

where Z denotes the between-epoch between-receivers differences of carrier phase residuals, e is the observation noise vector, $\Delta\nabla\rho$ is the double-difference distance between satellite and earth predicted by INS, A is the double difference observation design matrix, C_n^e is the rotation matrix of the navigation system to the earth system, and C_b^e is the rotation matrix of the system to the earth system; M is visible satellite number.

3 INS-Assisted BDS Cycle Slips Detection and Repair

3.1 Cycle Slips Detection Model Based on Compressive Sensing

For M observation satellites in the case of a short baseline, the BDS receiver phase observation equation after double difference, the carrier phase double difference residual components [9].

$$\nabla\Delta b_\phi = \lambda^{-1} E \cdot B \cdot \nabla\Delta dx + \lambda^{-1} E \cdot \nabla\Delta\delta t_u + \nabla\Delta N + \varepsilon_{\nabla\Delta\phi} \tag{6}$$

where $\nabla\Delta b_\phi$ denotes the M between-epoch between-receivers differences of carrier phase residuals, λ represents wavelength, E is the unit matrix of M dimensions, B is $M \times 3$ direction cosine matrix, $\nabla\Delta dx$ denotes the M between-epoch between-receiver increments of the corrections to the rover position, $\nabla\Delta\delta t_u$ denotes clock error of double difference receiver, $\nabla\Delta N$ denotes the cycle slip between the successive epochs,$\varepsilon_{\nabla\Delta\phi}$ denotes measurement noise.

$$\nabla\Delta b_\phi = \nabla\Delta\phi - \lambda^{-1} \cdot \nabla\Delta\rho = \begin{bmatrix} \nabla\Delta\phi_1 - \lambda^{-1} \cdot (\Delta\rho_{r1} - \Delta\rho_{b1}) \\ \nabla\Delta\phi_2 - \lambda^{-1} \cdot (\Delta\rho_{r2} - \Delta\rho_{b2}) \\ \vdots \\ \nabla\Delta\phi_M - \lambda^{-1} \cdot (\Delta\rho_{rM} - \Delta\rho_{bM}) \end{bmatrix} \tag{7}$$

where the subscript r stands for the rover, the subscript b stands for the base station. The geometric distance increment to the BDS satellite from the base station and the rover receiver are respectively expressed as:

$$\Delta\rho_b = \rho_b(t - \tilde{\tau}(t)) - \rho_b(t - 1 - \tilde{\tau}(t-1)) \tag{8}$$

$$\Delta\rho_r = \rho_r(t - \tilde{\tau}(t)) - \rho_r(t - 1 - \tilde{\tau}(t-1)) \tag{9}$$

where $\tilde{\tau}(t)$ is the signal travel time.

For Eq. (6), using notations

$$\begin{aligned} b &= \nabla\Delta b_\phi \in R^{M\times 1} \\ D &= \begin{bmatrix} \lambda^{-1} & \lambda^{-1}B \end{bmatrix} \in R^{M\times 4} \\ x &= \begin{bmatrix} \nabla\Delta\delta t_u & \nabla\Delta dx \end{bmatrix}^T = R^4 \\ \delta &= \nabla\Delta N \in R^{M\times 1} \\ \eta &= \varepsilon_{\nabla\Delta\phi} \in R^{M\times 1} \end{aligned} \tag{10}$$

So, we can present Eq. (6) in the form

$$b = Dx + \delta + \eta \tag{11}$$

suppose $\eta \sim n(0, \sigma)$, σ is of the order of a hundredth of a cycle.

Provided no cycle slips have occurred, note that between-epoch carrier phase increments for each satellite form the M-dimensional vector b, whereas the four-dimensional vector x, which varies arbitrarily, can form only a four-dimensional subspace in the M-dimensional space. In order to check if it is true, we must test the linear system for consistency, zero hypothesis is that $\delta = 0$ in the system (11).

$$b = Dx + \eta \tag{12}$$

Let $\hat{x}$ be the least squares solution to the system (12).

$$\hat{x} = \left(D^T D\right)^{-1} D^T b \tag{13}$$

$$r = b - D\hat{x} = \left(E_M - D\left(D^T D\right)^{-1} D^T\right) b \tag{14}$$

$$V = r^T F^{-1} r = \frac{1}{\sigma^2} r^T r \tag{15}$$

where r and V are the residual vector and weighted sum of squares, respectively. F is covariance matrix of measurement noise. If $\eta \sim n(0, \sigma)$, then the value (15) is distributed according to the χ^2 law with $M - 4$ degrees of freedom, we can say that the system (12) is consistent with accuracy σ. It also verifies the consistency of the linear system. If consistency of the system (12) is violated, then our assumption

about absence of cycle slips is not true, thus $\delta \neq 0$, if that happens, we decide that the presence of cycle slips has been detected.

Obviously, Eq. (11) belongs to the underdeveloped equations and can not be solved directly. However, the slips of integer ambiguity can be regarded as sparse. It is well known that compressive sensing is a kind of signal acquisition theory by refactoring, which is combined with sparse decomposition and optimization method. Therefore, it can obtain the position and size of the cycle slips from the undervaluation equation by using compressive sensing [11].

For Eq. (11), D has full rank. In order to solve the cycle slip δ, Consider the QR decomposition of the matrix D. where the matrix Q is orthogonal, the matrix U is upper-triangle, and the matrix O consists of zeros.

$$\begin{aligned} &QR = D, \quad Q \in R^{M \times M} \\ &Q^T = \begin{bmatrix} G \\ W \end{bmatrix}, \quad R = \begin{bmatrix} U \\ O \end{bmatrix} \end{aligned} \tag{16}$$

making $WD = 0$, we then apply W to both sides of the expression (12) resulting into equation

$$P = W\delta + \xi \tag{17}$$

where $P = Wb$, $\xi = W\eta$.

Based on compressive sensing theory, the vector δ itself is sparse, and the matrix W is both observation matrix and sensing matrix. If the arbitrary 2 K columns of the sensing matrix W are linearly independent, let the sparsity of the matrix δ is K $(K \ll M)$, the sparse vector δ can be uniquely reconstructed. It can be seen that the measurement matrix W is a standard orthogonal basis, and satisfies the linear independence condition, and the sparse vector δ can be uniquely reconstructed.

3.2 *Cycle Slips Repair Based on Bayesian Compressive Sensing*

Bayesian compressive sensing is from the perspective of Bayesian statistics to deduce the posterior distribution function of cycle slip under Bayesian framework, using the sparse prior and the measured values of the signal. In addition, the advantage is especially obvious in the noisy environment, which can basically eliminate the influence of noise on the reconstruction process [3].

Since the cycle slips δ has a sparse priori property, suppose the δ_s is equal to the K largest items in the cycle slips δ, the rest M–K items are 0; the δ_e is equal to the M–K minimum items in the cycle slips δ, and the rest K items are 0. Obviously $\delta = \delta_s + \delta_e$, so

$$P = W(\delta_s + \delta_e) + \xi = W\delta_s + \xi_e \tag{18}$$

According to the central limit theorem, ξ_e can be approximated as white noise with variance of σ^2. The Gauss likelihood function of formula (19) can be obtained by applying the theory of probability, so that the reconstruction of cycle slips δ are converted into Bayesian estimation based on compressive sensing.

$$p\left(P|\delta_s, \sigma^2\right) = \left(2\pi\sigma^2\right)^{-K/2} \cdot \exp\left(-\|P - W\delta_s\|^2/\left(2\sigma^2\right)\right) \tag{19}$$

In order to satisfy the Bayesian analysis, this paper introduces the hierarchical prior of the relevance vector machine in machine learning theory, and assumes that the cycle slips are the Gauss distribution with mean 0, and gives the variance of $\alpha = [\alpha_1, \alpha_2, \ldots \alpha_M]$

$$p(\delta_s|\alpha) = \prod_{i=1}^{M} N\left(\delta_{si}|0, \alpha_i^{-1}\right) \tag{20}$$

The noise variance $\alpha_0 = 1/\sigma^2$ can be obtained by the similar processing for noisy signals, so the reconstruction of the cycle slips δ are transformed into the reconstruction of the hyperparameters α and α_0, the posterior probability distribution of cycle slips δ can be obtained by using the Bayesian criterion:

$$\begin{aligned} p(\delta_s|P, \alpha, \alpha_0) &= p(P|\delta_s, \alpha_0)p(\delta_s|\alpha)/p(P|\alpha, \alpha_0) \\ &= (2\pi)^{\frac{M+1}{2}}|\Sigma|^{-\frac{1}{2}}\exp\left\{-\frac{1}{2}(\delta_s - u)^T(\Sigma)^{-1}(\delta_s - u)\right\} \end{aligned} \tag{21}$$

where u and Σ are mean and variance, respectively.

In the framework of support vector machine (SVM), the edge likelihood function of the superparametric α and α_0 is obtained by integrating the sparse cycle slips. In order to facilitate calculation, the logarithm of likelihood function is calculated:

$$\begin{aligned} L(\alpha, \alpha_0) &= \log\, p(P|\alpha, \alpha_0) \\ &= -\frac{1}{2}\left(K\, \log\, 2\pi + \log|U| + P^T U^{-1} P\right) \end{aligned} \tag{22}$$

where $U = \sigma^2 E + W\Lambda^{-1}W^T$, $\Lambda = diag(\alpha_1, \alpha_2, \ldots \alpha_M)$. The estimation of the super parameter is obtained by the iterative generalized maximum expectation algorithm, and then the cycle slips δ are estimated based on the posterior mean.

4 Measurement Analysis

In this experiment, the experimental data collected by two Trimble NetR9 BDS receivers in Yuci District, Jinzhong City, Shanxi Province was analyzed. The sampling interval was 1 s, the cut-off height angle was 15° and the observation time

was 5 min. The INS data acquisition used low-cost MEMS gyroscope inertial measurement unit, the sampling frequency of 100 Hz, but after testing zero bias, scaling factor and non-orthogonal degree are compensated. In the course of the experiment, 5 BDS satellites with PDOP value of 2.5–3 were selected.

Aiming at the effect of observation noise on cycle slips detection and repair, in order to verify the feasibility of the proposed method of cycle slips detection and repair based on Bayesian compressive sensing, amplitude of cycle slips from 1 to 5 is artificially added to the carrier phase observation of the rover receiver. In order to use more observation data, we use dual frequency carrier phase to detect and repair cycle slips. Consider the case where only one satellite adds the cycle slips, and then consider the situation where two satellites and multiple satellites simultaneously add cycle slips, as shown in Figs. 2 and 3. Taking cycle slips repair error rate as a measure of performance, the traditional base pursuit (BP), iterative hard thresholding (IHT), orthogonal matching pursuit (OMP), iterative re-weighted least squares (IRLS) and Bayesian compressed sensing (BCS) are compared. For the BDS system and the INS-aided BDS system, the cycle slips repair error rates of the five methods are corresponding to the (a) and the (b) in Fig. 4, respectively.

As the number of satellites with cycle slips increases, so does compression measurement noise. As can be clearly seen from Fig. 4a, b, BCS has a better performance of cycle slips repair than the other four methods despite the increasing compression noise. When two satellites occur cycle slips simultaneously, the repair error rates of the OMP and IHT start to increase dramatically. When the five satellites occur cycle slips simultaneously, the repair error rate is almost 100%, so the proposed Bayesian Compressive sensing can well detect and repair cycle slips, especially in the noisy case, showed an obvious advantage. The comparison between Fig. 4a and b shows that the repair error rate of cycle slips in INS-assisted BDS system is lower than that of BDS system, which shows the validity and feasibility of the detection and repair of cycle slips by INS-assisted BDS.

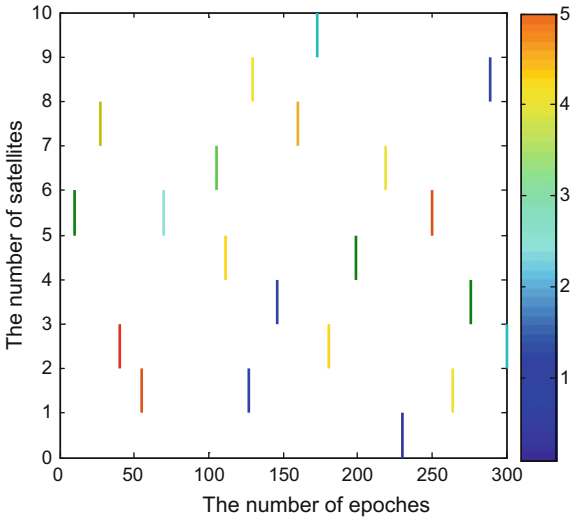

Fig. 2 A satellite adding cycle slips

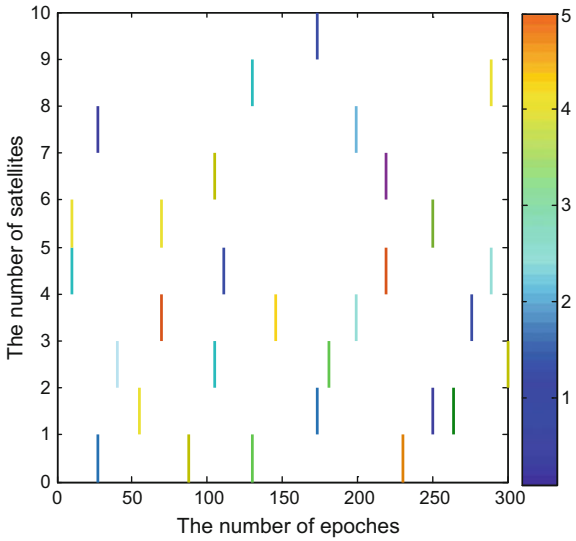

Fig. 3 Two satellites adding cycle slips

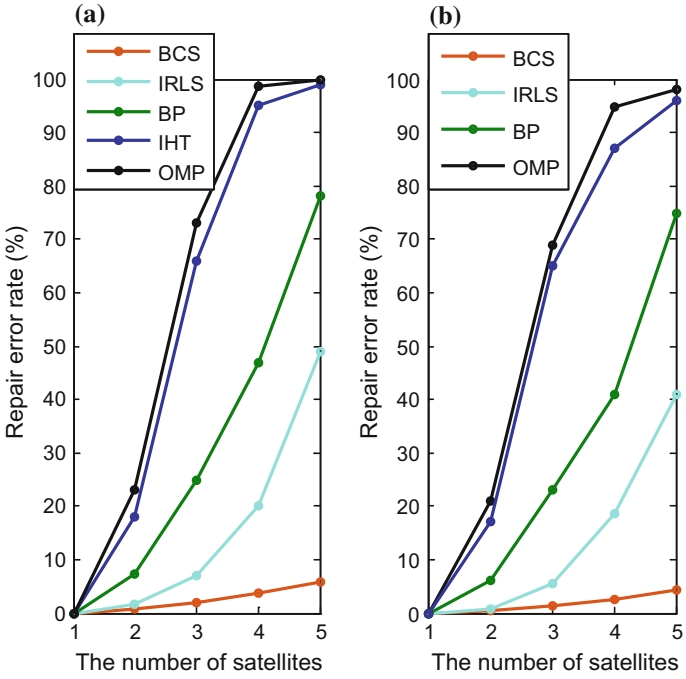

Fig. 4 Comparison of cycle slips repair error rate

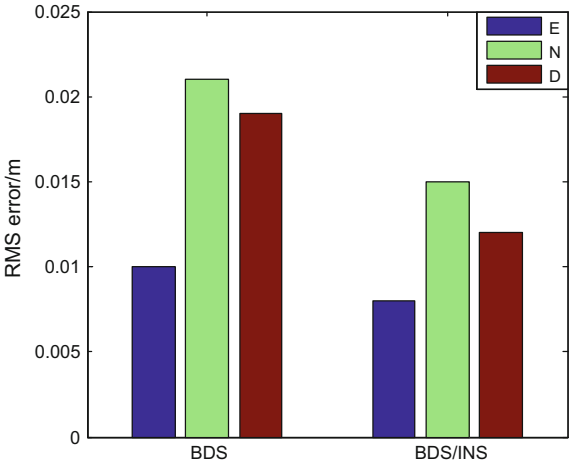

Fig. 5 Comparison of root mean square error

By using Bayesian compressive sensing to detect and repair BDS and BDS/INS cycle slips, navigation data are simply processed, and Fig. 5 is the RMS error of BDS and BDS/INS systems in three directions of E, N and D. The statistical results show that the RMS errors of BDS are 0.01, 0.021 and 0.019 m at E, N and D, respectively, and the RMS errors of BDS/INS at E, N and D are 0.008, 0.015, 0.012 m. Therefore it can be shown that INS-assisted BDS can improve navigation accuracy of BDS.

5 Conclusion

This paper presents an INS-assisted BDS cycle slips detection and repair method, focusing on the influence of observation noise on the detection and repair of BDS cycle slips. The Kalman filter is used to establish a tightly combined positioning model of BDS and INS. Then a sparse cycle slips detection model based on compressive sensing is constructed. Under the framework of Bayesian learning, we introduce the hierarchical priori in the relation vector machine of machine learning theory and transform the reconstruction of the cycle slips into the reconstruction of the hyperparameters. The estimation of the super parameter is obtained by the iterative generalized maximum expectation algorithm, and finally the cycle slips are repaired. The experimental results show that the Bayesian compressive sensing can well repair the INS-aided BDS cycle slips, and then improve the navigation and positioning accuracy of BDS.

Acknowledgements The study is supported by The National High Technology Research and Development Program ("863" Program) of China (2015AA016901): High linearity laser diode array and high saturation power photodiode array; The General Object of National Natural Science Foundation (61772358) Research on the key technology of BDS precision positioning in complex

landform; International Cooperation Project of Shanxi Province (Grant No. 201603D421012): Research on the key technology of GNSS area strengthen information extraction based on crowd sensing; The General Object of National Natural Science Foundation under Grants (61572347): Resource Optimization in Large-scale Mobile Crowdsensing: Theory and Technology.

References

1. Banville S, Langley RB (2013) Mitigating the impact of ionospheric cycle slips in GNSS observations. J Geodesy 87(2):179–193
2. Cederholm P, Plausinaitis D (2014) Cycle slip detection in single frequency GPS carrier phase observations using expected doppler shift. Nordic J Survey Real Estate Res 10(1)
3. Lacy MCD, Reguzzoni M, Sansò F et al (2008) The Bayesian detection of discontinuities in a polynomial regression and its application to the cycle-slip problem. J Geodesy 82(9):527–542
4. Lee JY, Kim HS, Choi KH et al (2016) Adaptive GPS/INS integration for relative navigation. GPS Solutions 20(1):63–75
5. Liu Z (2011) A new automated cycle slip detection and repair method for a single dual-frequency BDS receiver. J Geodesy 85(3):171–183
6. Moafipoor S, Grejner-Brzezinska DA, Toth CK (2004) Tightly coupled GPS/INS integration based on BDS carrier phase velocity update. Brzezinska 1094–1102
7. Shuang D, Yang G (2012) Inertial aided cycle slip detection and identification for integrated PPP GPS and INS. Sensors 12(11):14344–14362
8. Tan X, Wang J, Han H (2014) Improved neural network aided GPS/INS integrated navigation algorithm. J China Uni Mining Technol 43(3):526–533
9. Xie G (2009) GPS principle and receiver design. Electronic Industry Press
10. Xu G (2016) GPS: theory, algorithms, and applications. Springer Publishing Company, Incorporated, xiv, 209
11. Xu L, Liang Q (2010) Compressive sensing using singular value decomposition. In: International conference on wireless algorithms, systems, and applications. Springer-Verlag, 338–342
12. Younsil K, Junesol S, Changdon K et al (2015) GPS cycle slip detection considering satellite geometry based on TDCP/INS integrated navigation. Sensors 15(10):25336–25365
13. Zhang X, Qi Z, He J, Kang C (2017) Improving turboedit real-time cycle slip detection by the construction of threshold model. Geomatics Info Sci Wuhan Uni 42(3):285–292

Research on the Influence of Assigning Weight for BDS Satellites of Different Orbits on Baseline Processing and Software Designing

Yihao Tang, Jinsheng Zhang and Chenggang Li

Abstract GNSS relative positioning stochastic model reflects the noise level of observation data, in the process of baseline processing, reasonable stochastic model can improve the precision of calculating. Beidou navigation system (BDS) consists of three kinds of satellite: Geosynchronous Earth Orbit satellite (GEO), Medium Earth Orbit satellite (MEO) and Inclined Geosynchronous Satellite Orbit (IGSO). Due to the difference of orbits, it should be distinguished when select stochastic model for the three kinds of satellite. In this paper, the three kinds of satellite are assigned different weight based on posteriori root mean square error (RMS) of Beidou zero-difference phase observation combined with elevation angle stochastic model, and based on BDS baseline processing software, the conclusion is verified by experiment with 79.4 km baseline data of seven days. The experiment result shows that it can improve the precision and daily repeatability of BDS baseline result as the biggest, least and middle weight are assigned to IGSO, MEO and GEO respectively when processing data of BDS; the baseline result of BDS processed by the BDS baseline processing software are compared with baseline result of GPS processed by Bernese software, it shows that the difference of the two results is less than 1 cm in plane direction and less than 2.6 cm in up direction.

Keywords Weight of BDS satellite · Posteriori root mean square error
Elevation angle stochastic model · BDS baseline processing software

1 Introduction

China launched the 24th and 25th Beidou navigation satellite on November 6, 2017. BDS uses the structure of the mixed constellation, at present, there are 14 satellites can provide service, including: 5 GEO, 5 IGSO and 4 MEO satellites, but the navigation systems of other countries, such as: GPS, GLONASS, Galileo are

Y. Tang (✉) · J. Zhang · C. Li
Guangzhou Hi-Target Navigation Tech Co., Ltd., Guangzhou, China
e-mail: 13466278838@163.com

J. Sun et al. (eds.), *China Satellite Navigation Conference (CSNC) 2018 Proceedings*, Lecture Notes in Electrical Engineering 498,
https://doi.org/10.1007/978-981-13-0014-1_50

composed of MEO satellites. The orbit altitude of the three kinds of satellite of BDS is different, and the movement and the regression period are also different.

BDS and GPS satellite signal are code division multiple access mode, when processing relative positioning data, BDS and GPS have the same function model, and stochastic model is usually the elevation angle model or signal-to-noise ratio model. For BDS satellites, however, because of the difference of GEO, MEO and IGSO satellite orbits, the error effect on signal in the process of transmission will be different, it is not reasonable that the three kinds of satellite of BDS use the same stochastic model as GPS without distinction. Li Yan puts forward a method that iterative least squares (ILS) combines with minimum norm quadratic unbiased estimation (MINQUE) to estimate the observation variance components of BDS in real time, it can improve the precision 12.6 mm and stable performance 8.0 mm for BDS single epoch kinematic baseline result. But if the observation geometry information is not enough, the variance component estimation will be not convergent [1]. In this paper, the stochastic model that RMS of zero-difference phase observation of BDS combines with the elevation angle model is used for assigning weight for GEO, MEO and IGSO satellites and comparison experiment to research its effect on baseline result.

2 Weight of BDS GEO/MEO/IGSO

2.1 Characteristic of GEO/MEO/IGSO

GEO orbit altitude is 35,786 km, GEO satellites are distributed near the equator and move slowly relative to the land. Because of the high altitude of satellite orbit, the sunlight pressure has large effect on GEO satellites. In low latitude area, the correlation of received observation data from GEO satellite is strong, and it may generate morbid matrix when estimating parameters; in high latitude area, the observation angle from user to GEO satellite is small, it may lead to big observation error. In addition, the static characteristic may cause that it is difficult to calculate satellite clock error in GEO satellite orbit determination. Under the same condition, the ranging error introduced by ephemeris of GEO satellite is about twice of MEO satellite [2]. WeiPing Liu finds that GEO satellite orbit precision is obviously lower than IGSO satellite and MEO satellite in the experiment of BDS satellite precise orbit determination [3]. Relative to the static station, the geometry structure of GEO satellite is almost changeless, it causes that it is not sensitive to distinguish reflection and direct signal when the receiver receives them, that leads to obvious multipath effect [4, 5]. These reasons result that it is difficult to guarantee the precision of GEO satellite observation. In this paper, BDS satellite orbits are fitted by Bernese software with precise ephemeris of seven days, the precision of fitted orbits is listed in Table 1, and it can be found from the table that the error of GEO satellite is bigger than others.

Table 1 RMS (m) of orbits fitted by Bernese software with Beidou precise ephemeris

Date	C01	C02	C03	C04	C05	C06	C07	C08	C09	C10	C11	C12	C14
9-9	0.114	0.126	0.115	0.107	0.127	0.061	0.068	0.024	0.058	0.060	0.048	0.040	0.150
9-10	0.115	0.128	0.116	0.108	0.127	0.063	0.066	0.025	0.059	0.058	0.037	0.049	0.143
9-13	0.118	0.127	0.117	0.113	0.126	0.072	0.066	0.023	0.064	0.058	0.037	0.030	0.125
9-14	0.119	0.125	0.117	0.115	0.124	0.076	0.064	0.020	0.065	0.055	0.046	0.037	0.133
9-15	0.120	0.127	0.117	0.116	0.123	0.077	0.062	0.021	0.067	0.054	0.039	0.047	0.150
9-16	0.122	0.125	0.118	0.118	0.121	0.083	0.061	0.019	0.070	0.052	0.046	0.040	0.148

The orbit altitude of IGSO and GEO satellite is same, but movement track of IGSO satellite is "8" glyph that the equator is the axis of symmetry, and it can cover high latitude area and have good orbit stability [4]. IGSO satellite not only takes advantage of GEO that it is synchronous with earth and the coverage is fixed but also overcomes the defect that the elevation of GEO satellite is low in high latitude area. In addition, the precision of IGSO and MEO satellite orbit determination is almost same.

The regression period of MEO satellite is 7 days, it has wide coverage, its orbit altitude is 21,528 km and lower than that of GEO and IGSO. In addition, the proportion of low elevation angle observation of MEO satellite is larger, its pseudorange and carrier phase residual are generally larger than that of GEO and IGSO satellite [6].

2.2 Weight of GEO/MEO/IGSO

For short baseline, single-difference observation data between stations can eliminate the error of satellite, ionosphere and troposphere error, after deducting the receiver clock error, only the observation noise and multipath effect are left. Therefore, single-difference observation residual eventually is able to reflect the satellite observation noise level.

In the study of positioning performance of BDS, Yuanxi Yang has an experiment with single-difference static data of ultra-short baseline of eight days and uses the method of fixing known baseline to get the single-difference observation residual, then according to the law of error propagation, RMS of zero-difference phase observation is calculated (Table 2).

Table 2 RMS of zero-difference phase observation calculated by residual sequence of ultra-short baseline single-difference observation [5]

	BDS	B1 (mm)	B2 (mm)
GEO	C01	1.149	1.404
	C02	1.732	1.394
	C03	2.123	1.817
	C04	2.360	3.360
	C05	2.957	2.220
IGSO	C06	1.387	1.991
	C07	1.433	1.701
	C08	1.426	1.708
	C09	1.336	1.593
	C10	1.321	1.929
MEO	C11	2.377	2.744
	C12	2.165	3.209
	C13	2.341	2.903
	C14	2.343	2.759

Based on the research, the statistics precision of zero-difference phase observation of Beidou GEO/MEO/IGSO satellite is in Table 3.

In the experiment, it is found that Beidou GEO satellite carrier phase single-difference residual has daily periodical variation as it is affected by the multiple path effect. Due to the larger proportion of low elevation angle observation, the single-difference residual of MEO is bigger than which of GEO and IGSO satellite. The statistics of single-difference residual of IGSO is best as its proportion of low elevation angles is smaller [5].

In this experiment, weight is assigned to different types of satellite according to the method that RMS of zero-difference phase observation combines with the elevation angle model.

Elevation angle stochastic model is:

$$\omega(z) = \cos^2(z) \tag{1}$$

Set the weight of IGSO satellite as:

$$P_{IGSO} = 1 \cdot \omega(z) \tag{2}$$

Set the weight of GEO satellite as:

$$P_{GEO} = \frac{(RMS_{IGSO})^2}{(RMS_{GEO})^2} \cdot \omega(z) \approx 0.6 \cdot \omega(z) \tag{3}$$

Set the weight of MEO satellite as:

$$P_{MEO} = \frac{(RMS_{IGSO})^2}{(RMS_{MEO})^2} \cdot \omega(z) \approx 0.4 \cdot \omega(z) \tag{4}$$

'Z' represents the elevation angle of satellite.

Table 3 Zero-difference phase observation RMS of GEO/MEO/IGSO

Type of satellite	The RMS of phase observation (mm)
GEO	2.052
MEO	2.605
IGSO	1.5825

3 BDS Baseline Processing Software

3.1 Observation Model

The zero-difference phase observation equation can be represented as:

$$\begin{aligned}\lambda \cdot \varphi^s = \rho + c \cdot (\delta t_r - \delta t^s) - \lambda \cdot N + T + I + ant_r \\ + ant^s + rel + earth + M + \varepsilon\end{aligned} \tag{5}$$

In the equation, λ is wave length, φ^s is phase observation, c is speed of light, δt_r is receiver clock error, N is ambiguity, T is tropospheric delay parameter, I is ionosphere delay parameter, ant_r and ant^s are antenna phase center deviation of receiver and satellite, *rel* is relativistic effect, *earth* is Earth rotation correction term, M is multipath effect, ε is noise error. Besides, *ant* includes antenna phase center offset and antenna phase center variation, it can be corrected according to the calibration parameters in the antenna phase center correction file, *rel* and *earth* can be corrected according to correction model.

Single-difference phase observation equation between stations can be represented as:

$$\lambda \cdot \Delta\varphi^s = \Delta\rho + c \cdot \Delta\delta t_r - \lambda \cdot \Delta N + \Delta T + \Delta I + \Delta M + \Delta\varepsilon \tag{6}$$

Δ is single-difference item. The single-difference data between stations eliminates the satellite clock error. And then the double-difference phase observation equation can be represented as:

$$\lambda \cdot \nabla\Delta\varphi^s = \nabla\Delta\rho - \lambda \cdot \nabla\Delta N + \nabla\Delta T + \nabla\Delta I + \nabla\Delta M + \nabla\Delta\varepsilon \tag{7}$$

$\nabla\Delta$ is double-difference item. The double-difference data between satellites can eliminate the receiver clock error. For the short baseline, the effect of the double-difference troposphere and ionosphere delay can be ignored, but for long baseline, they need to be corrected by model and parameter estimation.

3.2 Development of BDS Baseline Processing Software

In this paper, the algorithm of processing BDS static data is researched, and the BDS baseline processing software is developed. The software interface is shown in Fig. 1 and processing flow diagram is in Fig. 2:

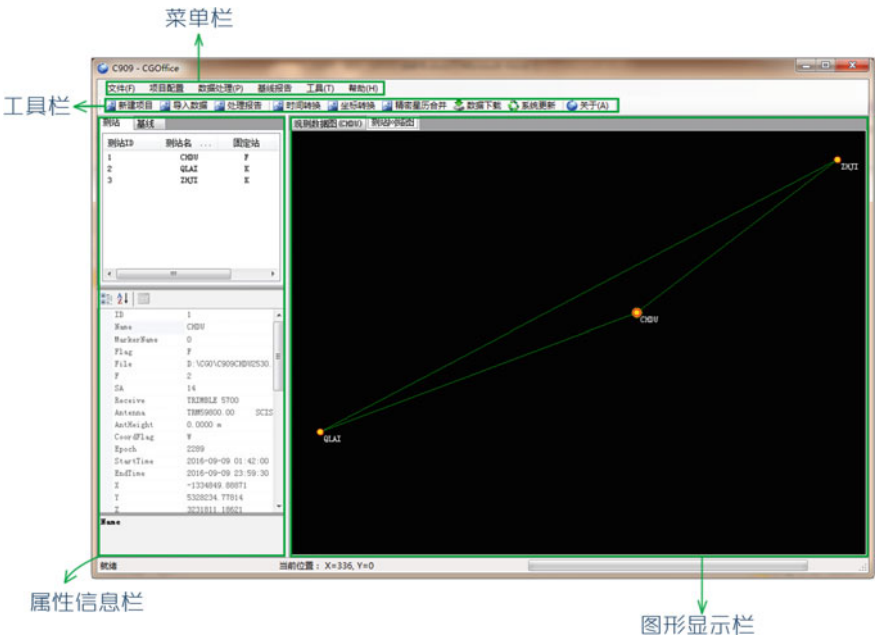

Fig. 1 Software interface

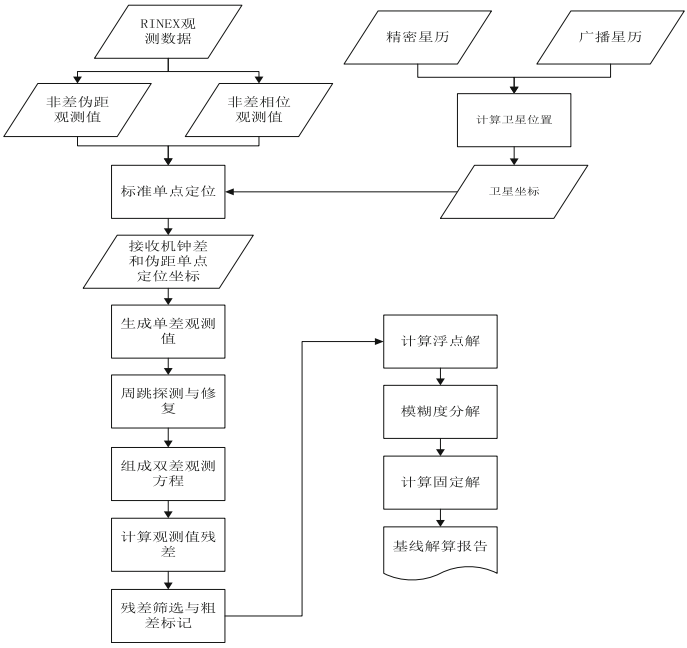

Fig. 2 Process flow of static data

4 Experiment and Test

4.1 Experiment of Assigning Weight to BDS

In the experiment, the data of seven days from September 09, 2016, to September 17 of CHDU station and QLAI station which belong to CORS of SiChuan Province is used, and four kinds of scheme are used for calculation and analysis, then the repeatability of baseline results of different schemes is analyzed and the results are compared with results calculated by Bernese software with GPS data:

1. Scheme A: the elevation angle stochastic model is used for GEO/MEO/IGSO.
2. Scheme B: the weight of GEO is $0.6 \cdot \omega(z)$, weight of IGSO is $\omega(z)$, weight of MEO is $\omega(z)$.
3. Scheme C: the weight of GEO is $\omega(z)$, weight of IGSO is $\omega(z)$, weight of MEO is $0.4 \cdot \omega(z)$.
4. Scheme D: the weight of GEO is $0.6 \cdot \omega(z)$, weight of IGSO is $\omega(z)$, weight of MEO is $0.4 \cdot \omega(z)$.

In Fig. 3a, b, c, d respectively represent bias between the BDS baseline results and Bernese-GPS baseline results of scheme A, B, C, D. Tables 4, 5, 6 and 7 respectively represent the repeatability of BDS baseline results of four schemes.

Comparing the results of scheme A and B, it can be found that lower weight for GEO satellite can improve external precision and baseline daily repeatability as external precision and repeatability are improved 3 mm; in scheme C, lower weight for MEO satellite only improve the repeatability slightly, because the regression

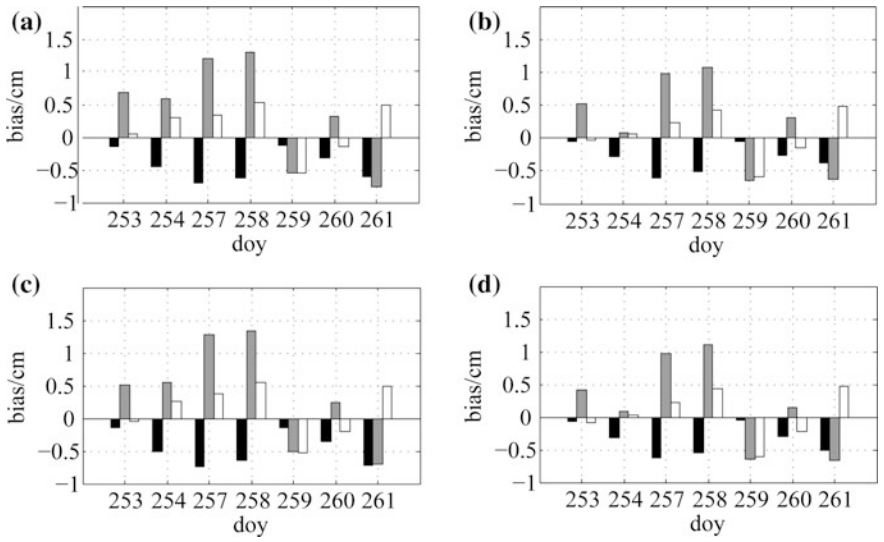

Fig. 3 Bias between baseline results of scheme A, B, C, D and Bernese-GPS baseline results

Table 4 Scheme A: daily repetitive difference of BDS baseline results

Day of year	254	257	258	259	260	261
ΔX (m)	0.00312	0.00733	0.00798	0.00516	0.0056	0.00426
ΔY (m)	−0.00136	0.00806	0.00301	0.01507	0.01609	0.01343
ΔZ (m)	−0.00172	−0.00329	−0.00714	0.00069	−0.00047	−0.00431

Table 5 Scheme B: daily repetitive difference of BDS baseline results

Day of year	254	257	258	259	260	261
ΔX (m)	0.00238	0.00715	0.0077	0.0052	0.00591	0.00262
ΔY (m)	0.00206	0.0087	0.00381	0.01445	0.01467	0.01059
ΔZ (m)	−0.00022	−0.00311	−0.00679	0.0003	−0.00137	−0.00506

Table 6 Scheme C: daily repetitive difference of BDS baseline results

Day of year	254	257	258	259	260	261
ΔX (m)	0.00365	0.00754	0.00817	0.00516	0.00582	0.00528
ΔY (m)	−0.00259	0.00572	0.001	0.01321	0.01527	0.01127
ΔZ (m)	−0.00228	−0.00466	−0.0083	0.0003	−0.00093	−0.00512

Table 7 Scheme D: daily repetitive difference of BDS baseline results

Day of year	254	257	258	259	260	261
ΔX (m)	0.00251	0.00715	0.00791	0.00507	0.00619	0.00388
ΔY (m)	0.00106	0.00777	0.00240	0.01340	0.01514	0.00990
ΔZ (m)	−0.00055	−0.00363	−0.00757	−0.00016	−0.00114	−0.00554

period of it is seven days; In scheme D, lower weight for GEO and MEO satellite, the external precision and repeatability are improved, but the difference compared with scheme B is not obvious. In conclusion, GEO satellite orbit error is bigger and observation precision is lower, the scheme of lower weight for GEO satellite can significantly improve precision of baseline processing.

4.2 Test and Analysis of BDS Baseline Processing Software

In order to test the BDS baseline processing software, in this experiment of single baseline processing, three different length baselines data that is from CHDU-ZHJI (61.5 km), CHDU-QLAI (79.4 km), QLAI-ZHJI (139.1 km) of seven days of SiChuan CORS are used. The strategy of baseline processing is as follows:

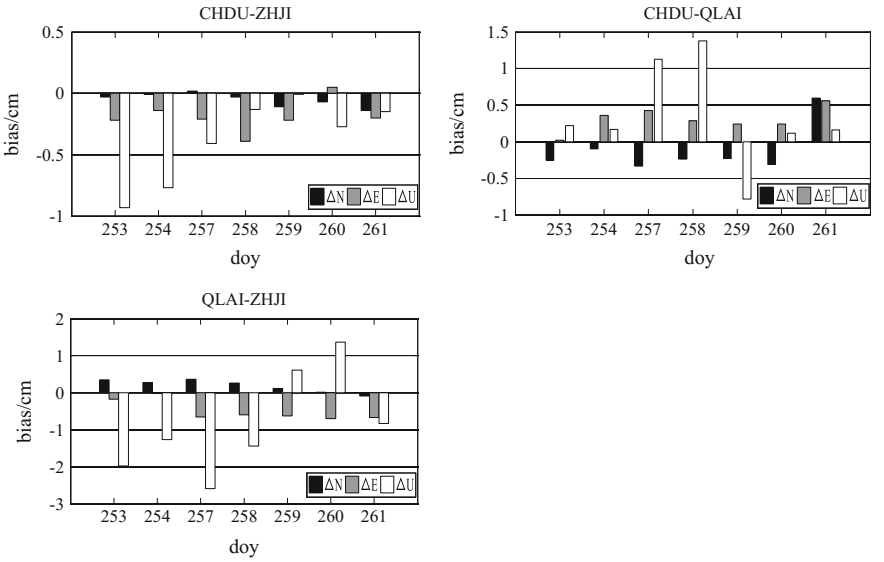

Fig. 4 Bias between baseline solution of BDS baseline processing software with BDS data and solution of Bernese with GPS data

Troposphere parameters estimation method: the method of additional parameter to estimate troposphere parameters every 1 h;

The cut-off elevation angle is set as: 10°;

Stochastic model: $0.6 \cdot \omega(z)$ for GEO satellite, $0.4 \cdot \omega(z)$ for MEO satellite, $\omega(z)$ for IGSO satellite, $\omega(z)$ for GPS satellite and combined with elevation angle stochastic model. The processing results are listed in Fig. 4:

Compared with Bernese-GPS results, the bias of BDS results of baseline CHDU-ZHJI are less than 2 mm in north direction, less than 4 mm in east direction, and less than 10 mm in up direction; For baseline CHDU-QLAI, the bias in the three direction has the tendency of increase and it is less than 4 mm in north direction, 6 mm in east direction and 14 mm in up direction; For baseline QLIA-ZHJI, the bias is less than 4 mm in north direction, 7 mm in east direction and 26 mm in up direction.

5 Conclusion

BDS consists of GEO/MEO/IGSO three kinds of mixed satellite constellation, because of different characteristics of them, it is need to assign weight for them reasonable when data processing. In this paper, the method of RMS of BDS zero-difference observation combined with elevation angle stochastic model is used to assign weight for BDS. By comparison with experiment, it can be found that

lower weight for GEO satellite can improve the baseline processing precision of millimeter; and it can improve precision and daily repeatability of BDS baseline results as assign the biggest, least and middle weight to IGSO, MEO and GEO respectively when processing data of BDS.

The bias between result of BDS calculated by BDS baseline processing software and result of GPS calculated by Bernese software is less than 10 mm in plane direction and 24 mm in up direction.

The above conclusion is only based on the current situation that BDS covers Asia and the Pacific regional. However, BDS will provide service for the world, the number of MEO satellite will increase and cover the whole world, it may be need to reconsider the weight of MEO satellite.

References

1. Yan L (2017) BeiDou/GPS combined precise positioning theory and algorithm. Southwest Jiaotong University, China
2. Zhao YQ (2013) Research of location algorithm and analysis of GDOP of the COMPASS satellite navigation system. Harbin Engineering University
3. Liu WP, Hao JM, Li JW et al (2014) Multi-GNSS joint precise orbit determination of Beidou navigation system. Acta Geodaetica Cartogr Sin 43(11):1132–1143. https://doi.org/10.13485/j.cnki.11-2089.2014.0186
4. Yang Y, Fan L, Dong XR (2008) IGSO constellation analysis and its optimal design. Netw Inf Technol 27(11):53–55
5. Yang YX, Li JL, Wang AB et al (2014) Preliminary assessment of the navigation and positioning performance of BeiDou regional navigation satellite system. Sci China: Earth Sci 57:144–152. https://doi.org/10.1007/s11430-013-4769-0
6. Li LY, Guo JM (2016) Influence of GEO satellites number on BDS single point positioning. Sci Surv Mapp 41(6):19–22

GNSS-Based Attitude Determination via Schmidt Kalman Filter

Yu Li, Huabo Wei, Min Wu, Huizhu Zhu and Jun Ye

Abstract The Schmidt Kalman Filter is presented in this study for float ambiguity resolution and attitude estimation of a multi-antenna platform using single-frequency GNSS measurements. The geometry information of the antenna configuration is fully exploited for ambiguity resolution via formulating the direct functional relationship between double-differenced carrier phase measurements and attitude quaternions. A first-order Gauss–Markov process is employed to model the remaining observation colour noise. The attitude parameters and the colored observation noise are decoupled in the state equation with Schmidt Kalman Filter. The Least-squares AMBiguity Decorrelation Adjustment (LAMBDA) algorithm is implemented for integer ambiguity resolution. The process of attitude determination algorithm via Schmidt-Kalman filter is designed and a static GNSS test is carried out to validate the filter performance. Results show that the Schmidt-Kalman filter performs better than the standard reduced-order Kalman filter and QUEST algorithm in terms of the integer ambiguity resolution (such as, the success rate and Time-to-Fix) and the accuracy of attitude angles for BDS, GPS and GPS + BDS. The double GNSS have better performance than single constellation, and there is no big difference between GPS and BDS for attitude determination.

Keywords Schmidt kalman filter · Float ambiguity resolution · GNSS Attitude determination

1 Introduction

The Global Navigation Satellite System (GNSS) plays an important role in the attitude determination, ranging from terrestrial to maritime (guidance of land vehicles, precise docking of vessels, and automatic pilot), and from air to space

Y. Li · H. Wei (✉) · M. Wu · H. Zhu · J. Ye
China Aeronautical Radio Electronics Research Institute, 432 Ziyue Road, Minhang District, Shanghai, China
e-mail: wei_huabo@126.com

J. Sun et al. (eds.), *China Satellite Navigation Conference (CSNC) 2018 Proceedings*, Lecture Notes in Electrical Engineering 498,
https://doi.org/10.1007/978-981-13-0014-1_51

(landing assistance, unmanned air vehicles (UAVs), and satellites) [1–8]. High-precision attitude estimation usually requires carrier phase observations, which have higher accuracy than code observations that rely on successful resolution of unknown integer ambiguities. After ambiguity resolution, the attitude of a multi-antenna platform can be derived via quaternions.

The key to integer ambiguities resolution (IAR) is the accuracy of the float ambiguity. Current approaches utilize differenced carrier phases to obtain precise baselines between antennas and then deduce the attitude matrix via solving the Wahba's problem [9, 10]. Within this method, the ambiguity resolution and the attitude matrix extraction are regarded as two individual parts, and the geometry information of the antenna configuration is only involved in the latter process.

Numerous studies have been conducted to investigate the feasibility of the GNSS-based attitude determination in which the geometry information also assists the ambiguity resolution and attitude estimation. Several researchers exploit the known baseline length to improve the accuracy of the float ambiguity by solving the constrained least-squares problem [11–13]. The known baseline length is also used to modify Least-squares AMBiguity Decorrelation Adjustment (LAMBDA) method, in which the baseline length is integrated into the ambiguity objective function with mixed integer parameters to improve the success rate of ambiguity resolution [5, 14–16]. Several researchers improve the accuracy of the baseline vector or attitude solution with the known integer ambiguity and the prior information [17, 18].

Recall that the double-differenced GNSS code and carrier phase observations contain autocorrelated noise. An augmented state space model can be formulated and a full-order Kalman filter can be used to estimate all the state variables. However, we do not really care about the colored noise. In addition, the first-order Gauss–Markov process model for the higher-order residual errors is only an approximation and is not rigorous. Thus a full-order filter may not be the best choice. The Schmidt-Kalman filter (SKF) is a reduced-order filter dealing with dynamic estimation of systems in which the subsets of state variables are decoupled from each other. The attitude determination problem in this study happens to be such a case, where the attitude parameters and the colored observation noise are decoupled in the state equation and are regarded as "solve-for" and "consider" variables, respectively.

In this study, we focus on float ambiguity resolution using SKF. The geometrical information, i.e., the baseline length and orientation, is not used as additional constraints but essential parameters to reconstruct the measurement model to improve the accuracy of the float ambiguities. The SKF algorithm is utilized to estimate float ambiguities and attitude quaternions simultaneously. The LAMBDA method is then used to fix the ambiguities and to further correct the attitude solutions. A static BDS experiment is carried out to test the performance.

2 GNSS-Attitude Model

In this section, we present the underlying model for GNSS-based attitude solution. The double-differenced carrier phase observation model for a multi-antenna system is firstly introduced. The antenna configuration, the definition of the body reference system, as well as the attitude model is then described.

2.1 Functional Model for GNSS Observations

The single-frequency GNSS carrier phase measurements used for receiver A tracking satellite j at time k are given as follows:

$$P_A^j = \rho_A^j + c(\delta t_A - \delta t^j) + I_A^j + T_A^j + v_P^j \tag{1}$$

$$\Phi_A^j = \rho_A^j + \lambda_{L1} N_A^j + c(\delta t_A - \delta t^j) - I_A^j + T_A^j + v_\Phi^j \tag{2}$$

where the superscript j indicates the GNSS satellite, the subscript A indicates the receiver, P_A^j, Φ_A^j represent the carrier phase observations and pseudorange (m), ρ_A^j the geometrical distance between the receiver and the satellite (m), c the vacuum speed of light (m/s), δt_A and δt^j the receiver and satellite clock offsets (s), I_A^j and T_A^j the ionospheric and troposphere error terms (m), v_Φ^j the thermal noise (m), N_A^j the ambiguity (cycles), and λ_{L1} is the nominal $L1$ carrier phase wavelength (m).

Suppose that the receivers A and B track m common GNSS satellites. The double-differenced (DD) carrier phase observations are constructed with differences between measurements collected by the two receivers from two different satellites as follows:

$$P_{BA}^{j\vartheta} = \rho_{BA}^{j\vartheta} + v_{\Phi_{BA}}^{j\vartheta} \tag{3}$$

$$\Phi_{BA}^{j\vartheta} = \rho_{BA}^{j\vartheta} + \lambda_{L1} N_{BA}^{j\vartheta} + v_{\Phi_{BA}}^{j\vartheta} \tag{4}$$

where $(*)_{BA}^{j\vartheta} = \left[(*)_B^j - (*)_B^\vartheta\right] - \left[(*)_A^j - (*)_A^\vartheta\right]$ is the double-differenced operator, ϑ is the reference satellite and is selected according to the maximum elevation. The clock offsets are eliminated in the equation and the number of unknown parameters to be determined is thus reduced. Moreover, the atmospheric errors become negligible in case of short baselines, since that the signals travel approximately along the same path from the satellites to the closely separated antennas.

For full attitude determination, at least three antennas are required. Therefore, model (4) needs to be extended to a multi-antenna system. Consider a set of $m + 1$ antennas tracking the same $n + 1$ GNSS satellites. Let M be the master antenna and i be the slave antenna ($i = 1, 2, \ldots, m$). The GNSS DD carrier phase observations formed with the m independent baselines are given as follows:

$$\begin{pmatrix} \Phi_{1M}^{j\vartheta} \\ \vdots \\ \Phi_{mM}^{j\vartheta} \end{pmatrix} \otimes \begin{pmatrix} 1 \\ \vdots \\ 1 \end{pmatrix}_{n\times 1} = \begin{pmatrix} \rho_{1M}^{j\vartheta} + \lambda_{L1} N_{1M}^{j\vartheta} \\ \vdots \\ \rho_{mM}^{j\kappa} + \lambda_{L1} N_{mM}^{j\vartheta} \end{pmatrix} \otimes \begin{pmatrix} 1 \\ \vdots \\ 1 \end{pmatrix}_{n\times 1} + \boldsymbol{v}_{mn\times 1} \tag{5}$$

where $\otimes$ indicates the Kronecker product, $\boldsymbol{v}_{mn\times 1}$ is DD observation noise vector.

2.2 Attitude Model

Suppose that there are $m+1$ antennas firmly mounted on a rigid platform. The lengths and the orientations of the baselines are known beforehand. The body reference frame of the platform is defined as follows: the first axis $\boldsymbol{e}_1$ is aligned with the first baseline, the second axis $\boldsymbol{e}_2$ is perpendicular to $\boldsymbol{e}_1$ lying in the plane formed by the first two baselines, and the third axis $\boldsymbol{e}_3$ together with $\boldsymbol{e}_1$ and $\boldsymbol{e}_2$ forms a right-handed orthonormal frame. The attitude matrix $\boldsymbol{A}$ ($\boldsymbol{A}^{\mathrm{T}}\boldsymbol{A} = \boldsymbol{I}$) is defined as the transformation matrix from the local East-North-Up (ENU) frame to the body frame. Let $\boldsymbol{B}$ and $\boldsymbol{D}$ denote the matrices consisting of the n baseline vectors in the body frame and in the ENU frame, respectively. Based on the above definitions, we have see Giorgi et al. [5].

$$\begin{aligned} m = 1,\ \boldsymbol{D} = \boldsymbol{AB} = \boldsymbol{A} &\begin{bmatrix} B_{11} \\ 0 \\ 0 \end{bmatrix} \\ m = 2,\ \boldsymbol{D} = \boldsymbol{AB} = \boldsymbol{A} &\begin{bmatrix} \boldsymbol{B_{11}} & \boldsymbol{B_{21}} \\ 0 & \boldsymbol{B_{22}} \\ 0 & 0 \end{bmatrix} \\ m \geq 3,\ \boldsymbol{D} = \boldsymbol{AB} = \boldsymbol{A} &\begin{bmatrix} B_{11} & B_{21} & B_{31} & \cdots & B_{m1} \\ 0 & B_{22} & B_{32} & \cdots & B_{m2} \\ 0 & 0 & B_{33} & \cdots & B_{m3} \end{bmatrix} \end{aligned} \tag{6}$$

The quaternion representation is of common use to attitude estimation and control applications, since that it guarantees high numerical robustness. In addition, the estimation of the orthonormal matrix $\boldsymbol{A}$ has low computational loads and no singularities with the quaternion parameterization. The attitude matrix $\boldsymbol{A}$ is parameterized in terms of quaternions as follows:

$$\boldsymbol{A}(\bar{\boldsymbol{q}}) = \begin{bmatrix} q_1^2 - q_2^2 - q_3^2 + q_4^2 & 2(q_1q_2 + q_3q_4) & 2(q_1q_3 - q_2q_4) \\ 2(q_1q_2 - q_3q_4) & -q_1^2 + q_2^2 - q_3^2 + q_4^2 & 2(q_2q_3 + q_1q_4) \\ 2(q_1q_3 + q_2q_4) & 2(q_2q_3 - q_1q_4) & -q_1^2 - q_2^2 + q_3^2 + q_4^2 \end{bmatrix} \tag{7}$$

where $\bar{\boldsymbol{q}} = (\boldsymbol{q},\ q_4)$, $\boldsymbol{q} = (q_1,\ q_2,\ q_3)$, $\overline{\boldsymbol{qq}}^{\mathrm{T}} = 1$.

The three Euler angles can be extracted from the attitude matrix $\boldsymbol{A}$ by

$$\psi = \arctan(-a_{21}/a_{22});\ \theta = \arctan(-a_{13}/a_{33});\ \varphi = \arcsin(a_{23}) \tag{8}$$

with a_{ij} the elements of $\boldsymbol{A}$.

3 SKF for GNSS-Attitude Determination

The DD carrier phase model and the attitude model described above are combined to formulate the direct quaternion parameterized observation equation. The state equation for kinematic attitude determination is also given. Then we utilize the SKF to deal with this recursive estimation problem.

3.1 The Quaternion Parameterized Observation Equation

The quaternion parameterized observation equation is formulated by fully exploiting the baseline length and orientation information. For ultra-short baselines, the double-differenced geometric distance $\boldsymbol{\rho}_{iM}^{\kappa j}$ in Eq. (4) can be linearized as

$$\rho_{iM}^{j\kappa} = \left[\rho_i^j - \rho_i^\kappa\right] - \left[\rho_M^j - \rho_M^\kappa\right] = \boldsymbol{L}_i^T \boldsymbol{u}_j \tag{9}$$

With

$$\boldsymbol{u}_j = \frac{\boldsymbol{r}^j - \boldsymbol{r}_M}{\rho_M^j} - \frac{\boldsymbol{r}^\kappa - \boldsymbol{r}_M}{\rho_M^\kappa} \tag{10}$$

where $\boldsymbol{r}_M$ is the known position vector of the master antenna, $\boldsymbol{r}^j$ and $\boldsymbol{r}^\kappa$ are the position vectors of the jth and reference satellites, and $\boldsymbol{L}_i$ is the unknown baseline vector between the ith antenna and the master antenna. All the vectors in Eq. (9) are expressed in the Earth-centered Earth-fixed (ECEF) frame. Combine the m baselines vector into a $3 \times m$ matrix.

$$\boldsymbol{L} = [\boldsymbol{L}_1 \quad \boldsymbol{L}_2 \quad \cdots \quad \boldsymbol{L}_m] \tag{11}$$

According to the definitions of coordinate systems in Sect. 2, we have

$$\boldsymbol{L} = \boldsymbol{TD} = \boldsymbol{TA}(\bar{\boldsymbol{q}})\boldsymbol{B} \tag{12}$$

where $\boldsymbol{T}$ is the rotation matrix from ENU to ECEF. Substituting Eqs. (9) and (11) into Eq. (4), then we obtain the direct functional relationship between the DD phases and the quaternions.

$$\Delta\nabla\boldsymbol{\Phi} = \left((\boldsymbol{TA}(\bar{\boldsymbol{q}})\boldsymbol{B})^T\boldsymbol{u}_j + \lambda_{L1}\boldsymbol{N}_j\right) \otimes \begin{pmatrix} 1 \\ \vdots \\ 1 \end{pmatrix}_{n\times 1} + \boldsymbol{v}_{mn\times 1} \tag{13}$$

where $\Delta\nabla\boldsymbol{\Phi}$ is the DD carrier phase vector, $\boldsymbol{N}_j = \begin{bmatrix} N_{1M}^{j\vartheta} & N_{2M}^{j\vartheta} & \cdots & N_{mM}^{j\vartheta} \end{bmatrix}$ the DD ambiguity vector for the jth satellite. The unknown parameters in Eq. (13) include the 4-dimensional quaternion $\bar{\boldsymbol{q}}$ and a total $m \times n$ dimensional DD ambiguity vector $\boldsymbol{N} = \begin{bmatrix} \boldsymbol{N}_1^T & \boldsymbol{N}_2^T & \cdots & \boldsymbol{N}_n^T \end{bmatrix}^T$.

The norm of $\bar{\boldsymbol{q}}$ always equals 1. This provides a nonlinear constraint for the quaternion estimation. In this study, the norm constraint is regarded as a virtual observation. The final observation equation can be written as

$$\boldsymbol{z} \equiv \begin{bmatrix} \Delta\nabla\boldsymbol{\Phi} \\ 1 \end{bmatrix} = \boldsymbol{h}(\boldsymbol{x}) + \tilde{\boldsymbol{v}} \tag{14}$$

with

$$\boldsymbol{h}(x) = \begin{bmatrix} \left((\boldsymbol{TA}(\bar{\boldsymbol{q}})\boldsymbol{B})^T\boldsymbol{u}_j + \lambda_{L1}\boldsymbol{N}_j\right) \otimes \begin{pmatrix} 1 \\ \vdots \\ 1 \end{pmatrix}_{n\times 1} \\ \bar{\boldsymbol{q}}^T\bar{\boldsymbol{q}} \end{bmatrix}, \ \tilde{\boldsymbol{v}} = \begin{bmatrix} \boldsymbol{v}_{mn\times 1} \\ 0 \end{bmatrix} \tag{15}$$

where $\boldsymbol{x} = \begin{bmatrix} \bar{\boldsymbol{q}} & \boldsymbol{N} \end{bmatrix}^T$ is the state vector, $\boldsymbol{h}(\cdot)$ is the nonlinear measurement function, $\tilde{\boldsymbol{v}}$ is the observation error and is assumed to be zero-mean Gaussian noise. The variance-covariance (V-C) matrix of the observations is constructed as [5]

$$\boldsymbol{R} = \begin{bmatrix} \boldsymbol{R}_{\Delta\nabla\boldsymbol{\Phi}} & \\ & 0 \end{bmatrix} \tag{16}$$

with

$$\boldsymbol{R}_{\Delta\nabla\boldsymbol{\Phi}} = \sigma_{\boldsymbol{\Phi}}^2\boldsymbol{I}_{m\times m} \otimes \begin{bmatrix} 4 & 2 & \cdots & 2 \\ 2 & 4 & \cdots & 2 \\ \vdots & \vdots & \ddots & \vdots \\ 2 & 2 & \cdots & 4 \end{bmatrix}_{n\times n} \tag{17}$$

where $\sigma_{\boldsymbol{\Phi}}$ is the standard deviation of the undifferenced carrier phase noise.

3.2 The Kinematic State Equation

The kinematic motion of the attitude quaternion and the ambiguities can be represented as a first-order differential equation.

$$\begin{aligned}\dot{\bar{\boldsymbol{q}}} &= \frac{1}{2}\boldsymbol{\Omega}\bar{\boldsymbol{q}} \\ \dot{\boldsymbol{N}} &= \boldsymbol{0}\end{aligned} \tag{18}$$

where $\boldsymbol{\Omega}$ is the angular velocity matrix. In order to propagate the state vector to the next measurement epoch, the discrete form of the kinematic equation is used as follows:

$$\begin{aligned}\bar{\boldsymbol{q}}_k &= \boldsymbol{e}^{\frac{1}{2}\boldsymbol{\Omega}\Delta t_k}\bar{\boldsymbol{q}}_{k-1} \\ \boldsymbol{N}_k &= \boldsymbol{N}_{k-1}\end{aligned} \tag{19}$$

where, the subscript k denotes the epoch number.

The generalized state equation can be obtained as

$$\boldsymbol{x}_k = \boldsymbol{F}_{k,k-1}\boldsymbol{x}_{k-1} + \boldsymbol{w}_{k-1} \tag{20}$$

with

$$\boldsymbol{F}_{k,k-1} = \begin{bmatrix} \boldsymbol{e}^{\frac{1}{2}\boldsymbol{\Omega}\Delta t_k} & \\ & \boldsymbol{I}_{mn\times mn}\end{bmatrix},\ \boldsymbol{w}_{k-1} = \begin{bmatrix}\boldsymbol{w}_\omega \\ \boldsymbol{0}_{mn\times 1}\end{bmatrix} \tag{21}$$

where $\boldsymbol{F}_{k/k-1}$ is the state transition matrix, $\boldsymbol{w}_\omega$ is the fictitious process noise due to the angular velocity uncertainty, and its standard deviation is denoted by σ_ω. For the static case, $\boldsymbol{\Omega} = \boldsymbol{0}$. Then we have

$$\boldsymbol{F}_{k,k-1} = \begin{bmatrix}\boldsymbol{I}_{4\times 4} & \\ & \boldsymbol{I}_{mn\times mn}\end{bmatrix} \tag{22}$$

The process noise matrix $\boldsymbol{Q}_{k-1}$ is defined as

$$\boldsymbol{Q}_{k,k-1} = \begin{bmatrix}\sigma_\omega^2\Delta t\cdot\boldsymbol{I}_{4\times 4} & \\ & \boldsymbol{0}_{mn\times mn}\end{bmatrix} \tag{23}$$

3.3 Schmidt-Kalman Filter Design

The DD carrier phase model and the attitude model described above are combined to formulate the direct quaternion parameterized observation equation. The state equation for kinematic attitude determination is also given. Then we utilize the SKF to deal with this recursive estimation problem. The double-differenced GNSS code and carrier phase observations contain autocorrelated noise. An augmented state space model can be formulated and a full-order Kalman filter can be used to estimate all the state variables. However, we do not really care about the colored

noise. In addition, the first-order Gauss–Markov process model for the higher-order residual errors is only an approximation and is not rigorous. Thus a full-order filter may not be the best choice.

The Schmidt-Kalman filter (SKF) is a reduced-order filter dealing with dynamic estimation of systems in which the subsets of state variables are decoupled from each other [19, 20]. The attitude determination problem in this study happens to be such a case, where the attitude parameters and the colored observation noise are decoupled in the state equation and are regarded as "solve-for" and "consider" variables, respectively. The solve-for states are updated at each time step, whereas the considered states are always set to zero. The update process also involves the covariances of the states. The detailed algorithm of the Schmidt-Kalman filter for linear system estimation is given in Simon [19], and its superior performance over the standard reduced-order Kalman filter.

This section presents the overall Schmidt-Kalman filter design for the single-frequency GNSS attitude determination. The solve-for state vector comprises the quaternion and the DD ambiguities.

$$\tilde{\boldsymbol{x}}^T = \begin{bmatrix} \bar{\boldsymbol{q}} & \widehat{\boldsymbol{N}} \end{bmatrix} \tag{24}$$

The estimate of $\tilde{\boldsymbol{x}}$ is denoted by $\hat{\tilde{\boldsymbol{x}}}$ and the accompanying covariance is denoted by $\widetilde{\boldsymbol{P}}$. Suppose there are n tracked GNSS satellites at the current epoch and the reference satellite is placed at the ϑth position in the visible satellites array. The DD ambiguity vector $\widehat{\boldsymbol{N}}$, thus contains $M-1$ unknowns baseline DD ambiguity vector $\widehat{\boldsymbol{N}}_{iM}$ $(i = 1, 2, \ldots, \mathrm{M}-1)$.

$$\begin{aligned} \widehat{\boldsymbol{N}} &= \begin{bmatrix} \widehat{\boldsymbol{N}}_{1M} & \cdots & \widehat{\boldsymbol{N}}_{iM} & \cdots & \widehat{\boldsymbol{N}}_{M-1M} \end{bmatrix}^T \\ \widehat{\boldsymbol{N}}_{iM} &= \begin{bmatrix} \widehat{\boldsymbol{N}}_{iM}^{\vartheta 1} & \widehat{\boldsymbol{N}}_{iM}^{\vartheta 2} & \cdots & \widehat{\boldsymbol{N}}_{iM}^{\vartheta j} & \cdots & \widehat{\boldsymbol{N}}_{iM}^{\vartheta m} \end{bmatrix}^T \end{aligned} \tag{25}$$

where $j \neq \vartheta$. The consider state vector comprises the $M-1 \times n-1$ double-differenced colored noise terms.

$$\begin{aligned} \tilde{\tilde{\boldsymbol{x}}} &= \begin{bmatrix} \boldsymbol{\xi}_{1M} & \cdots & \boldsymbol{\xi}_{iM} & \cdots & \boldsymbol{\xi}_{M-1M} \end{bmatrix} \\ \boldsymbol{\xi}_{iM} &= \begin{bmatrix} \xi_{iM}^{\vartheta 1} & \xi_{iM}^{\vartheta 2} & \cdots & \xi_{iM}^{\vartheta j} & \cdots & \xi_{iM}^{\vartheta n} \end{bmatrix}^T \end{aligned} \tag{26}$$

where $j \neq \vartheta$. The estimate of $\tilde{\tilde{\boldsymbol{x}}}$ is denoted by $\hat{\tilde{\tilde{\boldsymbol{x}}}}$ and the accompanying covariance is denoted by $\widetilde{\widetilde{\boldsymbol{P}}}$. The covariance between $\hat{\tilde{\boldsymbol{x}}}$ and $\hat{\tilde{\tilde{\boldsymbol{x}}}}$ is denoted by $\boldsymbol{\Sigma}$.

Given initial values of $\tilde{\boldsymbol{x}}$, $\widetilde{\boldsymbol{P}}$, $\boldsymbol{\Sigma}$, and $\widetilde{\widetilde{\boldsymbol{P}}}$, the filter processes the double-differenced carrier phase measurements at consecutive epochs and recursively updates the solve-for states and all the covariances. The initial values of $\boldsymbol{q}$ is obtained by body attitude angles. The initial value of $\boldsymbol{\Sigma}$ is set to zero. The initial value of $\widetilde{\widetilde{\boldsymbol{P}}}$ is set to

$$\widetilde{\widetilde{\boldsymbol{P}}} = \sigma_{\xi}^{2}\begin{bmatrix} 2 & 1 & \cdots & 1 \\ 1 & 2 & \cdots & 1 \\ \vdots & \vdots & \ddots & \vdots \\ 1 & 1 & \cdots & 2 \end{bmatrix}_{(n-1)\times(n-1)} \tag{27}$$

The recursive estimation at each step consists of time-update and measurement-update stages. At the time-update stage, the solve-for states are propagated from previous epoch $k-1$ to current epoch k, see Eqs. (19–23).

The covariance $\widetilde{\boldsymbol{P}}$ is propagated as follows:

$$\widetilde{\boldsymbol{P}}_{k}^{-} = \boldsymbol{F}_{k,k-1}\widetilde{\boldsymbol{P}}_{k-1}^{+}\boldsymbol{F}_{k,k-1}^{T} + \boldsymbol{Q}_{k,k-1} \tag{28}$$

The covariances, $\boldsymbol{\Sigma}$ and $\widetilde{\widetilde{\boldsymbol{P}}}$, are also propagated as follows:

$$\boldsymbol{\Sigma}_{k}^{-} = \boldsymbol{\Phi}_{k,k-1}\boldsymbol{\Sigma}_{k-1}^{+}\boldsymbol{M}_{k,k-1}^{T} \tag{29}$$

$$\widetilde{\widetilde{\boldsymbol{P}}}_{k}^{-} = \boldsymbol{M}_{k,k-1}\widetilde{\widetilde{\boldsymbol{P}}}_{k-1}^{+}\boldsymbol{M}_{k,k-1}^{T} + \boldsymbol{Q}_{\xi,k,k-1} \tag{30}$$

where $\boldsymbol{M}_{k,k-1}$ and $\boldsymbol{Q}_{\xi,k,k-1}$ are the mapping matrix and process noise matrix of $\tilde{\tilde{\boldsymbol{x}}}$

$$\boldsymbol{M}_{k,k-1} = e^{-(t_k - t_{k-1})/\tau}\boldsymbol{I}_{(n-1)\times(n-1)} \tag{31}$$

$$\boldsymbol{Q}_{\xi,k,k-1} = \sigma_{\xi}^{2}\left[1 - e^{-2(t_k - t_{k-1})/\tau}\right]\begin{bmatrix} 2 & 1 & \cdots & 1 \\ 1 & 2 & \cdots & 1 \\ \vdots & \vdots & \ddots & \vdots \\ 1 & 1 & \cdots & 2 \end{bmatrix}_{(m-1)\times(m-1)} \tag{32}$$

At the measurement-update stage, the solve-for state vector and its accompanying covariance are updated as follows:

$$\hat{\tilde{\tilde{\boldsymbol{x}}}}_{k}^{+} = \hat{\tilde{\tilde{\boldsymbol{x}}}}_{k}^{-} + \widetilde{\boldsymbol{K}}_{k}\left[z_k - \boldsymbol{G}\left(\hat{\tilde{\tilde{\boldsymbol{x}}}}^{-}\right)\right] \tag{33}$$

$$\widetilde{\boldsymbol{K}}_{k} = \left(\widetilde{\boldsymbol{P}}_{k}^{-}\widetilde{\boldsymbol{H}}_{k}^{T} + \boldsymbol{\Sigma}_{k}^{-}\widetilde{\widetilde{\boldsymbol{H}}}_{k}^{T}\right)\boldsymbol{\Lambda}_{k}^{-1} \tag{34}$$

$$\boldsymbol{\Lambda}_{k} = \widetilde{\boldsymbol{H}}_{k}\widetilde{\boldsymbol{P}}_{k}^{-}\widetilde{\boldsymbol{H}}_{k}^{T} + \widetilde{\boldsymbol{H}}_{k}\boldsymbol{\Sigma}_{k}^{-}\widetilde{\widetilde{\boldsymbol{H}}}_{k}^{T} + \widetilde{\widetilde{\boldsymbol{H}}}_{k}\left(\boldsymbol{\Sigma}_{k}^{-}\right)^{T}\widetilde{\boldsymbol{H}}_{k}^{T} + \widetilde{\widetilde{\boldsymbol{H}}}_{k}\widetilde{\widetilde{\boldsymbol{P}}}_{k}^{-}\widetilde{\widetilde{\boldsymbol{H}}}_{k}^{T} + \mathbf{R}_{k} \tag{35}$$

$$\begin{aligned}\widetilde{\boldsymbol{P}}_{k}^{+} = {} & \left(\mathbf{I} - \widetilde{\boldsymbol{K}}_{k}\widetilde{\boldsymbol{H}}_{k}\right)\tilde{\mathbf{P}}_{k}^{-}\left(\mathbf{I} - \widetilde{\boldsymbol{K}}_{k}\widetilde{\boldsymbol{H}}_{k}\right)^{T} - \left(\mathbf{I} - \widetilde{\boldsymbol{K}}_{k}\widetilde{\boldsymbol{H}}_{k}\right)\boldsymbol{\Sigma}_{k}^{-}\widetilde{\widetilde{\boldsymbol{H}}}_{k}^{T}\widetilde{\boldsymbol{K}}_{k}^{T} \\ & - \widetilde{\boldsymbol{K}}_{k}\widetilde{\widetilde{\boldsymbol{H}}}_{k}\left(\boldsymbol{\Sigma}_{k}^{-}\right)^{T}\left(\mathbf{I} - \widetilde{\boldsymbol{K}}_{k}\widetilde{\boldsymbol{H}}_{k}\right)^{T} + \widetilde{\boldsymbol{K}}_{k}\mathbf{R}_{k}\widetilde{\boldsymbol{K}}_{k}^{T}\end{aligned} \tag{36}$$

where $\widetilde{\boldsymbol{K}}_k$ is the filter gain, z_k is the actual measurement vector, $\boldsymbol{G}\left(\hat{\tilde{\boldsymbol{x}}}^-\right)$ is the predicted measurement vector, $\widetilde{\boldsymbol{H}}_k$ and $\widetilde{\widetilde{\boldsymbol{H}}}_k$ are the design matrices corresponding to $\tilde{\boldsymbol{x}}$ and $\tilde{\tilde{\boldsymbol{x}}}$, and $\boldsymbol{R}_k$ is the covariance of the measurement noise vector. In this study, the measurement vector $\boldsymbol{z}$ refers to the DD observations, see Eq. (14).

The design matrix $\widetilde{\boldsymbol{H}}$ is composed by

$$\widetilde{\boldsymbol{H}} = \begin{bmatrix} \boldsymbol{H}_q & \boldsymbol{I}_{(M-1\times n-1)\times(M-1\times n-1)} \end{bmatrix} \tag{37}$$

where $\boldsymbol{H}_{\mathbf{r}}$ contains the normalized line-of-sight vectors and single-differences thereof. The design matrix $\widetilde{\widetilde{\boldsymbol{H}}}_k$ is an identify matrix. The measurement covariance is given by Eq. (17).

The covariances $\boldsymbol{\Sigma}$ and $\widetilde{\widetilde{\boldsymbol{P}}}$ are updated as follows:

$$\boldsymbol{\Sigma}_k^+ = \left(\boldsymbol{I} - \widetilde{\boldsymbol{K}}_k\widetilde{\boldsymbol{H}}_k\right)\boldsymbol{\Sigma}_k^- - \widetilde{\boldsymbol{K}}_k\widetilde{\widetilde{\boldsymbol{H}}}_k\widetilde{\widetilde{\boldsymbol{P}}}_k^- \tag{38}$$

The filter starts with the initialization of the solve-for states and all the covariances and then enters cycles of time-update and measurement-update stages. Before the measurement-update stage, an additional check of the change in observed GPS satellites is required. A reordering operation will be implemented on $\widehat{\boldsymbol{N}}, \widetilde{\boldsymbol{P}}_{\mathbf{A}}, \boldsymbol{\Sigma}$, and $\widetilde{\widetilde{\boldsymbol{P}}}$ if new GNSS satellites are available, old satellites disappear, and the reference satellite changes.

3.4 Workflow of Algorithm

The workflow of the GNSS-based attitude determination by the SKF is presented as Fig. 1

- Initialization processing

A reasonable estimate may not be obtained with the SKF, if the initial estimation is not good. First, the install matrix $\boldsymbol{B}$ is calculated by means of the whole observation data. A good choice is to first initialize the quaternion by solving Eq. (12) with the Gauss–Newton method. Then the DD carrier phase and DD C/A code are combined to generate the initialization of DD ambiguities as follows:

$$\boldsymbol{N}_{iM}^{j\kappa} = \left(\boldsymbol{\Phi}_{iM}^{j\kappa} - \boldsymbol{P}_{iM}^{j\kappa}\right)/\lambda_{L1} + \varepsilon_{\Delta\boldsymbol{P}} \tag{39}$$

where $\boldsymbol{P}_{iM}^{j\kappa}$ is DD C/A code, $\varepsilon_{\Delta\boldsymbol{P}}$ is the DD code observation error.

Based on the above initialization, we get initialization state vector $\boldsymbol{x}_0$ and $\boldsymbol{P}_0$

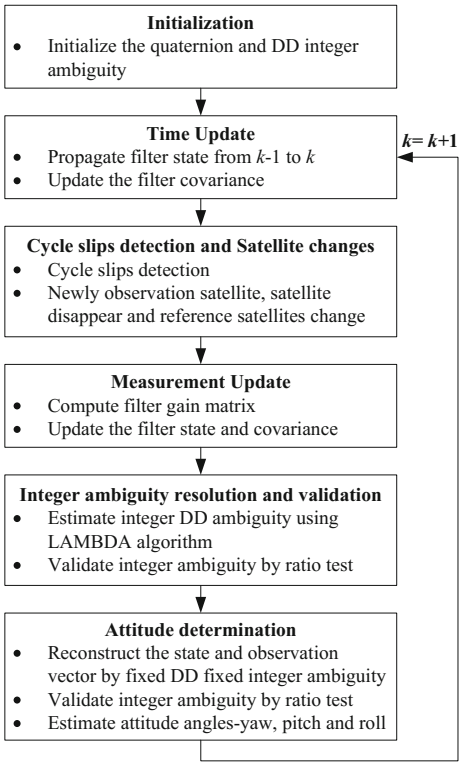

Fig. 1 The workflow of the proposed method

$$\hat{\boldsymbol{x}}_0 = E[\boldsymbol{x}_0], \boldsymbol{P}_0 = E\left[(\boldsymbol{x}_0 - \hat{\boldsymbol{x}}_0)(\boldsymbol{x}_0 - \hat{\boldsymbol{x}}_0)^T\right] \tag{40}$$

- Constructing the measurement model

At each epoch, the reference satellite and common tracking satellites for the baselines are obtained by Single Point Positioning. Then, the DD carrier phase can be calculated to construct measurement vector by Eq. (14).

- Cycle slip detection

Once the correct integer ambiguity vector is fixed, it can be used permanently until cycle slip occurrence. Thus the cycle slip detection is of importance to the attitude determination. We use the distance between the time-update DD float ambiguity $\widehat{\boldsymbol{N}}_{k,k-1}^{\vartheta i}$ and the $\boldsymbol{N}_{iM}^{\vartheta j}$ estimated by applying Eq. (41) to detect cycle slip as follows:

$$\left|\boldsymbol{N}_{iM}^{\vartheta j} - \widehat{\boldsymbol{N}}_{iM,k/k-1}^{\vartheta j}\right| > \zeta \tag{41}$$

where the ζ is the an empirical threshold, which is set to 3 [21]. If the distance value is larger than ζ, we deduce that a cycle slip occurred to the corresponding satellite and some operation will be implemented to repair it.

- Float ambiguity resolution by the SKF

When the observation vector and state vector have been constructed, the SKF is utilized to get high accuracy float solutions in which the filter contains time-update and measurement-update stages.

- Integer ambiguity resolution and validation

To exploit the full accuracy of the carrier phase observations, the filter has furthermore been supplemented with integer ambiguities. The most appropriate integer vector $\breve{\boldsymbol{N}}$ for the integer ambiguities is obtained by solving an ILS (integer least square) problem expressed as

$$\breve{\boldsymbol{N}} = \arg\min_{\mathbf{N}\in\mathbb{Z}^n} \left\|\boldsymbol{N} - \widehat{\boldsymbol{N}}_k\right\|^2_{\boldsymbol{Q}_{NN}} \tag{42}$$

A well-known efficient search strategy LAMBDA and its extension MLAMBDA are employed to solve the ILS problem. LAMBDA and MLAMBDA offer the combination of a linear transformation to shrink the integer vector search space and a skillful tree-search procedure in the transformed space [22]. Then the ratio test is used to test the reliability of the integer ambiguities [23].

- Attitude estimation

The correct DD ambiguity will be used to reconstruct the state and the observation equation. Then the high accuracy quaternion can be obtained by restarting SKF. The attitude yaw, pitch, and roll angles will be got via Eqs. (7) and (8).

4 Experimental Testing

In order to assess the performance of the proposed algorithm, a test is carried out for a platform in this section. Three antennas and GNSS receivers with the same performance are installed on the platform at Beihang university. The experimental configuration is depicted in Fig. 2. The single-frequency GNSS data are collected using the GNSS receivers M300, which are manufactured by ComNav company of China, with the sample interval of 1 s.

As illustrated in Fig. 2, the antenna $A1$ is the master antenna, and $A2$ and $A3$ are the slave antennas. The install matrix of the three antennas configuration is determined from the whole observation data with 5 mm accuracy and is given as follows:

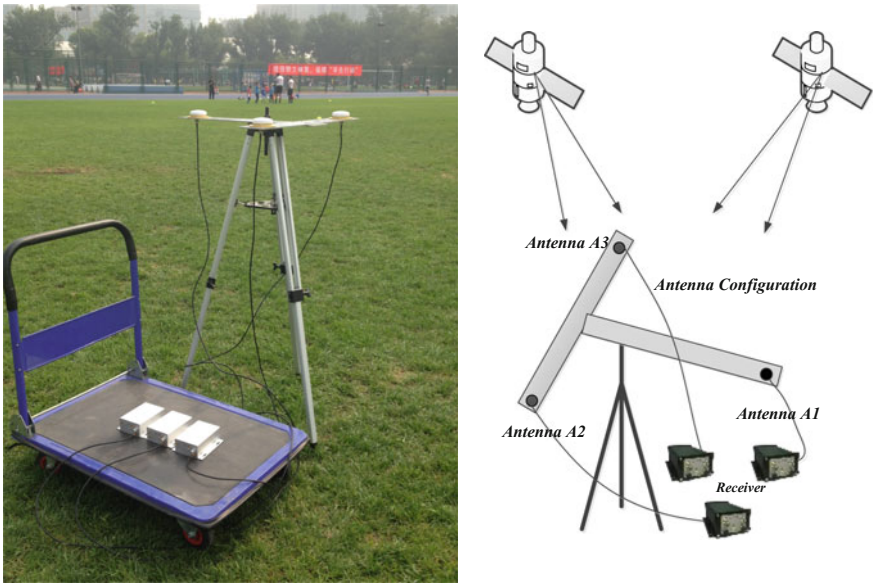

Fig. 2 The BDS measurement experiment

$$\boldsymbol{B} = \begin{bmatrix} 0.5101 & 0.2930 \\ 0 & 0.4935 \\ 0 & 0 \end{bmatrix} \tag{43}$$

A 1106 s dataset referring to August 29, 2015 starting from 11:28:17.000 UTC to 11:46:42.000 UTC has been provided. 9 BDS satellites and 8 GPS satellites are tracked in our experiment. The number of common tracking satellites ranges from 15 to 17. The BDS, GPS and GNSS (GPS + BDS) data will be used to make an analysis, respectively. After obtaining the float ambiguity by KF or SKF, integer ambiguities are resolved by the LAMBDA algorithm. For analysis of the performance of the proposed methods, we compare the correct integer ambiguity vector (the 'correct solution' estimated from post-processing with real data) and the estimated integer ambiguity vector at every epoch.

In this test, Time-To-Fix (TTF) is defined as the number of measurement epochs required to firstly fix the ambiguity. We define the empirical success rate as the ratio of the number of epochs with all correctly fixed ambiguity to the total epoch number as follows:

$$P = n_{cor}/n_{tot} \times 100\% \tag{44}$$

where n_{cor} and n_{tot} are the number of computations with all ambiguities being correctly fixed and the number of total computations.

The summary success rate and TTF of fixed ambiguity for the SKF and KF with the LAMBDA is given as Table 1.

Table 1 shows the success rate and TTF of the ambiguity resolution for two baselines with SKF or KF method. With the SKF, the success rate and TTF of the ambiguity resolution present higher performance than the full-order KF for BDS, GPS and GNSS. Note that the success rates and the ratio number for the baseline 2 are higher than those for the baseline 1 when employing the LAMBDA method. This is due to the more tracking GNSS satellites of the baseline 2 than the baseline 1. As expected, the SKF substantially affects the capacity of fixing the correct integer ambiguity vector. A benefit of the SKF is that it decouples the attitude parameters and the colored observation noise to only consider the attitude parameters. Then the accuracy of the float ambiguity is improved and the solutions are stabilized.

Table 1 also shows there is no big difference between BDS and GPS. When combining GPS and BDS, the success rate is much higher than either single constellation and the TTF is much lower than either single constellation. This improvement shows that the GPS + BDS combination provides the higher availability of satellites to improve the accuracy of float ambiguity and therefore increase the success rate of ambiguity resolution.

After getting fixed ambiguity, the state equation and the measurement equation of the SKF will be reconstructed using the fixed correct ambiguity vector. Then high-precision quaternion can be obtained by restarting the SKF filter.

Figure 3 describes the quaternion $\bar{\boldsymbol{q}}$ with correctly fixed ambiguity. Because there is no big difference for quaternion with different method and constellation, it could not be described in the same figure. Therefore, the statistic characteristics of quaternion are given and listed in Table 2.

Table 2 shows the quaternion performance of the correctly fixed solutions for different method and constellation.

As we can see from the Table 2, the accuracy of Quaternion with the SKF is much better than the full-order KF for BDS, GPS and GPS + BDS. Due to decoupling the attitude parameters and the colored observation noise, high accuracy of the quaternion can be also achieved. Some conclusion can be obtained that the SKF can achieve much more efficiency than the full-order KF for integer ambiguity resolution and attitude determination with GNSS.

Table 1 The success rate and TTF of fixed ambiguity

Success rate		SKF		KF	
		Success rate (%)	TTF/s	Success rate (%)	TTF/s
Baseline1 A1–A2	BDS	99.49	5	94.94	28
	GPS	99.73	3	97.65	26
	GNSS	99.9	1	98.55	16
Baseline2 A1–A3	BDS	99.82	2	95.04	25
	GPS	99.73	3	95.04	25
	GNSS	99.9	1	98.64	15

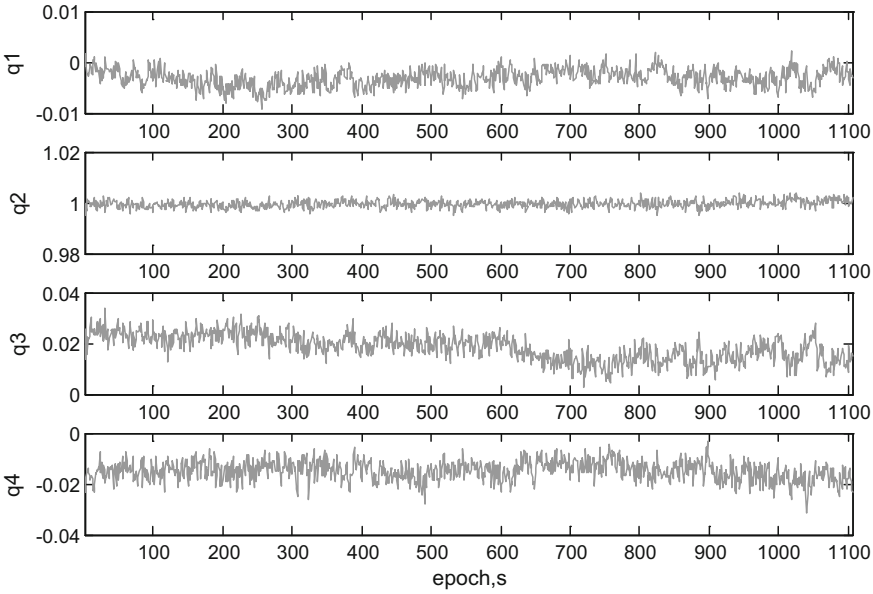

Fig. 3 The quaternion of the SKF with GPS + BDS

Table 2 The statistic characteristics of quaternion

Quaternion	SKF			KF		
	BDS	GPS	GNSS	BDS	GPS	GNSS
q1	0.0012	0.0012	0.001	0.0016	0.0015	0.0014
q2	0.0016	0.0013	0.0011	0.0017	0.0017	0.0015
q3	0.0039	0.0040	0.0035	0.0041	0.0038	0.0036
q4	0.0041	0.0038	0.0031	0.0042	0.0041	0.0037

Then, the Eqs. (7) and (8) are utilized to get yaw (ψ), pitch (θ) and roll (φ) angles. In order to analyze the performance of attitude angles, the epochs of the unfixed ambiguity are replaced by the correct ambiguity. In this case, the three attitude angles are characterized by standard deviations (Std). To assess the accuracy of this method, the QUEST algorithm was used to estimate attitude angles.

Figure 4 demonstrates that the value of yaw (ψ), pitch (θ), and roll (φ) angles with interval of 1 s. Because there is no bigger difference of the accuracy between SKF and full order KF for BDS, GPS and GPS + BDS, we cannot make difference use the same figure. So the Fig. 4 just concludes the attitude estimate with SKF and QUEST algorithm for GPS + BDS. The angles estimated with QUEST and SKF are described with the dotted line and solid line, respectively. The accuracy of the total attitude solutions is provided in Table 3.

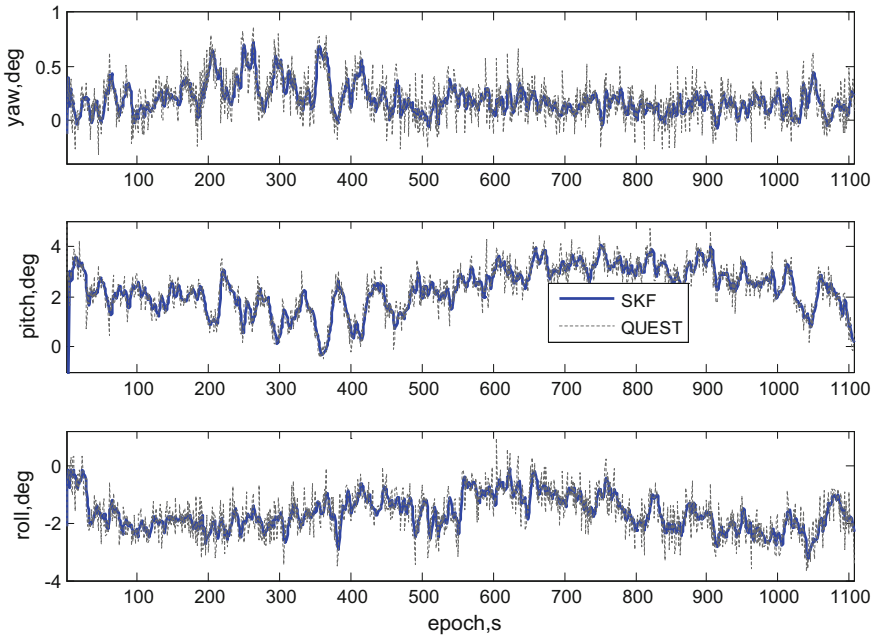

Fig. 4 The performance of yaw, pitch and roll angles with GPS + BDS

Table 3 The standard deviations of the attitude angle

Attitude	SKF			KF			QUEST
	BDS	GPS	GNSS	BDS	GPS	GNSS	
Yaw	0.1837	0.1831	0.1609	0.2046	0.1902	0.1721	0.2266
Pitch	0.5836	0.5766	0.5585	0.6039	0.5966	0.5786	0.6579
Roll	0.4244	0.424	0.4002	0.4548	0.441	0.4212	0.5527

From the Std in Table 3, the yaw angle is estimated with the highest precision, whereas the pitch estimation is characterized by the highest noise levels for both the SKF and the QUEST for BDS, GPS and GPS + BDS. According to the achieved performance of quaternion, the SKF can be got more accuracy of attitude angles than the full order KF. Moreover, the SKF and the full order KF have more superior performance than the QUEST for per-axis attitude angles. The higher precision of the yaw angle is due to the intrinsic characteristic of the GNSS working principle: the satellites cover, with respect to the receiver, only a hemisphere, causing higher dilution of precision in the vertical plane than in the horizontal plane.

5 Conclusions

In this paper, the SKF for GNSS-based attitude determination has been presented to float ambiguity resolution and attitude estimation. The geometry information of the antenna configuration is fully exploited for ambiguity resolution via formulating the direct functional relationship between double-differenced carrier phase measurements and attitude quaternions. By using the SKF, the attitude parameters and the colored observation noise can be decoupled in the state equation. The higher accuracy of attitude angles and float ambiguity vector with only considering attitude parameters can be achieved than the full order KF. The performance of the proposed method has been assessed by an actual GNSS experiment test. Results demonstrated that the higher success rate and the less Time-to-Fix ambiguity resolution are achievable than the current method for BDS, GPS and GPS + BDS. The distribution of the available GNSS satellites has an influence on the accuracy of attitude angles. The proposed method has better accuracy than the full order KF and the QUEST algorithm for BDS, GPS and GPS + BDS. The GPS + BDS combination have better performance than single BDS or GPS constellation, and there is no big difference between GPS and BDS for attitude resolution.

References

1. Axelrad P, Behre CP (1997) Attitude estimation algorithms for spinning satellites using global positioning system phase data. J Guid Control Dynam 20(1):164–169
2. Buist PJ, Teunissen PJG, Verhagen S, Giorgi G (2011) A vectorial bootstrapping approach for integrated GNSS-based relative positioning and attitude determination of spacecraft. Acta Astronaut 68(7):1113–1125
3. Buist PJ (2013) Multi-platform integrated positioning and attitude determination using GNSS. Ph.D. thesis. Delft University of Technology
4. Chiang K, Psiaki M, Powell S, Miceli R, O'Hanlon B (2014) GPS-based attitude determination for a spinning rocket. IEEE Trans Aerosp Electron Syst 50(4):2654–2663
5. Giorgi G, Teunissen PJG, Verhagen S, Buist PJ (2012) Instantaneous ambiguity resolution in global-navigation-satellite-system-based attitude determination applications: a multivariate constrained approach. J Guid Control Dynam 35(1):51–67
6. Giorgi G, Teunissen PJG, Verhagen S (2010) Testing a new multivariate GNSS carrier phase attitude determination method for remote sensing platforms. Adv Space Res 46(2):118–129
7. Madsen J, Lightsey EG (2004) Spacecraft attitude determination using global positioning system receivers. J Space Rockets 41(4):635–643
8. Unwin M, Purivigraipong P, da Silva Curiel A (2002) Stand-alone spacecraft attitude determination using real flight GPS data from UOSAT-12. Acta Astronaut 51(1):261–268
9. Bar-Itzhack IY, Montgomery P, Garrick J (1998) Algorithm for attitude determination using global positioning system. J Guid Control Dynam 21(6):846–852
10. Wahba G (1965) A least squares estimate of spacecraft attitude. SUM Review 7(3):409
11. Buist PJ (2007) The baseline constrained LAMBDA method for single epoch, single frequency attitude determination applications. In: Proceedings of ION GPS-2007, pp 2962–2973
12. Giorgi G, Teunissen PJG, Buist PJ (2008) A search and shrink approach for the baseline constrained LAMBDA: experimental results. In: Proceedings of the international symposium on GPS/GNSS

13. Teunissen PJG (2010) Integer least-squares theory for the GNSS compass. J Geod 84(7):433–447
14. Chen W, Qin H (2011) New method for single epoch, single frequency land vehicle attitude determination using low-end GPS receiver. GPS Solut 16(3):329–338
15. Teunissen PJG, Giorgi G (2011) Testing of a new single frequency GNSS carrier phase attitude determination method: land, ship and aircraft experiments. GPS Solut 15(1):15–28
16. Wang B, Miao LJ, Wang ST, Shen J (2009) A constrained LAMBDA method for GPS attitude determination. GPS Solut 13(13):97–107
17. Cheng J, Wang J, Zhao L (2014) A direct attitude determination approach based on GPS double-difference carrier phase measurements. J Appl Math 2014(1):1–6
18. Qin H, Chen W (2013) Application of the constrained moving horizon estimation method for the ultra-short baseline attitude determination. Acta Geod Geophys 48(1):27–38
19. Simon D (2006) Optimal state estimation: Kalman, H infinity, and nonlinear approaches. Wiley, Hoboken, New Jersey
20. Stauch J, Jah M (2015) Unscented Schmidt-Kalman filter algorithm. J Guid Control Dynam 38(1):117–123. https://doi.org/10.2514/1.G000467
21. Realini E, Reguzzoni M (2013) goGPS: open source software for enhancing the accuracy of low-cost receivers by single-frequency relative kinematic positioning. Meas Sci Technol 25 (11)
22. Verhagen S, Li B (2012) LAMBDA software package: Matlab implementation, version 3.0. Delft University of Technology and Curtin University, Perth, Australia
23. Verhagen S (2004) Integer ambiguity validation: an open problem? GPS Solut 8(1):36–43

Realization of Embedded RTK System and Performance Evaluation

Qingjiang Wang, Qinan Zhi, Pengfei Liu and Guoju Ma

Abstract High precision mobile mapping system has become an effective method for solving the data acquisition problem and the high precision position system is the key part of the mobile mapping system. In this paper, an embedded real-time RTK system is realized based on the FPGA and DSP architecture. The designation and realization of the hardware and the RTK algorithm are introduced in detail. The performance of the embedded RTK system was evaluated in open condition and typical complex urban conditions with 3G/4G method to transmit the differential correction datas. Results show the lagging time for most of the differential correction data is within 10 s in typical urban condition. The positioning precision of the single system and GPS/BDS system is also compared and it is showed that the GPS/BDS positioning method can effectively improve the visible satellite number and the positioning precision is much higher that single system. The positioning precision for the GPS/BDS system is better than 5 cm which can satisfy the requirement of the mobile mapping system.

Keywords RTK · Mobile mapping system · Real time

1 Introduction

Satellite navigation and positioning system occupies an important position in the national economic construction and national defense safety and is an important component and driving force for the information construction of the national economy [1]. It is a key technology platform directly related to national security and economic development [2, 3]. Beidou satellite navigation system is China's satellite

Q. Wang (✉) · Q. Zhi · P. Liu · G. Ma
The 54th Research Institute of CETC, Shijiazhuang 050500, China
e-mail: wangqjwhu@whu.edu.cn

Q. Wang · P. Liu · G. Ma
State Key Laboratory of Satellite Navigation System and Equipment Technology, Shijiazhuang 050500, China

J. Sun et al. (eds.), *China Satellite Navigation Conference (CSNC) 2018 Proceedings*, Lecture Notes in Electrical Engineering 498,
https://doi.org/10.1007/978-981-13-0014-1_52

navigation system that independently focuses on national security and economic and social development needs and operates independently.

With the continuous development of the concept of "digital city" and the concept of "digital earth", the process of digitization of the Earth's cities in our cities has been accelerating rapidly. However, the restriction of acquiring and updating of spatial information data based on mapping technology is becoming increasingly obvious. In this demand, MMS (Mobile Measurement System) came into being and becomes a typical representative of the new mapping technology [4, 5]. Nowadays with the development of laser measurement technology, GPS technology, inertial navigation technology and CCD technology, the multi-sensor integrated on-board 3D mobile measurement system has become the necessary complement to the earth observation technology [6, 7].

As a high-accuracy position, velocity and time measuring device, GNSS high-precision receiver is one of the key components in mobile measurement system. It is combined with measurement sensors such as inertial navigation system, CCD camera, laser radar and panoramic camera and loaded in the mapping car on the high-speed mobile state to complete the measurement and geographic information collection. The accuracy of the position, velocity and time information provided by the GNSS high-precision receiver is the time and space reference of the data processing of each measurement sensor, which is the basis for ensuring the accuracy of the mobile measurement data.

In this paper, a RTK system is designed and implemented using FPGA + DSP architecture. The RTK mathematical model of BDS/GPS dual system is researched and established. The BDS tri-frequency RTK mathematical model is established. The algorithm and system performance are tested by van test. It shows that BDS/GPS dual system can effectively increase the number of visible satellites in typical urban scenario. The dual system real-time navigation accuracy can achieve 5 cm in both horizontal and vertical direction, which can meet the needs of mobile mapping technology in urban scenes. It shows that BDS/GPS dual system can effectively increase the number of visible satellites in a typical urban scenario. The dual system real-time navigation accuracy can achieve horizontal and vertical accuracy of 5 cm, which can meet the needs of mobile mapping technology in urban scenes.

2 Designation

2.1 Overall Designation

The entire RTK system consists of a GNSS base receiver, a GNSS rover receiver, a data processing solution module, and a 3G/4G data transfer module. The data is processed using FPGA + DSP architecture. After FPGA receives the raw data of the base station and rover, it can be output to the computer through the serial port for saving. Afterwards, the FPGA analyzes the differential data of the base station to

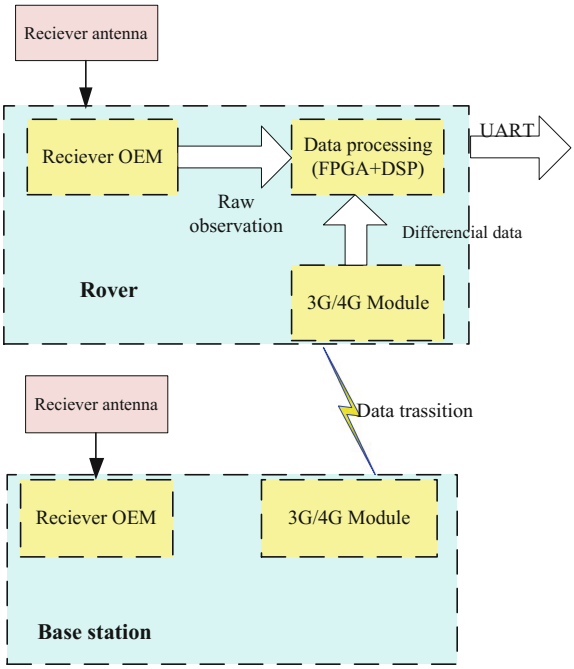

Fig. 1 System block diagram of the RTK

the DSP for RTK calculation. After finishing the RTK navigation solution, the DSP outputs the navigation results to the laptop through the UART serial port for saving. The whole system block diagram is shown as Fig. 1.

2.2 Differential Data Transmission Scheme

Conventional stations transmit differential data and require no obstructions between the base station and the rover and require direct transmission path. However, in complex urban environments, data transmission may be affected due to obstructions such as trees, high buildings and tunnels resulting in delayed base differential correction data, affecting real-time RTK positioning accuracy. At present, 3G/4G has been covered in most scenarios, so using 3G/4G transmission can effectively reduce the differential data delay time. In the process of data transmission, the mobile station and the rover are connected to the 3G/4G network through the network device, and after the fixed IP address is obtained, a data communication link is established between the base station and the rover to transmit the check correction data to the Rover.

3 Algorithm Design

3.1 Beidou/GPS Combination RTK Mathematical Model

The use of GPS and BDS dual system RTK joint solution in complex scenes such as cities can effectively increase the number of visible satellites and increase the system availability and navigation accuracy. Therefore, we need to establish BDS/GPS joint RTK positioning mathematical model.

BDS/GPS dual system combined RTK basic mathematical model is consistent with the single-system mathematical model, due to the GPS system and the Beidou system frequency is inconsistent so the receiver clock is inconsistent so the formation of double-difference equation requires the GPS system and Beidou system each have a reference satellite. When the number of visible satellites in two systems is n, n − 2 carrier phase double difference equations can be formed. The noise matrix corresponding to the observed values is also listed separately according to GPS system and Beidou system, which can be expressed as:

$$\boldsymbol{P} = \begin{bmatrix} \boldsymbol{P}_{GPS} & 0 \\ 0 & \boldsymbol{P}_{BDS} \end{bmatrix}$$

In this paper, satellite altitude angle-dependent sine function model weight:

$$R_i^2 = a^2 + b^2 / \sin^2(\theta)$$

Where, the variance of the observed noise representing the *i*-th satellite θ represents the altitude of the satellite. The values of a and b are generally set according to the experience value, which are taken as 5 mm in this paper, and the weight matrix corresponding to the double difference observation equation can be calculated according to the noise variance.

The specific process of BDS/GPS dual system combined RTK solution is as follows:

(1) Iteratively calculate the coordinates of the observed satellites using the observation data of the reference station. The coordinates of the rover station are obtained using the pseudoranges and double difference observations. The coordinates of the rover station are calculated using GPS and BDS double system data.
(2) Wide-lane ambiguity is calculated by using Melborne-Wubbena combination, in which the observations of M-W combination are as follows:

$$\lambda_{WL} N_{WL} = \frac{f_{L1} P_{L1} + f_{L2} P_{L2}}{f_{L1} + f_{L2}} - \lambda_{WL} \varphi_{WL}$$

Where, f_{L1} and f_{L2} are the frequencies of L1 and L2, respectively, $P_{L1}P_{L2}$ are the pseudorange observations; λ_{WL} is the wide-band combined wavelength; φ_{WL} is the wide-alley combined observation and φ_{WL} is the wide-alley combined ambiguity.

(3) After calculating the pseudorange of dual system and the observation equation of wide-lane of carrier phase, the floating-point solution of ambiguous wide-lane ambiguity and the corresponding covariance matrix of ambiguity are obtained by the least-squares method.
(4) After calculating the fixed solution of wide-lane ambiguity, we can establish the double-difference observation equation of wide lane and L1, L2, and then use LAMBDA method to fix the ambiguity of each system L1 as a whole, and then obtain the ambiguity of L2 according to the relationship.
(5) The method for determining the degree of ambiguity is the same as the method for determining the single system. It is worth to be clarified by comparing the ratio values of the residual values after the adjustment. It is worth noting that the fixed threshold of the ambiguity of the two systems can be reduced appropriately to 2.0.

3.2 Compass Tri-band RTK Positioning Algorithm

At present, GNSS has a wide range of applications for high-precision and rapid dynamic positioning, and the fast dynamic ambiguity solution is the key to high-precision positioning. Considering that China's BDS satellite navigation system has already started to broadcast three carrier signals at frequencies of B1 (1561.098 MHz), B2 (1207.140 MHz) and B3 (1268.520 MHz) respectively. The use of tri-band carrier signal can improve the success rate and reliability of ambiguity resolution, which is particularly important for real-time precision positioning.

The algorithm can be divided into three steps:

1. Firstly, a joint observation equation is constructed by using pseudo-range observation values of B1, B2, and B3 and wide-lane observation value $\varphi(0,-1,1)$, and the floating point solution of the ultra—using LAMBDA method to determine the ambiguity of ultra wide lane. And restore the observation of ultra-wide lane.
2. Construct the joint observation equation by using the observation data of the ultra-wide lane determined in step (1) and the observation data of wide alley $\varphi(1,-1,0)$ and calculate the wide-lane ambiguity $\mathrm{N}(1,-1,0)$ the ambiguity of wide lane is determined by LAMBDA method, $\mathrm{N}(1,-1,0)$ and another wide lane ambiguity $\mathrm{N}(0,-1,1)$.
3. Using the reconstructed two wide-lane observation values $\varphi(1,-1,0)$ and $\varphi(1,0,-1)$ and $\varphi 1$ to make a joint observation equation, the original ambiguity Floating point solution, fixed N1 ambiguity determined N2, N3 ambiguity.

4 Tests and Results

4.1 Test Description

To test the performance of real-time RTK algorithms, real-time RTK performance testing was conducted in Shijiazhuang on August 2, 2017. The van test takes about 1 h. Most of the test scenes are open scenes, covering a small part of the occlusion scene. The base coordinates are accurately known. The base station data is broadcasted through the 3G/4G moduler over received the correction data through the 3G/4G module for and real-time RTK solution. The baseline length is within 15 km. During the test, the raw data for the base and rover were saved for post-processing as reference data for real-time RTK results.

During the test, two rover receivers were equipped, and the rover receivers were respectively configured as BDS triple-frequency single-system working mode and BDS/GPS dual-system working mode. Test base is shown in Fig. 2.

4.2 Test Result

After the test, the commercial software IE (Inertial Explorer) reverse smooth result is used as a reference.

Sports car test track shown in Fig. 3.

The number of visible satellites is shown in Fig. 4. It can be seen from the figure that most of the visible stars in the BDS satellite system can have 5–10 visible satellites, while most of the visible satellites for the BDS/GPS dual system is 10–19, and visible number of stars significantly more than single-system. It can be seen that the dual system can effectively increase the number of visible satellites and improve the geometry of the satellite.

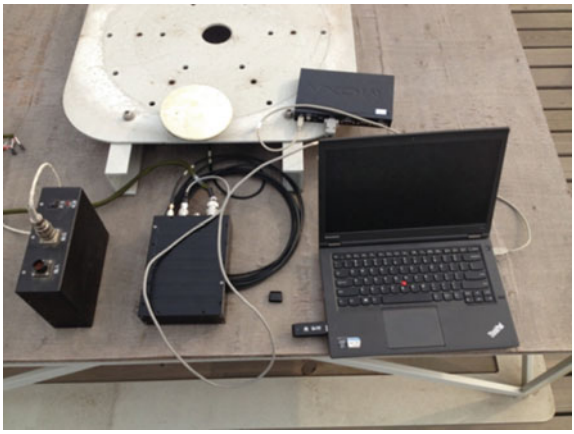

Fig. 2 Figure of base station

Fig. 3 Van test track

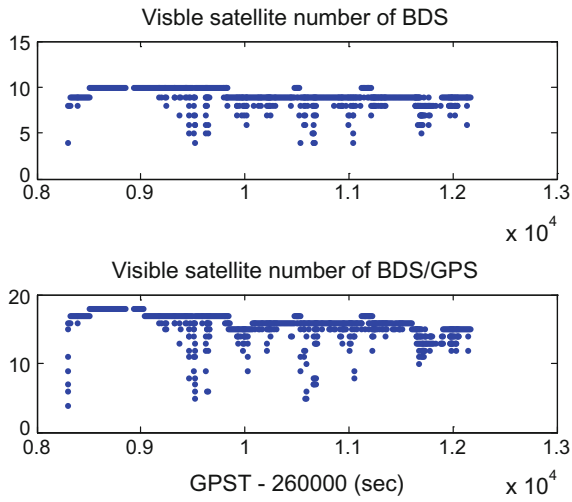

Fig. 4 Visible satellite number in van test

The differential time between the base and rover is also a key factor affecting the positioning accuracy, which cannot be guaranteed due to the blockage of tall buildings, trees and tunnels in urban scenes, so the radio station cannot guarantee Data transmission continuity between base and rover. The testing process uses 3G/4G module transmission, Fig. 5 shows the base station differential data delay time can be seen from the figure most of the data delay time within 10 s, only a very few part of the time is greater than ten seconds, and the test results It shows that even if the data delay time is more than 10 s, stable and reliable RTK solution can be obtained. The test results show that using 3G/4G method in real-time urban complex scenarios can ensure the stability and real-time performance of real-time RTK system for differential correction data.

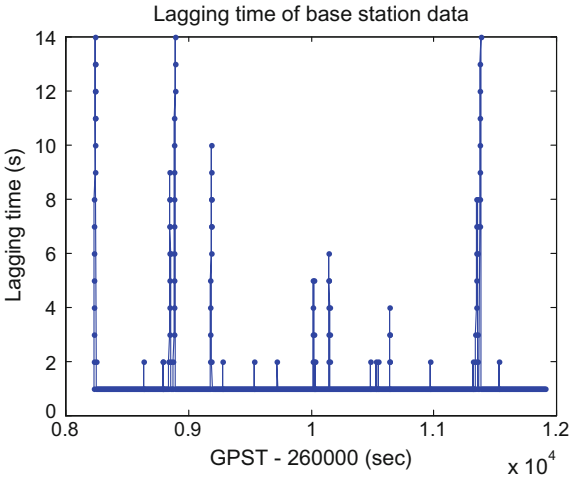

Fig. 5 Lagging time of base station data

Figure 6 give the results of BDS system tri-frequency positioning error and the dual positioning system of BDS/GPS respectively. It can be seen from Fig. 6 that the error of horizontal accuracy of the BDS tri-frequency positioning error is within 0.1 m and the vertical error is within 0.2 m. It can also be seen from Fig. 6 that the BDS/GPS dual system positioning accuracy in east, north and vertical are within 0.1 m. In order to further evaluate the BDS tri-frequency precision and BDS/GPS joint resolution accuracy, the positioning results were error statistics, the statistical

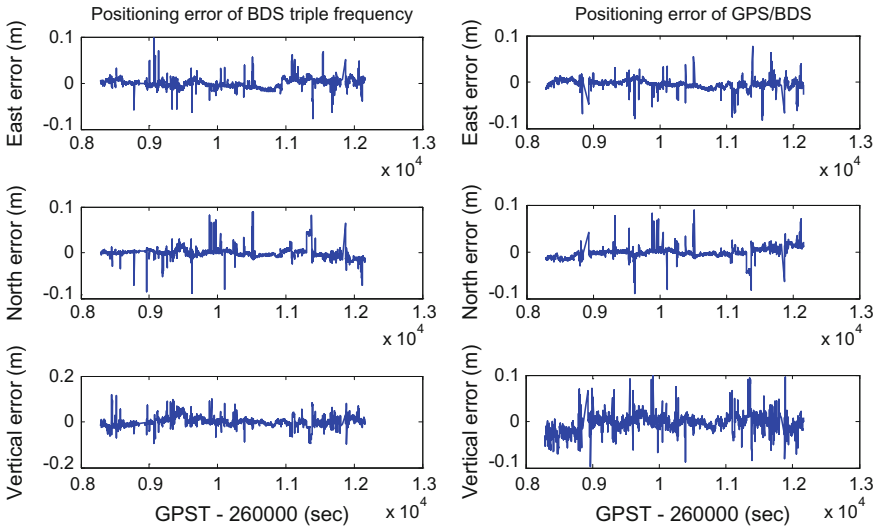

Fig. 6 Positioning error with BDS triple frequency and with BDS/GPS system

Table 1 Errors of positioning

定位模式	平均值 (cm)			RMS (cm)		
	E	N	U	E	N	U
北斗三频	0.03	0.08	0.05	1.61	1.81	2.32
北斗/GPS	0.02	0.03	0.04	0.92	1.33	1.64

results shown in Table 1. It can be seen from Table 1 that the RMS errors of the BDS tri-frequency positioning results in the three directions of east, north and vertical are 1.61, 1.81 and 2.32 cm, respectively. The RMS of BDS/GPS positioning error in east, north, and vertical direction followed by 0.92, 1.33 and 1.64 cm, the positioning result is better than BDS single system. The test results show that the 3D positioning accuracy of 5 cm can be achieved no matter whether the BDS single system or the BDS/GPS dual system is used. This positioning result can effectively meet the positioning accuracy requirements of mobile surveying vehicles in urban scenes.

5 Conclusion

This article designed and implemented a real-time BDS/GPS dual system RTK system. The establishment and realization of the BDS/GPS dual system joint positioning and the mathematical model of the BDS tri-band are carried out by programming and implemented in the embedded system. Test real-time RTK system performance with actual sports car tests. The test process uses 3G/4G module to transmit differential correction data in real time. The experimental results show that the transmission delay of 3G/4G module can meet the solution requirements of real-time RTK within 10 s in most typical scenarios. The test results show that the commercial software as a reference, the use of BDStri-frequency positioning and BDS/GPS can achieve the positioning accuracy of 5 cm, which verifies the correctness of the system and algorithm.

References

1. Wang H (2013) GPS navigation: principles and applications. Sci Press 2003(8):258–265
2. Kapland H (2012) Understanding GPS principles and applications (trans: Kou Y). Electronic Industry Press, Beijing (8): 130–134
3. Yan X, Cai B, Ning B, Wei S (2014) An autonomous positioning algorithm for GPS/INS deep-coupled train based on vector tracking. J China Railway Soc 1:63–65
4. Dong X, Sun X (2010) GPS/INS ultra-tight coupling method and its application analysis telemetry remote control 9 (6): 7–8; Giorgi G (2012) Instantaneous global navigation satellite system (GNSS)-based attitude determination for maritime applications. Oceanic Eng, IEEE J

5. Giorgi G, Teunissen PJG, Gourlay TP (2012) Instantaneous global navigation satellite system (GNSS)-based attitude determination for maritime applications. IEEE J Oceanic Eng 37 (3):348–362
6. Song G, Wang C, Xi F, Zhang A (2012) The performance of tracking loop filter for software GPS receiver simulation analysis, IEEE
7. Song Y, Li X, Yang Y, Liu L (2011) Enhanced full bit acquisition algorithm for software GPS receiver in weak signal environment. In: International conference on computational problem-solving (ICCP)

A Precise Regional Ionospheric Model Was Established Based on GNSS Technique

Liang Chen and Hailin Guo

Abstract Ionospheric delay is an important source of error in the positioning of the Global Navigation Satellite System (GNSS). In the case of active ionosphere, the ionospheric delay can be over 100 m, which has a great impact on the positioning accuracy of single-frequency GNSS users. At present, ionospheric observations based on dual-frequency carrier phase smoothed pseudorange are frequently used to estimate the ionospheric model, however, the ionospheric observations are susceptible to the precision of the pseudorange, the length of the smoothing arc and the multipath, which affect the accuracy of the estimated ionospheric model. In this paper, the UofC model of the precise point positioning is proposed for estimating carrier phase ambiguity to obtain high precision ionospheric observations. The IGS global tracking network data are combined to solve the problem of strong correlation in differential code bias (DCB) of the regional station receivers. A regional ionospheric model based on satellites was established considering the precision loss of the fitting of the ionospheric single-layer model in small area. The results show that the single-frequency pseudorange positioning based on the regional ionospheric model estimated in this paper are better than the positioning results based on IGS global ionospheric map (GIM).

Keywords Global positioning system (GPS) · Precise point positioning (PPP) UofC · Regional ionospheric model

1 Introduction

Ionospheric delay plays an important role in navigation and positioning, space atmosphere, signal propagation and other fields. The value and variation of ionospheric delay are closely related to the total electronic content (TEC) distribution in

L. Chen (✉) · H. Guo
GNSS Research Center of Wuhan University, Wuhan 430079, China
e-mail: chenliangchn@whu.edu.cn

H. Guo
e-mail: hailing@whu.edu.cn

J. Sun et al. (eds.), *China Satellite Navigation Conference (CSNC) 2018 Proceedings*, Lecture Notes in Electrical Engineering 498,
https://doi.org/10.1007/978-981-13-0014-1_53

the ionosphere space. Therefore, obtaining highly accurate TEC distribution is a hotspot in the field of ionospheric research. Using GNSS technology to estimate TEC and ionospheric delay model, is an effective method to monitor ionospheric variations and correct ionospheric delay errors.

Much progress has been made in the development of ionospheric models using GNSS at home and abroad. Georgiadou and Kleusberg [1] established a regional ionospheric model by using dual-frequency observation data and applied it to ionospheric correction of baseline. Lanyi [2] used polynomials to fit the ionospheric delay and compared it to ionospheric delay values obtained by other methods. Mannucci et al. [3] proposed a triangular grid interpolation method to establish the global ionospheric model. Wilson and Mannucci [4] put forward spherical harmonics function and triangular grid interpolation to estimate ionospheric model and DCB. Schaer [5] used the dual-frequency GPS observations to extract TEC, and forecast and analyze its changing trends and laws. In 1998, the IGS organization established the ionospheric working group to continuously monitor ionospheric changes and provide daily GIM products, the standard deviation is 2–8 TECU. Feltens [6] summarized the main activities since ionospheric working group had established. Komjathy and Herna´ndez-Pajares [7] summarized status of previous GIMs and perspective for the future. Recently, Herna´ndez-Pajares et al. [8] has given an overview of how GIMs are generated, overall validation with TOPEX/JASON, and evolution trends of VTEC during near one Solar Cycle.

At present, there are few studies of ionospheric modeling in a small area where the ionosphere is very active. Based on the establishment of the ionospheric delay model in Hongkong. This paper proposes a method to extract the slant TEC information by using UofC model of PPP. The IGS global tracking network data are combined to solve the problem of strong correlation in DCB of the regional station receivers. A regional ionospheric model based on satellites was established considering the precision loss of fitting of the single-layer model in a small area. The accuracy of single-frequency pseudorange positioning based on the regional ionospheric model estimated in this paper is 0.4 m.

2 Establishment of Regional Ionosphere Model Based on GNSS

2.1 Extraction of Ionospheric Observations Based on UofC Model

Due to the dispersion of the ionosphere, the ionospheric effects on pseudorange and carrier phase observations at different frequencies are different. Ionospheric observations is obtained by differencing the observed values of different frequencies:

$$\begin{aligned} P_{k,4}^{i} &= P_{k,1}^{i} - P_{k,2}^{i} = \frac{A}{f_1^2} - \frac{A}{f_2^2} - \left(\left(b_1^s - b_1^r\right) - \left(b_2^s - b_2^r\right)\right) \\ L_{k,4}^{i} &= L_{k,1}^{i} - L_{k,2}^{i} = \frac{A}{f_2^2} - \frac{A}{f_1^2} - (N_2 - N_1) \end{aligned} \tag{1}$$

In the above formula, i represents the satellite, k represents the station, P, L represent the pseudorange and carrier phase observation, f is the frequency, A is the slant ionospheric delay, b^s, b^r represent the satellite and receiver DCB; N is the integer ambiguity. We usually calculate the ionospheric TEC by using carrier phase smoothing pseudorange method, as follows:

$$A = (\overset{\wedge}{P_{k,4}^{i}} + (b_1^s - b_1^r) - (b_2^s - b_2^r))/(\frac{1}{f_1^2} - \frac{1}{f_2^2}) \tag{2}$$

In the above formula, $\overset{\wedge}{P_{k,4}^{i}}$ is the pseudorange observation smoothed by carrier phase, other symbols are the same as formula (1). Although the phase smoothing pseudorange method can reduce the influence of pseudorange noise and multipath error, the accuracy of the ionospheric observations is low when satellite appears. Therefore, we can consider the PPP method to estimate the ionospheric delay. The PPP method can calculate the carrier phase ambiguities faster and more accurately by using the known star-ground distance as the constraint condition. In this paper, UofC model is presented [9]:

$$\begin{aligned} \mathrm{P}_{IF,1} &= 0.5(\mathrm{P}_1 + \phi_1) = \rho + \mathrm{dx} - \mathrm{C}\cdot\mathrm{dt} + \mathrm{m}\cdot\mathrm{d}_{trop} + 0.5\cdot(\mathrm{N}_1 + b_1^s - b_1^r) + \varepsilon_{P_{IF,1}} \\ \mathrm{P}_{IF,2} &= 0.5(\mathrm{P}_2 + \phi_2) = \rho + \mathrm{dx} - \mathrm{C}\cdot\mathrm{dt} + \mathrm{m}\cdot\mathrm{d}_{trop} + 0.5\cdot(\mathrm{N}_2 + b_2^s - b_2^r) + \varepsilon_{P_{IF,1}} \\ \phi_{IF} &= \frac{f_1^2\phi_1 - f_2^2\phi_2}{f_1^2 - f_2^2} = \rho + \mathrm{dx} - \mathrm{C}\cdot\mathrm{dt} + \mathrm{m}\cdot\mathrm{d}_{trop} + \frac{f_1^2}{f_1^2 - f_2^2}\mathrm{N}_1 + \frac{f_2^2}{f_1^2 - f_2^2}\mathrm{N}_2 + \varepsilon_{\phi_{IF}} \end{aligned} \tag{3}$$

In the above formula, P_{IF}, ϕ_{IF} is the ionosphere-free pseudorange, carrier phase observation, respectively, $\varepsilon_{P_{IF}}$, $\varepsilon_{\phi_{IF}}$ is the noise of ionosphere-free pseudorange, carrier phase observation, respectively, ρ is the geometric distance, m is the troposphere projection coefficient, C is the speed of light, dx is the coordinate parameter. In this paper, we use the precise satellite orbit, clock products and station coordinate provided by IGS. Therefore, the unknown parameters are receiver clock error, tropospheric and ambiguity parameters. Receiver DCB and ambiguity parameters are combined into a new ambiguity parameters:

$$\begin{aligned} \mathrm{N'}_1 &= \mathrm{N}_1 + b_1^s - b_1^r \\ \mathrm{N'}_2 &= \mathrm{N}_2 + b_2^s - b_2^r \end{aligned} \tag{4}$$

The ionosphere-free combination ambiguity can be expressed as follows:

$$\begin{aligned}\frac{f_1^2}{f_1^2-f_2^2}N_1-\frac{f_2^2}{f_1^2-f_2^2}N_2=&\frac{f_1^2}{f_1^2-f_2^2}N_1^{'}-\frac{f_2^2}{f_1^2-f_2^2}N_2^{'}\\&-\left(\frac{f_1^2}{f_1^2-f_2^2}\left(b_1^s-b_1^r\right)-\frac{f_2^2}{f_1^2-f_2^2}\left(b_2^s-b_2^r\right)\right)\end{aligned} \tag{5}$$

$\frac{f_1^2}{f_1^2-f_2^2}\left(b_1^s-b_1^r\right)-\frac{f_2^2}{f_1^2-f_2^2}\left(b_2^s-b_2^r\right)$ is the ionosphere-free combination DCB, the precise orbit and clock products provided by IGS is based on dual-frequency ionosphere-free pseudorange, the ionosphere-free combination DCB is considered to be zero. Therefore, combination of DCB and ambiguity in the UofC model results in a new ambiguity parameter that does not affect the estimation of the position and tropospheric parameters.

2.2 DCB Estimation

When the carrier phase ambiguity is obtained, the slant TEC can be obtained according to the phase observations of two different frequencies.

$$A=\left(\left(\phi_1+N_1'\right)-\left(\phi_2+N_2'\right)\right)/\left(\frac{1}{f_1^2}-\frac{1}{f_2^2}\right) \tag{6}$$

A is the slant TEC, which still contains DCB information. To obtain the absolute ionospheric delay value, accurate satellite and station DCB delay are also required. DCB is usually estimated together with global or regional ionospheric models. In this paper, the spherical harmonic function is used to describe the global ionospheric delay. Combined with the DCB parameters, the function model is as follows [4]:

$$\begin{aligned}A(\beta,s)=&\sum_{n=0}^{n_{\max}}\sum_{m=0}^{n}\tilde{P}_{nm}(\sin\beta)\left(a_{nm}\cos ms+b_{nm}\sin ms\right)/M\\&+\left(DCB^s-DCB^r\right)/\left(\frac{1}{f_1^2}-\frac{1}{f_2^2}\right)\end{aligned} \tag{7}$$

β and s are the geomagnetic latitude and longitude of the piercing point, $\tilde{P}_{nm}$ is the regularized Legendre series, a_{nm} and b_{nm} are the coefficients parameters; $A(\beta,s)$ is the slant TEC obtained from formula (6), M is the projection function, DCB^s, DCB^r is related to satellites, receivers, respectively. Due to the strong correlation

between DCB^s and DCB^r parameters, IGS uses zero-mean constraint in ionospheric model estimation to separate DCB^s and DCB^r. In this paper, DCB^s are provided by IGS, only the DCB^r parameters are estimated.

2.3 DCB Estimation

The ambiguities and DCB are estimated from the above two sections, the absolute slant TEC can be calculated by the following formula.

$$STEC = ((\phi_1^s + N_1) - (\phi_2^s + N_2) - (DCB^s - DCB^r))/(\frac{1}{f_1^2} - \frac{1}{f_2^2}) \tag{8}$$

STEC is the absolute slant TEC. During the calculation of receiver DCB in the previous section, the Global Ionosphere Map (GIM) has been acquired in fact. GIM is based on the single-layer assumption, which has a large model error that affects the small area. For example, the distance between GNSS stations of the Hongkong Positioning Reference Station network is about 15 km, the base station covers about 50 km, assuming that the single-layer model height is 450 km, the cut-off height angle is 10°, and the maximum range of the satellite pierce point distribution is 3000 km. GIM has a low accuracy in the region-wide ionospheric delay through interpolation, therefore, it is necessary to establish an ionospheric model suitable for the region. In order to reduce the model error, this paper proposes a regional ionospheric model based on satellites. The slant TEC is used as observations to avoid the distribution and altitude of the pierce point and polynomial fitting function in order to fit regional ionospheric distribution.

$$STEC = \sum_{n=0}^{n_{\max}} \sum_{m=n}^{n_{\max}} \beta^m s^n a_{nm} n \tag{9}$$

β and s are the geographic latitude and longitude of station, a_{nm} are estimated parameters, n is a polynomial fitting order number determined by the complexity of the surface, the relationship between the number of estimated parameters and fitting order can be expressed as follows:

$$NumberX = \frac{(n+1) * (n+2)}{2} \quad \text{n} \in N \tag{10}$$

3 Results and Statistical Analysis

The observation data of the IGS global network and the Hongkong SatRef network are from September 1, 2015 to September 30, 2015. The coordinates of global stations, precise orbit, clock products are provided by IGS.

3.1 Comparison of Ambiguity Resolution

Figure 1 shows the ambiguities estimated by the carrier phase smoothing pseudo-range and the UofC method. It can be seen that the convergence speed of the two GPS satellites using the UofC method is faster than the carrier phase smoothing pseudo-range method. Especially the GPS Satellite PRN 24, the ambiguity estimated by the UOFC method converges after about 1000 epochs, whereas using the carrier phase smoothing pseudorange method converges after approximately 3000 epochs. The reason is the UOFC method uses the precise satellite ground distance information as the constraint condition that leads to faster convergence speed.

3.2 DCB Estimation

If only the Hongkong SatRef network is used to estimate the regional station receivers DCB, the observations of all regional stations are almost equivalent to the observations of one station on the satellite due to the strong correlation between the observation data of each station. Therefore, observation of IGS global stations is joined to estimate global and regional receivers DCB, distribution of IGS global stations is shown as in Fig. 2.

Based on the observation of 183 stations in IGS network and 12 stations in Hongkong SatRef, the 15 order spherical harmonic model is used to solve the receivers DCB parameters of global and regional stations. Figure 3 shows the difference between the estimated DCB parameters and the DCB provided by IGS. As shown in the figure, the accuracy of estimated DCB of global stations is 0.4 ns.

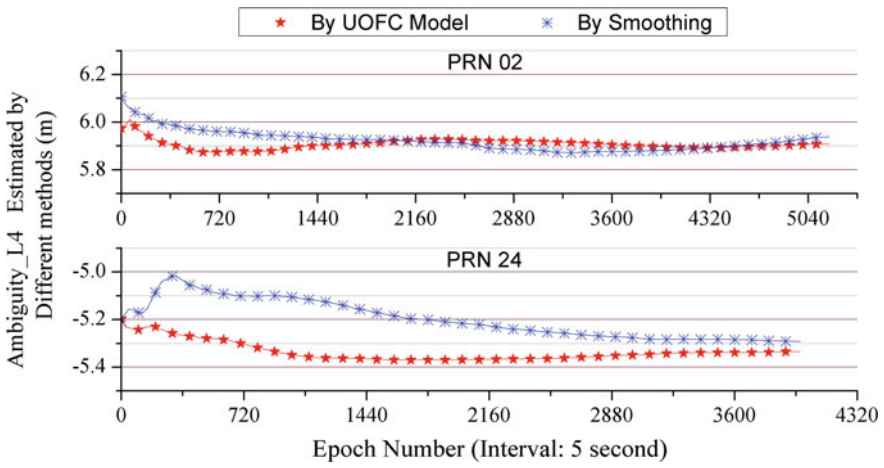

Fig. 1 Comparison of carrier phase ambiguities between carrier phase smoothed pseudorange and UofC Estimation

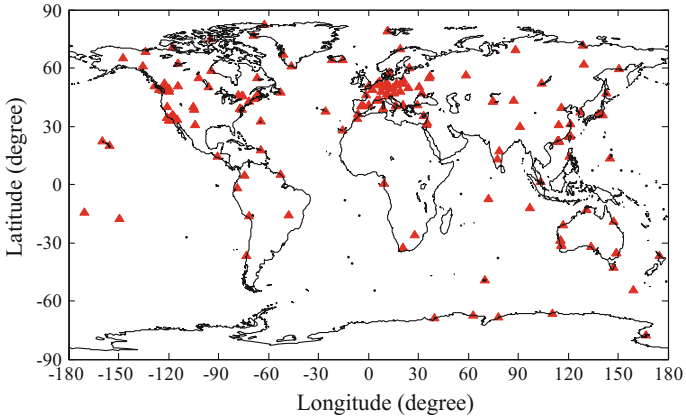

Fig. 2 Distribution map of global station involved in DCB estimation

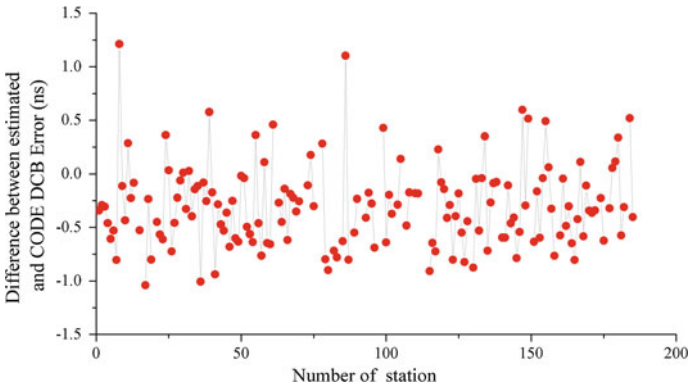

Fig. 3 Estimation accuracy of global stations receivers DCB

3.3 Ionosphere Model Estimation

According to the distribution of Hongkong SatRef, the regional ionospheric model is established based on satellites. In this paper, the second-order polynomial function is used to fit the Hongkong regional ionosphere model. Figure 4 is the distribution map of Hongkong regional stations involved in ionosphere model estimation. Figure 5 is the surface ionospheric model (Abbreviated as IonHk) fitted by polynomial function. The statistics of fitting residuals of the ionospheric model is 0.12 TECU.

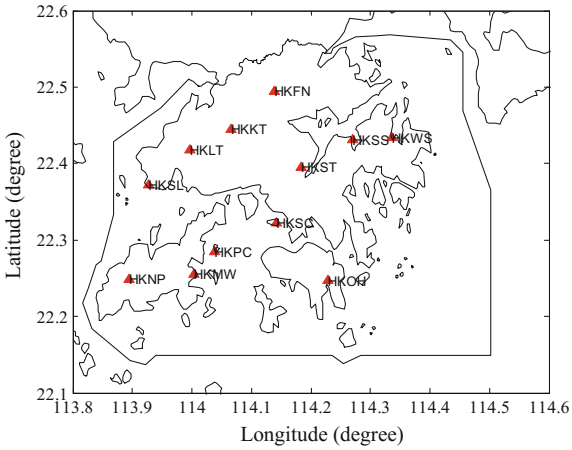

Fig. 4 Distribution map of Hongkong regional stations involved in ionosphere model estimation

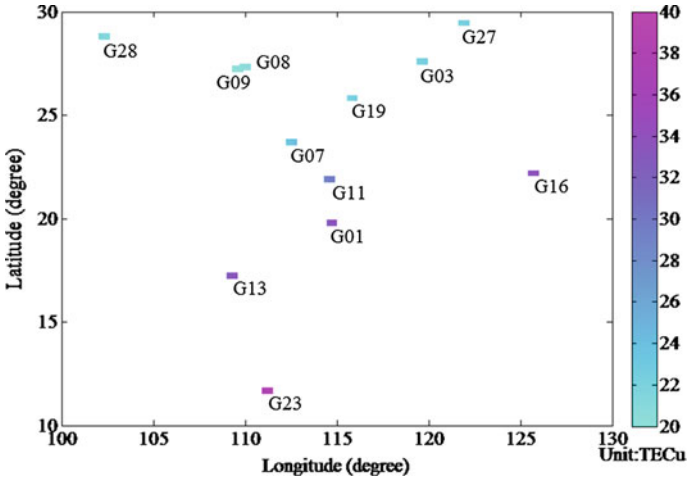

Fig. 5 Ionosphere surface model (local time 2015/9/9 11:0:0)

3.4 Pseudorange Positioning

In order to verify the accuracy of the regional ionospheric model estimated in this paper, we adopt four positioning algorithms shown in Table 1. The four algorithms are single-frequency pseudorange positioning without correction of ionospheric delay, dual-frequency ionosphere-free pseudorange positioning, single-frequency pseudorange positioning with GIM model and single-frequency pseudorange positioning with the IonHk model. Pseudorange positioning uses IGS precise orbit

Table 1 Solution strategies of pseudorange positioning

Abbreviation	Correction method of the ionospheric delay
P1	Without ionospheric correction
P ionosphere-free	Ionosphere-free
P1 GIM	GIM model
P1 IonHk	IonHk model

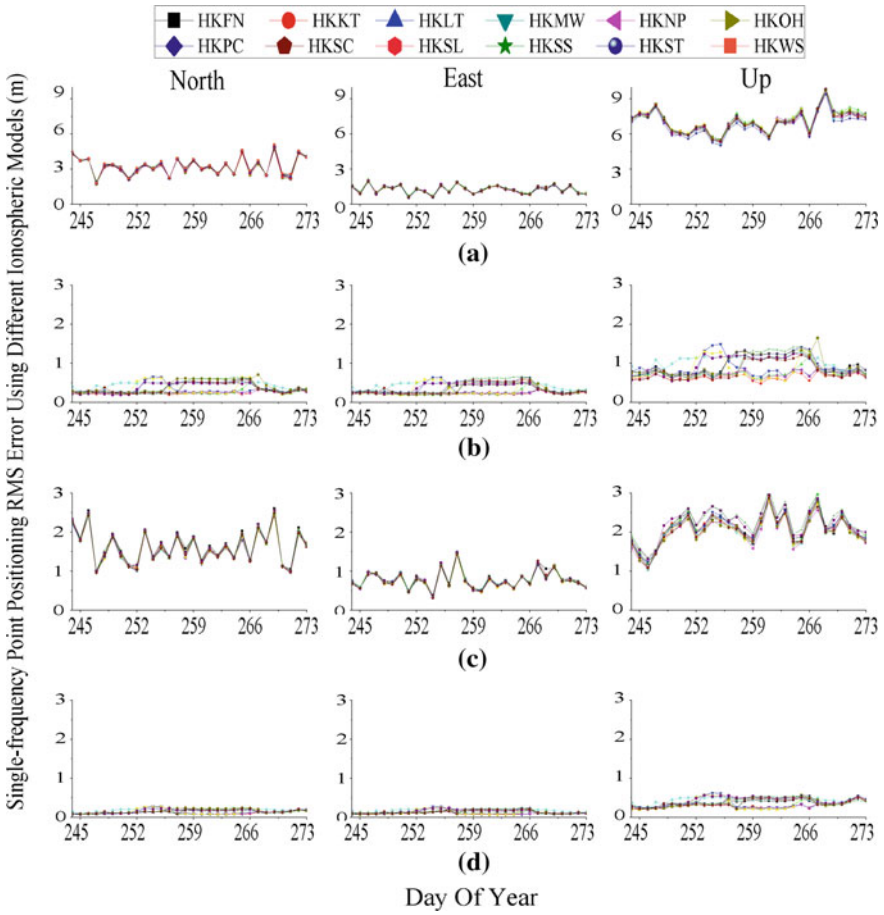

Fig. 6 Time series of pseudorange positioning accuracy of Hongkong regional stations using different solutions

and clock products, the tropospheric errors are corrected by the Saastamoinen model, the estimated parameters are station coordinates and receiver clock error.

Figure 6 shows the time series of the pseudorange positioning results of 12 stations in Hongkong using different solutions. Figure 6a shows that the positioning

result without ionospheric correction. The stations have almost the same positioning accuracy on the same day. The positioning accuracy of all the stations can reach a maximum of 9.86, 5.11 and 2.10 m in the vertical, north and east direction, respectively.

Figure 6b shows the ionosphere-free pseudorange positioning that reduces the effect of ionospheric delay. Since the noise of the ionosphere-free pseudorange observation is 3–4 times the noise of the P1 pseudorange observation. The positioning accuracy is determined mainly by the noise level of the pseudorange observation. The positioning accuracy of all stations in the north, east, vertical direction can up to 0.71, 0.66, 1.66 m.

Figure 6c shows the P1 pseudorange positioning with ionospheric corrections using the GIM model provided by IGS, and the positioning accuracy of each station is similar on the same day. The positioning accuracy of all stations in the north, east, the vertical direction can up to 2.61, 1.50, 3.09 m.

Figure 6d shows the P1 pseudorange positioning with ionospheric corrections using the IonHk model. The noise of P1 pseudorange is only a third to a quarter of the noise of ionosphere-free pseudorange, and the ionospheric delay through the IonHk model is also well weakened. The positioning accuracy of all stations in the north, east, the vertical direction can up to 0.28, 0.28, 0.63 m.

Figure 7 shows the pseudorange positioning accuracy statistics of Hongkong regional stations. The accuracy of P1 pseudorange positioning with ionospheric corrections using the IonHk model is only 0.15, 0.13, 0.37 m, respectively.

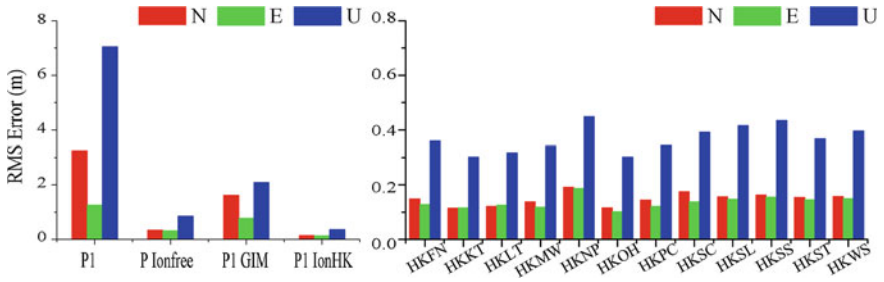

Fig. 7 Pseudorange positioning accuracy statistics of Hongkong regional stations using different solutions, left shows positioning accuracy statistics by using four solutions, right shows single-frequency pseudorange positioning accuracy statistics of each station using IonHk model

4 Conclusion

In this paper, the IGS global and Hongkong regional tracking station data are used to study the DCB estimation and regional ionospheric model. The carrier phase ambiguity is estimated by using the PPP UofC model in order to obtain high-precision ionospheric observations. The IGS global stations are combined to solve the problem of strong correlation in DCB of regional station receivers A regional ionospheric model based on satellites was established considering the precision loss of fitting of the ionospheric single-layer model in small area. The results show that the three-dimensional accuracy of single-frequency pseudorange positioning based on the regional ionospheric model is 0.4 m.

References

1. Georgiadou Y, Kleusberg A (1998) On the effect of ionospheric delay on geodetic relative GPS positioning. Manuscripta Geod 13:1–8
2. Lanyi G (1986). Total ionospheric electron content calibration using series GPS satellite data. Its the telecommunications & data acquisition report P
3. Mannucci AJ, Wilson BD, Edwards CD (1993) A new method for monitoring the earth ionosphere total electron content using the GPS global network. Proc Inst Navig 22(2):1323–1332
4. Wilson BD, Mannucci AJ (1993) Instrumental biases in ionospheric measurements derived from gps data. In: Proceedings of international technical meeting of the satellite division of the institute of navigation
5. Schaer S (1999) Mapping and predicting the earth's ionosphere using the global positioning system. Geod Geophys Arb Schweiz 59:59
6. Feltens J (2003) The activities of the ionosphere working group of the international GPS service (IGS). GPS Solutions 7(1):41–46
7. Komjathy A, Herna´ndez-Pajares M (2004) The IGS global TEC maps: present and future. In: National Radio Science Meeting, Boulder, CO, USA
8. Herna'ndez-Pajares M, Juan J, Sanz J, Orus R, Garcia-Rigo A, Feltens J, Komjathy A, Schaer S, Krankowski A (2009) The IGSVTEC maps: a reliable source of ionospheric information since 1998. J Geod 83(3–4), 263–275
9. Gao Y, Liu ZZ (2002) Precise ionosphere modeling using regional GPS network data. Positioning 1(1):18–24

The Algorithm Research of BDS/GPS Network RTK Real-Time Positioning with Centimeter Level

Tianming Ma, Chunmei Zhao and Huizhong Zhu

Abstract Compared with conventional RTK, Network RTK possesses the advantages of wide coverage, high real-time positioning accuracy, high reliability and etc., which becomes a hot spot in the field of high-precision positioning with its wide application range. The positioning principle of BDS/GPS Network RTK algorithm and the processing strategies of observation errors are explored, based on which, the resolution algorithm of integer ambiguities of double difference carrier phase between reference stations for BDS/GPS is researched. Then a high-precision BDS/GPS error processing model is established within the coverage range of reference stations. Further, the error processing of the mobile station is made by using the method of regional error correction between BDS/GPS reference stations. After that, the integer ambiguity resolution method of BDS/GPS carrier phase in mobile station is studied. Finally a set of BDS/GPS Network RTK data processing software is developed according to the algorithm proposed in this contribution, which is analyzed and verified with measured dual frequency observation data of BDS/GPS. The results show that the network RTK centimeter level positioning accuracy of BDS/GPS can be effectively achieved by the proposed algorithm.

Keywords Network RTK · BDS/GPS · Ambiguity · Tropospheric delay Ionospheric delay

1 Introduction

BeiDou navigation satellite system (BeiDou Navigation Satellite System, BDS) consists of Geostationary Earth Orbit (GEO) satellites, Inclined Geosynchronous Earth Orbit (IGSO) satellites and Medium Earth Orbit (MEO) satellites. As of

T. Ma (✉) · C. Zhao
Chinese Academy of Surveying and Mapping, Beijing, China
e-mail: 18941835327@163.com

T. Ma · H. Zhu
Liaoning Technical University, Fuxin, China

J. Sun et al. (eds.), *China Satellite Navigation Conference (CSNC) 2018 Proceedings*, Lecture Notes in Electrical Engineering 498,
https://doi.org/10.1007/978-981-13-0014-1_54

November 2017, there are 14 satellites in orbit in BDS. The BeiDou satellite navigation system with global positioning capabilities will be fully completed by around 2020, to form a global service capacity. Global Positioning System (Global Positioning System, GPS) only consists of Medium Earth Orbit (MEO) satellites. In the network RTK positioning of GPS and BDS single system, carrier phase difference technology is usually used for quick positioning, while the key problem and the hard part in the network RTK positioning is the accurate fix of the ambiguity of the carrier phase. Since the BeiDou satellite positioning system covers the entire Asian-Pacific region and provides navigation and positioning services, the positioning accuracy of BDS can be improved by using carrier phase observation data, and the key problem is the quick calculation of the integer ambiguity of the carrier phase.

Many scholars have studied the positioning of BDS/GPS network RTK. Han Shaowei proposed to use MW combined observation value to calculate the wide-lane ambiguity and then resolve the narrow-lane ambiguity. Because the accuracy of the measured pseudo distance observation is not high, the ambiguity fixed time is relatively longer [1]; Hern M proposed an algorithm based on the free electron change in the atmosphere, the success rate of which can reach about 95% in very good conditions [2]; Tang Weiming proposed the three-step method to calculate the ambiguity of GPS carrier phase, however, the problem of which is that the ambiguity of narrow-lane is not easy to fix and needs to be further improved [3]; Li Bofeng proposed a method to calculate the long-range base station ambiguity, which can control the failure rate, and the precise determination of narrow-lane is realized by limiting factors such as controllable error probability [4]; Zhu Huizhong, Gao Wang, Gao XingWei et al. proposed Network RTK integer ambiguity solution model, which can realize the network RTK integer ambiguity real-time single epoch solution, but the model is not stable enough and needs further improved [5–8]. This contribution proposes a network RTK real-time centimeter level positioning method, that is, the ambiguity of base station is calculated by using the MW combined observation value, the regional error is calculated by using the integrated error interpolation method, and the ambiguity of mobile station is calculated by using the improved LAMBDA algorithm, which makes the initialization time of the ambiguity calculation shortened and the results of real-time centimeter level positioning of BDS/GPS users realized.

2 BDS/GPS Network RTK Positioning Model

2.1 The Base Station Ambiguity Calculation

The calculation of the ambiguity of the base station is the key problem to be solved first. In this contribution, the double difference wide-lane integer ambiguity of the

base station is adopted by the MW combined observation value [9], as shown in Eqs. (1) and (2):

$$\Delta\nabla MW = \frac{f_1\Delta\nabla L_1 - f_2\Delta\nabla L_2}{f_1 - f_2} - \frac{f_1\Delta\nabla P_1 + f_2\Delta\nabla P_2}{f_1 + f_2} \tag{1}$$

$$\Delta\nabla N_w = \frac{(f_1 - f_2)\Delta\nabla MW}{c} \tag{2}$$

where f_1, f_2 is the frequency of carrier L_1, L_2, $\Delta\nabla L_1$, $\Delta\nabla L_2$ is double difference observation value in distance L_1, L_2, $\Delta\nabla P_1, \Delta\nabla P_2$ is double difference observation value of pseudo range P_1, P_2, $\Delta\nabla MW$ is MW combined observation value, and $\Delta\nabla N_w$ is double difference wide-lane integer ambiguity. The method of taking an average value by epoch is adopted to weak the noise effect of the double difference wide-lane integer ambiguity and the difference of the absolute value between the double difference wide-lane ambiguity float solutions and correct integer solutions is less than 0.25 cycles, therefore, the integer solution of the double difference wide-lane ambiguity can be obtained by directly taking the full integer of the ambiguity float solution [10, 11]. The double difference carrier phase observation equation of the base station can be written as Eq. (3):

$$\lambda_1\Delta\nabla L_1 = \Delta\nabla\rho - \lambda_1\Delta\nabla N_1 - \frac{\Delta\nabla I}{f_1^2} - \Delta\nabla T + \Delta\nabla_{\varepsilon L1} \tag{3}$$

Because the base station coordinates are known, the unknown parameters included in the Eq. (3), such as, the double difference carrier phase integer ambiguity, double difference ionospheric delay error and double difference tropospheric delay error, can be solved as follows: the double difference ionospheric delay error is estimated as a parameter, the dry delay error of double difference tropospheric was corrected by Sasstamonion model, and residual wet delay error is estimated as unknown parameters. Then, the least-square method is used to calculate the float solution of the double difference carrier phase ambiguity. In the end, the LAMBDA algorithm is used to search the fixed double difference carrier phase integer ambiguity.

2.2 *Regional Error Correction*

Based on the comprehensive comparison of the existing regional error correction models, the error correction of the base station and the mobile station is calculated by combined error interpolation algorithm, the characteristics of which is that all errors are not distinguished, but to be directly used to calculate the combined error of the base station and the mobile station [12, 13]. After the integer solution of the carrier phase ambiguity of the base station is accurately fixed, the calculation equation for the base station combined error is given below:

$$\begin{aligned}\Delta\nabla m_{s1s2} &= \lambda_1\Delta\nabla L_1 - \Delta\nabla\rho_{s1s2} + \lambda_1\Delta\nabla N_{s1s2}\\ \Delta\nabla m_{s2s3} &= \lambda_1\Delta\nabla L_1 - \Delta\nabla\rho_{s2s3} + \lambda_1\Delta\nabla N_{s2s3}\end{aligned} \tag{4}$$

where $s1, s2, s3$ refer to base stations, the calculation equation of integrated error of the mobile station is shown in Eq. (5):

$$\Delta\nabla m_{ss1} = [X_s - X_{s1}Y_s - Y_{s1}] \cdot \begin{bmatrix} X_{s2} - X_{s1}Y_{s2} - Y_{s1} \\ X_{s3} - X_{s1}Y_{s3} - Y_{s1} \end{bmatrix}^{-1} \cdot \begin{bmatrix} \Delta\nabla m_{s1s2} \\ \Delta\nabla m_{s2s3} \end{bmatrix} \tag{5}$$

where $(X_{s1}, Y_{s1}), (X_{s1}, Y_{s1}), (X_{s1}, Y_{s1}), (X_{s1}, Y_{s1})$ are coordinates of base stations $s1, s2, s3$ and mobile station s.

2.3 The Mobile Station Ambiguity Calculation

The combined error of the mobile station calculated by the combined error interpolation algorithm is used to correct its observation value, by which the accuracy of the value is greatly improved and the time of initialization of the mobile station is also shortened. Because the wavelength of the wide-lane is relatively long and easy to fix, the double difference wide-lane ambiguity of the mobile station is firstly fixed, and then the double difference carrier phase integer ambiguity of the station is calculated [14].

The double difference wide-lane observation equation is shown as Eq. (6):

$$V_{\mathrm{w}} = H\,\delta X - \lambda_{\mathrm{w}}\,\Delta\nabla N'_w - L_{\mathrm{w}} \tag{6}$$

where $\Delta\nabla$ represents double difference operator, V_{w} represents error of double difference observation equation, H represents the coefficient matrix combined by cosine of the three coordinates of the observed satellites, δX is the correction of the unknown parameters in the three directions of the station coordinates; λ_w is wide-lane carrier phase wavelength, $\Delta\nabla N'_w$ represents integer solution of double difference wide-lane ambiguity, and L_{w} is constant term. The Eq. (6) is written as the Eq. (7):

$$V_{\mathrm{w}} = [H - \lambda_{\mathrm{w}}] \cdot \begin{bmatrix} \delta X \\ \Delta\nabla N'_w \end{bmatrix} - L_{\mathrm{w}} \tag{7}$$

The unknown parameters, δX and $\Delta\nabla N'_w$ are calculated by least square method in Eq. (7).

$$Y = N^{-1}M \tag{8}$$

where:

$$Y = \begin{bmatrix} \delta X \\ \Delta\nabla\, N'_w \end{bmatrix}$$
$$N = [H - \lambda_{\mathrm{w}}]^{\mathrm{T}} P[H - \lambda_{\mathrm{w}}]$$
$$U = [H - \lambda_{\mathrm{w}}]^{\mathrm{T}}\, L_{\mathrm{w}}$$

where p is unit matrix, substitute integer solution of the double difference wide-lane ambiguity in Eq. (6):

$$V_{\mathrm{w}} = H\,\delta X - (\lambda_{\mathrm{w}}\,\Delta\nabla N'_{\mathrm{w}} + L_{\mathrm{w}}) \tag{9}$$

In Eq. (9), the unknown parameter is only the coordinate correction of the mobile station δX, therefore, the least square method is used to calculate the coordinate correction δX of the mobile station, as shown in Eq. (10):

$$\delta X = (H^{\mathrm{T}} PH)^{-1}[H^{\mathrm{T}} P(\lambda_{\mathrm{w}}\,\Delta\nabla N'_{\mathrm{w}} + L_{\mathrm{w}})] \tag{10}$$

After the integer ambiguity solution and the initial coordinate correction of the mobile station δX are obtained. The next step is to calculate the double difference L1 carrier phase ambiguity, the double difference L1 carrier phase observation equation is shown in Eq. (11):

$$V_{L1} = -\lambda_1 \Delta\nabla N'_1 - (L_1 - H\delta X) \tag{11}$$

For Eq. (11), use the least square method to calculate the double difference carrier phase float solution, as shown in Eq. (12):

$$\Delta\nabla N'_1 = [(-\lambda_1^{\mathrm{T}})P\,(-\lambda_1)]^{-1} \cdot [(-\lambda_1^{\mathrm{T}})P(L_1 - H\delta X)] \tag{12}$$

At present, the double difference carrier phase ambiguity float solution is obtained, but the carrier wavelength is shorter and the ambiguity is more difficult to fix, therefore, the improved LAMBDA algorithm is used to calculate the integer solution of the fixed carrier ambiguity.

2.4 The Improved LAMBDA Algorithm

First, the Eq. (11) is written as matrix form as Eq. (13):

$$VL1 = [C] \cdot \begin{bmatrix} \delta X \\ \Delta\nabla N'_1 \end{bmatrix} - L1 \tag{13}$$

Then the coefficient matrix $[C]$ of the unknown parameter is carried out as follows:

$$\underset{n\times(n+3)}{C} = \underset{n\times(n+3)}{U}\ \underset{(n+3)\times(n+3)}{D}\ \underset{(n+3)\times(n+3)}{V}$$

Then the following decomposition of the matrix D and V in the upper equation is shown as follows:

$$\underset{(n+3)\times(n+3)}{D} = \begin{bmatrix} \underset{n\times n}{D_1} & 0 \\ 0 & \underset{3\times 3}{D_2} \end{bmatrix} \quad \underset{(v+3)\times(n+3)}{V} = \begin{bmatrix} \underset{3\times 3}{V_{11}} & \underset{3\times n}{V_{12}} \\ \underset{n\times 3}{V_{21}} & \underset{n\times n}{V_{22}} \end{bmatrix}$$

Then the matrix M and matrix R are calculated:

$$\underset{3\times(n+3)}{M} = \underset{3\times 3}{D_2}\begin{bmatrix} \underset{3\times 3}{V_{11}^T} & \underset{3\times n}{0} \end{bmatrix} \quad R = M^T M$$

In matrix R, all elements are zero except the 9 elements of the top left 3 rows and 3 columns. The matrix R and Eq. (12) is used to calculate the unknown parameters by using the least square method, as show in Eq. (14):

$$\begin{bmatrix} \delta X \\ \Delta\nabla N_1' \end{bmatrix} = (\mathrm{C}^T PC + R)^{-1}(\mathrm{C}^T P_{L1}) \tag{14}$$

Therefore, the improved algorithm can obtain a more accurate ambiguity float solution. At the same time, the mean square error matrix is used to determine the range of the ambiguity of the covariance matrix, which improves search efficiency.

3 Algorithm Experiment

In order to verify the correctness and reliability of this algorithm, the CORS network observation data is used. The sampling interval of the data is 15 s. The satellite cut-off altitude angle is set at 15 degrees, and the station distribution is shown in Fig. 1.

By using the algorithm presented in this contribution, the ambiguity of the base station is firstly calculated, and the regional error is solved. Then the regional error is used to correct the observation value of the mobile station, in order to improve the accuracy of the observation data of the mobile station. Finally, the ambiguity of the mobile station is calculated by using the corrected mobile station observation data. The GPS is based on satellite No. 16, and the results of the double difference L1 carrier ambiguity of satellite No. 3 and satellite No. 6 are given; the BDS is based on satellite No. 7, and the results of the double difference B1 carrier ambiguity of satellite No. 1 and satellite No. 13 are given, see Figs. 2, 3, 4, and 5.

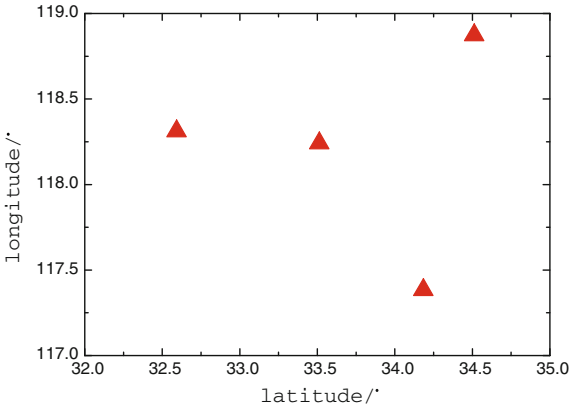

Fig. 1 Station distribution

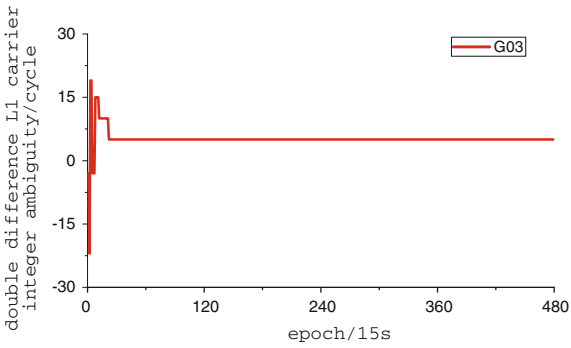

Fig. 2 The double difference L1 carrier ambiguity (PRN03)

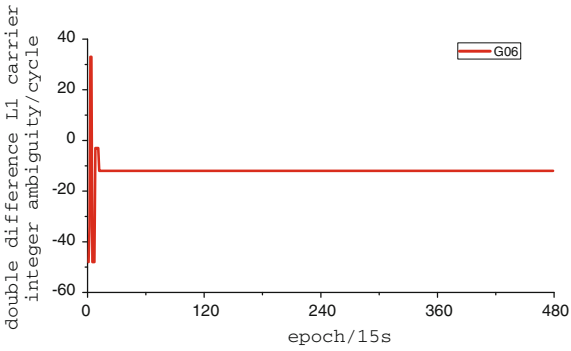

Fig. 3 The double difference L1 carrier ambiguity (PRN06)

It can be seen from Figs. 2, 3, 4, and 5, the double difference L1 carrier phase integer ambiguity of the GPS mobile station can quickly converge to complete the initialization. The initial time of the double difference B1 carrier phase integer ambiguity of BDS mobile station is slightly longer than GPS. The initial time of the

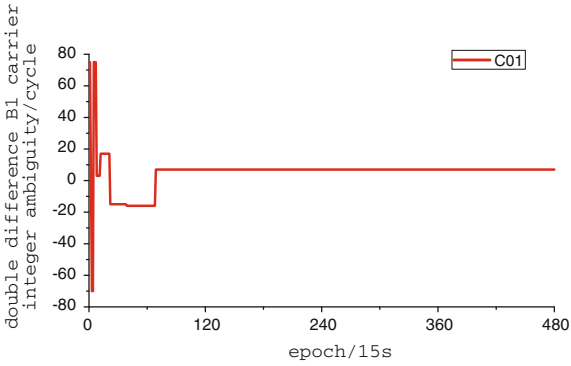

Fig. 4 The double difference B1 carrier ambiguity (PRN01)

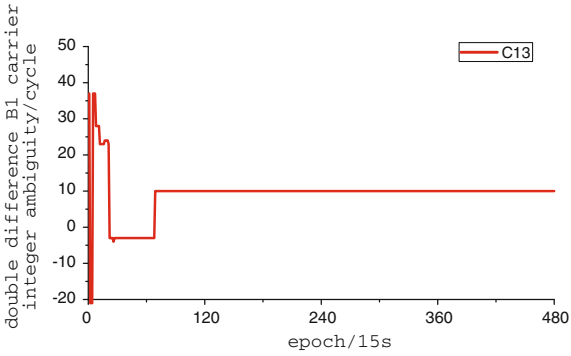

Fig. 5 The double difference B1 carrier ambiguity (PRN13)

fixed solution of the double difference carrier phase ambiguity of the mobile station in Figs. 2, 3, 4, and 5 is shown in Table 1.

It can be seen from Table 1, the double difference carrier ambiguity of GPS mobile station can be initialized by 21 epochs, and the correct ambiguity fixed solution is obtained. Because the time interval is 15 s, the initialization time of 21 epochs is about 5 min; BDS requires 62 epochs to be initialized, and the initialization time is about 15 min.

After the double difference carrier phase ambiguity of mobile station is fixed, a fixed solution of double difference carrier phase ambiguity of the mobile station is carried back to the Eq. (14) and the least square method is used to calculate the

Table 1 The initialization time of double difference wide-lane ambiguity fixed solution (epoch)

	Total epoch	Time/ epoch	Fix epoch	Success rate (%)
Double difference L1 carrier ambiguity	480	21	459	95.625
Double difference B1 carrier ambiguity	480	62	418	87.083

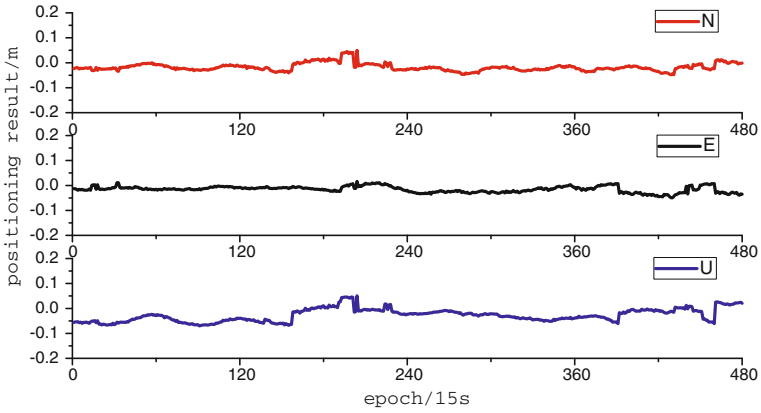

Fig. 6 2 h positioning results of GPS

positioning results of the final N, E and U of the mobile station. In this case, the positioning results of 2 and 12 h are given respectively, see Figs. 6, 7, 8, and 9.

It can be seen from Figs. 6, 7, 8, and 9, the two systems reach the accuracy of centimeter level positioning in the three directions of N, E and U. After the probability statistics of the positioning difference of these three directions, N, E and U, the average of one week's coordinates of the station solved by PANDA software is regarded as the true value. And the information of RMS values of the positioning results of the three directions of N, E and U can be obtained from the results the solved in this contribution minus the average, as shown in Table 2.

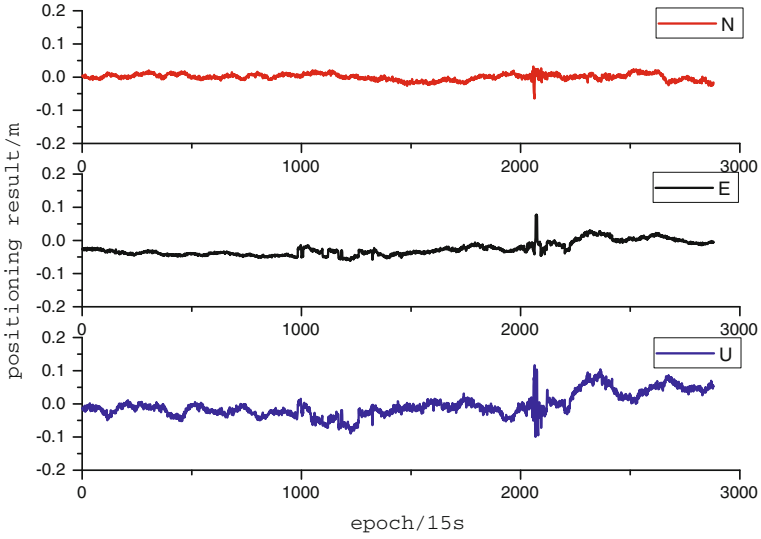

Fig. 7 12 h positioning results of GPS

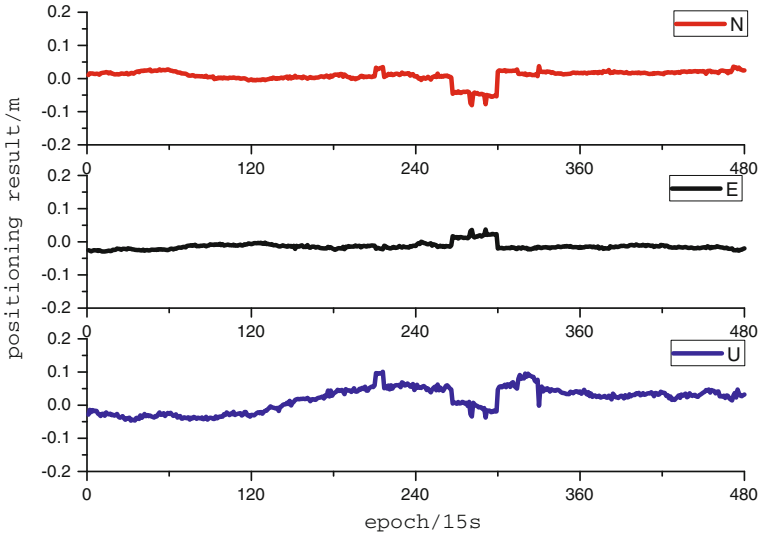

Fig. 8 2 h positioning results of BDS

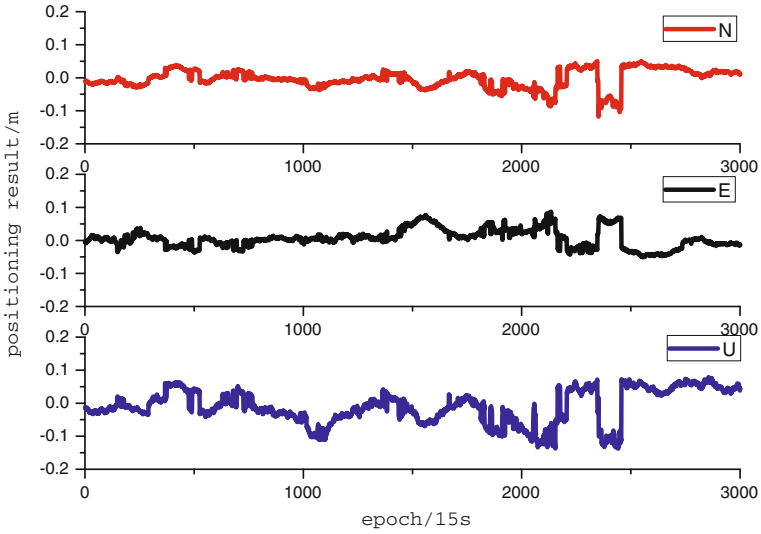

Fig. 9 12 h positioning results of BDS

It can be seen from Table 2, both systems reach the accuracy of centimeter level positioning in the three directions of N, E and U. The positioning results of BDS are slightly worse than that of GPS, and the positioning accuracy of the U direction of the BDS in the 12 h positioning results is up to 5 cm, probably because BDS has

Table 2 RMS of absolute bias of positioning results (m)

		N direction	E direction	U direction
GPS	2 h	0.0200	0.0236	0.0376
	12 h	0.0195	0.0326	0.0395
BDS	2 h	0.0145	0.0194	0.0301
	12 h	0.0281	0.0378	0.0519

fewer satellites than GPS, and BDS contains GEO and IGSO satellites. The geometry of these satellites is not good, so the positioning accuracy is slightly worse than GPS, but it also reaches the accuracy of centimeter level positioning.

4 Conclusion

This contribution systematically studies the network RTK positioning algorithm, including the ambiguity calculation of the base station, the calculation of regional error correction, the ambiguity resolution of the mobile station and the positioning results of the mobile station. The algorithm is verified by CORS network observation data. The experimental results show that the proposed network RTK positioning algorithm can realize the accuracy of centimeter level positioning in both BDS and GPS systems. Among them, the positioning results of BDS are slightly worse than GPS, mainly due to the influence of satellite number and satellite structure, but it still reaches the accuracy of centimeter level positioning, which verifies the validity and reliability of this algorithm.

Acknowledgements This contribution was supported by the National Natural Science Foundation of China (Grant No. 41774013 and 41504010).

References

1. Han S (1997) Carrier phase-based long-range GPS kinematic positioning. School of Geomatic Engineering, The University of New South Wales
2. Hern M, Juan J, Sanz J et al (2000) Application of ionospheric tomography to real-time GPS carrier-phase ambiguities resolution, at scales of 400–1000 km and with high geomagnetic activity. Geophys Res Lett 27(13):2009–2012
3. Tang WM (2006) The RTK technology research and software implementation of large range and long distance GNSS network. Wuhan University
4. Li B, Shen Y, Feng Y et al (2015) GNSS ambiguity resolution with controllable failure rate for long baseline network RTK. J Geodesy 89(6):607–635
5. Zhu HZ (2012) The study of GNSS network RTK algorithm between long range at single epoch using undifference error corrections. Wuhan University
6. Zhu HZ, Xu AG, Gao M (2016) The algorithm of single-epoch integer ambiguity resolution between middle-range BDS network RTK reference stations. Acta Geodaetica Cartogr Sin 45 (1):50–57

7. Gao W, Gao CF, Pan SG et al (2015) Single-epoch positioning method in network RTK with BDS triple-frequency wide-lane combinations. Acta Geodaetica Cartogr Sin 44(6):641–648
8. Gao XW, Liu JN, Ge MR et al (2002) An ambiguity searching method for network RTK baselines between base stations at single epoch. Acta Geodaetica Cartogr Sin 31(2):305–309
9. Deng J, Hong ZZ (2014) Long baseline network RTK ambiguity resolution use of ionosphere reweighted model. J Geodesy Geodyn 34(02):64–68
10. Gao M, Xu AG, Zhu HZ et al (2017) The algorithm of triple-frequency ambiguity resolution between BDS network RTK reference stations. Acta Geodaetica Cartogr Sin 46(04):442–452
11. Lv WC, Gao JX, Zhang SB et al (2014) A method of fixing integer ambiguity between base stations in network RTK with wide-lane ambiguity restriction. J China Univ Min Technol 43 (05):933–937
12. Feng YT, Liu H, Zhang HP et al (2013) Comparisons and analysis on network RTK combined bias interpolation algorithm. J Geomatics 38(01):20–22+26
13. Hu MX (2017) Algorithm and positioning accuracy analysis of GPS/BDS/GLONASS network RTK. Wuhan University
14. Tang WJ (2015) Analysis of positioning precision network RTK based on BDS CORS. China satellite navigation system management office Academic Exchange Center. In: Proceedings of the Sixth China satellite navigation Symposium-S01 BeiDou/GNSS navigation application. China satellite navigation system management office Academic Exchange Center. 5

A Tightly Combined GPS/Galileo Model for Long Baseline RTK Positioning with Partial Ambiguity Resolution

Qing Zhao, Chengfa Gao, Shuguo Pan, Ruicheng Zhang and Liwei Liu

Abstract Knowledge of differential inter-system biases (DISBs) is critical to integrate observations from mixed GNSS. If the corresponding DISB could be calibrated in advance, only one pivot satellite is sufficient for ambiguity resolution on overlapping frequencies, which is the so-called tight combining (TC) strategy. Considering that GPS and Galileo transmit signals on two identical frequencies (e.g. L1/E1 and L5/E5a), a tightly combined GPS/Galileo RTK positioning model is proposed in this paper. Traditional DD model has been slightly adjusted to avoid the hand-over problem of reference satellites. The estimation of code and fractional part of phase DISB is archived through zero and ultra-short baselines. Three long baselines were selected to verify the proposed model with DISB calibrated in advance. Moreover, to get better AR performance, a simple but robust procedure of PAR, where the satellite elevation, number of consecutive tracking, success rate and ratio test are all combined to determine the subset of ambiguity, is adopted in the long baseline experiments. Results shows that the code and fractional part of phase DISB is rather stable. The TC strategy do not significantly improve the value of ratio, but shorten the convergence time to reach the 100% success rate. Compared with results of loose combining (LC) strategy, time to first fix (TTFF) is further reduced by 54.3, 72.9, 69.0% respectively under TC strategy corresponding to different long baselines. Besides, TC strategy could slightly improve the fixing rate of epochs. In terms of accuracy, the precision in up direction is worse than that in north and east direction. Once the ambiguity is fixed correctly, both LC and TC strategy can achieve centimeter-level positioning accuracy.

Q. Zhao · C. Gao (✉) · R. Zhang
School of Transportation, Southeast University, 2 Sipailou,
Nanjing 210096, China
e-mail: 230169553@seu.edu.cn

S. Pan (✉) · L. Liu
School of Instrument Science and Engineering, Southeast University,
2 Sipailou, Nanjing 210096, China
e-mail: psg@seu.edu.cn

J. Sun et al. (eds.), *China Satellite Navigation Conference (CSNC) 2018 Proceedings*, Lecture Notes in Electrical Engineering 498,
https://doi.org/10.1007/978-981-13-0014-1_55

Keywords GPS · Galileo · Differential inter-system bias (DISB)
Long baseline · RTK · Partial ambiguity resolution (PAR)

1 Introduction

Today, the Global Navigation Satellite System (GNSS) has been widely used for a multitude of applications around the world. Multi-GNSS differential positioning requires different reference satellite for each system, which is referred to as loose combining (LC) [1], and the performance of BDS/GPS dual/triple frequency was investigated by Gao et al. [2, 3]. On the other hand, combining observations on same frequencies from multi-GNSS in one positioning model with a common pivot satellite, which is the so-called tight combining (TC) [4], can introduce at least one more redundancy and will be beneficial to ambiguity resolution (AR) performance which is essential to high-precision mixed-constellation RTK positioning. The performance in terms of accuracy, availability and reliability of GPS only is largely a function of the number of satellite being tracked. Thus, the GPS real-time kinematic (RTK) positioning solution is degraded in urban canyon environment or in deep open cut mines where the number of visible satellite is limited [5]. The Galileo in EU is a one of the aiding solutions to add more functioning satellites which shares two overlapping frequencies (e.g. L1/E1 and L5/E5a) with GPS [6]. However, proper handling of the GNSS hardware biases known as differential inter-system bias (DISB) [7] is the prerequisite for integrating GPS and Galileo in one rigorous model. Studies on DISB have become the focus in the GNSS community. The GPS-Galileo ISB was first carried out by Montenbruck in CONGO network experiment [8]. Odijk and Teunissen pointed out that the range ISB can be estimated along with the coordinate parameters, while the phase ISB can be lump together with ambiguity parameters [9], however, this will not do any impact on the positioning results. A particle filter-based method for estimation of ISB was proposed by Tian et al. [10]. In addition to identical frequencies, DISB model between GPS and BDS on different frequencies was also studied and verified by Gao et al. [11].

Correct estimates of the carrier phase integer ambiguities are the prerequisite for high-precision positioning, since incorrect ambiguity fixing can lead to largely biased positioning solutions. However, it is not easy to fix all ambiguities simultaneously. In such cases, it may be beneficial to consider partial ambiguity resolution (PAR) techniques, which resolve only a subset of ambiguities. The important thing is how to determine the subset. Choice of an ambiguity subset could be based on ambiguity variance, pre-defined subset sizes, elevation ordering and linear combinations [12]. Parkins proposed a PAR method to deal with the presence of biased observations [13], but it is very time-consuming. An elevation-based technique was applied to the GPS/BDS/GLONASS RTK positioning by Gao et al. [14]. Unlike the usual method, a modified partial ambiguity resolution procedure is proposed by Wang and Feng [15], where the indices of both the success rate and the ratio test are combined to find an optimal ambiguity subset to be fixed. It was

widely demonstrated that the PAR strategy could obviously shorten the time to reach centimeter level accuracy for long baselines, and considerably extend the range for instantaneous RTK positioning [16].

Although many studies have been focused on the DISB with zero/ultra-short or medium-baseline experiments, the effect of application under long baseline conditions remains to be further studied. Therefore, this paper aims to make a preliminary assessment of the DISB application in the case of long baseline. In the following, Sect. 2 details the mathematical derivations of TC observation model, DISB estimation model and PAR procedure; Sect. 3 presents the data and models used in the experiments; Sect. 4 analysis the results of estimated DISB, performance of AR and positioning accuracy; finally, Sect. 5 summarizes the main point of this paper.

2 Methods

2.1 Intra-system and Inter-system Observation Model

For GPS and Galileo, the discrepancy in coordinate and time systems may be negligible in most applications. They transmitted signals on identical frequencies of L1/E1 and L5/E5a, which enables only one common pivot satellite once the DISB is calibrated. For long baselines, the differential atmospheric delays between receivers need to be considered. The between-receiver SD observation equations for GPS or Galileo can be expressed as

$$\begin{aligned} \Delta L^S_{r_1r_2} &= \Delta\rho^S_{r_1r_2} + \Delta dt_{r_1r_2} + \Delta T^S_{r_1r_2} - \mu\cdot\Delta I^S_{r_1r_2} + \lambda\cdot\Delta N^S_{r_1r_2} + b^S_{r_1r_2} \\ \Delta P^S_{r_1r_2} &= \Delta\rho^S_{r_1r_2} + \Delta dt_{r_1r_2} + \Delta T^S_{r_1r_2} + \mu\cdot\Delta I^S_{r_1r_2} + B^S_{r_1r_2} \end{aligned} \tag{1}$$

where, Δ is the between-receiver SD operator; L is the carrier observation and P is pseudorange observation; The superscript S represents the satellite of GPS or Galileo and the subscript r represents different receivers; ρ is the distance between satellite and receiver; dt denotes the receiver clock error; λ denotes the wavelength; b denotes the hardware phase delay, which also contains the initial phase in the receiver; N denotes the integer phase ambiguity; T denotes the tropospheric delay, and I denotes the ionospheric delay; μ is the ionospheric scale factor; B denotes the hardware code delay in the receiver for GPS or Galileo.

Based on SD observation equations, the classical intra-system DD observation can be formed, where the receiver-dependent bias can be eliminated. Here, we choose G_1 as the reference satellite for GPS and E_1 for Galileo, we can obtain

$$\begin{aligned}
\nabla\Delta L_{r_1r_2}^{G_1G_s} &= \nabla\Delta\rho_{r_1r_2}^{G_1G_s} + \nabla\Delta T_{r_1r_2}^{G_1G_s} - \mu\cdot\nabla\Delta I_{r_1r_2}^{G_1G_s} + \lambda\cdot\nabla\Delta N_{r_1r_2}^{G_1G_s} \\
\nabla\Delta P_{r_1r_2}^{G_1G_s} &= \nabla\Delta\rho_{r_1r_2}^{G_1G_s} + \nabla\Delta T_{r_1r_2}^{G_1G_s} + \mu\cdot\nabla\Delta I_{r_1r_2}^{G_1G_s} \\
\nabla\Delta L_{r_1r_2}^{E_1E_s} &= \nabla\Delta\rho_{r_1r_2}^{E_1E_s} + \nabla\Delta T_{r_1r_2}^{E_1E_s} - \mu\cdot\nabla\Delta I_{r_1r_2}^{E_1E_s} + \lambda\cdot\nabla\Delta N_{r_1r_2}^{E_1E_s} \\
\nabla\Delta P_{r_1r_2}^{E_1E_s} &= \nabla\Delta\rho_{r_1r_2}^{E_1E_s} + \nabla\Delta T_{r_1r_2}^{E_1E_s} + \mu\cdot\nabla\Delta I_{r_1r_2}^{E_1E_s}
\end{aligned} \tag{2}$$

where, $\nabla\Delta$ is the double-differential operator; G and E represents satellites of GPS and Galileo respectively. The meaning of other characters is as described above.

The inter-system DD observation equations between GPS and Galileo on same frequencies can also be built in a similar way, but the hardware delays cannot be eliminated. The corresponding models can be expressed as

$$\begin{aligned}
\nabla\Delta L_{r_1r_2}^{G_1E_s} &= \nabla\Delta\rho_{r_1r_2}^{G_1E_s} + \nabla\Delta T_{r_1r_2}^{G_1E_s} - \nabla\Delta I_{r_1r_2}^{G_1E_s} + \lambda\cdot\nabla\Delta N_{r_1r_2}^{G_1E_s} + \nabla\Delta b_{r_1r_2}^{GE} \\
\nabla\Delta P_{r_1r_2}^{G_1E_s} &= \nabla\Delta\rho_{r_1r_2}^{G_1E_s} + \nabla\Delta T_{r_1r_2}^{G_1E_s} + \nabla\Delta I_{r_1r_2}^{G_1E_s} + \nabla\Delta B_{r_1r_2}^{GE}
\end{aligned} \tag{3}$$

where, $\nabla\Delta b_{r_1r_2}^{GE}$ and $\nabla\Delta B_{r_1r_2}^{GE}$ represent the phase and code DISB between GPS and Galileo on overlapping frequencies. Odijk and Teunissen [7] and Paziewski et al. [6] have studied the DISB on same frequencies and demonstrated that the DISB is rather stable in time and related to the receiver type and signal frequency. Therefore carrier phase and code ISBs for a particular receiver pair can be estimated once and introduced as a known correction in GPS/Galileo tightly combined processing.

In order to avoid the hand-over problem of reference satellites in traditional DD model, we made some adjustments where the estimated DD tropospheric delay is expressed in the form of zero-differenced and the estimated DD ionospheric delay, DD ambiguities are all maintain the form of between-receiver single difference.

$$\begin{aligned}
\nabla\Delta L_{r_1r_2}^{G_1E_s} - \nabla\Delta b_{r_1r_2}^{GE} &= \nabla\Delta\rho_{r_1r_2}^{G_1E_s} + \left(M_{r_2}^{E_s} - M_{r_2}^{G_1}\right)T_{r_2} - \left(M_{r_1}^{E_s} - M_{r_1}^{G_1}\right)T_{r_1} - \mu\cdot\left(\Delta I_{r_1r_2}^{E_s} - \Delta I_{r_1r_2}^{G_1}\right) \\
&\quad + \lambda\cdot\left(\Delta N_{r_1r_2}^{E_s} - \Delta N_{r_1r_2}^{G_1}\right) \\
\nabla\Delta P_{r_1r_2}^{G_1E_s} - \nabla\Delta B_{r_1r_2}^{GE} &= \nabla\Delta\rho_{r_1r_2}^{G_1E_s} + \left(M_{r_2}^{E_s} - M_{r_2}^{G_1}\right)T_{r_2} - \left(M_{r_1}^{E_s} - M_{r_1}^{G_1}\right)T_{r_1} + \mu\cdot\left(\Delta I_{r_1r_2}^{E_s} - \Delta I_{r_1r_2}^{G_1}\right)
\end{aligned} \tag{4}$$

where M is the mapping function of tropospheric delay, here the niell mapping function is used.

After making the above adjustments to the model, the unknown state x vector is defined as:

$$x = \left(X, Y, Z, T_{r_2}, T_{r_1}, I_1, I_2, \ldots, I_{Maxsat}, N_1, N_2, \ldots, N_{Maxsat\cdot numfreq}\right) \tag{5}$$

where, *Maxsat* and *numfreq* represents the number of satellites and frequencies respectively.

2.2 Estimation of DISB

The phase and code ISBs can be estimated precisely on zero or ultra-short baselines based on Eq. (3) where differential atmosphere errors could be ignored. Due to the integer part of DISB is linearly dependent with ambiguity so they can be lumped together, so we could only get the fractional part of the phase DISB. Of course, this rank deficiency problem do not exist in the estimation of code DISB. The code and fractional part of phase DISB can be calculated through the following equation,

$$\begin{aligned} \nabla\Delta b^{GE}_{r_1r_2,fractional} &= \left(\nabla\Delta L^{G_1E_s}_{r_1r_2} - \nabla\Delta\rho^{G_1E_s}_{r_1r_2}\right)/\lambda - \left[\left(\nabla\Delta L^{G_1E_s}_{r_1r_2} - \nabla\Delta\rho^{G_1E_s}_{r_1r_2}\right)/\lambda\right] \\ \nabla\Delta B^{GE}_{r_1r_2} &= \nabla\Delta P^{G_1E_s}_{r_1r_2} - \nabla\Delta\rho^{G_1E_s}_{r_1r_2} \end{aligned} \tag{6}$$

where, the $[\cdot]$ denotes rounding function.

2.3 Strategy of Partial Ambiguity Resolution

In the multi-constellation RTK processing, it is not easy to fix all ambiguities reliably, however, one could have sufficient confidence to fix a subset of the ambiguities, which is referred to as partial ambiguity resolution (PAR) [17]. As we all know, the low-elevation ambiguities suffer much more from observation noise, multipath effects and the residual atmospheric delays, and thus have lower accuracies and also take longer to converge to a certain degree of precision. Therefore it is generally hard to fix these ambiguities correctly due to its poor accuracy and high correlation with others. In the other hand, if we fix all the ambiguities simultaneously, the low-elevation ones may influence the search system and make the search result unable to pass the acceptance test [14]. Fortunately, the number of visible satellites greatly increases when both GPS and Galileo are used, which means a higher cut-off angle could be used. In this Section, a simple but robust PAR strategy with ambiguity subset selected based on the elevations and the number of consecutive tracking will be introduced. Figure 1 presents the flowchart of this procedure.

First, the procedure starts with SD float ambiguity and an initial elevation mask of 10 degrees, and the threshold number of consecutive locked is set to 10, then we could get the DD float solution and the corresponding variance. If the number of DD float ambiguity is greater than 6, the LAMBDA method is applied to get the optimal candidate. If the bootstrapping success rate and value of ratio is higher than the threshold (e.g., 0.99 and 3.0), tight constraints is applied on ambiguities which is the so-called “Fix and Hold”, and the ambiguity-fixed solution is achieved. Otherwise, the elevation mask of AR will increase by 5°, and repeat the LAMBDA search and AR test. Until the number of DD ambiguities is less than 6, the iteration will be terminated and only a float solution is achieved at this epoch.

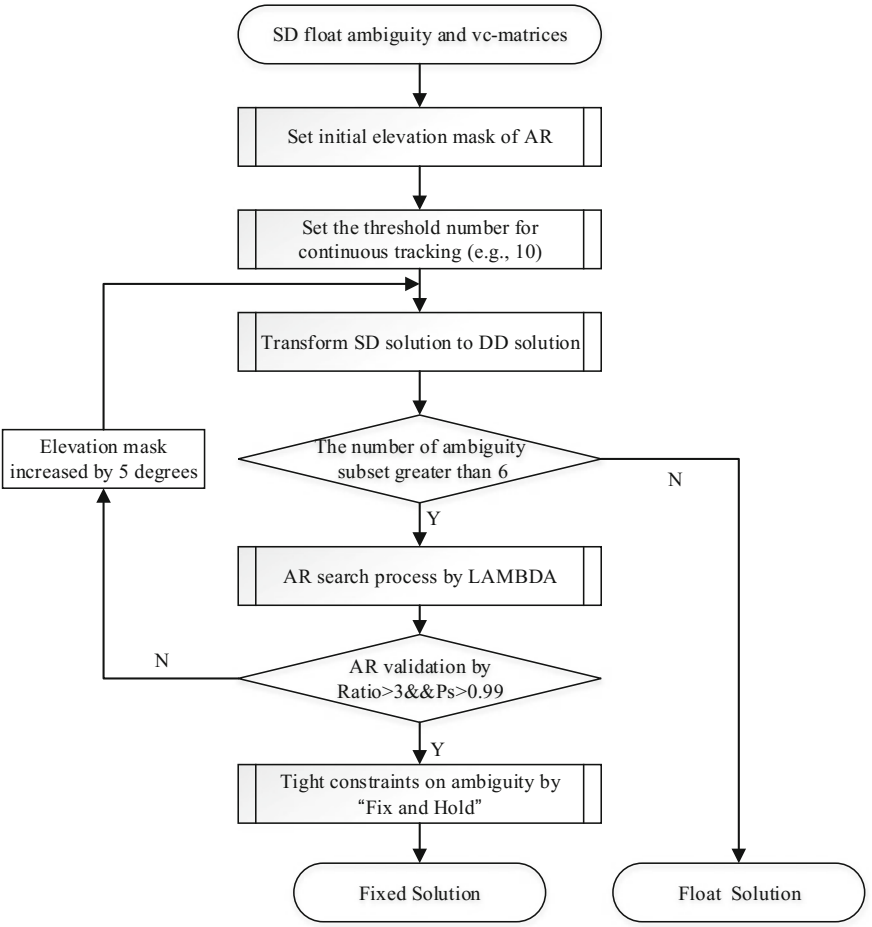

Fig. 1 The flowchart of PAR procedure

3 Data Processing

Similar to earlier DISB studies, the estimation of code and phase DISBs on overlapping frequencies L1/E1 and L5/E5a is achieved through zero and ultra-short baselines, since the atmospheric effects can be ignored. Here, three MGEX stations (CUT0, CUT2, CUTC) in campus of Curtin University, Australia is selected. As mentioned earlier, the purpose of DISB calibration is to improve the performance of ambiguity resolution which is essential to high-precision mixed-constellation RTK positioning. The calibration of DISB is verified with 3 long baselines range from 570 to 1200 km which is formed by PERT, MRO1 and KARR in Australia. It is worth mentioning that the coordinates of the MGEX stations are known and have

Table 1 Baselines used in the experiment of estimation and calibration of DISB

Baseline	Receiver Type1 (Version)	Receiver Type2 (Version)	Baseline Length	Remark
CUT2-CUT0	Trimble NETR9 (5.22)	Trimble NETR9 (5.22)	0 m	Estimation
CUTC-CUT0	Trimble NETR9 (5.30)	Trimble NETR9 (5.22)	8 m	
MRO1-KARR	Trimble NETR9 (5.22)	Trimble NETR9 (5.22)	634.484 km	Calibration
PERT-MRO1	Trimble NETR9 (5.30)	Trimble NETR9 (5.22)	570.399 km	
PERT-KARR	Trimble NETR9 (5.30)	Trimble NETR9 (5.22)	1203.129 km	

an accuracy of a few millimeters. Detailed information for each baseline is shown in Table 1. All stations are equipped with Trimble NETR9 receiver but different firmware version. The data were collected on DOY 300, 2017 with the sampling interval of 30 s.

Table 2 summarizes the detailed processing strategy for long baseline RTK positioning. Precise orbit at intervals 5 min provided by MGEX (e.g., GFZ) were used since the accuracy of broadcast ephemeris is limited. For data modeling, we applied the absolute phase centers [18], the phase-wind up effects [19] and the station displacement models proposed by IERS Convensions 2010 [20]. A cut-off angel of 10° was set for usable measurement and an elevation-dependent weighting strategy was applied to measurements where a priori precision of 3 mm and 3 m for raw phase and code, respectively. In addition, the station coordinate was estimated as white noise process with variance of 30^2 m^2. The bootstrapping success rate and ratio-test threshold were 0.99 and 3.0 respectively.

4 Results and Discussion

In this section, we first discuss the characteristics of the code/phase DISB estimated from zero or ultra-short baseline, then analysis the ambiguity performance of long baseline RTK positioning with DISB calibration, and finally address the statistical results of positioning accuracy under LC and TC strategy.

4.1 Results of Code/Phase DISB

The estimated code and phase DISB on frequencies L1/E1 and L5/E5a calculated from Eq. (6) are shown in Figs. 2 and 3 respectively. It is obviously that the DISB

Table 2 Tightly combined processing strategy for long baseline

Item	Models
Solution mode	Kinematic
Constellation	GPS & Galileo
Observations	Carrier phase and code observations
Estimator	Kalman filter
Frequency selection	GPS:L1/L2/L5; Galileo:E1/E5a/E5b
Elevation cutoff angle	10°
Sampling rate	30 s
Weighting scheme	Elevation-dependent weight: A priori precision of 3 mm and 3 m for raw phase and code, respectively
Ionospheric delay	Estimated as random-walk process
Tropospheric delay	Dry component: corrected with standard atmosphere and Saastamoinen model Wet component: estimated as random-walk process(10^{-8} m^2/s), NMF mapping function applied
Sagnac effect	Applied
Station displacement	Corrected by IERS Convention 2010
Satellite antenna PCO/PCV	Corrected by IGS 14.atx
Receiver antenna PCO/PCV	PCO/PCV values for GPS from IGS14.atx are used
Satellite orbit	Fixed to MGEX (GFZ) products
Satellite clock	DD eliminated or weakening
Receiver clock	DD eliminated or weakening
Station coordinate	Estimated as white noise process (30^2 m^2)
Phase ambiguity	Estimated, constant for each continuous arcs, Fix and Hold
Bootstrapping success rate threshold	0.99
Ratio test threshold	3.0

is rather stable over the whole observation period regardless of the random terms caused by observation noises. The mean of phase DISB over the day is close to zero indeed and the standard deviations for both L1/E1 and L5/E5a are all within 0.02 cycles. Compared with phase DISB, the code DISB show greater noise due to the pseudorange noise and the standard deviations are all within 0.6 m. Despite the larger noise in code DISB, the amplitude is still relatively stable. The detailed statistical results is summarized in Table 3.

It can be seen that the code and phase DISB on both frequencies estimated from CUTC-CUT0 show larger noise than that from CUT2-CUT0. This may be caused by the following two reasons: The first one is that the different firmware version over the both sides of the baseline CUTC-CUT0; The second is that the baseline CUT2-CUT0 is a zero baseline for which differential atmospheric errors are completely absent and multi-path errors are very minor while the baseline CUTC-CUT0

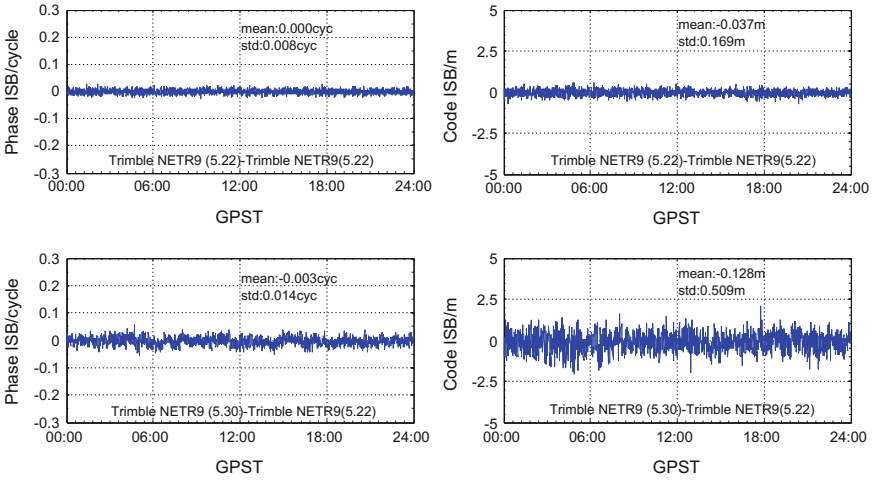

Fig. 2 Estimated fractional phase (left) and code (right) DISB on L1/E1 corresponding to CUT2-CUT0 (top) and CUTC-CUT0 (bottom)

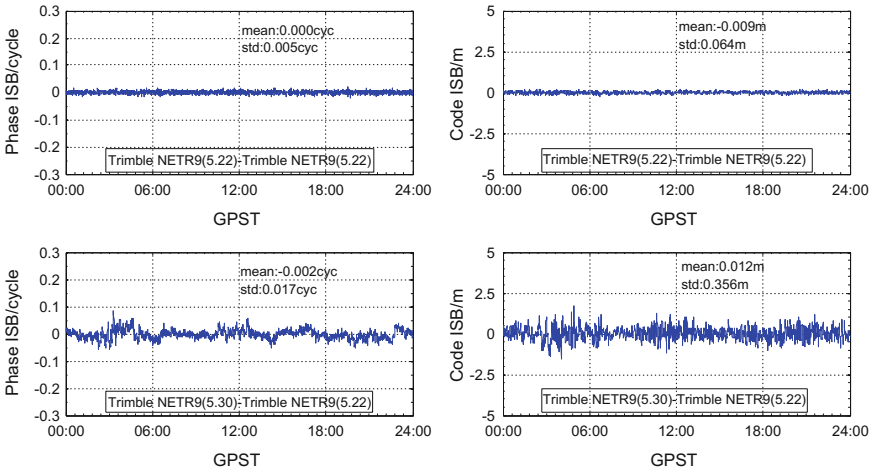

Fig. 3 Estimated fractional phase (left) and code (right) DISB on L5/E5a corresponding to CUT2-CUT0 (top) and CUTC-CUT0 (bottom)

Table 3 Statistical results of fractional phase and code DISB

Baseline	L1/E1 Phase		L1/E1 Code		L5/E5a Phase		L5/E5a Code	
	Mean/cyc	Std/cyc	Mean/m	Std/m	Mean/cyc	Std/cyc	Mean/m	Std/m
CUT2-CUT0	0.000	0.008	−0.037	0.169	0.000	0.005	−0.009	0.064
CUTC-CUT0	−0.003	0.014	−0.128	0.509	−0.002	0.017	0.012	0.356

is a nonzero-baseline. We adopted the DISB calibration in the long baseline experiments corresponding to the receiver firmware version.

4.2 Results of AR Performance

The AR results of LC and TC for three different long baselines are shown in this section. Figure 4 shows the value of ratio (left) over the day and success rate (right) for the first 6 h. From Fig. 4, we can find that TC strategy do not significantly improve the value of ratio, but shorten the convergence time to reach the 100% success rate. This is because that during the initial period, TC strategy could provide more observations, so additional redundancies are introduced which is beneficial to the ambiguity resolution.

Figure 5 shows the AR performance in terms of TTFF (left) and the fixing rate (right) of three different long baselines under LC and TC strategy. In this paper, the TTFF was defined as the time taken for the ambiguity-fixed solution to be successfully achieved and the following 10 epochs also keep fixed. The fixing rate was defined as the ratio of the number of fixed epochs to the number of total epochs during this period. Since we apply the DISB calibration advance in TC strategy,

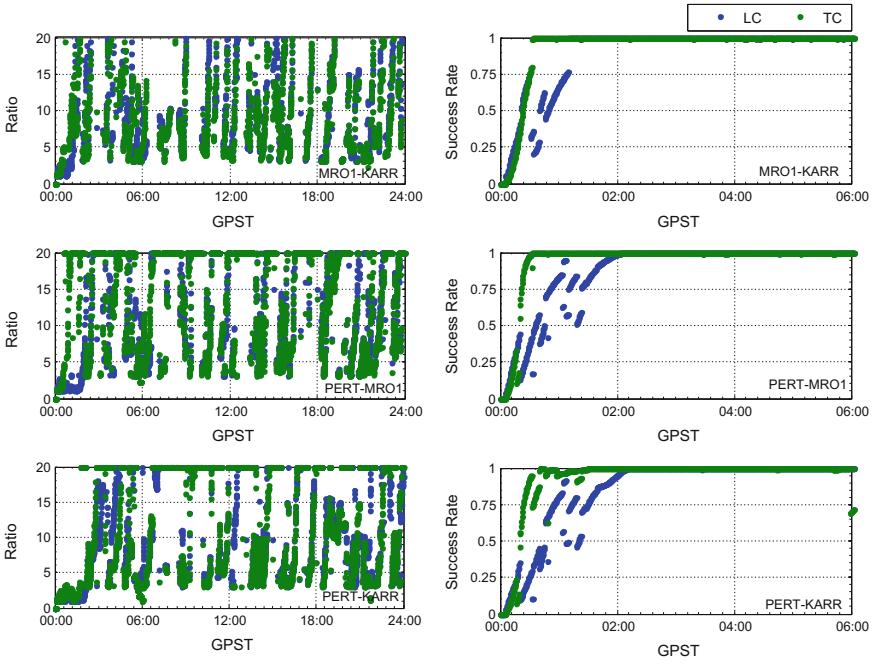

Fig. 4 Ratio value (left) and bootstrapping success rate (right) corresponding to MRO1-KARR (top), PERT-MRO1 (medium), PERT-KARR (bottom) under LC and TC strategy respectively

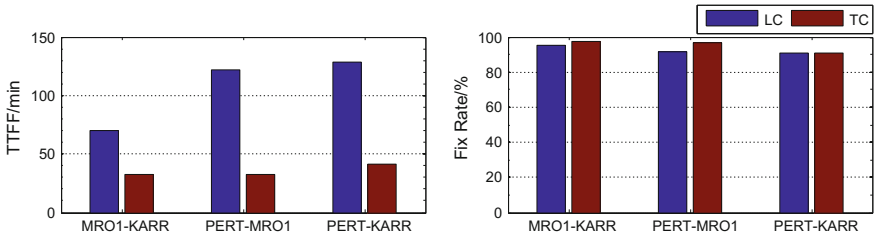

Fig. 5 TTFF (left) and fix rate (right) of epochs correspond to different baselines

there is more redundancies compared with LC strategy, which result in shorter convergence time to first fix, as shown in Fig. 5. The time to first fix is 70, 122, 129 min under LC strategy, while only 32, 33, 40 min under TC strategy corresponding to MRO1-KARR, PERT-MRO1, PERT-KARR baseline. Compared with results of LC strategy, TTFF is further reduced by 54.3, 72.9, 69.0% respectively. Figure 5 (right) also shows that TC strategy could slightly improve the fixing rate of epochs.

Figure 6 shows the common view satellite number of Galileo (top) and ambiguity fix period of Galileo (bottom) corresponding to MRO1-KARR baseline. It is easy to find that TC could achieve longer fixing period. During some period as checked in red rectangle in Fig. 6, there is only one common view Galileo satellite

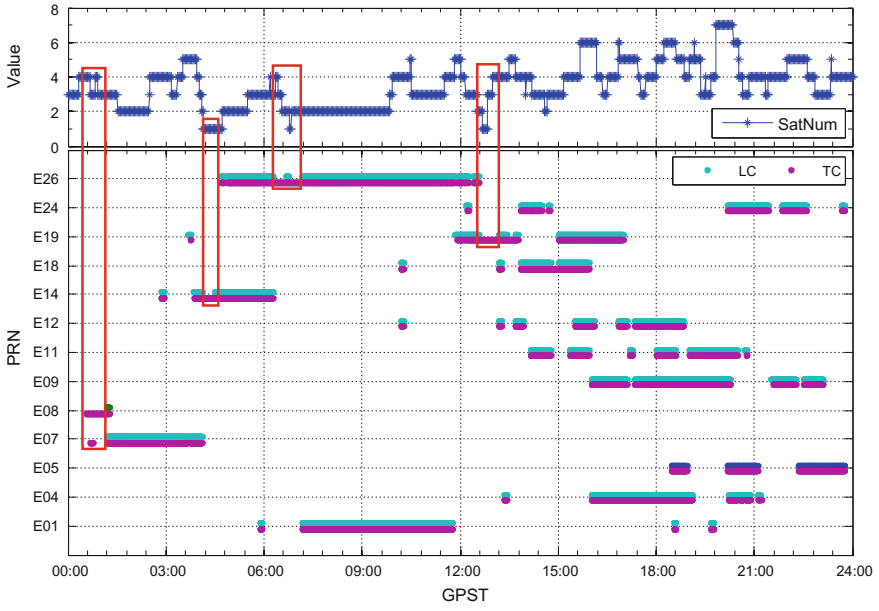

Fig. 6 Common view satellite number (top) and fixed period (bottom) of Galileo system corresponding to MRO1-KARR

where double-difference ambiguity could not be formed within Galileo system and the number of satellites is dramatically changing which lead to frequent reinitialization of new rise satellites, LC could only keep float solutions, while TC could still get the fixed solutions. It come to the following conclusion that compared with LC strategy, TC strategy has a better performance in AR.

4.3 Results of Positioning

As mentioned earlier, the coordinates of three stations are precisely known from the IGS weekly solution. Baseline errors are the difference between the estimated baseline length and precise reference baseline length. Baseline errors of different combination strategy are shown in Fig. 7. The light green dotted line in the figure marked the TTFF. It is easy to find that fluctuation in the up direction is larger than that in north and east direction. Detailed precision statistics are summarized in

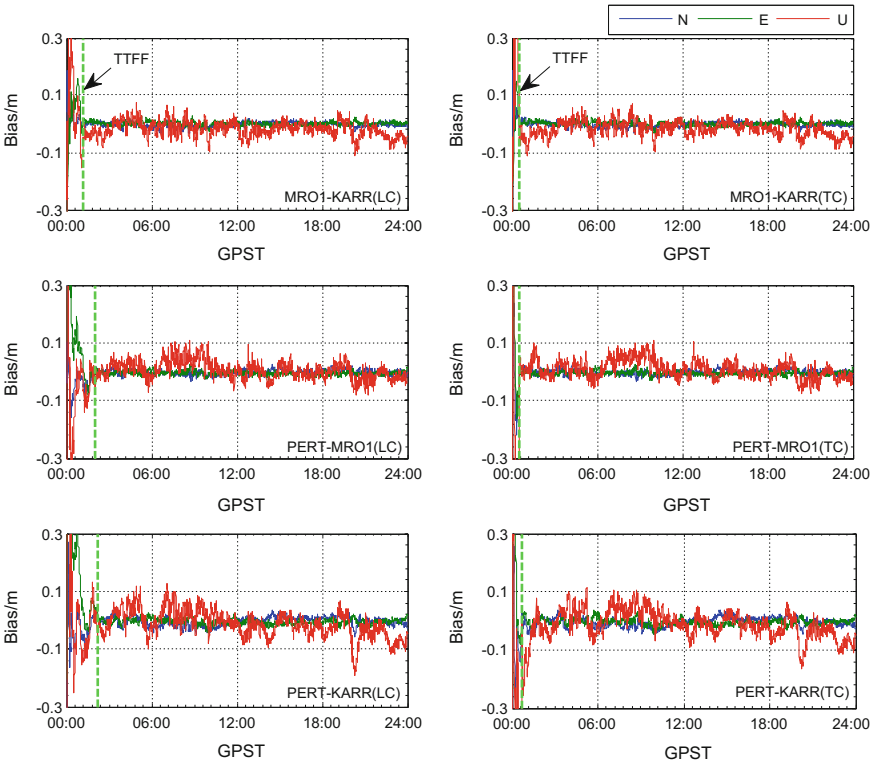

Fig. 7 Baseline errors for LC (left) and TC (right) strategy corresponding to MRO1-KARR (top), PERT-MRO1 (medium), PERT-KARR (bottom)

Table 4 RMS statistics of baseline error

Baseline	LC-RMS				TC-RMS			
	N/m	E/m	U/m	3D/m	N/m	E/m	U/m	3D/m
MRO1-KARR	0.009	0.007	0.032	0.034	0.008	0.007	0.031	0.033
PERT-MRO1	0.009	0.009	0.030	0.033	0.009	0.009	0.031	0.034
PERT-KARR	0.016	0.011	0.048	0.052	0.015	0.011	0.046	0.050

Table 4. It must be noted that only the ambiguity-fixed solution is contained in the statistics. The 3D positioning errors is 3.4, 3.3, 4.8 cm under LC strategy, while 3.3, 3.4, 5.0 cm under TC strategy corresponding to MRO1-KARR, PERT-MRO1, PERT-KARR baseline. LC and TC strategy could both achieve centimeter-level positioning accuracy in the case of ambiguity fixed correctly. The length of PERT-KARR is almost twice of that of other two baselines and the accuracy of PERT-KARR baseline is also worse than that of other two baselines due to residual atmospheric errors, such as residual tropospheric delay and ionospheric delay.

5 Conclusions

We first propose a GPS/Galileo tightly combined RTK positioning model with raw carrier phase and code observations for long baselines which avoid the hand-over problem of reference satellites in traditional DD model, then the estimation of DISB model based on zero or ultra-short baseline is developed. In order to get better AR performance, a simple but robust strategy of partial ambiguity resolution is suggested, where the satellite elevation, number of consecutive tracking, success rate and ratio test are all combined to determine the subset of ambiguity. The DISB results based on zero/ultra-short baseline with different receiver firmware version shows that the code and phase DISB is rather stable over time which means that it could be corrected in advance. Three long baselines range from 570 to 1200 km were tested with DISB calibration in advance to verify the proposed model. The results shows that TC strategy do not improve the value of ratio but shorten the time to reach 100% success rate, compared with the LC strategy. At the same time, TC strategy could significantly shorten the time to first fix and improve the fixing rate of epochs slightly, which means that under some circumstances, LC strategy could only keep float solutions while the TC strategy could still get ambiguity-fixed solutions. In term of positioning accuracy, the precision in up direction is worse than that in north and east direction. Once the ambiguity is fixed correctly, both LC and TC strategy can achieve centimeter-level positioning accuracy. This paper just gives the preliminary research results about the DISB application under long baseline circumstances. Using more data for experimental verification and investigating of what performance the real-time precise products could archive are the points that we will focus on and continue to research.

Acknowledgements The authors gratefully acknowledge IGS Multi-GNSS Experiment (MGEX) for providing GNSS data and products. We appreciate anonymous reviewers for their valuable comments and improvements to this manuscript. Thanks also go to the National Natural Science Foundation of China (No: 41574026, 41774027), Primary Research & Development Plan of Jiangsu province (Grant Number BE2016176), National Key Technologies R&D Program (Grant Number 2016YFB0502101) and Six Talent Peaks Project in Jiangsu Province (Grant Number 2015-WLW-002).

References

1. Pan SG, Meng X, Wang SL et al (2015) Ambiguity resolution with double troposphere parameter restriction for long range reference stations in NRTK system. Surv Rev 47 (345):429–437
2. Gao W, Gao C, Pan S et al (2015) Improving ambiguity resolution for medium baselines using combined GPS and BDS dual/triple-frequency observations. Sensors 15(11):27525–27542
3. Gao W, Gao C, Pan S et al (2017) Method and assessment of BDS triple-frequency ambiguity resolution for long-baseline network RTK. Adv Space Res
4. Julien O, Alves P, Cannon ME et al (2003) A tightly coupled GPS/GALILEO combination for improved ambiguity resolution. In: Proceedings of the European Navigation Conference (ENC-GNSS'03), pp 1–14
5. Liu H, Shu B, Xu L et al (2017) Accounting for inter-system bias in DGNSS positioning with GPS/GLONASS/BDS/Galileo. J Navig, 1–13
6. Paziewski J, Wielgosz P (2015) Accounting for Galileo–GPS inter-system biases in precise satellite positioning. J Geodesy 89(1):81–93
7. Odijk D, Teunissen PJG (2013) Estimation of differential inter-system biases between the overlapping frequencies of GPS, Galileo, BeiDou and QZSS. In: 4th international colloquium scientific and fundamental aspects of the Galileo programme, pp 4–6
8. Montenbruck O, Hauschild A, Hessels U (2011) Characterization of GPS/GIOVE sensor stations in the CONGO network. GPS Solutions 15(3):193–205
9. Odijk D, Teunissen PJG (2013) Characterization of between-receiver GPS-Galileo inter-system biases and their effect on mixed ambiguity resolution. GPS Solutions 17 (4):521–533
10. Tian Y, Ge M, Neitzel F et al (2017) Particle filter-based estimation of inter-system phase bias for real-time integer ambiguity resolution. GPS Solutions 21(3):949–961
11. Gao W, Gao C, Pan S et al (2017) Inter-system differencing between GPS and BDS for medium-baseline RTK positioning. Remote Sens 9(9):948
12. Mowlam AP, Collier PA (2004) Fast ambiguity resolution performance using partially-fixed multi-GNSS phase observations. In: International symposium on GNSS/GPS. Sydney, Australia, pp 6–8
13. Parkins A (2011) Increasing GNSS RTK availability with a new single-epoch batch partial ambiguity resolution algorithm. GPS Solutions 15(4):391–402
14. Gao W, Gao C, Pan S (2017) A method of GPS/BDS/GLONASS combined RTK positioning for middle-long baseline with partial ambiguity resolution. Surv Rev 49(354):212–220
15. Wang J, Feng Y (2013) Reliability of partial ambiguity fixing with multiple GNSS constellations. J Geodesy, 1–14
16. Brack A (2016) Partial ambiguity resolution for reliable GNSS positioning—a useful tool? In: Aerospace conference, 2016 IEEE. IEEE, pp 1–7

17. Teunissen PJG, Joosten P, Tiberius C (1999) Geometry-free ambiguity success rates in case of partial fixing. In: Proceedings of ION-NTM, pp 25–27
18. Schmid R, Steigenberger P, Gendt G et al (2007) Generation of a consistent absolute phase-center correction model for GPS receiver and satellite antennas. J Geodesy 81(12):781–798
19. Wu JT, Wu SC, Hajj GA et al (1992) Effects of antenna orientation on GPS carrier phase. Astrodynamics 1991, 1647–1660
20. Petit G, Luzum B (2010) IERS conventions. BUREAU INTERNATIONAL DES POIDS ET MESURES SEVRES (FRANCE)

A Method of Medium/Long Baseline Ambiguity Resolution Based on BDS Triple-Frequency

Dengao Li, Meng Shi, Wenjing Li, Jumin Zhao and Junbing Cheng

Abstract High precision positioning using carrier phase observations is the main method and approach of Beidou navigation satellite system (BDS) positioning. Especially, the ambiguity fixing has always been the focus, and it is always the key problem of the related research. In the medium/long baseline, the ionospheric delay error will affect the efficiency of ambiguity resolution seriously, and then affect the precision and efficiency of precise positioning. To solve this problem, this paper put forward a method of medium/long baseline ambiguity resolution based on the classical three-carrier ambiguity resolution (TCAR) model. To improve the reliability of wide-lane (WL) ambiguity fixing, a factor is introduced into the optimal linear combination for reducing noise, and the ionospheric priori standard deviation is used to minimize the effect of the length of the baseline. In order to verify the feasibility and effectiveness of the algorithm, the proposed algorithm is compared with the classical TCAR algorithm in several aspects such as the ambiguity fixed success rate. The results show that the proposed algorithm has the highest success rate in the case of medium/long baseline, and can fix the ambiguity instantly.

Keywords Ambiguity resolution · TCAR · BDS Triple-frequency
Medium/long baseline · Ionospheric delay

1 Introduction

The fast fixing of the ambiguity is the key to realize high precision real-time positioning, and is one of the hot issues in the research of global navigation satellite system (GNSS). At present, GNSS can send three or more frequency signals. The use of multi-frequency combination of signals can improve the reliability and

D. Li (✉) · M. Shi · W. Li · J. Zhao · J. Cheng
College of Information Engineering, Taiyuan University of Technology, Jinzhong, China
e-mail: lidengao@tyut.edu.cn

J. Sun et al. (eds.), *China Satellite Navigation Conference (CSNC) 2018 Proceedings*, Lecture Notes in Electrical Engineering 498,
https://doi.org/10.1007/978-981-13-0014-1_56

validity of ambiguity fixed [12]. The Beidou satellite navigation system (BDS) provides three frequency signals of B1, B2 and B3, which can form a combined observation value with longer wavelengths and smaller noise, which is conducive to ambiguity resolution.

At present, in the case of three-carrier ambiguity resolution (TCAR), most errors, including orbit errors, tropospheric delay errors and ionospheric delay errors, can be canceled or reduced by double-differences for short baselines. However, for the medium/long baseline, the ionospheric delay and noise error are the main limiting factors for the fixation of the ambiguity. Feng et al. [2] proposed a combination of pseudorange and carrier based on geometry-free and ionosphere-free model, which can effectively reduce the influence of medium/long baseline ionospheric delay on the ambiguity fixing. Based on the geometric model, Xie et al. [7] use the geometry-based model and obtained the optimal linear combination of observation of the original pseudoranges and the observation of the ambiguity solved extra-wide-lane (EWL) and wide-lane (WL). Tian et al. [5] smoothed the double-difference ionospheric delay to solve the floating-point ambiguity. Li et al. [4] used the partial ambiguity fixing method in the narrow-lane (NL) ambiguity resolution, and optimized the traditional TCAR algorithm. Wang et al. [6], by giving different weights to pseudorange observations to aid the WL and NL to eliminate the effects of ionospheric residuals, the solution of WL and NL is only affected by the observation noise. Then the ambiguity value of wide-lane and narrow-lane is obtained by the smoothing of multiple epochs. Zhuang [11] analyzed the factors affecting the long baseline ambiguity fixing, and studied the theory of the ambiguity resolution of the Geometry-based model in the TCAR method, and proposed a new ambiguity fixing method using the multi-epoch smoothing. Deng et al. [1] inherited the traditional TCAR method. According to the different characteristics and different purposes in each step of the ambiguity resolution, chose the optimal combination of observations, effectively improved the ambiguity of the solution rate.

In this paper, we proposed a new method of medium/long baseline ambiguity resolution followed the steps of solving the EWL, WL and NL ambiguity in TCAR. First, the combination ambiguity of two EWL is fixed and the double-difference ionospheric delay is solved. Secondly, the pseudoranges observation and ambiguity fixed EWL observation are linearly combined to obtain the combined observations of the lowest noise based on ionosphere-free or ionosphere-based model. Finally, the least squares criterion is used to solve the NL ambiguity, while the double-difference ionospheric delay, the NL ambiguity and the position parameters are taken as the unknowns. The ionospheric parameters are added, the virtual ionosphere priori standard deviation is determined by the length of the baseline, so as to improve the accuracy of NL ambiguity fixing.

2 Classic TCAR Algorithm

The main idea of classical TCAR algorithm is to combine the original carrier phase observation to get the optimal virtual observation of long wavelength, weak ionospheric delay and low observation noise. According to the wavelength from long to short, followed by EWL, WL and NL ambiguity fixing, the efficiency of ambiguity fixing can be improved significantly [3].

2.1 Linear Combination of Observations

Double-difference combined observations based on triple-frequency can be described as follows [9]:

$$\nabla\Delta P(i,j,k) = \frac{if_1\nabla\Delta P_1 + jf_2\nabla\Delta P_2 + kf_3\nabla\Delta P_3}{if_1 + jf_2 + kf_3} \tag{1}$$

$$\nabla\Delta\phi(i,j,k) = \frac{if_1\nabla\Delta\phi_1 + jf_2\nabla\Delta\phi_2 + kf_3\nabla\Delta\phi_3}{if_1 + jf_2 + kf_3} \tag{2}$$

where $\nabla\Delta$ is double-difference symbol, $\nabla\Delta P$ is double-difference pseudorange observation, $\nabla\Delta\phi$ is double-difference carrier phase observation, i, j, k are arbitrary integer combination coefficients, f_1, f_2, f_3 are frequencies of the three carriers.

The first ionospheric delay scale factor $\beta_{(i,j,k)}$ and the carrier noise factor $\mu_{(i,j,k)}$ of the combined measurement are:

$$\beta_{(i,j,k)} = \frac{f_1^2(i/f_1 + j/f_2 + k/f_3)}{if_1 + jf_2 + kf_3} \tag{3}$$

$$\mu_{(i,j,k)} = \frac{(if_1)^2 + (jf_2)^2 + (kf_3)^2}{(if_1 + jf_2 + kf_3)^2} \tag{4}$$

2.2 TCAR Algorithm Flow

The first step is to solve the ambiguity of EWL:

Because of the high accuracy of pseudorange observations at B3 frequency points in BDS, it can be used to solve ambiguity resolution of EWL. The EWL ambiguity parameter $\nabla\Delta N_{(0,1,-1)}$ is calculated as follows:

$$\nabla\Delta N_{(0,1,-1)} = \left[\frac{\nabla\Delta P_3 - \nabla\Delta\phi_{(0,1,-1)}}{\lambda_{(0,1,-1)}}\right] \tag{5}$$

where [ ] means rounding.

The second step is to solve the ambiguity of WL:

The ambiguity fixed EWL is regarded as a high precision pseudorange observation, which is used to calculate the WL ambiguity. The calculation is as follows:

$$\nabla\Delta\widetilde{\phi}_{(0,1,-1)} = \nabla\Delta\phi_{(0,1,-1)} + \lambda_{(0,1,-1)}\nabla\Delta N_{(0,1,-1)} \tag{6}$$

$$\nabla\Delta N_{(1,-1,0)} = [\nabla\Delta\widetilde{\phi}_{(0,1,-1)} - \nabla\Delta\phi_{(1,-1,0)} + (\beta_{(0,1,-1)} - \beta_{(1,-1,0)})\nabla\Delta I_1 \Big/ \lambda_{(1,-1,0)}] \tag{7}$$

The third step is to solve the ambiguity of NL:

The ambiguity fixed WL is regarded as a high precision pseudorange observation, which is used to calculate the NL ambiguity. The calculation is as follows:

$$\nabla\Delta\widetilde{\phi}_{(1,-1,0)} = \nabla\Delta\phi_{(1,-1,0)} + \lambda_{(1,-1,0)}\nabla\Delta N_{(1,-1,0)} \tag{8}$$

$$\nabla\Delta N_{(1,0,0)} = [\nabla\Delta\widetilde{\phi}_{(1,-1,0)} - \nabla\Delta\phi_{(1,0,0)} + (\beta_{(1,-1,0)} - \beta_{(1,0,0)})\nabla\Delta I_1 \Big/ \lambda_{(1,0,0)}] \tag{9}$$

$$\nabla\Delta N_{(0,1,0)} = \nabla\Delta N_{(1,0,0)} - \nabla\Delta N_{(1,-1,0)} \tag{10}$$

$$\nabla\Delta N_{(0,0,1)} = \nabla\Delta N_{(0,1,0)} - \nabla\Delta N_{(0,1,-1)} \tag{11}$$

In the first step, the success rate of ambiguity fixing in EWL mainly depends on the influence of noise. The combination of (0, 1, −1) is selected, because its wavelength is longer, so by direct rounding method the ambiguity can be accurately fixed [8].

In the second and third steps, the geometry containing the double-difference tropospheric errors can be eliminated. For short baselines, the double-difference ionospheric delay can also be neglected. However, as the baseline length increases, the effects of double-difference ionospheric delay and observed noises on the ambiguities are gradually increasing. In step 3, the double-difference ionospheric delay becomes more dominant. Therefore, TCAR algorithm is difficult to adapt to medium/long baseline conditions.

3 Improved Algorithm

Double-difference ionospheric delay and measurement noise are the main factors that limit the application of classical TCAR algorithm in medium/long baseline. Based on the classical TCAR algorithm, this paper reduces the influence of noise by using an adaptive factor, and adds the prior information of ionospheric delay to reduce the influence of ionospheric delay. Algorithm flow chart is as follows (Fig. 1):

3.1 EWL Ambiguity Fixing

Based on the geometry-free model, two easily fixed EWL ambiguity are fixed. In this step, the classical TCAR is used to solve the ambiguity of EWL directly. EWL combination (0, 1, −1) and (1, −6, 5) have longer wavelength, which is suitable for ambiguity fixing. So choose the two combinations to fix EWL ambiguities. The calculation is as follows:

$$\nabla\Delta N_{(0,1,-1)} = \left[\frac{\nabla\Delta P_3 - \nabla\Delta\phi_{(0,1,-1)}}{\lambda_{(0,1,-1)}}\right] \tag{12}$$

$$\nabla\Delta N_{(1,-6,5)} = \left[\frac{\nabla\Delta P_3 - \nabla\Delta\phi_{(1,-6,5)}}{\lambda_{(1,-6,5)}}\right] \tag{13}$$

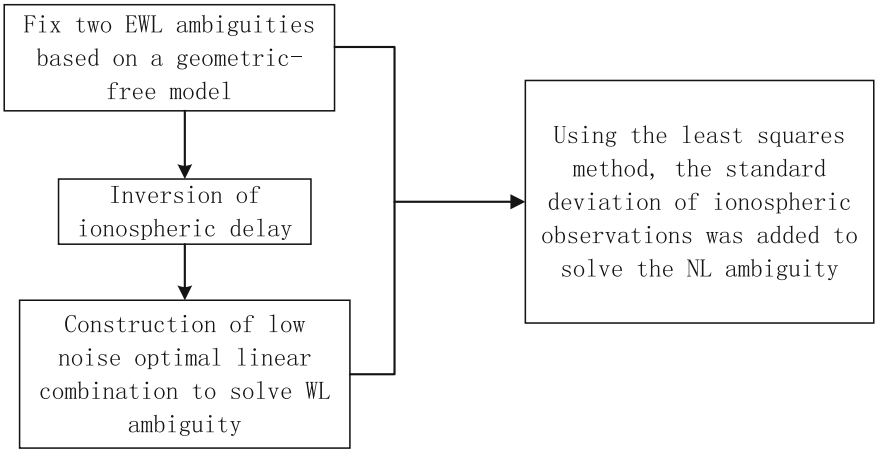

Fig. 1 Algorithm flow chart

After fixing two EWL ambiguities, the double-difference ionospheric delay is solved in real time according to the combined observation of the EWL. The calculation is as follows:

$$\nabla\Delta I_1 = \frac{\lambda_{(0,1,-1)}N_{(0,1,-1)} + \nabla\Delta\phi_{(0,1,-1)} - \lambda_{(1,-6,5)}N_{(1,-6,5)} - \nabla\Delta\phi_{(1,-6,5)}}{\beta_{(1,-6,5)} - \beta_{(0,1,-1)}} \quad (14)$$

3.2 WL Ambiguity Fixing

The three original pseudorange observations and the ambiguity fixed EWL observations are combined to obtain the optimal linear combination. The adaptive factor with the double-difference ionospheric delay variation is added to obtain the combined observations of the ionosphere-free or ionosphere-based with the lowest noise. WL ambiguity fixed calculation formula is as follows:

$$\nabla\Delta N_{(1,-1,0)} = [\frac{m_1\nabla\Delta P_{(1,0,0)} + m_2\nabla\Delta P_{(0,1,0)} + m_3\nabla\Delta P_{(0,0,1)} + m_4\nabla\Delta\widetilde{\phi}_{(0,1,-1)} - \nabla\Delta\phi_{(1,-1,0)}}{\lambda_{(1,-1,0)}}] \quad (15)$$

where m_1, m_2, m_3, m_4 are the weight factors in the linear combination, they satisfy the following constraints:

$$m_1 + m_2 + m_3 + m_4 = 1 \quad (16)$$

$$m_1\beta_{(1,0,0)} + m_2\beta_{(0,1,0)} + m_3\beta_{(0,0,1)} - m_4\beta_{(0,1,-1)} = -(1+\kappa)\beta_{(1,-1,0)} \quad (17)$$

$$(m_1^2\mu_{(1,0,0)}^2 + m_2^2\mu_{(0,1,0)}^2 + m_3^2\mu_{(0,0,1)}^2)\sigma_P^2 + m_4^2\mu_{(0,1,-1)}^2\sigma_\phi^2 = \min \quad (18)$$

Among them, the formula (16) is to avoid the unmodeled error (tropospheric error, orbital error, etc.); formula (18) is to make the combined noise minimum.

In formula (17), κ is the adaptive factor that varies with the delay level of the double-difference ionosphere to balance the double-difference ionospheric delay and the combined noise. Relative to the NL ambiguity fixed, WL ambiguity fixed process can withstand a certain double-difference ionospheric delay. Therefore, when the double-difference ionosphere delay is small, it is not necessary to completely eliminate the ionospheric delay. Therefore, the problem of noise increasing caused by deionization is reduced to a certain extent. The value of κ varies with the level of the double-difference ionospheric delay solved in the first step. When the double-difference ionosphere delay is large, κ is taken as 0 to construct the ionosphere-free model. When the double-difference ionosphere delay is small, κ takes a small value which does not affect the WL ambiguity fixation success rate to construct ionosphere-based model. The value of K is as follows:

$$\kappa = \begin{cases} 0.2, & \nabla\Delta I_1 < 1\,\mathrm{m} \\ 0.1, & 1\,\mathrm{m} < \nabla\Delta I_1 < 2\,\mathrm{m} \\ 0, & \nabla\Delta I_1 > 2\,\mathrm{m} \end{cases} \tag{19}$$

3.3 NL Ambiguity Fixing

For short baselines, ionospheric delay and tropospheric delay can be eliminated or reduced by double-difference, which makes it possible to accurately determine NL ambiguity in the third step. However, with the increase of baseline length, the double-difference ionospheric delay becomes the main constraint for the medium/long baseline NL ambiguity fixation.

The double-difference ionospheric delay in the first step is not precise enough to be used for the correction of NL ambiguities. So the position parameter, NL ambiguity and double-difference ionospheric delay are taken as unknowns parameters, use the EWL and WL observation which has been fixed in the first and second steps to fix NL ambiguity. And use the least square method to solve the problem. The ionospheric parameter is added in this step, the priori standard deviation of the observed value of the virtual ionosphere is determined by the length of the baseline, so as to improve the accuracy of NL ambiguity fixation. After the NL ambiguity floating-point solution is obtained, it is fixed with LAMBDA.

The observation equation for solving the NL ambiguity is:

$$\begin{bmatrix} \lambda_{(0,1,-1)}\nabla\Delta\phi_{(0,1,-1)} + \lambda_{(0,1,-1)}\nabla\Delta N_{(0,1,-1)} - \nabla\Delta\rho \\ \lambda_{(1,-1,0)}\nabla\Delta\phi_{(1,-1,0)} + \lambda_{(1,-1,0)}\nabla\Delta N_{(1,-1,0)} - \nabla\Delta\rho \\ \lambda_{NL}\nabla\Delta\phi_{NL} - \nabla\Delta\rho \end{bmatrix} = \begin{bmatrix} C & 0 & E\beta_{(0,1,-1)} \\ C & 0 & E\beta_{(1,-1,0)} \\ C & -E\lambda_{NL} & E\beta_{NL} \end{bmatrix} \begin{bmatrix} \Delta X \\ \nabla\Delta N_{NL} \\ \nabla\Delta I_1 \end{bmatrix} + \begin{bmatrix} \varepsilon_{\nabla\Delta\phi_{(0,1,-1)}} \\ \varepsilon_{\nabla\Delta\phi_{(1,-1,0)}} \\ \varepsilon_{\nabla\Delta\phi_{(NL)}} \end{bmatrix} \tag{20}$$

where C is design matrix, E is unit matrix, ΔX is baseline location parameters, $\nabla\Delta\rho$ is double-difference geometric distance.

$$\begin{bmatrix} v_1 \\ v_2 \end{bmatrix} = \begin{bmatrix} B_1 & B_2 \\ 0 & E \end{bmatrix} \begin{bmatrix} x \\ \nabla\Delta I_1 \end{bmatrix} - \begin{bmatrix} l \\ l_{I_1} \end{bmatrix} \tag{21}$$

where v_1, v_2 are corrections, l_{I_1} is the first frequency ionospheric observations, B_1, B_2, x, l are as follows:

$$B_1 = \begin{bmatrix} A & 0 \\ A & 0 \\ A & -E\lambda_{NL} \end{bmatrix}, B_2 = \begin{bmatrix} E\beta_{(0,1,-1)} \\ E\beta_{(1,-1,0)} \\ E\beta_{NL} \end{bmatrix}, x = \begin{bmatrix} \Delta X \\ \nabla\Delta N_{NL} \end{bmatrix}$$
$$l = \begin{bmatrix} \lambda_{(0,1,-1)}\nabla\Delta\phi_{(0,1,-1)} + \lambda_{(0,1,-1)}\nabla\Delta N_{(0,1,-1)} - \nabla\Delta\rho \\ \lambda_{(1,-1,0)}\nabla\Delta\phi_{(1,-1,0)} + \lambda_{(1,-1,0)}\nabla\Delta N_{(1,-1,0)} - \nabla\Delta\rho \\ \lambda_{NL}\nabla\Delta\phi_{NL} - \nabla\Delta\rho \end{bmatrix} \tag{22}$$

The corresponding random model of l_{I_1} is:

$$D\begin{bmatrix} \phi \\ P \\ l_{I_1} \end{bmatrix} = \begin{bmatrix} Q_\phi & & \\ & Q_P & \\ & & Q_{l_{I_1}} \end{bmatrix} \tag{23}$$

where D is a conversion matrix that makes the single difference to double-difference, $Q_{l_{I_1}}$ represents the variance of the virtual ionosphere observations. Virtual ionospheric observations taken as 0, the key lies in the setting of $Q_{l_{I_1}}$. Set the relationship between ionospheric priori standard deviation and the length of baseline as follows:

$$R_{l_{I_1}} = \begin{cases} 0.05, & 15\,\text{km} < L < 30\,\text{km} \\ 0.2, & 30\,\text{km} \le L < 100\,\text{km} \\ 0.5, & L \ge 100\,\text{km} \end{cases} \tag{24}$$

where $R_{l_{I_1}}$ is the ionospheric priori standard deviation, L is the length of baseline.

4 Experiment Analysis

In order to verify the validity and feasibility of the proposed algorithm, three groups of baselines with lengths of 17, 72 and 160 km were analyzed experimentally. The data acquisition uses Si Nan multimode receiver, the satellite cut-off angle is set to 15°. The baseline data used is summarized in Table 1.

Table 1 Overview of experimental baseline data

The length of baseline/km	Observation epoch/s	Sampling interval/s	The satellite cut-off angle/(°)
17	7320	1	15
72	9780	1	15
160	9800	1	15

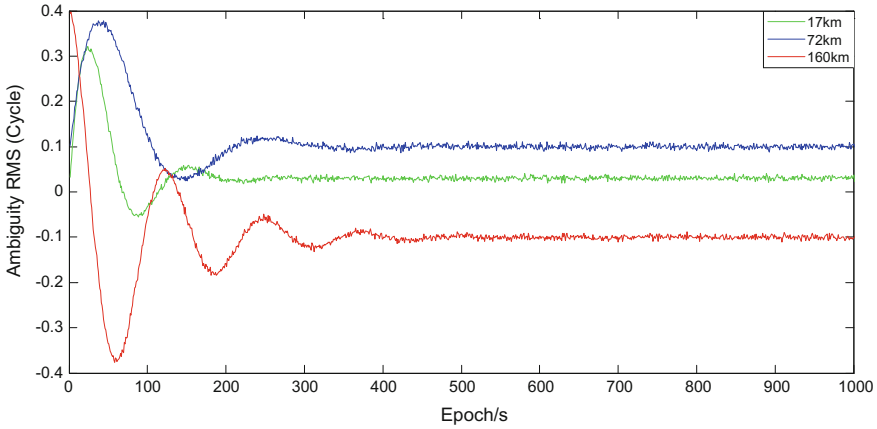

Fig. 2 Fixed error of WL ambiguity

The experiment is analyzed with the data of three groups of different lengths of baseline. The experimental results are shown in Figs. 2 and 3.

As can be seen from Figs. 2 and 3, with the increase of baseline length, WL and NL ambiguity floating error increases, but basically stable, and have a high fixed reliability.

As can be seen from Figs. 4 and 5, the positioning accuracy has been improved to a certain extent after the correction of the ionospheric prior standard deviation.

In the experiment, the fixed solution obtained by precise post-processing relative positioning is taken as the standard value, and the fixed value of the ambiguity obtained by each epoch is compared with the standard value to determine whether the ambiguity is fixed correctly. The ambiguity fixed success rate is used as an

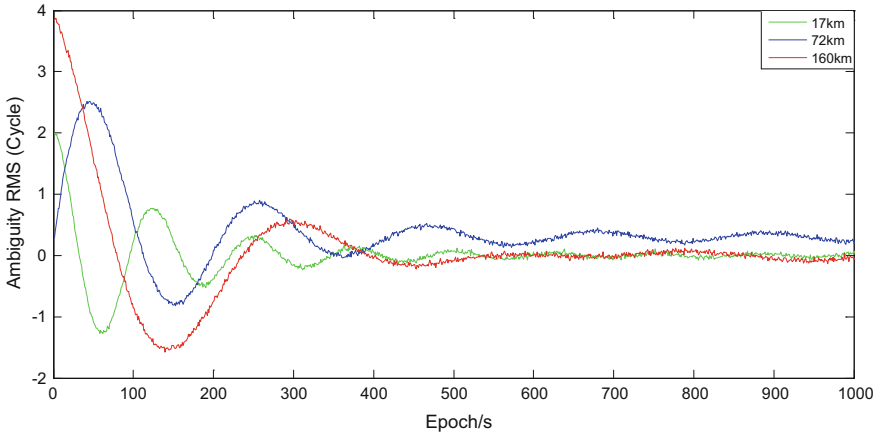

Fig. 3 Fixed error of NL ambiguity

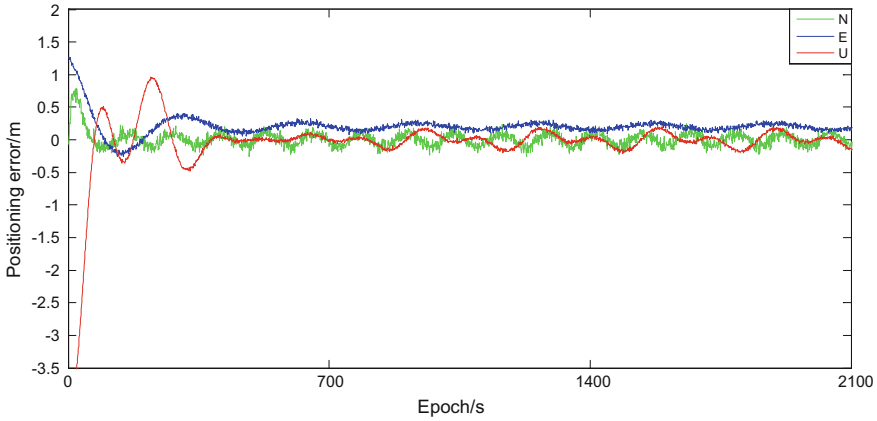

Fig. 4 Positioning error in the absence of ionospheric prior standard deviation

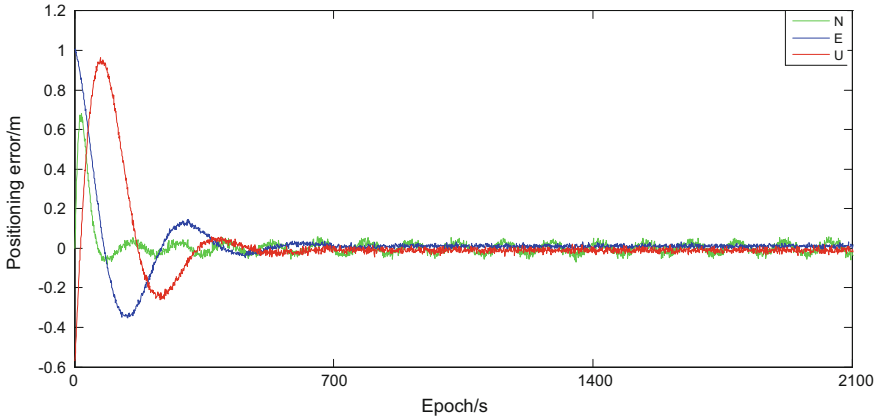

Fig. 5 Positioning error with the ionospheric prior standard deviation

index to evaluate the effectiveness and feasibility of the algorithm. Ambiguity fixed success rate is calculated as follows:

$$SR = \frac{N_s}{N_w} \times 100\% \tag{25}$$

where SR indicates the degree of ambiguity fixed success rate, N_s is the ambiguity fixing successful number of epochs, N_w is the total number of epochs.

Because EWL ambiguity can be reliably fixed with the classic TCAR method, the experimental part does not discuss the ambiguity fix success rate of EWL, only compared with the traditional TCAR and the proposed algorithm in the WL and NL ambiguity fixed Success rate. The experimental results are shown in Table 2.

Table 2 Fixed effect of ambiguity

Baseline/km	N_w/s	WL/NL	Classic TCAR		Proposed algorithm	
			N_s/s	SR/%	N_s/s	SR/%
17	7320	WL	7043	96.22	7305	99.79
		NL	6614	90.35	7088	96.83
72	9780	WL	9240	94.48	9607	98.23
		NL	8537	87.29	9223	94.30
160	9800	WL	8738	89.16	9551	97.46
		NL	8263	84.32	9131	93.17

As can be seen from the experimental data, the TCAR algorithm is affected by the length of the baseline, with the increase of baseline length, WL and NL ambiguity fixed success rate decreased significantly. The improved TCAR algorithm has a higher fixed success rate than the traditional algorithm. This shows that adding adaptive factor to reduce noise helps to improve the fixed success rate of ambiguity, and the ionospheric priori standard deviation could reduce the influence of the increase of baseline length on ambiguity fixing.

5 Conclusion

In the triple-frequency ambiguity resolution, the traditional TCAR algorithm has a high success rate of ambiguity fixation for short baselines. However, for the medium/long baselines, the ambiguity fixing of WL and NL are influenced by the ionospheric delay and combined noise, the fixing effect is bad. This paper is based on the traditional TCAR step-by-step ambiguity fixed method. First, two EWL ambiguities are fixed and the double differential ionospheric delay is solved. Then use these information to construct the optimal linear combination with the lowest noise to solve the WL ambiguity. Finally, the ionospheric priori standard deviation is introduced to solve the NL ambiguity by the least square method, which reduces the influence of the increase of baseline length on the ambiguity fixing of NL. The experimental results show that the proposed algorithm can effectively improve the validity and reliability of medium/long baseline ambiguity fixing.

Acknowledgements The study is supported by The National High Technology Research and Development Program ("863" Program) of China (2015AA016901): High linearity laser diode array and high saturation power photodiode array; The General Object of National Natural Science Foundation (61772358) Research on the key technology of BDS precision positioning in complex landform; International Cooperation Project of Shanxi Province (Grant No. 201603D421012): Research on the key technology of GNSS area strengthen information extraction based on crowd sensing; The General Object of National Natural Science Foundation under Grants (61572347): Resource Optimization in Large-scale Mobile Crowdsensing: Theory and Technology.

References

1. Deng J, Pan S-G, Wang S-L (2012) Fast solution to ambiguity of RTK triple-frequency carrier in long baseline networks based on optimal combination. Chin J Inertial Technol 20(5):587–592
2. Feng C, Huang L, Dong H et al (2017) The triple frequency in long baseline ambiguity research. J Geodesy Geodyn 37(8):824–829
3. Gao W, Gao C, Pan S et al (2017) A ambiguity resolution of wide-lane between BeiDou triple-frequency long-distance reference stations based on the step-by-step ionosphere-free combination. J Southeast Univ (Natural Science Edition) 47(1): 43–49
4. Li BF, Feng YM, Gao WG, Li Z (2015) Real-time kinematic positioning over long baselines using triple-frequency BeiDou signals. IEEE Trans Aerosp Electron Syst 51(4):3254–3269
5. Tian Y, Zhao D, Chai H et al (2017) BDS ambiguity resolution with the modified TCAR method for medium-long baseline. Adv Space Res 59(2):670–681
6. Wang P, Lv Z, Yang D et al (2017) A new long baseline BDS three frequency ambiguity resolution method. Bull Surv Mapp 4:25–29
7. Xie J, Hao JM, Han C et al (2016) Optimization of BDS single epoch TCAR algorithm. Surv Mapp Sci Technol J 33(1):6–10
8. Xie J, Hao J, Han C et al (2016) Research of BDS single-epoch and triple-frequency ambiguity resolution using the modified TCAR method. J Geomatics Sci Technol
9. Yu X (2011) Multi-frequency GNSS precision positioning theory and method. Wuhan University
10. Zhang M (2016) Long distance network RTK GPS/BDS key technology research. Wuhan University
11. Zhuang W (2016) Beidou triple-frequency long baseline ambiguity fixed algorithm and its application. Chang'an University
12. Zhai Y, Zhang F, Shen F (2014) Beidou system pseudorange multipath characteristics and its influence on positioning accuracy. J Navig Positioning 2(2):45–49

Real-Time Detection and Repair of Cycle-Slip Based on Pseudo-range Phase Combinations for Un-differenced GNSS Triple-Frequency Observations

Lingdong Meng, Junping Chen, Jiexian Wang and Yize Zhang

Abstract For the detection and repair of cycle-slip for un-differenced GNSS triple-frequency observations, current algorithms have difficulties in efficiency, stability and even some special cycle-slip combinations cannot be detected. This paper investigates the strategies in real-time detection and repair of cycle-slip. Geometry free ionospheric free code-phase combinations together with phase combinations are used, where the selection criteria of combination coefficients is based on the principle of the minimal condition number. Advantage of the method is that each cycle-slip value can be calculated without searching, thus the efficiency is improved and success rate is still high. Experiment results show that even under the severe ionospheric conditions, cycle-slips of triple-frequency un-differenced observations can be detected and repaired.

Keywords Un-differenced triple-frequency observations · Cycle-slip detection and repair · Code-phase combination

1 Introduction

Triple frequency data can form more combinations with longer wavelength, smaller noise and less affected by ionosphere, which is useful for cycle-slip detection [1] and integer ambiguity solution [2]. There have been many algorithms to detect and repair cycle-slips [3]. The high order-difference method is intuitive but it is difficult to realize in source coding [4]; Extrapolation method based on gray theory [5] cannot work well in carrier with irregular motion and when cycle-slip happened in

L. Meng · J. Wang
College of Surveying and Geo-Informatics, Tongji University, Shanghai 200092, China

J. Chen (✉) · Y. Zhang
Shanghai Astronomical Observatory Chinese Academy of Sciences, Shanghai 200030, China
e-mail: junping@shao.ac.cn

J. Chen
University of Chinese Academy of Sciences, Beijing 100049, China

J. Sun et al. (eds.), *China Satellite Navigation Conference (CSNC) 2018 Proceedings*, Lecture Notes in Electrical Engineering 498,
https://doi.org/10.1007/978-981-13-0014-1_57

the first few epochs; Triple-frequency TurboEdit cycle-slip processing method using searching way to calculate the value of each frequency [6] cycle-slips is of low efficiency, unstable and complicated; The influence of ionosphere is not fully considered in the method based on code-phase combinations for triple-frequency un-differenced observations [1]; The method of Geometry Free Ionospheric Free (GFIF) combinations united the real-time estimation of ionospheric variation delay [7] can overcome the effect of ionospheric delay but this method is too complicated with huge processing burden.

In this paper, the triple-frequency GFIF code combinations are based on the criteria of less pseudo-range noise. Phase combinations used in this paper is selected with the criteria of less ionosphere delay effects and noise. The principle of the minimal conditions of coefficient matrix are implemented for the definition of the equation to be used in the calculation of cycle-slip. Finally, the method of this paper is verified using the BDS and GPS triple-frequency observations of IGS.

2 The Cycle-Slip Detection Observations

2.1 Triple-Frequency GFIF Code-Phase Combination

Referred to the idea of dual-frequency MW combination, triple-frequency GFIF combinations can eliminate the geometric distance-related terms and the first order effects of ionospheric delay. The pseudo-range and phase observation equation can be shown as Eqs. (1) and (2) respectively.

$$P_i = \rho + \frac{f_1^2}{f_i^2} I + \varepsilon_{p_i} \tag{1}$$

$$\varphi_i = \frac{\rho}{\lambda_i} + N_i - \frac{f_1^2}{f_i^2} I' + \varepsilon_{\varphi_i} \tag{2}$$

where, P and φ is the raw pseudo-range and phase observation; ρ is the geometric distance between satellite and receiver antennas including the satellite clock error and tropospheric delay; I and I' are the ionospheric group delay on the first frequency in meters and ionospheric phase delay on the first frequency in cycles respectively; ε_{φ_i} and ε_{p_i} are the receiver code noise in meters and the receiver phase noise in cycles respectively; i refers to frequency number. According to Eqs. (1) and (2), the integer ambiguity can be calculated as Eq. (3).

$$N = aN_1 + bN_2 + cN_3 = a\varphi_1 + b\varphi_2 + c\varphi_3 - \frac{(lP_1 + mP_2 + nP_3)}{\lambda} \tag{3}$$

In Eq. (3), to keep the integer features of ambiguity, a, b and c must be integer, while l, m and n can be real number.

According to the [6], the GFIF code-phase combination coefficients follows the Eqs. (4) and (5).

$$l + m + n = 1 \tag{4}$$

$$l + m\frac{f_1^2}{f_2^2} + n\frac{f_1^2}{f_3^2} = -\frac{\lambda_{abc}}{\lambda_1}\left(a + b\frac{f_1}{f_2} + c\frac{f_1}{f_3}\right) \tag{5}$$

The estimation cycle-slip value of combination observations can be calculated by Eq. (6) which is the time-differenced equation between two consequent epochs.

$$\Delta N = a\Delta N_1 + b\Delta N_2 + c\Delta N_3 = a\Delta\varphi_1 + b\Delta\varphi_2 + c\Delta\varphi_3 - \frac{(l\Delta P_1 + m\Delta P_2 + n\Delta P_3)}{\lambda} \tag{6}$$

For a, b and c and l, m and n can be calculated with two Eqs. (4) and (5). The combinations which is less affected by noise are selected. Suppose the noise of code is 0.3 m and phase is 0.01 cycle, some typical combinations are listed in the Table 1 [6].

According to Table 1, the GFIF combination (0, −1, 1) is the best one for BDS and (0, 1, −1) for GPS. Even the code noise is as large as 1 m, the value of combination cycle-slip can still be fixed at the success rate of 95.5% [1]. If there are no cycle-slips the value calculated by Eq. (6) is close to zero. However, only one GFIF is far not enough, because cycle-slip combinations cannot be detected by GFIF combinations, i.e. $\Delta N_1 = \Delta N_2 = \Delta N_3$, on the other hand, GFIF combinations are not able to calculate cycle-slips of individual frequency.

Table 1 Triple-frequency GFIF code-phase combination of GPS and BDS

	(*a*, *b*, *c*)	*l*	*m*	*n*	λ (m)	Standard error (cycle)
GPS	(0, 1, −1)	0.012109	0.444991	0.54290	5.8610	0.0533
	(1, −3, 2)	0.842594	0.15314	0.001092	1.2211	0.3033
	(1, −4, 3)	1.061142	0.080347	−0.141489	1.5424	0.3033
	(1, −2, 1)	0.699407	0.206086	0.094507	1.0105	0.3100
BDS	(a, b, c)	l	m	n	λ (m)	Standard error (cycle)
	(0, −1, 1)	0.019945	0.552577	0.427478	4.8842	0.0633
	(1, 1, −2)	0.750616	0.041406	0.207978	1.2967	0.2567
	(1, 3, −4)	1.577791	−0.537279	−0.040512	2.7646	0.2667
	(1, 0, −1)	0.597328	0.148645	0.254027	1.0247	0.2767

2.2 Phase Combinations

To enable the cycle-slips detection for each frequency, another two phase combinations are needed in addition to the GFIF combination (0, −1, 1) of BDS and (0, 1, −1) of GPS. Referred to [8], the geometric distance term in the phase combination observations could be eliminated by the GFIF combination with cycle-slips being repaired. The cycle-slip value of combination can be estimated using the epoch-differences [8].

For different combination observations, there exists relation as the Eqs. (7) shown:

$$\lambda_{a1b1c1}\Delta N_{a1b1c1} + \lambda_{a1b1c1}\Delta\varphi_{a1b1c1} + \beta_{a1b1c1}\Delta I_1 \approx \lambda_{a2b2c2}\Delta N_{a2b2c2} + \lambda_{a2b2c2}\Delta\varphi_{a2b2c2} + \beta_{a2b2c2}\Delta I_1 \tag{7}$$

$$\beta_{abc} = \frac{f_1^2(a/f_1 + b/f_2 + c/f_3)}{af_1 + bf_2 + cf_3} \tag{8}$$

where β_{abc} is the coefficient of phase combination (a, b, c); ΔI_1 in unite of meters is the ionospheric phase delay on the first frequency in cycles. Δ is the epoch-difference operator. The cycle-slip value of combinations can be estimated by Eq. (9).

$$\Delta N_{a1b1c1} \approx \frac{\lambda_{a2b2c2}\Delta N_{a2b2c2} - \lambda_{a1b1c1}\Delta\varphi_{a1b1c1} + \lambda_{a2b2c2}\Delta\varphi_{a2b2c2} + (\beta_{a2b2c2} - \beta_{a1b1c1})\Delta I_1}{\lambda_{a1b1c1}} \tag{9}$$

And the Eq. (10) is used in the detection of cycle-slip.

$$\Delta N_{a1b1c1} \approx \frac{\lambda_{a2b2c2}\Delta\varphi_{a2b2c2} - \lambda_{a1b1c1}\Delta\varphi_{a1b1c1} + (\beta_{a2b2c2} - \beta_{a1b1c1})\Delta I_1}{\lambda_{a1b1c1}} \tag{10}$$

At least 3 linear independence equations are needed for the detection and repair of cycle-slip. Equations can be formed as Eq. (10), with the appropriate coefficients. Supposing the pseudo-range noise is 0.3 m and the phase noise is 0.01 cycle. The criteria in coefficients selection is shown as following:

(1) If ΔI_1 = 0.5 m, the noise of cycle-slip parameter ΔN_{a1b1c1} in Eq. (10) should be no more than 0.25 cycle. At this time, in the most of cases, the value of cycle-slip can be fixed at least at the success rate of 95.5% [8];
(2) The wavelength should be no less than 1 m in order to reduce the effect of ionospheric delay [9];

Table 2 The best combination coefficients of GPS and BDS

	Combination	The coefficients of phase combination (*a, b, c*)	The coefficients of code combination (*l, m, n*)	Threshold value
GPS	GFIF	(0, 1, −1)	(0.012109, 0.444991, 0.5429)	0.1800
	Phase combination 1	(1, −2, 1)		0.6300
	Phase combination 2	(−3, 3, 1)		0.3043
BDS	GFIF	(0, −1, 1)	(0.019945, 0.552577, 0.427478)	0.6636
	Phase combination 1	(1, 0, −1)		0.1553
	Phase combination 2	(−3, 2, 2)		1.0080

(3) The absolute value of the sum of combination coefficients should be no more than 1 and all combinations should be integer. In this case the ionospheric delay is reduced [1];
(4) The condition number of coefficients matrix composed by the coefficients of GFIF and phase combinations should be as small as possible.

Considering the signal feature of BDS and GPS, the coefficients can be searched in the range of [−10, 10]. The best coefficients is shown in the Table 2. If absolute value of cycle-slip parameter is larger than the threshold value, the cycle-slip is detected. All coefficients of three combinations is linear independence, when there is a cycle-slip in one frequency, the estimation of at least one combination cycle-slip value will be bigger than 1 cycle.

3 The Repair of Cycle-Slip

According to the relationship of combination ambiguity and ambiguity at each frequency, Eqs. (11) and (12) can be established. All coefficients are integer and $det(H) = \pm 1$, so each cycle-slip value can be calculated by $x = H^{-1}y$ which is more efficient compared with conventional searching method. Equation (11) is used for GPS and Eq. (12) is be used for BDS. The condition number of H in Eq. (11) is 44.9059, while the condition number of H in Eq. (12) is only 4.1982. From this point of view, the signal of BDS is better than GPS. When BDS-3 have been established, its signal will be different from BDS-2, the best combination need to be re-defined.

$$y = \begin{bmatrix} \delta N_{a1b1c1} \\ \delta N_{a2b2c2} \\ \delta N_{a3b3c3} \end{bmatrix} = \begin{bmatrix} 0 & 1 & -1 \\ 1 & -2 & 1 \\ -3 & 3 & 1 \end{bmatrix} \begin{bmatrix} \delta N_1 \\ \delta N_2 \\ \delta N_3 \end{bmatrix} = Hx \tag{11}$$

$$y = \begin{bmatrix} \delta N_{a1b1c1} \\ \delta N_{a2b2c2} \\ \delta N_{a3b3c3} \end{bmatrix} = \begin{bmatrix} 0 & -1 & 1 \\ 1 & 0 & 1 \\ -3 & 2 & 2 \end{bmatrix} \begin{bmatrix} \delta N_1 \\ \delta N_2 \\ \delta N_3 \end{bmatrix} = Hx \tag{12}$$

4 Data Processing and Analysis

The observation data of 1 s sampling rate of station WTZR (Germany) on the day of March 17, 2013 was used for validating of the model. Large magnetic storm happened on this day and TEC changed significantly over the equator, middle latitudes and auroral regions [6]. The data of GPS G24 phase data L1, L2, L5 and code data C1, C2, C5 were used from 15:00:00 to 20:00:00. Based on the file of ionosphere grid file of IGS on this day, with the calculation of GIM model, we found that TEC is large between 07:00:00 and 19:00:00. Therefore, this data could be used to check the capability of detection and repair of cycle-slips under the severe ionosphere environment. The second experiment is carried out using the 1 s sampling rate observations of station UNB3 (Canada) on March 13, 2016. BDS C12 is used include phase data L2, L6, L7 and code data C2, C6, C7 from 06:00:00 to 10:59:59. The third experiment used the data of AIRA (Japan) on August 17, 2017. The data of GPS G08 phase data L1, L2, L5 and code data Cl, C2, C5 were used from 00:00:00 to 04:59:59. For the data analysis, we used the software of Bernese 5.2 to detect the cycle-slips of the phase data of GPS G24, GPS G08 and no cycle-slip was found in the frequency of L1 and L2. Then we added cycle-slips in the phase data of GPS G24, GPS G08 and BDS C12 from the 5th epoch to 16875th epoch every 5 epochs, as followed: [0, 0, 1], [0, 0, 2],…,[14, 14, 15]. The number of manual-added cycle-slip was 3375.

4.1 Data Process

The calculation process is shown in Fig. 1. The first step is to read raw data and form combination observations. Secondly, cycle-slips are detected for current epoch. In the third step, the cycle-slips are determined and repaired in case that they exist. The process will be continued until the last epoch.

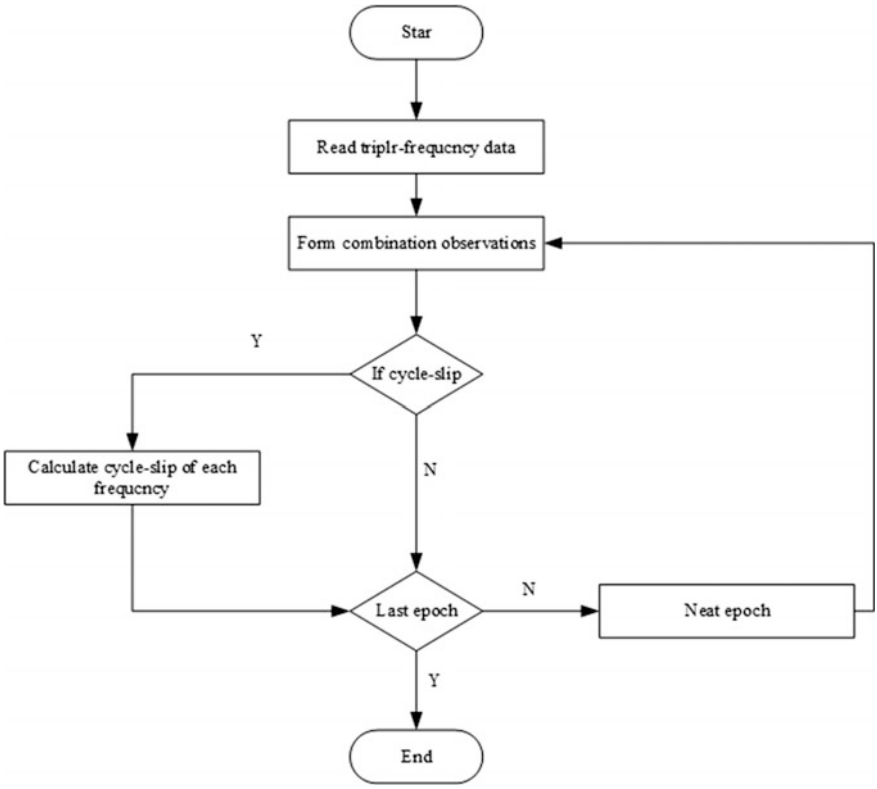

Fig. 1 Data processing flow chart

4.2 The Results of Cycle-Slip Detection and Repair

Based on the software of MATLAB 2016b and processor of CORE i3, taking the BDS data as an example, the processing time of cycle-slip detection and repair of 17,998 epochs data was 2.242 s, and the mean processing time for 1 epoch was around 125 microseconds. The cycle-slip parameters of GPS for the station WTZR are shown in Fig. 2 and BDS results for station UNB3, GPS results for AIRA are shown in Figs. 3 and 4. Shown in the figures all manual-added 3375 cycle-slips were precisely detected and repaired. Some of the results are shown in Tables 3, 4, and 5.

The difference the real and the fixed cycle-slip parameters of each frequency of station WTZR, UNB3 and AIRA are shown in Figs. 5, 6, and 7. As shown in the figures, the difference is between −0.5 cycle and 0.5 cycle for stations WTZR and UNB3. Due to poorer quality of the pseudo-range data of AIRA station, the difference is between −1.5 cycle and 1.5 cycle.

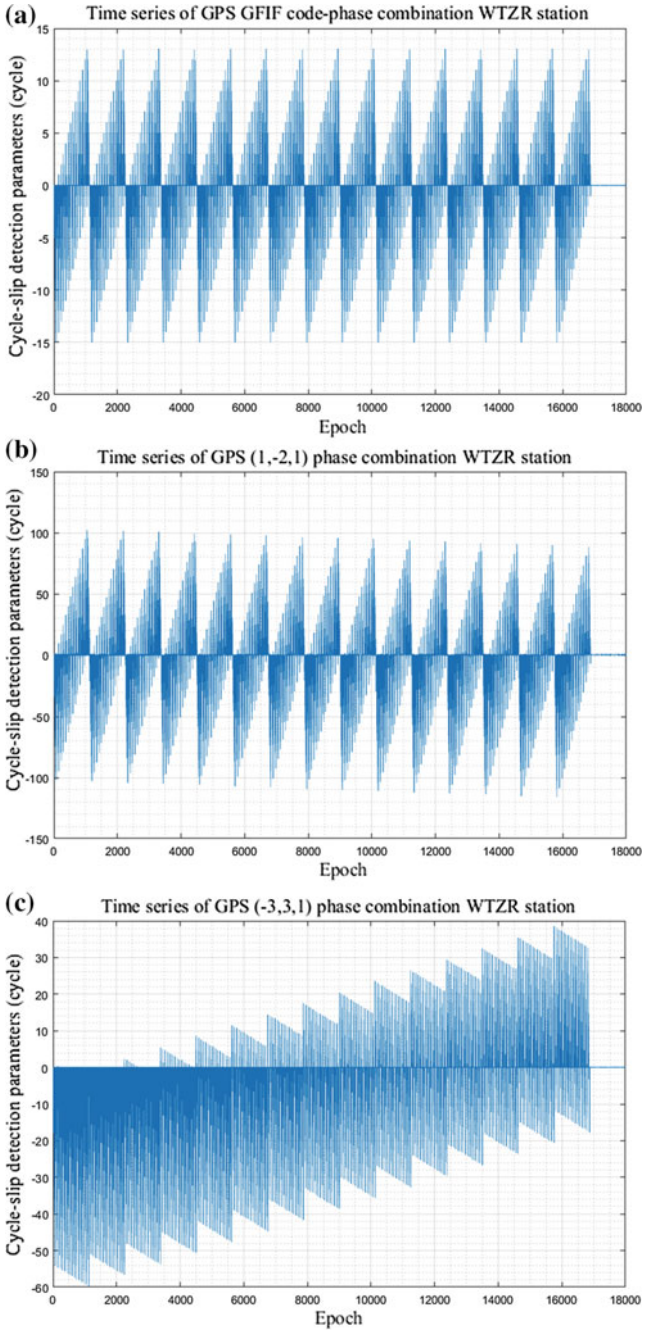

Fig. 2 Time series of all GPS cycle-slip detection parameters for station WTZR. **a** GFIF, **b** (1, −2, 1), **c** (−3, 3, 1)

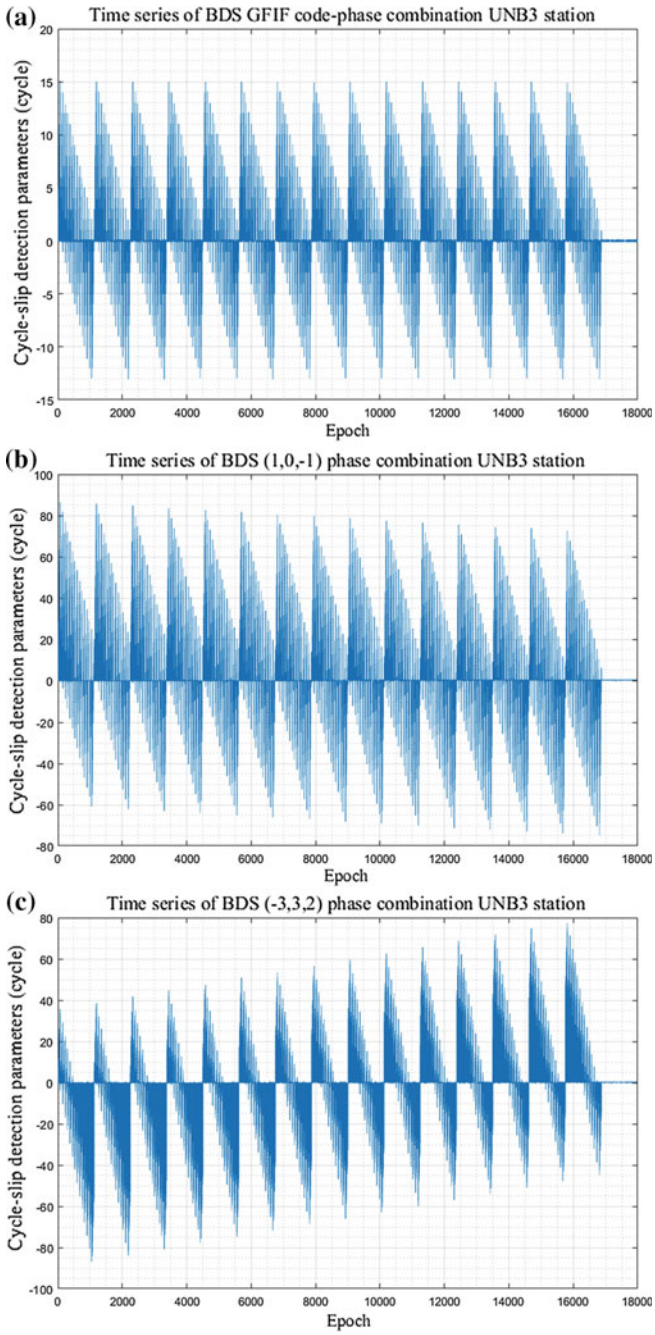

Fig. 3 Time series of all BDS cycle-slip detection parameters for station UNB3. **a** GFIF, **b** (1, 0, −1), **c** (–3, 3, 2)

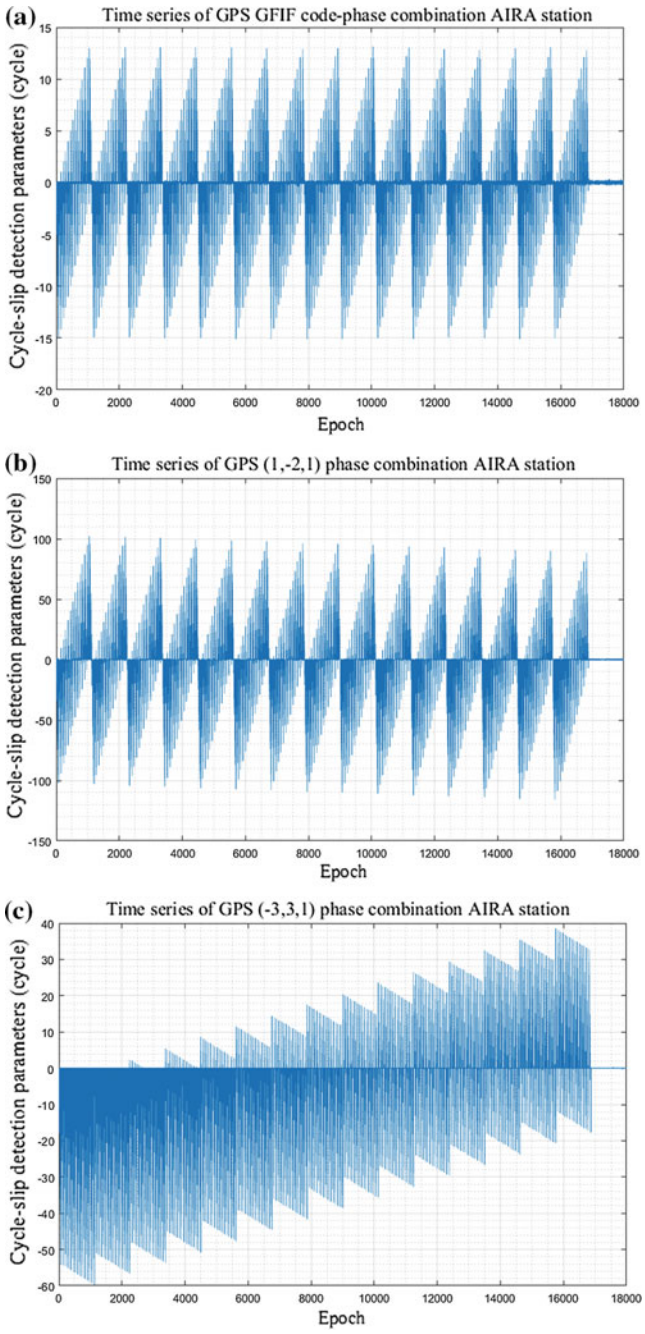

Fig. 4 Time series of all GPS cycle-slip detection parameters for station AIRA. **a** GFIF, **b** (1, −2, 1), **c** (−3, 3, 1)

Table 3 WTZR GPS G25 the results of cycle-slip detection and repair (parts)

Epoch	Point cycle-slip parameters (L1 L2 L5)			Fix cycle-slip parameters (L1 L2 L5)		
30	−0.1159	−0.0790	5.9244	0	0	6
35	−0.4539	−0.3446	6.6437	0	0	7
8035	6.9659	1.9737	1.9785	7	2	2
8040	7.1717	2.1321	3.1415	7	2	3
16,845	13.9789	13.9866	8.9826	14	14	9
16,850	14.0986	14.0757	10.0732	14	14	10

Table 4 UNB3 BDS C12 the results of cycle-slip detection and repair(parts)

Epoch	Point cycle-slip parameters (B1 B2 B3)			Fix cycle-slip parameters (B1 B2 B3)		
5	0.3963	0.3160	1.3399	0	0	1
10	−0.0485	−0.0272	1.9820	0	0	2
8010	6.7968	0.8418	11.8368	7	1	12
8015	7.1597	1.1206	13.1329	7	1	13
16,870	14.0817	14.0624	14.0607	14	14	14
16,875	14.3583	14.2758	15.2823	14	14	15

Table 5 AIRA GPS G08 the results of cycle-slip detection and repair(parts)

Epoch	Point cycle-slip parameters (L1 L2 L5)			Fix cycle-slip parameters (L1 L2 L5)		
20	−0.4265	−0.3127	3.6632	0	0	4
25	−0.3407	−0.2505	4.7544	0	0	5
8010	5.8949	0.1333	11.2570	7	1	12
8015	5.9712	0.2017	12.3046	7	1	13
16,840	15.0535	14.8138	8.7155	14	14	8
16,845	14.1006	14.0529	9.0651	14	14	9

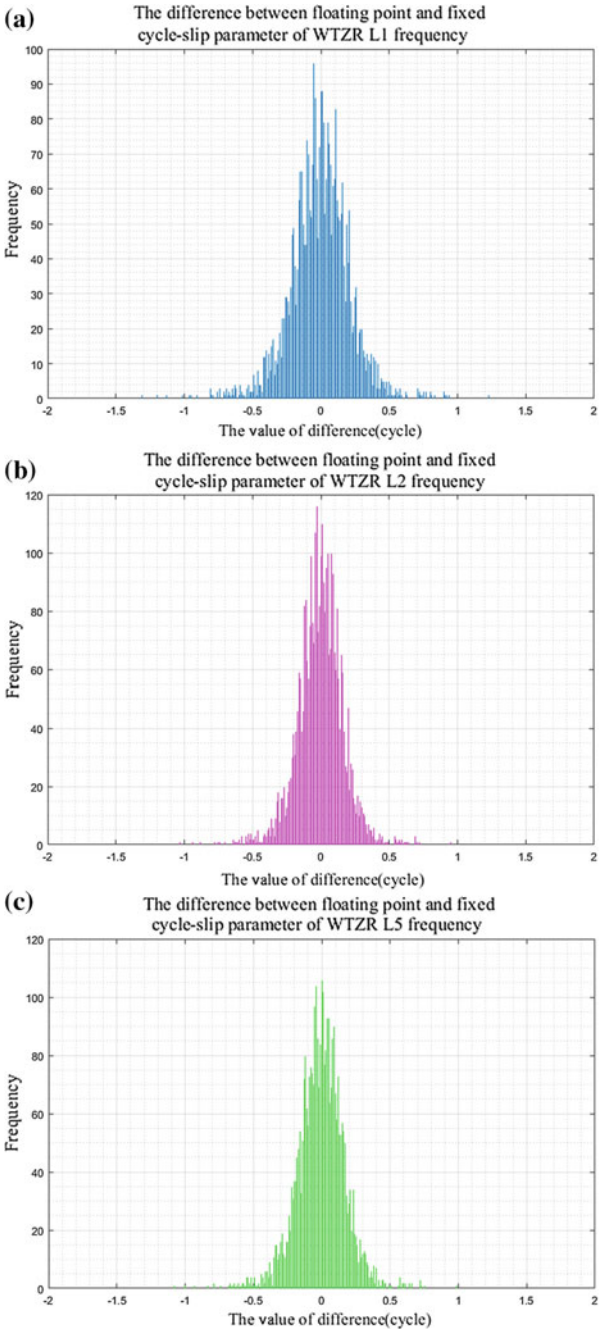

Fig. 5 The difference between the real and the fixed cycle-slip parameter of each frequency of WTZR station GPS G25. **a** L1, **b** L2, **c** L5

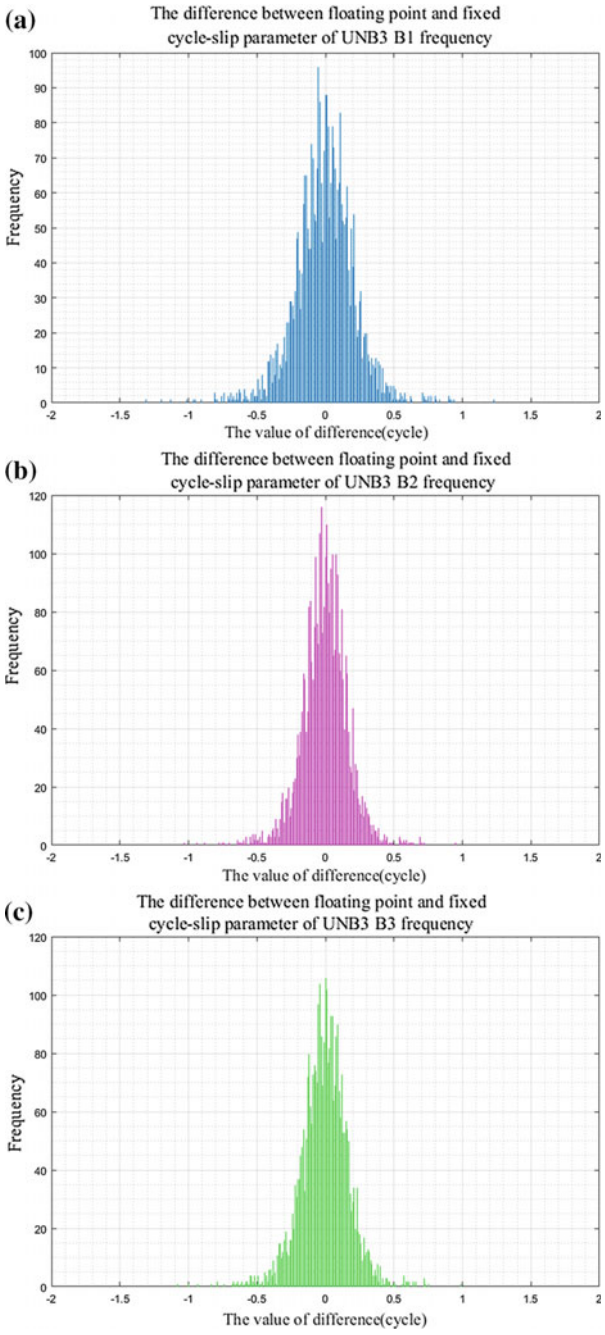

Fig. 6 The difference between the real and the fixed cycle-slip parameter of each frequency of UNB3 station BDS C12. **a** L2, **b** L6, **c** L7

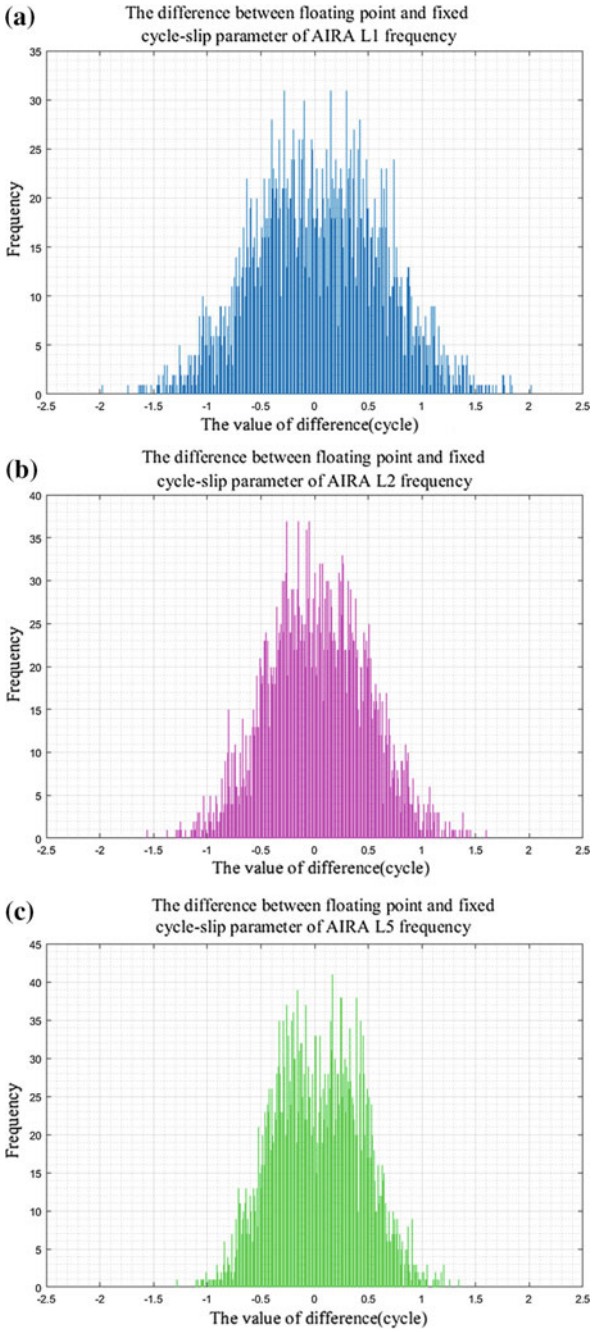

Fig. 7 The difference between the real and the fixed cycle-slip parameter of each frequency of AIRA station GPS G08. **a** L1, **b** L2, **c** L5

5 Conclusion

A more efficient method which is suitable for BDS and GPS for cycle-slip detection and repair is discussed in this paper. The cycle-slip parameters can be calculated without searching thus the efficiency is improved and stable. If some first epochs without cycle-slips or cycle-slips being repaired, using the method of phase smoothed pseudo-ranges can be applied to reduce the noise of pseudo-range and multipath. In addition, the results in the case of severe ionospheric delay with low sampling rate should be tested and the threshold value still can be optimized deeper.

Acknowledgements This work is support by the NSFC (No.11673050) and the 863 (No. 2014AA123102) projects.

References

1. Li J, Yang Y et al (2011) Real-time cycle-slip detection and repair based on code-phase combination for GNSS triple-frequency un-differenced observations. J Acta Geodaetica Cartogr Sin 40(6):717–722
2. Feng YM (2008) GNSS three carrier ambiguity resolution using ionosphere-reduced virtual signals. J Geodesy. https://doi.org/10.1007/s00190-008-0209-x
3. Zhang Y (2017) Research on real-time high precision BeiDou positioning service system. Tongji University, Shanghai
4. Li Z, Huang J (2016) GPS surveying and data processing. Wuhan University Press, Wuhan
5. Wang C, Wang J (2012) Cycle slip detection and correction of single-frequency undifferenced phase observation. J Tongji Univ (Natural Science). https://doi.org/10.3969/j.issn.0253-374x.2012.09.020
6. Huang L, Zhai G, Ouyang Y et al (2015) Triple-frequency TurboEdit cycle-slip processing method of weakening ionospheric activity. J Acta Geodaetica et Cartographica Sinica. https://doi.org/10.11947/j.AGCS.2015.20140380
7. Wang X, Wen Xiang LIU et al (2016) Detection and repair of cycle-slip for undifferenced BDS triple-frequency observations. J Nat Univ Defense Technol. https://doi.org/10.11887/j.cn.201603003
8. Wang X (2016) Research on high precision positioning data processing technology of Beidou satellite navigation system. National University of Defense Technology, Changsha
9. Yao Y, Gao J et al (2014) Real-time cycle-slip detection and repair for compass triple-frequency carrier pahse observations. J China Univ Minimaling Technol. https://doi.org/10.13247/j.cnki.jcumt.000242

Analysis of GPS Time Series Based on Spatio-temporal Filtering in Antarctic Peninsula

Wenhao Li, Fei Li, Shengkai Zhang, Jintao Lei and Qingchuan Zhang

Abstract The high-accuracy GPS velocity field is one of effective approaches to study the regional crustal displacement, and can provide validations and constraints for GIA models. There are spatially and temporally correlated errors in GPS data. Applying a spatiotemporal filter can reduce these effects and improve the accuracy of GPS time series. To obtain high-accuracy GPS vertical velocities in Antarctic peninsula, a "regional filter" is used to remove the spatially correlated errors in the selected 6 GPS time series, and the classic autocorrelation function is used to mitigate the temporally correlated errors of each GPS time series. The result shows that the scatter of GPS time series is reduced significantly after spatiotemporal filtering, the reduction of maximum RMS can reach up to 41.82%, and mean RMS reduction is 35.44%.

Keywords Antarctic peninsula · GPS vertical velocities · Spatiotemporal filtering Common mode errors

1 Introduction

Continuous GPS networks can be used to investigate geological and geophysical process, which provide unified frame to monitor surface deformation of Earth in different temporal and spatial scales [1]. The high-accuracy GPS velocity field is one of effective approaches to study the regional crustal displacement, and can provide validations and constraints for GIA models which always used as important corrections for plate movement, GRACE gravity field, satellite altimetry. There are spatially and temporally correlated errors in GPS data. Applying a spatiotemporal filter can reduce the effects and improve the accuracy of GPS time series. Dong et al. [2] filtered the GPS time series in southern California with the methods of principal comment analysis (PCA) and karhunen-Loeve(KLE),and subtracted the

W. Li · F. Li · S. Zhang (✉) · J. Lei · Q. Zhang
Chinese Antarctic Center of Surveying and Mapping, Wuhan 430079, China
e-mail: zskai@whu.edu.cn

J. Sun et al. (eds.), *China Satellite Navigation Conference (CSNC) 2018 Proceedings*, Lecture Notes in Electrical Engineering 498,
https://doi.org/10.1007/978-981-13-0014-1_58

common mode error of GPS coordinates. Hu S et al. [3] also used the regional filter to analysis GPS time series in this region and contrasted the stacking, PCA and KLE. Jiang et al. [4] removed the common mode error of GPS continuously operating reference station (CORS) coordinates time series, reduced the amplitude of annul periods in vertical displacements. Serplloni [5] removed the common mode error of 800 GPS stations time series in the Euro-Mediterranean region, improved the signal noise ratio of GPS data. Shen et al. [6] extracted the common mode error of using the crustal movement observation network of China (CMONOC) discontinuous time series with the improved PCA. To obtain high-accuracy GPS vertical velocities in Antarctic Peninsula, a "regional filter" is used to remove the spatially correlated errors in the selected 6 GPS time series, and the classic autocorrelation function is used to mitigate the temporally correlated errors of each GPS time series [7, 8].

2 Data Processing

2.1 Data Source

The GPS time series are downloaded from Nevada Geodetic Laboratory (http://geodesy.unr.edu/NGLStationPages/GlobalStationList). Base on the distribution and integrity of GPS time series, we select 6 GPS stations (DUPT, PAL2, PALV, PALM, ROTH, VNAD) in Antarctic Peninsula, with time span from 2010.02.06 to 2017.02.18. Figure 1 is the locations of 6 GPS stations in Antarctica Peninsula.

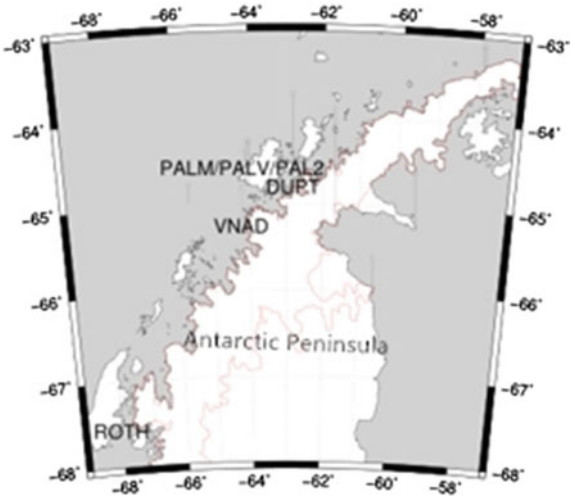

Fig. 1 The locations of 6 GPS stations in Antarctica Peninsula

2.2 Spatially Correlated Errors

We fit a secure trend, annual and semiannual terms to the daily vertical solutions. Figure 2 is time series of vertical positions at DUPT, each black dot represents a daily solution, the solid red line shows the fitting curve. Figure 3 shows the daily residuals at DUPT, obtained by removing the fitting curve from the daily values of vertical positions.

The daily residuals are not entirely random. They arise from measurement errors, tropospheric modeling errors, satellite orbit errors, and loading from the atmosphere, ocean et al. Some of these errors have similar effects at the different sites. By applying a regional mean signal, we can reduce some of these common errors in vertical time series.

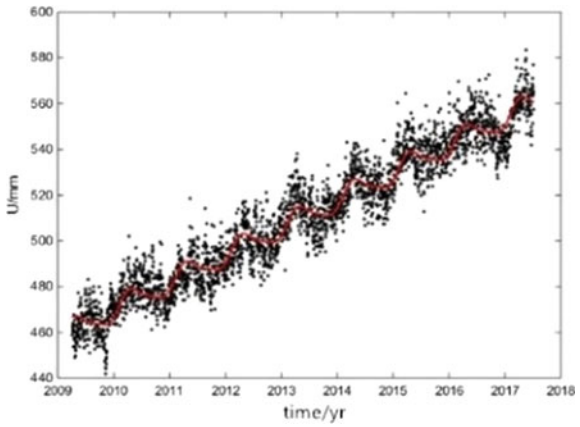

Fig. 2 Daily values of vertical positions at DUPT (the solid curve shows the best fitting offsets, and the secular, annual, and semiannual terms)

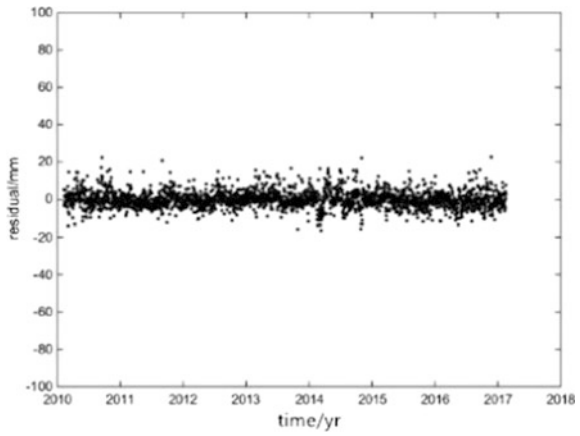

Fig. 3 Daily residuals after removing secure trend, annual and semiannual terms of DUPT

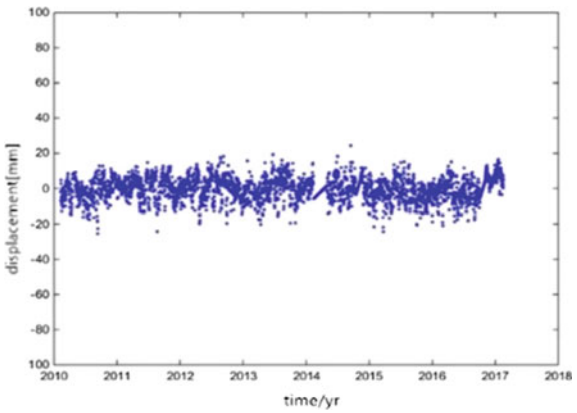

Fig. 4 Regional daily mean signal

(1) To get the daily residuals of the vertical positions, we remove the annual, semiannual and secular terms by using Eq. (1)

$$\mathrm{yt} = \mathrm{at} + \mathrm{b} + \mathrm{A1}\sin(\omega 1 - \varphi 1) + \mathrm{A2}\sin(\omega 2 - \varphi 2) + \varepsilon \mathrm{t} \tag{1}$$

Here yt is the displacement, A1, $\omega 1$, $\varphi 1$ and A2, $\omega 2$, $\varphi 2$ are the annual and semi-annual amplitude, angular frequency and initial phase, respectively. a, b and εt are the slope, intercept and random noise, respectively.

(2) Because time spans for those 6 stations are not exactly the same, and there are data gaps at different times, we first find the days where data from all 6 sites are available. We then correct each of the 6 residual time series for a mean value computed for only those days.
(3) We interpolate a complete time series for filtering model, the time span is 2010.02.06–2017.02.18, the reginal filtering is used in this time span.

Figure 4 is the regional daily mean signal, Fig. 5 Shows daily values of vertical positions at 6 GPS before (black lines) and after (red dots) regional spatial filtering, (a) DUPT, (b) PAL2, (c) PALM, (d) PALV, (e) ROTH, (f) VNAD, there is a clear reduction in scatter after applying the reginal filter, while the secular, annual, semiannual signals are kept fixed. Table 1 is the RMSs before and after regional spatial filter. After applying the regional spatial filter, the maximum reduction of RMS is 41.82%, and the mean value is 35.44%.

2.3 *Temporally Correlated Errors*

Besides spatially correlated errors, there are temporally correlated errors in GPS time series, if we assume the daily residuals are uncorrelated with one another, is likely to underestimate the uncertainties in the parameter values. We analysis the

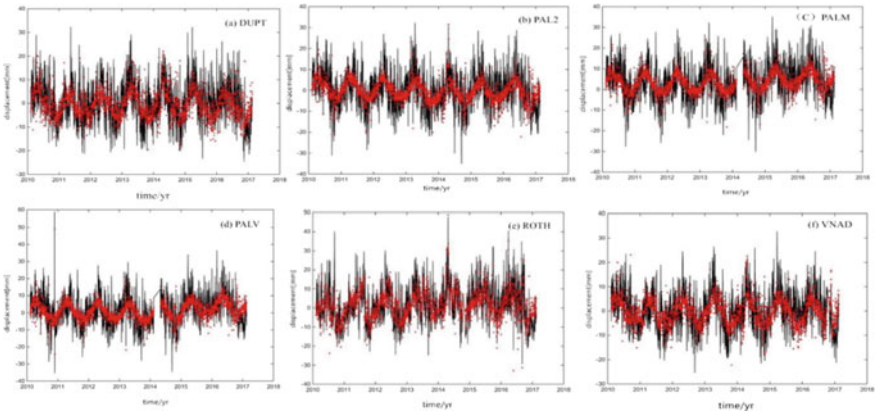

Fig. 5 Time series of vertical positions at 6 GPS before and after regional filter, **a** DUPT, **b** PAL2, **c** PALM, **d** PALV, **e** ROTH, **f** VNAD

Table 1 The varieties of RMS

Sites	Before filter	After filter	Reduction (%)
DUPT	8.43	5.75	31.79
PAL2	8.59	5.14	40.16
PALV	10.10	5.89	41.68
ALM	9.11	5.30	41.82
ROTH	9.95	7.52	24.42
VNAD	7.87	5.29	32.78

temporally correlated errors with autocorrelation functions and calculate a multiday averages model. Equation (2) is autocorrelation of the daily residuals

$$C(\tau) = \frac{\sum_t h(t)h(t-\tau)}{\sum_t h(t)^2} \tag{2}$$

where $h(t)$ is the residual at time t, τ is the time span, when $\tau = 0$, $C(\tau) = 1$, Fig. 6 is the autocorrelation functions at 6 stations, the dashed lines denote the 95% confidence interval.

The function for (a) DUPT, (b) PAL2, (c) PALM, (d) PALV, (e) ROTH, (f) VNAD reach the 95% confidence interval when the data span reach 24d, 24d, 133d, 120d, 24d, 25d respectively. We use these decorrelation times to calculate multiday averages of the daily residuals, for (a) DUPT, (b) PAL2, (c) PALM, (d) PALV, (e) ROTH, and (f) VNAD respectively.

Table 2 shows the fitting parameters at 6 GPS stations.

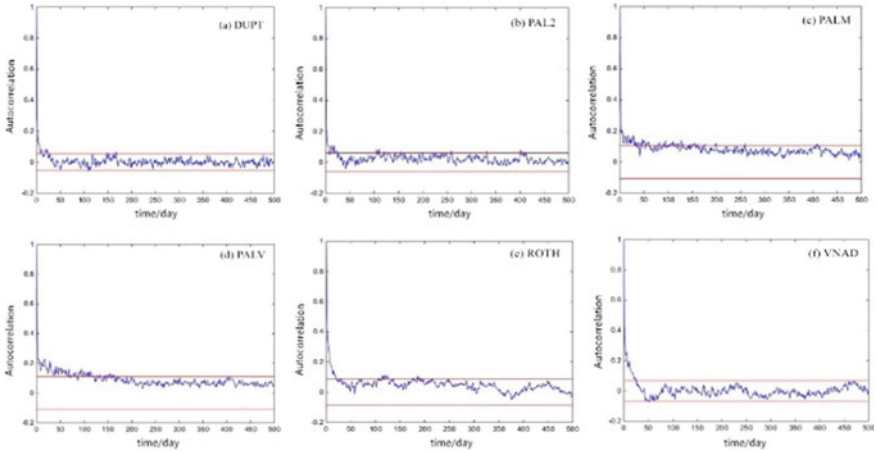

Fig. 6 Autocorrelation functions at **a** DUPT, **b** PAL2, **c** PALM, **d** PALV, **e** ROTH, **f** VNAD

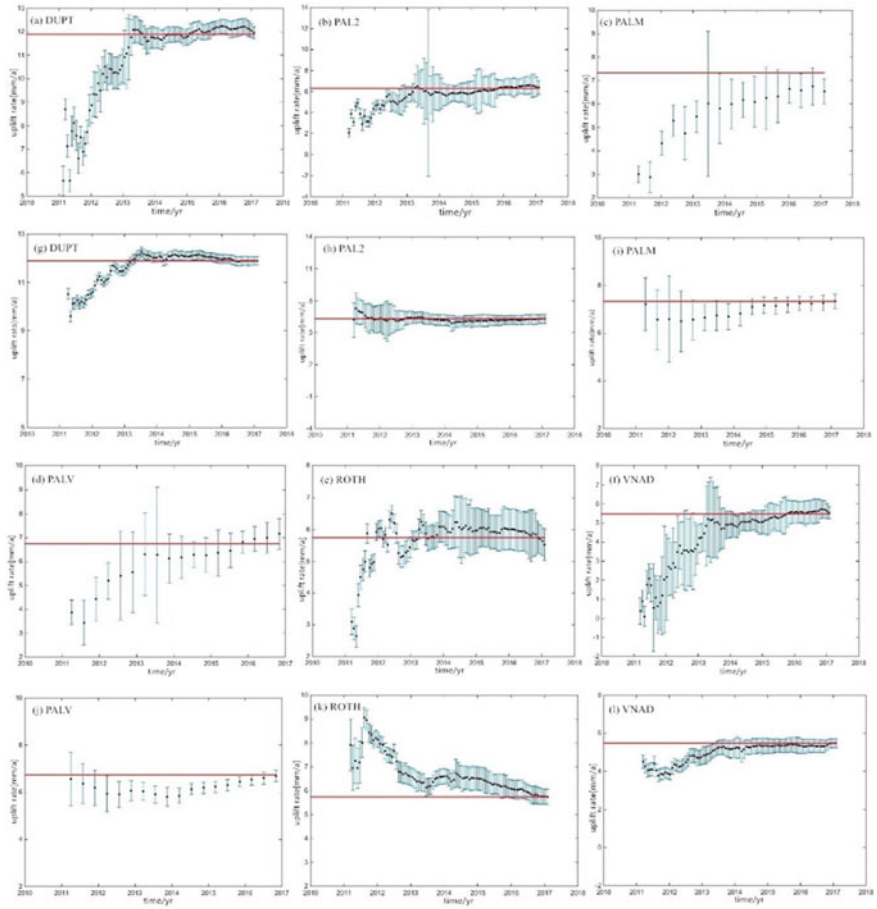

Fig. 7 Convergence plots of uplift rates before (left) and after (right) reginal filtering at 6 GPS stations

Table 2 Statistic results of fit at 6 GPS stations

Sites	A1/mm	φ_1/°	A2/mm	φ_2/°	a/mm/a	b/mm
VNAD	4.52 ± 0.29	0.36 ± 0.06	0.98 ± 0.29	8.95 ± 0.29	5.48 ± 0.10	−0.11 ± 0.41
ROTH	5.54 ± 0.42	−6.28 ± 0.08	0.95 ± 0.42	1.42 ± 0.44	5.74 ± 0.15	−0.42 ± 0.60
PAL2	4.71 ± 0.20	−5.85 ± 0.04	0.44 ± 0.20	−13.42 ± 0.45	6.31 ± 0.07	0.95 ± 0.28
DUPT	4.62 ± 0.24	0.35 ± 0.05	1.37 ± 0.24	0.07 ± 0.18	11.89 ± 0.09	0.56 ± 0.34
PALM	−4.00 ± 0.30	1.28 ± 0.54	0.58 ± 0.30	4.45 ± 0.08	7.33 ± 0.11	2.89 ± 0.42
PALV	4.61 ± 0.91	0.94 ± 1.00	0.94 ± 0.95	7.38 ± 0.21	6.74 ± 0.17	0.55 ± 0.64

A1, $\varphi 1$ and A2, $\varphi 2$ are the annual and semi-annual amplitude and initial phase, respectively. a, b are the slope and intercept, respectively. Table 2 shows that the maximum rate is DUPT 11.89 ± 0.09 mm/a, and the minimum rate is VNAD: 5.48 ± 0.10 mm/a.

Figure 7 is convergence plots of uplift rates before (up) and after (down) reginal filtering at 6 GPS stations.

a–f, g–l are the convergence plots of uplift rates before and after reginal filtering, respectively. Each estimate of the uplift rate is obtained by fitting the same terms discussed previously to the first 300 days of data, then adding the next 25 days for DUPT, PAL2 ROTH, VNAD,133 days for PALM and 120 days for PALV, and repeating the fit and so forth. Each estimate of the linear term is plotted as a dot and the vertical blue lines is the estimated uncertainties of the uplift, with the horizontal dashed lines is the uplift rates listed in Table 2.

Figure 7 suggests that there are inter-annual signals at 6 sites, and they have significant impacts on secular trend estimates when reginal filtering is not applied, these signals are regionally correlated, so the effect of signals is reduced after applying reginal filtering. The annual and linear terms are well separated, and that the fitted trends are insensitive to inter-annual, seasonal and other short-term variations.

3 Conclusion

To obtain high-accuracy GPS vertical velocities in Antarctic peninsula, a "regional filter" is used to remove the spatially correlated errors in the selected 6 GPS time series, and the classic autocorrelation function is used to correct the temporally correlated errors of each GPS time series. The result shows that

(1) After applying the regional filter, the maximum RMS of reduction is 41.82%, and the mean value is 35.44%. The spatially correlated errors are reduced significantly.
(2) The decorrelation times are 24, 24, 133, 120, 24, 25 at 6 sites, we construct 25 days multiday averages of the daily residuals for DUPT, PAL2, ROTH, VNAD, 133 days for PALM, and120 days for PALV, respectively.
(3) After applying the spatio-temporal filtering, the maximum rate in vertical direction is DUPT 11.89 ± 0.09 mm/a, and the minimum rate is VNAD 5.48 ± 0.10 mm/a.

Acknowledgements This work is supported by the State Key Program of National Science of China (41531069), the State Program of National Science of China (41176173), and Chinese Polar Environment Comprehensive Investigation and Assessment Programs (CHINARE2017).

References

1. Ma C, Li F, Zhang S et al (2016) The coordinate time series analysis of continuous GPS stations in the Antarctic Peninsula with consideration of common mode error. Chin J Geophys 59(8):2783–2795
2. Dong D, Fang P, Bock Y et al (2006) Spatiotemporal filtering using principal component analysis and Karhunen-Loeve Expansion approaches for regional GPS network analysis. J Geophys Res Solid Earth (1978–2012) 111(B3):B03405
3. Hu S, Wu C, Sun Y et al (2009) Comparison among three spatiotemporal filtering methods for regional GPS networks analysis. J Geodesy Geodyn 29(03):95–99
4. Jiang Z, Zhang P, Mi J et al (2010) Velocity estimation on the colored noise properties of CORS Network in China based on the CGCS2000 frame. Acta Geodaetica et cartographica Sinica 39(4):335–363 (in Chinese)
5. Serpelloni E, Faccenna C, Spada G et al (2013) Vertical GPS ground motion rates in the Euro-Mediterranean region: new evidence of velocity gradients at different spatial scales along the Nubia-Eurasia plate boundary. J Geophys Res Solid Earth 118(11):6003–6024
6. Shen Y, Li W, Xu G et al (2014) Spatiotemporal filtering of regional GNSS network's position time series with missing data using principle component analysis. J Geodesy 88(1):1–12
7. Khan SA, Wahr J, Leuliette E et al (2008) Geodetic measurements of postglacial adjustments in Greenland. J Geophys Res 113:B02402
8. Khan SA, Liu L, Wahr J et al (2010) GPS measurements of crustal uplift near Jakobshavn Isbræ due to glacial ice mass loss. J Geophys Res 115:B09405

Wide-Lane Ambiguity Fixing Method Based on BDS Triple Frequency Observations

Jianjian Jin, Chengfa Gao and Bo Chen

Abstract In this paper, based on the characteristics of easy to fix the ambiguity of BeiDou triple frequency ultra-wide lane, a fast solution method of wide lane ambiguity of BDS/GPS dual system based on BeiDou triple frequency is proposed. Firstly, the combination ambiguity of BeiDou (0, −1, 1) ultra-wide lane is fixed by using combination of wide-lane carrier and narrow-lane pseudo-range; Then, according to the principle of least squares, the ambiguity of Beidou (1, 4, −5) ultra wide lane is solved by constraint; Next, the ambiguities of Beidou (1, −1, 0) and (1, 0, −1) wide lane can be obtained by linear combination of the two ambiguities of fixed ultra wide lane; Considering the effects of tropospheric and ionospheric errors on long and medium baselines, the combined wide-lane ambiguity of Beidou (1, 0, −1) is taken as the optimal constraint, which is brought into the comprehensive constraint model to realize the fixed solution of GPS wide-lane ambiguity. Experimental results show that the method proposed in this paper can quickly fix the ambiguity of wide-lane GPS. Compared with the traditional MW method, this method greatly reduces the number of primitive epochs needed to correctly fix the wide-lane ambiguity, and improve timeliness of GNSS ambiguity resolution.

Keywords Triple-frequency · Integer ambiguity · Wide lane constraint
BDS · GPS

1 Introduction

Beidou Navigation Satellite System (BDS) is a satellite navigation system developed independently, operated independently and compatible with other satellite navigation systems in China. By the end of 2012, the Beidou Navigation Satellite System (BDS) officially provided continuous passive positioning, navigation and timing services to the Asia Pacific region. It is estimated that by 2020, a global

J. Jin (✉) · C. Gao · B. Chen
School of Transportation, Southeast University, 211189 Nanjing, China
e-mail: jinjj_seu@foxmail.com

J. Sun et al. (eds.), *China Satellite Navigation Conference (CSNC) 2018 Proceedings*, Lecture Notes in Electrical Engineering 498,
https://doi.org/10.1007/978-981-13-0014-1_59

satellite navigation and positioning system will be established [1]. At present, BDS is the only satellite navigation system that broadcasts triple frequency signals for all constellations. With the continuous improvement and development of satellite navigation systems such as GPS, GLONASS and GALILEO, Global Navigation Satellite System (GNSS) is entering the era of multi-system multi-frequency positioning [2].

At present, the most commonly used method of wide-lane ambiguity resolution is the combination of dual frequency pseudo-range and carrier (MW method). However, the result of the calculation is affected by the observed noise of pseudo-range, which makes it impossible for a single epoch to fix the wide-lane ambiguity. The use of GNSS multi-frequency signals, can be constructed with a number of long-wavelength, small noise, weak ionospheric effects of linear combination of observations, in order to improve the fixed efficiency of the ambiguity [3]. Therefore, how to give full play to the advantages of BDS triple frequency and establish the ambiguity resolution model with BDS triple frequency constraint to realize the rapid positioning of multi-system combination is very important for popularizing the application of BDS system in our country.

Based on the existing research, this paper makes full use of the characteristics of Beidou tri-frequency ambiguity easily fixed, and proposes a method of wide-line ambiguity fixing based on Beidou triple frequency observation so as to achieve a fast solution to mid-long baseline. The Beidou measured triple frequency data were verified.

2 BDS Triple Frequency Observation and Its Linear Combination

Considering the effect of ionosphere and troposphere on the refraction of satellite signals, we can get the carrier double differential observation equation as:

$$\Delta\nabla\phi_{(i,j,k)} = \Delta\nabla\rho + \Delta\nabla T - \eta_{(i,j,k)} \cdot \Delta\nabla I + \lambda_{(i,j,k)} \cdot \Delta\nabla N_{(i,j,k)} + \Delta\nabla\varepsilon_{\phi_{(i,j,k)}} \quad (1)$$

In the formula, $\Delta\nabla$ is a double difference operator. $\Delta\nabla\phi_{(i,j,k)}$ is a combination of carrier observations. $\Delta\nabla\rho, \Delta\nabla T$ are the double-difference station star-pitch and double-difference tropospheric delay values respectively. $\Delta\nabla I$ is the Beidou B1 frequency double difference ionospheric delay factor. $\Delta\nabla N_{(i,j,k)}$ is the integer ambiguity of the combined observations. $\eta_{(i,j,k)}$ is the ionospheric delay factor for combined observations. $\Delta\nabla\varepsilon_{\phi_{(i,j,k)}}$ is residual error.

Triple frequency combination of observations:

$$\Delta\nabla\phi_{(i,j,k)} = (i \cdot f_1 \cdot \Delta\nabla\phi_1 + j \cdot f_2 \cdot \Delta\nabla\phi_2 + k \cdot f_3 \cdot \Delta\nabla\phi_3)/f(i,j,k) \quad (2)$$

Triple frequency combination ambiguity:

$$\Delta\nabla N_{(i,j,k)} = i \cdot \Delta\nabla N_1 + j \cdot \Delta\nabla N_2 + k \cdot \Delta\nabla N_3 \tag{3}$$

The frequency and wavelength of the triple-frequency observations are expressed as:

$$\begin{cases} f_{(i,j,k)} = i \cdot f_1 + j \cdot f_2 + k \cdot f_3 \\ \lambda_{(i,j,k)} = \frac{c}{f_{(i,j,k)}} \end{cases} \tag{4}$$

It is commonly assumed that the observed values of Beidou are the same in all frequency bands and set as $\sigma\Delta\nabla\phi$, the triple-frequency's accuracy of the observed value is calculated as:

$$\begin{aligned} \sigma\Delta\nabla_{(i,j,k)} &= \pm \frac{\sqrt{(i \cdot f_1)^2 + (j \cdot f_2)^2 + (k \cdot f_3)^2}}{f_{(i,j,k)}} \sigma\Delta\nabla\phi \\ &= \mu_{(i,j,k)} \sigma\Delta\nabla\phi \end{aligned} \tag{5}$$

In the formula, $\mu_{(i,j,k)}$ is noise amplification factor for combined observation.

Comparing with the linear combination of the observed values of Beidou in the three frequency bands, several linear combinations as shown in Table 1 can be obtained.

3 Wide Lane Ambiguity Fixed

3.1 BDS Ultra-Wide Lane Ambiguity Fixed

For BDS triple frequency observations, the combination of carrier and pseudo-range can be used to solve the combination ambiguity $\Delta\nabla N_{(0,-1,1)}$ [4].

Table 1 BDS extra wide lane/wide lane carrier combination

Combination number	Combination factor (i, j, k)	Wavelength $\lambda_{(i,j,k)}/m$	Ionospheric factors $\eta_{(i,j,k)}$	Noise factor
1	(0, −1, 1)	4.8842	−1.5915	28.5287
2	(1, 4, −5)	6.3707	0.6521	172.6135
3	(1, 3, −4)	2.7646	−0.9698	59.2629
4	(1, 2, −3)	1.7654	−1.1348	28.0859
5	(−1, −5, 6)	20.9323	−8.9631	686.9493
6	(1, −1, 0)	0.8470	−1.2932	5.5752
7	(1, 0, −1)	1.0247	−1.2306	6.8751

$$\Delta\nabla N_{(0,-1,1)} = \left[\Delta\nabla\phi_{(0,-1,1)} - \frac{\Delta\nabla P_{(0,-1,1)}}{\lambda_{(0,-1,1)}}\right] \tag{6}$$

$\Delta\nabla P_{(0,-1,1)}$ is a combination of pseudo-range observations in meters. [ ] is rounding operator.

Formula 6, the effects of tropospheric and ionospheric delay are eliminated, and the accuracy is only affected by pseudo-range and carrier observations. The accuracy of the ambiguity using formula 6 is:

$$\sigma\Delta\nabla_{(0,-1,1)} = \pm\frac{1}{\lambda_{(0,-1,1)}} \cdot \sqrt{\frac{f_2^2+f_3^2}{f_{(0,-1,1)}^2}\sigma_{\Delta\nabla\phi}^2 + \frac{f_2^2+f_3^2}{f_{(0,-1,1)}^2}\sigma_{\Delta\nabla P}^2} \tag{7}$$

For non-difference carrier phase and pseudo-range observation noise errors are respectively 0.002 and 0.3 m. Based on the law of error propagation, it can be seen that the noise errors of carrier phase and pseudo-range observations are 0.004 and 0.6 m [5]. In Eq. 7, the calculated median error is 0.1737 weeks, so the rounding of the ambiguity by a single epoch can correctly fix the ambiguity of the (0, −1, 1) combined ultra wide lane of Beidou.

Although (1, 4, −5) combined observation has wavelengths longer than (0, −1, 1), its noise is amplified by approximately 6 times. $\Delta\nabla N_{(1,4,-5)}$ usually can be calculated using the similar formula (6), but its fixed success rate is not high, and for the medium-long baseline, the main influencing factor is residual tropospheric errors [3]. Here to improve the positioning accuracy, the idea of least squares adjustment is adopted and use Beidou ultra wide lane ambiguity $\Delta\nabla N_{(0,-1,1)}$ to constraint solution $\Delta\nabla N_{(1,4,-5)}$, the formula is:

$$\begin{bmatrix}\Delta P_{(0,-1,1)} - \Delta\rho_0 \\ \Delta\Phi_{(1,4,-5)} - \Delta\rho_0\end{bmatrix} = \begin{bmatrix}A & 0 \\ A & -\lambda_{(1,4,-5)}\end{bmatrix} * \begin{bmatrix}\delta x \\ \Delta\nabla N_{(1,4,-5)}\end{bmatrix} + \begin{bmatrix}\varepsilon_{\Delta P_{(0,-1,1)}} \\ \varepsilon_{\Delta\Phi_{(1,4,-5)}}\end{bmatrix} \tag{8}$$

In formula 8, A is the design matrix of coordinate correction, δx is the baseline unknown parameter, $\Delta P_{(0,-1,1)} = \Delta\Phi_{(0,-1,1)} - \lambda_{(0,-1,1)} \cdot \Delta\nabla N_{(0,-1,1)}$. According to the traditional method of solving ambiguity, ambiguity value is solved by single epoch error equation.

3.2 BDS Wide Lane Ambiguity Fixed

When BeiDou's two ultra-wide lane ambiguity $\Delta\nabla N_{(0,-1,1)}, \Delta\nabla N_{(1,4,-5)}$ are fixed, you can get a linear combination of the other wide lane ambiguity, Computation formula is:

$$\begin{cases} \Delta\nabla N_{(1,-1,0)} = 5\Delta\nabla N_{(0,-1,1)} + \Delta\nabla N_{(1,4,-5)} \\ \Delta\nabla N_{(1,0,-1)} = 4\Delta\nabla N_{(0,-1,1)} + \Delta\nabla N_{(1,4,-5)} \end{cases} \tag{9}$$

As can be seen from Table 1, Beidou's (1, 0, −1) combined wide-lane ambiguity has a wavelength larger than that of (1, −1, 0) and its ionospheric factor is smaller, so $\Delta\nabla N_{(1,0,-1)}$ is selected as the preferred constraint.

3.3 GPS Wide Lane Ambiguity Fixed

After the (1, 0, −1) wide-lane ambiguity resolution of BDS is fixed, it can be established with the observation equation of GPS system satellite to solve the wide-lane ambiguity of GPS. The GPS wide lane observation equation is:

$$\Delta\nabla\phi_{(1,-1,0)} = \Delta\nabla\rho + \Delta\nabla T - \eta_{(1,-1,0)} \cdot \Delta\nabla I + \lambda_{(1,-1,0)} \cdot \Delta\nabla N_{(1,-1,0)} + \Delta\nabla\varepsilon_{\phi_{(1,-1,0)}} \tag{10}$$

In the experiment, the fixed ambiguity of BDS wide alley as a priori information construct the baseline solution model with the constraint of BDS wide lane. In this way, the ill-posedness of the normal equations in the baseline solution model can be reduced and the ambiguity of wide-lane GPS can be effectively fixed. At the same time, in order to improve the precision of wide-lane ambiguity resolution, pseudo-range and carrier observation equations are established simultaneously. According to the measurement accuracy of pseudo-range and carrier phase, empirical weighting method is adopted, and the ratio is 1: 100 [6]. The comprehensive constraint model is:

$$\begin{bmatrix} A^C & 0 \\ A^C & 0 \\ A^G & 0 \\ A^G & diag(-\lambda^G_{(1,-1,0)}) \end{bmatrix} \cdot \begin{bmatrix} \Delta X \\ \Delta\nabla N^G_{(1,-1,0)} \end{bmatrix} = \begin{bmatrix} \Delta\nabla P^C \\ \Delta\nabla L^C - \lambda^C_{(1,0,-1)} \cdot \Delta\nabla N^C_{(1,0,-1)} \\ \Delta\nabla P^G \\ \Delta\nabla L^G \end{bmatrix} \tag{11}$$

In Eq. 11, A^C/A^G are the BDS and GPS coordinate increments respectively. $\Delta\nabla N^G_{(1,-1,0)}/\Delta\nabla N^C_{(1,0,-1)}$ are wide lane ambiguities for GPS and BDS, ΔX is the rover coordinate correction value, $\lambda^G_{(1,-1,0)}/\lambda^C_{(1,0,-1)}$ are the wide alley wavelength of GPS and BDS respectively, $\Delta\nabla L/\Delta\nabla P$ are pseudo-range and carrier observation equation constant term.

According to Eq. (11) to solve the GPS wide-lane ambiguity floating point solution and its corresponding variance and covariance matrix, we can take a single epoch to fix GPS wide lane ambiguity, as well as the LAMBDA method, to search and fix GPS wide-lane ambiguities [7]. Finally, GPS and BDS wide-lane ambiguity back to the observation equation, you can achieve wide lane combination of positioning.

4 Experiment Analysis

The experimental data used by the Nanjing Institute of Metrology CORS stations JN_NF and MQ_NF on December 7, 2016 collected a set of GPS/BDS/GLONASS medium baseline data, including the BDS contains three frequency observations, the baseline length of 17.8 km, The data sampling rate is 1 s.

In the experiment, the coordinates of the two stations are not known, and GAMIT software can be used to accurately solve the baseline vector solution. After the accurate baseline vector solution is well-defined, the ambiguity of wide lane or ultra wide lane can be solved according to the network RTK mode.

4.1 BDS Ultra-Wide Lane Ambiguity Fixed Results

In the experiment, because satellite No. 5 has the highest elevation angle, so it is used as a reference star, and non-reference stars are numbered 1, 2, 3, 4, 7, 9 and 10 in turn. The ambiguity of Beidou (0, −1, 1) combined ultra wide lane can be solved by Eq. (6), and the ambiguity deviation of combined ultra wide lane can be obtained by using the floating point solution of ultra wide lane. The result is shown in Fig. 1.

From Fig. 1, it can be seen that the ambiguity $\Delta\nabla N_{(0,-1,1)}$ of Beidou ultra wide lane is about ±0.15 weeks, and the deviation results are evenly distributed. Therefore, the single epoch rounding can be correctly fixed $\Delta\nabla N_{(0,-1,1)}$, which also

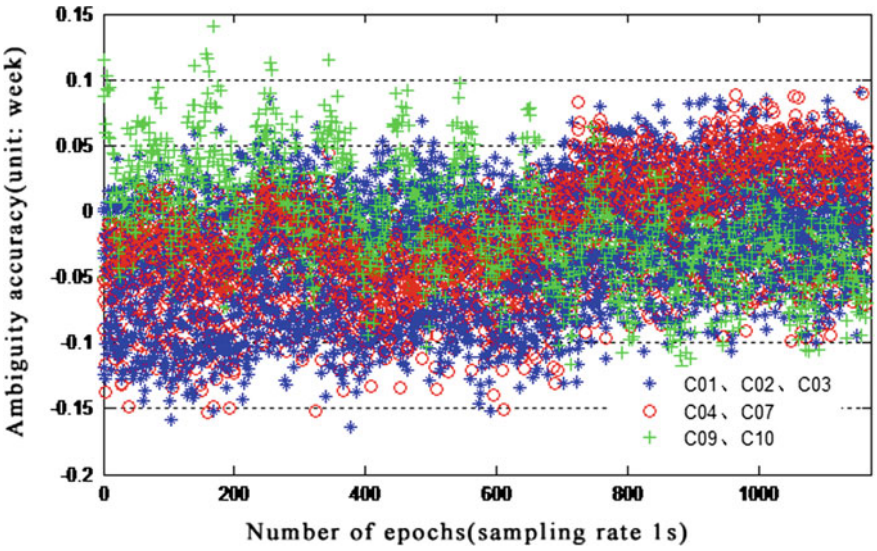

Fig. 1 BDS (0, −1, 1) extra wide lane ambiguity deviation

verifies the Beidou (0, −1, 1) combined observations longer wavelength, the conclusion is easy to fix the degree of ambiguity.

After the ambiguity of Beidou extra-wide lane is solved accurately, the ambiguity of BDS (1, 4, −5) combined extra-wide lane can be constrained using the least squares principle Eq. (8). As can be seen from Fig. 2, the combined ambiguity deviation is basically stable within ±0.2 weeks. Comparing the two picture, it is found that (1, 4, −5) combination ambiguity deviation is slightly larger than (0, −1, 1) combination ambiguity deviation, this is because the solution process is affected by the combined noise of (0, −1, 1) when the combined ambiguity of least squares (1, 4, −5) is used, resulting in a slightly poorer final resolution.

4.2 Wide Lane Ambiguity Fixed Result

After the ambiguities of the two ultra-wide lanes of the BDS are fixed, any one of the wide lane ambiguities whose combination coefficient is zero can be obtained through the integer combination. Since the ambiguities of the two ultra-wide lanes are rounded and fixed, the wide-lane ambiguity of BDS (1, 0, −1) can be obtained by the formula (9), and the result is an integer.

After the solution of (1, 0, −1) combined wide-area ambiguity of DBS is completed, we can use it as a priori information to construct the ambiguity resolution model Eq. (11) Ambiguity.

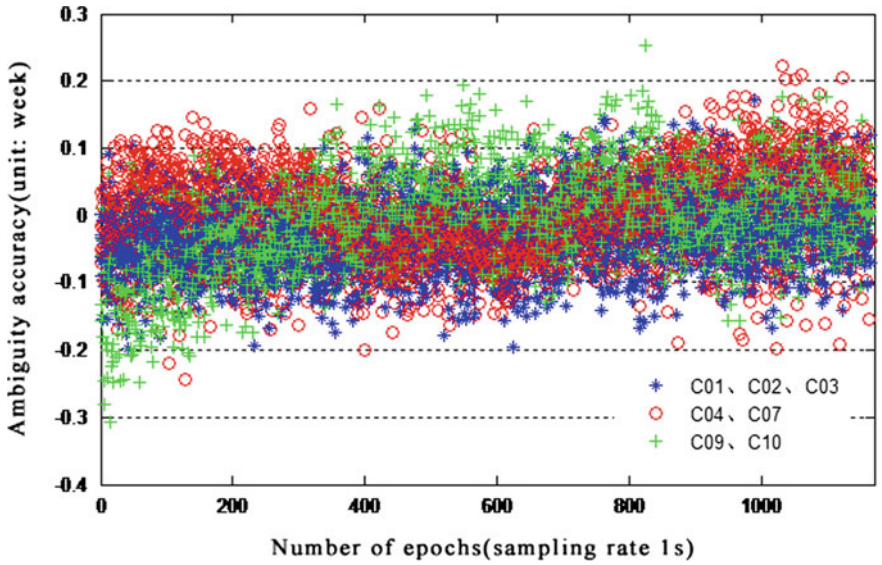

Fig. 2 BDS (1, 4, −5) extra wide lane ambiguity deviation

As can be seen from Fig. 3, the deviation of GPS wide-lane ambiguity solved by BDS (1, 0, −1) wide-lane ambiguity constraint can be fixed within ±0.15 weeks. As can be seen from Figs. 4 and 5, the deviation of GPS wide-lane ambiguity solved by MW method is within ±1.5 weeks. Single epoch can't be fixed round. Therefore, the method proposed in this paper can quickly fix GPS wide lane ambiguity and realize the solution of mid-long baseline.

Finally, the wide-lane ambiguity of GPS and BDS is returned to the observation equation to carry out wide-lane combination positioning. The deviation in each direction of N, E and U is shown in Fig. 6. In Fig. 6, the positioning accuracy of the wide-lane combined positioning plane is 2 cm, and the elevation direction is weaker than the plane, at about 6 cm, there is no big deviation in the whole, which also shows that the solution of wide-lane ambiguity is reliable.

In this experiment, the BDS ultra-wide lane ambiguities were linearly combined to solve the ambiguities of (1, −1, 0) and (1, 0, −1), and the (1, 0, −1) wide lane ambiguity is selected as the constraint condition to solve the GPS wide lane ambiguity. Compared with the traditional MW method to solve wide-lane ambiguity, the method proposed in this paper can effectively reduce the number of primitive epochs needed to correctly fix the ambiguity of wide-lane and achieve a fast solution to medium-long baseline, as well as laying the foundation for solving the network ambiguity of RTK.

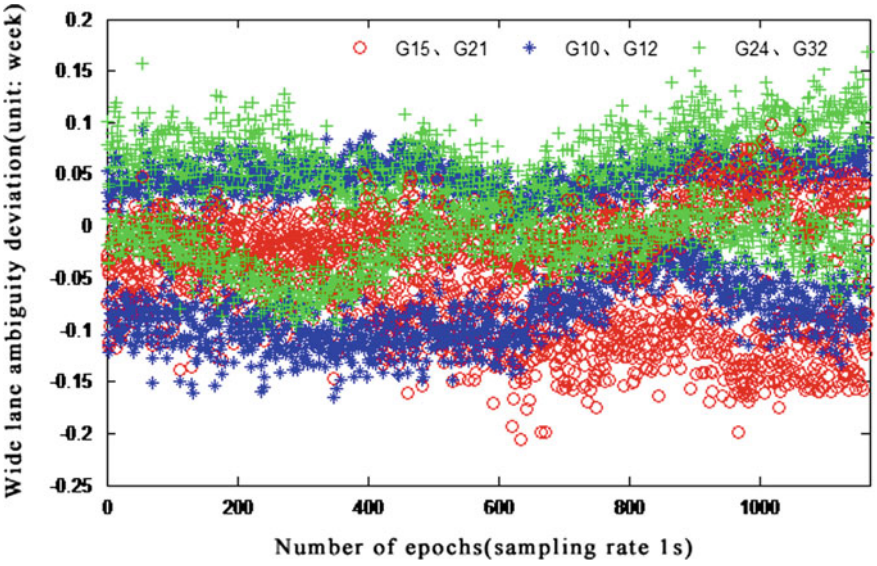

Fig. 3 GPS (1, −1, 0) wide lane ambiguity deviation

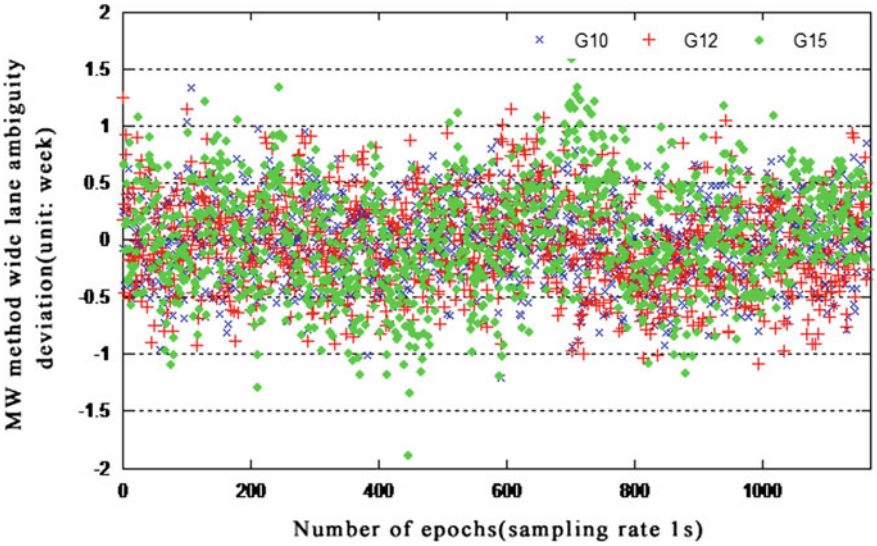

Fig. 4 GPS wide lane ambiguity deviation (MW method)

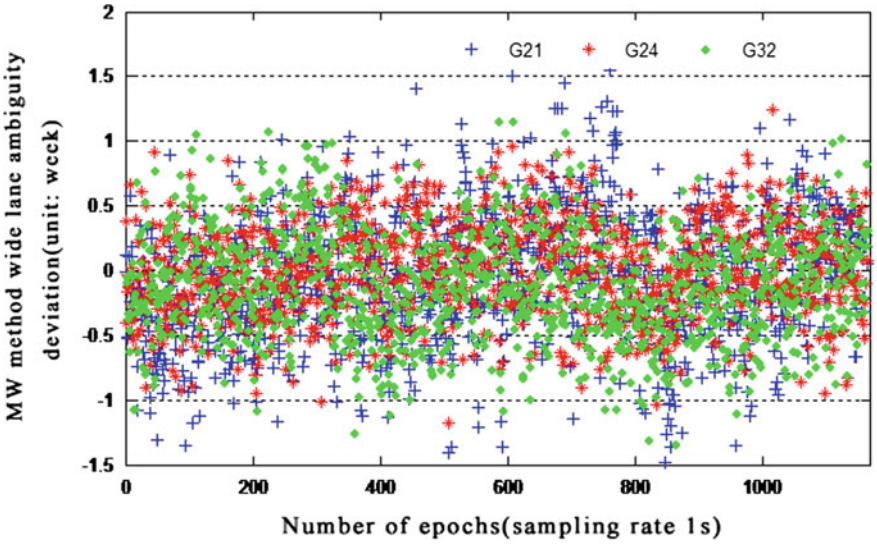

Fig. 5 GPS wide lane ambiguity deviation (MW method)

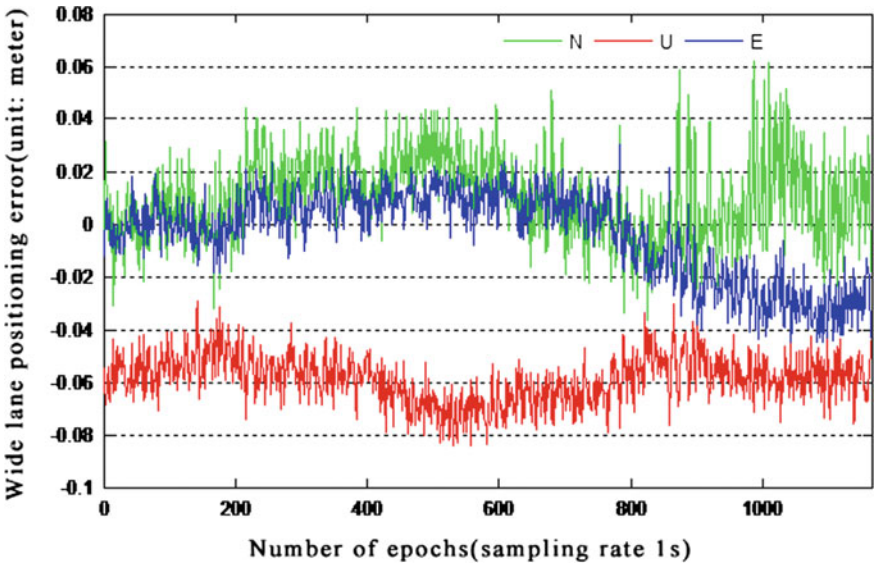

Fig. 6 Deviation of NEU directions in wide lane combination

5 Conclusion

In this paper, BDS triple frequency as the core, firstly introduced the BDS two ultra-wide lane ambiguity solution method, and then the two ultra-wide lane ambiguity linear combination to get BDS wide lane ambiguity, constrained GPS wide lane ambiguity. Finally, the wide-lane ambiguity of GPS and BDS is returned to the observation equation to realize the combination of fast lane widening. At last, the method proposed in the article is validated by the measured triple frequency data of BDS, and the following conclusions are drawn:

(1) For the combination of BDS (0, −1, 1) triple frequency observations, the delay between ionosphere and troposphere can be eliminated by combining wide-lane carrier with narrow-girth pseudo-range. The ambiguity deviation of single epoch calculation is within ±0.15 weeks, the ambiguity fixed success rate of 100%.
(2) Using the principle of least square adjustment, the $\Delta\nabla N_{(1,4,-5)}$ ambiguity is solved by the Beidou (0, −1, 1) ultra-wide lane ambiguity constraint, and the ambiguity deviation is controlled within ±0.2 weeks, which can be rounded and fixed by a single epoch.
(3) Taking the wide lane ambiguity of BDS (1, 0, −1) as a priori information, the ambiguity of GPS wide lane ambiguity solved in the ambiguity constraint model is ±0.15 weeks, which can be directly rounded and fixed.

(4) The model of ambiguity resolution with BDS wide-lane constraint proposed in this paper can quickly fix ambiguity of GPS wide-lane and contribute to the ambiguity decomposition of mid-long baselines, which lays the foundation for solving the ambiguity of network RTK.

References

1. Wang J, Fan X (2013) China compass system officially serves the Asia Pacific region. Geogr Teach 2013(4):4–6
2. Wang S (2015) Study on the computation method of BDS Tri—frequency ambiguity. J China Univ Min Technol
3. Li B, Shen Y, Zhou Z (2009) A new method for medium and long range three frequency GNSS rapid ambiguity resolution. Acta Geodaet Cartogr Sin 38(4):18–23
4. Gao W, Gao C, Pan S et al (2015) Single-epoch positioning method in network RTK with BDS triple-frequency wide-lance combinations. Acta Geodaet Cartogr Sin 44(6):641–648
5. Lv WC, Gao JX, Wang J et al (2015) The single epoch algorithm for short baseline ambiguity based on BeiDou three frequency constraint. J China Univ Min Technol 44(6):1090–1096
6. Feng Y (2008) GNSS three carrier ambiguity resolution using ionosphere-reduced virtual signals. J Geodesy 82(12):847–862
7. Teunissen PJG (1995) The least-squares ambiguity decorrelation adjustment: a method for fast GPS integer ambiguity estimation. J Geodesy 70(1–2):65–82

Part IV
Policies and Regulations, Standards and Intellectual Properties

Beidou+ Industry Convergence Development and Intellectual Property Protection

Yu Jinping, Wang Yuxuan and Yang Xianna

Abstract With the rapid development of global Beidou system construction and industrial development, the application of new technologies, new models, new products and new services emerge in an endless stream. The trend of "converging data, converging network, converging terminal, converging industry"s integration is becoming more and more pronounced. BDS is entering the emerging areas of shared bikes, unmanned aerial vehicles and automatic driving. Beidou high precision is also from the industry to enter the field of mass consumption, becoming a new growth point of technology, driving the growth of spatio-temporal information consumption. With the integration of the Beidou+ industry development, Beidou+ industry related patent applications increased rapidly, domestic innovation growth faster. Universities and Research Institute of patent ownership is more prominent, as the main body of market the enterprise's patent accumulation has a larger promotion space, foreign manufacturers to introduce new products into the domestic market at the same time, also in the footsteps of China area to speed up the layout of patent. Beidou module hardware and map navigation software, are intellectual property intensive industries, with large patent pool, related intellectual property rights litigation is also rising year by year. BDS is facing the challenge from the traditional ICT industry, facing the pressure of related industry of intellectual property litigation and open source software, at the same time, the SEP and NPE problems are unavoidable. Strengthen the core technology's patent layout, encourage resource sharing and balance intellectual property trade-offs, defense the intellectual property risks caused by the upstream and downstream industry chains, tracking the dynamics of competitors and making timely warning of intellectual property rights are the current urgencies.

Keywords BeiDou+ · Satellite navigation · Industry convergence
Intellectual property (IP)

Y. Jinping (✉) · W. Yuxuan · Y. Xianna
National Research Center for Industrial Information Security Development,
Electronic First Research Institute, Ministry of Industry and Information Technology,
Beijing 100040, China
e-mail: yujinping@infoip.org

J. Sun et al. (eds.), *China Satellite Navigation Conference (CSNC) 2018 Proceedings*, Lecture Notes in Electrical Engineering 498,
https://doi.org/10.1007/978-981-13-0014-1_60

1 Introduction

BeiDou is a satellite navigation system that is Chinese self-built, operated independently and compatible with other satellite navigation systems in the world. With the rise of wearable devices, drones, intelligent manufacturing and other kinds of intelligent hardware and terminals, the concept of "BeiDou+" surged through the integration with emerging technologies and industries, such as the Beidou shared bikes, Beidou watch, intelligent driver Test and promoted the supply-side structural reform, provided a positioning basis for the Internet of Everything. The convergence of Satellite navigation and multisensor, combined with the vast amount of location information generated by various application fields, can further tap its potential value and serve the public's life, and form a new ecological chain of industries, by combining with large data, cloud computing, artificial intelligence and machine learning technologies. This enables the integration development to become a new engine and booster for the rapid development of the Beidou industry.

Compared with the traditional industries, the converging industries have their own different characteristics. Due to the involved long industrial chain and the wide range of intellectual property rights, the intellectual property issues thus generated also deserve special attention.

2 The Status Quo of Beidou+ Industrial Convergence

With the rapid development of Beidou application and industrial development, the new technologies, new models, new products and new services applied by Beidou emerged one after another, and the converging development trend of "convergence of data, convergence of networks and convergence of terminals" becomes more and more remarkable. The intellectual property of Beidou has been deepen into the technical innovation, product applications and market competition in every aspect.

From the industrial chain analysis point of view, Beidou navigation industry segment can be broadly divided into upper, middle and lower parts. Upstream is a basis class product that produces independent or integrated reception systems for some systems, including chips, antennas, boards, and more. Midstream is a system integrator that integrates GNSS functions into more products such as car terminals and handheld terminals. Downstream is a value-added service provider whose value added services improve the use and coverage of GNSS, including map providers, enhanced service providers and GNSS calibration or test service providers (Fig. 1).

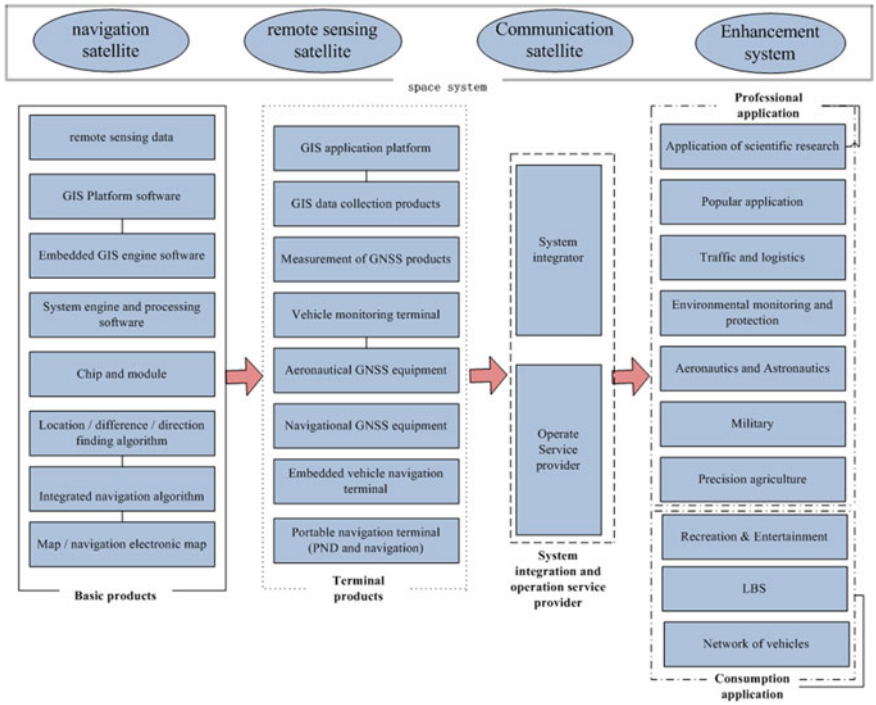

Fig. 1 China's satellite navigation industry distribution

Overall, the development of China's satellite industry started later, but there exist huge demand in the domestic market. Beidou application industry is entering a period of rapid growth. The output value of the industry has increased from 12.7 billion yuan in 2006 to 211.8 billion yuan in 2016, with an increase of more than ten times in just 10 years. The capacity of industry independent innovation has been greatly improved. The application exploitation and system research of Beidou compatible navigation terminals have reached the international advanced level. Breakthroughs are being made in key areas such as satellite positioning. China has constructed a Beidou industrial chain integrating chips, modules, boards, terminals and operation services. As a result, the industrial development has begun to take shape. The number of application terminal enterprises in the midstream is the largest while that of the downstream operation services is the fastest.

From the layout of the existing satellite navigation industry, regardless of the hardware of the chip module or the software of map navigation, all are intellectual property-intensive industries, with numerous patents and litigation disputes over intellectual property. In the future, in the development of satellite navigation system construction and industrialization, the basic reserves of intellectual property and the enhancement of comprehensive utilization capacity are all important components in boosting the internationalization of the satellite navigation industry.

3 Intellectual Property Protection Object of Converging Industry and Its Particularity

The object of the intellectual property protection in the converging industry is the result of the intellectual property of the relevant industries. It is the same intangible property as the general intellectual property object. However, it has its peculiarities compared with the general object of intellectual property. Compared with ordinary industries, the newly emerging converging industries' particularity is mainly manifested in the following characteristics:

(1) Cross-border
Both "Internet+" and "BeiDou+" have a clear cross-border nature. Technology has been fully integrated with all economic fields to further optimize and integrate the reconfiguration of production factors. At the same time, the problems of intellectual property brought about are also cross-border. Issues involved patents trademarks, copyrights, integrated circuit layout and technical secrets are also intertwined.

(2) Openness
The practical application and innovation of knowledge have promoted social and economic development. Break down monopolies and barriers, promote equal cooperation in the society, and encourage positive creation and promot information and knowledge balance. In the process of the development of industrial convergence, it provides opportunities and at the same time forces the intellectual property to be more public. With opening up and sharing become an important topic, the Beidou open source system came into being.

(3) Growth
Most of the converging industries are in a period of rapid development with more potential for development in the later stage and their growth rate will exceed that of the traditional industries. Many of the intellectual property issues derived from them also come up with new requirements as the industry develops. For example, the patentability of commercial methods of the internet industry have always been the subject of great attention and discussion.

(4) Dynamic
The converging industry is dynamic. The emerging industries may be transformed into traditional industries after long-term development and slowing of development. With the development of the industry, there are also related issues of intellectual property protection. For example, in the field of intelligent terminals, the objects of graphical user interface appearance patent are dynamically adjusted according to the needs of the industrial development.

(5) High Investment, High Return
As an emerging industry, the converging industry, is not mature in all aspects and it is very difficult to develop it. It will inevitably require a large amount of capital investment to develop a large-scale market. However, its guiding characteristics as well as its broad development space make it equally lucrative to invest once

successful. The input and output of IPRs also have the same characteristics. The transfer of IPRs has become the theme of development and plays an important role in M&A and development of enterprises.

4 Beidou+ Industry Development and Intellectual Property Status Quo

The data in this paper comes from the IPR research team of National Industrial Information Security Development Research Center. The search time for patents is up to October 25, 2017. The technical research and professional analysis of the related patent search are carried out. The retrieved data are filtered, cleaned and classified. By the analysis of the annual and technical dimensions of Beidou+ industry-related patents, the overall situation of Beidou+ industry intellectual property could be reflected.

4.1 The Overall Situation of Satellite Navigation Industry Patent Application

China's applications for satellite navigation-related patents in 2011 as the cut-off point, prior to China's annual acceptance has been lower than the United States, but from 2012 onwards, China's satellite navigation-related patents for the first time exceeded the United States in the annual figures, ranking first. However, as China's Beidou satellite navigation research and patent applications started late, before 2016, the total number of patent applications has been lower than the United States. According to the distribution of rights holders, the layout of domestic applicants of BeiDou satellite navigation has obvious advantages. Both inventions and licenses are higher than that of foreign applicants in invention disclosure (Figs. 2 and 3).

As of October 25, 2017, China's total amount of satellite navigation-related patent applications has reached 48,078, surpassing the five countries and regions such as the United States and Europe, ranking the first in the world. On the one hand, this is due to the rapid increase in the number of patent applications filed by Beidou+ and industrial innovation bodies in China. On the other hand, foreign manufacturers are accelerating the pace of patent distribution in China while putting new products into their domestic markets.

From the main body of the patent application for satellite navigation accepted in China, foreign companies such as Qualcomm, Tianbao and Samsung have begun to make their navigation products compatible with the Beidou system in order to achieve their strategic goal of docking with Beidou. These international companies are stepping up the patent layout while put their products into Chinese market. Compared with the emerging satellite navigation companies in China, foreign

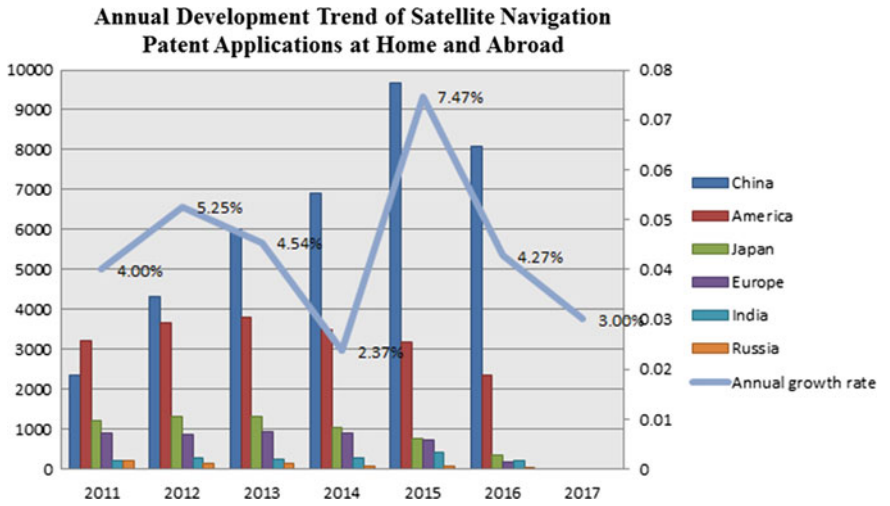

Fig. 2 Annual development trend of satellite navigation patent applications at home and abroad

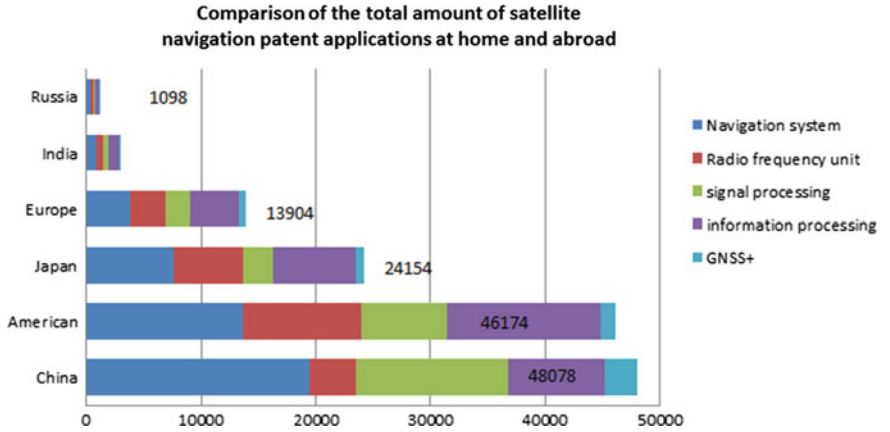

Fig. 3 Comparison of the total amount of satellite navigation patent applications at home and abroad

manufacturers have obvious advantages both in terms of the total amount of patents accumulated and the breadth and depth of the patent layout. Domestic satellite navigation patentees from colleges and universities are more prominent, including Beijing University of Aeronautics and Astronautics, Harbin Engineering University, Nanjing University of Aeronautics and Astronautics, Wuhan University and Tsinghua University. Only Haewei and ZTE enter the top ten applicants for navigation satellite patents. To some extent this shows that the key enterprises of Beidou are small and non-core enterprises. The fragmentation of the brand is serious. The core competitiveness based on intellectual property has not yet been

formed. There is a huge rift between the scale of the industry and the size of the enterprise, and the industrial consolidation has become inevitable.

4.2 China's Patent Applications Status of Enterprises Based Beidou Innovation Subject

Taking the 200 upstream and downstream enterprises of China's satellite navigation industry chain as a random sample, we conducted a survey and analysis of the patents they hold. The research shows that more than 70% of China's satellite navigation industry holds patents, and Enterprises hold more than 100 patents accounted for about 13.49% of the patents are in the state of authorization; the proportion of effective patent is as high as 83%, which reflects the main body of China's satellite navigation innovation in recent years is in intensive application period (Figs. 4 and 5).

From the geographical distribution of the patent of 200 satellite navigation companies, Beijing and Guangdong are the most prominent ones, and the amount of applications is far ahead of other provinces and cities. Sichuan, as the representative of the Midwest regions, is also the leader in the total number of applications, ranking third. With the rise of BeiDou+ concept, the development of satellite navigation industry is more and more closely linked with the Internet industry. This is reflected in the rise of emerging enterprises in Beijing and Guangdong and their rapid application of patents.

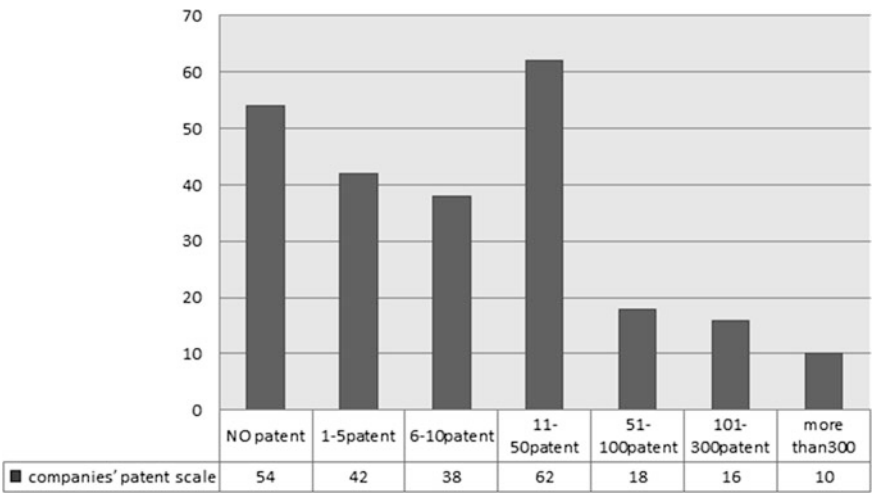

Fig. 4 Sample analysis of China's satellite navigation companies' patent scale

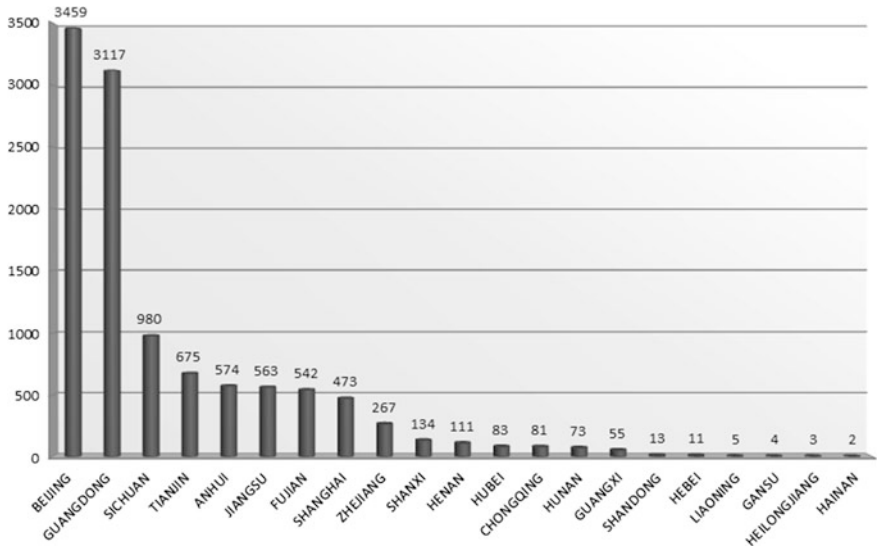

Fig. 5 Sample analysis of China's satellite navigation companies' patent holding

5 Beidou+ Intellectual Property Risk in Industrial Development

5.1 Emerging Firms Face Patent Competition from Traditional ICT Enterprises

RF unit, signal processing and information processing are the core technologies of "BeiDou+". It is also the field where the traditional information industry accumulates most patents and the market is the most active. Most of these patents are still in the hands of traditional communication enterprises and internet companies and will compete with BeiDou+ enterprise in the new business model. These companies for the intervention in the navigation field will be rolled-off and have tremendous impact. From the existing number of patents observed, Chinese domestic enterprises have not yet fully prepared, the main reason is the early accumulation of communications companies. The traditional communications and Internet enterprises have accumulated a large number of patents in the field of G01S (radio-oriented; radio navigation; use of radio-wave ranging or speed detection; positioning or presence detection using reflection or reradiation of radio waves; similar devices using other waves) and in the field of H04B (transfer). Taking the traditional enterprises as an example, in the existing patents, the number of applications under the G01S and H04B fields is, Quacomm 21872, Huawei Technologies 9546, Honeywell 2515. Patent accumulation of the new Beidou+ enterprises in this area is slightly less. As the leading enterprises in this field, the

number of patents of the four companies including BDStar Navigation Techtotop Microelectronics, Unistrong and Qianxun SI is 292, 119, 85 and 72 respectively, of which the highest is inferior to Huawei's one tenth of the quantity. And this gap is difficult to be exceeded within a short period of time. The accumulation of patents in the core technology fields takes time and capital investment as well as the accumulation of talent and technology, which is difficult to complete in a short period of time. Most of the Beidou+ industrial enterprises are emerging enterprises, and the weak accumulation of patents will inevitably make the enterprises at a comparative disadvantage in the future innovation and development.

5.2 Terminal Vendors Face Pressure from IP Litigations of Upstream and Downstream Enterprises

"Beidou+" has transformed and affected many industries. At present, industries familiar to the public such as intelligent transportation, precision agriculture, logistics control, people's livelihood care and intelligent driving test are all "BeiDou+" masterpieces, and industries related to Beidou+. The chain is very extensive. However, Beidou satellite navigation, as one of the four major navigation systems in the world, started late in the industry chain innovation and had poorer comprehensive utilization of intellectual property. Once intellectual property disputes occurs, the industrial chain will be affected from the front end to the back end, including the chip manufacturers, module manufacturers, terminal manufacturers, operators and depots, etc. And the most wrecked will be terminal manufacturers and depots, which will have a profound impact on the Beidou+ industry. Similar situation frequently occurs in the field of intelligent terminals. HTC, Samsung, ZTE, etc. has inevitably experienced intellectual property disputes from upstream and downstream. For example, the cases of Iwncomm v. Sony and 337 investigations toward electric self-balancing scooters, all suffered a lot due to the intellectual property problems of purchasing products upstream and downstream. In the "BeiDou+" industrial chain, terminal manufacturers are often fatal because of the impact of intellectual property risk. In particular, the problems caused by upstream hardware should not be overlooked.

5.3 Beidou+ Related Vendors Are Under Pressure from Open Source Software

In 2016, after more than two years' hard work and development, National Defense University CNETD team made a trial version of the global satellite navigation system simulation software platform (abbreviated as "BDSim"), which is officially launched on the satellite navigation simulation and testing open laboratory network platform. In order to reflect the development philosophy of "integration, openness,

cooperation and win-win" of Beidou Open Laboratory, users of Beidou Open Laboratory can download BDSim or BDSim source code freely through Beidou Open Lab Network Platform or Trustie Creative Practice Community. Similar to BDSim, most open source software developers related to China's BeiDou satellite navigation field are mostly completed by universities or research institutes and are in their infancy. Compared with the open source software developed by commercial companies, these research institutions have no litigation experience and no strong litigation funding backing. Once involved in patent litigations, there is no chance to fight back. For users of Beidou open source software, most of them do not have the capacity to judge whether the open source software infringes others' rights or not. The end user is "no fault" and cannot completely fight the responsibility of infringement, However the obligee can still seek the injunction protection through judicial channels to prohibit the use of infringing software.

In addition, there are a host of other innate problems with open source software such as the unclear legal validity of open source software licenses, incompatibility of open source software licenses, translation, interpretation, enforcement of open source software licenses, and open source software Permit "unsecured" and other issues, these issues could bring unknown risks for the future "Beidou+" related companies.

5.4 Issues from SEP and NPE Cannot Be Ignored

In the course of the continuous progress of "Beidou+" and "Internet+", the issue of the standard essential patent ("SEP") and the non-patent implementing entity ("NPE") still cannot be ignored.

After long-term investment in research and development, traditional communications companies have accumulated many basic patents, especially SEP in the field of communications and data transmission. Compared with this, the number of Chinese enterprises is far behind the number of patents. In the face of IPR infringement litigation from SEP, Beidou satellite navigation company's patent accumulation is often not a favorable negotiating capital.

For the NPE, the data show that NPE is highly concerned with the area of satellite navigation. Through the plaintiff's analysis of GPS-related products in U.S. patent litigation, more than 200 plaintiffs in patent litigation except for Broadcom and LunarEye and other related parties, all are NPE (Non-practical Entity) plaintiffs. Through the satellite navigation-related five cases of 337 investigation, the most affected is the car manufacturer. The respondent includes Audi, BMW, Ford, Daimler and other well-known manufacturers. As of now, there are no Chinese car manufacturers in the depot being sued. The reason may be that satellite navigation is mainly installed in high-end vehicles as a front-load and Chinese automakers export mainly in the low-end. In view of the further development of BeiDou, in the future in China's automobiles, more navigation products will be equipped and related intellectual property risks will need more attention.

6 Beidou+ Intellectual Property Protection Trend

With the continuous development of Beidou satellite navigation, satellite navigation has been widely applied and infiltrated into all walks of life, involving transportation, precision agriculture, emergency rescue, personal location services, etc., which has brought many positive effects to the development of related industries. The intellectual property protection involved in all fields, the content of its protection, the rights and boundaries have their own characteristics. In the context of convergence of the economy, how to further protect intellectual property is a major problem many enterprises faced.

On the one hand, the future of intellectual property will face the challenge of being weakened. Traditional IPR protection systems are constantly under the attack and influence of Internet+, BeiDou+ and other converging technologies. There is more overlap between personal interests and public interests. As a result, how to safeguard their rights is becoming more and more obscure. At the same time, patent holders will gradually give partial rights to intellectual property under the trade-offs of advantages and disadvantages, provide some room for development for the industry. This would break the traditional intellectual property protection mechanism and further promote the "Internet+", "Beidou+" and coordinated and healthy development of economic development of enterprises. For example, the Android operating system is to take the initiative to give up the software source code patents, to attract more developers and mobile phone users in the open source based on further analysis and research to achieve the purpose of joint development and resource sharing which has won a huge success. Therefore, under the perspective of convergence and development, in order to better protect intellectual property and promote coordinated development of industries, weakening the protection of intellectual property has become a huge challenge for the converging industry.

On the other hand, the future protection of intellectual property will be more stringent. Judging from the domestic legal environment, our country has developed to a stage highly dependent on intellectual property in the process of accelerating the implementation of an innovation-driven development strategy. To create a fair competition environment in the market, strict protection of intellectual property protection system is needed. From the perspective of market competition, the international and domestic pressures Beidou+ industrial development faced are still huge. In the process of "going global", from an international perspective, Beidou's terminal manufacturers' products face various challenges in the mature countries and regions in the intellectual property system of the United States, the European Union and Japan. At the domestic level, most of the patents in BeiDou and related innovation entities are weakly accumulated. The comprehensive capability of intellectual property is uneven, the common awareness of protecting intellectual property is weak and the mind of using other people's intellectual property rights legally is not strong, which not only seriously damages the interests of intellectual property owners and vast consumers, but also severely discourages the compliance operators and independent innovators. This will affect the overall development of the industry.

7 BeiDou+ Industry Intellectual Property Risk Prevention Suggestions

(1) Strengthen the core technology's patent layout. Internet of things era, in addition to the core technology of traditional satellite navigation hardware, related software technology is equally important. In order to grasp the timing of the transformation of the Internet of Things, although it will take time to accumulate the basic patents for navigation and applications, strategic investments in core technologies such as information processing and signal processing should be emphasized. Innovation in navigation systems and radio frequency units achievements should be transformed into independent intellectual property rights to firmly rooted in the foundation. In particular, the patent protection of Beidou's signal system is a long-term task. It should proceed from the overall national development strategy and establish an effective mechanism for organizing, coordinating and unified management. At the same time, emerging navigation companies should also consider the application-side technology research and development investment, according to enterprise development strategy and market positioning, on the basis of the core patent application, apply a patent with its own technical characteristics of peripheral patents to form a complete patent family, and constantly improve the layout of intellectual property. This would favor the Beidou+ whole industry chain development.

(2) Encourage resource sharing and balance intellectual property trade-offs. Under the new trend of "Internet+" economic development, the main body of Beidou+ industry innovation in China can learn from Japan's "abandonment model" of intellectual property and actively integrate into the Internet era. During the process of setting up patent pool and patent alliance, some patents, trademarks, software copyrights and other intellectual property rights could be shared. Strengthen mutual exchanges and cooperation among enterprises, create a benign environment for Beidou+ industrial development, promote the overall development of BeiDou+ industry and share industrial interests.

(3) Defense the intellectual property risks caused by the upstream and downstream industry chains. Beidou+ industry chain is long, in the terminal products, whether it is sharing bicycles, cars in the field of traffic or smart phones in the field of consumer electronics, in the process of basic product procurement and research we must carefully investigate the intellectual property risk from the upstream and downstream industry chains, to avoid the restrictions on the market because of the infringement of intellectual property after export overseas. Because this could bring devastating damages to the business. The contents of the investigation include whether the technology provided by the technology provider is original, whether it has obtained the permission of the other product, whether there is an exclusive licensee, whether the risk of patent infringement using this technology is to be circumvented. Fully understanding of the technical products provided by each other is needed. In addition, for the software, pay attention to open source software to comply with the requirements of the open

source agreement, especially to restrictions to the ownership of our rights and other issues. Beidou-related enterprises, on the one hand should rely on independent research and development to actively submit patent applications. On the other hand, also need to supplement their own short board through the purchase of patents, and comprehensively improve the intellectual property risk defense capabilities. Long-term development requires the adaption of patent competition laws.

(4) Tracking the dynamics of competitors, making timely warning of intellectual property rights. On the one hand, through patent analysis and other means to track patent litigation in the countries/regions, litigation companies, litigation and potential litigation could make advance risk aversion, thus could minimize the intellectual property risk in the field of advantage. On the other hand, China's Beidou enterprises should follow the investigation of the application status, legal status and lawsuits for the basic patents. Analyze and determine in detail the scope of protection of the patent claims obtained under the provisions of the prohibition of reverse prosecution. Comprehensively assess the validity of the patent and search the comparative documents that can destroy the novelty or inventiveness of the target patent. Promptly initiate the patent invalidation procedure to the patent administration departments of all countries or regions in accordance with the relevant laws of different countries or regions. Strengthen the technical accumulation of the enterprise, at the same time, defend NPE actively.

8 Conclusion

The intellectual property chain of converging industry represented by "IP+" and "BeiDou+" is longer than the traditional industries, the resulting intellectual property issues are all-encompassing and more complex. With the continuous development of converging industries, the issue of intellectual property becomes more prominent, which will attract more people's attention. Only by taking reasonable measures to protect intellectual property rights can we bring vitality to the development of the industry and enhance the overall competitiveness of enterprises. Further properly handle the relationship between the development of converging industries such as "Beidou+" and "Internet+" and the protection of intellectual property rights is still a long way to go.

References

1. Hu H, Xing H (2003) Industrial integration theory and its enlightenment on China's development of information industry. In: China Industrial Economics, Beijing
2. Chen L (Tianjin Academy of Social Sciences, Tianjin 300091, China) (2006) The mutual infiltration of industrial development: industrial integration. In: Guizhou University of Finance and Economics (3), Guiyang

3. Hao H (2013) Beijing satellite navigation productivity promotion center hot spot, navigation world hot-point perspective. In: GNSS WORLD, Beijing
4. Chu C (2016) “Internet +” and intellectual property protection. In: Civil and Commercial Law Theory and Practice, Beijing
5. Chen L (2006) mutual infiltration of industrial development: industrial integration. In: economics and management, Guizhou University of Finance and Economics, third period (total 122), Guiyang
6. Beidou web. http://www.beidou.gov.cn/. Cited 7 Dec 2017
7. Hu G, Wu H, Liu Y, Zhang Y, Nguyen H, Huang H (2017) Progress and prospect of Beidou application and promotion industrialization. In: Satellite navigation, vol 5, Issue 1, Beijing

Research on the Application of BeiDou High Precision Positioning Intellectual Property

Zhengfan Liu, Xueyong Xu, Ye Zhou, Jinchen Wang, Yu Xia and Yingying Zhang

Abstract This paper analyzes the number, the involved technical fields, the technical level and the ownerships of patents, which related to high-precision positioning applications of BeiDou Navigation Satellite System(BDS). We point out the deficiencies in the layout of the patents. As the international development of BDS high-precision positioning applications will be pushed forward in the future, we hope our work would be a reference to the protection of intellectual property rights.

Keywords BeiDou · Satellite navigation · High precision · Intellectual property Distribution

1 Introduction

At present, the global operational four Global Navigation Satellite Systems (GNSS) are GPS, GLONASS, Galileo and BDS. Among them, the earliest and most mature GPS of USA has been providing services for more than two decades, accounting for nearly 90% of the entire GNSS market [1, 2]. Therefore, in the current GNSS market, GPS occupies the dominant position. The other three global satellite navigation systems have their own characteristics and occupy only a small amount of market share.

In recent years, China has made great efforts to develop BDS in order to improve the positioning accuracy of the system, increase the system reliability, enhance the system service capabilities and enhance the international competitiveness of BDS, and completely solve the huge potential safety hazard in high precision satellite navigation applications. In September 2014, China formally started the development and construction of the national BDS ground-based augmentation system (BD-GBAS). The first phase of the system to realize the real-time meter level

Z. Liu (✉) · X. Xu · Y. Zhou · J. Wang · Y. Xia · Y. Zhang
North Information Control Institute Group Co., Ltd., Nan Jing 211153, China
e-mail: senseblaze900@163.com

J. Sun et al. (eds.), *China Satellite Navigation Conference (CSNC) 2018 Proceedings*, Lecture Notes in Electrical Engineering 498,
https://doi.org/10.1007/978-981-13-0014-1_61

accuracy positioning service in the major cities of China was completed. By the end of 2018, the construction of BD-GBAS will be fully completed. It will meet the needs of the industry users and the public users for BDS's real-time meter-/decimeter-/centimeter- and post-processing millimeter-level high precision positioning service. After the completion of the BD-GBAS, China will enter the "BeiDou high precision positioning application era".

The competition in the field of international GNSS will be fiercer with the development of the practical and the globalization of the BeiDou system and its high precision positioning application industries. The competition and cooperation between BDS and the other GNSS systems, such as GPS, GLONASS, GALILEO, will inevitably occur in the competition for market [3, 4]. Under the current environment of international competition in satellite navigation market, the use of intellectual property strategy to win market competition has become an important means of international competition. The flexible application of patent protection strategy to seize market and technical resources is an important way for enterprises in the market competition, "grasp the opportunities, and win the initiative" [5–7].

Compared with some developed countries, setting up intellectual property system in our country is relatively late. Only in the last six years, the patents have systematic layout. Especially in overseas, the related patent layout is still not perfect. There is a big gap between China and developed countries [8–10]. The United States has already made extensive patent arrangements. They have great advantages in the number of patents, core technologies and applications. This makes our enterprises face the huge risk of patent infringement while expanding the international market, hinder the "going out" of our BeiDou products [11, 12].

This paper is mainly based on the status of China's high-precision application of BDS patent, conducted in-depth analysis to explore the strategic significance of the deployment of high-precision applications; thus in the future patent disputes, we have more bargaining chips in the occurrence of patent disputes. Then it is possible to achieve the cross-licensing with foreign industrial giants in the use of patents for protecting the development of the BDS globalization.

2 Research Method

The data in this paper mainly comes from the public collection of data in the patent retrieval and service system of the State Intellectual Property Office. In order to retrieve the data of all BeiDou high precision positioning related patents in China, we searched the key words of "BeiDou", "high precision", "differential positioning" and other key words. The application time was up to January 01, 2017. We filtered the wrong and repetitive data. We focused on the number, category, type, industry, region and other characteristics of the BeiDou high precision positioning application related patents. We directly explained the relevant conclusions by introducing a large number of chart survey data.

3 Main Content

By using the patent retrieval and service system, we can get the total number of applications. It is 474 till Jan. 1, 2017. As shown in Fig. 1, we can see that from 2012 onwards, the number of patents related to BeiDou high precision positioning application shows a rapid growth trend.

The BeiDou-2 system began offering services in 2012. The service area covers most of the Asia-Pacific region. During this period the number of patents related to BeiDou high precision positioning application is a bit less. It is also the germination period of the development of BeiDou high precision positioning in China. Since the first phase of the BeiDou satellite navigation system was completed in 2012, the application of BDS has been greatly developed in both military and civilian markets.

To develop the BeiDou application market, Ministry of Equipment Development has united with Ministry of Transport (MOT), Ministry of Public Security (MOPS), Meteorological Administration and some other departments of China, and GuangDong, ShangHai, BeiJing, HuNan, GuiZhou, ShanXi and other provinces and cities to carry out the BeiDou satellite navigation demonstration application. This has prompted applications of BDS.

From Fig. 1 we can see that, from 2014 to 2015, the number of patents related to BeiDou high precision positioning applications has increased rapidly. This is mainly due to the construction of Continuously Operating Reference Stations (CORS) in various areas such as Jiangsu, Zhejiang, HuBei, HuNan, QingHai, SiChuan, GuangDong and other provinces in recent years, on purpose to provide the high precision positioning service of BDS. Especially in 2014, China began to build the national BD-GBAS, which has nurtured the development of the BeiDou high precision positioning application industry. In 2016 and 2017, the number of related applications reached 304, which accounted for 82% of the total patent applications of BeiDou high precision positioning application in recent three years. This shows that the BeiDou high-precision application industry has entered a rapid

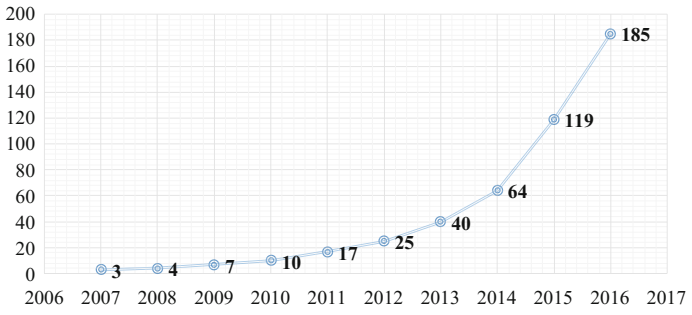

Fig. 1 The number of patents related to the BeiDou high precision positioning application

growth period. It also shows that the protection of intellectual property rights by domestic related enterprises and research institutes is increasing.

In terms of the total number of patent applications, the absolute number of high precision positioning related patent applications for the BeiDou is not much. This is mainly due to the fact that, most of the core technologies related to BeiDou high precision positioning are filed in the form of national defense patents. Since it forms a protective measure of important technical secrets, the patent data information is difficult to retrieve. Furthermore, the development of the related technology is mainly dependent on the development of BDS. The manufacture, production, launch, operation of BeiDou satellites and the construction of the BD-GBAS mainly dominated by the state. The main areas of enterprise participation are often limited to the application of terminal devices. Most of the patents they have applied are partial non-national defense patents. Therefore, the number of BeiDou high precision positioning application related patents was not much.

Figure 2 shows the number of patents, utility models and design patents related to the high precision positioning application from 2007 to the end of 2016. As can be seen from Fig. 2, the number of invention patents is higher than the number of the utility models. Prior to 2012, the number of both utility models and invention patents increased slowly. Since 2012, the number of both applications types has increased rapidly. In order to obtain more stable and long-term patent ownership, it is obvious that the application of the invention patent is the first choice. On the other hand, considering the shortcomings of the utility model patents such as the relatively short examination period, relatively low creativity, the low application fee and other advantages, BeiDou high precision industrial patent layout in the utility model should also be taken seriously.

Upon further analysis, it can be found that in the application data of utility model patents and invention patents, the case of applying for utility model and invention patent at the same time under the same applicant and the same name appears, so-called "One case, two applications". This is mainly because the patent for utility model acquired the right of first instance at the time of application but without any substantive examination. Comparing with invention patent, the patent right acquired by the utility model has lower patentability in terms of creativity, novelty and stability. "One case, two applications" can protect the patent applicant's product technical solutions with multiple levels and types of patents, and further

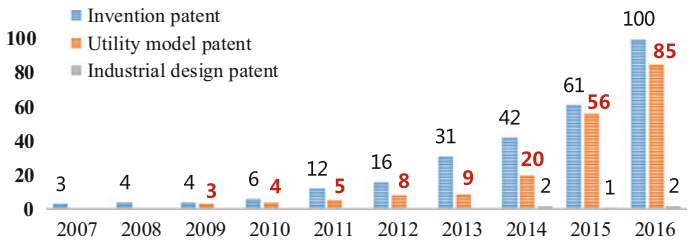

Fig. 2 The number of the patent for invention and the utility model patent

strengthen the insurance role of patent rights in stability. Although the application of utility model patent is easier to obtain the patent right, the patent does not have the same stability and authority as the invention patent, nor does it have a long time to effectively protect the invention patent.

In view of the above characteristics and current status of the two types of patents, China's enterprises, scientific research institutes and universities, should strengthen the long-term efficacy of patent protection. To achieve greater competitive advantage in the high precision satellite navigation technology, the quality and quantity of patent applications should be improved.

Figure 3 shows the situation of the top 18 applicant organizations (the number of applications for the same organization is more than 3), which have the patent applications related to BeiDou high precision positioning application. As can be seen from Fig. 3, the proportion of enterprises is higher than the proportion of scientific research institutes and universities. On the one hand, BeiDou high precision positioning technology has shifted from the theoretical stage to the market launch stage. More and more companies began to attach importance to the vast market brought by BeiDou high precision positioning application technology.

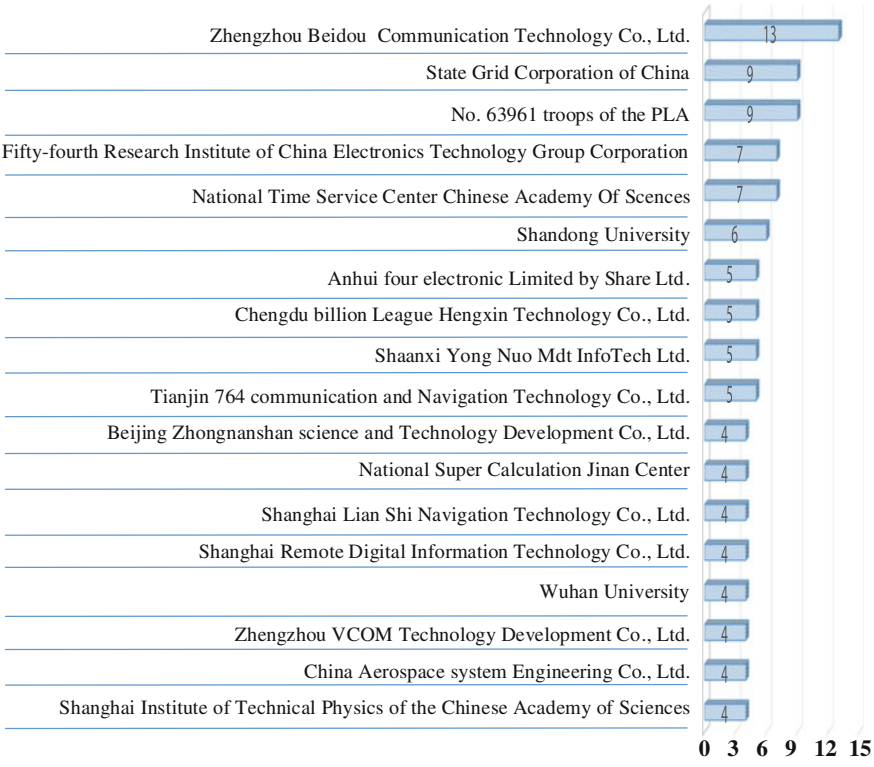

Fig. 3 The top 18 patent applicant organizations

On the other hand, it shows that scientific research institutes and universities pay less attention to intellectual property protection than enterprises. Because research institutes are more likely to publish in papers after obtaining scientific research results. Only a few choose to apply for patent protection to protect scientific achievements. This is also an important reason why scientific research institutes have fewer applications and authorized enterprises.

Enterprises become the main group of invention patent applications in BeiDou high precision positioning application field. This shows that the enterprises effort to increase research and innovation, the awareness of patent protection, the faster conversion of the scientific and technological achievements. It can be seen from Fig. 3 that the number of scientific research institutes and universities applying for high precision positioning related patents of the BeiDou is significant. The research and academic institutions in China have improved the research activity in the field of BeiDou satellite navigation technology in BeiDou, and the awareness of patent protection is increasing.

In recent years, scientific research institutes, universities and enterprises have been carrying out various research & development cooperation, giving full play to scientific research strength of institutes, colleges and universities, and to the strong market grasp ability of the enterprises. It realize the complementary advantages of enterprises and research institutions. Research institutes and universities vigorously implement the reform and innovation. Market-led, relying on national policies, they take a definite aim and make a comprehensive consideration in the core technology research. Most of their research results have been recognized by the market, which has played a certain pioneering role in the domestic BeiDou high precision satellite navigation industry.

In addition, from the proportion of the military applicants in Fig. 3, one can see that the development strategy of the national military and civilian integration in recent years has achieved good results.

Some military products have become civilianized. It embodies the overall advancement of military and civilian integration, accelerating the development, promoting the national economy development and the comprehensive national defense strength.

The military's absolute superiority in defense related technology is incomparable to other applicants. The BeiDou high precision positioning related technologies are gradually infiltrating into the civil market. Foreseeable, in the future they could be a dark horse that cannot be underestimated in the field of high precision satellite navigation applications.

Figure 4 shows the distribution of the provinces where the BeiDou high precision positioning application related patents are located. It can be seen from Fig. 4 that the research and development area of the high precision industry of BeiDou has traversed many provinces in China, from the southeast coast to the north China plain, and then to the Sichuan and Shaanxi region, and so on. Among them, Beijing, Shanghai, Guangdong, Shenzhen, Jiangsu, Hubei, Shandong, Shaanxi, Henan and Hebei accounted for nearly 76% of the applications. This shows that the economically and technically developed regions have played a crucial role in

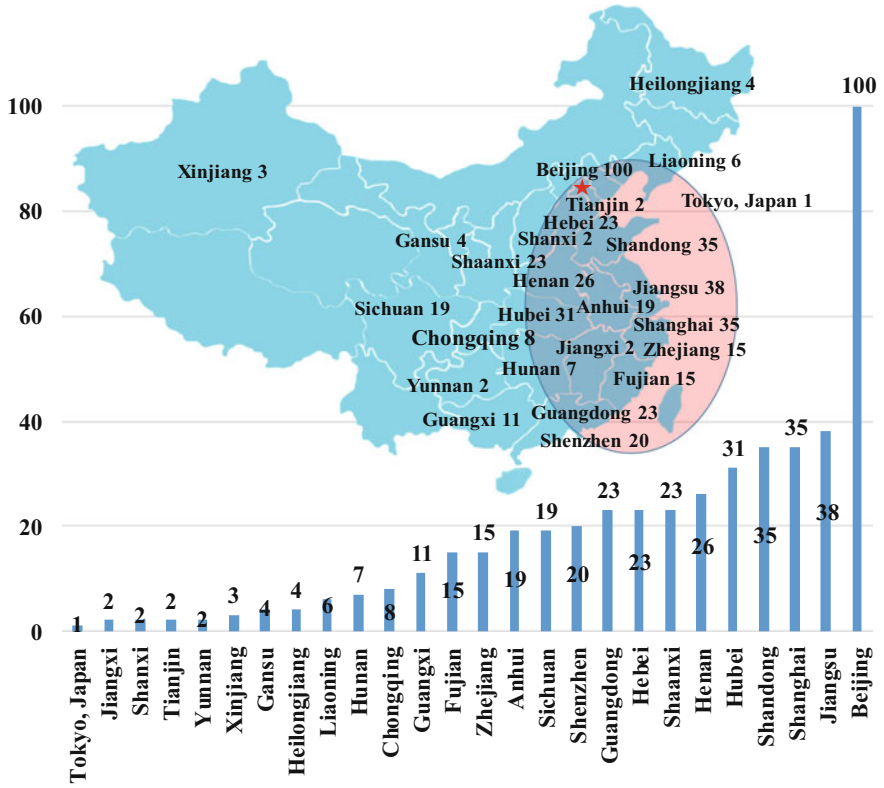

Fig. 4 Distribution of the applicant's location

promoting the development of the BeiDou high-precision industry. Beijing, the capital of China's political, military, scientific and cultural center, has the most authorized applications, followed by the Yangtze River Delta and the Pearl River Delta region. Because of the respective regional importance, Shaanxi, Shandong, Henan, Hebei, Hubei, and other provinces are also making great efforts to develop the BeiDou high precision positioning industry.

In addition, since 2012, Beijing, Shanghai, Guangdong and Jiangsu provinces have gradually formed the BeiDou Navigation Industry Alliance under the guidance of national policies and industrial development. With the strong support of local government and the relevant preferential policies, the BeiDou satellite navigation industry in these areas has reached a large-scale development. This is one of the reasons why the key enterprises and scientific research institutes in the field of satellite navigation are basically located in these provinces. In summary, besides Beijing, BeiDou high-precision satellite navigation related patents are mainly concentrated in the developed southeastern coastal areas of China. The number of patent applications in other provinces and cities is relatively less.

Figure 5 shows the distribution of high precision positioning industrial patent types and application fields in recent years. Among them, the amount of BeiDou high precision positioning service patents is far more than BeiDou high precision positioning algorithmic patents. The main reason is that the application of the positioning service patent is mainly involved in the most basic and relatively mature BDS navigation and positioning function. The positioning service related applications could put into operation and take effects quickly. However, the majority of algorithmic patent applications are about the optimization of baseband processing, differential positioning solution, timing accuracy and so on. They are more theoretical and the period of developing a stable and reliable algorithm product is relatively longer.

On the other hand, it can be seen from Fig. 5 that the main distribution fields of the high precision positioning application of BeiDou are timing/time keeping, algorithms, vehicle supervision, marine ships and deformation monitoring, etc. The applications of BeiDou high-precision application patent in mapping, geo-information, electric power, meteorology, communication, positioning and orientation are relatively few. Therefore, the patents that can be applied are relatively more.

By using the quantitative analysis method, this article has studied and analyzed the situation of BeiDou high precision positioning application related patents. We can see from the search data, with the government's policy support, special implementation and the emphasis on the satellite navigation market in recent years, the number of BeiDou high precision positioning application related patents is increasing year by year. However, under such rapid development situation, the quality of patent applications is not high and needs to be further promoted and

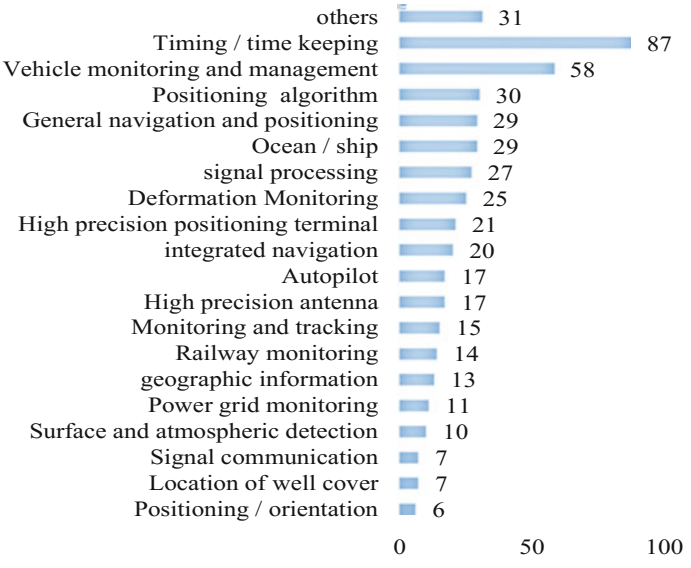

Fig. 5 Types and application fields

strengthened. The basis of the overall development of the satellite navigation industry needs to be strengthened. Exchanges and cooperation between enterprises and research institutes need to encourage, aiming at the key problem of which encountered in the development process of the related enterprises in the BeiDou high precision positioning application field. The integration of the dominant resources in the industry should be encouraged to carry out complementary advantages and optimization and to promote the maturity and development of the BeiDou high precision satellite navigation technology. In just a dozen years, the technology of the BeiDou satellite navigation and positioning is growing gradually and rapidly. Although there is still a certain gap between the BDS and other satellite navigation technologies, the BeiDou satellite navigation technology have more potential and space for development in the future, under the vigorous support of the national industrial policy, the unremitting breakthrough and innovation, tough tackling efforts by domestic enterprises and scientific research institutes.

4 Conclusions

Through the research on the application of BeiDou high precision satellite navigation intellectual property, it can be seen that nowadays, China has begun to pay attention to the high precision application related patents of BDS in the layout. Although the national BD-GBAS has not been fully completed, the related BeiDou high precision application intellectual property system has already completed the plan ahead of schedule, and some applications for intellectual property rights have been carried out.

Compared to the domestic situation, the overseas distribution of intellectual property of BeiDou satellite navigation is not yet mature. There is still a large layout space. This is a very good opportunity for BDS to go abroad and promote its application worldwide.

The government and relevant functional departments should promulgate as soon as possible the relevant policies, form overseas intellectual property alliance, establish a professional overseas intellectual property information platform, encourage and guide domestic enterprises and institutions to go abroad. The intellectual property rights layout of BDS in other countries should be immediately implemented, which would lay a solid foundation for the application of the high precision positioning of the BDS in foreign countries. And to circumvent the risk of intellectual property for domestic enterprises to expand overseas market of BDS and provide support for the implementation of new national strategies such as “the Belt and Road” and “interconnection and intercommunication”.

References

1. Liu C et al (2015) Research on the development of foreign satellite navigation application industry. Satell Appl 2:59–64
2. Yang T (2014) Industrial patent analysis report (volumes 20): satellite navigation terminal. Intellectual Property Publishing House, Beijing, p 514
3. Duan D et al (2013) Analysis of comparative advantage, intellectual property advantage and competitive advantage. China Inventions Pat 9:19–21
4. Zhou S et al (2015) Early warning and proposal for patent risk of Beidou satellite navigation system. Chinese Invention Pat 8:47–52
5. Fan C et al (2011) Research on intellectual property protection in international trade under the background of economic globalization. Dongbei University of Finance and Economics, p 64
6. Sun H et al (2009) Comparison and reference of intellectual property strategy in developed countries. J China Univ Polit Sci Law 6:133–136
7. Wu H et al (2015) The patent layout in the enterprise intellectual property strategy. Satell Netw Satell Navig Technol 12:60–63
8. Li D et al (2016) Literature retrieval and patent analysis of the satellite navigation industry development analysis. In: China satellite navigation conference based on 2016
9. Li F et al (2014) Analysis and reflection on the current status of China Beidou navigation chip technology patent. Electron Intellect Property Rights 9:91–95
10. Zhou L et al (2015) Analysis of the status of the patent industry of BeiDou satellite navigation industry and related suggestions. Chinese Invention Pat 9:44–48
11. Du L et al (2016) China enterprises “going out” of intellectual property rights should be “clear” and “fine” and “strong”. Chin Strateg Emerg Ind 9:74–76
12. Wang X et al (2014) Seize the historical opportunity to speed up the industrial patent layout of the dipper industry. China Patent Agent association of the annual meeting of intellectual property forum

Conception About Carrying Out Standardization of X-Ray Pulsar Navigation

Wei Jin, Ying Liu, Zhiheng Zhang, Xiaoxi Jin, Qiong Liu and Xiaochen Jin

Abstract X-Ray pulsar navigation is a new technology for astronavigation. It's an effective supplement to the satellite navigation which is widely used at present. It can provide autonomous navigation services for spacecraft that cannot be covered by satellite navigation system. China has started researching on engineering application since 2005, and sent specific satellites to carry out space experiments in 2016. Compared to theoretical research and engineering application, the standardization of X-Ray pulsar navigation is left behind. There are no relevant standards and top-level planning for X-Ray pulsar navigation in the standard systems at national level. Standardization is an important guarantee condition to ensure development of an industry and progress of a major project. The general departments take standardization as an important work in the major national projects, such as CMS, BeiDou, CHEOS and so on. As an important part of navigation project, the standardization of X-Ray pulsar navigation is to meet the needs of navigation engineering construction, and is an effective way to implement the requirements of navigation standardization. This paper explains how to carry out standardization by combining the technical characteristics and development status of X-Ray pulsar navigation.

Keywords X-Ray pulsar navigation · Standard · Standard internationalization

W. Jin (✉) · Z. Zhang · X. Jin
Beijing Satellite Navigation Center, Beijing 100094, China
e-mail: jinwei13370156609@163.com

Y. Liu
Beijing Institute of Tracking and Telecommunication Technology, Beijing 10094, China

Q. Liu · X. Jin
Beijing Institute of Space Science and Technology Information, Beijing 10094, China

J. Sun et al. (eds.), *China Satellite Navigation Conference (CSNC) 2018 Proceedings*, Lecture Notes in Electrical Engineering 498,
https://doi.org/10.1007/978-981-13-0014-1_62

1 Introduction

At present, there are many methods of achieving navigation, such as traditional astronomical navigation, satellite navigation, inertial navigation, geomagnetic navigation, and so on. However, most of these methods require the support of ground stations and cannot achieve true spacecraft autonomous navigation. As the natural clock, the pulsar is much more stable in the long-term than the existing time-frequency systems and does not require human maintenance. By using X-ray photons radiated by pulsars, spacecraft autonomous navigation achieved by estimating the arrival time of X-ray signal of 3–4 pulsars simultaneously has become the most likely breakthrough of deep space autonomous navigation technology in the future [1]. X-ray pulsar navigation (also referred as "pulsar navigation") is a new type of astronomical navigation technology, which is an effective supplement to the current satellite navigation technology. It can be used to provide autonomous navigation and positioning services for high-altitude orbit spacecraft and deep-space explorations which cannot be covered by the satellite navigation systems. Pulsar navigation has characteristics of being independent from ground operation, wide range of application, high precision, strong autonomy, simple structure, excellent reliability and so on. It is the most suitable navigation method for human being to go to deep space and achieve interstellar travel. Pulsar navigation would be widely used in the future [1].

Pulsar navigation research was started from "autonomous navigation based on X-ray source verification" program, proposed by the US Defense Advanced Research Projects Agency in 2004. China has also started research of engineering application of pulsar navigation and has developed various types of detectors since 2005. A special test satellite was successfully launched in 2016 for space experiments. Compared to theoretical research and engineering application, the standardization of X-Ray pulsar navigation is relatively left behind. There are no relevant standards and top-level planning for X-Ray pulsar navigation in the standard systems at national level. Standardization is an important guarantee condition to ensure development of an industry and progress of a major project. The general departments take standardization as an important work in the major national projects, such as CMS, BeiDou, CHEOS and so on. Pulsar navigation is an important part of navigation project. Pulsar navigation standardization is conducted to meet the needs of navigation engineering construction, and is also an effective way to implement navigation standardization requirements. This paper would make suggestions about carrying out standard work in this area in the light of the technical characteristics and development status of pulsar navigation.

2 Analysis of Standard Demands

The realization process of pulsar navigation is very complicated, as shown in Fig. 1. First of all, detect the X-ray photons radiated by a specific X-ray pulsar using a pulsar navigation detector mounted on the spacecraft. The X-ray photons contain pulse information and angular position information corresponding to the X-ray pulsar. For the pulse information, the arrival time of the detected X-ray photons is marked by the spaceborne atomic clock, and then correct the photon arrival time considering the solar system planet parameter database and the pulsar navigation database and extract the pulse profile to obtain the pulse arrival time. For the angular position information, the angular position of the corresponding pulsar in the spacecraft's coordinate system is obtained. Based on the angular position of the corresponding pulsar recorded in the reference frame of the centroid of the solar system in the pulsar database, the coordinate system is used to obtain the corresponding angular position information pulsar angular position in the inertial coordinate system. Finally, the spaceborne navigation algorithm is used to solve the measured data of multiple X-ray pulsars to calculate the navigation parameters such as the position, speed, time and attitude of the spacecraft so as to realize autonomous navigation. It can be seen from the entire implementation process of pulsar navigation that X-ray photon detection, pulsar navigation database determination and pulsar navigation data processing are the most important steps. The following would discuss pulsar navigation detector development, establishment of pulsar navigation database and algorithm of X-ray pulsar navigation.

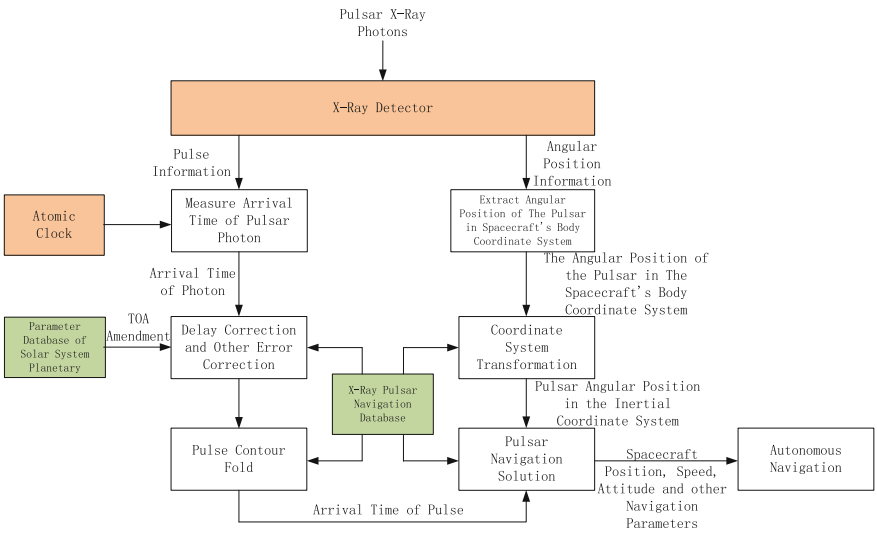

Fig. 1 Implementation process of pulsar navigation

2.1 Development of X-Ray Pulsar Navigation Detector

X-ray pulsar navigation detector (also referred as "navigation detector") used for X-ray photon detection, is the key equipment to achieve pulsar navigation. Only when the sensitivity of the navigation detector could meet certain requirements, valid data could be obtained and autonomous navigation could be achieved. After many years of accumulation, the level of development of navigation detectors in China is close to the top level in the world. The technical requirements of navigation detectors in terms of performance indicators, external interfaces, environmental adaptability and reliability have been well defined and have conditions for standardization. It is necessary to make standards for these indicators and propose specific requirements for these indicators. This not only consolidates and consolidates the existing research and development experience, but also sets necessary barriers for entering the entire industry, which is important to regulate the development of the entire industry.

Ground calibration and testing is an important part of the development process of navigation detector. It is not only verification of product performance, but also feedback of product design improvement, which runs through the entire development process of the navigation probe [2]. Ground calibration is the evidence for signal interpretation in the photoelectric conversion process through establishment of the corresponding relationship between energy of X-ray photon and output voltage signal amplitude of navigation detector. Ground test is mainly about testing whether view, energy resolution, detection efficiency, time resolution, response time and other technical indicators of navigation detector would meet the mission requirements. For ground calibration and testing, the choice of method directly determines the accuracy of calibration and test and plays a crucial role in calibration and test results. The unification of calibration and test methods is the basis for scientifically evaluating the performance of navigation detectors. It is necessary to unify and regulate calibration and test methods through making standards.

The ground test system is used to verify the function of the navigation detector and to calibrate and test the performance index. The ground test system is important infrastructure for the development of navigation detectors [3]. The ground test system is a large-scale integrated test platform including several functional modules such as space environment simulation, X-ray simulation, X-ray calibration, attitude adjustment and control, satellite platform simulation and pulsar navigation solution. The fifth institute of China Aerospace Science and Technology Corporation has constructed the most advanced and complete ground test system in China and provides free ground calibration and test services of navigation detectors to all domestic manufacturers.

In order to facilitate manufacturers to use the ground test system, it is necessary to develop standards about the ground test system functions, performance and navigation probe interface provided technical requirements to effectively guide manufacturers to conduct interface design and test program of navigation detectors. As the technical specifications of the ground test system will change over time,

periodic calibration should be conducted to ensure calibration and test of accuracy ground test system. In order to ensure the authority of the test accuracy of the ground test system, it is necessary to formulate standards to regulate the calibration items, calibration methods, time interval of re-calibration, etc., to effectively guide the calibration of the ground test system. In addition, installation interfaces of navigation detectors of different manufacturers are not exactly the same, it is necessary to achieve interface matching through tooling. The installation of navigation detectors in the ground test system is more complicated, including assembly, alignment, unloading and other stages, each stage has corresponding operational requirements, precautions, key record links and so on. In order to ensure that the installation accuracy of navigation detectors could meet the calibration and test requirements, standards need to be established for standardizing the installation operation.

2.2 Establishment of X-Ray Pulsar Navigation Database

The establishment of X-ray pulsar navigation database (also referred as "navigation database") belongs to the basic research work of pulsar navigation. The basic physical characteristics of X-ray pulsar need to be obtained through analysis and processing of long-term accumulated astronomical observation data. Pulse profile of signal-to-noise ratio, timing model of high precision, position of pulsar horn and preferred navigation pulsar. At the same time, it is necessary to organize and catalog these important data to form navigation database [4].

More than 1000 X-ray pulsars has been observed. Not every X-ray pulsar is suitable for navigation because of X-ray photon signal intensity and pulse period stability [5]. Therefore, time and energy are needed to invest in targeted observations and create the navigation database of chosen X-ray pulsars for maximum benefit. The workload of establishing a navigation database is very large. It is a process of gradual accumulation and continuous improvement. It requires a great deal of manpower, material and financial resources. It could only be completed through efforts from all parties rather than one single institute. In order to facilitate the collection of observation data of all parties, it is necessary to formulate standards for attributes of X-ray pulsar, what kind of metadata is described by these attributes, and what kind of data format are included in the navigation database. In addition, the unification of navigation database format and content also facilitates resource sharing, and facilitates all parties to make full use of the navigation database to solve the detected data. This is important to improving the development efficiency of related products and popularizing the application of pulsar navigation.

2.3 Algorithm of X-Ray Pulsar Navigation

X-ray pulsar navigation solution includes selecting the target pulsar according to the orbit of the spacecraft, using the detected X-ray photon signal to calculate the pulse arrival time and the angular position coordinates of the target pulsar, and comparing the measured data with the model data Calculate the spacecraft position, velocity, attitude and other navigation parameters, the use of navigation parameters for autonomous navigation path planning and other aspects of data processing [6, 7]. X-ray pulsar navigation algorithm (also referred as "navigation algorithm") is a concrete realization of the pulsar navigation solution function, and it is connected with the navigation probe, navigation database and other functional modules, which is important to achieve the function of pulsar navigation. The design of navigation algorithm is complicated, and it needs to consider the specific application scenarios, the physical characteristics of the target pulsar, the detection efficiency of the navigation detector, the processing capability of the spacecraft and so on. At present, the theoretical research of navigation algorithm is very developed, but it has not been verified by engineering due to lacking of measuring data. With the on-orbit application of subsequent pulsar navigation test satellites, the measured data is continuously enriched, and the algorithm for solving the problem will be continuously improved. For navigation solution algorithm, the specific realization of the manufacturers of research and development capabilities, are the core secrets of various manufacturers, do not have the conditions for standardization. However, the function of the algorithm to be solved and the effect to be achieved, the format of the input and output data need to be consistent. It is necessary to formulate standards to guide the development of related software products and hardware products.

3 Analysis of Standard Internationalization

In the field of satellite navigation, there are important international standards including ICD files released by service providers such as GPS and BeiDou, terminal data format standards promulgated by application associations such as NMEA, RTCM, RTCA, and IAG, and published by international application organizations such as ICAO, IMO and 3GPP Industry standards and so on. These international standards are the basis for interoperability between satellite navigation systems and user terminals, and also the basis for the development of related products. These standards play a crucial role in promoting and standardizing the development of the entire satellite navigation industry. Although it started late, China has also been devoted to the standardization of BeiDou Navigation System Internationalization and has made major breakthroughs in recent years. The Shipborne BDs Receiver Equipment Performance Standard was approved by IMO in 2014 and achieved a breakthrough of zero of Beidou International Standard. In addition, BeiDou System also passed IMO recognition and became the third global satellite navigation after

GPS and GLONASS system. The success of standard internationalization has played a crucial role in the promotion and application of BeiDou navigation system in the world. Compared with satellite navigation, pulsar navigation is still an emerging field, and would play an important role in the exploration of the vast universe by mankind in the future. After many inquiries and searches, various international standards organizations and industry bodies have not standardized their work in the field of pulsar navigation. At this time, the study on standardizing internationalization has made groundbreaking achievements. It reflects the historical responsibility and social responsibility of a major country to all mankind. In terms of engineering research on pulsar navigation, China is currently in the leading position in the world and possesses the technical conditions for the standardization of international standards in this field. At the same time, with the enhancement of China's overall national strength and improvement of its international status, China also needs to improve its soft power and international influence by leading the formulation of relevant international standards so as to complete the transition from a big country to a strong country in aerospace field.

The standard internationalization of pulsar navigation is a comprehensive, general, long-term and continuous work. It needs a comprehensive professional team to carry out special research to systematically demonstrate the standard internationalization of pulsar navigation.

Pulsar navigation is not yet put into practical application at present, it is not necessary to carry out standard internationalization. It is necessary to study necessity and feasibility of the internationalization of pulsar navigation standards from the perspective of long-term national interests and the significance of space development.

Pulsar navigation is a comprehensive area with many standardization requirements in many aspects. However, not every area is suitable for developing international standards. It is necessary to study from the technical characteristics and application fields of pulsar navigation areas to establish international standards.

The future of pulsar navigation will mainly be used in the areas such as deep space exploration. The corresponding international standardization organizations and agencies have great differences in the fields of navigation and satellite navigation. It is also necessary to study the business scope of the International Organization for Standardization (ISO) and agencies and find relevant international standardization organizations and agencies to join in and try their best to take important roles. China can also take the lead in setting up an international standardization organization or agency to lead the development of international standards in the entire pulsar navigation field.

4 Summary

With the rapid development of pulsar navigation technology and further application of engineering, standards as an example of technical regulations will play an increasingly important role. From the perspective of overall engineering, on the one hand, this paper analyzes requirements of the standard of pulsar navigation, puts forward the main directions of future standards development and the problems need to be considered, and on the other hand, the requirements of standard internationalization in the field of pulsar navigation are analyzed, puts forward some suggestions on how to carry out standard internationalization in this field according to the experience of Beidou in the standard internationalization process. Standardization of pulsar navigation in the field on the one hand could build the industry entry barriers and make requirements of acceptance of unified products to regulate the development of the entire industry through establishment of standards, the other hand, the product development cycle could be shortened through standardizing the interfaces of different products, enabling companies put more money and energy on technological innovation. At present, the condition and timing for formulating the standard of pulsar navigation are mature. The standards development work should be carried out by the related research developments and the application department base on the overall project organization. The publicity should be organized in time, so that everyone can understand the standards and apply the standards in the work. Carrying out the research of standard internationalization in the field of pulsar navigation can further enhance Chinese international influence in this field, especially in the early stage of engineering development, Chinese related technologies and products could be promoted simultaneously through advanced layout and formulation of international standards, and then lead the future of international cooperation in this field. Standard internationalization need to consider many objective factors. The overall project should start related work as soon as possible, and arrange a special person responsible for the standard internationalization of pulsar navigation matters. The standardization in the field of pulsar navigation is a complicated systematic project, which needs to consider actual situation of model development, the demand of international cooperation and the trend of technological development. At the same time, the planning and formulation of related standards are also a process with gradual improvement. The standard system needs to be revised and optimized with the occurrence of new technology, new products and new needs. The suggestions in this paper can be used as a reference for China to carry out standardization of pulsar navigation in the future.

References

1. Shuai P, Li M, Chen S et al (2009) X-ray pulsar navigation system principles and methods. China Aerospace Press, Beijing
2. Sheng LZ, Zhao B, Zhou F et al (2013) X-ray pulsar navigation detector performance. Phys J 42(9)
3. Hu H, Zhao B, Sheng L et al (2011) Ground simulation system based on X-ray pulsar navigation. Phys J 60(2)
4. Huan L, Shuai P, Lin Q, Zhang X (2015) X-ray pulsar navigation nominal database construction. Chin Space Sci Technol 32(3)
5. Xue S, Zhang K, Lv M (2014) Visibility of X-ray pulsar navigation in interplanetary exploration [J]. Photoelectric Eng 41(9)
6. Chu Y, Wang Y, Huang X (2011) Selection method of optimal combination about pulsar navigation. Chinese Space Sci Technol 31(5)
7. Wang P, Zhao B, Sheng L et al (2012) Research of accuracy of X-ray pulsar navigation system. Phys J 61(20)

China's Satellite Navigation Policy: Status Quo, Problems and Solutions

Wenbo Chen and Yuanyuan Jiang

Abstract To date, the United States, Russia and the European Union have promulgated or amended legislations, presidential decrees, administrative regulations and directives concerning the issue of satellite navigation, forming a relatively comprehensive administrative and legislative system. By delineating the executive missions, operation mechanisms and procedures for the satellite navigation sectors in the respective states, such system has laid a solid foundation and provided legal guarantees for the development of their satellite navigation systems. In China, there have already been some national, state-departmental and provincial policies and regulations of similar targets, such as *National Satellite Navigation Industry Mid-term and Long-term Development Plan*; however, insufficiencies in the legislative and administrative system of China's satellite navigation development still exist, namely, a lack of top-level laws or regulations, arbitrariness in policies, uneven organization of the policy structure, and imbalance of policy subjects. By applying the approach of quantitative research, this article conducts a systematical summary and analysis of the regulations, laws, and political documents concerning satellite navigation in China and to explore the transformation process and diffusion of the policies, as well as the relationship between the authorities involved. In so doing, it aims at figuring out the kernel problems of the political and legislative system of the current satellite navigation in China and putting forward corresponding solutions to them, including the need for an improved system with timely top-level policies, the need for the promotion of industrial development and optimization of the policy structure, and the need for a coordinated relationship between policy subjects and a guarantee for the implementation of policies.

Keywords Satellite navigation · Policy · Status quo · Problems Solutions

W. Chen (✉)
Beihang University, Beijing 100191, China
e-mail: wenbo.chen@buaa.edu.cn

W. Chen · Y. Jiang
School of Public Administration, Beihang University, Beijing 100191, China

J. Sun et al. (eds.), *China Satellite Navigation Conference (CSNC) 2018 Proceedings*, Lecture Notes in Electrical Engineering 498,
https://doi.org/10.1007/978-981-13-0014-1_63

1 Introduction

With successful launch of the two Beidou-3 satellites on November 5, 2017, the Beidou navigation system (BDS) has embarked on its global networking. It is proceeding towards the target that "18 satellites will be launched around 2018, and the BDS is to provide the countries in the 'Belt and Road initiative' with basic satellite navigation service; the global networking of 35 Beidou satellites will be completed, and the BDS will be capable of serving the entire world by 2020." This target is paving the way for the BDS towards a global satellite navigation system. In the field of global navigation satellite system (GNSS), in order to ensure a service of constant and uninterrupted stability, countries around the world have been making persevering efforts to promote the development of the GNSS by making policies—an essential component of the construction of the GNSS industry. Such policies have been penetrated in almost all aspects of satellite navigation, and play a significant role in assuring and guiding technological innovation and industrial development. Meanwhile, the characteristics of hi-tech, high-security request and civil-military integration of the GNSS demands the feasibility and adaptability to the uniqueness in the policy-making process, thus imposes a more demanding requirement on the establishment of its policy system.

2 Theoretical Review and Research Perspective

Since the strategic construction of the BDS, governments at all levels in China have issued corresponding policies along with the research and development of the GNSS technology, in the hope of safeguarding and promoting its continual development. Therefore, GNSS policies have been an issue of common concern in recent years. The research on GNSS policies generally fall into the three categories as follows:

2.1 Comparative Study of the GNSS Policy Systems in Countries Other Than China

This kind of research focuses on the analysis and interpretation of the GNSS management systems, strategic planning and policies in the United States, Russia and Europe [1–3]. Among them, studies of the American GPS policy system are the most thorough and profound. On the one hand, scholars analyze the background, specific content and influence of the relevant policies of the GPS from the perspective of historical development [4]. On the other hand, scholars induce and analyze the design of administrative institutions, policy system structure and the operation of the GPS policy system [5, 46–49]. Generally speaking, there are two

models of satellite navigation policy system for China to refer to: one is the comprehensive basic law-oriented model represented by Russia, and the other is the decentralized policy guidance model represented by the United States.

2.2 Research on the Policies of the GNSS Industry

As the BDS is still under construction and promotion, it faces the challenges from both domestic industry and international competition. Given such context, a complete and feasible policy system is in urgent demand for the further development of the BDS industry and the realization of the industrial cluster advantage. Upon this, researchers have proposed corresponding solutions of industrial policy. For instance, a policy system in accordance with the principles of government dominance, adaptation to the market economy system, [6] and a combination of compulsory application and voluntary application is needed; [7] an appropriate and effective allocation of the resources of the BDS industry to make up the market defects and industrial degeneration is in urgent demand through the construction of policy system [5, 46–49]. Thus, taking industry promoting policy as the approach and gradually constructing a comprehensive policy system is the essence for the construction of the BDS.

2.3 Research on the Construction of China's BDS Policy System

As a new high-tech field, the BDS has the urgent need of institutionalization and standardization. Therefore, scholars emphasize the great importance of the construction of a complete BDS policy system. Meanwhile, they expect to build a policy system which can make the BDS provide better services constantly. The current policy environment has been vigorously advancing the military-civilian integration. Under this circumstance, the focus of fundamental objectives of the BDS policy ought to be laid on safeguarding national security in military terms, ensuring the openness of satellite navigation services and promoting related industries in civilian terms. However, there are problems on the subject of the BDS policy in China, such as the ambiguity and intersection of duties, rights and obligations in the authorities involved, and ambiguous policy goal, unclear problem boundary, and weak policy enforceability in the policy-making process [8]. Therefore, the governments at all levels should cope with these problems when making the BDS policies, and adopt proper combination of policy tools, [9] including financial and taxation policies, goal programming, government procurement, statutory regulation and so on. In addition, the policy, as a kind of guiding administrative measures, should also take the coordination of interest relations into

consideration. In the field of the BDS, three major groups of relations are to be dealt with through the establishment of policy system: the relationship between system construction and application, the relationship between military and civil application and the relationship between market mechanism and government regulations.

On the basis of theoretical review above, this research aims to conduct an empirical exploration of the development status and characteristics of China's satellite navigation policies and provide an analysis of the existing problems of the policy system with a quantitative analysis of the BDS policies in China, and propose practical and feasible countermeasures correspondingly.

3 Quantitative Analysis of China's Satellite Navigation Policies

Derived from the *Government Literature Information System of Tsinghua University*, the data of this research cover comprehensively all the political documents containing the key words of "satellite navigation" promulgated by the government of all levels in China as of December, 2017. Among them, 909 political documents are selected as object of the quantitative study. Analyses are made upon the relevant information extracted from these policy documents including document titles, promulgation dates, sources, etc.

Through screening analysis, there are 31 documents whose titles clearly contain "navigation" or "satellite navigation," accounting for merely 3.4% of the samples selected. Such result indicates that there are few policies specifically aimed at satellite navigation. Moreover, among the 31 policies, most of them were introduced by the state ministries and departments, while only 6 pieces were promulgated by the provincial governments, such as Hunan,Hubei, Henan, Jiangsu, Guangdong Provinces, accounting for only 16% of the provincial administrative regions (Hong Kong, Macao and Taiwan excluded). In addition, it is demonstrated that 83.3% of the documents were promulgated in 2015 (see Table 1). In terms of the contents of the policies, the major focuses are laid on the applicative industry development of the satellite navigation technology.

The Ministry of Transport and the Civil Aviation Administration of China (CAAC) were involved in the design of 13 policies, which accounts for 52% of the 25 satellite navigation policies promulgated by the central ministries and commissions of China. Only two documents were co-issued by the central ministries, i.e., *Instructions from the Ministry of Transport and the General Administration of Quality Supervision, Inspection and Quarantine of P.R.C. (AQSIQ) on Improving the Quality of Satellite Navigation Products and Services in the Transport Industry* and *Announcement from the General Administration of Quality Supervision, Inspection and Quarantine of P.R.C. (AQSIQ) and Certification and Accreditation Administration of P.R.C. (CNCA) on the Establishment of National Satellite Navigation and Positioning Service Product Quality Supervision and Inspection*

Table 1 The satellite navigation policy documents promulgated by provincial governments in China

Province	Title of the document	Time
Guangdong	Guidelines from the General Office of People's Government of Guangdong Province for the Development of Satellite Navigation Application Industry	2008
Henan	Announcement from the General Office of People's Government of Henan Province on the Action Plan for the Three-Year Development of Beidou Navigation Industry in Henan Province (2016–2018)	2015
Hubei	Instructions from the General Office of People's Government of Hubei Province for the Development of Satellite Navigation Application Industry	2015
Hunan	Announcement from the Office of the Department of Land and Resources of Hunan Province on Accelerating the Construction and Application of Public Service Platform of Satellite Navigation and Positioning	2015
Changsha, Hunan	Instructions from Changsha Municipal Government on Promoting Beidou Navigation Application Industry	2015
Jiangsu	Reply from the Department of Information Industry of Jiangsu Province on Adjusting the Executives of Development and Industrialization Project of Satellite Navigation Positioning Terminal and Software Platform	2015

Center (Shanghai). However, major industry associations in satellite navigation—the GNSS&LBS Association of China (GLAC) introduced only one policy, which is directly related to satellite navigation, accounting for only 4% of the total (see Table 2).

The analysis of the 909 policy documents (see Table 3 and Fig. 1) reveals the trend of fluctuations in growth over time, which can roughly be divided into three phases: the first phase spans from 1987 to 2006, during which period governments at all levels promulgated few policies concerning satellite navigation, accounting for only 3.19% of the total. China officially embarked on the construction of the BDS with global navigation capability in 2004, which is accountable for the peaking of policies for the first time. The second phase ranges from 2006 to 2012, when the central and local authorities began to pay attention to satellite navigation policies, so the number of policies rose steadily. In particular, the application of the BDS has gradually been carried out in the fields of precision agriculture, ocean-going fishing and geographical mapping since 2006. Various departments and regions have been actively involved in the promulgation of application promotion and implementation plan of satellite navigation, so that the overall number of policies in this phase gradually increased and the coverage was expanded. The third phase started from 2012, with the number of policies in this period growing rapidly, and finally climaxing in 2016. As the BDS has formally provided free positioning, navigation and timing services to the Asia-Pacific region since 2012, governments at all levels and the authorities involved began to consciously and gradually formulate the relevant supporting policies of satellite navigation.

Table 2 The political documents of "satellite navigation" promulgated by the central ministries and commissions of China

Individual promulgation source			Promulgation source (including co-promulgation sources)		
Agency	Quantity	Proportion (%)	Agency	Quantity	Proportion (%)
CAAC	6	24	Ministry of Transport of P.R.C	7	28
Ministry of Transport of P. R.C	6	24	CAAC	6	24
NASG	3	12	NASG	3	12
CNCA	2	8	CNCA	3	12
NDRC	1	4	AQSIQ	3	12
AQSIQ	1	4	NDRC	1	4
Ministry of Science and Technology of P.R.C	1	4	Ministry of Science and Technology of P.R.C	1	4
Ministry of Civil Affairs of P.R.C	1	4	Ministry of Civil Affairs of P.R.C	1	4
PBC	1	4	PBC	1	4
GLAC	1	4	GLAC	1	4

Particularly, in April 2016, the general office of the State Council officially put the *Regulation of the People's Republic of China on Satellite Navigation* into the legislative plan. With the initiation of the specific legislation on satellite navigation and the need of The Belt and Road Initiative, the expansion of the number of the satellite navigation policies and the improvement of the policy system would be essential.

From the perspective of the central-local relationship, among the 909 political documents, the number of policies promulgated by the local governments is 606, exactly twice the number of policies made by the central government. In addition, the trend of the changing in the number of the local policies goes roughly in line with the one made by central government. But in terms of promulgation date, the local policies lag behind the ones made by the central government. This also reflects the central-to-local direction of policy diffusion of satellite navigation, instead of the bottom-up approach in the "policy pilot mode." In this way, some principal policies shall firstly be formulated at the central level, and then the local governments will promulgate specific and executable policies in accordance with the local characteristics. This phenomenon shows that critical significance of the guidance of top-level policies.

It also can be found that the number of political documents concerning satellite navigation is distributed unevenly in the 31 provinces, autonomous regions and

Table 3 Time distribution of satellite navigation policy documents

Year	State Council	Central ministries and commissions	Provinces	Cities	Total	Proportion (%)
1987	0	1	0	0	1	0.11
1994	0	1	0	0	1	0.11
1997	0	1	0	1	2	0.22
1998	0	0	1	0	1	0.11
1999	0	2	0	0	2	0.22
2001	0	4	0	0	4	0.44
2002	1	4	0	0	5	0.55
2003	0	0	1	0	1	0.11
2004	0	3	2	2	7	0.77
2005	0	1	2	2	5	0.55
2006	0	6	6	0	12	1.32
2007	2	8	5	3	18	1.98
2008	0	12	7	7	26	2.86
2009	0	13	9	6	28	3.08
2010	0	7	10	6	23	2.53
2011	2	16	13	8	39	4.30
2012	2	31	13	14	60	6.61
2013	1	33	16	12	62	6.83
2014	2	31	33	21	87	9.47
2015	0	39	63	23	125	13.77
2016	0	51	129	90	270	29.74
2017	0	29	54	47	130	14.32
Total	10	293	364	242	909	100

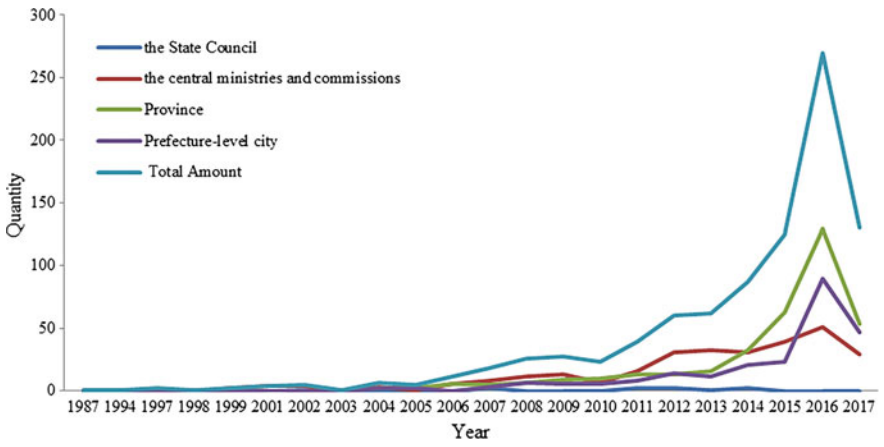

Fig. 1 Annual distribution of satellite navigation policy documents

municipalities. The number of policies introduced by Hebei, Guangdong, Jiangsu, Shanghai, Zhejiang Provinces is 223, accounting for 36.81% of the total (see Table 4). Meanwhile, the number of policies introduced by Tibet Autonomous Region, Tianjin Municipality, Yunnan Province, Xinjiang Uygur Autonomous Region, and Qinghai Province is 20, accounting for only 3.31%. The proportion of policies made in east China is 33.2%, while those of the northeast and southwest regions account for 6.61 and 7.11% respectively (see Table 5). Such results indicate that compared with less developed areas, the more developed regions have exerted greater effort on satellite navigation policies. In general, the political documents appear to be more in the east than those in the west and more in the coastal region than those in the inland.

In the 303 policies promulgated at the central level, as is shown in Table 6, the total number of the policies promulgated by the State Council is 10, accounting for 3.3%. This indicates that the top-level institutional design of satellite navigation policies is vacant. The National Administration of Surveying, Mapping and Geo-information and the Ministry of Transport promulgated the largest number of policies, making up more than one-third of the total of satellite navigation policies at the central level. On the one hand, it represents that the departments of transportation, surveying and mapping are the major users of satellite navigation services; on the other hand, it implies that the demand for administrative management of surveying, mapping and transportation departments has increased significantly with the opening of the free access to satellite positioning, navigation and timing services. However, it is notable that there is only 1 policy promulgated by the GLAC, demonstrating that industry associations play a rather limited role in the field of satellite navigation. At the central level, departments and sectors have consecutively promulgated instructional policies and documents in the industry of satellite navigation. This being considered, there are still prominent problems of absence of subjectivity and inappropriate administration. For instance, as regards the standardization of satellite navigation, the current authorities involved include Ministry of Transportation, Ministry of Industry and Information Technology, National Administration of Surveying, Mapping and Geo-information, Standardization Ministry, National Bureau of Quality Inspection, and State Administration of Work Safety. Such multi-authority situation may not only lead to the repetition of policy promulgation and redundancy of administrative resources, but also engender problems such as the inaction and unaccountability in the governmental sectors due to the limbo in the administrative functions.

As it shown in Table 7, there are 22 types of political documents involved, but 62.16% of them are announcements. Among them, departmental instructions rank the second, accounting for 22.11% of all the political documents. This indicates that there is a lack of scientific and reasonable design and standard in the institutional construction of satellite navigation. Government agencies tend to be arbitrary in the promulgation of policies. In addition, there are a large number of government internal working documents in the announcement category, such as the *Announcement of the Certification and Accreditation Administration of the P.R.C. on Authorization of National Satellite Navigation and Positioning Service Product*

Table 4 The location distribution of satellite navigation policy documents

Administrative region	Total	The number of documents in city	The ratio of the number of documents in city (%)	Proportion (%)	Administrative region	Total	The number of documents in city	The ratio of the number of documents in city (%)	Proportion (%)
Hebei	63	33	52.38	10.40	Sichuan	18	6	33.33	2.97
Guangdong	48	33	68.75	7.92	Guangxi Zhuang Autonomous Region	16	7	43.75	2.64
Jiangsu	41	29	70.73	6.77	Hainan	16	0	0.00	2.64
Shanghai	39	–	–	6.44	Anhui	13	5	38.46	2.15
Zhenjiang	32	22	68.75	5.28	Gansu	12	1	8.33	1.98
Shaanxi	31	10	32.26	5.12	Jilin	12	4	33.33	1.98
Fujian	30	14	46.67	4.95	Guizhou	11	3	27.27	1.82
Henan	27	18	66.67	4.46	Ningxia Hui Autonomous Region	9	1	11.11	1.49
Jiangxi	25	12	48.00	4.13	Chongqing	9	–	–	1.49
Hubei	22	5	22.73	3.63	Heilongjiang	7	1	14.29	1.16
Beijing	21	–	–	3.47	Inner Mongolia Autonomous Region	6	1	16.67	0.99
Liaoning	21	10	47.62	3.47	Qinghai	6	1	16.67	0.99
Shandong	20	11	55.00	3.30	Xinjiang Uygur Autonomous Region	5	1	20.00	0.83
Hunan	19	7	36.84	3.14	Yunnan	5	1	20.00	0.83
Shanxi	18	6	33.33	2.97	Tianjin	4	–	–	0.66

Table 5 Geographical distribution of satellite navigation policy documents

Region	Proportion (%)
East China (Zhejiang, Shanghai, Anhui, Fujian, Jiangxi, Shandong, Jiangsu)	33.2
South China (Henan, Hubei, Hunan, Guangdong, Guangxi, Hainan)	24.43
North China (Beijing, Tianjin, Hebei, Shanxi, Inner Mongolia)	18.49
Northwest (Shanxi, Gansu, Ningxia, Qinghai, Xinjiang)	10.41
Southwest (Chongqing, Sichuan, Guizhou, Yunnan, Tibet)	7.11
Northeast (Liaoning, Jilin, Heilongjiang)	6.61

Table 6 Top 10 policy-making central ministries and commissions

Department	Quantity
National Administration of Surveying, Mapping and Geo-information	60
Ministry of Transport	47
National Development and Reform Commission	16
Ministry of Industry and Information Technology	14
National Bureau of Quality Inspection	14
Ministry of Science and Technology of P.R.C	12
National Standards Commission	9
Certification and Accreditation Commission	9
Civil Aviation Administration, Ministry of Agriculture	8

Table 7 Types of political documents involved

Type	Quantity	Proportion (%)	Type	Quantity	Proportion (%)
Announcement	565	62.16	Guideline	5	0.55
Instruction	201	22.11	Executive response	4	0.44
Proclamation	58	6.38	Reply	2	0.22
Catalogue	12	1.32	Communique	2	0.22
Stipulation	11	1.21	Public note	2	0.22
Decision	11	1.21	Rules	1	0.11
Method	8	0.88	Scheme	1	0.11
Plan	7	0.77	Work	1	0.11
Letter	5	0.55	Condition	1	0.11
Regulation	5	0.55	Requirement	1	0.11
Circular	5	0.55	Policy	1	0.11

Quality Supervision and Inspection Center (Shanghai). The internal working documents are weak in their influence on the development of satellite navigation. Meanwhile, this kind of policy is more about industry development of satellite navigation instead of system construction, application promotion, and international cooperation.

4 Problems of China's Satellite Navigation Policies

Based on the empirical data analysis above,it can be concluded that although satellite navigation policies play an indispensable role in the administration, operation and application of satellite navigation in China, there are still some problems in practice, such as the lack of top-level policies, uneven organization of the policy structure and imbalanced policy subjects, etc.

4.1 Lack of Top-Level Policy

Only 1.1% of the 909 satellite navigation political documents introduced in China have been directly promulgated by the State Council, while the proportion of policy documents promulgated by local governments reaches 66.6%. Due to the low law enforcement and limited range of application, these policies have limited effects on the guidance and standardization of the BDS. In China's legal system, the major laws which are related to satellite navigation are *Surveying and Mapping Law of the People's Republic of China*, *Regulation of the People's Republic of China on the Management of Radio Operation* and *Regulation of the People's Republic of China on Controlling the Export of Guided Missiles and Related Items and Technologies*. But the main obligatory object of these laws is different from satellite navigation; therefore, these legislation play limited roles in the guidance and standardization of the system construction and industrial development of the BDS. In this empirical research, it is apparent that the policy diffusion of satellite navigation moves from the central to local, so it poses an urgent need for promulgating guiding policies at the central level. Although the *Regulations on Satellite Navigation of the People's Republic of China* has been included in the legislative plan of the State Council in 2016, it is still in the process of drafting.

4.2 Uneven Organization of Policy Structure and Arbitrariness in Policies

There is a structural imbalance in the distribution of industries and regions in the current satellite navigation policies of China. As regards the content of policies, they tend to focus on the application and industrial development of satellite

navigation while neglect the management system, intellectual property protection and international cooperation of satellite navigation. In terms of the regional distribution of policies, the policies introduced in the more developed areas (east China, south China, north China) account for 76% of the total, while those introduced in underdeveloped area (northeast, northwest, southwest) account for only 24%. In addition, there is no rigorous and uniform specification for the title and content of the political documents of satellite navigation, resulting in the uneven types and formats of the policies and the failure in the formation of a reasonable system. Moreover, the diversity of the titles of the political documents directly reflects the arbitrariness of the policy, which may leads to the deficiency in policy enforcement and the weakening of implementation.

4.3 Imbalanced Policy Subjects

The empirical study above demonstrates that the major policy subjects of satellite navigation are the user department, such as the NASG and the Ministry of Transport. The number of the policies promulgated by these two departments has exceeded 1/3 of the total number of policies at the central level. However, the specific supervision and management departments which are responsible for the operation, maintenance, infrastructure construction, industrial promotion of the BDS have only introduced few policies. What's more, the policies promulgated by these departments are relatively low at legal level and most of them are announcements and instructions. This indicates that there are some problems in the administrative subjects of satellite navigation, such as overlapping authorities and responsibilities, unclear responsibilities as well as multi-authority administration. In addition, the low policy-making participation of the major industry association of satellite navigation has hindered the functioning of industry association, which is not conducive to the development of satellite navigation.

5 Solutions

In order to solve the problems in the field of China's satellite navigation policies, this research attempts to propose concrete and feasible suggestions from the following three aspects: 1. the construction of the top-level policy system, 2. the optimization of the policy structure, 3. the coordination of policy subjects.

5.1 To Improve the Policy System with Timely Promulgation of Top-Level Policies

In order to provide a sound institutional environment for the construction, operation and development of the BDS and to adapt to the current policy diffusion characteristics in the field of satellite navigation, China is in urgent need of a top-level

national regulation on satellite navigation. The fact that the existing satellite navigation policies are mainly promulgated by the governmental sectors at the provincial and municipal levels indicates a lack of universal binding force in legislation and policy. Thus, the *Regulations on Satellite Navigation of the People's Republic of China* included in the legislation plan of the State Council in 2016 should be formulated in principles of strong guidance, wide coverage and high feasibility, and should be implemented as soon as possible. At the same time, it should stick to problem-orientation in the process of drafting and straighten out some significant relationships, such as compulsory application and voluntary application, the compatibility and interoperability between the BDS and other satellite navigation systems as well as military and civilian boundaries, etc.

In addition, the relationship with existing laws and regulations in the process of drafting should be properly handled. On the one hand, the regulation ought to absorb the opinions of various departments at all levels, avoiding conflicts with existing laws and regulations especially like the *Surveying and Mapping Law of the People's Republic of China* and the *Regulation of the People's Republic of China on the Management of Radio Operation*. On the other hand, the *Regulation* should give full play to the role of guidance and standardization, as well as absorb the achievements of the existing satellite navigation policies, guaranteeing the continuity, stability, timeliness, standardization and innovation of policies. After the regulation promulgating, departments of the State Council and local governments should be encouraged to promulgate relevant supporting and implementation policies on the basis of the *Regulation*. Finally, a policy system with clear hierarchy and comprehensive type will be formed. In order to gradually change from administered policy management to legalized governance, those policies that have a significant effect in implementation to legislation should be timely transferred.

5.2 To Promote Industrial Development and Optimize Policy Structure

The development of industry is the foundation and vital driving force for the technological progress and the promotion of satellite navigation. Thus, in order to serve the national strategy and promote the development of civil-military integration in the field of satellite navigation, it's necessary to continually make industrial policies of satellite navigation and take the industrial promotion policies of satellite navigation as a breakthrough to construct a comprehensive system of satellite navigation policies. To ensure the sustainable development of the satellite navigation industry, it's necessary to conduct standard norms and strict management on production and service quality standard of satellite navigation. In addition, it should take industry standards and application specifications in account, in order to avoid illegal conducts such as user privacy disclosure caused by improper transaction and the abuse of navigation data.

Meanwhile, the heavy reliance on announcement-dominated compulsory administrative policies should also be avoided in the choice of policy tools. Encouraging policies shall be multiply adapted to upgrading the satellite navigation industry from the aspects of markets regulation, fiscal and taxation support, programming and construction and personnel training. Domestically, regional industrial development policies should be made based on local conditions to balance the imbalance among regions. Internationally, it should take full advantage of international rules to cancel the contradictions between domestic rules and international rules by promulgating mandatory application polices of satellite navigation in a reasonable range to guarantee the international market share of the BDS.

5.3 To Coordinate the Relationships Between Policy Subjects and Guarantee the Implementation of Policies

As a means of administration, the effectiveness of polices depends on the implementation of functional departments. It is crucial to coordinate the relationship between policy subjects and clarify the responsibilities, rights and obligations. In order to solve the problems effectively in the current administrative system, it should follow the other satellite navigation systems to establish an inter-sectoral and civil-military integrated management agency and clarify its legal status, rights and obligations.

Secondly, a special policy supervision and enforcement office should be set up under the comprehensive and coordinated management agency. For both business and public users, on the one hand, the office implements the publicity and education of satellite navigation policies; on the other hand, it regularly evaluates the effects of satellite navigation policies. At the same time, it should also clearly endow the industry association the functions of coordination and supervision, in order to enhance the effect of coordination and support of industry associations. The clarity of authority and responsibility not only prevents the policy subjects from shifting the blame to each other, but also ensure the effectiveness of supervision.

Finally, the comprehensive and coordinated management agency should organize think-tanks of satellite navigation policies via recruiting technical, policy-making, and legislative experts. It shall then carry out the policy and strategic of satellite navigation research and provide consultation for the formulation, implementation and evaluation of satellite navigation policies. Meanwhile, targeting at the specific problems in the construction of satellite navigation policy system, the government shall also encourage non-governmental think-tanks to offer optimal policy options.

References

1. Wang J (2008) Management system and policies of foreign satellite navigation and positioning system. Aerosp Ind Manage 03:29–35
2. Wang J, Shi W (2009) Application management system and policies of overseas satellite navigation and positioning system. Aerosp Chin 06:12–15
3. Wang J, Wu W (2011) Policy progress study of overseas satellite navigation and positioning system. Aerosp Chin 01:15–18
4. Li Y, Liu W et al (2013) The evolution rules and implications of U.S. GPS policies. In: Proceedings of the Fourth China satellite navigation academic annual conference—S1 Beidou/GNSS navigation application: 4
5. Cao C (2014) Development and evolution of foreign satellite navigation policies. High-Technol Ind 06:46–49
6. Yang J, Hu X (2016) Six principles of industrial policy optimization for BDS. J Navig Positioning 03:40–44
7. Shui B (2014) The legal protection for the promotion of satellite navigation industry. In: J Nanjing Univ (Philosophy, Humanities and Social Sciences) 03:47–52
8. Xu H (2013) Some thoughts on improving the construction of China's Beidou satellite navigation industry system. Satell Netw 06:26–28
9. Yang J (2016) Mechanism, path and policy choice of military and civilian cooperation of China's Beidou satellite system. Financ Econ 10:25–27

On the Trademark Pledge for Beidou Satellite Navigation Industrialization

Huan Yan

Abstract Since deployed into use, Beidou navigation satellite system has gradually play its role in the field. However, there is still a long way to catch the advanced system like GPS in US or European Galileo. The industrialization of Beidou is the necessary way for further development. The foundation of the successful development of the industry is based on financing. And as a technical copyright, trademark in the course of enterprise development which is a sign of modern society. The use of trademark rights financing in the United States and other countries has become an important means of investment and financing of scientific and technological enterprises, but in China is still in the exploratory stage. This paper is based on the analysis of the current situation, and following the experience of United States, then propose some method to improve the Beidou trademark pledge.

Keywords Trademark right · Pledge financing · Pledge assessment

1 Introduction

In the life changing technology today, a variety of high-tech products into production market, bring convenience to life. For example, compared to early traffic is not convenient, to the distance is more restricted by time rather than travel. Nowadays, people use mobile phone navigation travel is very common, go all around the world are extremely easy. Instead of on the road do not understand, can only rely on the only data exploration. The reason to have such an advantage, all rely on the development of the navigation system.

The current global navigation system is Galileo navigation system GPS of the United States and Europe, especially the GPS system of the United States to pro-

H. Yan (✉)
Northwest University of Political Science and Law,
300 South Changan Road, Xi'an 710063, China
e-mail: cheerhh@sina.com

J. Sun et al. (eds.), *China Satellite Navigation Conference (CSNC) 2018 Proceedings*, Lecture Notes in Electrical Engineering 498,
https://doi.org/10.1007/978-981-13-0014-1_64

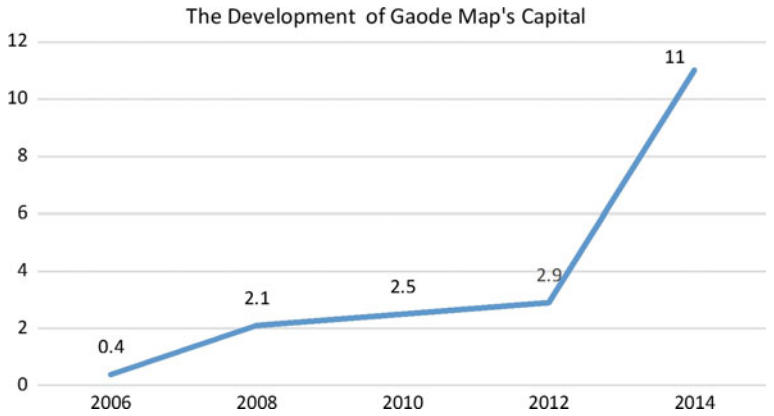

Fig. 1 The development of Gaode Map's Capital

vide services for a number of global navigation App Co, only in terms of travel is like Google maps, foreign GRT, High German map and all kinds of public services in China. While providing convenience for life, it is a great opportunity.

On this basis, derived from relying on the navigation system and the industrial chain, Beidou navigation satellite system developed in China is going to the world's three largest GPS and Galileo navigation system in the technical field, and its market prospect is optimistic. But in the competition to find a place to even win, rely on not only is the leading technology, is a kind of brand symbol is the legal! Brand trademark (Fig. 1).

2 Current Situation of Trademark Pledge

2.1 Trademark Pledge

A trademark is a kind of intangible assets has considerable economic value in the market. The products can be compared to the actual measure, the trademark is the product quality, a comprehensive reflection of the connotation and the enterprise culture, and the trademark is reusable, without space time constraints, and has received much attention in the modern market economy. The vast majority of enterprises a registered trademark moves in the beginning. But the trademark and the well-known trademark is still a big difference in the market economy, which directly determines the value of the trademark, the trademark can affect the success as a means of financing function for the development of enterprises.

Property as a trademark of intellectual property with the property, according to the provisions of the State Intellectual Property Office, trademark as intangible assets in bank financing, the trademark right is a right, according to the provisions of China's "guarantee law", the trademark rights in the bank as collateral financing should be used when the pledge.

2.2 Current Situation of Trademark Pledge

2.2.1 Imperfect Trademark Pledge Related Legal System

At present there is no legal norms about trademark right financing, the relevant legal provisions are limited to Trademark Law and the guarantee law, more reflected in the bank loan financing requirements, and more based on the terms of the contract, so it is difficult to avoid the one-sided situation, enterprises to obtain bank the loan support, it is difficult to avoid to give up self-rights as a condition that is not conducive to the protection of intellectual property rights, thereby affecting the long-term development of copyright, copyright and utility is also difficult to play.

Perfect laws and regulations is the best way to guarantee the rights and obligations, the protection of property rights is the development of the Trademark Law emphasizes the only way which must be passed. The application and validity of trademark, the trademark rights provisions of the lack of the use of the trademark. The property right is only legal support, is the attribute level textbooks, lack of mandatory legal provisions in practice. Support, and in the property or property rights is not clear but the proportion of unknown circumstances, will inevitably have the right to dispute, this is a big obstacle to the development of enterprises.

Guarantee law, the provisions of the right financing is vaguer, even often is mortgage or pledge of rights for debate. There is no doubt that the pledge, but because of the provisions of the fuzzy, a large number of manpower consumption in the aspects of the debate, it is more effect on the loss outweighs the gain, after the share of financing decisions.

2.2.2 Imperfect Trademark Pledge Related Policies

China's current economic system with the public ownership as the main body of common development of multi ownership economy, which determines the guidance and support of China's current economic development still needs government policy. Beidou navigation satellite system is the first military posture for the development, in all the key nodes are constrained by the national security legal system the system, such as "People's Republic of China state secrets law". In the critical period of conversion, some core technologies are required to facilitate the policy guidance of the government, enterprises, and then enter the field of financing. If only the brand effect of the Beidou navigation and lack of substantive support to the connotation of the brand, is the pledge of both sides is not ideal the situation will greatly affect the long-term development, and seriously influence the process of industrialization.

Now, our country from the central and local governments were not issued special copyright financing regulations, is only in the form of a document policy guidance is to encourage the emergence of posture, never have guidance or practical policy formal, in the actual operation, no relevant industry guild in this restriction. Cause

out of order in the actual operation, many previous mode states. China is a civil law country, the spirit of the subject is the standardization of regulations, but in practice the application case law of Anglo American law system, not many chaos laughable.

2.2.3 Lack of Pledge Assessment Professional

Still need professional personnel in participating in the assessment process, which requires the relevant staff not only need to have their own professional quality, but also to have the legal, economic and other knowledge, but in reality, the lack of these talents evaluation. In the past, the copyright in the process of financing, the evaluation is completed by financial institutions, bank employees the lending industry to understand the detailed rules, but the majority of bank lending for real estate mortgage, pledge loan business of the bank on the lack of, also is for the corresponding national call, provide the corresponding service, but the practice is less and less.

Which is the idea of operators, but require employees to have much knowledge is the ideal state. Most of the operators are hoping the ideal state, but its cost is enormous, investment return is whether you can get everyone in consideration. And hired as a versatile talent employment to parity work personnel to ensure the money is not paid.

Such embarrassing situation caused by a large loss of capital or value is reduced use are detrimental to industrial development.

3 Relevant Experience of Foreign Trademark Right Pledge

3.1 Relevant Laws and Regulations Policy

According to the latest statistics of American Google Corporation with a brand value of $229 billion to become the world's first. The Google Corporation mainly relies on the United States GPS satellite navigation market value of derivative products, the same industry occupies most of the market share, determines the development direction and trend of the industry to a certain extent. The success of the Google Corporation is not only its excellent technology advanced management results that is more legal guarantee. Throughout the United States, the laws on intellectual property development, in every important historical node have left traces of legal development progress.

The development of better protection of intellectual property rights, intellectual property rights amendment act, according to the characteristics of the rapid development of intellectual property rights, since the beginning of twentieth Century is the establishment of the intellectual property rights specialized

institutions, promote the development of copyright protection in the name of the country, this is the United States copyright has many enterprises laid a solid foundation.

After the United States in 1986 through the "technology transfer law", the research institutions will contract, trademark licensing and transfer are included in the work of scientific research institutions. Founded in 1992, the national technology transfer centre, specifically related to intellectual property management training, the American science and Technology Laboratory for unified management, combined with the existing research results the establishment of application technology consultation system, market assessment, market research and technology intermediary work. In cooperation with the Federal Laboratory Centre for technology transfer, technical cooperation through the six regional centre for technology transfer, market investigation and evaluation of technology intermediary and so on.

Research shows, copyright, patent, trademark occupy eighty percent of the market value of Listed Companies in the United States, this from the angle of economy greatly inspired the development of the legal system and mature. The huge market share and the need to regulate the legal constraints.

3.2 Perfect Policy Mechanism

The United States has a sound trademark protection bureau and related policy support mature, mainly be responsible for the administrative management of trademark and patent, trademark application and application of convenient service enterprises. The Trademark Office has now implemented enterprise management, market regulation aims to better follow the pace of the market, to provide the most effective protection for trademark management. According to the twenty-first Century strategic plan for U.S. trademark the Bureau, from a macro point of view, put forward to promote the continuous development of copyright, trademark of the impact of globalization, encourage innovation and investment.

At the institutional level, the United States established three outstanding systems.

3.2.1 First Invention Rule

Pay attention to the protection to the inventors, from the level of control, with the invention of confrontation is the importance of property rights registration, encourage a great performance of invention. In the American dream with the greatest interest to encourage expansion of new creation. If new inventions or to be a registered trademark has been registered in the Bureau of copyright or Trademark Management Council may raise objections, the burden of proof further proof, if there is ample evidence, can judge the first registration is invalid. This measure can

not only maximize the protection of the rights of human rights, it can promote the development of the United States registration management system, strict screening of the market, to provide a solid foundation for trademark rights financing. To avoid damage due to disputes caused by corporate interests, and then influence the development.

Especially in science and technology enterprises, the application of any trademark or patent is the enterprise survival guarantee, the trademark system is not only convenient smooth and clean enterprise investment and financing side, is a powerful means of enterprise competition. In the space science and technology enterprises, the navigation system used by enterprises accounted for the vast majority of market share, with navigation technology the basis of brand creation, brand effect to expand the development of navigation technology industrialization, is every practitioner direction. Even in successfully occupied the global market share today, also can not ignore the protection of trademark rights.

3.2.2 Grace Period Rule

In the vast majority of the world's legal system are required to complete the work in the creation of trademark registration before the registration, as an entity, not directly to the unknown state registration. The provisions of the United States a grace period of twelve months. At the same time, the Paris convention also provides a foreign inventor in the United States apply within one year.

Creation is the accumulation of a process, providing time convenience for the stakeholders, can better promote the creation of creative quality. Excellent works can play a greater role.

In the navigation enterprise, satellite navigation technology related are very strange market for ordinary consumers, one must understand the meaning of symbols is not possible, but through a sign can clear guidance of product attributes, it is possible. It condenses a wisdom of great intellectual achievements the author the use of the system. The grace period, great to meet the needs of the accumulation of the creation process.

3.2.3 First Usage Rule

The United States trademark law gives the right to use trademark user. First to use is a prerequisite for registration. After receiving the tort litigation, first use is important litigation evidence. It helps protect the interests of trademark rights, but also invest more in the industry after the first test in the market to be registered in the trademark. Mark after five years of challenge period, in five years, if the other enterprises registered trademark objection or unknown ownership situation, but judicial proceedings, if after five years, even if there are no dispute litigation rights of trademark rights in the market. This is a major feature, avoid confuse the public the phenomenon. After five years of market baptism, the same trademark has been

recognized, the related benefit derived have been produced, the open market attitude allows the existence of dispute, but the dispute cannot affect the fundamental and development of the market.

3.3 Perfect Assessment System

Germany, as an advanced capitalist country, has a unique appraiser system worth learning from.

3.3.1 Establishment of Evaluation Training Institutions

To the public in the form of government established assessment of professional training institutions, strictly regulate the assessment of the training system. It can realize the comprehensive development of the evaluation, but also avoid the market assessment of the phenomenon of uneven in quality.

3.3.2 Establishment Assessment System

Through the government assessment, assessment of occupation qualification only after the assessment work. In bank lending to the assessment of assets, only the professional assessment personnel issued results have legal effect.

4 Perfection of Trademark Right Financing System in China

In the last century, the United States in 60s film “graduates”, leading to everyone shouting “the future is plastic era, plastic industry influenced the whole generation lifestyle change, and now, the shouting will become” the present era is the era of intellectual property rights. “Copyright of life deep influence there is no comparison”. From a global perspective, the global top five brands are science and technology enterprises (Table 1):

Table 1 The global top five brands with their value

	Company	Value (Billion)
1	Google	2290
2	Apple	2280
3	Microsoft	1220
4	AT&T	1070
5	Facebook	1030

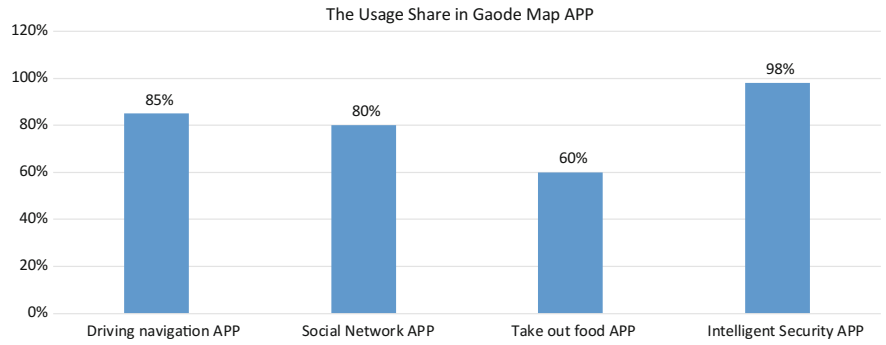

Fig. 2 The usage share in Gaode Map APP

The vigorous development of science and technology enterprises is the top priority of China's economic transformation, at present, relying on GPS satellite navigation system of High German location services, with absolute advantage occupies a large market share, its form as shown (Fig. 2).

Although China has broad market prospects, but there are deficiencies in the system norms, the need to learn from advanced foreign experience can play a role.

4.1 Improve Trademark Rights Pledge Financing Laws and Regulations

4.1.1 Form the Norms of Legal

The existing norms to regulate the form into law to restrict the legislation and related work. After amending the law is a law in the process of keeping pace with the times, is a necessary process. We should take a positive attitude to cope with this change. At the same time, combined with the reality of our country, drawing on the essence of his country's success take, summed up China's intellectual property rights pledge financing way.

4.1.2 Clear the Right with Legal

China's current "trademark law" and "guarantee law" is not clear right of trademark is to pledge financing way, only to clear the rights pledge rather than rights can be realized. The establishment of standardized way of financing regular financing behavior. Restrictions on borrowing rights and obligations of both parties, taxable behavior, delivery mode, result of behavior.

4.1.3 Clear the Obligation by Legal

To ensure the full compliance of the financing behavior, both parties must maintain their obligations. The obligation is the center of their own should do for others and society. But for now, the financing behavior of the trademark does not expressly prescribe by law, and the obligation has no definite regulations. Ensure for the rational allocation of interests, the obligations of the provisions and necessary.

4.2 Improve Policy Guidance and Establish Industry Norms

China is currently in the form of government policy guidance and other forms of business norms within the industry, that is, the system is not standardized. In order to ensure the development of industrialization, we must first establish the policy.

Government to establish tax, loan interest rates, customs and other related conducive to Beidou navigation satellite system of industrial development policy.

4.3 Perfecting the Training Mechanism of Appraiser

Government led, relying on financial institutions to support, improve the evaluation of training mechanisms.

Government official assessment training institutions, professional teacher policy interpretation, assessment mechanism, assessment of qualified people to grant the certificate form. Usually, this kind of assessment are not employed in various types of financial institutions to provide loans, both exist with independent third-party attitude. In order to ensure the interests of both sides by financing all.

References

1. Zhou L, Li S, Yang S (2015) The analysis and suggestions on patent status of Beidou satellite navigation industry. China Invitation & Patent, pp 44–48
2. Min X (2016) The Analysis of trademark pledge loan restricted. Chinese finance, pp 106–110
3. Tao L (2016) Research on legal risks and countermeasures of trademark guarantee value utilization. Intellectual property, pp 47–52
4. Wang L (2010) Research on the legal application of international guarantee financing of trademark right. Telemetry and remote control, pp 185–191
5. Liu L, Sub-Branch PZ (2015) Analysis of trademark pledge loans in the development of tea industry. J Reg Finan Res
6. Kong X (2016) An empirical analysis of trademark pledge value and financing body. J Beijing Instit Graph Commun

Study on the Development Strategy of Legal System of China's Satellite Navigation System Based on AHP-SWOT Analysis

Yingjie Du

Abstract The legal system of satellite navigation is the basis for the development and application of national satellite navigation. At present, the administerment and generalization about satellite navigation system still mainly depend on the policies of government. Lawlessness is the main problem of the construction of legal system of China's satellite navigation system. To get more scientific development strategy of legal system of satellite navigation, the treatise puts to use the method of SWOT to analysis the status quo of legal system of satellite navigation from the aspects such as the strength, weakness, opportunities and threats. Based on the analysis of the above, the treatise uses the method of AHP to get the sort of development strategy of the legal system of satellite navigation. Then based on the sort, the treatise not only gets the best development strategy of the legal system of satellite navigation, but also puts forward the concrete suggestions.

Keywords Satellite navigation system · Legal system · SWOT · AHP

The report of the 19th National Congress of the CPC has pointed out that we would carry out lawmaking in a well-conceived and democratic way in accordance with law, so that good laws are made to promote development and ensure good governance [2]. As the typical project of the national military and civilian integration and the major space-time infrastructure, the satellite navigation system is a matter of national security, the national economy and the people's livelihood. Therefore, it is necessary to not only give full play to the regulation, guidance and guarantee of the laws and regulations, but also bring the construction, development, application and promotion of the satellite navigation system into the track of the rule of law to ensure the healthy and safe development of the satellite navigation system. Lawlessness is the main problem of the development of legal system of satellite navigation system. To get more scientific development strategy of legal system of satellite navigation, the treatise puts to use the method of SWOT to analysis the

Y. Du (✉)
Political School of National Defense University, Xi'an 710068, Shaanxi, China
e-mail: duyingjie1979@163.com

J. Sun et al. (eds.), *China Satellite Navigation Conference (CSNC) 2018 Proceedings*, Lecture Notes in Electrical Engineering 498,
https://doi.org/10.1007/978-981-13-0014-1_65

status quo of legal system of satellite navigation from the aspects such as the strength, weakness, opportunities and threats. Based on the analysis of the above, the treatise uses the method of AHP to get the sort of development strategy of the legal system of satellite navigation. Then, the treatise not only gets the best development strategy of the legal system of satellite navigation, but also puts forward the concrete suggestions which is helpful to improve the level of legal system of the satellite navigation system.

1 Basic Models and Methods

The treatise uses the SWOT analysis method to qualitatively analyze the situation of China's satellite navigation legal system construction, and build the AHP model based on the analysis results, then conduct quantitative analysis of all the factors in the model, and put forward specific proposals for improving the legal system of China's satellite navigation.

1.1 SWOT Analysis Method

The SWOT analysis is also known as situation analysis. Among them, S is strength; W is weaknesses; O is opportunity, and T is threat. SWOT analysis method is firstly put forward by K·J·Andrews. It is based on the strength, weakness, opportunities and threats of its environment, so as to formulate development strategies. The basic principle is to make full use of external opportunities, effectively evade external threat and give full play to internal strength and overcome internal weakness. In the course of studying, the following theoretical model is used to analyze the factors that affect the development situation as shown in Fig. 1.

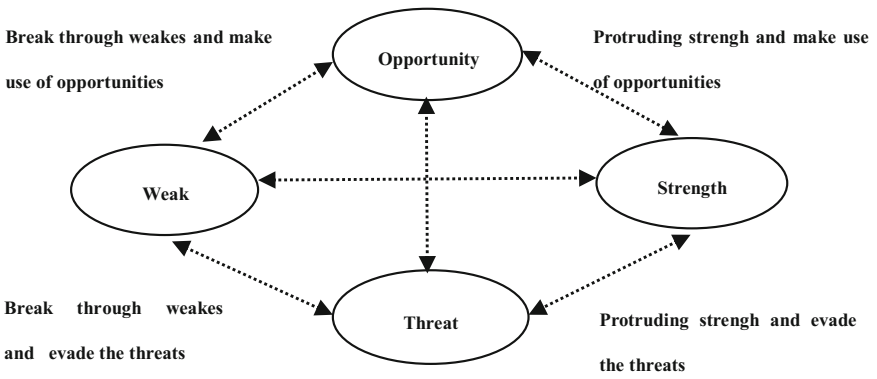

Fig. 1 Logical relation of SWOT

1.2 AHP Analysis Method

The analytic hierarchy process is referred as AHP. Its basic principle is based on the nature of the problems and achieves the overall objective of the problems. The problem is decomposed into different components. Then according to the relationship between influence factors and affiliation to the factors at different levels of aggregation combinations, forming a multi-layered structure model of the thus, the problem is reduced to the lowest level (for decision schemes and measures) relative to the top (target) to determine the relative merits of the order of the schedule or the relative weight, then get the solution or target the quantitative description of the relative importance. When using the analytic hierarchy process to build the system model, it can be generally divided into four steps: Firstly, establishing the hierarchical structure model; Secondly, constructing the judgement matrix (paired comparison); Thirdly, ranking single level and checking its consistency; Fourth, ranking and checking the consistency of the hierarchy.

1.3 Coordination Analysis Between SWOT and AHP

The advantage of the SWOT method is to consider the problem comprehensively and intuitively. It can combine closely the diagnosis and prescriptions of the problem with strong persuasiveness. The shortage lies in the qualitative analysis and the lack of quantitative analysis. The advantage of the AHP method is systematic, practical and succinct. Combining qualitative and quantitative methods, it can deal with many practical problems which cannot be started with traditional optimization technology. This treatise uses SWOT analysis method to analyze the strength, weakness, opportunities and threats of legal system of satellite navigation in our country, putting the AHP analysis method into the SWOT analysis method, to provide the best reference for strengthening the legal system of satellite navigation, and put forward the corresponding countermeasures suggestions, and strive to make the suggestions more targeted.

2 Status Quo of Legal System of Satellite Navigation Based on the SWOT

2.1 Strength

2.1.1 Exterior Environment of Law-Based Governance in All Fields

Since the 18th National Congress of the CPC, the CPC Central Committee with Xi Jinping as the core has risen to rule the country by law and become the basic strategy of governing the country. Ruling of law has become the basic way of

governing the country. The rule of law has appeared 55 times in the report of the 19th National Congress of the CPC. All these directly indicate a new era of rule of law is coming. The rule of law has been formed in accordance with the law, the finding of the law, the use of the problem and the solution of the contradiction. The change of external environment will inevitably require satellite navigation system to go on the track of rule of law. Relying on the perfect and sound legal system to ensure the healthy and rapid development of satellite navigation system, it objectively brings about the realistic need for the legal system of satellite navigation system.

2.1.2 Support from the Government and Army

As the typical project of the national military and civilian integration and the major space-time infrastructure, the perfection of legal system of China's satellite navigation system is supported by the government and army. The general secretary Xi has asked us to strengthen the construction and development of the legal system of satellite navigation. The Satellite Navigation Rules has been included in the legislation plan by the General Armaments Department. The State Council has the Satellite Navigation Rules be included in the 2016 legislative plan as the legislative project of the implementation of the national security strategy and the maintenance of national security. Yang Changfeng, as the chief designer of satellite navigation was the leader of the leading group of satellite navigation major projects. The drafting group was made up of the member units of the major special leading group of satellite navigation. The executive unit of drafting was Beijing University of Aeronautics and Astronautics.

2.1.3 Practical Need of the National Development Strategy

Achieving greater military-civilian integration and pursuing the Belt and Road initiative are the national development and major tasks. As the important part of project of the national military and civilian integration and the Belt and Road initiative, the satellite navigation system is a matter of national long-term development and the people's livelihood. Therefore, it is inevitable demand of the legal system of satellite navigation to ensure the realization of greater military-civilian integration and pursuing the Belt and Road initiative with the power of law. At present, the policies and regulations of the satellite navigation system are still not perfect, not necessary, not convergence, which has caused the channel of military-civilian integration is not smooth. To achieve greater military-civilian integration, it is urgent for advancing the relevant policies, laws and regulations to guide and standardize the construction, management and application of the satellite navigation. In addition, as the important content of Belt and Road Initiative, lawlessness will be the important problem when we render services for the counties and areas along the line of the Belt and Road.

2.2 Weakness

2.2.1 Lower Level of Administration by Law

Since the 18th National Congress of the CPC, the rule of law has been the basic way to rule the country. Under the background of law-based governance in all fields, the level of the administration by law in all walks of life has been greatly raised. However, in the field of satellite navigation, influenced by the long-term planned economic and the complexity of the satellite navigation, the level of administration by law is still lower than other fields. For example, in the existing regulation system, the Regulations on the Application of Satellite Navigation issued by the General Staff Department is in the scope of the law. Beyond that, they are all policies. The policy is still the main basis for the adjustment of the legal relations in the satellite navigation field. In view of the inherent defects in the execution of the policy, the level of administration by law has lagged far behind the construction and development of the satellite navigation system.

2.2.2 Imperfection of the Rule of Law

Although, in 2011 China had announced that the socialist legal system with Chinese characteristics which were made up with the constitution, constitutive law, civil law and other laws had been formed. Frankly, the level of the legal system is still relatively low. And it has not covered all areas. As a new field, satellite navigation has the characteristics of comprehensiveness. The legal system has not thorough covered this field. In practice, it mainly relies on administrative policies to adjust its construction, development, popularization and application. The way of relying mainly on habits and experience to solve the problems has not been changed significantly.

2.2.3 Incompetence of Legal Talent

Under the background of law-based governance in all fields, with the acceptance of the rule of law, the law literacy of the people has been generally promoted. However, as a job with professional and technical requirements, legislation not only requires the staffs have professional legal knowledge, but also must have corresponding technological knowledge. As the national high-end technology industry, satellite navigation has made unprecedented demands for the staffs—not only have the knowledge of legislation, but also have the knowledge of satellite navigation. However, incompetence of legal talent is far from the requirements which seriously has been the important factor of affecting the development of the legal system in the field of satellite navigation.

2.2.4 Disparity Between Our and Foreign Countries

At present, there are three satellite navigation systems in the world in addition Beidou which have been put into use of providing the service signal: GPS of US, GLONASS of Russia, and GALILEO of Europe. Among them, as the earliest GNSS developers, the GPS related legislation has been more mature; While the speed of development of the GALILEO of Europe lags behind slightly, its legal system is more perfect. Because the GLONASS of Russia has developed many years, its supporting policies and rules are also perfect [1]. We has not yet had a special regulation related to the satellite navigation. The deficiency of legislation has been unable to satisfy the development of satellite navigation.

2.3 Opportunities

2.3.1 Requirement of System of Rule of Law

The report of the 19th National Congress of the CPC has pointed out that we must improve the Chinese socialist system of laws, at the heart of which is the Constitution; establish a Chinese system of socialist rule of law [3]. As the typical project of the national military and civilian integration and the major space-time infrastructure, it is necessary to give full play to the regulation, guidance and guarantee of the laws and regulations to ensure the healthy and safe development of the satellite navigation system. Therefore, it is the objective and inevitable requirement of development of satellite navigation to perfect the system of legal. It is also the important content and concrete measures for carrying out great spirits of the 19th National Congress of the CPC and the Xi Jinping's great strategic thoughts of ruling the country of the law in the new era. It is also the important contents and concrete measures for establishing a Chinese system of socialist rule of law.

2.3.2 Requirement of Civil-Military Integration

The general secretary Xi has pointed that we would deepen reform of defense-related science, technology, and industry, achieve greater military-civilian integration. As a national civil military integration of major industrial projects, it is prerequisite for using the rule of law to promote and ensure the deep integration of satellite navigation system and speeding up the formation of the deep development pattern of the integration of military and civilian. The military and civilian integration of the satellite navigation system needs not only the support and encouragement of the policy platform, but also the guarantee of the legal system. Therefore, perfecting the legal system of satellite navigation, creating the atmosphere of civil military integration, giving full play to the role of laws and

regulations, are the inevitable requirement to ensure the healthy development of the satellite navigation system. It is also the objective needs of promoting the level of the depth development of civil military integration of the whole country.

2.3.3 Requirement of Development of Satellite Navigation System

The experience of human progress tells us that standardization, immobilization, normalization and scientization is the most scientific and convenient way to manage the rule of law. As the national construction of the important pillar industry and the major state space infrastructure, construction and application of satellite navigation system are related to thousands of people, the livelihood of every family. The construction and application of satellite navigation system is related to thousands of people, interests of everyone. It will also affect the security and development of the country. In this case, it is inevitable choice of solving all the problems of construction, promotion, development, construction and management with the rule of law to ensure the construction and management of the satellite navigation system.

2.3.4 Requirement of International Co-operation

As a global navigation satellite system, the technology and products of satellite navigation system must combine with international standards. Therefore, in order to ensure China's satellite navigation system to better the national market, especially with the further development of the Belt and Road initiative, to ensure the cooperation and compatibility with other satellite navigation systems, we must abide by the international treaties and international rules. Except that, we also need to transform them in the domestic legislation and take use of the mandatory, normalization and guidance of laws to guarantee the development of satellite navigation system. At present, the deficiency of legislation has been the important obstacle of creating a international brand, the initiative of international co-operation and the internationalization of satellite navigation system. We must break the current unfavorable situation that mainly takes policy as the main mean of adjustment to promote the level of the internationalization of the satellite navigation industry.

2.4 Threats

2.4.1 Aggravation of International Competition

With the development of satellite navigation system and pursuing the Belt and Road initiative, the pressure coming from international competition is growing. The competition between the owned satellite navigation systems countries are more fierce. As mentioned in the previous article, the legal system of satellite navigation

systems in our country has lagged behind other countries. The deficiency of legislation has been the important obstacle of creating a international brand, the initiative of international co-operation and the internationalization of satellite navigation system.

2.4.2 Swiftness of Industry Development

By 2020, our satellite navigation system will serve as a global user service. The system of policies, regulations and standards of the satellite navigation system is unperfect. The system including market access, application, policies supporting, technical standard and personnel training has not yet formed. Because of the deficiency of unified industrial organization policy, malign competition is popular in the practice. Due to the lack of unified market access criteria, excessive intervention, small scale and low level of business are pressing issues. It is urgent to establish an application system of satellite navigation.

2.4.3 Inadequateness of Theoretical Research

Although the satellite navigation system in China started late, the construction and development of satellite navigation system has made great achievements in recent years. However, the achievements and prosperity of the technical level did not bring about the same degree of development to the theory and practice of the construction of the satellite navigation system. At present, there are few theoretical results that can be found related to the construction of the satellite navigation system. The lack of theoretical research has also created a realistic obstacle for the development of satellite navigation system.

3 Selection of Development Strategies of Legal System

3.1 Building Model of SWOT Analysis

Based on the above analysis, we can get the analysis model of SWOT analysis about the development strategy of legal system of China's satellite navigation system as shown in Fig. 2.

3.1.1 SO Strategy

The SO strategy is based on the development strategy of intersecting the internal and external opportunities. According to the analysis, the development of legal system must be based on the construction of Chinese socialism law system, take

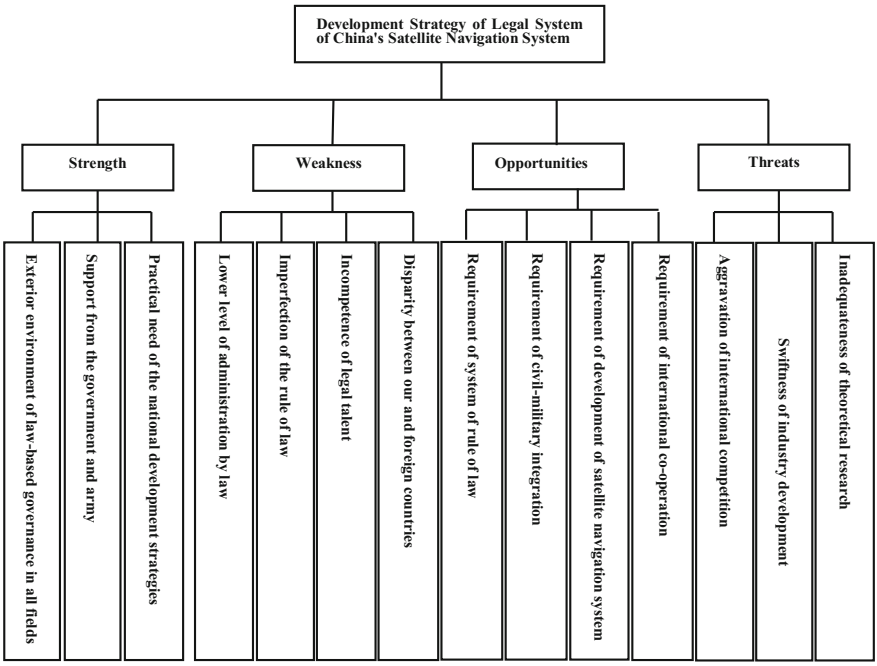

Fig. 2 Model of legal system of satellite navigation based on the SWOT

advantage of the support from the CPC and the country, satisfy the needs of national development strategy and the construction, abide by the practice of the development of the satellite navigation.

3.1.2 WO Strategy

The WO strategy is a development strategy based on the cross analysis of external opportunities. According to the analysis, we must deepen the rule of law and constantly improve the level of administration according to law, perfect the legal system, learn foreign advanced legislative experience, accelerate the law talent training, update the training concept, broaden the training channels, to meet the needs of personnel.

3.1.3 ST Strategy

The ST strategy is a development strategy based on the cross analysis of internal strength and environmental threats. According to the analysis, we should carefully analyze the development trend of the international satellite navigation, analyze and

compare the strength and weakness of our satellite navigation system and other satellite navigation systems, and strengthen the basic theoretical research on the legal system of the satellite navigation.

3.1.4 WT Strategy

WT strategy is the development strategy based on the cross analysis of the weakness and external threats. When perfecting the legal system satellite navigation, we must constantly strengthen thinking of the rule of law, learn from foreign advanced legislative experience, strengthen the training of rule of law talents in the field of satellite navigation, and constantly perfect the system of satellite navigation regulations.

3.2 Hierarchical Analysis of the Perfection Strategy of Legal System

Using the analytic hierarchy process, we will decompose the internal and external factors of the perfection of the legal system of the satellite navigation. Based on these, we will design a questionnaire, score according to the 1–4 scale method, build judgement matrix, calculate the maximum eigenvalue (λ_{max}) corresponding to the feature vector of W, and test the consistency as shown in Table 1.

The judgment matrix of each level is determined by the expert scoring method as shown in Tables 2, 3, 4, 5 and 6.

$W_S = [0.539 \quad 0.1634 \quad 0.297]^T$, $\lambda_{max} = 3.0092$, CI = 0.0046, RI = 0.58, CR = 0.008 < 0.1. The obtained outcome satisfies the consistency test.

$W_w = [0.1388 \ 0.3856 \ 0.3007 \ 0.1749]^T$, $\lambda_{max} = 4.165$, CI = 0.055, RI = 0.9, CR = 0.061 < 0.1. The obtained outcome satisfies the consistency test.

$W_o = [0.4152 \ 0.1263 \ 0.1933 \ 0.2652]^T$, $\lambda_{max} = 4.2298$, CI = 0.0766, RI = 0.9, CR = 0.085 < 0.1. The obtained outcome satisfies the consistency test.

Table 1 Index scale

	0	1	2	3	4
Strength	No strength	A little strength	Great strength	Striking strength	Absolute strength
Weakness	No weakness	A little weakness	Great weakness	Striking weakness	Absolute weakness
Opportunities	No opportunities	A little opportunities	Great opportunities	Striking opportunities	Absolute opportunities
Threats	No threats	A little threats	Great threats	Striking threats	Absolute threats

Table 2 Judgement matrix S for its own strength

S	S_1	S_2	S_3
S_1	1	3	2
S_2	1/3	1	1/2
S_3	1/2	2	1

Table 3 Judgement matrix W for its own weakness

S	W_1	W_2	W_3	W_4
W_1	1	1/2	1/2	1/2
W_2	2	1	2	2
W_3	3	1/2	1	2
W_4	2	1/3	1/2	1

Table 4 Judgement matrix O for external opportunities

O	O_1	O_2	O_3	O_4
O_1	1	2	2	3
O_2	1/2	1	1/3	1/2
O_3	1/2	2	1	1/2
O_4	1/2	2	2	1

Table 5 Judgement matrix T for external threats

T	T_1	T_2	T_3
T_1	1	2	1/2
T_2	1/2	1	1/2
T_3	2	2	1

Table 6 Judgement matrix A for the strategy selection of legal system of satellite navigation

A	S	W	O	T
S	1	3	2	3
W	1/3	1	1/3	1/2
O	1/2	3	1	2
T	1/3	2	1/2	1

$W_T = [03108 \quad 0.3916 \quad 0.4934]^T$, $\lambda_{max} = 3.0459$, CI = 0.023, RI = 0.58, CR = 0.04 < 0.1. The obtained outcome satisfies the consistency test.

$W_A = [0.4445\ 0.1072\ 0.2832\ 0.1651]^T$, $\lambda_{max} = 4.0712$, CI = 0.0237, RI = 0.9, CR = 0.0263 < 0.1. The obtained outcome satisfies the consistency test.

Finally, the overall ranking of the total objectives is carried out. The results are shown in Table 7.

From Table 7, we can see that the maximum weights are S3 = 0.24, W3 = 0.041, O3 = 0.118, T2 = 0.081, and now we can use SWOT quadrilateral to make choices as shown in Fig. 3.

Table 7 The overall ranking of strategy selection of legal system of satellite navigation

	ω_1	ω_2	ω_3	ω_4
S	0.24	0.073	0.132	0
W	0.15	0.041	0.032	0.019
O	0.118	0.036	0.055	0.075
T	0.051	0.065	0.081	0

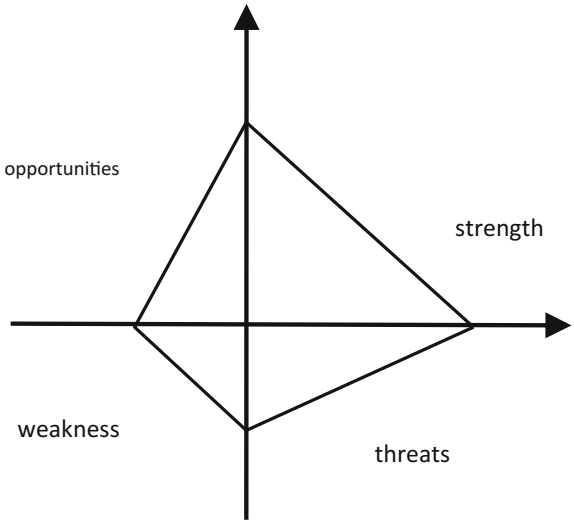

Fig. 3 SWOT quadrilateral strategy selection analysis diagram

Table 8 Triangle area of strategy selection basen on SWOT

	$S_{\Delta\ SAO}$	$S_{\Delta\ WAO}$	$S_{\Delta\ SAT}$	$S_{\Delta\ WAT}$
Area	0.014	0.002	0.002	0.01

According to Fig. 3, the area of the quadrant triangles is calculated respectively, and the results are obtained as shown in Table 8.

According to the order of area size, the SO strategy is selected as the best strategy.

4 Suggestions on Perfection the Legal System of Satellite Navigation

The rule of law is the important, good law is the premise of good governance. In view of China's current legislation situation of the satellite navigation, we should adhere to the approaches of giving priority to the theories, conceptual optimization

complete system, focused. Based on these, we will form the regulations of the satellite navigation system with the characteristics of the clarity of hierarchy, reasonable classification, specific and detailed to solve the problems of lawless of satellite navigation.

4.1 Establish the Legislative Model of Satellite Navigation

Before defining the specific content of the legislation of the satellite navigation system in China, we should firstly make clear what kind of legislative mode should be adopted. Through combing the legislation of the European Union, the US and the Russian satellite navigation, especially the domestic legislation of the US and Russia, we can find that there are mainly two models of the current world satellite navigation legislation: One is the sub—law integration mode, also known as the American model. It makes special legislation in accordance with its specific problems. The other is the mother law navigation model, also known as the Russian model which makes the basic law of guided satellite navigation be formulated. Considering our country's legislative tradition and national conditions, the author tends to the Russian model.

The reasons are as follows: Firstly, China has make the space legislation put on the legislative agenda. The Act of Space Activities is expected in recent years. As the part of the space activities, we can program the basic question of satellite navigation. Secondly, China's basic rules for regulating satellite navigation; the Satellite Navigation Ordinance has entered the stage of practical legislation, regulating and adjusting the basic laws and regulations in the field of satellite navigation. The Satellite Navigation Ordinance is expected to come out in the future. Lastly, in the history of Chinese legislation, the adoption of the Russian model accords with the legislative habits and legislative traditions of our country. Our country is accustomed to the introduction of a unified regulation, and then build up and perfect the relevant legal norms system.

4.2 Strengthen the Research of the Basic Theory of Legislation

According to the status of the satellite navigation, the research on the basic theory of legislation should be carried out in depth.

Firstly, we must further study the basic theory of the legal system of satellite navigation, analyze and study the characteristics of he legal system of satellite navigation, and study the special requirements of satellite navigation system with the rule of law system with Chinese characteristics. Secondly, we need to further study the shortcomings of the satellite navigation policies system, and study the

need for legislation in every aspect of the construction, development, application and promotion of the satellite navigation. Thirdly, we should study the major strategic needs of the state and the construction and development goals, and the specific requirements for the legislation of the Beidou satellite navigation. Lastly, we should study the experience and lessons of the satellite navigation legislation in developed countries, and analyze the availability of the construction of satellite navigation system in China.

4.3 Make a Scientific Plan for Legislative Planning

The legislative plan of the satellite navigation should be scientifically formulated in accordance with the practice of legislative work. According to the practical requirements, the plan for the legislative planning of the satellite navigation is scientifically formulated in accordance with the thought of the first urgent delay and the advance of maturity. Perfecting the legal system of satellite navigation should strengthen the research of satellite navigation system of laws and regulations, be guided by the satellite navigation law, be based on the upcoming satellite navigation regulations. The legal system of satellite navigation should include the regulations, standards, regulatory documents from the different departments, industry.

4.4 Perfect the Existing Policies and Regulations

We should strengthen the job of legalization based on the characteristics of the industry and the region. Based on the respective characteristics, we should accelerate the formulation of regulations and standard revision in urgent need of various professional fields, such as navigation application and industry promotion policy, mandatory applicable regulations or normative documents, industry standards, market access and other aspects. And clear up the outdated policies and regulations in time.

In addition, we should speed up the legislative process in accordance with the needs of construction and development in key areas such as follows: Firstly, it is necessary to clarify the legal status of the satellite navigation system which is beneficial to protect the related facilities, interstellar links and information transmission. Secondly, it is necessary to clarify the management system of the satellite navigation system. We should specific the code of conduct of the administrative departments, the navigation timing (PNT), service providers, users and the public participation. And it is necessary to clear up the border of their rights and obligations to realize the fundamental change from the industrial management, project management to business management. Thirdly, it is necessary to specific the promotion mechanism of the satellite navigation system. Through the means of rule of

law such as government procurement, we will promote the accumulation of technological innovation elements and expand the domestic and international market of the satellite navigation application industry, and establish and maintain a fair and orderly healthy competition environment. Finally, it is necessary to clarify the foreign policy and international policy of the satellite navigation system. We need to strengthen multilateral and bilateral exchanges and cooperation with GPS of US, GLONASS of Russia, and GALILEO of Europe and the specific regional satellite navigation system. And taking advantage of function of the rule of law, we can not only protect and promote the international application of the our satellite navigation system, but also effectively eliminate all kinds of international application barriers at home and abroad.

References

1. Liu S (2013) The legal regulation of global navigation system. Harbin Institute of Technology, Harbin, p 23
2. Xi J (2017) Secure a decisive victory in building a moderately prosperous society in all respects and strive for the great success of Socialism with Chinese characteristics for a new era. People's Publishing House, Perking, pp 38–39
3. Xi J (2017) Secure a decisive victory in building a moderately prosperous society in all respects and strive for the great success of Socialism with Chinese characteristics for a new era. People's Publishing House, Perking, p 22